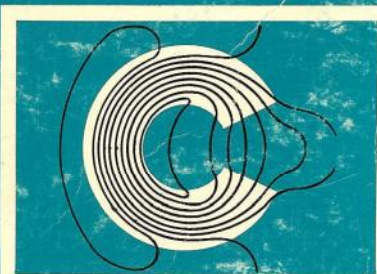


Published by the **Rutherford Laboratory**,
Science Research Council, Chilton, Didcot, Oxon. UK

Proceedings



COMPUTMAG

Conference on the Computation of Magnetic Fields

Oxford, 31 March to 2 April 1976

Proceedings

of the

COMPUMAG

**Conference on the Computation of
Magnetic Fields**

St Catherine's College, Oxford

31 March - 2 April 1976

Sponsored by:

The Science Research Council

The Institute of Physics

The Institute of Electrical and Electronic Engineers Inc., USA

Conference organised and Proceedings published by

Rutherford Laboratory, Chilton, Didcot, Oxon OX11 0QX, UK

© **The Science Research Council**

“The Science Research Council does not accept any responsibility for loss or damage arising from the use of information contained in any of its reports or in any communication about its tests or investigations.”

FOREWORD

The idea for this Conference arose from a desire by specialists in magnet computation at the Rutherford Laboratory to have discussions with their counterparts in industry and universities. Usually in the past this particular topic has been submerged in meetings catering for the much wider field of magnet technology, i.e. Intermag and Magnet Technology conferences. That we were justified in arranging Compumag has been demonstrated by the enthusiastic response - over 200 participants from 15 countries.

Whilst the standard achieved in the Conference must be judged by the quality of the papers appearing in these Proceedings, it can be said that most aspects of the field were covered and the discussions both in and out of the formal sessions were very valuable. A highlight of the conference was the specially set up magnet design work station, based on a GEC 4080 computer linked to the Rutherford Laboratory's IBM 360/195 computer. A series of demonstrations using these facilities served to indicate the importance of computer aided graphics techniques in magnet design. In this connection I should particularly like to thank the teams from the Central Electricity Research Laboratories, Leatherhead, Imperial College of Science and Technology, London and the Rutherford Laboratory.

I must express my appreciation to the delegates, the invited speakers, and members of the various organising committees for their efforts in making the Conference a success and to Dr. G. Manning, deputy director of the Rutherford Laboratory, for making the opening address. Finally my thanks to the Science Research Council without whose support this Conference could not have taken place.

18th May, 1976

C W Trowbridge

Editorial Note:

These Proceedings have been produced by direct photographic reproduction of material supplied by contributors, and no changes have been made in wording or presentation. This has enabled the Proceedings to be made available with minimum delay.

INTERNATIONAL STEERING COMMITTEE:

C W Trowbridge	Rutherford Laboratory, UK (Chairman)
Ch Iselin	CERN, Switzerland (Vice-chairman)
C J Carpenter	Imperial College of Science and Technology, UK
J Erb	University of Karlsruhe, West Germany
W Geysen	University of Leuven, Belgium
G Neyret	CEN/Saclay, France
S J Polak	NV Philips, Netherlands
U Ratti	University of Rome, Italy
J G Steel	Central Electricity Research Laboratories, UK
J Simkin	Rutherford Laboratory, UK (Secretary)

RUTHERFORD LABORATORY ORGANISING COMMITTEE:

F M Telling (Chairman)
F Harden
C Heming
T Moody
H Norris
J Simkin
J R Smith
C W Trowbridge

SESSION CHAIRMEN:

C J Carpenter
J Erb
W Geysen
Ch Iselin
S J Polak
U Ratti
J G Steel

SCIENTIFIC SECRETARIES:

A Armstrong
C S Biddlecombe
C J Collie
N J Diserens
M J Newman

COMPUTER WORKSTATION GROUP:

C Balderson
B J Day
P Gill
R G Smith
A R Thorne

The Organising Committee gratefully acknowledges the loan of a 4080 minicomputer from GEC Ltd.

LIST OF DELEGATES

C Anyega	Liverpool University	J Bidault	Thomson-CSF, Velizy-Villacoublay, France
M Aderholz	Max Planck Institut, Munich, West Germany	C Biddlecombe	Rutherford Laboratory, UK
B Alderfeld	Philips GmbH, Hamburg, West Germany	P Birien	CEN Saclay, Gif sur Yvette, France
R Allen	The Plessey Co. Ltd., Towcester, Northants, UK	P Blanchard	Lyon University, France
W D Allen	Rutherford Laboratory, UK	H Blok	Delft University of Technology, Holland
M Auriac	SEV MARCHAL, Toulouse, France	P Bonjour	Institut d'Electronique Fondamentale, Bures sur Yvette, France
A Armstrong	Rutherford Laboratory, UK	A Bossavit	Electricite de France, Clamart, France
R Ballisti	Swiss Federal Institute of Technology, Zurich, Switzerland	D Brombach	Swiss Institute for Nuclear Research Villigen, Switzerland
W Baran	Fried. Krupp GmbH, Essen, West Germany	P J Bryant	CERN, Geneva, Switzerland
D Barlow	Rutherford Laboratory, UK	J Bumby	IRD Co. Ltd., Newcastle-upon-Tyne, UK
J le Bars	CEN Saclay, Gif sur Yvette, France	J Brown	Rutherford Laboratory, UK
C Bazin	LAL, Orsay, France	M Caciotta	Rome University, Italy
E Becker	Texas University, Texas, USA	C J Carpenter	Imperial College, London, UK
D S Benaragama	Southampton University, UK	R G Carter	Lancaster University, UK
L Beretta	ENEL, Milan, Italy	N V Challis	British Gas Engineering Research Station, Newcastle-upon-Tyne, UK
		J L Chevalley	CERN, Geneva, Switzerland

U Christensen	Princeton University, New Jersey, USA	V Danilov	Joint Institute for Nuclear Research, Moscow, USSR
J Coleman	Lanchester Polytechnic, Coventry, UK	E M Deeley	King's College, London, UK
C J Collie	Rutherford Laboratory, UK	P Del Vecchio	Rome University, Italy
J S Colonais	Lawrence Berkeley Laboratory, Berkeley, USA	F Derksen	ESA/ESTEC, Noordwijk, Holland
P V Cooper	Plessey Memories Ltd., Towcester, Northants, UK	J Y E Durieu	MBLE, Brussels, Belgium
B J Couchman	CERN, Geneva, Switzerland	N J Diserens	Rutherford Laboratory, UK
E Coccorese	UKAEA, Culham Laboratory, UK	D Di Napoli	Rome University, Italy
J Coupland	Rutherford Laboratory, UK	J D Edwards	Sussex University, UK
J W Cox	RAE, Farnborough, Hampshire, UK	R A Early	SLAC, Stanford, USA
D S Craik	Nottingham University, UK	M H S El-Markabi	Imperial College, London, UK
H J Crawley	UKAEA Culham Laboratory, UK	K Endo	National Laboratory for High Energy Physics, Ibaraki, Japan
Z Csendes	GEC, Schenectady, New York, USA	J Erb	Karlsruhe University, West Germany
M D Cuthbert	RACAL Thermionic Ltd., Southampton, Hants, UK	B J Farrington	CEGB, Berkeley Nuclear Laboratories, Glos, UK
M Coulson	Strathclyde University, UK	L Fox	Oxford University, UK
A Dael	LAL, Orsay, France	E M Freeman	Imperial College, London, UK
G G Dal Mut	ANSALDO, Genoa, Italy		

G J Freestone	British Railways Board, Derby	Z Haznadar	Elektrotehnicki Fakultet, Zagreb, Yugoslavia
P Gara	Institut de Physique Nucleaire, Orsay France	W A L Heijnemans	Philips Research Laboratory, Eindhoven, Holland
W Geysen	Katholieke Universiteit Leuven, Heverlee, Belgium	P Henninger	Siemens AG, Erlangen, West Germany
R C Gibson	Electricity Council Research Centre, Capenhurst, Chester, UK	R Hindmarsh	CA Parsons & Co Ltd., Newcastle-upon-Tyne, UK
E V Gilbert	Oxford Instrument Co, Osney Mead, Oxford, UK	R Holsinger	Los Alamos Scientific Laboratory New Mexico, USA
W A Gilliespie	Glasgow University, UK	J.B Hicks	UKAEA, Culham Laboratory, UK
R Glowinski	Paris University, Le Chesnay, France	R A Hoult	Perkin-Elmer Ltd, Beaconsfield, Bucks, UK
J W Gray	UKAEA, Culham Laboratory, UK	D Howe	CA Parsons & Co Ltd., Newcastle-upon-Tyne, UK
M Gyr	CERN, Geneva, Switzerland	V A Hughes	GEC Power Engineering Ltd., Stafford, UK
D Hamels	Delft University of Technology, Holland	C Iselin	CERN, Geneva, Switzerland
P Hammond	Southampton University, UK		
B I Hassall	IRD Co Ltd, Newcastle-upon-Tyne, UK	D A Jacobs	CEGB, Leatherhead, Surrey, UK
L Hayali	King's College, London, UK	N Janssens	Universite Catholique de Louvain, Belgium
A Y Hannalla	Cairo University, UAR	M J Jevons	Aston University, Birmingham, UK

A Kaleck	Institut fur Plasmaphysik, Julich, West Germany	D Locke	CA Parsons & Co. Ltd., Newcastle-upon-Tyne, UK
T A Kitchens	US Office of Naval Research, London, UK	W Lord	University College, Cardiff, UK
E Knappek	Siemens AG, Munich, West Germany	M Lovenjak	Elektrotehnicki Institut "Rade Koncar", Zagreb, Yugoslavia
E D Krause	Siemens AG, Erlangen, West Germany	D A Lowther	Imperial College, London, UK
P J Kuypers	ACEC, Charleroi, Belgium		
		R Maas	Institute for Nuclear Physics Research, Amsterdam, Holland
B Langenbeck	Gesellschaft fur Schwerionenforschung, Darmstadt, West Germany	D C McDonald	Imperial College, London, UK
R J Lari	Argonne National Laboratory, Illinois, USA	I Mandic	Electrotechnical Institute "R. Koncar", Zagreb, Yugoslavia
J R Last	UKAEA, Culham Laboratory, UK	F Manero-Amoros	Junta de Energia Nuclear, Madrid, Spain
P J Lawrenson	Leeds University, UK	M Marinescu	Heidelberg-Ziegelhausen, West Germany
C Leloup	Euratom-CEA Collaboration, Fontenay aux Roses, France	N Marks	Daresbury Laboratory, UK
R Leyvraz	Brown Boverie et Cie, Zurich, Switzerland	A Marrocco	IRIA, Le Chesnay, France
		S Martin	KFA Julich, West Germany
D Lindholm	Ampex Corp, California, USA	T J Martin	UKAEA, Culham Laboratory, UK
P Little	UKAEA, Culham Laboratory, UK	S Mastero	Laborelec, Rhode St. Genese, Belgium
L Lhenry	CERCEM, Lyon, France	M Maestri	Rome University, Italy

J H McWhirter	Westinghouse Research Laboratories, Pittsburgh, USA	N H Nessler	Innsbruck University, Austria
K Mehlem	ESA/ESTEC, Noordwijk, Holland	R W Newport	Rutherford Laboratory, UK
J Meissburger	KFA Julich, West Germany	G Neyret	CEA, Gif sur Yvette, France
G Le Meur	LAL, Orsay, France	J A M Nieuwendijk	NV Philips, Eindhoven, Holland
A Middleton	Rutherford Laboratory, UK	M N Newman	Rutherford Laboratory, UK
T J E Miller	Leeds University, UK	M Ohayon	CEA, Orsay, France
H Mimmel	NV Philips, Eindhoven, Holland	H Oniwa	Cambridge University, UK
R H Minors	CEGB, Leatherhead, Surrey, UK	P Orecchia	ANSALDO, Genoa, Italy
A J Mitchell	UKAEA, Risley, UK		
J E Monson	Harvey Mudd College, Claremont, USA	E Pagano	Naples University, Italy
P Moro	Electricite de France, Clamart, France	J M Peel	Brighton Polytechnic, UK
R W Moses	Wisconsin University, USA	J Penman	Southampton University, UK
J Mulhaus	CERL, Leatherhead, Surrey, UK	R Perin	CERN, Geneva, Switzerland
E Munro	IBM, Thomas J Watson Research Center, Yorktown Heights, USA	T G Phemister	CA Parsons & Co. Ltd., Newcastle-upon- Tyne, UK
		G Piller	Ebauches Sa, Neuchatel, Switzerland
B M Neale	University College of North Wales, Bangor, UK	J Planchard	Electricite de France, Clamart, France
A Negro	Torino University, Italy	S J Polak	NV Philips, Eindhoven, Holland

M W Poole	Daresbury Laboratory, UK	R L Russell	Newcastle University, UK
B Popovic	Belgrade University, Yugoslavia		
T W Preston	GEC Power Engineering Ltd., Stafford, UK	J L Sabrie	Electricite de France, Clamart, France
D L Prior	Liverpool University, UK	H Schomberg	Philips GmbH, Hamburg, West Germany
		C A Scott	Rutherford Laboratory, UK
J P Radziwill	Philips GmbH, Aachen, West Germany	K O Sharples	City University, London, UK
P Rafinejad	ENSEGP, Grenoble, France	P Silvester	McGill University, Montreal, Canada
U Ratti	Rome University, Italy	G P Soardo	Instituto Elettrotecnico Nazionale, Torino, Italy
A B J Reece	GEC Power Engineering Ltd., Stafford, UK	M Soell	Max Planck Institut. Garching, West Germany
C Reece	IRD Co.Ltd., Newcastle-upon-Tyne, UK	J Steel	CERL, Leatherhead, Surrey, UK
K Reichert	AG Brown Boverie, Baden, Switzerland	R L Stoll	Southampton University, UK
M Renard	LAL, Orsay, France	B Streibl	MPG-IPP, Garching, West Germany
M V Ricci	CNEN, Frascati, Rome, Italy	M Szilagyi	Kalman Kando College of Electrical Engineering, Budapest, Hungary
J A R Riche	CERN, Geneva, Switzerland	J Simkin	Rutherford Laboratory, UK
D Rodger	Aberdeen University, UK		
G J Rogers	Southampton University, UK	M Tartaglia	Instituto Elettrotecnico Nazionale G. Ferraris, Torino, Italy
H Rosten	CHAM Ltd., New Malden, Surrey, UK		
N T Rowden	Leeds University, UK	M Teissier	Faculte des Sciences, Rabat, Morocco

C Ll Thomas	UKAEA, Culham Laboratory, UK	I A Vetlisky	IITEP, Moscow, USSR
D B Thomas	Rutherford Laboratory, UK		
T Tortschanoff	CERN, Geneva, Switzerland	A J H Wachters	NV Philips, Eindhoven, Holland
C W Trowbridge	Rutherford Laboratory, UK	A G Wardle	Daresbury Laboratory, UK
D R Turner	Liverpool University, UK	A C A Van Wees	FOM Laboratories, Jutphaas, Holland
L Turner	Argonne National Laboratory, Illinois, USA	P Th. Weggler	Contraves AG, Zurich, Switzerland
E F Troyanov	Serpukov, USSR	H J Wiesmann	Brown Boverie Research Centre, Baden, Switzerland
		A C Williamson	Manchester University, UK
H H Umstatter	CERN, Geneva, Switzerland	S Williamson	Aberdeen University, UK
		H Wind	CERN, Geneva, Switzerland
B Vaillant	SEV, Marchal, Toulouse, France	W Wolff	AEG Telefunken, Buchslag, West Germany
A Vanderput	Louvain University, Belgium	A Wright	Nottingham University, UK
J-C Verite	Electricite de France, Clamart, France	E A Wyatt	Imperial College, London, UK
S P Verma	Saskatchewan University, Canada		
G Veca	Rome University, Italy	H T Yeh	Oak Ridge National Laboratory, Tennessee, USA
A Viviani	Genoa University, Italy		
H de Vries	Institute for Nuclear Physics Research, Amsterdam, Holland		

N Zaplatin	Joint Institute for Nuclear Research, Moscow, USSR
B Zelenko	Produzece R Koncar, Zagreb, Yugoslavia
B N Zhukov	Institute of Electrophysical Apparatus, Leningrad, USSR
H Zijlstra	NV Philips, Eindhoven, Holland

CONTENTS

Paper	Author	Page
SECTION A - MAGNETOSTATICS		1
Invited Papers:		
Computation of Magnetostatic Fields	P Silvester Electrical Engineering Dept. McGill University, Montreal, Canada	2
Magnetostatic Fields Computing Using an Integral Equation Derived from Green's Theorems	J Simkin, C W Trowbridge Rutherford Laboratory, Chilton, Didcot, UK	5
A Scalar Integral Equation for Magnetostatic Fields	Ch Iselin CERN, Geneva, Switzerland	15
An Account of the Use of the FEM for Magnetostatic Problems	S J Polak, A Wachters, A de Beer Philips Gloeilampenfabrieken, Eindhoven, Netherlands	19
Physical Basis of the Variational Method for the Computation of Magnetic Field Problems	P Hammond Electrical Engineering Dept., Southampton University, UK	28
Some Techniques and Applications of the Finite Element Method for Solving Magnetic Field Problems	E Munro IBM Thomas J Watson Research Centre, New York, USA	35
Numerical Models of Three-Dimensional End Winding Arrays	C J Carpenter Electrical Engineering Dept, Imperial College, London, UK D H Locke CA Parsons & Co. Ltd., Newcastle-on-Tyne, UK	47
An Analytical Method of Calculating Magnetic Fields in Slotted Regions	T G Phemister CA Parsons & Co. Ltd., Newcastle-on-Tyne, UK	56
The Calculation of Forces and Torques within Numerical Magnetic Field Calculation Methods	K Reichert, H Freundl, W Vogt AG Brown Boverie, Baden, Switzerland	64

Paper	Author	Page
Contributed Papers:		
Calculation of the Magnetic System Elements of the Isochronous Cyclotron by the Grid Method	Y G Alenitsky, S B Vorozhtsov, N L Zaplatin Laboratory of Nuclear Problems, Joint Institute for Nuclear Research, Dubna, USSR	75
On the Computation of Three-Dimensional Magnetostatic Fields by the Integral Equation Field	V T Banchev, S B Vorozhsov Joint Institute for Nuclear Research, Dubna, USSR	81
Magnetic Fields and Potentials of Linearly Varying Current or Magnetisation in a Plane Bounded Region	C J Collie Rutherford Laboratory, Chilton, Didcot, UK	86
Non-Divergent Vector Finite Elements for Magnetic Field Calculations	Z N Csendes General Electric Co. Schenectady, New York, USA	96
A Generalised Finite Difference Method for the Computation of Electric and Magnetic Fields	G B Denegri, G Molinari, A Viviani Electrical Engineering Dept. Genoa University, Italy	104
Finite Element Approximation and Iterative Methods of Solution for 2-D Non-Linear Magnetostatic Problems	R Glowinski Laboratoire Analyse Numerique, Paris University, France A Marrocco IRIA/LABORIA, Rocquencourt, France	112
Magnetic Field Calculation for a Salient-Pole Hysteresis Coupling	M J Jevons Aston University, Birmingham UK	126
The Use of the Divided Differences in Finite Element Calculations	M J Long, K W Morton Mathematics Dept., Reading University, UK	132
Determination of Magnetic Fields at the Conductor for Solenoids and Toroids	R W Moses Jnr. R L Willig University of Wisconsin, Madison, USA	138
A Fortran Package for Solving Linear Algebraic Equations with a Large Dense Matrix Using Direct Access Storage	M J Newman Rutherford Laboratory, Chilton, Didcot, UK	144

Paper	Author	Page
Computation of the Integrated Multipole Field Components in a Superconducting Magnet with Constant Perimeter Coil Ends	T Tortschanoff CERN, Geneva, Switzerland	149
A Practical Method for the Determination of Stationary Two-Dimensional Magnetic Fields	B Zelenko OOUR Elektrotehnici Institut, Zagreb, Yugoslavia	154
A Method for Computation the Superconducting Magnets Winding Configuration to Create a Prescribed Magnet Field Distribution	B N Zhukov, V N Lebedev, I A Mozalevsky, D V Efremov Institute for Electrophysical Apparatus, Leningrad, USSR	159
SECTION B - MAGNETIC MATERIALS		163
Invited Papers:		
Permanent Magnets in Magnetic Field Calculations	H Zijlstra Philips Research Laboratories, Eindhoven, Netherlands	164
Computation of Magnetic Fields in Nonlinear Anisotropic Media with Field-Dependent Degree of Anisotropy	P Weggler Contraves AG, Zurich, Switzerland	168
Fields Computation of Magnet Made of Steel with Magnetic Anisotropy	T Kasuga, E Takasaki, A Ando, M Kihara, K Endo National Laboratory for High Energy Physics, Ibaraki, Japan	177
Fields Involved in Magnetic Recording on a Moving Steel Strip	E M Deeley, I Hayali Kings College, London, UK	183
Mathematical Modelling of Magnetic Hysteresis	N Janssens Faculty of Applied Sciences, Louvain University, Belgium	191
Permanent Magnet Modelling for Machine Applications	W Lord Electrical & Electronic Engineering Dept. University College, Cardiff, UK	198
SECTION C - STEADY STATE		205
Invited Papers:		
Solution of Transient and Steady-State Magnetic Fields with Particular Reference to Numerical Methods	R Stoll Electrical Engineering Dept., Southampton University, UK	206

Paper	Author	Page
The Prediction of Machine End-Region Fluxes, allowing for Eddy Current Losses in Thick Components	T W Preston, A B J Reece GEC Power Engineering Ltd., Stafford, UK	213
Semi-Analytical Computation of Magnetic Fields, Eddy Currents and Forces in Electrodynamic Levitation Systems	E D Krause, L Urankar Siemens AG, Erlangen, West Germany	221
Three Dimensional Eddy Current Calculations	W Wolff AEG Telefunken, Buchslag, West Germany	231
Efficiency of Numerical Techniques for Computing Eddy Currents in Two and Three Dimensions	C J Carpenter, E A Wyatt Electrical Engineering Dept, Imperial College, London UK	242
The Calculation of Magnetic Fluxes and Eddy Currents in Generator Stator Stores	D Jacobs CEGB, Leatherhead, UK	251
Determination of Magnetic Fields in Power Transformers	P B Johns, A Wright, J E Stitch Nottingham University, UK	261
Computation of Eddy Current Losses in Solid Iron under Various Surface Conditions	D A Lowther, E A Wyatt Electrical Engineering Dept, Imperial College, London UK	269
Evaluation of the Air Gap Field in Short Stator Asynchronous Motors	G Figalli, G Gentile, E Pagano, V Vaccaro Istituto Elettrotecnico, Naples, Italy	
Contributed Papers:		
Numerical Determination of an Equivalent Complex Permeability for Saturated Steel	A Bossavit Electricite de France, Clamart, France	282
A Computerised Program for the Numerical Solution of Harmonic Fields with Boundary Conditions Non-Properly Defined	A di Napoli, C Mazzetti, U Ratti Electrical Engineering Institute, Rome University, Italy	287
A Computer Method of Calculating the Eddy Current Heating of Magnetic materials, with a Comparison between Predicted and Measured Results in a 2MVA Induction Furnace	R C Gibson Electricity Council Research Station, Capenhurst, UK	294

Paper	Author	Page
A Method of Calculating Eddy Current Losses in the Rotor Retaining Ring of a Turbogenerator Due to the Tooth Ripple Field	D Howe, T G Phemister C A Parsons & Co. Ltd., Newcastle on Tyne, UK	301
An Analytical Approach for Solving Two-Dimensional Saturable Eddy-Current Problems	J Mulhaus Central Electricity Research Laboratories, Leatherhead, UK	309
Calculation of Eddy Currents in a Conductor and its Sheath by a Finite Element Method	J C Nederlec Ecole Polytechnique, Palaiseau, France J.L. Sabrie, J C Verite Electricite de France, Clamart, France	316
Simplified Integral Equations for Alternating Current Distribution in Strip-Conductors and Strip-Line with Minimised Proximity Effect	B Popovic Electrical Engineering Dept., Belgrade University, Yugoslavia	324
The Piece-by-Piece Solution of Eigenvalue Problems	G J Rogers, D S. Benaragama Electrical Engineering Dept, Southampton University, UK	329
SECTION D - TRANSIENT		333
Invited Papers:		
Use of the Fast Fourier Transform for Transient Magnetic Fields	T JE Miller, P Lawrenson Electrical Engineering Dept, Leeds University, UK	334
The Calculation of Magnetic Fields in Air-cored Electric Machines	D R Turner, D L Prior, Y H A Rahim Electrical Engineering and Electronics Dept., Liverpool University UK	344
Electromagnetic Behaviour of a Rotating Screen for a Superconducting Inductor of a Synchronous Machine	E del Vecchio, G M Vega Electrotechnics Institute, Rome University, Italy G Sacerdoti CNEN, Frascati, Italy	350

Paper	Author	Page
Computer Aided Steady-State and Transient Solutions of Quasi-One Dimensional Problems in Induction Devices	E M Freeman Electrical Engineering Dept, Imperial College, London UK	357
The Integral Equation Method Applied to Eddy Currents	C S Biddlecombe, C J Collie, J Simkin, C W Trowbridge Rutherford Laboratory, Chilton, Didcot, UK	363
A Perturbation Expansion with Separated Time Dependence for Eddy Current Calculations	K H Carpenter, H T Yeh Oak Ridge National Laboratory, Tennessee, USA	373
The Solution of Transient Fields by the Nodal Method	A Y Hannalla, D C Macdonald Ain Shams University, Cairo, UAR Imperial College, London UK	381
Calculation of the Dynamic Behaviour of Electromagnetic Actuators	B Aldefeld Philips Forschungslaboratorium, Hamburg, West Germany	389
A Three-Dimensional Analytic Model for Calculating Eddy-Current Effects Applied to a Tokamak Blanket and Shield	L R Turner, S T Wang, J R Purcell Argonne National Laboratory, Illinois, USA	394
Induction Motor Analysis and Field Calculation Using Anisotropic Layer Theory	S Williamson Engineering Dept, Aberdeen University, UK	400
Calculation of Transient Skin-Effect in Conductors Embedded in Slots	S P Verma, S E Abo-Shady Electrical Engineering Dept. Saskatchewan University, Canada	407
Contributed Papers:		
Magnetic Field Diffusion in Fast Discharging Homopolar Machines; a Finite Element Approach	E B Becker, R D Pillsbury, M D Driga University of Texas, Austin, USA	417
Field Penetration into a Variable- μ Material	I Gumowski CERN, Geneva, Switzerland	423
Use of Bubnow-Galerkin Method for Calculation of Transient Skin Effect in Foil-Wound Chokes	P Rolicz Electrical Engineering Dept, Bialystok Polytechnic, Poland	427

Paper	Author	Page
SECTION E - COMPUTER-AIDED DESIGN		431
Invited Papers:		
Application of Interactive Graphics Techniques to Magnet Design	M J Newman Rutherford Laboratory, Chilton, Didcot, UK	432
The Interactive Design of Magnetic Fields for Controlled Thermonuclear Research	T J Martin Culham Laboratory, Abingdon, UK	446
Design Methods for Tokamak Ohmic Heating Windings	A J Federowicz, L Linter, J H McWhirter Westinghouse Research Laboratories, Pittsburgh, USA	455
Magnetic Field Computation and Stress Analysis in Toroidal Circular and Dee-Shaped Coils for Tokamak Fusion Experiments	N J Diserens Rutherford Laboratory, Chilton, Didcot, UK	462
Iterative Generation of Optimal Triangular Grids for the Solution of 2-Dimensional Field Problems	R Levyraz Brown, Boveri et Cie, Zurich, Switzerland	472
Contributed Papers:		
Computation of Stresses Produced by a Superconducting Normal Single Coil Transition in a Toroidal Magnet for a Fusion Research Tokamak	M Caciotta, G Sacerdoti Istituto Elettrotecnico, Rome University, Italy	486
Mechanical and Thermal Stresses in Doubler Dipole	S C Snowdon Fermi National Laboratory, Illinois, USA	495

SECTION A MAGNETOSTATICS

COMPUTATION OF MAGNETOSTATIC FIELDS

P. Silvester

1. Mathematical Formulation of the Physical Problem.

Nearly all magnetostatic and quasi-static analyses presented to date have been based on scalar or vector potential formulations. These often appear in the forms

$$\operatorname{div} \mu \operatorname{grad} \phi = 0 \quad (1)$$

$$\operatorname{curl} v \operatorname{curl} A = J \quad (2)$$

Generally, these representations involving second order differential operators lead to simple discrete forms and favourable matrix properties (e.g. symmetry). In this form, the magnetic properties are easiest to represent as permeabilities or reluctivities. In contrast, the potentials may also be formulated in terms of integral equations; in that case, the magnetic properties are often easier to represent in terms of a magnetisation vector M , e.g.,

$$A = \frac{\mu_0}{4\pi} \int \left[\frac{J}{r} - \frac{4\pi M \times r}{r^3} \right] d\Omega \quad (3)$$

Such formulations frequently lead to iterative methods of solution, since M is implicitly related to A . In consequence, wide use has been made of the integral forms in two sets of circumstances; the nonmagnetic case, in which M vanishes, and the nonlinear case, in which iterative methods must be employed in any event. The vector potential formulation is clearly less economic computationally, since three components must be considered. On the other hand, it is very difficult to treat distributed currents by the scalar potential technique, so that it is most useful where magnetic fields exterior to relatively thin conductors are to be calculated.

The differential equation formulations (1) and (2) re-

quire solving a three-dimensional operator equation of the form

$$D V = G \quad (4)$$

where D is a differential operator and its associated boundary conditions, V is the variable sought, and G represents the given sources and boundary condition inhomogeneities. It is widely recognised that if G and D depend (in some coordinate system) only on two coordinate quantities, V does likewise, and the problem may be reduced to one in two dimensions. It is less well understood that an equivalent treatment is possible if G is quite general, but D depends on only two coordinate quantities. In such cases, V and G may be expanded in terms of suitable orthogonal functions, leading to replacement of the three-dimensional problem by a set of two-dimensional problems, which may be solved separately.

2. Discretisation of the Continuum Equations.

Two major discretisation methods have been widely employed: finite differences and finite elements. In the former, the solution is approximated at certain selected points in the region of interest, while in the latter, an approximation uniquely defined everywhere in the region is sought.

Finite difference methods tend to result in very large and very sparse systems of equations, for whose solution iterative methods have traditionally been employed. However, there exists good evidence that direct solution methods which take account of matrix sparsity are at least competitive with iteration techniques. Iteration methods suffer from two grave shortcomings in magnetostatics: their convergence is very slow, and there is no valid nonlinear theory to serve as a guide in choosing acceleration and stabilisa-

tion factors. The slowness of convergence is inherent in the interface conditions (large permeability ratios typically encountered, thus it is a result of the physical problem rather than of its mathematical treatment.

Finite element methods lend themselves well to the construction of Newton minimisation schemes, which do not suffer from the convergence troubles encountered by finite differences. They are geometrically flexible, allowing curved shapes to be modelled as well as rectilinear ones. The systems of algebraic equations to be solved are usually smaller and denser than with finite differences; thus sparsity-exploiting direct solvers are attractive, though some iterative techniques have been used as well (e.g., conjugate gradients). For integral equations, element functions need only possess C^0 continuity, and are thus relatively easy to construct (even though the resulting integrals are not always easy to evaluate) by Galerkin projections. For differential equation problems, C^1 continuity is required; suitable functions are easy to construct for the scalar case, but not for the vector case if restrictions are to be placed on the divergence of A .

3. Computational Considerations.

The mathematics of finite elements have now reached a level of development exceeding that of finite differences. Concurrently, practical algorithm development has been carried far by engineering analysts. Unfortunately, much less attention -- one might almost say none -- has been paid to establishing principles and standards of generally useful software. There are as many conventions and standards as programming groups, so that virtually every mathematical step has to be re-created by every programming group.

At present there exists no generally agreed language or terminology, oriented toward finite mathematics and computational solutions, for the description of magnetic field problems. This lack not only renders communication between

programs incredibly difficult, it also leads to much fruitless discussion between analysts. Much valuable manpower and ingenuity is at present being wasted in the creation of input languages and data structures suitable only for specific, strongly restricted, analysis programs. In the future, effort needs to be directed to producing well-documented, generally useful software modules, and on which specific applications programs can be based. The ability to create these, however, presupposes agreement on the form of data structure for representing problems to be analysed.

Only rarely is the field solution itself of use to the analyst. Much more often, he seeks functionals of the field -- inductance values, generated voltages, lifting forces, power losses. The calculation of such quantities again requires the problem description, as well as the computed solution for the field, to be embedded in a data structure of standard form.

4. Conclusions.

Many good static field analysis programs now exist, particularly for two dimensional problems. Further work on nonlinear problems, especially in three dimensions and using integral equation formulations, may be anticipated. However, the greatest need at present is for standardisation of data bases so as to permit analysts to link together already existing program segments.

Discussion following paper:

(Fox, Oxford) (1) I would comment that the strongly implicit methods of Stone and corresponding factorization methods of people like Golub and Concus should be included in your list of methods. They seem to me to form a very satisfactory balance between iterative methods and direct methods, with more connection with the latter. I agree that direct methods have many attractions.

(2) It surely isn't true that Newton's method always converges from an arbitrary start? The method might be slow if you have to compute the Jacobian matrix all that often and although Newton has quadratic convergence, ie $e_{v+1} = ke_v^2$ (where e_v is the error), this doesn't say that the number of significant figures is doubled at each stage. It is true for sufficiently small v if k is not too big.

(Silvester, McGill) (1) I agree that semi-iterative (or semi-direct?) methods have many attractions, even though they are not widely used at present.

(2) For magnetostatics problems, where reluctivity and its first derivative are monotonic, the usual finite-element functionals are convex. Thus Newton's method converges. Unless really extreme saturation levels are encountered, starting Newton from a null solution (ie assuming the magnetic material to be linear) often yields potentials accurate to within a factor of two. In other words, one correct binary digit is usually achieved on the first or second Newton step. This starting point appears to be sufficiently near the solution to produce nearly quadratic convergence subsequently. Typically, 16 correct bits are obtained in the fifth or sixth iteration, if the maximum flux density in the problem is around 2.0 - 2.5 tesla.

(Jacobs, CERL) I am interested in the second method you described for treating problems in infinite regions which utilizes a linear operator for the imposed boundary condition at the artificially included finite boundary. Yet another method utilizes the inversion in a circle for two dimensions (on a sphere for three dimensions) of the outer part of the problem which extends to infinity. Thus one obtains two finite problems forming a discus or hyperdiscus matched on the common boundary. The resulting movement of rectangular coordinate nodal points (if used) to model such a curved boundary concords with your comments on the longer time spent on deriving the algebraic equations. With finite element methods one can also develop specific "infinite" elements which extend to infinity.

(Silvester) I quite agree. Inversion mappings have been used for various problems with good success; their main disadvantage I believe is a fussy and uneconomic program structure. Infinite finite elements (defined on an unbounded geometric region but bounded in energy) have been successfully used for various two-dimensional problems; they produce the desired boundary operator directly.

MAGNETOSTATIC FIELDS COMPUTED USING AN INTEGRAL EQUATION DERIVED FROM GREEN'S THEOREMS.

J Simkin and C W Trowbridge

Rutherford Laboratory, Chilton, Didcot, Oxon, OX11 0QX

ABSTRACT

A method of computing magnetostatic fields is described that is based on a numerical solution of the integral equation obtained from Green's Theorems. The magnetic scalar potential and its normal derivative on the surfaces of volumes are found by solving a set of linear equations. These are obtained from Green's Second Theorem and the continuity conditions at interfaces between volumes. Results from a two-dimensional computer program are presented and these show the method to be accurate and efficient.

1. INTRODUCTION

The present generation of computer programs for calculating magnetostatic fields in three dimensions are expensive to use and they will continue to be until new algorithms are developed. Changes in computer hardware, eg. parallel processors, may make it possible to obtain solutions more quickly, but, it is doubtful whether the amount of storage available will change significantly. In this paper the numerical solution of an integral equation derived from Green's Theorems is shown to have many advantages over existing integral equation methods.

Integral equation methods are now widely accepted and the Rutherford Laboratory program GFUN3D⁽¹⁾, which solves the integral equation for the volume distribution of induced magnetisation, has been successfully used for the design of many magnets. As an example of the accuracy of this program the measured and computed results for the homogeneity of an essentially two-dimensional C shaped dipole magnet are shown in Figure 1. This accuracy (better than 1 part in 10^4) was obtained by using 10 minutes of CPU time on an IBM 360/195, a cruder model capable of 1% accuracy would typically require 10 seconds CPU time. In the case of strongly three-dimensional magnets however, 60 minutes of CPU time are probably required for an accuracy better than 1%. Furthermore, for complex problems even when the magnetisation distribution has been computed, the time taken to

compute fields at particular points is not trivial.

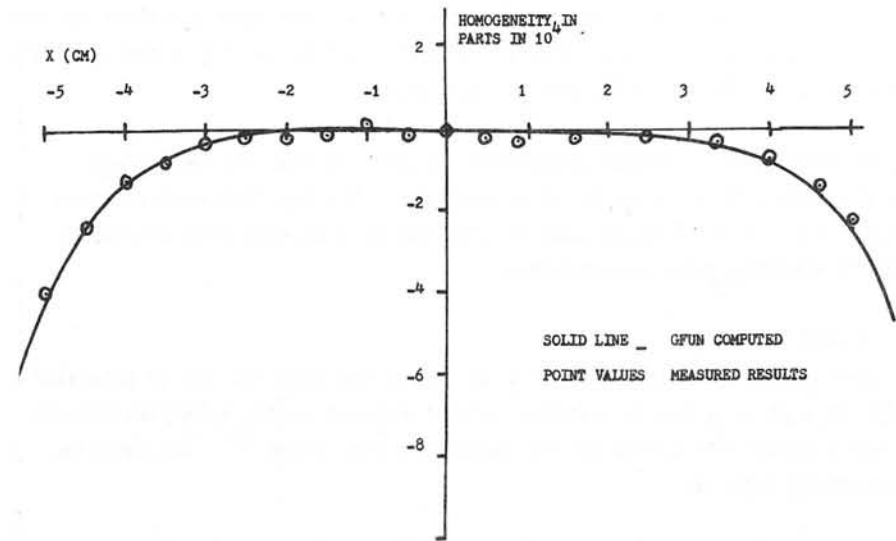


FIGURE 1 - MEASURED AND COMPUTED HOMOGENEITY OF THE FIELD PRODUCED BY A C-SHAPED MAGNET WITH SMALL POLE TIP SHIMS

Iselin⁽²⁾ has proposed a scalar potential method that may prove to be more efficient than GFUN3D which uses the three component magnetisation. An alternative approach is the Boundary Integral Method, this method is based on the numerical solution of an integral equation for the magnetic scalar potential, derived from Green's Theorems. This approach has already been used for the solution of linear flow and elasticity problems.^(3,4,5)

For linear problems, ie. constant permeability, it is only necessary to define the boundaries of regions with different permeability, together with a far field boundary condition - however the far field boundary can be expanded to infinity. A region may consist of several surfaces that do not touch or intersect and this fact together with the use of symmetry allows the calculation of fields with minimal effort. In an appendix an extension is discussed that will make it possible to include non-linear permeabilities.

To determine the magnetic field distribution in a region the magnetic scalar potential and its normal derivative to the boundary must be computed over the surface of the region. This is done numerically by sub-dividing the surface into small areas over which the potential and normal derivatives are assumed constant. The distribution is then found by solving a set of linear equations for the potential and its derivative.

A two-dimensional computer program was written to test the method and compare the accuracy with existing programs. Results from several tests are given. It is expected that this method will be even more attractive for three-dimensional calculations.

2. THEORY

Green's second theorem can be used to relate the magnetic scalar potential $V(p)$ at a point p inside a volume to the magnetic scalar potential and its outward normal derivative on the surface of the volume.⁽⁶⁾ The equation connecting them is:

$$V(p) = \frac{1}{4\pi} \int_{\text{volume}} \frac{1}{r} \nabla^2 V dV + \frac{1}{4\pi} \int_S \frac{1}{r} \frac{\partial V}{\partial n} ds - \frac{1}{4\pi} \int_S V \frac{\partial}{\partial n} \left(\frac{1}{r} \right) ds \quad (1)$$

where r is the distance between the point p and an element of the volume or surface of the region. If the permeability of a region is constant then:

$$\nabla^2 V = 0$$

and therefore the first integral in equation (1) is zero. In Appendix 1 the use of a perturbation term based on the volume integral is shown as a possible means of extending the method to non-linear permeabilities.

If a surface is defined just inside the boundary of a volume and this surface is subdivided into small areas over which V and $\frac{\partial V}{\partial n}$ are constant then equation (1) becomes:

$$V(p) = \frac{1}{4\pi} \left[\sum_{j=1, m} \frac{dV_j}{\partial n_j} \int_{s_j} \frac{1}{r} ds_j - V_j \int_{s_j} \frac{\partial}{\partial n_j} \left(\frac{1}{r} \right) ds_j \right] \quad (2)$$

where the surface is subdivided into m area elements. Equation (2) can also be used to express the potential of a point on this surface as a function of the potential and its outward normal derivative on each surface area element.

If the geometric factors relating to the potential and its derivative on every element of the surface are calculated for points at the centroid of every area element, then providing V or $\frac{\partial V}{\partial n}$ is known on every area element, the unknown values can be found by solving a set of exactly determined linear equations.

Of more interest is a problem consisting of regions with different permeability where there are interfaces between the regions. For example, consider a two-region problem, where region 1 has permeability μ_1 and region 2 has permeability μ_2 . (This could correspond to region 1 being iron and region 2 air.) There must be some driving field, however this is at present of no account expect that a distribution of field H_v is assumed to be produced by a set of current carrying conductors. A surface is defined just inside each region and this surface is subdivided into small elements with an exact correspondence between the elements across the interface between the regions.

Equation (2) then gives for each surface element:

$$V_j(R1) - \frac{1}{4\pi} \left(\sum_{i=1, n1} \frac{\partial V_i}{\partial n_i} (R1) \int_{s_i} \frac{1}{r} ds_i - V_i(R1) \int_{s_i} \frac{\partial}{\partial n_i} \left(\frac{1}{r} \right) ds_i \right) = 0 \quad (3)$$

$$V_k(R2) - \frac{1}{4\pi} \left(\sum_{i=1, n2} \frac{\partial V_i}{\partial n_i} (R2) \int_{s_i} \frac{1}{r} ds_i - V_i(R2) \int_{s_i} \frac{\partial}{\partial n_i} \left(\frac{1}{r} \right) ds_i \right) = 0 \quad (4)$$

where $V_j(R1)$ are the potentials in region 1 and $V_k(R2)$ are potentials in region 2. On the interface between the two regions V and $\frac{\partial V}{\partial n}$ on the surface elements are unknown in both regions. If V or $\frac{\partial V}{\partial n}$ is known on the surface elements that are not on the interface then the set of linear equations formed from (3) and (4) will still be under-determined. Two extra equations must be introduced for each interface element and these can be obtained from the interface continuity conditions. The equations are:

$$V_j(R1) = V_k(R2) \tag{5}$$

$$\mu_1 \left(-\frac{\partial V_j(R1)}{\partial n_j} + H_{n_j}(R1) \right) = \mu_2 \left(\frac{\partial V_k(R2)}{\partial n_k} + H_{n_j}(R1) \right) \tag{6}$$

where $H_{n_j}(R1)$ is the outward normal component of the driving field on element j of region 1. The same ideas can be applied to problems consisting of any number of regions.

It is interesting at this stage to examine the set of equations generated to determine V and $\frac{\partial V}{\partial n}$ in a two region problem, where there is an interface between the regions. A pictorial representation of the equations is shown in Figure 2. There are $n1$ and $n2$ sides and $m1$ and $m2$ unknowns in region 1 and 2 respectively. The submatrix (1) is dense and is formed from the coefficients from equation (3) applied to the element of region 1. Similarly submatrix (4) comes from region 2. The submatrices (2) and (3) are sparse (two unknowns per row) and are generated from the interface conditions. The other areas contain zeros. If on the boundary surfaces where the potential or its derivative is known the value is zero then all the right-hand sides are zero except those corresponding to the normal \bar{B} continuous boundary conditions.

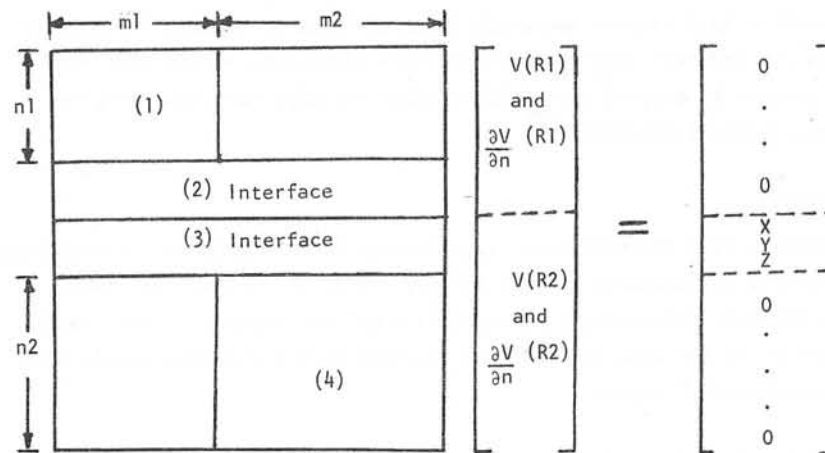


FIGURE 2 - A REPRESENTATION OF THE SET OF LINEAR EQUATIONS REQUIRED TO SOLVE FOR THE POTENTIAL AND ITS NORMAL DERIVATIVE IN A 2 REGION PROBLEM

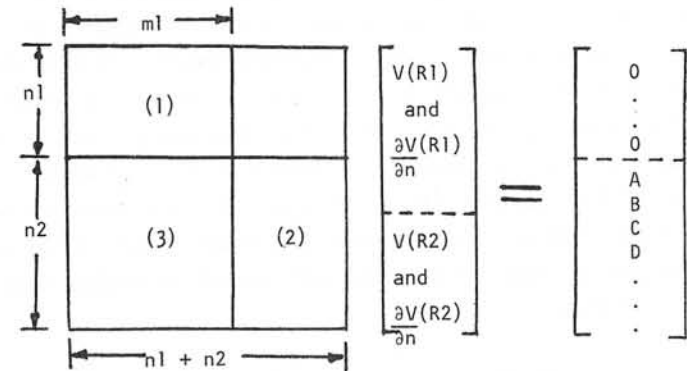


FIGURE 3 - SUBMATRICES (1) and (2) ARE DENSE, (3) IS SPARSE

In order to make the most efficient use of existing computer programs for solving linear equations the interface conditions can be used to replace unknowns on the interface in region 2 by the values in the equivalent elements in region 1. The order of the matrix can be reduced using this technique but at the expense of the loss of the blocking that previously existed. From a long term point of view it would be more efficient to use the blocked matrix and special factorising methods. Figure 3 shows the structure of the set of equations after order reduction has taken place. In the case of a problem only consisting of interfaces the order is reduced to half its previous size.

3. SYMMETRY

The number of unknowns in a problem can be reduced significantly when the geometry and its associated potential distribution possesses a known rotational or reflective symmetry. The two methods that can be employed to make use of this symmetry are shown pictorially in Figures 4 and 5. In Figure 4 a model of a dipole magnet is shown where the Dirichlet and Neumann boundary values have been used to imply the rest of the model. In Figure 5 the whole model is shown but, because the potentials in the 2nd, 3rd and 4th quadrants have an exact equivalence to those in the first quadrant, the potentials in the first quadrant are the only ones which must be computed explicitly.

The far field boundary shown in Figure 5 can be expanded to infinity because there are no boundary connections between it and the magnet; the far field boundary then has no effect on the problem whatsoever. This is obvious for real problems where the potential and its normal derivative to the far boundary can be defined as zero. It is not immediately clear in the two-dimensional infinite limit because the potential from a boundary side becomes infinite at large distances. However the divergence of the potential from a complete surface must be zero and therefore the contributions from all elements of a surface will cancel to produce zero potential at infinity.

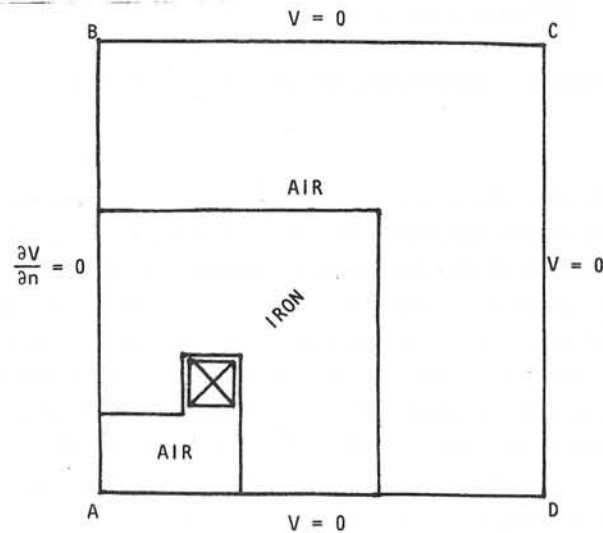


FIGURE 4 - BOUNDARY INTEGRAL METHOD MODEL USING NEUMANN AND DIRICHLET BOUNDARY VALUES

4. APPLICATIONS OF THE METHOD

A two-dimensional magnetostatic computer program was written to test the accuracy and efficiency of the method. The results for the program were very encouraging. In the program the fields from infinitely long conductors with polygonal cross section and curvilinear faces were computed using existing analytic expressions.⁽⁷⁾ The boundaries between regions of different permeabilities were subdivided into plane faces over which the potential and its normal derivative were assumed to be constant. The expression for the potential and field from such faces are given in Appendix 2. The integrals can be evaluated for higher order basis

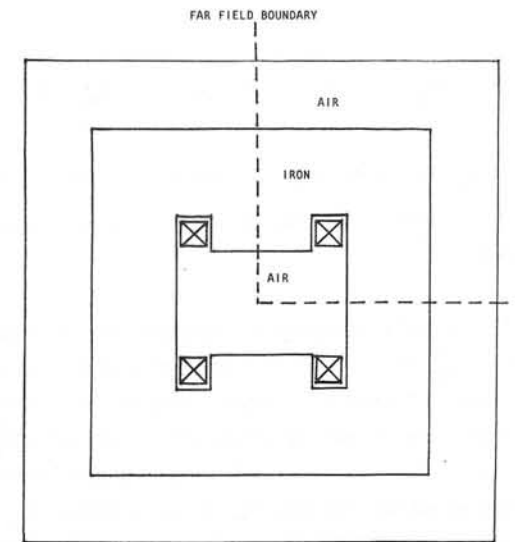


FIGURE 5 - BOUNDARY INTEGRAL METHOD MODEL USING EQUIVALENT ELEMENTS AND SYMMETRY - THE FAR FIELD BOUNDARY IS SHOWN BUT IT CAN BE AT INFINITY

functions but this leads to problems at external corners because the integrals have singular kernels. This problem can be solved but it was simply avoided in the present program by computing the potentials at the centroid of each element where the integral is well behaved. The program can be run interactively on the Rutherford Laboratory IBM 360/195 and in this version an elegant data input package was used for specifying the boundary data of polyhedra.⁽⁸⁾

5. RESULTS

The results from two test cases are included in this section; a comparison of analytic and computed results for the field in a hollow, infinitely long, constant permeability cylinder in a uniform external field; and a comparison of the GFUN and Boundary Integral Method computed fields for a two-dimensional C magnet.

(a) Hollow Cylinder. The fields in a hollow infinitely long constant permeability cylinder in a uniform field perpendicular to the axis of the cylinder were computed using the Boundary Integral Method. The inside radius of the cylinder was 5 cms and the outside radius 10 cms. The

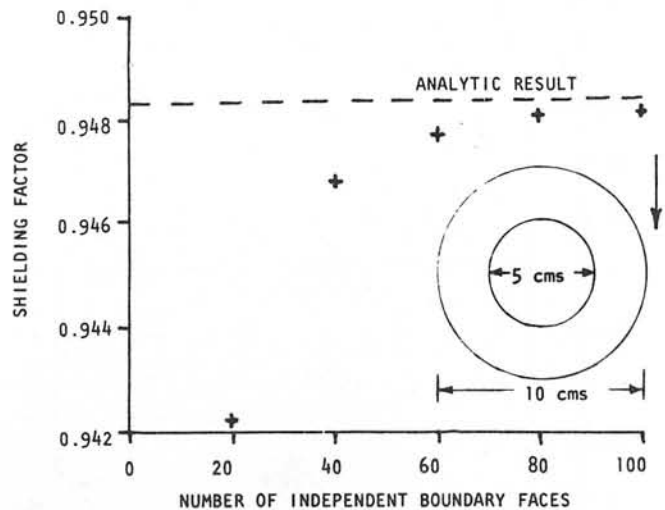


FIGURE 6 - SHIELDING FACTOR OF HOLLOW FERROMAGNETIC CYLINDER - INSIDE RADIUS 5 CMS, OUTSIDE RADIUS 10 CMS, PERMEABILITY 100 - AS A FUNCTION OF THE NUMBER OF INDEPENDENT BOUNDARY FACES IN THE MODEL.

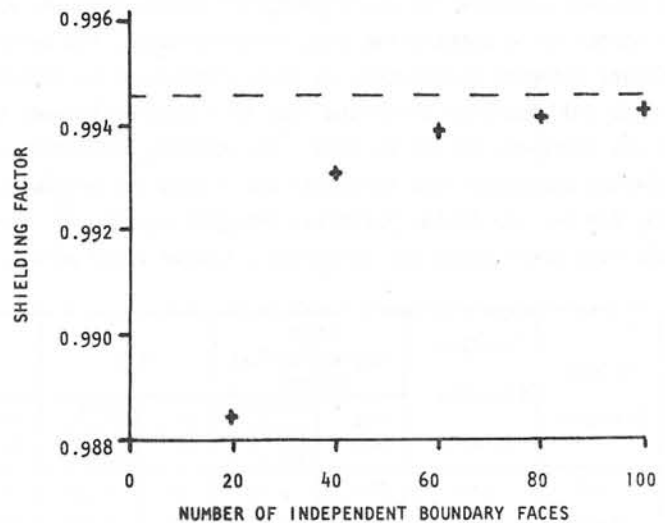


FIGURE 7 - SHIELDING FACTOR OF A HOLLOW FERROMAGNETIC CYLINDER - DIMENSIONS AS FIGURE 5, PERMEABILITY 1000 - AS A FUNCTION OF THE NUMBER OF INDEPENDENT BOUNDARY FACES.

cylinder was approximated by many-sided polyhedra and symmetry was used so that only potentials and derivatives in the first quadrant were computed explicitly. In Figures 6 and 7 the computed shielding factor of the cylinder is plotted as a function of the number of boundary faces for cylinders with relative permeabilities of 100 and 1000. The accuracy is very good, and most of the error is due to the polygonal approximation. The field in the hollow centre should be uniform and in the computed cases the homogeneity was always better than 2 in 10^4 . An interesting point to note about the results is that the fields at points inside the cylinder were obtained as accurately as the shielding factor, this is not true in the GFUN program where eigenvalue solutions can be obtained.

(b) C-Shaped Dipole Magnet. The geometry of this magnet is shown in Figures 8 and 9, Figure 8 shows the GFUN model and Figure 9 the Boundary Integral Method model. The results in Figure 1 have shown that GFUN gives accuracies of the order of 0.01% for the homogeneity of this type of C magnet. GFUN was therefore used to compute the field homogeneity of the magnet shown in Figure 8 for steel with a relative permeability of 1000.0. In Figure 10 the GFUN results are compared to those obtained using the Boundary Integral Method (BIM) for several different models. Symmetry was used and therefore only the upper Y plane was computed explicitly. (In both these cases the far field boundary was at infinity.) The results for this case are again good. Figure 11 shows a computed map of lines of constant scalar potential for the 140 element BIM model.

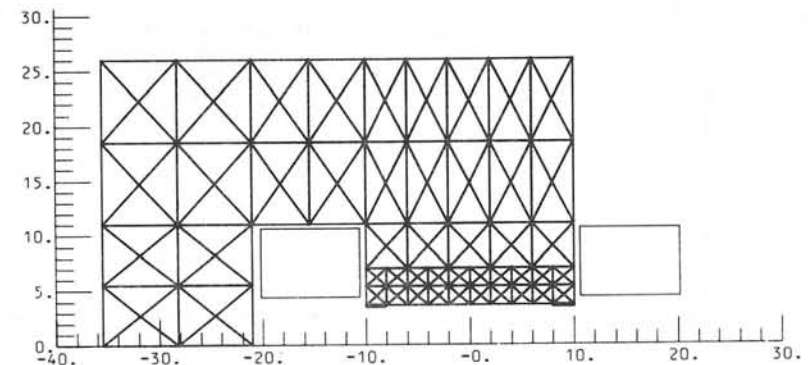


FIGURE 8 - GFUN MODEL OF A TWO-DIMENSIONAL C-MAGNET

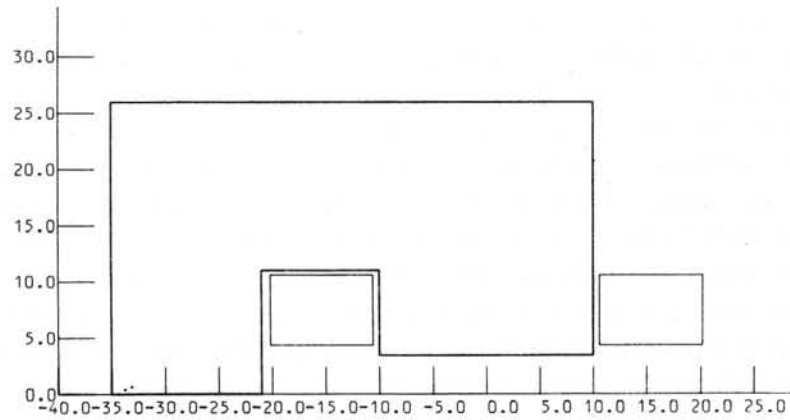


FIGURE 9 - BIM MODEL OF A TWO-DIMENSIONAL C-MAGNET

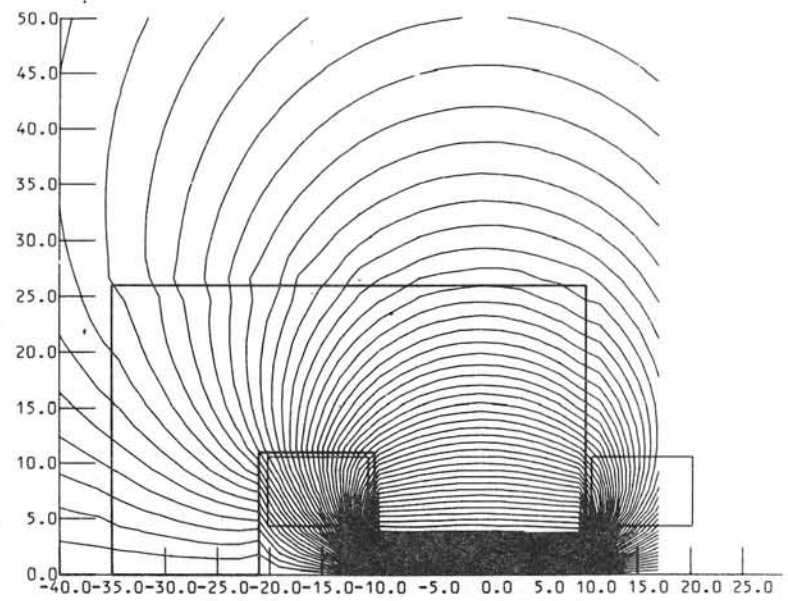


FIGURE 11 - A MAP OF THE COMPUTED MAGNETIC SCALAR POTENTIAL FOR A C-MAGNET

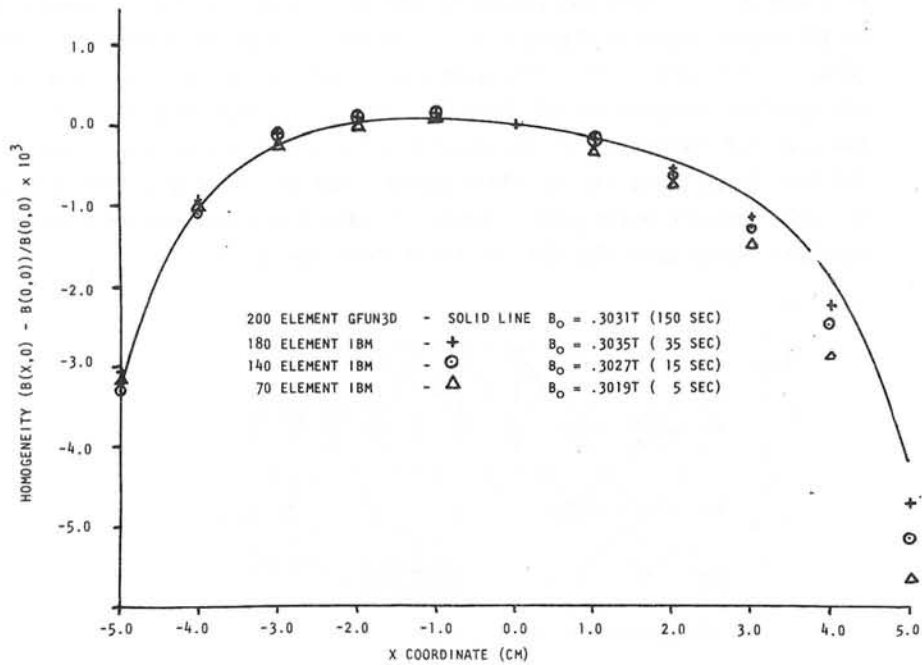


FIGURE 10 - COMPUTED HOMOGENEITY OF THE FIELD UNDER THE POLE TIP OF THE C MAGNET SHOWN IN FIGURE 8.

6. CONCLUSIONS

The results achieved for two-dimensional magnet problems are encouraging and appear to be competitive with other methods. The extension of the Boundary Integral Formulation to three dimensions is relatively straightforward and should in principle lead to a more efficient algorithm than the one currently in use in GFUN. For example, the following table compares predicted computing time (seconds) for a range of problems, ie. for existing GFUN, BIM and the Scalar Potential Integral Equation⁽²⁾ formulation. The table also gives times for computing a single field point.

Volume Elements	Surface Elements in BIM	GFUN Magnetisation Method		BIM		Scalar Int. Eq. Method	
		Int. Eq.	Single Field Point	Int. Eq.	Single Field Point	Int. Eq.	Single Field Point
216	216	114	2.16	12	0.36	4.2	2.16
343	294	450	3.43	30	0.49	18.0	3.43
512	384	1488	5.12	70	0.64	55.0	5.12
730	486	4320	7.30	133	0.80	162.0	7.30

It can be seen that, as the number of elements increases, BIM compares very favourably with the Scalar Integral Equation method both for the main solution and for fields at single points.

Since the existing program is restricted to constant permeability problems the best method for solving the non-linear problems must be established - the multi-region option outlined in Appendix 1 Section 2 will be tried first by modifying the existing two-dimensional program.

Finally, it should be emphasised that this method has a far wider range of applicability than magnetostatics; for example, solution of current flow potentials in association with eddy currents⁽⁸⁾; also it may be used to advantage in improving the efficiencies of programs already developed such as GFUN for computing the fields at single points.

7. ACKNOWLEDGEMENTS

The authors are indebted to the following Rutherford Laboratory staff: Dr D B Thomas, Head of Applied Physics Division for his encouragement throughout the work and to Mrs E Dawson for preparing the typescript.

8. REFERENCES

1. Armstrong, A G A M, Collie, C J, Diserens, N J, Newman, M J, Simkin, J and Trowbridge, C W. New Developments in the Magnet Design Computer Program GFUN. RL-75-066. Also in Proc. 5th Int. Conf. on Magnet Technology, Rome, 1975.
2. Iselin, Ch. A Scalar Integral Equation for Magnetostatic Fields. Proc. COMPUMAG Conf. on the Computation of Magnetic Fields, Oxford, April 1976.
3. Jawson, M A. Integral Equation Methods in Potential Theory I. Proc. Roy. Soc. A, 275 23-32, 1963.
4. Cruse, T A. Application of Boundary Integral Equation Method to 3D Stress Analysis. J. Computer and Structures, Vol.3, 509-527, Pergamon Press 1973.

5. Symm, G T. Potential Problems in Three Dimensions. Numerical Solution of Integral Equations, Chapter 24. Clarendon Press, Oxford 1974.
6. Smythe, W R. Static and Dynamic Electricity, page 53. McGraw Hill, 1968.
7. Collie, C J. A Program for Computing the Magnetic Fields of Two Dimensional Arrays of Conductors. RL-73-032.
8. Newman, M N. Application of Interactive Graphics Techniques to Magnet Design. Proc. COMPUMAG Conf. on the Computation of Magnetic Fields, Oxford, April 1976.

APPENDIX 1

EXTENSION OF THE GREEN'S THEOREM APPROACH TO NON-LINEAR MAGNETOSTATIC PROBLEMS.

There are two possible methods of extending the method to cover non-linear problems; the first involves using a perturbation term based on the volume integral in equation (1); the second would require the whole of an iron volume to be subdivided into separate volume elements on the surfaces of which the potential and its normal derivative are computed.

(1) Perturbation term method. The magnetic field H_T at a point can be divided into two parts - \bar{H}_C due to currents and \bar{H}_M due to the iron.

$$\bar{H}_T = \bar{H}_C + \bar{H}_M \quad (7)$$

Since:

$$\text{Div } \bar{B} = 0$$

Then:

$$\text{Div}(\mu\bar{H}_C + \mu\bar{H}_M) = 0 \quad (8)$$

(only isotropic materials are considered here)

From equation (8)

$$\begin{aligned}\text{Div}(\mu\vec{H}_M) &= (\nabla\mu) \cdot \vec{H}_M + \mu(\nabla \cdot \vec{H}_M) \\ &= (\nabla\mu) \cdot \vec{H}_M - \mu\nabla^2V = -\text{Div}(\mu\vec{H}_C)\end{aligned}$$

Since:

$$\text{Div}(\mu\vec{H}_C) = 0 \text{ then:}$$

$$\nabla^2V = \frac{1}{\mu} \nabla\mu \cdot \vec{H}_T \quad (9)$$

Combining equations (2) and (9):

$$4\pi V(p) = \int_V \frac{1}{\mu} (\nabla\mu \cdot \vec{H}_T) \frac{dV}{r} + \int_S \frac{1}{r} \frac{\partial V}{\partial n} ds - \int_S V \frac{\partial}{\partial n} \left(\frac{1}{r}\right) ds \quad (10)$$

This equation could be solved numerically by calculating the contributions of the volume integral when the solution for V and $\frac{\partial V}{\partial n}$ is known. Using a simple iterative scheme the values of V and $\frac{\partial V}{\partial n}$ could then be updated by resolving equations (3) and (4) with the volume integral contribution added to the right-hand sides and the continuity conditions modified.

(2) Volume subdivision method. The existing two-dimensional program can be used to evaluate this method. The ferromagnetic regions of a problem must be divided into small elements over which the change in permeability is small. The equations to be solved are unchanged but an iterative method must be used to converge the solutions for the permeabilities. This method has several advantages; the matrix to be solved is banded and sparse and has a similar structure to those obtained in finite element methods; a numerical calculation of the gradient of μ is not needed. It is hoped to try this second method if present improvements to integral equation methods (2) do not fulfill their promise.

APPENDIX 2

EXPRESSIONS FOR THE FIELD AND POTENTIAL FROM SINGLE AND DOUBLE LAYER SURFACE CHARGES ON INFINITELY LONG PLANE FACES OF FINITE WIDTH

A typical region consisting of many boundary faces is shown in Figure 12. All the expressions given below are for points in the local coordinate system of a boundary face - Figure 13. The faces are infinitely long and of the plane of the paper - in the Z direction:

(1) Potentials. The integrals to be evaluated are shown in equation (2). The potential at a point $p(x,y)$ is:

$$V(p) = \frac{1}{4\pi} [V_j(2\theta) + 2 \frac{\partial V_j}{\partial n} (x \ln(r_1/r_2) + b \ln(r_1 r_2) - 2b + y\theta)]$$

where $2b$ is the width of the face.

(2) Fields. The field at point $p(x,y)$ is:

$$\vec{H} = -\text{grad } V(p)$$

Therefore:

$$\begin{aligned}H_x &= \frac{1}{2\pi} [V_j \left\{ \gamma \left(\frac{1}{r_1^2} - \frac{1}{r_2^2} \right) \right. \\ &\quad \left. + \frac{\partial V_j}{\partial n} \left\{ x \left(\frac{(x+b)}{r_1^2} - \frac{(x-b)}{r_2^2} \right) + \ln(r/r) + b \left(\frac{(x+b)}{r_1^2} - \frac{(x-b)}{r_2^2} \right) \right. \right. \\ &\quad \left. \left. + \left(\frac{y^2}{r_1^2} - \frac{y^2}{r_2^2} \right) \right\} \right] \\ H_y &= \frac{1}{2\pi} [V_j \left\{ \frac{(x-b)}{r_2^2} - \frac{(x-b)}{r_1^2} \right\} \\ &\quad \left. + \frac{\partial V_j}{\partial n} \left\{ x \left(\frac{-y}{r_1^2} - \frac{y}{r_2^2} \right) + b \left(\frac{-y}{r_1^2} + \frac{y}{r_2^2} \right) + y \left(\frac{(x-b)}{r_2^2} - \frac{(x+b)}{r_1^2} \right) + \theta \right\} \right]\end{aligned}$$

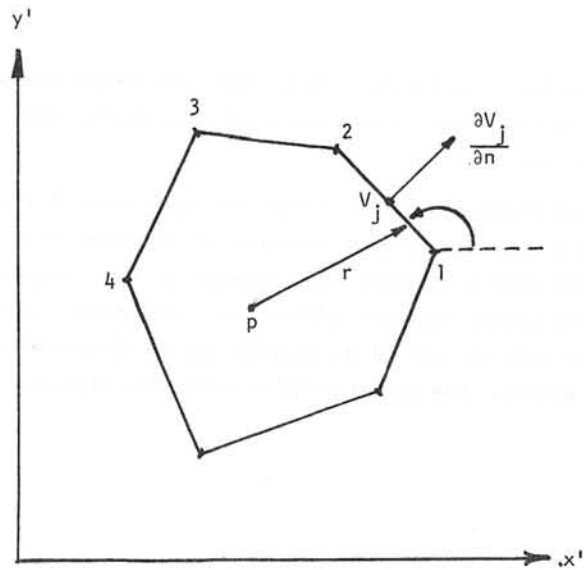


FIGURE 12 - GLOBAL COORDINATE SYSTEM.
A BOUNDARY SURFACE SUBDIVIDED INTO ELEMENTS

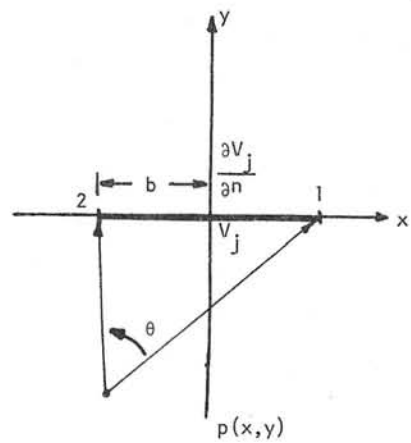


FIGURE 13 - LOCAL COORDINATE SYSTEM OF AN ELEMENT

Discussion following paper:

(Yeh, Oak Ridge) Please elaborate on the matching of the number of variables with the number of equations in your method.

(Simkin, Rutherford) If Neumann or Dirichlet boundary values are defined on every surface element the set of linear equations for the unknowns is exactly determined by the Green's theorem equations for every surface element. Where the potential and derivative are unknown on interfaces there must be an exact equivalence between elements forming surfaces on either side of the boundary. For each pair of equivalent elements two extra equations are obtained from continuity of V and B across the boundary. Thus for the pair of equivalent elements we have four unknowns and four equations - see the section of the paper on equation reduction.

(Rosten, CHAM Ltd) You mentioned the application of the IBM for computing the distribution of current within conductors. Would you elaborate this point.

(Simkin) The IBM can be used to compute the current flow at any position in the volume of a general 3-D variable cross section conductor. Having computed J , the conductor fields still need to be calculated using volume integration methods - see the paper by C J Collie on fields and potentials from hexahedra in the Proceedings.

(Rogers, Southampton) We have used an integral equation method based on Green's functions for each sub-region of the field. It has been successfully applied to the computation of functionals of the field (such as inductance) but we have found considerable errors in the local field at singular points. Do you have to take any special precautions to avoid this problem?

(Simkin) The fields and potentials are well behaved except at points close to areas of the surface where the potential or surface tangent changes discontinuously. At the moment the problem is avoided by displacing such points a very small distance. In future higher order basis functions will be used on our surface elements and it will be necessary to investigate methods of overcoming these weak singularities.

(Ohiwa, Cambridge) Could you give me some idea of the accuracy of the calculated field in terms of the number of mesh points, required storage and computer time.

(Simkin) The results included in the paper give some of the figures. Typically, for linear problems accuracies of the order of 1% can be obtained using 200K of storage and 6 seconds CPU time on an IBM 360/195. In solving the linear equations we have only used simple gaussian elimination and not made any use of the blocked and non-dense nature of the coefficient matrix. The method could be made more efficient.

A SCALAR INTEGRAL EQUATION FOR MAGNETOSTATIC FIELDS

Ch. Iselin

CERN, Geneva, Switzerland

Abstract

For the solution of magnetostatic field problems in three dimensions, integral equation methods have been used mainly because of the following advantages:

- i) The unknown quantities need to be calculated in iron only, i.e. the domain of calculation is finite.
- ii) The boundary conditions at infinity are taken care of automatically, and the magnetic field can be found correctly anywhere in space.

On the other hand, the following difficulties have been encountered with integral equation methods:

- i) The number of unknowns is large; it must be found by inverting a full matrix.
- ii) The condition number of the matrix to be inverted can be very large.
- iii) The magnetic field is infinite on iron edges. This makes it impossible to use certain, otherwise convenient, approximations to the magnetic field.

In this paper we propose to solve the integral equation for the scalar potential in iron by Galerkin's method. It is believed that this avoids the last two of the above problems.

1. BASIC EQUATIONS

The magnetostatic field obeys the two Maxwell equations

$$\operatorname{div} \vec{B} = 0 \quad (1)$$

$$\operatorname{curl} \vec{H} = \vec{j}, \quad (2)$$

where

\vec{B} : magnetic flux density

\vec{H} : magnetic field strength

\vec{j} : current density.

Furthermore, \vec{B} and \vec{H} are related by the material equation

$$\vec{B} = \vec{B}(\vec{H}). \quad (3)$$

We now introduce the magnetic field \vec{H}_0 of the coils alone, which obeys the equations

$$\operatorname{div} \vec{H}_0 = 0 \quad (4)$$

$$\operatorname{curl} \vec{H}_0 = \vec{j}. \quad (5)$$

The field \vec{H}_0 can be found by the law of Biot and Savart

$$4\pi\vec{H}_0 = \int_{\text{coils}} \frac{\vec{j} \times \vec{r}}{r^3} dV. \quad (6)$$

For any scalar potential ϕ the expression

$$\vec{H} = \vec{H}_0 + \operatorname{grad} \phi \quad (7)$$

fulfils eq. (2). Instead of using eq. (1), we can make use of the magnetization \vec{M} of the iron

$$\vec{M} = \vec{B} - \mu_0 \vec{H}, \quad (8a)$$

or

$$\vec{M} = \vec{M}(\vec{H}_0 + \operatorname{grad} \phi). \quad (8b)$$

Equation (8b) shows the functional dependence of \vec{M} upon \vec{H} .

Equation (1) may then be replaced by

$$\mu_0 \operatorname{div} \operatorname{grad} \phi = - \operatorname{div} \vec{M}. \quad (9)$$

This has the solution

$$4\pi\mu_0\phi = - \int_{\text{iron}} \frac{\vec{M} \cdot \vec{r}}{r^3} dV. \quad (10)$$

It is clear that neither the potential ϕ nor the magnetization \vec{M} is known at this stage. In this paper we are trying to give a method to find the scalar potential.

2. METHODS USED SO FAR

2.1 Halacsy's method

In the RENO computer program¹⁾, the unknown is the scalar potential. It is found by the following procedure:

i) Insert the definition $\vec{B} = \mu\vec{H}$ into eq. (1).

$$\text{div } \vec{B} = \text{div} [\mu(H_0 + \text{grad } \phi)] = 0 . \quad (11)$$

ii) Combine eqs. (8) and (10) giving

$$4\pi\mu_0\phi = - \int_{\text{iron}} \frac{(\mu - \mu_0)(\vec{H}_0 + \text{grad } \phi) \cdot \vec{r}}{r^3} dV . \quad (12)$$

iii) Insert eq. (12) into eq. (11), yielding a rather complicated equation for ϕ .

iv) Solve the equation resulting from step (iii) numerically.

The equation for the scalar potential is solved using a regular rectangular grid. This imposes important restrictions on the iron geometry. The method is very difficult to adapt for anisotropic iron.

Note that both eqs. (11) and (12) uniquely determine the scalar potential, and that both have the same solution. This may be the reason why the method often breaks down, due to an attempt to invert a singular matrix.

2.2 Magnetisation method

To our knowledge, the first author^{2,3)} to use integral equation methods with success was Trowbridge et al. The computer program GFUN solves the integral equation

$$\vec{H} = \vec{H}_0 - \frac{1}{4\pi\mu_0} \text{grad} \int_{\text{iron}} \frac{\vec{M} \cdot \vec{r}}{r^3} dV \quad (13)$$

combined with the material equation

$$\vec{M} = \vec{M}(\vec{H}) \quad (14)$$

in terms of the magnetization \vec{M} or of the total magnetic field strength \vec{H} . The method could easily be adapted for anisotropic iron. The GFUN program has been used with considerable success in several laboratories, but it still leaves some problems unsolved.

So far the program uses a piece-wise constant magnetization. The discontinuities of \vec{M} on element boundaries can cause problems by allowing some non-physical solutions to be generated and by making difficult an accurate field calculation in the iron. One cannot use more sophisticated approximations for the magnetization, as long as they depend on values on iron edges, since on iron edges the fields are discontinuous.

Another disadvantage of this method is that its unknown is a vector and that the number of unknowns is higher by a factor of three compared with a method searching for the scalar potential.

3. THE PROPOSED METHOD

3.1 Basic idea

We note that the scalar potential ϕ introduced in eq. (7) must be finite in all space. We shall therefore try to solve eq. (10)

$$4\pi\mu_0\phi + \int_{\text{iron}} \frac{\vec{M} \cdot \vec{r}}{r^3} dV = 0 \quad (15)$$

together with the material equation

$$\vec{M} = \vec{M}(H_0 + \text{grad } \phi) \quad (16)$$

iteratively in terms of the scalar potential ϕ .

Assume that after k iterations we have found a guess $\phi^{(k)}$. The magnetization is then

$$\vec{M}^{(k)} = \vec{M}(\vec{H}_0 + \text{grad } \phi^{(k)}) . \quad (17)$$

Inserting $\phi^{(k)}$ and $\vec{M}^{(k)}$ into eq. (15) we have

$$4\pi\mu_0\phi^{(k)} + \int_{\text{iron}} \frac{\vec{r} \cdot \vec{M}^{(k)}}{r^3} dV = f^{(k)} \neq 0 . \quad (18)$$

The idea is now to find a linear integral equation for the k^{th} correction $\Delta\phi^{(k)}$ by linearizing in the neighbourhood of our last guess:

$$f^{(k+1)} \approx f^{(k)} + 4\pi\mu_0 \Delta\phi^{(k)} + \int_{\text{iron}} \frac{\vec{r} \cdot [P^{(k)} \text{grad } \Delta\phi^{(k)}]}{r^3} dV = 0 . \quad (19)$$

Here $P^{(k)}$ is the (3×3) Jacobi matrix of partial derivatives of the components of \vec{M} with respect to the components of \vec{H} .

3.2 Methods of solution

Let us now choose a suitable function space with the finite dimension N to approximate our scalar potential. In this space we define a base

$$\{\phi_n(x,y,z), N = 1, 2, 3, \dots, N\} . \quad (20)$$

In terms of our base the k^{th} correction is approximated as

$$\Delta\phi^{(k)} \approx \sum_{n=1}^N c_n \phi_n(x, y, z) . \quad (21)$$

Further, we define the set of functions

$$\psi_n^{(k)} = \frac{\partial f^{(k+1)}}{\partial c_n} = 4\pi\mu_0\phi_n + \int_{\text{iron}} \frac{\vec{r} \cdot [P^{(k)} \text{grad } \phi_n]}{r^3} dV . \quad (22)$$

This allows us to write eq. (19) as

$$f^{(k)} + \sum_{n=1}^N c_n \psi_n^{(k)} = 0 . \quad (23)$$

We are left with a problem of linear algebra: that is to fit a function $f^{(k)}$ in the best possible way by a linear combination of (hopefully!) linearly independent functions $\psi_n^{(k)}$.

A solution to this fitting problem can be found by Galerkin's method. We define the inner product of two functions by

$$(u, v) = \int uv dV , \quad (24)$$

the integral being taken over the iron volume only, or over the whole space, whichever is more convenient for the functions concerned. We also select a linearly independent set of trial functions

$$\{t_m(x, y, z), m = 1, 2, 3, \dots, N\} . \quad (25)$$

Then the relations

$$(t_m, f^{(k)}) + \sum_{n=1}^N c_n (t_m, \psi_n^{(k)}) = 0 \quad (26)$$

provide us with a system of N linear equations in the N unknowns c_n .

The simplest choice for the trial functions t_m is to use N Dirac functions. The scalar products in eq. (26) then simply mean evaluation in N different points, i.e. the correction is such that eq. (23) becomes true in these N points.

A solution of eq. (23) in the least-squares sense means minimization of

$$(f^{(k)}, f^{(k)}) = \text{minimum} . \quad (27)$$

The trial functions are then $t_m = \psi_m^{(k)}$. This choice must usually be ruled out, because the trial functions are non-zero in whole space, and the computational effort to evaluate the inner products is prohibitive.

A compromise would be to take $t_m = \phi_m$. Further investigations will be necessary to find out if this choice is worth the effort.

4. CHOICE OF BASE FUNCTIONS

4.1 Linear base functions

For a first trial of the method the base of functions was defined in a straightforward way. The iron was cut into small tetrahedra, allowing a rather general geometry. On each tetrahedron the potential was taken to be a linear function of position, defined by its values in the four vertices of the tetrahedron. The magnetic field and the magnetization were thus both constant throughout each tetrahedron, in a similar way to the GFUN program.

The trial functions t_m were taken to be Dirac functions centred on the tetrahedron vertices, i.e. eq. (23) was solved for the tetrahedron vertices. For simple problems, such as an iron cube in a homogeneous magnetic field, the results were rather encouraging. For more realistic problems, such as, for example, a race track coil surrounded by a cylindrical iron shell, the potential values were still approximately correct in the solution points, but very large oscillations of the potential appeared close to the iron surface. This was because the tangential component of the magnetic field should be nearly zero on the iron surface, which is only possible if the potential is allowed to vary to a higher degree than linear.

The use of linear base functions seems not to be appropriate if the number of calculation points is small. For a very fine subdivision of the iron it may possibly give reasonable results.

4.2 Quadratic base functions

For the second test, the same subdivision of the iron into tetrahedra was used. This time the potential was allowed to be a quadratic function of position, defined by its values in the vertices, plus the values in the midpoints of the tetrahedron edges. This made the magnetic field a linear function of position in each tetrahedron. The magnetization was assumed to vary linearly with position as well. Equation (23) was again solved in all points with unknown potential values.

The solution using quadratic base functions gave much better results than the approach using linear base functions. Even for a rather coarse subdivision of the iron, the results were comparable with results found using the GFUN program, but there is still a problem left. Since the magnetic fields were only coupled through the potential, when going from one tetrahedron to the next, they were not smooth on the interface. It remains to be investigated whether a different method of numeric differentiation of the potential gives better results. These investigations are under way.

4.3 Isoparametric base

Investigations are also under way on the use of an isoparametric representation as has been used in the finite element method⁴⁾. This would permit one to use a very general geometry and still to have a smooth magnetic field all over the iron. Unfortunately, due to the lack of time, no numeric results can be presented yet.

REFERENCES

- 1) A.A. Halacsy, Three-dimensional analysis of magnetic fields with field-dependent permeability, Proc. 3rd Internat. Conf. on Magnet Technology, Hamburg, 1970 (DESY, Hamburg, 1972?), p. 113.
- 2) M.J. Newman, C.W. Trowbridge and L.R. Turner, GFUN: An interactive program as an aid to magnet design, Proc. 4th Internat. Conf. on Magnet Technology, Brookhaven, 1972 (U.S. Atomic Energy Commission, Washington, 1973), p. 617.
- 3) A.G.A.M. Armstrong, C.J. Collie, N.J. Diserens, M.J. Newman, J. Simkin and C.W. Trowbridge, New developments in the magnet design computer program GFUN3D, Proc. 5th Internat. Conf. on Magnet Technology, Rome, 1975 (Laboratori Nazionali del CNEN, Frascati, 1975), p. 168.
- 4) G. Strang and G.J. Fix, An analysis of the finite element method (Prentice Hall, Englewood Cliffs N.J., 1973).

Discussion following paper:

(Trowbridge, Rutherford) What set of basis functions did you chose and was the gain in efficiency expected with your method actually achieved?

(Iselin, CERN) I used three sets of base functions:

- (1) tetrahedral elements with linear ϕ variation
- (2) tetrahedral elements with quadratic ϕ variation
- (3) 'isoparametric' (r, ϕ , θ) elements.

So far only case (3) gave acceptable results. The time for setting up the matrix is comparable to GFUN, but the time for one iteration is cut down to about 4%.

An account for the use of the FEM for magnetostatic problems

S.J. Polak, A. Wachters, A. de Beer

N.V. Philips' Gloeilampenfabrieken, ISA-DSA/SCA

Abstract

The FEM is considered for magnetostatic problems involving both soft isotropic and hard anisotropic materials in this article. Special attention is paid to existence and uniqueness aspects for these non-linear problems. For hard anisotropic materials a new model is introduced. The program package MAGGY contains this model and has been used to compare calculated with measured data.

1. Introduction

In the last ten years numerous calculations have been performed, using the FEM for the numerical approximation of solutions of magnetostatic problems. These are e.g. mentioned in [1] - [7]. In most descriptions no attention is paid to the validity of this use w.r.t. existence, uniqueness and convergence aspects. These do not trivially fit in the usual theory because magnetostatic problems are non-linear. Only in [2] a special approximation of the B-H curve is used for this purpose. Here the FEM is considered for a very general class of magnetostatic problems while paying special attention to the above-mentioned aspects. For hard anisotropic materials a new, simple and usable model is introduced. The model is available in the program package MAGGY. Results from computations with MAGGY are compared with measured data.

2. Basic notions

2.1. Suppose V an open simply connected region in R_3 or R_2 with closure \bar{V} , $\delta V = \bar{V} \setminus V$. On V we have the usual spaces L_2 and W_2^1 (see e.g. [9]). The space L_2 has the usual inner product and associated norm defined by

$$(2.1.1.) \quad (f, g)_L = \int_V f g \, dv, \quad \|f\|_L = (f, f)_L^{\frac{1}{2}}.$$

The space W_2^1 has inner product and norm

$$(2.1.2.) \quad (f, g)_W = \int_V \text{grad } f \cdot \text{grad } g \, dv, \quad \|f\|_W = (f, f)_W^{\frac{1}{2}}$$

We will use P_k to denote some finite dimensional subspace of W_2^1 .

2.2. For a magnetostatic problem on $V \subset R_3$ we have

$$(2.2.1.) \quad \text{curl } H = j, \quad H \text{ the magnetic field,} \\ j \text{ the current density;}$$

$$(2.2.2.) \quad \text{div } B(H) = 0, \quad B \text{ the fluxdensity.}$$

Suppose B an invertible vector function of H in the sequel. B is continuously partially differentiable w.r.t. H . We note that $\int_V j^2 \, dv < \infty$.

2.3. In this section 2.3. we consider the case where the problem is two-dimensional for symmetry reasons and in cartesian coordinates. We identify V with the accompanying region in R_2 . Now j can have a component perpendicular to V only and thus is effectively a scalar function. A vector potential A is introduced with

$$(2.3.1.) \quad B = \text{curl } A \text{ on } V, \quad A \equiv 0 \text{ on } \delta V$$

which represents condition (2.2.2.). Because j is perpendicular to V , A only needs to have one component, perpendicular to V . Therefore also A is effectively a scalar function. However where necessary A is to be interpreted as the appropriate vector.

Remark: in this case we have $|\text{curl } A| = |\text{grad } A|$ such that $A \equiv 0$ on δV is sufficient to give: $\|\text{curl } A\|_L = 0 \iff A = 0$. Thus A is uniquely defined for a certain B . The equation (2.2.1.) then gives

$$(2.3.2.) \quad \text{curl } H(\text{curl } A) = j \text{ on } V, \quad A \equiv 0 \text{ on } \delta V \text{ with } j \in L_2.$$

The FEM is usually considered as the minimisation of the following energy integral:

$$(2.3.3.) \quad E(A) = \int_V \int_0^{B=\text{curl } A} H(b) \cdot db - 2jA \, dv$$

over some P_k . This is termed the energy formulation of the problem. The Galerkin formulation of (2.3.2.) is

$$(2.3.4.) \quad \int_V H(\text{curl } A) \cdot \text{curl } f \, dv = \int_V j \cdot f \, dv \quad \text{for all } f \in P_k$$

and f is interpreted as a vector perpendicular to V as usual. In §5 it is shown that these formulations are equivalent.

2.4. For a three dimensional problem (2.3.1.) does not uniquely define the vector potential. Thus we use a different approach. A "source field" H_c is established with

$$(2.4.1.) \quad \text{curl } H_c = j$$

This is e.g. done with Biot-Savart's law in vacuum. For the discussion of the FEM we assume this solution H_c with $H_c \in L_2$ available. Then we use (2.2.2.) giving

$$(2.4.2.) \quad \begin{aligned} \text{div } B(H_c + \text{grad } f) &= 0 & \text{on } V \\ f &\equiv 0 & \text{on } \delta V. \end{aligned}$$

The Galerkin formulation for this problem is

$$(2.4.3.) \quad \int_V B(H_c + \text{grad } f) \cdot \text{grad } g \, dv = 0 \quad \text{for all } g \in P_k.$$

3. B-H properties of various kinds of materials

3.1. Magnetic materials may be classified according to different criteria, either in the classes isotropic and anisotropic or in the classes of soft and hard. (see fig 1)

	soft	hard
isotropic		
anisotropic		

Fig.1. classes of magnetic materials

An isotropic material is characterised by the fact that a virginal sphere has no preferred direction. Other materials are anisotropic. Soft magnetic materials are characterised by the fact that no field in the material can exist if no external source for a magnetic field is present. Other materials are termed hard.

Here we will only discuss the B-H properties of materials belonging to the diagonal blocks of figure 1.

3.2. For soft isotropic materials the field dependence of the flux density is well-known:

$$(3.2.1.) \quad B(H) = \mu(|H|)H,$$

where the magnetic permeability μ is a scalar, so that B can be interpreted as a scalar function of H (B-H curve), which is differentiable and invertible.

3.3. For hard anisotropic materials the field dependence of the flux density may be formulated as follows:

$$(3.3.1.) \quad B(H) = \mu(H)H + B_r,$$

where B_r is the remanence and $\mu(H)$ a tensor. In general $\mu(H)$ can not be obtained from available experimental data for such materials. However, for sintered hard anisotropic materials containing single domain particles one may take:

$$(3.3.2.) \quad \mu(H) = \mu_0 \begin{bmatrix} \mu_{r//}(H_{//}) & 0 \\ 0 & \mu_{r\perp} \end{bmatrix}, \quad H_{//} = H \cdot B_r / |B_r|$$

where $\mu_{r//}$ can be obtained from the B-H curve and $\mu_{r\perp} = 1 + M_s / |H_A|$, in which M_s the saturation magnetic moment and $|H_A|$ the anisotropy field strength.

The approximation of $\mu(H)$ by e.g. (3.3.2.) is justified by experiments described in a paper of Zijlstra presented at this conference, and a model calculation described in the following sections.

3.4. The field dependence of the magnetic moment of a single domain particle can be obtained from a treatment similar to the one given by Stoner and Wohlfarth [18]. Since the anisotropy energy of a single domain particle is give to a first approximation by:

$$(3.4.1.) \quad E_A = k \sin^2 \psi_i,$$

where k is a parameter depending on the temperature, ψ_i is the angle between the magnetization vector M_i and the easy axis of the monocrystalline particle. In the presence of a magnetic field H, which makes an angle α_i with the easy axis, the equilibrium direction of M_i can be obtained from

$$(3.4.2.) \quad \frac{\partial}{\partial \psi_i} (E_A - M_i \cdot H) = 2k \cos \psi_i \sin \psi_i - |M_i| |H| \sin(\alpha_i - \psi_i) = 0,$$

so that as shown in figure 2 the magnetization is directed along the resultant of H and a hypothetical field $H_{A,i}$, the so-called anisotropy field of strength $2k \cos \psi_i / |M_i|$.

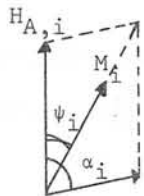


Fig. 2. Dependence of magnetic moment M_i of the magnetic field H and the anisotropy field $H_{A,i}$ for a single domain particle

If M_s is the spontaneous magnetisation per unit volume the magnetic moment M_i of a single domain particle per unit volume is:

$$(3.4.3.) \quad M_i = M_s \frac{H + H_{A,i}}{|H + H_{A,i}|} \quad ; \quad |M_i| = M_s.$$

3.5. The magnetic moment M per unit volume in a point in the material may be considered as the sum of the magnetic moments per unit volume of the particles, each with a volume τ_i , in a small volume V surrounding the point so that

$$(3.5.1.) \quad M = \frac{1}{V} \sum_i M_i \tau_i = M_s \sum_i \frac{H + H_{A,i}}{|H + H_{A,i}|} \tau_i / V$$

If $\tau_i \ll V$ the summation may be replaced by integration. For spherical coordinates θ and ϕ and the probability density function $f(\theta, \phi)$ for the distribution of the direction of the particle magnetic moments

$$(3.5.2.) \quad M(\bar{\alpha}, |H|) = M_s \int_0^\pi \int_0^{2\pi} \frac{H + H_A(\theta, \phi)}{|H + H_A(\theta, \phi)|} f(\theta, \phi) \sin \theta d\theta d\phi / \int_0^\pi \int_0^{2\pi} f(\theta, \phi) \sin \theta d\theta d\phi,$$

where

$$(3.5.3.) \quad |H_A(\theta, \phi)| = |H_A^0| \cos \phi(\theta, \phi) \quad , \quad |H_A^0| = 2k / M_s \quad ;$$

and due to (3.4.2.)

$$(3.5.4.) \quad \cos \phi(\theta, \phi) \sin \phi(\theta, \phi) = \frac{|H|}{|H_A^0|} \sin(\alpha(\theta, \phi) - \psi(\theta, \phi)).$$

$\bar{\alpha}$ is the angle between H and the direction of the average of $H_A(\theta, \phi)$, which is the direction of the remanence.

3.6. For a uniform distribution:

$$(3.6.1.) \quad f(\theta, \phi) = \begin{cases} 1, & \text{for } 0 \leq \theta \leq \theta_0 \text{ and } 0 \leq \phi \leq 2\pi \\ 0, & \text{for } \theta_0 \leq \theta \leq \pi \text{ and } 0 \leq \phi \leq 2\pi \end{cases}$$

the double integral of (3.5.2.) has been calculated by Gauss quadrature, after determination of the appropriate root of (3.5.4.), as function of H and $\bar{\alpha}$. Because of the appearance of Bloch walls for $|H|$ smaller than $0.5 H_A^0$ a reversal field H_r was introduced (see paper of Zijlstra).

The results of the calculations show the following relations for the components of $M(\bar{\alpha}, |H|)$ parallel and perpendicular to the direction of the remanence resp.

$$(3.6.2.) \quad M_{//}(\bar{\alpha}, |H|) = M_{//}(\bar{\alpha}, |H'|) \text{ for } |H| \cos \bar{\alpha} = |H'| \cos \bar{\alpha}',$$

$$(3.6.3.) \quad M_{\perp}(\bar{\alpha}, |H|) = M_S |H| \sin \bar{\alpha} / (|H_A^0| + |H| \cos \bar{\alpha}), (\bar{\alpha}, \theta_0 < \frac{1}{4}\pi).$$

From these relations it follows that the magnetic susceptibility, defined by $M = \chi H + M_0$ is a tensor of following form:

$$\chi = \begin{bmatrix} \chi_{//} (|H| \cos \bar{\alpha}) & 0 \\ 0 & M_S / (|H_A^0| + |H| \cos \bar{\alpha}) \end{bmatrix}$$

so that $\mu_{r//} \equiv 1 + \chi_{//} (|H| \cos \bar{\alpha})$ can be obtained from the B-H curve if as argument the projection is taken along the direction of the remanence. For $\mu_{r\perp}$ can be taken $1 + M_S / (|H_A^0| + |H| \cos \bar{\alpha}) \approx 1 + M_S / |H_A^0|$, since in practice $|H| \ll |H_A^0|$ for the anisotropic materials of interest.

4. Basic inequalities

4.1. For notational ease we consider only 2 dimensional problems in this §. This is no restriction because the 3 dimensional extension is trivial here.

The models presented in §3 are of the following form:

$$(4.1.1.) \quad B = Z(H)H + B_r$$

where $Z(H)$ is a matrix and B_r independant of H . In the soft isotropic case $Z(H) = \mu(|H|)I$ where I is the identity matrix. For the hard anisotropic case we consider

$$(4.1.2.) \quad Z(H) = \begin{bmatrix} \mu_{//} & 0 \\ 0 & c \end{bmatrix}, \quad \mu_{//} = \mu_0 \mu_{r//} (H_{//}), \quad c = \mu_0 \mu_{r\perp}$$

We note that there always exists a $d < c$ such that

$$(4.1.3.) \quad 0 < d \leq \mu \leq d^{-1}, \quad 0 < d \leq \frac{d|B|}{d|H|} \leq d^{-1} \text{ in the soft isotropic case and } 0 < d \leq \frac{dB_{//}}{dH_{//}} \leq d^{-1} \text{ for the hard anisotropic case.}$$

The properties stated in the following lemma are used in §6.

Lemma (4.1.) If $\Delta H = H(B_2) - H(B_1)$

$$\Delta B = B_2 - B_1 \quad \text{then}$$

$$(4.1.4.) \quad \Delta H \cdot \Delta B \geq d^{-1} |\Delta B|^2,$$

$$(4.1.5.) \quad \Delta H \cdot \Delta B \geq d |\Delta H|^2,$$

$$(4.1.6.) \quad |\Delta H| \leq 2d |\Delta B| \text{ and } |\Delta B| \leq 2d^{-1} |\Delta H|$$

proof: We first consider the jacobian matrix $((\frac{\partial B}{\partial H}))$

In the soft isotropic case

$$(4.1.7.) \quad ((\frac{\partial B}{\partial H})) = \mu(|H|) (I - \frac{1}{|H|^2} Z'(H)) + \frac{1}{|H|^2} \frac{d|B|}{d|H|} Z'(H)$$

where $Z'(H) = \begin{bmatrix} H_x^2 & H_x H_y \\ H_x H_y & H_y^2 \end{bmatrix}$ is a semi-positive definite

matrix. Also $I - Z'(H)/|H|^2$ is semi-positive definite, using

$$(4.1.3.) \text{ we therefore have } |((\frac{\partial B}{\partial H}))| = \max_x ((\frac{\partial B}{\partial H}))_{x \cdot x} / |x|^2 \geq d > 0 \text{ or}$$

$$(4.1.8.) \quad ((\frac{\partial B}{\partial H}))_{x \cdot x} \geq d |x|^2$$

From (4.1.7.) it also follows that

$$(4.1.9.) \quad |((\frac{\partial B}{\partial H}))| \leq \mu + \frac{d|B|}{d|H|} \leq 2 d^{-1}$$

In the hard anisotropic case we chose a coordinate system with $x_{//} B_r$ and $y_{\perp} B_r$. In this coordinate system we have

$$((\frac{\partial B}{\partial H})) = \begin{bmatrix} \frac{\partial B_{//}}{\partial H_{//}} & 0 \\ 0 & c \end{bmatrix}$$

where with (4.1.3.) we have again (4.1.8.) and (4.1.9.).

Using a Taylor development and $((\frac{\partial H}{\partial B})) = ((\frac{\partial B}{\partial H}))^{-1}$ we find
(4.1.4.) - (4.1.6.)

5. Equivalence of the Galerkin and energy formulation in the two dimensional case.

5.1. For the proof of theorem (5.1.) we need the following equality on $V \subset R_3$

$$(5.1.1.) \quad \int_V \text{curl } H \cdot f \, dv = \int_V H \cdot \text{curl } f \, dv + \int_{\delta V} (\Delta A \times H) \cdot n \, d\sigma$$

For the two dimensional case we can still use this formula by interpreting the vectors A, B and H as in (2.3.) and $f // A$. We assume the volume to have unit length perpendicular to $V \subset R_2$ and note that the contributions from top and bottom planes cancel.

5.2. The operator T is defined by

$$(5.2.1.) \quad TA = \text{curl } H (\text{curl } A) - j$$

Theorem (5.1.)

$$(5.2.2.) \quad E(A) \leq E(f) \quad \text{for all } f \in \hat{W}_2^1 \iff$$

$$(5.2.3.) \quad (TA, f)_L = 0 \quad \text{for all } f \in \hat{W}_2^1$$

Proof: a. Suppose for a certain A and j we have (5.2.3.), then define

$$\Delta E = E(A) - E(f) = \int_V \int_{B-\Delta B}^B H(b) \cdot db - j \cdot \Delta A \, dv$$

where $\Delta A = A - f$ and $\Delta B = \text{curl } \Delta A$.

We also have, using (5.1.1.) and $\Delta A = 0$ on δV that

$$\int_V j \cdot \Delta A \, dv = \int_V H \cdot \Delta B \, dv$$

Therefore

$$\Delta E = \int_V \int_{B-\Delta B}^B H(b) \cdot db - H(B) \cdot \Delta B \, dv$$

which with (4.1.8.) gives $\Delta E \leq 0$.

b. Now suppose $E(A) \leq E(f)$ for all $f \in \hat{W}_2^1$. With (4.1.8.) we have

$$\int_{B-\Delta B}^B H(b) \cdot db \geq H(B-\Delta B) \cdot \Delta B$$

therefore

$$\int_V H(B-\Delta B) \cdot \Delta B - j \cdot \Delta A \, dv = \int_V H(B) \cdot \Delta B - \Delta H \cdot \Delta B - j \cdot \Delta A \, dv \leq \Delta E \leq 0$$

where $\Delta H = H(B) - H(B-\Delta B)$ or using

$$\int_V H \cdot \Delta B \, dv = \int_V \text{curl } H \cdot \Delta A \, dv$$

we find

$$\int_V \Delta H \cdot \Delta B - (\text{curl } H - j) \cdot \Delta A \, dv \geq 0$$

for all ΔA . Using a Taylor development for ΔH and taking ΔB small enough this implies

$$\int_V ((\frac{\partial H}{\partial B})) \cdot |\Delta B|^2 - (\text{curl } H - j) \cdot \Delta A \, dv \geq 0$$

we write $\Delta A = \epsilon \Delta A'$ and see that we have, $\epsilon^2 p + \epsilon q \geq 0$ for all ϵ . Therefore $q \geq 0$ or $(TA, f)_L = 0$

6. Existence, uniqueness and convergence

6.1. In this § the theory from §2 of [10] is applied for the magnetostatic problem. This theory is used in the following form

Theorem (6.1.)

Let T be a mapping from \hat{W}_2^1 into L_2 satisfying

Q_1 : there exists a $c_1 > 0$ such that

$$(6.1.1.) \quad (Tu - Tv, Z)_L \leq c_1 \| |u-v| \|_W \| |Z| \|_W$$

for all u, v and $Z \in \hat{W}_2^1$ and

Q_2 : there exists a c_2 such that

$$(6.1.2.) \quad (Tu - Tv, u-v)_L \geq c_2 \| |u-v| \|_W^2$$

for all $u, v \in \hat{W}_2^1$
then the problems

$R : (Tu, v)_L = 0$ for all $u \in \hat{W}_2^1$ and

$R_k : (Tu_k, v)_L = 0$ for all $u_k \in P_k$ have unique solutions, and

$$(6.1.3.) \quad \| |u_k - u| \|_W \leq D \inf \{ \| |z - u| \|_W \mid z \in P_k \}$$

for some fixed $D > 0$

6.2. The problem posed in (2.3.) is considered here again.
The operator T is defined by

$$TA = \text{curl } H(\text{curl } A) - j$$

Then

$$(TA_1 - TA_2, A_3)_L = \int_V (H(\text{curl } A_1) - H(\text{curl } A_2)) \text{curl } A_3 \, dv$$

and (4.1.6.) gives

$$|H(\text{curl } A_1) - H(\text{curl } A_2)| \leq 2d |\text{curl}(A_1 - A_2)|$$

we find, using Schwartz inequality

$$(TA_1 - TA_2, A_3)_L \leq \| |A_1 - A_2| \|_W \| |A_3| \|_W$$

which is property Q_1 .

$$(TA_1 - TA_2, A_1 - A_2)_L = \int_V (H(\text{curl } A_1) - H(\text{curl } A_2)) \cdot \text{curl}(A_1 - A_2) \, dv$$

and (4.1.5.) gives

$$H(\text{curl } A_1) - H(\text{curl } A_2) \cdot \text{curl}(A_1 - A_2) \geq d (\text{curl}(A_1 - A_2))^2$$

which implies property Q_2 .

6.3. In this section we consider the problem (2.4.). The operator T is defined by

$$Tf = \text{div } B(H_c + \text{grad } f)$$

As in section (6.2.) we may conclude that properties Q_1 and Q_2 are satisfied, this time using (4.1.4.) and (4.1.6.).

6.4. Thus for the problems posed in (2.3.) and (2.4.) we may apply theorem (6.1.). Convergence of approximate solutions depends on the spaces P_k . It follows from (6.1.3.) that, if $P_k \subset P_{k+1}$ and $\lim_{k \rightarrow \infty} P_k$ is dense in \hat{W}_2^1 then $\lim_{k \rightarrow \infty} u_k = u$, see e.g. [11].

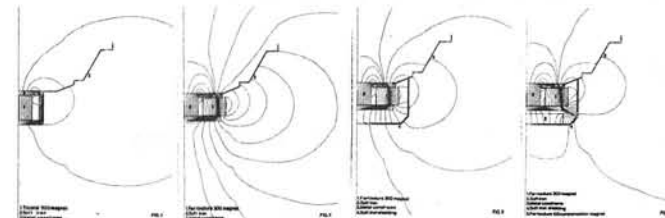


Fig. 3.

7. The program package MAGGY

7.1. The package MAGGY offers facilities for the approximation of 2-dimensional magnetostatic problems. These problems may be either in polar, cylindrical or cartesian coordinates. Calculations are performed using isoparametric bilinear quadrilaterals in either of these coordinates. The previous existence etc. considerations only apply in the cartesian case. The problem and algorithm information have to be given in a problem oriented language, MAGLAN.

The package contains an interpreter program which checks and expands the input and also generates part of the calculating program (e.g. dimension statements). Then a set of secondary programs is available for plotting, printing and the calculation of some secondary results. The package is completely written in Fortran. MAGGY2 is an open package in the sense that it is possible to give user chosen function names for most numbers in the input. The accompanying functions have to be given, immediately following the MAGLAN input.

7.2. The choice of elements in the FEM was done with ease of specification of the mesh as criterium rather than optimum flexibility. However structures of complicated nature have been analysed using MAGGY as can be seen in fig.3,5) In [3] an easy way of specifying a quadrilateral mesh can be found. Here an improved version is given.

A coarse quadrilateral mesh, topologically equivalent to a square mesh, has to be provided. An example is shown in fig. 4. The mesh is completed by the program with linear interpolation.

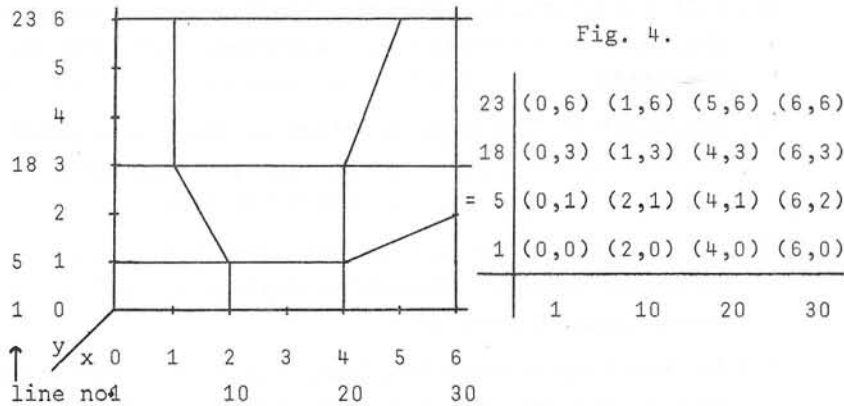
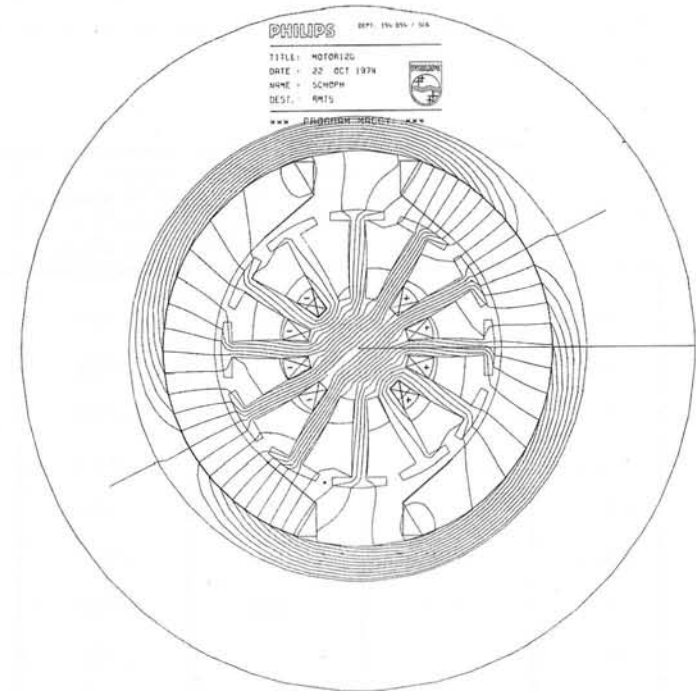


Fig. 4.

This mesh can be specified to the program by giving
 $x(1) = 4*0, x(10) = 2*2, 2*1, x(20) = 3*4, 5, x(30) = 4*6,$
 $y(1) = 4*0, y(5) = 3*1, 2, y(18) = 4*3, y(23) = 4*6.$

This is all the mesh information needed for MAGGY, is short and readable.

Fig. 5.



8. A comparison between computed and measured data

The flux, $A(z,R) \approx 2\pi \int_0^R B(z,r)r dr$, in a cylindrical Ticonal 900 bar has been measured at a number of points in the axial direction, z. The flux also has been computed with MAGGY using the model for permanent magnets discussed in §3. The results obtained for three different meshes are shown in Tabel 1, column two, three and four; $(z_1, r_2)/(z_2, r_2)$ indicates the total number of mesh lines in z- and r-direction within a region of $200 \times 130 \text{mm}^2$ surrounding the magnet, and the number of meshlines within the magnet of $44.875 \times 10.875 \text{mm}^2$ respectively.

The measured flux is shown in the last column of table 1. Except for the last two points near the pole of the magnet the results for the finest mesh agree with experiment to within 1%, and the difference is almost constant.

Table 1

Tinocal 900 bar with radius of 10.875mm and half length of 44.875. Flux measured through a cylinder with radius of 11mm is given in 10^{-3} Tesla.

z-coord	Flux calculated by MAGGY			Flux measured
	(11,11) /(5,4)	(21,19) /(9,6)	(43,37) /(19,12)	
0.0	.382	.393	.396	.392
2.5			.396	.392
5.0			.396	.392
7.5		.391	.395	.392
10.0			.394	.390
12.5			.392	.389
15.0	.374	.386	.390	.388
17.5			.387	.384
20.0		.380	.384	.380
22.5			.379	.375
25.0	.349	.368	.373	.369
27.5			.364	.360
30.0		.346	.353	.348
32.5			.337	.333
35.0	.284	.308	.317	.314
37.5			.290	.287
40.0		.245	.253	.249
42.5			.206	.195
44.875	.111	.124	.130	.120

Acknowledgement

We wish to thank mr. P.J. Schophuizen for the permission to publish fig.3,5 which stem from his use of MAGGY. We also wish to express our gratitude towards Dr. Zijlstra for his contributions in the development of the model presented in §3 and mr. Mimmel for the measurements shown in Tabel 1.

References

- [1] C.Iselin, Some recent developments in computation of two dimensional fields in iron magnets, Third int. conf. on magnet technology, Hamburg, May 1970.
- [2] R.Glowinski et A.Marocco, Analyse numerique du champ magnetique d'un alternateur par elements finis et surrelaxation ponctuelle nonlineaire, Computer methods in applied mechanics and engineering, vol3 no1 Jan.1974.
- [3] E.Munro, B.A., Computer aided design methods in electron optics, Ph.D.Thesis, Cambridge University.
- [4] P.Silvester and M.V.K.Chari, Analysis of a turbo alternator magnetic field by finite elements, IEEE, PAS 90, 1971, 454-464.
- [5] P.Silvester and M.V.K.Chari, Finite element analysis of magnetically saturated D.C. machines, IEEE, PAS 90, 1971 2362-2372.
- [6] A.M.Winslow, Numerical solution of the quasi-linear Poisson equation in a non-uniform triangle mesh, Journal of Comp. Phys. 2 (1967) 149-172.
- [7] W.Kammaing, Finite element solutions for devices with permanent magnets. Journal of Physics D, Applied Physics Vol18, number 7, May 1975.
- [8] Jerzyna Slomczynska. Nonlinear analysis of the magnetic flux in the magnetized magnet stabilised in air. IEEE, Vol MAG-10, No 4, December 1974.
- [9] J.Neças. Les methodes directes en theorie des equations elliptiques, MASSON et CIE, 1967.

- [10] P.G.Ciarlet, M.H.Schultz and R.S.Varga, Numerical methods of high order accuracy for nonlinear boundary value problems V, Numer. Math. 51-77 (1969).
- [11] P.G.Ciarlet & P.A.Raviart, General Lagrange and Hermite interpolation in R^n with applications to finite element methods, 12 Arch. Rat. Mech. Anal. vol 46.
- [12] G.Strang, G.J.Fix, An analysis of the finite element method, Prentice Hall Series in automatic computation, 1973.
- [13] MAGGY2, user manual, Philips, UDV-DSA-SCA/AdB/SP/AW/75/022/jf.
- [14] MAGGY2, example set, Philips, UDV-DSA-SCA/AdB/SP/AW/75/025/jf.
- [15] S.J.Polak, MAGGY-A system for magnetic circuit computer aided design, Philips, ISCA-general 003, March 1974.
- [16] S.J.Polak, Some aspects in developing MAGGY, Philips, ISCA MAC-CAD, December 1974.
- [17] S.J.Polak, J.van Welij, Recent developments, Philips, ISCA MAG-CAD 1975, to appear.
- [18] E.C.Stoner and E.P.Wohlfarth, Phil. Trans A240, 599-642, 1948.
- [19] M.Bakker, P.W.Hemker, P.J. van der Houwen, S.J.Polak, M. van Veldhuizen, Colloquium discretiseringsmethoden, MC Syllabus 27, Mathematisch Centrum, Amsterdam 1976.

Discussion following paper:

(Becker, Texas) The issue of loss of accuracy in obtaining gradients of the finite element solution (by numerically differentiating the solution) is a serious one in the analysis of stress and flow problems as well as in the present context. Some techniques that have been used (with a mixed degree of success) includes:

- (a) Use of higher order Lagrangian elements (usually isoparametric) with gradients calculated at appropriate interior points.
- (b) Use of conjugate approximation or other projection methods (as in the work of Oden or of Wheeler).
- (c) Use of mixed or mixed-hybrid models in which the gradients are solved directly.

Have you considered any of these techniques and, if so, how do you view their usefulness?

(Polak, Philips, Eindhoven) The problem mentioned is often encountered by us.

B values can be obtained by higher order Lagrange elements inside the elements.

If $\int H \cdot ds$ has to be calculated over element boundaries I think that Hermite elements with interface conditions would be a good choice.

I am not sufficiently familiar with conjugate approximations and therefore cannot give an opinion on their value for this problem. Then of course in integral methods as in GFUN H is solved directly. However for larger problems the full matrix involved will compare unfavourably with the sparse FEM matrices.

As integral methods and GFUN are enjoying some prominence at this conference it is worthwhile clarifying this point.

For an $n \times n$ problem, the FEM with Choleski and simple elements used $\frac{1}{2}n^4$ operations. For the same problem the integral method would typically involve only $n^2/5$ unknowns which would require $1/3 (1/5n^2)^3$ operations. The factor 5 chosen here is problem dependent but there is always an n for which the FEM becomes cheaper.

Therefore we can say that up to a certain magnitude integral methods should be good for calculating H directly and in general using FEM one has to use appropriate elements.

PHYSICAL BASIS OF THE VARIATIONAL METHOD FOR THE
COMPUTATION OF MAGNETIC FIELD PROBLEMS

P. Hammond, Department of Electrical Engineering,
University of Southampton, England.

1. Introduction

The hallmark of good computational work is accuracy and attention to detail. The skilled worker who has these qualities in mind cannot easily take a detached view of the computation as a whole. In particular he is unlikely to question the need for the computation. Yet such questioning is essential if the physical concepts are to be disentangled from the algebraic and numerical techniques. Engineers who design such devices as transformers and rotating machines are used to thinking in terms of physical models. They use such terms as leakage flux and they represent the device by equivalent circuit parameters. To determine these parameters they need information about the magnetic field. Before the advent of computers this information was difficult to obtain and crude approximations had to be made. Now the opposite difficulty exists. Engineers are often swamped with information, which is not only useless in itself, but actually blocks the design process, because data-handling has become the over-riding difficulty. Under such circumstances the designer turns his back on computation and relies on intuition and experience, much as a physician may do when presented with a large array of chemical test results on a patient. This is of course a pity, but nevertheless it is a real problem. This paper is a plea for better co-operation between computer analysts and designers. It is a plea that the designer should explain to the analyst what information he needs and that the analyst should restrain his desire to show what the computer can do and concentrate instead on providing simple and elegant programs for particular needs. This does not necessarily mean that the big 'suite of programs' should be ignored, but it does mean that the analyst should seek to understand that the pressing need is for solutions to particular problems rather than for information which may be useful one day. Of course this is a big theme and cannot be dealt with in one paper. What can be done here is to illustrate the theme by a particular example. The

example which has been chosen is the method of the calculus of variations which underlies the method of finite elements.

2. The variational method

The development of numerical methods for the solution of magnetic field problems has in general started from a consideration of the differential equations describing the field. These equations have been discretised and by this means a finite-difference mesh has been generated to replace the continuous field distribution. More recently the finite-element method has become popular, which is based on a definite integral or 'functional' of the field energy. Algebraically both methods may lead to similar computation schemes involving the solution of many simultaneous equations. If these equations are taken as the starting point of the computation the choice of method depends only on the past experience of the analyst and the characteristics of the digital computer available.

One might conclude that the physical content of the two methods would also be very similar, but a close examination shows that this is not so. Indeed, the differences can be put to good use in certain cases. Let us consider these differences. The finite-difference method starts with the differential relationships which relate the local field curvature, i.e. the divergence and curl, and the local time-variation of the field, to the local source density. In order to obtain the field in a region the numerical process scans the local source densities and then anchors the mesh to the boundary by imposing given boundary conditions. The finite-element method on the other hand depends on formulating an energy functional and finding its maximum or minimum by a variational technique. In this variational process the differential equation appears as the Euler-Lagrange equation of the functional. If the object of the method were to recover a known equation via an often unknown functional, this would be a strangely circuitous route. A physical interpretation of the functional is needed to make sense of the method.

To arrive at such an interpretation let us take the particular case of a Poissonian field. The functional is known to be $F = \iiint \phi \rho \, dv + \frac{1}{2} \iiint \phi \epsilon \nabla^2 \phi \, dv$, where ϕ is a scalar potential and ρ is a source density. It is convenient to write this in 'inner product' notation

$$F = \langle \phi, \rho \rangle + \frac{1}{2} \langle \phi, \epsilon \nabla^2 \phi \rangle$$

If ρ is taken as an assigned source density and ϕ as a variable, the first

variation of F is given by

$$\delta F = \langle \delta\phi, \rho \rangle + \langle \delta\phi, \epsilon \nabla^2 \phi \rangle.$$

Thus for zero first variation, we have $\epsilon \nabla^2 \phi + \rho = 0$, which is of course Poisson's equation. Thus the functional F is the required one. But where did it come from? Its stationary value is given by

$$F_s = \langle \phi, \rho \rangle - \frac{1}{2} \langle \phi, \rho \rangle = \frac{1}{2} \langle \phi, \rho \rangle,$$

and this is the potential energy of a set of known sources ρ . The potential energy is the 'inter-action' of the sources in terms of the scalar potential ϕ , which in elementary field theory is defined as potential energy per unit source. It is therefore reasonable to start from the functional rather than from the field quantity itself, because the functional has physical significance in terms of energy.

But more remains to be said. Let us generalise the field equation $-\epsilon \nabla^2 \phi = \rho$ by adopting the operator notation $L\phi = \rho$. We then have

$$F = \langle \phi, \rho \rangle - \frac{1}{2} \langle \phi, L\phi \rangle$$

which can be recast into the form

$$F = \frac{1}{2} \langle \phi, \rho \rangle - \frac{1}{2} \langle \phi, L\phi - \rho \rangle.$$

The first term gives the potential energy and the second term introduces the constraint $L\phi = \rho$ by means of the familiar method of a Lagrange multiplier. The method, therefore, seeks the energy of the system of sources ρ subject to the operator equation of the field. Since the designer generally needs to know this energy rather than the field distribution, the method is well adapted to meet his needs. It should be noted that the functional is essentially a system parameter. It is of course possible to divide any system into smaller sub-systems, and if this is done the method is akin to the differential finite-difference method. But the functional can be of arbitrary size and does not need to be subdivided.

3. The adjoint problem

The meaning and the possibilities inherent in the variational method become even clearer if a more general functional is considered. Let there be two sets of sources designated by ρ and ρ^a , and let their associated field quantities be ϕ and ϕ^a . Consider the mutual energy of the two sets of sources. This mutual energy is given by $\langle \phi, \rho^a \rangle = \langle \phi^a, \rho \rangle$. Consider the functional

$$F = \langle \phi, \rho^a \rangle - \langle \phi^a, L\phi - \rho \rangle$$

where ρ^a and ρ are the assigned known values of the sources. To find the stationary value of F we put

$$\delta F = 0 = \langle \delta\phi, \rho^a \rangle - \langle \delta\phi^a, L\phi - \rho \rangle - \langle \phi^a, L\delta\phi \rangle$$

If in the last term we transpose the operator L to another operator L^a , such that

$$\langle \phi^a, L\delta\phi \rangle = \langle L^a \phi^a, \delta\phi \rangle$$

we obtain the two conditions

$$L\phi = \rho \text{ and } L^a \phi^a = \rho^a.$$

The physical significance of this is clear. The first term of the expression

$$F = \langle \phi, \rho^a \rangle - \langle \phi^a, L\phi - \rho \rangle$$

gives the inter-action energy of the sources ρ and ρ^a . Hence the stationary value F_s determines this energy parameter. The parameter is subject to the two-fold condition that ϕ obeys $L\phi = \rho$ and ϕ^a obeys $L^a \phi^a = \rho^a$. The second system is called the adjoint system. The adjoint sources ρ^a are associated with their own field ϕ^a and an adjoint operator L^a . In many cases, such as Laplacian and Poissonian fields, $L = L^a$ and the operators are said to be self-adjoint. An important exception is the diffusion equation, which is not self-adjoint. If $\rho = \rho^a$ the stationary value of the functional F_s gives the self-energy of the system. Otherwise F_s gives the mutual energy of two systems.

On first meeting the adjoint field quantities one may regard them as a peculiarity of the variational method. More than that one may even decide that the appearance of the adjoint problem is a drawback of this method. Such a conclusion is very wide of the mark. The adjoint problem draws attention to the physical basis of field calculation methods in general and provides valuable guidance for the formulation of efficient computation schemes. To understand what is happening it is necessary to go back to the experimental basis of field theory.

Consider for instance the electrostatic field. The entire theory is built on the experimentally observed inter-action of electric charges. In the simplest case two charges act on each other and a mutual potential energy can be associated with the system formed by the two charges. The notion of an electric field only arises when the problem of inter-action is separated into two problems, in which one charge acts as a source for a field which then acts on the other charge. The field is no more or no

less than a useful mental construct which enables the problem to be separated into two stages.

It is therefore not surprising that information about a field distribution is of use to the designer only as far as it can be made to yield further information about such physical matters as force and energy. To put it very bluntly, the designer does not require the field map at all. This is at the root of much of the misunderstanding between computer analysts and designers, which is so common in industry. Of course we are overstating the difficulties, because to the experienced eye a field map does present useful information. Nevertheless it also contains much information which is not useful, namely the field distribution in a region free of matter. Moreover if the information is presented in numerical form, the problem of interpretation becomes well-nigh insoluble.

Since inter-action is the basis of both theory and practice in field problems, it is not surprising that the variational method draws attention to two field equations which have to be satisfied in order to determine the mutual energy for the equilibrium condition. Unless there is an adjoint source, there is no system. A single source by itself is an abstraction which has no counterpart in the physical world. The adjoint problem draws attention to the principle of reciprocity. The energy of a system is always a mutual relationship. Thus the self-energy, as for instance the self-inductance of a circuit is really a mutual energy of the parts of the circuit. The self-inductance is not a property of the material of the wire, but a property of the geometrical arrangement of the parts of the wire relative to each other. In the integration process the elements of the circuit fulfil the role of the adjoint sources as well as the original sources. The adjoint problem therefore coalesces with the original problem. If on the other hand mutual inductance is to be calculated each coil is the adjoint of the other.

4. The adjoint source as a probe of the field

The notion of mutual inductance leads to another important observation about field calculations. Suppose we regard the 'secondary' coil as a probe to be used in examining the field of a set of 'primary' coils. For every position of this probe there will be a mutual inductance between it and the primary coils. We can set up the energy functional as

$$F = \langle \underline{A}, \underline{J}^a \rangle - \langle \underline{A}^a, L \underline{A} - \underline{J} \rangle$$

where \underline{J} are the primary current densities and \underline{J}^a the current densities in the probe. \underline{A} and \underline{A}^a are the vector potentials due to these current densities and L is the operative $\frac{1}{\mu} \nabla \times \nabla \times$ which is also L^a . $\delta F = 0$ leads to $L \underline{A} = \underline{J}$ and $L^a \underline{A}^a = \underline{J}^a$. Suppose we require a map of the field parameter \underline{A} . In order to find \underline{A} at a point, we need to shrink the probe to an infinitesimal current element. However, the probe must carry finite current in its infinitesimal cross-section, because if the current itself were to be infinitesimal there would be no measurable inter-action. Thus the current will have to have infinite density and can be represented by a Dirac δ function. Thus by requiring information about the local distribution of \underline{A} , we have decided that the probe must have the properties of a δ function. Similarly an electrostatic field map requires a probe which is a charge of infinite density and zero volume.

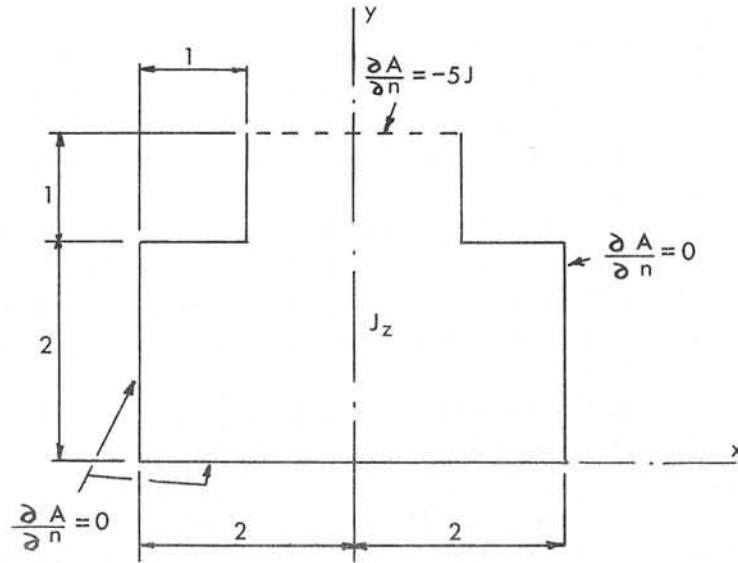
The inter-action energy can be written as either $\langle \underline{A}, \underline{J}^a \rangle$ or $\langle \underline{A}^a, \underline{J} \rangle$. The first form requires the use of the δ function probe and the second requires the use of the Green's function \underline{A}^a . This may be the better choice, but Green's function solutions tend to have slow convergence. The trouble is due to the stringent requirement to find the field at every point. All this information has to be paid for.

If the adjoint source is thought of as a probe designed to elicit information about the field, we notice at once how important it is that the designer should specify to the computer analyst what information he requires. If, for instance, the mutual inductance between two windings of a machine is required, the analyst can choose one of the windings as the 'probe'. Such a large probe will be insensitive to local field variations and this will reduce the computational effort. It would be wasteful to explore the field with a tiny probe and then derive the large-scale energy parameter.

5. An example of a self-inductance calculation

In problems of self-inductance the natural choice of probe is in terms of the assigned current density itself. We then obtain the energy in terms of the integral $\frac{1}{2} \langle \underline{A}, \underline{J} \rangle$. This integral may be insensitive to the actual distribution of \underline{A} and it becomes possible to use a fairly rough approximation for \underline{A} which will still give a close value for the energy and hence the inductance. As an example consider the internal inductance of a T-shaped conductor in a slot in highly-permeable iron as shown in the

figure.



The slot is open at the top and we have assumed that the magnetic field is constant across the opening. There is a uniform current density $J_z = J$ across the section of the conductor, so that the total current is $10J$. The iron is assumed to be infinitely permeable, so that the tangential H along the iron boundary is zero. Hence the tangential field across the opening of the slot is $H_x = -10J/2 = -5J$.

To calculate the internal inductance we have to isolate the conductor from the outside region. This can be done by assuming there to be a surface current across the opening of the slot which gives the correct magnetic field inside the slot and zero field outside. This means there is a current $I = H_x = -5J$ at the slot opening.

The internal inductance of such a conductor has been carefully investigated by various writers. Thus we have accurate values for purposes of comparison with the approximate values we shall derive by means of the variational method. In particular a paper⁽¹⁾ by Jones, Reed, Mullineux and Stoll gives a method from which we deduce that the internal inductance is $L = 0.570 \mu_0$ H/m.

For the variational method we set up the usual functional

$$F = \frac{1}{2} \langle \underline{A}, \underline{J} \rangle + \frac{1}{2} \left| \underline{A}, \underline{I} \right| - \frac{1}{2} \langle \underline{A}, \underline{L} \underline{A} - \underline{J} \rangle$$

where the second term describes the energy associated with the surface current at the slot opening. Thus

$$\begin{aligned} F &= \langle \underline{A}, \underline{J} \rangle + \frac{1}{2} \left| \underline{A}, \underline{I} \right| - \frac{1}{2\mu_0} \langle \underline{A}, \nabla \times \nabla \times \underline{A} \rangle \\ &= \langle \underline{A}, \underline{J} \rangle + \left| \underline{A}, \underline{I} \right| - \frac{1}{2\mu_0} \langle \underline{B}, \underline{B} \rangle \end{aligned}$$

The first variation of F is given by

$$\delta F = \langle \delta \underline{A}, \underline{J} \rangle + \left| \delta \underline{A}, \underline{I} \right| - \frac{1}{\mu} \langle \underline{B}, \delta \underline{B} \rangle = 0$$

We note that $A_x = A_y = 0$ and therefore $B_z = 0$. Also $B_x = \frac{\partial A_z}{\partial y}$ and $B_y = -\frac{\partial A_z}{\partial x}$.

To find an approximate value for the functional and therefore for the inductance we must choose appropriate functions for A_z . A constant value for A_z gives zero magnetic field and therefore does not contribute to the solution. We consider next $A_z = ax + by$. From symmetry $a = 0$, so that we have $A_z = by$. This implies that $B_y = 0$ and $B_x = b$ is a constant. Then

$$\begin{aligned} F &= \langle by, \underline{J} \rangle - \left| 3b, 5J \right| - \frac{1}{2\mu_0} \langle b^2 \rangle \\ &= \int_0^2 \int_{-2}^{+2} J b y \, dx \, dy + \int_2^3 \int_{-1}^{+1} J b y \, dx \, dy - \int_{-1}^{+1} 15 b J \, dx - \frac{5b^2}{\mu_0} \\ &= 8 J b + 5 J b - 30 J b - \frac{5b^2}{\mu_0} \\ &= -17 J b - \frac{5b^2}{\mu_0} \end{aligned}$$

For $\delta F = 0$ we put $\frac{\partial F}{\partial b} = 0$, hence $-17J - \frac{10b}{\mu_0} = 0$ and $b = -1.7\mu_0 J$

Substituting in F we obtain $F = 14.45\mu_0 J^2$ and $L = 0.289\mu_0$, which should be compared with the accurate value $L = 0.570\mu_0$.

We have deliberately chosen a poor approximation in order to illustrate the method. It will have been noted that our choice of A_z implied a constant magnetic field everywhere in the conductor. Since we know that the field is zero at the bottom of the slot and that it has a finite value at the top, our choice is a poor one.

Let us consider an improved trial function $A_z = ay + by^2$, for which $B_x = a + 2by$. In the variational process we put $\frac{\partial F}{\partial a} = 0$ and $\frac{\partial F}{\partial b} = 0$ to obtain a and b . This gives $F = 24.25\mu_0 J^2$ and $L = 0.485\mu_0$. This is

already within 15% of the correct value and may be sufficient for practical purposes. The power of the method is shown by the fact that a close approximation of the inductance has been obtained, although the field pattern is highly inaccurate. For instance at $y = 0$ we know that $B_x = 0$ but on approximation gives $B_x = a = 0.57\mu_0 J$. The reason for the power of the method lies in the fact that it has been designed to find the best value of the energy or the inductance and does not seek to find an accurate flux map. If the designer needs the inductance it is unnecessary and wasteful to find a field. Of course it is desirable to choose a reasonable trial function for the field, but the method is not very sensitive to the actual choice.

In this example we have used the variational method in exactly the same way as it is used in the method of finite elements. The only difference is that the shape of the conductor is somewhat unusual. Moreover most finite-element calculations use a linear relationship for the trial function. Clearly a linear relationship will give adequate closeness of fit over smaller regions. In any case finite-element solutions are not limited to linear representations of the potential. The difference between our method and that of the usual finite-element method does not lie in the mathematical technique, but in the approach to the problem. The finite-element method is generally used to obtain a field map and this, as has been mentioned before, implies a desire for information about the distribution of energy in a region. Our approach on the other hand is to regard the variational method as dealing with a system and seeking the energy of that system in an equilibrium condition.

6. Upper and lower bounds for the functional

One objection which could be raised to the method illustrated by the example of the T-shaped conductor is that the degree of approximation to the accurate solution is in general not known. This is a common failing in numerical methods and is similar to the uncertainty that exists in manufacturing processes. The correct choice of tolerances comes with experience. It is both expensive and useless to call for closer tolerances than those that are needed. But happily the variational method suffers less from uncertainty than many other methods. So far we have used only the equilibrium relationship which sets the first variation of the functional to zero. Further information can be obtained by

considering the second variation. The sign of this variation determines whether the functional is a maximum or a minimum. Thus the functional $F = \langle \underline{A}, \underline{J} \rangle + \left| \underline{A}, \underline{J} \right| - \frac{1}{2\mu_0} \langle \underline{B}, \underline{B} \rangle$ is a maximum at its stationary value, because only the third term contributes to the second variation and its sign is negative.

It is a valuable property of the magnetostatic problem that a dual functional can be formulated which has the same stationary value but as a minimum. Thus the approximate functionals can be used to provide both a lower and an upper bound for the correct value. This greatly reduces the uncertainty.

The dual functional is given by $F' = \frac{\mu_0}{2} \langle \underline{H}, \underline{H} \rangle$. Reverting to our example, the simple choice of $H_y = 0$, $H_x = -\frac{5}{3} y J$ gives $F' = 32.41\mu_0 J^2$ and $L' = 0.648\mu_0$. This provides an upper bound for the inductance. It is interesting to note that if we take the average of this upper bound and the lower bound $L = 0.485\mu_0$ previously obtained, we arrive at $L = 0.567\mu_0$ which is within 1% of the correct value. For a fuller discussion of dual upper and lower bounds the reader is referred to a paper 'The calculation of inductance and capacitance by means of dual energy principles' by the present author and Dr. J. Penman to be published shortly in the Proceedings of the Institution of Electrical Engineers.

7. Variational treatment of the diffusion equation

Finally it may be of interest to look at the treatment of diffusion problems by means of the variational method. Consider an assigned harmonic current distribution $\underline{J}e^{j\omega t}$. In order to obtain a functional independent of time we must choose an adjoint current which has a negative time variation. Thus $\underline{J}e^{-j\omega t}$ is a possible choice. \underline{J} and \underline{J}^* are complex conjugates. The vector potential and the adjoint vector potential are chosen similarly. The operator equation $\underline{L}\underline{A} = \underline{J}$ is given by $\frac{1}{\mu} \nabla \times \nabla \times \underline{A} + j\omega\sigma\underline{A} = \underline{J}$ where σ is the conductivity and hence the operators are $L = \frac{1}{\mu} \nabla \times \nabla \times + j\omega\sigma$, and $L^a = \frac{1}{\mu} \nabla \times \nabla \times - j\omega\sigma$. The complex functional is given by $F = \langle \underline{A}, \underline{J}^* \rangle - \frac{1}{2} \langle \underline{A}, L^a \underline{A} \rangle$. This functional contains both the inductance and resistance. It is very interesting that in this instance the adjoint quantities use a negative time. But of course this is exactly what is done by using the complex conjugate in phasor calculations. Once again the adjoint problem is an essential feature in the determination of the system parameters.

8. Conclusion

In this paper a plea has been made for a better understanding between computer analysts and designers of electrical machines. In particular it is urged that the designer often needs large-scale system parameters rather than the details of a field map. Variational methods are well-adapted to provide this information economically.

9. Reference

1. Jones, D.E., Mullineux, N., Reed, J.R., and Stoll, R.L. : 'Solid rectangular and T-shaped conductors in semi-closed slots', J. Engineering Mathematics 3, 2, 1969, pp.123-135.

Discussion following paper:

(Yeh, Oak Ridge) Could the variational bound approach be as useful when the quantity of interest is not the energy of interaction but some other quantity, eg the field in some region?

(Hammond, Southampton) The variational method seeks a functional, ie a quantity which can be described by a real or complex number. Thus the parameter of interest must be such a number if it is to be obtained by this method. If it is desired to find the field at a point, then this can be done by using a source which has strength unity and placing it at that point. The interaction energy is then equal to the field at the point. A scalar field can be found by a single functional, a vector field needs a vector probe and in general will need three functionals. The method is essentially an energy method, but this is not restrictive if it is realised that energy is what fields are all about.

(Popovic, Belgrade) I should like to agree with Prof Hammond that physical insight is often very important in making useful approximations for magnetic field problems. Frequently we are inclined to write a paper which should be entitled "A very general method for solving arbitrarily large problems with an application to a very small problem", when the small problem could be solved with a much simpler theory.

(Carpenter, Imperial College) The method gives a very neat way of deriving what appears to be a surprisingly accurate solution by simple approximations. But the accuracy depends on the upper and lower approximations being equally displaced from the exact solution. Is this a fortunate accident in the examples given, or can Prof Hammond obtain two solutions generally which are merely equally displaced?

(Hammond) I suspect that one needs to acquire experience with the method and I am still rather inexperienced. However, if the variable function is expressed as a polynomial then the order of the polynomial should probably be the same for the same physical quantity in both the upper and the lower bound. Thus in a linear magnetic material H and B should have the same type of approximation. It is also important to pay attention to the boundary conditions and use the same accuracy, or lack of it, in modelling the two functionals.

(Silvester, McGill) Would Prof Hammond care to indicate the extent of applicability of this theory to non-linear problems?

(Hammond) The method depends on the geometrical relationships of the field, ie on its curl and divergence. It is independent of the constitutive relationships. An analogous statement for networks says that Tellegen's theorem is independent of the linearity of the circuit elements. All that matters is that both Kirchhoff laws hold. If hysteresis is present, the problem would have to be specified by giving information about the initial state as well as the shape of the hysteresis loop.

(Jevons, Birmingham) A practical example of approaching the accurate solution from both sides and averaging the result, occurs in the use of resistance networks to determine circuit parameters of fields problems. Suppose a 'straight' analogue is made and the resistance measured, and then the dual made by interchanging equipotential and flow line boundaries and the resistance again measured. The average of the two measured values is very close to the accurate value for even very coarse meshes. One or two mesh refinements gives rapid convergence to the accurate value.

(Hammond) I have no first-hand experience of resistance analogues and am very grateful to Dr Jevons for confirming that the method works well in such an application.

(Reece, GEC) The machine designer would wish to know not only the self inductance of a tee-bar but also the AC resistance. Is it possible to use the method described in dissipative situations, and hence to obtain AC resistance?

(Hammond) Yes, the functional can be complex and embody both resistance and inductance. This is briefly treated in the last section of the paper. I do not think it is possible to obtain a doubly-bounded solution, however.

(Steel, CERN) Prof Hammond makes an important contribution to the conference in that he reminds us that we should always be aware of the questions which underlie the investigation of fields. This can be illustrated by one of many classical examples in the literature. I chose the determination of the maximum temperature of a thermally well insulated conductor carrying an electric current. If the non-linear relation between thermal and electric conductivities is taken into account then it has been shown by Raymond Holm that

(Steel, continued)

$$V^2 = 8 \int_{T_0}^{T_m} \rho \lambda \, dT$$

V is the potential across the conductor

T_m is the maximum temperature

T_0 is the end temperature.

Note that for pure metals $\rho \lambda \propto T$ and the relation between T_m and V is algebraic and independent of the shape of the conductor!

(Hammond) The example cited by Mr Steel is new to me. It certainly reinforces Mr Steel's comments. It seems to me that the greatest challenge to a teacher is how to foster the gift of physical understanding with which some of his students are endowed.

SOME TECHNIQUES AND APPLICATIONS OF THE FINITE ELEMENT METHOD FOR SOLVING MAGNETIC FIELD PROBLEMS

Eric Munro

IBM Thomas J. Watson Research Center,
Yorktown Heights, New York 10598, U.S.A.

1. Introduction

The finite element method¹ provides a powerful numerical technique for solving magnetic field problems. The author's work in this field has been concerned mainly with using the method to calculate field distributions in magnetic electron lenses^{2,3}, and the computer programs developed for this purpose have recently been published⁴. In this paper, the principles of the method are summarized, the derivation of the finite element equations is explained, and techniques for solving the equations are discussed. Extensions of the method for handling the properties of materials with non-linear magnetization characteristics and permanent magnet materials are described. A technique for calculating the fields due to toroidal deflection coils inside rotationally-symmetric magnetic electron lenses is also presented. Each technique is illustrated by typical computed results, to show the wide range of applications of the method.

2. Principles of the finite element method

The partial differential equation of the boundary-value field problem is first replaced by a corresponding functional, whose minimization is equivalent to solving the original differential equation. The entire region inside the boundary is then divided into many small sub-regions called finite elements. These finite elements may be triangles, quadrilaterals or more complicated shapes. The potential distribution within each element is then approximated by some simple function of position, e.g. a first-order polynomial (first-order elements), a second-order polynomial (second-order elements), or a higher-order polynomial if extreme accuracy is required. Using this approximation, the potential distribution within each element is then expressed as a function of the potentials at mesh-points associated with the element. In this way, the contribution from each element to the overall value of the functional is expressed in terms of the mesh-point potentials. The requirement that the functional is to be minimized is then used to derive a set of algebraic equations, inter-relating the potentials at adjacent mesh-points. These equations are then solved to give the potential at each mesh-point.

3. Derivation of the finite element equations

The derivation of the finite element equations will be illustrated using the magnetic electron lens shown in Fig. 1 as an example. This lens consists of a magnetic circuit, polepieces and coil windings, which all have rotational symmetry about the axis XYZ. If the field distribution is required only in the polepiece region ABCD, this can be calculated using a scalar potential. If the fields are required throughout the entire magnetic circuit region EFGH which includes the coil windings, then a vector potential must be used. Each of these cases will be considered in turn.

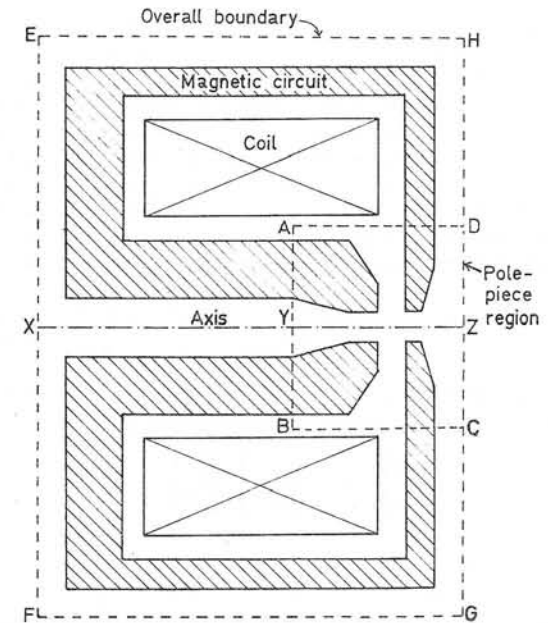


Fig. 1 Cross-section of a typical magnetic electron lens

3.1 Scalar potential formulation

The polepiece region ABCD contains no coil windings. The magnetic field strength \underline{H} throughout this region can therefore be expressed as the gradient of a scalar potential V , i.e.

$$\underline{H} = \underline{\text{grad}} V \quad (1)$$

V satisfies the differential equation

$$\text{div} (\mu \underline{\text{grad}} V) = 0 \quad (2)$$

where μ is the permeability at any point. For linear problems, in which μ is assumed to be independent of \underline{H} , the solution of (2) subject to prescribed boundary conditions can be obtained by minimizing the functional

$$F = \iiint \frac{1}{2} \mu \underline{\text{grad}} V \cdot \underline{\text{grad}} V \, dv \quad (3)$$

subject to the same boundary conditions. (A proof of this can be found in Ref. 2.) For the rotationally-symmetric lens of Fig. 1, (3) becomes

$$F = \iint \frac{1}{2} \mu \left[\left(\frac{\partial V}{\partial z} \right)^2 + \left(\frac{\partial V}{\partial r} \right)^2 \right] 2\pi r \, dz \, dr \quad (4)$$

The functional (4) must now be minimized numerically by the finite element method. To do this, the region to be analyzed is divided by a mesh into small quadrilateral regions (Fig. 2). The mesh lines are chosen to coincide with the polepiece profiles. A fine mesh is used where high accuracy is required; a coarser mesh is used elsewhere. Each quadrilateral is subdivided into two triangular finite elements. This subdivision is done in two separate ways (Fig. 3). A typical finite element is shown in Fig. 4. Let the potentials at the vertices be denoted by $V_i(z_i, r_i)$, $V_j(z_j, r_j)$ and $V_k(z_k, r_k)$. Since in our example we are using first-order finite elements, we make the approximation that the potential varies linearly over the element. With this approximation, the contribution ΔF from a single finite element to the value of the functional (4) is

$$\Delta F = \frac{\pi \mu r_0}{4a} \left[\left(\sum_{i=1}^3 b_i V_i \right)^2 + \left(\sum_{i=1}^3 c_i V_i \right)^2 \right] \quad (5)$$

where μ = permeability of element, r_0 = value of r at centroid of element, a = area of element, $b_i = r_j - r_k$ and $c_i = z_k - z_j$. Differentiating (5) gives

$$\left[\frac{\partial \Delta F}{\partial V_i} \right] = \left[F_{ij} \right] \left[V_i \right] \quad (6)$$

where

$$F_{ij} = \mu \frac{\pi r_0}{2a} (b_i b_j + c_i c_j) \quad (7)$$

Using (7), a 3×3 matrix F_{ij} is calculated for every element of the mesh. Since F_{ij} is symmetric, only six coefficients need be stored for each matrix.

The matrices F_{ij} are now used to set up the finite element equations, by imposing the condition that the functional is to be minimized. To illustrate how this is done, let V_0 be the potential at a general mesh-point (see Fig. 3) and let V_1, V_2, \dots, V_8 be the potentials at the eight adjacent mesh-points. The condition for minimizing the functional is

$$\frac{\partial F}{\partial V_0} = 0 \quad (8)$$

Now, if V_0 is changed, keeping all the other potentials constant, then the corresponding change in the functional will be due only to the changes in the contributions from the twelve shaded elements E_1 - E_{12} in Fig. 3. Thus from equation (8) we obtain

$$\left(\frac{\partial \Delta F}{\partial V_0} \right)_{E_1} + \left(\frac{\partial \Delta F}{\partial V_0} \right)_{E_2} + \dots + \left(\frac{\partial \Delta F}{\partial V_0} \right)_{E_{12}} = 0 \quad (9)$$

By substituting equation (6) for each of the elements E_1 - E_{12} into equation (9), we obtain a nine-point finite element equation of the form

$$\sum_{m=0}^8 P_m V_m = 0 \quad (10)$$

where each coefficient P_m is the sum of appropriate terms of F_{ij} . In this way, a finite element equation is generated for every mesh-point which is not a boundary point. Points which lie on the symmetry axis YZ in Fig. 2 are treated as a special case, and at each of these points a six-point equation is obtained. The prescribed boundary potentials on the boundaries AY , AC and CZ (see Fig. 2) are then inserted into the equations. These equations are then solved, as described in Section 4, to give the potential

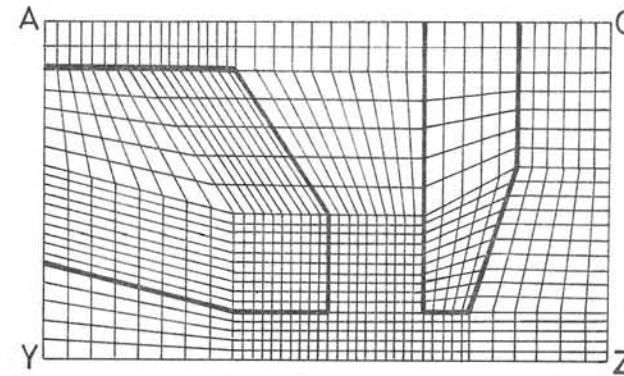


Fig. 2 Finite element mesh for calculating the scalar potential distribution in the polepiece region of the lens of Fig. 1

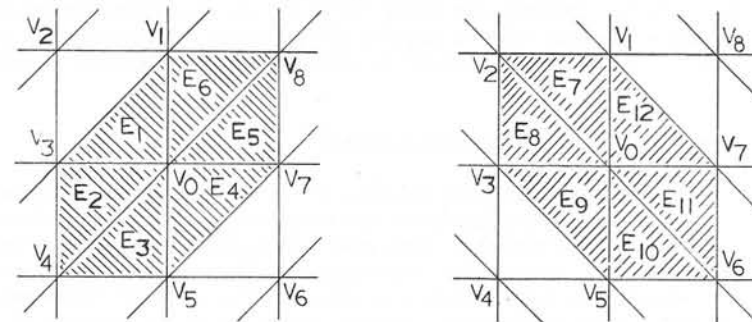


Fig. 3 Subdivision of the quadrilateral regions into triangular finite elements

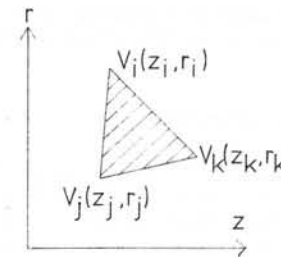


Fig. 4 A typical finite element for the scalar potential formulation

at each mesh-point. The scalar equipotentials can then be plotted out on a computer graph plotter, as shown in Fig. 5, and the field components at any point can be obtained by numerical differentiation of the computed mesh-point potentials.

A similar technique is used for calculating two-dimensional scalar potential distributions in planar (x,y) coordinate systems. In such cases, instead of using the functional (4), the following functional is used:

$$F = \iint \frac{1}{2} \mu \left[\left(\frac{\partial V}{\partial x} \right)^2 + \left(\frac{\partial V}{\partial y} \right)^2 \right] dx dy \quad (11)$$

and equation (7) is replaced by

$$F_{ij} = \frac{\mu}{4a} (b_i b_j + c_i c_j) \quad (12)$$

where μ = permeability of element, a = area of element, $b_i = y_j - y_k$ and $c_i = x_k - x_j$. In all other respects, the analysis of planar fields is identical to the analysis of rotationally-symmetric fields.

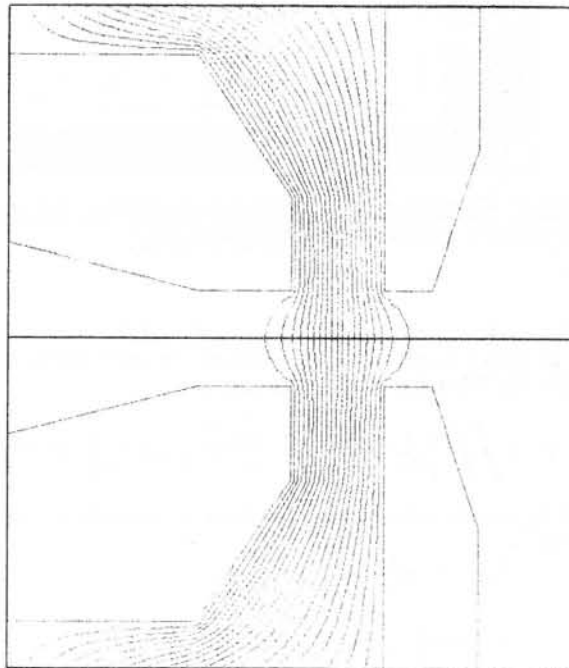


Fig. 5 Computed scalar equipotentials in the polepiece region of the lens of Fig. 1

3.2 Vector potential formulation

To calculate the field distribution throughout the the region EFGH in Fig. 1, which encloses the coil windings, a vector potential must be used, since a scalar potential cannot be used in regions containing currents. The vector potential \underline{A} is defined such that the flux density \underline{B} is the curl of \underline{A} , i.e.

$$\underline{B} = \text{curl } \underline{A} \quad (13)$$

\underline{A} satisfies the differential equation

$$\text{curl } \left(\frac{1}{\mu} \text{curl } \underline{A} \right) = \underline{J} \quad (14)$$

where μ = permeability and \underline{J} = current density at any point. For linear problems, in which μ is assumed to be independent of \underline{B} , the solution of (14) subject to prescribed boundary conditions can be obtained by minimizing the functional

$$F = \iiint \left(\frac{1}{2\mu} \text{curl } \underline{A} \cdot \text{curl } \underline{A} - \underline{J} \cdot \underline{A} \right) dv \quad (15)$$

subject to the same boundary conditions. (A proof of this can be found in Ref. 2.) For the rotationally-symmetric lens of Fig. 1, (15) becomes

$$F = \iint \left\{ \frac{1}{2\mu} \left[\left(\frac{\partial A_\theta}{\partial z} \right)^2 + \left(\frac{\partial A_\theta}{\partial r} + \frac{A_\theta}{r} \right)^2 \right] - J_\theta A_\theta \right\} 2\pi r dz dr \quad (16)$$

where J_θ and A_θ are the θ -components of \underline{J} and \underline{A} respectively. The functional (16) must now be minimized numerically by the finite element method. The procedure for doing this is analogous to that used in the scalar potential formulation. The region to be analysed is first divided into quadrilateral regions (Fig. 6). The mesh lines are chosen to coincide with the profiles of the magnetic circuit and coil windings. A fine mesh is

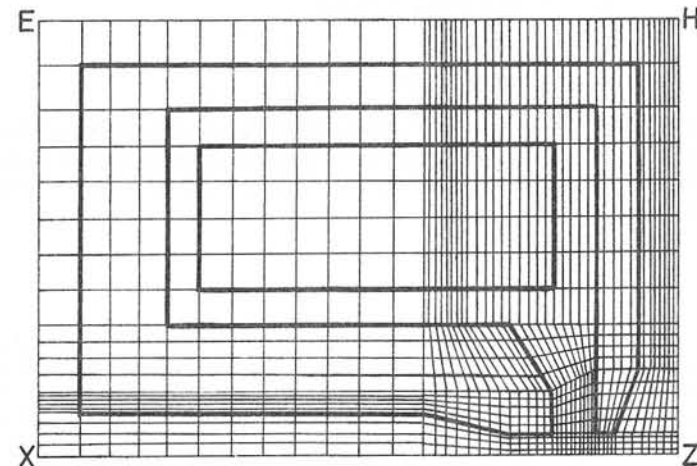
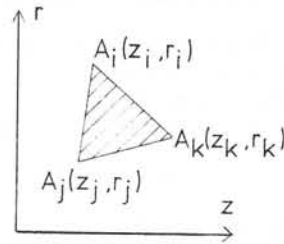


Fig. 6 Finite element mesh for calculating the vector potential distribution throughout the magnetic circuit and coil windings of the lens of Fig. 1

Fig. 7 A typical finite element for the vector potential formulation



used where high accuracy is required; a coarser mesh is used elsewhere. Each quadrilateral is subdivided into two triangular finite elements. This subdivision is done in two ways (Fig. 3). A typical finite element is shown in Fig. 7. Let the values of A_θ at the vertices of the element be denoted by $A_i(z_i, r_i)$, $A_j(z_j, r_j)$ and $A_k(z_k, r_k)$. Making the first-order finite element approximation, i.e. assuming that A_θ varies linearly over the element, we find that the contribution ΔF from a single element to the value of the functional (16) is

$$\Delta F = \frac{\pi r_0}{4\mu a} \left[\left(\sum_{i=1}^3 b_i A_i \right)^2 + \left(\sum_{i=1}^3 d_i A_i \right)^2 \right] - \frac{2}{3} J_\theta \pi r_0 a \left(\sum_{i=1}^3 A_i \right) \quad (17)$$

where μ = permeability of element, r_0 = value of r at centroid of element, a = area of element, $b_i = r_j - r_k$ and $d_i = z_k - z_j + 2a/3r_0$. In obtaining (17) from (16), we have made the approximation that $\int r^m z^n dr dz = z_0^m r_0^n a$, where (z_0, r_0) is the centroid of the element. This approximation is satisfactory provided that the elements are sufficiently small. Differentiating (17) gives

$$\left[\frac{\partial \Delta F}{\partial A_i} \right] = \left[F_{ij} \right] \left[A_i \right] + \left[G_i \right] \quad (18)$$

$$\left. \begin{aligned} \text{where } F_{ij} &= \frac{\pi r_0}{2\mu a} (b_i b_j + d_i d_j) \\ \text{and } G_i &= -\frac{2}{3} J_\theta \pi r_0 a \end{aligned} \right\} \quad (19)$$

Using (19), a 3×3 matrix F_{ij} and a value of G_i are calculated for each finite element. We then proceed to set up the finite element equations, using exactly the same reasoning as for the scalar potential formulation. In this case, each finite element equation has the general form

$$\sum_{m=0}^8 P_m A_m = Q \quad (20)$$

where each coefficient P_m is the sum of appropriate elements of F_{ij} , and Q is the sum of appropriate elements of G_i . The boundary conditions are that $A_\theta = 0$ on the outer boundaries EX, EH and HZ (see Fig. 6), and $A_\theta = 0$ on the axis XZ. These boundary conditions are inserted into the finite element equations. The equations are then solved, as described in Section 4, to give the vector potential A_θ at each mesh-point. The magnetic flux lines (lines of constant rA_θ) can then be plotted on a computer graph plotter, as shown in Fig. 8, and the flux density components at any point can be obtained by numerical differentiation of the computed mesh-point potentials.

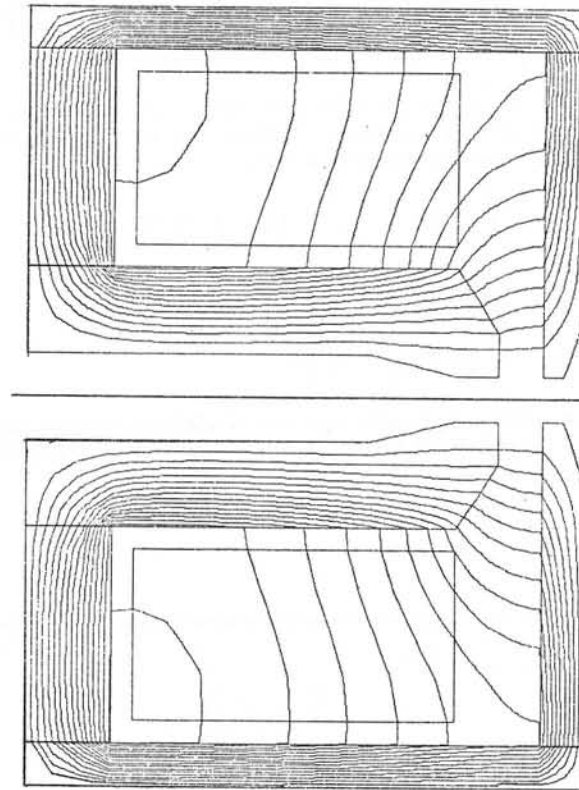


Fig. 8 Computed flux distribution throughout the magnetic circuit and coil windings of the lens of Fig. 1

An analogous technique is used for calculating two-dimensional vector potential distributions in planar (x,y) coordinate systems. In such cases, instead of using the functional (16), the following functional is used:

$$F = \iint \left\{ \frac{1}{2\mu} \left[\left(\frac{\partial A_z}{\partial x} \right)^2 + \left(\frac{\partial A_z}{\partial y} \right)^2 \right] - J_z A_z \right\} dx dy \quad (21)$$

where J_z and A_z are the z -components of J and A respectively; the expressions (19) are replaced by

$$\left. \begin{aligned} F_{ij} &= \frac{1}{4\mu a} (b_i b_j + c_i c_j) \\ \text{and } G_i &= -\frac{1}{3} J_z a \end{aligned} \right\} \quad (22)$$

where μ = permeability of element, a = area of element, $b_i = y_j - y_k$ and $c_i = x_k - x_j$; and the magnetic flux lines are lines of constant A_z . In all other respects, the calculation of vector potential distributions for planar fields is identical to that for rotationally-symmetric fields.

4. Methods for solving the finite element equations

Let there be $I \times J$ mesh-points in Fig. 2 or Fig. 6, and let them be numbered sequentially, column by column, as shown in Fig. 9. Then, if the finite element equations for each mesh-point are arranged in this same order, the matrix of coefficients will appear as shown in Fig. 10. This matrix contains nine non-zero diagonals, corresponding to the nine coefficients in each equation. This matrix will always be symmetric, because the constituent finite element matrices F_{ij} (see equation (7) or (12)) are themselves symmetric. Consequently, only five coefficients need be stored for the left-hand side of each equation. The equation for the $(i,j)^{th}$ mesh-point can therefore be written in the following form:

$$\begin{aligned}
 &P_{i-1,j-1,5} V_{i-1,j-1} + P_{i,j-1,4} V_{i,j-1} + P_{i+1,j-1,3} V_{i+1,j-1} \\
 &+ P_{i-1,j,2} V_{i-1,j} + P_{i,j,1} V_{i,j} + P_{i,j,2} V_{i+1,j} \\
 &+ P_{i,j,3} V_{i-1,j+1} + P_{i,j,4} V_{i,j+1} + P_{i,j,5} V_{i+1,j+1} = Q_{i,j} \quad (23)
 \end{aligned}$$

The most straightforward way of solving these equations is by gaussian elimination and backward substitution, using a symmetric banded matrix subroutine⁵. This is the approach adopted by the author in his programs⁴. As the gaussian elimination proceeds, all the coefficients which lie between the outermost non-zero diagonals in Fig. 10 become filled with non-zeros. Since the matrix is symmetric, it is sufficient to store only the upper half of the band. Thus $(I+2)$ coefficients must be stored per equation, or a total of $(I+2)IJ$ coefficients for all the equations. Hence this method becomes very expensive on storage if large numbers of mesh-points are used. For example, the maximum mesh-size which the author has used with this method is 70×100 mesh-points. With each variable stored in double precision mode (8 bytes), approximately 4 megabytes of storage were required; this is feasible on a large computer, such as an IBM 370/168, with virtual storage capability⁶. Despite the expensive storage penalty, the gaussian elimination method has the great advantage that the solution is obtained directly, so that there are no questions of convergence or choice of iteration parameters to consider.

Polak⁷ has greatly alleviated the storage problem for the gaussian elimination technique by storing most of the band matrix on a disc file, and only operating on a small block of the matrix in main storage at any given time.

For very large mesh-sizes, it may be preferable to use some iterative technique, such as successive over-relaxation⁸, the alternating-direction implicit method⁹, or approximate matrix factorization techniques, such as Stone's method¹⁰ or Dupont, Kendall and Rachford's method¹¹. With such techniques, the storage required is directly proportional to the number of mesh-points. The author has experimented with these techniques, and the general conclusion is that they work satisfactorily if suitable iteration parameters are chosen, but in all cases the convergence is slow and no rational basis has been found for choosing the iteration parameters in the case of complicated problems of practical importance. More study is required before the relative advantages of each method can be satisfactorily compared. The storage requirements and number of arithmetic operations for each method is summarized in Table 1.

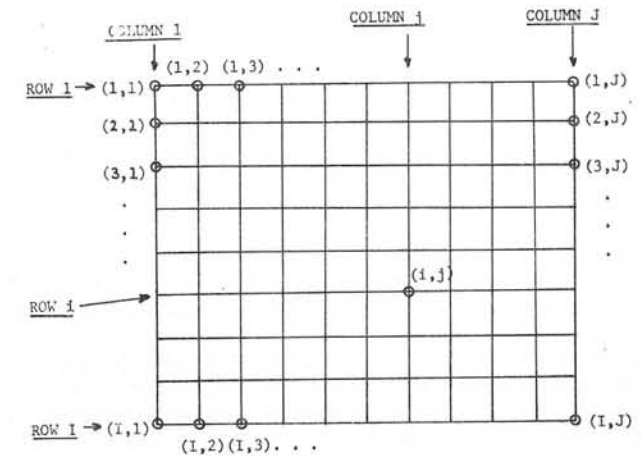


Fig. 9 Numbering of the $I \times J$ mesh-points column by column

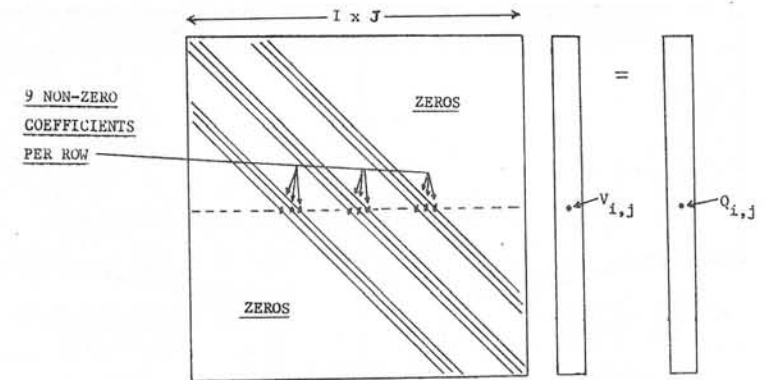


Fig. 10 The finite element equations written in matrix form

Method	No. of variables to be stored	No. of arithmetic operations required
Gaussian elimination	$(I+3) IJ$	$I^3 J$
Successive over-relaxation	6 IJ	19 IJN
Alternating-direction implicit method	7 IJ	20 IJN
Stone's method	14 IJ	40 IJN
Dupont, Kendall and Rachford's method	11 IJ	34 IJN

Table 1 Storage and time requirements for various methods of solving the equations ($I \times J$ = no. of mesh-points; N = number of iterations)

5. Illustrative examples of computed flux distributions

A useful application of the vector potential formulation has been the analysis of electron lenses with superconducting polepieces¹². Fig. 11 shows a typical example. The superconducting polepieces exclude magnetic flux (the Meissner effect), thus producing a very concentrated focusing field in the centre of the lens. The Meissner effect is simulated in the program simply by setting the relative permeability of the superconducting polepieces to a very small value, e.g. 10^{-6} .

The vector potential formulation has also proved particularly useful in analysing a type of electron lens called a 'snorkel lens', which was invented by Mulvey¹³. Fig. 12 shows a typical example, together with the computed flux distribution. A beam of electrons approaching the lens from the left is focused by the magnetic field in front of the 'snout' of the snorkel lens. Since the direct influence of the coil windings on the focusing field must be taken into account, such lenses could not be analysed by previous finite difference methods which used a scalar potential formulation. The properties of a range of such snorkel lenses have been calculated by the finite element method, and the results have been published in a recent paper¹⁴.

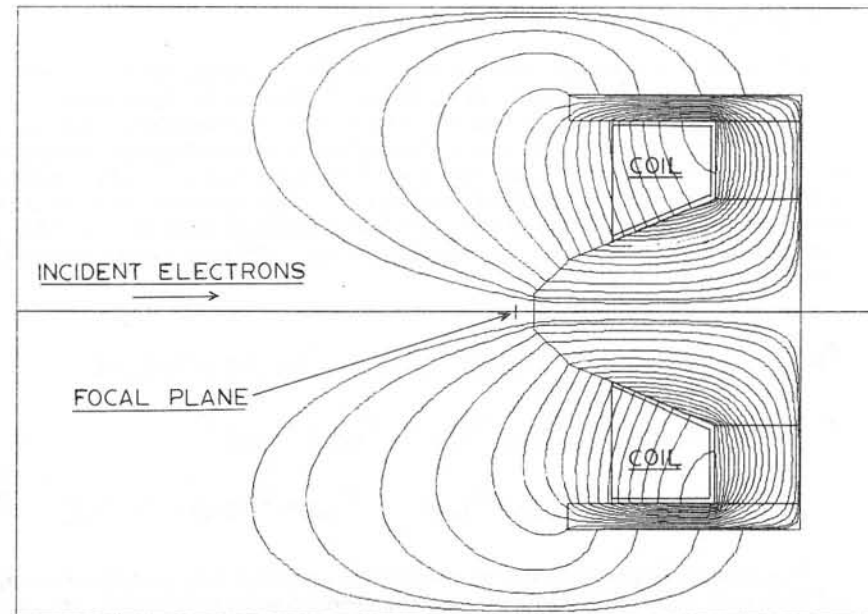


Fig. 12 Computed flux distribution for a snorkel lens

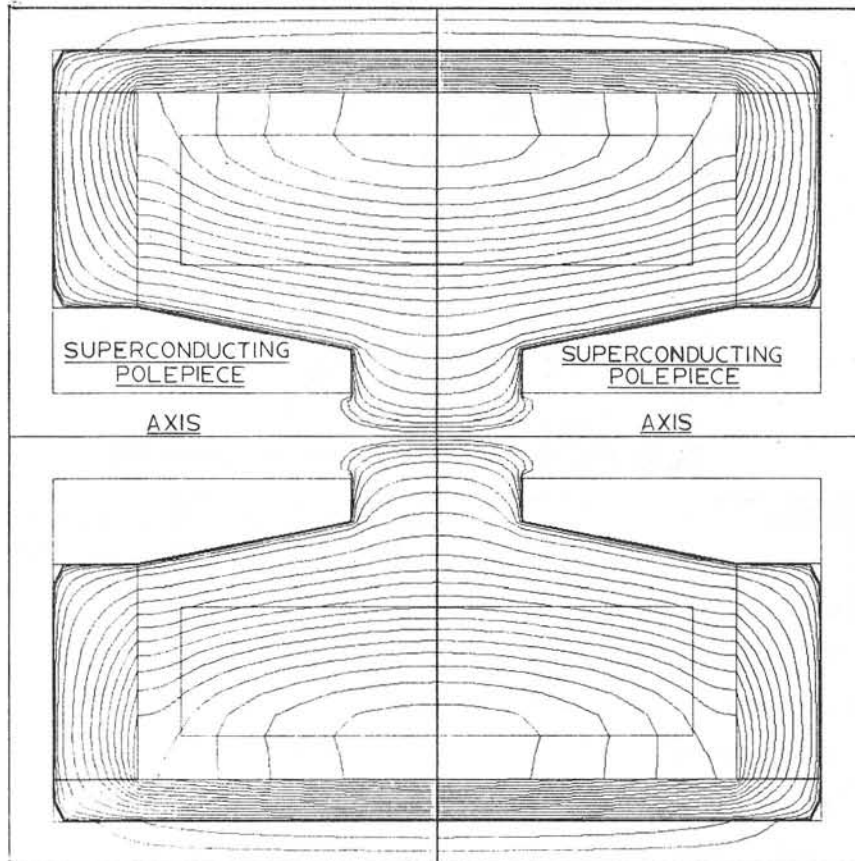


Fig. 11 Computed flux distribution in a lens with superconducting polepieces

6. Solution of non-linear problems

The functionals (3) and (15) are valid only for linear problems, for which the permeability μ is assumed to be independent of the field strength H . In this section, the method is extended to solve field problems involving magnetic materials with non-linear magnetization characteristics, such as shown in Fig. 13. We define two quantities U_c and U (see Fig. 13) as follows:

$$\left. \begin{aligned} U_c(H_1) &= \int_0^{H_1} B \, dH = \text{complementary energy/unit volume} \\ U(B_1) &= \int_0^{B_1} H \, dB = \text{stored energy/unit volume} \end{aligned} \right\} (24)$$

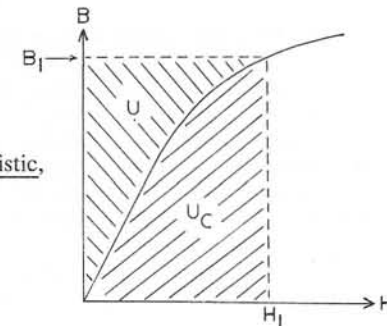


Fig. 13 A non-linear magnetization characteristic, showing the definitions of U and U_c

Then the appropriate functionals to be minimized for non-linear problems are as follows:

For scalar potential problems, the linear functional (3) is replaced by

$$F = \iiint U_c \, dv \tag{25}$$

and for vector potential problems, the linear functional (15) is replaced by

$$F = \iiint (U - \underline{j} \cdot \underline{A}) \, dv \tag{26}$$

(A proof of the validity of these functionals can be found in Ref. 2.) Since the functionals (25) and (26) are non-linear, the resulting finite element equations are also non-linear. These equations have the general form

$$\frac{\partial F}{\partial V_i} = f_i(V_1, V_2, \dots, V_n) = 0, \quad i=1, n \tag{27}$$

where F is the value of the functional, V_i is the potential at the i^{th} mesh-point, f_i is a non-linear function of the mesh-point potentials and n is the number of finite element equations. These non-linear equations can be solved iteratively by Newton's method. To do this, an initial approximation to the solution is calculated using a constant permeability. Let this initial approximation be denoted by $[V_i^I]$. A set of residuals $[r_i]$ and a Jacobian matrix $[J_{ij}]$ are then calculated, whose general elements are defined as

$$r_i = f_i(V_1^I, V_2^I, \dots, V_n^I) \tag{28}$$

$$J_{ij} = \frac{\partial f_i}{\partial V_j} (V_1^I, V_2^I, \dots, V_n^I) \tag{29}$$

From equation (27), it follows that

$$r_i = \frac{\partial F}{\partial V_i} (V_1^I, V_2^I, \dots, V_n^I) \tag{30}$$

$$J_{ij} = \frac{\partial^2 F}{\partial V_i \partial V_j} (V_1^I, V_2^I, \dots, V_n^I) \tag{31}$$

To calculate r_i and J_{ij} , we invoke the fact that if V_i is changed, the resulting change in F is due solely to changes in the contributions ΔF to the functional from the twelve finite elements E_1 - E_{12} in the neighbourhood of V_i (see Fig. 3). Thus from (30) and (31) we obtain

$$r_i = \left(\frac{\partial \Delta F}{\partial V_i} \right)_{E_1} + \left(\frac{\partial \Delta F}{\partial V_i} \right)_{E_2} + \dots + \left(\frac{\partial \Delta F}{\partial V_i} \right)_{E_{12}} \tag{32}$$

$$J_{ij} = \left(\frac{\partial^2 \Delta F}{\partial V_i \partial V_j} \right)_{E_1} + \left(\frac{\partial^2 \Delta F}{\partial V_i \partial V_j} \right)_{E_2} + \dots + \left(\frac{\partial^2 \Delta F}{\partial V_i \partial V_j} \right)_{E_{12}} \tag{33}$$

r_i and J_{ij} are calculated for each finite element equation using (32) and (33). The changes δV_i to be applied to the mesh-point potentials are then calculated by solving the matrix equation

$$\begin{bmatrix} J_{ij} \end{bmatrix} \begin{bmatrix} \delta V_i \end{bmatrix} = - \begin{bmatrix} r_i \end{bmatrix} \tag{34}$$

The matrix $[J_{ij}]$ has the same symmetric banded structure as the finite element coefficients, and so (34) can be solved using any of the methods discussed earlier. Having solved for $[\delta V_i]$, the new approximation to the potentials is given by

$$\begin{bmatrix} V_i^{II} \end{bmatrix} = \begin{bmatrix} V_i^I \end{bmatrix} + \begin{bmatrix} \delta V_i \end{bmatrix} \tag{35}$$

$[V_i^{II}]$ is then used as the starting point for the next iteration. This cycle is repeated until all the residuals are negligibly small. The resulting potential distribution is the solution of the finite element equations (27). As an example, Fig. 14 shows the flux distribution in the lens of Fig. 1 at a very high excitation, computed using a non-linear magnetization characteristic. Comparison with the corresponding linear solution of Fig. 8 shows that the magnetic saturation at high excitations produces non-linear flux leakage in the back bore of the lens.

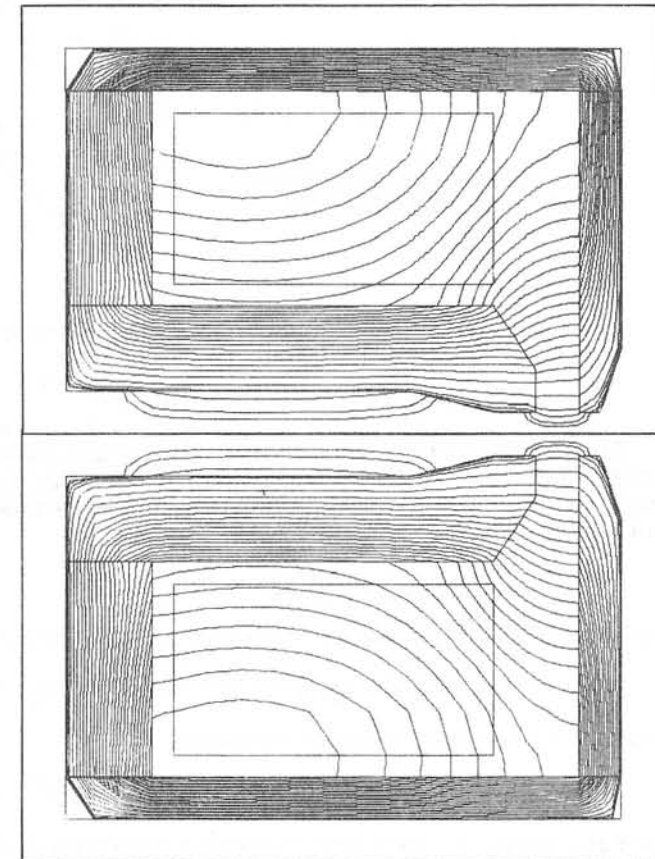


Fig. 14 Computed flux distribution for the lens of Fig. 1 under saturation conditions

7. Solution of problems involving permanent magnet materials

In Section 3, we described how to solve field problems involving magnetic materials with linear magnetization characteristics of the form

$$\underline{B} = \mu \underline{H} \tag{36}$$

where \underline{B} = flux density, \underline{H} = field strength and μ = permeability. In this section, we extend this method to the solution of problems involving permanent magnet materials with magnetization characteristics of the form

$$\underline{B} = \mu (\underline{H} + \underline{H}_c) \tag{37}$$

where \underline{H}_c = 'coercive field strength', which is assumed to be a constant for the material. The type of magnetization characteristic corresponding to (37) is shown in Fig. 15.

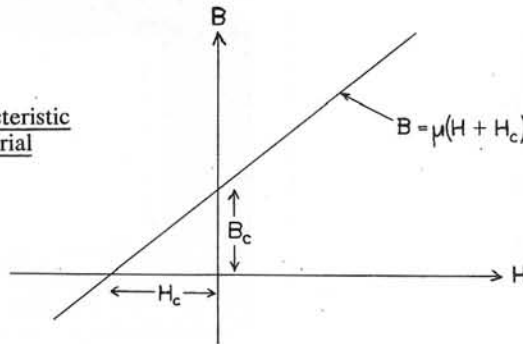


Fig. 15 Magnetization characteristic for a permanent magnet material

For the scalar potential formulation, we proceed in a manner analogous to that described in Section 3.1. The scalar potential V is still defined as in equation (1), but since \underline{B} and \underline{H} are now related by (37) instead of (36), the differential equation (2) must be replaced by

$$\text{div} \left[\mu (\underline{\text{grad}} V + \underline{H}_c) \right] = 0 \tag{38}$$

The functional whose minimization corresponds to the solution of (38) is

$$F = \iiint \frac{1}{2} \mu (\underline{\text{grad}} V + \underline{H}_c) \cdot (\underline{\text{grad}} V + \underline{H}_c) dv \tag{39}$$

For rotationally-symmetric systems, (39) becomes

$$F = \iint \frac{1}{2} \mu \left[\left(\frac{\partial V}{\partial z} + H_{cz} \right)^2 + \left(\frac{\partial V}{\partial r} + H_{cr} \right)^2 \right] 2\pi r dz dr \tag{40}$$

where H_{cz} and H_{cr} are the z and r components respectively of the coercive field \underline{H}_c . For a triangular finite element, the contribution ΔF to the value of the functional (40) is

$$\Delta F = \mu \pi r_0 a \left\{ \left[\frac{1}{2a} \left(\sum_{i=1}^3 b_i V_i \right) + H_{zc} \right]^2 + \left[\frac{1}{2a} \left(\sum_{i=1}^3 c_i V_i \right) + H_{rc} \right]^2 \right\} \tag{41}$$

where r_0 , a , b_i and c_i are as defined for equation (5). Differentiating (41) gives

$$\left[\frac{\partial \Delta F}{\partial V_i} \right] = \left[F_{ij} \right] \left[V_j \right] + \left[G_i \right] \tag{42}$$

where

$$\left. \begin{aligned} F_{ij} &= \frac{\mu \pi r_0}{2a} (b_i b_j + c_i c_j) \\ \text{and } G_i &= \mu \pi r_0 (b_i H_{zc} + c_i H_{rc}) \end{aligned} \right\} \tag{43}$$

The 3×3 matrix F_{ij} and the 3-component vector G_i are calculated using (43) for every finite element. The finite element equations are then set up using F_{ij} and G_i in exactly the same way as described in Section 3.1.

For permanent magnet problems in planar (x,y) coordinates, the expressions for F_{ij} and G_i corresponding to (43) are

$$\left. \begin{aligned} F_{ij} &= \frac{\mu}{4a} (b_i b_j + c_i c_j) \\ \text{and } G_i &= \frac{\mu}{2} (b_i H_{xc} + c_i H_{yc}) \end{aligned} \right\} \tag{44}$$

where b_i and c_i are as defined for equation (12), and H_{xc} and H_{yc} are the x and y components of the coercive field \underline{H}_c .

For the vector potential formulation for permanent magnet materials, we rewrite (37) in the form

$$\underline{H} = \frac{1}{\mu} (\underline{B} - \underline{B}_c) \tag{45}$$

where $\underline{B}_c = \mu \underline{H}_c$ is the 'remanent flux density' (see Fig. 15). The vector potential \underline{A} is still defined as in equation (13). However, since \underline{B} and \underline{H} are now related by (45), the differential equation (14) must be replaced by

$$\underline{\text{curl}} \left[\frac{1}{\mu} (\underline{\text{curl}} \underline{A} - \underline{B}_c) \right] = \underline{J} \tag{46}$$

The functional whose minimization corresponds to the solution of (46) is

$$F = \iiint \left[\frac{1}{2\mu} (\underline{\text{curl}} \underline{A} - \underline{B}_c) \cdot (\underline{\text{curl}} \underline{A} - \underline{B}_c) - \underline{J} \cdot \underline{A} \right] dv \tag{47}$$

For rotationally-symmetric systems, (47) becomes

$$F = \iint \left\{ \frac{1}{2\mu} \left[\left(\frac{\partial A_\theta}{\partial z} + B_{c\theta} \right)^2 + \left(\frac{\partial A_\theta}{\partial r} + \frac{A_\theta}{r} - B_{c\theta} \right)^2 \right] - J_\theta A_\theta \right\} 2\pi r dz dr \tag{48}$$

where B_{cz} and B_{cr} are the z and r components of the remanent flux density \underline{B}_c . For a triangular finite element, the contribution ΔF to the value of the functional (48) is

$$\Delta F = \frac{\pi r_0 a}{\mu} \left\{ \left[\frac{1}{2a} \left(\sum_{i=1}^3 b_i A_i \right) + B_{cr} \right]^2 + \left[\frac{1}{2a} \left(\sum_{i=1}^3 d_i A_i \right) - B_{cz} \right]^2 \right\} - \frac{2}{3} \pi J_\theta r_0 a \left(\sum_{i=1}^3 A_i \right) \tag{49}$$

where r_0 , a , b_i and d_i are as defined for equation (17). Differentiating (49) gives

$$\left[\frac{\partial \Delta F}{\partial A_i} \right] = \left[F_{ij} \right] \left[A_j \right] + \left[G_i \right] \tag{50}$$

where

$$F_{ij} = \frac{\pi r_0}{2\mu a} (b_i b_j + d_i d_j)$$

and

$$G_i = \frac{\pi r_0}{\mu} (b_i B_{cr} - d_i B_{cz}) - \frac{2}{3} J_\theta \pi r_0 a$$

$$\left. \begin{aligned} & \\ & \end{aligned} \right\} (51)$$

The expressions (51) then replace the expressions (19) in the generation of the finite element equations.

For problems involving permanent magnet materials in planar (x,y) coordinates, the expressions corresponding to (51) are

$$F_{ij} = \frac{1}{4\mu a} (b_i b_j + c_i c_j)$$

$$G_i = \frac{1}{2\mu} (b_i B_{cy} - c_i B_{cx}) - \frac{1}{3} J_z a$$

$$\left. \begin{aligned} & \\ & \end{aligned} \right\} (52)$$

where b_i , c_i and J_z are as defined for equation (22), and B_{cx} and B_{cy} are the x and y components of the remanent flux density \underline{B}_c .

A typical application of this technique is shown in Figs. 16 and 17. It is a solution in planar (x,y) coordinates of a magnetic circuit containing an outer soft iron yoke of square cross-section, four tapered permanent magnets oriented so as to produce a quadrupole field, and four tapered soft iron polecaps. This might represent, for example, a permanent magnet quadrupole electron lens, or a permanent magnet four-pole stator for an electric motor. Fig. 16 shows the computed scalar potential distribution and Fig. 17 shows the computed vector potential distribution.

8. Calculation of the fields due to toroidal deflection coils inside rotationally-symmetric electron lenses

The concept of deflecting an electron beam by a toroidal deflection yoke located centrally inside a magnetic lens (Fig. 18) as a means of reducing the aberrations of an electron beam scanning system was first proposed by Pfeiffer¹⁵. In such systems, the rotationally-symmetric magnetic circuit of the lens has a significant influence on the deflection field. A method which has been devised for analysing such systems¹⁶ will be summarized here. The current loading in the yoke is first expressed as a Fourier series of harmonic components, thus:

$$f(\theta) = (NI)_1 \sin \theta + (NI)_3 \sin 3\theta + (NI)_5 \sin 5\theta + \dots \quad (53)$$

where $(NI)_n$ represents the number of ampere-turns in the n^{th} harmonic. Then it can be proved that the field components due to the n^{th} harmonic of the current loading have the general form:

$$\left. \begin{aligned} H_z &= \frac{\partial \Phi}{\partial z} \cos n\theta & H_r &= \frac{\partial \Phi}{\partial r} \cos n\theta \\ H_\theta &= -\frac{1}{n\mu} \left[\frac{\partial}{\partial r} (\mu r \frac{\partial \Phi}{\partial r}) + \frac{\partial}{\partial z} (\mu r \frac{\partial \Phi}{\partial z}) \right] \sin n\theta \end{aligned} \right\} (54)$$

where Φ is a scalar function of z and r , and μ is the permeability at any point. $\Phi(z,r)$ satisfies the following differential equation:

$$\frac{\partial}{\partial r} (\mu r \frac{\partial \Phi}{\partial r}) - \frac{n^2 \mu \Phi}{r} + \frac{\partial}{\partial z} (\mu r \frac{\partial \Phi}{\partial z}) = -\frac{n\mu (NI)_n g(r,z)}{r} \quad (55)$$

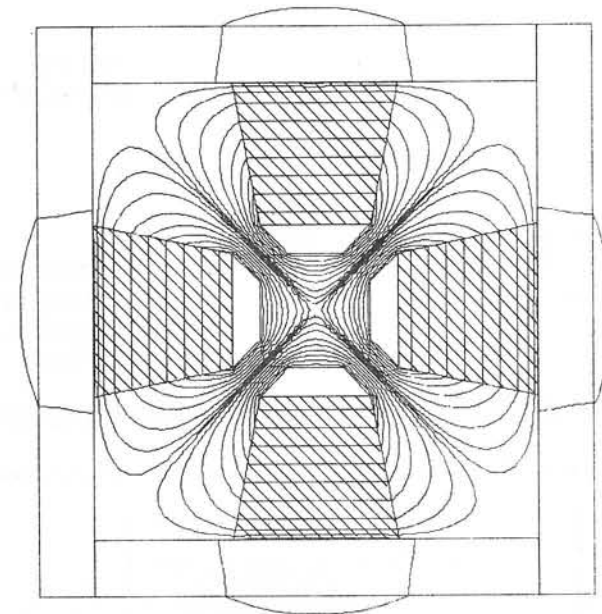


Fig. 16 Computed scalar potential distribution in a permanent magnet quadrupole lens (the permanent magnets are indicated by cross-hatching)

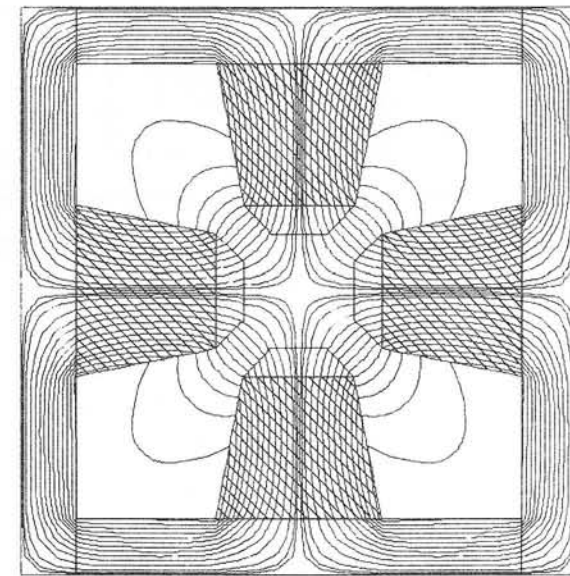


Fig. 17 Computed vector potential distribution in a permanent magnet quadrupole lens (the permanent magnets are indicated by cross-hatching)

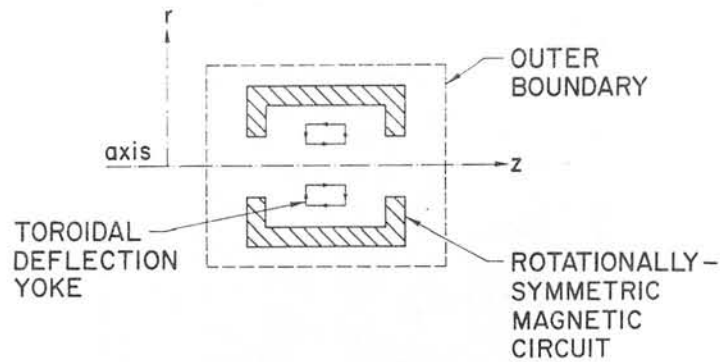


Fig. 18 A toroidal deflection coil inside a rotationally-symmetric magnetic electron lens

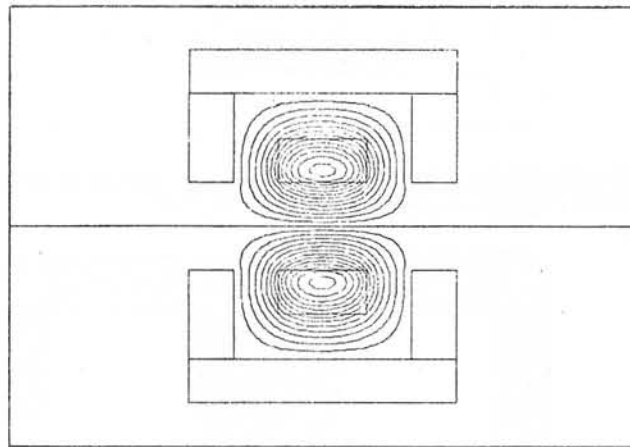


Fig. 19 Computed distribution of $\Phi(z,r)$ for a toroidal-coil-in-lens problem

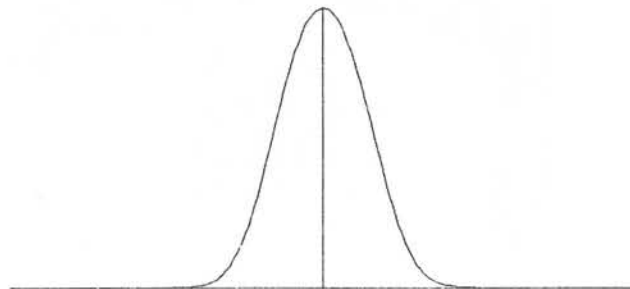


Fig. 20 Computed deflection field at the axis for the system shown in Fig. 19

where $g(z,r) = 1$ inside the cross-section of the deflection coil and $g(z,r) = 0$ outside the coil, and $\Phi(z,r) = 0$ on the outer boundary and also on the axis. The functional whose minimization corresponds to the solution of (55) is

$$F = \iiint \left\{ \mu r \left[\left(\frac{\partial \Phi}{\partial r} \right)^2 + \left(\frac{n \Phi}{r} \right)^2 + \left(\frac{\partial \Phi}{\partial z} \right)^2 \right] - \frac{2n\mu (NI)_n \Phi g}{r} \right\} dr dz \quad (56)$$

The functional (56) can then be minimized numerically using the finite element method to give the function $\Phi(z,r)$, and then the field components can be calculated using (54).

As an example, Fig. 19 shows the computed distribution of $\Phi(z,r)$ for the first harmonic ($n=1$) of a typical toroidal-yoke-in-lens problem, and Fig. 20 shows the corresponding computed transverse deflection field at the axis.

9. Conclusions

The principles of the finite element method and some of its applications in solving boundary-value static magnetic field problems have been described. The method can handle complicated magnetic circuit geometries, finite permeabilities, magnetic saturation effects and the properties of permanent magnet materials.

References

1. O.C. Zienkiewicz and Y.K. Cheung (1965), *The Engineer*, **220**, 507-510.
2. E. Munro (1972), 'Computer-Aided Design Methods in Electron Optics', Ph.D. Thesis, Cambridge.
3. E. Munro (1973), 'Computer-Aided Design of Electron Lenses by the Finite Element Method', in 'Image Processing and Computer-Aided Design in Electron Optics', P.W. Hawkes, ed., Academic Press, London, 284-323.
4. E. Munro (1975), 'A Set of Computer Programs for Calculating the Properties of Electron Lenses', Cambridge University Engineering Department Report CUED/B-ELECT/TR 45 (1975).
5. IBM Publication GH20-0205-4, 'System/360 Scientific Subroutine Package' (1970), 137-142.
6. IBM Publication GC20-1800-1, 'IBM Virtual Machine Facility/370 Introduction' (1973), 10-11.
7. S.J. Polak (1974), Private Communication.
8. S.P. Frankel (1950), *Math. Tables Aids Comput.*, **4**, 65-75.
9. D.W. Peaceman and H.H. Rachford (1955), *J. Soc. Indust. Appl. Math.*, **3**, 28-41.
10. H.L. Stone (1968), *SIAM J. Numer. Anal.*, **5**, 530-558.
11. T. Dupont, R.P. Kendall and H.H. Rachford (1968), *SIAM J. Numer. Anal.*, **5**, 559-573.
12. I. Dietrich, H. Pfisterer and R. Weyl (1969), *Z. angew. Phys.*, **28**, 35-39.
13. T. Mulvey (1972), British Patent Application 40888/72, 'Improvements in or relating to magnetic lenses'.
14. E. Munro and O.C. Wells (1976), 'Some Comments on the Design of Magnetic Lenses for the Scanning Electron Microscope', Proc. 9th Annual Scanning Electron Microscope Symposium, IIT Research Institute, Chicago.
15. H.C. Pfeiffer (1974), Proc. 8th International Congress on Electron Microscopy, Canberra, Australia, 56-57.
16. E. Munro (1975), *J. Vac. Sci. Technol.*, **12**, 1146-1150.

Discussion following paper:

(Ohiwa, Cambridge) In the field of electron optics, the quantities required are the magnetic field and its derivatives with respect to Z rather than magnetic potential. Therefore, it is necessary to carry out numerical differentiation to obtain these quantities; losing significance in doing so. How do you cope with this? Could you give me some idea of the accuracy of the calculated field in terms of the number of mesh points, required storage, and computer time?

(Munro, IBM, USA) I have carried out the numerical differentiation with respect to Z by using a cubic spline technique which ensures continuity of the first and second derivatives. For most applications, I generally have used a mesh of about 25×50 points, which generally enables the axial field distribution to be calculated to an accuracy of about 1%. For this mesh size, the storage required on an IBM 370/168 is approximately 250 kilobytes with all the variables stored in double precision mode, and the solution time is of the order of a few seconds. The maximum mesh size I have handled is about 80×100 points. In any given application, the accuracy of the results can be estimated by first solving the problem with a relatively coarse mesh, and then repeating the calculation with twice as many mesh points in each direction. In the latter case, the result will be about four times more accurate than in the former case, and this enables an estimate of the upper bound of the errors to be obtained.

(Diserens, Rutherford) When you calculate the fields from potentials do you apply any smoothing at this stage? How many points do you use in each field calculation?

(Munro) I have generally calculated the field distribution along the axis using a cubic spline technique which ensures continuity of the first and second derivatives. In this technique, I have not used any initial smoothing of the potential values at the mesh points. In the case of field components at internal mesh points, I have calculated the field components at the centroid of each quadrilateral region using the computed potential values at the four corners of the quadrilateral.

(Trowbridge, Rutherford) The calculation of magnetic lens aberrations requires the integral of the field to be calculated through the fringe field of the magnet - how did you ensure that the remote boundary in your computer model was sufficiently far away?

(Munro) No special techniques were used, however the position of the external boundary was varied to ensure that this effect could be made negligible.

(Jacobs, CERL) Dr Munro illustrates some interesting comparisons of various direct and iterative solution procedures. For the nine diagonal coefficient matrix with its special symmetric sparsity layout, the Strongly Implicit Procedure (Stone's method) would generally use a factorization into lower and upper triangular factors each with only five non-zero diagonals. Alternatively the factorization of the standard five diagonal matrix would be used in conjunction with a "modified" iterative scheme, where in essence, the other diagonal coefficients are relegated to the right hand side of the equation to add to the excitation source term. The important attribute of SIP is the marked lack of importance of accurate parameter selection. However, I believe the very special form of the matrix enables Gaussian elimination to be used with only very limited fill in. The method would eliminate the elements of the 1st column using the first row, then the elements of the $(I + 1)$ st column using the $(I + 1)$ st row; etc. The total number of operations is then proportional to IJ .

(Munro) I appreciate your comments on alternative implementations of Stone's method as it applies to nine-point equations, and I intend to try out both your suggestions, namely using triangular matrices with fine non-zero diagonals instead of four, and relegating the potentials at the corner nodes to the right-hand side of the equation. As regards your comments about the ability to perform Gaussian elimination of my banded matrix equation in a number of operations proportional to IJ , I do not think that this is possible, but I would very much like to hear a detailed algorithm for your proposed scheme, since if what you suggest is in fact possible, it would certainly represent a significant breakthrough in the direct solution of banded sparse matrix equations.

(Fox, Oxford) (1) I would like to ask if you used any special ordering in the equations for Gauss elimination. This is important, and for example the "optimal" ordering of F A George involves much less computer time and storage. (2) Following up Dr Jacob's remarks on the Stone method, it appears that the parameters are less important than the B matrix in $LU = A + B$, where L and U are your triangular matrices. It seems to be desirable, in current language, for $A + B$ to have second-order comparability

(Fox, continued) with A, and I am not sure whether or not you looked into this. (3) You also mentioned a method by Dupont et al. They virtually put a parameter on the right-hand side of the equations, and Stone puts one on the left. I have heard of recent work in America in which somebody is trying to get the best of both worlds by putting parameters on both sides. I haven't seen the paper, but I could give you a reference.

(Munro) (1) I simply ordered the equations by numbering the mesh points sequentially column by column. I had believed that this ordering would result in the most efficient Gaussian elimination, because of its topological simplicity. However, if the method of George is more efficient, I will be very interested to incorporate it in my programs. (2) Up till now, my investigations of Stone's method have been somewhat limited and I am not sure whether the B matrix I have chosen ensures second-order comparability of $(A + B)$ with A. I intend to investigate this as a result of your comment. (3) The method of Dupont et al does in fact allow for the possibility of variable iteration parameters on both sides of the equation. I will be interested to receive the reference on the recent paper published on this subject.

NUMERICAL MODELS OF THREE-DIMENSIONAL END WINDING ARRAYS

by

C.J. Carpenter* and D.H. Locke**

Abstract

The three-dimensional magnetic fields in machine end regions can be most conveniently solved in differential terms by computing a magnetic scalar potential. The complexity of the end winding shapes makes it difficult to translate the three components of the current density vector into suitable field sources in a simple and systematic way. For many purposes it is convenient to treat the field in travelling wave terms, and it is necessary to extract the fundamental and harmonic components of the sources. The paper examines the general problem of translating complex current distributions into equivalent sources for a numerical scalar potential computation. The method is applied to a turbogenerator end region and illustrated by field solutions.

Principle symbols

B	magnetic flux density	S	mesh coefficient matrix
F	network branch m.m.f	T	electric vector potential (eqn. 1)
H	magnetic field strength	w	separation direction
J	current density	∇	differential vector operator
m	harmonic number	μ	permeability
R_e	real part of complx quantity	Ω	magnetic scalar potential
r, θ, z	cylindrical coordinates	n, θ, t	local coordinate system (Fig. 1)
\tilde{T}	indicates phasor quantity	\underline{T}	indicates vector quantity
T', T''	T functions defined by equations 2 and 16 respectively		

1 INTRODUCTION

The magnetic fields in the end regions of electrical machines are generated by winding end-connections of complex shape, and these give a three-dimensional flux pattern whose computation is of increasing importance in the design of turbogenerators and other large machines. The field in the vicinity of the windings can be predicted satisfactorily by numerical integration using current elements and simple image sources to model the nearest iron surface, and this method has long been used to obtain winding inductances and conductor forces. It is much less well suited, however, to the problem of predicting the fields and losses in the stator core, and in other materials exposed to the leakage field. Differential methods are then more convenient, preferably formulated in terms of a magnetic scalar potential^{1,2}, since this reduces the magneto-static problem to the calculation of a single function with simple and well-behaved boundary and interface conditions. Eddy currents are easily incorporated^{2,3}.

The use of a scalar function transfers attention from the problem of making three-dimensional field calculations to that of describing their sources. The current density vector \underline{J} within the end windings has three components defined by the machine geometry. Each component varies in a complex manner, but not independently of the others. The extraction and translation of this data into a form suitable for a numerical model is tedious and prone to error. The sources can be expressed in terms of travelling waves, thus reducing the field computation from three dimensions to two, but this requires the extraction of the \underline{J} components as a function of position in the end winding cross-section. The analysis can be carried out independently for many different sections through the winding, but this is often unnecessary.

It is shown in this paper that the practical problems of providing an economic description of the current density vector in an arbitrary winding configuration, and of translating these sources into a scalar potential computer program, are closely related. Although the principles of the field transformation from a solenoidal to a scalar potential form can be stated very simply in terms of a separation of field components^{1,2}, its practical application in a general purpose program, particularly one

* Electrical Engineering Department, Imperial College, London, SW7 2BT

** C.A. Parsons and Co. Ltd., Heaton Works, Newcastle upon Tyne, NE6 2YL.

with irregular elements, requires an operational and systematic formulation of the various ways in which the sources can be generated. The very flexibility of the method, and the range of choice in applying it, can be an embarrassment in preparing algorithms, and one objective is to combine this flexibility with the statement of precise computational instructions.

For present purposes it is assumed that the currents are all specified. The principles discussed are directly applicable to three-dimensional eddy current problems, and some aspects are examined in a companion paper⁴. The wider implications, however, require a more extensive treatment than can be given here.

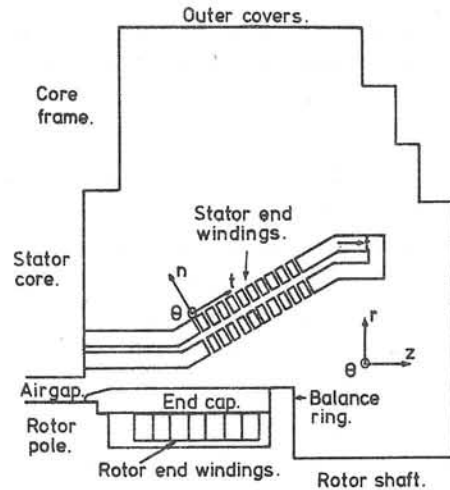


Figure 1. Turbogenerator end region.

invariably, have the same shape. The rotor coils are confined to a single layer and form a concentric end winding, as illustrated in the developed view shown in Figure 2. The m.m.f. distribution produced by both windings varies approximately sinusoidally with θ in the airgap, but the variation in the end region depends on the actual coil shapes, and the separation of the two layers of the stator end winding. The problem is to translate this distribution of current carrying conductors into a numerical form in terms of some arbitrary distribution of nodes forming a rectangular, triangular or some other irregular two or three dimensional mesh.

2.2 Current describing function

The simplest describing function, \underline{T} , is one defined by:

$$\text{curl } \underline{T} = \underline{J} \quad \dots(1)$$

where \underline{J} is the current density vector. \underline{T} is an electric vector potential, or analogue of the magnetic vector potential \underline{A} (defined by $\text{curl } \underline{A} = \underline{B}$), and, just as \underline{A} provides a convenient flow function description in two-dimensional transverse magnetic field problems so the vector \underline{T} can be used in a similar way by limiting it to a direction \underline{n} normal to the plane in which the current flows. That is, everywhere in the end windings a local coordinate direction \underline{n} is specified at right-angles to \underline{J} and to the θ axis, and \underline{T} is limited to the \underline{n} direction (Figure 1). This condition, namely:

$$\underline{T}' \times \underline{n} = 0 \quad \dots(2)$$

defines a particular \underline{T} function consisting of a single quantity T' from which the three components of \underline{J} can be derived. For example, J_t and J_θ are given by:

$$J_t = -\frac{1}{r} \frac{\partial T'}{\partial \theta} \quad \dots(3a)$$

$$J_\theta = \frac{\partial T'}{\partial t} \quad \dots(3b)$$

with the coordinate sequence n, θ, t (Figure 1), and the components of the \underline{J} vector derived in this way necessarily satisfy the current continuity condition:

$$\text{div } \underline{J} = 0$$

T' is constant outside the windings and here is assigned zero value.

2 CURRENT DISTRIBUTION AND DESCRIBING FUNCTION

2.1 Machine geometry

The cross-sectional geometry of the machine, (Figure 1), including both stator and rotor end windings, may be assumed to be invariant with angular displacement θ , but the current distributions within the two windings vary with θ in different ways. The stator end winding is formed in a two-layer configuration in which all the coils usually, although not

The requirement imposed by equation 2 is possible since the divergence of \underline{T}' is otherwise undefined. Taking the divergence of $\underline{T}' \times \underline{n}$:

$$\nabla \cdot (\underline{T}' \times \underline{n}) = \underline{n} \cdot (\nabla \times \underline{T}') - \underline{T}' \cdot (\nabla \times \underline{n}) = 0$$

from equation 2. $\underline{T}' \cdot (\nabla \times \underline{n})$ is zero, so that equation 1 and 2 together require that:

$$\underline{n} \cdot \underline{J} = 0 \quad \dots\dots(4)$$

a condition which \underline{n} has been chosen to satisfy. The divergence of \underline{T}' is zero in the conductor interior where the winding is flat, but is non-zero at any bends in the winding and also at the winding surface.

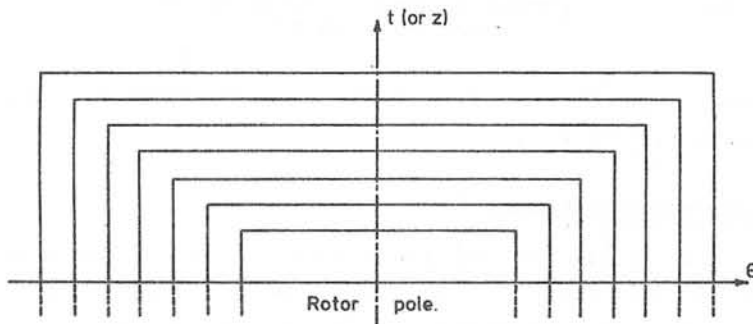


Figure 2. Rotor end winding drawing showing idealised conductor shapes and $T'(\theta,z)$ map. Contours of equal T' plotted for equal increments of T' .

2.3 Rotor end winding

A drawing of the rotor coil ends (Figure 2) can be interpreted as a map of lines of constant T' as a function of t (or z) and θ . This map is valid for all n (or r) values in the winding, and T' does not vary in time in a reference system moving with the rotor. In practice the variation of $T'(\theta, z)$ in both the θ and z directions is discontinuous in slope because of the coil insulation, but T' is everywhere defined.

A harmonic analysis of m.m.f. wave in the θ direction for different values of z gives the magnitude T'_m or the m th space harmonic:

$$T'_m(r, \theta, z) = R_e \left\{ \hat{T}'_m(z) \exp(-jm\theta) \right\} \quad m = 1, 3, 5 \quad \dots\dots(5)$$

where $R_e \left\{ \dots \right\}$ denotes the real part. The harmonics give travelling waves when transformed to a stationary reference system. Because of the symmetry of the winding, the phase angle is not a function of z , and there are no even harmonics. The first seven terms of $T'_m(z)$, together with the major

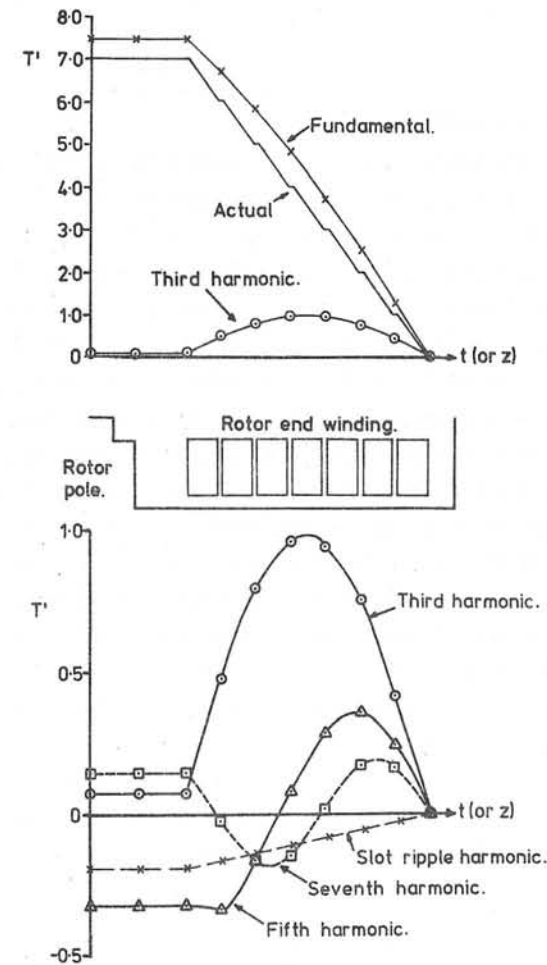


Figure 3. Rotor end winding harmonic analysis. $T'(t)$ function and harmonics, $T'_m(t)$.

ripple harmonic (of slot frequency), are plotted in Figure 3 for a typical rotor end winding. The two current density components, J_z (or J_t) and J_θ are given by equation 3 and this shows that, at a given radius r , J_z is proportional to T' but phase shifted;

$$(\tilde{J}_z)_m = -\tilde{J}_m \tilde{T}'_m / r \quad \dots (6)$$

where \tilde{J} denotes a phasor. The T' and J_z diagrams are thus nearly interchangeable.

2.4 Stator end winding

The stator end winding is of more complex shape, but the n, t coordinate grid can be chosen arbitrarily since it provides only an intermediate step in the process of expressing T' as a function of r and z . The constant T' contours pass across the winding cross-section along the copper-insulation boundaries in the regions where J_θ is non-zero. This is in the sloping section (Figure 1) where the directions of the T' contours are defined by a rectangular n, t grid in which T' is independent of n . In other parts of the winding T' is constant. The $T'(t)$ values can be inserted from a knowledge of the $T'(\theta)$ function in the airgap (calculated from the airgap current distribution, using equation 3a), together with a diagram of the end winding coil shapes drawn in a typical θ, t surface (Figure 4). As in Figure 2, the coil shapes define the lines of constant T' in Figure 4, but the stator currents pulsate sinusoidally in time and the T' values are instantaneous when viewed from a stationary reference point. In general the actual coil shapes should be inserted in Figure 4, but a linearised winding outline such as that illustrated is sufficient for most purposes.

If the coils all have the same shape, so also have the constant T' contours, and $T'(t)$ varies only in phase. That is, the typical term of the Fourier series is now:

$$\tilde{T}'_m(r, \theta, z) = \hat{T}'_m \exp j[\phi_m(t) - m\theta] \quad \dots (7)$$

in which the magnitude \hat{T}'_m is not a function of t , and is given by the Fourier coefficients computed in the airgap. The lines of constant phase ϕ are given by the coil shapes, $\theta(t)$, so that these shapes define $\phi_m(t)$. The function is approximately piece-wise linear with few segments as

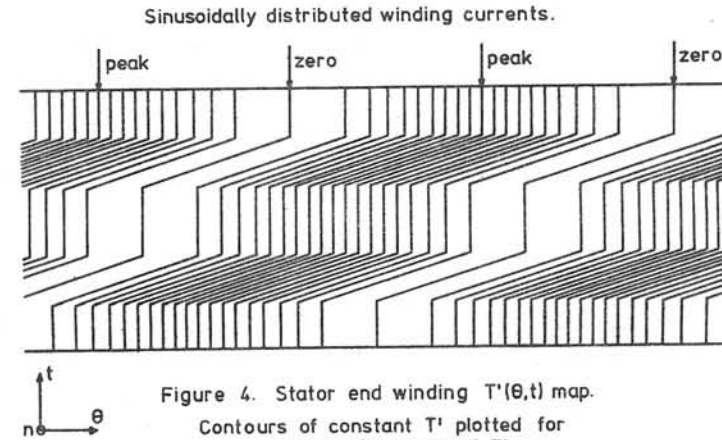


Figure 4. Stator end winding $T'(\theta, t)$ map. Contours of constant T' plotted for equal increments of T' .

indicated in Figure 4. Used in association with the n, t grid, it gives T'_m in terms of r and z .

3 SCALAR POTENTIAL SOURCES

One of the roles of the electric vector potential \underline{T} is that of a current describing function for end windings of large cross-section. It extends to these the concept of m.m.f. distribution which is conventionally associated with current sheets, or with windings in air-gaps. T' is essentially the m.m.f. per unit thickness of the winding. But it also provides directly the transformation from the solenoidal field to a scalar potential equivalent. As the field \underline{H} produced by the windings is given by:

$$\text{curl } \underline{H} = \underline{J} \quad \dots (8)$$

it follows from equation 1 that, for all T functions including T' :

$$\underline{H} = \underline{T} - \text{grad } \Omega \quad \dots (9)$$

and the problem posed numerically is that of computing Ω . Since:

$$\text{div } \underline{B} = 0 \quad \dots (10)$$

the equation to be solved is:

$$\nabla \cdot (\mu(\underline{T} - \nabla\Omega)) = 0 \quad \dots (11a)$$

Commonly T is non-zero only inside windings of non-magnetic material, which reduces equation 11a to:

$$\nabla^2 \Omega = \nabla \cdot \underline{T} \quad \dots (11b)$$

so that the equivalent magnetic poles, which are the sources of Ω , are generated by the divergence of \underline{T} .

One way to compute Ω is to find the equivalent pole distribution from \underline{T} , and model this in the usual way as a Poisson-type field source in finite element, or finite difference, terms. But this gives some difficulty in formulation, and is liable to lead to unnecessary numerical errors, as $\text{div } \underline{T}$ is a discontinuous function confined largely to the surfaces of the windings, whereas the Poisson-type source function is usually assumed to be continuous over the elements in which it is non-zero.

An approach in terms of branch quantities provides a different method of deriving the node equations and a further insight into the nature and accuracy of the Ω model. It shows that, in two-dimensional problems in which a first-order finite element, or finite difference description is used, the accuracy is identical to that of a magnetic vector potential calculation on a network of similar size; more specifically, one which is the dual of that chosen for the Ω solution⁵. Since T can be regarded as a magnetic field component:

$$\int \underline{T} \cdot d\underline{L} = F_b \quad \dots\dots(12)$$

is an m.m.f. which can be evaluated for each mesh branch b . It follows from equation 1 that the sum of the F_b quantities acting around any mesh is equal to the current enclosed, which is the current associated with the corresponding node in the dual network. Hence the branch flow quantities in the Ω model are the same as the corresponding branch potential differences in its dual, or magnetic vector potential equivalent⁶ (provided that the problem is two-dimensional so that a simple dual can be derived).

Where F_b is zero, the network models the second term in equation 9 in the usual way and we obtain, either by finite element or finite difference methods, a set of nodal equations:

$$[S] \{ \Omega \} = 0$$

in which the off-diagonal terms of the coefficient matrix $[S]$ represent the branch "conductance" values of the network⁵, so that the equation for node p can be written

$$\sum_k S_{pk} (\Omega_p - \Omega_k) = 0$$

In regions where F_b is not zero, the effect of the additional m.m.f.s. is to change the branch quantities, giving:

$$\sum_k S_{pk} (\Omega_p - \Omega_k) + \sum_k S_{pk} F_{pk} = 0 \quad \dots\dots(13)$$

as the discrete form of equation 11. Calculating the sources of Ω requires the integration of T' along all the element edges, or lines joining adjacent nodes.

When using rectangular meshes, it is often inconvenient or impractical to choose them in such a way that the winding surfaces intersect the branches only at the network nodes. The branch-source method is then both the simplest and the most accurate way of deriving the source constant in the node equations. The result expresses the very simple requirement that, to define a scalar potential function, the current linkages with the network meshes must be replaced by F_b sources chosen so that their algebraic sum around every mesh is equal to the current linkage which is replaced. T' is one of any number of T functions defining a set of branch sources which will meet this condition. A general rule for defining the sources is to imagine that the current carrying conductors are separated from the network by tearing. As the current is withdrawn, we place in each intersected branch, an m.m.f. source F_b equal in magnitude to the current intersecting it. These sources are the network equivalent of dipoles, and a set of dipoles (of dipole moment T') defined in this way constitutes a magnetic shell equivalent of the winding^{1,6}. When the windings are replaced by current sheets, F represents the magnitude of the potential discontinuity across a current sheet (a quantity which has previously² been denoted $\Delta\Omega$; however this notation is unsatisfactory when the current is spread out in a winding of finite thickness).

4 SOLUTION OF TURBOGENERATOR END REGION FIELD

Fundamental travelling wave solutions have been computed in cylindrical coordinates by the methods described in Sections 2 and 3. Equation 11 becomes:

$$\frac{1}{r} \frac{\partial}{\partial r} \left[\mu r \left(\frac{\partial \tilde{\Omega}}{\partial r} - \tilde{T}'_r \right) \right] + \frac{\partial}{\partial z} \left[\mu \left(\frac{\partial \tilde{\Omega}}{\partial z} - \tilde{T}'_z \right) \right] = \mu \frac{m^2}{r^2} \tilde{\Omega} \quad \dots\dots(14)$$

since the sinusoidal variation of Ω with θ demands no variation in μ in this direction. The travelling-wave term on the right-hand side of

equation 14 can be treated as a source term in the usual way, and gives network branches to ground. The remainder can be expressed numerically in the manner described for equation 11.

The r, z plane mesh used for these solutions was square, with a node spacing equal to one half of the machine airgap length. Eddy current effects⁴ have been omitted and all boundaries are assumed to be infinitely permeable except for the rotor end cap, which is non-magnetic (the effects of saturation in a magnetic and cap have been studied separately in a three-dimensional mesh). When the machine is on load the amplitudes, and relative angular positions, of the stator and rotor m.m.fs. vary with changing load, but by ignoring saturation the effect of each winding can be studied separately and the two load solutions combined linearly after appropriate scaling and angular displacement. The rotor end winding field is required in only one r, z plane since this winding generates a monophasic flux pattern (equation 5), but the stator end winding field has both real and imaginary parts (equation 7). These three basic solutions are stored and combined as needed to give the field under any given operating conditions. Radial and axial flux densities are obtained directly from equation 9, whilst in the circumferential direction the flux density is given by:

$$B_{\theta} = j\mu\frac{\Omega}{r}z \quad \dots\dots(15)$$

Flux density components are commonly required for comparison with measurements, but since all three components are complex (requiring six field plots in all) there are difficulties in displaying them diagrammatically).

Figure 5 shows the Ω equipotentials plotted in the plane of peak winding m.m.f. (acting in the airgap) under short circuit conditions, when the two windings act nearly in opposition. The flux density maps which are reproduced in Figure 6 give the magnitudes of the three flux density phasors when the machine is operating at rated load with rated terminal voltage. These diagrams show contours of equal flux density, plotted without regard to phase angle. Comparisons of flux density calculations such as these with measurements will be reported elsewhere.

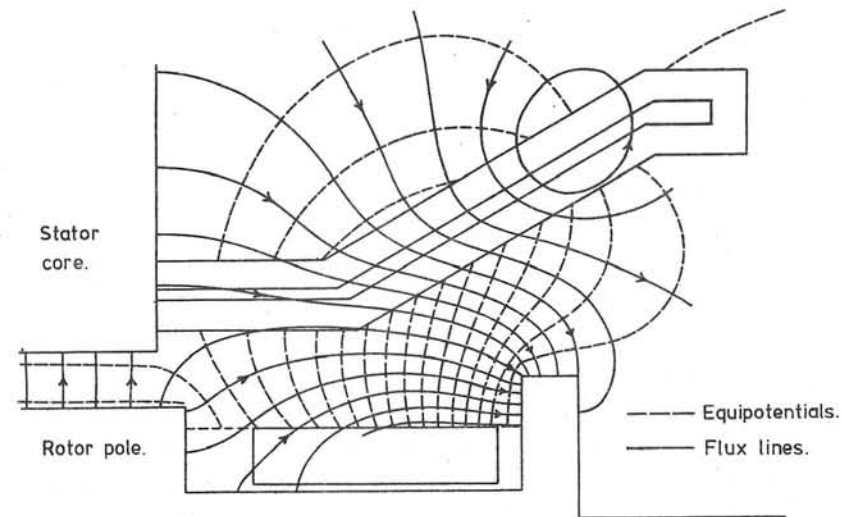


Figure 5. Short circuit rated current. End field in plane of maximum winding m.m.f.

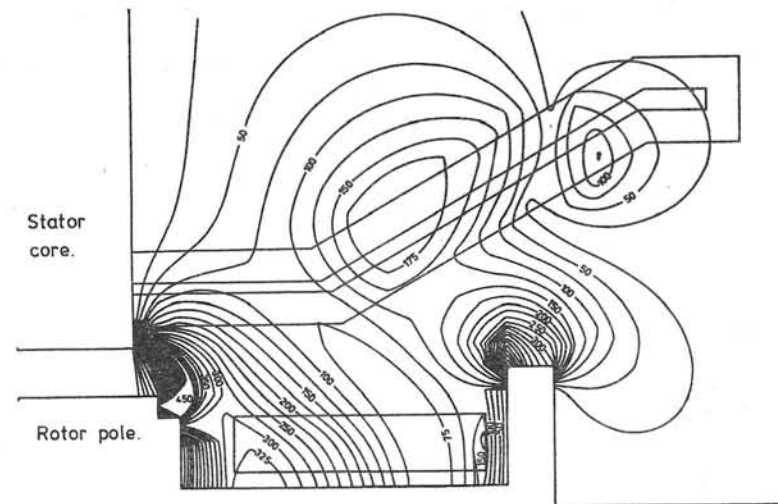


Figure 6a. Rated power 0.95p.f. lag. Peak radial flux density, \hat{B}_r .

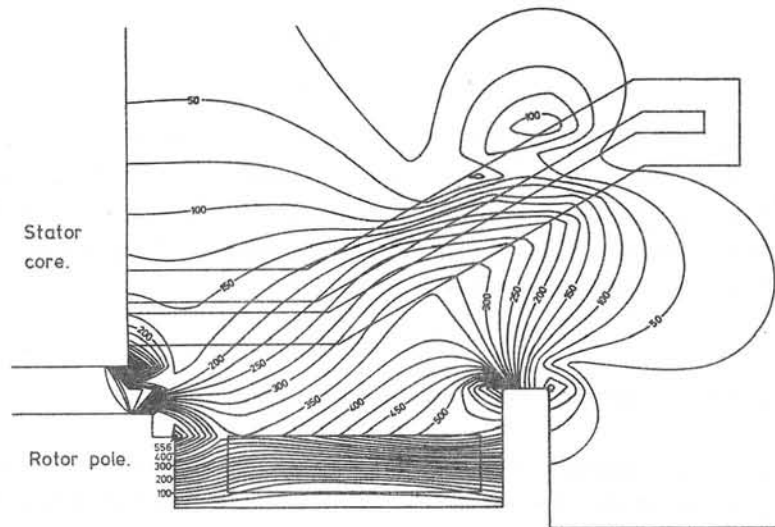


Figure 6b. Rated power 0.95 p.f. lag. Peak axial flux density, \hat{B}_z .

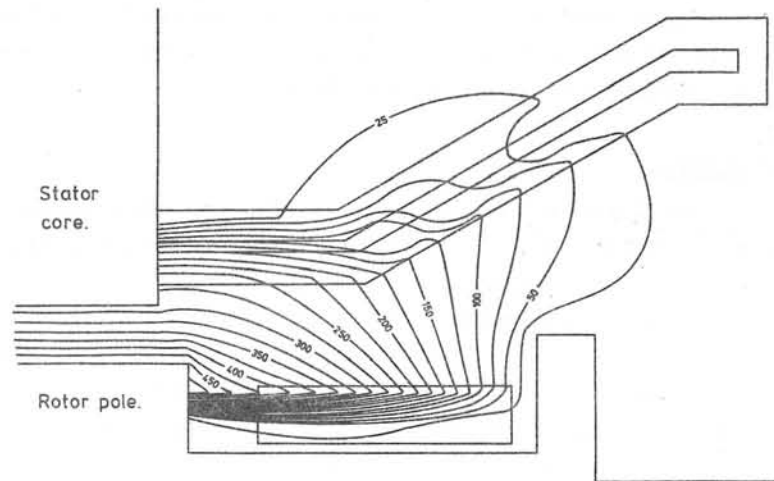


Figure 6c. Rated power 0.95 p.f. lag. Peak circumferential flux density, \hat{B}_θ .

5 ALTERNATIVE SEPARATION METHODS

The \underline{T}' vector has only one component in the local coordinate system, but its direction changes with position in the stator end winding. This complicates the computation of \underline{E} , and the combination of \underline{T} and $\text{grad } \Omega$ within the elements when \underline{H} is required, particularly when using a triangular instead of a rectangular mesh. There are then some advantages in separating the two roles for \underline{T}' using one \underline{T}' as a current describing function and another, \underline{T}'' , to provide input data for the field calculation. Various possibilities are currently being explored. By withdrawing the end winding current in a direction orientated relative to the r, z instead of the local n, t coordinates, \underline{T}'' can be given a constant direction. The current may, for example, be withdrawn in the $-z$ direction towards the stator. Alternatively it can be withdrawn in the $-r$ direction towards the axis, and then in the $-z$ direction through the airgap, giving some advantages in accuracy¹ since \underline{T}'' approximates to the required \underline{H} field in the airgap. There are also various advantages in reducing the winding to an equivalent current sheet by first withdrawing the current inwards parallel to the n , instead of the t , direction in Figure 1. This replaces the distributed current by a simple scalar potential discontinuity, together with additional sources whose effect is small, so that the accuracy with which they have to be specified is much reduced. The current sheet approximation provides a convenient idealisation of the winding in several respects, and by carrying the withdrawal in the n direction further, the two layers can be reduced to a single current sheet as the major field source, together with additional sources whose effect is relatively localised.

These possibilities require a more general method of generating \underline{T} than that defined by equation 2. This is the only simple and convenient way of generating a describing function, but for other purposes the condition imposed by equation 4 is too restrictive. Because of the freedom of choice in the divergence of \underline{T} , any number of different functions can be defined to satisfy equation 1. The magnetic shell principle offers useful guidance, but it is not easily converted into an algorithm for constructing the scalar potential sources. The simplest way of providing for a more general orientation of the \underline{T} vector is to define a direction \underline{w}

in which all the currents are withdrawn, using the tearing principle stated in section 3. The direction \underline{w} can be aligned parallel to one coordinate axis; for example, choosing \underline{w} in the t or θ direction generates the same \underline{T}' function as before. One consequence of equation 2 is that \underline{T}' can be obtained by withdrawal in any direction within the surface defined by the \underline{n} vector. This property we now relinquish.

The withdrawal concept shows that there can be no component of \underline{T}'' in the withdrawal direction, as no network branch orientated in this direction is intersected or "torn" by any current. That is, having chosen the direction \underline{w} , we define \underline{T}'' so that:

$$\underline{T}'' \cdot \underline{w} = 0 \quad \dots\dots(16)$$

This, coupled with equation 1, is both a possible and a sufficient definition of a set of branch sources (from equation 12) equivalent to the current linkages which they replace. Two consequences of the replacement of equation 2 by equation 16 is that \underline{J} can have any arbitrary direction relative to \underline{w} , and \underline{T} now has two components, whereas it was previously restricted to one in the local coordinate system. The modified definition is particularly important in three-dimensional eddy current problems in which the direction of the \underline{J} vector is, in general, undefined, but here the treatment is restricted to magnostatic aspects.

From equations 1 and 16, it follows that:

$$\underline{J} \times \underline{w} = (\underline{w} \cdot \nabla) \underline{T}'' \quad \dots\dots(17)$$

and the T''_x and T''_y components can be constructed by dividing equation 17 by the magnitude of w and integrating:

$$T''_1 - T''_2 = \int_1^2 \underline{J} \times \frac{d\underline{w}}{w} \quad \dots\dots(18)$$

Where J is zero T'' is constant, and is assigned zero value in the region 'upstream' of the winding, that is, before the displacement vector \underline{w} intersects it: \underline{T}'' , and hence F , are then completely defined. Equations 16, 17 and 18 express symbolically the possibility of defining any vector \underline{T} to satisfy equation 1 by suppressing one component, leaving the other two defined independently of each other by one-dimensional integration. If \underline{w} is chosen so that it is parallel to one of the coordinate axes (although not necessarily the same one throughout the withdrawal process), the F quantities are obtained directly in the branches of a rectangular network.

For example, if \underline{w} is in the $-z$ direction in Figure 1, equation 3 is then replaced by:

$$J_r = \frac{\partial T''_R}{\partial z} \quad \dots\dots(19a)$$

$$J_\theta = -\frac{\partial T''_\theta}{\partial z} \quad \dots\dots(19b)$$

(from equation 17). The \underline{T}'' function for the rotor winding is the same as \underline{T}' , since J_r is zero, and when using a two-dimensional travelling wave description, \underline{T}'' due to the stator winding consists of only one component, T''_r , in the plane in which the solution is computed. T''_r depends on J_θ , which in turn, is given by equations 3 and 7:

$$J_\theta = -j \left(\frac{\partial \phi_m}{\partial t} \right) T'_m \quad \dots\dots(20)$$

where the $\phi(t)$ curve is the coil shape shown in Figure 5.

Only one component, T''_r is needed to compute F . The other, T''_θ , affects the \underline{H} vector in the peripheral direction, and hence the travelling wave term on the right-hand side of equation 14. This becomes:

$$\mu \frac{1}{r} \frac{\partial H_\theta}{\partial \theta} = \mu \left(\frac{m^2}{r^2} \Omega - j \frac{m}{r} \frac{T''_\theta}{\theta} \right) \quad \dots\dots(21)$$

so that, in network terms, T''_θ is equivalent to generators connected in series with the branches to ground. The withdrawal in the $-z$ direction would normally be terminated at the stator lamination surface leaving a current sheet which is represented by a simple scalar potential discontinuity whose magnitude is everywhere specified.

6 CONCLUSIONS

It has been shown that the problem of describing a three-dimensional current distribution economically is closely allied to that of translating the field problem into magnetic scalar potential terms. The three components of the current density vector can be replaced by a single current describing function, T' , which corresponds to a (scalar) current flow function when T' is appropriately defined. This extends to bulky windings the simple potential-jump concept associated with current sheets, and it assists the production of a numerical description of the current distribution from the actual winding geometry. The sources of the magnetic scalar potential, Ω , can be derived directly from T' , but it is

sometimes more convenient to use for this purpose a less restrictive way of generating the \underline{T} vector. Both methods can be stated concisely in vector terms, and hence translated into algorithms.

The method has been used to compute turbogenerator end fields, and is illustrated in these terms, but is applicable to all magnostatic problems in which the current distribution is specified. The replacement of T' by alternative T'' functions is, however, particularly appropriate to three dimensional eddy current problems in solids, where the direction of the current density vector is not specified, as distinct from laminated materials where \underline{T}' is at right angles to the plane of the laminations⁴.

Acknowledgements

The authors wish to thank both the Science Research Council and C.A. Parsons and Co. Ltd. for financial support, and the latter for permission to publish the computed results.

References

- 1 CARPENTER, C.J. Numerical solution of magnetic fields in the vicinity of current carrying conductors. Proc. IEE, 1967, 114 (11), pp1793-1800
- 2 CARPENTER, C.J. Computation of magnetic fields and eddy currents. 5th International Conference on Magnetic Technology. Rome, April 1975, pp 147-158
- 3 CARPENTER, C.J. and DJUROVIC, M. Three-dimensional numerical solution of eddy currents in thin plates, Proc. IEE, 1975, 122 (6) pp681-688
- 4 CARPENTER, C.J. and WYATT, E.A. Efficiency of numerical techniques for computing eddy currents in two and three dimensions. Compumag 1976.
- 5 CARPENTER, C.J. Finite element network models and their application to eddy-current problems. Proc. IEE, 1975, 122 (4), pp 455-462
- 6 CARPENTER, C.J. and RATTI, U. Comparison of scalar and vector potentials for the numerical solution of magnetic fields. L'Energia Elettrica, 1974, No. 4, pp 200-212.

Discussion following paper:

(Trowbridge, Rutherford Lab) Does the computer program based on your T junction method take into account iron?

Has the technique any advantages over other methods ie Biot Savart Law interpolation in the special case of conductor fields?

(Carpenter, Imperial College) Yes, the results described include the effect of unsaturated iron surfaces, and we have made separate studies of saturation effects in highly saturated parts. Here a full three-dimensional mesh is necessary in place of the travelling-wave approximation, which depends on linearity. Usually T is zero inside the iron, but the only effect of removing this restriction is to add the T vector in equation 9 when calculating B from the B/H curve.

When there is no iron present then I think there is usually no advantage in any other method over the simple Biot-Savart (or Neumann) type of integration.

Occasionally a T vector can be easily constructed which is a close approximation to the required field, and the grad Ω term then represents a small correction. This has obvious advantages. Examples are given in reference 1 of the paper.

(Polak, NV Philips) Is there any comparison between calculated and measured data which gives an idea of the accuracy?

(Carpenter) Yes, we have made comparisons and we hope to publish these shortly. It is very difficult to summarise them in any brief statement because the results depend on the position at which B is measured, the component measured, and on the magnitude and phase angle of this load on the machine.

AN ANALYTICAL METHOD OF CALCULATING
MAGNETIC FIELDS IN SLOTTED REGIONS

by

T.G. Phemister

C.A. Parsons and Co. Ltd., Newcastle upon Tyne

The magnetic field in slotted regions is defined by Fourier series with unknown coefficients. Continuity of the field at the top of the slots is used to set up infinite matrices relating the unknown coefficients to the boundary conditions. The infinite matrices are inverted analytically to give an explicit solution for the coefficients. The method is rapid and its theoretical accuracy is within the uncertainties in the manufacture of large generators.

1 Introduction

The origin of the work to be described was a requirement to calculate the three-dimensional magnetic field near the ends of large generators in more detail than existing computer programs permitted. The geometry of a generator is complicated, with its slotted structure and cooling ducts, and a program based on the straightforward application of finite difference or finite element methods demands too much computer time to be an ordinary design tool; the band-width of the resulting equations is uncomfortably large. If, however, a rapid method can be found for calculating the field in the slots and air-gap together, then an efficient scheme of iteration can be set up between the magnetic and non-magnetic regions.

The method to be described was designed for an iterative scheme in which, with normal flux density as the boundary condition for the magnetic regions, finite element methods were used to calculate surface magnetising forces for the next stage of iteration. The problem was, therefore, to calculate rapidly the magnetic field in the slots and air-gap when the surface magnetising forces were known on all boundaries. The method adopted was based on Fourier analysis. Systems of equations were set up for the Fourier coefficients and the matrix of left-hand sides was inverted analytically. The method is explained by applying it to the simplest problem in which its value is apparent; the problems in extending it to

more complicated geometries are discussed afterwards.

2 Specification of problem

The simplest problem to which the method has been applied was a calculation of the two-dimensional magnetic field in the centre of a generator. To avoid obscuring the algebra by inessential detail, the following simplifications will be made.

- (a) The generator is a perfect two-pole machine.
- (b) The rotor is cylindrical and the currents in its windings are represented by a distribution of magnetic scalar potential on its surface.
- (c) The fields are two-dimensional.
- (d) The stator slots are rectangular.
- (e) Curvature will be neglected at the top of the slots and a rectangular system of coordinates in each slot will be assumed compatible with polar coordinates in the air-gap.
- (f) The air-gap length is greater than the width of the stator slots, the width of the tooth tips is not much less than the width of the slots, and the slots are deep with respect to their width.

None of these simplifications except (f) is necessary for the success of the method. A related method has been developed for geometries in which (f) does not hold.

The problem can be summarised as follows. A two-dimensional magnetic scalar potential is specified on the surface of a cylindrical rotor, on the stator tooth tips, and on all sides of the stator slots. Currents are specified in the stator slots. The magnetic field is to be calculated in the slots and air-gap.

3 Coordinate system

Polar coordinates r, θ will be used in the air-gap. The surface of the rotor is at $r = t$ and the stator tooth tips lie on $r = s$.

The centre of the stator slot numbered n lies on $\theta = c_n$ and the top

corners are at $r = s$, $\theta = c_n \pm d_n$. Rectangular coordinates x_n down the slot and y_n across the slot will be used. Thus, at the boundary between the slot and the air-gap, $x_n = 0$ and $y_n = s(\theta - c_n + d_n)$. The width of the slot is $w_n = 2sd_n$. There are N slots in a half circumference.

4 Schematic solution

The first step in solving the problem is to impose an arbitrary distribution of scalar potential on the boundaries between the slots and air-gap; the simplest is a linear variation between the corners of each slot. Unique solutions for the magnetic field can then be found in each slot separately and in the air gap separately. Since these regions are of a simple shape, the solutions can be obtained expeditiously by traditional methods. If these solutions are written as

$$\underline{H} = \underline{H}_n = \begin{pmatrix} H_{xn} \\ H_{yn} \end{pmatrix} \text{ in slot } n,$$

$$\text{and } \underline{H} = \underline{H}_g = \begin{pmatrix} H_{gr} \\ H_{g\theta} \end{pmatrix} \text{ in the air-gap,}$$

then the complete solution can be expressed as:

$$\underline{H} = \underline{H}_n - \nabla\phi_n \text{ in slot } n$$

$$\text{and } \underline{H} = \underline{H}_g - \nabla\phi_g \text{ in the air gap,}$$

$$\text{where } \phi_n = \sum_{i=1,3}^{\infty} a_{ni} \sin \left(\frac{i\pi y_n}{w_n} \right) \exp \left(\frac{-i\pi x_n}{w_n} \right) + \sum_{j=2,4}^{\infty} b_{nj} \sin \left(\frac{j\pi y_n}{w_n} \right) \exp \left(\frac{-j\pi x_n}{w_n} \right)$$

$$\text{and } \phi_g = \sum_{k=1}^{\infty} \frac{\left(\frac{r}{t} \right)^K - \left(\frac{t}{r} \right)^K}{\left(\frac{s}{t} \right)^K - \left(\frac{t}{s} \right)^K}$$

$$\times \left[\sum_{n=1}^N \frac{2d_n}{\pi} \cos K(\theta - c_n) \sum_{i=1,3}^{\infty} a_{ni} Q_{nik} \right]$$

$$+ \sum_{n=1}^N \frac{2d_n}{\pi} \sin K(\theta - c_n) \sum_{j=2,4}^{\infty} b_{nj} R_{nj k} \Big],$$

in which

$$K = 2k - 1,$$

$$Q_{nik} = \frac{-i\pi \cos K d_n}{d_n^2 \left[K^2 - \frac{i^2 \pi^2}{4d_n^2} \right]},$$

$$R_{nj k} = \frac{j\pi \sin K d_n}{d_n^2 \left[K^2 - \frac{j^2 \pi^2}{4d_n^2} \right]}.$$

The limit is to be understood when the denominator is zero. The odd and even coefficients are treated separately because the terms to which they are attached behave differently.

A solution of this form satisfies all the boundary conditions except continuity for H_r between each slot and the air-gap. Fourier analysis of this remaining condition gives the equations required for calculating the unknown coefficients a_{ni} and b_{nj} . It will be found that $a_{ni} = O(i^{-5/3})$ and $b_{nj} = O(j^{-5/3})$. Using this, it is straightforward to prove that the order of summation in the series can be changed.

Up to this point, the method has been similar to work previously published, for example, by Midgley and Smethurst (1963) and Jones et al. (1969). As far as the writer is aware, however, what follows is new.

5 Explicit equations for the unknown coefficients

Equating the normal flux density across the top of each slot by Fourier analysis gives a set of equations which can be expressed in matrix form as:

$$\begin{bmatrix} E_{11} & F_{11} & E_{12} & F_{12} & \dots & \dots \\ G_{11} & H_{11} & G_{12} & H_{12} & \dots & \dots \\ E_{21} & F_{21} & E_{22} & F_{22} & \dots & \dots \\ G_{21} & H_{21} & G_{22} & H_{22} & \dots & \dots \\ \dots & \dots & \dots & \dots & \dots & \dots \\ \dots & \dots & \dots & \dots & \dots & \dots \end{bmatrix} \begin{bmatrix} a_{1p} \\ b_{1q} \\ a_{2p} \\ b_{2q} \\ \dots \\ \dots \end{bmatrix} = \begin{bmatrix} s_{1i} \\ t_{1j} \\ s_{2i} \\ t_{2j} \\ \dots \\ \dots \end{bmatrix}$$

where E_{nm} , F_{nm} , G_{nm} , H_{nm} ($n = 1, N$ and $m = 1, N$) are infinite square matrices, $\begin{bmatrix} a_{mp} \end{bmatrix}$ and $\begin{bmatrix} b_{mq} \end{bmatrix}$ are infinite column matrices of the unknown coefficients, and $\begin{bmatrix} s_{ni} \end{bmatrix}$ and $\begin{bmatrix} t_{nj} \end{bmatrix}$ are infinite column matrices which come from Fourier analysis of $H_{xn} - H_{gn}$ at the top of slot n .

If E_{nmip} is the i, p element of E_{nm} , then

$$E_{nmip} = \frac{1}{2} \delta_{nm} \delta_{ip} + \frac{2d_n d_m}{i\pi^2} \sum_{k=1}^{\infty} K(1 + P_k) \cos K(c_n - c_m) Q_{nik} Q_{mpk},$$

$$\text{where } P_k = \frac{2}{\left(\frac{s}{t}\right)^{2K} - 1}.$$

By expressing $Q_{nik} Q_{mpk}$ as three partial fractions, and by using their properties as Fourier coefficients, it may be shown that

$$\frac{2d_n d_m}{i\pi^2} \sum_{k=1}^{\infty} K \cos K(c_n - c_m) Q_{nik} Q_{mpk} = \frac{-p}{2d_n d_m \left(\frac{2\pi}{2d_n} + \frac{p\pi}{2d_m}\right)} \sum_{k=1}^{\infty} \frac{\left[\cos K\left(\frac{c_n - c_m + d_n + d_m}{n}\right) + \cos K\left(\frac{c_n - c_m - d_n - d_m}{n}\right) \right] + \cos K\left(\frac{c_n - c_m - d_n + d_m}{n}\right) + \cos K\left(\frac{c_n - c_m + d_n - d_m}{n}\right)}{\left(K + \frac{i\pi}{2d_n}\right) \left(K + \frac{p\pi}{2d_m}\right)}.$$

Uniform convergence ensures that this remains true in all cases, except $n = m$ and $i = p$ in which $\frac{1}{2}$ is added.

Phemister (1972) has shown that

$$\sum_{k=1}^{\infty} \frac{\cos Kx}{K+a} = \frac{1}{2}g(ax) - \frac{1}{2}g(a\pi - ax) + \frac{S(x)}{a^2} + O\left(\frac{1}{4}\right), \quad 0 < x < \pi,$$

where $g(x)$ is the second generating function of the sine and cosine integrals and $|S(x)| < 0.04$. Now $g(x) = \frac{1}{x^2} + O\left(\frac{1}{x^4}\right)$ and so, if $n \neq m$ and the teeth are not greatly narrower than the slots, this part of E_{nmip} can be approximated as $\frac{\text{constant}}{i^2 p}$. The series with P_k , which is rapidly convergent, can also be so approximated, even when $n = m$.

Thus the submatrices E_{nm} can be written approximately as

$$E_{nm} = \frac{\begin{bmatrix} e_{nm} \end{bmatrix}}{i^2 p}, \quad n \neq m.$$

It can be shown similarly that, approximately,

$$F_{nm} = \frac{\begin{bmatrix} f_{nm} \end{bmatrix}}{i^2 q} \text{ for all } n, m,$$

$$G_{nm} = \frac{\begin{bmatrix} g_{nm} \end{bmatrix}}{j^2 p} \text{ for all } n, m,$$

$$\text{and } H_{nm} = \frac{\begin{bmatrix} h_{nm} \end{bmatrix}}{j^2 q}, \quad n \neq m.$$

In the present application, F_{nm} and G_{nm} are, by symmetry, null matrices whenever $n = m$ but in general they can be expressed approximately in the forms given above even when $n = m$.

The submatrices E_{nm} and H_{nm} must be studied in more detail. With the extra $\frac{1}{2}$ that has been mentioned

$$E_{nmip} = \delta_{ip} - \frac{2p}{\pi d_n (i+p)} \sum_{k=1}^{\infty} \frac{1 + \cos 2Kd_n}{\left(K + \frac{i\pi}{2d_n}\right) \left(K + \frac{p\pi}{2d_n}\right)} + \frac{2p}{d_n^2} \sum_{k=1}^{\infty} \frac{KP_k \cos^2 Kd_n}{\left(K^2 - \frac{i^2 \pi^2}{4d_n^2}\right) \left(K^2 - \frac{p^2 \pi^2}{4d_n^2}\right)}.$$

Since F_k tends exponentially to zero and

$$\frac{\pi}{2d_n} \gg 1,$$

the second series can be approximated by

$$\frac{1}{i^2 p} \times \frac{32d_n^2}{\pi^4} \sum_{k=1}^{\infty} KP_k \cos^2 kd_n.$$

The first series gives

$$- \frac{2p \left[\ln \left(\frac{i}{p} \right) + g(p\pi) - g(i\pi) \right]}{\pi^2 (i^2 - p^2)} + \frac{\text{constant}}{i^2 p} + \text{negligible terms}.$$

The formula $\lim_{x \rightarrow 0} (g(ix) - g(px)) = - \ln \left(\frac{i}{p} \right)$ has been used in obtaining this and $g(x)$ has been expressed asymptotically when its argument is large.

Thus, if A is the matrix whose i, p element is

$$\delta_{ip} - \frac{2p}{\pi^2 (i^2 - p^2)} \left[\ln \left(\frac{i}{p} \right) + g(p\pi) - g(i\pi) \right],$$

the submatrix E_{nn} can be approximated as

$$A + \begin{pmatrix} e_{nn} \\ i^2 p \end{pmatrix}.$$

It may be shown that, if B is the matrix whose j, q element is

$$\delta_{jq} - \frac{2q}{\pi^2 (j^2 - q^2)} \left[\ln \left(\frac{j}{q} \right) - g(q\pi) + g(j\pi) \right],$$

the submatrix H_{nn} can be approximated as

$$B + \begin{pmatrix} h_{nn} \\ j^2 q \end{pmatrix}.$$

The matrices A and B are independent of the geometry and only the constants e_{nm} etc. are required to give an explicit formulation of the equations for the unknown coefficients. There is only a finite number of these coefficients and not many of them are needed, since they tend

rapidly to zero as $|n - m|$ increases. The simplest way to calculate them is to set

$$e_{nm} = E_{nm11},$$

$$f_{nm} = 2F_{nm12},$$

$$g_{nm} = 4G_{nm21},$$

$$h_{nm} = 8H_{nm22},$$

with suitable modifications for e_{nn} and h_{nn} . By using asymptotic forms, this can be done rapidly.

The equations can then be expressed explicitly as

$$\left[\text{diag } (A, B, A, B, \dots) + \begin{pmatrix} \begin{pmatrix} e_{nm} \\ i^2 p \end{pmatrix} & \begin{pmatrix} f_{nm} \\ i^2 q \end{pmatrix} \\ \begin{pmatrix} g_{nm} \\ j^2 p \end{pmatrix} & \begin{pmatrix} h_{nm} \\ j^2 q \end{pmatrix} \end{pmatrix} \right] \begin{pmatrix} a_{mp} \\ b_{mq} \end{pmatrix} = \begin{pmatrix} s_{ni} \\ t_{nj} \end{pmatrix}.$$

6 Solution of the equations for the unknown coefficients

It has been shown by Phemister (1972) that an asymptotic form for the i, p element of A^{-1} when i and p are large is

$$\delta_{ip} + \frac{2p \left[\left(\frac{i}{p} \right)^{\frac{1}{3}} - \left(\frac{p}{i} \right)^{\frac{1}{3}} \right]}{\pi\sqrt{3} (i^2 - p^2)},$$

that B^{-1} has the same asymptotic form, and that A^{-1} and B^{-1} can be approximated by the matrices C and D , where the i, p element of C is

$$\delta_{ip} + \frac{2p \left[\left(\frac{i}{p} \right)^{\frac{1}{3}} - \left(\frac{p}{i} \right)^{\frac{1}{3}} \right]}{\pi\sqrt{3} (i^2 - p^2)} + \frac{0.014718 p}{(ip)^{\frac{5}{3}}} - \frac{0.001893 p}{(ip)^{\frac{7}{3}}}$$

and the j, q element of D is

$$\epsilon_{jq} + \frac{2q \left[\left(\frac{f}{q} \right)^{\frac{1}{3}} - \left(\frac{q}{j} \right)^{\frac{1}{3}} \right]}{\pi \sqrt{3} (j^2 - q^2)} - \frac{0.037705 q}{(jq)^{\frac{5}{3}}} + \frac{0.014055 q}{(jq)^{\frac{7}{3}}}$$

The numerical constants were obtained by a least squares minimisation of the elements of $CA - I$ and $DB - I$, where I is the unit matrix.

The equations can be solved by expanding the reciprocal of the square matrix on the left hand side, to give, as the first two terms of the binomial series,

$$\begin{bmatrix} a_{ni} \\ b_{nj} \end{bmatrix} = \left\{ M - M \begin{bmatrix} \frac{e_{nm}}{i^2 p} & \frac{f_{nm}}{i^2 q} \\ \frac{g_{nm}}{j^2 p} & \frac{h_{nm}}{j^2 q} \end{bmatrix} M \right\} \begin{bmatrix} s_{mp} \\ t_{mq} \end{bmatrix}$$

where $M = \text{diag} (C, D, C, D, \dots)$. Thus the unknown coefficients have been expressed explicitly in terms of known quantities.

The matrices A and B are those that arise in the problem of a single infinitely deep slot in a semi-infinite slab. The binomial expansion is the equivalent of solving first for each slot separately as if the stator bore were the only boundary and no other slots existed and afterwards correcting for the effect of other slots and other boundaries.

7 Types of a_{ni} , etc.

The solution that has been found is still expressed in terms of infinite matrices and would be difficult to handle as it stands. Phemister (1972) proposed, and Drumm (1973) confirmed, that the column matrices $\begin{bmatrix} s_{mp} \end{bmatrix}$ and $\begin{bmatrix} t_{mq} \end{bmatrix}$ could each be expressed to the required accuracy as the linear combination of four different types:

$$\begin{bmatrix} \frac{ln p}{p^2} \end{bmatrix}, \begin{bmatrix} \frac{1}{p^2} \end{bmatrix}, \begin{bmatrix} \delta_{1p} \end{bmatrix}, \begin{bmatrix} \frac{1}{p^4} \end{bmatrix}, \text{ and } \begin{bmatrix} \frac{ln q}{q^2} \end{bmatrix}, \begin{bmatrix} \frac{1}{q^2} \end{bmatrix}, \begin{bmatrix} \delta_{2q} \end{bmatrix}, \begin{bmatrix} \frac{1}{q^4} \end{bmatrix}.$$

It was established further that the products $C \begin{bmatrix} s_{mp} \end{bmatrix}$ and $D \begin{bmatrix} t_{mq} \end{bmatrix}$ could each be expressed to the required accuracy as a linear combination of four different types of column matrix:

$$\begin{bmatrix} i^{-\frac{5}{3}} \end{bmatrix}, \begin{bmatrix} i^{-\frac{7}{3}} \end{bmatrix}, \begin{bmatrix} \delta_{1i} \end{bmatrix}, \begin{bmatrix} \delta_{3i} \end{bmatrix} \text{ and } \begin{bmatrix} j^{-\frac{5}{3}} \end{bmatrix}, \begin{bmatrix} j^{-\frac{7}{3}} \end{bmatrix}, \begin{bmatrix} \delta_{2j} \end{bmatrix}, \begin{bmatrix} \delta_{4j} \end{bmatrix}.$$

It follows that the products $C \begin{bmatrix} e_{nm} \\ i^2 p \end{bmatrix} C \begin{bmatrix} s_{mp} \end{bmatrix}$ etc. can each be expressed as a linear combination of the same four odd or four even types of column matrix. Hence $\begin{bmatrix} a_{ni} \end{bmatrix}$ and $\begin{bmatrix} b_{nj} \end{bmatrix}$ can also be so expressed.

If all the algebra is performed on these types of infinite column matrix, then $\begin{bmatrix} s_{mp} \end{bmatrix}$ and $\begin{bmatrix} t_{mq} \end{bmatrix}$ can each be represented by a column matrix of only four elements, which are the parameters of the different types of infinite column matrix arising from $H_{xn} - H_{gr}$. Similarly, $\begin{bmatrix} a_{ni} \end{bmatrix}$ and $\begin{bmatrix} b_{nj} \end{bmatrix}$ can each be represented by a column matrix of four elements. C and D can be represented by 4×4 matrices whose elements are known absolutely and are independent of the problem. Similarly, any of the four products $C \begin{bmatrix} f_{nm} \\ i^2 q \end{bmatrix} D$ etc. can be represented by the product of the appropriate scalar, f_{nm} etc., with one of four 4×4 matrices whose elements are known absolutely.

Thus, if $\begin{bmatrix} a_{nu}^* \end{bmatrix}$ and $\begin{bmatrix} b_{nu}^* \end{bmatrix}$, $u = 1, 4$, $n = 1, N$, denote the four-element column matrices of parameters of the different types of $\begin{bmatrix} a_{ni} \end{bmatrix}$ and $\begin{bmatrix} b_{nj} \end{bmatrix}$, respectively, and if $\begin{bmatrix} s_{mv}^* \end{bmatrix}$ and $\begin{bmatrix} t_{mv}^* \end{bmatrix}$, $u = 1, 4$, $m = 1, N$, denote the four-element column matrices of parameters of the different types of $\begin{bmatrix} s_{mp} \end{bmatrix}$ and $\begin{bmatrix} t_{mq} \end{bmatrix}$, respectively, then the solution can be expressed in the simple form:

$$\begin{bmatrix} a_{nu}^* \end{bmatrix} = C^* \begin{bmatrix} s_{nv}^* \end{bmatrix} - \sum_{m=1}^N e_{nm} E^* \begin{bmatrix} s_{mv}^* \end{bmatrix} + f_{nm} F^* \begin{bmatrix} t_{mv}^* \end{bmatrix},$$

$$\begin{bmatrix} b_{nu}^* \end{bmatrix} = D^* \begin{bmatrix} t_{nv}^* \end{bmatrix} - \sum_{m=1}^N g_{nm} G^* \begin{bmatrix} s_{mv}^* \end{bmatrix} + h_{nm} H^* \begin{bmatrix} t_{mv}^* \end{bmatrix},$$

where C^* , D^* , E^* , F^* , G^* , H^* are 4×4 matrices whose elements are known absolutely.

8 Calculation of the magnetic field

In the method which has been described, there are five steps in calculating the magnetic field.

- (1) The constants e_{nm} , f_{nm} , g_{nm} , h_{nm} must be calculated. Since they depend only on the geometry, the calculation need be performed only once.
- (2) For particular boundary conditions the fields H_n and H_g or the related vector potential must be calculated where required. The parameters, (s_{mv}^*) and (t_{mq}^*) , of the types of (s_{mp}) and (t_{mq}) must also be found.
- (3) The parameters, (a_{nu}^*) and (b_{nu}^*) , of the types of (a_{ni}) and (b_{nj}) can then be calculated by, at worst, 80 N² multiplications in total. In practice only about 300 N multiplications are required because most interactions between slots are negligible.
- (4) The magnetic field or the related vector potential must be calculated where required from (a_{nu}^*) and (b_{nu}^*) .
- (5) Local corrections must be made by numerical methods to allow for irregularities in the slots, such as wedge notches.

Step (4) needs further description. Within each slot, series such as

$$\sum_{i=1,3}^{\infty} \frac{z^i}{i^3}$$

appear, where z is complex and $|z| < 1$. On the stator bore series such as

$$\sum_{i=1,3}^{\infty} \frac{g(ix)}{i^3}$$

appear. Plemister (1972) and Drumm (1973) have established simple expressions for the functions defined by these series.

The time taken on an IBM 370/145 computer when the method was applied to a generator stator with 21 slots in a half circumference, was 2½ seconds (£0.02) for the initial calculations of Step (1) and 17 seconds (£0.12) for the calculations of Steps (2) to (5) inclusive.

9 Assessment of errors

The error in using C and D for A^{-1} and B^{-1} can be determined by calculating the elements of $CA - I$ and $DB - I$. The largest element of $CA - I$ is 0.0001816 in the 3, 3 position. Since the column matrix (s_{mp}) which it multiplies behaves like $\frac{1}{p^2}$ for small values of p and is

$$O\left(\frac{\ln p}{p^2}\right)$$

for large p , this is roughly equivalent to an element one ninth as great in column 1. The greatest element in column 1 is 0.0000208 in row 5. The largest element in $DB - I$ is 0.0000475 in the 4, 6 position and the largest element in column 2 is 0.0000097 in row 6. The error in using C and D for A^{-1} and B^{-1} is, accordingly, much less than 10⁻⁴.

The errors in replacing the matrices E_{nm} etc by $\left(\frac{e_{nm}}{i^2 p}\right)$ etc. and in stopping at the second term of the binomial series were investigated extensively by Drumm (1973). Within the range of air-gap lengths, slot widths, and tooth widths foreseeable on large generators, it was found that the worst error would be 2.5 × 10⁻⁴ and that the probable error was about 10⁻⁴. The error in expressing the infinite column matrices as linear combinations of four types was similar.

The error in ignoring curvature at the top of the slots was difficult to estimate but was less than 10⁻³. If this error proved troublesome in applications to smaller machines, it could be absorbed either by the local correction for the wedge notch or by a method discussed in Section 10.

There is an inconsistency in using expressions for the field which assume singularities of order $\frac{1}{2}$ at the corners of the teeth (corresponding to an infinitely permeable right-angle) when the boundary conditions arise from saturation and the angle is not exactly a right-angle. Taking the correct angle would make the order of the singularity about 0.328 and would certainly reduce it by less than 2%. The magnetic field tends to be rearranged to reduce saturation near the corners and magnetising forces of the order of 10⁵ A/m exist only very near a corner. For right-angles of constant permeability the order of the singularity remains greater

than 0.3 in absolute value for relative permeabilities as low as 21. Moreover, the singularity cannot be allowed for exactly in the finite element solution in the teeth, since its nature is undefined. It seems almost certain for these reasons, though it has not been verified, that the error caused by the inconsistency is local to the corners and smaller than the error of the finite element solutions in the teeth.

To sum up, the errors in the method are almost certainly less than those in the accompanying finite element solutions and less than the uncertainties in the manufacture of the machines. For example, the rotor can sag by more than 3 mm between the main bearings in the longest generators.

10 Extensions of the method

Including the slots in the rotor is straightforward but the interactions between stator and rotor slots change as the rotor turns. There is no limitation to two-pole machines or to a cylindrical geometry.

Three-dimensional fields which vary exponentially or sinusoidally - most can be expressed as a linear combination of such fields - can be calculated in the same way by altering the constants e_{nm} etc.

Non-rectangular slots or compensation for curvature at the top of the slot can be treated either by local corrections or by incorporating a numerical solution within the slot in the general solution and so altering the constants e_{nm} etc.

For slots that are not deep or are insufficiently separated, a related method can be employed which has proved successful for calculating fields in the end regions of generators. This will be published as early as possible.

The method cannot be applied without further development to slots in which the wedge notches are so close to the corners that effectively they change the nature of the singularities.

11 Comparisons with measurements

Calculations by computer programs based on the method have been compared regularly with measurements on large generators. They have mostly agreed within experimental accuracy. For one machine, however, they differed by as much as 15% in the 5th harmonic on short circuit, a discrepancy which has never been explained.

12 Conclusion

A rapid and accurate method has been developed for calculating magnetic fields in slotted regions.

Acknowledgements

The work formed part of a collaborative programme of research by C.A. Parsons and Company Limited and the Central Electricity Generating Board. The writer wishes to thank C.A. Parsons for permission to publish, Mr. J.G. Steel of the CEGB for his encouragement, and Dr. M.J. Drumm, who prepared the method for the digital computer.

References

- DRUMM, M.J. 1973, C.A. Parsons Working Paper.
- JONES, D.E., MULLINEUX, N., REED, J.R. and STOLL, R.L. 1969, J. Eng. Maths., vol. 3, p123-135.
- MIDGLEY, D. and SMETHURST, S.W. 1963, Proc. IEE., 110(8), p1465-1472.
- PHEMISTER, T.G. 1972, C.A. Parsons Working Paper.

Discussion following paper:

(Fox, Oxford) There are numerical methods which solve problems in adjoining regions and then satisfy the conditions at the interface. They effectively work out a few columns of the inverse matrix corresponding to the finite difference operation, and these are analogous to the Green's function at relevant points of the boundary. Is there any relation between this numerical method and your analytical method?

(Phemister, Newcastle-upon-Tyne) There is a relation. The functions used here for correcting the first simple solutions are limits of sums of Green's functions, with the properties:

- (1) They satisfy Laplace's equation everywhere: except at the interface.
- (2) They are continuous everywhere.
- (3) They have defined discontinuities of their normal derivatives at the interface.
- (4) Four of the functions are chosen in such a way that they account for the singularities of order $\pm 1/3$ at each corner

The method is, therefore, the analytical counterpart of the numerical methods which Professor Fox describes, provided that the numerical method also accounts for the singularities.

(Moses, Wisconsin) Would the method of Schwarz-Christoffel transformations be applicable to field computation for slots?

(Phemister) Yes, in two-dimensional problems it can sometimes be used as an approximation. The author's experience, however, has been that field calculations from Schwarz-Christoffel transformations are cumbersome if the boundaries are neither equipotentials nor flux lines.

(Rogers, Southampton University) The singularities introduced by the corners of the slots do give rise to involved calculation if the local field is required. Very often in machine problems only an average field is necessary and in such cases the infinite matrices may be truncated drastically with very little loss in accuracy.

(Phemister) One result of the work that has been described is that singularities need not give rise to involved calculations. The seemingly difficult functions, defined by infinite series, have all been approximated in simple forms. Certainly truncation of the infinite set of equations is sometimes justified- in a calculation of the total magnetic energy, for example, the contribution of A_{ni} would be of order $i^{-10/3}$.

(Lindholm, Ampex Corp) The method appears similar to that of FAN used to analyze the field of a two-dimensional recording head with Fourier series. Although the potential is developed in a Fourier series, the magnetic field being the spatial derivative of the potential, is singular on the corners of the magnetic material. Consequently, the magnetic field on the corners cannot be represented by a finite Fourier series. The question is: how is this singularity treated in the present method?

(Phemister) The singularity is treated by using four infinite Fourier series for each slot; collectively they can account for the singularities of order $\pm 1/3$ at each corner.

The calculation of forces and torques within numerical magnetic field calculation methods

K. Reichert, H. Freundl, W. Vogt
AG Brown Boveri
Baden/Switzerland

1) Forces and torques in magnetic fields

Magnetic fields give rise to locally varying force densities \mathbf{f} in magnetizable and current carrying bodies and consequently to body forces \mathbf{F} and torques \mathbf{T} :

$$\mathbf{F} = \int \mathbf{f} dV \quad (1) \quad \mathbf{T} = \int \mathbf{r} \times \mathbf{f} dV \quad (2)$$

These actions are of great importance in all kinds of electromagnetic devices such as electrical machinery and magnetic levitation systems (Fig. 1). The more complex magnet fields in such equipment is nowadays computed by means of numerical methods as finite difference or element methods. It is therefore desirable to have available a simple method to compute forces \mathbf{F} and torques \mathbf{T} from discrete field-quantities obtained from these computations.

2) The general expression for the force density \mathbf{f} [1,2,4]

There are several possibilities to derive expressions for the force density \mathbf{f} . Usually one starts from the power balance and then applies the principle of virtual displacement.

The power balance of a magnetic system (displacement current $\partial D/\partial t = 0$; electric energy density $\int \mathbf{E}d\mathbf{D} = 0$) can be written in the form for rigid bodies:

$$\int \left\{ \text{div} (\mathbf{E} \times \mathbf{H}) + \frac{d}{dt} \int_0^{\mathbf{B}} \mathbf{H} \cdot d\mathbf{B} + \mathbf{E} \cdot \mathbf{J} + \frac{d\mathbf{s}}{dt} \cdot \mathbf{f} \right\} dV = 0 \quad (3)$$

with: \mathbf{E} = el. field strength, \mathbf{H} = magn. field strength
 \mathbf{B} = magn. induction, \mathbf{J} = current density

$$\int_0^{\mathbf{B}} \mathbf{H} \cdot d\mathbf{B} = \text{magn. energy density}$$

$$\mathbf{E} \cdot \mathbf{J} = \text{joule power}$$

$$\frac{d\mathbf{s}}{dt} \cdot \mathbf{f} = \text{mechanical power}$$

$$\text{div} (\mathbf{E} \times \mathbf{H}) = \text{inflowing power}$$

Using Maxwells equations:

$$\text{rot } \mathbf{E} = - \frac{\partial \mathbf{B}}{\partial t} + \text{rot} (\mathbf{v} \times \mathbf{B}) \quad (4) \quad \text{rot } \mathbf{H} = \mathbf{J} \quad (5)$$

We can transform:

$$\text{div} (\mathbf{E} \times \mathbf{H}) = \mathbf{H} \cdot \text{rot } \mathbf{E} - \mathbf{E} \cdot \text{rot } \mathbf{H} = - \mathbf{H} \cdot \frac{\partial \mathbf{B}}{\partial t} - \mathbf{E} \cdot \mathbf{J} + \mathbf{H} \cdot \text{rot} (\mathbf{v} \times \mathbf{B})$$

and get

$$\int \frac{d\mathbf{s}}{dt} \cdot \mathbf{f} dV = \int \left\{ \mathbf{H} \cdot \frac{\partial \mathbf{B}}{\partial t} - \frac{d}{dt} \int_0^{\mathbf{B}} \mathbf{H} \cdot d\mathbf{B} - \mathbf{H} \cdot \text{rot} (\mathbf{v} \times \mathbf{B}) \right\} dV \quad (6)$$

In (6) the velocity $d\mathbf{s}/dt$ can be interpreted as a virtual velocity \mathbf{v} .

If the magnetic material is modeled by

$$\mathbf{B} = \mu \mathbf{H} + \mathbf{M}_p \quad (7)$$

the first two terms on the right-hand side of (6) can be transformed as follows:

$$\int \left\{ \mathbf{H} \cdot \frac{\partial \mathbf{B}}{\partial t} - \frac{d}{dt} \int_0^{\mathbf{B}} \mathbf{H} \cdot d\mathbf{B} \right\} dV = \int \left\{ \mathbf{H} \cdot \frac{\partial \mathbf{B}}{\partial t} - \frac{d}{dt} (\mathbf{H} \cdot \mathbf{B} - \int_0^{\mathbf{H}} \mathbf{B} \cdot d\mathbf{H}) \right\} dV =$$

$$= \int \left\{ \frac{\partial \mathbf{B}}{\partial t} \cdot \mathbf{H} dV = \int \left\{ \int_0^{\mathbf{H}} \frac{\partial \mu}{\partial t} \mathbf{H} d\mathbf{H} + \frac{\partial \mathbf{M}_p}{\partial t} \cdot \mathbf{H} \right\} dV =$$

$$= - \int \mathbf{v} \cdot \left\{ \text{rot } \mathbf{H} \times \mathbf{M}_p + \mathbf{H} \text{div} \mathbf{M}_p + \int_0^{\mathbf{H}} \text{grad } \mu \mathbf{H} d\mathbf{H} \right\} dV \quad (7)$$

$$\text{with } \frac{\partial \mu}{\partial t} = -\mathbf{v} \cdot \text{grad } \mu - \mu \text{ div } \mathbf{v}$$

$$\frac{\partial \mathbf{M}_p}{\partial t} = \text{rot}(\mathbf{v} \times \mathbf{M}_p) - \mathbf{v} \text{ div } \mathbf{M}_p$$

$$\int \mu \text{ div } \mathbf{v} \, dV = \oint \mu \, \mathbf{v} \cdot d\mathbf{f} = 0$$

$$\begin{aligned} \int \mathbf{H} \cdot \text{rot}(\mathbf{v} \times \mathbf{M}_p) \, dV &= \int \text{div}(\mathbf{H} \times (\mathbf{v} \times \mathbf{M}_p)) \, dV + \int (\mathbf{v} \times \mathbf{M}_p) \cdot \text{rot } \mathbf{H} \, dV \\ &= - \int \mathbf{v} \cdot (\text{rot } \mathbf{H} \times \mathbf{M}_p) \, dV \quad (8) \end{aligned}$$

The term $\mathbf{H} \cdot \text{rot}(\mathbf{v} \times \mathbf{B})$ in (6) can be similarly transformed:

$$\int \mathbf{H} \cdot \text{rot}(\mathbf{v} \times \mathbf{B}) \, dV = - \int \mathbf{v} \cdot (\text{rot } \mathbf{H} \times \mathbf{B}) \, dV \quad (9)$$

Introducing (5) in (8) and (9), (8) in (7), (7) + (9) in (6) we get

$$\int \mathbf{v} \cdot \mathbf{f} \, dV = \int \mathbf{v} \cdot \left\{ \mathbf{J} \times (\mathbf{B} - \mathbf{M}_p) - \mathbf{H} \text{div } \mathbf{M}_p - \int_0^H \text{grad } \mu \, \mathbf{H} dH \right\} \, dV \quad (10)$$

and thus the expression for the force density \mathbf{f} :

$$\mathbf{f} = \mathbf{J} \times (\mathbf{B} - \mathbf{M}_p) - \mathbf{H} \text{div } \mathbf{M}_p - \int_0^H \text{grad } \mu \, \mathbf{H} dH \quad (11)$$

by comparing the terms on both sides of (10).

The different terms in the force density (11) can be interpreted as follows:

- $\mathbf{J} \times \mathbf{B}$ is the force on a current carrying conductor in air
- $\mathbf{H} \text{div } \mathbf{M}_p$ is the force on a permanent magnet ($\mathbf{J} = 0, \text{grad } \mu = 0$)
- $\int_0^H \text{grad } \mu \, \mathbf{H} dH$ is the force in iron ($\mathbf{J} = 0, \mathbf{M}_p = 0$)

but in general it is not possible to so assign the terms of (11).

3) The calculation of forces \mathbf{F} and torques \mathbf{T} by means of surface integration [1..4]

The calculation of forces and torques by means of eg. (1) and (2) using (11) in numerical field calculations is inadvisable and inefficient because:

- Eq. (1) and (2) require volume integration
- in non linear cases ($\mu = f(H \text{ or } B)$) the magnetic history should be known, otherwise (10) can not be evaluated i.e. several field calculations.

The solution to this problems is

- calculation of \mathbf{F} and \mathbf{T} by means of surface integration
- surface integration in $\mu = \text{const}$ (air).

The volume integrals (1) and (2) can be transformed into surface integrals as the integration of a surface stress p over an arbitrary surface enclosing the body (Fig. 2) should result in the same forces and torques as the volume integration over the body using the force density \mathbf{f} (11). i.e.:

$$\mathbf{F} = \int_V \mathbf{f} \, dV = \oint_A \mathbf{p} \, dA \quad (12)$$

$$\mathbf{T} = \int_V \mathbf{r} \times \mathbf{f} \, dV = \oint_A \mathbf{r} \times \mathbf{p} \, dA \quad (13)$$

By defining the tensor $\phi : \mathbf{f} = \text{div } \phi$ the volume integral can be converted into a surface integral using gauss integral formulae. This results in:

$$\mathbf{p} = \mathbf{H} (\mathbf{n} \cdot \mu \mathbf{H}) - \mathbf{n} \int_0^H \mu \, \mathbf{H} dH \quad (14)$$

with \mathbf{n} the unit outward vector normal to the surface A . If the integration surface A is outside the material the expression for the surface stress \mathbf{p} (14) can be simplified to:

$$\mathbf{p} = \mu_0 (\mathbf{n} \cdot \mathbf{H}) \mathbf{H} - \frac{1}{2} \mu_0 H^2 \mathbf{n} = \frac{1}{\mu_0} (\mathbf{n} \cdot \mathbf{B}) \mathbf{B} - \frac{1}{2\mu_0} B^2 \mathbf{n} \quad (15)$$

It is interesting to note that in eq. (15) the non linear character of the body which is enclosed by the surface A is not directly expressed.

Eq. (15) together with (12) or (13) is best suited to the calculation of forces and torques of discrete field values resulting from numerical field calculations because

- only surface integration is required
- in nonlinear cases ($\mu = f(B \text{ or } H)$) one field calculation is sufficient if the integration surface A is in air.
- Any integration surface A will result in the same force if the body is fully enclosed.

However this method also has some limitations:

- The result is always a total force F or torque T acting on a simple connected body.
- Fictive air gaps are not allowed if they are disturbing the field.
- The method does not provide information over the body stress as eq. (11).
- The body has to be rigid.

4) The calculation of forces \mathbf{F} and torques \mathbf{T} within numerical field calculations

4.1 Procedure in general

The calculation of a body force \mathbf{F} or torque \mathbf{T} by means of eq. (12), (13) and (15) is straightforward.

- Calculate discrete values of potentials (vector- or skalarpotential \mathbf{A} , φ) or other descriptive field quantities, by means of finite difference, finite element or other numerical techniques using a grid or element distribution.
- Define the integration surface A around the body. Any A should result in the same force and torque as long as the body is enclosed. Therefore simplified integration surfaces A can be chosen (Fig.2,3). The surface A should pass through the centers of the elements.
- Calculate the magnetic field strength \mathbf{H}_i or the induction \mathbf{B}_i in the elements i crossed by A .
- Calculate the surface stress \mathbf{p}_i (15) in the element i .
- Calculate the force \mathbf{F} and the torque \mathbf{T} :

$$\mathbf{F} = \sum \Delta \mathbf{F}_i = \sum_{i=1}^N \mathbf{p}_i \Delta A_i \quad (16) \quad \mathbf{T} = \sum \Delta \mathbf{T}_i = \sum_{i=1}^N \mathbf{r}_i \times \mathbf{p}_i \Delta A_i \quad (17)$$

4.2 Procedure for some typical elements

a) Two-dimensional rectangular element: $\mathbf{p} = (p^x, p^{y'})$

With the vectorpotentials A_{ik} , $A_{i, k+1}$, $A_{i+1, k}$, $A_{i+1, k+1}$ in the corners of the rectangular element (Fig. 4), one calculates the components of the induction:

$$B_{i,k}^x = \frac{A_{i, k+1} + A_{i+1, k} - A_{i, k} - A_{i+1, k+1}}{2 h_k}$$

$$B_{i,k}^y = \frac{A_{i,k+1} + A_{i,k} - A_{i+1,k+1} - A_{i+1,k}}{2 h_i}$$

If the integration surface A has the direction of the x-axis, we have $\mathbf{n} = e_y$

$$p_{i,k}^{xy} = \frac{1}{\mu_0} B_{i,k}^x \cdot B_{i,k}^y ; \quad p_{i,k}^{yy} = \frac{1}{2\mu_0} (B_{i,k}^{y2} - B_{i,k}^{x2})$$

$$\Delta F_{i,k}^{xy} = \ell \cdot p_{i,k}^x \cdot h_i ; \quad \Delta F_{i,k}^{yy} = \ell \cdot p_{i,k}^y \cdot h_i$$

ℓ is the length perpendicular to the xy plane.

For $\mathbf{n} = e_x$ we get:

$$p_{i,k}^{xx} = \frac{1}{2\mu_0} (B_{i,k}^{x2} - B_{i,k}^{y2}) = -p_{i,k}^{yy} \quad (18)$$

$$p_{i,k}^{yx} = \frac{1}{\mu_0} B_{i,k}^x B_{i,k}^y = p_{i,k}^{xy} \quad (19)$$

$$\Delta F_{i,k}^{xx} = \ell \cdot p_{i,k}^{xx} h_k ; \quad \Delta F_{i,k}^{yx} = \ell \cdot p_{i,k}^{yx} \cdot h_k$$

b) Two-dimensional triangular element: $\mathbf{p} = (p^x, p^y)$ (Fig. 5)

The path of integration can be:

1-s-2, 1-s-3, 2-s-3 or any others.

In a first-order element the induction B is constant and given by:

$$B^x = \frac{\partial A}{\partial y} = \frac{1}{2F} \sum_{i=k,n,m} c_i A_i ; \quad B^y = \frac{\partial A}{\partial x} = \frac{1}{2F} \sum_{i=k,n,m} b_i A_i$$

with $b_k = y_m - y_n ; \quad c_k = x_n - x_m$

$b_m = y_n - y_k ; \quad c_m = x_k - x_n$

$b_n = y_k - y_m ; \quad c_n = x_m - x_k$

F = Fläche Δ

The normal vector to the integration path 1-s is:

$$\mathbf{n}_{1s} = \frac{i(y_n - \frac{y_m + y_k}{2}) - j(x_n - \frac{x_m + x_k}{2})}{\sqrt{(x_n - \frac{x_m + x_k}{2})^2 + (y_n - \frac{y_m + y_k}{2})^2}}$$

or $\mathbf{n}_{1s} = i n_{1s}^x + j n_{1s}^y$

The contribution ΔF_{1s} of the integration path 1-s to the force F is therefore:

$$\mathbf{F}_{1s} = \frac{\ell \cdot \ell_{1s}}{u_0} (n_{1s}^x B^x + n_{1s}^y B^y) (i B^x + j B^y) - \frac{1}{2} (B^{x2} + B^{y2}) \cdot (i n_{1s}^x + j n_{1s}^y)$$

with $\ell_{1s} = \frac{1}{3} \sqrt{(x_n - \frac{x_m + x_k}{2})^2 + (y_n - \frac{y_m + y_k}{2})^2}$

Similar expressions can be derived for the contributions of 2-s and 3-s.

c) Complex field quantities

If the variation of the field is quasistationary sinusoidal, the situation can best be described by complex quantities:

$$B^x = \text{Re } \underline{B}^x e^{j\omega t} \quad (20)$$

Where \underline{B}^x is complex: $= B^x e^{j\varphi_x}$. Introducing this in eq. (18) we receive for the components of $p_{i,k}$

$$p_{i,k}^{xx} = \frac{1}{2\mu_0} (\text{Re } \underline{B}^x e^{j\omega t} \cdot \text{Re } \underline{B}^x e^{j\omega t} - \text{Re } \underline{B}^y e^{j\omega t} \cdot \text{Re } \underline{B}^y e^{j\omega t}) \quad (21)$$

$$p_{i,k}^{yx} = \frac{1}{\mu_0} \text{Re } \underline{B}^x e^{j\omega t} \cdot \text{Re } \underline{B}^y e^{j\omega t} \quad (22)$$

with $\underline{n} = e_x + e_y$

If Z_1 and Z_2 are to complex numbers we have the relationship:

$$\text{Re } (Z_1) \text{Re } (Z_2) = \frac{1}{2} \text{Re } (Z_1 \cdot Z_2 + Z_1 \cdot Z_2^*)$$

* means conjugate complex.

Using this relation we receive for $p_{i,k}^{xy}$:

$$p_{i,k}^{yx} = \frac{1}{2\mu_0} B^x B^y \left\{ \cos (2\omega t + \varphi_x + \varphi_y) + \cos (\varphi_x - \varphi_y) \right\}$$

This means that the method is also applicable to sinusoidal fields, if we use a complex potential \underline{A} :

$$A = \text{Re } \underline{A} e^{j\omega t}$$

with $\underline{A} = AR + jAI$ we can calculate:

$$B_{i,k}^x = \frac{1}{2h_k} \sqrt{\frac{(AR_{i,k+1} + AR_{i+1,k} - AR_{i,k} - AR_{i+1,k})^2 + (AI_{i,k+1} + AI_{i+1,k} - AI_{i,k} - AI_{i+1,k})^2}{}}$$

and $B_{i,k}^y$ in the same way if we have a rectangular grid.

5) Application

A system of subroutines has been written to compute forces and torques from discrete field quantities based on a certain element type. The method has been applied to a number of magnetic field and eddycurrent problems.

Fig. 6 shows an example, the magnetic field in a cross-section of a magnetic levitation system. The main problem was there the calculation of the forces F^x and F^y between the rail and the magnet especially for different off-set positions x/b because in this design the magnet is also supposed to keep the train in the middle of the rail. Using a rectangular grid, the vector potential approach and the finite element method the discrete field distribution was calculated considering saturation in the iron. From these quantities the forces F^x and F^y were derived by means of surface integration. The results (Fig. 7) did agree very well with measurements.

Literature:

- [1] Diesselhorst, H. : Magnetische Felder und Kräfte
J.A. Barth-Verlag, Leipzig, 1939
- [2] Stratton, J.A. : Electromagnetic Theory
- [3] Carpenter, C.J. : Surface integration methods of calculating forces on magnetic iron parts
Proc. I.E.E. 106C (1960)
- [4] Kamerbeek E.M.H. : On the theoretical and experimental determination of electromagnetic torques in electrical machines
Philips. Res. Rept. Suppl. 1970, No.4

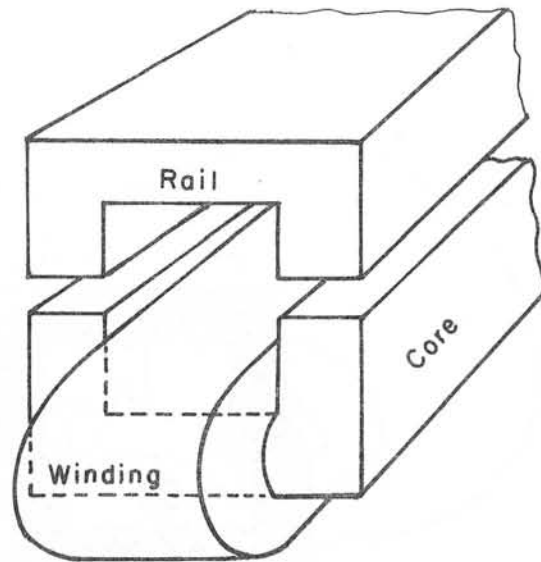


Fig.1 : Magnetic levitation system

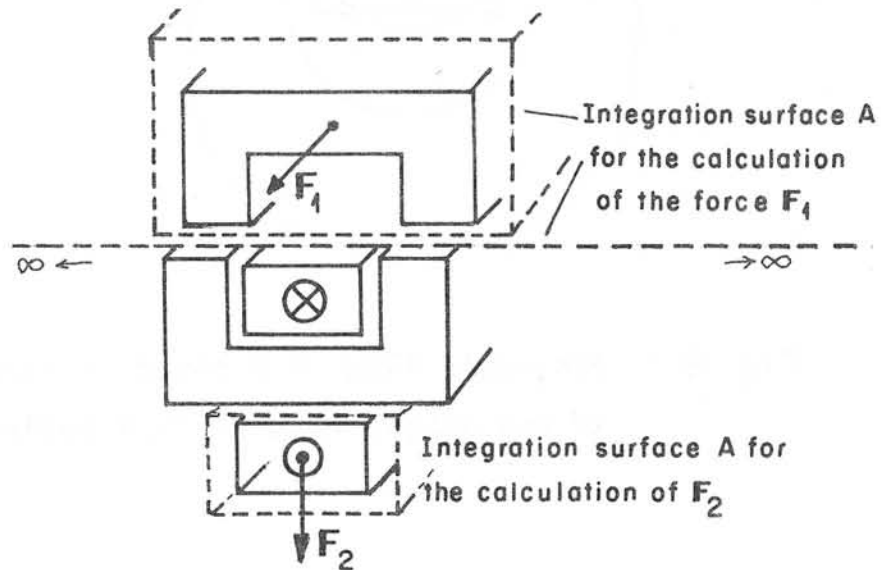


Fig. 2 : Definition of the surface integration

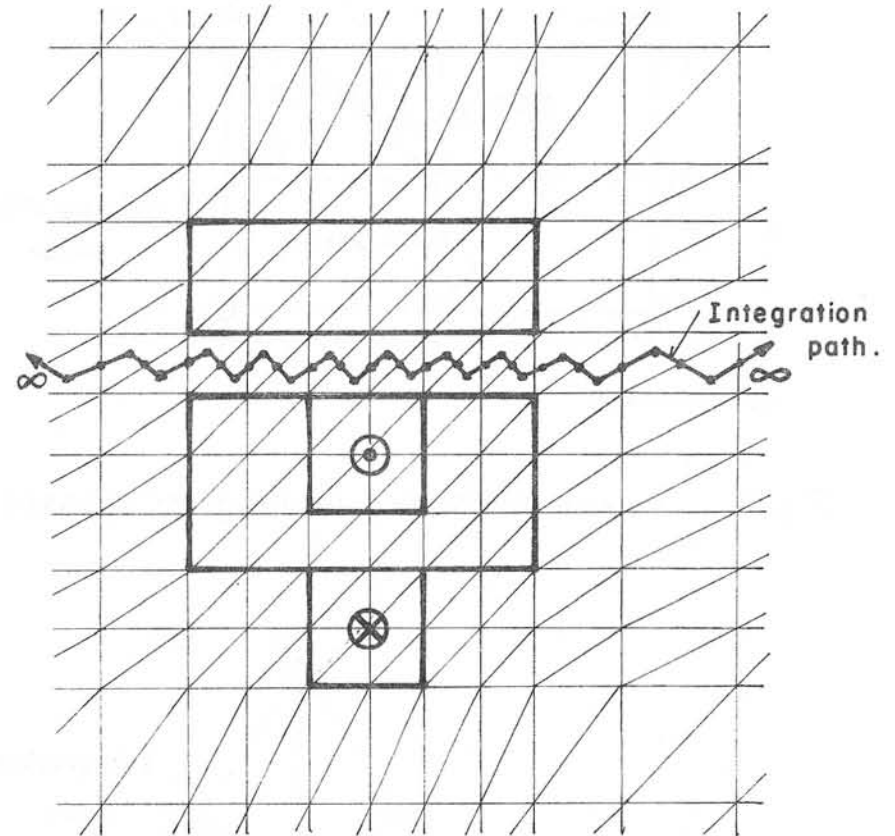


Fig. 3 : Finite element grid, integration path for force calculation by surface integration.

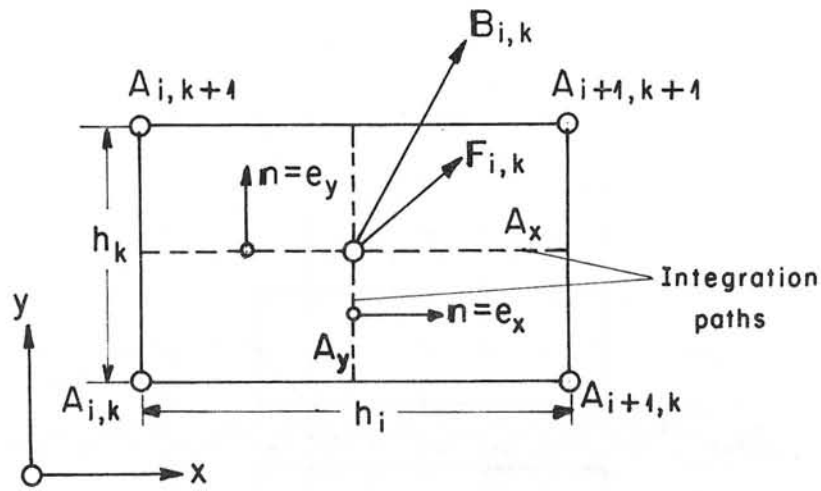


Fig. 4 : Two-dimensional rectangular element

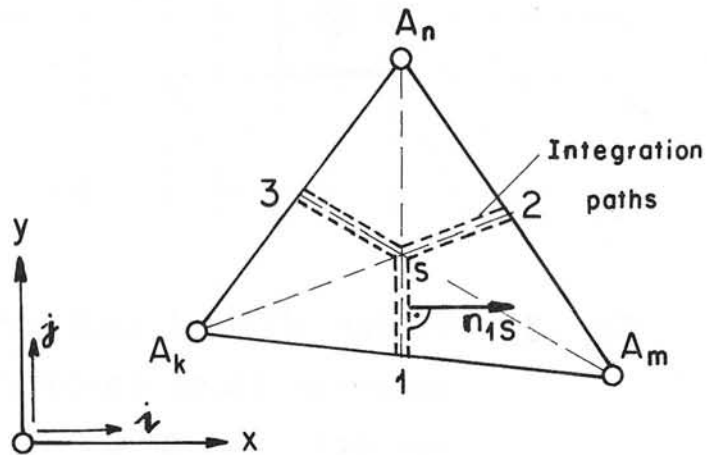


Fig. 5 : Two-dimensional triangular element

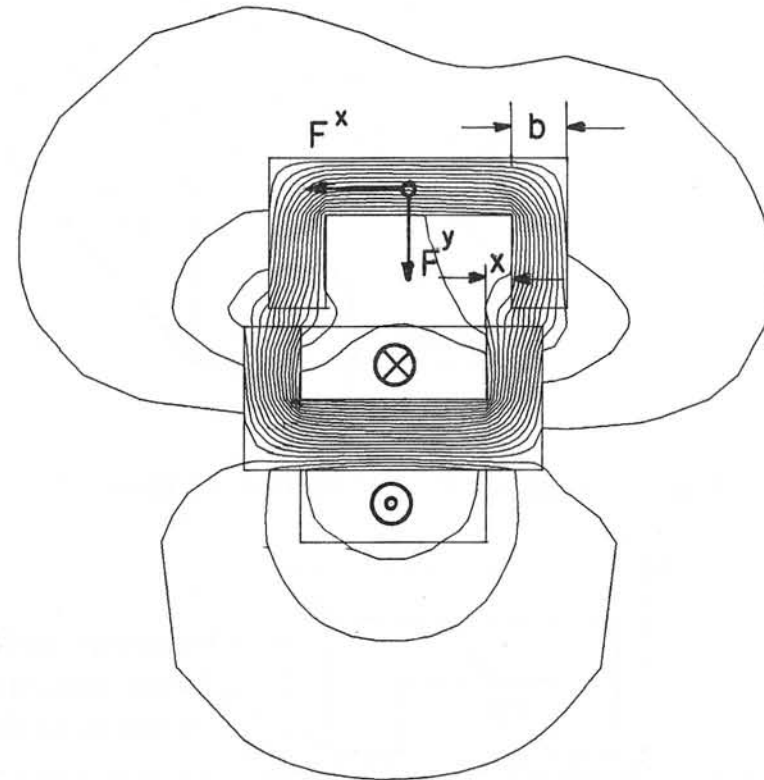


Fig. 6 : Magnetic field in a cross-section of the magnetic levitation system

tional definition, all methods lead to the same result. Moreover, if we define "Stress" in any looser way, then I have found that, where the stresses are large enough to be of importance in engineering applications (i.e. near failure) then the differences which we obtain by using different models are too small to be experimentally significant.

I suggest that simple energy arguments can be misleading in these contexts and that deriving the Maxwell stress equations this way can imply unnecessary limitations, because of problems associated with energy loss in eddy currents and hysteresis. I am sure Dr Reichert will agree that surface integration will always give the force on whatever is enclosed by the surface, whether the energy is conserved or not.

Dr Reichert referred to the need to make air gaps around the part of the interest as a limitation of the method. I regard it, on the contrary, as an asset. If the force which we compute is to be observable (and therefore meaningful) we must be able to separate the part from the rest of the device. In practice we always have air gaps, however, small they may be, and the method draws attention to any peculiarities, such as domain effects which may be associated with iron surfaces (nearly) in contact with each other.

My final point concerns the shape of the surfaces which we choose to integrate over. These do not have to conform with the iron surfaces, and there are sometimes substantial advantages to be gained by choosing other shapes, particularly when calculating "sideways" forces, as in Dr Reichert's two C-cores. The possibilities can be illustrated most clearly by tracing a simplified example. The sideways force on a slot carrying a current (Fig A) can be shown, usually by energy arguments, to be the same as if the conductor were placed in the gap and the slot filled in. This is difficult to show by an integration surface which passes straight through the gap or by one which follows the slot surface. But, the integration surface shown in Fig A gives the force by inspection:

$$F = \frac{1}{2} g (H_1^2 - H_2^2) = I \frac{H_1 + H_2}{2} \quad \text{N/m}$$

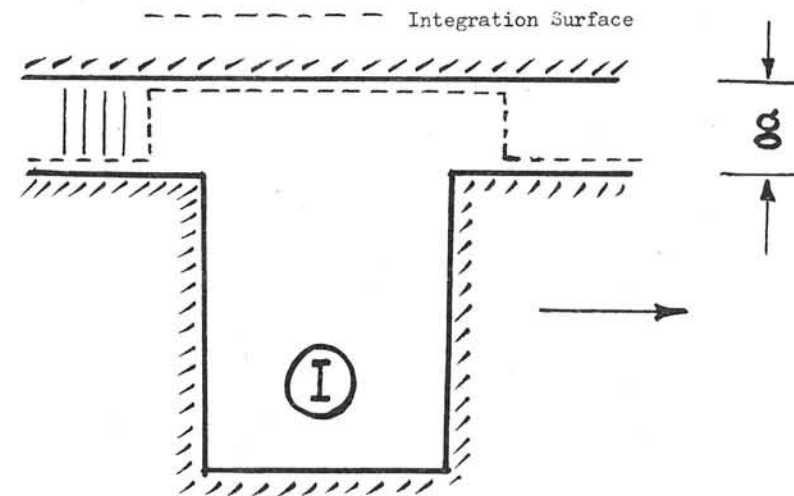


Fig A Conductor in Slot

(Reichert/Freundl) Our eq (11) gives the force density in an infinitesimal volume element dV . Therefore we cannot distinguish between different forces. The situation is different if one is interested in the force on a finite volume. A permanent magnet for example can be modelled either by surface charges or by Ampere's currents. The total force in both cases is the same but the stress inside is different. Therefore, we agree that the distinction between magnetic and mechanical forces inside is "model depending" and therefore meaningless.

(Perin, Cern) 1. Does your method assume that all the magnetic flux which crosses the integration surface passes through the ferro-magnetic body?

2. How close has the surface in air to be to the body?

(Reichert) 1. No, any field situation can be handled.

2. The path of integration has to be in air, it has to be closed but it can be arbitrary within this limit. The resulting force is independent

of the path of integration but can depend on the accuracy of the discrete field quantities as calculated by the FE-method.

(Chevalley, Cern) Have you ever looked at the contributions of the difficult terms in the equation?

In a particular case I found that the integral $\int \text{grad } \mu \text{ HdH}$ is small ($\sim 3\%$) and could be ignored.

(Reichert) The contribution of the different terms in the volume element force equation is problem dependent. Therefore a general answer cannot be given to the answer. In an electric machine for example the term $F \times \mu H$ is only important if the conductor is exposed to the field H (open slot).

(Armstrong, Rutherford) How do you deal with the singularity at the corners of the surface of integration?

Your general method is given in J Strattan, Electromagnetic Theory (McGraw Hill 1941).

(Reichert) In a FE solution a singularity does not show up unless the element size is not zero. The result is always a finite magnetic field distribution in the grid, even at the corners. With reference to your statement there are a number of textbooks which are describing the method in general, but to my knowledge up to now nobody has mentioned the application of the method within the FE - or FD - method.

CALCULATION OF THE MAGNETIC SYSTEM ELEMENTS OF THE
ISOCHRONOUS CYCLOTRON BY THE GRID METHOD

Yu.G.Alenitsky, S.B.Vorozhtsov, N.L.Zaplatin
Laboratory of Nuclear Problems
Joint Institute for Nuclear Research, Dubna, USSR

I. Introduction

The calculation of magnetic fields by the grid method in systems containing ferromagnetic and current elements allows one to analyse the effect of iron saturation and magnetic flux distribution when induction is varied in a wide range. By using the available programmes for calculating the two-dimensional configuration, ref. /1,2,3,4,5/, one can obtain good quantitative results. By separating the cross section for calculations from the whole three-dimensional configuration and choosing for it some realistic boundary conditions one can obtain the results coinciding with the experiment to an accuracy of (1±5)%.

II. Short Description of the Programme

The TRIMA programme system, a modified version of the TRIMD^{/2/} programme which in its turn had been written basing on ref. /1/, has been developed at the Laboratory of Nuclear Problems, JINR.

The programme solves the nonlinear differential equation of elliptical type in private derivatives presented in the finite-difference form. The equation is as follows:

For the Cartesian system of coordinates (x,y)

$$\frac{\partial}{\partial x} \left[\frac{1}{\mu} \frac{\partial u(x,y)}{\partial x} \right] + \frac{\partial}{\partial y} \left[\frac{1}{\mu} \frac{\partial u(x,y)}{\partial y} \right] = -0,4\pi J(x,y)$$

For the cylindrical system of coordinates (r,z)

$$\frac{\partial}{\partial z} \left[\frac{1}{\mu r} \frac{\partial [r \cdot u(r,z)]}{\partial z} \right] + \frac{\partial}{\partial r} \left[\frac{1}{\mu r} \frac{\partial [r \cdot u(r,z)]}{\partial r} \right] = -0,4\pi J(r,z)$$

where U is the vector potential of the magnetic field (G × cm), $\mu = \mu(B)$ is the permeability of ferromagnetic, J is current density (a/cm²), U and J are the normal planes (x,y) or (r,z).

Fig. 1 shows the diagrams of possible boundary conditions. The Dirichlet zero boundary condition is set at all boundaries (fig.1-A) in usual cases. If the axis y=0 is the symmetry axis, the Neumann zero condition is set at this boundary. For the cylindrical system of coordinates with $r \rightarrow 0$ the vector potential is found from the condition $rU(r,z) = a(z) \times r^2$ which results from the fact that at the r=0 axis the field is an even function.

The TRIMA programme approximates the $u(B^2)$ dependence by the analytic expression proposed in^{/6/}. As a result of the optimization of the programme part, the time consumption for calculations is reduced about 4 times, the number of grid points was increased up to 1600 (without using the external computer memory). The programme has been written for the BESM-6 computer.

III. Calculation of the Magnetic System Elements

As has been shown in ref. /7/, the amplitude of the magnetic field variation of spiral shims is fairly well described by the infinite system of rectilinear ferromagnetic bars. To choose preliminary the azimuthal width and the height of the spiral shims of the "F" facility some experiments have been performed by using 4 pairs of rectilinear bars^{/8/}.

A similar mathematic modelling may be performed by using the computer programme. Fig. 2 shows the experimental lay out with ferromagnetic bars in the electromagnet gap and the calculation region shown by the dashed line. The results of calculations are presented as a function of $B_1 = F(B)$, where

$$B_1 = 0.5 / B(0,0) - B(X_{\max}, 0) / ,$$

$$B = 0.5 / B(0,0) + B(X_{\max}, 0) / .$$

For the programme calculation of the configuration of this type a scheme of boundary conditions is envisaged, which is shown in fig. 1.B.

The left and right boundaries of the calculation region are set by $U(0,y) = \text{const}_1$, $U(x_{\text{max}},y) = \text{const}_2$ which indicates the absence of the flux going through these boundaries. At the $y = 0$ boundary the Neumann zero condition is possible, when $y = 0$ is the symmetry axis or the Dirichlet zero condition. For $y = y_{\text{max}}$ the Neumann zero condition or the Dirichlet condition is possible $U(x, y_{\text{max}}) = f(x)$.

The calculation of our rectilinear bars was made for the following boundary conditions:

$$U(0,y) = 0, U(x_{\text{max}},y) = B_0 \times x_{\text{max}}, \frac{\partial U(x,y)}{\partial y} \Big|_{y=0} = 0$$

at the $y = y_{\text{max}}$ boundary the following two boundary conditions were set:

$$U(x, y_{\text{max}}) = B_0 \times x, \frac{\partial U(x,y)}{\partial y} \Big|_{y=y_{\text{max}}} = 0$$

In this case the calculation results remained the same. This may be explained by the fact that the upper boundary is located sufficiently far so that no redistribution of the magnetic flux at the pole caused by bars located in the electromagnet gap, at the upper boundary of the calculation region occurs.

The calculation shows fairly well the state of ferromagnetic elements and the redistribution of the μ magnetic permeability and the magnetic fluxes when the field level is changed. Fig. 3 shows the flux distribution for run I (fig.2) at the average induction level in the gap (1.0T, 1.3T, 1.6T). As the calculations show, with the average level of the induction $B = 1.3T$, the rectilinear bar approaches saturation, the induction inside the bar is $B=(2.0-2.1)T$. For the calculation of $B_1(B)$ (800 mesh points, five induction levels) twelve minutes of the BESM-6 computer time are required.

The comparison of calculation and experimental dependences (fig.2) shows that the curves are identical.

The difference of the value $2B_1$ obtained by calculation from that obtained experimentally is (1-3)% and may be explained by the finiteness of ferromagnetic bars used in the

experiment, by the decrease of the field in the flat gap of the electromagnet and the discrepancy of the $\mu(B)$ properties of the applied ferromagnetic and calculation approximation.

An example of the calculation of the electromagnet pole edge is shown in fig. 4. The mesh of 1500 points is used, the BESM-6 computer time is about 10 minutes. The boundary conditions differ from those used above only at the upper boundary which is distributed into two parts (fig. 1-C).

1) $x < x_k$ is the constant flux,

2) $x > x_k$ is the flux determined by the potential of

the magnetic dipole.

As is seen from Fig.4, in the radial region of the $r < r_k$, where r_k is the radius of the electromagnet pole, the difference of calculations from the curve obtained experimentally by using the electromagnet ($\emptyset 1200\text{mm}$) does not exceed 0.5%. However, the great divergence of the experiment and calculation curves for $r > r_k$ is seen. This means that the boundary potential given as a dipole potential differs from real conditions at the electromagnet.

It is necessary to mention that when using the boundary conditions of this type, it is desirable to fulfil the following correlations:

$$Z_{\text{max}} > 2 h_M, r_{\text{max}} > 1.2 r_k$$

When developing the magnet system for the U-120M isochronous cyclotron it is important to select such a configuration of spiral shims which could provide the minimum relative changing of the magnetic fields when varying the induction level.

As has been shown in ref. /9/, one may achieve this for the central region of the magnetic system by varying the angular width of spiral shims and using the axial grooves in them.

The general schematic view of the cross section along

the spiral axis line of the U-120M magnetic system is shown in fig. 5, the dashed line shows the calculation region. The boundary conditions are given as shown in fig.1-B.

The results of calculations for the shims with grooves and without them at two limit induction levels are shown in figs. 6,7^{10/}. Comparing figs. 6-C and 6-D, one may see the essential increase of the horizontal component of the flux at the low induction level, which results in field increase in the median plane at small radii (fig. 8-A).

As is seen from figs. 6-A and 6-C, the vertical grooves reduce the fraction of the flux hitting the centre from large radii at low induction.

Thus, in the case of shims with grooves (figs.6-A,B) one observes less essential change of the pattern of magnetic flux distribution with increasing the induction level.

Figs. 7-C and 7-D show the distributions of magnetic permeability for shims without grooves. With $B = 1.0$ T (Fig.7-C) a sharp increase of permeability is observed with decreasing the radius. The gradient is $d\mu/dr = -250 \text{ cm}^{-1}$ with $r = 7$ cm, therefore, the magnetic flux lines are directed to the centre. At large induction levels $B = 2.2$ T (fig. 7-D) the shim is saturated, and μ at a larger shim section does not exceed 10 and nearly uniform distribution of permeability is observed. In this case the gradient $d\mu/dr = -2.0 \text{ cm}^{-1}$ over the larger part of the central shim region. Consequently, the horizontal component of the flux is reduced which results in field increasing at small radii.

A similar μ distribution at the same induction levels for shims with grooves are shown in figs. 7-A and 7-B. Comparing fig.7-C and 7-A relating to low induction one observes the following:

- 1) the distributions, μ , at the pole are of similar kind,
- 2) the central part and the shim teeth are not saturated, axial grooves in the shims prevent the passage of the horizontal component in the teeth region. Such unsaturated teeth promote the uniform passage of the flux through the

shim and pole contact region. This is proved by the reduction of the pole permeability in the regions opposite the teeth and the increase of the pole permeability over the grooves (the reflection effect).

3. The general state of the shim section under the grooves is described by a lower average value of the permeability $\mu = 15$ at the same excitation level which impedes the deflection of the magnetic flux lines in the horizontal direction.

4. The radial gradients μ of the shims under the grooves are considerably smaller than those in the shims without grooves.

With large induction levels (fig. 7-B) the shim teeth are saturated approximately equally with the lower part of the shim. Horizontal fluxes similar to the case with shims without grooves are impeded. Special attention should be paid to the region of larger μ in the shim body directly under the grooves as well as a more noticeable effect of reflecting the teeth at the pole.

The calculational distribution of magnetic field intensity in the median plane for the case under consideration are shown in fig. 8-A. The curves are matched in pairs at the field level for $r = 16$ cm. For the shim with grooves (curves 3 and 4) the field difference in the radial range of 3-10 cm is reduced about 300 Oe, and the field peak due to the horizontal component of the flux disappears.

Fig. 8-B shows the experimental values of the field peak for configurations and excitation levels under consideration. The comparison with calculational data shows the coincidence of the dependences. However, in the range of $r = (30-35)$ cm noticeable distortions are observed which are caused by artificial conditions of flux absence through the right-hand side boundary taken in the calculation scheme.

In conclusion it is worth mentioning that the given calculations do not claim for complete quantitative

description of 3-dimensional structure of the magnetic system and are just a model for clearing out the physical phenomenon in this part of the magnetic system. The calculation model makes it possible to determine the variations of magnetic field intensity and the redistribution of μ in iron when varving the shim geometry.

The calculations of the chosen parts of the magnetic system performed by using the TRIMA programme do not consume much computer time. Hence, this method can be extensively used when modelling complicated magnetic systems. Despite the fact that the accuracy of calculations (1+5)% is much poorer than that for field shaping (0.02%) required for accelerators, such calculations are the only method permitting the analysis of the magnetic state of ferromagnetic when varying its configuration and the level of the external magnetizing field.

References

1. A.M.Winslow, J. Computer Phys., V 1, No.2(1966)pp.149-172.
2. S.B.Vorozhtsov, L.T.Zakamskaya, N.L.Zaplatin. JINR Communication P9-5013, Dubna, 1970.
3. M.T.Diserens, RMEL/R, 171(1969).
4. John S.Colonias. "Partical Accelerator Design.Computer Program". Academic Press, New-York and London, 1974.
5. Y.T.Puzynovich. NIIIEFA Preprint B-0178, Leningrad, 1973.
6. Y.S.Derendyaev, B.A.Klenin. JINR Communication, P-11-6579, Dubna, 1972.
7. V.P.Dmitrievsky, et al. JINR Communication, 1431, Dubna, 1960.
8. S.B.Vorozhtsov, N.I.Dyakov, N.L.Zaplatin, JINR Communication, 9-4517, Dubna, 1969.
9. Y.G.Alenitsky, N.L.Zaplatin, A.A.Kropin, N.A.Morozov. Proc. III Working Meeting on the U-120M Isochronous Cyclotron, Czeske Budejovic, CSSR, 14-18 May, 1973. JINR Communication P9-7339, Dubna, 1973.
10. Y.G.Alenitsky, S.B.Vorozhtsov, N.L.Zaplatin, JINR Communication P9-7412, Dubna, 1973.

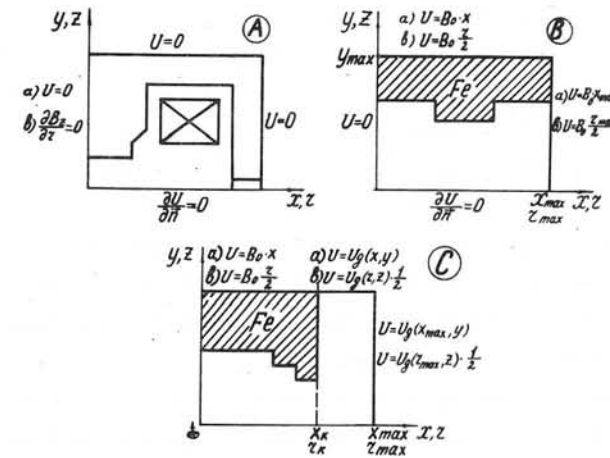


Fig. 1

- 1) Boundary conditions: a) Cartesian system of coordinates
- b) cylindrical system of coordinates.

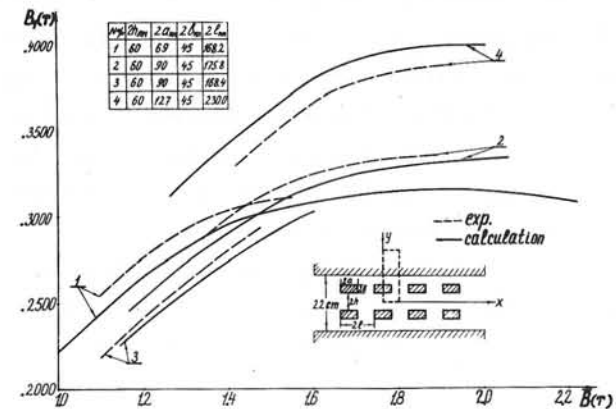


Fig. 2 .

Experimental procedure and the calculation of the rectilinear bar system. The dependences $B_1(B)$.

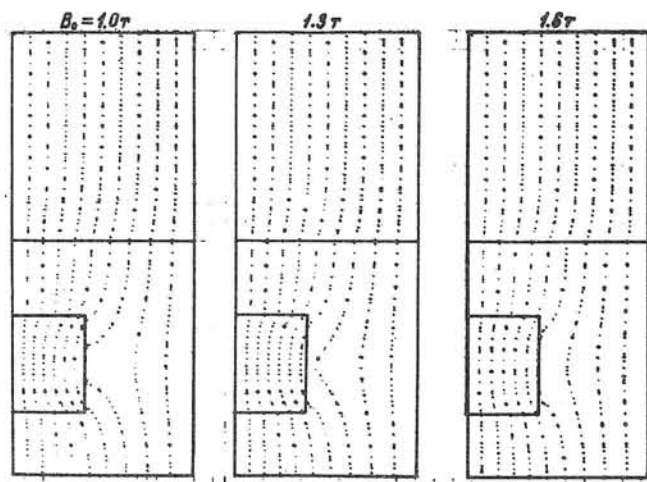


Fig. 3

Distribution of magnetic flux lines for the following levels: $B = 1.0 \text{ T}$, 1.3 T , 1.6 T

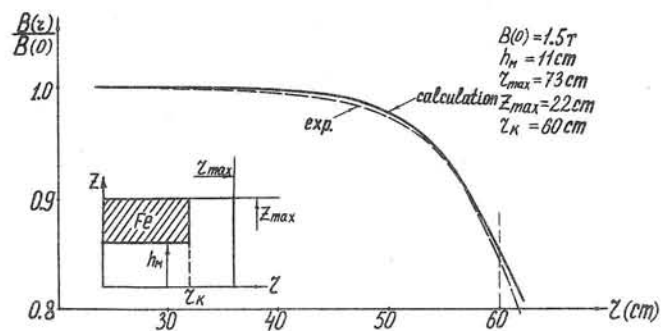


Fig. 4

Electromagnetic pole edge, the calculation procedure and the obtained characteristics of $B(r)/B_0$.

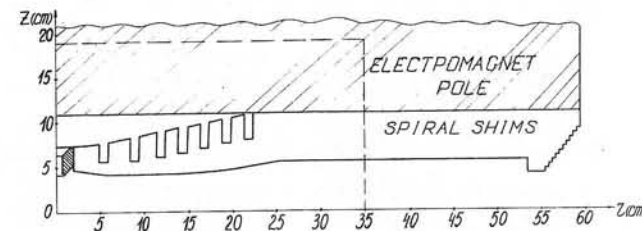


Fig. 5

Cross section of the U-120M magnetic system, the dashed line is the calculation region.

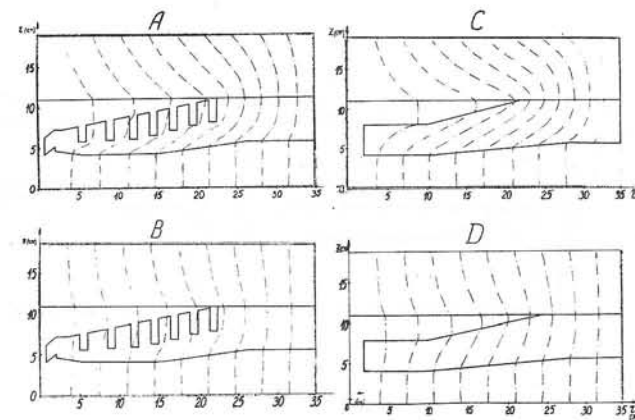


Fig. 6

The distribution of the magnetic flux lines

A, C - $B_0 = 1.0 \text{ T}$

B, D - $B_0 = 2.27 \text{ T}$

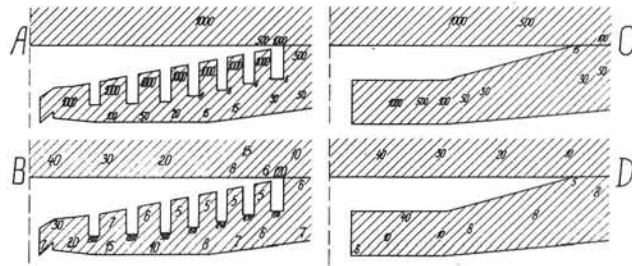


Fig. 7

Distribution of magnetic permeability

A, C - $B_0 = 1.0 \text{ T}$
 B, D - $B_0 = 2.27 \text{ T}$

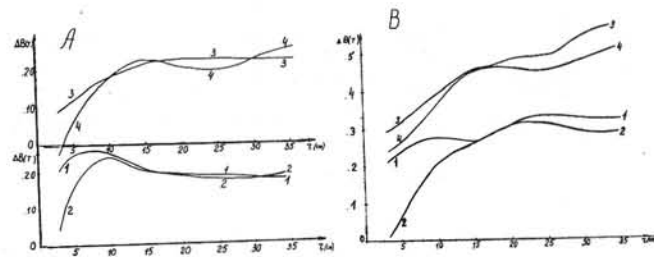


Fig. 8

Magnetic field intensity in the median plane

A- calculation , B -measured magnetic field in the hill

1,2 - shims without grooves

3,4 - shims with grooves

1,3 - $B_0 = 1.0 \text{ T}$

2,4 - $B_0 = 2.27 \text{ T}$.

ON THE COMPUTATION OF THREE-DIMENSIONAL MAGNETOSTATIC FIELDS BY THE INTEGRAL EQUATION METHOD

V.Ts.Banchev, S.B.Vorozhtsov

Joint Institute for Nuclear Research, Dubna, USSR

The integral equation method for the computation of 3-dimensional magnetostatic fields in the presence of iron has been mostly developed during the last years^{/1-3/}. In this paper the polyhedron of an arbitrary form is suggested to be used as a region with uniform magnetization. Two numerical methods for the solution of the resulting system of simultaneous nonlinear algebraic equations were tried.

Dividing a magnetic body into polyhedral regions with a constant magnetization vector in each one, the problem of finding the magnetic field intensity inside the magnet iron is reduced to the solution of the following set of simultaneous nonlinear algebraic equations (the Gaussian system of units).

$$\mu_a H_a - \frac{1}{4\pi} \sum_{q=1}^N (\mu_q - 1) \sum_{\xi=x,y,z} H_{\xi q} f_{\xi x} (D_{\xi a q_1}^{\xi}, D_{\xi a q_2}^{\xi}, \dots, D_{\xi a q_M}^{\xi}) = H_{\xi ca}, \quad (1)$$

where $\xi = x, y, z, \quad a = 1, 2, \dots, N,$

$$\mu_a = \mu_a \left(\sqrt{\sum_{\xi} H_{\xi a}^2} \right) \quad (2)$$

is the known permeability curve of the specific magnetic material, $D_{\xi a q_i}^{\xi} = \xi_a - \xi_{q_i}, \quad i = 1, 2, \dots, M,$ i denotes the vertex number of the "q" polyhedron, a denotes the number of the polyhedron for the central point of which equation (1) is written, N is the total number of polyhedrons, $f_{\xi x}$ is the demagnetization coefficients or the field strength component H_{ξ} in the "a" polyhedron produced by the magnetization component $M_x = 1.0$ of the "q" polyhedron. The procedure for the calculation of $f_{\xi x}$ has been described in ref.^{/4/}.

$H_{\xi ca}$ is the magnetic field of the magnet excitation coil at the "a" polyhedron centroid in the absence of the magnet iron

The method for the $H_{\xi ca}$ computation for a coil of an arbitrary 3-dimensional configuration has been given in ref.^{/5/}.

$H_{\xi a}, H_{\xi q}$ are the known field intensity components at the polyhedron centroids. Their total number is $3N$. The nonlinearity of system (1) is due to the nonlinear dependence in (2).

In order to reduce the number of equations and unknowns in the cases, when the magnet configuration has planes of symmetry in a properly chosen coordinate system, set (1) is written only for the polyhedrons in the first octant. For the calculation of the contribution to the second term and the right-hand side in (1) from the remaining part of the magnet, situated in the other octants, it is convenient to express the coordinates, the field components and the current densities in these octants by the corresponding quantities in the first octant. If there is only one plane of symmetry (fig.1a) this is achieved by means of the transformations

$$\vec{X}_{1\xi} = I_x \cdot \vec{X}_0, \quad (3)$$

$$\vec{H}_{1\xi} = N_{\xi} \cdot I_x \cdot \vec{H}_0, \quad (4)$$

$$\vec{J}_{1\xi} = -N_{\xi} \cdot I_x \cdot \vec{J}_0, \quad (5)$$

where $\vec{X}_0 = \left(\frac{x}{z}, \frac{y}{z} \right)$ is the radius vector of a point in the first octant, $\vec{X}_{1\xi}$ is the radius vector of the point reflected in the coordinate plane, which is normal to the ξ axis,

$$I_x = \begin{pmatrix} 1-2\delta_{x\xi} & 0 & 0 \\ 0 & 1-2\delta_{y\xi} & 0 \\ 0 & 0 & 1-2\delta_{z\xi} \end{pmatrix}, \quad (6)$$

where

$$\delta_{x\xi} = \begin{cases} 0, & x \neq \xi \\ 1, & x = \xi \end{cases}, \quad (7)$$

$$N_{\xi} = \begin{cases} 1 & \text{in the case of reflection of the field vector in the} \\ & \text{specified plane,} \\ -1 & \text{in the case of antisymmetry,} \end{cases} \quad (8)$$

\vec{j} is the current density vector. The sign of reflection in the current transformation is opposite to the sign of field reflection according to

$$\vec{H} = 4\pi / C \cdot \text{rot } \vec{j} \quad (9)$$

Reflection in two coordinate planes is characterized by the following transformations:

$$\vec{X}_{2\xi} = I_{xx} \cdot \vec{X}_0, \quad (10)$$

$$\vec{H}_{2\xi} = N_{\xi} \cdot N_{\xi 1} \cdot I_{xx} \cdot \vec{H}_0, \quad (11)$$

$$\vec{j}_{2\xi} = N_{\xi} \cdot N_{\xi 1} \cdot I_{xx} \cdot \vec{j}_0, \quad (12)$$

where ξ_1 is obtained from ξ by cyclic permutation according to the following rule

$$x \rightarrow z \rightarrow y \rightarrow x, \\ I_{xx} = \begin{pmatrix} (1-2\delta_{x\xi})(1-2\delta_{y\xi}) & 0 & 0 \\ 0 & (1-2\delta_{y\xi})(1-2\delta_{z\xi}) & 0 \\ 0 & 0 & (1-2\delta_{z\xi})(1-2\delta_{x\xi}) \end{pmatrix} \quad (13)$$

In this case the reflection in the specified planes of symmetry is carried out at first according to (3)-(5) and then according to (10)-(12) (fig.1b).

For the reflection in all coordinate planes we have

$$\vec{X}_{3\xi} = I_{xxx} \cdot \vec{X}_0, \quad (14)$$

$$\vec{H}_{3\xi} = N_x \cdot N_y \cdot N_z \cdot I_{xxx} \cdot \vec{H}_0, \quad (15)$$

$$\vec{j}_{3\xi} = -N_x \cdot N_y \cdot N_z \cdot I_{xxx} \cdot \vec{j}_0, \quad (16)$$

where

$$I_{xxx} = (1-2\delta_{x\xi})(1-2\delta_{y\xi})(1-2\delta_{z\xi}). \quad (17)$$

The reflection is carried out successively according to (3)-(5) and (10)-(12) in all coordinate planes and

according to (14)-(16) in any, but only one symmetry plane (fig. 1c).

Some remarks on the numerical solution of the system of nonlinear equations (1) will be made now. The strong nonlinearity and the great number of the unknowns, in general, make the problem of finding a solution to system (1) a difficult task even when using powerful computers. Therefore, the choice of a suitable numerical method with fast convergence which requires small storage and allows comparatively crude initial approximations, is of great importance. In this connection the method of conjugate gradients (Klessig-Polak's algorithm^{/6/}) and a modification of the Gauss-Newton method, the so-called autoregularized Gauss-Newton iterative process (ARP-F), implemented in the REGN subroutine^{/7/}, were tried. Both methods are computationally stable. The method of conjugate gradients requires smaller storage (of the order of the number of unknowns, i.e. about 3N) than the Gauss-Newton process, which requires storage of the order of 9N² (note that by the method of conjugate gradients the sum of residuals of equations (1) was minimized). But the second method converges faster than the first one. Moreover, the automatic choice of the regularization parameter, depending on the behaviour of iterative process criteria, is an advantage of the second method as well. The demagnetization coefficients $f_{\xi\alpha}$ and the right-hand side $H_{\xi ca}$ were calculated in advance and were kept in the external memory of the CDC-6400 computer. The solution was considered to be found when

$$\max_i |\varepsilon_i| \leq 10^{-9} \text{ and } \sum_{i=1}^{3N} \varepsilon_i^2 \leq 10^{-19}, \quad (18)$$

where ε_i are the residuals of equations (1).

The numerical experiments showed that the method of conjugate gradients converges much more slowly and requires greater computer time than the autoregularized Gauss-Newton process. This has led to the conclusion that

that its application for the solution of system (1) is inexpedient, though it requires smaller storage than the Gauss-Newton method. Besides, for the solution of (1), when the number of the unknowns is great, the autoregularized Gauss-Newton iterative process can be modified with the help, e.g., of the method described in ref.^{/8/}, for the inversion of large matrices with the use of the external memory.

Finally, mention that in some particular cases, e.g., when iron is saturated, system (1) can be solved by the method of successive approximations, which does not require large storage (as to the conditions of its application, see ref.^{/9/}).

Here are the results of some numerical experiments, carried out with the use of the REGN subroutine (an autoregularized Gauss-Newton process). As a test problem, a pair of ring-shaped shims, placed in a uniform external magnetic field with the following components $H_x = 0$, $H_y = 0$, $H_z = 12050.7$ Oe, was chosen. A part of this system situated in the first octant was divided into 4 polyhedrons, as shown in fig. 2. The calculation was made by taking into account the field symmetry with respect to the planes XOZ, YOZ and its antisymmetry with regard to the XOY plane. The right-hand side of set (1) multiplied by 0.1 was used as an initial approximation. The solution of (1) for this problem was obtained in 7 iterations for 9 seconds CDC-6400 computing time. As a verification the same configuration was calculated by the difference method implemented in the POISSON program^{/10/} in the cylindrical coordinate system with the boundary conditions shown in fig. 2. In the absence of the ring-shaped shims these boundary conditions produce a uniform field having the components $H_x = 0$, $H_y = 0$, $H_z = 12050.7$ Oe.

In both calculations the distributions of the fields at $z = 0$, reduced to the same external field level, coincide everywhere, except the region of $10 \text{ cm} < r < 13 \text{ cm}$ with an accuracy of 1% from the contribution of the shims to the

field. The difference in the results near the boundary ($A_r = \text{const.}$) is due to the calculation error in the POISSON program which arises from the artificial localization of the field by the boundary conditions. Magnetization inside the shims computed by the difference method varied within the limits $4\mathcal{I}M_z = 14.0-16.6$ kGauss. By the integral equation method it was found to be $4\mathcal{I}M_z \approx 14.3$ kGauss. This is a satisfactory coincidence keeping in mind the small number of polyhedrons. The results were additionally checked by computing the field of a pair of ring-shaped shims, whose magnetization was $4\mathcal{I}M_x = 0$, $4\mathcal{I}M_y = 0$, $4\mathcal{I}M_z = 14.3$ kGauss by the method described in ref.^{/11/}. The result obtained nearly coincides with that of the calculation by the integral equation method.

A serious test for the developed system of programs was the computation of a real C-shaped magnet, the configuration of one quarter of which is shown in fig. 3. The first octant of the magnet was divided into 48 polyhedrons with constant magnetization, as shown in fig. 3. Most of the elements of the division were situated near the working gap of the magnet at $z = 0$. The initial approximation was $H_{\xi a} = 0.001$ Oe, $\xi = x, y, z$, $a = 1, 2, \dots, N$. The calculation of this problem required about 6 hours of the CDC-6400 computing time and about 200 iterations. The results of the computation of the magnetic field in the $z = 0$ plane along the mid-line of the magnet pole $x = 0$ is given in fig. 4, in comparison with the experimental curve for the same Ampere-turns $Iw = 11985$. As is evident from the figure, the field dependence on "y" has wavy behaviour in accordance with the structure of the magnet pole division into polyhedrons. In order to obtain the computed field close to the experimental one, the gap between the magnet poles being so small and the magnetization distribution inside the magnet iron being strongly non-uniform, it is necessary, apparently, to increase the

number of elements, into which the pole is divided, approximately twice. However, as it follows from the experience gained during the calculation of the magnet divided into 48 polyhedrons such a problem cannot be solved with the use of the CDC-6400 computer because of the central memory and computing time limitations. Its solution requires the use of a computer of CDC-7600 type. In fact, it turns out that with the help of the created system of programmes 3-dimensional configurations with a comparatively large working region, free of iron (e.g., magnets of bubble chambers), can be calculated using the CDC-6400 computer.

The authors are pleased to thank E.P.Zhidkov and N.L.Zaplatin for their continuous interest and encouragement during the preparation of this work. The authors are also indebted to T.N.Dudareva for her help in carrying out the calculations and designing the results.

References

1. A.G.A.Armstrong, C.J.Collie et al., Proc. 5th Int.Conf. on Mag.Tech.,Frascati, 1975.
2. O.V.Tozoni, "CALCULATION OF 3-DIMENSIONAL ELECTROMAGNETIC FIELDS", "Technica" Publishing House, Kiev, 1974.
3. N.J.Newman, C.W.Trowbridge, L.R.Turner. Proc. 4th Int. Conf. on Mag.Tech., Brookhaven, 1972.
4. M.Odyniec, S.B.Vorozhtsov, JINR Communication E9-8811, 1975.
5. A.A.Halacsy, Univ. of Nevada, Reno, Engineering Rep. No.40, 1970.
6. E.Polak, "NUMERICAL METHODS OF OPTIMIZATION", "Mir" Publishing House, 1974, p.351.
7. L.Aleksandrov, JINR preprint P9-7259, Dubna, 1973.
8. L.Fox. An Introduction to Numerical Linear Algebra. Oxford University Press, 1965.
9. A.U.Luccio. University of Maryland, Technical Report No. 74-104, 1974.

10. K.Halbach, R.Holsinger, S.Magyary. Proceedings of the 5th Int. Conf. on Magnet Technology, Frascati, 1975.
11. V.I.Danilov, N.L.Zaplatin et al. Preprint P-702, JINR, Dubna, 1961.

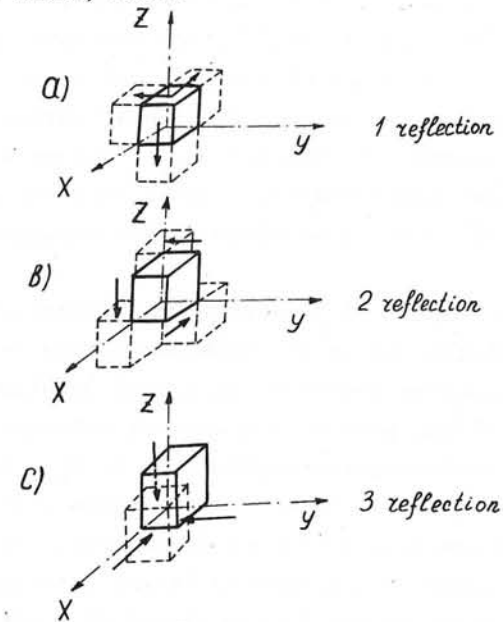


Fig.1. Magnet symmetry.

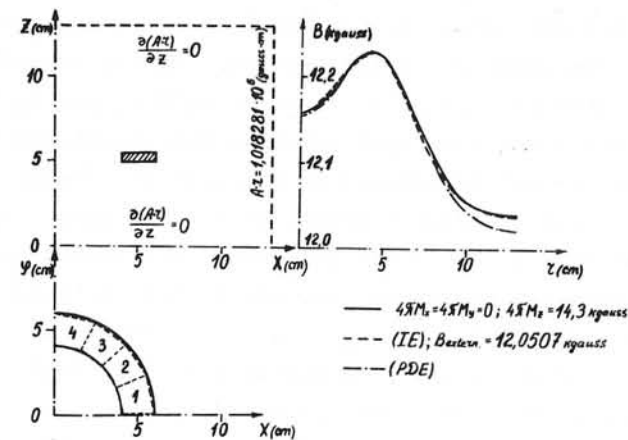


Fig. 2. Test problem .

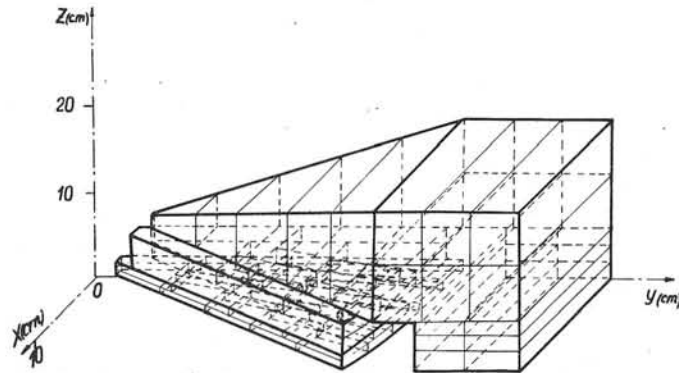


Fig. 3. C-shaped magnet .

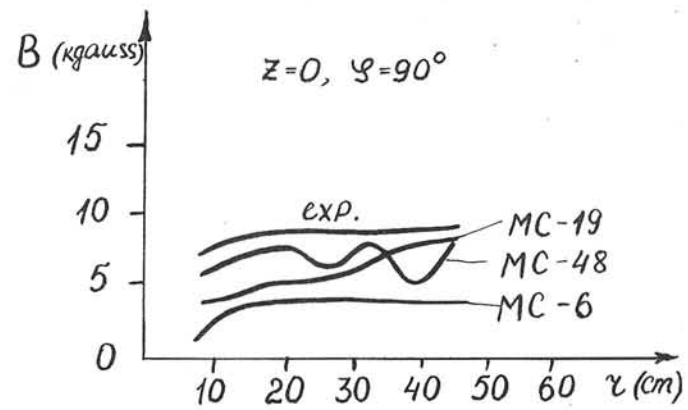


Fig.4. Results of calculations of the C-shaped magnet .

MAGNETIC FIELDS AND POTENTIALS OF LINEARLY VARYING CURRENT OR MAGNETISATION IN A PLANE BOUNDED REGION

C J Collie

Rutherford Laboratory, Chilton, Didcot, Oxon, OX11 0QX

ABSTRACT

In magnetic field problems solutions are obtained using the integral equation method by discretising the material and by assuming the functional form of the source (current or magnetisation) in each element.

The assumptions made here are that the source density is a linear function of the coordinates and that the elementary volume has plane sides (that is either a polyhedron or its limiting cases of plane polygon and infinite prism). The potentials and field are then expressed as a summation over the faces, edges and corners of the elements involving only elementary functions, and all the coefficients are tabulated.

It is also shown that the same technique is applicable to integral boundary method problems making the same assumptions.

1. INTRODUCTION

1.1 Task. The task of this paper is to calculate the effect of current or magnetisation sources at a point in terms of the density of the sources: which is the central task in solving magnetic field problems by integral equation methods. This cannot be done explicitly in general so simplifying assumptions must be made. Those used here are:

(a) The material is divided into elements with plane sides. In the general case treated in paragraphs 2-3, 5-7, this is a polyhedron. The special cases of a plane polygon, eg. a current sheet, and an infinite prism are examined in paragraphs 4 and 8 respectively.

(b) The source density is a linear function of the coordinates. This includes constant density as a special case and the method could be extended to higher order polynomials. In paragraph 7 the parameters of the linear function are assumed to be the values of the source at the corners, elsewhere this is immaterial.

1.2 Notation. This is exemplified in Figure 1.2.1, which shows a typical face and edge of the elementary volume. The field point x has Cartesian coordinates x_i ($i = 1, 2, 3$) and a typical source point x' has coordinates x'_i . Most of the analysis is performed in terms of the relative coordinate $U_i = x'_i - x_i$. The summation convention is used throughout. Thus for example:

$$(\nabla \times \underline{A})_i = \epsilon_{ijk} \frac{\partial A_k}{\partial x_j}, \text{ with } \epsilon_{ijk} \text{ the totally antisymmetric form.}$$

$$r = (U_i U_i)^{\frac{1}{2}} = \text{distance between } x \text{ and } x'$$

$$R = (U_i U_i)^{\frac{1}{2}} \quad (i = 1, 2) \text{ used in paragraph 8.}$$

(ξ, η, ζ) are the coordinates in a rotated frame with the ζ axis normal to a face and the η axis perpendicular to an edge. The differentials of volume, surface normal, and 2-dimensional edge normal are denoted by dV , dS_i , dL_i . Other symbols are defined as they are introduced.

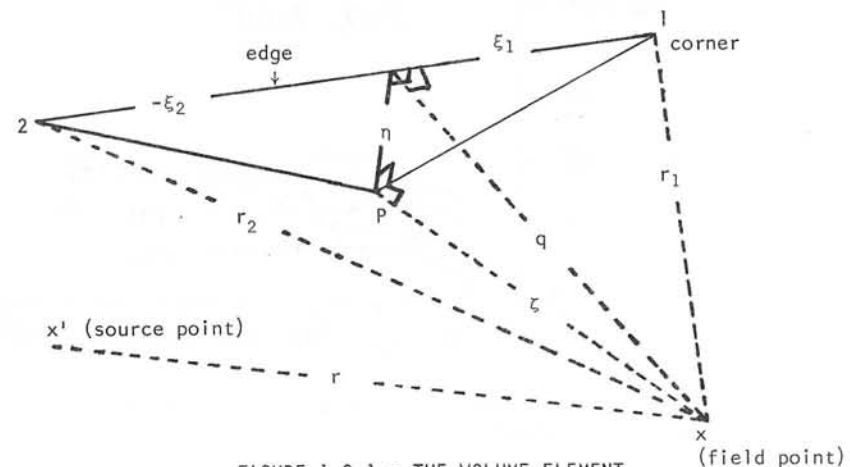


FIGURE 1.2.1 - THE VOLUME ELEMENT

2. FORMULATION OF POTENTIALS AND FIELDS IN 3 DIMENSIONS

The integral forms for relating current and magnetisation to potential and field may be found in (1) or (5) e.g. In SI units they are:

Vector potential due to current:

$$A_i(x) = \frac{\mu_0}{4\pi} \int J_i(x') \left\{ \frac{1}{r} \right\} dV \quad (2.1)$$

Field due to current:

$$B_i(x) = \epsilon_{ijk} \frac{\partial A_k}{\partial x_j} = \epsilon_{ijk} \frac{\mu_0}{4\pi} \int J_k(x') \left\{ \frac{U_j}{r^3} \right\} dV \quad (2.2)$$

Magnetic scalar potential due to magnetisation:

$$U(x) = \frac{-1}{4\pi} \int M_i(x') \left\{ \frac{U_i}{r^3} \right\} dV \quad (2.3)$$

Vector potential due to magnetisation:

$$A_i(x) = \frac{-\mu_0}{4\pi} \int \epsilon_{ijk} M_j(x') \left\{ \frac{U_k}{r^3} \right\} dV \quad (2.4)$$

Field due to magnetisation:

$$B_i(x) = \epsilon_{ijk} \frac{\partial A_k}{\partial x_j}(x) = -\mu_0 \frac{\partial U(x)}{\partial x_i} \\ = \frac{\mu_0}{4\pi} \int M_j(x') \left\{ \frac{3U_i U_j}{r^5} - \frac{\delta_{ij}}{r^3} \right\} dV \quad (2.5)$$

Evaluation of these integrals is to be carried out for the volume described in paragraph 1 for the case when the sources J_i and M_i are linear functions of x' . Since $U_i = x'_i - x_i$ the sources are therefore also linear functions of U . The integrals needed are thus just the terms in braces in (2.1) - (2.5), and U_m multiplied by these terms.

3. REDUCTION OF VOLUME TO SURFACE INTEGRALS

All the integrals which are shown to be needed in paragraph 2 can be obtained by successive differentiation of the source point - field point distance r . To avoid confusion with the components of some vector r_i we

denote this by R and indicate differentiation with respect to U_i by a subscript. That is R_{ij} means $\partial^2 R / \partial U_i \partial U_j$. We then obtain the following scheme:

$R = r = (U_i U_i)^{\frac{1}{2}}$ Differentials of R	
General Forms	Contractions
$R_i = \frac{U_i}{r}$	$R_{ii} = \frac{2}{r}$
$R_{ij} = \frac{-U_i U_j}{r^3} + \frac{\delta_{ij}}{r}$	$R_{ijj} = -\frac{2U_i}{r^3}$
$R_{ijk} = \frac{3U_i U_j U_k}{r^5} - \frac{\delta_{ij} U_k}{r^3} - \frac{\delta_{jk} U_i}{r^3} - \frac{\delta_{ki} U_j}{r^3}$	$R_{ijjj} = -8\pi \delta(r)$
$R_{ijkk} = 2 \left\{ \frac{3U_i U_j}{r^5} - \frac{\delta_{ij}}{r^3} \right\}$	

TABLE 3.1 - DIFFERENTIALS OF r . ($\delta(r)$ IN THE THREE-DIMENSIONAL DIRAC δ FUNCTION)

Since all the integrands of paragraph 2 are either entries in Table 3.1 or combinations of them, and all the entries are differentials of the line above, their integrals are immediately expressible as integrals over the surface. R_{ij} is given as an example to explain the method and notation, and the results for all of them are tabulated in Table 3.2:

$$\int R_{ij} dV = \int \partial/\partial U_j (R_i) dV = \int R_i dS_j = \int (U_i/r) dS_j \quad (3.2)$$

Since the surface consists of plane faces, the direction of dS_j is constant over each face. Introducing new axes so that the new U_3 axis is parallel to dS_j , (that is along the outward normal) the face will have the equation $U_3 = \zeta$, where ζ is the distance from the field point to the face (see Figure 1.2.1). The rotation is carried out using the rotation matrix a_{ij} defined so that the relation between the new (starred) axes and the old is:

$$U_i^* = a_{ji} U_j ; U_i = a_{ij} U_j^* , a_{ik} a_{jk} = a_{ki} a_{kj} = \delta_{ij} \quad (3.3)$$

Then (3.2) gives:

$$\int R_{ij} dV = \sum_{\text{faces}} \int (1/r) a_{im} U_m^* a_{j3} dS \quad (3.4)$$

Where $dS_3 = dS$ and a_{j3} are the direction cosines of the outward normal to the face. A two-dimensional vector $V_i = [U_1^*, U_2^*]$ is introduced and $U_3^* = \zeta$. (3.4) then becomes:

$$\int R_{ij} dV = \sum_{\text{faces}} \int a_{j3} (a_{i3} \frac{\zeta}{r} + a_{ip} \frac{V_p}{r}) dS \quad (3.5)$$

(p = 1,2 only)

Note that $a_{ip} V_p = (U_i - a_{i3}\zeta)$ and is invariant under rotations about the U_3^* axis, which leave a_{j3} unchanged. a_{ip} is therefore a two-dimensional vector. In Table 3.2 the integrands of the other R's are similarly decomposed into ζ and V_p parts.

Term	Integrand of dS for face with normal along a_{j3}
R_i	$a_{i3} r$
R_{ij}	$a_{i3} (a_{j3} \frac{\zeta}{r} + a_{jp} \frac{V_p}{r})$
R_{ii}	$\frac{\zeta}{r}$
R_{ijk}	$a_{i3} (-a_{j3} a_{k3} \frac{\zeta^2}{r^3} - \zeta a_{j3} \zeta a_{kp} \frac{V_p}{r^3} - a_{k3} \zeta a_{jq} \frac{V_q}{r^3} - a_{jp} a_{kq} \frac{V_p V_q}{r^3} + \frac{\delta_{jk}}{r})$
R_{ijj}	$a_{i3} (\frac{2}{r})$
R_{ijkk}	$a_{i3} (-2a_{j3} \frac{\zeta}{r^3} - 2a_{jp} \frac{V_p}{r^3})$
R_{ijjj}	$-2 \frac{\zeta}{r^3}$ (integrates to $-2 \times$ solid angle subtended by the face)

TABLE 3.6 - FIRST INTEGRALS OF THE DIFFERENTIALS OF R

The entries in this table are not unique since it is only over a closed surface that the integral theorem:

$$\int \frac{\partial \phi}{\partial U_i} dV = \int \phi dS_i$$

can be applied. Thus the entry for R_{ij} is not symmetrical, and it would even be possible to write perversely:

$$\begin{aligned} \int R_{ijj} dV &= \int \frac{\partial}{\partial U_j} R_{ij} = \int (- \frac{U_i U_j}{r^3} + \frac{\delta_{ij}}{r}) dS_j \\ &= \int (- \zeta a_{ip} \frac{V_p}{r^3} + a_{i3} (- \frac{\zeta^2}{r^3} + \frac{1}{r})) dS \end{aligned}$$

instead of:

$$\int R_{ijj} dV = \frac{\partial}{\partial U_i} R_{jj} dV = \int \frac{2}{r} dS_i = \int a_{i3} (\frac{2}{r}) dS$$

The forms chosen are the simplest ones.

4. SURFACE INTEGRALS IN THREE DIMENSIONS

The expressions (3.6) may arise without immediately deriving from integration of (2.1) - (2.5). Thus in solving problems by Green's theorem methods the starting point will be Green's second theorem:

$$4\pi\phi(x) = - \int \nabla^2 \phi \frac{1}{r} dV + \int \frac{1}{r} \frac{\partial \phi(x')}{\partial x'_i} dS_i + \int \phi(x') \frac{U_i}{r^3} dS_i \quad (4.1)$$

relating the value of the potential $\phi(x)$ to its value and normal gradient on the surface of the volume. For linear problems the first right-hand side term is zero. The solution of the simplified equation so obtained may be attempted by approximating the surface by a set of plane facets and assuming constant or linearly varying behaviour for ϕ and $\partial\phi/\partial x'_i$ on each facet. When this is done all the required integrals occur in (3.6).

Another case is the idealization called a current sheet. A surface current density K_i , has potentials and fields corresponding to (2.1) - (2.2):

$$A_i = \frac{\mu_0}{4\pi} \int K_i(x') \left\{ \frac{1}{r} \right\} dS \quad (4.2)$$

$$B_i = \epsilon_{ijk} \frac{\partial A_k}{\partial x_j} = \epsilon_{ijk} \frac{\mu_0}{4\pi} \int K_k(x') \frac{U_j}{r^3} dS \quad (4.3)$$

Again, on the assumption of linear variation for K_i , all the integrals are in (3.6). A magnetostatics program based on (4.1) is described in⁽²⁾ and the eddy current program of⁽³⁾ includes current sheets.

5. REDUCTION OF SURFACE TO LINE INTEGRALS

The integrals of (3.6) may be integrated further by an extension of the technique of paragraph 3. Corresponding to R we now need two generating functions denoted by M and Q and defined in (5.1)

$M = r^3/9 + \zeta^2 r/3 - \frac{1}{3} \zeta ^3 \log(\zeta + \zeta) ; r = (V_i V_i + \zeta^2)^{\frac{1}{2}}$	
$M_i = r V_i/3 + \zeta^2 V_i/3r - \zeta ^3 V_i/3r (r + \zeta)$	
$Q = \zeta \log(r + \zeta)$	
$Q_i = \frac{ \zeta V_i}{r(r + \zeta)} \quad \text{(Definitions of M and Q)}$	
$M_{ii} = r \equiv P \quad \text{(Definition of P)}$	
$P_i = \frac{V_i}{r}$	
$P_{ij} = -\frac{V_i V_j}{r^3} + \frac{\delta_{ij}}{r}$	
$P_{ii} = \frac{\zeta^2}{r^3} + \frac{1}{r}$	$Q_{ii} = \frac{\zeta^2}{r^3}$
$(P_{ii} - Q_{ii}) = \frac{1}{r} \equiv T \quad \text{(Definition of T)}$	
$T_i = -\frac{V_i}{r^3}$	

TABLE 5.1 - DIFFERENTIALS OF M AND Q

Every entry in (3.6) can be expressed as a combination of those in (5.1), so they can all be integrated. P_{ij} is given as an example:

$$\int P_{ij} dS = \int \partial P_i / \partial V_j dS = \int P_i dL_j = \int V_i / r dL_j \quad (5.2)$$

Since the boundaries of the face are the edges of the polyhedron, the direction of dL_j is constant for each edge. If a_{ij} is chosen so that the V_2 axis is along the outward normal to edge, then the equation of the edge is $V_2 = \eta$ with $\eta = a_{j2} U_j$, a constant. Call this new rotation matrix b_{ij} ; it is a particular a_{ij} which is completely determined while a_{ij} fixed only the 3-axis in the transformed system. For convenience c_{ij} is introduced to connect a_{ij} and b_{ij} :

$$U_i^{**} = b_{ij} U_j = c_{ki} U_k^* = c_{ki} a_{jk} U_j$$

with

$$U_3^{**} = U_3^* = \zeta, U_2^{**} = \eta; c_{k3} = c_{3k} = \delta_{3k} \quad (5.3)$$

Of course only b_{ij} , the fully determined form, can occur in the results. Note that there is a b_{ij} for every edge in every face. (5.2) to (5.3) give:

$$\int P_{ij} dS = \sum_{\text{edges}} \int c_{ik} \frac{V_k^*}{r} c_j dw = \sum_{\text{edges}} \int (c_{i1} \frac{w}{r} + c_{i2} \frac{\eta}{r}) c_{j2} dw \quad (5.4)$$

where $w = V_1^* = b_{i1} U_i$ is the remaining variable. The w axis is along the edge and the perpendicular from field point to the edge has $w = 0$ (see Figure 1.2.1).

The tables which follow give firstly the separation into η and w parts for the entries in (5.1), secondly the expressions for the first integrals of R in terms of the differentials of M and Q, and thirdly the second integrals of R.

Integrand	Integral for edge normal to b_{i2}
M_{ii}	$n \frac{r}{3} + \frac{\zeta^2 n}{3} - \frac{ \zeta ^3 n}{3r(r+ \zeta)}$
P_i	$c_{i2} r$
P_{ij}	$c_{i2} (c_{j2} \frac{n}{r} + c_{j1} \frac{w}{r})$
P_{ii}	$\frac{n}{r}$
Q_{ii}	$\frac{ \zeta n}{r(r+ \zeta)}$
T	$\frac{n}{r} - \frac{ \zeta n}{r(r+ \zeta)}$
T_i	$c_{i2} \frac{1}{r}$

TABLE 5.5 - INTEGRALS OF M AND Q DIFFERENTIALS

TERM	INTEGRAND OF dw FOR EDGE NORMAL TO b_{j2}
R_i	$b_{i3} (n \frac{r}{3} + \zeta^2 \frac{n}{3r} - \frac{ \zeta ^3 n}{r(r+ \zeta)})$
R_{ij}	$b_{i3} (b_{j3} \zeta (\frac{n}{r} - \frac{ \zeta n}{r(r+ \zeta)}) + b_{j2} r)$
R_{ii}	$\zeta (\frac{n}{r} - \frac{ \zeta n}{r(r+ \zeta)})$
R_{ijk}	$b_{i3} (b_{j3} b_{k3} (\frac{n}{r} - \frac{2 \zeta n}{r(r+ \zeta)}) + (b_{j3} b_{k2} + b_{k3} b_{j2}) \frac{\zeta}{r} + b_{j2} (b_{k2} \frac{n}{r} + b_{k1} \frac{w}{r}))$
R_{ijj}	$b_{i3} (\frac{2n}{r} - \frac{2 \zeta n}{r(r+ \zeta)})$
R_{ijkk}	$b_{i3} (-2b_{j3} \frac{ \zeta }{\zeta} \frac{n}{r(r+ \zeta)} + 2b_{j2} \frac{1}{r})$
R_{ijjj}	$-2 \frac{ \zeta }{\zeta} \frac{n}{r(r+ \zeta)}$

TABLE 5.7 - SECOND INTEGRALS OF THE DIFFERENTIALS OF R

Integrand	Integral
R_i	$a_{i3} M_{pp}$
R_{ij}	$a_{i3} (a_{j3} \tau T + a_{jp} P_p)$
R_{ii}	ζT
R_{ijk}	$a_{i3} (a_{j3} a_{k3} (2T - P_{pp}) + (a_{j3} a_{kp} + a_{k3} a_{jp}) \zeta T_p + a_{jp} a_{kq} P_{pq})$
R_{ijj}	$a_{i3} (2T)$
R_{ijkk}	$a_{i3} (-2a_{j3} \frac{Q_{pp}}{\zeta} + 2a_{jp} T_p)$
R_{ijjj}	$-2 \frac{Q_{pp}}{\zeta}$

TABLE 5.6 - FIRST INTEGRALS IN M Q FORM

6. FORM OF RESULTS

6.1 Third Integration. To complete the derivation of closed expressions for integrals of all the required forms it is necessary to give the definite integrals of the 4 functions appearing in (5.7) or (5.5) and to show that the original symmetries are restored when the sums over the edges and faces are performed.

Taking the integrals first we have simply:

$$\int_{\zeta_2}^{\zeta_1} r \, dw = \frac{(r_1 + r_2)}{4\ell} ((r_1 - r_2) + \ell^2) + \frac{q^2}{2} \log \left(\frac{(r_1 + r_2 + \ell)}{(r_1 + r_2 - \ell)} \right)$$

$$\int_{\zeta_2}^{\zeta_1} \frac{dw}{r} = \log \left(\frac{r_1 + r_2 + \ell}{r_1 + r_2 - \ell} \right)$$

$$\int_{\zeta_2}^{\zeta_1} \frac{w}{r} \, dr = r_1 - r_2 \tag{6.1.1}$$

$$\int_{\zeta_2}^{\zeta_1} \frac{\eta}{r(r + |\zeta|)} = 2 \left[\tan^{-1} \frac{\xi_1}{(r_1 + |\zeta|)} \frac{\eta}{(r_1 + q)} - \tan^{-1} \frac{\xi_2}{(r_2 + |\zeta|)} \frac{\eta}{(r_2 + q)} \right]$$

Where ξ_1, ξ_2 are the w coordinates of the end points of the edge, $\ell = \xi_1 - \xi_2$ is the length of the edge, and $q = (\zeta^2 + \eta^2)^{1/2}$ is the distance of the field point from the line. (See Figure 1.2.1). The last expression in (6.1) is $|\zeta|/\zeta$ x the solid angle subtended by the area P12 in Figure 1.2.1. Note that the log term in (6.1.1) is unbounded on the edge. R_{ijkk} and T_i are the only forms containing this term without a protecting factor.

6.2 Restoring Symmetry. The only apparently unsymmetric form in (5.5) is P_{ij} which is:

$$\int P_{ij} \, dS = \sum_{\text{edges}} \int c_{i_2} \left(c_{j_2} \frac{\eta}{r} + c_{j_1} \frac{w}{r} \right) dw$$

Only the second term in this is unsymmetrical. Its value by (6.1.1) is $c_{i_2} c_{j_1} (r_1 - r_2)$. The same value of r as r_1 occurs in the adjacent side of the face (see Figure 6.2.1) as r_2 . So each corner coordinate occurs in a combination like:

$$c_{i_2} c_{j_1} - c_{i_2}^i c_{j_1}^i \tag{6.2.1}$$

Now c_{ij} rotates simply in the plane of the face. So (6.2.1) is of the form:

$$\begin{bmatrix} -\sin\theta & \cos\theta & -\sin^2\theta & 0 \\ \cos^2\theta & \sin\theta\cos\theta & 0 & 0 \\ 0 & 0 & 1 & 1 \end{bmatrix} - \begin{bmatrix} -\sin\theta' & \cos\theta' & \sin^2\theta' & 0 \\ \cos^2\theta' & \sin\theta'\cos\theta' & 0 & 0 \\ 0 & 0 & 1 & 1 \end{bmatrix}$$

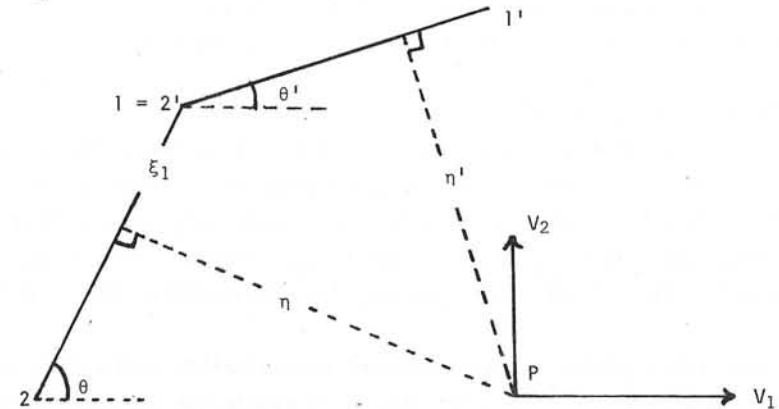


FIGURE 6.2.1 - RELATION BETWEEN ADJACENT c_{ij}

which is symmetrical on interchange of 1 and 2. The same argument shows the symmetry in jk of the last term of R_{ijk} in (5.7), since the b_{ij} for different edges in the same face are different c_{ij} multiplied by the same a_{ij} .

A different argument is required to restore the symmetry in i, j of the terms in (5.7). Thus the last term in R_{ij} is by (6.1.1).

$$\sum_{\text{faces}} \sum_{\text{edges}} \log \left(\frac{r_1 + r_2 + \ell}{r_1 + r_2 - \ell} \right) b_{i_3} b_{j_2} \tag{6.2.2}$$

The same log term will thus occur twice for each edge, with the $b_{i_3} b_{j_2}$ for the two faces which join along the edge. Now the b_{j_2} in this case are not independent: since b_{j_3} is normal to the face, the edge $b_{j_1} = -b_{j_1}^i$ must be parallel to $(b_{j_3} \wedge b_{j_3}^i)$, and b_{j_2} is $(b_{j_3} \wedge b_{j_1})$. Carrying out the vector products gives:

$$b_{i_3} b_{j_2} + b_{i_3}^i b_{j_2}^i = \frac{b_{i_3} b_{j_3}^i + b_{j_3} b_{i_3}^i - (b_{k_3} b_{k_3}^i)(b_{i_3} b_{j_3} + b_{i_3}^i b_{j_3}^i)}{(1 - (b_{k_3} b_{k_3}^i)^2)^{1/2}} \tag{6.2.3}$$

which is symmetrical in i and j . The only remaining case is the symmetry between i and k of R_{ijk} . It has been shown to be symmetrical in j and k when the summation is carried out over all the edges on a face, by the argument of (6.2.1), and in i and j by that of (6.2.2) when both contributions to an edge are summed, from which it follows that it must be symmetrical in i and k when the whole summation is complete.

7. SINGULARITIES IN THE RESULTS

The integrals of (6.1.1) contain a solid angle term, which is discontinuous on the surface, and a log term which is unbounded on the edges of the volume. Inspection of (5.7) shows that these terms only occur without a protecting factor in R_{ijkk} and its trace R_{iikk} , which derive from the magnetisation field (2.5), and these only from the constant term in $M_j(x')$.

This means that a method based on constant magnetisation within each volume element, such as GFUN⁽⁴⁾ can obtain the field within the iron only by an indirect averaging process, analogous to the Lorentz averaging by which H_i is derived from B_i within material, as described for example in⁽⁵⁾. Since a linear dependence for $M_j(x')$ also contains a constant term it might appear that the same is true for this case, but in fact these singularities and discontinuities can cancel out on internal edges and boundaries.

To see this it is necessary to look more fully at the linear magnetisation supposition. While any polyhedron can be used as element in the constant magnetisation case, the linear magnetisation case is likely to be used only with a tetrahedral element, the 4 corner values of magnetisation being just sufficient to determine the 4 parameters of the linear function $a_0 + a_i x_i$. Thus on defining $x'_0 \equiv 1$, the supposition of linear magnetisation within the element amounts to saying that for some constants $N_{\alpha\beta}$

$$M_i(x') = M_{\alpha} N_{\alpha\beta} x'_{\beta} \quad (\alpha, \beta \text{ summed from } 0-3) \quad (7.1)$$

with $M_{\alpha} = M_i(x_{\alpha})$; its value at the α^{th} corner. Setting $x' = x_{\gamma}$ in (7.1)

$$M_{\gamma} = M_{\alpha} N_{\alpha\beta} x_{\gamma\beta}$$

$$\therefore N_{\alpha\beta} x_{\gamma\beta} = \delta_{\alpha\gamma} \quad (7.2)$$

Substitute (7.1) into (2.5) and obtain:

$$B_i(x') = \frac{\mu_0}{4\pi} \int M_{\alpha} N_{\alpha\beta} (U_{\beta} + x_{\beta}) \left(\frac{3U_i U_j}{r^5} - \frac{\delta_{ij}}{r^3} \right) dV \quad (7.3)$$

where $U_0 = 0, x_0 = 1$.

The coefficient of $\int R_{ijkk} dV$ (see (3.7)) in B_i is therefore:

$$\frac{\mu_0}{8\pi} M_{\alpha} N_{\alpha\beta} x_{\beta} \equiv W(x) \quad (\text{definition of } W) \quad (7.4)$$

Imagine the field point x approaching the corner x_{γ} , that is $x_{\beta} = x_{\gamma\beta} + \epsilon_{\beta}$ ($\epsilon_0 = 0$), where ϵ is an infinitesimal vector. Then by (7.2):

$$W(x_{\gamma} + \epsilon) = \frac{\mu_0}{8\pi} (M_{\gamma} + M_{\alpha} N_{\alpha\beta} \epsilon_{\beta}) \quad (7.5)$$

Referring now to (5.7), consider the contributions to the field of the common face of 2 adjacent elements. The b_{j_3} are along the outward normal and thus simply change sign and the solid angle also changes sign. The b_{j_2} are equal since they are the outward normal to the edge, and the log term is the same for the two elements. The M_{γ} contribution in (7.5) will thus exactly cancel, and the contributions from other corners are $O(\epsilon)$.

Now imagine x approaching not a corner but an edge. That is $x_{\beta} = (px_{\gamma\beta} + qx_{\delta\beta} + \epsilon_{\beta})$ with $p + q = 1$. Then similarly to (7.5) we have:

$$W(px_{\gamma} + qx_{\delta} + \epsilon) = \frac{\mu_0}{8\pi} (pM_{\gamma} + qM_{\delta} + M_{\alpha} N_{\alpha\beta} \epsilon_{\beta}) \quad (7.6)$$

Again, considering adjacent elements, it is only the common corners which make finite contributions to W , and these exactly cancel. Similarly the field is continuous on crossing a face.

So the only troublesome points are on external corners and edges where physically iron will be saturated. Some special procedure must be adopted to deal with these, such as radiusing the corners or placing the nodes of

the mesh a little inside the material boundaries. Elsewhere the linear magnetisation supposition should provide directly values for the field within the iron and as (5.7) shows, requires the evaluation of exactly the same transcendental functions, and no others, as constant magnetisation. A given mesh will generally contain fewer nodes than elements, so it should also be economical.

8. THE TWO DIMENSIONAL LIMIT

8.1 Formulation in two dimensions. A case of considerable practical interest, because set ups which approximate to it allow considerable computational savings, occurs when there is no variation of any quantity in one direction, so that the volume of interest becomes an infinite prism. The form the results obtained take in this case is not immediately apparent because such systems only approximate to reality when they are balanced. Without this restraint (2.1) diverges.

It is easier to start again with the relationships which connect sources, and fields in this case. They are ⁽¹⁾, with subscripts indicating 2 vectors throughout.

Vector potential due to current:

$$A_i(x) = -\frac{\mu_0}{2\pi} \int j_i(x') \log R/a \, dS \tag{8.1.1}$$

Field due to current:

$$B(x) = \epsilon_{ij} \frac{\partial A_j}{\partial x_i} = \frac{\mu_0}{2\pi} \epsilon_{ij} \int j_i(x') \frac{U_j}{R^2} \, dS \tag{8.1.2}$$

(There is also the case when j_3 exists, but exactly the same integrals occur, so it is omitted.)

Magnetic Scalar potential due to magnetisation:

$$U(x) = \frac{-1}{2\pi} \int M_i(x') \frac{U_i}{R} \, dS \tag{8.1.3}$$

Vector Potential due to magnetisation:

$$A(x) = -\frac{\mu_0}{2\pi} \int \epsilon_{ij} \frac{M_j(x')}{R^2} U_j \, dS \tag{8.1.4}$$

Field due to magnetisation:

$$B_i(x) = \epsilon_{ij} \frac{\partial A_j(x)}{\partial x_i} = -\mu_0 \frac{\partial U(x)}{\partial x_i} = \frac{\mu_0}{2\pi} \int M_j(x') \left(\frac{2U_i U_j}{R^4} - \frac{\epsilon_{ij}}{R^2} \right) dS \tag{8.1.5}$$

In which the constant a in (8.1.1) is quite arbitrary and is the trace of the fact that only balanced systems are meaningful, when it will cancel. The evaluations are to be carried out for $j_i(x')$ and $M_i(x')$ linear functions of x' , or U . The area of integration is the polygon of Figure 8.1.1, with the prism extending to \pm infinity in the x_3 direction.

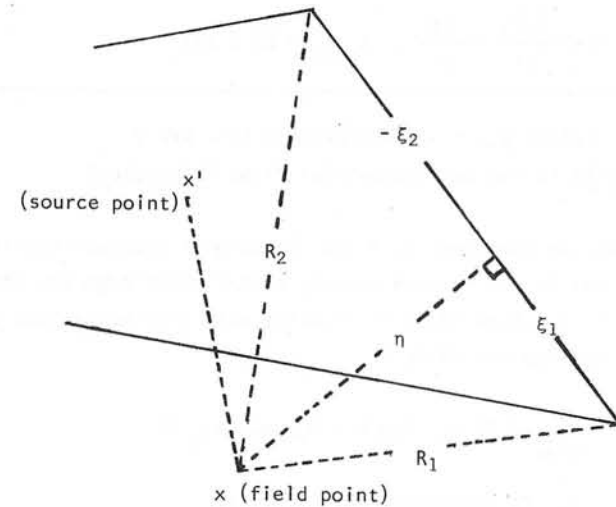


FIGURE 8.1.1 - REGION OF INTEGRATION FOR THE TWO-DIMENSIONAL LIMIT

8.2 Reduction of surface to line integrals. Analogously to the treatment of paragraph 3, all the required integrands can be derived in differentials of R^2 and $R^2 \log R$, according to the scheme of (8.2.1), setting the arbitrary constant a to 1.

$X = R^2 \log R, \quad Y = R^2$ <p style="text-align: center;">(Definition of X and Y)</p>
$X_i = 2U_i \log R + U_i \qquad Y_i = 2 U_i$
$X_{ij} = 2 \frac{U_i U_j}{R^2} + \delta_{ij} (1 + 2 \log R), \quad X_{ii} = 4 + 4 \log R, \quad Y_{ii} = 4$
$X_{ijk} = 2 \left(-2 \frac{U_i U_j U_k}{R^4} + \delta_{ij} \frac{U_k}{R^2} + \delta_{jk} \frac{U_i}{R^2} + \delta_{ki} \frac{U_j}{R^2} \right)$
$X_{ijj} = 4 \frac{U_i}{R^2}$
$X_{ijkk} = 4 \left(-2 \frac{U_i U_j}{R^4} + \frac{i_j}{R^2} \right), \quad X_{iijj} = 8\pi \delta(\underline{R})$

TABLE 8.2.1 - DIFFERENTIALS OF X AND Y
 ($\delta(\underline{R})$ is the two dimensional Dirac δ function)

Again analogously to paragraph 3, a two dimensional rotation matrix is introduced so that in the rotated system, a particular edge has the equation $U_2 = \eta = a$ constant. Then (3.3) still holds with sums understood as from 1 to 2 and the analogue of (3.4) is

$$\int X_{ij} dS = \sum_{\text{edge}} \int (2 U_m^* \log R + U_m^*) a_{im} a_{j2} dL \tag{8.2.2}$$

Introducing $V = U_1^*$, this becomes, since $dL = dL_1$

$$\int X_{ij} dS = \sum_{\text{edges}} \int a_{j2} (a_{i2} (2 \eta \log R + \eta) + a_{i1} (2 V \log R + V)) dV \tag{8.2.3}$$

Carrying out a similar procedure for each item in (8.2.7) gives Table 8.2.4, choosing the simplest of the non unique forms as in (3.6)

Term	
X_i	$a_{i2} (\eta^2 \log R + V^2 \log R)$
Y_i	$a_{i2} (\eta^2 + V^2)$
X_{ij}	$a_{i2} (a_{j2} (2 \eta \log R + \eta) + a_{j1} (2 V \log R + V))$
X_{ii}	$2 \eta \log R + \eta$
Y_{ii}	2η
X_{ijk}	$a_{i2} (2 a_{j2} a_{k2} \frac{\eta^2}{R^2} + 2 a_{j2} a_{k1} \frac{\eta V}{R^2} + 2 a_{k2} a_{j1} \frac{\eta V}{R^2} + 2 a_{j1} a_{k1} \frac{V^2}{R^2} + \delta_{jk} (1 + 2 \log R))$
X_{ijj}	$a_{i2} (4 + 4 \log R)$
X_{ijkk}	$a_{i2} (4 a_{j2} \frac{\eta}{R^2} + 4 a_{j1} \frac{V}{R^2})$
X_{iijj}	$4 \eta / R^2$

TABLE 8.2.4 - FIRST INTEGRALS OF THE DIFFERENTIALS OF X AND Y

The singular and discontinuous forms arising in (8.2.4) are:

$$\int_{\zeta_2}^{\zeta_1} \frac{V}{R^2} = \log R_1/R_2 \quad \text{and} \quad \int_{\zeta_2}^{\zeta_1} \frac{\eta}{R^2} = \frac{|\eta|}{\eta} \times |\text{angle subtended by edge}| \tag{8.2.5}$$

which can be shown to give rise to continuous fields internally for linear magnetisation in the same way as in paragraph 7.

9. REFERENCES

1. W R Smythe. Static and Dynamic Electricity
McGraw Hill 1968.
2. J Simkin, C W Trowbridge. Magnetostatic fields computed using an
integral equation derived from Green's Theorems.
(These Proceedings)
3. C S Biddlecombe, C J Collie, J Simkin, C W Trowbridge. The Integral
Equation Method Applied to Eddy Currents. (These Proceedings)
4. A G A M Armstrong, C J Collie, N J Diserens, M J Newman, J Simkin,
C W Trowbridge. New Developments in the Magnet Design Computer
Program GFUN. RL-75-066 and Proc. 5th Int. Conf. on Magnet
Technology, Frascati, Rome, 1975.
5. F N H Robinson. Macroscopic Electromagnetism. Pergamon Press 1973.

Non-divergent Vector Finite Elements for
Magnetic Field Calculations

Z. J. Csendes

General Electric Company
Schenectady, New York 12345

Abstract

In this paper, a novel set of two and three-dimensional approximation functions are derived which satisfy the condition that their divergence equals zero. These functions are useful for approximating operator equations involving non-divergent magnetic field quantities. The application of these functions to two-dimensional finite element analysis is presented and the procedure is illustrated with the two-component vector magnetic field solution of a stranded, slot-embedded conductor.

1. Introduction

A large number of magnetic field problems are formulated in terms of non-divergent vector field quantities. Often the most convenient representation of these quantities is in terms of an operator equation in which the non-divergent nature of the field is not specified. For example, in three-dimensional magnetostatic problems, the vector potential must independently satisfy both a vector Poisson equation and the Coulomb gauge, and in magnetic field induction calculations [1,2], the current distribution must separately satisfy both a vector integral equation and a zero-divergence condition. For this reason, the numerical solution of vector magnetic field problems has remained limited to a few isolated cases [3,4], and most numerical work in magnetic field analysis has involved only the direct solution of one-component field quantities.

In this paper, a complete set of interpolatory polynomial vectors are derived which satisfy the condition that their

divergence equals zero in a rectangular region. These polynomials form a natural set of approximating functions for non-divergent magnetic field quantities and eliminate the difficulty of imposing the zero-divergence condition on a numerical solution. Coupled with solution techniques derived from the finite element method, these polynomials constitute a powerful method of solving many two and three-dimensional magnetic field problems.

The remainder of this paper is divided into three main parts. Section 2 contains the definition and the derivation of interpolating non-divergent vector polynomials as well as a brief examination of some of their properties; Section 3 presents the application of these polynomials to the finite element method; and Section 4 describes the numerical solution of the two-component magnetic field distribution in a stranded, slot-embedded conductor.

2. Non-divergent Polynomial Vectors

2.1 Definition

The finite element analysis of a two-component non-divergent vector field requires the evaluation of polynomial vectors of the form

$$\bar{\alpha}_{ij}(x,y) = p_{ij}(x,y) \bar{I}_x + q_{ij}(x,y) \bar{I}_y \quad (1)$$

in which $p_{ij}(x,y)$ and $q_{ij}(x,y)$ are polynomials of minimal order satisfying the following properties:

- (i) $p_{ij}(x,y)$ and $q_{ij}(x,y)$ are product separable, i.e., it is possible to write $p_{ij}(x,y)$ and $q_{ij}(x,y)$ in the form

$$p_{ij}(x,y) = X_i(x) Y_j(y) \quad (2)$$

$$q_{ij}(x,y) = -W_i(x) Z_j(y) \quad (3)$$

- (ii) The functions $p_{ij}(x,y)$ and $q_{ij}(x,y)$ interpolate on an m by n grid of points (a_i, b_j) :

$$p_{ij}(a_k, b_\ell) = \delta_{ij}^{k\ell} \quad \begin{matrix} i, k = 1, \dots, m \\ j, \ell = 1, \dots, n \end{matrix} \quad (4)$$

$$q_{ij}(a_k, b_\ell) = 0$$

It is assumed throughout that $a_i \neq a_j$ and that $b_i \neq b_j$ if $i \neq j$.

(iii) The vector $\bar{\alpha}_{ij}(x, y)$ has zero divergence

$$\nabla \cdot \bar{\alpha}_{ij}(x, y) = 0 \quad (5)$$

2.2 Admissible Forms

Conditions (i) and (iii) may be combined to yield the following equations

$$\frac{\partial X_i(x)}{\partial x} = \lambda W_i(x) \quad (6)$$

$$\frac{\partial Z_j(y)}{\partial y} = \lambda Y_j(y) \quad (7)$$

Equations (6) and (7) provide the divergence condition in terms of the functions $X(x)$, $Y(y)$, $W(x)$ and $Z(y)$. Since the relative magnitudes of X and Y and of W and Z are arbitrary, without loss of generality it is possible to set $\lambda = 1$.

Since $p_{ij}(x, y)$ and $q_{ij}(x, y)$ are polynomials, the functions $X_i(x)$ and $Z_j(y)$ may be represented as

$$X_i(x) = \sum_{k=0}^M \alpha_k^i x^k \quad (8)$$

$$Z_j(y) = \sum_{k=0}^N \beta_k^j y^k \quad (9)$$

where M and N are the orders of $X_i(x)$ and of $Z_j(y)$, respectively, and the coefficients α_k^i and β_k^j are to be determined. According to equations (6) and (7) the functions $W_i(x)$ and $Y_j(y)$ are polynomials of order one less than the polynomials $X_i(x)$ and $Z_j(y)$, respectively.

The interpolation conditions (ii) may be stated in terms of the functions $X_i(x)$, $Y_j(y)$, $W_i(x)$ and $Z_j(y)$ by substituting (2) and (3) into (4). This gives

$$\begin{aligned} X_i(a_k) &= \delta_{ik} \\ Y_j(b_\ell) &= \delta_{j\ell} \\ W_i(a_k) &= 0 \\ Z_j(b_\ell) &= 0 \end{aligned} \quad (10)$$

These equations imply, respectively, that (a) the points $x = a_k$, $k=1, \dots, i-1, i+1, \dots, m$ are the roots of the polynomial $X_i(x)$; (b) the points $y = b_k$, $k=1, \dots, j-1, j+1, \dots, n$ are roots of the polynomial $Y_j(y)$; (c) the points $x = a_k$, $k=1, \dots, m$ are roots of $W_i(x)$; and that (d) the points $y = b_k$, $k=1, \dots, n$ are roots of $Z_j(y)$. Thus there are $M+m+1$ free parameters x_k in $X_i(x)$ and $M+m+1$ free parameters w_k in $W_i(x)$. Equating the derivative of $X_i(x)$ to $W_i(x)$ results in $M-1$ equations in $2M-2m$ unknowns. (The value of $\alpha_M^i \beta_N^j$ is set in the normalization $p_{ij}(a_i, b_j)=1$). A unique solution of this system is therefore possible if and only if

$$M = 2m-1 \quad (11)$$

A similar reasoning with $Y_j(y)$ and $Z_j(y)$ implies that

$$N = 2n-1 \quad (12)$$

2.3 Explicit Representation

Evaluating the derivative of $X_i(x)$ at the points $x=a_p$ and setting the result equal to $W_i(a_p)$ leads to the equations

$$X_i'(x) = \alpha_m^i (x-x_i) A_i(x) \quad (13)$$

$$W_i(x) = \alpha_m^i A_i(x) + (x-x_i) A_i'(x) \quad (14)$$

where $A_i'(x)$ is the derivative of $A_i(x)$ and

$$A_i'(x) = \prod_{\substack{k=1 \\ k \neq i}}^m (x-a_k)^2 \quad (15)$$

$$x_i = a_i + \frac{A_i(a_i)}{A_i'(a_i)} \quad (16)$$

In the same way, it follows that

$$Z_j(y) = \beta_N^j (y-b_j) B_j(y) \tag{17}$$

$$Y_j(y) = \beta_N^j B_j(y) + (y-b_j) B_j'(y) \tag{18}$$

where

$$B_j(y) = \prod_{\substack{k=1 \\ k \neq j}}^n (y-b_k)^2 \tag{19}$$

One final condition needs to be imposed on the polynomials. This is the condition that

$$p_{ij}(a_i, b_j) = 1 \tag{20}$$

Evaluating the expressions $X_i(a_i)$ and $Y_j(b_j)$ and substituting into (20) gives

$$\alpha_M^i \beta_N^j = \frac{A_i'(a_i)}{A_i^2(a_i) B_j(b_j)} \tag{21}$$

One possible set of solutions of this equation is

$$\alpha_M^i = \frac{A_i'(a_i)}{A_i^2(a_i)} \tag{22}$$

$$\beta_N^j = \frac{1}{B_j(b_j)}$$

2.4 Further Properties

One of the most interesting properties of non-divergent vector interpolation polynomials is their relationship to Gaussian quadrature formulas. Since the polynomial $X_i(x)$ is of order $2m-1$, it can be integrated exactly by the quadrature formula

$$\int w(x) X_i(x) dx = \sum_{\ell=1}^m X_i(a_\ell) C_\ell^m \tag{23}$$

where $w(x)$ is a weighting function and the C_ℓ^m are quadrature weights with a degree of precision $2m-1$. Taking the points a_i to coincide with the nodes a_ℓ used in the quadrature, (23) reduces to

$$\int w(x) X_i(x) dx = C_i^m \tag{24}$$

A similar reasoning with $Y_j(y)$, $W_i(x)$ and $Z_j(y)$ gives

$$\begin{aligned} \int w(y) Y_j(y) dy &= C_j^n \\ \int w(x) W_i(x) dx &= 0 \\ \int w(y) Z_i(y) dy &= 0 \end{aligned} \tag{25}$$

Thus, there obtains the following remarkable result: the application of a Gaussian quadrature formula to a two-dimensional scalar field is equivalent to approximating the scalar field with one component of a two-component non-divergent polynomial vector field, the integral of the second component of which is zero.

In three dimensions, non-divergent vector interpolation polynomials are obtained by taking

$$\begin{aligned} \bar{Y}_{ijk}(x,y,z) &= X_i(x) Y_j(y) Y_k(z) \bar{I}_x \\ &+ W_i(x) [X_j(y) - Z_j(y)] Y_k(z) \bar{I}_y - W_i(x) W_j(y) Z_k(z) \bar{I}_z \end{aligned} \tag{26}$$

Furthermore, in the cylindrical coordinate system, the following three-component vector is both interpolatory and non-divergent

$$\begin{aligned} \bar{Y}_{ijk}(r,z,\theta) &= \frac{1}{r} X_i(r) Y_j(z) Y_k(\theta) \bar{I}_r \\ &+ \frac{1}{r} W_i(r) [X_j(z) - Z_j(z)] Y_k(\theta) \bar{I}_z - W_i(r) W_j(z) Z_k(\theta) \bar{I}_\theta \end{aligned} \tag{27}$$

3. Vector Finite Element Formulation

3.1 Variational Expression

In a number of magnetic field problems, a two-component vector field \bar{V}

$$\bar{V} = \begin{bmatrix} v_x \\ v_y \end{bmatrix} \tag{28}$$

must be both non-divergent

$$\frac{\partial v_x}{\partial x} + \frac{\partial v_y}{\partial y} = 0 \tag{29}$$

and satisfy the operator equation

$$(\mathcal{L} + \lambda)\bar{V} = \bar{F} \quad (30)$$

where λ is a constant, \bar{F} is a two-component forcing function and \mathcal{L} is the operator

$$\mathcal{L} = \begin{bmatrix} \nabla^2 & 0 \\ 0 & \nabla^2 \end{bmatrix} \quad (31)$$

It is well known that an energy functional corresponding to the operator equation (30) is given by [5]

$$\mathcal{G}(\bar{V}) = \int \bar{V}^T (\mathcal{L} + \lambda)\bar{V} d\Omega - 2 \int \bar{V}^T \bar{F} d\Omega \quad (32)$$

where Ω is the region of integration. Applying Green's first identity to equation (32) results in

$$\mathcal{G}(\bar{V}) = - \int (G\bar{V})^T (G\bar{V}) d\Omega + \lambda \int \bar{V}^T \bar{V} d\Omega - 2 \int \bar{V}^T \bar{F} d\Omega \quad (33)$$

where G is the matrix

$$G = \begin{bmatrix} \partial/\partial x & 0 \\ \partial/\partial y & 0 \\ 0 & \partial/\partial x \\ 0 & \partial/\partial y \end{bmatrix} \quad (34)$$

Consequently, an approximate solution of the operator equation (30) subject to the divergence condition (29) may be obtained by extremizing the functional $\mathcal{G}(\bar{V})$ in equation (33) in the space of non-divergent two-component vectors \bar{V} .

3.2 Non-divergent Basis Functions

An arbitrary, non-divergent two-component vector \bar{V} may be approximated in a rectangular region by the vector

$$\bar{V}(x,y) = \sum_{i=1}^m \sum_{j=1}^n K_{ij} \bar{\alpha}_{ij}(x,y) + \sum_{i=1}^m \sum_{j=1}^n L_{ij} \bar{\beta}_{ij}(x,y) \quad (35)$$

where K_{ij} and L_{ij} are arbitrary coefficients and $\bar{\alpha}_{ij}(x,y)$ and $\bar{\beta}_{ij}(x,y)$ are the vectors

$$\bar{\alpha}_{ij}(x,y) = \begin{bmatrix} P_{ij}(x,y) \\ Q_{ij}(x,y) \end{bmatrix} \quad (36)$$

$$\bar{\beta}_{ij}(x,y) = \begin{bmatrix} Q_{ji}(x,y) \\ P_{ji}(x,y) \end{bmatrix} \quad (37)$$

Substituting equation (35) into equation (33), differentiating $\mathcal{G}(\bar{V})$ with respect to K_{rs} and setting the result equal to zero yields

$$\begin{aligned} & - \sum_{i=1}^m \sum_{j=1}^n K_{ij} \int \left\{ \frac{\partial p_{ij}}{\partial x} \frac{\partial p_{rs}}{\partial x} + \frac{\partial p_{ij}}{\partial y} \frac{\partial p_{rs}}{\partial y} + \frac{\partial q_{ij}}{\partial x} \frac{\partial q_{rs}}{\partial x} + \frac{\partial q_{ij}}{\partial y} \frac{\partial q_{rs}}{\partial y} \right\} d\Omega \\ & + \lambda \sum_{i=1}^m \sum_{j=1}^n K_{ij} \int \{ p_{ij} p_{rs} + q_{ij} q_{rs} \} d\Omega \\ & = \sum_{i=1}^m \sum_{j=1}^n F_{x_{ij}} \int \{ p_{ij} p_{rs} + q_{ij} q_{rs} \} d\Omega \end{aligned} \quad (38)$$

where $F_{x_{ij}}$ are the coefficients of the x-component of \bar{F} . A similar equation is obtained for L_{ij} .

3.3 Vector Notation

Introducing the vector notation

$$\begin{aligned} \tilde{X}(x) &= [X_1(x) \quad X_2(x) \quad \dots \quad X_m(x)] \\ K &= \begin{bmatrix} K_{11} & \dots & K_{1n} \\ \vdots & & \vdots \\ K_{m1} & \dots & K_{mn} \end{bmatrix} \end{aligned} \quad (39)$$

equation (38) may be written in the matrix form

$$\begin{aligned}
 & -2 I_{WW} K J_{YY}^T - I_{XX} K J_{UU}^T - I_{VV} K J_{ZZ}^T \\
 & + \lambda (I_{XX} K J_{YY}^T + I_{WW} K J_{ZZ}^T) \\
 & = I_{XX} F_x J_{YY}^T + I_{WW} F_x J_{ZZ}^T
 \end{aligned} \tag{40}$$

where I_{AA} and J_{AA} are the integrals

$$I_{AA} = \int \tilde{A}^T(x) \tilde{A}(x) dx \tag{41}$$

$$J_{AA} = \int \tilde{A}^T(y) \tilde{A}(y) dy$$

and $\tilde{U}(y)$ and $\tilde{V}(x)$ are the vectors

$$\tilde{U}(y) = \frac{\partial \tilde{Y}(y)}{\partial y} \tag{42}$$

$$\tilde{V}(x) = \frac{\partial \tilde{W}(x)}{\partial x}$$

Finally, applying the vec operation to both sides of equation (40) gives (vec $M = [M_1^T \dots M_n^T]^T$ where M_i is the i^{th} column of a matrix M)

$$\begin{aligned}
 & - (2 J_{YY} \otimes I_{WW} + J_{UU} \otimes I_{XX} + J_{ZZ} \otimes I_{VV}) \text{vec } K \\
 & + \lambda (J_{YY} \otimes I_{XX} + J_{ZZ} \otimes I_{WW}) \text{vec } K \\
 & = (J_{YY} \otimes I_{XX} + J_{ZZ} \otimes I_{WW}) \text{vec } F_x
 \end{aligned} \tag{43}$$

where \otimes denotes the Kronecker product $A \otimes B = (a_{ij} B)$ [6].

A very similar development differentiating $\mathcal{Q}(\tilde{V})$ with respect to the coefficients L_{rs} results in the equation

$$\begin{aligned}
 & - (2 J_{WW} \otimes I_{YY} + J_{VV} \otimes I_{ZZ} + J_{XX} \otimes I_{UU}) \text{vec } L \\
 & + \lambda (J_{WW} \otimes I_{ZZ} + J_{XX} \otimes I_{YY}) \text{vec } L \\
 & = (J_{WW} \otimes I_{ZZ} + J_{XX} \otimes I_{YY}) \text{vec } F_y
 \end{aligned} \tag{44}$$

Equations (43) and (44) provide two uncoupled matrix equations to be solved for the unknown coefficients K_{ij} and L_{ij} .

4. Application to Slot-Embedded Conductors

4.1 Discretization

Figure 1(a) provides a descriptive picture of a slot-embedded conductor including the adjacent air-gap region, indicating the locations of the conducting strands and the regions of insulation. A finite element discretization corresponding to this conductor using rectangular elements is presented in Figure 1(b). This Figure also presents the boundary conditions which need to be satisfied by the magnetic field components B_x and B_y .

Assuming that there are no source currents, the magnetic field in a slot-embedded conductor satisfies equations (29) and (30) with $\bar{V} = \bar{B}$, $\bar{F} = 0$ and $\lambda = -j\omega\mu\sigma$ in the conducting regions, $\lambda = 0$ in the non-conducting regions. Consequently, the analysis in the previous sections may be applied directly to solve the slot-embedded conductor problem in Figure 1.

The lowest order non-divergent polynomial vectors occur by taking $m=n=2$ in equation (4). In this case, letting the interpolation nodes correspond to the corners of the rectangle $-a \leq x \leq a$, $-b \leq y \leq b$, the interpolation polynomials become

$$\begin{aligned}
 X_1(x) &= X_2(-x) = (x-a)^2 (x+2a)/4a^3 \\
 Y_1(y) &= Y_2(-y) = (y-b)(3y+b)/4b^2 \\
 W_1(x) &= W_2(-x) = 3(x-a)(x+a)/4a^3 \\
 Z_1(y) &= Z_2(-y) = (y+b)(y-b)/4b^2 \\
 V_1(x) &= V_2(-x) = 3x/2a^3 \\
 U_1(y) &= U_2(-y) = (3y-b)/2b^2
 \end{aligned} \tag{45}$$

Using these polynomials, the integrals I_{AA} and J_{AA} in equations (43) and (44) are easily evaluated; the numerical values obtained are presented in Table 1.

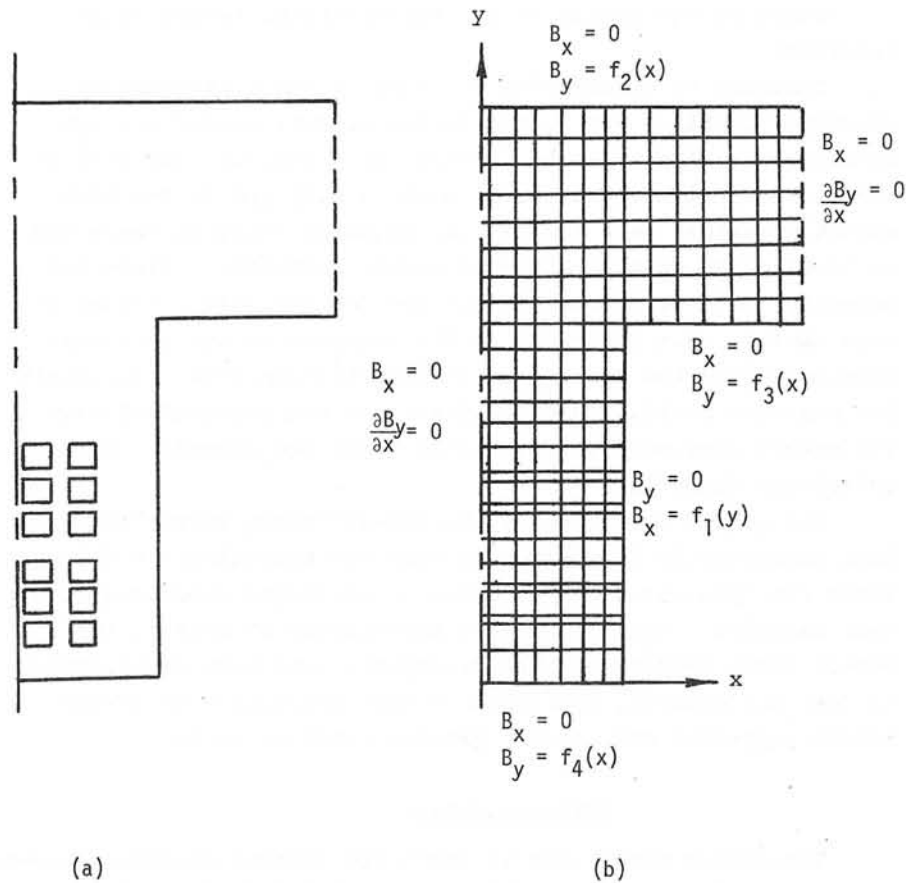


Figure 1. (a) Typical slot-embedded conductor geometry showing the conducting strands, the liquid cooling ducts and the adjacent airgap.

(b) Rectangular finite element subdivision of the slot-embedded conductor geometry in (a) and a description of the boundary conditions satisfied by the magnetic field.

Table 1. Numerical values of the matrices I_{AA} (or of J_{AA} with a replaced by b) evaluated using the interpolation polynomials in equation (45). The matrices are symmetric with $I_{AA}(2,1) = I_{AA}(1,2)$ and $I_{AA}(2,2) = I_{AA}(1,1)$.

A	$I_{AA}(1,1)$	$I_{AA}(1,2)$
X	$26a/35$	$9a/35$
Y	$4a/15$	$-a/15$
W	$3/5a$	$3/5a$
Z	$8a^3/105$	$6a^3/105$
V	$3/2a^3$	$-3/2a^3$
U	$2/a$	$-1/a$

4.2 Solution

For the purposes of the present investigation, a computer program was written to assemble and solve equations (43) and (44) for the x and y components of the magnetic field for the problem in Figure 1. The program accepts as data the slot width and the slot depth, the airgap thickness and the tooth spacing, as well as the locations of the conducting strands.

Taking the boundary condition forcing functions to be of the form

$$\begin{aligned}
 f_1(y) &= C_1 x + C_2 \\
 f_2(x) &= -1.0 \\
 f_3(x) &= -0.37 \\
 f_4(x) &= -0.10
 \end{aligned}
 \tag{46}$$

where C_1 and C_2 are constants, the magnetic field distribution in Figure 2 results. In this Figure, lines of equal magnetic flux magnitude have been plotted, since this plot is easier to comprehend than separate plots of the x and y components of the complex-valued magnetic field.

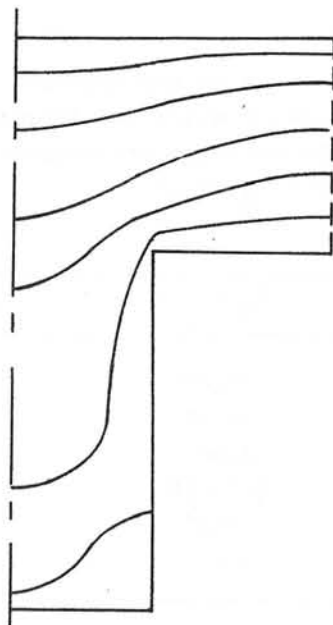


Figure 2. A plot of the equi-magnitude lines of the magnetic field for the problem in Figure 1.

5. Conclusions

A finite element method has been developed for the solution of magnetic field problems involving non-divergent vector field quantities. The method is based on the use of non-divergent vector approximation polynomials, which are derived in this paper. Although the finite element formulation presented is specifically designed to solve two-component vector field problems, extension to three-component vector fields is straight-forward since three-component non-divergent polynomials may be obtained from the two-component non-divergent polynomials, as shown in Section 2.4.

As a simple illustration of the application of the vector finite element method, a two-component vector solution of the magnetic field in a slot-embedded conductor is presented in this paper. Although the procedure employed treats the x and y -components of the magnetic

field independently, non-divergence of the solution vector is assured by the choice of the non-divergent vector basis functions.

Compared to alternative analyses of the slot-embedded conductor problem, the vector finite element method has two advantages. First of all, in both the classical analysis of the slot-embedded conductor problem [7,8,9] and in the more recent numerical work [10,11] the magnetic field is described in terms of an axially directed vector potential. Since the magnetic field is defined as the curl of the vector potential, this implies that the error in the computer vector potential is exaggerated by the process of differentiation used to obtain the magnetic field. This limitation is not encountered with the method presented in this paper since the magnetic field is solved for directly.

The second advantage of the non-divergent vector formulation presented in this paper is that the approximation functions are "pre-screened" in order to eliminate undesired divergent behavior. The alternative possibility of solving the vector field problem and the divergence condition simultaneously (as, for example, described in [4]) presents much larger matrix equations and, hence, greater computer costs.

Acknowledgement

The author would like to thank the General Electric Company for permission to publish this paper and M.V.K. Chari for discussions about the slot-embedded conductor problem.

References

1. Z.J. Csendes, A. Gopinath and P. Silvester, "Generalized matrix inverse techniques for local approximations of operator equations", in The Mathematics of Finite Elements and Applications, J.R. Whiteman (ed.), London: Academic Press, pp. 189-199, 1973.
2. A. Gopinath and P. Silvester, "Calculation of inductance of finite-length strips and its variation with frequency", IEEE Trans. Microwave Theory Tech., vol. MTT-21, pp. 380-386, 1973.
3. S. Sackett, "Solution of the magnetostatics problem in three space dimensions", Proceedings of the Second Conference on Analysis of Magnetic Fields, University of Nevada, Reno, Nevada, pp. 67-75, 1969.
4. H. Okuda, T. Kawamura and M. Nishi, "Finite element solution of magnetic field and eddy current problems in the end zone of turbine generators", IEEE Power Engineering Society Winter Meeting, Paper A 76 141-2, New York, 1976.
5. I. Stakgold, Boundary Value Problems of Mathematical Physics, New York: MacMillan, 1968.
6. C.R. Rao and S.K. Mitra, Generalized Inverse of Matrices and its Applications, New York: John Wiley, 1971.
7. L.V. Bewley, Two-dimensional Fields in Electrical Engineering, New York: Dover, 1963.
8. J. Lammeraner and M. Stafl, Eddy Currents, London: Iliffe Books, 1966.
9. R.L. Stoll, The Analysis of Eddy Currents, Oxford: Clarendon Press, 1974.
10. P. Silvester, "Dynamic resistance and inductance of slot-embedded conductors", IEEE Trans. Power Apparatus and Systems, vol. PAS-87, pp. 250-256, 1968.
11. A. Konrad, J.L. Conlomb, J.C. Sabonnadiere, and P. Silvester, "Finite element analysis of steady state skin effect in a slot-embedded conductor", IEEE Power Engineering Society Winter Meeting, New York, 1976.

A GENERALIZED FINITE DIFFERENCE METHOD
FOR THE COMPUTATION OF ELECTRIC AND MAGNETIC FIELDS

by G.B. Denegri, G. Molinari, A. Viviani

Electrical Engineering Department, University of Genoa

Viale Causa 13, 16145 Genoa, Italy

1. Abstract

A generalized form of the finite difference method is proposed to solve boundary value problems of the elliptic type, such as stationary magnetic or electric field problems.

The new method allows us to use grid forms of the type usually adopted by the finite-elements method.

In such a grid, the internal elliptic equations and the boundary and interface conditions can be discretized by expressing the potential V by a Taylor series expansion stopped at the N -order terms around any gridpoint. The particular procedure used produces an algebraic system which is better conditioned with respect to the ones typical of traditional finite-difference problems, and is very similar to those common to the finite-elements method. The new method eliminates completely the difficulties usually presented by the finite-difference method in the treatment of boundary and interface conditions. A comparison with the finite-elements method can give various results, because both methods present various implementation forms. However, the proposed method seems to warrant higher precision, especially when interface conditions are involved.

2. Introduction

At the present time, as far as the numerical solution of field problems is concerned, the finite-elements method is generally considered more powerful than the finite-difference one. This is essentially due to the fact that the finite-elements method allows us to introduce a non-ordered set of gridpoints; on the contrary, the finite-difference method requires a set of gridpoints arranged at the intersections of two or three orthogonal sheaves of straight lines. Almost any other advantage of the finite-

elements method depends on this fact. It allows us to optimize the grid-points distribution on the basis of the geometry of the problem. Besides, it eliminates the cumbersome interpolation procedures required by the finite-difference method at the boundary and interface conditions, which cause difficulties in inverting the algebraic system obtained by the discretization, owing to the increase in the matrix band amplitude.

The introduction of curvilinear grids into the finite-difference method^{1,2} reduces the difficulties in adapting the grid to the problem, though the interpolation procedures at the boundary and interface conditions are still necessary.

As a consequence, the finite-elements grid structure remains more versatile, especially when complicated boundary shapes are concerned.

However, the finite-difference method turns out to be inadequate especially because it is applied in a restrictive version, which wastes some of the method's features.

A generalized form of the finite-difference method is presented here, which can be considered on the same level as the finite-elements one, and can be more suitable to particular problems.

For the sake of simplicity, the generalized procedure is described in the case of bidimensional problems requiring only scalar potentials. Its extension to tridimensional problems is an easy matter.

3. The definition of the problem

Let us consider a boundary value problem defined at any continuity point of a set D in the x - y -plane by a second order linear partial differential equation of the elliptic type, given in the form:

$$a_{20} \frac{\partial^2 V}{\partial x^2} + a_{02} \frac{\partial^2 V}{\partial y^2} + a_{11} \frac{\partial^2 V}{\partial x \partial y} + a_{10} \frac{\partial V}{\partial x} + a_{01} \frac{\partial V}{\partial y} + a_{00} V = f_0 \quad (3.1)$$

where a_{20} , ..., a_{00} and f_0 are constant or given functions of x , y . On the boundary of the set D , the following general conditions are imposed:

$$b_1 V + b_2 \frac{\partial V}{\partial n} = f_1 \quad (3.2)$$

where b_1, b_2 and f_1 are constant or given functions of x, y , and n is the inward normal to the boundary. The set D can be divided into partial subsets D_i . On their interfaces, the following conditions hold:

$$V_j = V_k + f_2 \tag{3.3}$$

$$c_j \frac{\partial V_j}{\partial n_j} + c_k \frac{\partial V_k}{\partial n_k} = f_3 \tag{3.4}$$

where j and k are subscripts referring to regions D_j and D_k ; c_j, c_k, f_2, f_3 are constant or given functions of x, y , and n_j, n_k are the inward normals to the boundaries of D_j and D_k .

4. The discretization of the partial differential problem

The generalization of the finite-difference method proposed requires the introduction of a grid of the type used in the finite elements procedure (Fig. 1).

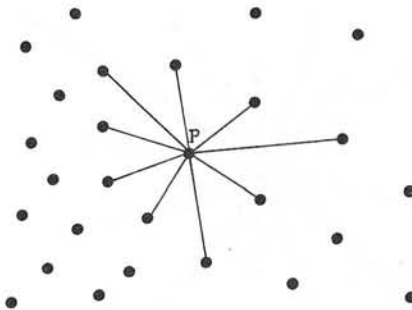


Fig. 1 - M-point star around an internal gridpoint P (case with N=3, M=9)

At any internal gridpoint P, the potential V can be expressed by a Taylor series expansion, stopped at the N-order terms, of the form:

$$V = \sum_{n=0}^N \sum_{l+m=n} \frac{1}{l!m!} \left. \frac{\partial^n V}{\partial x^l \partial y^m} \right|_P (x - x_P)^l (y - y_P)^m \tag{4.1}$$

Then, the potential must be computed at $M=(N+1)(N+2)/2-1$ gridpoints around P, generally at the M gridpoints nearest to P (Fig. 1). At the gridpoints P_i ($i=1, M$), we have:

$$V_{Pi} - V_P = \sum_{n=1}^N \sum_{l+m=n} \frac{1}{l!m!} \left. \frac{\partial^n V}{\partial x^l \partial y^m} \right|_P (x_{Pi} - x_P)^l (y_{Pi} - y_P)^m \tag{4.2}$$

Eqs. (4.2) form a system of M equations in the M unknowns $\left[\frac{\partial^n V}{\partial x^l \partial y^m} \right] \Big|_P$. This system can be solved and gives the M potential derivatives as functions of the potential values at the M gridpoints around P

$$\left. \frac{\partial^n V}{\partial x^l \partial y^m} \right|_P = \sum_{i=1}^M A_{lmi} (V_{Pi} - V_P) \tag{4.3}$$

Then, eq. (3.1) can be discretized by using eqs. (4.3). Substitution into eq. (3.1) gives an algebraic equation of the form:

$$V_P = \sum_{i=1}^M B_i V_{Pi} + B_0 \tag{4.4}$$

where

$$B_i = \frac{\sum_{n=1}^2 \sum_{l+m=n} a_{lm} A_{lmi}}{\sum_{n=1}^2 \sum_{l+m=n} a_{lm} \sum_{i=1}^M A_{lmi} - a_{00}} \tag{4.5}$$

$$B_0 = - \frac{f_0}{\sum_{n=1}^2 \sum_{l+m=n} a_{lm} \sum_{i=1}^M A_{lmi} - a_{00}} \tag{4.6}$$

The coefficients A_{lmi} are functions of the coordinates of the gridpoints x_{Pi}, y_{Pi}, x_P, y_P , and consequently the coefficients B_i and B_0 can be computed as functions of the above coordinates and of the values of a_{lm} and f_0 at P.

5. The discretization of the boundary conditions

The boundary conditions of the type (3.2) can be imposed provided that a suitable number of gridpoints are arranged on the boundary lines (Fig. 2). The discretization procedure, which must be applied to any boundary gridpoint where $b_2 \neq 0$, is similar to the one described in the previous Section.

By means of the expansion (4.1) applied to a boundary gridpoint P, we can compute the potential at M-1 gridpoints P_i ($i=1, M-1$) around P, ge-

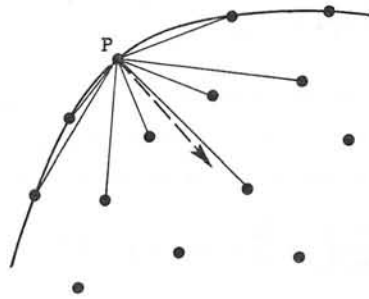


Fig. 2 - (M-1)-point star around a boundary gridpoint P (case with N=3, M=9).

generally at the M-1 gridpoints nearest to P (Fig. 2). This procedure gives M-1 equations of the type (4.2). A system of M equations is obtained by introducing the following expression of the normal potential derivative:

$$\frac{\partial V}{\partial n} \Big|_P = \frac{\partial V}{\partial x} \Big|_P \frac{\partial x}{\partial n} \Big|_P + \frac{\partial V}{\partial y} \Big|_P \frac{\partial y}{\partial n} \Big|_P = \frac{\partial V}{\partial x} \Big|_P n_x + \frac{\partial V}{\partial y} \Big|_P n_y \quad (5.1)$$

where $\bar{n}=(n_x, n_y)$ is the unit vector normal to the boundary at P (Fig. 2). The inversion of the system made up of eqs. (4.2) and (5.1) gives the M potential derivatives as functions of both the potential values at the M-1 gridpoints around P and the normal derivative:

$$\frac{\partial^n V}{\partial x^l \partial y^m} \Big|_P = \sum_{i=1}^{M-1} A_{1mi} (V_{Pi} - V_P) + A'_{1mM} \frac{\partial V}{\partial n} \Big|_P \quad (5.2)$$

The substitution of eq. (3.2) into eq. (5.2) gives:

$$\frac{\partial^n V}{\partial x^l \partial y^m} \Big|_P = \sum_{i=1}^{M-1} A_{1mi} (V_{Pi} - V_P) + A_{1mM} \left(\frac{f_1}{b_1} - V_P \right) \quad (5.3)$$

with

$$A_{1mM} = A'_{1mM} \frac{b_1}{b_2} \quad (5.4)$$

Finally, the substitution of eqs. (5.3) into eq. (3.1) gives an algebraic equation of the form:

$$V_P = \sum_{i=1}^{M-1} B_i V_{Pi} + B_0 \quad (5.5)$$

where the coefficients B_i ($i=1, M-1$) are defined by relations of the form (4.5), whereas B_0 is given by:

$$B_0 = \frac{\sum_{i=1}^2 n \sum_{l+m=n} a_{1m} A_{1mM} \frac{f_1}{b_1} - f_0}{\sum_{i=1}^2 n \sum_{l+m=n} a_{1m} \sum_{i=1}^M i A_{1mi} - a_{00}} \quad (5.6)$$

The above coefficients are functions of the coordinates of the gridpoints and of the values a_{1m}, f_0, f_1, b_1 and b_2 at P.

When $b_2=0$, the condition (3.2) reduces to a Dirichlet boundary condition, which can be directly introduced into the system.

6. The discretization of the interface conditions

The interface conditions (3.3), (3.4) must be imposed by introducing a suitable number of gridpoints on any interface line (Fig. 3). Due to eq. (3.3), which introduces a discontinuity into the potential, any interface

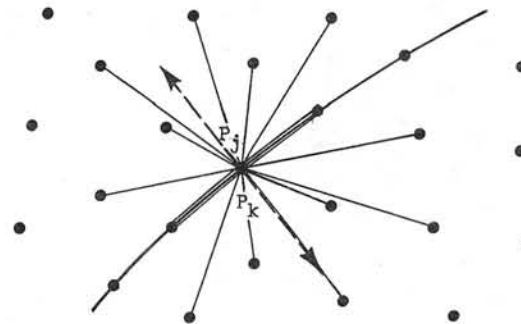


Fig. 3 - 2(M-1)-point star around an interface gridpoint P (case with N=3, M=9).

gridpoint P must be replaced by two separate gridpoints P_j and P_k , belonging to the two regions D_j and D_k separated by the interface line. The discretization procedure, which must be applied to any couple of interface gridpoints, follows directly from the one described in the previous Section.

By means of the expansion (4.1) applied to an interface gridpoint P_j (or P_k), we can compute the potential at M-1 gridpoints P_{ij} (or P_{ik}) ($i=1, M-1$) around P_j (or P_k), generally at the M-1 gridpoints nearest to P_j (or

P_k), all belonging to D_j (or D_k). A system of M equations is obtained by means of $M-1$ equations of the type (4.2) and of one equation of the type (5.1), obtained by suitably defining the normal derivative as function of the unit vector $\bar{n}_j = (n_{xj}, n_{yj})$ or $\bar{n}_k = (n_{xk}, n_{yk})$ normal to the boundary at P_j (or P_k) (see Fig. 3). The inversion of the system gives the M potential derivatives in D_j (or D_k) in a form similar to the one of eqs. (5.2). Then, the substitution of these equations into eq. (3.1) gives two equations of the form:

$$\left. \frac{\partial V_j}{\partial n_j} \right|_{P_j} = \sum_{i=1}^{M-1} c_{ij} (V_{Pij} - V_{Pj}) + C_{Mj} V_{Pj} + C_{0j} \quad (6.1)$$

$$\left. \frac{\partial V_k}{\partial n_k} \right|_{P_k} = \sum_{i=1}^{M-1} c_{ik} (V_{Pik} - V_{Pk}) + C_{Mk} V_{Pk} + C_{0k} \quad (6.2)$$

where, with reference to eqs. (5.2), it is, for j :

$$c_{ij} = - \frac{\sum_{n=1}^2 \sum_{l+m=n} a_{lmj} A_{lmij}}{\sum_{n=1}^2 \sum_{l+m=n} a_{lmj} A'_{lmMj}} \quad (6.3)$$

$$C_{Mj} = - \frac{a_{00j}}{\sum_{n=1}^2 \sum_{l+m=n} a_{lmj} A'_{lmMj}} \quad (6.4)$$

$$C_{0j} = \frac{f_{0j}}{\sum_{n=1}^2 \sum_{l+m=n} a_{lmj} A'_{lmMj}} \quad (6.5)$$

and analogously for k .

The substitution of eqs. (6.1), (6.2) into eqs. (3.3), (3.4) gives the algebraic equations:

$$V_{Pj} = \sum_{i=1}^{M-1} B_{ij} V_{Pij} + \sum_{i=1}^{M-1} B_{ik} V_{Pik} + B_0 \quad (6.6)$$

$$V_{Pk} = V_{Pj} - f_2 \quad (6.7)$$

where:

$$B_{ij} = \frac{c_j c_{ij}}{c_j \sum_{i=1}^{M-1} c_{ij} + c_k \sum_{i=1}^{M-1} c_{ik} - c_j C_{Mj} - c_k C_{Mk}} \quad (6.8)$$

$$B_{ik} = \frac{c_k c_{ik}}{c_j \sum_{i=1}^{M-1} c_{ij} + c_k \sum_{i=1}^{M-1} c_{ik} - c_j C_{Mj} - c_k C_{Mk}} \quad (6.9)$$

$$B_0 = \frac{c_j C_{0j} + c_k C_{0k} + c_k \sum_{i=1}^{M-1} c_{ik} f_2 - c_k C_{Mk} f_2 - f_3}{c_j \sum_{i=1}^{M-1} c_{ij} + c_k \sum_{i=1}^{M-1} c_{ik} - c_j C_{Mj} - c_k C_{Mk}} \quad (6.10)$$

The above coefficients are functions of the coordinates of the grid-points, of the values of a_{lm} and f_0 at P_j and P_k , of c_j at P_j , of c_k at P_k , and of f_2 and f_3 at P_j (or P_k , which is the same).

7. General features of the proposed method

On the whole, the algebraic equations (4.4), (5.5), (6.6) and (6.7) form an algebraic system of the type:

$$[B] [V] = [F] \quad (7.1)$$

whose solution can be found by various methods, depending on the properties of matrix $[B]$. Such properties are quite various, depending on the shape of the grid used; however, they generally seem very similar to those resulting from the finite-elements applications. The large number of implementation forms make difficult a general comparison between the new method and the most commonly used ones.

Once the solution of the system (7.1) has been obtained by direct or iterative methods, the new finite-difference scheme is particularly suitable to evaluate the field everywhere in the space. The potential and the field components at a given point Q can be computed by using the Taylor series expansion (4.1) and its derivatives relevant to the gridpoint P nearest to Q . The partial derivatives present in that series can now be evaluated as functions of the potential of the gridpoints near P by means of eqs. (4.3), (5.3), and so on.

The above potential and field computation procedure, which is valid for points not belonging to the grid, presents the same degree of approximation as that typical of the discretization procedure, and is particularly suitable to compute field values near a boundary or interface line, which

can be of notable interest and are usually computed with some difficulties.

8. Some remarks on the grid form

The method proposed can be implemented in various forms, depending on the grid chosen for the discretization.

The simplest form can be obtained in the case of a Taylor series expansion (4.1) stopped at the second order terms ($N=2, M=5$). In this case, the internal equations (4.4) involve five gridpoints P_i , in addition to the central one, P (Fig. 4). The boundary equations (5.5) involve four gridpoints (Fig. 5), and the interface equations (6.6) involve eight gridpoints

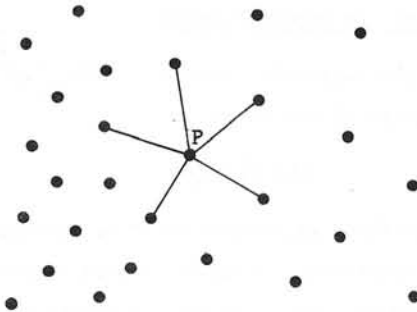


Fig. 4 - 5-point star around an internal gridpoint P (case with $N=2, M=5$).

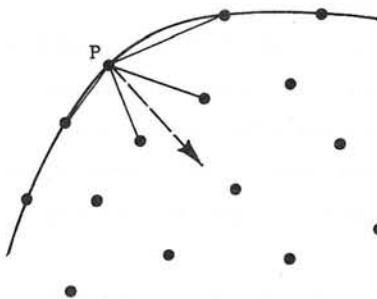


Fig. 5 - 4-point star around a boundary gridpoint P (case with $N=2, M=5$)

(Fig. 6). However, if f_2 is zero in eq. (6.7), only six gridpoints are necessary instead of eight. In this implementation form, if four gridpoints are placed on two orthogonal straight lines passing through the central

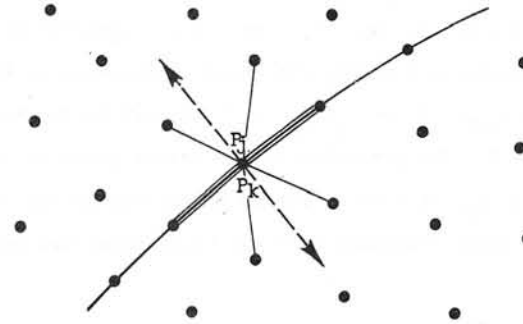


Fig. 6 - 8-point star around an interface gridpoint P (case with $N=2, M=5$).

gridpoint P , the equation (4.4) degenerates into the form typical of the traditional finite-difference method, and the coefficient of the fifth gridpoint tends to zero. It must be noted that the difference between the discontinuity equations and the internal ones is much smaller than in traditional finite-difference methods, where the equations involving normal derivatives are derived from interpolation procedures which need many gridpoints, for instance, six in the boundary equations, and twelve in the interface ones, precision being equal.

An application of the new method can be limited to the introduction of the boundary and interface conditions involving normal derivatives. In this case, the internal equations remain unchanged with respect to the traditional finite-difference ones, and the new method is used only to simplify the discontinuity conditions.

Less simple forms of the method involve a Taylor series expansion stopped at higher order terms. This choice yields higher precision of the results with a smaller gridpoints number. For instance, it is possible to take into account second, third and fourth order terms in the expansion by taking $N=4$ and $M=14$. Then, the internal equations involve 14 gridpoints, the boundary ones 13, and the interface ones 26; the difference between the equations increases notably.

9. A comparison with traditional numerical methods

The new method proposed presents such a variety of implementation forms that a comparison with previous methods should now be untimely. However, we can outline the problem as follows.

With respect to traditional finite-difference schemes, the new method seems to be much more powerful. It coincides with the traditional method only in its simplest form ($N=2$) applied to a Cartesian grid, and only in the internal equations. The discontinuity equations are already simpler, and allow us to reduce notably the iteration number required for convergence by overrelaxation iterative methods, owing to a reduction in the band amplitude of the matrix B .

The differences between the proposed method and the finite-elements one are not easily definable: both methods may be applied in many different ways, so that their comparison depends essentially on the particular implementation used.

Both methods introduce an approximate expansion of the potential in the grid. Probably, the finite-elements method can use a larger number of different approximating functions. However, in the authors' opinion, the new finite-difference method can generally warrant higher precision of the results. This assertion is first based on the complete form of the Taylor series expansion, stopped at the N -order terms, which is used in the method, and then on the high precision with which the boundary and interface conditions are locally imposed.

Besides, the new finite difference method seems to simplify the implementation for various differential problems, and for various degrees of approximations. Finally, it seems to allow us a very simple and accurate procedure of potential and field evaluation at points, not belonging to the grid.

Anyhow, most of the drawbacks of the finite-difference procedure with respect to the finite-elements one seem to have been eliminated.

10. Examples

The implementation of the new method proposed is presently under way. As an example, in the following we shall apply our method to a simple case where a comparison with a theoretical solution is possible.

The problem is one of computing the magnetic field produced by a rectangular wire of circular cross section carrying a time-constant current I .

The problem can be solved by the introduction of a vector potential A with only the axial component A_z different from zero.

To obtain a comparison with a finite-elements solution of the same problem, we resort to a computation, carried out by means of first order triangular elements, which is available in the literature³. Indeed, to facilitate the comparison, we have used the same gridpoints also for our finite-difference application. The grid used is shown in Fig. 7, where we have indicated, at any gridpoint, the composition of the relevant star by means of segments directed towards the gridpoints involved in the discretized equation. We have used a second order discretization ($N=2$, $M=5$),

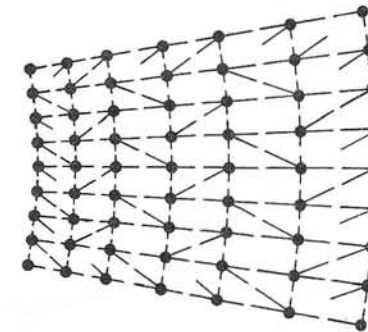


Fig. 7 - An example of field computation by the method proposed. The gridpoints coincide in both the finite-elements and the finite-difference computation.

which is the most consistent with the finite-elements solution considered.

The boundary conditions imposed have been $A_z=100$ on the internal circle of Fig. 7, $A_z=0$ on the external one, and $\partial A_z/\partial n=0$ on the two radii which delimitate the definition set of the problem.

In Fig. 8, we show the relative errors on the potential obtained by

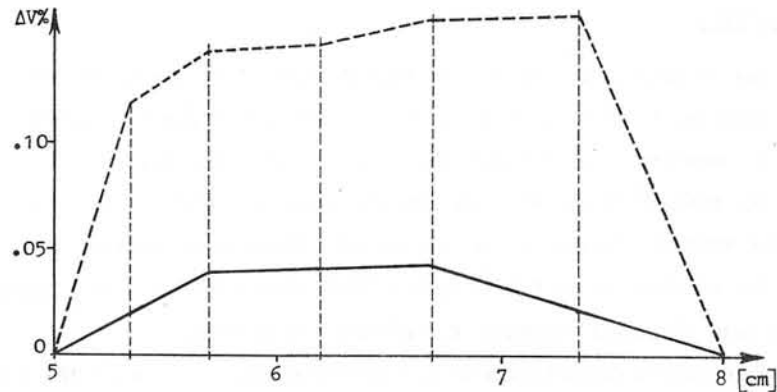


Fig. 8 - Comparison between the absolute value of the relative errors on the potential for the problem of Fig. 7.
Continuous curve: finite-difference solution.
Dashed curve: finite-elements solution³.

the method proposed (continuous curve) and the ones of the finite-elements solution (dashed curve). They are relevant to the gridpoints placed on the symmetry axis of the problem (horizontal axis in Fig. 7).

Analogous results, relating to the magnetic field on the same symmetry axis, are plotted in Fig. 9.

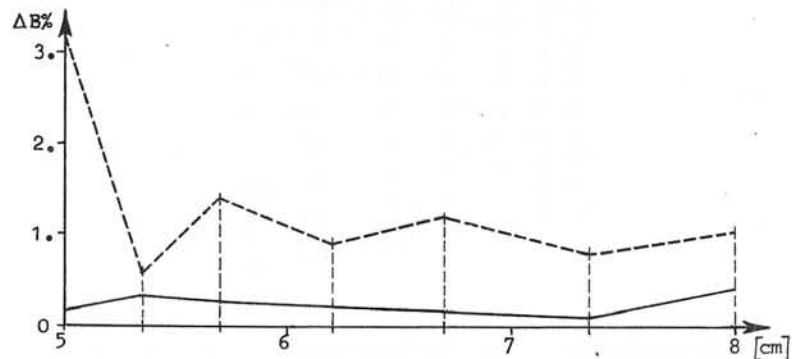


Fig. 9 - Comparison between the absolute value of the relative errors on the magnetic field for the problem of Fig. 7.
Continuous curve: finite-difference solution.
Dashed curve: finite-elements solution³.

As we can see, the new method gives satisfactory results in the example presented above. They exhibit a non-negligible improvement with re-

spect to the ones obtained by the finite-elements method, especially as far as the field is concerned.

Other examples carried out by the authors have also provided good results. In particular, the new method lends itself to grid optimization, and in this connection the present authors have already obtained very satisfactory results, which are described elsewhere⁴.

11. Conclusions

The introduction of a finite-elements grid form in the finite-difference procedure seems particularly useful to blend the best features of the two methods and to obtain a new powerful field computation procedure.

This has been accomplished by means of a discretization procedure, which has allowed us to use irregular grids and to obtain various orders of approximation, depending on the truncation errors in the series expansion of the potential around any gridpoint.

The new method exhibits too many implementation ways to allow an immediate, conclusive description of its features. However, the results obtained seem to show that the old disadvantages of the finite-difference procedure with respect to the finite-elements one have been eliminated. Indeed, some advantages should be obtained, such as higher precision of the results, an easier implementation procedure, and a better flexibility in adapting the method to various problems and to various computation requirements, especially when derivatives of the potential are necessary. It is too early to give a positive statement of the qualities of the new method. However, there are indications that the good results obtained so far may be confirmed in the future.

12. Acknowledgment

The authors acknowledge the financial support of the Gruppo Macchine Elettriche of CNR (Electric Machinery Research Group of the Italian Research Council).

13. References

1. L. Ceriturioni and A. Viviani: "Contribution to numerical computation of Laplacian fields". Proc, IEE. Vol. 122, 1975, p. 1327.
2. G.B. Denegri, G. Molinari and A. Viviani: "A program for electric field computation using a finite-difference method with curvilinear grid", 1975 International High Voltage Symposium, Zurich, Vol. 1, p. 6.
3. M. Fanelli: "Il metodo degli elementi finiti: possibilita di applicazione a problemi di interesse degli elettrotecnici", L'Elettrotecnica, Vol. 62, 1975. p. 513.
4. B. Delfino, G.B. Denegri, G. Molinari, .A. Viviani: "A contribution to high precision numerical computation of Laplacian fields", to be presented at the International Conference on Numerical Methods in Electrical and Magnetic Field Problems, Santa Margherita (Italy), May-June 1976.

FINITE ELEMENT APPROXIMATION AND ITERATIVE METHODS OF SOLUTION FOR 2-D NON-LINEAR MAGNETOSTATIC PROBLEMS

R. Glowinski - A. Marrocco
Univ. PARIS VI - IRIA/LABORIA

I. INTRODUCTION

The numerical analysis of the magnetic field in a tetrapolar alternator is presented here. The actual problem is a tridimensional one, but in this paper we study only the middle cross-section of the machine and the problem is reduced to a two-dimensional one. (see fig.1). The approximation is made by the technique of finite elements (conformal P_1 finite element). For the engineer this choice corresponds to the following approximation : in the iron (stator or rotor), the magnetic permeability will be constant over each element. The numerical solution of the resulting algebraic (non-linear) system is carried out by different methods (linearization, Newton-Raphson, point over-relaxation method, penalty-duality).

II. STATEMENT OF THE PROBLEM

The Maxwell's equations (for magnetostatic) are the following

$$\nabla \times \vec{H} = \vec{j} \quad (2.1)$$

$$\vec{B} = \mu \vec{H} \quad (2.2)$$

$$\nabla \cdot \vec{B} = 0 \quad (2.3)$$

where

- . \vec{H} is the magnetizing force (or magnetic field intensity),
- . \vec{j} is the current density vector and (2.1) is the Maxwell-Ampere relation,
- . \vec{B} is the flux density (or magnetic induction) and μ is the magnetic permeability (scalar function for isotropic material)

Equation (2.2) gives the relation between magnetizing force \vec{H} and flux density \vec{B} . This relation is linear in air where we have $\mu = \mu_0 = 4\pi \cdot 10^{-7}$ MKSA, but it becomes non linear in iron because the magnetic permeability is a function of $|\vec{H}|$ (or a function of $|\vec{B}|$). This dependence of μ versus \vec{H} or \vec{B} can be extracted from characteristic curves - see fig. 2 and 3 - (the hysteresis effect is not considered). With (2.3) it is classical (see Durand (1)) to introduce the potential vector A such that

$$\vec{B} = \nabla \times \vec{A} \quad (2.4)$$

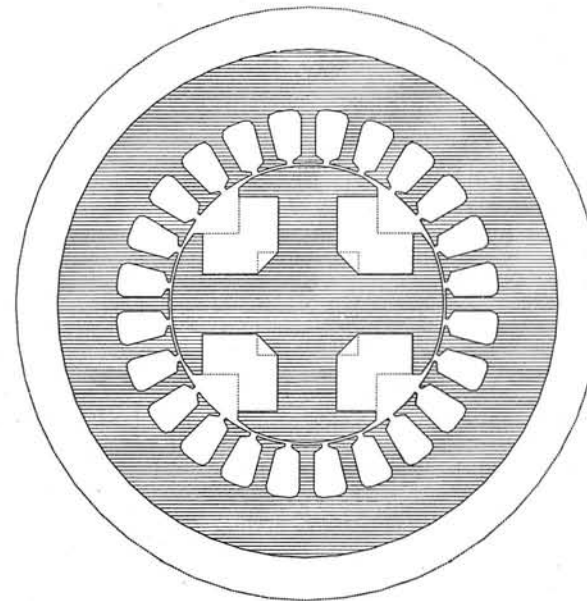


Figure 1
Tetrapolar alternator

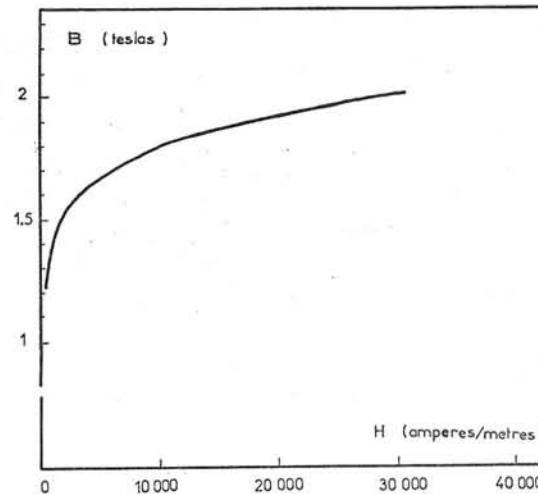


Figure 2
Stator B-H characteristic

With this relation, (2.1), (2.2), (2.3) is reduced in :

$$\nabla \times (\nu \nabla \times \vec{A}) = \vec{j} \quad (2.5)$$

where ν is the magnetic reluctivity ($\nu = \frac{1}{\mu}$).

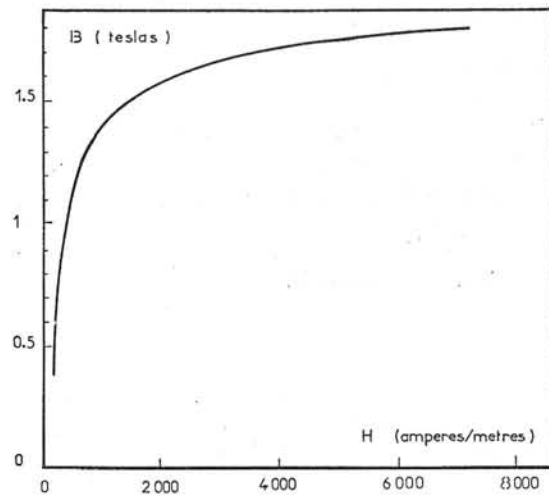


Figure 3
Rotor B-H characteristic

In our 2.D problem the potential vector \vec{A} and current density \vec{j} have a particular structure

$$\vec{A} = (0, 0, A_3)$$

$$\vec{j} = (0, 0, j_3)$$

where A_3 and j_3 depend only of x_1, x_2 .

In this case (2.5) may be written in the following way.

$$-\sum_{i=1}^2 \frac{\partial}{\partial x_i} \left(v \frac{\partial A_3}{\partial x_i} \right) = j_3 \quad \text{or} \quad -\nabla \cdot (v \nabla A_3) = j_3, \quad (2.6)$$

(2.6) is the partial differential equation we have to study. This equation (2.6) (or 2.5) is theoretically given for the whole space. In practice we take a bounded domain Ω and the potential vector must satisfy suitable properties on the boundary. See fig. 1 for the domain considered.

There is an air-region in the outside of the stator and on its boundary we take $A_3 = 0$. The physical meaning of this condition is : all flux lines are in the domain shown on fig. 1 (there is no magnetic phenomenon outside Ω). The numerical results show that this condition $A_3 = 0$ could be prescribed in fact on the stator boundary.

From a theoretical point of view, we study the problem in the domain Ω with homogeneous Dirichlet condition ; for computations it will be sufficient to take only a quarter of circle.

III. MATHEMATICAL MODEL

III.1. Partial differential equations

The domain Ω is a disk in \mathbb{R}^2 , and we denote by Γ the boundary of Ω . The magnetic field determination is equivalent to the solution of the partial differential equation

$$\left. \begin{aligned} -\frac{\partial}{\partial x_1} \left(v(x,A) \frac{\partial A}{\partial x_1} \right) - \frac{\partial}{\partial x_2} \left(v(x,A) \frac{\partial A}{\partial x_2} \right) &= j \quad \text{in } \Omega \\ A|_{\Gamma} &= 0, \end{aligned} \right\} \quad (3.1)$$

where A is a function of x_1, x_2 . The reluctivity v is a function of the space variable $x = \{x_1, x_2\}$ and also of the function $|\vec{B}|$ in the iron. In 2.D we have $|\vec{B}| = |\nabla \times \vec{A}| = |\nabla \cdot \vec{A}|$ if $\vec{A} = (0, 0, A)$, so that v is also a function of A .

If we factorize the reluctivity v by

$$v = v_o v_r$$

where $v_o = \frac{1}{\mu_o} = \frac{1}{4\pi \cdot 10^{-7}}$ MKSA is the reluctivity of air and v_r is the relative reluctivity with respect to air, in iron v_r is a non linear function of $|\vec{B}|$; it is more convenient to express v_r as a function of $|\vec{B}|^2 = |\text{grad } A|^2$ and we can write (3.1) as

$$\left. \begin{aligned} -\frac{\partial}{\partial x_1} \left(v_r(x, |\text{grad } A|^2) \frac{\partial A}{\partial x_1} \right) - \frac{\partial}{\partial x_2} \left(v_r(x, |\text{grad } A|^2) \frac{\partial A}{\partial x_2} \right) &= \mu_o j \quad \text{in } \Omega \\ A|_{\Gamma} &= 0 \end{aligned} \right\} \quad (3.2)$$

III.2. Energy functional

Solving (3.2) is equivalent to the minimization in a suitable space of the magnetic energy given by

$$\mathcal{F}(A) = \int_{\Omega} \left[\int_0^{|\vec{B}|} v_r(x, b) b db \right] dx - \int_{\Omega} \mu_o j \cdot A dx \quad (3.3)$$

where $|\vec{B}| = |\nabla \times \vec{A}|$, $\vec{A} = (0, 0, A)$ (see for instance CHARL-SILVESTER (2)). The Euler equation of the optimisation problem gives equation (3.2). With our choice of v_r , if we denote by ψ the function such that :

$$\left. \begin{aligned} \frac{\partial \psi}{\partial |\vec{B}|^2} (x, |\vec{B}|^2) &= v_r(x, |\vec{B}|^2) \\ \psi(x, 0) &= 0, \end{aligned} \right\} \quad (3.4)$$

then the energy functional becomes

$$\mathcal{F}(A) = \frac{1}{2} \int_{\Omega} \psi(x, |\text{grad } A|^2) dx - \int_{\Omega} \mu_0 \mathbf{j} \cdot \mathbf{A} dx \quad (3.5)$$

III.3. Reluctivity approximation

Let us take the B-H characteristics of stator and rotor. We assume that these curves are single-valued (no hysteresis effect). We take points from these characteristic curves and put these points in a $(|\vec{B}|^2, v_r)$ space.

The distribution of these points in the $(|\vec{B}|^2, v_r)$ space, the physical properties of v_r lead us to approximate $v_r(|\vec{B}|^2)$ by a function belonging to the family defined by

$$\tilde{v}_{\epsilon, \alpha, c, T}(x) = \epsilon + (c - \epsilon) \frac{x^\alpha}{x^\alpha + T} \quad (3.6)$$

(with constraints of positiveness on parameters ϵ, α, c, T).

The approximation is made by a least-square method. A typical set of value (ϵ, α, c, T) obtained for stator characteristic approximation is

$$\begin{aligned} \epsilon &= 5.163619 \cdot 10^{-4} \\ c &= 0.175775 \\ \alpha &= 5.419241 \\ T &= 8.758756 \cdot 10^3 \end{aligned}$$

The mean relative error when comparing to the experimental data is 3,5% (see fig. 4 and 5).

Remark 3.1 : ψ defined in (3.4) will be in fact the primitive function of $\tilde{v}_{\epsilon, \alpha, c, T}$.

IV. THEORETICAL RESULTS

IV.1. Rigorous formulation

Let $H_0^1(\Omega)$ be the classical SOBOLEV space defined by :

$$H_0^1(\Omega) = \{v | v \in L^2(\Omega), \frac{\partial v}{\partial x_i} \in L^2(\Omega), v|_{\Gamma} = 0\} \quad (4.1)$$

with Hilberts' norm

$$\|v\|_{H_0^1(\Omega)}^2 = \int_{\Omega} |\text{grad } v|^2 dx. \quad (4.2)$$

The precise formulation of our optimization problem is :

Find a function A such that $A \in H_0^1(\Omega)$, and

$$\mathcal{F}(A) \leq \mathcal{F}(v) \text{ for every } v \in H_0^1(\Omega), \quad (4.3)$$

where \mathcal{F} is given by

$$\mathcal{F}(v) = \frac{1}{2} \int_{\Omega} \psi(x, |\text{grad } v|^2) dx - \int_{\Omega} \mu_0 \mathbf{j} \cdot \mathbf{v} dx.$$

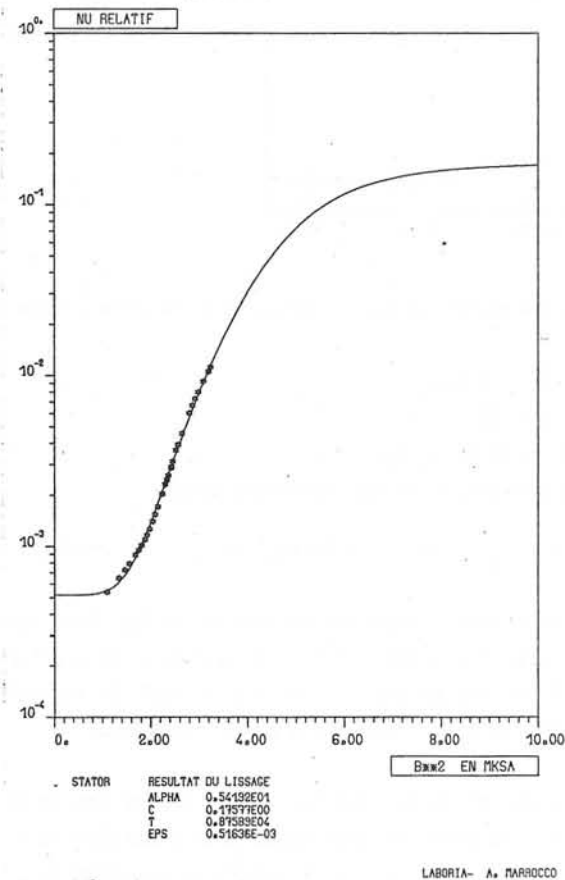


Figure 4
Reluctivity approximation
(stator)

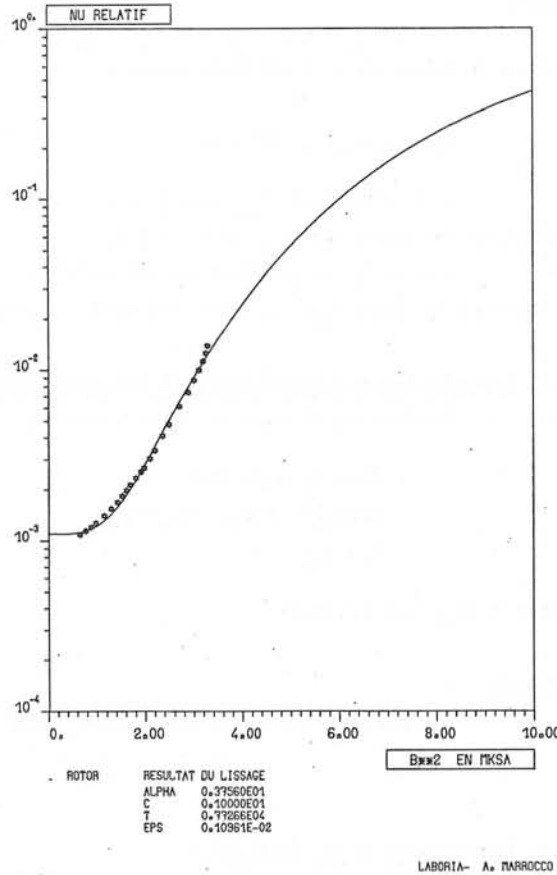
IV.2. Existence and uniqueness results for the problem (4.3)

Theorem : The optimization problem (4.3) has a solution and this solution is unique

Very briefly this result comes directly from the following properties

- a) \mathcal{F} is strongly continuous on $H_0^1(\Omega)$,

Figure 5
Reluctivity approximation
(rotor)



- b) \mathcal{F} is strictly convex,
- c) $\mathcal{F}(v) \rightarrow +\infty$ when $\|v\|_{H^1_0(\Omega)} \rightarrow +\infty$.

IV.3. Relations between the non linear partial differential equation formulation (3.2) and the optimization (or variational) formulation (4.3)

Theorem. - A, solution of (4.3) is the unique solution of (3.2) in $H^1_0(\Omega)$.

Proof : \mathcal{F} is gateaux-differentiable, i.e.

$\forall u \in H^1_0(\Omega)$, here exists $\mathcal{F}'(u) \in H^{-1}(\Omega)$ such that

$$\lim_{\substack{t \rightarrow 0 \\ t \neq 0}} \frac{\mathcal{F}(u+tv) - \mathcal{F}(u)}{t} = (\mathcal{F}'(u), v)$$

for each $v \in H^1_0(\Omega)$

If A is solution of (4.3) we have

$$\frac{\mathcal{F}(A+tv) - \mathcal{F}(A)}{t} \geq 0 \quad \forall t > 0, \forall v \in H^1_0(\Omega)$$

At the limit we have

$$(\mathcal{F}'(A), v) \geq 0 \quad \forall v \in H^1_0(\Omega)$$

In the same way for $t < 0$, we have

$$(\mathcal{F}'(A), v) \leq 0 \quad \forall v \in H^1_0(\Omega)$$

It follows that

$$(\mathcal{F}'(A), v) = 0 \quad \forall v \in H^1_0(\Omega) \tag{4.4}$$

so that we have :

$$\mathcal{F}'(A) = 0 \quad (\text{equality in } H^{-1}(\Omega)). \tag{4.5}$$

The explicit form of (4.4) and (4.5) are respectively given by (4.6) and (4.7)

$$\int_{\Omega} v_r(x, |\text{grad } A|^2) \text{grad } A \cdot \text{grad } v \, dx - \int_{\Omega} \mu_0 j \cdot v \, dx = 0 \tag{4.6}$$

$\forall v \in H^1_0(\Omega),$

$$- \sum_{i=1}^2 \frac{\partial}{\partial x_i} (v_r(x, |\text{grad } A|^2) \frac{\partial A}{\partial x_i}) - \mu_0 j = 0 \tag{4.7}$$

$A|_{\Gamma} = 0.$

Actually A is completely characterized by (4.4), because \mathcal{F} is strictly convex.

V. FINITE ELEMENT APPROXIMATION

V.1. Triangulation of Ω and notations (see fig. 6)

The triangulation \mathcal{T}_h will be a set of triangles T such that

$$\bigcup_{T \in \mathcal{T}_h} T \subset \bar{\Omega} \tag{5.1}$$

If T_1 and $T_2 \in \mathcal{T}_h$ we have

$$\left. \begin{aligned} T_1 \cap T_2 &= \emptyset \\ \text{or } T_1 \text{ and } T_2 &\text{ have a common edge} \\ \text{either } T_1 \text{ and } T_2 &\text{ have a common vertex.} \end{aligned} \right\} \tag{5.2}$$

As usual, h will be the largest edges' length of \mathcal{T}_h .

We define

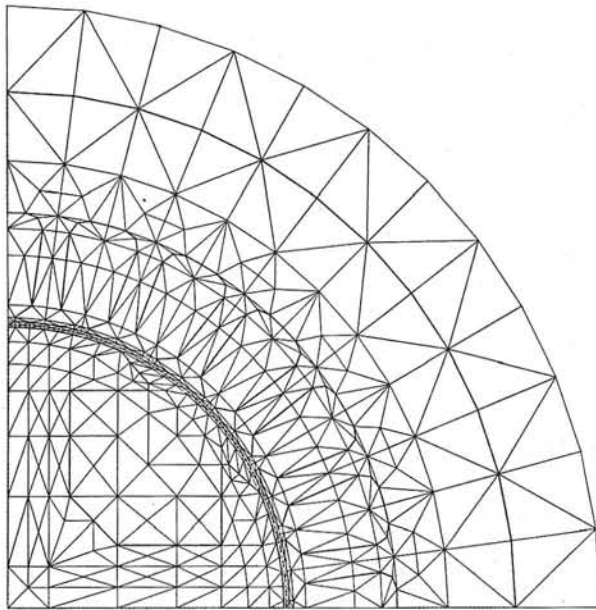


Figure 6
Triangulation of the domain

$$\Omega_h = \bigcup_{T \in \mathcal{T}_h} T, \quad \Gamma_h = \partial\Omega_h \quad (5.3)$$

$$\omega_h = \{P \mid P \in \Omega_h, P \text{ vertex of } T, T \in \mathcal{T}_h\} \quad (5.4)$$

$$\gamma_h = \{P \mid P \in \Gamma_h, P \text{ vertex of } T \in \mathcal{T}_h\} \quad (5.5)$$

$$\bar{\omega}_h = \omega_h + \gamma_h \quad (5.6)$$

Remark.

With the triangulation used, the boundaries between air and iron, air and cooper, never cross a triangle and are unions of edges of triangles which belong to \mathcal{T}_h .

V.2. Approximation of $H_0^1(\Omega)$

$H_0^1(\Omega)$ is approximated by

$$V_{oh} = \{v_h \mid v_h \in C^0(\bar{\Omega}_h), d^\circ v_h \leq 1 \text{ on } T, T \in \mathcal{T}_h, v_h = 0 \text{ on } \Gamma_h\} \quad (5.7)$$

Remarks

. $\dim V_{oh} = \text{Card}(\omega_h)$ and $v_h \in V_{oh}$ is completely determined by the values it takes on ω_h ; we shall denote

$$v_i = v_h(M_i), \quad \forall M_i \in \omega_h \quad (5.8)$$

. As classical, V_{oh} may be considered as a subspace of $H_0^1(\Omega)$ obtained by extending $v_h \in V_{oh}$ by 0 on $\Omega - \Omega_h$

. $\text{grad } v_h$ is constant on each element $T \in \mathcal{T}_h$, so that v_h which is a function of $|\text{grad } v_h|^2$ is also constant on each triangle.

V.3. Formulation and solvability of the approximated problem

Problem (4.3) will be approximated by

$$\left. \begin{aligned} \text{Find } A_h \text{ such that} \\ \mathfrak{F}(A_h) \leq \mathfrak{F}(v_h) \quad \forall v_h \in V_{oh} \\ A_h \in V_{oh} \end{aligned} \right\} \quad (5.9)$$

where \mathfrak{F} is given by (3.5).

Theorem

The problem (5.9) has one and only one solution characterised by:

$$\frac{\partial \mathfrak{F}}{\partial v_i}(A_h) = 0 \quad (5.10)$$

V.4. Convergence of A_h when $h \rightarrow 0$

Theorem

If :

- i) $\Omega - \Omega_h \rightarrow 0$ when $h \rightarrow 0$ (i.e. $\forall K \subset \Omega$, K compact, we have $K \subset \Omega_h$ for h small enough).
- ii) The angles of all $T \in \mathcal{T}_h$ are bounded below by some $\theta_0 > 0$, θ_0 independent of h , then

$$A_h \rightarrow A \text{ strongly in } H_0^1(\Omega) \text{ when } h \rightarrow 0. \quad (5.11)$$

VI. NUMERICAL SOLUTION OF THE APPROXIMATED PROBLEM

VI.1. Solution by linearization

A variational formulation of the approximated problem is

$$\left. \begin{aligned} \int_{\Omega} \tilde{v}_r(x, |\text{grad } A_h|^2) \text{grad } A_h \cdot \text{grad } v_h \, dx &= \int_{\Omega} \mu_o j \cdot v_h \, dx \quad \forall v_h \in V_{oh} \\ A_h \in V_{oh} \end{aligned} \right\} \quad (6.1)$$

Then it is natural to use the following algorithm

$$A_h^o \text{ given in } V_{oh} \quad (A_h \equiv 0 \text{ for example}) \quad (6.2)$$

A_h^n known, A_h^{n+1} is computed by solving the linear problem

$$\left. \begin{aligned} \int_{\Omega} v_r(x, |\text{grad } A_h^n|^2) \text{grad } A_h^{n+1} \cdot \text{grad } v_h &= \int_{\Omega} \mu_o j \cdot v_h \, dx \quad \forall v_h \in V_{oh} \\ A_h^{n+1} \in V_{oh} \end{aligned} \right\} \quad (6.3)$$

If we make use of an iterative method for solving the linear system (6.3) (overrelaxation method for instance), an obvious variant is to make only one cycle to find A_h^{n+1} , using as initial value A_h^n . For both techniques, convergence is obtained only if j is small enough ($j \leq j_o = 0.5 \text{ A/mm}^2$). For these values of j we have not magnetic saturation in iron and the problem is only a practically linear problem with non constant coefficients. For small values of j we have small flux density B in the machine and the relative reluctivity v is quasi-constant, and this lead to a linear problem. When we take greater j , the process does not converge any more and oscillations appear (the value of v_r may change very much from one iteration to the following). A remedy for this oscillation is to under-relax the reluctivities, for example in (6.3) we replace

$$\begin{aligned} \tilde{v}_r(x, A_h^n) \text{ by } v_n \text{ evaluated by} \\ v^n(x) = \rho_n v^{n-1}(x) + (1-\rho_n) v_r^n(x, A_h^n) \quad , \quad 0 < \rho_n < 1 \end{aligned} \quad (6.4)$$

or by

$$v^n(x) = \tilde{v}_r(x, \rho_n A_h^{n-1} + (1-\rho_n) A_h^n). \quad (6.5)$$

Such algorithms can be found for example in ERDELY and FUCHS [3]. The parameter ρ_n is chosen independent of n (value 0.1) and the overrelaxation factor is 1.3 for A_h , but theoretical results of convergence for such an algorithm are known.

VI.2. Newton-Raphson method

The explicit form of the Newton Raphson algorithm is the following :

$$A_h^o \text{ given in } V_{oh} \quad (A_h^o \equiv 0 \text{ for example}),$$

we suppose A_h^n known and we compute A_h^{n+1} by solving the linear system

$$\left. \begin{aligned} \int_{\Omega} \left[\tilde{v}_r(x, |\text{grad } A_h^n|^2) + 2\tilde{v}_r'(x, |\text{grad } A_h^n|^2) \cdot |\text{grad } A_h^n|^2 \right] \text{grad } A_h^{n+1} \cdot \text{grad } v_h \, dx \\ = \int_{\Omega} \mu_o j \cdot v_h \, dx + 2 \int_{\Omega} \tilde{v}_r'(x, |\text{grad } A_h^n|^2) \cdot |\text{grad } A_h^n|^2 \text{grad } A_h^n \cdot \text{grad } v_h \, dx \\ \forall v_h \in V_{oh}, \quad A_h^{n+1} \in V_{oh} \\ \tilde{v}_r'(x, |\text{grad } A|^2) = \frac{\partial}{\partial |\text{grad } A|^2} v_r(x, |\text{grad } A|^2). \end{aligned} \right\} \quad (6.6)$$

A variant of the Newton-Raphson method is to make only one cycle of point, overrelaxation to find A_h^{n+1} .

VI.3. Solution by non linear point over-relaxation

We denote $N = N_h = \dim V_{oh}$ and $v_h = (v_1, v_2, \dots, v_N)$, so we have to solve

$$\frac{\partial \mathcal{F}}{\partial v_i} (A_1, A_2, \dots, A_N) = 0 \quad i = 1, 2, \dots, N \quad (6.7)$$

Algorithm SNL1

$$A_h^o \text{ given in } V_{oh} \quad (A_h^o \equiv 0 \text{ for example}) \quad (6.8)$$

A_h^n known, A_h^{n+1} is computed, component by component by

$$\left. \begin{aligned} \frac{\partial \mathcal{F}}{\partial v_i} (A_1^{n+1}, A_2^{n+1}, \dots, A_{i-1}^{n+1}, \bar{A}_i^{n+1}, A_{i+1}^n, \dots, A_N^n) &= 0 \\ A_i^{n+1} = A_i^n + \omega (\bar{A}_i^{n+1} - A_i^n) \quad , \quad i=1, 2, \dots, N. \quad 0 < \omega < \omega_M \leq 2 \end{aligned} \right\} \quad (6.9)$$

The convergence of this algorithm can be proved using theoretical results obtained by SCHECHTER [4].

Algorithm SNL2

$$A_h^o \text{ given in } V_{oh} \quad (A_h^o \equiv 0) \quad (6.10)$$

A_h^n known, A_h^{n+1} is computed component by component by solving

$$\frac{\partial \mathcal{F}}{\partial v_i} (A_1^{n+1}, \dots, A_{i-1}^{n+1}, A_i^{n+1}, A_{i+1}^n, \dots, A_N^n) = (1-\omega) \frac{\partial \mathcal{F}}{\partial v_i} (A_1^{n+1}, \dots, A_{i-1}^{n+1}, A_i^n, \dots, A_N^n) \quad (6.11)$$

$$0 < \omega < 2 \quad i=1,2,\dots,N.$$

The convergence of SNL2 is not proved (if $\omega \neq 1$), but practically it runs like SNL1. For problems completely non linear, SNL2 seems more robust than SNL1. In SNL1 we have a relaxation of the variables and in SNL2 a relaxation of the equations. This is the same for the linear case.

Some remarks on SNL1 and SNL2

The use of SNL1 or SNL2 leads to solve for each i , a non linear equation (non linear in only one variable \bar{A}_i^{n+1} or A_i^{n+1}).

In this condition it is natural to use the well known Newton method (in only one variable). To solve

$$\left. \begin{aligned} f(x) &= 0 \text{ we use} \\ x_0 &\text{ given} \\ x_{m+1} &= x_m - \frac{f(x_m)}{f'(x_m)} \end{aligned} \right\} \quad (6.12)$$

The iterations are stopped when $\frac{|x_{n+1} - x_n|}{|x_{n+1}|} \leq 10^{-4}$ (if $x_{n+1} \neq 0$)

In our particular problem, the use of (6.12) gives the results in only 2 or 3 iterations for the starting point

$$x_0 = A_1^n.$$

These remarks lead evidently to consider a variant of algorithms SNL1 and SNL2 :

we take for \bar{A}_i^{n+1} or A_i^{n+1} the first iterate of Newton algorithm with an initialization by A_i^n , then we obtain the same algorithm, which will be denoted by EGSN (extrapolated Gauss Seidel Newton).

The explicit form of EGSN is given by

$$A_h^0 \text{ given in } V_{oh} \quad (A_h^0 \equiv 0). \quad (6.13)$$

$$A_i^{n+1} = A_i^n - \omega \frac{\frac{\partial \mathcal{F}}{\partial v_i} (A_i^{n+1}, \dots, A_{i-1}^{n+1}, A_i^n, A_{i+1}^n, \dots, A_N^n)}{\frac{\partial^2 \mathcal{F}}{\partial v_i^2} (A_i^{n+1}, \dots, A_{i-1}^{n+1}, A_i^n, A_{i+1}^n, \dots, A_N^n)}.$$

$$0 < \omega < \omega_M \leq 2, \quad i=1,2,\dots,N.$$

The proof of the convergence of this algorithm can be obtained by using SCHECHTER [4].

The numerical results we obtained prove that EGSN is more efficient than SNL1 and SNL2.

VI.4. Penalty-duality algorithm.

We apply here a penalty-duality method which is proposed for example in R. GLOWINSKI-A. MARROCCO [5].

We have to minimize on V_{oh} the functional

$$\mathcal{F}(v_h) = \frac{1}{2} \int_{\Omega} \psi(x, |\text{grad } v_h|^2) dx - \int_{\Omega} \mu_0 j \cdot v_h dx ; \quad (6.14)$$

$\text{grad } v_h$ is constant on each $T \in \mathcal{T}_h$, we denote by χ_T the characteristic function of T and define

$$L_h = \{z_h | z_h = \sum_{T \in \mathcal{T}_h} z_T \chi_T, z_T \in \mathbb{R}^2\}. \quad (6.15)$$

We define the application $J : V_{oh} \times L_h \rightarrow \mathbb{R}$ by

$$J(v_h, z_h) = \frac{1}{2} \int_{\Omega} \psi(x, |z_h|^2) dx - \int_{\Omega} \mu_0 j \cdot v_h dx \quad (6.16)$$

The optimization problem on V_{oh} is equivalent to

$$\left. \begin{aligned} J(A_h, y_h) &\leq J(v_h, z_h) \quad \forall z_h \in L_h, \forall v_h \in V_{oh}, \\ \text{grad } v_h - z_h &= 0, (A_h, y_h) \in V_{oh} \times L_h, \text{ grad } A_h - y_h = 0. \end{aligned} \right\} \quad (6.17)$$

For the problem (6.17) we can introduce the Lagrangian

$$\mathcal{L}(v_h, z_h; \mu_h) = J(v_h, z_h) + \int_{\Omega} \mu_h (z_h - \text{grad } v_h) dx.$$

By dualization and penalisation of the constraint $\text{grad } v_h - z_h = 0$, we introduce, for $\epsilon > 0$,

$$J_{\epsilon}(v_h, z_h) = J(v_h, z_h) + \frac{1}{\epsilon} \int_{\Omega} |z_h - \text{grad } v_h|^2 dx, \quad (6.18)$$

and then an augmented Lagrangian

$$\mathcal{L}_{\epsilon}(v_h, z_h; \mu_h) = J_{\epsilon}(v_h, z_h) + \int_{\Omega} \mu_h (z_h - \text{grad } v_h) dx. \quad (6.19)$$

For the penalisation (6.18), it is in fact more convenient to define J_ϵ by

$$J_\epsilon(v_h, z_h) = J(v_h, z_h) + \frac{1}{\epsilon} \int_\Omega \eta(x) |z_h - \text{grad } v_h|^2 dx \quad (6.20)$$

with $\eta(x) > 0$ on Ω

In the numerical applications, $\eta(x)$ will be a function constant over each triangle and will permit a homogeneous penalisation. For the engineer this function $\eta(x)$ is more important, it has the same signification than the relative reluctivity ν_r , and could be estimated by him ; if this estimation is good, the following process of resolution converge very quickly.

Algorithm of penalty-duality method

$$A_h^0 \equiv 0, \quad y_h^0 \equiv 0, \quad \lambda_h^0 \equiv 0 \quad (6.21)$$

$$A_h^n, \quad y_h^n, \quad \lambda_h^n \text{ known}$$

1°) A_h^{n+1} is solution of the linear problem.

$$\left. \begin{aligned} \int_\Omega \eta(x) \text{grad } A_h^{n+1} \cdot \text{grad } v_h \, dx &= \frac{\epsilon}{2} \int_\Omega \mu_{oj} \cdot v_h \, dx + \int_\Omega \left(\frac{\epsilon \lambda_h^n}{2} + \eta(x) y_h^n \right) \cdot \text{grad } v_h \, dx \\ \forall v_h \in V_{oh}, \quad A_h^{n+1} \in V_{oh} \end{aligned} \right\} \quad (6.22)$$

2°) We compute y_h^{n+1} by solving the non linear equations

$$\left. \begin{aligned} \int_\Omega \tilde{\nu}_r(x, |y_h^{n+1}|) y_h^{n+1} \cdot z_h \, dx + \frac{2}{\epsilon} \int_\Omega \eta(x) \cdot (y_h^{n+1} - \text{grad } A_h^{n+1}) \cdot z_h \, dx \\ + \int_\Omega \lambda_h^n z_h \, dx = 0 \\ \forall z_h \in L_h; \quad y_h^{n+1} \in L_h \end{aligned} \right\} \quad (6.23)$$

3°) We compute λ_h^{n+1} , triangle by triangle by

$$\lambda_{h,T}^{n+1} = \lambda_{h,T}^n + \rho \eta_T (y_{h,T}^{n+1} - \text{grad } A_{h,T}^{n+1}) \quad (6.24)$$

If we take $\rho = \frac{2}{\epsilon}$ in (6.24) we can prove the convergence of this algorithm as in MERCIER [6].

The non-linear problem (6.23) is in fact a system of Card \mathcal{C}_h non linear equation, in only one variable, and these equations are independent.

If we denote by $|q_T|$ the modulus of a on $T \in \mathcal{C}_h$, the non linear equation we have to solve for each triangle is

$$|q_T| \cdot (\tilde{\nu}_r(x, |q_T|^2) + \frac{2\eta_T}{\epsilon}) = \sqrt{\left[\frac{2\eta_T}{\epsilon} \frac{\partial A_h^{n+1}}{\partial x_1} \Big|_T - \lambda_{1,T}^n \right]^2 + \left[\frac{2\eta_T}{\epsilon} \frac{\partial A_h^{n+1}}{\partial x_2} \Big|_T - \lambda_{2,T}^n \right]^2} \quad (6.25)$$

It is possible to use Newton's method to solve (6.25) but we have to handle this algorithm with care (because the function $q \mapsto q \cdot (\tilde{\nu}_r(x, q^2) + 2\alpha)$ has a derivative which is not monotone).

For this penalty-duality algorithm we have to solve a each step

- . a linear problem (always the same)
- . Card(\mathcal{C}_h) n.l.-equation (only one variable)
- . 2 Card \mathcal{C}_h instruction

With this decomposition of the problem it is easy to implement this new algorithm on a parallel computer.

VII. NUMERICAL RESULTS

For a quarter of alternator, the triangulation has 812 triangles and 384 interior nodes.

The stopping test for all algorithm described in VI is

$$\left. \begin{aligned} \text{Res}(n) &= \frac{\sum_{i=1}^N |A_i^{n+1} - A_i^n|}{\sum_{i=1}^N |A_i^{n+1}|} \\ \text{Res}(n) &\leq \epsilon. \end{aligned} \right\} \quad (7.1)$$

We choose $\epsilon = 10^{-5}$ in (7.1) ; this test is very strong. To obtain 10^{-6} of 10^{-7} it is necessary to compute with double precision.

The algorithm VI.1 (linearization) gives acceptable results for only $j \leq 0.5$.

VII.1. Results for Newton-Raphson algorithm.

The linear system at each step is solved by a direct method (CHOLESKY BAND - a renumerotation of nodes is made to reduce the band width).

The computing time from A_h^n to A_h^{n+1} is 13 s. on CII IRIS 80 computer. See on table VII.1 the results obtained with Newton-Raphson algorithm. The algorithm is started with $A_h^0 \equiv 0$.

For large values of the current density j , the starting point $A_h^0 \equiv 0$ is a bad one, and we observe large oscillations of A_h^n .

RES \ J	$5 \cdot 10^{-4}$	10^{-4}	$5 \cdot 10^{-5}$	10^{-5}
0.5			2 it	3 it
1	3 it		4 it	6 it
2	6 it	7 it	8 it and oscillation	
3	8 it	11 it	14 it	22 it
4	9 it	12 it	15 it	19 it
5	10 it	14 it	16 it	22 it
7.5	9 it	12 it	14 it	19 it
10	13 it	17 it	19 it	28 it
15	51 it	55 it	56 it	62 it
20	big oscillations			

TABLE VII.1. : Newton-Raphson results.

On fig. 7, we give the variation of RES(n) (7.1) when using Newton-Raphson algorithm.

For large values of j we can use the following process (interpolation or under-relaxation).

$$A_h^0 \equiv 0 \text{ given}$$

$$A_h^n \text{ known, } A_h^{n+1} \text{ is computed by}$$

$$\left. \begin{aligned} 1^\circ) & A_h^{n+1} \text{ solution of (6.6)} \\ 2^\circ) & A_h^{n+1} = A_h^n + \omega(A_h^{n+1} - A_h^n) \quad 0 < \omega < 1 \end{aligned} \right\} (7.2)$$

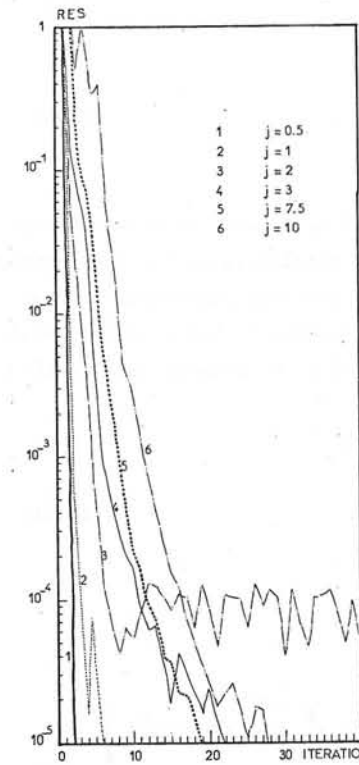


Fig. 7 - Newton Raphson algorithm

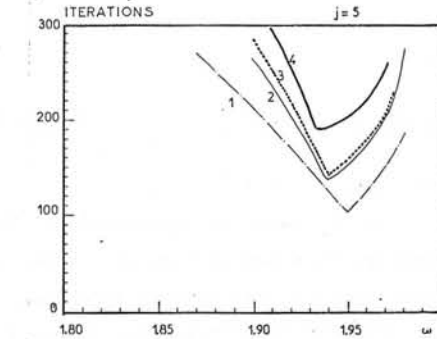


Fig. 8 - Iterative variant of Newton-Raphson

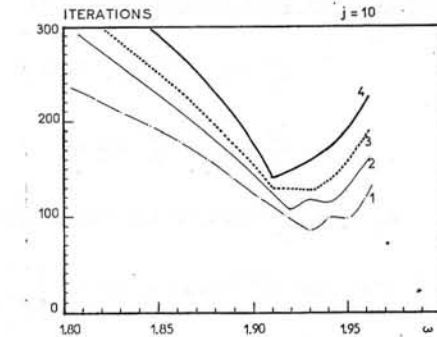


Fig. 9 - Iterative variant of Newton-Raphson

We choose $\omega = 0.5$ in (7.2), this is not optimal, and we obtain the results shown in table VII.2.

Another variant of the algorithm is the following : if we take the linear system (6.6), A_h^{n+1} is obtained from A_h^n by only one cycle of point over-relaxation process. The computing time from A_h^n to A_h^{n+1} is 0.9 s. on CII IRIS 80 computer. With the starting point $A_h^0 \equiv 0$, this variant (iterative variant of Newton) is always more efficient than Newton-Raphson method for large values of the current density j (which leads to a strongly non-linear problem). We can see on fig. 8, 9, 10 the variation of the number of cycles needed for the convergence, for the current density $j=5,10,20$.

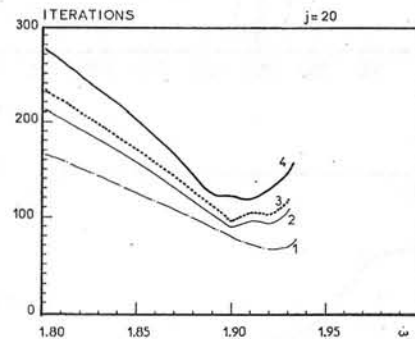
VII.2. Non-linear point over relaxation

For EGSN process the computer time from A_h^n to A_h^{n+1} is 0.65 s. on CII IRIS 80. For SNL1 and SNL2 this time is not constant and depends on the in-

RES \ J	$5 \cdot 10^{-4}$	10^{-4}	$5 \cdot 10^{-5}$	10^{-5}
0.5	11 it	14 it	15 it	16 it
2	11 it	14 it	15 it	18 it
7.5	13 it	19 it	23 it	31 it
15	17 it	22 it	25 it	34 it
20	16 it	21 it	24 it	34 it

TABLE VII.2. : Newton-Raphson with under-relaxation $\omega = 0.5$

Fig. 10 - Iterative variant of Newton-Raphson



ternal Newton process. We can see on fig. 11, 12, 13, 14, 15, 16, 17, 18 results obtained with SNL2 and EGSN.

These algorithms, in particular EGSN, are very efficient and do not need very much storage on the computer. We have also solved the problem for the complete machine. The number of triangles is then 3240, the number of interior nodes is 1597. This algorithm was run on the middle size computer CII 10070 (128K words), without auxiliary memory. For $j=10$, $\omega=1.93$ and $\epsilon=10^{-5}$ in (7.1), EGSN needs 162 iterations and the computing time is about 16 mn. (less than 10 mn. on CII IRIS 80).

VII.3. Results obtained with penalty-duality algorithm

This method need more computer storage, but presents the following interesting particularities

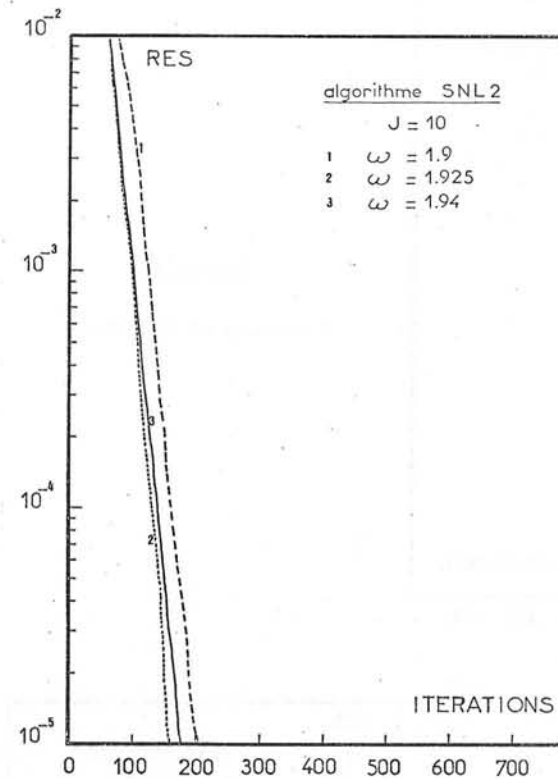


Figure 11
Variation of RES (7.1)

a) each step of the algorithm (6.22), (6.23), (6.24) is easy to solve, since we have to solve

- . a linear problem (with a fixed matrix)
- . a set of non linear independent equations
- . explicit calculation for λ^{n+1}

b) This algorithm is easy to implement on a parallel computer

c) The electrical engineer has the possibility of choosing the function $\eta(x)$ which has a concrete signification for him (he can estimate the solution of his problem in term of flux density repartition).

The results presented here are made with constant value of $\eta(x)$ in air (the value is 1) and in stator, and in rotor the value is $[k \cdot \text{minimal value of } v_r]$ in respective material, with $k > 0$.

The number of iterations necessary to achieve the convergence is shown in fig. 19-29. We give the variation of the number of iterations in

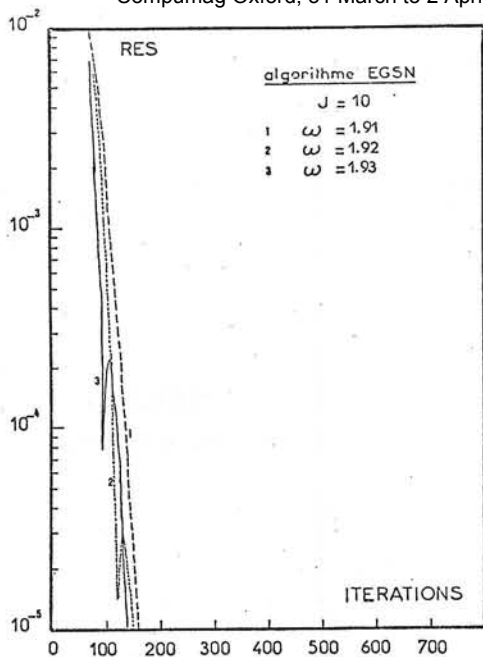


Figure 12

Variation of RES (7.1)

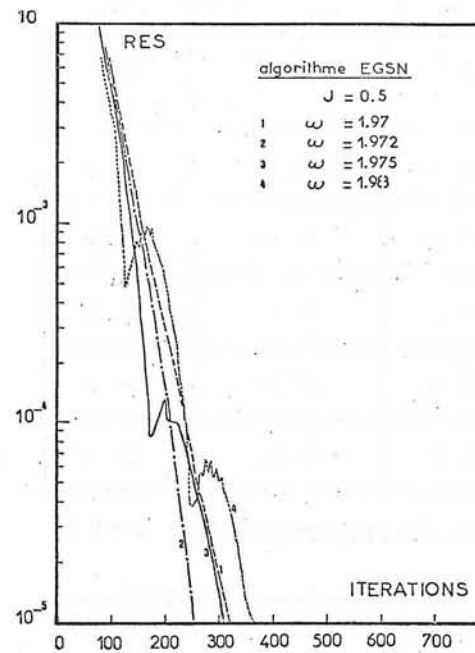


Figure 14

Variation of RES (7.1)

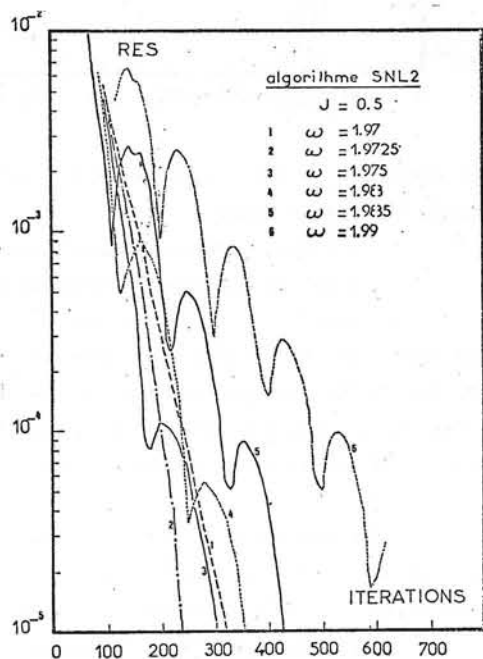


Figure 13

Variation of RES (7.1)

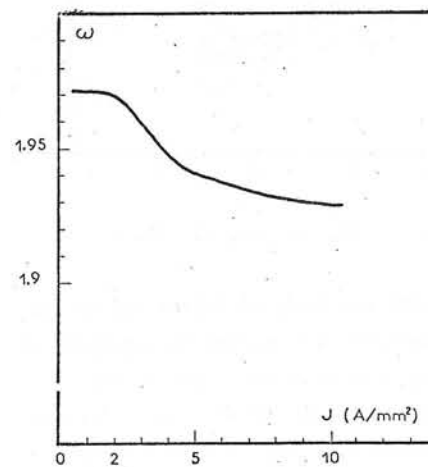


Figure 15

Optimal choice of relaxation parameter for EGSN algorithm.

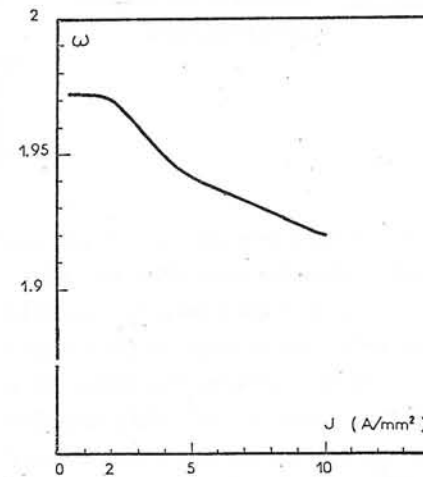


Figure 16

Optimal choice of relaxation parameter for SNL2 algorithm.

function of the penalisation parameter ϵ . We give in table VII.3, computing time on CII IRIS 80 for different values of parameters ϵ , k , j . The stopping test in (7.1) is 10^{-5} .

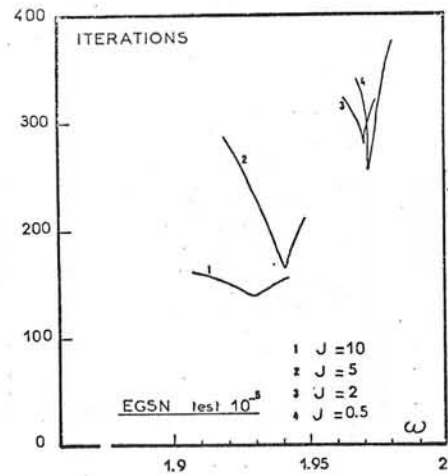


Figure 17

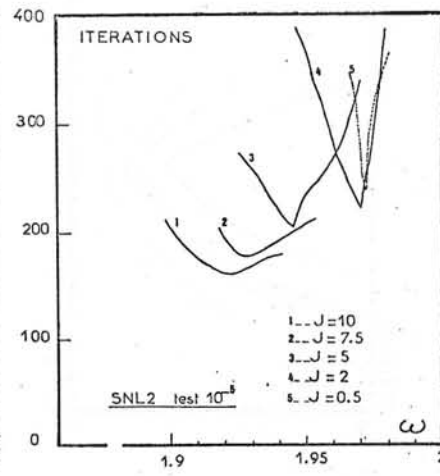


Figure 18

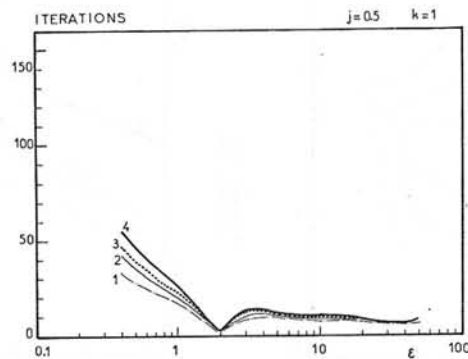


Figure 19

Current density: $j = 0.5$			
$k=1$	$k=10$	$k=20$	$k=50$
$\epsilon = 2$ 2 it. 17s	$\epsilon = 3$ 20 it. 51s		
	$\epsilon = 4$ 18 it. 49s		
	$\epsilon = 5$ 23 it. 56s		
Current density : $j = 2.$			
$\epsilon=0.1$ 152it.363s	$\epsilon=0.75$ 60 it.126s	$\epsilon= 1$ 77 it. 176s	$\epsilon= 5$ 40 it. 95s
$\epsilon=0.2$ 90it.215s	$\epsilon=1$ 55 it.115s	$\epsilon= 2$ 53 it. 121s	$\epsilon=7.5$ 38 it. 91s
$\epsilon=0.3$ 111it.258s	$\epsilon=2$ 79 it.156s	$\epsilon= 3$ 63 it. 139s	$\epsilon=10$ 45 it.106s
Current density : $j = 7.5$			
$\epsilon=0.075$ 137it.329s	$\epsilon=0.4$ 59 it.126s	$\epsilon= 0.5$ 67 it. 142s	$\epsilon= 1$ 74 it.154s
$\epsilon=0.1$ 131it.265s	$\epsilon=0.5$ 49 it.105s	$\epsilon= 0.75$ 53it. 113s	$\epsilon= 2$ 54 it.113s
$\epsilon=0.2$ 133it.267s	$\epsilon=0.75$ 70 it.140s	$\epsilon= 1$ 56 it. 117s	$\epsilon= 3$ 65 it.142s
Current density : $j = 20$			
$\epsilon=0.1$ 114it.232s	$\epsilon=0.3$ 53 it.116s		$\epsilon= 1$ 57 it.123s
$\epsilon=0.2$ 93it.191s	$\epsilon=0.4$ 47 it.104s		$\epsilon= 2$ 43 it. 95s
$\epsilon=0.3$ 124it.248s	$\epsilon=0.5$ 53 it.115s		$\epsilon= 3$ 65 it.136s

TABLE VII.3. Results with duality-penalty algorithm.

We give in Figure 30 an example of repartition of flux lines, for current density $j = 10$.

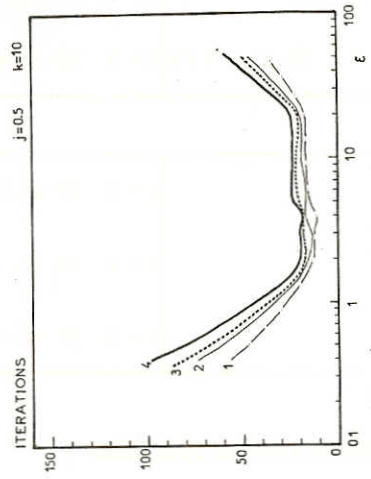


Figure 20

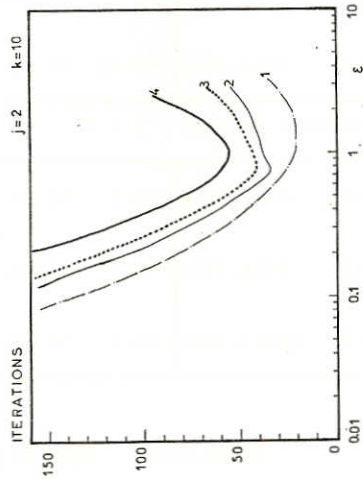


Figure 22

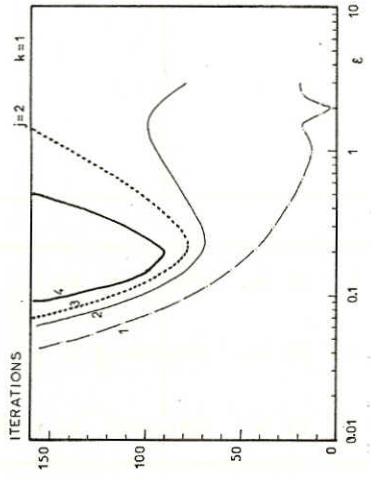


Figure 21

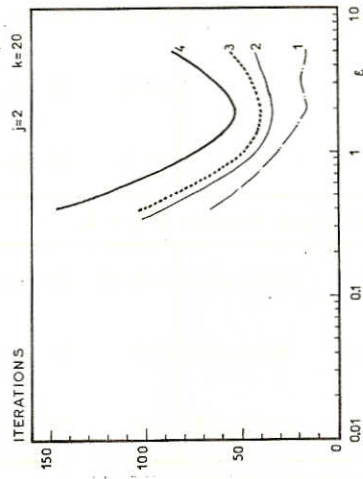


Figure 23

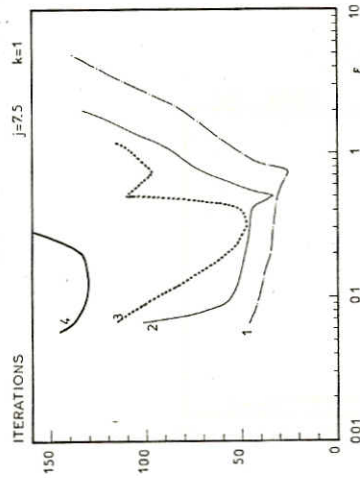


Figure 24

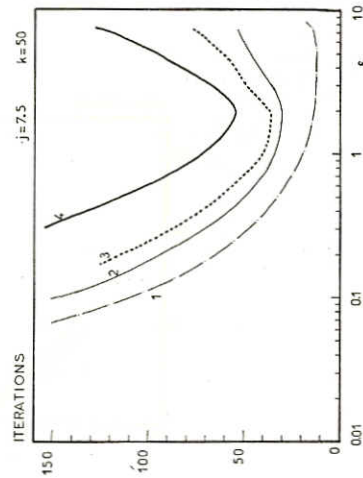


Figure 26

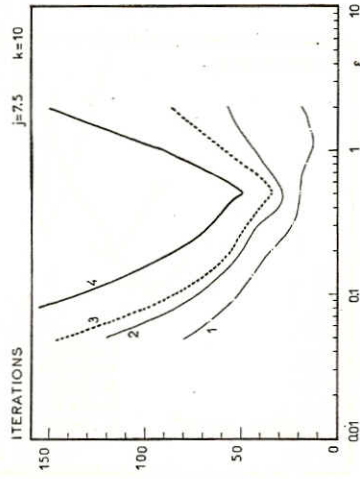


Figure 25

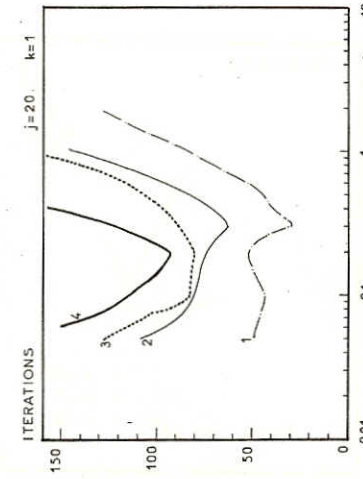


Figure 27

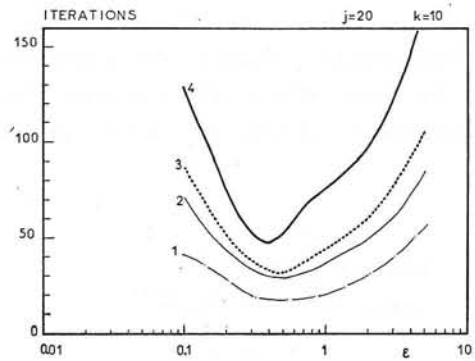


Figure 28

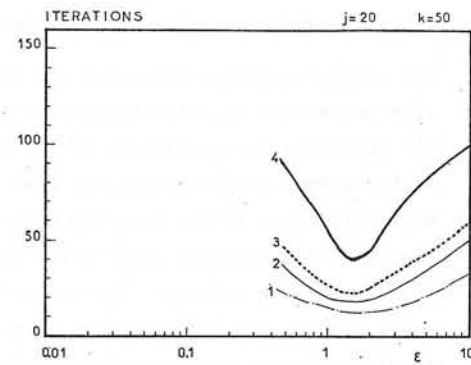


Figure 29

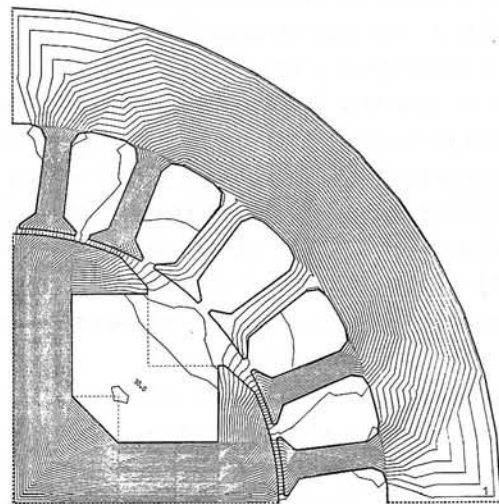


Figure 30
Flux line for $j=10 \text{ A/mm}^2$

REFERENCES

0 - R. GLOWINSKI - A. MARROCCO - Analyse numérique du champ magnétique d'un alternateur par éléments finis et surrelaxation ponctuelle non linéaire. Computer methods in applied mechanics and engineering, 3, 1, (1974)

1 - E. DURAND - Magnétostatique. Masson & Cie, Paris 1968.

2 - P. SILVESTER - MVK CHARI - Analysis of turbo-alternator magnetic fields by finite elements. IEEE PAS, 90, 2, (1971).

3 - E.A. ERDELY - E.F. FUCHS - Non linear field analysis of D.C. machines. IEEE PAS, 80, N° 7 (1546-1583), 1970.

4 - S. SCHECHTER - Minimisation of convex functions by relaxation. Ch. 7 of Integer and non linear programming. J. ABADIE, North-Holland, 1970.

5 - R. GLOWINSKI - A. MARROCCO - Sur l'approximation par éléments finis d'ordre 1 et la résolution par pénalisation dualité d'une classe de problèmes de Dirichlet non linéaires. C.R.A.S. Paris, T. 278, 26 Juin 1974, Série A, 1949-1652. RAIRO, R-2, Août 1975.

6 - B. MERCIER - On the finite element approximation and the solution by a penalty duality algorithm of an elasto-plastic problem. Rapport Laboria, N° 149, Janvier 1975.

R. Glowinski - Université Paris VI, U.E.R. 48, Laboratoire Analyse Numérique, Paris.
 A. Marrocco - IRIA/LABORIA, Domaine de Voluceau, Rocquencourt, 78150 Le Chesnay.

MAGNETIC FIELD CALCULATION FOR A SALIENT-POLE HYSTERESIS COUPLING

M.J.Jevons

The University of Aston in Birmingham, Birmingham B4 7PB, England

1 The hysteresis coupling

One form of salient-pole circumferential-flux hysteresis coupling is shown in fig. 1⁽¹⁾. The stator is made of soft magnetic material and each pole has an exciting coil supplied with dc. The rotor comprises a thin annular ring of hard magnetic material on a non-magnetic arbor.

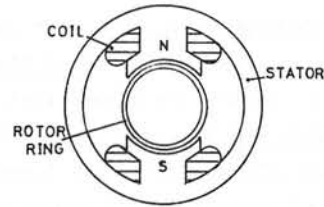


Fig. 1 Salient-pole hysteresis coupling

As the relative magnetic permeability of the ring is low, the airgap flux density waveforms - illustrated in fig. 2 for the outer surface of the rotor - are quite different from those of conventional salient-pole machines and the usual design procedures are not applicable.

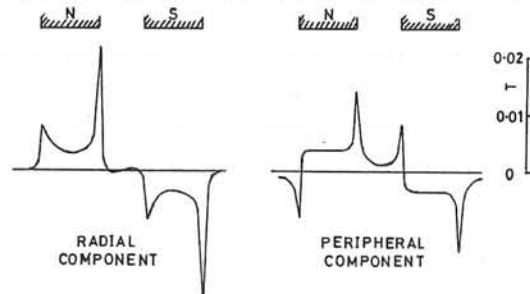


Fig. 2 Airgap flux density waveforms

The waveforms exhibit large peaks in the vicinity of the pole-tips, and the size of the peak in the radial component at the lagging pole-tip largely determines the torque/excitation characteristic of the coupling⁽²⁾. The size can be estimated from the values obtained from an actual machine without a rotor and the rotor saturation magnetization. The problem is to predict this value, and the total permeance as part of the design.

A qualitative theory has been based on a 2-pole idealized machine in which the stator is assumed to be infinitely permeable and the magnetic

field to result from surface polarity and not current sources. End effects have been neglected to permit a 2-dimensional approach. Two mathematical models have been used to predict the airgap flux density waveform. The first simply consists of two equipotential circular arcs which represent the pole-faces (see fig. 3).

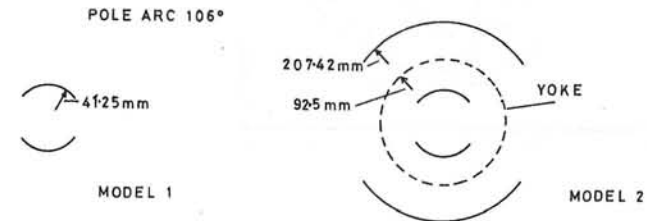


Fig. 3 Mathematical models for the idealized machine without a rotor

The complex magnetic potential and the vector magnetic field are evaluated from an inverse elliptic function transformation⁽³⁾ (see App.7.1). Although the waveforms are apparently of the required shape, detailed comparison with observed results shows the need for an improved model. In the second model (see fig. 3) the yoke has been simulated by including another pair of equipotential circular arcs formed by the inversion of the first pair about the axis of the machine. The radius of inversion equals the radius of the yoke. There does not appear to be a tractable solution for the Laplace equation in this case and the magnetic field has been evaluated numerically. Differences still exist between the predicted and observed waveforms, but are to be expected in view of the initial assumptions.

In the numerical solution adopted - the method of sub-elements - the surface polarity is assumed to vary in a known manner over short lengths (sub-elements) of the replica pole-arcs. A finite number of simultaneous equations are then formed which relate the potentials of the several surfaces to the values of surface polarity. Once these are known, the magnetic field can be calculated at any point in the model. In particular, values of the radial magnetic field strength (or flux density) can be calculated along the circumference of a pitch circle corresponding to the outer surface of the rotor and the maximum value found.

Various aspects of the method of sub-elements are considered in this paper, all with reference to the models described above. Working formulae for two different representations of the surface distribution are derived and their relative merits discussed. Results for both models have been

included; for although the first is an oversimplification, numerical results can be checked against theoretical values, and comparison of the different field distributions enables the practical effect of the yoke to be assessed.

2 Basic theory

There is no simple expression for the distribution of surface polarity (m) over the pole-face (fig. 4a). The shape of the curve is predictable: away from the pole-tips m changes only slightly, it exhibits a minimum at the pole centre-line and is symmetrical about this line; at the pole-tips m is theoretically infinite.

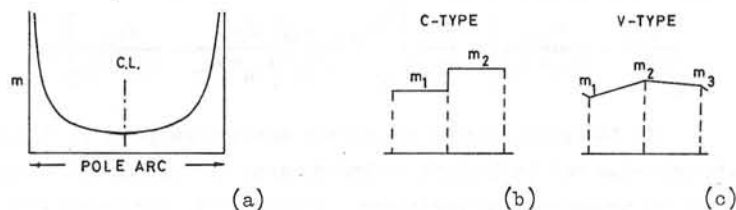


Fig. 4 Surface polarity on the pole-arc

To facilitate numerical evaluation of m , each pole-arc is divided into sections (sub-elements) over which m is assumed to have a known variation. For example; m could be constant - m_1, m_2, \dots (fig. 4b); or vary linearly - m_1, m_2, m_3, \dots (fig. 4c). These are the approximations considered here and are subsequently referred to as C- and V-type. Both are inadequate near to the pole-tips, because of the singularity, but this difficulty has been overcome by assuming m to vary as $x^{-1/2}$ (see App.7.2) in V-type sub-elements which include the pole-tips. The widths of the sections need not be the same and are chosen to anticipate a good fit.

2.1 Evaluation of potential

Each of the magnetized sub-elements contributes to the total potential of a given sub-element, but because of the discrete approximation of m , the potential is not constant over the width. If constant values of m have been assumed then the potential of a sub-element is taken as the value calculated at the mid-point of the width (see fig. 5a).

$$\phi_p = \sum_i - \frac{R_n m_n}{2\pi} \int_{-\frac{1}{2}A_n}^{\frac{1}{2}A_n} \ln(R_n^2 + X^2 - 2R_n X \cos(f_n + f))^{1/2} df \quad (2.1)$$

The summation includes all of the sub-elements on each arc of the model -

$(2n_{actual} + 2n_{image})$, but because of symmetry the potentials are only determined at $\frac{1}{2}n$ (n even) or $\frac{1}{2}(n+1)$ (n odd) points as there are only these distinct values of m . The product $|R_n m_n|$ is the same for a sub-element and its image. Eq. (2.1) is integrated numerically using Bode's quadrature formula⁽⁴⁾, except when $f_n=0$ and $R_n=X$. Then the integral is evaluated as

$$A_n \left[\ln\left(\frac{1}{2}R_n A_n\right) - 1 - \sum_{q=1}^{\infty} \frac{B_{2q-1} A_n^{2q}}{2^{2q+1} n (2q+1)!} \right] \quad (2.2)$$

where B_{2q-1} is a Bernoulli number. Usually 2 terms of the series give sufficient accuracy.

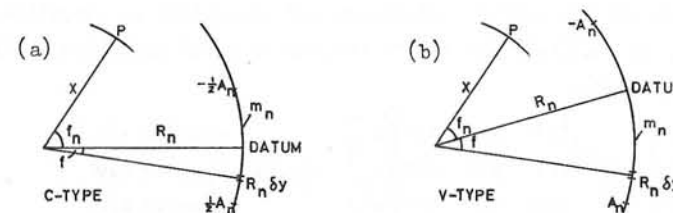


Fig. 5 Meaning of symbols used in equations (2.1) and (2.3)

When a linear variation of m is assumed, the potential is calculated at each end of the sub-element. If the mid-point were used then the solution of the equations for m_n would become unstable as the number of sub-elements is increased. Sub-elements which include the pole-tips are treated similarly except that the potential is calculated at the 'finite' end only. The potential equation corresponding to (2.1) is (see fig. 5b)

$$\phi_p = \sum_i - \frac{R_n m_n}{2\pi} \int_0^{A_n} \left(1 - \frac{f}{A_n}\right)^v \ln(R_n^2 + X^2 - 2R_n X \cos(f_n + f))^{1/2} df \quad (2.3)$$

$$= \sum_i - \frac{R_n m_n A_n}{2\pi} \left[\frac{1}{1+v} \ln(R_n^2 + X^2)^{1/2} + \frac{1}{2} \int_0^1 (1-t)^v \ln(1 - G_n \cos(f_n + tA_n)) dt \right] \quad (2.4)$$

where m_n is the value of m at one end of the sub-element, v is either 1 (linear) or $-1/2$ (pole-tip) and $G_n = 2R_n X / (R_n^2 + X^2)$. The singularity which occurs with $-ve$ v is removed by integrating by parts, when

$$\phi_p = \sum_i - \frac{R_n m_n A_n}{2\pi(1+v)} \left[\ln(R_n^2 + X^2 - 2R_n X \cos(f_n)) + \frac{1}{2} A_n \int_0^1 \frac{(1-t)^v G_n \sin(f_n + tA_n)}{1 - G_n \cos(f_n + tA_n)} dt \right] \quad (2.5)$$

These equations are also integrated numerically using Bode's formula, except when $f_n=0$ and $R_n=X$. Then the integral in eq. (2.3) is evaluated as

$$-A_n \left[\frac{1}{1+v} \left[\ln(R_n A_n) + \psi(1) + \psi(2+v) \right] - \sum_{q=1}^{\infty} \frac{1}{2^q} B_{2q-1} A_n^{2q} \sum_{k=0}^{2q} \frac{(-1)^k}{(2n-k)! k! (1+k+v)} \right] \quad (2.6)$$

where $\psi(j)$ is the digamma function.

At distances large in comparison with the sub-element widths the surface polarity could be considered concentrated into magnetic poles at the ends of the sub-elements and the calculation simplified. This has not been done in the present work.

Because each of the discrete surface distributions contributes to the potential of every sub-element, the coefficient matrices are dense. The equations are poorly conditioned and ill-suited to iterative solution schemes, as eq. (2.7) for 3 sub-elements of equal width (over half of the pole-arc) shows.

$$\begin{bmatrix} 1.0 \\ 1.0 \\ 1.0 \end{bmatrix} = \frac{10^{-4}}{2\pi} \begin{bmatrix} 917 & 346 & 148 \\ 651 & 615 & 265 \\ 577 & 531 & 467 \end{bmatrix} \begin{bmatrix} m_1 \\ m_2 \\ m_3 \end{bmatrix} \quad \text{whence} \quad \begin{matrix} m_1 = 58.2 \text{ A/m} \\ m_2 = 48.6 \text{ A/m} \\ m_3 = 46.9 \text{ A/m} \end{matrix} \quad (2.7)$$

This is for Model 1 - 120° pole-arc and V-type sub-elements. The coefficient matrix is unsymmetrical because the symmetry of the model has been used to reduce the number of equations. Multiplication by the transpose would make it symmetrical but would not improve its poor condition.

As there is no need for a large number of equations with the present simplified models, Gauss elimination has been used in the computer programs to evaluate the unknown surface polarities.

2.2 Evaluation of magnetic field strength

The radial component of the magnetic field strength at p (fig. 5b) is deduced from $\vec{H} = -\nabla\phi$ and eq. (2.3) as

$$H_r = \sum_{n=1}^{\infty} \frac{R_n m_n}{4\pi X} \int_0^{A_n} \left(1 - \frac{r}{A_n}\right)^v \left[1 - \frac{R_n^2 - X^2}{R_n^2 + X^2 - 2R_n X \cos(f_n + f)} \right] dr \quad (2.8)$$

Again the summation includes all of the sub-elements. The assumption of C-type sub-elements leads to poor results and is not pursued.

In the present application H_r is calculated close to the pole surface and this can cause loss of accuracy in the numerical evaluation of eq. (2.7), because $X \rightarrow R_n$ and $2R_n X \rightarrow (R_n^2 + X^2)$. Simpson's $\frac{1}{3}$ formula is used in the computer program, with the panel width automatically halved⁽⁵⁾ until the relative error between successive computations is less than a given value. This is based on a compromise between accuracy and fast running time -

$|0.5| \times 10^{-3}$ has been found suitable, together with a maximum of 7 halving cycles.

$$\begin{aligned} \text{New variables} \quad x_{1n} &= (R_n^2 - X^2) / 2R_n X, & x_{2n} &= (R_n - X)^2 / 2R_n X \\ y_{1n} &= 1 - \cos(f_n + f), & y_{2n} &= 1 - \cos(f_n - f) \end{aligned}$$

are defined and the integral (eq. (2.8)) is evaluated in the form

(i) +ve v (e.g., v=1)

$$\frac{A_n}{1+v} \left[1 - \frac{x_{1n}}{x_{2n}} \right] + \frac{x_{1n}}{x_{2n}} \int_0^{A_n} \left(1 - \frac{r}{A_n}\right)^v \frac{y_{1n}}{y_{1n} + x_{2n}} dr \quad (2.9)$$

(ii) -ve v (e.g., v=-1/2)

$$\frac{A_n}{1+v} \left[1 - \frac{x_{1n}}{y_{2n} + x_{2n}} \right] + \frac{x_{1n}}{x_{2n}} \int_0^{A_n} \left(1 - \frac{r}{A_n}\right)^v \left[\frac{y_{1n}}{y_{1n} + x_{2n}} - \frac{y_{2n}}{y_{2n} + x_{2n}} \right] dr \quad (2.10)$$

At the pitch circle radius the maximum value of H_r occurs just under the pole-tip and is located in the program by testing the slope of the H_r curve at predetermined positions. Values of H_r are calculated at the pole-tip and at angular increments of 0.2° toward the pole centre-line. A change in the sign of the slope locates the maximum within the last two angular increments. This smaller section of the H_r curve is then examined using an increment of 0.1°. The process is repeated twice more.

3 Computer results

Details of the models reported on are given in Fig. 3 and the chief results are tabulated in App.7.3. The numbers of sub-elements referred to are for half of the pole-arc.

3.1 Surface polarity

The principal use of the first model was to assess the correlation between numerical and theoretical values. In this respect the permeance shape factor (S_p - App.7.3) is a useful concept, being numerically equal to half the total surface polarity on one pole. It does not provide a check on the correctness of the distribution.

Both methods of representing the surface distribution were used in the calculations. There was close agreement for the surface polarity on the centre-line of the pole even with 4 sub-elements. However considerable error was noted in the shape factor for the C-type distribution when used with equal width sub-elements. This was not so with the V-type, and the advantage of a simple computer program in the first case is diminished by the larger number of sub-elements necessary and the increased running time.

The distributions for Model 2 using 8 sub-elements are shown in Fig. 6.

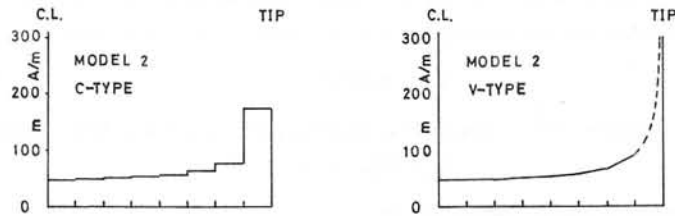


Fig. 6 Surface polarity using 8 equal width sub-elements

The almost constant value of polarity near the centre of the pole arc suggests that the widths of the sub-elements could be progressively increased from the pole-tip toward the pole centre-line. One example of this is shown in Fig. 7. The accuracy of the solution has been increased without increasing the number of equations, but there is a limit as the linear representation of the distribution just away from the pole-tip is inaccurate and introduces error. Further increase in accuracy then requires an increase in the number of equations.

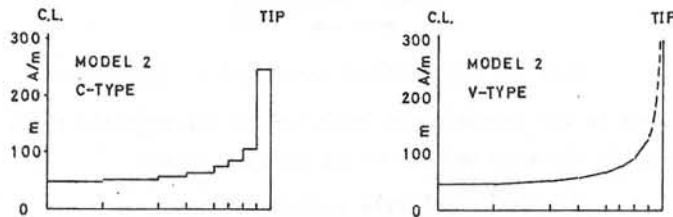


Fig. 7 Surface polarity using 8 variable width sub-elements

3.2 Magnetic field strength H_r

The variation of H_r along the rotor pitch circle is shown in Fig. 8 for Model 2, using eq. (2.9) and (2.10) with 8 equal width sub-elements. The shape is similar to that of the surface polarity because of the proximity of the pole-arc. In the interpole region H_r falls almost to zero, exhibiting a sign change with Model 2 but not Model 1. The position of the peak is slightly away from the pole-tip toward the pole centre-line. There is good correlation between the numerical and theoretical values of the peak obtained with Model 1 for a small number of sub-elements. The effect of the yoke, introduced in Model 2, is to increase the peak value by about 5% at this radius. The calculated position and size of the peak depend principally on the assumed variation of m near to the pole-tip, i.e., on the size of sub-elements and on the value of v (eq. (2.5)) for the

sub-element at the pole-tip. A \ln/\ln graph of m_n and pole-arc measured from the pole-tip shows that as the number of sub-elements is increased the assumed variation ($v = -\frac{1}{2}$) is substantially correct up to 1° of arc. A decreased value of v would slightly decrease the peak value. In practice the presence of pole-sides and a definite angle at the pole-tip will reduce the peak value.

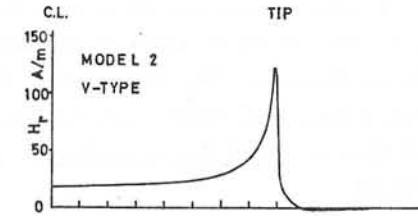


Fig. 8 Variation of H_r along the rotor pitch circle

4 Conclusion

The method of sub-elements is attractive because the surface polarity can be represented by simple functions; because the number of equations which have to be solved can be kept small by varying the widths of the sub-elements; and because the magnetic field strength can be calculated anywhere in the air region. It is clear from the present work that a better representation of the machine geometry would not lead to an unmanageable problem. The main disadvantage is that the coefficient matrices are ill-suited to iterative schemes and direct methods of solution must be used.

Certain improvements to the method are being examined. Representing the surface polarity over a sub-element by a polynomial may enable the number of equations to be further reduced, but at the expense of a more complicated computer program. A present weakness is that the potential is calculated only at points where the polarity is defined. Calculations based on the potential at the mid-points of V-type sub-elements were unstable, but the use of a weighting factor could give improved results. The extension of sub-elements to 3-dimensions - sub-areas - is well known⁽⁶⁾ but the author is not aware of literature describing the use of V-type representations of surface polarity or charge density.

Even without these improvements the calculated peak value of H_r is sufficiently accurate for design purposes. The permeance shape factor for the improved model is high, but this can be modified empirically to allow for the pole-cores.

5 Acknowledgements

The author wishes to thank S.S.Gill and B.S.Jeer for verifying the sub-element formulae as part of an undergraduate project, and Dr.S.C.Bhargava for the waveforms in Fig. 2 and the analysis in App. (7.1).

6 References

- 1 S.C.Bhargava, "Non-Synchronous Operation of a Hysteresis Machine", Ph.D. Thesis, The University of Aston in Birmingham, 1972.
- 2 M.J.Jevons and S.C.Bhargava, "The Salient-Pole Hysteresis Coupling", IEEE Trans (Magnetics), Vol. Mag-11, pp. 1461-3, 1975.
- 3 P.Moon and D.E.Spencer, Field Theory Handbook, Springer-Verlag, 1961, pp. 51,54,73.
- 4 M.Abramowitz and I.A.Stegun, Handbook of Mathematical Functions, Dover, 1965, p. 886.
- 5 Modern Computing Methods, HMSO, 1961, p. 130.
- 6 R.F.Harrington, Field Computation by Moment Methods, Macmillan, 1968, Ch. 2.

7 Appendices

7.1 Analysis of Model 1

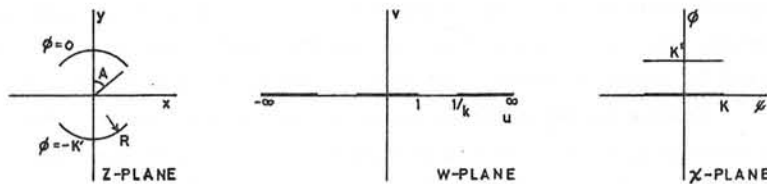


Fig. 9 Inverse sn transformation

The field due to two circular arcs on a pitch circle of radius R in the z-plane is transformed to a uniform field in the X-plane (see fig. 9) by the transformation

$$\text{sn } \chi = \frac{j}{k^{\frac{1}{2}}} \left[\frac{jR + z^*}{jR - z^*} \right] \quad (7.1)$$

where $k = \tan^2(\frac{1}{2}A)$ = modulus of the Jacobian elliptic function
 $K' = K(k')$ = associated complete elliptic integral of the first kind (see fig. 9).

Using $\vec{H} = -\nabla\phi$

$$H_r - jH_\theta = j e^{-j\theta} \frac{\partial \chi}{\partial r} = j e^{-j\theta} \frac{(1 - j k^{\frac{1}{2}} \text{sn } \chi)^2}{2R k^{\frac{1}{2}} \text{sn}' \chi} \quad (7.2)$$

This is readily evaluated at any point because $\text{sn } \chi$ is given by eq. (7.1).

In particular at the centre of the pole-arc, for potentials of 0, -K',

$$H_r = 1/2Rk^{\frac{1}{2}} \quad (7.3)$$

For the model:- $k^{\frac{1}{2}} = \tan 26.5^\circ = 0.498\dots$, $R = 41.5 \text{ mm}$, $K' = 2.8066\dots$

$$H_r = 24.311\dots$$

The permeance shape factor S_p is

$$S_p = \frac{4K}{K'} \approx 2\pi / (\ln \frac{4}{k} - \frac{k^2}{4}) \quad (7.4)$$

the approximation being sufficiently accurate when $k < 0.2$.

For the model $S_p = 2.274\dots$

7.2 Surface polarity at the pole-tip

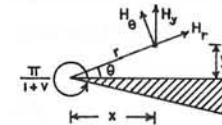


Fig. 10 Mathematical treatment of the pole-tip

Near to the pole-tip the variation of the magnetic field is approximately the same as that of an isolated corner

$$\phi = C r^{1+v} \sin(1+v)\theta + \text{constant terms} \quad (7.5)$$

Using $\vec{H} = -\nabla\phi$ and noting that $H_y = H_r \sin \theta + H_\theta \cos \theta$

$$H_y = -(1+v)C r^v \cos v\theta \quad (7.6)$$

If the pole-tip angle is 2π then $v = -\frac{1}{2}$ and $H_y \propto x^{-\frac{1}{2}}$.

Equating the derivative of H_y with respect to x , to zero shows that the peak occurs for

$$x_m = y \cot \frac{\pi}{2(1-v)} \quad (y \text{ constant}) \quad (7.7)$$

or at an angular increment

$$\delta A = \frac{y}{R} \cot \frac{\pi}{2(1-v)} \quad (7.8)$$

from the pole-tip.

For $v = -\frac{1}{2}$, $\delta A = 0.3207\dots$. This compares with a theoretical value of 0.3219 from eq. (7.2) and a practical value of 0.322.. for 8 sub-elements.

7.3 Results

The chief results are given below for the two models. The potentials are $-1, +1$ A, and the units of H_r are A/m.

Pole centre-line - H_r

(i) pole surface	R=41.25 mm			
number of sub-elements		4	8	16 (theory)
model 1		17.198	17.298	17.319 17.324
(ii) rotor pitch circle	R=40.85 mm			
number of sub-elements			8	(theory)
model 1			17.485	17.493
model 2			17.567	

Peak values of H_r

(i) pitch circle radius	40.85 mm			
number of sub-elements			8	16 (theory)
model 1		114.563	115.092	116.135
model 2		123.94	122.67	
(ii) pitch circle radius	40.45 mm			
number of sub-elements				16
model 2				86.259

Permeance shape factor - S_p

(i) C-type sub-elements				
number of sub-elements		4	8	16 (theory)
model 1		2.191	2.232	2.253 2.274
model 2		2.683	2.731	2.761
(ii) V-type sub-elements				
number of sub-elements		4	8	16 (theory)
model 1		2.270	2.273	2.274 2.274
model 2		2.793	2.783	2.781

The Use of Divided Differences in Finite Element Calculations

M.J. Long and K.W. Morton

Department of Mathematics, University of Reading

Summary

Divided differences are used to calculate gradients of functions computed by finite element methods. On regular elements the finite element equations can be interpreted as finite difference equations with local truncation errors. Examples of this are given together with the results of numerical trials for gradient approximations.

1. Introduction

The work presented in this paper was prompted by considering the relationships which exist between finite difference and finite element methods. The use of divided differences for calculating the gradients of functions which have been computed by finite element schemes provides an opportunity to pool the advantages of the two approaches. This is of great practical interest since in many cases it is the gradient of the calculated quantity which is most useful - e.g., electric and magnetic fields obtained from their scalar and vector potentials. With higher order finite element methods, these quantities are often carried as nodal parameters, but we are concerned here with lower order methods where they are normally obtained by actual or approximate differentiation.

In [3] we consider quite general boundary value problems and finite element methods on regular meshes: we shall in this paper, however, concentrate on specific second order problems in the plane - typically, Poisson's equation ($-\nabla^2 u = f$) with homogeneous boundary conditions. In weak form this problem becomes

$$a(u, v) = \langle f, v \rangle \tag{1.1}$$

where

$$a(u, v) = \int_{\Omega} \left(\frac{\partial u}{\partial x} \frac{\partial v}{\partial x} + \frac{\partial u}{\partial y} \frac{\partial v}{\partial y} \right) dx dy, \tag{1.2}$$

$$\langle f, v \rangle = \int_{\Omega} f v dx dy \tag{1.3}$$

and Ω is the region of interest (with boundary Γ). We limit our

attention in the main to cases where Γ is a polygonal boundary such that Ω can be exactly subdivided into a regular mesh of finite elements and this can be done for a sequence of mesh sizes characterised by element diameter h , with $h \leq h_0$ and tending to zero. We consider nodal finite element approximations to u of the form

$$u^h(x, y) = \sum_{\{j\}} u_j \phi_j(x, y) \tag{1.4}$$

where the parameters u_j are function values or derivatives of u^h at nodes labelled by the index j . The basis functions ϕ_j are polynomial in each element, with support localised to the elements neighbouring the point j - they span a space of functions which includes all piecewise polynomials of degree less than k . The specific finite element approximation to the solution u of (1.1) is determined by the Galerkin equations

$$a(u^h, \phi_j) = \langle f, \phi_j \rangle, \text{ for all } \phi_j, \tag{1.5}$$

and standard error analysis (see [4]) gives

$$\|u - u^h\|_0 = O(h^k), \quad [a(u - u^h, u - u^h)]^{\frac{1}{2}} = O(h^{k-1}), \tag{1.6}, (1.7)$$

where $\|v\|_0 = \langle v, v \rangle$: (1.7) expresses the lower order of accuracy of the derivatives of u^h .

Now let us suppose we can define D_h , a difference operator approximating the differential operator $D (= \partial/\partial x \text{ or } \partial/\partial y)$ to formal order of accuracy k : then in [3] we have shown that

$$\|D_h u^h - Du\|_0 = O(h^k). \tag{1.8}$$

The proof of (1.8) develops after applying the triangle inequality to $\|D_h u^h - Du\|_0$ several times: if we firstly define the interpolant of a function $v(x, y)$ to be

$$v^I(x, y) = \sum_{\{j\}} \bar{v}_j \phi_j(x, y), \tag{1.9}$$

where \bar{v}_j is the value of v (or one of its derivatives) at node j , then

$$\|D_h u^h - Du\|_0 \leq \|D_h u^h - D_h u^I\|_0 + \|D_h u^I - (D_h u)^I\|_0 + \|(D_h u)^I - D_h u\|_0 + \|D_h u - Du\|_0. \quad (1.10)$$

The third and fourth terms are $O(h^k)$ from the approximating properties of the basis functions and the local accuracy of D_h ; the second term is $O(h^k)$ for suitable choices of D_h - examples of these are given in section 3; the first term is the most interesting: due to the ellipticity of the initial problem, this term is $O(h^k)$ if we can show that

$$a(u^I - u^h, u^I - u^h) = O(h^{2k}). \quad (1.11)$$

Now $a(u^I, \phi_j) - \langle f, \phi_j \rangle = h^2 T_j$ (1.12)

where T_j is the truncation error of the finite difference scheme to which this Galerkin equation is equivalent. Thus

$$a(u^I - u^h, u^I - u^h) = h^2 \sum_{(j)} e_j T_j \quad (1.13)$$

where $e_j = \bar{u}_j - u_j$, the finite element error in \bar{u}_j . The proof of (1.8) therefore hinges on the structure of the Galerkin equations and their corresponding truncations errors. In section 2 we examine some important particular cases to illustrate certain special features of these equations. In section 3 we summarise the results of numerical trials for a simple model problem. Finally, some consideration is given in the last section to the use of divided differences when irregular elements are used. Few theoretical results are then possible but the difference technique is still almost as simple to apply and a practical test has shown encouraging results.

2. Explicit forms of the Galerkin Equations

We consider Poisson's equation defined on a region in the plane. A regular square mesh is superimposed on the domain - a typical 'patch' of elements is shown in figure 1. In this section we look at some examples of individual Galerkin equations obtained using a series of standard two dimensional elements; we shall ignore boundaries and examine typical internal nodes and their associated finite element equations.

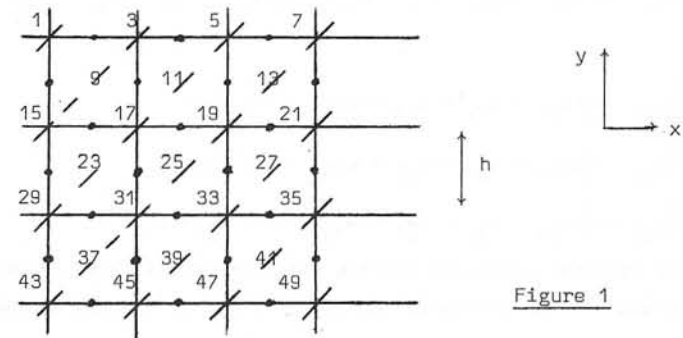


Figure 1

(a) Bilinear on a square:

The nodal parameters are the function values at the mesh points. There is only one type of node and corresponding Galerkin equation - typically node 31 of fig. 1; the equation here is

$$\frac{8}{3}u_{31} - \frac{1}{3}(u_{15} + u_{29} + u_{43} + u_{45} + u_{47} + u_{33} + u_{19} + u_{17}) = \langle f, \phi_{31} \rangle. \quad (2.1)$$

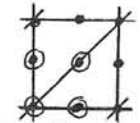
By expanding $a(u^I, \phi_{31}) - \langle f, \phi_{31} \rangle$ in a Taylor series expansion about node 31 we obtain

$$T_{31} = -\frac{h^2}{48}(3u_{xxxx} + 14u_{xxyy} + 3u_{yyyy})_{31} + O(h^4) \quad (2.2)$$

where $u_{xxxx} = \partial^4 u / \partial x^4$, etc. As the degree of approximation for this element is $k = 2$, the order of accuracy of T_{31} corresponds to the standard error estimate shown in (1.6).

(b) Quadratic on a right triangle:

For this element the nodal parameters are again just function values but there are now four types of node - typically, points 31, 32, 24 and 25 in fig. 1. The corresponding Galerkin equations are respectively



$$4u_{31} - \frac{4}{3}(u_{30} + u_{38} + u_{32} + u_{24}) + \frac{1}{3}(u_{29} + u_{45} + u_{33} + u_{17}) = \langle f, \phi_{31} \rangle \quad (2.3)$$

$$\frac{16}{3}u_{32} - \frac{4}{3}(u_{31} + u_{39} + u_{33} + u_{25}) = \langle f, \phi_{32} \rangle \quad (2.4)$$

$$\frac{16}{3}u_{24} - \frac{4}{3}(u_{23} + u_{31} + u_{25} + u_{17}) = \langle f, \phi_{24} \rangle \quad (2.5)$$

$$\frac{16}{3}u_{25} - \frac{4}{3}(u_{24} + u_{32} + u_{26} + u_{18}) = \langle f, \phi_{25} \rangle \quad (2.6)$$

Thus for mid-edge nodes one has the familiar second order, five-point scheme. The truncation errors of these difference schemes are

$$T_{31} = \frac{h^2}{48}(u_{xxxx} + u_{yyyy})_{31} + O(h^4) \quad (2.7)$$

$$T_j = -\frac{h^2}{144}(u_{xxxx} + u_{yyyy})_j + O(h^4), \quad j = 32, 24, 25. \quad (2.8)$$

The order of accuracy of this element is ordinarily $k = 3$ but the truncation errors are one order lower. The Galerkin equations can however be combined into a reduced set relating the nodal parameters at points of type 25: by combining equation (2.7) with a linear combination of the surrounding equations of type (2.4), (2.5), (2.6), it is found that

$$\frac{10}{3}u_{25} - \frac{2}{3}(u_{23} + u_{39} + u_{27} + u_{11}) - \frac{1}{6}(u_9 + u_{37} + u_{41} + u_{13}) = \langle f, \phi_{25} \rangle \quad (2.9)$$

where

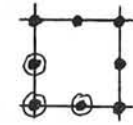
$$\begin{aligned} \phi_{25} = & \phi_{25} + \frac{3}{8}(\phi_{24} + \phi_{32} + \phi_{26} + \phi_{18}) + \frac{1}{4}(\phi_{17} + \phi_{31} + \phi_{33} + \phi_{19}) \\ & + \frac{1}{16}(\phi_{10} + \phi_{16} + \phi_{30} + \phi_{38} + \phi_{40} + \phi_{34} \\ & + \phi_{20} + \phi_{12}). \end{aligned} \quad (2.10)$$

Equation (2.9) is the familiar nine-point difference scheme; its truncation error (T_{25}) combines $3(=1 + 4 \times \frac{3}{8} + 8 \times \frac{1}{16})$ times (2.8) with $1(=4 \times \frac{1}{4})$ times (2.7), and because of the symmetry we obtain $T_{25} = O(h^4)$. Other combinations of the original equations (2.3)-(2.6) relate all the remaining nodal parameters to this reduced set. It follows that all the nodal errors are of the same order if

those for the reduced system are of fourth order.

(c) Quadratic on a square:

This element is at first glance very similar to the previous one except that there are only three types of node, that corresponding to the middle of the square being omitted. The Galerkin equations however take the more complicated form



$$\begin{aligned} 208u_{31} - 74(u_{30} + u_{38} + u_{32} + u_{24}) + 45(u_{29} + u_{45} + u_{33} + u_{17}) \\ - 23(u_{22} + u_{36} + u_{44} + u_{46} + u_{40} + u_{26} + u_{18} + u_{16} \\ - u_{15} - u_{43} - u_{47} - u_{19}) = 45\langle f, \phi_{31} \rangle \end{aligned} \quad (2.11)$$

$$\begin{aligned} 208u_{32} - 74(u_{31} + u_{33}) + 16(u_{18} + u_{46}) \\ - 23(u_{17} + u_{45} + u_{47} + u_{19}) = \langle f, \phi_{32} \rangle \end{aligned} \quad (2.12)$$

with a similar equation using ϕ_{24} . The truncation errors are

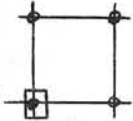
$$T_{31} = \frac{h^2}{360}(25u_{xxxx} + 92u_{xxyy} + 25u_{yyyy}) + O(h^4) \quad (2.13)$$

$$T_{32} = -\frac{h^2}{360}(5u_{xxxx} + 46u_{xxyy} + 20u_{yyyy}) + O(h^4). \quad (2.14)$$

Unlike the previous example, none of the nodal parameter sets can be eliminated, but combinations of the equations can yield a system where all the truncation errors are of fourth order.

(d) Hermite Cubic on a square:

With this element there is only one type of node (typically node 31) but there are three types of Galerkin equation associated with each one of these points. The parameters at each node are the function value and the x - and y -derivatives. The Galerkin equations are



$$\begin{aligned} 4416u_{31} - 696(u_{29} + u_{45} + u_{33} + u_{17}) - 408(u_{15} + u_{43} + u_{47} \\ + u_{19}) + 6h(u_{33}^x - u_{29}^x + u_{17}^y - u_{45}^y) \\ + 60h(u_{19}^x - u_{15}^x + u_{47}^x - u_{43}^x + u_{19}^y - u_{47}^y + u_{15}^y - u_{43}^y) \\ = 1260\langle f, \phi_{31} \rangle \text{ [function value]} \end{aligned} \quad (2.15)$$

$$h^2[272u_{31}^x - 46(u_{33}^x + u_{29}^x) + 32(u_{17}^x + u_{45}^x) + 2(u_{15}^x + u_{43}^x + u_{47}^x + u_{19}^x)] - h[6(u_{33} - u_{29}) + 60(u_{19} - u_{15} + u_{47} - u_{43})] = 1260\langle f, \phi_{31}^x \rangle$$

[x-derivative] (2.16)

with a similar equation for $\phi_{31}^y - \phi_{31}^x, \phi_{31}^x, \phi_{31}^y$ are the three types of basis function at node 31; u_j^x and u_j^y are the parameters associated with the x- and y-derivatives at node j. In all cases

$$a(u^I, \phi_{31}^*) - \langle f, \phi_{31}^* \rangle = O(h^6),$$

(2.17)

However, only the first of these three equations is consistent with $-\nabla^2 u = f$; the other two are consistent with $-(u_{xxx} + u_{yyx}) = f_x$ and $-(u_{xxy} + u_{yyx}) = f_y$ respectively.

The first three examples given in this section are generalised in [3] to produce the theoretical arguments in proving (1.11). The last example is a case where we would not really expect to use divided differences, though in the next section this element provides a comparison with the accuracies achieved by differencing with lower order elements.

3. Numerical results for a simple model problem

Numerical experiments were conducted with Laplace's equation $\nabla^2 u = 0$ on the square $0 \leq x, y \leq 3$ with the natural or symmetry boundary condition $\frac{\partial u}{\partial y} = 0$ along $y = 0$ and u set equal to the solution $\ln[(x - \frac{7}{2})^2 + y^2]$ on the other three sides of the square. Computations were carried out with $h^{-1} = 1, 2, 3, 4$ and 5 so that convergence tests could be made for overall and pointwise errors. We use the same elements as discussed in the previous section.

(a) Bilinear elements ($k = 2$):- we begin by checking whether (1.11) is approximately true for this element and compare the results with the error $a(u - u^h, u - u^h)$ [c.f. (1.7)]:

h^{-1}	1	2	3	4	5
$a(u^I - u^h, u^I - u^h)$	0.025	0.0249	0.0213	0.0347	0.0320
Convergence between last pair : $O(h^{3.8})$					
$a(u - u^h, u - u^h)$	1.1	0.29	0.13	0.017	0.046
Convergence between last pair : $O(h^{2.0})$					

This table confirms our expectations of the asymptotic behaviour of the error.

Three pairs of difference schemes were used for the gradients - these are all suitable for internal gradient approximations:

$$D_x^{(1)} v = [v(x+h, y) - v(x-h, y)]/2h, \quad \left. \begin{array}{l} \\ \\ \end{array} \right\} \quad (3.1)$$

$$D_y^{(1)} v = [v(x, y+h) - v(x, y-h)]/2h, \quad \left. \begin{array}{l} \\ \\ \end{array} \right\}$$

$$D_x^{(2)} v = [v(x + \frac{h}{2}, y) - v(x - \frac{h}{2}, y)]/h, \quad \left. \begin{array}{l} \\ \\ \end{array} \right\} \quad (3.2)$$

$$D_y^{(2)} v = [v(x, y + \frac{h}{2}) - v(x, y - \frac{h}{2})]/h, \quad \left. \begin{array}{l} \\ \\ \end{array} \right\}$$

$$D_x^{(3)} v = [v(x + \frac{h}{2}, y + \frac{h}{2}) + v(x + \frac{h}{2}, y - \frac{h}{2}) - v(x - \frac{h}{2}, y + \frac{h}{2}) - v(x - \frac{h}{2}, y - \frac{h}{2})]/2h \quad (3.3)$$

and similar expression for $D_y^{(3)} v(x, y)$; each is second order accurate to their respective derivatives. In table 1 we give the maximum error for $h^{-1} = 1, 3, 5$ over points which are the 'natural' centres for each scheme for all three values of h . Thus for $D_x^{(1)}$ and $D_y^{(1)}$ the points considered are (1, 1), (1, 2), (2, 1), (2, 2); for $D_x^{(2)}$ they are ($\frac{1}{2}, 1$), ($1\frac{1}{2}, 1$), ($2\frac{1}{2}, 1$), ($\frac{1}{2}, 2$), ($1\frac{1}{2}, 2$), ($2\frac{1}{2}, 2$), and for $D_y^{(2)}$, (1, $\frac{1}{2}$), (1, $1\frac{1}{2}$), etc.; for $D_x^{(3)}$ and $D_y^{(3)}$ they are the centres of the nine unit squares which make up Ω . In the final columns of the tables are given the worst convergence rates over the same set of points, calculated from the errors for $h^{-1} = 3$ and 5.

Table 1 : Maximum errors for difference approximations to derivatives using bilinear elements.

	h ⁻¹			Conv Rate		h ⁻¹			Conv Rate
	1	3	5			1	3	5	
D _x ⁽¹⁾	.046	.0244	.0215	2.0	D _y ⁽¹⁾	.16	.020	.0272	1.8
D _x ⁽²⁾	.080	.0241	.0215	2.0	D _y ⁽²⁾	.15	.020	.0274	1.9
D _x ⁽³⁾	.041	.0282	.0233	1.6	D _y ⁽³⁾	.13	.0277	.0230	1.8

There would seem to be little to choose between the accuracies of the schemes, bearing in mind the differences between the points considered. However, by further comparison over the whole of Ω, the most compact schemes D_x⁽²⁾ and D_y⁽²⁾ appear to be the most reliable. It should be noted that the maximum error for the function values over the same set of points for h⁻¹ = 5 is 0.0374. The differencing errors are somewhat larger than this, but at (1, 0) the function error does increase to 0.0238.

(b) Quadratic triangle elements (k = 3):- the Galerkin equations studied in the previous section suggested that the nodal errors for function values should converge like O(h⁴): this is in fact confirmed by the numerical experiments. One cannot expect this order of convergence between the nodal points where it drops to O(h³) - this is an example of the phenomenon of superconvergence (c.f. [1]). Similarly, we expect a(u^I - u^h, u^I - u^h) to converge like O(h⁶) and not at an enhanced rate - the table below indicates the actual behaviour:

	h ⁻¹	1	2	3	4	5
a(u ^I - u ^h , u ^I - u ^h)		0.0238	0.0327	0.0446	0.0412	0.0537
Convergence between last pair : O(h ^{5.3})						
a(u - u ^h , u - u ^h)		0.073	0.0294	0.0223	0.0380	0.0334
Convergence between last pair : O(h ^{3.8})						

The only difference schemes we have considered for the gradient are the usual fourth order approximations

$$D_x^{(4)}v(x, y) = [8v(x + \frac{h}{2}, y) - 8v(x - \frac{h}{2}, y) - v(x + h, y) + v(x - h, y)]/6h \quad (3.4)$$

and a similar expression for D_y⁽⁴⁾v(x, y). In table 2 we give the errors obtained for h⁻¹ = 1, 3, 5 at the central point (1½, 1½), which is one of the reduced set, and the maximum over the subsidiary points (1, 1), (1, 2), (2, 1), (2, 2). Except where noted convergence rates are calculated for the last pair of errors.

Table 2 : Maximum errors for difference approximations to derivatives using quadratic triangle elements.

		h ⁻¹			Conv Rate		h ⁻¹			Conv Rate
		1	3	5			1	3	5	
(1½, 1½)	D _x ⁽⁴⁾	.0389	.0529	.0632	4.3	D _y ⁽⁴⁾	.0389	.0511	.0612	4.3
Subsid.	D _x ⁽⁴⁾	.0251	.0474	.0411	3.7	D _y ⁽⁴⁾	.0228	.0527	.0518	4.6

* between h⁻¹ = 1 and 5

Clearly superconvergence also occurs for these gradient approximations, but the error increases between the nodes to give approximately the O(h³) convergence rate predicted by the analysis.

(c) Quadratic square elements (k = 3):- the results of numerical experiments were very similar to those for the previous element, all the function errors actually being O(h⁴). We give only the difference approximation errors, which were substantially larger, in table 3. The same difference schemes (3.4) were used.

Table 3 : Maximum errors for difference approximations to derivatives using quadratic square elements.

		h ⁻¹			Conv Rate		h ⁻¹			Conv Rate
		1	3	5			1	3	5	
(1½, 1½)	D _x ⁽⁴⁾	.0236	.0444	.0557	4.0	D _y ⁽⁴⁾	.0274	.0623	.0631	6.2*
Subsid.	D _x ⁽⁴⁾	.031	.0335	.0437	4.4	D _y ⁽⁴⁾	.0268	.0455	.0573	4.0

* between h⁻¹ = 1 and 5

(d) Hermite Cubic elements ($k = 4$):- the numerical results showed that both function and derivative errors at nodes converged like $O(h^4)$. However, one important point arises: over the four points (1, 1), (1, 2), (2, 1), (2, 2), the divided difference results for quadratics were more accurate than the direct derivative approximations achieved with this element.

4. Concluding Remarks

To be of practical utility, the divided difference techniques described above must be applicable to a finite element solution obtained with irregular elements. Very few theoretical results are then possible, though in one-dimension certain hypotheses can be deduced. Basically, there are two general rules here: (1) there needs to be a smooth variation of the mesh over the domain; (2) the step length and difference scheme used at any point should be determined by the most closely approximating uniform mesh. Many automatic element generators start with a basic mesh which is regular over large regions and incorporate smoothing algorithms to be applied to irregularities introduced at boundaries, interfaces, etc.; in these cases the rules should be easy to apply. A simple practical example in the computation of surface velocities over an aerofoil has produced encouraging results (c.f. [2]). More computational experience is needed, however, before being too definite or attempting to obtain theoretical results.

References

- [1] Douglas, J.H. and Dupont, T. : 1972, Proc. Conf. on Numerical Analysis, (ed. J.J.H. Miller) Royal Irish Academy, Dublin.
- [2] Long, M.J. : 1975, Ph.D. thesis, University of Reading.
- [3] Long, M.J. and Morton, K.W. : 1975, Numerical Analysis Report 2/75, Dept. of Maths., University of Reading.
- [4] Strang, G. and Fix, G.J. : 1973, 'An analysis of the finite element method', New York, Prentice-Hall.

DETERMINATION OF MAGNETIC FIELDS
AT THE CONDUCTOR FOR SOLENOIDS AND TOROIDS

R. W. Moses, Jr. and R.L. Willig
University of Wisconsin, Madison, Wisconsin, U.S.A.

ABSTRACT

Superconducting magnets must have the magnetic field smaller than the critical field the conductor is designed for. For optimal use of material the maximum field should be known everywhere along the length of the conductor. Here large single layer solenoids with superconductive energy storage applications are considered. An analytic expression is given for the midplane field correction due to conductor separation. Similar expressions are presented for sectorized toroidal tokamak coils. Numerical examples are given to demonstrate the large fields found at the ends of single layer solenoids. Optimization procedures are used to redistribute conductors to reduce the end fields to acceptable levels.

INTRODUCTION

In most discussions of the magnetic fields and forces for solenoids and toroids it is assumed that the current flows in a continuous sheet at the surface of the magnet. Although this simplifies many computations it does not account for field variations near individual conductors. Also large radial fields at the ends of a solenoid are often neglected. These effects and some means of compensating them will be examined in detail in this paper.

First let us consider a solenoid or toroid with current distributed uniformly over the surface in a thin sheet. There are N turns of conductor carrying a current I . For a solenoid of length ℓ and diameter D , the aspect ratio is defined as $\beta \equiv \ell/D$. When β is large the internal field away from the ends is $B \approx \mu_0 NI/\ell$. For smaller values of β the maximum field on the midplane, B_M , is at the inner surface of the wall and is expressed as follows

$$B_M = \mu_0 NI K'(\beta)/\ell. \quad (1)$$

$K'(\beta)$ is a correction factor between 0.5 and 1 (Moses, 1975).

The field in a toroid with uniform surface currents is expressed in terms of the radius, as measured from the major axis, R . Once again taking N turns of current I one gets

$$B = \mu_0 NI/2\pi R. \quad (2)$$

The purpose of this paper is to present corrections to Eqs. (1) and (2), accounting for the use of conductors of finite size and separation. We also discuss the reduction of the end fields of solenoids. These can be substantially greater than the expression given in Eq. (1) (Walstrom and Lubell, 1973). As an example it is commonplace to see field increases of more than 100% over Eqs. (1) for energy storage magnets. When the conductor critical field is exceeded anywhere in a superconducting magnet part, if not all, of the magnet goes normal. For this reason it is essential to know the maximum field at each segment of conductor and be able to design magnets free of unnecessarily high fields.

MIDPLANE CORRECTION

We now consider a single layer solenoid made of a circular cable of radius c . The number of conductors per unit length is $n = N/\ell$, then the center to center separation of the cables is $s = 1/n$. The fraction of magnet surface covered by conductor is defined as the ratio $\gamma \equiv 2c/s$.

To obtain the correction for the discrete conductor field, consider an infinite plane of straight parallel cables next to a conducting sheet, see Fig. 1. The maximum field, B_m , is on the leftmost edge of each conductor, and it is given by

$$\begin{aligned} B_m &= \mu_0 nI \left[\frac{1}{2} + \frac{\gamma}{\pi} \sum_{j=-\infty}^{\infty} \frac{1}{\gamma^2 + 4j^2} \right] \\ &= \mu_0 nI [1 + K''(\gamma)]. \end{aligned} \quad (3)$$

Equation (3) can be solved for K'' ; the results are plotted in Fig. 2. An approximate expression of K'' is also shown,

$$K'' = \frac{1}{\pi\gamma} + \frac{\pi\gamma}{12} - \frac{1}{2}. \quad (4)$$

This is accurate to 10% for $\gamma \leq 0.7$.

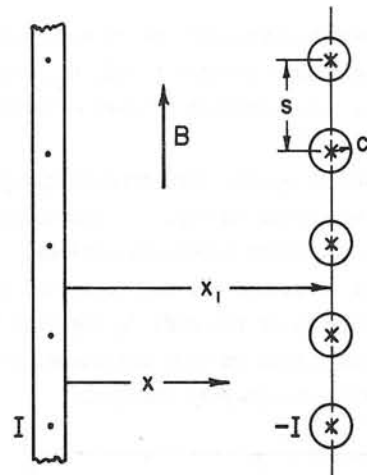


Fig. 1. Cross section of a set of straight conductors parallel to a uniform conducting sheet.

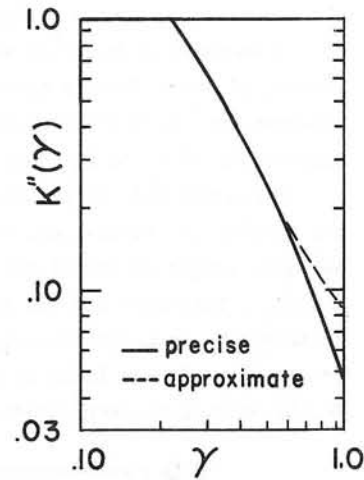


Fig. 2. Discrete coil correction factor as a function of γ .

Equation (3) is arranged to define K'' as a correction to the field between two parallel conducting planes, $\mu_0 nI$. Most of the value of K'' is attributable to conductors close to the point where B_m is measured, thus the cables of Fig. 1 could be wrapped into a solenoid without changing the meaning of K'' . Now Eq. (1) is rewritten to give the maximum field at the conductor on the midplane of a solenoid

$$B_M = \mu_0 nI [K'(\beta) + K''(\gamma)] \quad (5)$$

This and Fig. 2 make it clear that single layer solenoids with $\gamma < 1$ have maximum midplane fields substantially larger than those found in the continuous sheet model, Eq. (1). Throughout the paper B_m defines the maximum field on any segment of conductor while B_M defines the maximum midplane field.

END FIELD

If a thin walled solenoid is wound with turns evenly distributed along its length, very large radial fields are obtained at the ends of the magnet. A computer program was written to give the field on the inner side of the conductor at all points along the length of a solenoid.

Figure 3 illustrates these results for solenoids formed by continuous sheets of current. When a solenoid is infinitesimally thin there is a logarithmic singularity in the end field. This is shown for a variety of aspect ratios in Fig. 3.

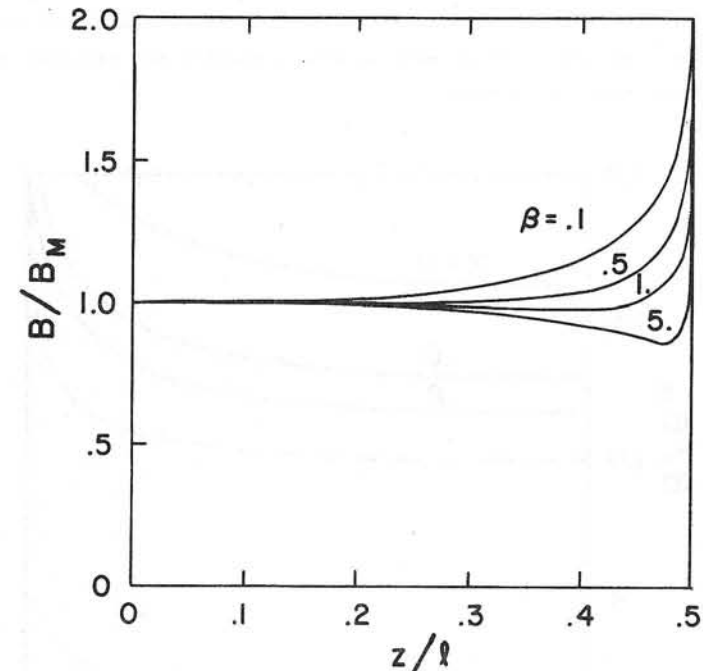


Fig. 3. Magnetic field along the inside surface of an infinitesimally thin solenoid with a uniform continuous current distribution.

As in the case of Eqs. (1) and (5) the conductor fields change for single layer solenoids made of discrete circular cables. Approximate values for the maximum field at each conductor are plotted for a $\beta = 0.3$ solenoid with several values of γ in Fig. 4.

The data in Figs. 3 and 4 make it clear that end fields can be very large in thin single layer solenoids. Such devices are particularly of interest for energy applications (Boom et al. 1974, 1976). Single layer magnets with nearly a thousand closely spaced turns are envisioned, certainly matching the severe field conditions shown in Fig. 4.

By varying the spacing of conductors along the length of a solenoid it is possible to manipulate the fields of Figs. 3 and 4 to

more desirable distributions. Since we are primarily concerned with energy storage, we want to store the maximum amount of energy with a given amount of conductor. In a solenoid one always maximizes the stored energy by placing the conductors as close together as possible. This is limited by the boundary condition that the critical field cannot be exceeded. Assuming there is one critical field, the stored energy is a maximum when the field at each conductor reaches the critical value (or a specified design limit).

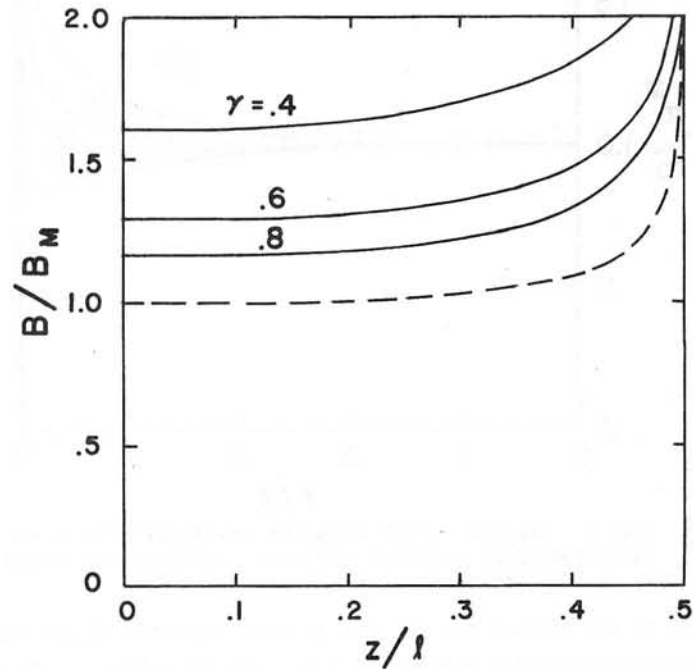


Fig. 4. Maximum field at the conductors of a single layer solenoid with current uniformly distributed in round conductor ($N = 200$). Here B_M in the midplane maximum for the current sheet model.

A smooth current distribution can be obtained by placing flat conductors close together. This gives a good mathematical model but is physically unrealistic. It is anticipated that large energy storage magnets would have a single layer of round superconducting cable embedded in a high purity aluminum stabilizer (Boom et al., 1975). Since the current is concentrated in the superconducting cable, we neglect the

stabilizer. The variable current distribution is obtained by control of the conductor spacing $s = 1/n$.

A computer program was written which expresses the current per unit length, nI , as a Fourier series. A midplane maximum field, B_M , was selected and the Fourier coefficients were adjusted to make a least squares fit of B_m to B_M along the solenoid.

Solenoids made of continuous current sheets were studied first and the results for several values of β are given in Fig. 5. The current per unit length is normalized to the specified mid-field maximum, $\mu_0 nI/B_M$. Typically the rms deviation is $\leq 0.03\%$ for ten expansion coefficients. As expected, only a reshaping of the ends is required to bring the conductor field to a constant value in long solenoids, $\beta = 5$. On the other hand, very short solenoids are grossly reshaped.

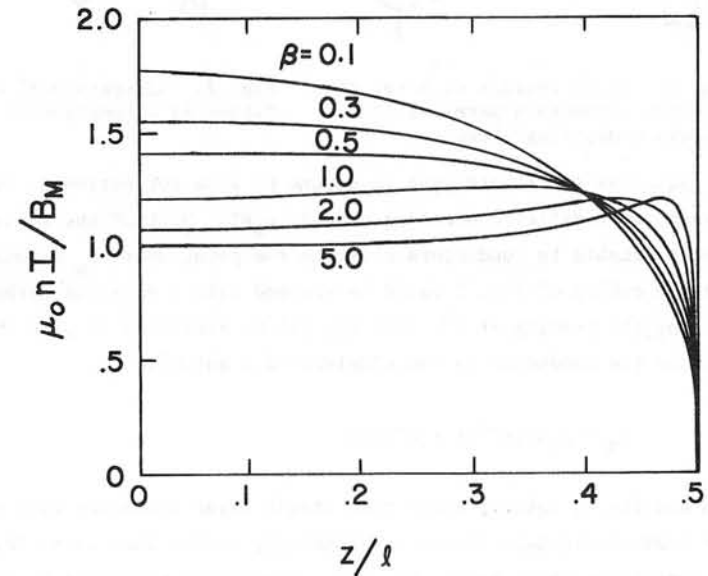


Fig. 5. Current distribution required to make the magnetic field constant along the inside surface of an infinitesimally thin solenoid.

The case of discrete round conductors was also studied and results are given for $\beta = 0.3$ and several values of γ_0 in Fig. 6. Here $\gamma_0 = 2c/s_0$ only represents the midplane value of γ . Each conductor carries the same current introducing a self field that is the same for all conductors. This leads to the radically different nI values in Fig. 6. Here

the end effects alter a much larger portion of the magnet than in the case of a continuous sheet conductor.

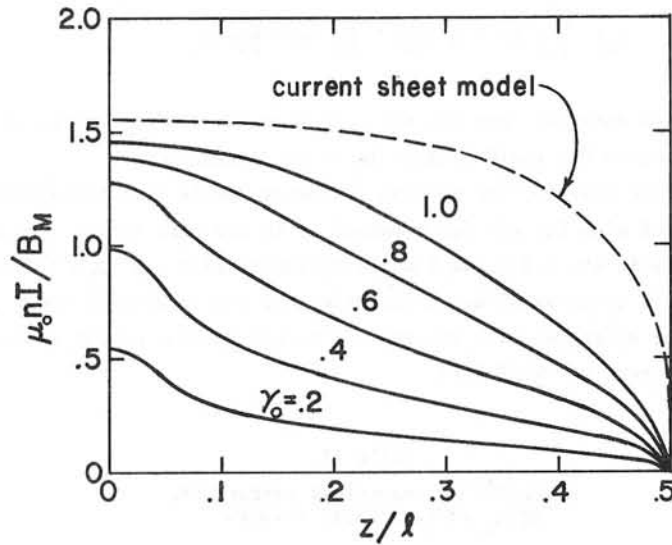


Fig. 6. Current distribution required to make the maximum magnetic field the same at every turn of a single layer solenoid.

Numerical computations for Fig. 6 were more difficult with rms errors of $\leq 1\%$. Detailed information on the numerical techniques will be published at a later date.

To quantify the above results we note that the ampere meters of conductor required to store a given amount of energy at a specific maximum field are (Moses, 1975)

$$IS = Q_{is} E^{2/3} / B_M^{1/3} \tag{6}$$

Also the radius of a solenoid is given by the expression

$$r = GE^{1/3} / B_M^{2/3} \tag{7}$$

The quality factor Q_{is} and the coefficient G are presented in Table I for the solenoids described in Figs. 3-6.

Table I

Conductor and radius factors for solenoids with constant field distributions as compared to those with constant current distribution

	Constant Current		Constant Field	
	Q_{is}	G	Q_{is}	G
β	$\text{AmT}^{1/3} / J^{2/3}$	$\text{mT}^{2/3} / J^{1/3}$	$\text{AmT}^{1/3} / J^{2/3}$	$\text{mT}^{2/3} / J^{1/3}$
Continuous Current Sheet Model	0.1	604	624	0.0205
	0.3	576	582	0.0119
	0.5	592	593	0.00954
	1.0	651	646	0.00732
	2.0	759	751	0.00578
	5.0	974	966	0.00428
Discrete Conductor Model, $\beta = 0.3$	γ			
	0.2	806	1009	0.0402
	0.4	675	807	0.0255
	0.6	627	706	0.0193
	0.8	606	645	0.0159
	1.0	599	622	0.0144

It must be emphasized that B_M represents the maximum midplane field in all cases. However, the end fields will be larger than B_M when the current distribution is uniform, Figs. 3 and 4. B_M for uniform current distributions is given by Eqs. (1) and (3). These formulae were used in earlier studies to establish values for Q_{is} and G . It was assumed that end fields would be compensated at a later date. Now Table I shows the minimum adjustments required to keep the field at all conductors within the limit of B_M .

It is very unlikely that a practical magnet would be built to the specifications outlined above. However, we have placed lower bounds on the conductor requirements, Q_{is} , and given an indication of the overall current distribution to strive for.

The problem of end fields may be partially solved by adding more superconductor in the ends of a magnet. That is, the field design limit of the composite superconductor is brought closer to the critical field

in the end turns. A tailored conductor design along with a compromise between the conductor and field distributions of Figs. 4 and 6 may give optimal results.

TOROIDAL FIELDS

Although toroidal magnets do not have the end field problems associated with solenoids, there can be a substantial field correction due to the discrete nature of a conductor. Equation (2) can be corrected in a manner similar to Eq. (1). A toroid can be treated as a solenoid with a component of toroidal curvature. Such a procedure gives very accurate expressions of the magnetic force on a sectored toroid (Moses and Young, 1975).

The midplane cross section of a toroidal field magnet is shown in Fig. 7, and a horizontal view is given in Fig. 8. Here ρ is the radius of curvature of the conductor which can vary along the coil, and the angle ϕ describes locations on the coil.

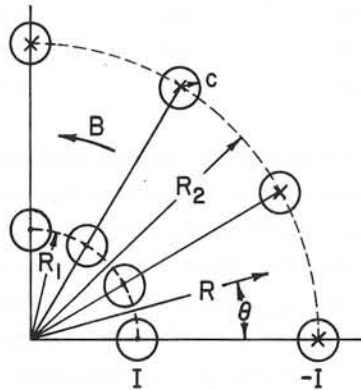


Fig. 7. Midplane cross section of a toroidal field magnet.

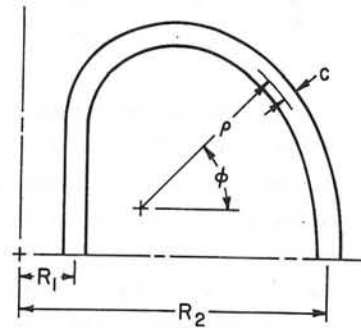


Fig. 8. Horizontal view of a toroidal field coil.

Equations (2) and (3) provide the basis for the expression of conductor field, but we add a correction for solenoidal curvature

$$\frac{\mu_0 I}{2\pi\rho} \ln \frac{1.284R}{cN}$$

see Moses and Young (1975) Eq. (14). Incorporating the equations listed

above one can approximate the field on the inner surface of a conductor as follows

$$B_m = \frac{\mu_0 NI}{2\pi R} \left[1 + K'' \left(\frac{Nc}{\pi R} \right) + \frac{R}{N\rho} \ln \frac{1.284R}{cN} \right]. \tag{8}$$

Here R is measured from the major axis to the inside surface of the conductor where the field maximum is to be determined.

As an example, the maximum conductor fields were calculated numerically and with Eq. (8) for a toroid of 18 circular coils. The major and minor radii are 1.5 m and 1 m respectively while $c \equiv \pi\rho/N = 8.73$ cm. Here I is taken as 10^6 A. A comparison of the results is shown in Table II. The numerical data are accurate to better than 0.01%; hence, Eq. (8) has an error of $\leq 2\%$ here.

Table II
Analytic and numerical expressions of B_m on an 18 coil toroid.

ϕ	R/m	$N_c/\pi R$	K''	B_m/T	
				analytic	numerical
0	2.413	0.2072	1.090	3.25	3.31
$\pi/2$	1.500	0.333	0.540	3.74	3.80
π	0.573	0.851	0.0752	6.44	6.51

With the expression of Eq. (8) one now has a simple accurate formula for the maximum field on toroidal coils. This can serve as a replacement for many of the extensive computer field computations previously required to get the same data.

CONCLUSION

In this paper we have outlined semianalytical techniques for obtaining local fields in solenoids and toroids. A systematic reduction of the severe end fields of thin walled solenoids was presented. The results given here should enable the magnet designer to approach predetermined conductor field limits with greater precision and optimum use of material.

ACKNOWLEDGEMENTS

The authors would like to thank Professors R.W. Boom, H.A. Peterson and W.C. Young and Dr. M.A. Hilal for many helpful discussions of this work. We are also grateful to the Wisconsin Alumni Research Foundation, the National Science Foundation and the Wisconsin Electric Utilities Research Foundation for supporting this work.

REFERENCES

- R.W. Boom, et al., "Wisconsin Superconductive Energy Storage Project," Feasibility Study Report, Volume 1, Madison, Wisconsin (July 1, 1974).
- R.W. Boom, et al., "Magnet Design for Superconductive Energy Storage for Power Systems," 5th International Conference on Magnet Technology, Rome (April, 1975).
- R.W. Boom, et al., "Wisconsin Superconductive Energy Storage Project," Feasibility Study Report, Volume 2, Madison, Wisconsin (1976).
- R.W. Moses, "The Configurational Design of Superconductive Energy Storage Magnets," to be published in Advances in Cryogenic Engineering, Vol. 20, Plenum Press (1975).
- R.W. Moses and W.C. Young, "Analytic Expressions for Magnetic Forces on Sectorized Toroidal Coils," presented at the Sixth Symposium on Engineering Problems of Fusion Research, San Diego, Calif. (November 18-21, 1975).
- P.L. Walstrom and M.S. Lubell, "Calculation of Radial Magnetic Fields for Axisymmetric Solenoids with Rectangular Cross-Section," ORNL-TM-4198, Oak Ridge National Laboratory (April, 1973).

A FORTRAN PACKAGE FOR SOLVING LINEAR ALGEBRAIC EQUATIONS WITH A LARGE DENSE MATRIX USING DIRECT ACCESS DISK STORAGE

M J Newman

Rutherford Laboratory, Chilton, Didcot, Oxon, OX11 0QX

1. INTRODUCTION

In solving the non-linear integral equation occurring in the GFUN^{1,2,3,4} magnet design program, a requirement arose for solving large linear problems with a general dense matrix of coefficients. The matrix was too large to be held in main memory, and was stored on a direct access disk dataset. The method to be described uses Gaussian Elimination and Back Substitution. The matrix is partitioned so that only a fraction of the whole matrix need be in main memory at any time. The method has been optimised to minimise the total elapsed time required for solution. To solve a problem of order 1000 on an IBM 360/195 computer using 516k bytes of main memory and 4M bytes of a 3330 disk took 19 minutes, of which 5.6 minutes was central processor activity.

The computer package is coded in Fortran and all input and output is handled in a single routine. It should be a simple matter to implement the package on any computer.

An additional facility is provided whereby having solved a system $A\underline{x} = \underline{b}$, a similar system $A\underline{x} = \underline{c}$ can be solved very economically using the factorised matrix which is stored on the disk.

2. METHOD

Since, for the particular problem in hand, the matrix had no convenient properties such as symmetry or sparseness, the method used is Gaussian Elimination with Back Substitution. The complete matrix is partitioned into square sub-matrices. Each sub-matrix forms a single record on the disk. The order of the sub-matrix can be chosen by the user subject to a maximum of 32767 bytes (order = 90) imposed by the Fortran Direct Access system. At any time, four sub-matrices are present in main memory. It is convenient to consider the complete matrix A (of order n) being partitioned as follows:

$$A = \begin{pmatrix} a_{11} & a_{12} & a_{13} & \dots & a_{1m} \\ a_{21} & a_{21} & a_{23} & \dots & a_{2m} \\ \vdots & \vdots & \vdots & \ddots & \vdots \\ a_{m1} & a_{m2} & a_{m3} & & a_{mm} \end{pmatrix}$$

where a_{ij} is a square sub-matrix of order p . Then $m = n/p$. At a general stage in the elimination process the four sub-matrices in main memory will be:

1. A Pivotal sub-matrix a_{ii} ($1 \leq i \leq m-1$)
2. A Sub-Pivotal sub-matrix a_{ki} ($i < k \leq m$)
3. A Cross-Pivotal sub-matrix $a_{i\ell}$ ($i < \ell \leq m$)
4. A Cross Sub-Pivotal sub-matrix $a_{k\ell}$

Suffix i ranges from 1 to $m-1$. For every value of i , suffix k ranges from $i+1$ to m . For every value of k , suffix ℓ ranges from $i+1$ to m . For each new value of i , when $k = i+1$, the two sub-matrices a_{ii} and a_{ki} are searched to find the element in each column below the diagonal which has the largest modulus. The row number is stored in work space provided by the user and that row is exchanged to become the pivotal row. The search for largest element has been restricted to two sub-matrices in order to restrict the number of disk accesses. For the application in mind it was thought to be extremely unlikely that this limitation will be noticeable. As a precaution the package prints out the maximum multiplying factor used as an indication of how effective this restricted search has been. Values are typically between 1 and 2. In the event of no non-zero elements being found an error diagnostic is printed and the program stops. As elements which lie below the diagonal are eliminated they are over-written with the appropriate multiplying factor. As many operations as possible are performed on each sub-matrix before returning it to the disk. The complete algorithm can be best understood by referring to diagrams 1 to 4.

In order to reduce the accumulated rounding error, each sub-matrix is stored with double precision (64 bit) accuracy in main memory. However, to reduce the number of disk accesses, each sub-matrix is truncated to

single precision (32 bit) accuracy before storing it on the disk. The total number of disk accesses is:

$$\frac{1}{6}[8m^3 - 3m^2 + 13m - 6]$$

for an order of 1000, where $m = 12$, this is 2257. The average number of truncations is:

$$\frac{1}{6}[4m - 3 + \frac{5}{m} - \frac{6}{m^2}]$$

which for the same problem is 7.5 truncations. Since the number of numerical operations is approximately $\frac{1}{3} \times 10^9$, it will be seen that the saving in the number of disk accesses does not introduce an unacceptable decrease in accuracy. It should be noted, however, that troubles may be expected if the facility for resolving similar problems with the same matrix is used for iterative refinement.

Since on most machines the residuals could only be calculated with 64 bit accuracy, this may not be sufficiently greater than the overall accuracy of the factorisation, and the refinement procedure may not converge.

3. EFFICIENCY

The efficiency of the package is best illustrated by some statistics from sample runs.

Order of main matrix n	Order of sub-matrix p	Total No. of sub-mcs. m	Disk space (Mbytes)	Main memory (Kbytes)
200	20	100	0.16	70
500	50	100	1.0	194
1000	90	144	4.67	516

Order of main matrix	Solve $Ax = b$			Resolve $Ax = c$		
	CPU time (mins)	Lapsed time (mins)	Total No. of disk access	CPU time (mins)	Lapsed time (mins)	Total No. of disk access
200	0.0766	0.856	1304	0.00342	0.0737	110
500	0.801	5.25	1304	0.0136	0.55	110
1000	5.56	19.10	2257	0.0509	0.302	156

The elapsed time for a solution will depend on the number of disk accesses, the size of each record, and the intensity of activity from concurrent jobs on the shared channel to the disk.

4. USER INTERFACE

The matrix must first be stored on a disk dataset in the required format. First, p , the order of each sub-matrix should be chosen as large as the main memory allows. The maximum value which p can take is 90. This results in a record size of 32400 bytes. Next the value of m must be calculated. This is n/p rounded up to the nearest integer if necessary. The package allows for m not being a factor of n . The dataset is then created with code similar to the following:

```
REAL*4 C4 (90,90)
DO 1 J = 1, M
DO 2 I = 1, M
[here fill C4 array with appropriate coefficients]
NREC = (J - 1)*M + I
WRITE (KSTR1,NREC) C4
2 CONTINUE
1 CONTINUE
STOP
END.
```

Next, in order to solve a system $Ax = b$, the user must call subroutine DSKSOL. The argument list is as follows:

No.	Name	Type	Dimensions	Purpose
1	C11	Real*8 array	(MD,MD)	Work space for a sub-matrix
2	C21	"	"	" " " " " "
3	C12	"	"	" " " " " "
4	C22	"	"	" " " " " "
5	C4	Real*4 array	"	Work space for a record
6	MD	Integer variable	-	Dimension of above arrays
7	SOL	Real*8 array	(IORD)	Contains solution on return
8	B	"	"	Contains vector <u>b</u> on calling
9	USED	Integer*2 array	(MSQ)	Work space(see note 1 below)
10	IPIV	"	(IORD)	Work space
11	KSTR1	Integer variable	-	Stream No.of dataset with matrix A
12	KSTR2	"	-	" " " "for factorised matrix
13	M	"	-	Order of sub-matrix
14	IORD	"	-	Order of complete matrix

Notes:

1. $MSQ \geq M^2$
2. $MD \geq M$
3. B must contain the values of the vector b before DSKSOL is called. These values are destroyed by DSKSOL.
4. The dataset on KSTR2 must be identical in structure to that on KSTR1. If the original matrix A is not required after the solution is obtained, set KSTR2 = KSTR1 and only supply one dataset.

In order subsequently to solve a similar system $Ax = c$, the user must call subroutine NEWRHS with a very similar argument list. This routine will destroy the values in the array c.

5. CONCLUSIONS

This package allows the solution of linear problems for which the coefficient matrix is larger than that which can be held in main memory. It is optimised towards minimising the total elapsed time for a solution. The accuracy obtained is close to that when the whole problem is solved in main memory with a word length of 64 bits.

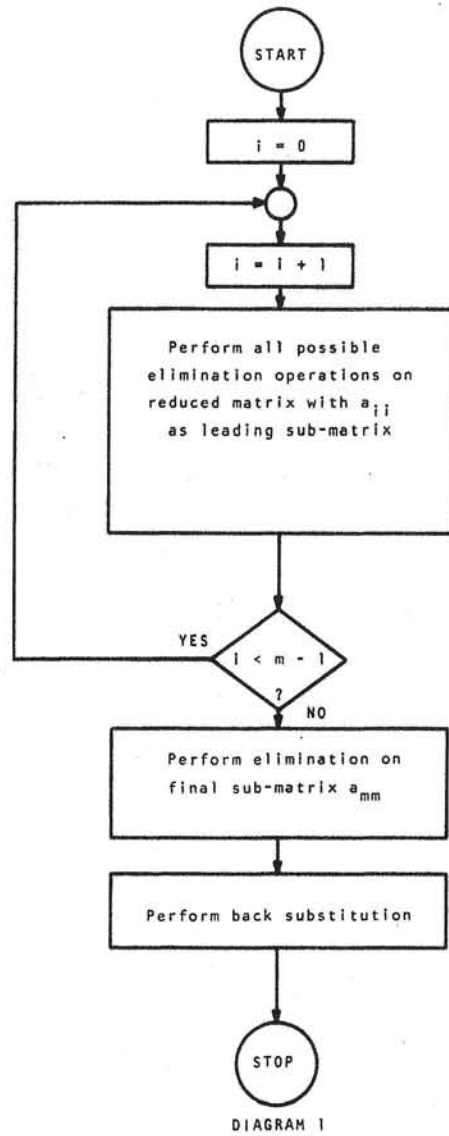
6. REFERENCES

1. M J Newman, C W Trowbridge, L R Turner. GFUN: An Interactive Program as an aid to Magnet Design. RPP/A94. Also in Proc. 4th Int. Conf. on Magnet Technology, Brookhaven, 1972.
2. M J Newman, J Simkin, C W Trowbridge, L R Turner. GFUN Users Guide - A user guide to an Interactive Graphics Program for the Computer Aided Design of Magnets. RHEL/R244, 1972.
3. C J Collie, N J Diserens, M J Newman, C W Trowbridge. Progress in the Development of an Interactive Computer Program for Magnetic Field Design and Analysis in Two and Three Dimensions. RL-73-077. Also in Proc. Conf. on Analysis of Magnetic Fields, Nevada, 1973.
4. A G A M Armstrong, C J Collie, N J Diserens, M J Newman, J Simkin, C W Trowbridge. New Developments in the Magnet Design Computer Program GFUN. RL-75-066. Also in Proc. 5th Int. Conf. on Magnet Technology, Frascati, Rome, 1975.

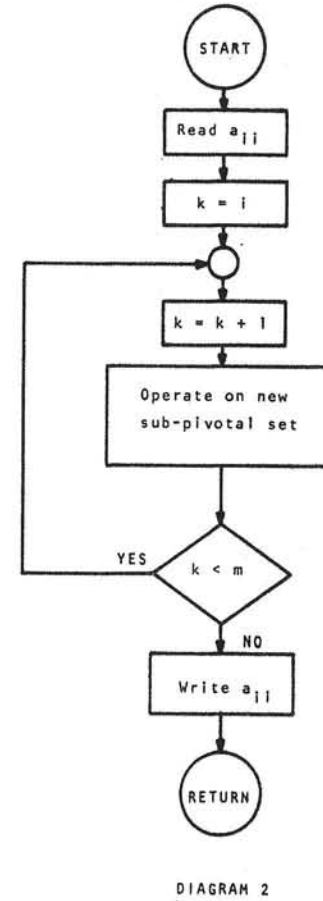
7. ACKNOWLEDGEMENTS

The author wishes to thank Mr C W Trowbridge, Applied Physics Division, Rutherford Laboratory, for the motivation and encouragement to complete this work, and Dr J K Reid, Theoretical Physics, AERE Harwell, for the suggestion of the optimum algorithm.

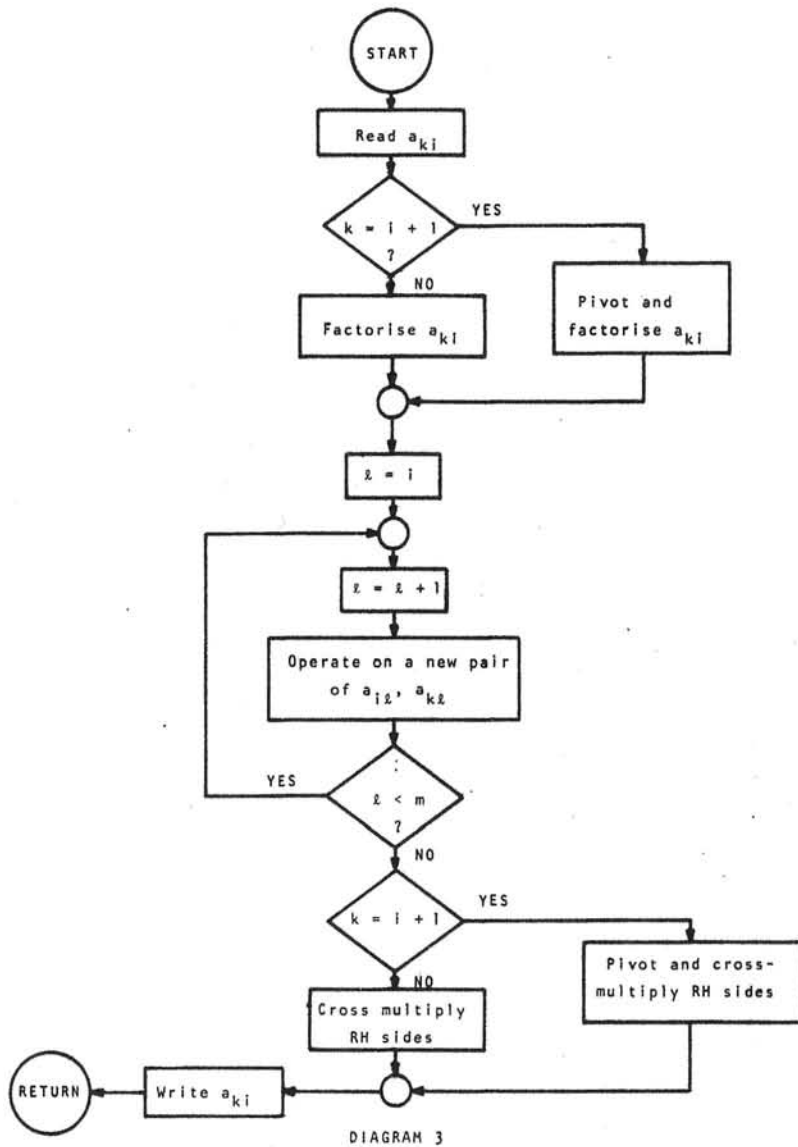
MAIN FLOW DIAGRAM



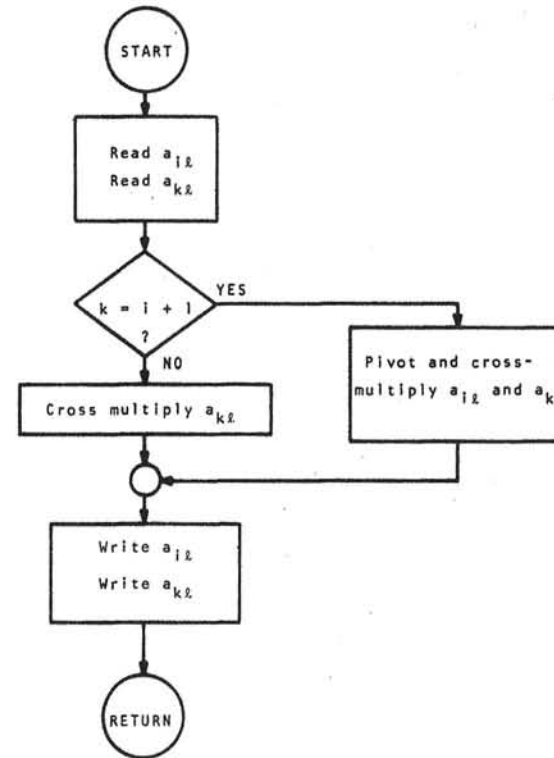
PERFORMING ALL POSSIBLE ELIMINATION OPERATIONS ON REDUCED MATRIX WITH a_{ij} AS LEADING SUB-MATRIX



OPERATION ON NEW SUB-PIVOTAL SET



OPERATIONS ON A NEW PAIR a_{iz} AND a_{kz}



COMPUTATION OF THE INTEGRATED MULTIPOLE FIELD COMPONENTS IN A SUPERCONDUCTING QUADRUPOLE MAGNET WITH CONSTANT PERIMETER COIL ENDS

T. Tortschanoff
CERN
Geneva, Switzerland

INTRODUCTION

Several attempts have been made to calculate the multipole field components produced by a quadrupole geometry including the contribution of the ends of windings. In particular, at Saclay and Rutherford Laboratory the constant perimeter geometry has been extensively treated^{1,2}). However, none of these calculations can be adapted to treat the geometry of the coil ends as they are actually manufactured at CERN and which represent a practical approximation of the ideal constant perimeter geometry.

For this reason, it was necessary to develop a special computer program to calculate the multipole components of the geometry which describes the quadrupole magnet in question. This calculation is especially important for the optimization of the space between each end of winding for the compensation of higher multipole components: by variation of the straight lengths, which determine the position of the ends of winding, one can eliminate a number of integrated multipole components which equals the number of coils per pole minus one. Thus, in the case of three windings per quadrant, the 12- and 20-pole components can be eliminated theoretically. In practice, however, this will not usually be feasible and other criteria for the optimization of the straight length have to be taken into account. In our case, the sum of the integrated gradient errors and the sum of their absolute values inside the useful region were taken as criteria.

1. METHOD OF CALCULATION

The method applied in these calculations is first to separate the straight part and the ends. The ends are treated as a series of very short straight parts by cutting them into a great number of thin slices perpendicular to the longitudinal axis of the magnet.

According to the complex variable method^{3,4}), for the two-dimensional case of a cylindrical geometry, the magnetic field produced by a sector winding can be written:

$$\vec{F} = B_y + i B_x = - \sum_{n=1}^{\infty} (a_n + b_n) z^{n-1}, \quad z = x + iy, \quad (1.1)$$

where, in the case of quadrupole windings, the contribution of each block of winding is (see Fig. 1)⁵):

$$a_n = \frac{4 \mu_0}{\pi} \frac{j_0 (r_2^{2-n} - r_1^{2-n})}{n(2-n)} (\sin n \phi_2 - \sin n \phi_1) \quad n \neq 2, n = 6, 10, 14, \dots$$

$$a_2 = \frac{2 \mu_0}{\pi} j_0 \ell n \frac{r_2}{r_1} (\sin 2 \phi_2 - \sin 2 \phi_1) \quad (1.2)$$

$$b_n = \frac{4 \mu_0}{\pi} \frac{j_0 (r_2^{n+2} - r_1^{n+2})}{R^{2n} n(n+2)} (\sin n \phi_2 - \sin n \phi_1) \quad n = 2, 6, 10, 14, \dots$$

j_0 is the current density in the longitudinal direction
 R is the inner radius of a $\mu = \infty$ cylindrical iron screen.

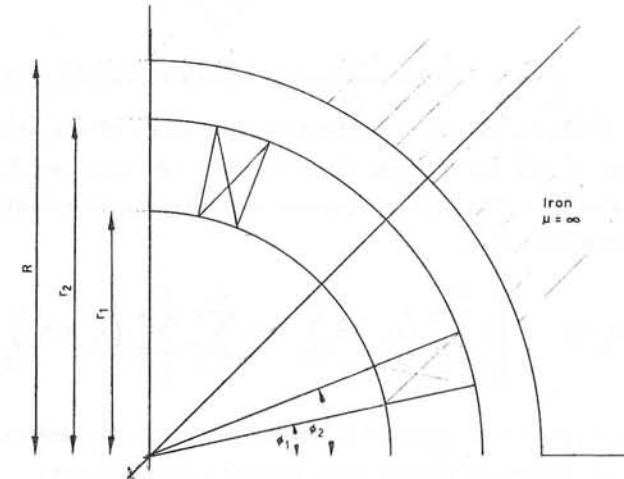


Fig. 1 Scheme for computation.

In order to extend these two-dimensional formulae to our three-dimensional problem, the a_n and b_n values have to be multiplied by the straight length, ℓ , and by the thickness of the thin slices, Δs , into which the ends are cut.

The geometry of the straight part of the coil is determined by the conductor which, in our case, is solid with rectangular cross-section. As shown in Fig. 2, the lateral sides of the blocks are parallel. Therefore, the blocks must be approximated by a suitable number of concentric layers which are treated as sectors. For each layer, the angles ϕ_1 and ϕ_2 can easily be determined from the design data (Fig. 2).

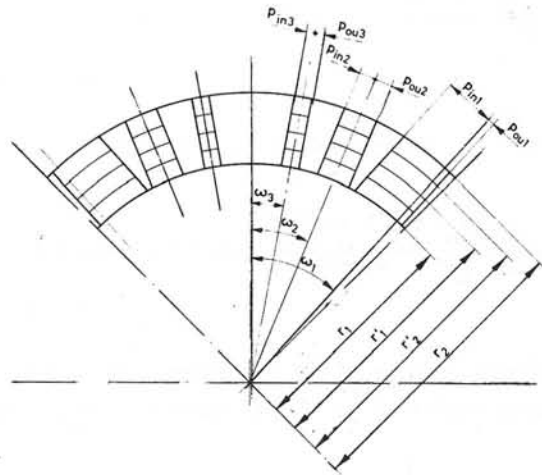


Fig. 2 Cross-section of straight part of coil.

By adding up the contributions of each layer of the straight part and each layer of all slices into which the ends are cut, one obtains the integrated multipole field components for each winding at a distance ρ from the longitudinal axis:

$$\int_{-\infty}^{\infty} B_n ds = - \left[\ell \sum_{i=1}^{n_\ell} (a_n + b_n)_i + \Delta s \sum_{j=1}^{n_s} \sum_{i=1}^{n_\ell} (a_n + b_n)_{ji} \right] \rho^{n-1}, \quad (1.3)$$

where n_ℓ = number of concentric layers per block of winding, and n_s = number of slices into which the ends are cut.

2. THE ENDS

The shape of the ends is determined by the condition that each turn of conductor must have the same circumference. It is obvious that in windings of considerable thickness this condition cannot be fulfilled for all

wires in the block¹⁾. For the calculation of the constant perimeter it seems, therefore, advantageous to take the centre vertical layer as a reference, which in the straight part is at an angular position ω .

It is also obvious that this constant perimeter layer has an inclination at the end, which is pointing to the inside of the coil (Fig. 3).

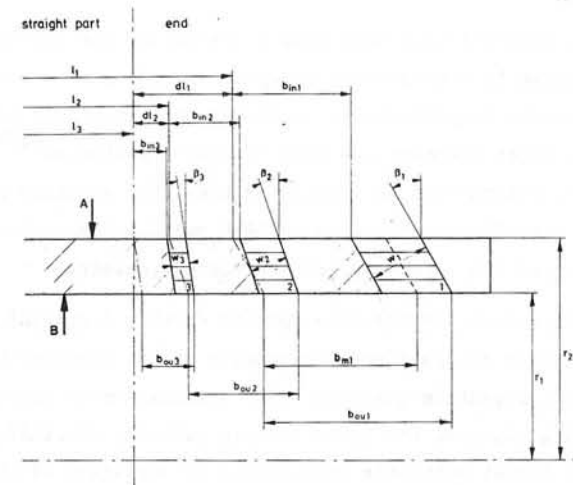


Fig. 3 Coil end cut along the 45° plane.

When making a constant perimeter end, one is free to decide at which cylinder radius of the coil the windings are describing an arc of circle. If it is intended to have the largest possible inclination to dilute the current density at the ends and thus decrease somewhat the magnetic field inside the winding, the arc of circle has to be at the outer surface of the cylinder (r_2).

For the layer which is on the inner cylinder (r_1), the end has the shape of a developed semi-ellipse with the centre displaced by the inclination β (Fig. 3). This end inclination, which produces the constant perimeter for the vertical layer of conductor, at the angular position ω in the straight part, is⁶⁾:

$$\tan \beta = \frac{\pi}{4} \omega. \quad (2.1)$$

The plane separating the straight part and the end (by definition) passes through the centre of the arc of circle describing the smallest

winding (No. 3 in Fig. 4) at the outer layer of the coil cylinder. Thus, if one starts to cut the end at a certain distance s from this separation plane, the cross-sections appear as shown in Fig. 5. If the cross-sections of the blocks of conductor at these cuts are subdivided into concentric layers, these cross-sections of blocks can also be approximated by a suitable number of circular sectors.

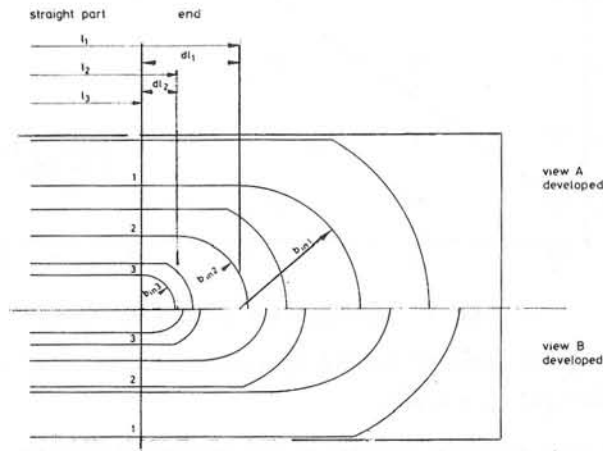


Fig. 4 Developed views of the coil end.

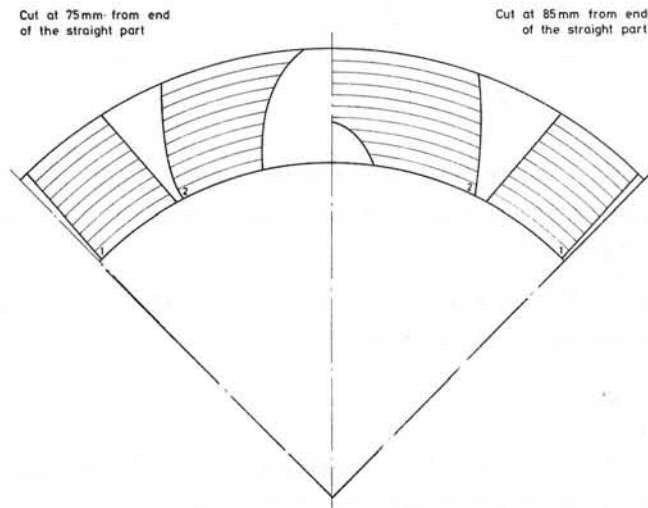


Fig. 5 Sections across the coil end.

Knowing the inner and outer radii of these sectors, the cut position, s , the parameters of the ellipses (on the developed surface of each concentric layer) and the displacement of the ellipse centres according to the end inclination β , one can easily calculate the approximated ϕ_1 and ϕ_2 angles for each circular sector.

Where the width of block is increased at the ends to a value w (by placing specially shaped spacers between the conductors), the parameters of the ellipses have to be corrected accordingly.

For each cut, one has to check:

- how many windings are concerned;
- whether the cut is performed in a straight or partially straight part of one winding;
- whether the peak of a winding is touched or partially touched ("tangential cut").

For each sector element, an average current density in longitudinal direction must be computed and applied in formula (1.2).

Now, the contributions of all sector elements have to be summed up according to formula (1.3).

4. COMPUTER PROGRAM ENDEF

A computer program was written to do the step-by-step integration along the quadrupole magnet. The input, consisting of 5 cards only per case, contains the basic geometric parameters of the coil as shown in Figs. 2 and 3, the current density for the straight part, the useful radius of aperture, the number of order (n) to which the multipole components will be calculated, the number of concentric layers (n_k) into which each block of winding has to be divided and the distance between cuts (Δs) performed in the end region.

The computing time depends mainly on the last two data. With three windings per coil, 30 concentric layers per block of winding and 1 mm cut-distance, Δs , in the end region, the time needed is about 6 seconds for the CERN CDC-7600 computer.

The output of the program consists of the integrated field components at the radius of the useful aperture, of the relative multipole field components and the relative gradient errors. Further the sum of the gradient errors and that of the absolute values of the gradient errors are given. All these results are separately printed out for the straight part and for the total quadrupole magnet.

4. RESULTS

For the superconducting quadrupole for the CERN Intersecting Storage Rings (ISR), the optimization was performed by variation of the straight length l_1 and l_2 , while the length of the smallest block, l_3 , was kept constant. The sum of the gradient errors and the sum of their absolute values for different straight lengths l_1 and l_2 are shown in the diagrams of Figs. 6 and 7.

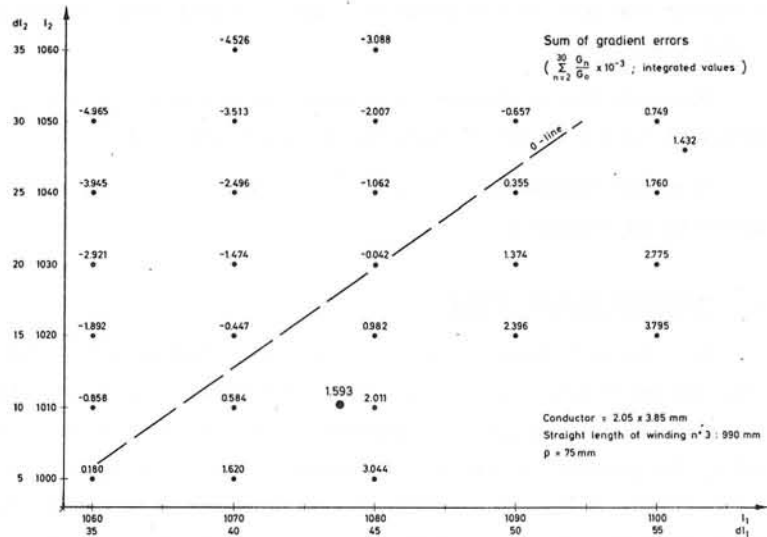


Fig. 6 Optimization of straight length

It can be seen that decreasing one length requires also a smaller length for the other block. A compromise had to be found which was compatible with the additional constraint that a certain free distance had to be kept for mechanical reasons between the ends of the blocks of windings. The straight length of the small blocks was kept at 990 mm, the other two blocks were finally chosen at 1010.6 mm and 1077.5 mm.

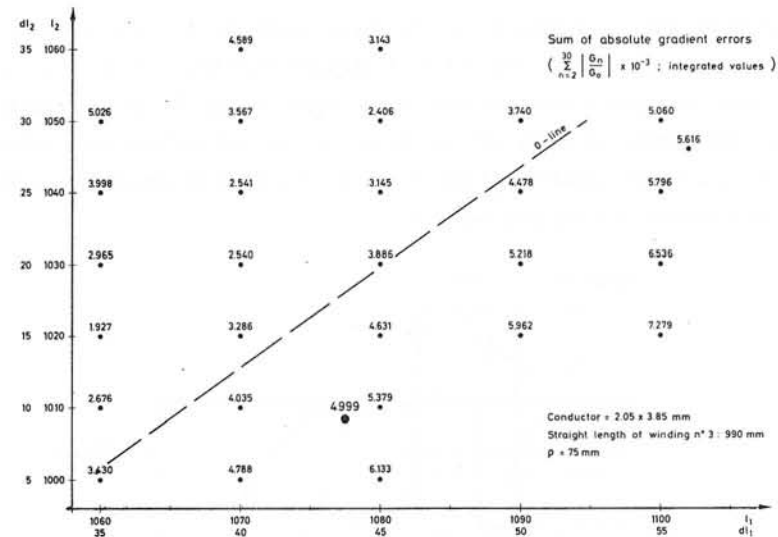


Fig. 7 Optimization of straight length

The inclinations of the end were calculated to be $\beta_1 = 29.17^\circ$, $\beta_2 = 18.54^\circ$ and $\beta_3 = 9.12^\circ$.

For this geometry, the sum of the integrated gradient error at a radial distance $\rho = 75$ mm is:

$$\frac{\int_{-\infty}^{\infty} G_{\rho=75} dz - \int_{-\infty}^{\infty} G_{\rho=0} dz}{\int_{-\infty}^{\infty} G_{\rho=0} dz} = 1.59 \times 10^{-3} \quad (4.1)$$

The sum of the integrated absolute values of the gradient errors (indicating the error outside the median plane) was calculated to be 5.00×10^{-3} .

Table 1 shows the parameters for the final quadrupole geometry (notations - Figs. 1, 2, 3 and 4).

REFERENCES

- 1) G. Bronca, J. Hamelin, S. Jaidane, M. Renard, Fringing fields and iron saturation in air core magnets, Proc. 3rd Int. Conf. on Magnet Technology, Hamburg, p. 64 (1970).

TABLE 1
Parameters for final quadrupole geometry

Parameter	Value	Parameter	Value
r_1	116.0 mm	Δs	1.0 mm
r_2	154.5 mm	j	195 A/mm ²
β_1	29.17°	l_1	1077.5 mm
β_2	18.41°	l_2	1010.6 mm
β_3	9.12°	l_3	990.0 mm
ω_1	42.0 °	w_1	43.24 mm
ω_2	25.0 °	w_2	26.92 mm
ω_3	10.5 °	w_3	12.64 mm
P_{in1}	27.70 mm	R	176.0 mm
P_{ou1}	5.10 mm	ρ	75 mm
P_{in2}	14.70 mm	n	30
P_{ou2}	3.75 mm	n_λ	30
P_{in3}	4.10 mm		
P_{ou3}	4.10 mm		

- 2) H.I. Rosten, The constant perimeter end, RL-73-096 (1973).
- 3) R.A. Beth, Evaluation of current-produced two-dimensional fields, J. Appl. Phys., Vol. 40, p. 4782 (1970).
- 4) K. Halbach, Fields and first order perturbation effects in two-dimensional conductor dominated magnets, Nucl. Instr. and Meth. 78, p. 185 (1970).
- 5) R. Perin, Private communication.
- 6) P. Pugin, Private communication.

A PRACTICAL METHOD FOR THE DETERMINATION OF STATIONARY TWO-DIMENSIONAL MAGNETIC FIELD

B. Zelenko

Poduzeće R.Končar, OOUR Elektrotehnički institut, Zagreb, Yugoslavia

ABSTRACT

A method for the determination of magnetic field in a sector of an annulus with usual assumptions about magnetic properties of materials is described. The grid in a two dimensional polar coordinate system may be chosen according to the configuration of magnetic materials and each rectangular element of the grid may be divided in two triangular parts. A set of nonlinear equations is obtained by means of integral of the magnetic field strength along a closed curve around each node. This set is solved iteratively by the method of overrelaxation of potentials and underrelaxation of reluctivities.

Some node potentials may be corrected by the addition of an amount which is in accordance with the nonlinear equations. The method is successfully applied to practical problems.

1. INTRODUCTION

The magnetic field in electrical machines is very often simplified and investigated in a two-dimensional region. The following equation

$$\frac{\partial \mathcal{V}}{\partial x} \frac{\partial A}{\partial x} + \frac{\partial \mathcal{V}}{\partial y} \frac{\partial A}{\partial y} = -J \tag{1}$$

holds for a stationary two-dimensional magnetic field. The variable A is the magnetic potential, J is the current density. We neglect the hysteresis effect so that the reluctivity \mathcal{V} is determined by the flux density only.

In this paper we consider the magnetic field in a sector of an annulus. This region is chosen in accordance with many problems on electrical machines.

In a polar coordinate system (r,φ) the region (fig. 1) is covered with a net of circle arcs r = const and straight lines φ = const. The con-

figuration of magnetic materials in this region can be irregular and therefore we suppose that a rectangular part of the net can be divided in two triangular parts (fig. 2). Of cause this division may be performed in two ways: from node (i, j) to (i+1, j+1) or from (i+1, j) to (i, j+1). We wish to determine the magnetic potentials belonging to the nodes. The potentials at other points of the region shall be interpolated linearly or bilinearly by means of its values at the nearest nodes.

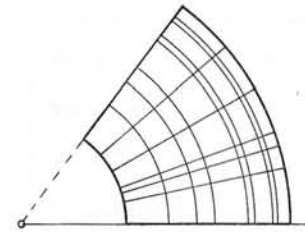


Figure 1. Sector of an annulus in a polar coordinate system

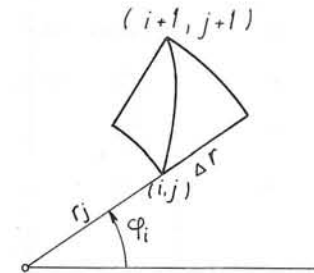


Figure 2. Division of a rectangular part (i, j) in two triangular ones

The equations between potentials at adjoining nodes are obtained by a line integral along a closed path. These equations are nonlinear if reluctivity depends on flux density and they can be solved by an iterative process only.

2. OBTAINING THE SET OF EQUATIONS

The value of the magnetic potential A is to be determined for each node of the net (fig. 1). Then the potential is approximately known at each point of the region by means of a bilinear interpolation:

$$A = a + b\varphi + cr + dr\varphi \tag{2}$$

In a rectangular part (fig. 3) the coefficients a, b, c and d are determined by four potentials A_{ij} , $A_{i+1,j}$, $A_{i+1,j+1}$ and $A_{i,j+1}$.

In a triangular part (fig. 2) d equals to zero and the values of a , b , and c are determined by the three potentials in the nodes of that part.

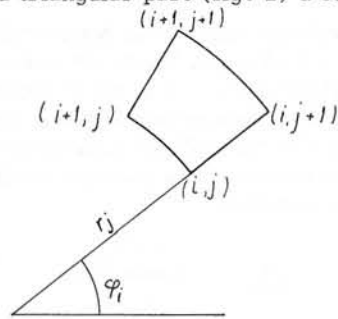


Figure 3. A rectangular part of the net

Due to continuity of the potential at the boundary of two adjoining parts, the curve that divides a rectangular part in two triangular ones has to be an Archimedes's spirale i.e. $r = e + f\varphi$. By means of such a subdivision of the net in triangular parts a good representation of the magnetic material configuration can be obtained.

The equations which include the value of potentials at the nodes can be obtained by considering the adjoining parts of a node.

Figure 4 shows a node and a curve KLMN which goes by the middle of those parts. The points L and M lie on the dividing spirales.

The curve KLMN is composed of arcs $r = \text{const}$ and $\varphi = \text{const}$ so that the following integral can be easily calculated:

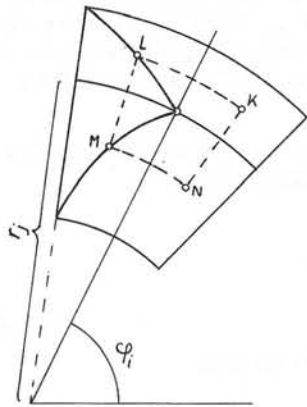


Figure 4. Node (i, j) and its adjoining parts

$$\int_{KLMN} \vec{H} \cdot d\vec{l} = I. \quad (3)$$

Here I is the current surrounded by this curve, $\vec{H} = \nabla \vec{B}$ is the magnetic strength, and the components of the flux density \vec{B} are

$$B_r = \frac{\partial A}{r \partial \varphi} \quad \text{and} \quad B_\varphi = - \frac{\partial A}{\partial r}.$$

If the potentials at the boundary of the region are given, then equation (3) gives as many equations as unknown node potentials exist. These equations are nonlinear if in some parts

there are ferromagnetic materials. The variable reluctivity in the inner of a certain part is approximated with a constant amount determined by the mean flux density in that part. The current density J for each part of the net is known and therefore it is easy to determine the right hand side of the equation (3). One equation connects 9 potentials of the neighbouring nodes (fig. 5) if all the four parts are nondivided. If some of

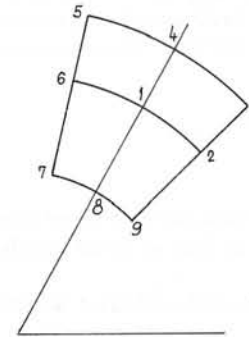


Figure 5. Neighbouring nodes in a net

them are divided in two triangular parts, the corresponding potentials at nodes 3, 5, 7 or 9 do not appear in the equation.

Similar relations appear at the application of finite element method when the basis of the vector space, the set of functions w_{ij} , is chosen in the following manner. Each function $w = w_{ij}(r, \varphi)$ is equal to zero at all nodes except at node (i, j) where $w_{i,j}$ is equal to 1. $w_{i,j}$ is interpolated linearly or bilinearly by means of the amounts at the neighbouring nodes in other points of the region. The equations obtained by means of the finite element method are some-

what different from (3). In the case of rectangular parts, a negative potential can be obtained at a node although the neighbouring potentials are not negative and $J = 0$. This is not physically acceptable. Similar results have been obtained with the method described in this paper, but because the equations (3) are physically clear and can be explained to every engineer, the finite element method has been avoided. An accurate comparison of these two methods is complicated. It is possible to prove the decrease of the difference between the equations

obtained by these two methods if $\Delta\varphi$ and Δr tend to zero in the simplest case of triangular parts without current. Speaking more precisely, if the biggest coefficients of the two compared equations are equal to 1, then the differences of the corresponding coefficients tend to zero with the same order of magnitude as $\Delta\varphi$ and Δr .

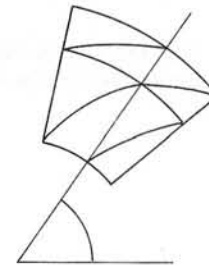


Figure 6. A simple triangular division

3. SOLVING THE EQUATIONS

The equations (3) are nonlinear and therefore they have to be solved iteratively. The well known method [1] with overrelaxation of potentials and underrelaxation of reluctivities has been applied. The overrelaxation factor ω :

$$(A_{ij})_{new} = (A_{ij})_{old} + \omega \cdot (A' - (A_{ij})_{old}), \quad (4)$$

$(A' \text{ obtained from (3)})$

was determined by computing experiment at each particular problem. In large nets, e.g. with more than 2000 nodes, ω had to be as small as 1.5.

The reluctivity ν is stored for each part of the net and after a complete potential iteration (4) it is corrected to

$$(\nu_{ij})_{new} = (\nu_{ij})_{old} + (\nu' - (\nu_{ij})_{old})/F, \quad (5)$$

$(\nu' \text{ corresponds to the mean calculated flux densities of that part}).$

The underrelaxation factor F was also experimentally determined. In large nets F is large, e.g. 30.

Beside the iterations (4) we also apply an additive correction of potentials in analogy to [3] for the net of rectangles. Namely, by adding some of equations (3) it is possible to obtain a new one which is very simple and which has a similar physical meaning as (3) :

$$\oint \vec{H} \cdot d\vec{l} = I. \quad (6)$$

The convergence of the iterative process can be accelerated by means of this procedure, e.g. in cases that nonmagnetic materials are surrounded with magnetic ones.

According to figure 7 one determines

$$I_1 = \oint_{KLMN} \vec{H} \cdot d\vec{l}, \quad (7)$$

$$I_0 = \oint_{KLMN} \vec{H}_0 \cdot d\vec{l}, \quad (8)$$

The calculated magnetic field strength \vec{H} is determined with the approximated values of A and ν after an iteration step (4), (5) for all the

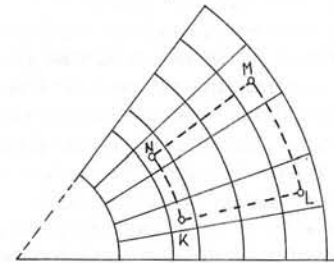


Figure 7. The integration path for additive correction for potentials

nodes. The fictitious magnetic force strength \vec{H}_0 is calculated with the same ν as before but with $A = 1$ at nodes inside the curve KLMN and $A = 0$ at other nodes. Then the potentials at nodes inside the curve KLMN have to be corrected with a common additive constant

$$\Delta = \frac{I - I_1}{I_0}, \quad (9)$$

where I is the total current surrounded by KLMN.

This procedure corresponds to adding some of equations (3) as follows. Let

$$x = C x + b \quad (10)$$

represent the linear system of equations (3) with constant reluctivities. x is the vector of unknown potentials A_{ij} and C is a matrix with diagonal elements equal to 0. We choose a vector z which has the components equal to 1 for nodes inside the curve KLMN, and the others equal to 0.

If an iteration vector $x^{(n)}$ is already known, by means of (9) we find the vector $d = \Delta z$ which is to be added to the vector x' :

$$x' = C x^{(n)} + b, \quad (11)$$

so that a new iteration vector is obtained :

$$x^{(n+1)} = x' + d. \quad (12)$$

Let z^T be the transpose of z . Then from (9) we have

$$= (z^T(x' - Cx^{(n)}) - z^T(x' - Cx'))/k, \quad k = z^T(z - Cz).$$

The procedure (11), (12) is linear:

$$x^{(n+1)} = D x^{(n)} + E b \quad (13)$$

where

$$Dx = Cx - (z^T(C - C^2)x)/k \cdot z, \quad Eb = b + (z^T C b)/k \cdot z.$$

Hence the additive correction corresponds to adding some of equations (3) .

Here z^T is the transpose of z and I is the unit matrix.

It would be advantageous if z were an eigenvector of C with an eigenvalue not equal to 1. Then z would be an eigenvector of D with eigenvalue 0. But unfortunately we can choose z approximately equal to an eigenvector of C in some cases only. This is fulfilled in the above mentioned case of nonmagnetic material surrounded with magnetic one.

Some of such additive corrections can be tied together because of the proximity of the corresponding curves. If these curves are ill chosen, the additional corrections may even prevent the convergence of the iterative process. This may happen if we choose for example two additive corrections according to figure 8. If we first correct in the region KLMN and then in the region K'L'M'N' it may happen that the iterative process does not converge.

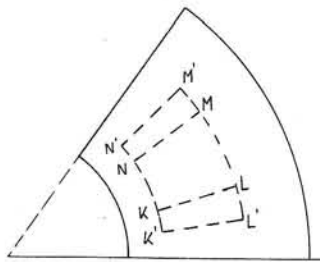


Figure 8. An example of ill chosen paths for additive corrections

4. CRITERIA FOR THE TERMINATION OF THE COMPUTATION

The magnetic field computation may serve for determination of flux densities locally or for global determination of the m.m. force. The very amounts of the magnetic potential is by no means important. Therefore any criterion for the termination of the computation should not be based on the amounts of the potential only.

According to our computations these criteria have been:

- small maximal correction of flux density
- small maximal correction of reluctivity
- the m.m. forces over various integration paths:

$$\theta = \int \vec{H} \cdot d\vec{l} \quad (14)$$

have to be in mutual accordance. For example in regions without current the m.m.f. can depend only on two end points of a curve along which θ is calculated.

We emphasize that the result θ in (14) is calculated in full accordance with equations (3) and formulae (6) to (9).

In practical applications the correction of flux density may be decreased at about 0.01 T. The correction of the reluctivity may be decreased so that the corresponding flux densities differ in amount of 0.001 T only. The m.m.f. along various paths with the same end points may differ from 2 to 5%.

5. APPLICATIONS

The described method is used for the determination of the flux density and m.m.f. in core backs of rotating machines. The holes are bored for the cooling improvement in the core back and they influence the flux density distribution, the thermal losses and the m.m. force.

In practical problems the number of nodes varies up to more than 2000. The computed m.m.f. θ_c differs in most cases from the m.m.f. θ_o determined by usual calculations. θ_c is sometimes much greater and sometimes much smaller than θ_o . Up to now the measurements have conformed our computations, and the magnetizing current calculated by means of θ_1 was greater than the measured one while the current calculated by means of θ_o was much smaller than the measured one.

The computed maximal flux density in the core back was in accordance with the measured one.

Figure 9 shows the cross-section of a part of a stator core back with holes. For this core back it was computed $\theta_1 = 1100$ A and $\theta_o = 500$ A.

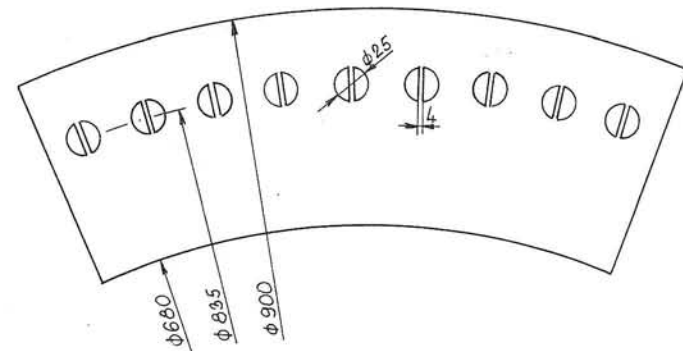


Figure 9. A part of a stator core back with holes

The calculating net for this example had 1000 nodes. The magnetic field computation lasted 6 minutes on Univac III computer. This time includes 320 iterations with all results, tables and figures.

6. CONCLUSIONS

A practical method for the determination of stationary two-dimensional magnetic field is described. This method is based on clear physical representation of used equations. The setting of the configuration is not complicated since the net in the sector of an annulus is based on circle arcs and straight lines. Practical applications give satisfactory results until now.

References

- [1] S.V.Ahamed, E.A.Erdélyi : Flux distribution in dc machines at no-load and overloads, IEEE Trans. Power Apparatus and Systems, vol. PAS-85, pp. 960-967, September 1966.
- [2] I. Mandić: Izrada programa za proračun magnetskog polja u zoni zuba za digitalno računalo C 90-40, elaborat E 32052, Poduzeće "R. Končar", Elektrotehnički institut, 1967.
- [3] E. de la Vallée-Poussin, A. Lion: Calcul itératif de l' induction magnétique dans les machines électriques, Revue générale de l' électricité, 731-739, avril 1967.
- [4] F. Melkes: Metoda konečných prvku⁰ pri řešení magnetickeho pole. Interni rad VUEST, Brno 1968.

A METHOD FOR COMPUTATION THE SUPERCONDUCTING MAGNETS
WINDING CONFIGURATION TO CREATE A PRESCRIBED MAGNET
FIELD DISTRIBUTION

B.N.Zhukov, V.N.Lebedev, I.A.Mozalevsky

D.V.Efremov Scientific Research Institute for
Electrophysical Apparatus

A number of ways is known to generate a given magnet field distribution in a given aperture by choosing adequate winding configuration. We shall discuss briefly some of these ways.

I. HOMOGENOUS CURRENT DENSITY WINDINGS
(IDEAL WINDINGS)

1. It is well known that homogenous and linear field distribution can be obtained in a system of intersecting circular or elliptical current blocks. In this case the region free of currents, where the specified field exists, is wider than the aperture, the later being commonly circular or elliptical. The stored energy and the superconductor weight are, therefore, greater than those in a winding lying close to the aperture boundary.

2. In the work [1] the computation method is described in which the set of parameters of the winding configuration is the solution of the system of nonlinear equations representing relation of the multipole field coefficients and these parameters. This method can be easily modified to enable the computation of the winding configuration for noncircular apertures and unsaturated circular iron shell. The approximate solution of the system is obtained by modified Newton method which takes a lot of computer time and is very sensitive to the choice of the initial approximation.

3. In the work [2] the configuration of the closely lying winding is the approximate solution of the system of equations

derived from condition of continuity of the vector potential on the outer winding boundary.

The real magnet windings are wound of the conductor of rather large cross-section to satisfy various technology and economical demands, and hence the above discussed methods are not applicable to real magnets design, the field error going up to few per cent if the ideal winding is simply "stuffed" with conductor.

II. WINDINGS OF REAL CONDUCTOR

1. One of the possible real winding configurations is an approximation of a harmonic current distribution with the set of current blocks of constant radial thickness and varying angular width. Such windings do not fit from economical point of view; besides, in case of noncircular apertures the solution analogous to harmonic current distribution cannot be easily obtained.

2. A lot of methods for discrete closely lying winding computation is developed based on minimization of some functional of field. (For instance [3], the energy stored in the aperture, on condition that the field magnitude (or gradient) in the aperture center is kept fixed, has minimum, when the higher harmonics are equal to zero). The minimization is proceeded by one or another gradient method requiring big computers.

We have developed a group of methods for computation the real magnet winding configurations to create any specified field in arbitrary aperture, with or without unsaturated iron shell. All of these methods are various modifications of a simple and fast working algorithm of computation an ideal winding for the circular aperture.

Basic algorithm description

Let us consider the algorithm for calculating the outer boundary of the ideal winding lying close to the circular aperture of the ironless magnet. Let the required field be

$$H(Z) = H_y + i H_x = \sum_{\kappa \in K} \alpha_\kappa Z^\kappa, \quad (1)$$

where $\{\alpha_\kappa\}_{\kappa \in K}$ is a finite set of given multipole coefficients. For instance, we want to create a homogeneous field $H(Z) \equiv H_0$, so we shall require $\alpha_0 = H_0$, and $\alpha_1 = \alpha_2 = \alpha_3 = \alpha_4 = \alpha_5 = \alpha_6 = \alpha_7 = \alpha_8 = \alpha_9 = \alpha_{10} = \alpha_{11} = \alpha_{12} = \alpha_{13} = \alpha_{14} = \alpha_{15} = \alpha_{16} = \alpha_{17} = \alpha_{18} = \alpha_{19} = \alpha_{20} = \alpha_{21} = \alpha_{22} = \alpha_{23} = \alpha_{24} = \alpha_{25} = \alpha_{26} = \alpha_{27} = \alpha_{28} = \alpha_{29} = \alpha_{30} = \alpha_{31} = \alpha_{32} = \alpha_{33} = \alpha_{34} = \alpha_{35} = \alpha_{36} = \alpha_{37} = \alpha_{38} = \alpha_{39} = \alpha_{40} = \alpha_{41} = \alpha_{42} = \alpha_{43} = \alpha_{44} = \alpha_{45} = \alpha_{46} = \alpha_{47} = \alpha_{48} = \alpha_{49} = \alpha_{50} = \alpha_{51} = \alpha_{52} = \alpha_{53} = \alpha_{54} = \alpha_{55} = \alpha_{56} = \alpha_{57} = \alpha_{58} = \alpha_{59} = \alpha_{60} = \alpha_{61} = \alpha_{62} = \alpha_{63} = \alpha_{64} = \alpha_{65} = \alpha_{66} = \alpha_{67} = \alpha_{68} = \alpha_{69} = \alpha_{70} = \alpha_{71} = \alpha_{72} = \alpha_{73} = \alpha_{74} = \alpha_{75} = \alpha_{76} = \alpha_{77} = \alpha_{78} = \alpha_{79} = \alpha_{80} = \alpha_{81} = \alpha_{82} = \alpha_{83} = \alpha_{84} = \alpha_{85} = \alpha_{86} = \alpha_{87} = \alpha_{88} = \alpha_{89} = \alpha_{90} = \alpha_{91} = \alpha_{92} = \alpha_{93} = \alpha_{94} = \alpha_{95} = \alpha_{96} = \alpha_{97} = \alpha_{98} = \alpha_{99} = 0$, if the required field symmetry differs from the aperture symmetry, and thus guarantee the zero total current.

We choose the initial approximation for the outer boundary $r(\varphi) \equiv z_0$, z_0 being the aperture radius. The work of the algorithm is the successive approximate compensation of the field disturbing harmonics. Let the outer boundary be, after the n-th step of iterations, $r^{(n)}(\varphi) = z_0 + |\sum_{\kappa \in K} c_\kappa^{(n)} \cos(\kappa+1)\varphi|$, and the current density $j^{(n)}$ be $j^{(n)} = |j| \cdot \text{sign}(\sum_{\kappa \in K} c_\kappa^{(n)} \cos(\kappa+1)\varphi)$. The winding produces the field $H^{(n)}(Z) = \sum_{\kappa=0}^{\infty} a_\kappa^{(n)} Z^\kappa$, where

$$a_\kappa^{(n)} = -0.2 \int_0^{2\pi} \int_{z_0}^{r^{(n)}(\varphi)} j^{(n)} \cos(\kappa+1)\varphi d\varphi dz, \quad \kappa \geq 0. \quad (2)$$

Formula (2) can be derived by expanding the Poisson integral $H(Z) = -0.2 \iint j(\zeta) dS / (\zeta - Z)$, into Taylor series. As it is known [4], the field disturbances $\Delta a_\kappa^{(n)} = a_\kappa - a_\kappa^{(n)}$ would be compensated, if we put current with the surface density

$$\sigma^{(n)}(\varphi) = \sum_{\kappa \in K} \sigma_\kappa^{(n)} \cos(\kappa+1)\varphi,$$

$$\sigma_\kappa^{(n)} = \Delta a_\kappa^{(n)} z_0^\kappa / 0.2\pi \quad (3)$$

onto aperture boundary. This compensation can be approximated by altering the winding outer boundary

$$r^{(n+1)}(\varphi) = z_0 + |\sum_{\kappa \in K} (c_\kappa^{(n)} + \frac{\sigma_\kappa^{(n)}}{|j|}) \cos(\kappa+1)\varphi| = z_0 + |\sum_{\kappa \in K} c_\kappa^{(n+1)} \cos(\kappa+1)\varphi| \quad (4)$$

and this accomplishes the n-th step of iteration. We have distributed the current with the density $\sigma^{(n)}(\varphi)$ along the strip of width depending on φ and carrying constant current density $|j|$.

The iteration is repeated until the field deviation $\max_{|Z| < z_w} |\Delta H^{(n)}(Z)|$ becomes less than permitted. The field error of about 0.01% at $z_w = z_0$ is achieved in 1+2 minutes with the BESM-4 computer ($2 \cdot 10^4$ op.per sec).

Noncircular aperture. Round iron shell

With the iron shell presence the field $H^{(n)}(Z)$ and the compensating current $\sigma^{(n)}(\varphi)$ are calculated with the shell contribution taken into account [5], and the iron inner radius $R_s^{(n)}$ is determined at each step by the condition $\max_{\varphi} |H^{(n)}(R_s^{(n)} e^{i\varphi})| = H_p$, where H_p is a given value less than iron saturation field.

If the aperture boundary is described by equation $z = z_\varphi(\varphi)$ we have to substitute $z_\varphi(\varphi)$ instead of z_0 into (2) and into the formula for $r^{(n)}(\varphi)$. The compensating current $\sigma^{(n)}(\varphi)$ in (3) is calculated for more or less arbitrary z_0 , the later

becoming a parameter, having no geometrical significance.

The ideal winding configurations computed as discussed above for various types of field, aperture shapes and values of $|j|$ are shown in figs 1 and 2.

Real windings

The real superconducting windings are wound of cable of finite cross-section and, as a rule, are provided with some spacers and channels of cooling system. The commonest types of windings are pancake and shell windings. Both types are characterized by the number of layers N and the number of turns W_i in each i -th layer. To define these parameters we "fill" the ideal winding with the conductor at each step of iteration according the chosen winding structure. The coefficients $\alpha_n^{(m)}$ are calculated following actual conductor position; it can be easily done for simple shapes of the conductor cross-section [5]. After that the iteration step is completed according formulae (2), (3); $|j|$ value in (3) should be taken equal to j_{av} - the average current density in winding.

The available field forming accuracy (i.e. the error magnitude does not decrease when one turn is added or removed) depends on conductor size and is about 0.1+0.01% if the current in a single conductor is in the interval 500 to 5000 amps. The computer time is 1+3 minutes for BESM-4 computer.

Fig.3 represents the real windings computed for both winding structures of a dipole magnet of the accelerator-storage unit [6].

Magnet field in current region

Such characteristics as forces in the winding, stored energy, residual field, etc., are of importance when the magnet is designed. These values can be easily obtained if the field distribution in winding is known. However, the direct summing of the elemental fields of each conductor for every point of winding takes too much computer time. Luckily, we can approximate the magnet field in real winding with the field in the ideal winding producing the same field in the aperture and carrying the current density $j = j_{av}$.

The field in the ideal winding can be easily found:

$$H(z, \bar{z}) = \tilde{H}(z) + 0.2\pi j (\bar{z} - f(z)). \quad (5)$$

Here $f(z)$ is analytical in current region, $\bar{z} = f(z)$ being the aperture boundary equation; $\tilde{H}(z)$ is the analytic continuation of $H(z)$ into current region. The above mentioned continuation obviously exists if $H(z) = \sum_{n=0}^{\infty} \alpha_n z^n$, where all but a finite subset of α_n are equal to zero. If the described $f(z)$ exists also, then formula (5) really represents the magnet field in current region, for $H(z, \bar{z})$ satisfies there the Maxwell equation $\partial H(z, \bar{z}) / \partial \bar{z} = 0.2\pi j$ and is continuous on the aperture boundary. The function $f(z)$ can be explicitly written down for simple shapes of the aperture. In case of the circular aperture we have $\bar{z} = z_0^2 / z$, and for elliptical

$$\bar{z} = \frac{\alpha^2 + b^2}{\alpha^2 - b^2} z - \frac{2ab}{\alpha^2 - b^2} \sqrt{z^2 - \alpha^2 + b^2},$$

a and b being major and minor radii of ellipse respectively.

So, for circular aperture the field in the winding is

$$H(z, \bar{z}) = \tilde{H}(z) + 0.2\pi j (\bar{z} - z^2/z) \quad (6)$$

and for elliptical aperture -

$$H(z, \bar{z}) = \tilde{H}(z) + 0.2\pi j \left(\bar{z} - \frac{a^2+b^2}{a^2-b^2} z + \frac{2ab}{a^2-b^2} \sqrt{z^2-a^2+b^2} \right).$$

REFERENCES

1. G.H.Morgan, IEEE Trans., 1969. Part.Accel.Conf.
2. V.G.Davidovsky, Preprint INP 40-70. SOAN USSR.
3. W.W.Lee and Snowdon. IEEE Trans. on Nucl.Sci., 1973, vol.NS-200, No.3, p.726.
4. R.A.Beth, Proc. of the Nat.Part.Accel.Conf., Washington D.C. March 1-3, 1967.
5. B.N.Zhukov, V.N.Lebedev, Preprint NIIEFA, 1972, E-0I49, E-0I56, Leningrad.
6. Y.M.Ado et al. Proc. of the IV all - Union Conf. on Charged Part.Accel. vol.1, p.44, Moskow, "Nauka", 1975.

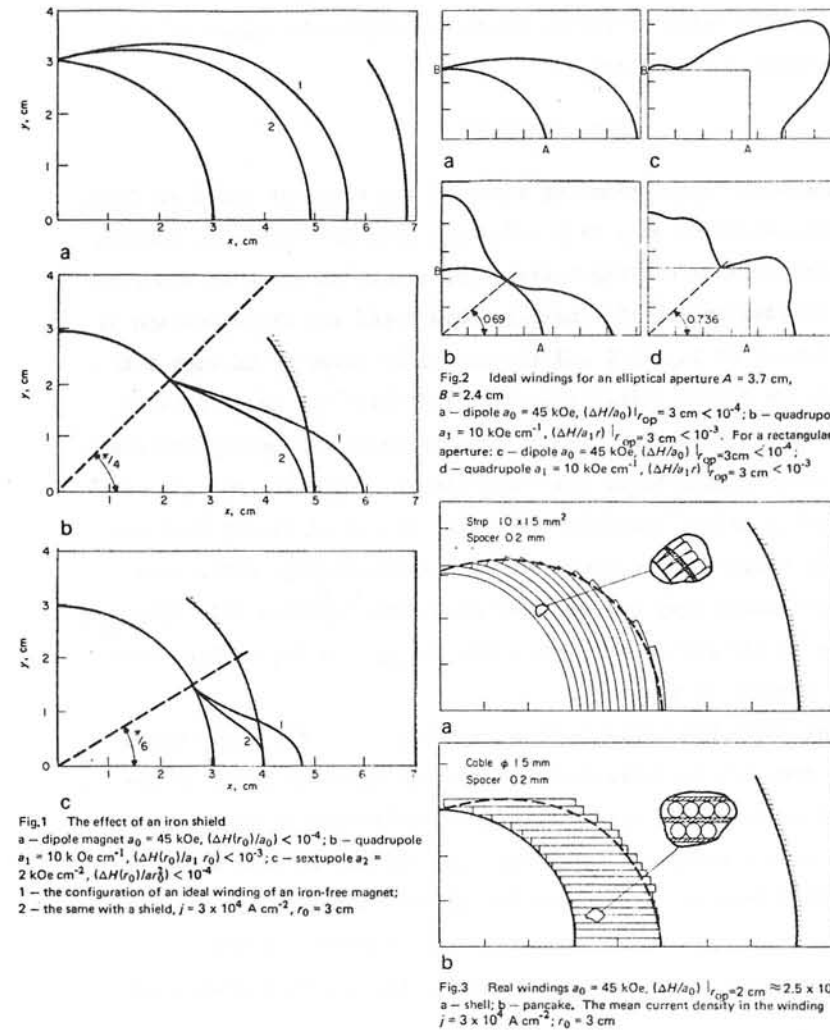


Fig.2 Ideal windings for an elliptical aperture $A = 3.7$ cm, $B = 2.4$ cm
 a - dipole $a_0 = 45$ kOe, $(\Delta H/a_0) |_{r_{op}} = 3 \text{ cm} < 10^{-4}$; b - quadrupole $a_1 = 10$ kOe cm^{-1} , $(\Delta H/a_1 r) |_{r_{op}} = 3 \text{ cm} < 10^{-3}$. For a rectangular aperture: c - dipole $a_0 = 45$ kOe, $(\Delta H/a_0) |_{r_{op}} = 3 \text{ cm} < 10^{-4}$; d - quadrupole $a_1 = 10$ kOe cm^{-1} , $(\Delta H/a_1 r) |_{r_{op}} = 3 \text{ cm} < 10^{-3}$

Fig.1 The effect of an iron shield
 a - dipole magnet $a_0 = 45$ kOe, $(\Delta H(r_0)/a_0) < 10^{-4}$; b - quadrupole $a_1 = 10$ kOe cm^{-1} , $(\Delta H(r_0)/a_1 r_0) < 10^{-3}$; c - sextupole $a_2 = 2$ kOe cm^{-2} , $(\Delta H(r_0)/a_2 r_0^2) < 10^{-4}$
 1 - the configuration of an ideal winding of an iron-free magnet; 2 - the same with a shield, $j = 3 \times 10^4$ A cm^{-2} , $r_0 = 3$ cm

Fig.3 Real windings $a_0 = 45$ kOe, $(\Delta H/a_0) |_{r_{op}} = 2 \text{ cm} \approx 2.5 \times 10^{-4}$
 a - shell; b - pangake. The mean current density in the winding $j = 3 \times 10^4$ A cm^{-2} ; $r_0 = 3$ cm

SECTION B MAGNETIC MATERIALS

PERMANENT MAGNETS IN MAGNETIC FIELD CALCULATIONS

H. Zijlstra

Philips Research Laboratories, Eindhoven, The Netherlands

Abstract

The presence of a permanent magnet in an electromagnetic system complicates the field calculations. The properties of the permanent magnet material that affect the calculations are analyzed theoretically. The results are tested by experiments with Ferroxdure magnets. A magnet model characterized by four parameters can be incorporated into field calculations. The customary manufacturer's data seem to be sufficient to deal with practical systems.

Introduction

The ever increasing quality of permanent magnet materials has led to a great expansion of the area of applications. Magnets are used in loudspeakers, electric motors and generators, relays, bearings and couplings, magnetic chucks and clamps, ore separators, microwave tubes, to name only a few. In all these applications the magnet serves to generate a magnetic field in an airgap by which a mechanical force is exerted on electric conductors or on magnetizable bodies.

The desire for better performance and also the occasionally high price of the magnet materials call for optimum design of the device containing the magnet.

In the past such optimizations were made by simple calculations on crude models and by experiments. Increasing complexity, however, and seeking for the ultimate percent have created a need for more rigorous methods. In the meantime computer programs have been developed for calculating field distributions in electromagnetic systems. Such programs work satisfactorily as long as the source of magnetomotive force is an electric current and provided that isotropic soft-magnetic materials are used.

But the introduction of a permanent magnet as an MMF source is a complication and this paper attempts to contribute to the solution of the problem. In particular, we shall consider which material properties are relevant and should be supplied by the manufacturer of permanent magnets.

The Permanent Magnet

The magnetic flux density \mathbf{B} in any magnetizable material can be written as

$$\mathbf{B} = \mu_0(\mathbf{H} + \mathbf{M}), \quad (1)$$

where $\mu_0\mathbf{H}$ is the contribution from the field and $\mu_0\mathbf{M}$ the contribution from the material. For a permanent magnet \mathbf{M} can be written as

$$\mathbf{M} = \mathbf{M}_0 + \chi\mathbf{H}, \quad (2)$$

where \mathbf{M}_0 is called the remanence and χ the susceptibility, which is a function of \mathbf{H} as well.

Fig. 1 shows the first and second quadrant of a typical hysteresis loop of a permanent magnet material. This curve is known as the demagnetization curve.

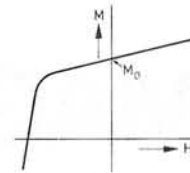


Fig. 1 Demagnetization curve of a permanent magnet material (schematic).

The permanent magnet differs from a soft magnetic material in having a magnetic moment when no magnetizing field is present. It is the magnetic moment \mathbf{M}_0 that serves as the source of the magnetomotive force.

Substituting \mathbf{M} into \mathbf{B} we obtain

$$\mathbf{B} = \mu_0(\mu_r\mathbf{H} + \mathbf{M}_0), \quad (3)$$

where we have written μ_r for $1+\chi$. Introducing the vector potential \mathbf{A} by $\mathbf{B} = \text{curl } \mathbf{A}$ and applying the curl operator on both sides we have

$$\text{curl}(\mu_0^{-1}\mu_r^{-1}\text{curl } \mathbf{A}) = \text{curl}(\mu_r^{-1}\mathbf{M}_0) + \text{curl } \mathbf{H}. \quad (4)$$

This is the vector equation that is to be solved by the computer. This paper is limited to the discussion of μ_r or rather χ .

We consider the source term with \mathbf{M}_0 . If we have an ideal magnet, i.e. a magnet that maintains a constant magnetic moment \mathbf{M}_0 in any field that might work on it, then μ_r is equal to one and a scalar. The curl of \mathbf{M}_0 is then zero throughout the magnet and differs from zero only at the magnet's boundary. The magnet can be considered as carrying a current sheet at its surface that generates its remanent magnetic moment. The density \mathbf{j} of this current is given by

$$\mathbf{j} = \text{curl } \mathbf{M}_0 \quad (5)$$

or, by applying Stokes' theorem,

$$\mathbf{j} = \mathbf{M}_0^t, \quad (6)$$

where \mathbf{M}_0^t is the tangential component of \mathbf{M}_0 at the surface and the current density \mathbf{j} flows at right angles around \mathbf{M}_0 in a right-hand screw relation. Thus a cylindrical magnet magnetized along its axis is equivalent to a homogeneous cylindrical current sheet of a total strength \mathbf{M}_0l , where l is the length of the magnet.

Now if the magnet is not ideal μ_r is greater than one and trouble may arise in several ways.

- 1) If μ_r depends on \mathbf{H} and \mathbf{H} is not uniform throughout the magnet, the equivalence of a magnet and a current sheet no longer holds.
- 2) If \mathbf{B} and \mathbf{H} have not the same orientation the curve of fig. 1 gives insufficient information, as in such curves one always measures the \mathbf{B} component along the field \mathbf{H} . For complete information curves for all combinations of \mathbf{B} and \mathbf{H} orientations would be required.

- 3) If the magnet has anisotropic μ_r , matters become even more complicated, because then the orientations relative to the magnet axes have to be taken into account as well.

It will be clear that it is virtually impossible to require such information from a magnet supplier and to feed it into the program. It seems more practical to try to find a magnet model that is characterized by a few parameters and that generates the B-H curves for any combination of B and H to a good approximation of what would be found in a real experiment. To that end we shall first take a closer look into what a permanent magnet material actually is.

What is a Permanent Magnet Material?

A permanent magnet consists of many small crystallites of a highly anisotropic magnetic material. Each of these crystallites has an individual crystallographic axis along which it prefers to be magnetized, its easy axis. The crystallites are compacted to a solid body with their easy axes more or less aligned with respect to each other. The magnet thus has an average easy axis around which the local easy axes of the crystallites are oriented according to a certain distribution function. For practical purposes this function can often be approximated by assuming that the individual orientations are distributed with uniform density inside a cone with semi-apex angle Θ^* , with no orientations outside (see figure 2). The cone axis coincides with the average easy axis of the magnet.



Fig. 2 First-order approximation to the distribution of easy axes of crystallites in an anisotropic polycrystalline permanent magnet.

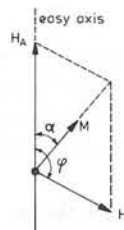


Fig. 3 Orientation of magnetization vector M under the combined action of the anisotropy field H_A and an applied field H.

We now consider one crystallite. It is uniformly magnetized with a magnetization M_s (s for saturation). The magnetization can vary under the influence of an externally applied field by two processes:

- a) uniform rotation, where M_s maintains its modulus and only varies its orientation;
- b) reversal, where M_s reduces its modulus to zero and grows in the reverse direction to acquire the value $-M_s$.

When no field is applied M_s is oriented along one of the two possible directions of the easy axis. Rotation of M_s requires energy because of the magnetic anisotropy. The strength of the anisotropy is often expressed in terms of anisotropy field H_A . This is a fictitious field, imagined to be oriented along the easy axis and to bind the magnetization vector to this axis. The strength of the anisotropy field is chosen such that the vector sum of an applied field H and the anisotropy field determines the correct orientation of M_s under the combined action of the anisotropy and the applied field (fig. 3). For small angles α between M_s and the easy axis, H_A can be considered as a constant field. For larger angles H_A has to depend on this angle, but this situation is of no practical importance to our problem; fields are always small compared to

H_A . It should be emphasized that H_A is a fictitious field and may not be introduced as such in a calculation. Its influence has rather to be incorporated in terms of susceptibility or permeability, as we shall see later.

Apart from the gradual rotation of the magnetization vector M_s under the influence of an applied field H another process may occur. If the applied field has a component opposite to M_s the latter will suddenly reverse its sign when H exceeds a certain critical value H_r , which value depends on the angle φ between H and the easy axis. The vector M_s then seeks a new equilibrium orientation under the combined action of H and H_A , the latter now pointing along the easy axis opposite to its orientation before the reversal jump (see fig. 4).

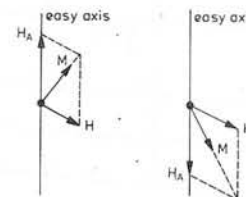


Fig. 4 Relative orientations of H_A , M and H before (left) and after (right) a reversal jump.

This reversal of the magnetization vector is a process entirely independent of the gradual rotation. It is associated with certain processes inside the crystal initiated by the presence of lattice defects. The reversal jumps occur at field strengths that are rarely higher than $0.2 H_A$ and are to be distinguished from rotation jumps, which can only occur at field strengths higher than $0.5 H_A$. The latter jumps are seldom of practical importance in the discussion of permanent magnets and will be ignored in the present discussion.

We have thus completely described the behaviour of one crystallite in terms of three parameters:

- a) the modulus of the magnetization M_s ,
- b) the strength of the anisotropy field H_A ,
- c) the critical field H_r for reversal of M, and its dependence on the angle φ between H and the easy axis.

A real magnet is assumed to behave as the sum of its individual crystallites, with their easy axes distributed uniformly inside a cone with semi-apex angle Θ^* , and is thus characterized by four parameters.

Experimental

The behaviour of a polycrystalline magnet as described above is based, of course, on approximations and assumptions. It is worth seeing whether a magnet behaves experimentally in accordance with this scheme.

We have made samples of two different qualities of Ferroxdure (a sintered Ba- or Sr-ferrite), labeled Fxd 1 and Fxd 2. The anisotropy field of these materials is known to be about 1.7 Tesla. ¹⁾

Fxd 1 was a commercial quality and from measurements of the remanent magnetization after magnetizing parallel and perpendicular to the easy axis, respectively, we found a value of Θ^* of about 33° and a saturation magnetization $\mu_0 M_s = 0.415$ Tesla. Fxd 2 was a laboratory sample with $\Theta^* = 15^\circ$ and a saturation magnetization $\mu_0 M_s = 0.465$ Tesla.

Of these materials we cut small spheres with a diameter of about 3 mm. The M vs H curves were measured using a PAR vibrating-sample magnetometer. This instrument measures the projection M_{ex} of M on the applied field H_{ex} . Before each measurement the samples were magnetized in a field of 2 Tesla along the easy axis and, at zero or small field, rotated to a fixed angle Θ between externally applied field H_{ex} and easy axis. Then H_{ex} was varied and the corresponding variation of M_{ex} recorded. Two sets of curves thus obtained are shown in figs. 5 and 6.

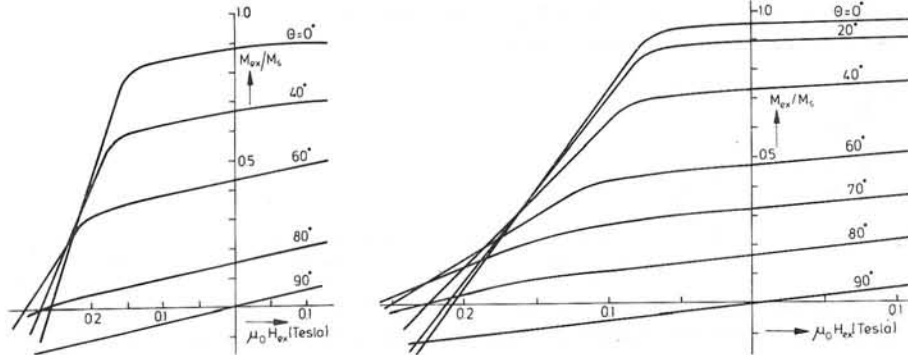


Fig. 5 M_{ex} vs H_{ex} curves of Fxd 1 spherical sample with the angle Θ between applied field H_{ex} and the easy axis as a parameter, each curve after magnetizing in a strong field along the easy axis.

Fig. 6 As fig. 5, for Fxd 2 spherical sample.

The actual field acting upon the material is the vector sum of the applied field H_{ex} and the self-demagnetizing field H_D , arising from the poles of the sample itself (fig. 7). Only for $\Theta = 0$ the vectors H_{ex} , H_D and M are parallel.

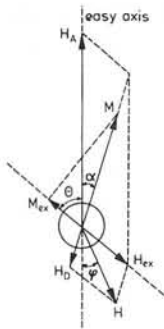


Fig. 7 Relative orientations of anisotropy field H_A , demagnetizing field H_D , applied field H_{ex} , vector sum H of H_{ex} and H_D , magnetization vector M , and its projection M_{ex} upon H_{ex} .

From the M_{ex} vs H_{ex} curves we derived the modulus of M as a function of the modulus of the total field H (figs. 8 and 9).

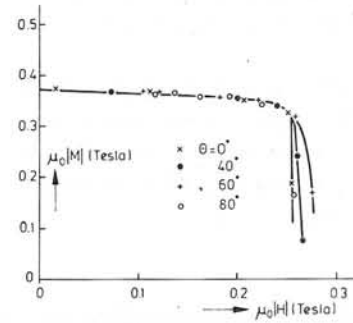


Fig. 8 Modulus of magnetization vector M versus modulus of total field H , with the angle Θ between applied field H_{ex} and easy axis as a parameter, for Fxd 1 sample.

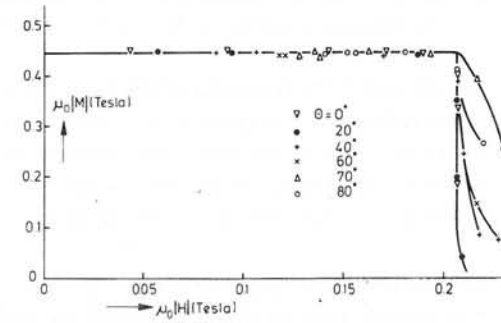


Fig. 9 As fig. 8, for Fxd 2 sample.

The curves are found to be independent of the angle Θ between H_{ex} and the easy axis, and $|M|$ is fairly constant up to a critical value H_r where its magnitude suddenly decreases. Obviously the individual crystallite magnetizations which together add up to M perform small rotations in fields up to H_r , at which value the reversal process occurs. A surprising fact is that H_r is practically independent of Θ .

This notion of small reversible rotations is further supported by the observation that a sample, being in its remanent state after having been magnetized along its easy axis, conserved this state after application and removal of any field H with modulus smaller than H_r .

These experiments thus confirm the validity of our model.

Model for a Polycrystalline Anisotropic Magnet

The behaviour of a single crystallite can generally be described as

$$M = M_0 + \underline{\chi} (H) \cdot H, \tag{7}$$

where $\underline{\chi}$ is a non-symmetric matrix dependent on H .

If we take M_0 as the main axis of the description and we expand the components of M up to terms quadratic in H/H_A we obtain

$$\underline{\chi} = \begin{vmatrix} 0 & -\frac{1}{2} M_s \frac{|H|}{H_A^2} \sin\Theta \\ -M_s \frac{|H|}{H_A^2} \sin\Theta & M_s/H_A \end{vmatrix} \tag{8}$$

For $|H| \ll H_A$, as we assumed, the non-diagonal elements remain small with respect to M_s/H_A and may be ignored. We then have for a single crystallite

$$\underline{\chi} = \begin{vmatrix} 0 & 0 \\ 0 & M_s/H_A \end{vmatrix} \tag{9}$$

For an aligned polycrystalline sample we assume that the non-diagonal elements may be neglected as well, and we write

$$\underline{\underline{\chi}} = \begin{vmatrix} \chi_{\parallel} & 0 \\ 0 & \chi_{\perp} \end{vmatrix}, \quad (10)$$

where χ_{\parallel} is the susceptibility along the easy axis and χ_{\perp} the susceptibility perpendicular to it. The spread in the individual crystallite orientations gives rise to a non-zero susceptibility along the average easy axis, but to a first approximation the contribution to the non-diagonal elements cancels out.

The usefulness of this matrix is experimentally confirmed by the agreement between a calculated and a measured M_{ex} vs H_{ex} curve for $\Theta^* = 33^\circ$ (fig. 10).

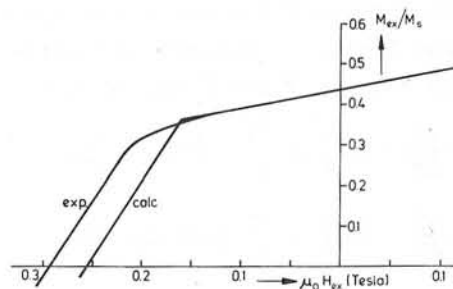


Fig. 10 M_{ex} vs H_{ex} calculated on the basis of the proposed model (see text) for $\Theta = 60^\circ$, compared with experiment. Difference in steep part of curves is due to arbitrary choice of reversal critical field H_r in model.

Incorporation of the Model into a Computer Program

A program for computing the field distribution in electromagnet systems consisting of isotropic soft magnetic material and electrical conductors can be used for permanent magnets by simply replacing M_0 by a current sheet and ignoring any $M(H)$. The magnet is then considered as ideal. This approach has been followed by Reichert²⁾ and Kamminga³⁾. A refinement was introduced by Slomczynska⁴⁾, which in our context is represented by the matrix of eq. (10) with χ_{\parallel} derived from the demagnetization curve along the easy axis of the magnet, and χ_{\perp} equal to the differential susceptibility of the same curve at $H = 0$.

Polak⁵⁾ has used a somewhat different approach, with χ_{\parallel} and χ_{\perp} both equal to the value of χ derived from the demagnetization curve along the easy axis, but with $H \cos \beta$ as argument (β being the angle between B and the easy axis). Polak's model was used by Schophuizen⁶⁾ for the analysis of loudspeaker systems, who obtained the satisfactory result of only a few percent difference between calculation and measurement.

Introduction of the present model with anisotropic χ , for which not only the $M-H$ curve parallel to the easy axis but also the perpendicular one is required, (on the understanding that initial magnetizing is done along the easy axis), might give more accurate results in more complicated designs where the magnetic vectors are expected to deviate substantially from the easy axis.

For Ferroxdure magnets, which are used in the majority of applications, knowledge of the M vs H curve perpendicular to the easy axis is not strictly required, as this curve is a straight line

with slope very close to M_s/H_A , even if alignment is not so perfect (see fig. 5). Technical data provided by the manufacturer therefore suffice in giving M_s , H_A , and the M vs H curve parallel to the easy axis (the second quadrant of the hysteresis loop), which also yield H_r .

Acknowledgement

Discussions with A.J.H. Wachters have greatly contributed to this paper.

References

- 1 J. Smit and H.P.J. Wijn, Ferrites (Wiley, New York, 1959) p. 204
- 2 K. Reichert, IEEE Trans. Mag. MAG-6, 283 (1970)
- 3 W. Kamminga, J. Phys. D (Appl. Phys.) 8, 841 (1975)
- 4 J. Slomczynska, IEEE Trans. Mag. MAG-10, 1109 (1974)
- 5 S.J. Polak, ISCA General 003, 11 (1974)
- 6 P.J. Schophuizen, private communication

Discussion following paper:

(Jannsens, Belgium) What is your position towards the model of Stomer and Wohlfarth? This model describes a hard magnetic material by means of an assembly of ellipsoids. The magnetization curve of such an ellipsoid exhibits reversible rotation and a sudden jump. May such an approach be compared with your model?

(Zijlstra, Philips, Eindhoven) The jumps in the SW model are rotation jumps that occur only at fields greater than $0,5H_A$. The reversal jumps discussed in my paper are independent from the rotation process and occur at fields on the order of $0,1 - 0,2 H_A$. They are associated with wall processes inside the crystal.

COMPUTATION OF MAGNETIC FIELDS IN NONLINEAR ANISOTROPIC MEDIA WITH FIELD DEPENDENT DEGREE OF ANISOTROPY

Peter Th. Weggler, CONTRAVES AG, Zurich, Switzerland

1. Summary [1]

Cold-rolled steel sheets with Goss texture are treated as non linear anisotropic media. Anisotropy, that is, the dependence of the permeabilities on the direction and magnitude of the vectors of the magnetic flux density \vec{B} and the magnetic field strength \vec{H} , is fully taken into account. In the algorithm for computing the field, the magnetic properties are separated into properties for the x-direction and properties for the y-direction (\equiv rolling direction). On the area in question a grid with meshes of different size is applied, which can be adjusted according to the geometrical structure and the convergence properties of the problem. The vector potential is used for the representation of the magnetic field. For the determination of the vector potential at each point of the grid a two step iterative procedure of pointwise successive over-relaxation is applied. The determination of the over-relaxation factor of each grid point is based on the geometrical structure near that point and on the history of the iteration process. The values of the magnetic properties are under-relaxed. Usually different under-relaxation factors are applied for the x- and y-directions. The field lines in a 45°-joint of a transformer are computed for various magnetic excitations.

2. Mathematical Formulation

Two dimensional static magnetic fields are computed. Equation (1) gives the vectorial relation between the magnetic flux density \vec{B} and the magnetic field strength \vec{H} .

$$\vec{B} = \mu_0 \cdot \|\mu_r\|(\vec{H}, \vec{B}) \cdot \vec{H} \quad (1)$$

In this equation the relative magnetic permeability is represented by a matrix. The elements of this matrix depend on the absolute value of \vec{B} and \vec{H} as well as on the direction of \vec{B} and \vec{H} relative to the rolling direction.

$$\vec{B} = \text{curl } \vec{A} \quad (2) \quad \text{div } \vec{A} = 0 \quad (3)$$

Equations (2) and (3) define the magnetic vector potential which is used for the representation of the magnetic field.

$$\text{curl } \vec{H} = \vec{J} \quad (4)$$

Equation (4) gives the relation between \vec{H} and the distributed current densities \vec{J} . By applying Stokes' s theorem and equations (1,2,4) a direct relation between \vec{J} and \vec{A} can be derived:

$$\oint_C (\nu_x \cdot \frac{\partial A}{\partial y} \cdot dx - \nu_y \cdot \frac{\partial A}{\partial x} \cdot dy) = \iint j \cdot dx \cdot dy \quad (5)$$

$$\sum_C (\nu_x \cdot \frac{\Delta A}{\Delta y} \cdot \Delta x - \nu_y \cdot \frac{\Delta A}{\Delta x} \cdot \Delta y) = \sum j \cdot \Delta x \cdot \Delta y \quad (8)$$

$$B_x = \frac{\partial A}{\partial y} \quad (6) \quad B_y = -\frac{\partial A}{\partial x} \quad (7)$$

ν_x and ν_y are the reciprocal permeabilities for the x- and y-directions respectively. Due to the representation of the magnetic properties the path C for computing the line integral (eq. (5)) is divided into components parallel to the x-direction and to the y-direction (\equiv rolling direction). If the differential expressions in equation (5) are replaced by difference expressions, we get equation (8) which is the basis for the numerical solution of the problem.

For the determination of the vector potential \vec{A} a grid divided into subsections with meshes of different size is applied on the area in question.

3. Magnetic Properties of Nonlinear Anisotropic Media [2], [3]

In ordinary soft magnetic materials the directions of the vectors of the magnetic flux density \vec{B} and the magnetic field

strength \vec{H} are parallel. In anisotropic materials the vectors \vec{B} and \vec{H} are generally not parallel to each other. Anisotropy is caused by a special crystalline structure of the material which can be obtained by means of different rolling processes and suitable annealings. Only properties of sheets with Goss texture are dealt with in this paper.

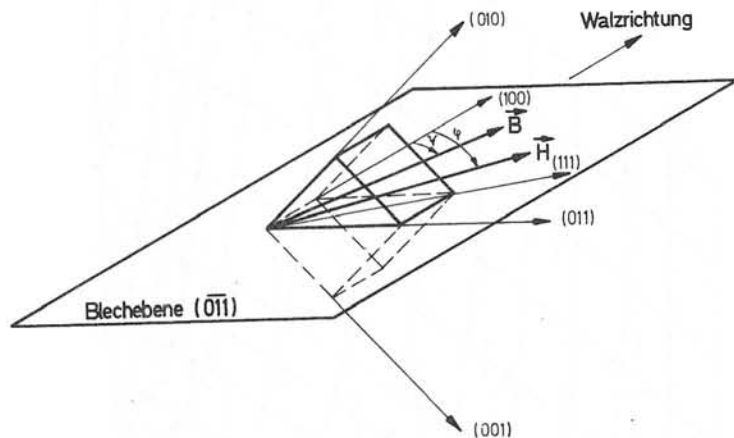


Fig. 1: Iron crystal in Goss position

Fig. 1 shows an iron crystal in Goss position. The (100)-direction is parallel to the rolling direction and represents the direction of light magnetization. The (011)-direction represents the direction of medium magnetization. The (111)-direction is the direction of strong magnetization. The (111)-direction and the (100)-direction form an angle of about 55°. All three directions are parallel to the surface of the sheet. ψ is the angle between \vec{B} and the rolling direction. φ is the angle between \vec{H} and the rolling direction. The properties of anisotropic materials can be represented by two sets of curves. Depending on the methods of measurement result the following sets of curves.

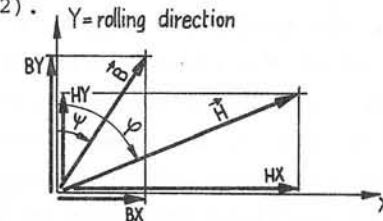
$$|\vec{B}| = |\vec{B}(\vec{H})|$$

$$\psi = \psi(\vec{H}) \quad \psi = \text{parameter}$$

$$\text{or } |\vec{B}| = |\vec{B}(\vec{H})|$$

$$\psi = \psi(\vec{H}) \quad \psi = \text{parameter}$$

The vectors \vec{B} and \vec{H} can be split into components parallel to and into components perpendicular to the rolling direction (see fig. 2).



$$URX = HX/BX$$

$$URY = HY/BY$$

Fig. 2: Split of \vec{B} and \vec{H}

The quotients URX and URY are the reciprocal values of the permeabilities in the x-direction and y-direction, provided that the y-direction is identical with the rolling direction of the sheet. Circle diagrams for \vec{B} are very useful for the description of the magnetic behavior of anisotropic sheets.

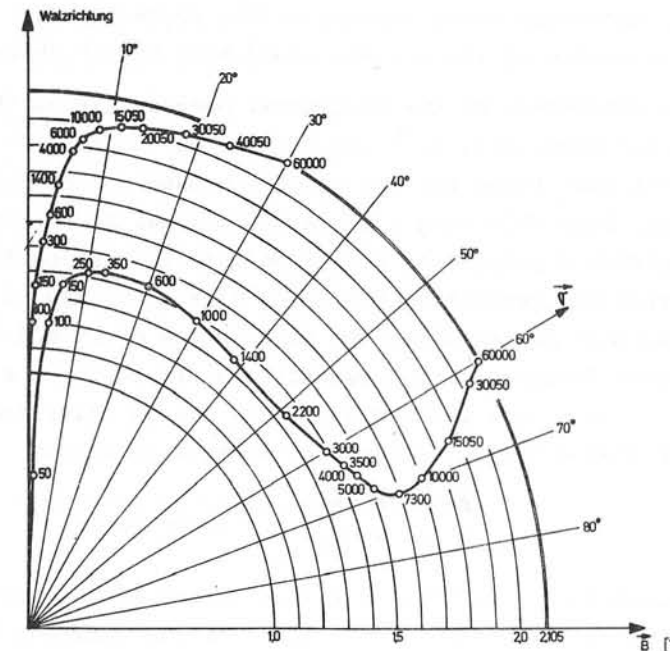


Fig. 3: Circle diagram for \vec{B} for $\varphi = 30^\circ$ and $\varphi = 60^\circ$

The curves in fig. 3 show the course of the top of the vector \vec{B} on the assumption that the direction of \vec{H} forms fixed angles of 30° and 60° with the rolling direction and that the absolute value of \vec{H} varies from zero to saturation. The figures on the curves are the absolute values of \vec{H} . The absolute values of \vec{B} are marked in the radial direction. If the fixed direction of \vec{H} forms an angle of less than 55° with the rolling direction (30° in fig. 3) the growing vector \vec{B} first remains near the rolling direction and then turns towards the fixed direction of \vec{H} . If the fixed direction of \vec{H} forms an angle of more than 55° with the rolling direction (60° in fig. 3) the growing vector \vec{B} first remains near the rolling direction too, but for increasing absolute values of \vec{H} the direction of \vec{B} turns away from the rolling direction and crosses the fixed direction of \vec{H} before falling together with it. It is remarkable that the absolute value of \vec{B} decreases in the area of strong angle deviation. The curves in fig. 3 are valid for sheets of the quality ARMCØ M6X, 0,014" thick.

A direct dependence of the reciprocal permeabilities (URX, URY) on the components of \vec{B} (BX, BY) and on the angle ψ respectively has been found for the algorithm used for computing the field. From this result three dimensional representations of the magnetic properties separated into properties for the x-direction and properties for the y-direction. Fig. 4 shows the reciprocal permeability URY in function of BY and ψ . These three dimensional representations are called magnetization surfaces. They can be calculated by means of linear interpolations in the sets of curves

$$\begin{aligned} |\vec{B}| &= |\vec{B}(\vec{H})| \\ \psi &= \psi(\vec{H}) \end{aligned} \quad \psi = \text{parameter}$$

The expression $P = URX/URY$ is called degree of anisotropy. It is defined as the ratio between the relative permeability in the rolling direction and the one perpendicular to the rolling direction. Fig. 5 shows the shape of P in function of

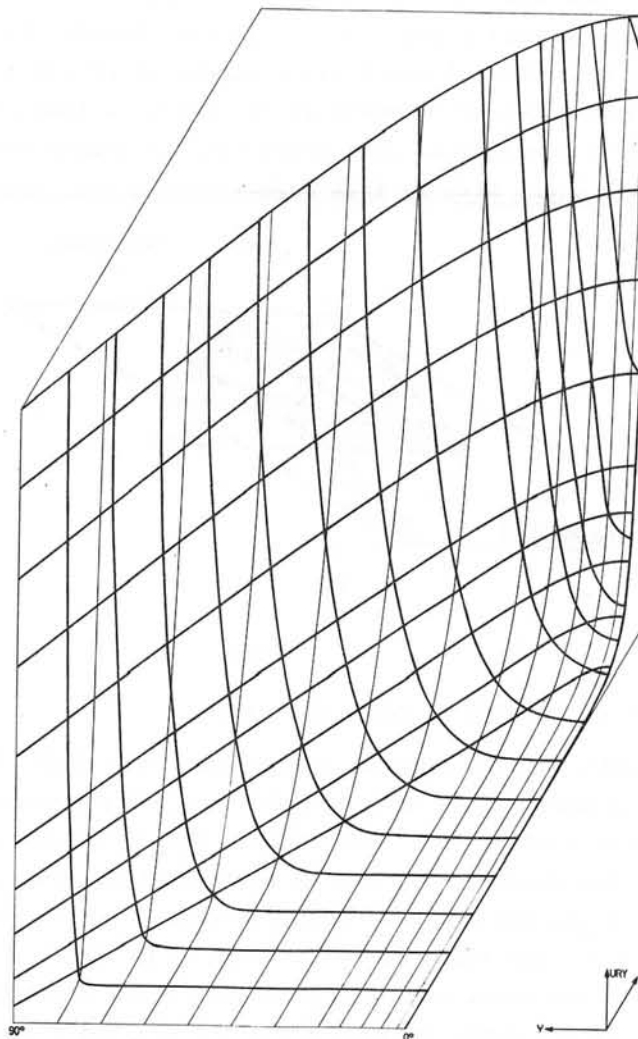


Fig. 4: Magnetization surface $URX = URX(BX, \psi)$

the absolute value of \vec{B} with ψ as parameter. For $\psi = 60^\circ, 70^\circ$ and 80° P can be less than 1. That means that the relative permeability perpendicular to the rolling direction is greater than the one parallel to the rolling direction.

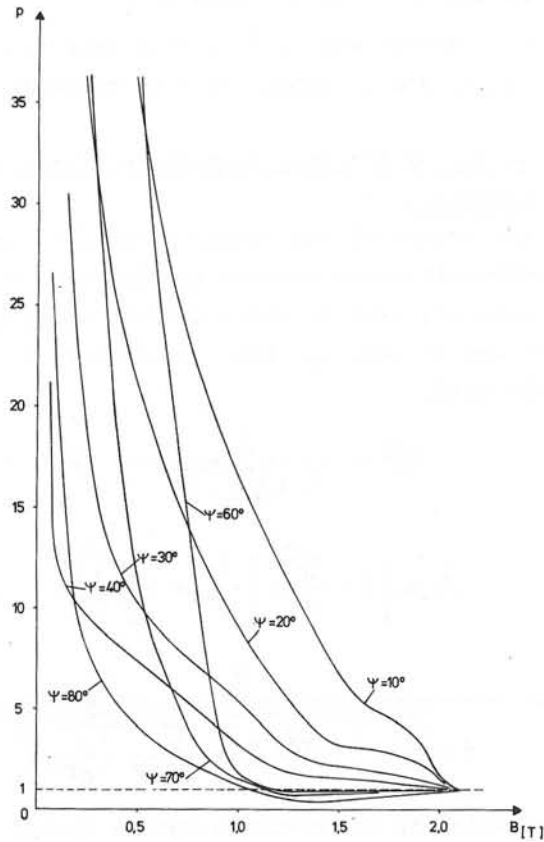


Fig. 5: Degree of anisotropy $P = P (|\vec{B}|), \psi$

4. Numerical solution

Fig. 6 shows the meshes surrounding a certain point of the grid used for the field computation. The procedure of computation of the vector potential $A (I)$ can be explained by means of the vector potential at point 27 in fig. 6. The diagonal which goes from point 27 to point 82 may be a boundary between two areas of iron in which the rolling directions form different angles with the y-axis of the coordinate system. Several auxiliary quantities must be determined. One of them is the vector potential $AS ()$ in the centers of gravity of

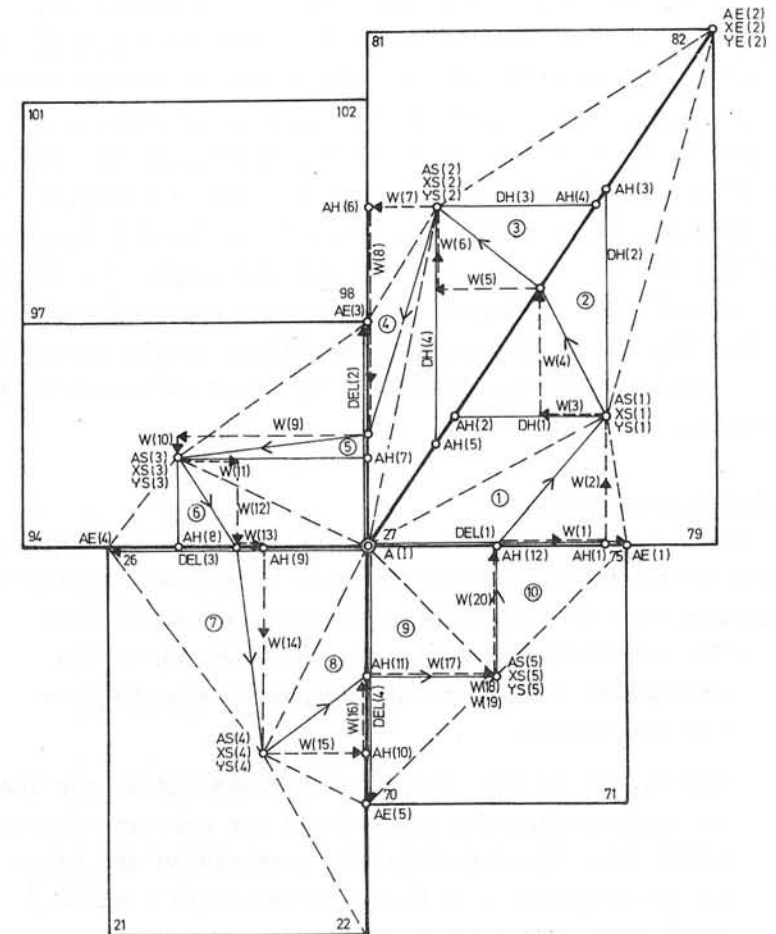


Fig. 6: Part of the grid

the rectangles or triangles, which is determined by means of the potentials on their contours. Because of the representation of the magnetic properties the path for computing the line integral (see eq. (8)) must be divided into components parallel to the x-direction and components parallel to the y-direction. ($W (1) \dots W (20)$ in fig. 6). A subdivision of the rectangles and triangles results from the position of the

centers of gravity within the rectangles and triangles and the mutual geometrical positions of the rectangles and triangles. The contours of these new basic triangles (1...10) caused by the subdivision are represented by dotted lines. Within such a basic triangle the magnetic properties are assumed to be constant. Crossing the boundaries the magnetic properties change discontinuously. For the determination of the permeabilities within the basic triangles the components of \vec{B} for the x- and y-directions and the angle ψ in the geometric centre of the basic triangle must be calculated. To do this the vector potential in auxiliary points called AH (1)... AH (12) must be calculated by means of linear interpolation.

5. Iteration procedure

For the computation of \vec{A} a two step iterative procedure of pointwise successive over-relaxation is applied. During one iteration step the following operations are performed:

- The components of the vector \vec{B} belonging to the grid point considered are computed from the vector potentials.
- The values of the reciprocal permeabilities for the x- and y-directions (called URX and URY) are determined from the magnetization surfaces on the basis of the components of \vec{B} and of the angle ψ which \vec{B} forms with the rolling direction. Appropriate transformations are necessary if the rolling direction doesn't correspond with the y-direction of the coordinate system.
- The values URX and URY are under-relaxed by the factors FX and FY. The values of the under-relaxation factors are computed during each iteration step. They depend on the nonlinearity of the magnetization surfaces, on the over-relaxation factor for \vec{A} and on the

acquired relative accuracy of \vec{A} .

- The vector potential \vec{A} is then computed with a line integral and is generally over-relaxed.

6. Determination of the over-relaxation factor for the vector potential

As a rule the values of the vector potentials are over-relaxed. Two over-relaxation factors are defined. The first one called WF (see eq. (9)) is valid for the whole grid. The second one called WL (see eq. (11)) is different at every point of the grid.

$$WF = \frac{2}{1 + \sqrt{1 - \lambda}} \quad (9)$$

$$\lambda = \left[1 - \frac{\pi^2}{4} \cdot \left[\frac{1}{P^2} + \frac{1}{Q^2} \right] \right]^2 \quad (10)$$

$$WL = \frac{2}{1 + \sqrt{1 - \left[1 - S^2 + 2S^2 \cdot \sqrt{\frac{1}{WF} - \frac{1}{WF^2}} \right]^2}} \quad (11)$$

The determination of the over-relaxation factor WF (see eq. (9)) for the whole grid is based on an average mesh and on the theory for the computation of linear fields. P and Q are expressions for the number of average meshes in the x- and y-directions respectively. For the determination of the local over-relaxation factor WL (see eq. (11)) a quantity S must be found which relates the specific geometrical configuration in the vicinity of a certain point to the geometrical configuration of the whole grid. During the iteration procedure the values of WF and WL are adjusted to the convergence.

7. Determination of the under-relaxation factor for the reciprocal permeabilities

The values of the reciprocal permeabilities (URX, URY) are under-relaxed.

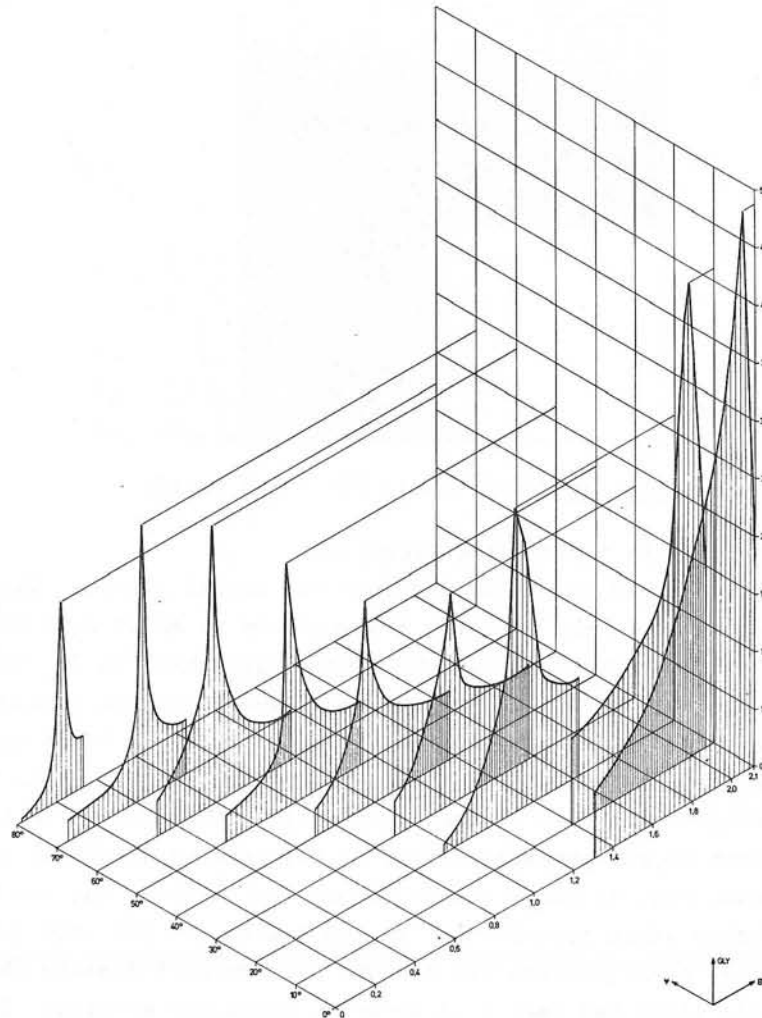


Fig. 7: Nonlinearity $GLY = GLY(BY), \psi$

Usually different under-relaxation factors (FX, FY) are applied for each point of the grid and for the x- and y-directions at each point (see eq. (12, 13)).

$$FX = \frac{WL - \beta}{\beta \cdot GLX} \quad (12) \quad FY = \frac{WL - \beta}{\beta \cdot GLY} \quad (13)$$

$$GLX = \frac{\partial URX}{\partial BX} \cdot \frac{BX}{URX} \quad (14) \quad GLY = \frac{\partial URY}{\partial BY} \cdot \frac{BY}{URY} \quad (15)$$

The values of the under-relaxation factors depend on the nonlinearity of the magnetic surfaces (GLX, GLY; see eq. (14, 15)), on the values of the local over-relaxation factors WL and on the acquired relative accuracy of A. β is a weight for the correction of the value of the reciprocal permeabilities and depends on the acquired relative accuracy of A and on the over-relaxation factor WL. Fig. 7 shows the nonlinearity GLY for the y-direction in function of BY for different values of ψ . The values of the under-relaxation factors are computed during each iteration step.

8. Computed examples

A 45° -joint of a transformer has been chosen as an example. Fig. 8 shows the grid used for the computation for two examples. The iron boundary is marked by fat lines. The rolling direction of the sheet is marked by arrows. The current regions are marked by 1 and 2. The meshes are large in the yoke and in the limb and smaller near the joint. The values for the reciprocal permeabilities correspond with the properties of sheets of the type UNISIL 51.

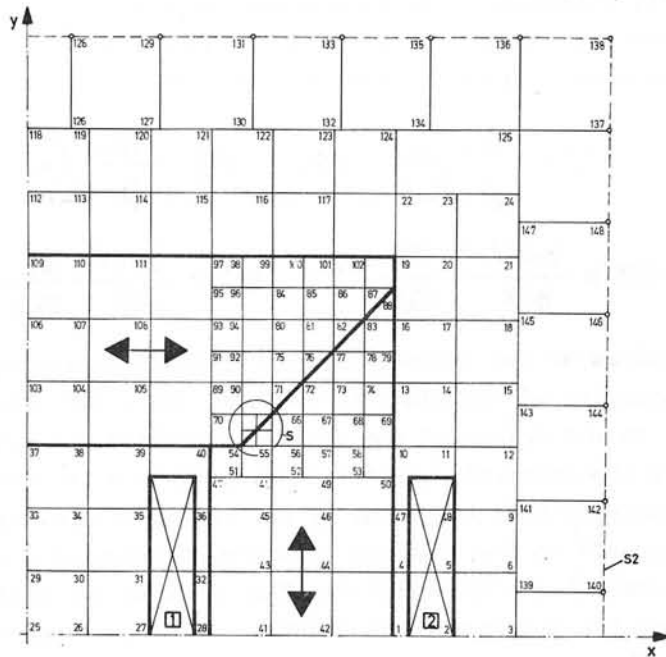
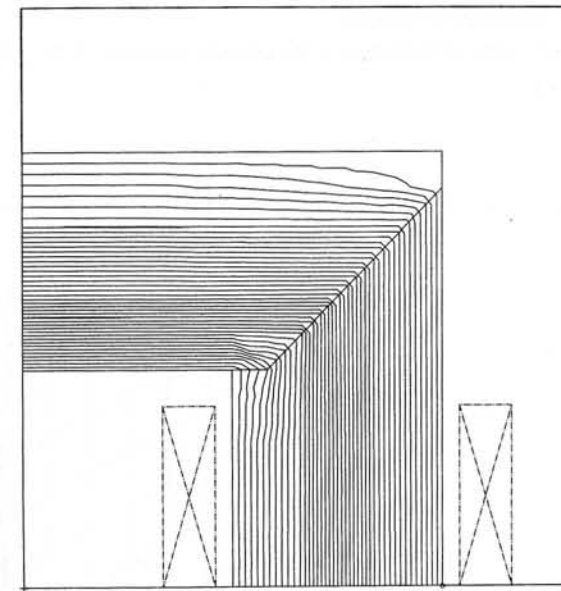


Fig. 8: Grid

The properties of the anisotropic material become evident especially with small values of the magnetic flux density. Fig. 9 shows the field lines of the first example. The average value of the magnetic flux density is about 0.9 Teslas. The relative accuracy of the vector potentials is about 10^{-4} . To get this result about 1600 iteration steps had been necessary. In the yoke as well as in the limb the field lines run almost parallel to the rolling direction. In the joint the field lines bend almost perpendicularly. This behavior has been proved by means of experiments with iron powder [4]. A compression of field lines can be observed near the inner iron boundary of the yoke, which indicates a concentration of flux. In the joint the flux distribution changes considerably. In the limb the main part of the flux runs in the middle. Only a small part of the flux in the yoke is forced to run perpen-

Fig. 9: Field lines; $|\vec{B}| = 0.9$ Teslas

dicularly to the rolling direction.

Fig. 10 shows the field lines of the second example. The average value of the magnetic flux density is about 1.75 Teslas. The relative accuracy of the vector potentials is $7 \cdot 10^{-5}$. To get this result about 1350 iteration steps had been necessary. In the vicinity of the junction the field lines in the yoke are displaced from the inner iron boundary towards the middle of the yoke. Thereby the part of the flux which is forced to run perpendicularly to the rolling direction is reduced. Fig. 11 shows the B-vectors (fat arrows) and the H-vectors (thin arrows) near the junction. For the same geometrical configuration and for the same current density the field lines had been calculated in isotropic material. If the two plots are laid one upon the other something like interference lines (see fig. 12) result. They clearly show the difference in the shape of field lines in anisotropic and isotropic material.

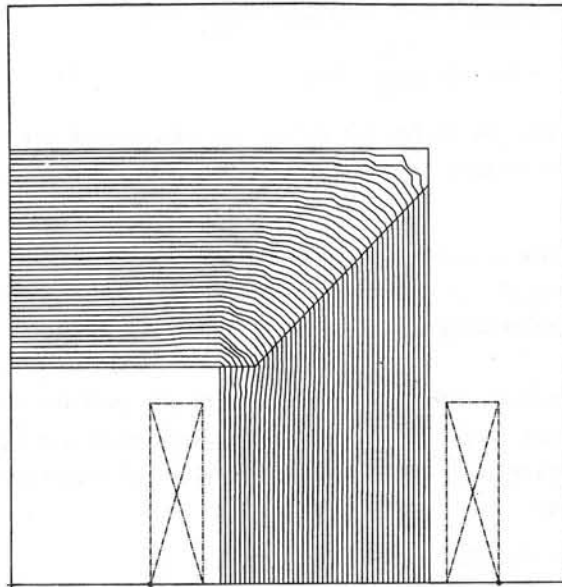


Fig. 10: Field lines; $|\vec{B}| = 1.75$ Teslas

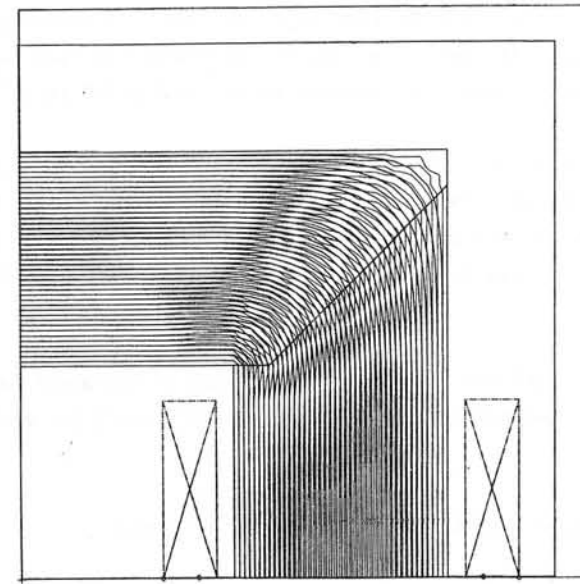


Fig. 12: Interference lines

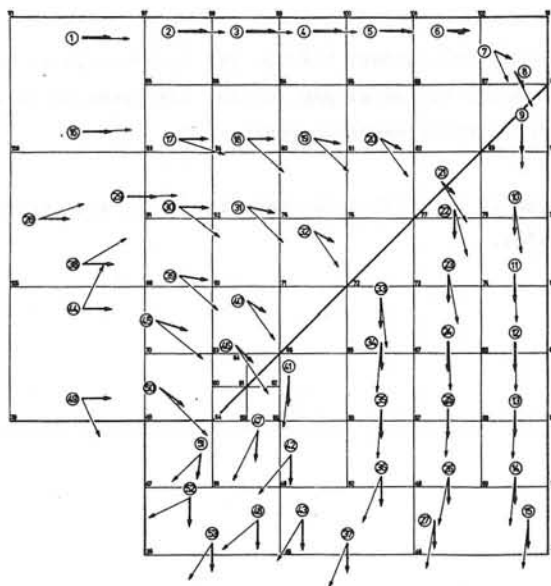


Fig. 11: B -and H-vectors

References

- [1] Weggler Peter Th.: "The computation of magnetic fields in nonlinear anisotropic media with field dependent degree of anisotropy". Thesis 5119/1973, Swiss Federal Institute of Technology.
- [2] Fasching, G.M. and H. Hofman: "Messeinrichtung für anisotrope Elektrobleche". Archiv für techn. Messen und industr. Messtechnik (ATM) 1969 R57 - R68, Lieferung 400
- [3] Gibler, F.: "Das magnetische Verhalten mechanisch beanspruchter anisotroper Ferromagnetika". Diss. TH. Wien, 1967.
- [4] Fasching, G.M., H.Hofman und M. Schückher: "Die magnetische Bezirksstruktur in der Umgebung eines Diagonalschnittes". Elektrotechnik und Maschinenbau 68 (1969), 41-44.

Discussion following paper:

(Lord, Cardiff) Has your approach been extended to 3 dimensions? In practice the joints are overlapped and the flux moves in (and out) to the next lamination - hence the problem is inherently 3-D in nature.

(Wegglar, Contraves AG) The problem is solved only for two dimensions. The airgap in the joint is assumed to be extremely small. The part of flux which moves in (and out) to the next lamination depends on the geometry of the air gap as well as on the flux density and is not taken into account.

(Phemister, C.A. Parsons) I should be grateful if you would say something about the measurement of the angle between \underline{B} and \underline{H} for various directions.

(Wegglar) Please consult the references in my paper.

(Polak, Philips) Could you tell us why the formulas shown were used for the computation of the different under relaxation factors.

(Wegglar) A basic five point representation of a grid point is assumed. For each point of the grid a residuum R can be defined:

$$R = \iint j \cdot dF - (By_1 \cdot vy_1 - Bx_1 \cdot vx_1 - - - - + By_4 \cdot vy_4)$$

$$\Delta R = -\Delta By_1 \cdot vy_1 - By_1 \cdot fy_1 \cdot \Delta vy_1 + \Delta Bx_1 \cdot vx_1 + - - - - - \\ -\Delta By_4 \cdot vy_4 - By_4 \cdot fy_4 \cdot \Delta vy_4$$

fx_i = under-relaxation factor for vx_i

fy_i = under-relaxation factor for vy_i

$$\Delta R \cdot \alpha = (\Delta R_A + \Delta R_{UR}) \cdot \beta \tag{1}$$

α = local over-relaxation factor for \vec{A}

β = weights for the indirect correction.

Direct correction:

$$\Delta R_A = -\Delta By_1 \cdot vy_1 + \Delta Bx_1 \cdot vx_1 + - - - - - -\Delta By_4 \cdot vy_4 \tag{2}$$

Indirect correction:

$$\Delta R_{UR} = -By_1 \cdot fy_1 \cdot \frac{\partial vy_1}{\partial By_1} \cdot \Delta By_1 + Bx_1 \cdot fx_1 \cdot \frac{\partial vx_1}{\partial Bx_1} \cdot \Delta Bx_1 \\ + - - - - - -By_4 \cdot fy_4 \cdot \frac{\partial vy_4}{\partial By_4} \cdot \Delta By_4 \tag{3}$$

If Eq. (2) and (3) are put in Eq. (4) we get the expressions for the under-relaxation factors fx_i and fy_i for the x - and y - directions.

(Endo, Japan) How to control the under-relaxation factors of transverse directions separately? I think it is difficult to control them for large "degree of anisotropy".

(Wegglar) Different under-relaxation factors are used for the x- and y- direction. They depend on the over relaxation factor for \vec{A} and on the relative accuracy of \vec{A} . The non linearity of the magnetic surfaces can be described by

$$\frac{\partial Vx}{\partial Bx} \cdot \frac{Bx}{Vx} \text{ for the x- direction and by}$$

$$\frac{\partial Vy}{\partial By} \cdot \frac{By}{Vy} \text{ for the y- direction.}$$

(Zijlstra) In practice the contact between the iron sheets is not perfect. What influence has an airgap, which, even when it is small, must represent a considerable magnetic resistance?

(Wegglar) An airgap is a considerable magnetic resistance especially at low magnetic fields.

Field Computation of Magnet made of Steel with Magnetic Anisotropy

T. Kasuga, E. Takasaki, A. Ando, M. Kihara and K. Endo

National Laboratory for High Energy Physics
Oho-machi, Tsukuba-gun, Ibaraki, Japan

Abstract

The grain oriented low carbon steel has been developed for the magnet core material of the proton synchrotron and proved to have superior magnetic properties when used properly. The grain orientation brings on the magnetic anisotropy which often leads to the different results against expectations. In order to get the clear view about the field properties of the quadrupole magnet made of the grain oriented steel, computations were carried out numerically by solving a set of difference equations on the square meshes of two dimensions. Computations were tried on the models with different orientations of magnetic anisotropy and compared with the magnetic field measurements on the full scale model magnets. In accordance with the experimental results, the marked differences were obtained for the different orientations of the grain.

§1. Introduction

Since an alternating gradient principle has been applied to a circular high energy particle accelerator, the weight of the magnet has been saved greatly. This advantage, however, requires higher quality of the magnetic field than ever met, in both bending and focusing fields. As inhomogeneities in the magnetic field will cause an undesirable effect on the beam behavior, the magnet should maintain good field configuration over the required aperture during the whole of an accelerating cycle. Steel for the iron core of the accelerator magnet has to be choosed carefully from the magnetic requirement such as low coercivity with small spread and high permeability with small spread at both low and high inductions. In addition to these magnetic properties, is also required good machinability to allow the precision stamping under the clearance of 0.02 mm or less. From these points of view, low silicon steel and low carbon steel have been used. These two kinds of steel show almost the same isotropic magnetic properties except that permeability is higher for low carbon steel.

On the other hand, iron in high purity form has superior magnetic properties in itself at both low and high fields, though its production needs very careful heat treatments for reduction of the harmful nonmetallic

impurities such as carbon and nitrogen which cause magnetic aging. And contents of carbon and nitrogen may be readily 0.003 and 0.005 %, respectively. Coercive force of this decarburized steel lowers remarkably by grain-growing treatment. During this grain-growing process which consists of cold rolling and hot annealing, anisotropy of the magnetic properties is developed. Permeability in the preferred direction raises and coercive force lowers appreciably without changing an ultimate saturation limit. The orientation of each grain in iron with preferred texture is within about 3 degrees to the rolling direction — (110)[001] textured iron. This type of steel is called as grain oriented (low carbon) steel.

Grain oriented steel has very large permeability to the direction of easy magnetization in accordance with the rolling direction, while its transverse has lower permeability. The merit of using grain oriented steel as the core material for the magnet of the proton synchrotron has been tested on the full scale models of the gradient dipole magnet.¹⁾ If the rolling direction of steel is aligned in the pole of the magnet to be perpendicular to the median plane in the air gap, the field quality is improved very much at high field. The same results were obtained from the calculations with an aid of the SIBYL program by assuming that permeability was isotropic one taken to the direction perpendicular to the median plane throughout the iron core. This assumption was based on the computational result that the flux lines inside the magnet pole was almost perpendicular to the median plane.

In the case of the quadrupole magnet, however, the magnetic properties of both transverse directions of steel have a role on the field in the air gap. Therefore, the same assumption must be avoided on this case, despite that the field computations were carried out by assuming the isotropic magnetic properties in the previous report²⁾ and showed the need for more detailed study to take the magnetic anisotropy of steel into consideration. First trial towards this problem was to take account of the directional dependence of the $B-\mu$ relation which was obtained experimentally.³⁾ This approach is rather easy because the $B-\mu$ relation to any direction can be calculated from the interpolation of the experimental data. This approach assumes the coincidence of the directions of the magnetic field and the magnetization. In general, these two directions do not coincide except for the direction of the easy magnetization. This indicates the second approach which treats permeability as a tensor quantity. In the case, the difference equations solving the vector potential in iron must be altered to deal with the tensor permeability. In this manuscript, both treatments are described

and tried by modifying the relaxation program LINDA.

§2. Computation of vector potential in anisotropic iron

For convenience of the computation, the air and iron regions are treated separately in two dimensions. That is, the magnetic field is treated by the modified scalar potential in the air and by the vector potential in the iron region both in square meshes. The computation mainly concerns with the iron region and the magnetic anisotropy is brought in the process of solving the vector potential field in iron.

2-1. Non-tensor form

An attempt to introduce the grain orientation effect into the field computation was undertaken by taking account of the directional dependence of the B-H characteristics shown in Fig.1 which were obtained by the Epstein test.⁴⁾ In the iron region where current does not exist, the Poisson equation describing the vector potential \vec{A} (0, 0, A) is transformed to

$$\nabla^2(\gamma A) = 0 \quad , \quad (1)$$

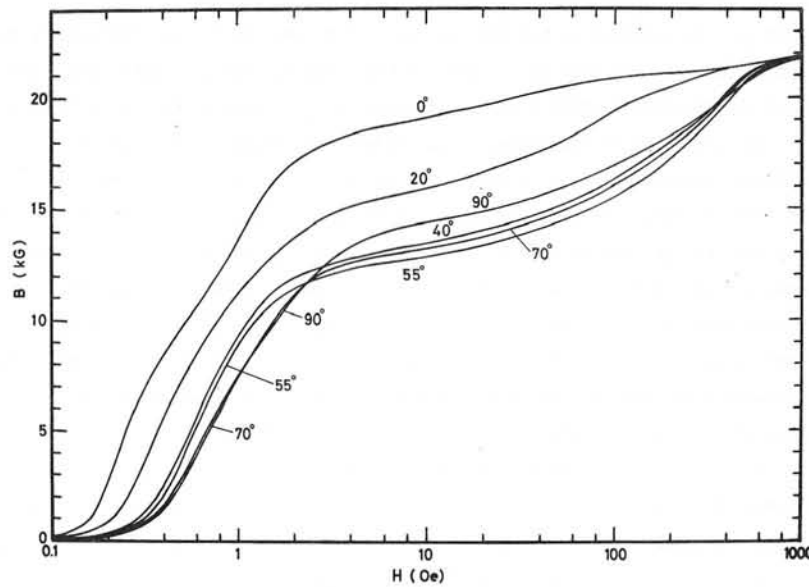


Fig.1 The B-H relation of the grain oriented steel. Figures mean the angles made by the rolling direction and the direction of the magnetizing force.

if the average reluctivity γ , reciprocal of permeability, is assumed between the adjacent mesh points.

Solving a set of the finite difference equations of eq.(1) by the successive over-relaxation method, components of the flux density at each mesh rectangle, B_x and B_y , are obtained from

$$\vec{B} = \nabla \times \vec{A} \quad . \quad (2)$$

Therefore, the direction of the flux line is given by

$$\theta = \tan^{-1} \left| \frac{B_y}{B_x} \right| = \tan^{-1} \left| \frac{dA}{dx} / \frac{dA}{dy} \right| \quad (3)$$

and the field strength by

$$H = \sqrt{H_x^2 + H_y^2} = \gamma \sqrt{B_x^2 + B_y^2} \quad . \quad (4)$$

Thus, the new γ is obtained by the linear interpolation between the input data of $B^2 - \gamma$ relations of both transverse directions, rolling and its perpendicular taken in the plane of the lamination.

In this treatment, the flux density along the direction with the angle θ with respect to the rolling direction at the field strength H can be represented as

$$B = (B_L(H) \cos^2\theta + B_C(H) \sin^2\theta) f(\theta, H) \quad , \quad (5)$$

where $B_L(H)$ and $B_C(H)$ stand for the flux density along the rolling direction and its transverse, respectively. An analytic function $f(\theta, H)$ is determined to reproduce the experimental B-H relations.⁵⁾

By using new γ values in every iteration cycle, the whole process in the iron region is repeated until the change in reluctivity per cycle become below a specified value for all mesh rectangles.

2-2. Tensor form

If the tensor quantity of permeability is given by ${}^2\mu$, the flux density is

$$\vec{B} = {}^2\mu \vec{H} \quad (6)$$

where

$${}^2\mu = \begin{pmatrix} \mu_{11} & \mu_{12} \\ \mu_{21} & \mu_{22} \end{pmatrix} \quad ,$$

$$\vec{B} = \begin{pmatrix} B_x \\ B_y \end{pmatrix} \quad \text{and} \quad \vec{H} = \begin{pmatrix} H_x \\ H_y \end{pmatrix} \quad . \quad (7)$$

In order to satisfy the symmetry for the rotation of the coordinates, tensor must be diagonal, that is,

$${}^2\mu = \begin{pmatrix} \mu_x & 0 \\ 0 & \mu_y \end{pmatrix}, \quad (8)$$

when the direction of the easy magnetization coincides with the axis of the coordinate. If μ_x refers to permeability in the direction of rolling, μ_y is taken to be its transverse. Tensor of reluctivity ${}^2\gamma$ is obtained from the relation

$$\gamma_{ik} = \frac{1}{|{}^2\mu|} \frac{\partial |{}^2\mu|}{\partial \mu_{ki}}. \quad (9)$$

Then,

$${}^2\gamma = \begin{pmatrix} \frac{1}{\mu_x} & 0 \\ 0 & \frac{1}{\mu_y} \end{pmatrix} = \begin{pmatrix} \gamma_x & 0 \\ 0 & \gamma_y \end{pmatrix}. \quad (10)$$

Using these expressions, the Poisson equation in the iron region is expressed as follows,

$$\frac{\partial}{\partial x} (\gamma_y \frac{\partial A}{\partial x}) + \frac{\partial}{\partial y} (\gamma_x \frac{\partial A}{\partial y}) = 0. \quad (11)$$

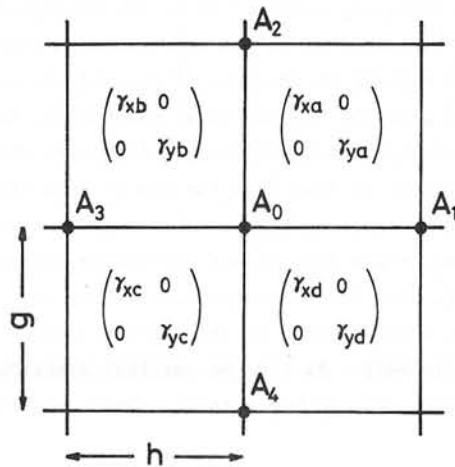


Fig.2 Tensor reluctivity in each mesh rectangle to derive the finite difference equation.

In the mesh rectangles shown in Fig.2, the finite difference equation of eq.(11) is given by

$$\frac{\gamma_{ya} + \gamma_{yd}}{h^2} A_1 + \frac{\gamma_{xa} + \gamma_{xb}}{g^2} A_2 + \frac{\gamma_{yb} + \gamma_{yc}}{h^2} A_3 + \frac{\gamma_{xc} + \gamma_{xd}}{g^2} A_4 - 4 \left(\frac{\bar{\gamma}_y}{h^2} + \frac{\bar{\gamma}_x}{g^2} \right) A_0 = 0, \quad (12)$$

where γ_x and γ_y in each mesh rectangle are expressed by adding suffixes (a,b,c and d) as shown in Fig.2, and

$$\bar{\gamma}_x = \frac{1}{4} (\gamma_{xa} + \gamma_{xb} + \gamma_{xc} + \gamma_{xd})$$

$$\bar{\gamma}_y = \frac{1}{4} (\gamma_{ya} + \gamma_{yb} + \gamma_{yc} + \gamma_{yd}). \quad (13)$$

h and g are the horizontal and vertical mesh sizes, respectively. If permeability is isotropic, that is, $\gamma_x = \gamma_y (\equiv \gamma)$, eq.(12) becomes the difference equation of the ordinary isotropic problem,

$$\frac{\gamma_a + \gamma_d}{h^2} A_1 + \frac{\gamma_a + \gamma_b}{g^2} A_2 + \frac{\gamma_b + \gamma_c}{h^2} A_3 + \frac{\gamma_c + \gamma_d}{g^2} A_4 - 4\bar{\gamma} \left(\frac{1}{h^2} + \frac{1}{g^2} \right) A_0 = 0, \quad (14)$$

where

$$\bar{\gamma} = \frac{1}{4} (\gamma_a + \gamma_b + \gamma_c + \gamma_d). \quad (15)$$

In order to solve eq.(12), the initial values of γ_x and γ_y are assumed to be 0.0002. After every iteration, angles given by eq.(3) are calculated at all meshes and new reluctivities of both transverse directions are recalculated by the linear interpolation of $B_x^2 - \gamma_x$ and $B_y^2 - \gamma_y$ tables which are obtained experimentally. The problem is likely to diverge unless the iterative increments or decrements of reluctivities of both directions are limited each other. Among several trials, limitations such as

$$\langle \Delta\gamma_x \rangle = \frac{\beta |\Delta\gamma_x \cdot \Delta\gamma_y|}{(|\Delta\gamma_x| + |\Delta\gamma_y|)^2} \Delta\gamma_x$$

$$\langle \Delta\gamma_y \rangle = \frac{\beta |\Delta\gamma_x \cdot \Delta\gamma_y|}{(|\Delta\gamma_x| + |\Delta\gamma_y|)^2} \Delta\gamma_y$$

(16)

seems to be good. $\Delta\gamma_x$ and $\Delta\gamma_y$ are the changes of the transverse reluctivities at some mesh rectangle after iteration and β is the under-relaxation factor. The problem converges very slow, so the iteration cycles are limited to a few hundreds.

After computation of the iron region, the vector potential is transformed to the scalar potential to get the scalar boundary values on the air-iron interface. Changes of the scalar potential along the horizontal and vertical mesh lines are given by $-\int \gamma_x \frac{\partial A}{\partial y} dx$ and $\int \gamma_y \frac{\partial A}{\partial x} dy$, respectively. If the scalar potential is obtained according to these integrals, the boundary conditions at the air-iron interface are satisfied in the following iterative relaxation in the air region.

§3. Field problems and their results

At the medium field level for which permeabilities of both transverse directions are expected to be very high, the field distribution in the air gap is mainly determined by the shape of the pole profile. So, the design calculations on the quadrupole magnet for the lattice focusing element to be used in the main ring of KEK proton synchrotron were carried out regardless of the magnetic anisotropy. Fig.3 shows the pole profile and the cross-sectional view of the quadrupole magnet. The rolling direction of the grain oriented steel was selected to be perpendicular to the horizontal median plane. The magnet of this type is referred as the vertically oriented one. In the same meaning, the horizontally oriented one means that the rolling direction is parallel to the horizontal median plane. The full scale models of both types were made of the laminated steel with the magnetic anisotropy shown in Fig.1. Thickness of the lamination is 1 mm.

Magnetic field was computed for the asymmetric configuration of Fig.3, although the pole profile underwent the slight modification so as to correct the field quality at the high field by using the experimental data on the full scale models. The field quality deteriorates due to the saturation

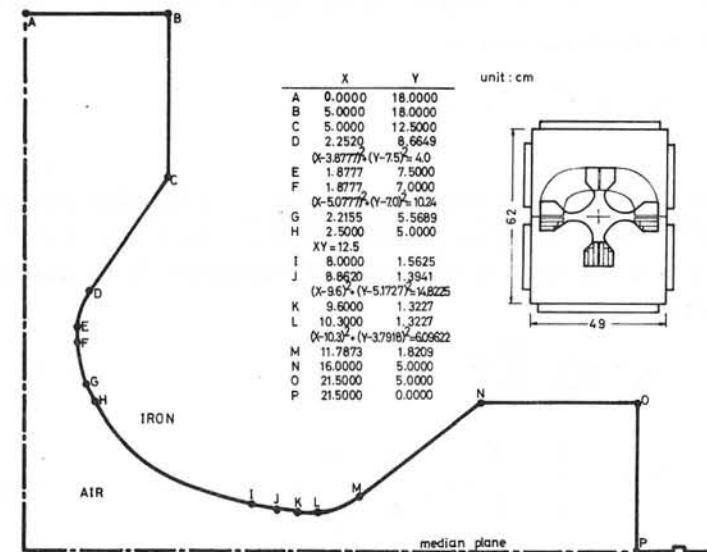


Fig.3 The pole profile and the cross-sectional view of the quadrupole magnet.

around the minimum gap on the horizontal median plane where the flux density in iron becomes high, say about 19 kG at the maximum excitation level. While the field distribution on the vertical axis does not deteriorate, because the flux density at the nose of the pole is not so high.

Fig.4 and 5 give the computational results for the vertically and horizontally oriented magnet, respectively. Also, are shown the experimental data⁶⁾ whose accuracy is $\pm 0.1\%$ by the search coil method. The difference between two approaches is evident for the horizontal distribution of the vertically oriented case (Fig.4) and the tensor approach fits in the experimental data well. For the horizontally oriented case (Fig.5), however, they give the similar distributions of the field gradients and explain the experimental data fairly well. As for the vertical distributions, the difference between the computation and the magnetic field measurement is very small in two cases.

To compare the grain oriented cases with the non-oriented case, the quadrupole magnet with the same size was made of the low silicon steel and its field was measured. Fig.6 contains the results of the experiment and

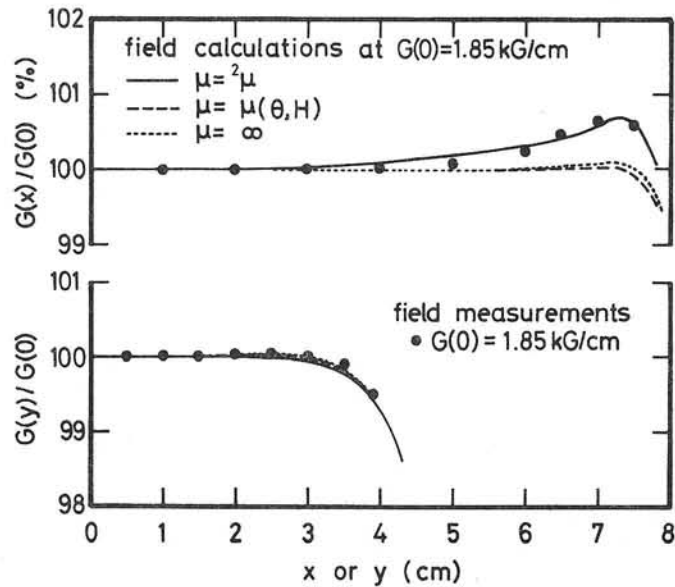


Fig.4 Distributions of field gradients on the horizontal (upper) and vertical (lower) median planes for the vertically oriented quadrupole magnet. Solid circles are the experimental data.

the computation. As the magnetic properties of the non-oriented magnet, was assumed the compiled $B^2 - \gamma$ table in the original program.

Generally, the magnetic flux lines are not parallel with the magnetizing force in the media with magnetic anisotropy. In computation, two curves of 0 and 90 deg. in Fig.1 were assumed for the transverse magnetic properties. But it is difficult to derive another curves from these ones at the present stage of the work even if the angular difference between B and H is taken into account. It is rather interesting that the second approach gives the good coincidence with the magnetic measurement.

Authors should like to express their thanks to Prof. T. Nishikawa for his continuous interest and invaluable discussions. They also acknowledge Messrs T. Igarashi and A. Araki for their efforts paid to the field measurements.

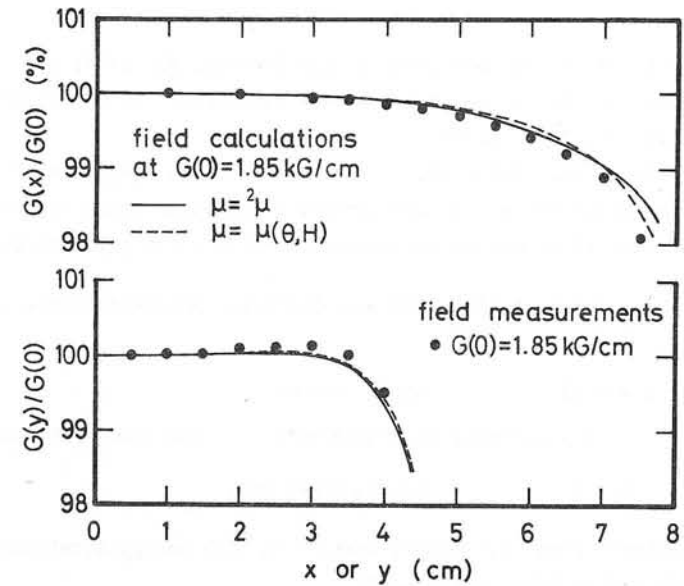


Fig.5 Same as in Fig.4 for the horizontally oriented quadrupole magnet.

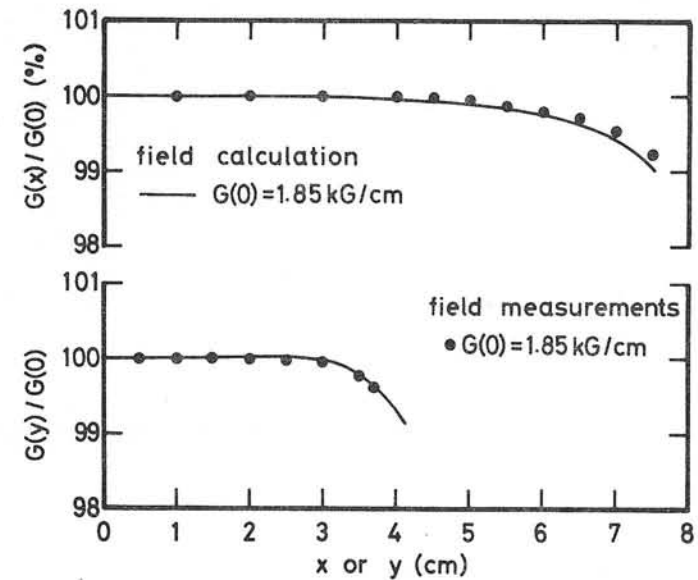


Fig.6 Same as in Fig.4 for the non-oriented quadrupole magnet.

References

- 1) T. Doke et al, Nuclear Instrum. and Methods, 83 (1970) 300
- 2) K. Endo and M. Kihara, Proc. of 4th Intl. Conf. on Magnet Technology, Brookhaven, 1972, p.306
- 3) K. Endo et al, IEEE Trans. on Nuclear Science, NS-20 (1973) 716
- 4) The experimental curves were provided by Nippon Steel Corporation.
- 5) Function $f(\theta, H)$ may be approximated within a few percents by

$$f = 0.025 \sin 6\theta + 1/\{0.4+2.35\alpha+(0.6-2.35\alpha)(\sin\theta+\cos\theta)\},$$

where

$$\begin{aligned} \alpha &= 0.25 \quad , \quad \text{for } H > 600 \text{ Oe} \\ &= -5.3 \times 10^{-7} H^2 + 7.3 \times 10^{-4} H + 2 \times 10^{-3} \quad , \quad \text{for } 40 < H \leq 60 \text{ Oe} \\ &= 0.0 \quad , \quad \text{for } 0 \leq H \leq 40 \text{ Oe} . \end{aligned}$$

- 6) M. Kihara, Proc. U.S.-Japan Seminar on High Energy Accelerator Science, Tokyo and Tsukuba, 1973, p.134

Fields Involved in Magnetic Recording on Moving Steel Strip

by E. M. Deeley and L. Hayali

Summary

A finite-difference method is described for solving field distributions relating to magnetic recording on steel strip, in which hysteresis, eddy-currents, and strip motion are taken into account. The method is sufficiently general to allow other nonlinear phenomena to be studied. A hysteresis model based on the arctan function is used which can be adjusted to approximate practical loops sufficiently closely.

An implicit time-stepping method is used together with nonlinear over-relaxation which gives convergence rates comparable with those for linear problems, even when the medium is heavily saturated. The inherent stability of the implicit method allows large time steps to be taken, particularly during the initial transient period.

An alternative method using equivalent currents to represent magnetization has also been used.

1. INTRODUCTION

The accurate measurement of the speed of moving steel strip by pulse or sinusoidal magnetization methods has led to the need for a better understanding of the recording process itself. Various studies of recording on non-conducting media have been made^{1,2,3} but the process of recording onto steel does not appear to have been studied in detail. The representation of hysteresis is a necessary feature of the computation, but as remnant magnetization is fundamental to the process it is not possible to employ complex permeability and a more physical model of hysteresis must be used. In addition, eddy-currents and the motion of the recording medium must be taken into account.

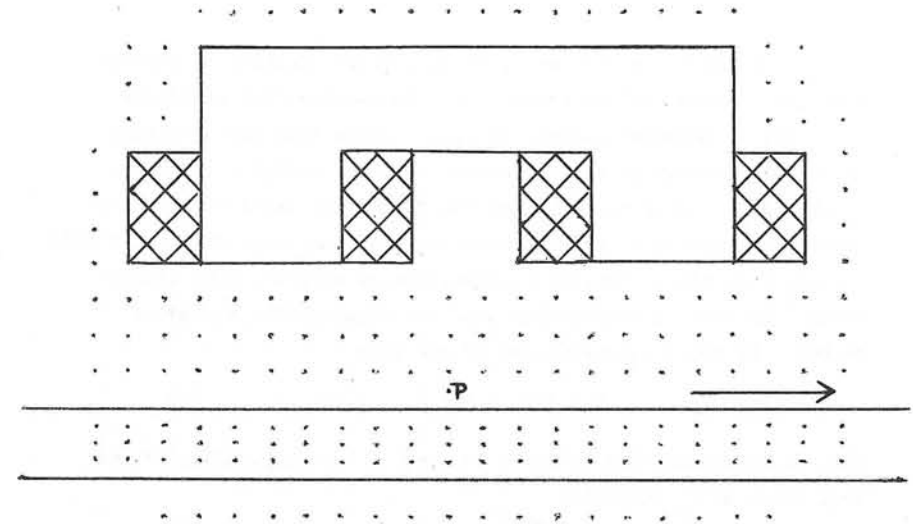


Fig. 1. Recording Head and Strip (current coils shown hatched)

The arrangement of the ferrite recording head, exciting coils, and steel strip is illustrated in fig. 1. A square mesh is used with a 3mm spacing, reducing to a rectangular mesh in the strip. This reduction ratio, and the node spacing in general, can be easily modified. In practice it is desired to study the effect of the separation between recording head and strip over a frequency range of approximately 4-250 Hz, and of strip speed.

The programme developed to simulate this process has also been used to study other nonlinear phenomena.

2. THE COMPUTATIONAL METHOD

Various finite-difference methods have been used to solve nonlinear magnetic field problems, including alternating-direction and extended Liebmann methods. In the present work the parabolic diffusion equation :

$$u_{xx} = k_1 u_t + k_2 u_x \quad (1)$$

is solved by an implicit time-stepping method. The simplest scheme

is that described by O'Brien ⁴, while greater accuracy is possible with the Crank-Nicholson scheme ⁵ at the expense (for nonlinear problems) of somewhat greater storage. These have the advantage that the equations solved are essentially the elliptic equations of the equivalent static problem, the additional terms due to time variation behaving as source terms, so that the computation is stable for any time step. Nonlinear relaxation as originated by Lieberstein ⁶ is used in conjunction with the Gauss-Seidel iterative method. If the N equations are of the form :

$$g_p(x_1, x_2, \dots, x_N) = 0 \quad p = 1, 2, \dots, N \quad (2)$$

then an overrelaxation factor ω is used in the computation of the next value of x_p such that :

$$(x_p)_{n+1} = (x_p)_n - \omega \left(\frac{dx_p}{dg_p} \right) (g_p)_n \quad (3)$$

where n refers to the nth iteration. The derivative appearing in this equation is calculated node by node, making use of the most recently corrected results as in the linear SOR method. This calculation is straightforward if analytic expressions are used for the non-linearities present, and the rate of convergence is comparable with that for linear problems.

Writing the non-linear relationship between B and H as :

$$B = \mu_o f(H) \quad (4)$$

then for the conventional

five-point star in the

x-y plane as shown in fig. 2,

for which the node spacing, h, is the

same for each connection, the z-component of Curl H becomes :

$$\begin{aligned} (\text{Curl H})_z &= \frac{1}{\mu_o h} \left[f^{-1}(B_{03}) - f^{-1}(B_{20}) \right] - \frac{1}{\mu_o h} \left[f^{-1}(B_{10}) - f^{-1}(B_{04}) \right] \\ &= \frac{1}{\mu_o h} \sum_{i=1}^4 f^{-1} \left(\frac{A_o - A_i}{h} \right) \end{aligned} \quad (5)$$

which can be equated to J_z in accordance with Maxwell's equation.

For moving media the vector current density is :

$$\bar{J} = \sigma(\bar{E} + \bar{v} \times \bar{B}) \quad (6)$$

where \bar{v} is the velocity vector. If the only component of \bar{v} in the two-dimensional case is v_x , then (6) becomes :

$$J_z = -\sigma \frac{\delta A}{\delta t} - \sigma v_x \frac{\delta A}{\delta x} \quad (7)$$

Using a backwards difference expression for $\delta A/\delta t$, and a central difference expression for $\delta A/\delta x$, averaged between the present and previous time steps, equation (7) becomes :

$$J_z = -\frac{\sigma}{\Delta t} \left[(A_o)_{k+1} - (A_o)_k \right] - \frac{\sigma v_x}{4h} \left[(A_3)_{k+1} + (A_3)_k - (A_1)_{k+1} - (A_1)_k \right] \quad (8)$$

where k and k+1 refer to successive time steps and Δt is the length of the step. Combining this with equation (5) to form Curl H - J=0 gives

$$g_p(A_o) = 0 \quad (9)$$

The values of $(A)_k$ in the conducting region, must therefore be stored, and this formulation is then essentially that of O'Brien et al. If values of Curl H at the kth step are also stored and averaged with those calculated by equation (5), the Crank-Nicholson form is obtained. In this method independent values of H, and hence of incremental permeability, are attributed to each connection in the 5-point star.

Differentiating $g_p(A_o)$ with respect to A_o gives :

$$\frac{dg(A_o)}{dA_o} = \frac{1}{\mu_1} + \frac{1}{\mu_2} + \frac{1}{\mu_3} + \frac{1}{\mu_4} + \frac{\sigma \mu_o h^2}{\Delta t} \quad (10)$$

where $\mu_1 \dots \mu_4$ are the slopes df/dH of the nonlinear B-H functions at the four operating points, and is the factor required for the nonlinear over-relaxation of equation (3).

Modified forms of equations (5) can be found for nodes on the boundary of the non-linear medium, or where a change of mesh size takes place, or where both occur together. In computing vector potential it is convenient to allow the numerical values to represent A/h at each node, as this quotient appears in the non-linear functions. This representation is therefore also used in the remainder of the field, the exciting current appearing in the form I/h , where I is the actual current concentrated at a node.

An Equivalent Current Method

By using for Curl H the expression :

$$\text{Curl H} = \frac{1}{\mu_0} \text{Curl B} - \text{Curl M}$$

and representing Curl M by an equivalent current, J_e , there results :

$$\text{Curl B} = \mu_0 (J + J_e)$$

or in vector potential terms :

$$\nabla^2 A = -\sigma\mu_0 \frac{\delta A}{\delta t} - \sigma\mu_0 v_x \frac{\delta A}{\delta x} + \mu_0 J_e \quad (11)$$

In this approach, which has been used in an integral method by Robertson and Zaky⁷, the nonlinear properties of the medium are contained in J_e . In the finite difference version of this method the equivalent currents are calculated after each complete sweep of the field used to calculate the values of A , so that acceleration of both A and J_e can be used. If a node-by-node computation of J_e is used the method reduces to a Curl H formulation similar to that already described.

The equivalent current method has proved successful for thin structures of not more than two node spacings in depth, where with appropriate choice of both acceleration factors it converges rapidly. For thicker regions however, the method traps residuals so that the convergence rate is slow.

3. THE HYSTERESIS MODEL

Several hysteresis loop models of varying degrees of complexity have been proposed to represent metallic and non-metallic magnetic materials. These include piecewise-linear^{2,8}, simple algebraic and trigonometrical functions used in conjunction with variable control parameters^{1,9,10}, and more complex models using two or more non-linear functions¹¹. A necessary feature of any model is the ability to represent minor loops, and in the simulation of a hysteresis motor Jackson⁸ has used a piecewise-linear model with five control parameters which operates in any of nine different modes. Sawamura and Iwasaki have also used such a model in studying tape recording processes². Simple algebraic expressions may not fit practical loops particularly closely but have the advantage of simplicity and speed when the hysteresis routine is to be accessed many times. The model described by Everatt based on the Fröhlich equation⁹ is probably the most suitable. Certain simple functions fit practical loops more closely^{1,12} at the expense of greater computing time, particularly if the inverse of the function is required. This is usually a problem if H is to be computed from B . Chua and Bass have described a very comprehensive model¹¹ making use of several functions which also represents dynamic effects, but would be prohibitively time-consuming in an iterative process.

In the present work the arctan function is used, shifted in position along the H -axis when the flux change is reversed in order to follow the major and minor loops¹. This is used to represent magnetization, to which $\mu_0 H$ is added to obtain flux density. The model can be adjusted to provide a close fit to actual static loops, such as those obtained for a steel sample by Zakrzewski and Pietras¹³.

4. TRANSPORT EFFECTS

The magnetization of the strip is transported at the strip velocity and this effect must be represented at each time step. This is particularly easily arranged when the velocity is one node per time step, interpolation being necessary for other speeds.

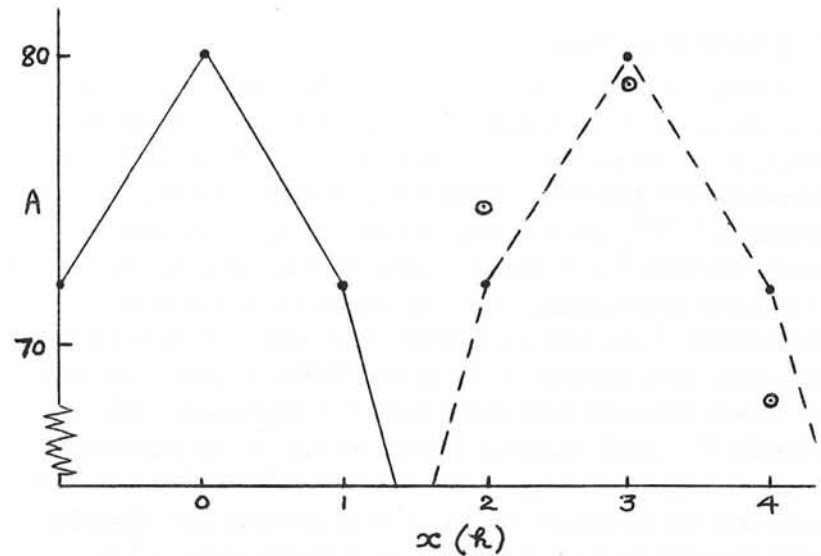


Fig. 3 Original distribution - solid line
Ideal distribution - broken line
Actual nodal values - circles

In the equivalent current method the J_e values represent the magnetization. Another transport effect is represented by the terms containing σ , and for an idealized situation when σ becomes infinite equation (9) reduces to :

$$-\frac{\partial A}{\partial t} = v_x \frac{\partial A}{\partial x} \quad (11)$$

In these circumstances the vector potential pattern should be transported in the x -direction with velocity v_x , unchanged in form. The accuracy with which this transport effect is simulated depends on the truncation errors introduced by the finite-difference approximation to equation (11) and has been studied using a one-dimensional model. Figure 3 shows how the peak of a gaussian-shaped potential distribution starting a node 0 is modified after being transported over a distance $3h$ in 15 time steps. The solid curve indicates the initial distribution with the actual values at nodes indicated by circles, while the broken line shows the ideal distribution 15 time steps later. The backward time difference

and central space difference averaged between time steps used in equation (8) leads to actual potential values illustrated by circles in Figure 3. An attenuation of the distribution by about $\frac{1}{2}\%$ at its peak is observed, while there is a lagging effect in the velocity of the distribution of approximately 10% below the expected velocity. When a higher order approximation to $\partial A/\partial x$ is used however, so that the truncation error is reduced to $O(h^3)$, the error in the velocity is reduced to less than 1%.

Experiments with higher order approximations to both derivatives indicate that the amplitude error is reduced by reducing the truncation error in $\partial A/\partial t$, while the velocity error responds to improved expressions for $\partial A/\partial x$. Various methods have been devised for reducing errors in the computation of equation (11), which have been summarized by Ames¹⁴ and further reduction of the above errors is possible, although not necessary in the present study where the major transport effect is by remnant magnetization.

A further effect caused by the moving medium is the build-up of spurious vector potential values at points of entry to, and exit from, the computed field. This is particularly severe if a boundary condition of $A=0$ is imposed, but can be reduced by employing a derivative boundary condition.

The use of a hysteresis loop necessitates storing values of B and H at each iteration in order to define the point reached on the loop. These values must be moved with the strip at each time step, but the presence of the $\partial A/\partial x$ term in equations (7) and (11) removes the need to move values of A . If the values of A stored at the end of a time step are also moved with the strip; however, the $\partial A/\partial x$ term can be deleted.

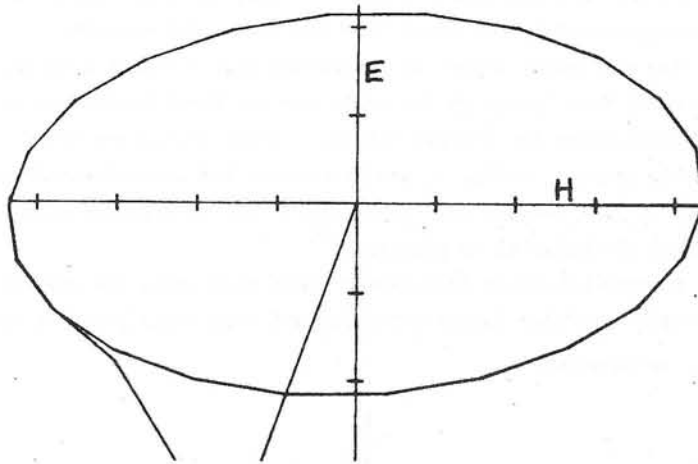


Fig. 4 - E/H Relation using O'Brien method

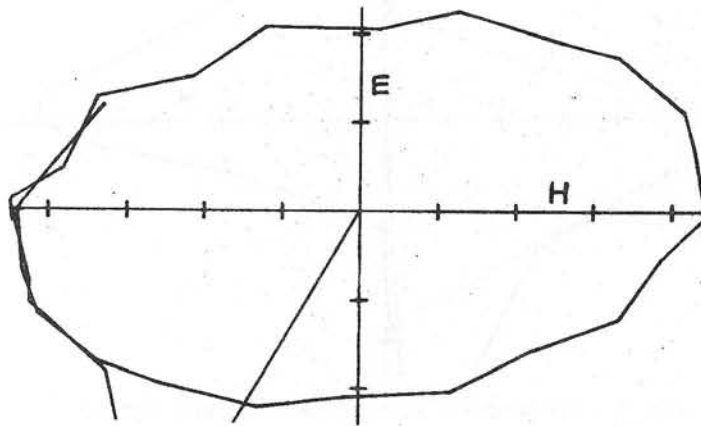


Fig. 5 - E/H Relation using Crank-Nicholson method

5. RESULTS

For comparison purposes various studies have been carried out using linear material for the strip, as well as non-linear material without hysteresis. The equivalent current method has also been used for moving material with hysteresis.

(a) Studies with Linear Material

Results for linear material were obtained using the model

shown in figure 1, with the same mesh spacing throughout the region. The frequency used was such that the strip thickness equalled twice the penetration depth at a relative permeability of 1000, and 22 time steps per cycle were employed.

In order to study the behaviour of different computational schemes, the relationship between tangential electric and magnetic fields was observed at a distance $h/2$ above the top surface of the strip, at a point between the poles (marked by P in figure 1). Simple finite difference expressions using the nodes above and below P, and those stored for the previous time step, were used. This relation is illustrated in figure 4 using the method of O'Brien et al, from which it is seen that after an initial transient the computation rapidly settles to its steady-state condition. The apparent phase angle between E and H is more nearly equal to 90° than 45° , this being due to the mesh representation of the region. (A very much finer mesh in the strip region would improve this situation, which in network terms would cause the strip to appear more as a transmission line than as a capacitance as seen from the air region).

A similar result is illustrated in figure 5 for the Crank-Nicholson method which, while employing more exact finite difference expressions with smaller truncation errors, is seen to follow a zig-zag oscillatory path before reaching its steady-state response after about one cycle. This numerical oscillation is considerably worse in parts of the field where only small differences are taken to calculate E and H, and appears mainly in the calculation of H. Inadequate convergence at each time step, which is not easily detectable in the O'Brien method, very much increases the amplitude of numerical oscillations in the Crank-Nicholson method.

Consideration of the corresponding network model of the field distribution indicates how a more accurate relation between tangential E and H can be found by also making use of values of vector potential at neighbouring nodes on the surface of the strip. By this means a phase angle of 42° is measured on the surface below point P, which is close to that expected. Where the component of

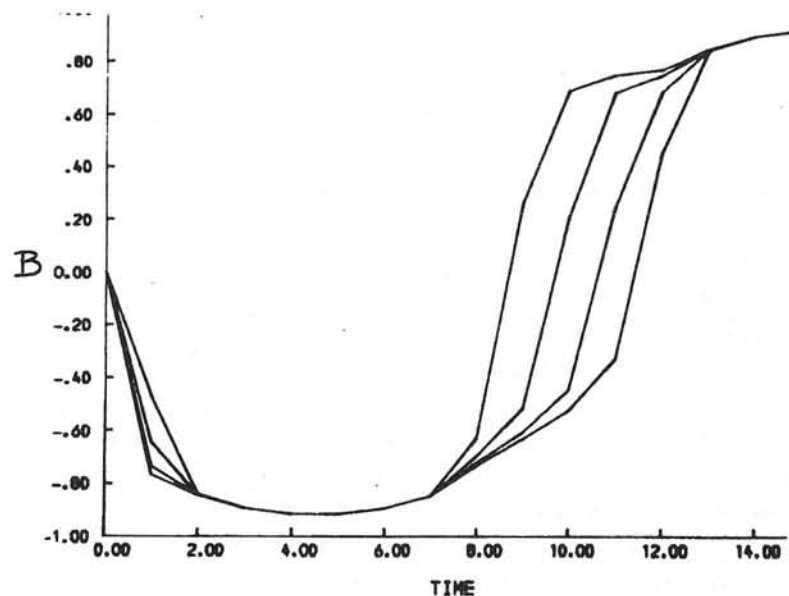


Fig. 6 - A wave of flux change in nonlinear material

normal flux is large, such as below the poles, further errors are introduced into the calculation of the tangential fields, the measured phase angle at these particular points being 57° .

(b) Non-linear material

For studies with non-linear material the B-H curve was represented by the particular Frölich equation:

$$B = \frac{H}{300 + 1.25|H|} + \mu_0 H$$

where B is Teslas and H in A/m. This gives an initial permeability of about 1000 and a saturation magnetization of 0.8T. Using an exciting current which would have produced a maximum flux density of approximately 2.5T in linear material having the same initial permeability the non-linear over-relaxation procedure worked well, the rate of convergence being approximately 0.6 that for the linear problem. The optimum acceleration factors were 1.88 (linear) and 1.85 (non-linear) respectively. Experiments with very deep saturation using a current drive ten times greater still necessitated

a reduction in acceleration factor to 1.65, the convergence rate being approximately 0.3 times that for the linear problem.

For the lesser degree of saturation fig. 6 illustrates the flux density at four levels in the strip for the first half cycle of excitation using the O'Brien method. These levels are those directly beneath P (fig. 1) and illustrate the characteristic rapid change in flux between the saturation levels at progressively later times as the material is penetrated¹⁵.

Similar behaviour is observed under each pole, and greater excitation produces faster switching and more rapid progress of the wave, as expected.

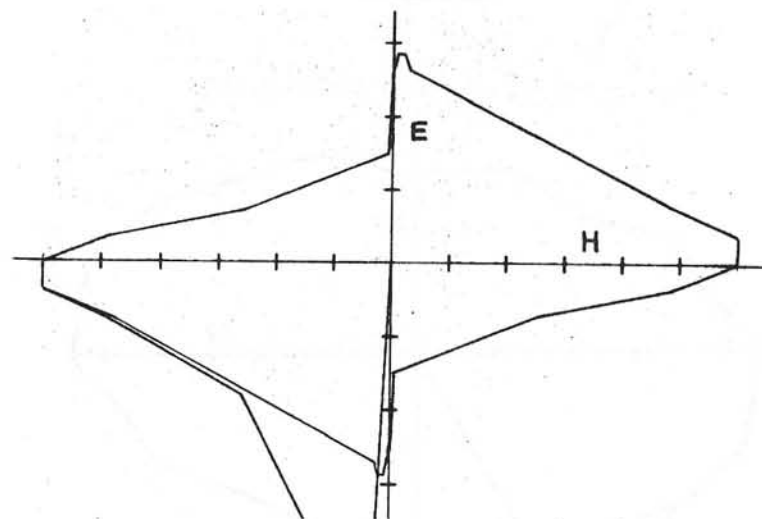


Fig. 7 - E/H Relation on Non-linear Material Surface

The relation between tangential E and H on the surface below Point P is illustrated in fig. 7, although no attempt has been made to measure the phase angle between the fundamental components. This might be expected to lie between 26.6° and 45° .

(c) Hysteretic Material

The arctan hysteresis loop model has so far been used only in conjunction with the equivalent current method. Preliminary results

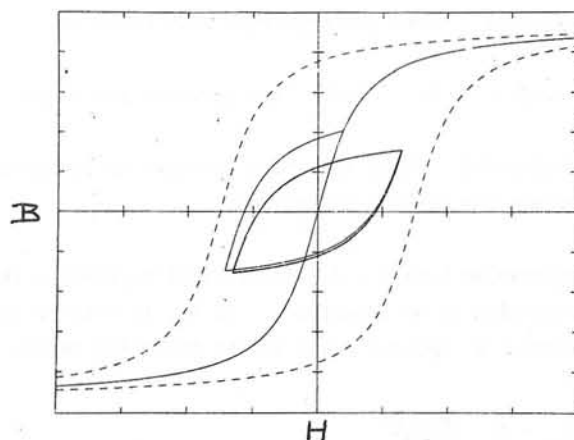


Fig. 8 - Transient and Minor loop in stationary strip

for a simple model employing a single coil recording head and strip of thickness equal to $2h$ have been obtained for various frequencies, for both stationary and moving strip. For a frequency at which the thickness is approximately one-half of the penetration depth for the initial permeability used, figure 8 illustrates the form of the magnetization loop reached after an initial transient, at a point on the surface of stationary material in the vicinity of the exciting coil. It has also been found practicable to examine the variation of magnetization in moving strip at a point remote from the exciting coil, which is the essential requirement for studying magnetic recording phenomena. No detailed studies of this have yet been made, however.

CONCLUSIONS

Implicit time-stepping methods have been used on linear, non-linear, and hysteretic material with the object of studying the magnetic recording produced on moving steel strip by a writing head. An equivalent current representation of magnetization has been used in conjunction with an arctan hysteresis model to obtain preliminary results using both stationary and moving strip, but the poor convergence rate of this method when the strip is greater than

two nodes in thickness preclude its use for more detailed studies. This disadvantage is found to be due to the trapping of residuals within the magnetic material when the equivalent currents are computed alternately with vector potential on a field-by-field basis.

The use of a formulation based on Curl H together with non-linear over-relaxation is found to give excellent convergence using either the O'Brien et al or Crank-Nicholson implicit schemes, although the latter is found to go through a number of numerical oscillations before reaching a steady state. There appears to be no difficulty in principle in extending this approach to moving hysteretic material, which represents the next stage of the present work.

7. ACKNOWLEDGEMENTS

The authors would like to thank Mr. J. Carpenter of Imperial College for many useful discussions.

8. REFERENCES

1. George, D.J., King S.F., and Carr, A.E. "A self-consistent calculation of the magnetic transition recorded on a thin film disk". I.E.E.E. Trans. MAG-6 pp.240-3 (1970).
2. Sawamura, S., and Iwaraki, S-I. "Application of the internal reaction field on the Analysis of Anhyseretic Magnetizing Process". I.E.E. Trans. MAG-6 pp.646-49 (1970).
3. McCary, R.O. "Saturation Magnetic Recording Process" I.E.E.E. Trans. MAG-7 pp.4-16, (1971).
4. O'Brien, G.G., Hyman, M.A., and Kaplan, S. "A Study of the Numerical Solutions of Partial Differential Equations." J. Math. Phys. 29 p.223 (1950)
5. Crank, J. and Nicholson, P. "A Practical Method for numerical evaluation of solutions of partial D.E. ^S of the heat conduction type". Proc. Camb. Phil. Soc. 43 pp.50-67(1947)
6. Lieberstein, H.M. "Over-relaxation for non-linear elliptic partial differential equations". Tech-Rept. No. MRC-TR-80. University of Wisconsin Mathematical Research Centre (1959).
7. Zaky, S.G. and Robertson, S.D.T. "Integral Equation formulation for the solution of magnetic field problems" (Part I). Trans. I.E.E.E. PAS-92 pp.808-815 (1973).

8. Jackson, R.D. "Digital Simulation of the hysteresis motor"
Proc. I.E.E. 120 p.1533-7 (1973).
9. Everatt, J.S. "Computer Simulation of non-linear inductors
with hysteresis". Electron. Lett. 6 pp.833-4 (1970).
10. Curland, N. and Speliotis D.E. "A theoretical study of an
isolated transition using an iterative hysteretic model".
I.E.E.E. Trans. MAG-6 pp.640-46 (1970).
11. Chua, L.O. and Bass, S.C. "A generalized hysteresis model"
I.E.E. Trans. CT-19 pp.36-48 (1972).
12. Stoll, R.L. "The Analysis of Eddy Currents".
(Clarendon Press, Oxford) p.90 (1974).
13. Zakrzewski, K. and Pietras, F. "Method of calculating the
electromagnetic field and power losses in ferromagnetic
material, taking into account magnetic hysteresis".
Proc. I.E.E. 118 pp.1679-85 (1971)
14. Ames, W.F. "Numerical Methods for Partial Differential
Equations". (Nelson) pp.232-38 (1969).
15. Agarwal, P.D. "Eddy Current losses in solid and laminated
iron".
Trans- Amer. Inst. Elect. Engrs. 78 (Pt.II) pp.169-8 (1959)

discussions following paper:

(Reichert, Brown Boveri) Have you neglected Eddy Currents?

(Deeley, Kings College) No. $\partial A/\partial t$ term accounts for these.

(Polak, Philips Eindhoven) Which equations are used at the material
interfaces to complete the problem definition.

(Deeley) The expression $\text{Curl } H = J$ is sufficient to specify the
vector potential equation at an interface. If H_{01} is written in terms
of the vector potential at nodes 0 and 1 in the following manner (for
linear material):

$$H_{01} + \frac{1}{\mu} B_{01} = \frac{1}{\mu} \frac{A_0 - A_1}{h}$$

and similar expressions written for the other connections to node 0, then
substitution into $\text{Curl } H=J$ yields the familiar expressions for vector
potential relations at interfaces and corners.

MATHEMATICAL MODELLING OF MAGNETIC HYSTERESIS

by N. JANSSENS
Faculty of Applied Sciences
University of Louvain

Abstract

The aim of this study is to build, for polycrystalline ferromagnetic bodies, a general model of hysteresis to be used as a framework for comparing the various mathematical models which have been proposed.

One only relies upon the properties of the experimental magnetization curves since the value of a given model is ultimately measured by the accuracy with which experimental curves can be predicted.

This approach makes it possible to prove on purely phenomenological grounds, without any recourse to microscopic physics, the validity of a generalized Preisach model.

This leads to a model of hysteresis which is fully justified and relatively easy to handle. Furthermore, it shows which experimental characteristics are the most relevant for the calculation of the "Preisach density".

1. Magnetization curves

In order to build models of the magnetic hysteresis phenomenon, we will begin with a detailed analysis of experimental magnetization curves and point out their fundamental characteristic features.

1.1. A property of almost every magnetic material is symmetry with respect to the origin ($H=0$, $M=0$) of the magnetization curves for evolutions of opposite signs.

Although this simplifies the models, the following developments do not refer to this property so that we will, for instance, be able to represent the asymmetric cycle of a permanent magnet cooled in a magnetic field.

The symmetry property will thus provide us with an additional relation within every model.

1.2. Another fundamental characteristic can be idealized by stating that :

Secondary cycles are closed and, after being closed, have no more influence on the subsequent evolution (we will say they are forgotten).

Figure 1 shows how accurately this statement is verified for a given material (ARMCO.0202). A model having such a property eliminates the accommodation phenomena (stabilization and drift of successive cycles).

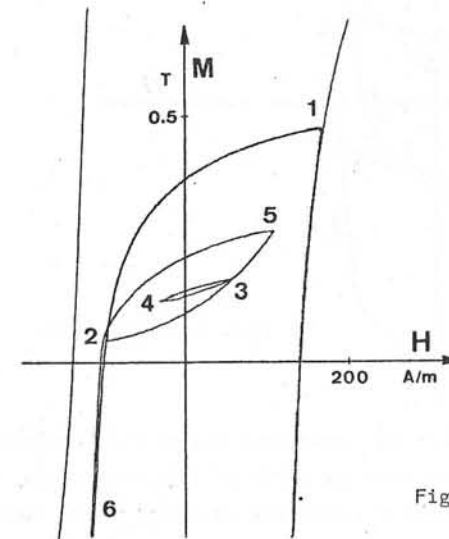


Fig. 1 Secondary cycles

Some hitherto proposed representations of magnetic hysteresis do not comply with this requirement. For instance, the model proposed by Duhem [1] aims to describe the magnetic state of a material with the only two variables H and M by considering two curves passing through each point inside the limit cycle, one to be used for increasing, the other for decreasing field and magnetization. Other models [2, 3, 4] are similar to the preceding one or particular cases of it. Their utility seems limited since, for some kinds of evolutions, their predictions are far from approximating the real behaviour of the material. This is shown on figure 2 by evolution 12345 which is based on a model of this type and deviates appreciably

from any experimental curve.

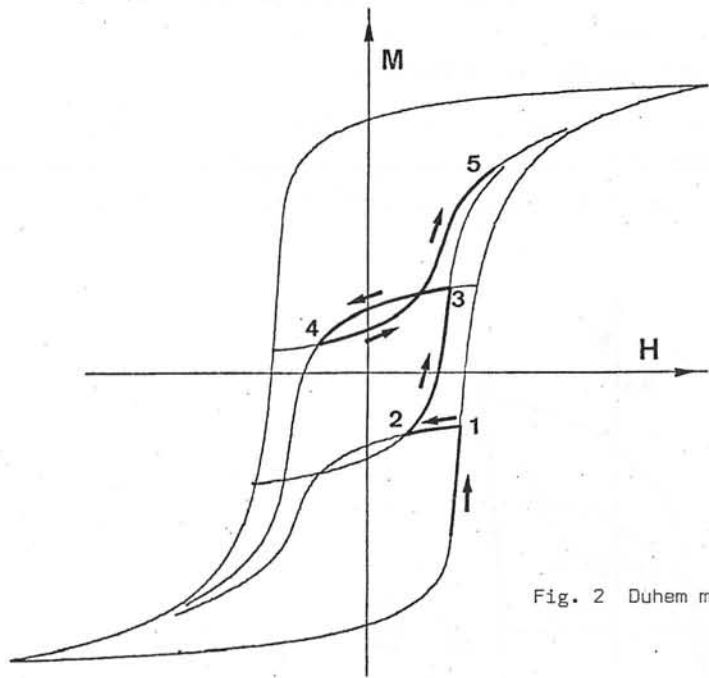


Fig. 2 Duhem model

Such models may only be used when the monotonous parts of an evolution are of great amplitude, compared with the width of the limit cycle. In this case, indeed, the magnetization curves are so close to the limit cycle that the closing and forgetting of the secondary cycles becomes of little importance.

Let us notice that the model we will establish (par.2) makes it possible to give a very simple (although rather crude) description of hysteresis with H and M uniquely determining the magnetic state and where the secondary cycles are closed and forgotten. This is shown on figure 3 : the evolutions are reversible inside the limit cycle and irreversible on this cycle.

1.3. A statement which is satisfied with the same accuracy as the closing and forgetting of the secondary cycles is the following :

Inside a secondary cycle, the magnetization curves depend only on their starting point.

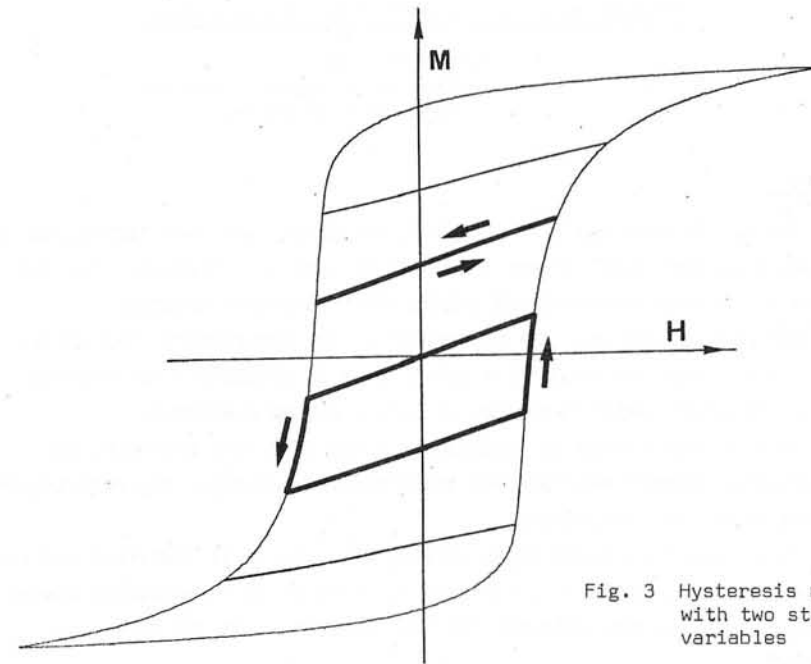


Fig. 3 Hysteresis model with two state variables

Figure 4, for instance, shows that the evolutions 12324 and 1'3'1' practically coincide upon the path 32. There is a certain analogy between this property and the ideas which form the basis of Duhem's model. In both cases, indeed, the curves depend only on the starting point in a given direction. However, here, the utilization of the curves to be followed is so restricted that the physionomy of the model is entirely different.

1.4. The preceding idealization requires the knowledge of a double infinity of curves. It may be seen that an important simplification is introduced at the expense of a small reduction in accuracy if one states that :

The curves issued from points located on each of the straight lines of fixed slope $-1/k$ are deduced from each other by translation

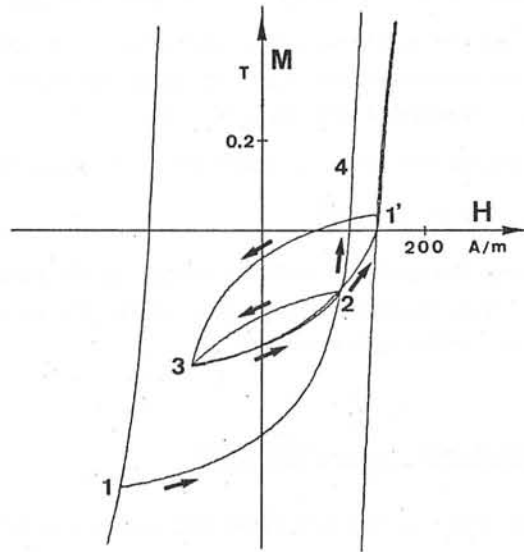


Fig. 4

Evolutions inside secondary cycles

If (H_e, M_e) is a point of the descending (ascending) limit cycle, the equation of the ascending (descending) curve starting from (H_i, M_i) located on the straight line with slope $-1/k$ passing through H_e, M_e has thus the form :

$$M - M_i = f(H - H_i, H_e + kM_e) \quad (1)$$

(The use of $H_e + kM_e$ as a parameter instead of H_e or M_e will prove to be convenient at a later stage).

Figure 5 shows that the last statement is in good agreement with experiment. The value of the parameter k is chosen from the magnetization curves in such a manner that one gets the best possible verification.

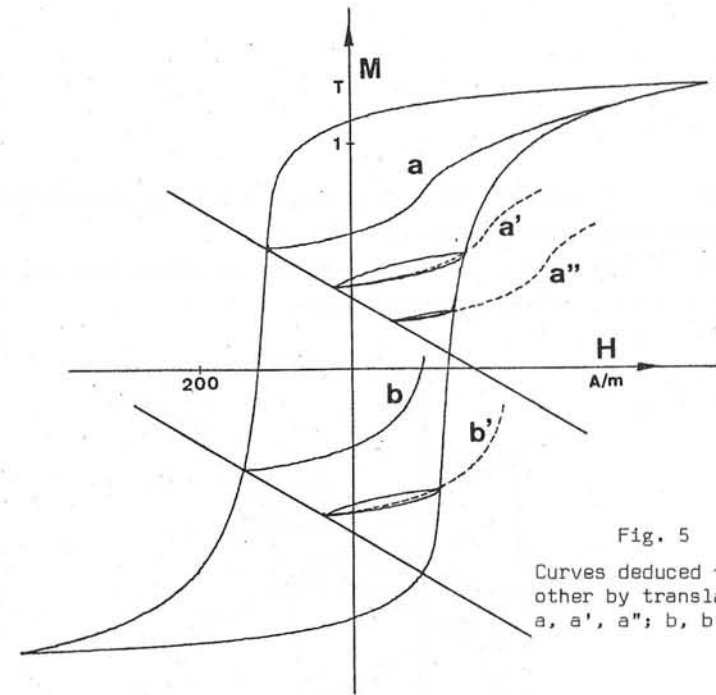


Fig. 5

Curves deduced from each other by translation :
a, a', a''; b, b'.

2. Proposed Model.

The above statements leads us to the following model.

We consider the family of experimental ascending and descending curves starting from each point (H_e, M_e) of the left respectively right side of the limit cycle. Their equations are given by (1) for $(H_i, M_i) = (H_e, M_e)$ and by introducing for every pair of (H, M) the new variable

$$H' = H + kM$$

they can be transformed into

$$M - M_e = g(H', H'_e) \quad (2)$$

According to statement 1.4, the ascending evolution starting, after reversal of the direction, from point (H_A, M_A) located on the straight line with slope $-1/k$ passing through (H_e, M_e) , has to be given by

$$M - M_A = g(H', H'_e)$$

or, since $H'_A = H'_e$,

$$M - M_A = g(H', H'_A) \tag{3}$$

The construction is shown on figure 6 as well as the curve corresponding to the following reversal at point B.

As indicated on the figure, the use of experimental curves does not in general give exactly closed secondary cycles.

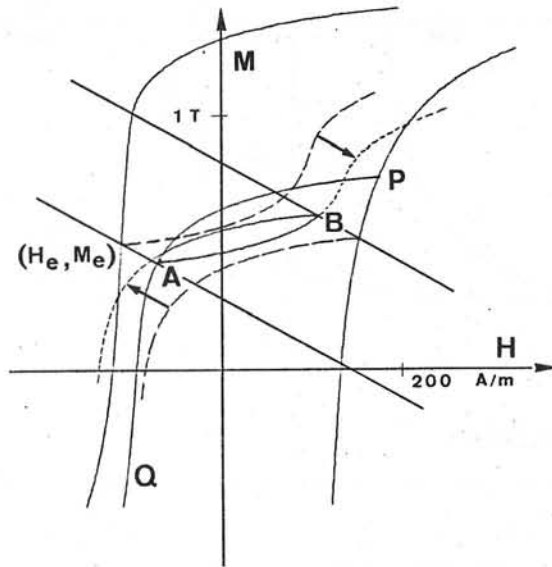


Fig. 6 "Construction" of the magnetization curves

In order to satisfy statement 1.2, the curves (3) must obey the relation

$$M_B - M_A = g(H'_B, H'_A) = -g(H'_A, H'_B)$$

To obtain this result we modify the experimental curves (2) and use for the model the expression

$$M - M_e = g_c(H', H'_e) = \frac{1}{2} [g(H', H'_e) - g(H'_e, H')]$$

This change affects the curves only slightly (in fact to the extent the previous statements are not fully verified experimentally).

To complete the model, we only have to add that, after coming back to point A, the subsequent evolution is the continuation of curve P A followed before reaching A for the first time.

If applicable, the symmetry statement (1.1) takes the form

$$g(H'_B, H'_A) = -g(-H'_B, -H'_A)$$

In summary, the proposed model is formed by the family of almost experimental curves issued from the limit cycle, the parameter k and a simple rule for combining the curves.

3. Identification with the Preisach model

3.1. One knows that the Preisach model represents a polycrystalline ferromagnetic material by an assembly of dipoles having rectangular hysteresis loops displaced a distance h_f away from the origin and with a coercive force h_c (figure 7). The fluctuation field h_f takes into account the interaction of the neighbouring dipoles [5,6]. The density $\phi(h_c, h_f)$ of the dipoles characterized by h_c and h_f can be represented in a plane where a line formed by segments alternatively at 45° and -45° provides the state of the system (figure 8).

In order to get a good agreement with experiment, this model has to be expanded in two ways. Firstly, we take the reversible permeability into account [7,8] by adding on the axis $h_c=0$ a line distribution of dipoles $\phi(h_f)\delta(h_c)$. Secondly, as indicated in [10] and used in [9], we replace the variable H by $H' = H + k'M$. This introduces a mean interaction field proportionnal to M.

The differential expression of a magnetization curve has then the form (figure 9) :

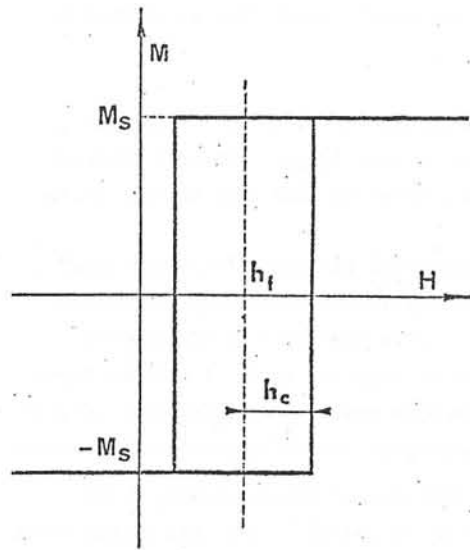


fig. 7 Elementary Preisach dipole

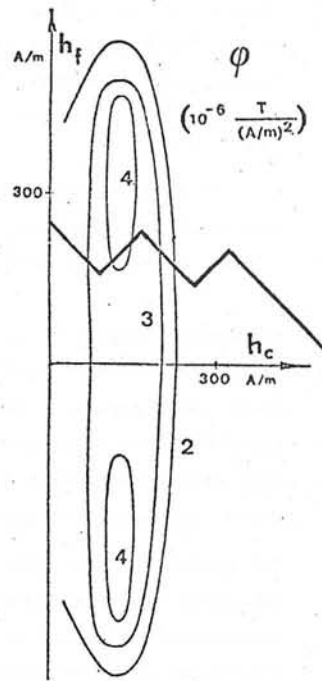


fig. 8 Preisach diagram : constant ϕ -lines and state line

$$\frac{dM}{dH'} = 2 \phi(H') + 2 \int_0^{\frac{|H' - H'_1|}{2}} \phi(h_c, H' \mp h_c) dh_c \quad (4)$$

where H'_1 corresponds to the last extremum retained and the - sign is to be used for ascending curves, the + sign for descending curves.

3.2. The Preisach model generalized as in paragraph (3.1) is completely identical with that of paragraph 2 if we take $k'=k$. Indeed, inside a secondary cycle, the predicted magnetization curves depends only on the value of $H' = H + kM$ at the starting point (statements 1.3 and 1.4). Furthermore, the secondary cycles are closed because the variation of M during either the ascending or the descending part are given by twice the surface integral of the Preisach density on the same triangle H'_A, H'_B, N (figure 9). Finally, the mechanism of displacement of the state line insures that the secondary cycles are "forgotten" (statement 1.2).

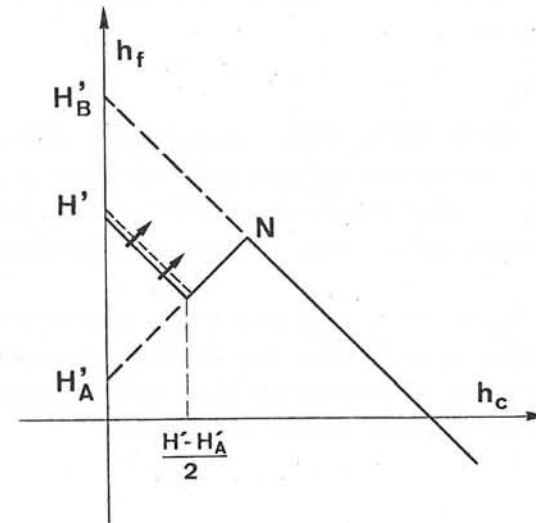


Fig. 9 Preisach diagram : interval of integration for the calculation of magnetization curves

The Preisach density can thus be viewed as a convenient means of specifying the single infinity of magnetization curves $g_c(H', H'_B)$ characterizing the proposed model. The relation between the Preisach density and the function g_c is obtained from equation (4) :

$$\phi(h_f) = \frac{1}{2} \frac{\partial g_c}{\partial H'} \quad \text{for } H'_e = H' = h_f$$

$$\varphi(h_c, h_f) = - \frac{\partial^2 g_c}{\partial H' \partial H'_e} \quad \text{for } H' = h_f + h_c$$

and $H'_e = h_f - h_c$

The introduction of the Preisach density is useful to simplify the model. For instance, the magnetization curves represented on figure 3 corresponds to a Preisach density given by two line distributions. Less drastic approximations can be obtained by giving ϕ and φ various analytical expressions.

4. Conclusions.

The mathematical model of hysteresis which is presented here is independent from any physical interpretation which is always open to criticism. Its formulation makes possible to introduce judicious approximations while retaining for every evolution the characteristic features of hysteresis.

On the other hand the Preisach interpretation leads to a very useful diagram. Furthermore it can be shown that the Preisach densities are more convenient to handle than the magnetization curves themselves, especially when approximated by simple analytical functions.

References

- 1 : P. DUHEM, Mémoires Acad. Belg en 4^o, Mem I, 54 (1896)
- 2 : R. BOUC, Acustica 24, 16 (1971)
- 3 : R. POTTER & R. SCHMULIAN, IEEE Trans. MAG 7, 873 (1971)
- 4 : W. THOMPSON, IEEE Trans. MAG 10, 332 (1974)
- 5 : P. WEISS & J. de FREUDENREICH, Arch. Sc. Nat. (Genève), 42, 449 (1916)
- 6 : F. PREISACH, Z. Physik, 94, 277 (1935)
- 7 : L. NEEL, Cah. Phys. 12, 1 (1942); 13, 18 (1943)
- 8 : S. OTHERU, AIEE Trans. PAS 78, 1809 (1960)
- 9 : N. GERMAI, S. MASTERO, J.VROMAN, CIGRE 1974, rapport 33-18
- 10 : H. GIRKE, Z. Angew. Physik 12, 502 (1960)

Discussions following paper:

(Teape, British Rail) 1. Could M Janssens comment on the significance of the 'real behaviour of magnetic materials, that is the closing and 'forgetting' of minor loops which his model caters for, as opposed to the behaviour of a Duhem model.

2. It would appear that the computation time involved in the use of this model in time-varying problems is very large. Could M Janssens comment on the practicability of his model in this type of application.

(Janssens, Belgium) 1. The differences between a "Preisach type" model and a "Duhem type" model are significant especially when small minor loops appear. For instance, if we superpose an alternative field of small amplitude to a constant magnetic field, the minor loops will drift appreciably for a "Duhem type model" while, for the Preisach model, the secondary cycles will superpose (no accommodation phenomena).

Let us mention that Van Dang (11) has studied experimentally drift phenomena, explained theoretically by Veel (12). But this second older phenomenon should not be compared with the discrepancies, the Duhem model introduces into the magnetization curves.

2. The Duhem Model is very simple to handle in a computation while the general model presented in the text is more "heavy" to use. Nevertheless, when assuming the Preisach densities in some simple forms (see for instance fig 3 which is obtained for a Preisach density composed of two lines distributions, it is possible to obtain models which are easily treatable. In fact, it is possible to build a family of models having various complexity.

Before choosing a model, one has to consider the kind of evolution to be simulated and the accuracy needed to resolve the problem in a convenient manner.

(11) B Van Dang J Phys. Rad. 20 (1959) 222

(12) L Veel J Phys. Rad. 20 (1959) 215

(Coulson, Strathclyde) Has Mr Janssens found that by using the Girke modification to Preisach theory (ie the inclusion of a KB term in the "line of state"), most of the anomalies of the unmodified model are overcome?

(Janssens) The primitive Preisach model is obtained by setting $K = 0$ in the model presented here. That is, this primitive model predicts that the curves issued from points located on the straight lines having a slope: $-1/k$ (ie straight lines parallel to the axis $H = 0$) are deduced from each other by translation. It may be seen that such a statement is not very adequate. When the value of k is properly chosen, we obtain a quite good result (see fig 5). The considerations can also be made in terms of the Preisach density. For a symmetric material (see par. 1.1) Girke (10) found that the primitive Preisach model gives an asymmetric dipole density. With the introduction of the modified field variable $H^1 = H + kM$, the Preisach density becomes more or less symmetric towards the axis $hf = 0$.

But, as I mentioned in par. 3.1 we have to introduce another generalization of the primitive Preisach model so that the magnetisation curves have a finite initial slope. The simplest way of doing this is to add a line distribution of dipoles on the axis $hc = 0$.

(Popovic, Belgrade) I would be grateful for your comments on the accuracy of the approximation in general. Particularly, does it apply and to what extent, to a material having a hysteresis loop very much differing from the standard one?

(Janssens) The model we have presented starts from experimental magnetization curves but does not require any assumption on the shape of the hysteresis loops. So that the model is valid to represent the hysteresis phenomenon of special materials. Feldtkeller, for instance used a Preisach density equal to a constant on two squares, and equal to zero elsewhere, to represent a hysteresis loop having a "narrowing". However, we may not forget that the Preisach model, built on statistical backgrounds, is valid for polycrystalline materials only.

(Baran, Essen) In the known Preisach - Model B and H are always parallel.

Do you believe that it could be possible to generalise the Preisach-Model to the case, where we have an angle between B and H , as it is for instance in permanent magnet material.

(Janssens) The experimental curves shown in the text have been obtained with a material which may be considered isotropic; the sample was a toroid so that H and B were parallel and with a constant direction.

I do not have any information about the validity of the Preisach model when these conditions are not verified.

PERMANENT MAGNET MODELLING FOR MACHINE APPLICATIONS

W. Lord

Hoover Electrical Machines Group
Department of Electrical and Electronic Engineering
University College, Cardiff

ABSTRACT

Permanent magnet materials are used widely in the construction of all types of electrical machinery, from fractional horsepower stepping motors for incremental motion control to dc machines of 100 horsepower for rolling mill applications. With the increasing availability of high energy ferrite, alnico and rare earth magnets, it is imperative that design techniques for magnetic structures containing permanent magnets be improved to yield optimum utilization of the permanent magnet materials.

This paper reviews the application of permanent magnet materials to electrical machinery, particularly with regard to the complex recoil behaviour which exists in dc machines, alternators and stepper motors under dynamic operating conditions. Suggestions are made for adapting finite element algorithms to include the effects of complex recoil phenomena caused by the heavy demagnetization forces experienced in practice and other problem areas relevant to permanent magnet design are identified for further consideration.

INTRODUCTION

Future advances in permanent magnet technology as applied to electrical machine design will come, not only from the development of new materials, but also from improved design techniques. With the increasing availability of high energy ferrites, columnar crystal alnicos and rare earth magnets, it is imperative that advantage be taken of modern numerical analysis techniques in the design of permanent magnet (p.m.) poles for electrical machines in order to minimize the volume of magnet required. Current 'trial-and-error' approaches to p.m. design, although contributing to the 'black-art' aura surrounding the subject, do very little in terms of providing a sound basis on which to build the

flexible, iterative design strategy needed for economical utilization of modern p.m. materials.

Considerable work still has to be done before the finite element and difference techniques, which have been so successfully applied to transformer and alternator design studies,¹⁻⁷ can be applied with equal success to permanent magnet structures. This paper discusses some of the factors affecting the use of numerical analysis techniques for p.m. design, including demagnetization forces in electrical machines and recoil loop modelling. Suggestions are made for incorporating these factors into finite element algorithms.

CURRENT DESIGN PRACTICE

Major aspects of permanent magnet design as applied to electrical machinery are summarized in Figure 1, with a typical p.m. motor construction shown in Figure 2.⁸ It is normally assumed that

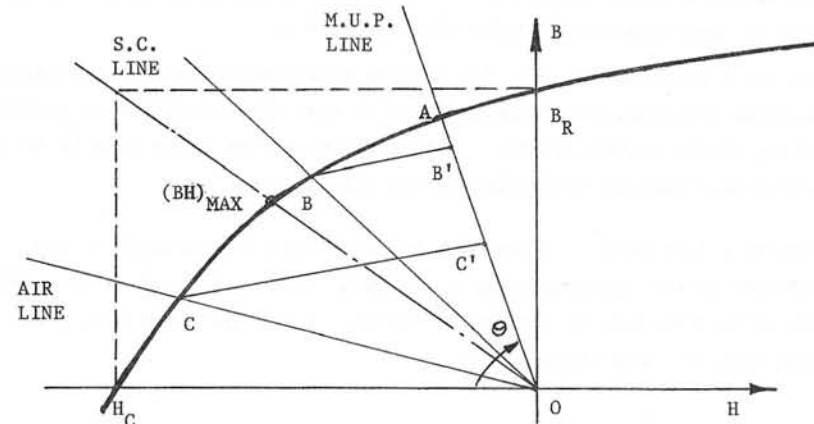


FIGURE 1 Permanent magnet design factors

all poles are initially in an unmagnetised state characterized by Point 0 at the origin of the B-H coordinates. Subsequent magnetization is assumed to take all poles into saturation, with a uniform flux density distribution resulting throughout the p.m. material. After magnetization it is assumed that all points on the surface of the pole work at point A, the intersection of the maximum unit permeance line with the major loop in the second quadrant.

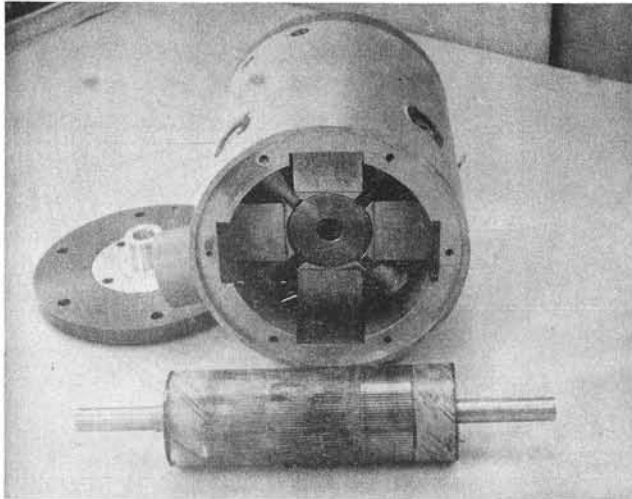


FIGURE 2 Permanent magnet motor construction

The angle θ can be used to define the maximum unit permeance line:

$$\tan \theta = \mu_o \frac{A L}{g m} / \frac{A L}{m g} \quad (1)$$

Leakage and iron m.m.f. are often taken into account by using appropriate constants in equation 1. Stabilization of the magnet poles is then achieved by subjecting them to a demagnetization force greater than any likely to be experienced during operation. Short circuit and air stabilization lines are shown in Figure 1; demagnetization forces after stabilization, such as armature reaction m.m.f.'s, cause the magnets to work along lines BB' or CC'.⁹ Ideally, for minimum magnet volume, the p.m. poles should be stabilized to operate close to the $(BH)_{\max}$ point.

$$\text{Minimum P.M. Volume} = B_g^2 L_g A_g / \mu_o (BH)_{\max}. \quad (2)$$

Assumptions and approximations in this treatment are related to:

- flux density distribution in the p.m. poles after magnetization
- estimates of leakage factor and iron m.m.f.
- recoil loop representation by a line
- recoil line slope
- demagnetization effects in electrical machinery.

All of these factors require further study in order to optimize the use of p.m. materials for machine excitation. Demagnetization forces are discussed in the following section as an illustration of how the physical phenomena associated with permanent magnet poles would affect numerical analysis techniques.

DEMAGNETIZATION PHENOMENA

Zakharov¹⁰ first reported the excessive demagnetization effects in dc machines during reversal, and their effect on the flux density distribution under p.m. poles. This work has been substantiated by the author^{11, 12} and Figure 3 shows the effects of reversal on the second quadrant operation of permanent magnet poles in a dc motor.

After short circuit stabilization all points on the surface of the p.m. poles would recoil to B', the flux distribution in a smooth rotor machine being similar to that shown in Figure 4.¹³ On reversal, currents approaching twice the short circuit value are present in the armature giving a resultant flux distribution similar to that shown in Figure 5; one pole tip becomes heavily magnetized (point C in Figure 3) and the other heavily demagnetized (point D in Figure 3). After several reversals a non uniform flux density distribution exists over the magnet pole face, the centre of the pole working along recoil line BB', the pole tips working along DE. Attempts have been made to derive empirical relationships describing these effects,¹⁴⁻¹⁶ but the results are not generally applicable to p.m. design.

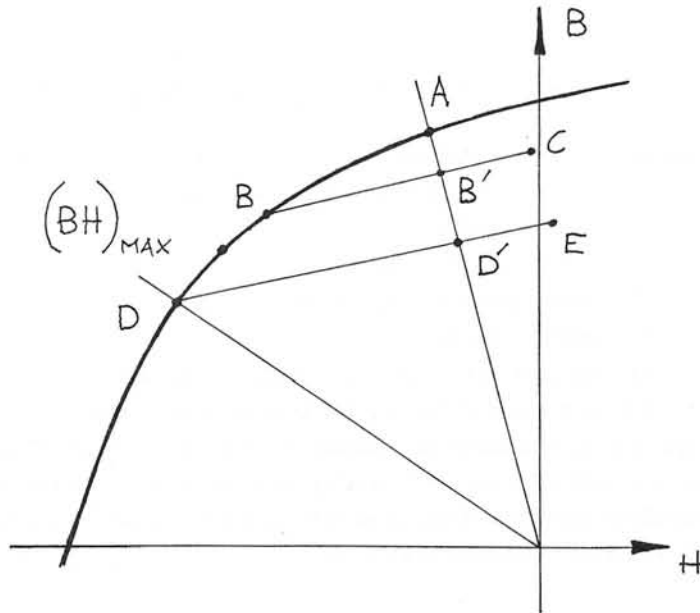


FIGURE 3 Demagnetization Phenomena in a Permanent Magnet DC Motor

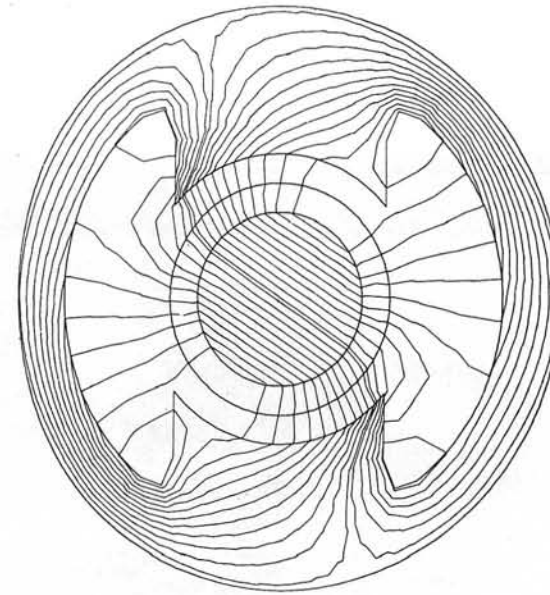


FIGURE 5 Flux distribution in a dc motor with heavy armature reaction

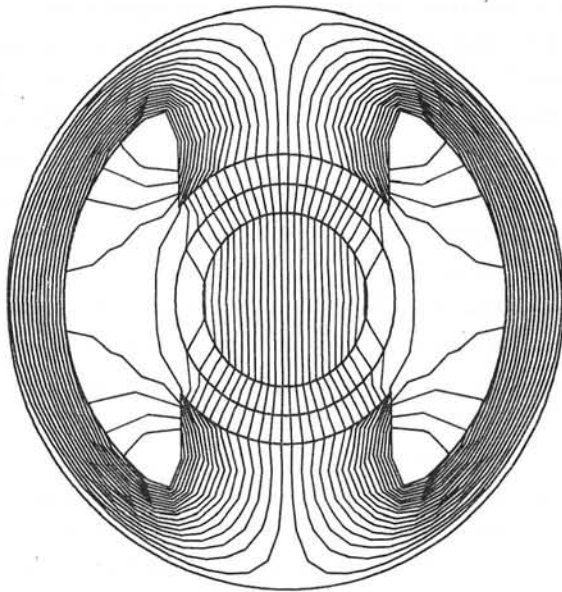


FIGURE 4 Flux distribution in an unloaded dc motor

Similar effects are present during 'pull-in' and 'pull-out' modes of operation of p.m. stepper motors and synchronous machines. Figure 6 shows a simulated flux distribution in one quadrant of a four phase reluctance stepper motor,¹³ and it is clear that the recoil behaviour of p.m. material on the rotor would be rather complex over the surface of the poles.

It is quite possible that with each part of a p.m. pole working along a separate recoil line, a 'minimum volume' design would entail the positioning of a band of recoil lines around the $(BH)_{max}$ point, as shown in Figure 3 for the dc motor case.

The problem of optimum design becomes even more complex when rotor and/or stator slots are present and when it is realized that recoil line slopes can change by as much as 25% depending upon the point of origin on the major loop.¹⁷

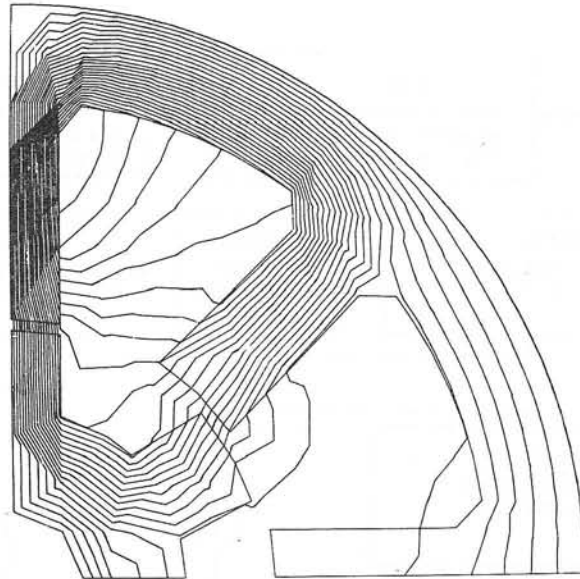


FIGURE 6 Flux distribution in one quadrant of a fourphase stepper motor

FACTORS AFFECTING NUMERICAL ANALYSIS OF P.M. STRUCTURES

Analysis of magnetic circuits in electrical machinery is based upon finding solutions of the nonlinear, poissonian-type equation

$$\frac{\partial}{\partial x} \left(v \frac{\partial A}{\partial x} \right) + \frac{\partial}{\partial y} \left(v \frac{\partial A}{\partial y} \right) = - J \quad (3)$$

where A is the magnetic vector potential, v is the reluctivity found from the nonlinear H/B characteristic in the case of the magnetic portions of the region being analysed, and J is the current density associated with the conducting portions of the circuit.

In finite difference methods^{1,3} of analysis the partial derivatives of equation 3 are modelled over a rectangular mesh to yield a set of nonlinear algebraic equations of the form:

$$[SK] [U] = [F] \quad (4)$$

where [SK] is a square matrix containing nonlinear reluctivity terms, [U] is a column matrix of nodal vector potentials and [F] is a column matrix of current density terms.

A similar equation results from a finite element approach,^{2,4,5,6,7} where equation 3 is satisfied when an energy functional is minimized over a triangular mesh covering the region of interest (see Figures 7 and 8).

Figure 9 shows the elements of a computer algorithm used to obtain the flux plots of Figures 4, 5 and 6 based on the mesh configurations of Figures 7 and 8. In the iteration procedure used to solve equation 4 the H/B characteristic of the iron parts can be modelled in a number of different ways.¹⁸⁻²³

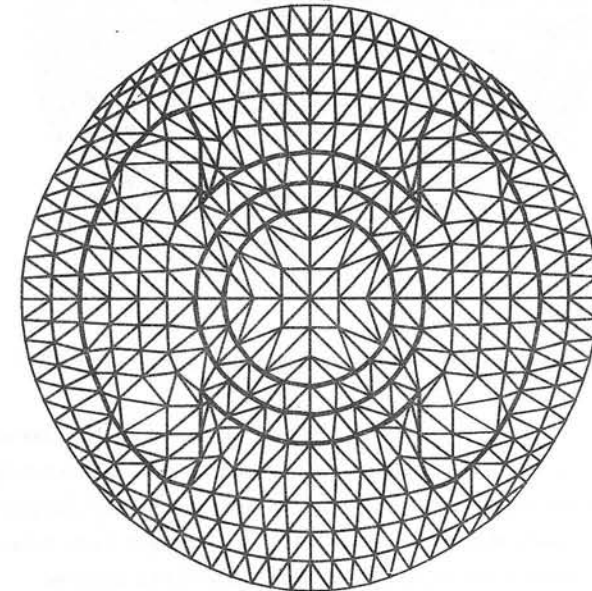


FIGURE 7 Mesh configuration for dc motor flux plot

Application of such an algorithm as a design aid in the construction of electrical machines with p.m. excitation would require modifications to be made depending upon the designers requirements. For example, the prediction of leakage factors might be made by assuming all parts of the magnet to be working at point A in Figure 1. In this case equation 3 is simply modified to include an additional current density term J_m representing the effect of the p.m. material.²⁴ Prediction of leakage factors after several cycles of operation however, would require accurate knowledge of the demagnetization effects so

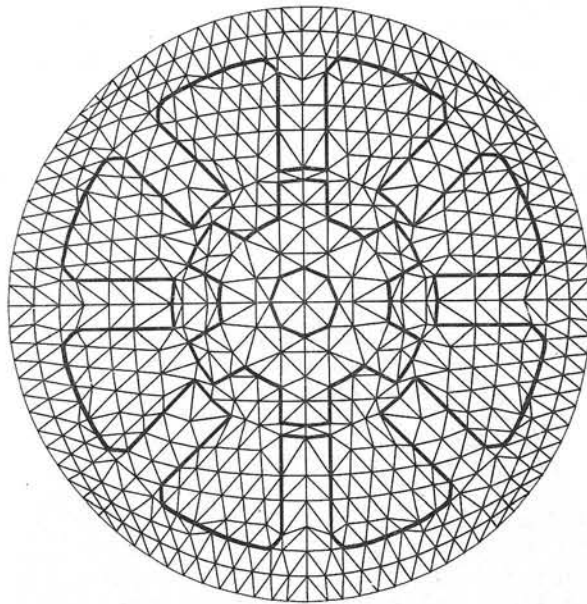


FIGURE 8 Mesh configuration for stepper motor flux plot

that each mesh element within the p.m. material could be characterized correctly. Estimation of leakage reactances in p.m. alternators and stepper motors would also require the development of individual recoil loop models for each element. Some work has already been done on modelling p.m. recoil behaviour by linear approximations and Fröhlich-type equations,²⁵⁻²⁷ and perhaps recent work on exponential series representations²⁸ and phenomenological modelling²⁹ could be adapted for p.m. machine design.

CONCLUSIONS

The author's purpose in presenting this paper is to indicate some of the areas of p.m. machine design which need additional attention before numerical analysis techniques can be successfully applied. Knowledge of both demagnetization phenomena in electrical machinery and magnetization effects in permanent magnets, coupled with accurate recoil loop modelling techniques will represent a further step towards on-line, interactive design of p.m. structures.

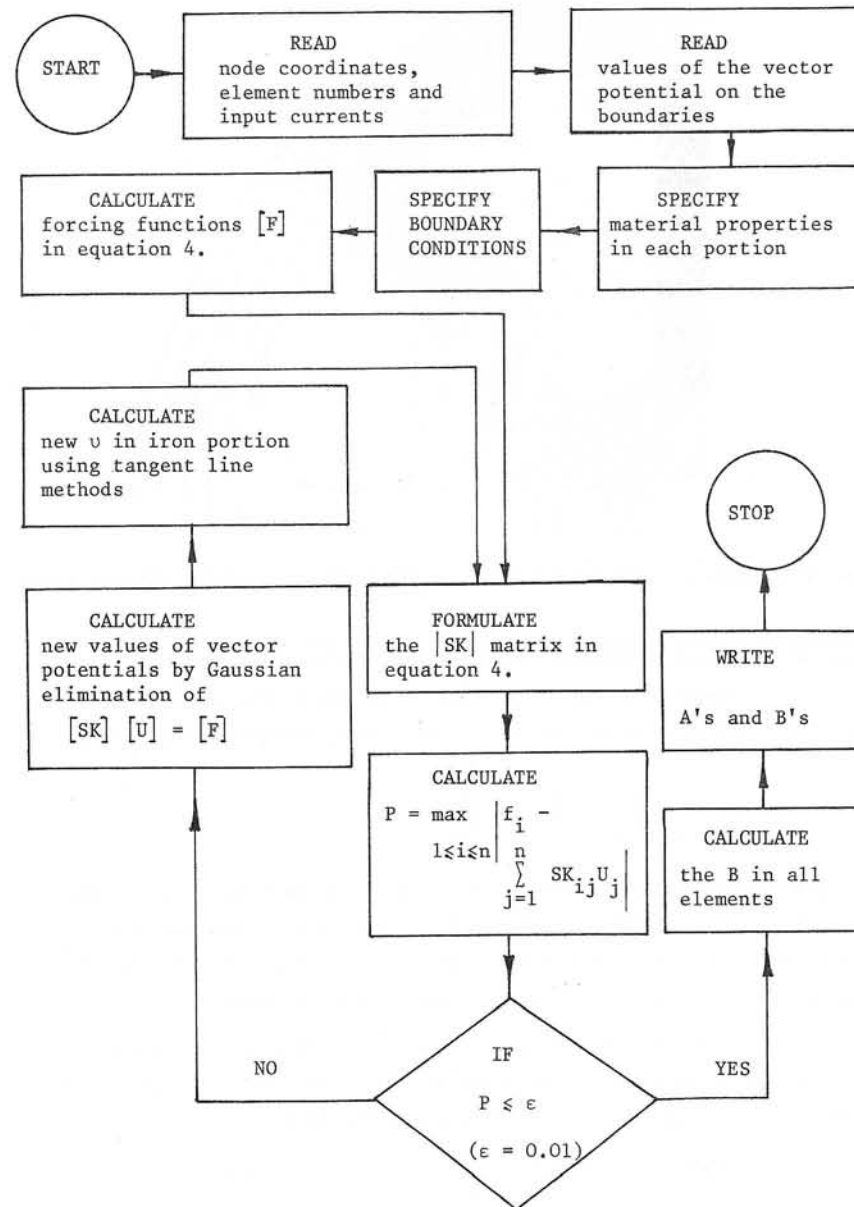


FIGURE 9 Flow chart for finite element program

REFERENCES

1. E.A. ERDELYI, S.V. AHAMED, R.D. BURTNESS, Flux distribution in saturated dc machines at no-load, IEEE Transactions on Power Apparatus and Systems, Vol. 84, May 1965, pp. 375-381.
2. A.M. WINSLOW, Numerical solution of the quasilinear Poisson equation in a nonuniform triangle mesh, Journal of Computational Physics, Vol. 2, 1967, pp. 149-172.
3. E.A. ERDELYI et al., Nonlinear magnetic field analysis of dc machines Parts, I, II, III, IEEE Transactions on Power Apparatus and Systems, Vol. 89, September/October 1970, pp. 1546-1583.
4. M.V.K. CHARI, P. SILVESTER, Finite element analysis of magnetically saturated dc machines, IEEE Transactions on Power Apparatus and Systems, Vol. 90, 1971, pp. 2362-2372.
5. O.W. ANDERSON, Transformer leakage flux program based on the finite element method, IEEE Transactions on Power Apparatus and Systems, Vol. 92, March/April 1973, pp. 682-689.
6. P. SILVESTER, H.S. CABAYAN, B.T. BROWNE, Efficient techniques for finite element analysis of electric machines, IEEE Transactions on Power Apparatus and Systems, Vol. 92, July/August 1973, pp.1274-1281.
7. P. SILVESTER, A. KONRAD, Analysis of transformer leakage phenomena by high-order finite elements, IEEE Transactions on Power Apparatus and Systems, Vol.92, November/December, 1973, pp. 1843-1855.
8. P.Y. HU, Printed circuit motor-disk vs cylinder, Proceedings of the Fourth Annual Symposium on Incremental Motion Control Systems and Devices, University of Illinois, April 1-3, 1975, pp. R.1. - R.8.
9. B.W. WENTWORTH and E.L. ELLIS, Stabilization prediction for permanent-magnet field motors and generators, Journal of Applied Physics, Vol. 37, No.3, March 1966, pp. 1143-1146.
10. Y.S. ZAKHAROV, "The influence of armature reaction on the operation of d.c. motors with permanent magnets", Elektrichestvo, 1958, 78, pp. 34-36.
11. W. LORD, Application of modern p.m. materials to the excitation of a slow-speed servomotor, Journal of Applied Physics, Vol. 37, No.3., March 1966, pp. 1151-1153.
12. W. LORD, Demagnetization phenomena in high-performance dc servomotors, Proc. IEE, Vol. 122, No.4. April 1975, pp.392-294.
13. W. LORD and J.H. HWANG, Leakage field analysis of magnetic circuits by variational methods, Proceedings of the Fourth Annual Symposium on Incremental Motion Control Systems and Devices, University of Illinois, April 1-3, 1975, pp. P1 - P9.
14. V.V. FETISOV, Calculation of commutation reaction in d.c. machines with a brush overlap greater than unity, Elektrichestvo, 1960, 80 pp. 46-50.
15. S. HALASZ, Influence of armature reaction on the stability of d.c. motors, Elektrotechnika, 1963, 56 pp. 157-164.
16. T. ONUKI, A theoretical design of the airgap shape of d.c. machines, Electrotech, J. Japan, 1954, 5 pp. 22-26.
17. D.J. HANRAHAN and D.S. TOFFOLO, Permanent magnet generators - Pt. 2 Optimum design, IEEE Trans. 1963, 82 pp. 68-74.
18. J. FISCHER, H. MOSER, Die Nachbildung von Magnetisierungskurven durch einfache algebraische oder transzendente funktionen, Archiv für Elektrotechnik, Vol. 42, No.5, 1956, pp. 286-299.
19. F.C. TRUTT, E.A. ERDELYI, R.E. HOPKINS, Representation of the magnetization characteristic of dc machines for computer use, IEEE Transactions on Power Apparatus and Systems, Vol. 87, March 1968, pp. 665-669.
20. G.F.T. WIDGER, Representation of magnetisation curves over extensive range by rational-fraction approximations, Proc. IEE, Vol. 116, No.1, January 1969, pp. 156-160.
21. M.K. EL-SHERBINY, Representation of the magnetization characteristic by a sum of exponentials, IEEE Transactions of Magnetics, Vol.9, No.1, March 1973, pp. 60-61.

22. W.K. MACFADYEN, R.R.S. SIMPSON, R.D. SLATER, W.D. WOOD,
Representation of magnetisation curves by exponential series,
Proc. IEE, Vol. 120, No.8, August, 1973, pp. 902-904.
23. T.S. KRISHNAMOORTHY, M. VENNGOPAL, Determination of best fit
parameters of a model for excitation curve, Proceedings of the IEEE,
Vol. 61, No.12, December 1973, pp. 1762-1784.
24. K.J. BINNS et al, A rapid method of computation of the magnetic
field of permanent magnets, IEEE Transactions on Magnetics, Vol.11,
No.5, September 1975, pp. 1538-1540.
25. W.J. HARROLD, Calculation of equipotentials and flux lines in
axially symmetrical permanent magnet assemblies by computer, IEEE
Transactions of Magnetics, Vol.8, No.1. March 1972, pp.23-29.
26. S.A.Y. SABIR and W. SHEPHERD, Magnetic properties of Alcomax 111
with dynamic excitation, Proc. IEE, Vol. 121, No.8, August 1974,
pp. 907-912.
27. J. SLOMCZYNSKA, Nonlinear analysis of the magnetic flux
distribution in the magnetized magnet stabilized in air, IEEE
Transactions on Magnetics, Vol.10, No.4., December 1974,
pp. 1109-1113.
28. J.W. TEAPE et al, Representation of magnetic characteristic,
including hysteresis, by exponential series, Proc. IEE, Vol.121,
No.9, September 1974, pp. 1019-1020.
29. W.H. DIERKING and C.T. KLEINER, Phenomenological magnetic core model
for circuit analysis programs, IEEE Transactions on Magnetics,
Vol.8, No.3, September, 1972, pp.594-596.

ACKNOWLEDGEMENTS

The author gratefully acknowledges the assistance of J.H. Hwang of Tuboscope Inc., for producing the flux plots in this paper. He would also like to thank Professor B.C. Kuo of the University of Illinois, for permission to publish Figures 4, 5, 6, 7 and 8.

SECTION C STEADY STATE

THE SOLUTION OF TRANSIENT AND STEADY-STATE MAGNETIC FIELDS
WITH PARTICULAR REFERENCE TO NUMERICAL METHODS

R.L. Stoll

Department of Electrical Engineering,
University of Southampton.

1. Introduction

The vector diffusion equation for a low frequency magnetic field \underline{H} can be written in the form (1)

$$\nabla^2 \underline{H} = \sigma \frac{dB}{dH} \frac{\partial H}{\partial t} - \text{grad} \left(H \cdot \frac{1}{\mu} \text{grad} \mu \right) - \frac{1}{\sigma} (\text{grad} \sigma) \times \text{curl} \underline{H} \quad (1)$$

Although the conductivity σ is usually constant within each conductor, it is expressed here as a function of space because this can sometimes facilitate setting up the computation scheme. The permeability μ is similarly treated, but, in addition, may be a function of \underline{H} . The constituent equation is assumed to take the form $\underline{B} = \mu \underline{H}$ where \underline{B} and \underline{H} are not necessarily linearly related but the magnetic material is isotropic and has no hysteresis effect. For example, the magnetisation characteristic may be approximated by the Frohlich curve

$$\underline{B} = \frac{\underline{H}}{a + bH} \quad (2)$$

from which $\mu = (a + bH)^{-1}$.

Problems in which the magnetic field is described by eqn.1 are known as initial boundary value problems: the initial ($t = 0$) state of \underline{H} must be defined over the space domain and Dirichlet, Neumann or mixed boundary conditions specified for $t > 0$. However, in the special case of sinusoidal excitation, with the additional constraint $\mu = \mu_0 \mu_r$, a simpler boundary value problem can be achieved by defining a complex vector $\underline{\bar{H}}$ which is related to the instantaneous vector \underline{H} by

$$\underline{H} = \text{Re} \left[\underline{\bar{H}} e^{j\omega t} \right] \quad (3)$$

so that eqn.1 reduces to

$$\nabla^2 \underline{\bar{H}} = j\omega\sigma\mu\bar{H} - \text{grad} \left(\bar{H} \cdot \frac{1}{\mu} \text{grad} \mu \right) - \frac{1}{\sigma} (\text{grad} \sigma) \times \text{curl} \bar{H} \quad (4)$$

Use of the vector potential \underline{A} , defined as $\text{curl} \underline{A} = \underline{B}$ and $\text{div} \underline{A} = 0$ (Sarma (2) shows that a nonzero divergence may be helpful in some low frequency problems), also yields similar real and complex second-order partial

differential equations, the real equation being

$$\nabla^2 \underline{A} = \sigma \mu \left(\frac{\partial A}{\partial t} + \text{grad} V \right) - \frac{1}{\mu} (\text{grad} \mu) \times \text{curl} \underline{A} \quad (5)$$

where V is a scalar electric potential.

Considering problems involving two space co-ordinates x and y and time, then if there is only one component of \underline{H} , H_z say, which is independent of z , i.e. the current density is a function of x and y , eqn.1 reduces to the convenient symmetrical form

$$\frac{\partial}{\partial x} \left(\rho \frac{\partial H_z}{\partial x} \right) + \frac{\partial}{\partial y} \left(\rho \frac{\partial H_z}{\partial y} \right) = \frac{dB_z}{dH_z} \frac{\partial H_z}{\partial t} \quad (6)$$

where ρ is the resistivity. Alternatively, if there is only one component of current density \underline{J}_z , it is convenient to use the resulting single component of vector potential A_z , and eqn.5 yields

$$\frac{\partial}{\partial x} \left(v \frac{\partial A_z}{\partial x} \right) + \frac{\partial}{\partial y} \left(v \frac{\partial A_z}{\partial y} \right) = \sigma \frac{\partial A_z}{\partial t} + \sigma \frac{\partial V}{\partial z} = \sigma \frac{\partial A_z}{\partial t} - \underline{J}_s \quad (7)$$

where v is the reluctivity. The term $\frac{\partial V}{\partial z}$ is the negative of the impressed electric field strength E_z , so that $-\sigma \frac{\partial V}{\partial z} = \underline{J}_s$ is the impressed source current density, if any.

Where a problem has natural boundaries, the differential formulation is preferable, especially in view of the research effort that has been put into the theory of differential equations, but it is also possible to set up an integral equation that sums the contribution of all the field sources. Interesting examples of integral formulations solved numerically are given by Haznadar (3) and Silvester (4).

2. Types of Solution

At the risk of oversimplification we can divide the various types of mathematical solution into three categories.

(a) First there is the analytical solution in which the independent variable or parameter of interest, e.g. the magnetic field distribution or a single quantity such as impedance, can be expressed algebraically in terms of the system constants (conductivity, frequency etc.) and the independent variables (the space and time co-ordinates). Needless to say the expression involved may be a complicated series, for example, and numerical substitution may be necessary before the influence of a given parameter can be determined. Examples of this type of solution are the separation of variables method and the finite, or infinite, Fourier

transform. Such methods are limited to relatively simple linear problems.

(b) Secondly, there is the almost entirely numerical approach in which the problem is discretised in some way so that we can work with a set of numbers instead of with a continuous variable and therefore with a matrix equation instead of a partial-differential equation. This is the basis of the finite-difference and finite-element methods which will be discussed in Section 3. An interesting variation is the coupled electric and magnetic network approach developed by Carpenter^(5,6) which makes use of the magnetic scalar potential, instead of the vector potential, by **confining** the current flow to thin conducting sheets and is a powerful way of translating an eddy-current problem into numerical form.

(c) Thirdly, there is the type of method that can most appropriately be described as mixed, containing both analytical and numerical components. They usually arise because a full numerical method is found to be too time consuming on the available computer system, or because the analyst is determined not to obey Parkinson's law but to seek an economic solution. An outstanding example is the method outlined by Hockney⁽⁷⁾ for the solution of Poisson's equation in a rectangular region, but also applicable to Helmholtz equation and to other two-dimensional co-ordinate systems, in which one dimension of the problem is reduced by the application of a finite Fourier transform. The partial-differential equation is thus reduced to a set of ordinary-differential equations which can then be solved numerically. There are various refinements which increase the speed of the solution, and the method should be appropriate for multi-region eddy-current problems, where the interfaces are parallel to the direction in which the transform is applied.

A different approach due to Silvester^(8,9) regards each term in a double Fourier series solution for a long rectangular bar as a single eddy-current mode for which an equivalent R-L circuit can be set up. The terms in the series form a complete set of orthogonal functions and so there is no coupling between the set of equivalent circuits. In more general terms we can say that the current in a conductor flows in an infinite number of independent spatial patterns (modes), its distribution between the modes being dictated by the form of the excitation. Thus the method had the advantage that any form of time-dependent excitation can be handled by the same set of circuit equations or matrix equation, and it is

particularly useful in being able to handle situations in which it is either not possible or not convenient to formulate an initial boundary value problem. In this sense the method is an alternative to the numerical solution of an integral equation formulation of the problem.

We will now briefly consider some numerical methods which are particularly important if we wish to include magnetic saturation.

3. Numerical Solutions

Problems that require numerical treatment divide naturally into two broad classes; linear steady state, and nonlinear steady state and transient. All nonlinear solutions are essentially the same because a steady-state solution must pass through a numerical transient which will be similar to the real transient for the given initial (switch-on) conditions.

Time-dependent magnetic field equations of the diffusion type have been solved numerically by both finite differences and finite elements, although the time co-ordinate has always been discretised by finite differences. The common feature of the methods is that, at each time step, they yield a large set of difference equations which are usually arranged to be linear and have to be solved either by elimination or by an iterative process of some sort.

In the finite-difference method, the complete differential operator is replaced by a finite-difference operator which sets up discrete values of the dependent variable at the nodes of a regular grid consisting (usually) of rectangular cells. The derivation and programming of the method is relatively straightforward compared with the finite-element approach, which, in its simplest form, sets up an array of triangular elements covering the space domain of the problem and forces the dependent variable to vary linearly over the surface of each element. Thus the local variable is defined by its values at the three vertex nodes. One of the advantages of finite elements is that their size is readily varied so that the field can be accurately represented in regions of rapid spatial variation without using an excessive number of elements. In a nonlinear quasi-static problem the set of algebraic equations is generated by minimising the energy functional⁽¹⁰⁾

$$F = \iint \left\{ \int_0^B v_B dB - AJ \right\} dx dy \quad (8)$$

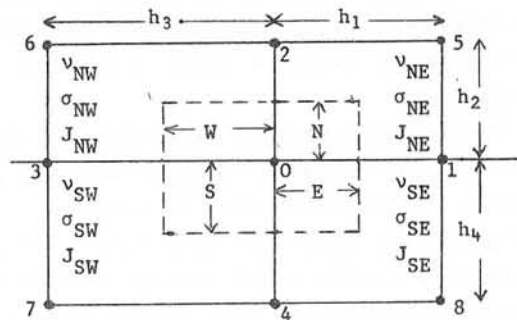
for which the original partial-differential equation is the Euler equation. One way of introducing the time dependence is to regard J in eqn.8 as consisting of, both the source current density J_s and the eddy current density $-\sigma \frac{\partial A}{\partial t}$ from eqn.7, i.e. $J = J_s - \sigma \frac{\partial A}{\partial t}$, and to 'graft on' a finite-difference expression for the time derivative after the minimisation process⁽¹¹⁾. Eqn.8, with J regarded as an instantaneous injected current, must now more properly be referred to as a functional associated with energy because, due to the ohmic losses, the new system is no longer energy conserving. Whatever the formal difficulties the hybrid scheme appears to work. Results for linear complex problems have already been reported^(12,13), and a relatively simple nonlinear problem has been solved using the Galerkin technique⁽¹⁴⁾.

3.1 A finite-difference algorithm for eqn.7.

It is possible to proceed directly via Taylor's theorem, but a simpler result can be achieved if eqn.7 is written in the form

$$\text{curl}_z \left(a_{-x} v \frac{\partial A_z}{\partial y} - a_{-y} v \frac{\partial A_z}{\partial x} \right) = J_s - \sigma \frac{\partial A_z}{\partial t} \quad (9)$$

FIG. 1



Integrating eqn.9 over the cross-section of the secondary cell shown dotted in Fig.1, applying Stokes' theorem and following a procedure similar to that given in Reference 1 for the complex form of eqn.9, the following explicit finite-difference equation for advancing from time step k to $k + 1$ is obtained.

$$\begin{aligned} & (\alpha_1 + \alpha_2 + \alpha_3 + \alpha_4) A_{o,k} - (\alpha_1 A_{1,k} + \alpha_2 A_{2,k} + \alpha_3 A_{3,k} + \alpha_4 A_{4,k}) \\ & = I_{o,k} - Q_{o,k} \frac{A_{o,k+1} - A_{o,k}}{\Delta t} \end{aligned} \quad (10)$$

$$\begin{aligned} \text{where } \alpha_1 &= (Nv_{NE} + Sv_{SE}) h_1^{-1} \\ \alpha_2 &= (Ev_{NE} + Wv_{NW}) h_2^{-1} \\ \alpha_3 &= (Nv_{NW} + Sv_{SW}) h_3^{-1} \\ \alpha_4 &= (Ev_{SE} + Wv_{SW}) h_4^{-1} \\ I_o &= NE J_{NE} + NW J_{NW} + SE J_{SE} + SW J_{SW} \\ \text{and } Q_o &= NE \sigma_{NE} + NW \sigma_{NW} + SE \sigma_{SE} + SW \sigma_{SW} \end{aligned}$$

All these parameters can be functions of time, i.e. the time-step counter k , including the coefficients α_1, α_2 , etc. if the problem is nonlinear. The truncation error of the algorithm is $O(h^2 + \Delta t)$ when h is the larger of h_1, h_2 , etc. The algorithm is also explicit in the sense that the new potential $A_{o,k+1}$ at node 0 can be obtained directly. However, such a scheme is known to have a very limited stability range, and modifications are necessary. These are most conveniently discussed in terms of a one-dimensional field solution.

3.2 One-dimensional algorithms and comments on extension to two dimensions

Consider the one-dimensional version of eqn.6 with constant conductivity, namely:-

$$\frac{\partial^2 H_z}{\partial y^2} = \sigma \frac{dB_z}{dz} \frac{\partial H_z}{\partial t} = \beta \frac{\partial H_z}{\partial t} \quad (11)$$

The simple explicit difference form of eqn.11 is

$$H_{i,k+1} = rH_{i+1,k} + (1 - 2r) H_{i,k} + rH_{i-1,k} \quad (12)$$

where $r = \Delta t / \beta h^2 < \frac{1}{2}$ for stability. Alternatively, the simple implicit equation using a backward instead of forward time difference equation is^(15,23)

$$H_{i+1,k+1} + \left(-2 - \frac{1}{r}\right) H_{i,k+1} + H_{i-1,k+1} = -\frac{1}{r} H_{i,k} \quad (13)$$

with no restriction on r . The penalty we have to pay for this stability is to solve all the new values at time $k+1$ simultaneously. However, the coefficient matrix is tridiagonal and so the matrix equation is simple to solve.

Application of eqns.12 and 13 at alternate time steps produces the well-known Crank-Nicolson algorithm

$$H_{i+1,k+1} + 2\left(-1 - \frac{1}{r}\right) H_{i,k+1} + H_{i-1,k+1} = -H_{i+1,k} + 2\left(1 - \frac{1}{r}\right) H_{i,k} - H_{i-1,k} \quad (14)$$

which has an improved truncation error $O(h^2 + (\Delta t)^2)$ and is stable for all linear problems and a wide range of nonlinear ones. When r is a function of H , a two-step predictor-corrector algorithm is usually incorporated⁽¹⁵⁾ in order to be able to maintain a relatively large time step.

The Crank-Nicolson equation is an implicit one so that its extension to two-dimensional problems is rather inefficient because of the large number of equations to be solved simultaneously at each time step. For this an iterative solution (e.g. successive over-relaxation) is faster than elimination because, since the change in nodal values from one time step to the next is small, only a few iterations are needed. However, a modified version of the method in two dimensions is the Peaceman-Rachford alternating-direction implicit (ADI) method^(16,24) where the nodal equations on first the rows and then the columns of the space grid are treated alternately as implicit sets.

It is tempting to seek an explicit method that is stable and can be extended to two-dimensional solutions. One possibility is the hopscotch method devised by Gourlay⁽¹⁷⁾ and summarised in Reference 1. Basically it derives from the alternate application of eqns.12 and 13 to the nodes on each time step so that the space-time plane can be pictured as a chess board of black (explicit) and white (implicit) squares. The resulting scheme is explicit and is effectively a faster version of the DuFort-Frankel^(18,25) scheme (although some of this advantage is lost in nonlinear problems) where $H_{i,k}$ in eqn.12 is replaced by $\frac{1}{2}(H_{i,k+1} + H_{i,k-1})$ to give

$$H_{i,k+1} = H_{i,k-1} + \frac{2r}{2r+1} (H_{i+1,k} - 2H_{i,k-1} + H_{i-1,k}) \quad (15)$$

The truncation error is $O(h^2 + (\Delta t)^2 + (\Delta t/h)^2)$ which indicates that Δt must be much smaller than h . Closer investigation shows that the optimum value of Δt for minimum error lies near $\frac{\beta h^2}{\sqrt{12}}$ for a linear problem⁽¹⁸⁾. For nonlinear solutions with high saturation, where β may decrease to a low value (typically about 4) for part of the cycle, the situation is not clear. The above condition would suggest $\Delta t \approx h^2$, but the method then involves as much computation as the simple explicit method. The time step must therefore be larger and a greater error tolerated, although the error can still be less than that with the simple scheme.

3.3. Analytical expression for the magnetisation curve

Numerical methods are both faster and less likely to become unstable if an analytical expression is used for the magnetisation curve instead of interpolating from a set of experimental values. In any case the experimental values should be smoothed before use, especially if the incremental permeability is required. A large number of mathematical expressions have been examined by Trutt, Erdelyi and Hopkins⁽¹⁹⁾ and the Frohlich curve (eqn.2) emerges as a good compromise between accuracy and simplicity. In fact the curve is excellent for materials like mild steel but not so good for silicon steels (electrical machine laminations) which have a pronounced 'knee' in their characteristic. It will be seen from eqn.2 that as H increases the magnitude of B tends to the constant value b^{-1} , i.e. the curve has zero slope. On the other hand, the magnetisation curve for steel maintains a constant slope μ_0 after the saturation point (B_s, H_s) . When working well into saturation, it is therefore essential to make up the characteristic in two parts; the Frohlich curve for $B < B_s$ and the straight line $B = B_0 + \mu_0 H$ when $B > B_s$. The constant B_0 can be shown to be given by bB_s^2 . Thus the incremental slope and reluctivity when $B < B_s$ are given by

$$\frac{dB}{dH} = \frac{a}{(a + bH)^2} \quad (16)$$

$$\text{and} \quad v = \frac{a}{1-bB} \quad (17)$$

and, when $B > B_s$ by

$$\frac{dB}{dH} = \mu_0 \quad (18)$$

$$\text{and} \quad v = \frac{1}{\mu_0} \left(1 - \frac{B_0}{B}\right) \quad (19)$$

The constants in the Frohlich equation must be such that the saturation point (B_s, H_s) lies on the curve and the slope is μ_0 when $H = H_s$. After a little manipulation we obtain

$$\left. \begin{aligned} a &= \mu_0 (H_s/B_s)^2 \\ b &= (1 - \sqrt{\mu_0 a}) B_s^{-1} \end{aligned} \right\} \quad (20)$$

An important point to note is that, if the problem is being solved in terms of the vector potential, H or v should be expressible explicitly

in terms of B, and hence the derivatives of A, and preferably not in a form that necessitates making successive approximations to H.

3.4 The DuFort-Frankel scheme in two dimensions with variable coefficients

The two-dimensional equation in H_z for constant conductivity is, from eqn.6,

$$\frac{\partial^2 H_z}{\partial x^2} + \frac{\partial^2 H_z}{\partial y^2} = \sigma \frac{dB_z}{dH_z} \frac{\partial H_z}{\partial t} \quad (21)$$

For a square mesh in the x,y plane of side h, the DuFort-Frankel finite-difference equation is

$$\left. \begin{aligned} H_{i,j,k+1} &= H_{i,j,k-1} + \frac{2r}{4r+1} \\ (H_{i-1,j,k} + H_{i,j-1,k} + H_{i,j+1,k} + H_{i+1,j,k} - 4H_{i,j,k}) & \end{aligned} \right) \quad (22)$$

where i,j is the integer address of a node in the x,y plane. The coefficient r is the same as in eqn.15 for the one-dimensional solution and contains the incremental permeability, which, if the Frohlich representation is being used, is given by eqns.16 and 18. However, we need to express H in eqn.16 in terms of the nodal values. Examining eqns.15 and 22 we see that they involve nodal values on three time levels (k-1,k, and k+1), and, if we view the space-time domain as a multi-dimensional chess board, the finite-difference equations separate into two sets, one associated with the white cubes and the other with the black. Thus, if we allow r to be expressed as a function of $H_{i,j,k}$ we are forcing a white value into the black set, or vice-versa. Such a mixture has been found to cause instability and it is therefore necessary for r to contain black (or white) values only. The unknown $H_{i,j,k+1}$ cannot appear in r because the finite-difference equation would no longer be linear in the unknown value, and therefore the average

$$H = \frac{1}{4} (H_{i-1,j,k} + H_{i,j-1,k} + H_{i,j+1,k} + H_{i+1,j,k}) \quad (23)$$

is used in eqn.16.

If we now turn to a two-dimensional finite-difference scheme in terms of the vector potential component A_z , again taking a square mesh and constant conductivity, and assuming zero source current density for simplicity, eqn.10 reduces to the simple explicit form

$$\begin{aligned} A_{o,k+1} &= \frac{1}{2}C \{ (v_{NE}+v_{SE})A_{1,k} + (v_{NE}+v_{NW})A_{2,k} \\ &+ (v_{NW}+v_{SW})A_{3,k} + (v_{SE}+v_{SW})A_{4,k} \} \\ &+ \{1-C (v_{NE}+v_{NW}+v_{SE}+v_{SW})\}A_{o,k} \end{aligned} \quad (24)$$

where $C = \Delta t / \sigma h^2$. The DuFort-Frankel equation is obtained by replacing $A_{o,k}$ by $\frac{1}{2}(A_{o,k+1} + A_{o,k-1})$.

Whereas the incremental permeability in eqn.22 (in the coefficient r) is effectively a node centred value, the reluctivities in eqn.24 are cell centred (see Fig.1). For example, using eqn.17,

$$v_{NE} = \frac{a}{1-bB_{NE}}$$

where B_{NE} is the magnitude of the flux density in cell NE of Fig.1. Since $B_x = \partial A / \partial y$ and $B_y = -\partial A / \partial x$, the most obvious finite-difference expression for B_{NE} is given by

$$\begin{aligned} B_{NE} &= (B_{xNE}^2 + B_{yNE}^2)^{\frac{1}{2}} = \left[\left\{ \frac{1}{2} \left(\frac{A_{2,k} - A_{o,k}}{h_1} + \frac{A_{5,k} - A_{1,k}}{h_1} \right) \right\}^2 \right. \\ &\left. + \left\{ \frac{1}{2} \left(\frac{A_{1,k} - A_{o,k}}{h_2} + \frac{A_{5,k} - A_{2,k}}{h_2} \right) \right\}^2 \right]^{\frac{1}{2}} \end{aligned} \quad (25)$$

In the DuFort-Frankel equivalent of eqn.24 use of eqn.25 involves a mixture of black and white nodal values. However, in practice, this mixture appears weak enough to avoid instability if the scheme is used with care, particularly in the choice of h (typically 0.5mm).

3.5 Two-dimensional linear steady-state solutions

The complex equivalent of eqn.10 can be obtained by inspection. The set of finite-difference equations is now stationary in the sense that a single elimination process only is required. However, due to the sparsity of the coefficient matrix, iterative methods are usually preferable where each iteration can be thought of as a step forward in solution time. Indeed iterative methods have been found to converge faster for complex than for real arrays of the same size. Apart from the A D I method already mentioned which has been found suitable for problems involving several thousand equations, there is the simpler complex version of the well-known successive over-relaxation (SOR) method⁽²⁰⁾. The only difficulty with SOR is the estimation of the complex accelerating factor⁽²¹⁾.

A method of interest, proposed by Stone⁽²²⁾, is based on the realisation that the relatively good convergence of ADI methods is due to the component of direct elimination in the iterative process. Stone's strongly implicit iterative method (SIIM) has an increased implicit content and excellent convergence, but at the expense of a substantial increase in computer store requirement (about five times that for SOR). In a simple problem involving 600 internal nodes, SOR required 53 and SIIM 14 iterations, the latter being approximately 10 per cent faster in time⁽¹⁾. However, as the number of nodes increases the time advantage of SIIM also increases.

REFERENCES

1. STOLL, R.L. : 'The analysis of eddy currents', Clarendon Press, Oxford, 1974, pp. 5, 99, 83, 112.
2. SARMA, M.S. : 'Potential functions in electromagnetic field problems', IEEE Trans. on magnetics, Vol. MAG-6, 1970, pp.513-18.
3. HAZNADAR, Z. and MATJAN, J. : 'Numerical solution of skin effect in systems of straight conductors, Elektrotehnika, Zagreb, Vol. 5, 1970.
4. SILVESTER, P. : 'Dynamic resistance and inductance of slot-embedded conductors', IEEE Trans. Power App. Syst., Vol.87, 1968, pp. 250-56.
5. CARPENTER, C.J. : 'Three-dimensional numerical solution of eddy-currents in thin plates', Proc. Instn. Elect. Engrs, Vol.122, 1975, pp.681-8.
6. CARPENTER, C.J. : 'Finite-element network models and their application to eddy-current problems', *ibid.* Vol.122, 1975, pp. 455-62.
7. HOCKNEY, R.W. : 'A fast direct solution of Poisson's equation using Fourier analysis', Journal of the Association for Computing Machinery, Vol.12, 1965, pp.95-113.
8. SILVESTER, P. : 'Eddy-current modes in linear solid iron bars', Proc. Instn. Elect. Engrs., Vol.112, 1965, pp.1589-94.
9. SILVESTER, P. : 'The accurate calculation of skin effect in conductors of complicated shape', IEEE Trans. Power App. Syst., Vol. PAS-87, 1968, pp.735-41.
10. SILVESTER, P. and CHARI, M.V.K. : 'Finite element solution of saturable magnetic field problems', *ibid.*, Vol.89, 1970, pp. 1642-48.
11. FLATABO, N. : 'Transient Heat conduction problems in power cables solved by the finite element method', *ibid.*, Vol.92, 1973, pp. 56-63.
12. CHARI, M.V.K. : 'Finite-element solution of the eddy-current problem in magnetic structures', *ibid.*, Vol.93, 1974, pp.62-69.
13. DONEA, J., GIULIANI, S., and PHILIPPE, A. : 'Finite elements in the solution of electromagnetic induction problems', Int. Journal for numerical methods in Engineering, Vol.8, 1974, pp.359-67.
14. FOGGIA, A., SABONNADIERE, J.C. and SILVESTER, P. : 'Finite element solution of saturated travelling magnetic field problems', *ibid.*, Vol.94, 1975, pp.866-71.
15. ROSENBERG, D.U. von : 'Methods for the numerical solution of partial differential equations', Elsevier, New York, 1969, pp.20, 57.
16. PEACEMAN, D.W. and RACHFORD, H.H. : 'The numerical solution of elliptic differential equations', J. Soc. ind. appl. math., Vol.3, 1955, pp. 28-41.
17. GOURLAY, A.R. : 'Hopscotch: a fast second-order partial differential equation solver', J. Inst. Math. Appl., Vol.6, 1970, pp. 375-90.
18. DUFORT, E.C. and FRANKEL, S.P. : 'Stability conditions in the numerical treatment of parabolic differential equations', Mathl. Tabl. Natn. Res. Coun., Wash., Vol. 7, 1953, pp. 135-52.
19. TRUTT, F.C., ERDELYI, E.A., and HOPKINS, R.E. : 'Representation of the magnetic characteristics of D.C. machines for computer use', IEEE Trans. Power App. Syst., Vol.87, 1968, pp.665-9.
20. AMES, W.F. : 'Numerical methods for partial differential equations' Nelson, 1969.
21. STOLL, R.L. : 'Solution of linear steady-state eddy-current problems by complex successive over-relaxation', Proc. Instn. Elect. Engrs, Vol. 117, 1970, pp. 1317-23.
22. STONE, H.L. : 'Iterative solution of implicit approximations of multidimensional differential equations', SIAM J. Numer. Anal., Vol.5, 1968, pp. 530-58.
23. ZAKRZEWSKI, K. and PIETRAS, F. : 'Method of calculating the electromagnetic field and power losses in ferromagnetic materials, taking into account magnetic hysteresis', Proc. Instn. Elect. Engrs., Vol. 118, 1971, pp.1679-85.
24. MUHLHAUS, J. : 'On the solution of 2-dimensional saturable eddy-current problems by the ADI technique', *ibid.* Vol. 123, 1976, pp.183-6.
25. LIM, K.K., and HAMMOND, P. : 'Numerical method for determining the electromagnetic field in saturated steel plates', *ibid.*, Vol.119, 1972, pp.1667-74.

Discussion following paper:

(Munro, IBM) 1. The method which you described for generating the finite difference equations was for rectangular meshes. Is this method also applicable to general quadrilateral meshes which are not necessarily parallel to the coordinate axes?

2. Can you comment on the speed of convergence of the ADI method for problems in which there are large changes in material properties (eg permeability) within the solution region?

(R Stoll) In reply to Dr Munro's first question, the method I describe for setting up a finite-difference equation in 2 dimensions using surface integration and Stokes' theorem can be applied in 3 dimensions and other coordinate systems. However, the 'box' used should conform to the coordinate systems selected.

In the second case, I have not used the ADI method sufficiently to be able to give a firm answer, but I suspect ADI will suffer in the same way as other iterative schemes in static or steady-state problems, although probably rather less so in view of the direct component of the method.

(Miller, University of Leeds) I would like to comment briefly on Mr Munro's question. The integration method described by Dr Stoll for discretising the differential equation can indeed be used for irregular polygonal meshes.

It has been claimed that discretisation by the integration method automatically gives properties to the coefficient matrix of the linear equations which guarantee convergence in iterative solution. Certainly this appears to be in tune with 2-D problems but at Leeds we have had the difficulty that these properties (in particular, diagonal dominance) appear to be lost when going to 3-D problems.

Refs Bronne, B T Ph D Thesis Leeds University
Varga, Matrix Iterative Analysis

(Schomberg, Philips GmbH) You mentioned the Hopscotch method, where one has "white" and "black" mesh points arranged in such a way that the white mesh points are surrounded by black ones and vice versa, and where one updates the corresponding "white" and "black" potentials alternatively. There seems to be a strong resemblance to the SOR method with "white-black" (or "odd-even") ordering of the mesh points, which is applicable to elliptic finite difference equations. Could you comment on this?

(Stoll,) Although Hopscotch is primarily designed for use with parabolic equations, the question concerns its use for stationary problems, ie as an iterative method. It can be shown to be equivalent to the Gauss-Seidel and SOR methods with odd-even ordering of the nodes.

The Prediction of Machine End-region
Fluxes, allowing for Eddy Current
Losses in Thick Components

by

T.W. Preston, A.B.J. Reece

1. Introduction

As unit ratings of turbine-generators increase, it is becoming essential to make accurate prediction of flux distribution, and associated induced losses in the machine end-zone, so that the risk of damage from overheating of components can be avoided.

Prediction of end-region leakage fields, allowing for irregular boundaries and internal components, such as the screen and clamping plate, can only be carried out numerically. The work described in Ref. (1) outlines a finite-element method for determining the scalar potential distribution in the end-region: scalar potential was used because it allows simple treatment of boundaries, and, compared with vector potential, only a single function has to be calculated. Economy of nodes was obtained by assuming that all end-zone functions vary sinusoidally around the periphery, thereby reducing the problem to one in the radial-axial plane only, whilst still retaining the essential 3-dimensional geometry of the end-region. In this way, the complex boundary outline can be represented adequately, but the magnetic effect of the boundary can only be represented by either an infinitely-permeable surface (the Dirichlet condition) or an infinitely-conducting surface (the Neumann condition).

The infinitely-conducting boundary condition has often been used to allow for eddy current effects in conducting boundaries, by setting a surface which has wholly tangential flux at a depth related to the skin depth below the real surface. This treatment is very approximate, and falls down badly when dealing with a highly permeable conducting surface,

since no allowance can be made for the high permeability within the skin depth. A fully 3-dimensional vector potential approach would overcome this difficulty, but it would prove expensive to use, as three solutions would be required to obtain all flux densities, and boundary conditions could prove awkward. Although scalar potential is not normally used in problems involving eddy currents, the following sections show that the use of complex potential with a new boundary condition which allows for frequency, permeability and resistivity to represent "thick" components can give excellent results.

2. Development of Boundary Condition

The effect of induced currents beneath the surface of a conducting surface is dealt with by relating the flux distribution beneath the surface to the density normal to the surface. In the formulation of the boundary condition, the following assumptions are made:-

- (i) The thickness of the conductor is greater than the depth of penetration.
- (ii) Flux flows entirely parallel to the surface once inside the member.
- (iii) Flux decays exponentially with depth, as in 1-dimensional theory.

The flux entering normal to the surface of a conducting member can be equated to the integrated value of the tangential flux from the surface to an infinite depth. Fig. 1 shows a tiny element of the conducting member, and by consideration of flux entering and leaving the element, the following equations are derived:-

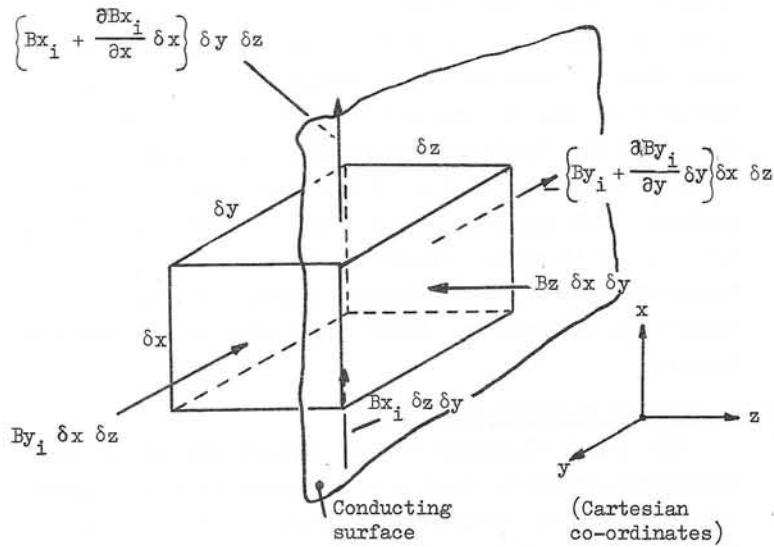


Fig. 1

Therefore, equating fluxes:

$$B_z \delta y \delta x = \int_0^{\infty} \frac{\partial B_{y_i}}{\partial y} \delta x \delta y dz + \int_0^{\infty} \frac{\partial B_{x_i}}{\partial x} \delta x \delta y dz$$

which, with Assumption (iii) and the continuity conditions at the interfaces, reduces to:

$$B_{z(\text{air})} = \frac{\mu_i (1 - j)\delta}{2} \left\{ \frac{\partial B_{y(\text{air})}}{\partial y} + \frac{\partial B_{x(\text{air})}}{\partial x} \right\} \dots (1)$$

where: μ_i = relative permeability of conducting member

$$\delta = \left[\frac{2\rho}{\mu_o \mu_i \omega} \right]^{\frac{1}{2}}$$

ρ = resistivity

ω = angular frequency

Thus the effect of induced currents beneath a surface can be represented by a boundary condition at the surface.

3. Analytic Check

To check the validity of the assumptions made in formulating the boundary condition, the expression for flux density in a machine gap (obtained by using the derivative boundary condition) was compared with the exact analytical solution.

(i) Exact solution

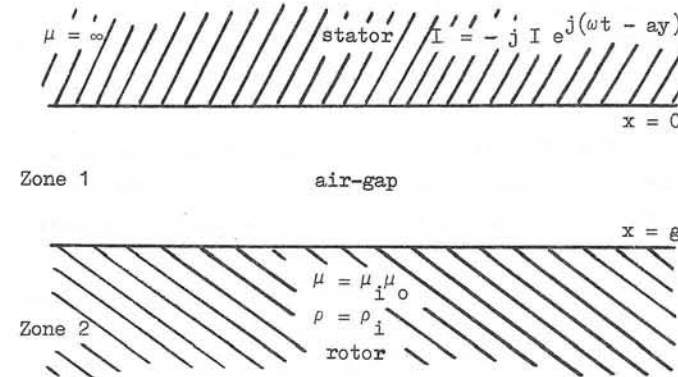


Fig. 2

Fig. 2 shows the air-gap and rotor iron in a Cartesian co-ordinate system, and the resulting equation for flux density in Zone 1 is:

$$B_x = \frac{\mu_o I \left[\cosh a(x - g) - \frac{c}{a \mu_i} \sinh a(x - g) \right]}{\sinh ag + \frac{c}{a \mu_i} \cosh ag} \dots (2)$$

where: $c^2 = a^2 + j \omega b^2$

$$a = 2\pi/T$$

$$b^2 = \mu_o \mu_i / \rho_i = 2/\delta^2 \omega$$

$$\delta = (2 \rho_i / \mu_o \mu_i \omega)^{\frac{1}{2}}$$

T = double pole pitch

(ii) Boundary solution

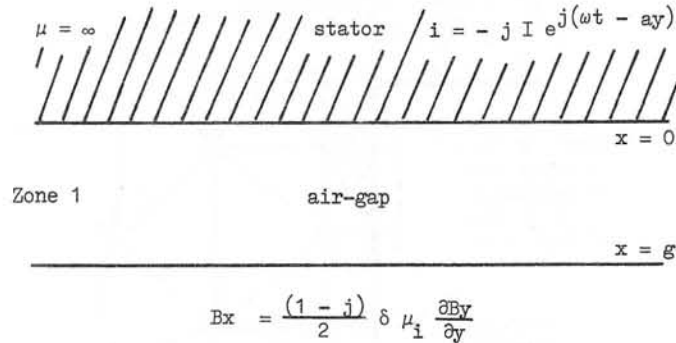


Fig. 3

Fig. 3 illustrates the same example, treated as a single-zone problem, with the boundary condition given by Eqn. (1) representing the rotor. The resulting equation for the air-gap density is:

$$B_x = \frac{j \mu_0 I \left[\cosh a(x-g) - \frac{(1+j)}{a \delta \mu_i} \sinh a(x-g) \right]}{\sinh ag + \frac{(1+j)}{a \delta \mu_i} \cosh ag} \dots (3)$$

Eqns. (2) and (3) differ only in the coefficients of the $\sinh a(x-g)$ and $\cosh ag$ terms, and if a^2 is negligibly small compared with the ωb^2 term, the equations become identical: this requires δ/T to be small.

In order to establish a value of δ/T which will give acceptable accuracy, calculations were made on the problem illustrated in Fig. 2, with the permeability of the rotor iron varied from 1-1,000 (this gives a variation of δ/T of about 30:1).

The results of these calculations are given in Fig. 4, and show that there is little error introduced in the real component of B_x over the whole range, but the error in the imaginary component becomes significant for $\mu_i < 10$: this corresponds to a δ/T ratio of 0.09. Thus, if the δ/T ratio is less than about 0.09, the error resulting from the use of the boundary method should be insignificant. Typically, the δ/T ratio for the screen of a turbine-generator is 0.0018.

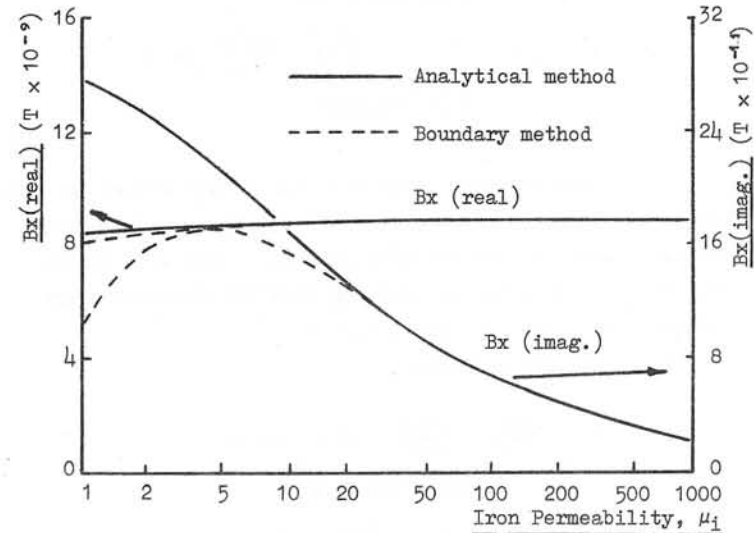


Fig. 4

4. Finite-element Representation of the Boundary Condition

In Ref. (1), a conducting boundary was considered as infinitely-conducting, i.e there was no allowance for flux penetration into the conducting boundary. The new boundary condition, which allows for flux penetration, can be written in scalar potential form by re-arranging Eqn. (1) as:

$$\frac{\partial U}{\partial z} = \frac{(1-j)}{2} \delta \mu_i \left\{ \frac{\partial^2 U}{\partial y^2} + \frac{\partial^2 U}{\partial x^2} \right\} \dots (4)$$

To enable this type of boundary to be represented in finite-element terms requires Eqn. (4) to be re-formulated in variational form and added to the existing functional. The basis of the method is outlined in Ref. (2), and when applied to the present problem results in the following functional:-

$$X = \frac{1}{2} \iiint_V \left\{ \left(\frac{\partial U}{\partial x} \right)^2 + \left(\frac{\partial U}{\partial y} \right)^2 + \left(\frac{\partial U}{\partial z} \right)^2 \right\} dx dy dz$$

end-region term

$$- \frac{(1-j)}{2} \delta \mu_i \iint_S \left\{ \left(\frac{\partial U}{\partial x} \right)^2 + \left(\frac{\partial U}{\partial y} \right)^2 \right\} dx dy$$

boundary term

..... (5)

The volume integral relates to the volume within the end-region, whereas the surface integral relates only to those boundary surfaces carrying eddy currents. Eqn. (5) can be reduced by a dimension by assuming that all functions vary sinusoidally around the periphery.

Thus Eqn. (5) becomes:

$$X = \frac{1}{2} \iint \left\{ \left(\frac{\partial U}{\partial x} \right)^2 + \left(\frac{\partial U}{\partial z} \right)^2 + a^2 U^2 \right\} dx dz$$

end-region term

$$- \frac{(1-j)}{2} \mu_i \frac{\delta}{2} \int \left\{ \left(\frac{\partial U}{\partial z} \right)^2 + a^2 U^2 \right\} dx$$

boundary term

..... (6)

The above functional is extremised by differentiating with respect to the unknown potential, U, and equating to zero, i.e.

$$\frac{\partial X}{\partial U} = 0$$

..... (7)

The numerical form of Eqn. (7) is obtained, as described in Ref. (1), by representing the area within the end-region term (Eqn. (6)) by triangular elements, but the boundary term is given by a line integral only, and thus has to be represented by a "line" or "bar" element, as shown in Fig. 5:

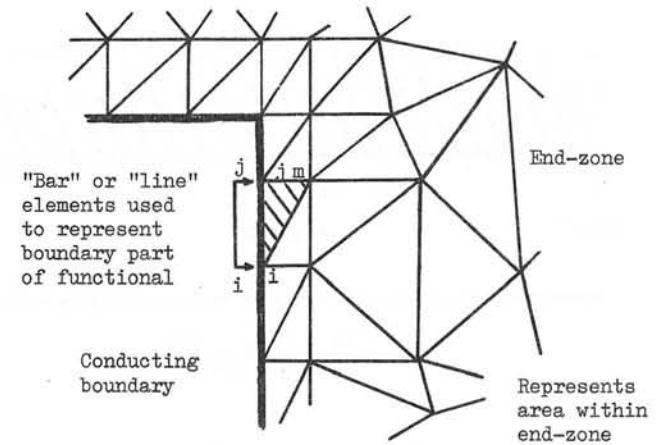


Fig. 5

As with the triangular element, the "bar" element can be represented in numerical form by assuming the potential varies linearly between the nodes. This leads to the following expression, which is added to the extremised functional only for nodes on conducting boundaries:-

$$\frac{\partial X(\text{boundary})}{\partial U_i} = \frac{(1-j)}{12l} \delta \mu_i \times \{ (6 + 2a^2 l^2) U_i + (-6 + a^2 l^2) U_j \}$$

where l = length of "bar" element

The validity of the bar element representation of conducting boundaries was checked by calculating the scalar potential within the air-gap of a turbine-generator for which an analytical solution was available. Several solutions were obtained for various values of pole-pitch, permeability and resistivity. Figs. 6-7 show that the bar element representation agrees well with the analytical solution, and better than the extreme boundary conditions previously used.

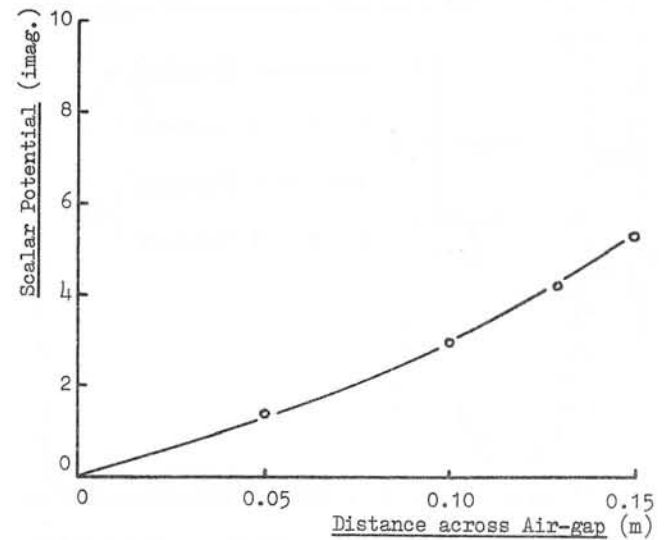
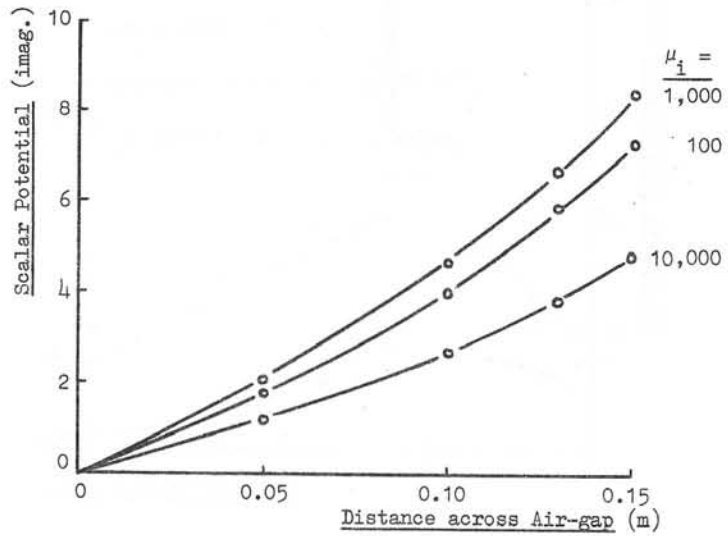
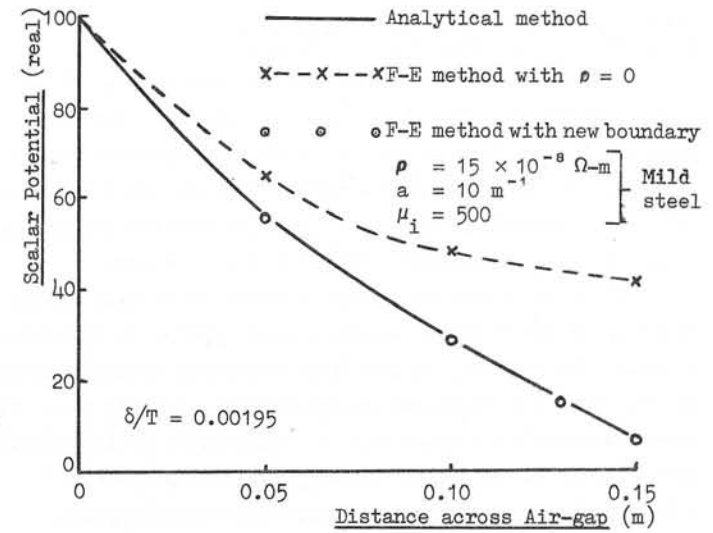
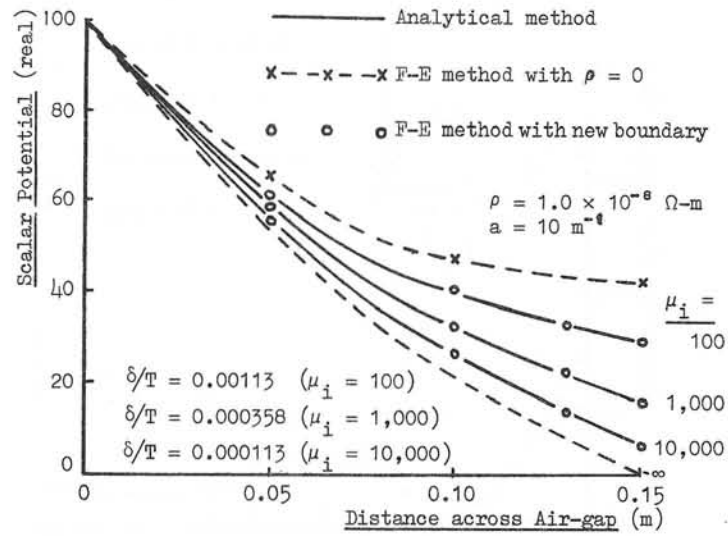


Fig. 6

Fig. 7

5. Application of New Boundary Approach to a 660 MW Turbine-generator End-region

Recently the stator-core and end-region of a 660 MW turbine-generator was extensively instrumented, and all components of flux density near the screen surface and (where possible) the clamping plate surface were measured under open- and short-circuit excitations. Loss intensities around the screen were also measured, using the $\partial\theta/\partial t$ method.

These measurements enabled a check to be made on the validity of the boundary approach when applied to an actual machine. To do this, it was first necessary to re-formulate all the previous equations in cylindrical co-ordinates. With these re-formulated equations, all components of flux density were calculated within the end-region, with particular attention being given to the screen and clamping plate surfaces. Figs. 8-10 compare the numerical and measured values of flux density near the screen surface for open- and short-circuit excitations. In all cases the agreement is good. Similarly, Figs. 11-12 compare the surface loss intensity around the screen for open- and short-circuit excitations respectively.

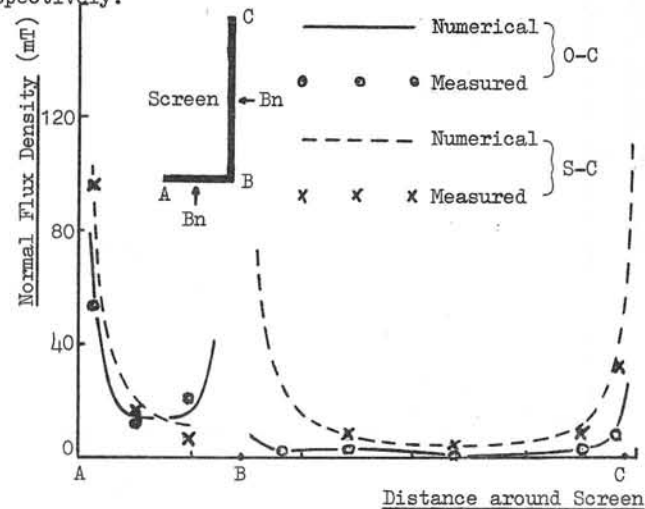


Fig. 8

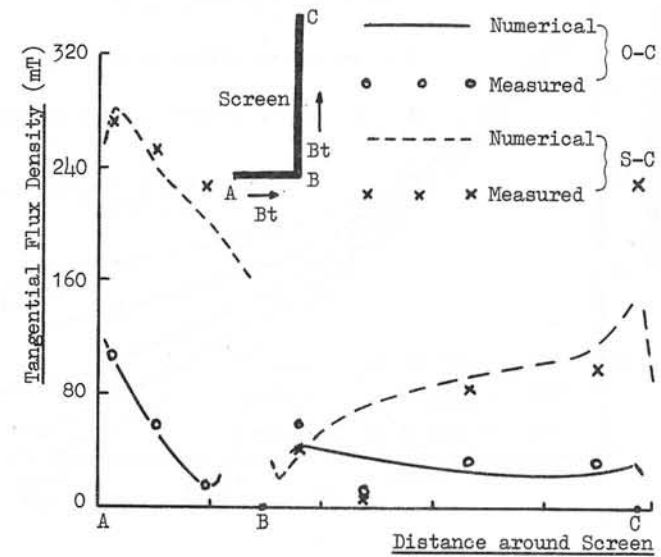


Fig. 9

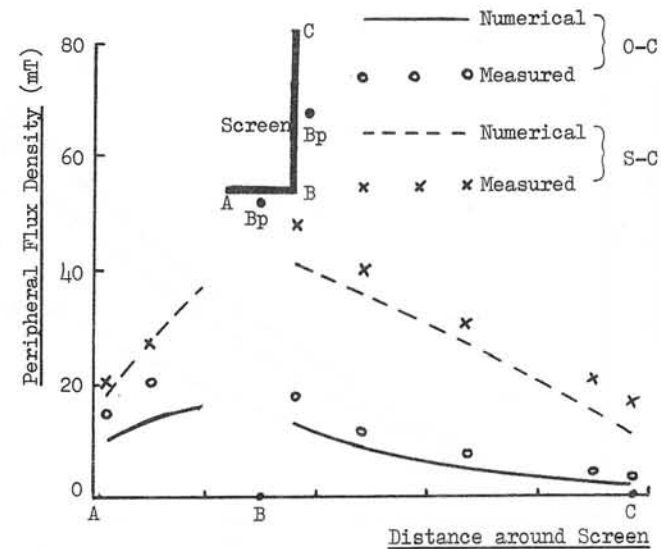


Fig. 10

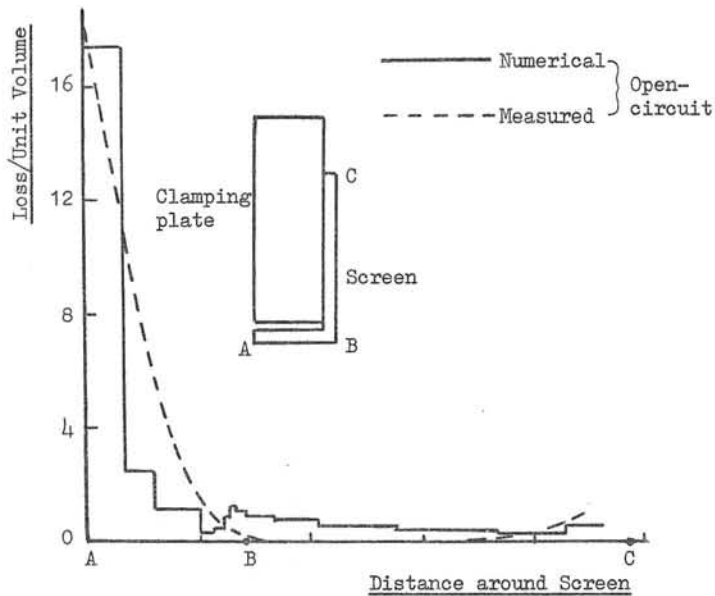


Fig. 11

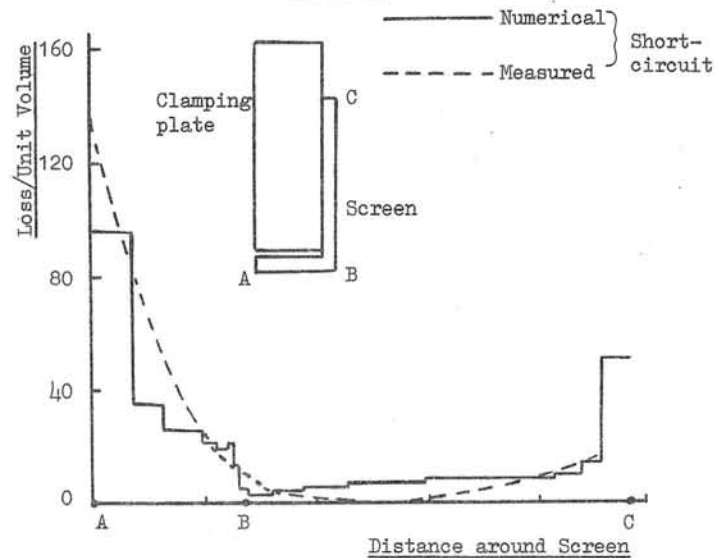


Fig. 12

From Figs. 8-11 it is evident that the new boundary method gives very satisfactory agreement with measurements.

The advantage of the boundary approach is its ability to represent the effect of induced currents in "thick" conducting members, without having to arbitrarily position the boundary surface below the physical surface, as was done in the earlier treatment of conducting boundaries. Also, the magnetic property of the member is more accurately represented.

6. Conclusions

A method has been developed in which the effect of induced currents in conducting magnetic members can be represented in terms of the normal derivative of scalar potential. It has been shown to give reasonable accuracy for various test cases, providing the δ/T ratio is smaller than about 0.09, and when applied to a specially instrumented 660 MW generator gave results in good agreement with the measured values of flux density and loss intensity.

References

- (1) Preston, T.W.,
"The prediction of turbine-generator end-winding fields",
Universities Power Engineering Conference - 1975:
The University of Aston in Birmingham.
- (2) Berg, B.W.,
"Calculus of variations",
Chapter 16 - 'Handbook of Engineering Mechanics',
W.Flügge, McGraw-Hill.

This work was carried out in the Stafford Laboratory of G.E.C. Power Engineering Ltd. with the support of the C.E.G.B.

Discussions following paper:

(Miller) The paper raises the question, under what conditions can the surface of a magnetic material be represented by a 'zero-permeability' boundary condition, established by the reaction of eddy currents? There is evidence that under certain conditions, for example, when the magnetic 'circuit' is mainly in air, the classical skin-depth parameter $\delta = \sqrt{\rho/\omega\mu}$ is less significant than the product $\mu_r \delta$ (μ_r = relative permeability), in the sense that the criterion $h/\mu_r \delta > 1$ implies 'zero permeability' or inductance - limited eddy current reaction field. (h is a characteristic dimension of the conducting material). It has been found both theoretically and experimentally* that the criterion $h/\mu_r \delta > 1$ gives a reliable indication of 'inductance limited' eddy currents in the particular application of finding underground insulated pipes inductively.

* Glennie E B and Miller T J E 'Inductive detection of Buried Metallic pipes' Proc. IEE May 1975.

(Preston, GEC Stafford) I thank Mr Miller for his remarks on the representation of a magnetic boundary by a zero permeability surface. If reference is made to Fig (6) in the paper it is clearly shown that the more permeable the surface becomes the larger is the error introduced by the use of a zero permeability boundary. Thus for magnetic materials the $\mu_r \delta$ product is a better criterion than δ in assessing the suitability of the zero permeability boundary condition.

Semi-analytical Computation of Magnetic Fields, Eddy Currents and Forces in Electrodynamical Levitation Systems

by

E.-D. Krause and L. Urankar
Siemens AG, Erlangen (W. Germany)

1. Introduction

In the last few years various magnet and track configurations have been proposed for magnetically levitated high-speed vehicles for future transport systems. The basic principles of all such arrangements fall into two categories (Figure 1):

Attractive (Ferromagnetic) Principle and
Repulsive (Inductive) Principle.

In systems using the first, attractive forces between magnets mounted on the vehicle and a ferromagnetic track (solid or laminated) produce levitation.

Systems using the repulsive principle depend upon Lenz's law, which implies that a magnetic field generated by induced currents opposes the primary field.

Two essentially different basic classes of track configurations have been suggested for systems of the second category. One uses metallic loops, the other compact metallic sheets.

Among the magnet arrangements there are again two classes: single magnet and double magnet, respectively. The single magnet class consists of a magnet on the vehicle which moves above a metallic track. Such a system is called the normal flux system. The other system comprises two magnets between which the track is located. The polarity of the magnets, i.e. the direction of the energising currents is such that the fields tend to cancel each other (null flux system) or such that the fields add up (brake flux system).

All these basic systems may be used either for lift of guidance alone or for both lift and guidance together.

In order to simplify the mathematical formulation of the problem, we restrict ourselves to the electromagnetic aspect only and to basic systems with infinite sheet track of arbitrary thickness. Then the basic systems between the dotted lines in Figure 1 can be treated mathematically together as a boundary value problem for magnetic fields. The geometrical arrangement for a theoretical analysis is

shown in Figure 2. An infinite metallic sheet of arbitrary thickness d , conductivity σ_S and permeability μ_S is situated between two excitation current systems which are mounted on the moving vehicle in a distance $2h_0$ apart and which consist of plane magnet coils of arbitrary form. The midplane of the sheet corresponds to the $z=0$ plane of the coordinate system which is assumed to be moving with the coils. The excitation systems denoted by $j=1$ above and 2 below are in parallel planes at distances h_j from the sheet track surfaces, move with a constant velocity in any direction and carry currents, the number of ampere turns being I_j .

A general velocity vector in any direction has been introduced in the model so that intrinsic damping in the levitation systems can be analysed. But the lateral and vertical components of the velocity are assumed to be small compared with the forward velocity, say in the x -direction.

2. Basic Equations

In the following analysis we assume the excitation system to be stationary, so that the sheet track moves with a velocity \underline{v} in the opposite direction. The electric and magnetic fields in the moving sheet track are obtained through Lorentz transformation. Since the track is a good electrical conductor, the displacement current is zero and hence the magnetic field at any fixed point in the moving track is equal to that in the stationary one.

The eddy current in the track is

$$\mu_S \underline{J}^{(S)} = \mu_S \sigma_S \underline{E} + (\underline{\Lambda} \times \underline{B}^{(i)}) \quad (1)$$

where $\underline{\Lambda} = \mu_S \sigma_S \underline{v}$ and $\underline{B}^{(i)} = \underline{B}^{(S)} + \underline{B}^{(E)}$ i.e. the total magnetic flux density in the track is the sum of magnetic flux densities due to the eddy current and excitation current, respectively.

Since now $\mu_S \underline{J}^{(S)} = \nabla \times \underline{B}^{(S)}$, we obtain from (1) after taking the rotation and noting that $\nabla \cdot \underline{B} = 0$ and $\nabla \times \underline{E} = 0$, the differential relation

$$\nabla^2 \underline{B}^{(S)} = (\underline{\Lambda} \cdot \nabla) \underline{B}^{(i)} \quad (2)$$

Inside the track sheet the excitation magnetic flux density satisfies $\nabla^2 \underline{B}^{(E)} = 0$, so that (2) reduces to the following Maxwell-Minkowski wave equation for the magnetic flux density in the track

$$\nabla^2 \underline{B}^{(i)} - (\underline{\Delta} \cdot \nabla) \underline{B}^{(i)} = 0 \quad (3)$$

Outside the sheet track we have to solve

$$\nabla^2 \underline{B}^{(e)} = 0 \quad (4)$$

Both the exterior and interior flux densities, $\underline{B}^{(e)}$ and $\underline{B}^{(i)}$, are divergence free and are interconnected through the following boundary conditions

$$\underline{n} \cdot \underline{B}^{(i)} = \underline{n} \cdot \underline{B}^{(e)} \quad (5a)$$

$$\underline{t} \cdot \underline{B}^{(i)} = \mu_R (\underline{t} \cdot \underline{B}^{(e)}) \quad (\mu_R = \mu_S / \mu_0) \quad (5b)$$

where \underline{n} and \underline{t} are outward normal and tangent unit vectors, respectively, at any arbitrary point on the sheet track surface.

3. Analytical Part of the Method

The central point of the method is a two-dimensional infinite Fourier transform defined by

$$\underline{B}(\underline{k}; z) = \frac{1}{4\pi^2} \int_{-\infty}^{+\infty} dx \int_{-\infty}^{+\infty} dy e^{-ik_x x} e^{-ik_y y} \underline{B}(\underline{r}) \quad (6a)$$

(where $\underline{k} = (k_x, k_y)$ and $\underline{r} = (x, y, z)$) and its inverse

$$\begin{aligned} \underline{B}(\underline{r}) &= \text{Re} \int_{-\infty}^{+\infty} dk_x \int_{-\infty}^{+\infty} dk_y e^{+ik_x x} e^{+ik_y y} \underline{B}(\underline{k}; z) \\ &= \text{Re} \int_{-\infty}^{+\infty} dk_x \int_{-\infty}^{+\infty} dk_y \underline{B}(\underline{k}; \underline{r}) \end{aligned} \quad (6b)$$

The functions $\underline{B}(\underline{k}; \underline{r})$ are then taken to be the Fourier components of the magnetic flux densities constituting the solutions of the equations (3), (4) and the boundary conditions (5a, b).

3.1. Ansatz for Solutions

In order to solve the boundary value problem we now make, similar to [1], following Ansatz for the solutions $\underline{B}(\underline{k}; \underline{r})$ in regions 1, 2 and 3 (s. Figure 2).

Regions 1 and 2:

$$\begin{aligned} \underline{B}_p^{(ej)} &= \underline{B}_p^{(Ej)}(\underline{k}; \underline{r}) + \tilde{\underline{B}}_p^{(j)}(\underline{k}; \underline{r}) \\ &= [\underline{B}_p^{(Ej)}(\underline{k}; z) + a_p^{(j)}(\underline{k}) e^{\mp kz}] e^{ik_x x} \begin{cases} \cos(k_y y) \\ \sin(k_y y) \\ \cos(k_y y) \end{cases} \quad (p=x, y, z) \quad (7) \end{aligned}$$

where $k = (k_x^2 + k_y^2)^{1/2}$ and the column term corresponds, from the top, to the components $p = x, y, z$. $\underline{B}^{(Ej)}$ is the excitation field of the excitation coil j in region j and thus $\tilde{\underline{B}}^{(1)}$ ($\tilde{\underline{B}}^{(2)}$) corresponds to the contribution from the field components in the upper (lower) region due to the eddy current in the track sheet and the lower (upper) excitation coil. The upper sign corresponds to $j=1$ while the lower one to $j=2$.

Region 3:

$$\underline{B}_p^{(i)} = [\underline{b}_p(\underline{k}) e^{\alpha z} + c_p(\underline{k}) e^{-\alpha z}] e^{ik_x x} \begin{cases} \cos(k_y y) \\ \sin(k_y y) \\ \cos(k_y y) \end{cases} \quad (p=x, y, z) \quad (8)$$

The subsidiary condition $(\nabla \times \underline{B})_z = 0$ (which is not a real restriction in the infinite sheet model because of the natural boundary conditions at infinity) allows us to determine the Fourier coefficients in the Ansatz uniquely for each (k_x, k_y) -pair.

3.2. Eddy Current and Force Expressions

The forces between the track sheet and the excitation current system can be calculated in two different ways.

I. The eddy current density in the track sheet is given by

$$\underline{J}^{(S)} = \frac{1}{\mu_S} (\nabla \times \underline{B}^{(i)}) \quad (9)$$

Substituting the inverse transform of (8) in this expression, we get the Fourier representation of the eddy current density.

With the help of the inverse transform of the excitation field the force density \underline{P} on the track sheet can now be calculated as

$$\underline{P}(\underline{r}) = \underline{J}^{(S)}(\underline{r}) \times \underline{B}^{(E)}(\underline{r}) \quad (10)$$

where $\underline{B}^{(E)} = \underline{B}^{(E1)} + \underline{B}^{(E2)}$. Integrating over the volume of the sheet track we obtain the global force between the track and the excitation system

$$\underline{F} = \iiint_{R_S} dx dy dz \underline{P}(x, y, z) \quad (11)$$

This approach is used when the spatial distribution of the eddy current and force components in the track are needed. This is the case during mechanical outlay of the track system.

II. If, on the contrary, only global forces are to be calculated, the expression

$$\underline{F} = \iiint_{R_E} dx dy dz [\underline{J}^{(E)} \times (\underline{B}^{(e)} - \underline{B}^{(E)})]$$

is much more convenient to use. With the help of (7), this then reduces to

$$\underline{F} = \sum_{j=1}^2 \iiint_{R_{Ej}} dx dy dz [\underline{J}^{(Ej)} \times \underline{B}^{(j)}] \quad (12)$$

which is physically equivalent to (11), as action and reaction are equal and opposite.

For sufficiently simple systems, the volume integral in (12) can be performed before calculating the inverse Fourier transform. In this case (12) can be expressed as

$$\underline{F} = \int_{-\infty}^{+\infty} dk_x \int_{-\infty}^{+\infty} dk_y \underline{f}(\underline{k}; B_x^{(E1)}(\underline{k}; d/2), B_x^{(E2)}(\underline{k}; -d/2)) \quad (13)$$

where $B_x^{(E1)}(\underline{k}; d/2)$ and $B_x^{(E2)}(\underline{k}; -d/2)$ are Fourier transforms of the x-components of the excitation field at the upper and lower track sheet surfaces, respectively.

4. Numerical Part of the Method

Now we discuss the numerical computations of eddy current and force densities as well as the global force. The former shall be dealt with fast Fourier transform, the latter by means of numerical quadrature. Finally, we compare both methods from the standpoint of computation time and efficiency.

4.1. Fast Fourier Transform (FFT)

To calculate the eddy current and force densities in the track it is necessary to compute several integrals of the type

$$\left. \begin{aligned} A^{(\cos)}(x,y) \\ A^{(\sin)}(x,y) \end{aligned} \right\} = \int_{-\infty}^{+\infty} dk_x \int_{-\infty}^{+\infty} dk_y e^{ik_x x} \begin{Bmatrix} \cos(k_y y) \\ \sin(k_y y) \end{Bmatrix} A(k_x, k_y) \quad (14a)$$

$$(14b)$$

Introducing the total inverse Fourier transform $A^{(tot)}(x,y)$, we obtain

$$A^{(\cos)}(x,y) = \frac{1}{2} [A^{(tot)}(x,y) + A^{(tot)}(x,-y)] \quad (15a)$$

$$A^{(\sin)}(x,y) = -\frac{i}{2} [A^{(tot)}(x,y) - A^{(tot)}(x,-y)] \quad (15b)$$

We now choose two even numbers n_1 and n_2 , and calculate the integral (14) on a net of $n_1 \cdot n_2$ equidistant points ordered symmetrically

about the origin:

$$x_{l_1} = \Delta x \cdot (l_1 - 1 - n_1/2)$$

$$y_{l_2} = \Delta y \cdot (l_2 - 1 - n_2/2)$$

For each (x,y)-pair we integrate in k-space by applying the trapezoidal rule to a similar net of $n_1 \cdot n_2$ equidistant points:

$$k_{x,j_1} = \Delta k_x \cdot (j_1 - 1 - n_1/2)$$

$$k_{y,j_2} = \Delta k_y \cdot (j_2 - 1 - n_2/2)$$

$$A^{(tot)}(x_{l_1}, y_{l_2}) = \Delta k_x \Delta k_y \sum_{j_1=1}^{n_1} \sum_{j_2=1}^{n_2} W_{j_1, j_2} e^{i(k_{x,j_1} \cdot x_{l_1} + k_{y,j_2} \cdot y_{l_2})} \cdot A(k_{x,j_1}, k_{y,j_2}) \quad (16)$$

$$(l_1 = 1, \dots, n_1; l_2 = 1, \dots, n_2)$$

Herein W_{j_1, j_2} are weight factors of the trapezoidal rule (1, 1/2 or 1/4).

The $n_1 \cdot n_2$ double sums (16) can be evaluated most effectively in the formalism of fast Fourier transform (FFT) which is applicable under following conditions

$$\Delta x \cdot \Delta k_x = 2\pi/n_1, \quad \Delta y \cdot \Delta k_y = 2\pi/n_2$$

If, in addition, the numbers n_1 and n_2 are powers of two, the computation time is minimum and (16) takes the form

$$A^{(tot)}(x_{l_1}, y_{l_2}) = (-1)^{l_1+l_2} \Delta k_x \Delta k_y \sum_{j_1=1}^{n_1} \sum_{j_2=1}^{n_2} (-1)^{j_1+j_2} W_{j_1, j_2} \cdot A(k_{x,j_1}, k_{y,j_2}) \cdot \exp\{2\pi i [(j_1-1)(l_1-1)/n_1 + (j_2-1)(l_2-1)/n_2]\} \quad (17)$$

4.2. Numerical Quadrature

The double integral (13) for the global force is not in the form of an inverse Fourier transform. Figure 3 shows the structure of one such typical integrand which must be computed by means of numerical quadrature.

For this purpose the first quadrant in the k_y -direction is separated into different strips of width $2\Delta k_y$ as shown in Figure 4. In each strip the step length for k_x -integration is adjusted to the structure of the integrand. The starting step length $\Delta k^{(a)}$ is chosen same for both the coordinates in such a way that for the oscillating function of the highest frequency occurring in the

integrand there are at least 3 integration nodes in a quarter period. Each strip is divided into rectangles of size $4\Delta k_x \cdot 2\Delta k_y$. For an integral over such a rectangle two approximate values are determined from integrals over elementary rectangles (denoted by the subscript ereco) according to product Simpson's rule (s. Figure 4).

$$F_{\text{rec}}^{(\text{coarse})} = F_{\text{ereco}}(2\Delta k_x)$$

$$F_{\text{rec}}^{(\text{fine})} = F_{\text{ereco}}^{(1)}(\Delta k_x) + F_{\text{ereco}}^{(r)}(\Delta k_x)$$

The integrals $F_{\text{rec}}^{(\text{fine})}$ over each rectangle are then summed to give the strip integral F_{str} ; the strip integrals in turn are summed to give the total integral F_{tot} . Integration over all the 4 quadrants is performed by taking together in each integral F_{ereco} the integrals over the mirror elementary rectangles I-IV.

The k_x -step length is controlled with the help of both the approximate values $F_{\text{rec}}^{(\text{fine})}$ and $F_{\text{rec}}^{(\text{coarse})}$. Let

$$\Delta F_{\text{rec}} = F_{\text{rec}}^{(\text{fine})} - F_{\text{rec}}^{(\text{coarse})}$$

and

$$F_{\text{temp}} = F_{\text{tot}} + F_{\text{str}} + F_{\text{rec}}^{(\text{fine})}$$

where F_{temp} is the temporary value of the total integral. We also introduce 3 accuracy parameters $\mathcal{E}_1, \mathcal{E}_2$ and \mathcal{E}_3 satisfying $\mathcal{E}_1 < \mathcal{E}_2 < \mathcal{E}_3$. Then, if $|\Delta F_{\text{rec}}| < \mathcal{E}_1 |F_{\text{temp}}|$, the step length Δk_x is doubled; if $|\Delta F_{\text{rec}}| > \mathcal{E}_3 |F_{\text{temp}}|$, then Δk_x is halved; in all other cases it remains unchanged.

The integration in a strip stops when

$$|F_{\text{rec}}^{(\text{fine})}| \leq \mathcal{E}_2 |F_{\text{temp}}|$$

is fulfilled. In the computer code we use

$$\mathcal{E}_1 = 10^{-(p+1)}, \quad \mathcal{E}_2 = 10^{-p}, \quad \mathcal{E}_3 = 10^{-(p-1)}$$

where p can be freely choosen.

If the k_y -step is also determined with the help of approximate values of the integral, the computation time would become unduly large. To avoid it, we use an heuristic way. If w_{max} is the highest frequency of the oscillating functions in the integrand depending upon k_y , an upper bound for the k_y -step length is defined by

$$\Delta k_y^{(\text{sup})} = \frac{\pi}{8w_{\text{max}}}$$

dividing the quarter period of the function $\sin(w_{\text{max}} \cdot k_y)$ into four

parts. Starting with step length $\Delta k^{(a)}$ in the first strip, the step length in each following strip is doubled so long as it does not exceed $\Delta k_y^{(\text{sup})}$. Integration is then performed over strips of constant width $2\Delta k_y^{(\text{sup})}$ until the strip integral becomes sufficiently small i.e.

$$|F_{\text{str}}| \leq \mathcal{E}_2 |F_{\text{temp}}|$$

4.3. Computation Time and Efficiency

Computation of the global force from (10) and (11) requires five two-dimensional FFT's (2 FFT's for the eddy current density and 3 FFT's for the excitation field) and one volume integral. On our computer SIEMENS 4004/55 we can execute an in-core FFT of maximum 128·128 complex data. All the 5 FFT's and the volume integral then require 10 minutes computation time. According to (13) the global force is given by a single two-dimensional integral requiring about 40 seconds of computation time only. Compared with (10) and (11), this represents a saving in computer time of a factor of 15.

Therefore our method of computation is highly suitable if only the global force and not the eddy current or force density is required to be analysed. An extensive parameter study of basic systems was done by us on the basis of global force, the results of which are available in a series of papers [2].

5. Results

The results presented below illustrate a variety of subproblems occuring in magnetic levitation. For a complete discussion of the physical aspects of these results we refer to [2, 3] and other references therein. The system data used in the illustrations are as follows.

Figure 5. Normal flux system with rectangular magnet:

$$2l = 2 \text{ m}, \quad 2b = 0.3 \text{ m}, \quad I = 0.3 \text{ MA}, \quad h_1 = 0.2 \text{ m}, \quad d = 20 \text{ mm},$$

$$\sigma_S = 31 \text{ MA/Vm}, \quad \mu_r = 1$$

Null flux system with circular magnet:

$$2r = 0.5 \text{ m}, \quad I = 0.6 \text{ MA}, \quad 2h_0 = 0.5 \text{ m}, \quad \Delta h = 20 \text{ mm}, \quad d = 5 \text{ mm},$$

$$\sigma_S = 31 \text{ MA/Vm}, \quad \mu_r = 1$$

Ferromagnetic system with rectangular magnet:

$$2l = 1 \text{ m}, 2b = 0.1 \text{ m}, I = 0.3 \text{ mA}, h_2 = 0.1 \text{ m}, d = 20 \text{ mm}, \\ \epsilon_S = 10 \text{ MA/Vm}, \mu_r = 1000$$

Figure 6. Null flux system with 5 rectangular magnets of alternating polarity:

$$2l = 1.15 \text{ m}, 2b = 0.3 \text{ m}, q = 0.25 \text{ m}, I = 0.6 \text{ MA}, \\ 2h_0 = 0.5 \text{ m}, \Delta h = 50 \text{ mm}, d = 5 \text{ mm}, \epsilon_S = 31 \text{ MA/Vm}, \mu_r = 1, \\ F_{LO} = 125 \text{ kN}$$

Figure 7. Normal and null flux:

$$2l = 1.15 \text{ m}, 2b = 0.3 \text{ m}, \epsilon_S = 31 \text{ MA/Vm}, \mu_r = 1 \\ \text{Ferromagnetic:} \\ 2l = 1 \text{ m}, 2b = 0.1 \text{ m}, \epsilon_S = 0.1 \text{ MA/Vm}, \mu_r = 1000 \\ \text{Normal flux and ferromagnetic:} \\ I = 0.3 \text{ MA}, d = 20 \text{ mm} \\ \text{Null flux:} \\ I = 0.6 \text{ MA}, d = 5 \text{ mm}, 2h_0 = 0.5 \text{ m}$$

Figure 8. Normal flux (upper row): $h_1 = 0.2 \text{ m}, d = 20 \text{ mm}$

Null flux (lower row): $2h_0 = 0.4 \text{ m}, \Delta h = 20 \text{ mm}, d = 5 \text{ mm}$

Normal and null flux: $2l = 1 \text{ m}, 2b = 0.3 \text{ m}, \epsilon_S = 31 \text{ MA/Vm}, \\ \mu_r = 1$

— $v_x = 30 \text{ m/s}, v_p = 0; \quad \text{---} v_x = 30 \text{ m/s}, v_p = 2 \text{ m/s}$

-o- $v_x = 150 \text{ m/s}, v_p = 0; \quad \text{-x-} v_x = 150 \text{ m/s}, v_p = 2 \text{ m/s}$

where $p=z$ and y for left and right column, respectively

Figures 9 and 10. Null flux system with two rectangular magnets of different polarity:

$$2l = 1.5 \text{ m}, 2b = 0.3 \text{ m}, q = 0.75 \text{ m}, I = 1 \text{ MA}, 2h_0 = 0.7 \text{ m}, \\ \Delta h = 10 \text{ mm}, d = 12 \text{ mm}, \epsilon_S = 31 \text{ MA/Vm}, \mu_r = 1, v_x = 140 \text{ m/s}$$

5.1. Global Forces

The Figures 5 and 6 show velocity characteristics for lift and drag forces and specific losses in basic levitation systems.

In Figure 5a the situation in a normal flux system with rectangular magnet is illustrated. The effect of magnet form on the forces was also investigated. For example, Figure 5b shows the forces in a null flux system with a pair of circular excitation magnets. Figure 5c represents the forces which act upon a rectangular coil situated below a ferromagnetic track sheet. The lift force decreases because

the electrodynamic repulsion between the coil and the track sheet is superimposed on the magnetostatic attraction between them.

Figure 6 shows the transition of a conceptual vehicle with a null flux system from the rolling into the freely floating state. As long as the lift force is smaller than the vehicle weight G , the vehicle rolls on wheels with a fixed sag Δh (deviation from the midplane of the track sheet). When the lift force exceeds the weight, the sag adjusts itself according to the relation

$$F_L(\Delta h) - G = 0 \quad (18)$$

and the vehicle starts floating. In our computer codes, the relation (18) is solved by Newton's iteration. As a consequence of this method we obtain the derivative of the lift force w.r.t. sag which is physically the mechanical stiffness of the system. With decreasing sag the stiffness increases; with increasing velocity both the quantities approach saturation values.

5.2. System Stiffness

Figure 7 shows suspension stiffness as a function of velocity under constant load conditions for the basic levitation systems. All the 3 diagrams correspond to a constant load of $F_{LO} = 25 \text{ kN}$. For the normal flux system stiffness remains almost constant with a mean value 0.25 kN/mm corresponding to an eigenfrequency of 1.6 Hz . The system stiffness for the null flux system is much higher (at $v_x = 50 \text{ m/s}$ about 6 times larger) and strongly velocity dependent. The stiffness value at $v_x = 150 \text{ m/s}$ corresponds to an eigenfrequency of 4.4 Hz which is about 3 times higher than that of a normal flux system. The stiffness of a ferromagnetic system is almost velocity independent with a mean value 0.593 kN/mm corresponding to an eigenfrequency of 2.5 Hz .

5.3. Intrinsic Damping

In Figure 8 we illustrate the dependence of normalized side and lift forces on transverse and vertical velocities at constant forward velocity in normal and null flux systems. The perturbing velocities v_y and v_z are assumed to be very small as compared with the forward velocity v_x and taken to be in the range $0-10 \text{ m/s}$. The normalization constant for the forces is $F_0 = \mu_0 I^2 / 2\pi$. From these curves intrinsic damping of the levitation system may be analysed if the quasi static

forces thus calculated are assumed to remain essentially unchanged in the dynamic situation involving time dependent transverse and/or vertical perturbations (such as side winds etc.). Restricting the perturbation velocity v_p ($p=y,z$) to a range of about 0-2 m/s where the curves are nearly linear with slope K_p , we can calculate, using Newton's law, the damping time τ_p in seconds for the perturbation velocity v_p as

$$\tau_p = \frac{F_L/F_0}{g \cdot K_p} \quad (p=y,z) \quad (19)$$

where g is the gravity acceleration. Since τ_p depends on the normalized lift force, it is independent of the excitation current of the magnets, other parameters remaining constant. An analysis of the physics of intrinsic damping in basic levitation systems is presented in [3].

5.4. Eddy Current and Force Density

Figures 9 and 10 show the eddy current and force density, respectively, in the track for a null flux system with two rectangular magnets of different polarity. Figure 9a is an orthographic projection of the x-component of the eddy current density which shows clearly that the x-component is maximum under the longitudinal conductors of the excitation magnet coils.

The y-component of the eddy current density (Figure 9b) is largest under the transverse conductors of the excitation magnet coils. Since for different polarity of the excitation magnets the currents in the neighbouring pair and in the far pair of transverse conductors each flow in the same direction, both pairs of the inner and external peaks in the y-component each have the same sign. For same polarity the signs, for example of both the right peaks, will be reverse. The eddy current stream lines shown in Figure 9c have a twofold meaning. Firstly they give the direction of the eddy current field; secondly between two neighbouring flow lines the same amount of current always flows i.e. the nearer the lines, the higher is the eddy current density.

The orthographic representation of the lift force distribution (Figure 10a) shows that the major contribution to the lift comes from the longitudinal conductors of the excitation coils while the drag force mainly stems from the transverse conductors. Figure 10b

shows lines of constant lift force acting upon a volume element of the track sheet.

6. Track of Finite Width

Recently, we have extended the above semi-analytical method of computation to sheet tracks of finite width. The main difficulty had been as follows: Whereas in the case of infinite sheet track the Fourier components of the exterior and interior magnetic field show a unique one to one correspondence via the boundary conditions, such a correlation does not exist for a track of finite width. It is therefore necessary to reduce the problem to a mathematically well defined interior boundary value problem, the solution of which does not require any knowledge of the exterior field. The results of this calculation will be presented elsewhere.

This work has been supported under the technological program of the Federal Department of Research and Technology of the FRG. The authors alone are responsible for the contents.

References

- [1] Reitz, J.R.; Davies, L.C.: J. Appl. Phys. 43 (1972), pp. 1547 - 1553
- [2] Urankar, L.: Siemens Forsch.- u. Entw. Ber. 4 (1975), pp. 25 - 32; s. also references herein
- [3] Urankar, L.: Siemens Forsch.- u. Entw. Ber. 5 (1975), pp. 110 - 119

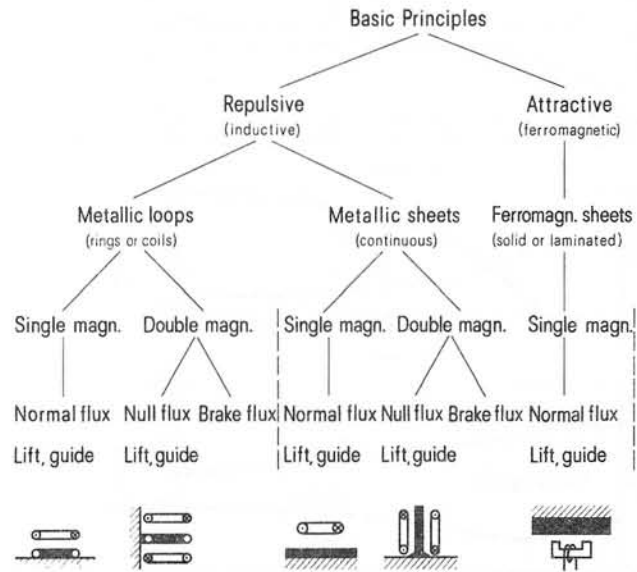


Figure 1: Basic types of magnetic levitation systems

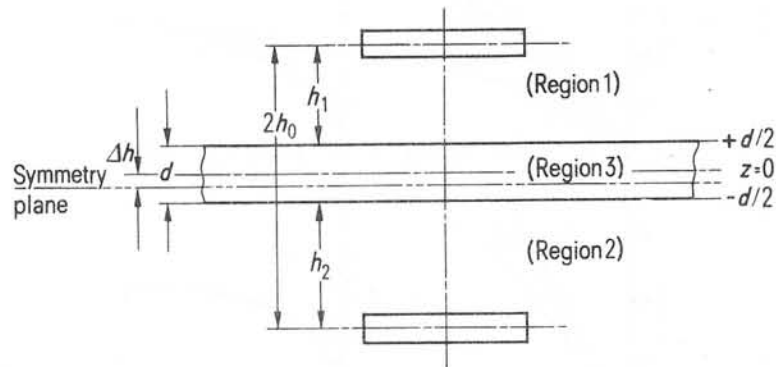


Figure 2: Schematic diagram of arrangement used in this analysis

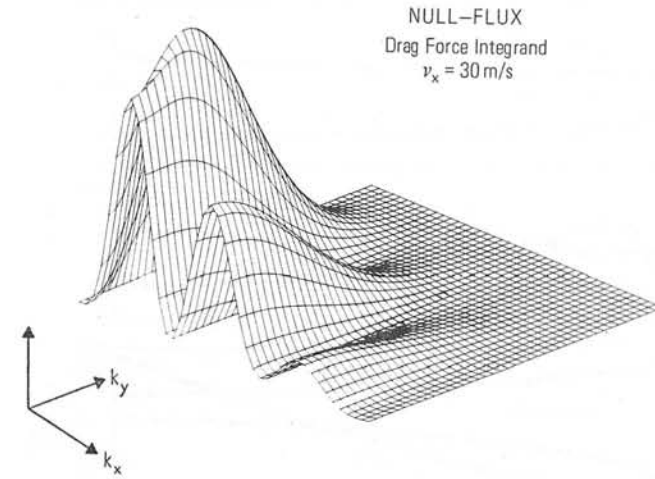


Figure 3: Typical integrand in k-space for global drag force

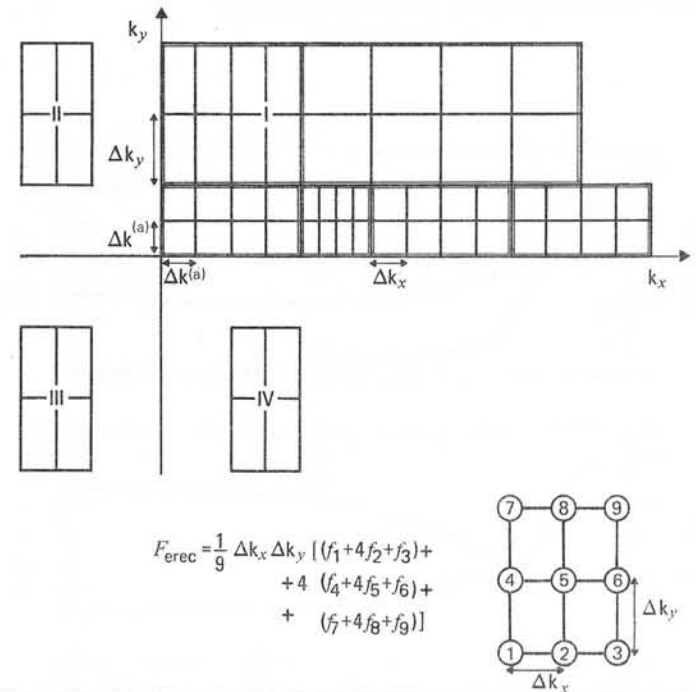


Figure 4: Numerical quadrature in k-space

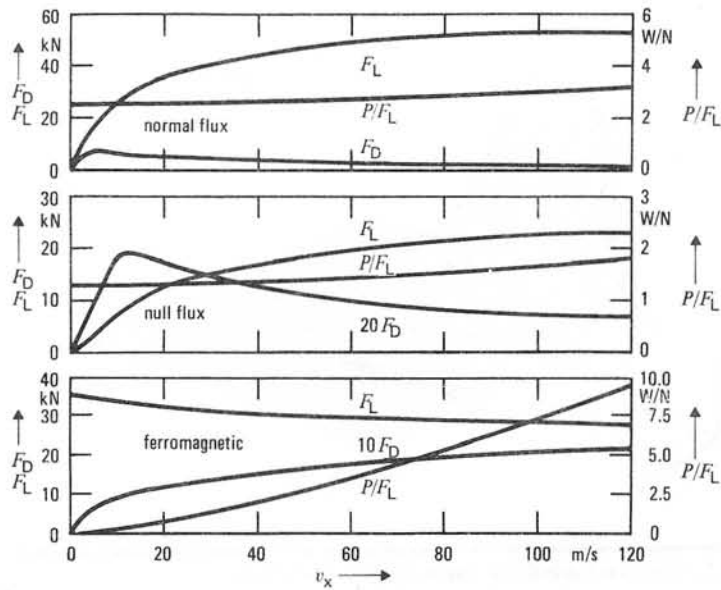


Figure 5: Velocity characteristics for basic levitation systems

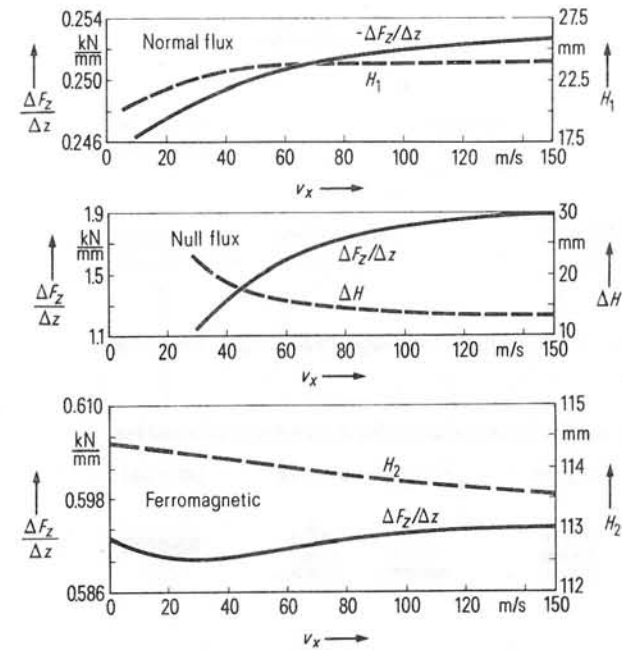


Figure 7: Velocity dependence of system stiffness and levitation height at constant load 25 kN

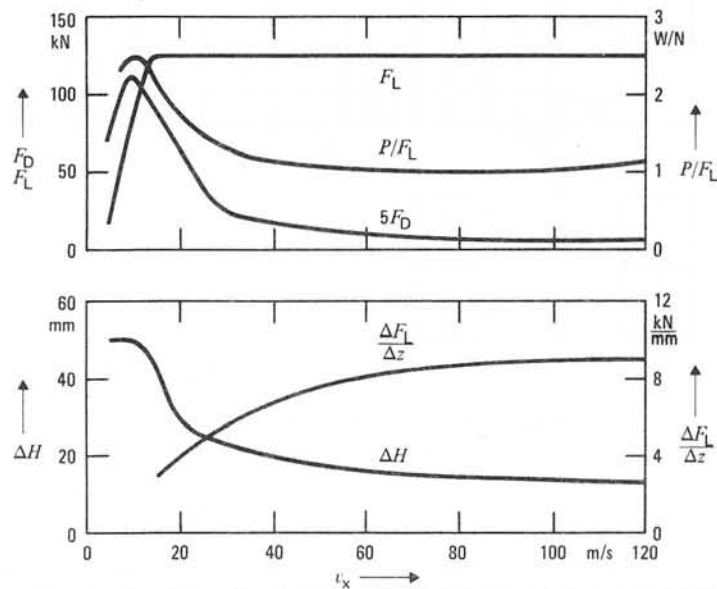


Figure 6: Transition from rolling to freely floating state

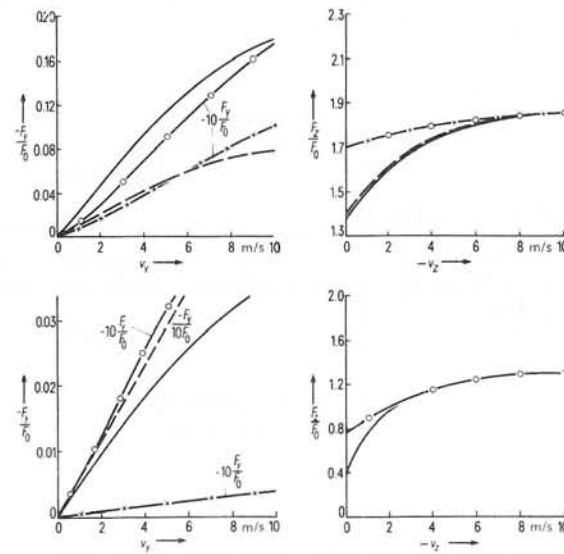


Figure 8: Effect of lateral and vertical velocities on side and lift forces

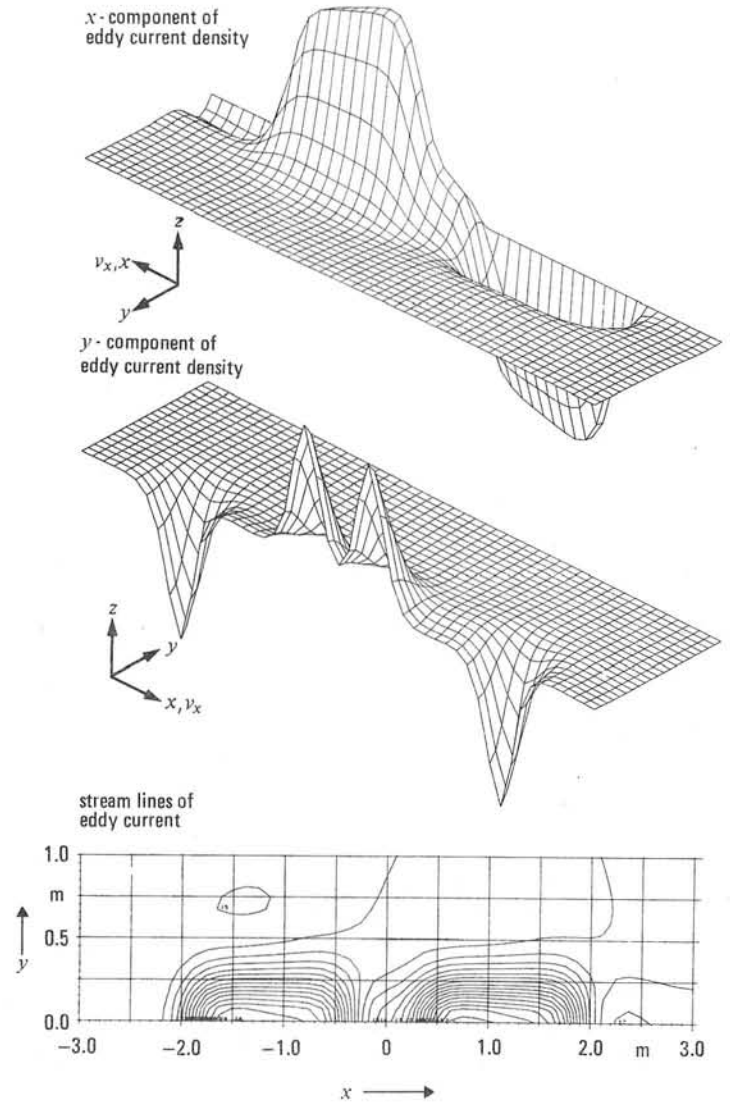


Figure 9: Eddy current density and stream lines in track sheet

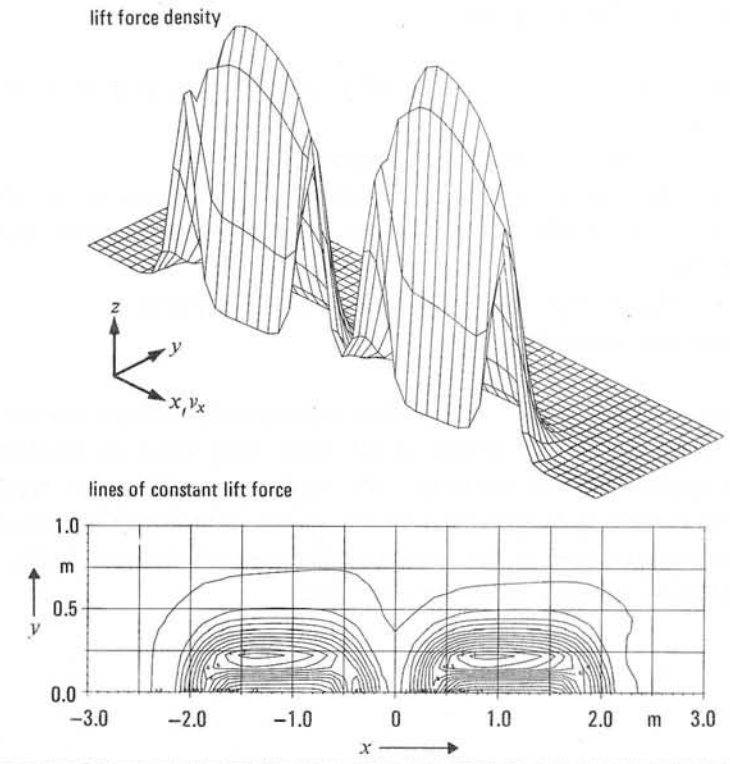


Figure 10: Distribution of lift force acting on track sheet

Discussions following paper:

(Roster, Chain Ltd) Your expression for the force density on the conductor is,

$$\underline{P}(x,y,z) = \underline{J}(\text{eddy}) \times \underline{B}(\text{excitation})$$

This does not appear to account for the self-interaction of the eddy currents. An expression for the force density which includes this effect is,

$$\underline{P}(x,y,z) = \underline{J}(\text{eddy}) \times \underline{B}(\text{excitation}) + \underline{B}(\text{eddy})$$

Why have you neglected $\underline{B}(\text{eddy})$?

(Krause, Siemens) The cross-product between eddy current and its own field leads to internal stress in the sheet track which is uninteresting in the problem at hand and hence left out in eqn. (10). The force density we want to analyse here is due to the interaction between the current distribution in the sheet and the excitation magnet field. An analogous argument holds for eqn. (12).

Three dimensional eddy current calculations

W Wolff, AEG Telefunken, Buchslag, West Germany

I) The solution of the magnetostatic equations

For the solution of the three dimensional magnetostatic equations we used the scalar potential as system quantity.

The basic idea of the applied method is the following.

$$\begin{aligned}
 & \text{a) } \underline{H} = \underline{H}_i - \text{grad } \phi \\
 1) & \text{ b) } \text{curl } \underline{H} = \text{curl } \underline{H}_i = \underline{i}_{St} \\
 & \text{c) } \text{div } \mu \text{ grad } \phi = \text{div } \mu \underline{H}_i
 \end{aligned}$$

The magnetostatic field \underline{H} is split up into two parts. The first one \underline{H}_i only has the same curls as the magnetic field has. Therefore the remaining part is eddy-free and can be expressed by the gradient of a scalar potential ϕ . The scalar potential is defined by an elliptic differential equation (eq. 1c), for which optimized numerical solution methods are well known. Because the curl-field \underline{H}_i can have any sources there is an infinite number of solutions fulfilling eq. 1b). This fact can be used to pick a simple

one calculable in a negligible time. Eq. 1b) was solved by discretization, too. Since the solution is not unique, the resulting linear equation system has more unknowns than equations. It is possible to combine the unknowns systematically in such a way that this linear equation system becomes recursive, and so the solution is uncomplicated.

In short, one can say : the magnetostatic problem is solved in a satisfactory way.

II) Extension to the solution of the time dependent Maxwell-equations

a) Basic equations

The question is:
can the described method be extended to the solution of the time dependent Maxwell-equations.

To solve the time dependent Maxwell-equations we

have to distinguish between a given current density \underline{i}_{St} as already introduced in equation 1b) and a current density \underline{i}_w , induced by the resulting magnetic field. From here on, the displacement current will be neglected, so the divergence must be zero for both the given and the induced current density and the curl-field \underline{H}_i can also be split up into two parts.

- a) $\underline{H}_i = \underline{H}_{iSt} + \underline{H}_{iw}$
- b) $\text{curl } \underline{H}_{iSt} = \underline{i}_{St}$
- 2) c) $\text{curl } \underline{H}_{iw} = \underline{i}_w$
- d) $\underline{H} = \underline{H}_{iSt} + \underline{H}_{iw} - \text{grad } \phi$
- e) $\text{div } \mu \text{ grad } \phi = \text{div } \mu (\underline{H}_{iSt} + \underline{H}_{iw})$

For a known vectorfield \underline{H}_{iw} the equation system does not differ from the magnetostatic one. That means, the solution of the time dependent Maxwell-equations requires the additional calculation of the vectorfield \underline{H}_{iw} , only.

According to equation 2c) \underline{H}_{iw} is the vectorpotential of the induced density. To eliminate \underline{i}_w , we substitute $\text{curl } \underline{H}_{iw}$ in the second Maxwell-equation for \underline{i}_w and obtain eq. 3b).

- a) $\underline{E} = 1/\epsilon \underline{i}_w = 1/\epsilon \text{curl } \underline{H}_{iw}$
- 3) b) $\text{curl } 1/\epsilon \text{curl } \underline{H}_{iw} = -\frac{d}{dt} \mu (\underline{H}_{iw} + \underline{H}_{iSt} - \text{grad } \phi)$
- c) $\text{curl } \text{curl } \underline{H}_{iw} = -\epsilon \frac{d}{dt} \mu (\underline{H}_{iw} + \underline{H}_{iSt} - \text{grad } \phi)$

The total time derivative is allowed if the velocity is low compared with the velocity of light. If the space, in which the eddy current calculations take place, is surrounded by insulators, boundary conditions at its surface can be formulated. With the further assumption of constant conductivity ϵ inside this space equation 3b) can be multiplied by ϵ and we have the more simple equation 3c).

- b) Boundary conditions

Outside the eddy current space the eddy current density is zero. So $\text{curl } \underline{H}_{iw}$ is zero, too, and \underline{H}_{iw} can be represented by the gradient of a scalar function ϕ_w . Then for the magnetic field we have, according to eq. 2d)

$$\underline{H} = \underline{H}_{iSt} + \text{grad } \phi_w - \text{grad } \phi$$

Because \underline{H} is defined uniquely by the potential equation 2b), for each ϕ_w the potential ϕ is determined accordingly.

We put $\phi_w = \text{const}$ for the sake of simplicity. That means that outside the eddy current space $\underline{H}_{iw} = 0$ is valid.

Because $\text{curl } \underline{H}_{iw}$ is a limited quantity the tangential component H_{iwt} of \underline{H}_{iw} must pass the surface of the eddy current region steadily. So we have the boundary condition, that the tangential component H_{iwt} must be zero at the total surface of the eddy current space.

c) Time dependence

I suppose, for optional time dependence and field dependent permeability the problem is not yet soluble in an acceptable computation time. For the solution of this four dimensional problem additional numerical methods have to be developed especially those, concerning the solution of large linear equation-systems and a suitable discretization of differential equations. Provided all the field quantities have the same time dependence the problem can be reduced to the solution of a three dimensional one. This assumption includes a permeability depending on locus

only and is strictly valid for non-ferromagnetic. For ferromagnetic the usual conversion of the permeability curve has to be carried out.

The following considerations provide both a sinusoidal time dependence and time dependent effects caused by moving bodies. In the latter case the restriction has to be made, that the cross section of the moving parts must be constant in the direction of movement.

For all the quantities the time-dependence is expressed by $e^{j\omega t}$ and all the movements are assumed in the X-direction, having the velocity v_x . Eq. 3c) can then be written in the final form eq. 4a)

$$\begin{aligned} \underline{H}_{iw} &= \tilde{\underline{H}}_{iw} e^{j\omega t} \\ 4) \quad \text{a) } \text{curl } \text{curl } \tilde{\underline{H}}_{iw} + j\omega \mu \tilde{\underline{H}}_{iw} + v_x \frac{\partial}{\partial x} \mu \tilde{\underline{H}}_{iw} &= \\ & - j\omega \mu (\tilde{\underline{H}}_{iSt} - \text{grad } \tilde{\phi}) - v_x \frac{\partial}{\partial x} \mu (\tilde{\underline{H}}_{iSt} - \text{grad } \tilde{\phi}) \\ \text{b) } \text{div } \mu \text{ grad } \tilde{\phi} &= \text{div } \mu (\tilde{\underline{H}}_{iSt} + \tilde{\underline{H}}_{iw}) \end{aligned}$$

The sign above the quantities signifies that these quantities are the complex amplitude, only.

d) Solution

One is used to the divergence of a vectorpotential being arbitrary. If this holds in our case, too, according to equation 4b), a suitable selection would be $\text{div } \mu \tilde{\underline{H}}_{iw} = 0$, because then the potential $\tilde{\phi}$ does not depend on $\tilde{\underline{H}}_{iw}$, and the calculation of $\tilde{\phi}$ would be definitive. We had the following direct way of calculation: First the computation of $\tilde{\underline{H}}_{iSt}$ needing the given current density, only. Then the computation of $\tilde{\phi}$ for the known $\tilde{\underline{H}}_{iSt}$ and at last the calculation of $\tilde{\underline{H}}_{iw}$.

In reality the solution is more complicated. Because we put $\tilde{\underline{H}}_{iw} = 0$ outside the eddy current space, $\text{div } \mu \tilde{\underline{H}}_{iw}$ cannot be made zero at the surface.

At the surface the normal component of $\tilde{\underline{H}}_{iw}$ jumps according to the jump of the tangential component of the eddy current density, that means, the eddy current causes sources of the magnetic field at the surface, which depend on the resulting field. So we have to solve the two

equations 4a) + b) by iteration. We start with an estimated value for $\tilde{\underline{H}}_{iw}$, solve equation 4b) and substitute the result for $\tilde{\phi}$ in equation 4a). The iteration-prescription is:

$$5) \quad \begin{aligned} a) \quad & \text{div } \mu \text{ grad } \tilde{\phi}^{(\nu)} = \text{div } \mu (\tilde{\underline{H}}_{iSt} + \tilde{\underline{H}}_{iw}^{(\nu-1)}) \\ b) \quad & \text{rot rot } \tilde{\underline{H}}_{iw}^{(\nu)} - \mu \nabla_x \frac{\partial}{\partial x} \tilde{\underline{H}}_{iw}^{(\nu)} = \\ & \mu \nabla_x \frac{\partial}{\partial x} (\tilde{\underline{H}}_{iSt} + \text{grad } \tilde{\phi}^{(\nu)}) \end{aligned}$$

With the yielded value for $\tilde{\underline{H}}_{iw}$ we calculate an improved approximation for $\tilde{\phi}$ by means of equation 4b) and start again. The procedure will be stopped if the power balance is fulfilled sufficiently.

e) Discretization

For discretization of equation 5b) the same grid is used as for discretizing the potential equation 5a). In this grid the scalar potential $\tilde{\phi}$ is defined at the nodes, marked as dots in Fig. 5. The components of the magnetic field $\tilde{\underline{H}}$ are calculated by dividing the difference of two neighbouring potentials by their distance. So the component directed from one node to the other one is defined in the

middle of the two nodes. Because of this lay down the according components of \tilde{H}_{iSt} and \tilde{H}_{iw} are defined at the same positions.

In order to calculate the x-components of \tilde{H}_{iw} , for example, one has to integrate over all the planes parallel to the grid planes $x = \text{constant}$. At the boundary of each integration plane, \tilde{H}_{iwx} is tangential component with respect to the total eddy current space and therefore zero. So we obtain equation systems containing the unknown components of one plane only.

By introducing a suitable numbering at each integration plane, it is possible to calculate the components of \tilde{H}_{iw} directly, for example, by means of Gaussian algorithm.

If no moving bodies are present convergence is uncritical. With a velocity unequal zero, however, the

above mentioned iteration procedure diverges if one starts with $\tilde{H}_{iw}^{(0)} = 0$. Convergence is obtained, if one starts with $\tilde{H}_{iw}^{(0)}$ necessary for total field displacement in the eddy current spaces, the so called ideal diamagnetic case ($\mu = 0$).

III) Some results

a) Electrodynamic levitation systems

For example the forces in electrodynamic levitation systems were calculated. Fig. 1 shows the set-up as used for basic experiments.

In principle, it is a rectangular coil moving with constant velocity above a conducting plate. The plate is infinite in the direction of movement and has constant cross section. It is 10 mm thick and 160 mm wide. The coil has a length of 200 mm, a width of 85 mm and a cross section of $15 \times 15 \text{ mm}^2$. The exciting current is 48000 A.

The complete lines of Fig. 2 show the levitation force and the drag force, caused by the eddy current in the plate, versus the velocity of the coil. The parameter is the distance Z_0 between the coil and the plate. In the lower curves the distance is 90 mm and in the upper curves 70 mm. The levitation force increases constantly with increasing velocity.

The drag force has a maximum at about 15 m/sec. The broken lines show the respective measured results. The discrepancies are mainly caused by the limitations of the experimental model set-up:

The infinite plate was represented by a round strip mounted on a rotating disc, so that the velocity was not uniform and the distance Z_0 was enlarged by the reaction force, during experiment.

Fig. 3 shows the current flow patterns at the upper surface of the plate for 18 km/h, 36 km/h and 540 km/h. In the patterns for 18 km/h two eddies can be seen, caused by the increase and decrease of the magnetic field of the coil. The centre of the eddies moves with increasing velocity opposite the direction of movement, as it can be seen comparing the patterns for 36 km/h with those for 18 km/h. At 540 km/h the rear-eddy has vanished and the front-eddy has shifted its centre to the centre of the coil.

Because of the symmetric set-up with regard to the y-direction, the side forces are zero in the cases dealt with before. For small displacements a linear increasing destabilizing side force occurs. Fig. 4 shows the side force versus the displacement .

b) Eddy current calculations in iron rotors

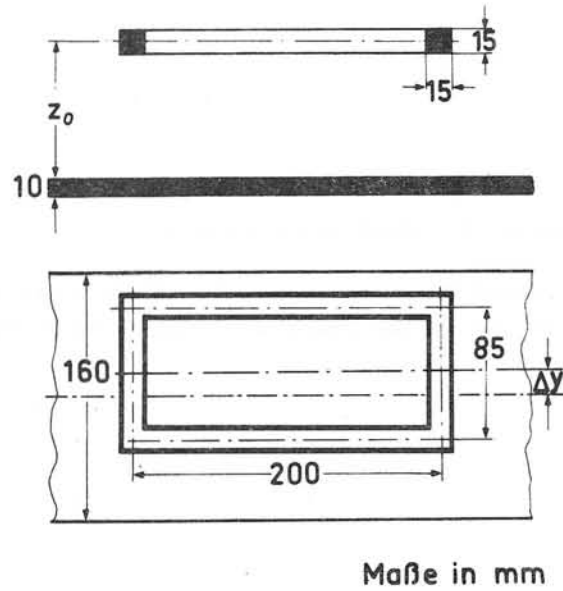
To demonstrate an application in material with locus dependent permeability the eddy current distribution was calculated in an iron rotor. For sake of simplicity rotor and stator are fixed and the excitation consists of one coil, only.

At first, the magnetic field was calculated for dc-excitation regarding a field dependent permeability. This permeability distribution remained unchanged during the eddy current calculations.

Fig. 6 shows the real component of the magnetic field in the symmetry plane caused by an ac-excitation and the eddy current. In the rotor the magnetic field is mainly displaced.

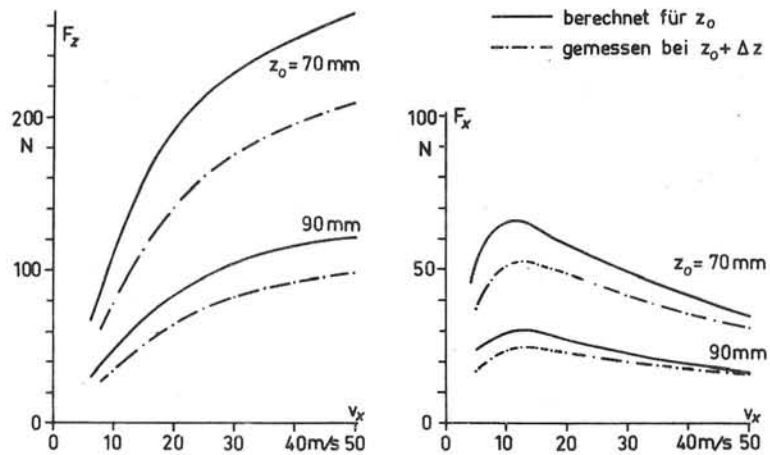
Fig. 7 shows the imaginary component.

Fig. 8 shows the real component of the eddy current at the surface of the rotor and fig. 9 the imaginary component.



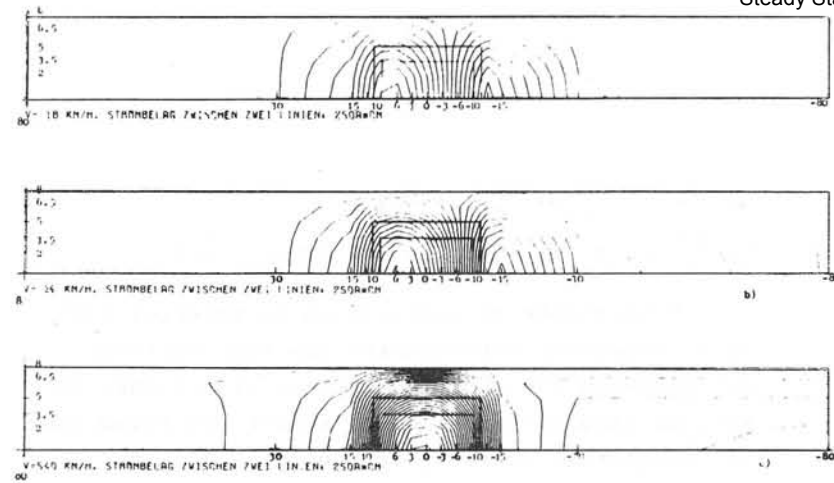
The model set up

Fig 1



Levitation- and drag-force versus v_x

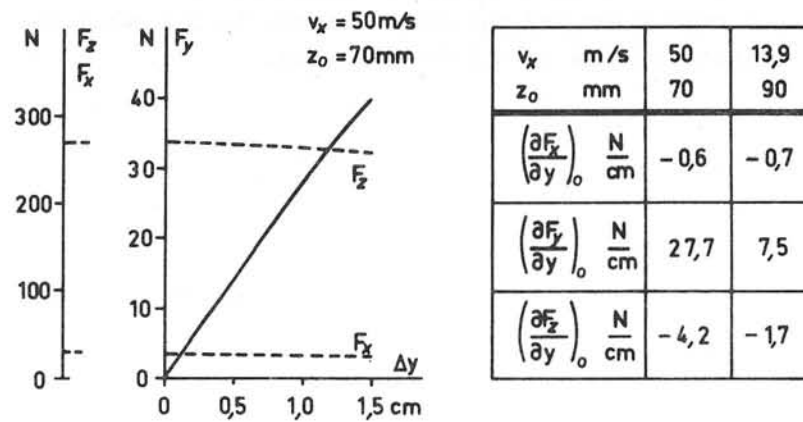
Fig 2



Eddy current patterns

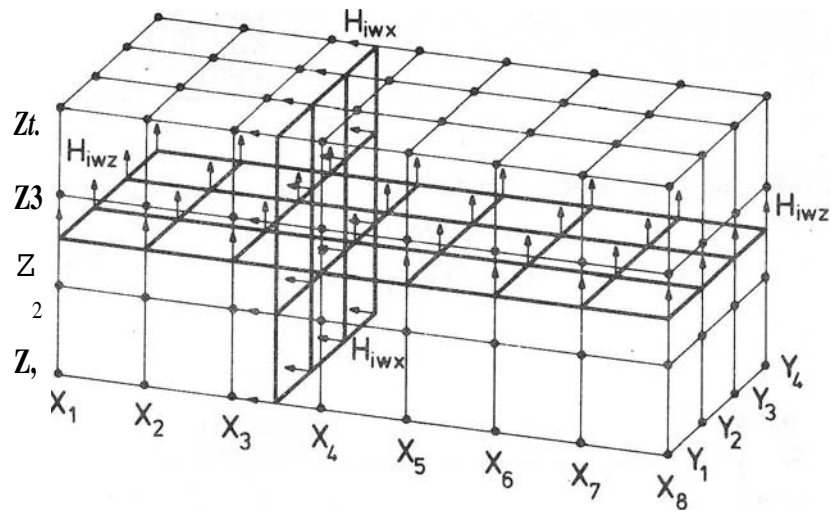
- a) $v_x = 18 \text{ km/h}$
- b) $v_x = 36 \text{ km/h}$
- c) $v_x = 540 \text{ km/h}$

Fig 3

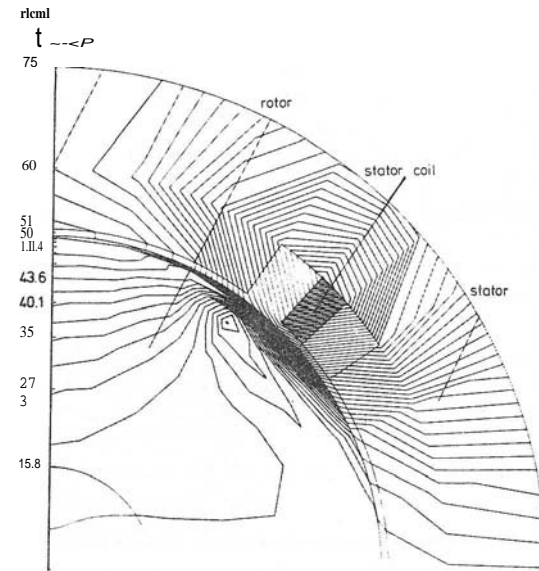


Side-drag- and levitation-force versus eccentricity Δy

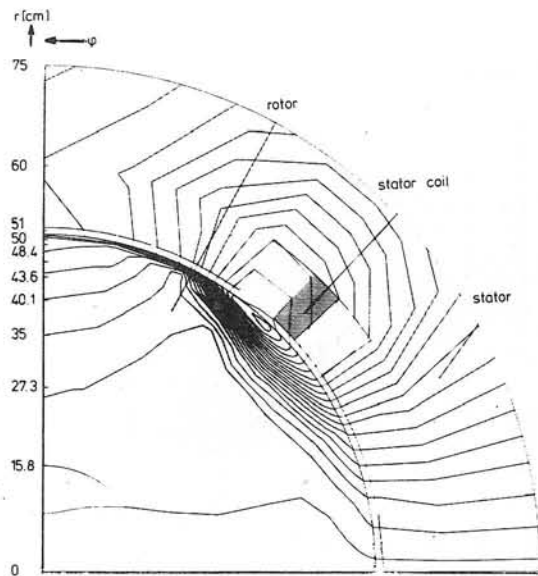
Fig 4



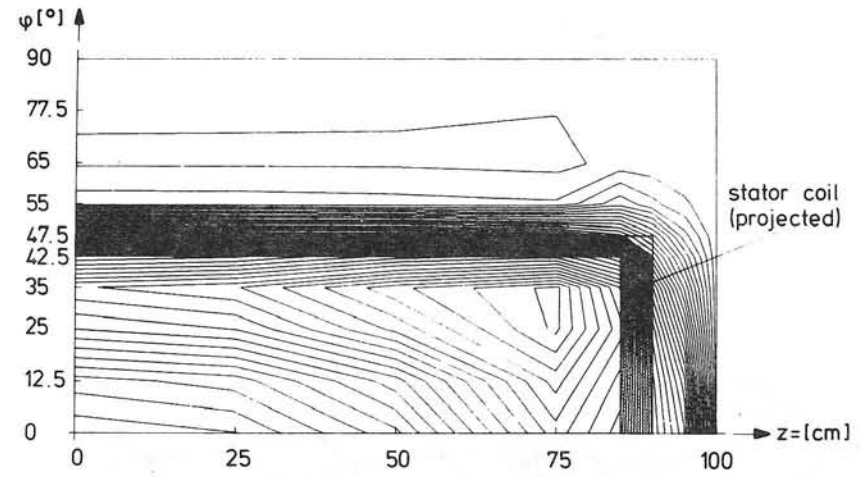
Integration planes for discretization of the vectorpotential equations concerning the components H_{iwx} and H_{iwz} Fig 5



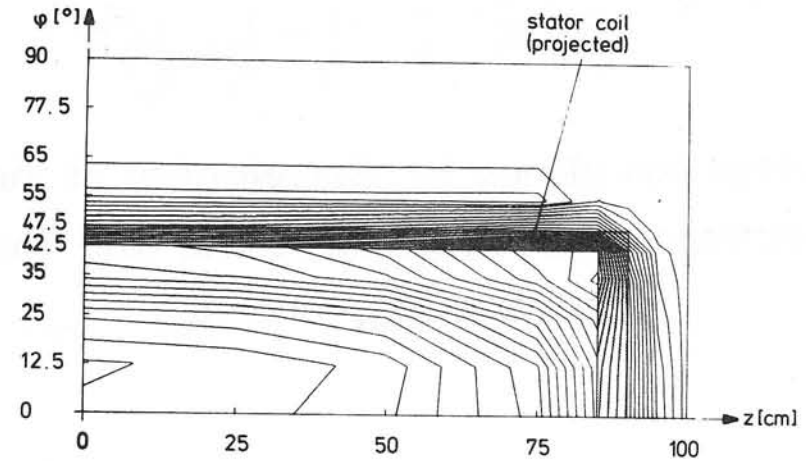
Induction (real component) I_n
symmetry-plane $z=0$ cm
0.5T.cm Fig 6



Induction (imaginary component) in
symmetry-plane $z=0\text{cm}$
 $0.6\text{T}\cdot\text{cm}$ Fig 7



Eddy - current (real component) at the rotor surface
($r=50\text{ cm}$)
 $0.5\text{kA}\cdot\text{cm}$ Fig 8



Eddy - current (imaginary component) at the rotor surface
($r=50\text{ cm}$)
 $0.5\text{kA}\cdot\text{cm}$ Fig 9

Discussions following paper:

(Miller, Leeds) I would like to ask Dr Wolff what boundary condition he uses at the edges of the strip conductor, where the eddy-current is deflected into the transverse direction. When this problem is approached using magnetic vector potential A there appears to be some uncertainty about this boundary condition. In physical terms my question asks whether charge appears on the strip edges.

(Wolff) The above derived boundary conditions for the vector potential are also valid at the edges. Whether charge appears or not cannot be answered by me, because we do not calculate the electrical field especially.

(Carpenter, IC) Dr Wolff's formulation is somewhat similar to that which we shall describe in paper number 38, but with one important difference. The electric vector potential function which Dr Wolff denotes H_{1st} is, as he points out, one of a range of possible functions. We have used the symbol T in conducting plate problems such as that described by Dr Wolff the component of current normal to the plate surface is usually negligible, and, as we have shown in paper no 7, this makes it possible to restrict T to a single component. The calculation is then reduced to two functions only (T and Ω , in our notation). I would like to ask Dr Wolff if he has considered this possibility. In general (as shown in paper 7) the three components of J can always be described by a T function which is limited to two components, and I wonder if there is any advantage in using three.

It is perhaps worth pointing out that Dr Jacob's equations in terms of a current flow function (paper 38) is essentially the same as Dr Wolff's but with the equivalent of the single-component T function.

(Wolff) Because of the lay boundary condition that the vector-potential is zero outside the eddy current space the three components of the vector-potential are determined uniquely. The advantage of the boundary condition at the surface of the eddy current space are the small equation systems for calculating the components of the vector-potential.

EFFICIENCY OF NUMERICAL TECHNIQUES FOR COMPUTING EDDY CURRENTS
IN TWO AND THREE DIMENSIONS

C.J. Carpenter* and E.A. Wyatt*

ABSTRACT

The paper reports recent work on numerical techniques for solving eddy current problems in terms of a scalar, instead of the conventional vector, magnetic potential function. A method described previously for thin plates has been extended to large-section conductors, and gives high convergence rates when solved by iterative methods provided that suitable numerical techniques are used. These techniques are described in the paper. The method is particularly well suited to three-dimensional problems, but it also gives better convergence than the conventional method of calculation in many two-dimensional problems of practical interest, particularly in electrical machines.

PRINCIPLE SYMBOLS:

B	magnetic flux density	T	electric vector potential (equ.6)
d	depth of penetration (equ.10)	\underline{x}	solution vector
E	electric field intensity	x,y,z.	coordinates
\underline{f}	column vector of constants	α	travelling-wave term (equ.22)
\underline{H}	magnetic field intensity	β	constant given by equ.23
h	mesh interval	μ	permeability
J	current density	σ	conductivity
L	coefficient matrix	τ	time
N	mesh element ratio (fig.1)	Ω	magnetic scalar potential
p	pole pitch	ω	angular frequency

1) Introduction

Eddy currents induced by leakage fluxes are of increasing importance in large electromagnetic devices such as turbo-generators, transformers, and the like, where increasing sizes and ratings may lead to severe heating problems. Eddy currents are induced in all conducting parts in the vicinity of the windings, particularly in the end-regions; and the end-surfaces of the core commonly need some form of screening. The eddy current and loss densities are difficult to predict because the problem is three-dimensional and the iron parts may be laminated and are liable to severe saturation. The magnetic vector potential, like the field vectors, has three components and, in general, it has to be supplemented by an electrostatic scalar potential, so that field calculations in these terms become formidable.

The obvious advantages of a magnetic scalar-potential formulation in magnetostatic problems, some aspects of which are discussed in a companion paper¹, assume an even greater significance in computing eddy currents. It is necessary to compute only one function outside the conductors, and excellent convergence is normally obtained when the differential equation is solved iteratively. A supplementary current-flow function has to be used inside the conducting regions, and this is, in general, a vector quantity, but it can usually be limited to one component, and it has been found to be well-behaved numerically when applied to problems in which the current flow is confined to thin sheets². This formulation can be applied to conductors of large cross-section either by assuming continuous conducting properties, by replacing them by a stack of thin plates, or using an "onion skin" model consisting of a set of concentric layers. Some of the possibilities have been discussed elsewhere^{1,3}.

In the type of problem considered here the more important conductors consist of laminated iron cores, or non-magnetic plates whose thickness is limited (although it may often be substantially greater than the depth of penetration at the working frequency). Under these conditions the current density component normal to the major conductor surfaces is negligible (i.e. the z-component in fig.1), and it is

* Electrical Engineering Department, Imperial College, London SW7 2AZ.

convenient to assume that it is zero in all conductors, whether laminated or not. The effect of removing this restriction will be discussed separately.

One of the devices of interest is a linear induction motor consisting of a conducting plate in an air gap between two iron surfaces, one carrying a winding in slots. This machine has been studied partly because the flux distributions are easily obtained experimentally. The principal parameters are given in figure 1. The winding generates a flux wave travelling in the y direction, and gives three-dimensional flux and current-flow patterns for which a two-dimensional description is adequate. This simplifies experimental work and is directly applicable to many end-field problems.¹ Varying the pole-pitch in the numerical model of the machine changes the field conditions from a rapid variation in the y direction, at one extreme, to a simple two-dimensional

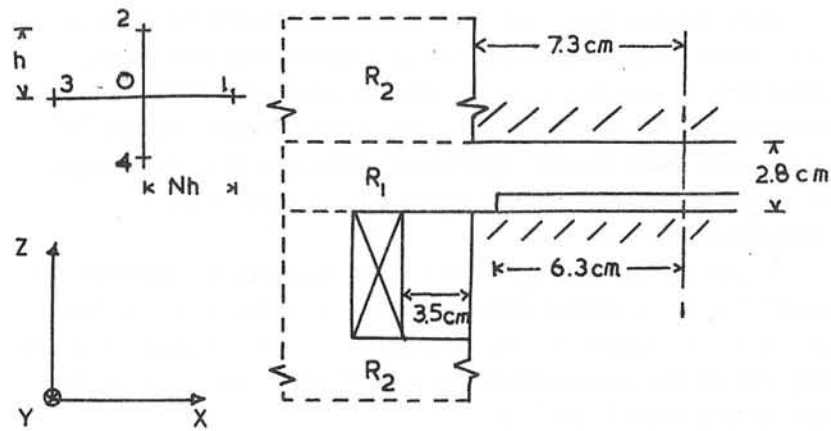


Fig. 1 Induction machine geometry.

Machine 380 mm long, pole pitch 95 mm
 "Duralumin" plate, resistivity $3.02 \times 10^{-8} \Omega\text{m}$, thickness 6.35 mm
 Mesh Nh = 4.67 mm $h = 2 \text{ mm}$ in region R_1
 $h = 4.5 \text{ mm}$ in region R_2

result, at the other, when the pole-pitch is infinite. The more general three-dimensional problem has been studied previously² using thin plates.

Early experience³ with the scalar-potential method suggested that it had very considerable advantages in eddy-current problems not only in three dimensions, but also in two, because of its numerical behaviour when solved iteratively. This has now been more closely studied and the behaviour of different numerical formulations compared. The object of the paper is to report some of the results of these studies, and the preferred numerical formulation. The method is applicable to both transient and steady-state problems, but for the present purpose all time variations are assumed to be sinusoidal, with angular frequency ω .

2) Formulation

The problem is to solve simultaneously the magnetic field equations

$$\text{curl } H = J \quad (1)$$

$$\text{div } B = 0 \quad (2)$$

together with

$$\text{curl } E = -j \omega B \quad (3)$$

$$\text{div } J = 0 \quad (4)$$

in which all the quantities are vectors with three space components, each of which is complex. The usual two-dimensional method is to satisfy equation 2 implicitly by expressing B as the curl of the magnetic vector potential, A, giving

$$\nabla^2 A = (j/d^2)(A - \text{grad } V) \quad (5)$$

where A is assumed to have zero divergence (Coulomb gauge). The electrostatic potential, V, adds an electric field component which is constant inside each conductor in a two-dimensional problem, but is not in three dimensions, where surface charges appear at all the conductor surfaces as a consequence of equation 4.

One alternative is to use an electric vector potential, T, defined by

$$\text{curl } T = J \quad (6)$$

and to confine T to a simple function by placing some other constraints on it and allowing it to have an arbitrary divergence. As is shown in

reference 1, T can be restricted to one component, T_z , inside the conductor, with zero value outside and a constant value in any conductor hole, provided that J_z is zero. Assuming uniform conductivity, σ , equation 3 becomes

$$\nabla_{x,y}^2 T_z = \partial^2 T_z / \partial x^2 + \partial^2 T_z / \partial y^2 = j \omega \sigma B_z \quad (7a)$$

when expressed in terms of T in Cartesian co-ordinates. Here T_z is operated on only in the x and y directions. From equations 1 and 6

$$H = T - \text{grad } \Omega \quad (8)$$

where Ω denotes a magnetic scalar potential function. It follows from equation 2 that, in a non-magnetic conductor,

$$\nabla^2 \Omega = \partial T_z / \partial z \quad (9)$$

where the ∇^2 operator refers to all three directions, in the usual way. Outside the conductors (or in windings in which J, and therefore T, is specified¹) H can be obtained by computing Ω , whilst in the eddy-current regions both equations 7a and 9 have to be solved. The sources of Ω - i.e. the right hand side of equation 9 - are equivalent to magnetic poles distributed through the volume of the conductor, but concentrated primarily at the upper and lower surfaces where T is discontinuous. Substituting from equation 8 in 7a,

$$\nabla_{x,y}^2 T_z = (j/d^2)(T_z - \partial\Omega/\partial z) \quad (7b)$$

where d is the depth of penetration defined by

$$d^2 = 1/\omega\mu\sigma \quad (10)$$

The pair of equations, 9 and 7b have to be solved simultaneously for Ω and T_z , respectively. One is Poisson's equation, and the other a form of the Helmholtz equation, but with a two-dimensional operator and an additional source term.

In a travelling-wave type of solution all quantities are assumed to vary sinusoidally with y, and with time τ , so that T_z , for example,

takes the form

$$T_z(x,z)\exp j(\omega\tau - \pi y/p + \phi)$$

so that the second derivative terms in y can be written

$$\partial^2 T_z / \partial y^2 = -(\pi/p)^2 T_z \quad (11)$$

and likewise for Ω .

In expressing these equations in discrete form the Ω and T_z functions inside the conductors are not restricted to a common node array, and the first-order derivatives on the right-hand sides of equations 9 and 10 suggest some advantages in computing them in two staggered arrays. The directional properties of the various terms, together with the discontinuities in both $\text{grad } \Omega$ and T at the conductor surfaces, introduce a range of possible numerical treatments, and each of the pairs of simultaneous equations obtained can be solved by elimination, line, or point iteration in various combinations.

These possibilities have been somewhat restricted by adopting a first-order (linear) interpolation in a rectangular node array, since this is well suited to the problem under consideration. An investigation of staggered meshes (the "split-branch" formulation⁴) showed that these have no significant advantages in either accuracy or numerical behaviour over a single mesh in which Ω and T_z are computed at the same nodes.

In general the conductor surface may intersect the mesh between nodes, but it is usually convenient to place nodes on it, as shown in fig 1. To compute T_z from equation 7 at a surface node, 0, H_z is required at the discontinuity. From equation 8, the H_z value mid-way between nodes 0 and 2 is

$$(H_z)_{02} = (\Omega_0 - \Omega_2)/h \quad (12)$$

and between 0 and 4,

$$(H_z)_{40} = (T_0 + T_4)/2 - (\Omega_0 - \Omega_4)/h \quad (13)$$

Here the z suffix has been dropped from T_z as it is superfluous. The two values can be averaged, or alternatively H_z at node 0 can be

derived from the underside values according to

$$(H_z)_0 = (H_z)_{40} + (\partial H_z / \partial z)_0 h/2 \quad (14)$$

where

$$(\partial H_z / \partial z)_0 = -(\partial H_x / \partial x + \partial H_y / \partial y)_0$$

since div H is zero. Hence

$$(\partial H_z / \partial z)_0 = (\partial^2 \Omega / \partial x^2 + \partial^2 \Omega / \partial y^2)_0 \quad (15)$$

and this can be expressed in terms of the nodal values of Ω in the usual way. The required H_z can likewise be derived entirely in terms of Ω from values on the surface and above by substituting from equations 12 and 15 in

$$(H_z)_0 = (H_z)_{02} - (\partial H_z / \partial z)_0 h/2 \quad (16)$$

The results obtained from equations 14 and 16 will be identical when the solution has converged and the continuity condition (equation 2) has been met, and likewise adding 14 and 16 together shows that averaging the H_z values above and below the node also gives the same final result. But at the earlier stages of the calculation the continuity condition is not satisfied, and it has been found that the different formulations give very large differences in numerical behaviour when iterated. In general, the use of asymmetric expressions for H_z has been found to produce poor convergence, and can lead to numerical instability, depending on the sequence and method by which the Ω and T functions are computed. No such difficulty has been encountered when using the symmetrical expressions

$$(H_z)_0 = [(H_z)_{02} + (H_z)_{40}]/2 \quad (17)$$

where the two terms are given by equations 12 and 13, and this form of dependence has therefore been adopted.

At the conductor surface the discontinuity in the right-hand side of equation 9 can be represented by treating it as a sheet source, in which the equivalent pole density is numerically equal to T_z , per

unit area. Alternatively, from equation 8,

$$\partial H_z / \partial z = \partial T_z / \partial z - \partial^2 \Omega / \partial z^2$$

so that equation 9 can be written

$$\nabla_{x,y}^2 \Omega = \partial H_z / \partial z \quad (18)$$

where

$$(\partial H_z / \partial z)_0 = [(H_z)_{02} - (H_z)_{40}] / h \quad (19)$$

Hence the nodal forms of equations 7 and 9 at the conductor surfaces are

$$T_1 + T_3 + jN^2 \beta [(\Omega_2 - \Omega_4)/h - T_4/2] - (2 + jN^2 \beta/2 + \alpha)T_0 = 0 \quad (20)$$

$$\Omega_1 + \Omega_3 + N^2 [\Omega_2 + \Omega_4 + (T_0 + T_4)h/2] - (2 + 2N^2 + \alpha)\Omega_0 = 0 \quad (21)$$

where

$$\alpha = (\pi N h / p)^2 \quad (22)$$

and

$$\beta = h^2 / 2d^2 \quad (23)$$

When equation 21 is derived by the equivalent pole-sheet approach the $(T_0 + T_4)/2$ term is replaced by T_0 , and this provides an alternative approximation of the same accuracy. More general expressions for T_0 and Ω_0 can be derived in the same way for conductor interfaces at which the conductivity takes different values on the two sides, neither zero. At nodes at which the conductivity is uniform, equations 7 and 9 become:

$$T_1 + T_3 + jN^2 \beta (\Omega_2 - \Omega_4) / h - (2 + j2N^2 \beta + \alpha)T_0 = 0 \quad (24)$$

$$\Omega_1 + \Omega_3 + N^2 [\Omega_2 + \Omega_4 + (T_4 - T_2)h/2] - (2 + 2N^2 + \alpha)\Omega_0 = 0 \quad (25)$$

3. Methods of solution

The method was compared with the conventional magnetic vector potential (A) formulation in an initial study of the linear motor. To simplify the A calculation the problem was assumed to be two-dimensional. Consequently the pole pitch was made infinite. The scalar potential, when calculated by simple point iteration with unity acceleration factor, required 850 iterations to reduce the maximum error to 2×10^{-5} of the maximum potential in a rectangular mesh of 202 nodes (with machine proportions somewhat different from those shown in fig.1). The dominating effect of the iron surface made the convergence of the A calculation too slow to be practicable without various acceleration techniques (including specifying the flux linkage instead of the excitation current), so that quantitative comparison is difficult and is not necessarily very meaningful because it is problem-dependent. But, in general terms, the well-known advantages of the scalar-potential formulation in regions bounded by iron, because the Neumann condition which is imposed on A is replaced by the Dirichlet condition, are retained in eddy-current calculations. It has been found that the ratio of the convergence rates is reduced as the frequency is raised, but it is greatly in favour of the scalar potential formulation at the working frequency of the machine.

Nevertheless, the preliminary results showed room for further improvement, and experimentation with different methods of computing Ω and T_z showed that not all of them converged well, whilst some diverged. The numerical behaviour was therefore examined more closely. The full set of finite difference equations for all nodal T_z and Ω values takes the form

$$L_1 \underline{x}_1(\Omega, T_z) = \underline{f}_1 \quad (26)$$

where L_1 is a sparse coefficient matrix, \underline{x}_1 is the vector of T_z and Ω values, and \underline{f}_1 is a constant vector that incorporates the boundary conditions. Although the values of the elements of L_1 depend on the way in which H_z and $\partial H_z / \partial z$ are approximated numerically, L_1 has some properties that are independent of the finite difference approximation used. The finite direction graph technique described by Varga⁵ shows that L_1 is not consistently ordered and does not satisfy Young's "Property A." Furthermore, L_1 cannot be diagonally dominant, though

it may approach this condition when the simultaneous equations are suitably manipulated. The manipulation takes the form of elimination of some T_z and Ω terms. The equations are derived from two different coupling conditions, namely the induced current equation 7, and the magnetic continuity equation 9, and numerical experimentation has shown that best convergence rates can be achieved if these are separated. That is, 26 is separated into two simultaneous matrix equations of the form

$$L_2 \underline{x}_2(T_z) = \underline{f}_2 + \underline{g}_2(\Omega) \quad (27)$$

$$L_3 \underline{x}_3(\Omega) = \underline{f}_3 + \underline{g}_3(T_z) \quad (28)$$

where \underline{f}_2 and \underline{f}_3 incorporate the boundary conditions, whilst \underline{g}_2 and \underline{g}_3 are functions of Ω and T_z respectively. The coefficient matrices L_2 and L_3 depend on the numerical approximation adopted. It is found that L_2 and L_3 are consistently ordered and satisfy Young's "Property A", although neither is diagonally dominant. Furthermore, L_2 , but not L_3 , can be tri-diagonal. It has been found that the T_z calculation is less well-conditioned than the Ω one (partly because the operator differentiating T_z has one less dimension than that operating on Ω) and improvements depend on an increase in the number of T_z iterations. This causes relatively little increase in the computing time per complete cycle because the T_z calculation is confined to nodes in conductors. There are advantages in solving equation 27 by matrix inversion, particularly when the finite-difference approximation chosen makes L_2 tri-diagonal, and this gives a part line-iteration method.

In a typical calculation, the substitution of equations 27 and 28 for 26 and computing T_z by 10 Gauss-Seidel iterations per step of the main iteration cycle improved convergence by a factor of 5 (to 173 cycles). The computing time was reduced by a factor of 3.5.

One consequence of the consistent ordering of the L_3 matrix is that the Carré-Stoll method^{6,7} may be used to calculate the best acceleration factor, and this has been found to work well in practice.

4) Results

The linear motor used for test purposes was excited by a 3-phase winding arranged in 3 slots per pole in the laminated block on the underside of the air gap (fig.1). The computation method was tested for various thicknesses and positions of the conducting plate as well as at different frequencies, but experimental measurements were limited to a plate having the thickness shown in fig. 1 placed on the lower iron surface. This left an air gap above the plate in which the flux density measurements were relatively unaffected by slot harmonics. The plate width was reduced below the normal value to increase leakage effects. For the field calculation a mesh of 661 interior nodes was chosen with approximately square elements in the end-region R_2 , and rectangular elements with a length-breadth ratio N of 2.25 in the air-gap region R_1 . The scalar potential field sources consisted of current sheets on the surface of the bottom laminated core, together with sheet pole-type sources on the end-winding surfaces (the T' function of ref.1).

A contour plot of the real part of the Ω function is given in fig.2. Here the field in the R_2 regions is compressed by treating all nodes, for plotting purposes, as having the same spacing as in the region R_1 . The imaginary part of Ω in the air gap and in the plate is drawn to an enlarged scale in fig. 3. The diagrams show the discontinuity in the normal gradient of Ω at the plate surface which is caused by the discontinuity in T .

As is typical with these proportions, the variation of T with z is comparatively small, although the depth of penetration d is only 20% greater than the plate thickness. The variation of T with x and y over the entire plate is shown in fig.4 for one instant of time (the calculation assumes no end-effects in the y direction). Since T varies sinusoidally with y , as well as in time, the real and imaginary parts are obtained by choosing appropriate sections of the diagram. It is noteworthy that $T(x)$ is approximately sinusoidal.

The solution converged to a potential error of 2×10^{-5} of the

maximum potential in 74 iterations, and the convergence rate was found to be virtually independent of frequency over a range of 40 to 1. The acceleration factor, computed by the Carré-Stoll method, settled to a final value of $1.707 + j 0.0047$, with a sufficiently high convergence rate to make its initial value (unity) unimportant.

Computed and measured values of the magnitudes of the two large flux-density components are plotted in fig. 5 as a function of x . The measurements shown were made in the mid-plane of the machine, where end-effects were expected to be least. Somewhat higher values were observed in other planes. Under travelling-wave conditions, equation 8 reduces to

$$H_y = -j(\pi/p)\Omega$$

so that the y component of B provides a direct measure of Ω . The purpose of the machine is to produce force in the y direction, and this force was measured and compared with the computed value to obtain a convenient criterion of solution accuracy averaged over the plate. The calculated force was 4.4% less than that measured.

The agreement between the calculations and measurements provided adequate confirmation of the former, in view of the approximations made, particularly the neglect of end-effects. Since the programme is a small one it could be readily extended to include these², but a more detailed study was not considered worthwhile. The principal objective was to investigate the numerical behaviour of the Ω and T functions for plate thicknesses representative of practical devices, and this behaviour is little affected by the way in which the y variations are modelled.

5) Conclusions

When computing eddy currents numerically the formulation can be expressed in terms of one of a range of possible quantities, all vectors, including the four field vectors (H, B, E, J) and the two vector potentials (A and T). The work described has confirmed the substantial advantages in choosing an electric vector potential, T , as the current describing function, defined so that it is constant or zero outside the conductors.

As in magnetostatic applications, this reduces the field problem in the non-conducting regions to that of computing a function Ω which is both a scalar and which is well-behaved numerically in regions bounded by iron. Inside laminated and plate conductors the associated T function can be limited to one component. Its interaction with Ω can be expressed numerically in a variety of ways, and many, although by no means all, of these possibilities have now been explored. Poor convergence, and even divergence, has been experienced with some, but the preferred methods give excellent convergence in a device which typifies many power-frequency applications.

The method assigns Ω and T values to the same nodes and is suitable for line iteration of the T values. Accelerated point iteration gives convergence which is very much better than that of the magnetic vector potential A function in regions bounded by iron, and the technique is well suited to both two- and three-dimensional calculations. The form of the matrices is such that the Carré-Stoll method for computing acceleration factors automatically is very effective.

6) Acknowledgements

The work has been supported financially by the Science Research Council. The authors are grateful to many colleagues for helpful discussions, particularly Dr. C.W. Norman (Westfield College) and Dr. D. A. Lowther (Imperial College).

7) References

- 1) Carpenter, C.J. and Locke, D. "Numerical models of 3-dimensional end-winding arrays" Compumag 1976
- 2) Carpenter, C.J. and Djurović, M "3-dimensional numerical solution of eddy currents in thin plates" Proc.I.E.E. 1975 122 pp 681-688
- 3) Carpenter, C.J. "Computation of magnetic fields and eddy currents" 5th Int.Conf. on Magnet Technology Rome 1975 pp 147-158
- 4) Carpenter, C.J. "A network approach to the numerical solution of eddy-current problems" Trans. I.E.E.E.1975 MAG-11 pp 1517-1522

- 5) Varga, R.S."Matrix Iterative Analysis", Prentice Hall 1962.
- 6) Carré, B.A. " The determination of the optimum accelerating factor for successive over-relaxation" Cmput.J. 1961 4 pp 73-8
- 7) Stoll,R.L. "Solution of linear steady-state eddy-current problems by complex successive overrelaxation" Proc.I.E.E. 1970 117 pp 1317-23

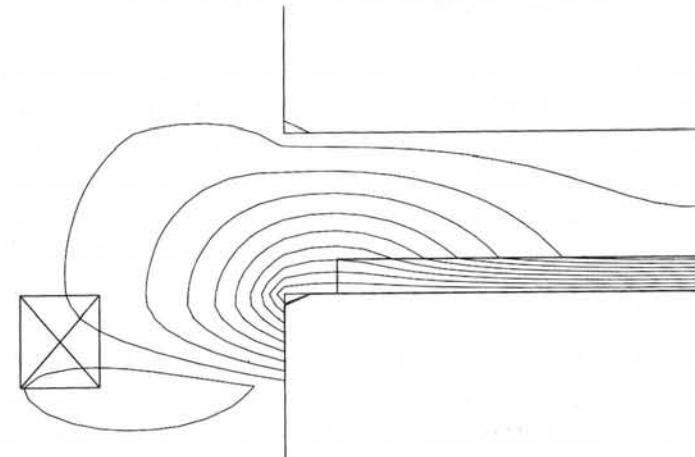


Fig. 2 Real part of Ω
 $\beta = 0.0276$

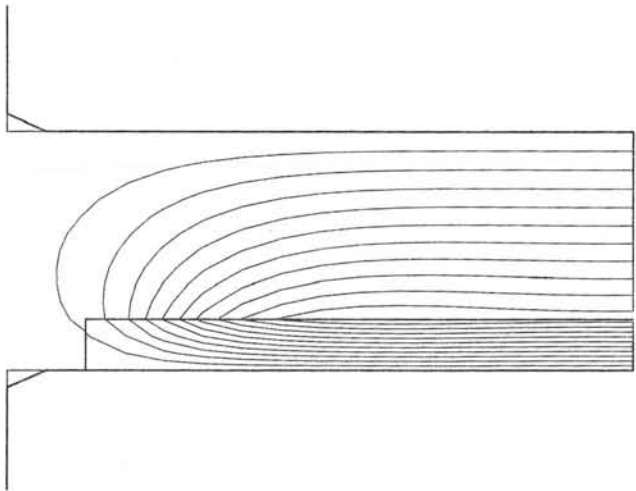


Fig. 3 Imaginary part of Ω
 $\Omega_{\max} = -29.2$ $\Omega_{\min} = 0$

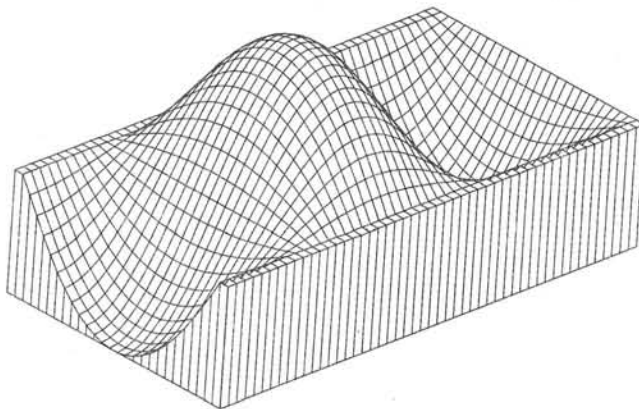


Fig. 4 T variation in typical layer of plate
 $T_{\max} = 6520$

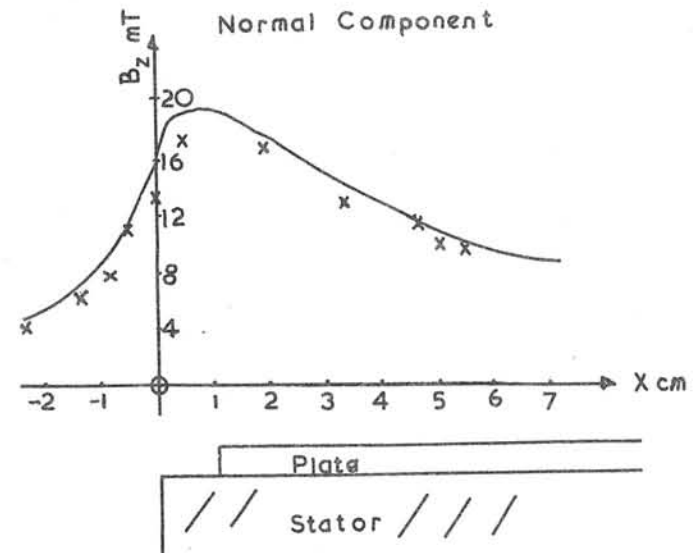
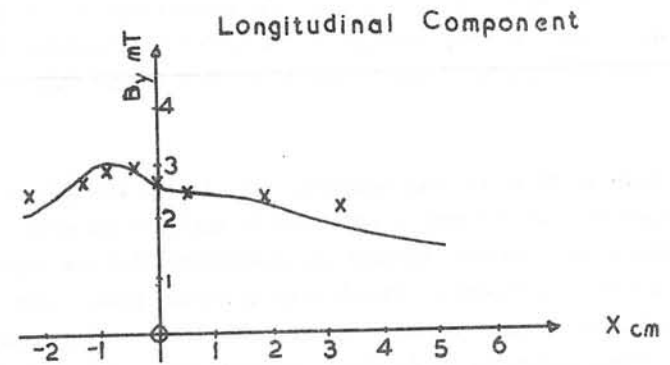


Fig. 5 Magnitude of B in air gap
 Measured in machine centre-plane 2mm below top iron surface

Discussions following paper:

(Perin, CERN) I should like to point out that the vector T was used, for the static case, about 20 years ago for the computation of the AGS magnets at BNL. Again a long time ago it was used by R Christian in his magnetostatic program Sybil and by myself at CERN in the MARE program.

(Wyatt) I thank Mr Perin for his comments. It is all too easy to give the impression that the method presented is entirely new when this is not the case. Maxwell himself was responsible for the idea of using a current flow function, though only in scalar form. Our contribution is that we have extended the flow function concept, using the electric vector potential T , in order to solve eddy currents in two and three dimensions.

THE CALCULATION OF MAGNETIC FLUXES AND
EDDY CURRENTS IN GENERATOR STATOR CORES

DAVID A.H. JACOBS

Research Department, C.E.G.B., Leatherhead, Great Britain

ABSTRACT

The time dependent electromagnetic fields in stator cores of large generators have been determined by a numerical solution procedure. The outline complex three dimensional geometry is modelled, and the saturable laminated structure of the core is included. The method has been ratified with measurements from large generators, and can be used to investigate the changes in the electromagnetic characteristics of generators occasioned by design modifications, changes in material, or material properties, and other alterations.

NOMENCLATURE

\underline{A}	Vector potential
\underline{B}	Magnetic flux density vector
\underline{E}	Electric field strength vector
\underline{H}	Magnetic field strength vector
H_o	Saturation magnetic field in the Fröhlich permeability relation
i	$= \sqrt{-1}$
\underline{J}	Current density vector
q	Source term in the stream function equation
r	Radial coordinate
t	Time
$\underline{x} = (r, \theta, z)$	Position vector
z	Axial coordinate
$\underline{\hat{z}}$	Unit axial vector
γ	Stacking factor
$\underline{\mu}$	Permeability tensor
$\bar{\mu}, \mu_{21}, \mu_{22}$	Fourier components of permeability components
μ_o	Permeability of free space
μ_1	Zero field relative permeability of iron
μ_2	Limiting relative permeability of iron
$\xi = \psi_{11} + i\psi_{12}$	
$\underline{\sigma}$	Electrical conductivity tensor
ϕ	Magnetic scalar potential
ϕ_{11}, ϕ_{12}	Fourier components of ϕ
ψ	Eddy current stream function
ψ_{11}, ψ_{12}	Fourier components of ψ
ω	Angular velocity of rotor
Superscript e	Induced eddy current component
Superscript i	Value in iron
Superscript n	Iteration number
Subscripts	Vector components
r, θ, z	

1. INTRODUCTION

It is highly desirable to put the art of designing large generators onto a firm scientific footing. Moreover during the life of a generator, the type of use and the load conditions it has to meet are likely to vary very considerably, and in order to be able to use the generator most efficiently it is necessary to predict the behaviour and characteristics under these different conditions. In this paper we concentrate on the derivation of the electromagnetic solution in the end region of a generator, including the radial air gap, the stator conductor slots and the stator core. The model developed includes a description of the three dimensional geometry, the radial cooling ducts, Pistoye slots, variations in the laminate constitution of the stator core, and the eddy currents in the laminate.

The aim of this work is to determine the relationships between the electromagnetic state of a generator and the thermal losses, both total and also local distribution, due to the induced eddy currents in the stator core. In principal, since some electromagnetic losses are inevitable, at least in conventional machines, suitable forms of cooling must be used where necessary to dissipate the induced thermal generation, and the channels incorporated in, for example, the stator through which the coolant passes, interact with the electromagnetic characteristics. It is therefore necessary to consider the cooling arrangements, together with the thermal conduction and convection treatment of the stator core and coolant, bound in with the electromagnetics. However in this paper, for simplicity and brevity, we only consider the electromagnetic problems.

2. REDUCTION OF THE BASIC FIELD EQUATIONS

The iron stator of a generator is not only a complicated geometrical shape, being basically cylindrical with axial teeth cut on the inside bore, together with radial and axial cooling ducts, Pistoye slots, etc., but it is also composed of a laminated material designed to confine the induced eddy currents to flow in planes normal to the machine axis. With existing computers it is not possible to represent the individual laminations explicitly, nor is it strictly necessary; instead in our model the laminated structure of the core is replaced by an equivalent homogeneous material with anisotropic non-linear properties. This will be considered more fully in section 7. We use cylindrical polar coordinates (r, θ, z) to describe the geometrical configuration which together with the associated simplifications will be considered in section 3.

The effect of hysteresis is ignored throughout the calculation, although as explained in section 9 the thermal generation caused by hysteresis effects can be estimated from the derived electromagnetic field solution.

We now derive the partial differential equations from the basic field equations. Within the stator core we assume that no eddy currents flow in the axial direction because of its laminated structure, so that the conservation of charge gives

$$\text{div } \underline{J}^e = \frac{1}{r} \frac{\partial}{\partial r} (r J_r^e) + \frac{1}{r} \frac{\partial J_\theta^e}{\partial \theta} = 0 \quad \dots (2.1)$$

This implies that \underline{J}^e can be defined by an eddy current stream function $\psi(r, \theta, z, t)$ with

$$\underline{J}^e = \hat{z} \times (\text{grad } \psi) \quad \dots (2.2)$$

where ψ can be defined to be continuous in the axial direction in accordance with the homogeneous laminated representation of the core. Maxwell's third equation gives, ignoring displacement currents, that

$$\text{curl } \underline{H} = \underline{J} \quad \dots (2.3)$$

Away from the regions in which stator currents are present, using equation (2.2) this implies that

$$\hat{z} \cdot (\text{curl } \underline{H}) = 0 \quad \dots (2.4)$$

so that a magnetic scalar potential ϕ can be defined where

$$H_r = \frac{\partial \phi}{\partial r} \quad \text{and} \quad H_\theta = \frac{1}{r} \frac{\partial \phi}{\partial \theta} \quad \dots (2.5)$$

By using the other two components of equation (2.3) we find that

$$\underline{H} = \text{grad } \phi - \hat{z} \psi \quad \dots (2.6)$$

[Currents in the stator bar conductors are incorporated by defining 'cuts' along specific coordinate lines which connect the conductors to the boundary and across which the magnetic potential is made discontinuous, the magnitude of the discontinuity being proportional to the stator current.] The relation (2.6) is a mathematical expression for the fact

that in addition to the magnetic scalar potential contributing to the magnetic field, the eddy currents generated in the lamination by the impinging axial flux act in a manner to reduce the magnitude of this axial flux (Lenz's Law).

The remaining Maxwell equations

$$\text{div } \underline{B} = 0 \quad \text{and} \quad \text{curl } \underline{E} = - \frac{\partial \underline{B}}{\partial t} \quad \dots (2.7) \text{ and } (2.8)$$

together with the constitutive relations

$$\underline{J} = \underline{\sigma} \underline{E} \quad \text{and} \quad \underline{B} = \underline{\mu} \underline{H} \quad \dots (2.9) \text{ and } (2.10)$$

give two partial differential equations for the magnetic scalar potential ϕ and the eddy current stream function ψ , namely

$$\frac{1}{r} \frac{\partial}{\partial r} \left(r \mu_r \frac{\partial \phi}{\partial r} \right) + \frac{1}{r^2} \frac{\partial}{\partial \theta} \left(\mu_\theta \frac{\partial \phi}{\partial \theta} \right) + \frac{\partial}{\partial z} \left(\mu_z \frac{\partial \phi}{\partial z} \right) = \frac{\partial}{\partial z} \left(\mu_z \psi \right) \quad \dots (2.11)$$

$$\text{and} \quad \frac{1}{\gamma \sigma_r} \frac{\partial}{\partial r} \left(r \frac{\partial \psi}{\partial r} \right) + \frac{1}{\gamma \sigma_\theta} \frac{\partial^2 \psi}{\partial \theta^2} = -\mu_o \frac{\partial}{\partial t} \left(\mu_z \left(\frac{\partial \phi}{\partial z} - \psi \right) \right) \quad \dots (2.12)$$

We have assumed that $\underline{\mu}$ the permeability tensor for the equivalent homogeneous material is

$$\underline{\mu} = \mu_o \begin{bmatrix} \mu_r & 0 & 0 \\ 0 & \mu_\theta & 0 \\ 0 & 0 & \mu_z \end{bmatrix} \quad \dots (2.13)$$

and that the conductivity tensor $\underline{\gamma \sigma}^i$ for this material is

$$\underline{\gamma \sigma}^i = \gamma \begin{bmatrix} \sigma_r^i & 0 & 0 \\ 0 & \sigma_\theta^i & 0 \\ 0 & 0 & 0 \end{bmatrix} \quad \dots (2.14)$$

The important characteristics of equations (2.11) and (2.12) are:

- (a) The electromagnetic solution in the three dimensional region is given in terms of only two quantities, ϕ and ψ , in place of the three components of the vector potential \underline{A} where $\underline{B} = \nabla \times \underline{A}$, or of the magnetic field \underline{H} .

- (b) The equation (2.11) is a second order partial differential equation with only spatial derivatives, i.e. there are no time derivatives; considering ϕ as the dependent variable, given ψ , the equation is a non-linear three dimensional Poisson type elliptic equation.
- (c) The equation (2.12) is a second order partial differential equation with only two second spatial derivative terms; considering ψ as the dependent variable, given ϕ , the equation is a second order equation in the spatial variables (r, θ) and first order in the time derivative: it is a second order parabolic equation of the heat conduction form. It will be seen later (Section 7) that μ_z is almost constant in an axial plane, and hence the equation is virtually linear.

3. REPRESENTATION OF THE GEOMETRY

To obtain a reasonably tractable problem for the finite difference representation using cylindrical polar coordinates (r, θ, z) all boundaries in the problem are assumed to lie along cylindrical coordinate surfaces, i.e. they are either parts of (a) surfaces of cylinders ($r = \text{constant}$), or (b) planes through the machine axis ($\theta = \text{constant}$), or (c) planes perpendicular to the machine axis ($z = \text{constant}$). Thus, in particular, the stator conductor slots are not parallel sided, as in reality, but lie on radial lines from the centre of the generator. A three dimensional perspective view of the region considered is shown in Fig. 1. The stator core can have a stepped end, and radial ducts and steps can be incorporated at axial nodal positions, i.e. the bore can be of variable diameter. The boundary just above the magnetic material of the rotor body can also have a varying diameter. A typical cross section along the axis is illustrated in Fig. 2. An eddy current screen at the end of the stator can be incorporated by using a stepped stator and by specifying different properties at different axial positions in the "stator". In practice the radial cooling ducts have not been modelled explicitly because of the restricted number of axial nodes. A typical cross-section normal to the axis of the machine through the stator core is shown in Fig. 3 where we have assumed that only one tooth pitch of the stator is being considered. The Pistoye slot, if present, is modelled by a line cut in the core material in a plane $\theta = \text{constant}$, of specified axial and radial extent across which no eddy currents pass. The radial penetration of the slot can vary with axial distance. The Pistoye slot has no direct effect on the magnetic potential ϕ . The offset of the Pistoye slot from the centre of the core teeth is not explicitly

represented where this offset alternates on adjacent laminations; however the homogeneous laminated material used to represent the core means that a centrally positioned slot models the 'average' position.

Other minor and non-imperative assumptions on the geometrical configuration are described in Section 8.

4. THE TEMPORAL VARIATION-FOURIER SYNTHESIS

The magnetic scalar potential and the eddy current stream function are dependent on the three spatial coordinates (r,θ,z) and, in addition, they vary temporally since the magnetic field generated by the currents in the rotor windings rotate at the machine speed. The rate of rotation is relatively large, and we are predominantly interested in the limiting periodic behaviour of the fields when a periodic input is imposed by the rotor. An expansion in a Fourier time series is therefore used with

$$\left. \begin{matrix} \phi(\underline{x},t) \\ \psi(\underline{x},t) \end{matrix} \right\} = f(\underline{x},t) = \sum_{\substack{n=1 \\ n \text{ odd}}}^{\infty} (f_{n1}(\underline{x})\cos n\omega t + f_{n2}(\underline{x})\sin n\omega t) \dots (4.1)$$

The series is truncated after a finite number of terms: typically either only the first, or the first and third harmonics are sought. Substituting the relevant expansions of the form of (4.1) into equations (2.11) and (2.12), and then by multiplying each equation by cosnwt or sinnwt and integrating with respect to time over a period of oscillation, we obtain partial differential equations involving the Fourier components of φ and ψ. Considering only the first harmonic variations here, and throughout the remainder of the paper, we obtain the equations

$$\begin{aligned} & \frac{1}{r} \frac{\partial}{\partial r} \left(r(\bar{\mu}_r + \mu_{22r}) \frac{\partial \phi_{11}}{\partial r} \right) + \frac{1}{r^2} \frac{\partial}{\partial \theta} \left((\bar{\mu}_\theta + \mu_{22\theta}) \frac{\partial \phi_{11}}{\partial \theta} \right) \\ & + \frac{\partial}{\partial z} \left((\bar{\mu}_z + \mu_{22z}) \frac{\partial \phi_{11}}{\partial z} \right) \\ & + \frac{1}{r} \frac{\partial}{\partial r} \left(r\mu_{21r} \frac{\partial \phi_{12}}{\partial r} \right) + \frac{1}{r^2} \frac{\partial}{\partial \theta} \left(\mu_{21\theta} \frac{\partial \phi_{12}}{\partial \theta} \right) + \frac{\partial}{\partial z} \left(\mu_{21z} \frac{\partial \phi_{12}}{\partial z} \right) \\ & = \frac{\partial}{\partial z} \left((\bar{\mu}_z + \mu_{22z}) \psi_{11} + \mu_{21z} \psi_{12} \right) \dots (4.2a) \end{aligned}$$

and a similar equation (4.2b) with φ₁₁ and φ₁₂ interchanged, ψ₁₁ and ψ₁₂ interchanged and with the sign of the terms involving μ₂₂'s changed. For the stream function components we use the complex variable

$$\xi = \psi_{11} + i\psi_{12} \dots (4.3)$$

which enables the two equations for the components to be written in compact form as

$$\frac{1}{\sigma_r} \frac{1}{i} \frac{\partial}{\partial r} \left(r \frac{\partial \xi}{\partial r} \right) + \frac{1}{\sigma_\theta} \frac{1}{i} \frac{\partial}{\partial \theta} \left(\frac{\partial^2 \xi}{\partial \theta^2} \right) + i\mu_o \omega \bar{\mu}_z \gamma \xi = q + i\mu_o \omega \bar{\mu}_z \gamma \frac{\partial}{\partial z} \left(\phi_{11} + i\phi_{12} \right) \dots (4.4)$$

$$\text{with } q = \omega \gamma \mu_o \left\{ (i\mu_{22z} - \mu_{21z}) \left(\frac{\partial \phi_{11}}{\partial z} - \psi_{11} \right) + (i\mu_{21z} + \mu_{22z}) \left(\frac{\partial \phi_{12}}{\partial z} - \psi_{12} \right) \right\} \dots (4.5)$$

$$\text{where } \bar{\mu}_* = \frac{\omega}{\pi} \int_0^{\pi/\omega} \mu_*(H) dt \dots (4.6a)$$

$$\text{and } \mu_{22*} = \frac{\omega}{\pi} \int_0^{\pi/\omega} \mu_*(H) \cos 2\omega t dt, \mu_{21*} = \frac{\omega}{\pi} \int_0^{\pi/\omega} \mu_*(H) \sin n\omega t dt, \dots (4.6b)$$

(where the * can be r, θ or z).

Note that the expressions (4.6) are the Fourier coefficients of the permeability components, and are functions of the field values H. Hence the equations (4.2) and the associated equation, are grossly non-linear for typical B ~ H relationships (see Section 8).

The equations (4.2) and (4.4) have been written in the form in which they are solved: the right hand side is regarded as a source term, and the Fourier components of the permeability are held fixed for each cycle of iterations. This iterative procedure is based on the premise that the equations for the magnetic potential and the eddy current stream function are only relatively weakly linked in most of the region under consideration, and that this linking can be relegated to a 'source' term in each equation only recalculated after each cycle of iterations.

5. BOUNDARY CONDITIONS

The external boundaries of the region considered have been selected to be those at which the values of φ and ψ or their gradients

are known to a good degree of accuracy: this implies that the normal or tangential component of the field must be known. However the region must be as small as possible so that the maximum resolution and accuracy can be attained consistent with the numerical solution procedure employed, and the computer available.

With reference to Fig. 4 which illustrates the region considered, the boundary conditions on the magnetic scalar potential ϕ are:

- (a) $\frac{\partial \phi}{\partial z} = 0$ on the outer axial casing of the generator, ABCD.
- (b) $\frac{\partial \phi}{\partial z} = 0$ at the axial 'centre' of the stator core, LMNP.
- (c) $\frac{\partial \phi}{\partial r} = 0$ at the radial extremity of the core, BCNM.

[These three conditions are the mathematical expression for the boundary condition that no magnetic flux leaves these surfaces.]

- (d) The potential, or its normal gradient must be specified on the rotor surface AEFLPKD. This can be derived from models in which the rotor is treated in considerable detail, but the stator is modelled more crudely; or, alternatively, at least to a first approximation, we can assume that all the potential is lost in the radial air gap and hence derive the boundary potential given the magnitude of the radial flux entering the stator tooth.
- (e) The magnetic potential on one plane ($\theta = \text{constant}$) which bisects a stator tooth is phase displaced from that of the other mid tooth face according to the formula

$$\phi_{BMLFEA}(r,z,t) = \phi_{CNPJKD}(r,z,t - \frac{\theta_1}{\omega})$$

where θ_1 is the angle \widehat{AOD} . This is a periodic boundary condition. (For open circuit calculations, this boundary condition is accurate when the mid planes of adjacent teeth are considered, and so only one tooth pitch need be examined, whereas on load it is strictly only correct when all the teeth within one phase band are considered.)

The boundary conditions on the eddy current stream function ψ are:

- (a) $\psi = 0$ on the surfaces of the stator core parallel to the axis of the machine, namely the surfaces GMNH,UVWQ,XYZT,QQ₁R₁R,TT₁S₁S and on the base and sides of the conductor slot. Across all these surfaces,

which include the Pistoye slot, no eddy currents pass.

- (b) $\psi_{GMRWVU}(r,z,t) = \psi_{HNSZYX}(r,z,t - \frac{\theta_1}{\omega})$ as for (e) above.

Internal material boundaries must also be treated with care. At the boundaries between materials of different permeabilities, the tangential component of \underline{H} and the normal component of \underline{B} are continuous. When working in terms of the magnetic scalar potential ϕ and seeking solutions satisfying $\text{div } \underline{B} = 0$, where $\underline{B} = \underline{u}(\text{grad } \phi - \hat{z}\psi)$, these internal boundary conditions are automatically satisfied by ensuring that all boundaries are defined by nodal points.

6. THE FINITE DIFFERENCE DISCRETIZATION

In place of deriving an analytic solution to equations (4.2) and (4.4) for the Fourier components of ϕ and ψ , we characterize the variables by a finite set of values, and use finite difference methods to derive the algebraic equations for these nodal values. The nodal points used to describe the region are defined by the intersection of coordinate planes in the cylindrical polar coordinate system. With the region as shown in Fig. 1, about 18 radial nodal lines, 21 circumferential and 14 axial are used. These are spaced non-uniformly so as to obtain the greatest resolution in the regions of most interest. Thus about 5000 nodes are used, of which about one half are within the stator core.

[These restrictions on the number of nodal coordinates produce a computer code which occupies less than 250 K bytes of core, which happens to be both convenient and beneficial on our computer, an IBM 370/168.]

The finite difference equations are derived from the analytic equations producing sets of difference equations for the nodal values of the variables $\phi_{11}, \phi_{12}, \psi_{11}$ and ψ_{12} . (Note that the eddy current stream function is only defined in the stator core region.) The coefficients of the difference equations for the potential components depend on the local values of the permeability, and have therefore to be recalculated after each cycle of iterations.

7. THE HOMOGENEOUS LAMINATE REPRESENTATION

The differential equations (4.2) and (4.4) require knowledge of the values of the Fourier components of the vector components of permeability. If we assume that $\mu_r = \mu_\theta$ (see Section 8), then the transverse permeability μ_r and the axial permeability μ_z of the laminated core must be related to the field magnitude in the core material. However the D.C. saturation characteristics of the core plate iron are generally

known, not those of the laminated material. The magnitude of the magnetic field in the iron is related to the vector components by

$$(H^i)^2 = (H_r^i)^2 + (H_\theta^i)^2 + (H_z^i)^2 \quad \dots (7.1)$$

The transverse field in the iron is equal to the transverse field in the equivalent homogeneous material ($H_r^i = H_r$, $H_\theta^i = H_\theta$),

$$\dots (7.2)$$

but in the axial direction, across the laminations, the magnetic flux density is continuous so that $\mu_z^i H_z^i = \mu_z H_z$.

$$\dots (7.3)$$

From the definition of the stacking factor

$$1/\mu_z = 1 - \gamma + \gamma/\mu^i \quad \text{and} \quad \mu_\theta = \mu_r = \gamma\mu^i + (1-\gamma) \quad \dots (7.4)$$

$$\text{so that} \quad H_z^i = \frac{H_z}{\gamma + (1-\gamma)\mu^i} \quad \dots (7.5)$$

If a specified saturation relation between μ^i and the magnitude of H^i is used (see Section 8), the equations can be formed into an iterative procedure for H^i and μ^i given H_r , H_θ and H_z . The permeability components μ_r, μ_θ, μ_z of the equivalent material are then derived from equations (7.4).

8. FURTHER APPROXIMATIONS

To facilitate the derivation of the difference equations, and their subsequent solution, several further approximations listed below are used. None of these is essential, and given the facilities to run larger computer programs, they could all be relaxed.

(a) $\mu_r = \mu_\theta$ This simplification models a non-grain orientated core plate, and can easily be relaxed at the expense of increased computer run time.

(b) $\mu^i = \mu_1 + \frac{\mu_2}{1 + |H^i|/H_0}$ Namely the D.C. permeability in the iron

comprising the laminated core is related to the instantaneous magnitude of the local magnetic field by a Fröhlich law with the addition of a constant. This algebraic relationship can be fitted to the $B \sim H$ curves of most core plate iron with a reasonable degree of accuracy. Being algebraic, it is easily evaluated on the computer which has to be done very frequently since the Fourier components of the A.C. permeability are taken as the weighted integrated averages (expressions 4.6) over a cycle. In fact to save computation, the

latter integrals can be approximated analytically given the above permeability relationship for the first few iterations.

- (c) The separate core plate sections which make up the core are not modelled explicitly, so that the butt joints between them, and the eddy current circuit closures are not modelled.
- (d) The radial cooling ducts and any magnetically transparent laminations are not explicitly incorporated because of the restriction on the number of axial coordinate positions. Instead they are implicitly incorporated by suitable adjustments to the axial stacking factor. Their effect is therefore spread over a portion of the core.
- (e) The axial cooling ducts are not modelled in the electromagnetic computer codes.
- (f) Tooth wedge notches and other small geometrical non-uniformities are not included in the electromagnetic solution.

Both the features (e) and (f) could be included at the expense of program complexity.

- (g) At present, the generator is only being considered in open circuit mode. Thus the stator current bars and end connections are not modelled, and, in addition, the periodic boundary conditions on both ϕ and ψ can be accurately applied to adjacent teeth, thus only one tooth pitch is considered. On load conditions can be considered by including the model of the stator conductors and end conditions described in Section 2.

9. THE NUMERICAL SOLUTION PROCEDURE

The finite difference equations are solved in as implicit a form as possible, that is in the equations (4.2) and (4.4) only the terms on the right hand side are calculated with the values of ϕ and ψ from the old iterative solution, except for the Fourier components of the permeability.

To proceed from one solution (ϕ^n, ψ^n) the following steps are followed:

- (i) Derive the required Fourier components of the permeability components throughout the iron from the local value of the magnetic field vector and the permeability law.
- (ii) Calculate the 'source' terms (the right hand sides) of equations (4.2) and (4.4) at each nodal point.
- (iii) Determine a new solution to the magnetic potential, ϕ^{n+1} to a reasonable degree of accuracy.

(iv) Determine a new solution to the eddy current stream function ψ^{n+1} to a reasonable degree of accuracy.

The cycle (i)-(iv) is then repeated until convergence.

The iterative procedure used for steps (iii) and (iv) has been selected to be that most suited to the geometry of the region (which is relatively very thin in the circumferential direction compared to typical radial and axial distances, and this non-uniformity is even further accentuated by the anisotropic permeability), and to the boundary conditions (in particular the periodic boundary conditions which relate the values of the dependent variables at the extremities of circular arcs); namely a line iterative technique, with the implicit lines of nodal points taken as arcs of circles. The subsystems of equations comprising the pairs of algebraic equations for the two Fourier components of each variable ϕ and ψ for the nodes which lie on one such arc are solved simultaneously. This ensures that the periodic boundary conditions are satisfied exactly. An acceleration parameter is used, and new values are used as soon as they are available in all subsequent calculations. Because ϕ_{11} and ϕ_{12} do not have the same differential operator on the left hand side of equations (4.2a) and (4.2b) (the sign of the μ_{22} components are opposite in the two equations), the solution for the components of the potential requires the inversion of a nine diagonal matrix. Whereas for the stream function, we can work with the complex variable ξ and for which the inversion of a tri-diagonal matrix with the additional terms representing the periodic boundary conditions is only required.

It is difficult to optimise the iterative acceleration parameters, especially those for the potential ϕ , because of the non-linear form of the equations. Many acceleration devices are also incorporated to enhance the rate of convergence.

Typically one starts with a reasonably good initial approximation, or from the previous solution with different geometry, etc., on backing store in the computer. A subsequent solution can then be obtained in about 3 to 5 minutes on an IBM 370/168 computer. The program derives the values of ϕ and ψ at the nodal points of the grid, and these are then transferred to backing store. A second program processes these results and calculates the vector components of the magnetic field, of the magnetic flux density, of the eddy currents, and from the latter, the rate of thermal generation in the stator core can be determined. The thermal generation caused by hysteresis effects can be calculated from an empirical expression (Steel,

1974) involving the magnitude of the transverse magnetic field. A third program comprises a heat conduction calculation of the core, using the thermal generation rates previously obtained. A finer grid is used for this purpose, and, of course, radial cooling ducts, axial cooling ducts, and tooth wedges, etc., are all modelled. This program gives the temperature at up to 10000 nodal points per packet, a packet comprising those laminations between two radial cooling ducts.

10. VALIDATION OF THE NUMERICAL MODEL

A comprehensive series of investigations has been made with the programs to ensure satisfactory operation. The electromagnetic solution procedure has been used to solve several problems in which a known analytic solution was sought, for example the derivation of two dimensional (r, θ) magnetic fields in a pair of adjacent annuli with known, but different, permeabilities. Subsequently the results have been compared with measured variations on 500 MW generators on open circuit test. The results (which are to be reported elsewhere) indicate acceptably good agreement considering the simple boundary condition imposed on the rotor surface, namely zero axial field and the potential calculated to produce the necessary radial magnetic flux in the centre of the generator and assuming that all the potential is lost in the radial air gap. Typical results will not be discussed here since they also will be described elsewhere; instead some of the salient features already resulting from our investigations are described; other investigations yet to be made will be detailed. They indicate the great generality and versatility of the method, and the increased understanding which the results produce.

11. SOME RESULTS OBTAINED, INVESTIGATIONS TO FOLLOW

One of the purposes of this programme of work has been to increase our understanding of the factors determining the variations in thermal generation in large generators, and several investigations have already been made with regard to the Pistoye slot length, both radial depth and axial extent, and variations in stacking factor. The results to be described were derived for geometry typical of 500 MW generators. Only open circuit conditions have been considered, and the stator end screen has not been modelled.

It is evident, for example, from the results obtained so far that the Pistoye slot is an important feature in predicting the thermal generation rate. These subdivide the laminated area in the stator tooth, typically, into two parts in which the eddy currents can circulate. The

magnitude of these currents are therefore reduced, and the results demonstrate this. However, because the eddy currents are reduced, so the axial flux is allowed to penetrate further. (The Pistoie slots need not necessarily be in the centre of the tooth, nor need they extend radially to the base of the conductor slot, they could extend further, or less far, or they could be of varying length. However, here we only consider the simple case in which they divide the tooth into two equal parts.) At some point axially the Pistoie slots are not cut in the laminations (unless they extend the whole axial length of the machine) and at that point, if any axial flux is still present, there is bound to be an increased thermal generation because of the enlarged eddy current circulations, all other things remaining unchanged. The program can, and has, been used to estimate the magnitude of this increase for various configurations.

Test results have been obtained with different configurations of radial cooling ducts. Their effect on the electromagnetic solution has been through the stacking factor which is decreased to model the ducting arrangement; the presence of the air is thus smeared out over an axial interval. Thus the amount of core plate is reduced, and it is therefore to be expected, and this has been verified, that the thermal generation rates decrease. Temperature calculations show these effects are generally amplified since the cooling efficiency is enhanced. The inclusion of asbestos laminations carrying instrumentation in the core plate has also been demonstrated to have significant effects on the thermal generation.

These examples are just a brief illustration of the type of results which can be derived from our model.

Planned future investigations include on-load calculations, calculations with radial cooling ducts included explicitly, the effect of axial cooling ducts, stepped stator ends, end screen designs, etc. As computers increase in size and more detailed investigations are sought, it is envisaged that the program will be enlarged to incorporate many additional details.

12. ACKNOWLEDGEMENTS

The development of the work described in this paper owes much to the invaluable contributions by Dr C.J. Myerscough, Dr M.L.J. Rollason and Mr J.G. Steel, and the programming has been assisted by Mrs M.E. Down, Mrs J. Linn and Mr P. Rutter.

The work was carried out at the Central Electricity Research Laboratories and the paper is published by permission of the Central Electricity Generating Board.

13. REFERENCE

Steel, J.G., 1974, 'Soft Magnetic Materials in Large Turbo-Alternators', Trans. I.E.E.E. MAG-10 (2) pp. 151-154.

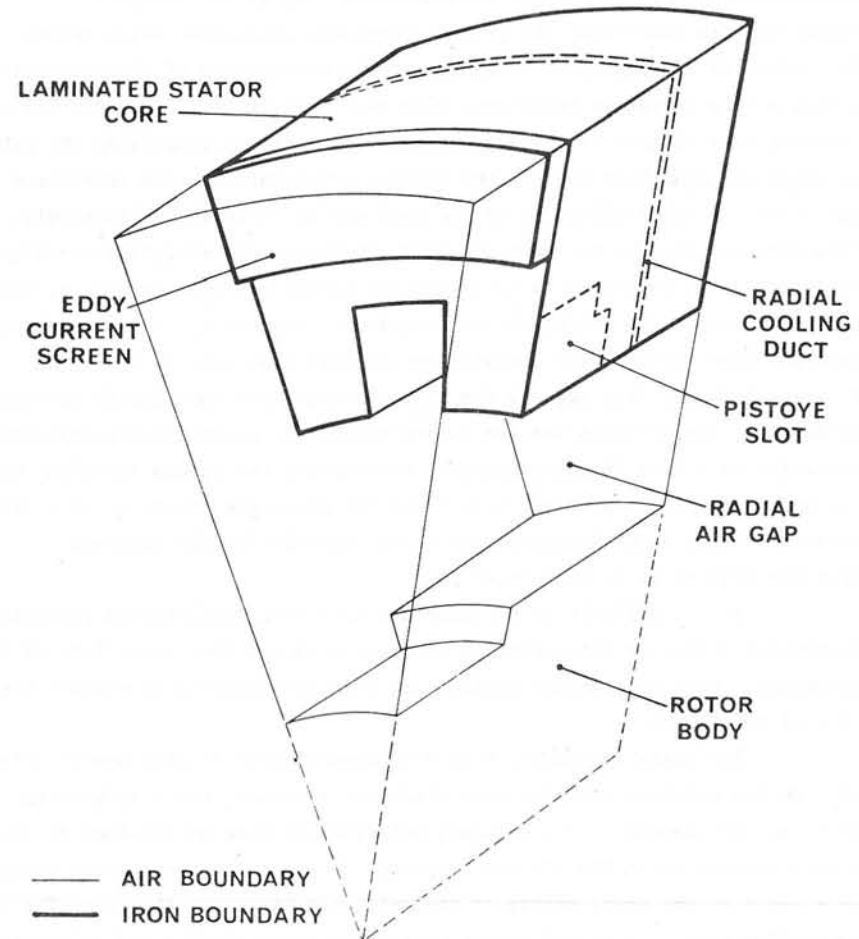


FIG1 A PERSPECTIVE VIEW OF THE REGION IN WHICH THE ELECTROMAGNETIC FIELD SOLUTION IS SOUGHT
(THE STATOR AND ROTOR CONDUCTORS ARE NOT SHOWN)

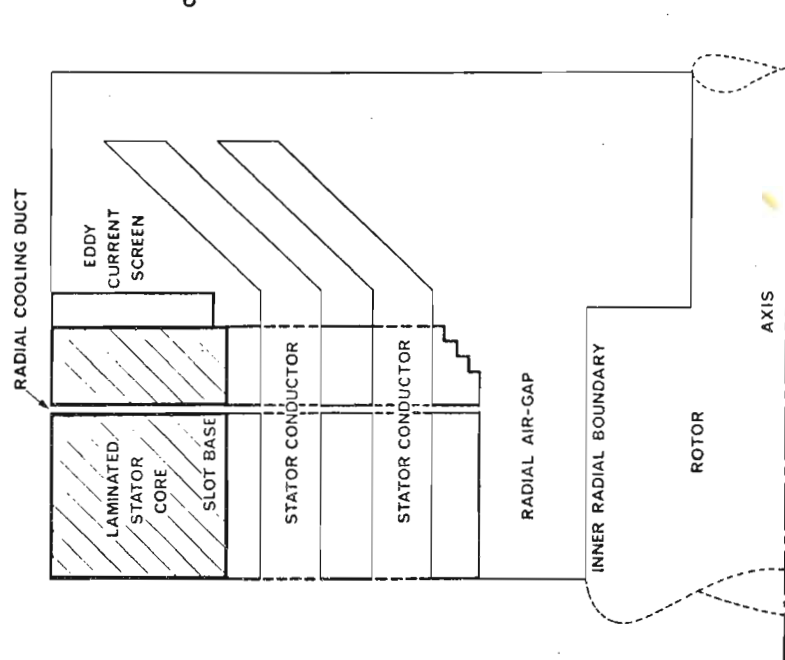


FIG 2 CROSS SECTION THROUGH THE ROTOR AXIS AND THE CENTRE OF A STATOR SLOT

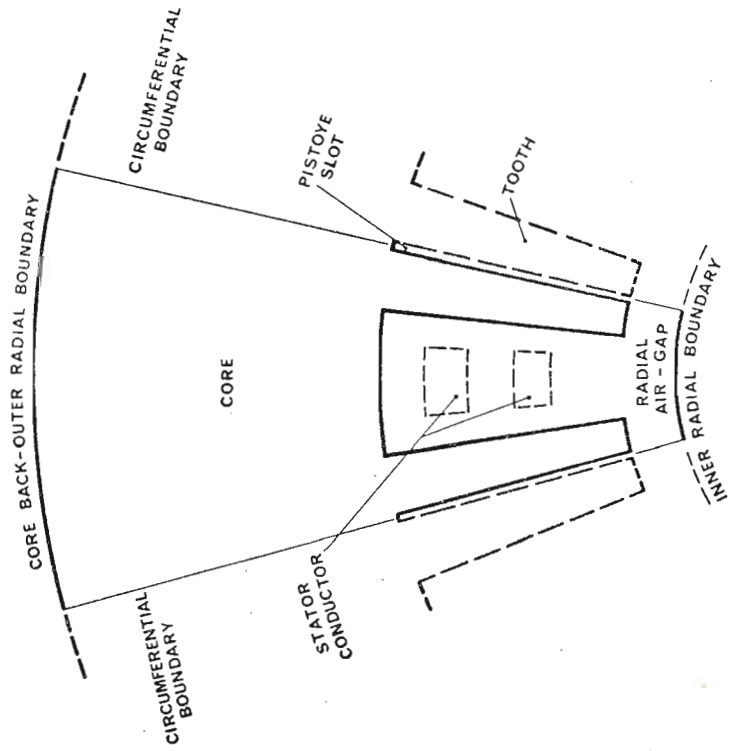


FIG 3 CROSS SECTION NORMAL TO THE ROTOR AXIS OF THE REGION CONSIDERED (THROUGH THE STATOR CORE)

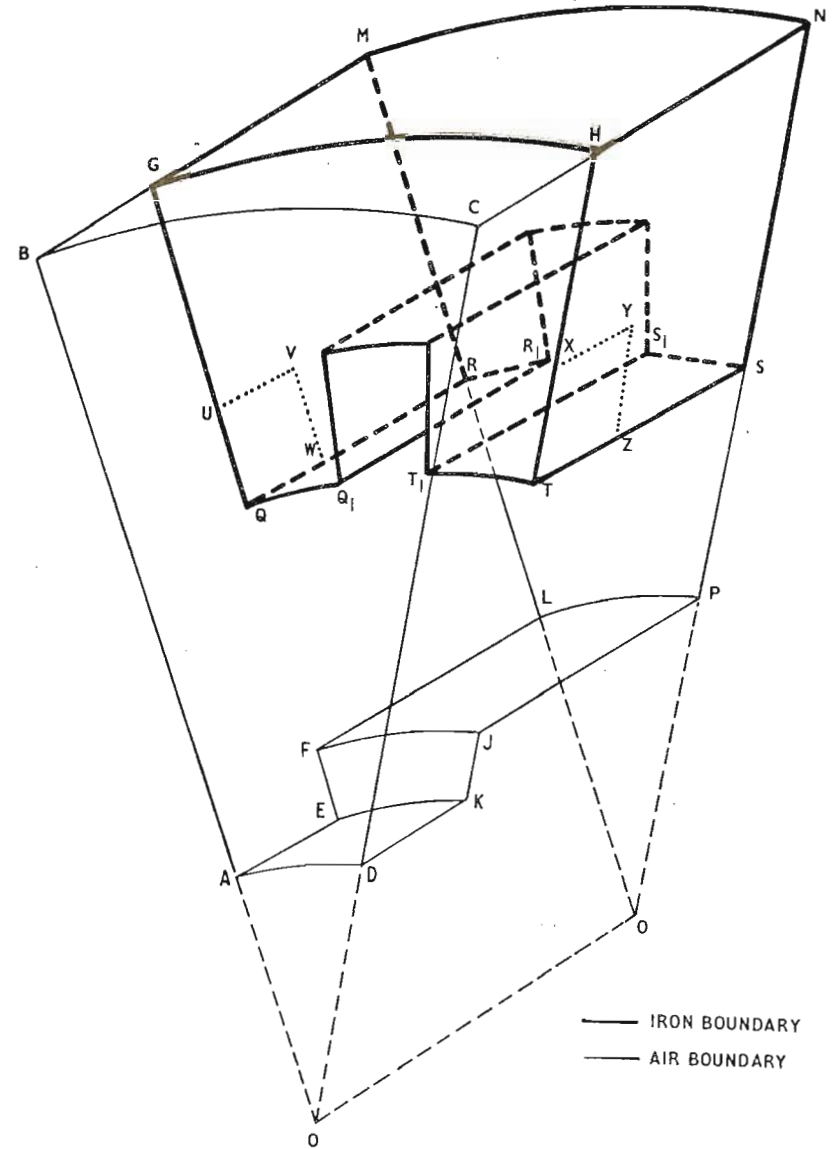


FIG. 4 REGION OF THE GENERATOR IN WHICH THE FIELD SOLUTION IS SOUGHT

Discussions following paper:

(Trowbridge) Will you comment on the use of your program for 3D conductor regions ie when there are no constraints on the direction of current flow.

(Jacobs) Such a problem would require additional dependent variables if one is going to consider eddy currents flowing in all three directions and not confined to laminations. Concerning three dimensional conductors these will be included in the next version of the program to be released which is now in an advanced stage of development. There are no inherent difficulties foreseen, and a method similar to that described by Dr Carpenter earlier is being used.

(Ratti, Univ Rome) The author has presented a nice piece of work, for which he must be congratulated.

On these two points we would like to have more detailed information:

- (a) The check of convergence is one of the various refinements spoken of by the Author, to reduce the run time: how is this check achieved and what are the benefits obtained?
- (b) The program is said to be expensive (something which is rarely recognised by research workers): can the author compare the cost with other methods and/or with the overall cost of the machine under investigation?

(Jacobs) (a) The primary initial check on the rate of convergence is based on the normalized residual and the maximum percentage charge actually applied at any point of the grid. Subsequently we compare the results from such a "well-converged" solution with one for which a further significant set of iterations have been used. As we proceed with the iteration those lines for which convergence is satisfied are not considered again for several further iterations thus saving computation. The fields, fluxes and thermal generation rates often seem to be "better" converged than the potential.

(b) Compared with typical computer programs it seems expensive; but it is not a typical program! A generator costs the order of $\pounds 10^6$ and

replacement costs for a 660 Mw machine per day are substantially more than the cost of running our IBM 370/168 computer for a day. They are therefore cheap in that sense.

(Reece, GEC) The work described assumes that the density on the rotor surface is known. When both conductors are studied, with the need to represent both stator and rotor current effects, what is the procedure proposed and what will be the effect on computation time and cost?

(Jacobs) In order to include both rotor and stator conductors, we are developing another program similar to that described by Mr Preston earlier today in which the circumferential variation is treated as a Fourier series and thereby reduce the problem to two space dimensions and time. We will ignore eddy currents in the stator initially at least, and from the imposed stator and rotor conductors and the phase difference between them we will derive the scalar potential on the rotor surface. This will be in the form of circumferential harmonics which will then be used as the boundary condition or the inner radial boundary in the three space dimensional problem.

The determination of magnetic fields in power transformers

by

P.B.Johns, M.Sc., Ph.D., C.Eng., MIEE, A.Wright, Ph.D., D.Sc., C.Eng., FIEE
and J.E.Sitch, B.A., M.Eng., Ph.D.
of the University of Nottingham.

1. Introduction

There are many situations where designers must assess the densities of magnetic and/or electric fields. As an example, it is necessary to determine the mechanical forces which may be exerted on the windings of large power transformers. These forces may reach very high levels during system fault conditions and they must be assessed with reasonable accuracy so that the windings may be braced to withstand them. Clearly the forces can be readily determined by calculating the magnetic flux densities at the positions of the individual conductors for various operating conditions.

There are a considerable number of possible numerical methods which may be used for tackling dynamic magnetic problems of this type and in particular there are several well-developed finite-difference routines for solving both transient and steady state eddy-current problems in two dimensions¹. One of the difficulties encountered, especially with transient analyses, centres around the stability of the method. The fastest finite-difference routines are those which are explicit but they are inherently unstable for large time steps. Implicit finite-difference routines, whilst stable, can require an unacceptable amount of computation.

Recently a method in which the space to be considered is assumed to contain a matrix of transmission lines (TLM method) has been developed for use in communication studies. The method is explicit and also unconditionally stable. The purpose of this paper is to describe the TLM method and show how it may be used to deal with power-frequency problems such as that referred to above.

2. Transmission line modelling of fields

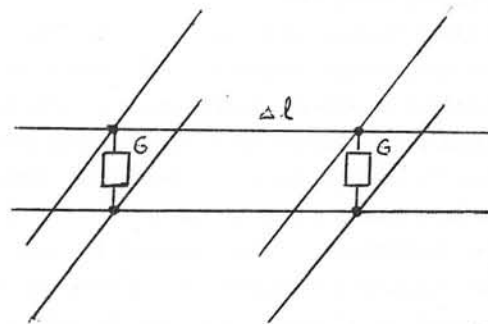
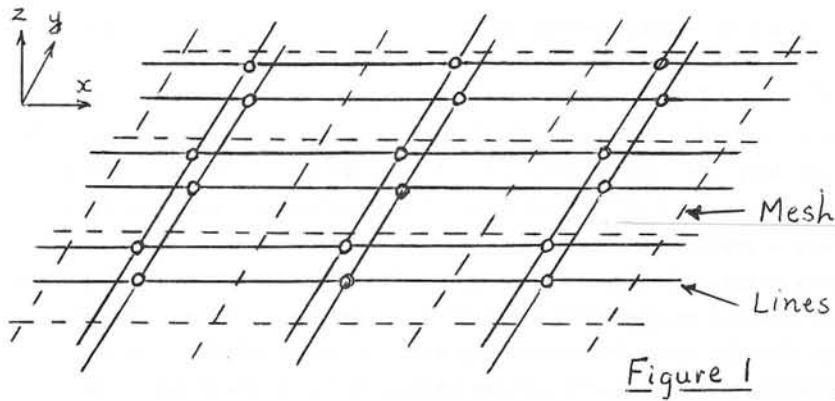
In the TLM method a region to be studied is divided into a mesh of equal-sized volumes, or areas in the case of two-dimensional problems, and a corresponding matrix of loss-free transmission lines, which are

appropriately interconnected at their junctions, is assumed to exist.

For a two-dimensional study, four transmission lines are assumed to meet at the mid-points of each of the elements in the mesh as shown in Fig.1. All lines associated with mesh elements in a particular uniform medium have the same propagation velocity and characteristic impedance, proportional to $(\mu\epsilon)^{-0.5}$ and $(\mu/\epsilon)^{0.5}$ respectively. For a medium of infinite permeability the propagation velocity would be zero and the characteristic impedance infinite, which implies that currents would not flow into any transmission lines used to represent such a region and open circuits could therefore be placed at its boundaries. This representation is clearly correct because H fields could not be set up in an infinitely permeable material.

The network of lines is excited by launching ideal delta functions (impulses) into it at appropriate points and these travel along the lines until they reach junctions or nodes. Scattering processes then take place and the scattered pulses travel on to neighbouring nodes. A numerical routine must be employed to keep track of the impulses and scattering processes in a somewhat similar manner to that which is used in the Bewley Lattice diagram when actual transmission lines are studied.

If the model was completely loss free, the pulses would not be damped and permanent oscillatory conditions would be set up. Considering the transformer problem as an example it is clear that eddy currents would flow in conducting material in the window due to the changing magnetic field and there would be a resultant power loss. Similarly any conductors forming a winding connected to a load would carry current, leading to the dissipation of power and damping. It could therefore be considered that the window space contains a lossy dielectric. Difficulties would be introduced if allowance was made for this by assuming lines with distributed conductance (G) because of the distortion of the pulses which would result. This may be overcome however if the mesh is fine enough by including lumped conductances at the junctions of the lines as shown in Fig.2. In practice the conductors and dielectric are not uniformly distributed across the window space and allowance may be made for this by including shunt conductances (G) at the appropriate nodes. In many problems the values assigned to these conductances may be made artificially high to increase the damping and accelerate the computations.



If fields set up by direct currents are to be determined then the input pulses to the model should be maintained constant and the phenomena by which the fields are set up in spaces are being correctly modelled. This process may be done in real time. When fields set up by time varying currents are to be calculated however it may be necessary to introduce time-scaling because the actual time needed to propagate a flux wave across a space will be so short relative to the period of the input signal that an extremely large number of time steps would have to be used to obtain a solution. This topic is dealt with in more detail later.

2.1. Inputs to model

To determine the magnetic fields set up when currents are driven into certain conductors, e.g. into the primary-winding conductors of a

transformer, pulses of current are injected into the appropriate elements of the mesh. The magnitude of the pulse injected into any element, at any instant, is made equal to the m.m.f. provided by the conductors in the element at the instant, i.e. the total current flowing into the element. Scattering of the pulses then proceeds as described in the next section.

2.2. Scattering process in a two dimensional space

At a node with no shunt conductance an incoming current wave on one line sees the three other lines in parallel and consequently the reflection coefficient (R) is given by :-

$$R = \frac{3Y_0 - Y_0}{3Y_0 + Y_0} = 0.5$$

where $Y_0 (= 1/Z_0)$ is the characteristic admittance of each line.

The transmission coefficient (T) to each of the three parallel output lines is :-

$$T = \frac{-2 \times 3Y_0}{3(3Y_0 + Y_0)} = -0.5$$

The above expressions are based on the convention that currents flowing towards a node are regarded as positive.

When a shunt conductance of GY_0 is present at a function the reflection and transmission coefficients are then modified to :-

$$R = \frac{Y_0(3 + G) - Y_0}{Y_0(3 + G) + Y_0} = \frac{2 + G}{4 + G}$$

$$\text{and } T = \frac{-2Y_0}{Y_0(3 + G) + Y_0} = \frac{-2}{4 + G}$$

If the conductors in the window are connected to an external source or load the currents flowing in them depend on external factors as well as the material parameters. The type of node used in this case has a current generator connected across the junction as shown in Fig.3. Any shunt conductance is effectively in series with the current source and may therefore be ignored in the scattering equations. The resulting outgoing waves ($b_1 \rightarrow b_4$) are given by expressions of the form

$$b_1 = Ra_1 + Ta_2 + Ta_3 + Ta_4 - \frac{I}{4}$$

$$b_2 = Ta_1 + Ra_2 + Ta_3 + Ta_4 - \frac{I}{4}$$

in which $a_1 \rightarrow a_4$ are the incoming waves to the node.

It is shown in Appendix 1 that the above procedure accurately models Maxwell's equations.

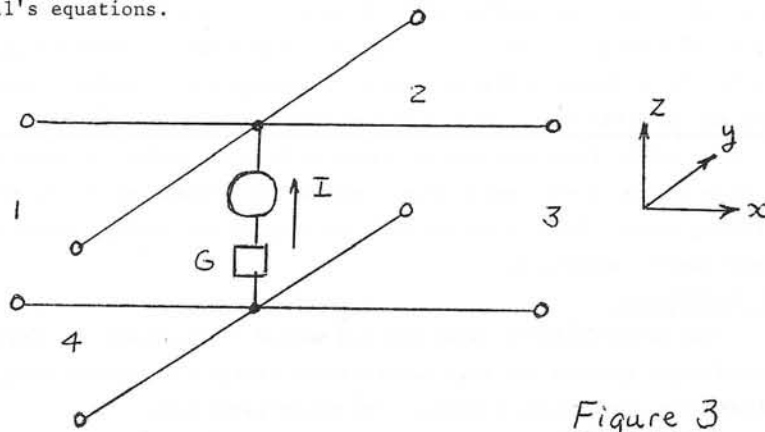


Figure 3

2.3. Time scaling

When dealing with direct current conditions it is possible as in microwave studies to calculate in real time. When solving behaviour obtained with power-frequency inputs however, the number of time steps involved would be excessive. This can readily be seen from the following illustration. For a mesh with 1 cm centres the time steps would have to be $(3 \times 10^{10})^{-1}$ s assuming propagation to be at the velocity of light and to calculate 40 ms of real time, i.e. 2 cycles, would require 1.2×10^9 steps.

This situation can be avoided by assuming high values of permeability and permittivity for the medium and thus artificially reducing the propagation velocity. To keep the levels of the travelling waves of current and voltage unchanged the characteristic impedance, which is proportional to $(\mu/\epsilon)^{0.5}$, should be maintained constant. It will be seen therefore that if μ and ϵ are multiplied by the same factor k , time steps may be increased by the same factor.

It must be realised that this change has the effect of increasing the displacement currents in steady state because of the increased shunt capacitances of the transmission lines and as a result they do not bear the correct relationships to the conduction currents. In practice however the displacement currents in power-frequency problems are extremely small relative to the conduction currents and they can be increased by several orders of magnitude without becoming sufficiently

large relative to the conduction currents to cause significant errors in computing magnetic field distributions. An indication of these effects is given in the later sections dealing with actual calculated values.

3. Power transformer studies

While the TLM method can be applied to three-dimensional problems initial studies of power transformer magnetic fields have been done on a two-dimensional basis. It was assumed that the transformer had an infinitely permeable core surrounding a rectangular window through which the conductors of the primary and secondary windings passed. It was thus necessary to divide the window area into a mesh of square elements with transmission lines between their centres. At the boundary of the window the lines were terminated in open circuits.

In practice one of the windings may be tapped to allow the transformation ratios to be varied and in these circumstances some of the conductors might not be carrying current at particular times. To allow complete generality the model was therefore arranged with input impulse currents at each of the nodes where primary winding conductors are present. At any instant each of these currents is made equal to the ampere conductors (ampere turns) present in the particular element of the mesh. As stated earlier each of the secondary winding conductors must carry the same current because of the series connection of the turns. This result would not be obtained by connecting equal conductances across each of the nodes at the positions of the secondary winding conductors, because of the different voltages which appear across the nodes. In the model therefore it is necessary to include a path at each of these nodes through which flows a current equal to the product of the sum of the voltages across the nodes and the conductance of the secondary winding and load. In addition, conductances may be included in parallel with these current paths to allow for eddy currents within the conductors.

The computation proceeds by injecting the appropriate current impulses at each particular time step and taking account of the currents present because of the impulses injected at earlier time steps. In this way the complete current pattern is determined for each time step and the program runs until the changes over a time step are below a particular level in the case of d.c. problems or until repetitive behaviour is obtained in a.c. steady-state studies.

3.1. D.C. Magnetic field calculations

In these examples, time only enters into the problem as a means of proceeding to a solution; although the time taken to reach a steady state may be of some interest to designers of pulse-transformers, the time scaling in these examples has been chosen to ensure the fastest possible convergence rather than accurate modelling of transients. All the results shown here are in windows in an infinitely permeable medium. The first example is of a situation where the individual conductors are smaller in cross section than the mesh size, consequently the current in each element is easily defined. Tables 1, 2 and 3 show the current density and H-field profiles for this model. Part of the "primary" is unexcited to simulate the effect of using a tapped winding. We may check the results by integrating $H \cdot dl$ along rectangular paths, this indicates errors of less than 0.5%, due to incomplete convergence. In this model mesh size is not fixed by any external consideration, the current density is in units of $A/\Delta l^2$ and $H \cdot \Delta l$ is printed out for the H-field, this easy spatial scaling only applies to D.C. models. The second example is a window with comparatively large conductors. The primary winding is driven from a voltage source and the secondary drives a resistive load. In the steady D.C. state the current density is constant across the conductor; the results presented below Tables 4, 5 and 6 were obtained after 300 iterations, the solution is within 1% of its steady value after 200 iterations.

3.2. Transient calculations

These are very similar to the D.C. computations with the exception that the time evolution of the solution is now of interest. Tables 7 and 8 show the build-up of H-field in a window filled with short-circuited windings. The units of time are seconds for a mesh size of 0.1 m.

The tables are drawn for different time scalings table 7 has c "slowed down" to $0.0707 \text{ m sec}^{-1}$ while in table 8 the modified propagation velocity is 0.707 m sec^{-1} . The agreement between the results shows that if the problem is correctly specified the use of time scaling can result in economical transient models.

3.3. A.C. models

To date A.C. modelling has been restricted to the time domain, although steady-state modelling is also possible. The primary voltage is input as a function of time and the primary and secondary currents, and

secondary voltage are found as functions of time. If the time-scaling is done correctly, the displacement current may be kept to a small fraction of the conduction current, and although this means the transmission line matrix is no longer critically damped, convergence to within a few percent is achieved in about 500 time steps for the 9×9 element model.

The leakage reactance may be computed from the model, it increases in size relative to the copper resistance as the inverse of the velocity scaling ratio. Thus it is possible to compute the leakage reactance under fault conditions.

4. Conclusions

The feasibility of using the TLM method to calculate the fields in transformer windows has been demonstrated by the preliminary results which have been obtained using a two-dimensional mesh.

The method models the way in which the fields build up and steady-state behaviour is approached through the transient conditions. Although time scaling is necessary in dealing with power-frequency problems it has been shown that this may be done with acceptable accuracy and the method provides an explicit and unconditionally stable routine. This is thought to be unique and of considerable importance.

The method may be extended to deal with non-uniform media and three-dimensional meshes.

5. Acknowledgements

Dr. Johns is spending a year on sabbatical leave at the University of Manitoba. He wishes to thank Dr. A. Wexler for the many interesting discussions on this and like topics, and the Department of Electrical Engineering for their hospitality.

Thanks are also due to Dr. S. Akhtarzad of the University of Nottingham for helpful comments on this paper and to the University of Nottingham for facilities made available during its preparation.

6. References

1. R. L. Stoll, 'The analysis of eddy currents', Clarendon Press, Oxford, 1974.
2. M. Djurovic and C. J. Carpenter, '3-dimensional computation of transformer leakage fields and associated losses', Trans. I.E.E.E., Mag-11, 5, p.1535-1537, September 1975.
3. S. Akhtarzad and P. B. Johns, 'Three-dimensional TLM computer analysis of microstrip resonators', Trans. I.E.E.E., MTT-23, 12, p.990-997, December 1975.

4. C. J. Carpenter and M. Djurovic, 'Three-dimensional numerical solution of eddy currents in thin plates', Proc. IEE, Vol.122, No.6, p.681-688, June 1975.
5. S. Akhtarzad and P. B. Johns, 'Generalised elements for the TLM method of numerical analysis', Proc. IEE, Vol.122, No.12, p.1349-1352, December 1975.
6. P. B. Johns, 'The solution of inhomogeneous waveguide problems using a transmission-line matrix, Trans IEEE, MTT-22, 3, p.209-215, March 1974.
7. S. Akhtarzad and P. B. Johns, 'The solution of Maxwell's equations in three space dimensions and time by the TLM method of numerical analysis', Proc. IEE, Vol.122, No.12, p.1344-1348, December 1975.
8. G. F. Slater, 'The use of finite transmission-line elements in numerical analysis', Ph.D. thesis, Nottingham University, 1973.

7. Appendices

Appendix 1. Modelling Equations

Consider an element, such as the one shown in Fig.A.1.

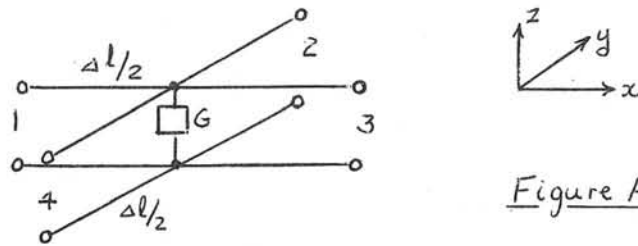


Figure A1

The incident current wave at port 1 is denoted by $a_1(t)$, while the scattered wave is $b_1(t)$. The voltage across the junction may be expressed in terms of the ingoing waves :-

$$V_c(t + \frac{\tau}{2}) = (a_1(t) + a_2(t) + a_3(t) + a_4(t)) \cdot T \cdot Z$$

where $\tau = \frac{\Delta l}{v}$, the time step.

It may also be expressed as a function of the outgoing waves

$$V_c(t = \frac{\tau}{2}) = -(b_1(t) + b_2(t) + b_3(t) + b_4(t)) \frac{T}{R+3T} \cdot Z$$

Now

$$\frac{T}{R+3T} = \frac{2}{4-G}$$

These two equations may be combined to give :-

$$2(V_c(t + \frac{\tau}{2}) - V_c(t - \frac{\tau}{2})) + \frac{G}{2} (V_c(t + \frac{\tau}{2}) + V_c(t - \frac{\tau}{2})) = (a_1(t) + b_1(t) + a_2(t) + b_2(t) + a_3(t) + b_3(t) + a_4(t) + b_4(t))Z$$

This simplifies to

$$2\tau \frac{\partial V_c(t)}{\partial t} + G V_c(t) = Z \Delta l \left(-\frac{\partial I_x}{\partial x} - \frac{\partial I_y}{\partial y} \right)$$

$$\frac{2}{vZ} \frac{\partial V_c}{\partial t} + \frac{G}{\Delta l Z} V_c = -\frac{\partial I_x}{\partial x} - \frac{\partial I_y}{\partial y}$$

So setting

$$\frac{2}{vZ} \equiv \epsilon, \quad \frac{G}{\Delta l \cdot Z} \equiv \sigma, \quad V_c \equiv E_z / \Delta z, \quad I_x \equiv H_y \cdot \Delta l, \quad I_y \equiv -H_x \cdot \Delta l$$

where $\Delta x = \Delta y = \Delta l$, the space step and $\Delta z = 1m$, we obtain the magnetic circuit law assuming no external electric sources or sinks.

At a point where there is a conductor connected to an external circuit the node has a current generator connected across it, and the following equations apply :-

$$V_c(t + \frac{\tau}{2}) = (\frac{1}{2}(a_1(t) + a_2(t) + a_3(t) + a_4(t)) + \frac{I}{4}(t - \frac{\tau}{2}))Z$$

$$V_c(t - \frac{\tau}{2}) = -(\frac{1}{2}(b_1(t) + b_2(t) + b_3(t) + b_4(t)) + \frac{I}{4}(t - \frac{\tau}{2}))Z$$

$$\frac{2}{vZ} \frac{\partial V_c}{\partial t} - \frac{I}{\Delta l} = -\frac{\partial I_x}{\partial x} - \frac{\partial I_y}{\partial y}$$

So we may set $-\frac{I}{\Delta l} \equiv J_z$ to obtain the general magnetic circuit law.

Similarly we may compute the currents at an intersection

$$I_x(t + \frac{\tau}{2}) = \frac{1}{2}(a_1(t) + b_1(t + \tau) - a_3(t) - b_3(t + \tau))$$

Substituting for the reflected waves $(1 + T - R = 2)$:-

$$I_x(t = \frac{\tau}{2}) = (a_1(t) - a_3(t))$$

Also

$$I_x(t - \frac{\tau}{2}) = (-b_1(t) + b_3(t))$$

Using central differences we may combine these two equations to yield :-

$$(I_x(t - \frac{T}{2}) - I_x(t + \frac{T}{2})) = (a_3(t) - b_3(t)) - (a_1(t) - b_1(t))$$

$$- \frac{\partial I_x}{\partial t} \cdot \frac{Z}{v} = \frac{\partial V}{\partial x}$$

So with the same equivalents as before and with $\frac{Z}{v} \equiv \mu$, we get the law of electromagnetic induction.

Combining our equations together we may obtain expressions for the characteristic impedance and velocity of propagation of the transmission lines in the matrix in terms of the characteristic impedance of the medium and the velocity of electromagnetic propagation within the medium

$$Z = \sqrt{2} Z_0 = \sqrt{\frac{2\mu}{\epsilon}}$$

$$v = \sqrt{2} c = \sqrt{\frac{2}{\mu\epsilon}}$$

Appendix 2. Time scaling

We wish to keep the magnetic relaxation time ($\tau_m = \sigma \cdot \mu$) constant, but vary σ and μ to reduce the propagation velocity. Denoting time-scaled quantities by a prime we may write :-

$$\tau_m = \sigma \cdot \mu = \sigma' \cdot \mu'$$

$$\mu' = \mu \left(\frac{c}{c'}\right)^2, \quad \sigma' = \sigma \left(\frac{c'}{c}\right)^2$$

$$Z_0' = Z_0 \frac{c}{c'}$$

Now we require $\sigma' \gg \omega\epsilon$ which means $c' \gg \sqrt{\frac{\omega\epsilon}{\sigma}} \cdot c$

For copper ($\omega = 2\pi \cdot 50$ radians sec^{-1} , $\epsilon = \epsilon_0$, $\sigma = 5.8 \times 10^7 \text{ S m}^{-1}$, $c = 3 \times 10^8 \text{ m sec}^{-1}$) we obtain

$$c' \gg 2.07 \text{ m sec}^{-1}.$$

Table 1. Jz

1.0	1.0	1.0	1.0	-0.733	-0.733	-0.733	-0.733	-0.733
1.0	1.0	1.0	1.0	-0.733	-0.733	-0.733	-0.733	-0.733
1.0	1.0	1.0	1.0	-0.733	-0.733	-0.733	-0.733	-0.733
1.0	1.0	1.0	1.0	-0.733	-0.733	-0.733	-0.733	-0.733
1.0	1.0	1.0	1.0	-0.733	-0.733	-0.733	-0.733	-0.733
1.0	1.0	1.0	1.0	-0.733	-0.733	-0.733	-0.733	-0.733
1.0	1.0	1.0	0	-0.733	-0.733	-0.733	-0.733	-0.733
1.0	1.0	1.0	0	-0.733	-0.733	-0.733	-0.733	-0.733
1.0	1.0	1.0	0	-0.733	-0.733	-0.733	-0.733	-0.733

Table 4. Jz

0	0	0	0	0	0	0	0	0
0	3.339	3.339	3.339	0	-3.339	-3.339	-3.339	0
0	3.339	3.339	3.339	0	-3.339	-3.339	-3.339	0
0	3.339	3.339	3.339	0	-3.339	-3.339	-3.339	0
0	0	0	0	0	0	0	0	0
0	3.339	3.339	3.339	0	-3.339	-3.339	-3.339	0
0	3.339	3.339	3.339	0	-3.339	-3.339	-3.339	0
0	3.339	3.339	3.339	0	-3.339	-3.339	-3.339	0
0	0	0	0	0	0	0	0	0

Table 2. Hx

--023	--023	--023	--022	--020	--018	--016	--014	--013
--064	--065	--066	--066	--061	--054	--047	--042	--039
--101	--105	--111	--112	--103	--090	--077	--067	--062
--137	--147	--161	--170	--151	--126	--103	--087	--079
--167	--185	--220	--255	--207	--158	--122	--100	--089
--176	--206	--276	--425	--263	--177	--128	--100	--088
--153	--183	--253	--402	--242	--159	--112	--086	--075
--103	--120	--154	--190	--146	--104	--075	--058	--050
--036	--042	--051	--058	--048	--036	--026	--020	--018

Table 5. Hx

.349	.809	.881	.698	0	--698	--881	--809	--349
.585	1.145	1.226	.941	0	--941	-1.226	-1.145	--585
-263	.289	.268	.170	0	--170	--268	--289	--263
--0855	--520	--612	--528	0	.528	.612	.520	.0855
0	0	0	0	0	0	0	0	0
.0855	.520	.612	.528	0	--528	--612	--520	--0855
--263	--289	--268	--170	0	.170	.268	.289	.263
--585	-1.145	-1.226	--941	0	.941	1.226	1.145	.585
--349	--809	.881	--698	0	.698	.881	.809	.349

Table 3. Hy

--479	-1.437	-2.394	-3.351	-3.443	-2.671	-1.904	-1.141	--380
--479	-1.437	-2.393	-3.348	-3.438	-2.667	-1.900	-1.138	--379
--480	-1.440	-2.394	-3.345	-3.431	-2.657	-1.892	-1.133	--377
--483	-1.447	-2.400	-3.341	-3.416	-2.640	-1.877	-1.123	--374
--490	-1.463	-2.418	-3.335	-3.387	-2.609	-1.853	-1.109	--369
--502	-1.500	-2.470	-3.328	-3.319	-2.555	-1.819	-1.090	--363
--519	-1.564	-2.636	-3.322	-3.139	-2.474	-1.777	-1.069	--357
--531	-1.599	-2.680	-3.317	-3.075	-2.425	-1.747	-1.053	--352
--536	-1.614	-2.706	-3.314	-3.053	-2.403	-1.731	-1.044	--349

Table 6. Hy

--349	-1.506	-3.195	-4.774	-5.472	-4.774	-3.195	-1.506	--349
.112	--974	-3.306	-5.655	-6.869	-5.655	-3.306	--974	4.112
.211	--865	-3.399	-6.000	-7.354	-6.000	-3.399	--865	.211
.138	--968	-3.424	-5.923	-7.210	-5.923	-3.424	--968	.138
--223	-1.392	-3.407	-5.388	-6.299	-5.388	-3.407	-1.392	--223
.138	--968	-3.424	-5.923	-7.210	-5.923	-3.424	--968	.138
.211	--865	-3.399	-6.000	-7.354	-6.000	-3.399	--865	.211
.112	--974	-3.306	-5.655	-6.869	-5.655	-3.306	--974	.112
--349	-1.506	-3.195	-4.774	-5.472	-4.774	-3.195	-1.506	--349

Time	<u>Table 7</u>				
	1	2	<u>Node</u> 3	4	5
5	-9.30	3.78	20.27	9.37	5.38
10	-8.57	8.04	26.63	17.43	15.47
15	-7.97	9.83	29.61	21.68	18.84
20	-7.57	10.41	29.80	22.10	20.12
25	-7.58	10.52	30.0	22.17	20.20

Time	<u>Table 8</u>				
	1	2	<u>Node</u> 3	4	5
5	-9.18	5.86	22.83	13.20	10.16
10	-8.35	8.24	26.54	17.87	15.34
15	-7.97	9.34	28.26	20.03	17.73
20	-7.79	9.87	29.09	21.07	18.90
25	-7.70	10.14	29.50	21.59	19.46

THE COMPUTATION OF EDDY CURRENT LOSSES IN SOLID IRON
UNDER VARIOUS SURFACE CONDITIONS

Dr. D.A. Lowther* and E.A. Wyatt*

Abstract

The paper compares the computation of eddy current losses by different methods. The rectangular B-H curve approximation is used to study the effects of sinusoidal and non-sinusoidal surface electric and magnetic fields.

The non sinusoidal form is convenient both for external field calculations and the analysis of experimental data. The Frohlich curve approach is examined under similar conditions of non-sinusoidal surface H. The extension of both methods to two-dimensions is examined.

1) Introduction

The severe heating problems which can occur in large transformers and turbo-alternators have given rise to the need for an accurate prediction of the power losses. This requires a detailed description of the field distribution both inside, and external to, the core.

The problem may be conveniently divided into two parts in order to simplify the calculations. The first part involves predicting the loss distribution inside a magnetically non-linear core for a given surface field distribution. The second is to find a simple model which allows the calculation of the exterior field, avoiding complex interface conditions.

*Department of Electrical Engineering,
Imperial College of Science and Technology,
London. S.W. 7

At the levels of magnetisation encountered in these applications the hysteresis loss is negligible and the eddy current loss is the major component. The purpose of this paper is to compare different methods of computing the losses in a non-linear medium. The resultant solutions may be expressed in terms of surface impedance. This concept is useful for comparing the various methods and can be used in the computation of the external field.

Two different approaches have been used in the published work. These may be classed according to the way in which the magnetisation characteristic is represented. In the simpler, and historically earlier method described by MacLean, Agarwal et al (references 1-6) a rectangular approximation to the characteristic is used. This leads to an algebraic solution in one-dimension and can give a useful indication of the behaviour of the field inside the material.

The more complex method employs a more realistic representation of the magnetisation characteristic and uses time stepping techniques (references 7-12). This method has become popular as large computers have become available and it gives the field distribution in the material accurately.

Because many electromagnetic devices operate under "current forced" conditions, attention has been restricted to the boundary condition of sinusoidal surface H in most of the published analyses. However, this can be considered as a limiting condition; the other limit being that of sinusoidal surface E (or total flux). Because, in practice, the surface conditions may vary between the two extremes and are, in general, non-sinusoidal, the analysis in this paper deals mainly with the sinusoidal surface E situation. In addition, the analysis is extended to include surface waveforms which are non-sinusoidal in time. This is useful as far as comparisons with experimental results are concerned.

In regions in which the non-linear medium is subject to a high level of incident normal flux, which turns along the surface after entering,

a two-dimensional analysis is required. Such an analysis will be considered briefly.

2) The Finite Difference Model

The finite difference model is taken to include all those models using time-stepping techniques (references 7-12) and in this approach the magnetisation curve may be represented by a single function or, alternatively, the actual curve may be stored at discrete points and curve fitting employed. Many different finite difference schemes have been employed. Examples include the Crank-Nicolson⁹ and DuFort-Frankel techniques⁷. In practice both the E and H surface waveforms are non-sinusoidal in time.

2.1) The Sinusoidal Surface E Analysis

When the sinusoidal surface E condition is imposed a difficulty arises which is not present if the sinusoidal surface H solution is sought. The difficulty is that the non-linearity considered is magnetic and thus concerns the relationship between B and H rather than E and J. The method used here is similar to that described by Lim and Hammond⁷ who used a DuFort-Frankel time-stepping scheme in conjunction with a Frohlich magnetisation characteristic.

If the material conductivity, σ , is assumed constant and the permeability is a function of B as well as the spatial coordinates, the following governing equation for E may be derived from Maxwell's Equations used in conjunction with the constitutive relations;

$$\nabla^2 \underline{E} = \frac{\partial}{\partial t} (\text{curl } \underline{\mu H}) \quad (1)$$

which can be further modified to give

$$\nabla^2 \underline{E} = \frac{\partial}{\partial t} (\mu \sigma \underline{E} - \underline{H} \times \text{grad } \mu) \quad (2)$$

If (2) is applied in conjunction with

$$\text{div } \underline{B} = 0 \quad (3)$$

all of Maxwell's equations are satisfied.

A convenient experimental model of the one-dimensional diffusion problem is a steel rod of circular cross-section subject to sinusoidal surface conditions. It is thus appropriate to consider the circular cylindrical coordinate form of equation (2) which is:

$$\frac{1}{r} \frac{\partial}{\partial r} \left(r \frac{\partial E}{\partial r} \right) = \frac{\partial}{\partial t} (\mu \sigma E_z + H_\theta \frac{\partial \mu}{\partial r}) \quad (4)$$

The subscripts may be dropped because there is only one component of E and one of H. Equations (2) and (4), however, require that the time derivative of the permeability be known and this is an inconvenience.

A simpler equation can be obtained from equation (1) by substituting \underline{B} for $\underline{\mu H}$ and noting that

$$\frac{\partial B}{\partial r} = \frac{dB}{dH} \frac{\partial H}{\partial r}$$

The equivalent form of equation (4) is then;

$$\frac{1}{r} \frac{\partial}{\partial r} \left(r \frac{\partial E}{\partial r} \right) = \sigma \frac{dB}{dH} \frac{\partial E}{\partial t} \quad (5)$$

from which the following finite difference equation may be derived using central differences:

$$E(i, j+1) = Q(E(i, j-1) (\beta r (\Delta r)^2 2r \Delta t) + \Delta t E(i+1, j) (2r + \Delta r) + E(i-1, j) (2r - \Delta r)) \quad (5a)$$

where

$$\beta = \sigma \frac{dB}{dH}, \quad Q = \frac{1}{r(2\Delta t + \beta(\Delta r)^2)}$$

The relationship between B and H is defined by the Frohlich curve:

$$B = \frac{H}{a+b|H|}$$

in which H and B are in the same direction.

At each step the H distribution must be calculated from that of E so that the magnetisation curve can be used. Because $\text{curl } \underline{H} = \underline{J}$

$$E = \frac{1}{r} \frac{\partial (rH)}{\partial r} \quad (7)$$

and integration with respect to r yields

$$H = \frac{\sigma}{r} \int_0^r r E dr \quad (8)$$

With this modification the calculation of the field distribution follows the method of Lim and Hammond⁷, using the DuFort-Frankel time-stepping scheme.

2.2) Surface Impedance.

From the solution, the fundamental components of the field vectors at the surface can be obtained by harmonic analysis. If either E or H is sinusoidal at the surface, the total power loss in the material may be determined by applying the Poynting Vector to their fundamental components. This loss can be regarded as occurring in the real part of a complex surface impedance. The quadrature component of the impedance may be used to describe the reactive volt-amp absorption. This surface impedance can then be used to terminate the exterior network.

The concept of a surface impedance is useful as a basis for comparison of methods and as a check against experimental results.

3) The Approximate Model

The approximate model in which the magnetisation curve is represented by a rectangular characteristic has been described by several authors (references 1-6). It restricts the flux penetration to a surface layer in which the material is saturated either one way or the other; the switching point between the two magnetisation directions defining a wavefront. An algebraic expression is obtained for the E and H waveforms.

As with the finite difference methods, much of the published literature considers the sinusoidal surface H condition. The following analysis considers the condition of sinusoidal surface E (as in the preceding section) and, in addition, the analysis is extended to include the non-sinusoidal surface fields.

3.1) Sinusoidal Surface E

Using a modified form of Maxwell's equations and the co-ordinate system of figure 2, the field at a distance x from the surface is given by:

$$\frac{H}{x} = \sigma E \quad (9)$$

$$\text{and } E = \frac{2Bdx}{dt} = E_0 \sin \omega t \quad (10)$$

After integration these equations give a wavefront depth of

$$x = \frac{E_0}{2\omega B_0} (1 - \cos \omega t) \quad (11)$$

and the solution for H is

$$H = \frac{\sigma E_0^2}{\omega B_0} \sin \omega t \sin^2 \frac{\omega t}{2} \quad (12)$$

As in the finite difference method the resultant solutions for the surface values of E and H may be harmonically analysed. If either waveform is purely sinusoidal, the loss may be obtained from the fundamental components by Fourier analysis. The fundamental component of H is:

$$H = H' (-4 \cos \omega t + 3\pi \sin \omega t) \quad (13)$$

where H' is defined in equation (A.1) of the appendix. If E = E, i.e. is purely real

$$H = H' (3\pi - 4j) \quad (14)$$

Again a surface impedance may be used to describe the resistive and reactive components of the total volt-amps. If this impedance is considered to consist of series components, their values are given by

equation (A.2). The impedance shows the power factor to be 0.9206 so that the phase angle is 23° . This result may be compared with that for the sinusoidal H condition given by McConnell⁴ and Agarwal⁵. In the latter case the impedance is that given in equation (A.3) and the power factor is 0.8944 giving a phase angle of 26.6° .

These two solutions can be compared on a basis of the same peak value of the fundamental component of E and the ratio of the magnitudes of the two impedances is then

$$|Z_{se}| / |Z_{sh}| = 2.04745 \quad (15)$$

This indicates that the power loss for the condition of sinusoidal surface E is double that for sinusoidal surface H. This point is confirmed by the finite difference solutions.

3.2) Non-sinusoidal Surface Fields

The above approach allows a further generalisation to include non-sinusoidal surface excitations by expressing the surface waveforms in Fourier series form.

The derivation described below is in terms of H although the treatment for E follows a similar procedure.

If the surface H distribution is given by

$$H = H_{1s} \sin \omega t + H_{1c} \cos \omega t + H_{3s} \sin 3\omega t + H_{3c} \cos 3\omega t + \dots \quad (16)$$

and equation (10) is modified to become

$$\frac{H}{x} = 2\sigma B_0 \frac{dx}{dt} \quad (17)$$

the resultant equation for the depth of penetration any time, E, is given by

$$x = \sqrt{\frac{2}{\omega\sigma B_0}} H^{1/2} \quad (18)$$

where H is defined by equation (A.7) of the appendix. The solution for E is then

$$E = \sqrt{\frac{\omega B_0}{2\sigma}} \frac{H}{H^{1/2}} \quad (19)$$

Equation (18) assumes that $x = 0$, and hence $H = 0$, at time $t = 0$ so that the time origin has to be displaced to the point at which $H = 0$.

As before, a harmonic analysis can be used to yield a surface impedance, although the impedance now has harmonic components so that the surface layer must include a series of harmonic generators.

Agarwal⁵ has modified the saturation flux density by a factor of 0.75 so as to predict the loss (but not the VAR's) accurately when the surface H is sinusoidal. This factor has been shown to be dependant on the magnetisation level¹³. In the sinusoidal surface E condition a similar approach can be employed to model the loss accurately.

The advantage of the rectangular magnetisation characteristic lies in the simplicity with which the surface impedance may be derived. The approximation is satisfactory at the large values of surface magnetisation which occur in many problems of interest.

4) Results

The results in figures 3 to 6 show the E and H waveforms predicted for a specific B - H curve for sinusoidal surface E and H. As can be seen, the waveforms are similar in form for both methods and as the magnetisation level is increased the similarity increases. The effect is shown more clearly in the surface impedance results.

The method of section 2 can be adapted so that a finite final slope is included on the B - H curve but the effect is small, as has been noted elsewhere⁶. It would seem that the difference between the approximate and finite difference methods is largely due to the fact that the finite difference solution allows for the initial slope in the B - H characteristic.

The extra loss caused by assuming a step change in flux density requires a reduction in the saturation flux density to obtain accurate predictions.

This result suggests that a modification of the rectangular curve to one having a finite initial slope would improve the agreement between the two methods considerably.

5) Extensions To Two-dimensions

Both methods may be extended to give field solutions in two dimensions, as is necessary when the flux density normal to the surface is large. This condition is commonly met in practice in the end region of a turbo-alternator or around a transformer leg.

The finite difference approach in two-dimensions may be formulated in terms of magnetic vector potential, A , which has only one component. This function was chosen because it is often employed in two-dimensional linear eddy-current problems.

The governing equation for A is

$$\nabla^2 A_z = \mu \sigma \left[\frac{\partial A_z}{\partial t} + \frac{\partial V}{\partial z} \right] - \left[\frac{\partial A}{\partial x} z \frac{\partial 1/\mu}{\partial x} - \frac{\partial A}{\partial y} z \frac{\partial 1/\mu}{\partial y} \right] \quad (20)$$

which may be approximated by a nodal (DuFort-Frankel) finite difference method. Care is needed in the treatment of interface conditions which include restrictions both on μ and the normal gradient of A .

The approximate approach may also be adapted to two-dimensions although the wavefront, which is the key to the algebraic treatment of the one-dimensional problem, no longer becomes as clearly defined since the angle through which the magnetisation vector switches is not necessarily 180 degrees. The evaluation of H is complicated by the variation of the current density within the saturated region. The solution is still of the surface layer type and is only applicable to high magnetisation level problems.

Two-dimensional calculations using these two approaches are being made and it is hoped to publish the results at a later date.

6) Conclusions

The foregoing analyses have shown that the most commonly used methods of treating non-linearity can be adapted to allow for any specified surface E or H time variation. A comparison between the results for sinusoidal H and E (the two limits) indicates a region within which the practical condition must occur. The methods have concentrated on the fact that sinusoidal surface E may be regarded as a limiting condition on the waveforms encountered in practice.

The surface layer concept, together with that of a characteristic surface impedance, can simplify external field calculations considerably. In addition, they provide an extremely useful point of reference between different analyses and experimental measurements.

7) References

- Rosenberg E. "Eddy Currents in Iron Masses", The Electrician, 1923, pp 188-191
- Haberland G. and Haberland F. "Alternating fields in Saturated Solid Iron", Archiv fur Elektrotechnik, Berlin, Germany, Vol 30, 1936, pp 126-133.
- Maclean W. "Theory of Strong Electromagnetic Waves in Massive Iron", Journal of Applied Physics, 25 (10) 1954, pp 1267-1270
- McConnell M.M. "Eddy Current Phenomena in Ferromagnetic Materials", Trans AIEE pt I (Mag) 73, 1954 pp 226-235.
- Agarwal P. "Eddy Current Losses in Solid and Laminated Iron", Trans AIEE, pt I (Mag) 78, 1959, pp 169-181
- Shevez W.L. "A Modified Limiting Non-Linear Theory of Eddy Current Phenomena in Solid Iron", Trans AIEE pt (Mag) 81, 1962 pp 48-55
- Lim K.K. and Hammond P. "Numerical Method for determining the Electromagnetic field in saturated Steel Plates." Proc IEE, 119, (11), 1972 pp 1667-1673.
- Neyfem A.H. and Asfar O.R. "An analytical solution of the Nonlinear

Eddy Current Losses in Ferromagnetic Materials"

IEEE Trans Mag - 10, 1974 pp 32- 331

9. Poritsky H. and Butler J.M. "A-C Flux Penetration into Magnetic Materials with Saturation" Trans AIEE, 1964, COM - 83, pp 99-111.
10. Gillott D.M. and Calvert J.F. "Eddy Current Loss in Saturated Solid Magnetic Plates, Rods, and Conductors". AIEE 1965, MAG - 1, pp 126-137
11. Ahamed S.V. and Erdelyi E.A "Non-Linear Theory of Salient Pole Machines", IEEE Trans PAS - 85, 1966, pp 61-70
12. Bullingham J.M. and Bernal M.J.M. "Investigation of the Effect of Non-Linear B-H Loops on the calculation of Eddy Current Losses", Proc IEE 114 (8) 1967, pp 1174-1176
13. Freeman E.M. "Universal Loss Chart for the calculation of Eddy Current Losses in thick steel plates", Proc IEE, 118 (1), pp278-279

Appendix

The following equations are used in the approximate model of section 3.

$$\frac{H'}{H} = \frac{\sigma E_0^2}{12 \omega B_0 \sigma \pi} \quad (A.1)$$

$$Z_{se} = \frac{E}{H} = \frac{12 \omega B_0 \pi}{\sigma E_0} \left[\frac{3\pi^2 + 4j}{9\pi^2 + 16} \right] \quad (A.2)$$

$$Z_{sh} = \frac{E}{H} = \frac{16}{3\pi} \left[\frac{\omega B_0}{2H_0 \sigma} \right]^{\frac{1}{2}} [1 + j\frac{1}{2}] \quad (A.3)$$

for the same peak fundamental component of E

$$Z_{sh} = \frac{E}{H} = \frac{16 B_0 \omega \sqrt{80}}{9\pi^2 E_0 \sigma} [1 + j\frac{1}{2}] \quad (A.4)$$

$$\frac{|Z_{se}|}{|Z_{sh}|} = \frac{27\pi^3}{40 (9\pi^2 + 16)^{\frac{1}{2}}} = 2.0475 \quad (A.5)$$

for the same condition, the ratio of penetration depths is

$$\frac{\delta_e}{\delta_h} = 0.949 \quad (A.6)$$

$$H' = \sum_{n=1,3,5}^{\infty} (H_{ns} \sin^2 \frac{n\omega t}{2} + H_{nc} \sin \frac{n\omega t}{2} \cos \frac{n\omega t}{2}) \quad (A.7)$$

Acknowledgements

The authors would like to thank Mr. C.J. Carpenter of Imperial College for helpful discussions, and the Science Research Council for financial support.

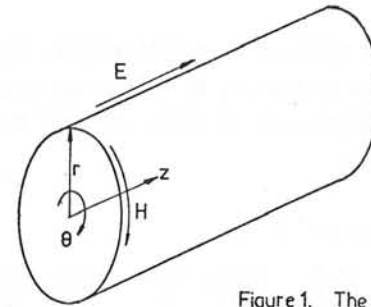


Figure 1. The sinusoidal E model

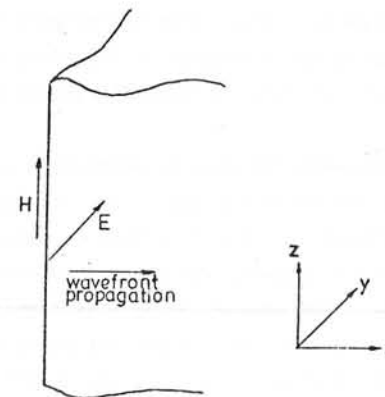


Figure 2. The rectangular B-H curve model

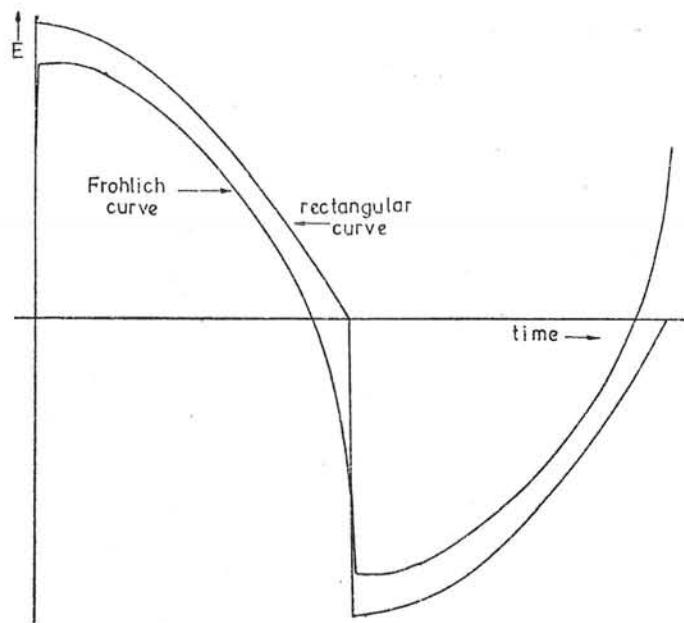


Figure 3. Surface E waveforms for sinusoidal surface H

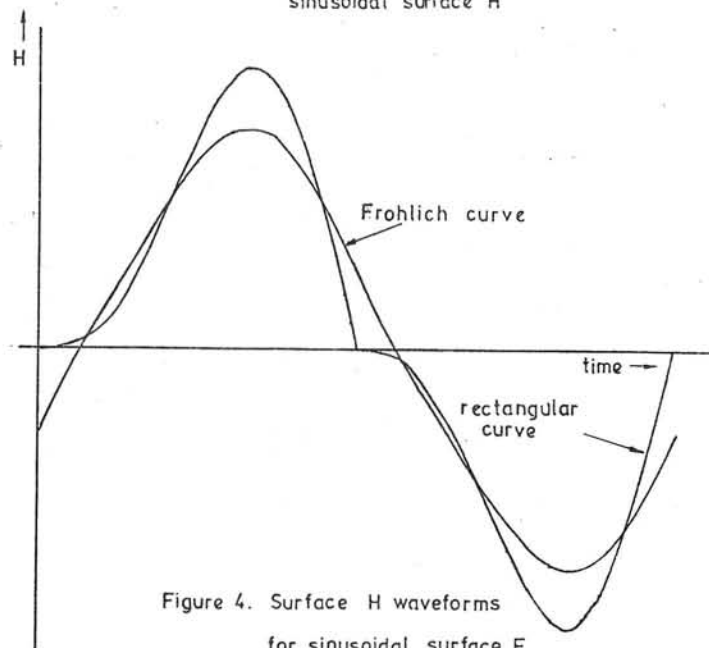


Figure 4. Surface H waveforms for sinusoidal surface E

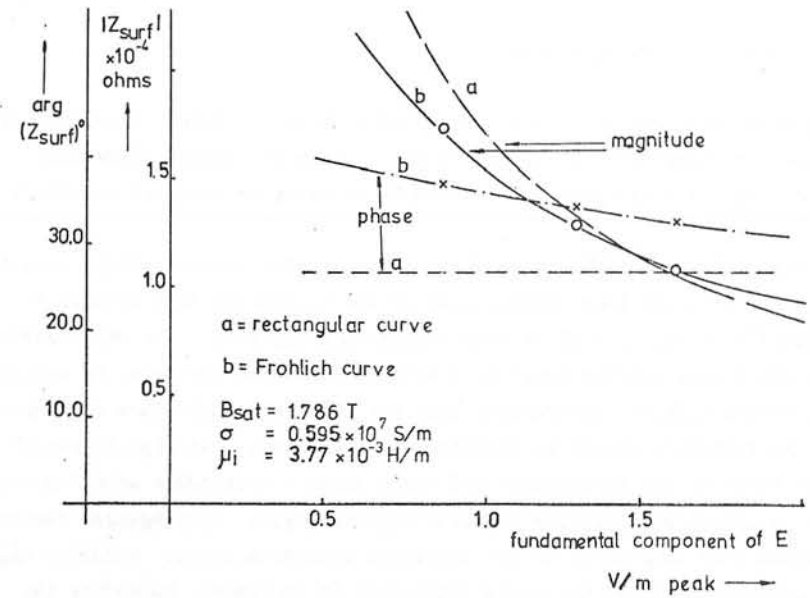


Figure 5. Surface impedance against E for sinusoidal surface H

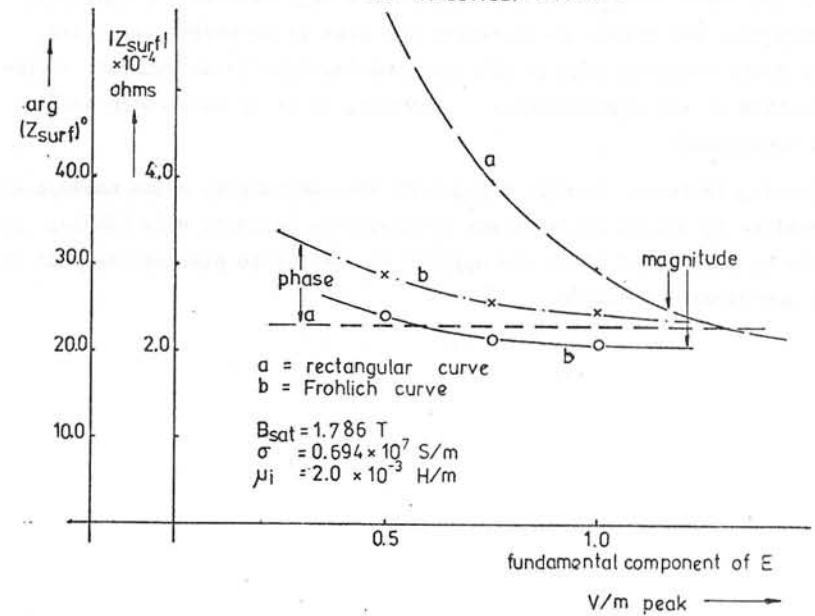


Figure 6. Surface impedance against E for sinusoidal surface E

Discussions following paper:

(Hammond, Southampton) The loss in solid iron is closely predicted by using a rectangular B-H characteristic. Does the author think that this loss could be obtained very simply by using an energy functional?

(Lowther, Imperial College) The rectangular B-H characteristic predicts the loss in solid iron closely only if the saturation flux density is reduced by a factor such as that suggested by Agarwal. In representing the non-linear surface layer by a surface impedance (in order to simplify the exterior field calculation) both the phase and quadrature components of the impedance should be accurately represented. At high levels of magnetisation the rectangular B-H curve gives a reasonable solution for the magnitude but produces an error in phase angle. The Agarwal factor reduces both components of the impedance whereas a better solution might be a method in which the phase angle only is increased, improving the accuracy of both components of the impedance.

With the above proviso the concept of an energy functional, employing a rectangular B-H curve, to represent the loss is an interesting idea. This would overcome some of the problems involved in an accurate representation of the non-linearity. However, it is an idea which we have not considered.

Following Professor Hammond's paper at the conference, which employs this technique to obtain the relevant parameter of interest very simply; we would be interested if he has applied the method to predict the loss in the non-linear situation.

EVALUATION OF THE AIR-GAP FIELD IN SHORT-STATOR LINEAR ASYNCHRONOUS MOTORS

G. Figalli - G. Gentile - E. Pagano - V. Vaccaro

1. Generalities

One of the essential problems to be considered in the study of the performances of short-stator linear asynchronous motors, is the determination of the air-gap magnetic field. In this evaluation, it is necessary to take into account the actual geometry of the stator and therefore the real map of the magnetic field both at the end and at the top and bottom sides. This implies that the air-gap magnetic field can not be identified with an ideal field in which all the lines are parallel and have equal and finite lengths. By introducing suitable simplified hypotheses, different approximate solutions can be obtained if the motor has a periodical configuration. These hypotheses have been validated by the agreement between the theoretical and experimental results obtained up to now.

A mathematical model based on an improved representation of the air-gap field map can be useful for application to a wide range of motor configuration. For this purpose the air-gap permeance can be expressed by means of a function of exponential type, which satisfactorily expresses the actual air-gap magnetic field. Allowing for symmetric conditions, the air-gap permeance can be approximated by an even function of x and z (see fig. 1), which vanishes at infinity. This function can be expressed in the form:

$$\lambda(x,z) = \frac{1}{\delta(x,z)} \lambda_0 \sum_{i=1}^n \exp\left[-\left(\frac{x-x_i}{A_0}\right)^2\right] \sum_{j=1}^m \exp\left[-\left(\frac{z-z_j}{B_0}\right)^2\right] \quad (1)$$

In this relation for each given pair of values of n and m , the constants A_0, B_0, x_i, z_j , are calculated to obtain the nearest approximation. A constant trend of the air-gap permeance inside the dominion D ($|x| \leq l_x/2, |z| \leq l_z/2$) is imposed together with a more or less quickly decreasing trend at the outside. For this purpose, first of all, a study has been done to determine the optimum value of x_i, A_0 , and z_j, B_0 , which give the minimum of the functions:

$$\Delta_x(x_i, A_0) = \int_0^{l_x/2} [\lambda(x,0) - \lambda(0,0)]^2 dx + k_x \int_{l_x/2}^{\infty} \lambda^2(x,0) dx,$$

$$\Delta_z(z_j, B_0) = \int_0^{l_z/2} [\lambda(0,z) - \lambda(0,0)]^2 dz + k_z \int_{l_z/2}^{\infty} \lambda^2(0,z) dz.$$

In these expressions, k_x and k_z are two constants chosen to give the decided weight of the error of the approximation inside the dominions D and D_{∞} ($|x| \geq l_x/2, |z| \geq l_z/2$). The air-gap field in the dominion D_{∞} is supposed to be zero.

2. Mathematical Model

In the study of steady-state operations of short stator linear induction motors, it is useful to make some approximations, i.e. neglect saturation phenomena and displacement currents, assign an infinite permeability to the inductor. If the z -component of the inductor current is only considered, the second Maxwell equation is:

$$\frac{\partial}{\partial x} [B(x,z,t) \cdot \delta(x,z)] = \mu_0 A_{z1}(x,z,t) + \mu_0 y_1 G_{z2}(x,z,t) \quad (2)$$

In this equation, it is also assumed that the induction field B has the same direction as the y -axis. This assumption generally made in the technical literature, does not alter the B distribution on the rotor. Ohm's law combined with the first Maxwell equation gives the following equation:

$$\frac{\partial^2 G_{z2}}{\partial x^2} + \frac{\partial^2 G_{z2}}{\partial z^2} - \chi \frac{\partial}{\partial x} \left(\frac{\partial B}{\partial t} + v \frac{\partial B}{\partial x} \right) = 0 \quad (3)$$

This equation together with equation (2) makes it possible to determine the function $B(x,z,t)$ on the rotor whenever the function A_{z1} is assigned. The latter depends on the time variation law of the inductor currents and on the geometric structure of the inductor windings. Referring to a symmetrical system of sinusoidal currents, one can write the linear current density as:

$$A_{z1}(x,z,t) = \sqrt{2} I \sum_{i=1}^p \sum_{j=1}^q \sum_{l=1}^q f_x(x) f_z(z) \exp[j(\omega t - 2\pi(i-1)/3)]$$

if all the pole windings are series connected and if we set:

$$f_x(x) = \frac{1}{\sqrt{2\pi} S_c g'} \left\{ \exp[-(x-x_{e,l,r})^2 / (2S_c^2 g'^2)] - \exp[-(x-x_{e,l,r}) / (2S_c^2 g'^2)] \right\}$$

$$f_z(z) = \frac{1}{\sqrt{2\pi} a f'} \int_{-\infty}^{\infty} \left\{ \exp[-(z+a)^2 / (2a^2 f'^2)] \exp[-(z-a)^2 / (2a^2 f'^2)] \right\} dz$$

This assumption implies that the distribution of the inductor currents is supposed to give rise to a Gaussian distribution of linear current density in the slot opening along the x-axis and to an integrated Gaussian distribution along the z-axis (see fig. 2).

Since at the steady-state the forcing variables are sinusoidal, all other variables will be also, i.e.:

$$B(x, z, t) = \dot{B}(x, z) \exp[j\omega t]$$

$$G_{z2}(x, z, t) = \dot{G}_{z2}(x, z) \exp[j\omega t]$$

$$A_{z1}(x, z, t) = \dot{A}_{z1}(x, z) \exp[j\omega t]$$

Some other properties are now examined. The vector B has zero divergence. Due to the magnetic symmetry with respect to the z axis, this property is summarized in the following equation:

$$\int_{-\infty}^{\infty} \dot{B}(x, z) dx = 0 \quad (4)$$

Performing the Fourier transform along the x-axis, the equation (4) becomes $\dot{B}(0, z) = 0$. The intrinsic structure of the physical model implies that the B_1 and B_2 components of the resulting air-gap induction field, separately generated by the current distributions on the stator and in the rotor, are zero i.e.:

$$\dot{B}_1(0, z) = \dot{B}_2(0, z) = 0 \quad (5)$$

On the other end the equation (2) can be written in the form:

$$\dot{B}(x, z) = \lambda(x, z) \left\{ \mu_0 \left[\int_{-\infty}^x \dot{A}_{z1}(x, z) dx + y_1 \int_{-\infty}^x \dot{G}_{z2}(x, z) dx \right] + k_1(z) + k_2(z) \right\} \quad (2')$$

In this equation we denote with k_1 and k_2 two integration functions. These functions must satisfy the condition (5), namely

$$k_1(z) = -\mu_0 \int_{-\infty}^0 \frac{\dot{A}_{z1}(\xi, z)}{j\xi} \exp\left[-\frac{A_0^2}{4} \xi^2 - j\xi x_1\right] d\xi \quad (6)$$

$$k_2(z) = -\mu_0 y_1 \int_{-\infty}^0 \frac{\dot{G}_{z2}(\xi, z)}{j\xi} \exp\left[-\frac{A_0^2}{4} \xi^2 - j\xi x_1\right] d\xi \quad (6)$$

Performing the double Fourier-transform of equations (2) and (3) and taking into account the properties of the integration functions we obtain as a result the integral equation:

$$\begin{aligned} \tilde{B}(\xi, \eta) = & \mu_0 \int_{-\infty}^{\infty} \int_{-\infty}^{\infty} \frac{\tilde{A}_{z1}(\gamma, \nu)}{j\gamma} \tilde{\lambda}(\xi - \gamma, \eta - \nu) d\gamma d\nu + \mu_0 y_1 \int_{-\infty}^{\infty} \int_{-\infty}^{\infty} \frac{\tilde{B}(\gamma, \nu) (\nu \gamma + \omega)}{j(\gamma^2 + \nu^2)} \\ & \cdot \tilde{\lambda}(\xi - \gamma, \eta - \nu) d\gamma d\nu \quad (7) \end{aligned}$$

where the function G_{z2} is eliminated.

To solve the equation (7) it is necessary to assign an adequate form to the function $\lambda(x, z)$, which represents the air-gap permeance. Referring to the relation (1), performing the double Fourier-transform, introducing in the equation (7) and making a normalization of the variable ξ, η over the quantities $A_0^2/4$ and $B_0^2/4$ we obtain the final equation. This equation is an integral equation of the Fredholm type, second kind, of two variables. The inspection of the kernel suggests an expansion of Hermite polynomials as functions of ξ, η . Performing the same expansion of the forcing function $\tilde{A}_{z1}(\xi, \eta)$ we can predict the form of the function $\tilde{B}(\xi, \eta)$:

$$\begin{aligned} \tilde{\lambda}(\xi, \eta) = & \lambda_0 A_0 B_0 \pi \frac{n}{\gamma} \frac{m}{\gamma} \exp\left[-(A_0^2 \xi^2 + B_0^2 \eta^2)/4\right] \exp\left[-j(x_1 \xi + z_1 \eta)\right] \\ \tilde{B}(\xi, \eta) = & C \exp\left[-(\xi^2 + \eta^2)\right] \sum_{i,k} \exp\left[-j(Dx_1 \xi + Fz_1 \eta)\right] \sum_{n,l} \tilde{H}_n(\xi) H_l(\eta) B_{n,l,i,k} \quad (8) \\ \tilde{H}_h(\xi) = & H_h(\xi) - H_h(0) \end{aligned}$$

where the quantities $B_{n,l,i,k}$ are the unknowns to be determined and where $D = 2/A_0, F = 2/B_0, C = \frac{h_1 l_1 i_1 k_1}{\mu_0 A_0 B_0 \pi \lambda_0}$ is set. Inserting the expression found in equation (2') and performing all the eventual algebra, the procedure leads to a system of infinite equations with infinite unknowns $B_{n,l,i,k}$. Truncation of the system which is equivalent to a degeneration of the kernel and an approximation of the forcing function leads to the matrix equation:

$$B = H + \Delta k B$$

whose solution is:

$$B = [I - \lambda k]^{-1} H$$

whose [I] is the identity matrix

LIST OF SYMBOLS

- a halfwidth of the rotor.
- $A_{z1}(x, z)$ linear current density at the stator air-gap surface.
- $B(x, z)$ air-gap induction.
- f', g' numerical coefficients.
- $\tilde{f}, \tilde{\tilde{f}}$ single and double Fourier-Transform of the function f .
- $G_{z2}(x, z)$ current density.
- I effective value of the inductor phase current.
- p number of pole-pairs.
- q number of slots per pole and per phase.
- S_c halfwidth of inductor slots.
- $x'_{e,r,i}, x''_{e,r,i}$ abscissae of the slots for clockwise and counterclockwise currents.
- v mutual velocity between stator and rotor.
- $\delta(x, z)$ length of the air-gap field-lines.
- $\lambda(x, z)$ air-gap permeance.
- μ_0 permeability.
- χ electric conductivity.
- ω angular frequency.

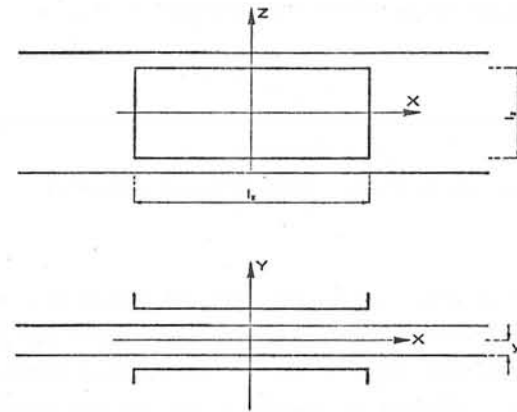


fig. 1

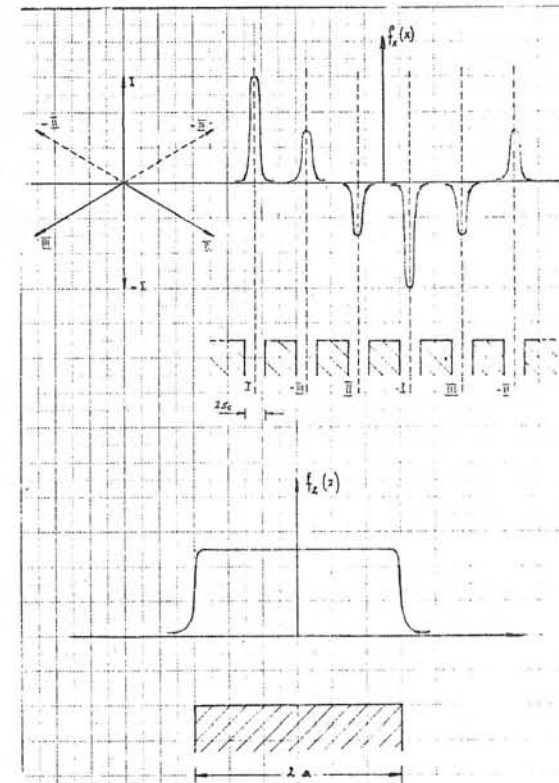


Fig. 2

NUMERICAL DETERMINATION OF AN EQUIVALENT
COMPLEX PERMEABILITY FOR SATURATED STEEL

Alain BOSSAVIT

Electricité de France (92140 Clamart, France)

This work has been done in relation with the design of a mathematical model of an induction furnace for slabs. The geometry of the furnace is such that a monodimensional study is valid, leading to a coupled system of non-linear partial differential equations, one for the temperature, one for the magnetic field.

A numerical treatment of this system is quite feasible, but time-consuming. The introduction of an *equivalent permeability* (see [1]) for saturated steel is a useful device to reduce the complexity of this system, for it allows one to solve the field equation in closed form, leaving only the heat equation to be solved.

The organization of the paper will be described at the end of the first paragraph.

1. - DEFINITION OF THE EQUIVALENT PERMEABILITY. ITS PURPOSE

We consider an infinite steel block, limited by the yOz plane, and a current sheet parallel to this plane, at the abscissa $-l$, l being the air-gap. Its resistance is r and its inductance s per square-meter and a voltage $v(t) = V \sin \omega t$ is applied.

The steel is characterized by its (constant) resistivity σ and its magnetization curve, linking the induction $b(t,x)$ and the magnetic field $h(t,x)$ by the relation

$$(1) \quad b(t,x) = b(h(t,x))$$

The evolution of the field is given by the parabolic equation

$$(2) \quad \frac{\partial}{\partial t} b(h(t,x)) - \frac{\partial}{\partial x} (\sigma^{-1} \frac{\partial h}{\partial x}) = 0, \quad x \geq 0,$$

with the boundary condition

$$(3) \quad (\mu_0 l + s) \frac{\partial h}{\partial t}(t,0) + r h(t,0) - \sigma^{-1} \frac{\partial h}{\partial x}(t,0) = v(t).$$

Having obtained the *periodic solution* of (2) (3), we can compute the *mean power* P and the *quadratic mean intensity* J under the applied voltage V .

Let us now imagine a steel of complex permeability

$$(4) \quad \mu = \mu_0 \mu_r \exp(i\theta)$$

heated by the same inductor. In this ideal material, the field would be $\text{Re} [\exp(i\omega t) H(x)]$ where H is the solution of

$$(5) \quad \begin{cases} i \omega \sigma \mu H(x) - \frac{\partial^2}{\partial x^2} H(x) = 0, & x \geq 0, \\ [i \omega (\mu_0 l + s) + r] H(0) - \sigma^{-1} \frac{\partial H}{\partial x}(0) = V \end{cases}$$

From (5) the mean power P' and the mean quadratic intensity J' are easily found, as functions of μ_r and θ .

We define the *equivalent complex permeability* as the solution of the system of two equations

$$(6) \quad P = P'(\mu_r, \theta), \quad J = J'(\mu_r, \theta)$$

A priori, μ_r and θ depend on a lot of parameters, and we shall examine this dependence in the next paragraph.

Let us remark that this ideal steel with equivalent permeability behaves like real steel with respect to P and J . These are the major parameters in heating applications, for J determines the power loss in the

coil, so that the heating power can be exactly determined. The comparison between P and J is also important to design the compensating capacitors.

This approach has a flaw : the exact *distribution* of power in the steel is not accurately predicted if one refers to (5) instead of (2) (3), but this is a minor disadvantage, for this power is dissipated in a very narrow skin depth (an the heat diffusion helps to smooth off the differences).

On the other hand, the simplification brought on by (5) in comparison with (2) (3) is obvious, *if the equivalent permeability is known.*

We shall attempt, in the coming paragraphs, to compute this permeability. In § 2, we put the equations in non-dimensional form, and make apparent the occurrence of a *small parameter* ϵ . Setting $\epsilon = 0$, we obtain a *classical formula* for the equivalent permeability. In § 3, we expose an approximate method, valid for small ϵ , which results in *corrections* to this formula. Detailed charts and curves for these correcting terms are given in § 4.

2. - EQUATIONS IN NON-DIMENSIONAL FORM. THE SMALL PARAMETER

Let us define new variables by

$$(7) \quad b = b_0 \bar{b}, \quad \bar{t} = \omega t, \quad h = H \bar{h}, \quad v = V \bar{v}, \quad x = \delta \bar{x}$$

and introduce the classical penetration depth

$$(8) \quad \delta_0 = \sqrt{2/\sigma \omega \mu_0} .$$

Three non-dimensional parameters appear :

$$(9) \quad \rho = r \sigma \delta_0, \quad \lambda = \sigma \omega \delta_0 (\mu_0 l + s), \quad \epsilon = \delta/\delta_0$$

If we decide that

$$(10) \quad \delta = (H/\sigma \omega b)^{1/2}, \quad H = \sigma \delta V = \sigma V^2/\omega b,$$

the equations (2) and (3) become (ignoring the bars)

$$(11) \quad \frac{\partial}{\partial \bar{t}} \beta_\epsilon(h) - \frac{\partial^2 h}{\partial x^2} = 0, \quad x \geq 0,$$

$$(12) \quad \lambda \epsilon \frac{dh}{d\bar{t}} + \rho \epsilon h - \frac{\partial h}{\partial x} = \sin \bar{t}, \quad \text{for } x = 0$$

where β is the non dimensional magnetization characteristic. For saturated steel under high applied fields, it is customary to adopt the following representation of the b-h relation (figure 1) :

$$(13) \quad b = b_0 \operatorname{sgn}(h) + \mu_0 h$$

If b_0 is taken as the new induction unit, (13) takes the non-dimensional form

$$(14) \quad \beta_\epsilon(h) = \operatorname{sgn}(h) + 2 \epsilon^2 h$$

When $\epsilon = 0$, (11) (12) reduce to a classical equation (cf.

Agarwal, [2]). The instantaneous field is (cf. fig. 2).

$$(15) \quad h(t,x) = (\sin^2 t/2 - x) \sin t \quad \text{if } x < \alpha(t) = \sin^2 t/2$$

$$= 0 \quad \text{if } x \geq \alpha(t)$$

This allows to interpret δ and H in (7) : δ is the maximum depth of penetration of the field and $H = (32/5)^{1/2} H_m$, where $H_m = J$ is the mean quadratic field on the edge of the slab.

The factor ϵ is thus a *ratio of two penetration depths* (under and above the point of Curie) and it takes small values (0.1 to 0.3) in standard situations.

This fact justifies Agarwal's approximation ($\epsilon = 0$). A straight-forward computation leads to the following expression for the equivalent

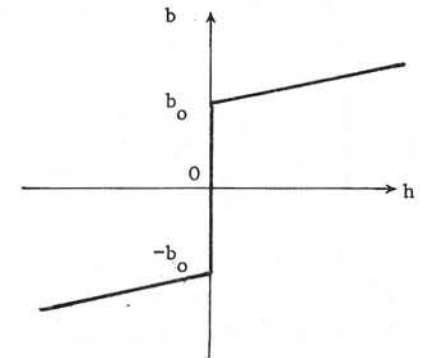


Figure 1

The b-h curve for intense fields

permeability when ϵ tends to zero :

$$(16) \quad \mu = 1.6 \frac{\mu_0}{\epsilon^2} \exp [i(2 \operatorname{Arctan} 1/2 - \pi/2)]$$

This must be understood as the first term of an asymptotic series in ϵ and we shall attempt to estimate the next term.

3. - A CORRECTION TO FORMULA (16)

Let us return to (11) (12). If we introduce the zeros $\{\alpha_i(t), i = 1, 2, \dots\}$ of h in x , (11) is equivalent to

$$(17) \quad \begin{cases} 2 \epsilon^2 \frac{\partial h}{\partial t} - \frac{\partial^2 h}{\partial x^2} = 0 & \text{if } x \neq \alpha_i \\ 2 \frac{d\alpha_i}{dt} + \frac{\partial h}{\partial x} (\alpha_i + 0) - \frac{\partial h}{\partial x} (\alpha_i - 0), i = 1, 2, \dots \end{cases}$$

It is physically obvious (but hard to prove) that h is negligible for all $x > \alpha_1$. So that (11) (12) can be restated in the following form, keeping only the first abscissa α in consideration :

$$(18) \quad 2 \epsilon^2 \frac{\partial h}{\partial t} - \frac{\partial^2 h}{\partial x^2} = 0, \quad x > 0, \quad 0 \leq t \leq \pi,$$

$$(19) \quad 2 \frac{d\alpha}{dt} + \frac{\partial h}{\partial x} (\alpha(t)) = 0, \quad 0 \leq t \leq \pi,$$

$$(20) \quad h(\alpha(t)) = 0, \quad 0 \leq t \leq \pi,$$

$$(21) \quad \lambda \epsilon \frac{dh}{dt}(0, t) + \rho \epsilon h(0, t) - \frac{\partial h}{\partial x}(0, t) = \sin(t + \gamma(\epsilon))$$

$$(22) \quad h(0, 0) = h(0, \pi) = 0$$

(A shift $\gamma(\epsilon)$ in the origin of times has been introduced in (21) to satisfy (22), which ensures the necessary periodicity).

To study (18)... (22) we introduce a new parameter $\zeta = 2 \epsilon^2$ and set

$$(18') \quad \zeta \frac{\partial h}{\partial t} - \frac{\partial^2 h}{\partial x^2} = 0$$

Developping formally the solution h in terms of ζ and ϵ , we have

$$(23) \quad h_{\zeta, \epsilon} = h_{0, \epsilon} + \zeta \frac{\partial}{\partial \zeta} h_{0, 0} + O(\epsilon^3)$$

As we wish to obtain $h_{2\epsilon^2, \epsilon}$, the following procedure stems from (23) :

- Solve (18') ... (22) with $\zeta = 0$ to get $h_{0, \epsilon}$

- Differentiate (18') ... (22) with respect to ζ and set ϵ to zero, to get $\frac{\partial h}{\partial \zeta}$,

- combine the results according to (19).

The solution found is accurate to the third order in ϵ .

The term $h_{0, \epsilon}$

Let us introduce the new unknown function.

$$(24) \quad u(t) = \int_0^t h(s, 0) ds$$

The system (18') ... (22) with $\zeta = 0$ becomes

$$(25) \quad \begin{cases} \lambda \epsilon \frac{du}{dt} + \rho \epsilon u + 2\sqrt{u} = \int_0^t \sin(s + \gamma(\epsilon)) ds, & 0 \leq t \leq \pi, \\ u(0) = 0 \\ u'(\pi) = 0 \end{cases}$$

a two-point boundary value problem. It has been solved by a shooting method, with a standard iterative procedure on the phase shift γ , and a Runge-Kutta scheme (with precautions near the origin to cope with the stiffness of the differential equation).

The term $\partial h / \partial \zeta$

It can be obtained in closed form easily.

Combination

A computer program has been written for the IBM 370-168 of Electricité de France to carry through these operations, to compare the results with the solution of (5), and to derive the equivalent permeability as a function of the three parameters ϵ , ρ and λ . About 0.4 second of CPU-time is used for each triplet. It is convenient to express the results in the following form

$$(26) \quad \mu(\epsilon, \rho, \lambda) = \frac{\nu^2(\epsilon, \rho, \lambda)}{\epsilon^2} \exp i \theta(\epsilon, \rho, \lambda)$$

The curves below show how ν et θ vary with ϵ , ρ and λ .

4. - RESULTS

For a numerical example, let us use the MKSA System.

Reasonable values are :

Frequency	: $\omega = 100 \pi$
Resistance of the sheet	: $r = 10^{-6} \text{ (}\Omega \text{ m}^{-2}\text{)}$
Inductance of the sheet	: $s = r/\omega \text{ (}\Omega \text{ m}^{-2}\text{)}$
Airgap	: $l = 0.1 \text{ (m)}$
Conductivity	: $\sigma = 10^6 \text{ (}\Omega^{-1} \text{ m)}$
Applied voltage	: $V = 10 \text{ (V)}$
Induction at saturation	: $b = 1.5 \text{ (T)}$

With these values, knowing that $\mu_0 = 4\pi 10^{-7}$, we obtain

Penetration depth	: $\delta = 0.021 \text{ (m)}$
Mean magnetizing field	: $H_m = 83000 \text{ (A/m)}$

and for the dimensionless parameters

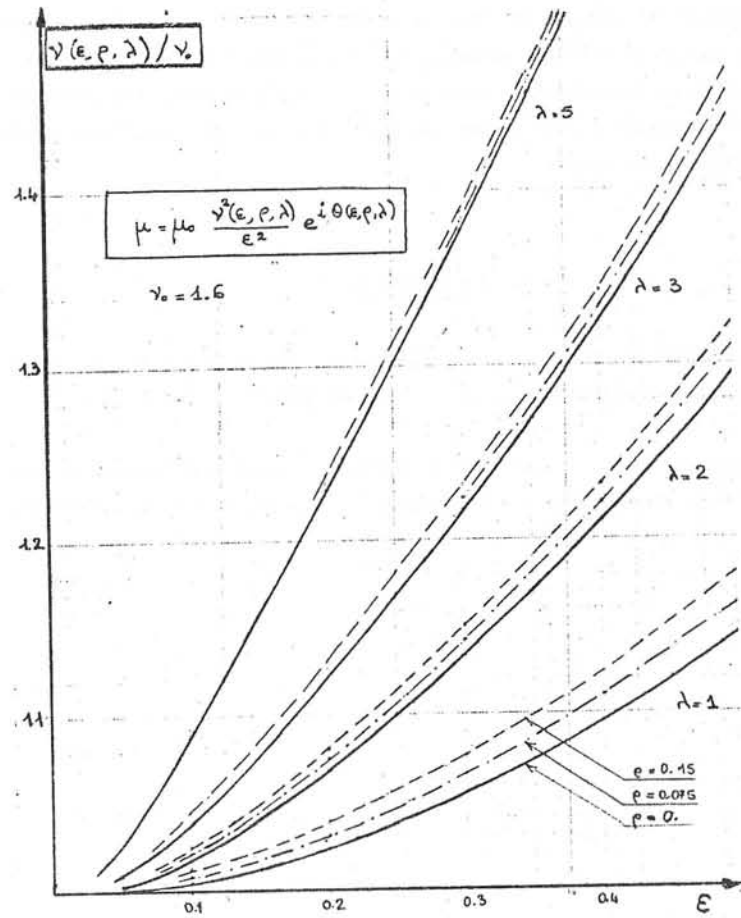
$$\epsilon = 0.298, \lambda = 2.88, \rho = 0.0712.$$

From these figures, and from the examination of our results, we can draw the following conclusion :

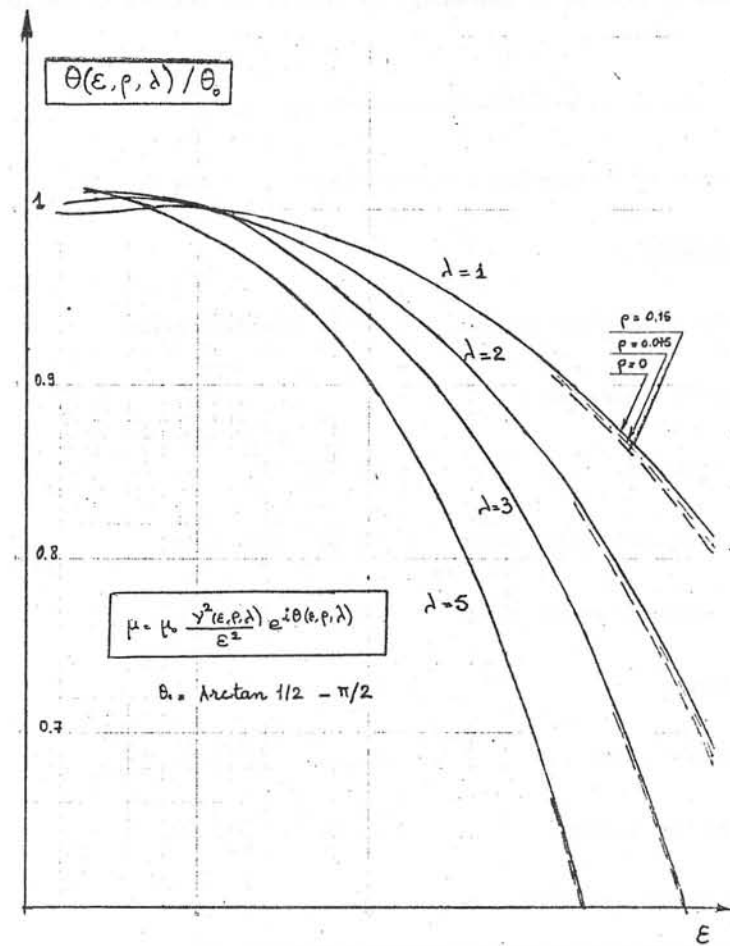
Agarwal's formula is valid only for weak magnetizing fields (but strong enough to achieve saturation, of course). For strong fields, as in heating applications, a correction must be provided. This correction depends strongly on the airgap and only to a negligible extent on the impedance of the coil.

REFERENCES

- [1] BARRET(P.), Contribution à l'étude du comportement du fer massif en régime alternatif saturé, note HM 010.49, E.D.F., 1972.
- [2] AGARWAL (P.D.), Eddy-current losses in solid and laminated iron, *Trans. Amer. Inst. Elect. Engrs.*, 1959, 78, Pt.II, pp. 169-181.



Variation of the modulus of the equivalent permeability



Variation of the argument of the equivalent permeability

A COMPUTERIZED PROGRAM FOR THE NUMERICAL SOLUTION OF
HARMONIC FIELDS WITH BOUNDARY CONDITION NON PROPERLY
DEFINED

A. Di Napoli, C. Mazzetti, U. Ratti
Electrical Engineering Institute - University of Rome
ROME

Summary

In a previous paper, /1/, an automatic computerized program was defined that, making use of the finite element technique, allows the study of the electromagnetic field relative to large-sized structures involved in high-frequency phenomena.

This program had been used for the determination of the electromagnetic field of a simple resistive divider for high-voltage measurement.

In this paper new devices are introduced that allow to markedly reduce both the storage area involved in the program and the computation time. This proved necessary in so much as the use of the program was so extended as to include the determination of the electromagnetic field of resistive dividers in the presence of electrodes and screens of various shapes and placed in different positions.

Introduction

The present paper represents an intermediate stage for the study of the electromagnetic field relating to large-sized structures involved in high-frequency phenomena. The computation methodology set forth here and applied to the solution of an electromagnetic field of a resistive voltage divider, was extensively illustrated under /1/; Fig. 6 shows the flow-chart, and Appendix 1, the relative equations.

In this paper, a computation subprogram was defined that, through the coefficient matrix inversion, directly solves the system of algebraic equations obtained, by means of the finite element technique, starting from the following differential equations:

$$\nabla^2 V = 0 \quad ; \quad \nabla^2 \dot{H} = \mu \varepsilon \frac{\delta^2 H}{\delta t^2} \quad (1)$$

The program was applied to the study of the electromagnetic field in a system consisting of a resistive voltage divider placed in a test laboratory, in which, unlike the work /1/, there are also present an HV electrode and ring-shaped screens. The system configuration, with the relative boundary conditions, are shown in Fig. 1.

The screens and the electrode are assumed to be made of fiber glass whose surface is metalized by means of a high-conductivity aluminium paint; in this way, they have a mere electrical and non magnetic function /2,3/.

The field distribution analysis was performed concomitantly with the frequency change; it is well known, in fact, that an impulsive wave may be always regarded as a sum of signals having a different frequency, amplitude and phase it ensues that the behaviour of the system under review, vis-à-vis this type of signal, provided that the system may be regarded as linear, is inferred from the results as a function of frequency. The interval considered is that comprised in the range of 0 to 250 kHz: such an interval also involves pulse waves with a rise time in the order of microseconds.

GEOMETRY OF THE SYSTEM AND BOUNDARY CONDITIONS

A system similar to that considered under /1/ was taken into examination, namely, a resistive divider with an anti-inductive winding, placed in a high-voltage laboratory, with both walls and ceiling assumed to be at zero potential.

In respect of the system analyzed under /1/, the resistive column is completed with an electrode placed in correspondence of a high-voltage terminal, as shown under Fig. 1 and 2.

The presence is subsequently considered of an annular screen positioned as in Fig. 1, and the influence is verified that it exerts on the behaviour of the field (Fig.3) and on the potential distribution along the divider (Fig.4), in the assumption of keeping it at the high-voltage terminal potential.

It should be noted that the system thus schematized presents a symmetry axis, and it is therefore possible to study the field behaviour in relation to any planes containing this axis, and to convert the problem under examination from bidimensional to tridimensional. Furthermore, in the plane under review, the system is still symmetrical in respect of the axis of the divider, and it is therefore possible to confine the study to one half plane only. In other words, it is possible to tackle the study of the field in cylindrical coordinates. Moreover, on the basis of the previous assumption of a perfectly anti-inductive winding, it is sufficient to study the phenomenon only in the region external to the divider, as schematically indicated in Fig. 1, where the part of the plane under examination is shown. This region, for

the purpose of the application of the finite element technique, was in fact discretized into triangular elements of the first order, as shown in Fig. 2, where it looks thickened in the areas in which a higher electrical gradient was assumed to be present.

The presence of the screens or of the H V electrode has obviously modified in part the boundary conditions and the previously described /1/ field equations, without, however, any changes being made to the functional to be minimized /4,5,6/.

Concerning the boundary conditions relative to the HV electrode and the fixed potential screen, it proved sufficient to impose to the nodes placed on the conducting surfaces a potential equal to that of the high-voltage terminal of the resistive column.

As to segment OO', representing the divisor-air separation surface, it is quite impossible to define "a priori" the value of the displacement currents flowing from such surface, hence the V electric potential and the H_e magnetic field among it. As previously indicated under /1/, it was initially assumed to consider a purely linear potential distribution, and hence, by means of the iterative procedure described in the flow-chart, the actual distribution along the divider was calculated by successive approximations.

The electromagnetic field equations throughout the region under review, are represented by (1) equations, except for the areas placed internally to high-voltage electrode and screens. In this region, owing to the absence of displacement currents, equations (1) are replaced by:

$$\nabla^2 V = 0; \quad \nabla^2 \dot{H} = 0 \quad (2)$$

Computation Program

The flow chart of the computation program is shown in Fig. 6. In this paragraph two peculiar features of the worked out program are emphasized: the storing of the coefficient matrix of the finite elements and the solution of the two following equation systems obtained by means of the finite element technique (5,6), starting from (1) equations:

$$|N| \cdot |V' + jV''| = 0 \quad (3)$$

$$\left(|M| + \omega^2 |T| \right) \cdot |H'_0 \cdot r + jH''_0 \cdot r| = 0 \quad (4)$$

With regard to the first point, it may be observed that we succeeded in considering a high number of nodes, occupying rather reduced storage areas /7/, by storing only the values of the coefficients different from zero that appear in matrices !M! and !N!.

Let us consider, in fact, the node i, j, Fig. 5, being the vertex of six triangles forming the drawn hexagon; it is in fact pointless to assign storage areas to the coefficient tying node i, j to node i+2, j+2 which is certainly equal to zero. In this way, it was possible to store, making use only of triangular elements of the first order, only seven coefficients for each node, thus obtaining a remarkable saving in storage that becomes greater and greater as the number of nodes increases.

The solution of the system of equations (3) and (4) was performed making use of Choleski's decomposition /8/.

It should be reminded that the matrix !N! of (3) is a symmetrical matrix, decomposable in a univocal way into the product of two triangular matrices, of which one is the transposition of the other; equation (3) may be thus

written as follows:

$$|N| \cdot |V' + jV''| = |m|^T \cdot |m| \cdot |V' + jV''| = 0 \quad (5)$$

Premultiplying (5) by the reverse of !m!^T, we obtain:

$$|m| \cdot |V' + jV''| = 0 \quad (6)$$

that, being a triangular matrix, is directly soluble.

In view of the previously mentioned storing of the matrix of only the coefficient different from zero, the one difficulty presented by such a way of working was that of obtaining the algorithms for the computation of matrix !m! from !N!, writing in !m! only the coefficients different from zero.

Such a way of working involved a storage increase that was, however, offset by a decrease in computation time; this time was reduced to 2/3 of the computation time previously required, by having recourse to the over-relaxation method. It should be also noted that in so doing, the uncertainty is eliminated, that is due to the imperfect knowledge of the overrelaxation coefficient. It should be finally observed that this type of solution is particularly suitable for the problem under examination: in fact, owing to the lack of knowledge of the potential distribution along OO', recourse must be had to successive iterations, during which the matrix to be inverted remains unchanged, and hence, for each iteration, it will suffice to solve the system in respect of the new values of V and of H, calculated along the OO' boundary.

Conclusions and Further Developments

The work carried out highlighted two particular features of the system under review:

- the methodology used for the solution of the system of equations (1);
- the application of the program formulated under /1/, as modified for the study of the divider-screen-electrode-laboratory system.

Concerning the first point, one can be fully satisfied, in view of the saving obtained both in machining time and in the storage area occupied.

As to the second point, although the influence the screen and the electrode exert upon the field behaviour and upon the potential distribution, was duly ascertained, some doubtful points, already present in /1/, still remain in existence. In fact, for frequencies below 1kHz, there still exist uncertainties due to the error in the computation of the derivative of Φ (eq. I.6); such uncertainties would be at least reduced by using elements of a higher order than the first one, and we intend to work in the future along these lines.

References

- /1/ A. Di Napoli, C. Mazzetti, V. Ratti, "Electromagnetic Field Computation of HV Resistive Divider" - I.C.C.A. D., S. Margherita Ligure, 1976.
- /2/ C. Mazzetti, U. Ratti, A. Tomassi, "Dividers for High-Voltage Measurements" - La Goliardica, Roma, 1973.
- /3/ B. Heller, A. Veverka, "Les phénomènes de choc dans les machines électriques" - Dunod, Paris, 1963.

- /4/ P. Silvester, M.V.K. CHARI, "Finite Element Solution of Saturable Magnetic Field Problems" - I E E E , Paper 70, TP 130, PWR.
- /5/ C.J. Carpenter, "Computer Solution of Field Problems", - Notes of Power System Equipment, London, 1971.
- /6/ J.O.C. Zienkiewicz, "The Finite Element Method in Engineering Science" - McGraw-Hill, London, 1971.
- /7/ A. Di Napoli, "The Finite Element Method in the Study of Electromagnetic Fields" - La Goliardica, Roma, 1975.
- /8/ "Calcul Matricial", Dunod, Paris.

APPENDIX

The flow-chart of the computation program and the algorithms referred to therein, are reported hereunder (Fig. 6) for a correct understanding of the work.

The equation systems (3), (4), by making use of Choleski's decomposition, may be respectively written as follows:

$$|m| |V' + jV''| = |V'_c + jV''_c| \quad (I.1)$$

$$|n| |H'_\vartheta + jH''_\vartheta| = |H'_c + jH''_c| \quad (I.2)$$

where, as a second member, there are placed the voltage and magnetic field vectors fixed at any iteration; $|m|$ and $|n|$ are triangular matrices. From the computation of potential V one goes back to the value of the electric field E_z in the barycenter of the triangles adjacent to the instrument

$$E_r = - \frac{\delta V}{\delta r} \quad (I.3)$$

and, hence, to the displacement currents value:

$$I_s = \frac{dQ}{dt} = \frac{d}{dt} (\epsilon E_r \cdot 2\pi r l) = j\omega \epsilon E_r \cdot 2\pi r l \quad (I.4)$$

The H values along OO' may be calculated from:

$$H_\vartheta = \frac{I}{2\pi r} \quad (I.5)$$

where I is the current flowing through the divider, less the quantity I_s that flows out of the latter by the capacitive route.

Starting from the value of the magnetic field H_e the electric field E is determined along OO' :

$$- \frac{1}{r} \frac{\delta}{\delta r} (H'_\vartheta + jH''_\vartheta) \cdot r = \epsilon \frac{\delta}{\delta t} (\tilde{E}'_z + j\tilde{E}''_z) \quad (I.6)$$

The knowledge of this component allows to calculate the electromotive force $\Delta V = E_z \cdot \Delta l$ induced by the magnetic field that is added to the resistive dump:

$$V_{\text{new}} = V_R + \Delta V \quad (I.7)$$

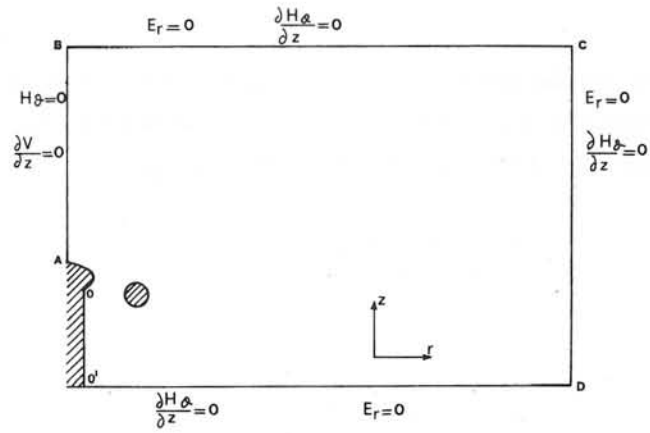


Fig. 1

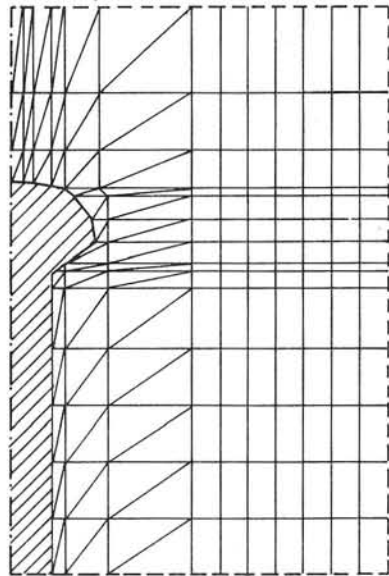


Fig. 2

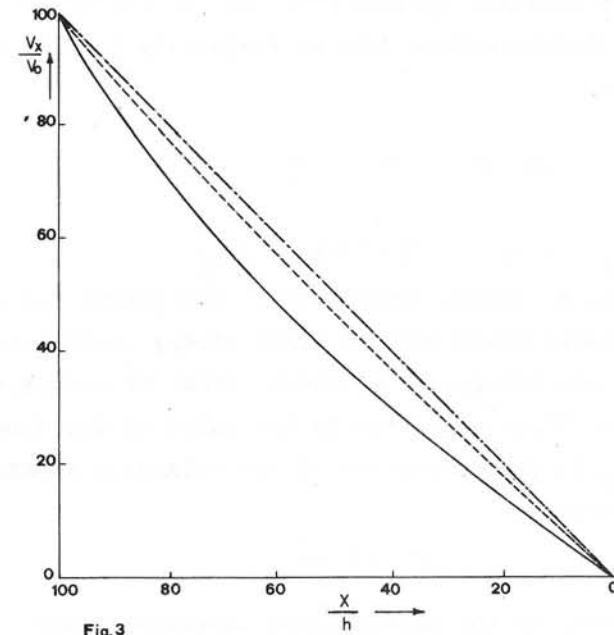


Fig.3

Fig. 3

Potential distribution along the resistive divider at 250 kHz

- without screen
- - - - - with screen

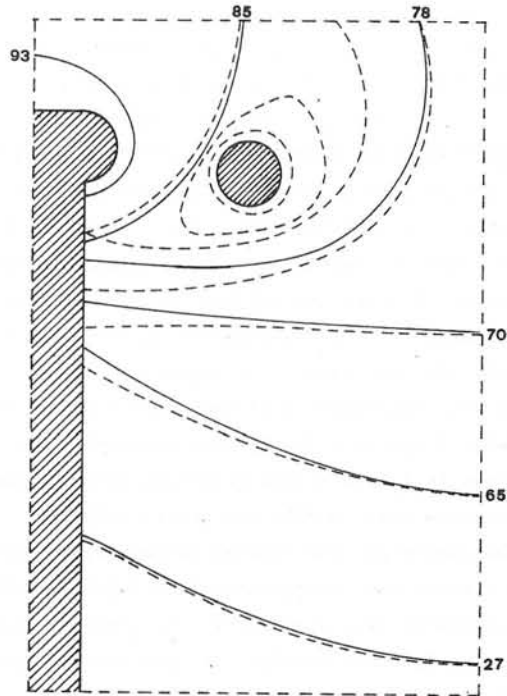


Fig. 4
Equipotential lines at 250 kHz
———— without screen
----- with screen

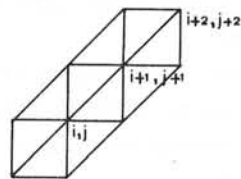


Fig. 5

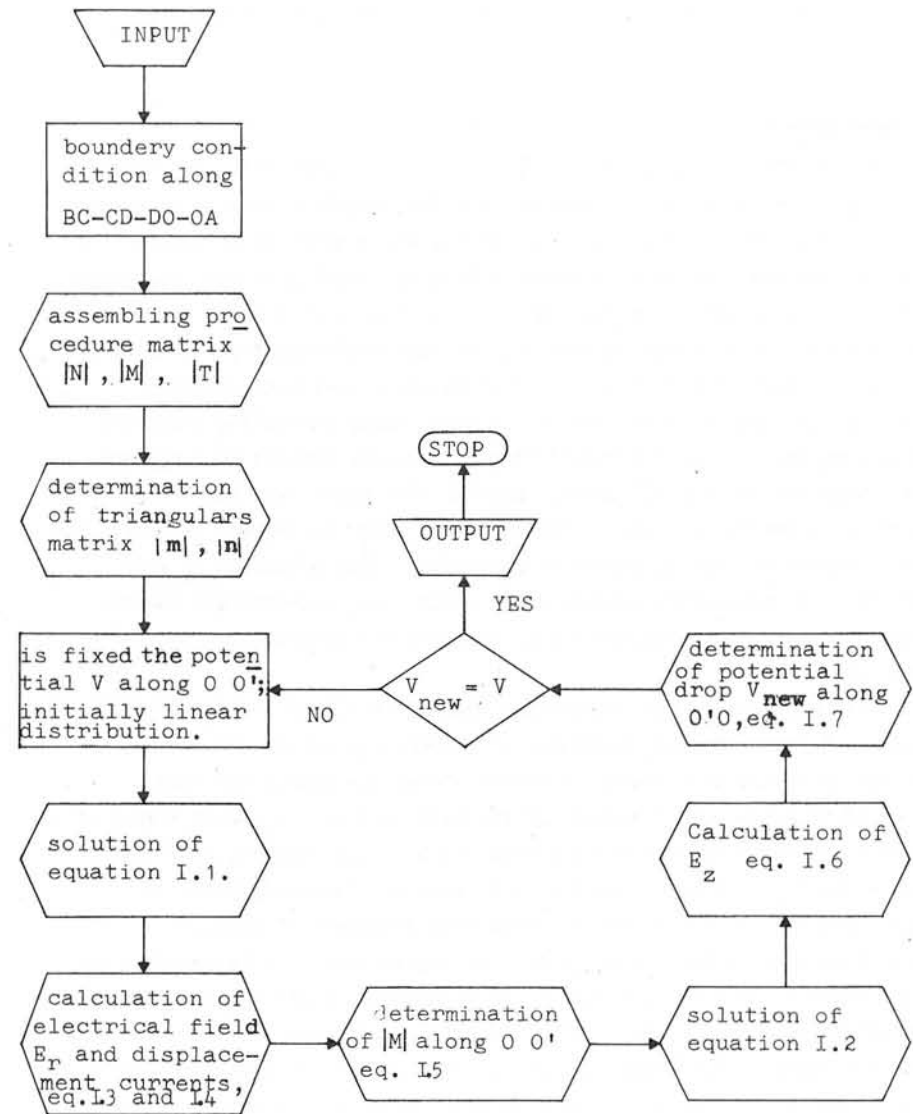


Fig. 6

A COMPUTER METHOD OF CALCULATING THE EDDY CURRENT HEATING OF MAGNETIC MATERIALS, WITH A COMPARISON BETWEEN PREDICTED AND MEASURED RESULTS IN A 2MVA INDUCTION FURNACE

R C GIBSON

1. Introduction

At the Electricity Council Research Centre, Capenhurst, considerable effort is being expended on research into the induction heating of metals. Much of this work is of a practical nature, concerning the development of existing and novel induction heating techniques, leading to the production of full scale industrial prototypes. In parallel with this, a theoretical analysis of induction heating methods has been undertaken by the author.

As a result of this theoretical analysis, a series of computer programs have been written to model various induction heating processes. These programs include the calculation of the eddy current heating, and the subsequent thermal diffusion, together with facilities for controlling the furnace power, frequency and other parameters necessary to model industrial heating processes accurately. Due allowance is made both for the temperature dependence of electrical, magnetic and thermal properties during the heating cycle, and also for saturation of magnetic materials.

This paper describes the methods used to calculate the two-dimensional magnetic field, with eddy currents, in a short cylindrical or flat wide coil of an induction furnace. A finite difference method has been selected as being most suitable for this application. A direct method of solution of the complex coefficient matrix has been adopted, as it has been found to be more efficient of both user and computing time. A detailed analysis is made of the simplified treatment of magnetic saturation used in the method, and it is argued that this is suitable for cases where a low cost calculation giving greater accuracy than orthodox design methods is required. Details are given of tests performed with both non-magnetic and magnetic loads in a 2MVA multilayer billet heater, and the measured results are compared with those calculated using the methods given in this paper.

2. Description of Program and Mathematical Model Used.

The program is essentially in two halves. First the eddy current power distribution is evaluated, and then this is used as source terms in the thermal diffusion equation to calculate the temperature rise in the

furnace charge. After a suitable interval, the eddy current heating is recalculated using updated values of physical properties appropriate to the new node temperatures. This cycle of alternate solution of magnetic and thermal fields is continued until the required temperature is obtained. During this heating cycle, such parameters as supply voltage and frequency, furnace power etc. can be altered to model the particular induction heating process being followed. In addition, the program permits furnace power to be controlled in order to provide rapid heating under such thermal constraints as a maximum temperature gradient or a maximum surface temperature. Heat losses from the furnace charge through a thermally insulating refractory are also taken into account.

Figure 1 shows the cross-section of the short circular furnace for which the calculated and measured results are compared in Section 5. A finite difference mesh is fitted to the cross-section as shown, the mesh extending beyond the coil to take adequately into account the stray magnetic field. The electrical and thermal conductivity, heat capacity etc. for each mesh element are interpolated from tabulated values. The derivation of the effective mesh permeability is given in Section 4. The magnetic field equations are written for each node in terms of the vector potential so that in the usual notation

$$\text{curl} (1/\mu \text{ curl } A) = -j 2\pi f \sigma A + J_s \quad 2.1$$

where μ and σ are assumed constant in time, but can differ for each mesh element. A and J_s are assumed to be sinusoidal functions at frequency F . The method of solution of these equations is given in Section 3.

The thermal diffusion equation can be integrated by a variety of means, in this case a variant of the Runge-Kutta method.

2.1. Calculation of Coil Losses.

The coil losses can be calculated by covering the winding with a finely divided mesh and allowing the program to calculate the eddy current losses in the winding strands in the same way as for the furnace charge. However in a case such as that of Figure 1, where the windings are reasonably well stranded (each strand being not deeper than one penetration depth) a more economic coarse mesh can be used. It is sufficient to assume initially that each strand is perfectly insulating but carrying the requisite source current. Once the magnetic field and the eddy currents in the furnace charge has been evaluated, the ohmic

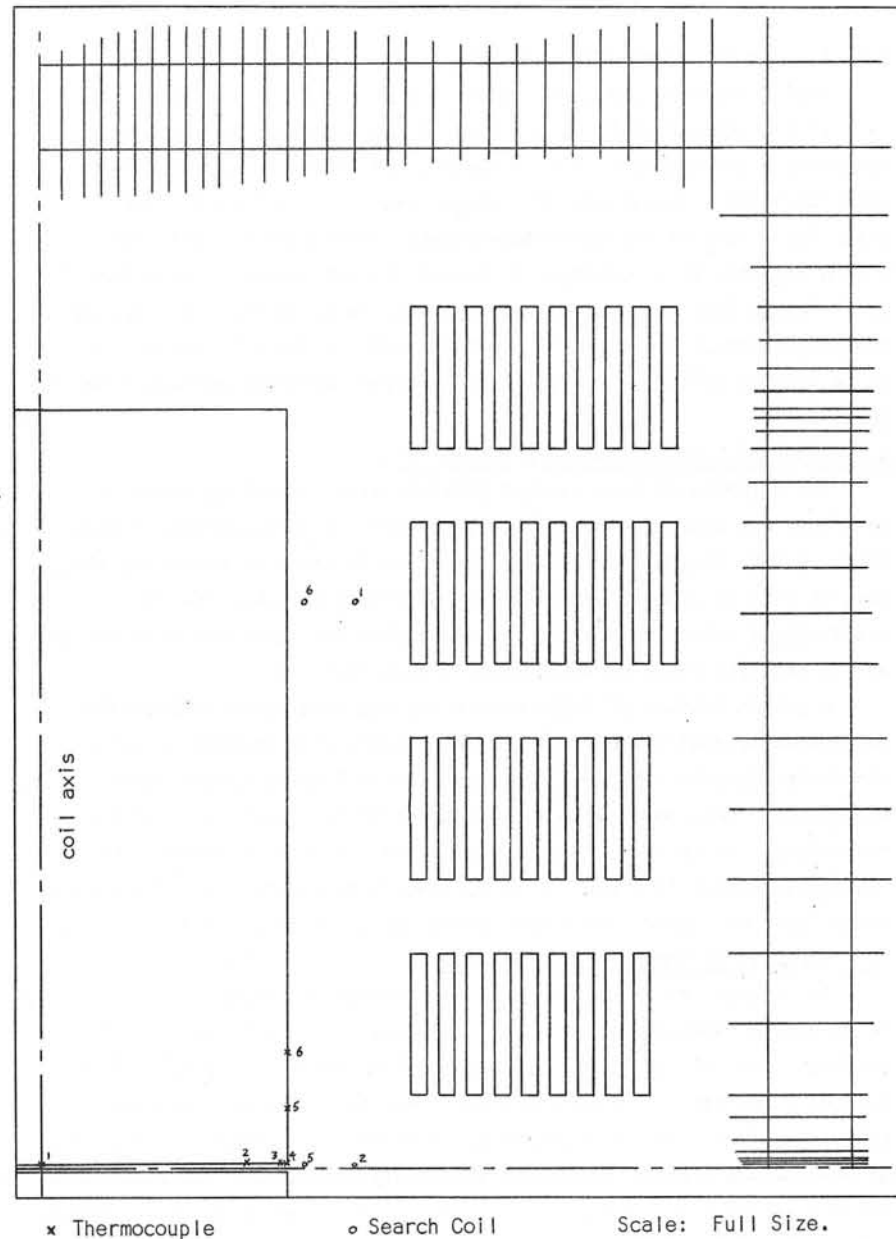


Figure 1 Cross-section of Top Half of 2 MVA Inductor showing Billet, Multi-layer Winding and Finite Difference Mesh

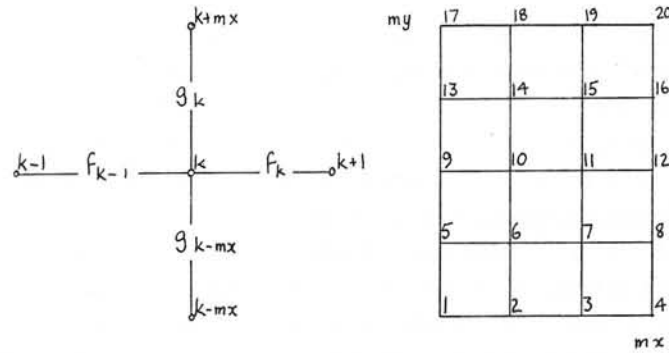
and eddy current winding losses can be simply calculated using the magnetic field passing through each strand. The slight difference between the current distribution initially assumed within each strand, and that which actually occurs as a result of the eddy currents, has negligible effect on the actual magnetic field distribution.

3. Method of Solving Node Equations

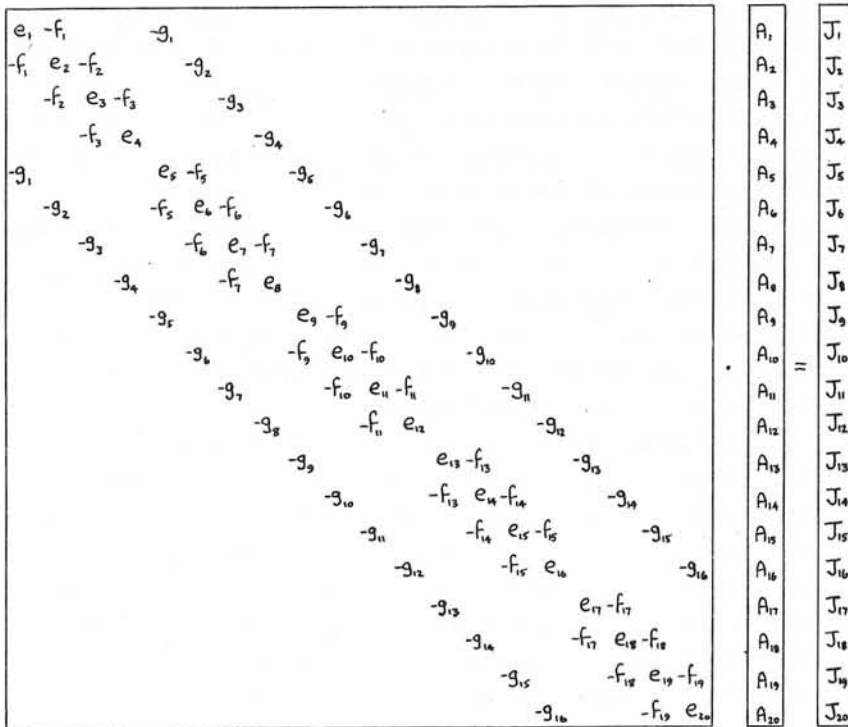
A finite difference method was selected, as, although finite element methods are advantageous with irregular geometries, the regular shapes of induction furnaces, with current flows parallel to the surfaces, allow a rectangular mesh to be suitably graded so that the use of excessively fine meshes in unimportant regions can be minimised. The use of a rectangular grid considerably simplifies mesh preparation, an essential feature if the performance of a furnace is to be assessed at short notice. Another important advantage of using a rectangular grid is that more efficient algorithms can be written for the solution of the node field equations; the problems of optimising the band width due to the use of an irregular mesh being avoided.

Iterative methods for solving the matrix of node coefficients have been attempted, but in spite of using line relaxation and other aids, it was found that convergence was relatively slow for complex coefficients with non-uniform meshes and varying physical properties. Problems were also experienced with defining convergence and selecting convergence factors in the complex plane.

A direct method of solution was adopted, and implemented on a UNIVAC 1108 computer as follows. A coefficient matrix for a small problem is shown in Fig. 2. The only core storage required to set up the matrix is for the real arrays f , g , r and the complex array A , A being used both for the source terms J and the solution. A Gaussian elimination method is used, and each line of $m \times$ coefficients of the upper triangular matrix is written to the NTRAN backing store while the next line is being formed, using a local complex array of size $m \times 2$. The rapid data transfer to the NTRAN drum occurring simultaneously with the main core calculations and combined with the low core storage requirement allows sets of up to 3000 equations of complex variables to be solved. The time taken on the UNIVAC 1108 is approximately $35 m \times 3 \mu s$. Fortunately, many induction furnace applications require



$$e_k = f_k + f_{k-1} + g_k + g_{k-mx} + Jr_k$$



To set a boundary node to zero, the coefficient e for that node is multiplied by 10^6 and the source term J is set to zero.

Figure 2. Coefficient Matrix for Small Finite Difference Grid.

long thin grids and so the band width mx is kept relatively small.

When evaluating the matrix coefficients, f, g and r, values of resistivity and permeability are taken appropriate to the local node temperature and magnetic field strength. An extensive error analysis undertaken for a one-dimensional case shows that the second order error for a node at the Curie temperature, where eddy currents pass from a magnetic to a non-magnetic region are not excessive provided a sufficiently fine mesh is taken. It should be noted that in a typical induction furnace the magnetic field strength in the coil airgap can be as high as 10^6 Am^{-1} , giving a billet surface relative permeability of about 3.

4. Method of Treating Magnetic Saturation.

The solution of eddy current problems with saturating magnetic materials has been attempted by many methods. A disadvantage of most of these is that they are relatively expensive in terms of computing time, and, as will be readily appreciated, not really suitable for the modelling of Induction heating processes with the attendant recalculation of the magnetic field as the furnace charge heats up.

A common feature of these more elaborate treatments of magnetic saturation is that the magnetic field strength H is assumed to be a sinusoidal function of time, the flux density B being grossly non-sinusoidal. Less commonly B is considered to be sinusoidal with H non-sinusoidal. It is the author's opinion that in reality, neither of these assumptions is true. It is considered that both H and B are near sinusoidal, or rather that H and $\partial B / \partial t$ are near sinusoidal.

4.1 Analysis of Magnetic Field Waveforms.

It is usual to connect power factor correction capacitors across the mains supply terminals of induction furnaces, and other low power factor devices. For optimum power factor correction the reactive components of current circulate in the series circuit formed by the coil and the capacitors, the value of capacitance being chosen so that the reactance of this series circuit is zero at the supply frequency. The magnitude, however, of this series reactance is much greater at higher frequencies, and so any higher harmonics in the current, and hence airgap and furnace charge surface magnetic field strength waveforms are heavily damped.

Two other features of induction furnace installations merit attention. Firstly, the voltage applied to the coil is known to be

sinusoidal as the load taken by the furnace has little or no effect on the supply system. Secondly it is usual to leave a fairly substantial distance between the furnace charge and the coil to allow for mechanical clearances and thermal insulation.

The significance of these last two points can be demonstrated by considering a very long uniformly wound coil of cross-section area A_c . Inside this coil, parallel to its axis is placed a magnetic core of uniform cross-section area A_m . This magnetic core has a typical B-H characteristic, but has infinite resistivity so that no eddy currents are induced in it. In such a case the magnetic field strength H inside the coil is therefore everywhere parallel to the axis of the coil and of constant magnitude both within the magnetic core, and in the airgap between the coil and the core. The flux density in the magnetic core is μH where μ is a function of H . The instantaneous voltage/turn in the coil is given by

$$v = \frac{\partial}{\partial t} (H(\mu A_m + \mu_0(A_c - A_m))) \quad 4.1$$

$$= A_m \frac{\partial}{\partial t} (\mu H) + \mu_0(A_c - A_m) \frac{\partial}{\partial t} (H) \quad 4.2$$

Now if

$$v = V \cos \omega t \quad 4.3$$

both sides of equation 4.1 can be integrated with time, and if μ is represented as a function of H by, for instance, the Fröhlich equation

$$\mu = a/(b + |H|) + c \quad 4.4$$

a table of instantaneous values of H can be calculated corresponding to a number of points on the voltage cosine wave. It is then a simple matter using fast Fourier transforms to obtain a Fourier series expansion for H . From the table of instantaneous values of H it is possible to tabulate the flux density in the magnetic core from the product μH . Furthermore, the instantaneous values of flux density can be numerically differentiated to tabulate the expression $\partial(\mu H)/\partial t$. The accuracy of all these numerical calculations can be checked by evaluating v from the computed values of the right hand side of equation 4.2.

This analysis was carried out for a wide range of typical magnetic field strengths, B-H characteristics (including hysteresis), and magnetic core cross-sectional areas. Characteristic waveforms of magnetic field strength, permeability, magnetic core flux density and the time derivative of magnetic core flux density, are shown in Figure 3. Although the wave

forms may look distorted, examination of the harmonic content shows in particular that the magnitude of the third harmonic of the H and $\partial(\mu H)/\partial t$ wave forms is less than 30% of the fundamental, no other harmonic being greater than 10%. Also the r.m.s. value of the fundamental is greater than 95% of the r.m.s. value of the total waveform.

4.2 Derivation of Concept of Effective Permeability.

Returning now to the eddy current analysis, equation 2.1 can be rewritten as

$$\text{curl}(\rho \text{curl} H) = -\partial(\mu H)/\partial t \quad 4.5$$

Now if H is $H' \sin \omega t$ and μ is constant in time, the right hand side of equation 4.5 becomes

$$\mu \partial(H' \sin \omega t)/\partial t = \omega \mu H' \cos \omega t \quad 4.6$$

or using the notation $H = \int (H' e^{j\omega t})$ the right hand side of equation 4.5 becomes $-j \omega \mu H$.

However if μ is a function of H , the above analysis of equation 4.5 is invalid. Looking again at Figure 3, it can be seen that if higher harmonic components are ignored H can still be written as $H' \sin \omega t$. Also $\partial(\mu H)/\partial t$ can be written as $H'' \cos \omega t$. If we define

$$H'' = \omega \mu' H' \quad 4.7$$

then a new right hand side of equation 4.5 can be written as $-j \omega \mu' H$.

μ' is defined as the effective permeability. In the analysis of Section 4.1 it was found that for a wide range of cases, μ' corresponded to the permeability calculated for a value of magnetic field strength equal to 0.75 to 0.85 of that of the peak of the fundamental component of the magnetic field strength wave form. It was also found that, for a wide range of typical B-H characteristics, this value of effective permeability is independent of the exact form of the B-H characteristic below the saturation knee.

It is admitted that the extension of the analysis of the magnetic core without eddy currents to cover the case of a magnetic core with eddy currents is not strictly valid. The significant point, however, is that although the relationship between B and H is grossly non-linear, there can exist waveforms of $\partial B/\partial t$ and H which are simultaneously near sinusoidal. As has been noted in Section 4.1 the physical mechanisms occurring in induction furnaces and other similar devices are such as to reduce the magnitude of higher harmonic components of magnetic field

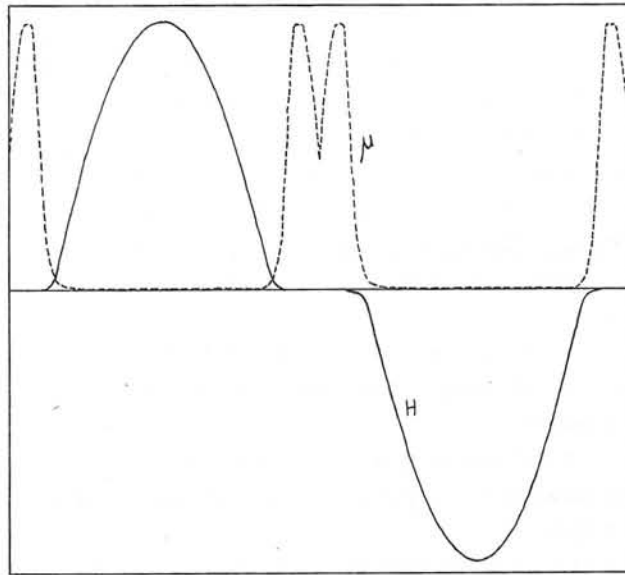


Figure 3(a) Waveform of Magnetic Field Strength H with Corresponding Permeability Waveform μ

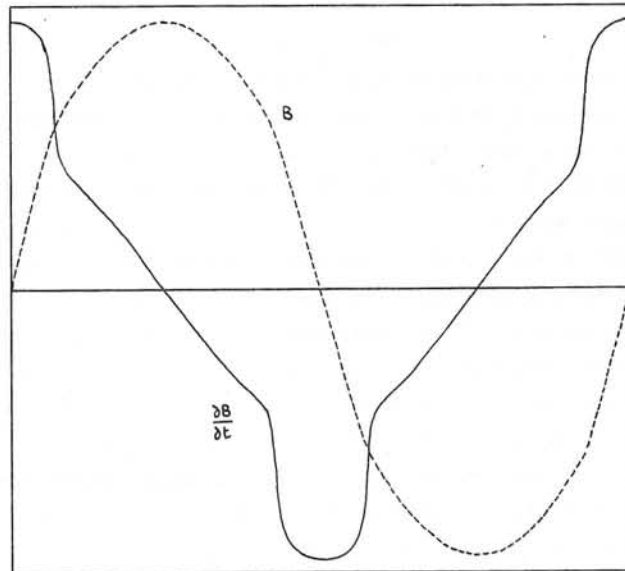


Figure 3(b) Waveforms of Magnetic Flux Density B and $\frac{\partial B}{\partial t}$ Corresponding with Magnetic Field Strength above.

strength and flux density.

It therefore seems reasonable to assume that for problems similar to those encountered in induction furnace analyses, that is with sinusoidal voltages, and with power factor convection tuned to the supply frequency, it is possible to use the simple concept of a constant effective permeability.

4.3 Simplified Treatment of Magnetic Saturation Used in Program.

The program only considers the fundamental of the magnetic field waveform and uses the concept of effective permeability introduced in Section 4.2. The permeability for each mesh element is calculated using a value 0.8 times the most up to date peak value of the magnetic field strength stored for that mesh element. After solution of the magnetic field, new values of the permeability are calculated and compared with the old values. If agreement is within previously determined limits, (usually 10% is adequate) the program continues to calculate the eddy current power distribution. Should agreement not be achieved, the process is repeated, convergence usually being very rapid with the direct method of solution of the node field equation used.

4.4 Representation of B-H characteristic.

Various methods of expressing permeability as a function of magnetic field strength have been tried, but it has been found adequate to use the simple Fröhlich expression of equation 4.3 where c tends to μ_0 for optimum fit for high values of H ($10^4 - 10^6 \text{ Am}^{-1}$). A rapid method of obtaining the coefficients a , b and c is to plot $1/(\mu - c)$ against H for various values of c and to select the value of c that gives the best straight line fit in the region near the maximum value of H that is expected. The slope of this straight line is $1/a$ and the y-intercept b/a .

5. Comparison of Predicted Performance with Measurements made on a 2 MVA Induction Furnace.

The validity of the mathematical model used in the analysis of induction furnaces, and the accuracy of the method of solution, were tested by comparing predicted performance with measurements taken during heating trials on the prototype 2 MVA 50 Hz cylindrical billet heater with coils using multi-layered windings shown in Figure 1. The winding losses, the terminal voltage, current and power, search coil voltages,

and temperature distribution in the billet, were continuously metered during the course of several heating cycles.

5.1 Tests with Non-magnetic Billets.

The programs were first tested comprehensively with non-magnetic billets, before the complications of magnetic saturation were introduced. The initial tests were made with copper billets, as the physical properties are well documented for the commercially pure metal. Excellent agreement was achieved with electrical measurements such as coil voltage, total power, power factor, coil losses and search coil voltages, and with the rate of temperature rise. A less constructive interpretation could be made of the temperature gradient through the billet however, as the high thermal conductivity of the copper prevented the surface to centre temperature difference from exceeding about 10°C. This was about the same value as the estimated error in the measurements.

In an attempt to increase the surface to centre temperature difference, the tests were repeated using a metal with a much lower thermal conductivity, namely stainless steel. As the physical properties are variable from sample to sample, it was necessary to have the thermal and electrical properties accurately measured as functions of temperature, specimens for this purpose being cut from the billet after the heating tests were completed. To facilitate the measurement of the thermal gradient, the billet was cut into two equal lengths. After thermocouples had been attached to the surfaces thus exposed, the two halves were packed closely together again as shown in Figure 1. A detailed study was also made of temperature corrections for heat lost along the thermocouple wires. The stainless steel billet was heated up to 1200°C and excellent agreement was again obtained, the predicted values of electrical and thermal parameters being within the estimated accuracy of the measured results.

5.2. Tests with Magnetic Billets.

A mild steel billet was prepared in a similar way to the stainless steel billet, and heated from cold, through the Curie temperature, in the 2MVA billet heater. Additional measurements were made by logging the coil voltage and current, together with five search coil voltages on a multi-track tape recorder. This enabled the waveforms to be analysed, and also the inductor power to be determined accurately by

taking a true product of the instantaneous current and voltage, and analysing the waveform of this product. Figure 4 shows the terminal voltage and current waveforms, together with the waveform of search coil 5 shown in Figure 1. The values of the third harmonics are 1%, 4% and 15% of the respective fundamentals. It can be seen that the harmonic content is small.

The calculated values of furnace power and voltage, winding losses and search coil voltages taken through the heating cycle were within 15% of the measured values. The coil current was taken as the common parameter for predicting the results. A comparison between calculated and measured values of temperature through the heating cycle can be seen in Figure 5 where the temperatures measured by thermocouples 1, 2 and 3-6, positioned as in Figure 1, are shown. The disparity between predicted and measured values around the 80 second mark largely reflects errors in the measured value taken for the Curie temperature of the billet material. This is a critical comparison as not only does the temperature rise show the instantaneous eddy current power and power distribution, but the graphs also reflect the time integral of power and power distribution.

While agreement is not perfect, the accuracy is quite adequate for predicting furnace performance. In particular the thermocouple readings giving the temperature distribution through the billet indicate that the eddy current heating has been calculated with reasonable accuracy.

While calculating the results discussed above, the effect of varying the values of physical properties of the billet material were assessed. The permeability measurements are the most difficult to obtain accurately, but it was found that for the above heating cycle the billet power varied as $\sqrt{\mu}$ for small changes in permeability. This agrees with the analytical results obtained for a cylindrical billet where the penetration depth

$$\delta = (2\rho/w\mu)^{\frac{1}{2}}$$

is small compared with the billet diameter.

As the sensitivity of the results to changes in the value taken for billet permeability is small, and as noted in Section 4.2 the results are independent of the exact shape of the B-H characteristic below the saturation knee, it is only necessary to measure values of permeability near the peak value of H expected during the course of the heating cycle.

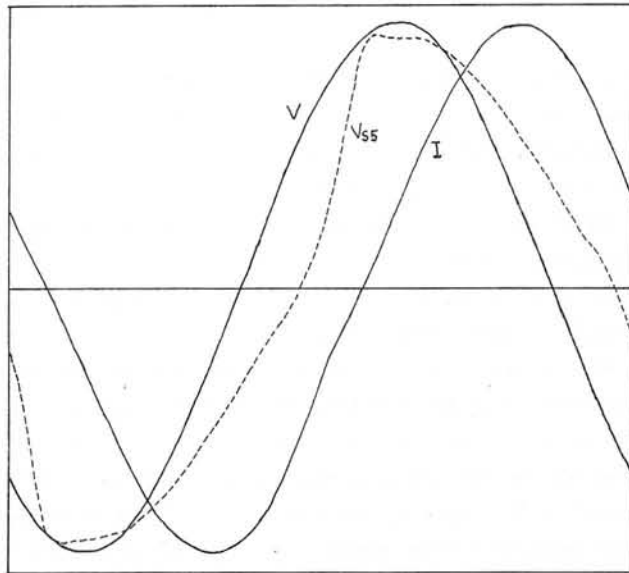


Figure 4. Waveforms of Coil Voltage V, Coil Current I and Search Coil 5 Voltage V_{ss} Taken 4 Seconds from Start of Test with Magnetic Billet.

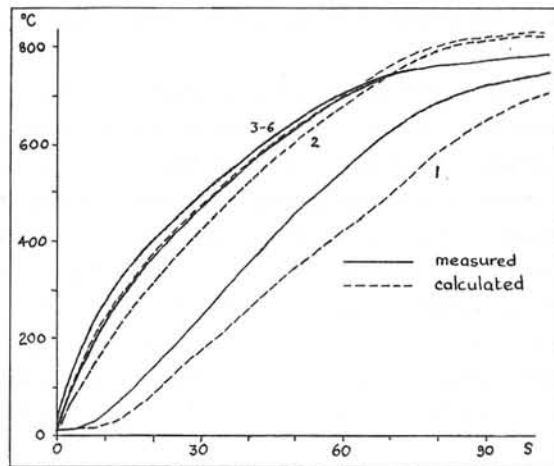


Figure 5. Comparison of Measured and Calculated Temperatures during test with Magnetic Billet.

6. Conclusions

The analytical techniques for modelling induction heating processes, and in particular the treatment of magnetic saturation giving rise to the concept of a linear effective permeability have been tested by comparing predicted and measured results of tests on a 2MVA 50 Hz billet heater.

With non-magnetic billets the agreement between measured and predicted results is very close, being within the accuracies of the techniques used to monitor the heating cycle, and also to measure the physical properties used for the theoretical calculations. Less good agreement is achieved for magnetic billets. The measurements are also more troublesome in this case, and it is difficult to separate out the errors due to the analytical methods used. However, the overall accuracy of the results is within the general tolerances within which the physical properties of industrial steels are known.

The analytical techniques outlined in this paper can therefore be used to compare different furnace designs and the performance of a furnace with different billet materials. While these techniques may not be applicable to all electromagnetic field problems, their use is recommended in many cases where, as in the prediction of induction furnace performance, it is necessary to obtain a theoretical assessment of problems to a greater accuracy and detail than by conventional design methods, and yet remain within a realistic costing for the study of a complete industrial process.

Acknowledgments

The author wishes to thank the Electricity Council for permission to publish this work. The author is also indebted to his colleagues, in particular Mr. I.G. Harvey, for providing the test results.

A METHOD OF CALCULATING EDDY CURRENT LOSSES IN THE ROTOR
RETAINING RING OF A TURBOGENERATOR DUE TO THE TOOTH RIPPLE FIELD

BY

D. Howe and T.G. Phemister

C.A. Parsons and Co. Ltd., Newcastle upon Tyne

A method has been developed for calculating the eddy current loss in the rotor retaining ring of a turbogenerator. The airspaces and the conducting ring are considered independently, the two regions being connected by the continuity of the field between the regions.

The airspace has a complicated geometry and a solution of the Laplacian field in this region has been based on the finite element method. The retaining ring has a simple geometry and a solution of the linear diffusion field has been obtained by an analytical method derived from the boundary conditions in that region. Interaction between the regions is calculated by iteration.

The method may have wider application to more general problems.

List of symbols

a	thickness of retaining ring.
a_i, b_i, c_i	coefficients.
A_m, B_m, C_m, D_m	
\underline{B}	magnetic flux density.
t	pole pitch of field component $\times 1/2 \pi$
B_x, B_y, B_z	components of flux density
c	length of retaining ring.
\underline{E}	electric field strength.
E_m, F_m, G_m, H_m	coefficients.
\underline{H}	magnetic field strength.
\underline{J}	current density
J	Lagrangian
k	harmonic number, number of stator slots

L	linear operator
p	radius of rotor surface.
P, Q, R, S	coefficients.
r, θ, z	cylindrical polar coordinates.
s	radius of stator bore.
t	time.
V_m	magnetic scalar potential.
V_m'	approximation to V_m
x, y, z	Cartesian coordinates.
Δ	element area.
θ	phase angle.
$\phi_m, \eta_m, \psi_m, \xi_m$	coefficients.
μ_0	permeability of free space.
μ_1	incremental relative permeability along x and z direction.
μ_2	incremental relative permeability along y direction.
ρ	resistivity.
ω	angular frequency.
∇^2	Laplacian operator.

Introduction

The continuing increase in the unit size of turbogenerators is being made possible by the use of improved materials and cooling methods, and by more sophisticated design techniques. With the development of more reliable methods of calculation it is possible to extend the limits of safe design.

The rotor end retaining ring is the most highly stressed component in the generator¹. The ring is normally shrunk on the end of the rotor body and incorporates some form of bayonet retention against axial forces. It is usual practice to use a non-magnetic steel, although a number of recent designs employ magnetic rings. Serious damage would result should the ring fail. It is important, therefore, to avoid possible areas of locally high temperature. One source of heating is produced by eddy currents induced in the ring by the stator tooth ripple flux.

Tooth ripples are pulsations of the main air-gap flux due to stator slotting. The flux density at points opposite a tooth is greater than at

those opposite adjacent slots, and the resultant ripple travels across the surface of the rotor and induces eddy currents therein. In order to calculate these eddy currents it is necessary to calculate the total field including the reaction field of the unknown eddy currents. The eddy current loss and heating will be strongest in the nose of the retaining ring, which extends into the air-gap, where the tooth ripple field is strongest. Unfortunately, because of differential thermal expansion, a concentration of loss in this area may impair the shrink fit.

The calculation of the eddy current losses is complicated, requiring the solution of Maxwell's equations in three-dimensional cylindrical coordinates. The approach which is described in this paper is based on solving the field in the airspaces and in the conducting ring independently; continuity of the magnetic field between the two regions is established by an iterative process. All fields within the end-region are assumed to vary sinusoidally around the periphery. The electromagnetic equations are formulated in terms of scalar potential, and a finite element numerical method is used for determining the field distribution in the airspaces. The eddy currents induced in the retaining ring are calculated analytically.

2 Method of analysis

Apart from the assumptions which have already been mentioned, two further simplifications have been introduced in order to make the problem mathematically tractable.

Firstly, the analysis is restricted to linear electromagnetic conditions. Except near the polar direct axis a magnetic ring will be heavily saturated by the excitation field. Since the tooth ripple flux is superimposed on this main flux the ring can be considered incrementally linear. The incremental permeability in the peripheral direction is assumed to be dB/dH . In the radial and axial directions the incremental permeability is taken as B/H .

Secondly, the rotor retaining ring of Fig. 1 is represented as a tubular region concentric with the rotor. Such a shape is amenable to analysis, and should not introduce undue error. No attempt has been made, however, to model the singularities at corners in the mathematical analysis.

The fundamental time component of the inducing field at the stator surface will have two harmonics $k \pm 1$, where k is the number of stator slots. Since they are of similar magnitude, they can be treated approximately as a single time and space harmonic $e^{j(\omega t - \theta)k}$; the relative error is at its greatest on the rotor surface, where it is about $2(s-p)^2/s^2$, p and s being the radii of the rotor surface and stator bore respectively. This fundamental harmonic will have a wavelength equal to the stator slot pitch, and may be calculated, in the air-gap, by the method described by Phemister². Alternatively, this field may be calculated by conformal transformation or, if saturation of the stator teeth is important by a numerical method such as finite elements. The distribution of the tooth ripple flux density around the stator end-surface may similarly be calculated by any appropriate technique. The fundamental component will be obtained from the Fourier expansion of the tooth ripple flux. Since the theory is in terms of sinusoidal functions of arbitrary wavelength and velocity it is possible to combine several such components together to represent any waveform of ripple flux density. In practice, however, only the fundamental is likely to be of importance.

2.1 Equations to be solved

Fig. 2 shows the model of the problem. In the airspace, region 1, cylindrical polar coordinates will be used. The magnetostatic field is described by Laplace's equation,

$$\nabla^2 V_m = 0.$$

When the scalar magnetic potential V_m varies sinusoidally in both space and time

$$V_m = V_m e^{j(\omega t - \theta)k}$$

and Laplace's equation can be reduced to two dimensions

$$\text{i.e. } \frac{\partial^2 V_m}{\partial r^2} + \frac{1}{r} \frac{\partial V_m}{\partial r} + \frac{\partial^2 V_m}{\partial z^2} - \frac{k^2}{r^2} V_m = 0 \quad \dots (1)$$

In the retaining ring, region 2, rectangular Cartesian coordinates are used as shown in Fig. 3. The skin depth at the frequencies considered is low enough to make this a good approximation. The tooth ripple frequency

is low enough for displacement currents to be neglected, and Maxwell's equations take the form

$$\text{Curl } \underline{H} = \underline{J}, \quad \dots (2)$$

$$\text{Curl } \underline{E} = - \frac{\partial \underline{B}}{\partial t} \quad \dots (3)$$

$$\text{and } \text{Div. } \underline{B} = 0. \quad \dots (4)$$

For the anisotropic permeabilities considered,

$$B_x = \mu_1 H_x, \quad \dots (5)$$

$$B_y = \mu_2 H_y$$

$$\text{and } B_z = \mu_1 H_z.$$

By manipulating equations 2 to 5, it can be shown that

$$\nabla^2 H_x - \frac{\mu_1}{\rho} \frac{\partial H_x}{\partial t} = \frac{\mu_1 - \mu_2}{\mu_1} \frac{\partial^2 H_y}{\partial x \partial y}, \quad \dots (6)$$

$$\frac{\partial^2 H_y}{\partial x^2} + \frac{\partial^2 H_y}{\partial z^2} + \frac{\mu_2}{\mu_1} \frac{\partial^2 H_y}{\partial y^2} - \frac{\mu_2}{\rho} \frac{\partial H_y}{\partial t} = 0, \quad \dots (7)$$

$$\nabla^2 H_z - \frac{\mu_1}{\rho} \frac{\partial H_z}{\partial t} = \frac{\mu_1 - \mu_2}{\mu_1} \frac{\partial^2 H_y}{\partial z \partial y}. \quad \dots (8)$$

Since all the field components are proportional to $e^{j(\omega t - y/b)}$, where $2\pi b$ is the wavelength of the spatial distribution, equations 6 to 8 can be written as

$$\frac{\partial^2 H_x}{\partial x^2} + \frac{\partial^2 H_x}{\partial z^2} - \left(\frac{1}{b^2} + \frac{j\omega\mu_1}{\rho} \right) H_x = - \frac{j}{b} \left(\frac{\mu_1 - \mu_2}{\mu_1} \right) \frac{\partial H_y}{\partial x}, \quad \dots (9)$$

$$\frac{\partial^2 H_y}{\partial x^2} + \frac{\partial^2 H_y}{\partial z^2} - \left(\frac{\mu_2}{\mu_1 b^2} + \frac{j\omega\mu_2}{\rho} \right) H_y = 0, \quad \dots (10)$$

$$\frac{\partial^2 H_z}{\partial x^2} + \frac{\partial^2 H_z}{\partial z^2} - \left(\frac{1}{b^2} + \frac{j\omega\mu_1}{\rho} \right) H_z = - \frac{j}{b} \left(\frac{\mu_1 - \mu_2}{\mu_1} \right) \frac{\partial H_y}{\partial z}, \quad \dots (11)$$

where H_x, H_y, H_z are now functions of r and z only.

Valid solutions of these equations must also satisfy the condition

that the normal component of current density is zero on all surfaces, which implies that

$$H_z = j b \frac{\partial H_y}{\partial z} \text{ at } x = 0 \text{ and } x = a \quad \dots (12)$$

$$\text{and } H_x = j b \frac{\partial H_y}{\partial x} \text{ at } z = 0 \text{ and } z = c. \quad \dots (13)$$

2.2 Solution for potential field in airspace

The general Lagrangian function for Laplace's equation is

$$J(V_m') = 2 \langle V_m', g \rangle - \langle V_m', L V_m' \rangle.$$

Therefore the variational expression for equation (1) is

$$J(V_m') = \iint_R \left[r \left(\frac{\partial V_m'}{\partial x} \right)^2 + r \left(\frac{\partial V_m'}{\partial z} \right)^2 + \frac{k^2}{r} (V_m')^2 \right] dx dz - \int_L V_m' r \frac{\partial V_m'}{\partial n} dl \quad \dots (14)$$

the line integral is zero for the appropriate boundary conditions. Natural Neumann boundary conditions are given by including the additional term

$$\int_L V_m' \frac{\partial V_m'}{\partial n} dl$$

If 1st order triangular elements are assumed, the trial function V_m' is expressed as a linear function in r and z of the three vertex values.

$$\text{i.e. } V_m'(r, z) = \frac{1}{2\Delta} \sum_{i=1}^3 (a_i + b_i r + c_i z) V_{mi}'$$

in which the coefficients depend on the vertex coordinates according to,

$$a_1 = r_3 z_2 - r_2 z_3,$$

$$b_1 = z_3 - z_2,$$

$$c_1 = r_2 - r_3, \text{ etc.}$$

By minimizing the Lagrangian equation 14, with respect to the vertex values of V_m' at each node the problem is reduced to the inversion of a matrix of finite order. The coefficients of the resulting matrix can be derived explicitly in terms of the vertex coordinates.

2.3 Boundary conditions on the surface of the retaining ring

It is shown in the appendix that, if a certain condition is satisfied, the following iterative process is exponentially convergent:

- (1) An assumed normal flux density on the surface of the retaining ring is used as a boundary condition for the solution of Laplace's equation in the airspace.
- (2) H_y on the surface of the retaining ring is calculated from this solution.
- (3) Equations 9 to 11 are solved with this H_y as a boundary condition. This gives a new normal flux density to continue the iteration.

Zero normal flux density is a convenient starting point. Convergence can be improved by a suitable weighting of two consecutive solutions.

Over the rotor pole, where the retaining ring is little saturated, the condition for convergence breaks down. An alternative iterative process, with normal flux density used as the boundary condition for the retaining ring, and H_y as boundary condition for the airspace, is then exponentially convergent; this is not discussed in the present paper.

2.4 Solution for the diffusion field in the retaining ring

Completely general solutions of the field equations 9, 10 and 11 for the conducting region of Fig. 3 are presented, and then these solutions are reduced for the particular case of tooth ripple losses.

The method of solution begins by assigning a system of parameters that define H_y at the surface of the ring of Fig. 3:

$$\begin{aligned} H_y &= P \text{ at } x = 0, z = 0, \\ &Q \text{ at } x = 0, z = c, \\ &R \text{ at } x = a, z = 0, \\ &S \text{ at } x = a, z = c, \end{aligned}$$

$$\begin{aligned} H_y &= P + (Q - P)\frac{z}{c} + \sum_{m=1}^M A_m \sin \frac{m\pi z}{c} \text{ at } x = 0, \\ &= R + (S - R)\frac{z}{c} + \sum_{m=1}^M B_m \sin \frac{m\pi z}{c} \text{ at } x = a, \\ &= P + (R - P)\frac{x}{a} + \sum_{n=1}^N C_n \sin \frac{n\pi x}{a} \text{ at } z = 0, \\ &= Q + (S - Q)\frac{x}{a} + \sum_{n=1}^N D_n \sin \frac{n\pi x}{a} \text{ at } z = c. \end{aligned}$$

At each iteration these parameters can be obtained by Fourier analysis of the H_y from the solution in the airspace.

It may be verified that, if

$$\begin{aligned} \phi_m &= \sqrt{\frac{m^2\pi^2}{c^2} + \frac{\mu_2}{\mu_1 b^2} + \frac{j\omega\mu_2}{\rho}}, \quad \dots(15) \\ \psi_n &= \sqrt{\frac{n^2\pi^2}{a^2} + \frac{\mu_2}{\mu_1 b^2} + \frac{j\omega\mu_2}{\rho}}, \end{aligned}$$

$$\begin{aligned} \text{then } H_y &= \left[P + (Q - P)\frac{z}{c} \right] \frac{\sinh \phi_0 (a - x)}{\sinh \phi_0 a} + \left[R + (S - R)\frac{z}{c} \right] \frac{\sinh \phi_0 x}{\sinh \phi_0 a} \\ &+ \sum_{n=1}^{\infty} \frac{2\phi_0^2}{n\pi\psi_n^2} \left[P - (-1)^n R \right] \frac{\sinh \psi_n (c - z)}{\sinh \psi_n c} \sin \frac{n\pi x}{a} \\ &+ \sum_{n=1}^{\infty} \frac{2\phi_0^2}{n\pi\psi_n^2} \left[Q - (-1)^n S \right] \frac{\sinh \psi_n z}{\sinh \psi_n c} \sin \frac{n\pi x}{a} \\ &+ \sum_{n=1}^N \left[\frac{C_n \sinh \psi_n (a - z) + D_n \sinh \psi_n z}{\sinh \psi_n c} \right] \sin \frac{n\pi x}{a} \\ &+ \sum_{m=1}^M \left[\frac{A_m \sinh \phi_m (a - x) + B_m \sinh \phi_m x}{\sinh \phi_m a} \right] \sin \frac{m\pi z}{c}. \quad \dots(16) \end{aligned}$$

It follows that, if

$$\eta_m = \sqrt{\frac{m^2\pi^2}{c^2} + \frac{1}{b^2} + \frac{j\omega\mu_1}{\rho}}$$

$$\text{and } \xi_n = \sqrt{\frac{n^2\pi^2}{a^2} + \frac{1}{b^2} + \frac{j\omega\mu_1}{\rho}},$$

$$H_x = \frac{j}{b\eta_0^2} \frac{\partial H_y}{\partial x} + \sum_{m=1}^{\infty} \left[\frac{E_m \cosh \eta_m (a-x) + F_m \cosh \eta_m x}{\sinh \eta_m a} \right] \sin \frac{m\pi z}{c} + \sum_{n=0}^{\infty} \left[\frac{G_n \sinh \xi_n (c-z) + H_n \sinh \xi_n z}{\sinh \xi_n c} \right] \cos \frac{n\pi x}{a} \quad \dots (17)$$

and similarly for H_z .

The coefficients of equation (17) can be found from equations (16) and (13). Similarly the coefficients of the expression for H_z can be found from the condition of equation (12). Equation (17) then becomes

$$H_x = \frac{j\sqrt{\frac{\mu_2}{\mu_1}}}{b\eta_0 \sinh \phi_0 a} \left\{ \left[R + (S-R)\frac{z}{c} \right] \cosh \phi_0 x - \left[P + (Q-P)\frac{z}{c} \right] \cosh \phi_0 (a-x) \right\} - \frac{\omega\mu_1 b}{\rho a \eta_0^2 \sinh \xi_0 c} \left[(R-P) \sinh \xi_0 (c-z) + (S-Q) \sinh \xi_0 z \right] + \frac{2j\mu_2}{ab\mu_1} \sum_{n=1}^{\infty} \left\{ \left[P - (-1)^n R \right] \sinh \psi_n (c-z) + \left[Q - (-1)^n S \right] \sinh \psi_n z \right\} \frac{\cos \frac{n\pi x}{a}}{\psi_n^2 \sinh \psi_n c} + \frac{\pi j}{ab\eta_0^2} \sum_{n=1}^N n \left\{ \left[\frac{C_n \sinh \psi_n (c-z) + D_n \sinh \psi_n z}{\sinh \psi_n c} \right] + \frac{j\omega\mu_1 b^2}{\rho} \left[\frac{C_n \sinh \xi_n (c-z) + D_n \sinh \xi_n z}{\sinh \xi_n c} \right] \right\} \cos \frac{n\pi x}{a}$$

$$+ \frac{j}{b\eta_0^2} \sum_{m=1}^M \left\{ \phi_m \left[\frac{B_m \cosh \phi_m x - A_m \cosh \phi_m (a-x)}{\sinh \phi_m a} \right] - \frac{j m^2 \pi^2 \omega \mu_1 b^2}{\rho c^2 \eta_m} \left[\frac{A_m \cosh \eta_m (a-x) - B_m \cosh \eta_m x}{\sinh \eta_m a} \right] \right\} \sin \frac{m\pi z}{c}, \quad \dots (18)$$

and similarly for H_z .

For the particular case of tooth ripple, considerable simplifications can be made since P, Q, A_m and D_n are all zero, and the hyperbolic functions of z and c can be replaced by exponentials, to give:

$$H_x = j\sqrt{\frac{\mu_2}{\mu_1}} \left[\frac{R + (S-R)\frac{z}{c}}{b\eta_0 \sinh \phi_0 a} \right] \cosh \phi_0 x - \frac{\omega\mu_1 b}{\rho a \eta_0^2} \left[R e^{-\xi_0 z} + S e^{-\xi_0 (c-z)} \right] - \frac{2j\mu_2}{ab\mu_1} \sum_{n=1}^{\infty} \frac{(-1)^n}{\psi_n^2} \left[R e^{-\psi_n z} + S e^{-\psi_n (c-z)} \right] \cos \frac{n\pi x}{a} + \frac{\pi j}{ab\eta_0^2} \sum_{n=1}^N n C_n \left[e^{-\psi_n z} + \frac{j\omega\mu_1 b^2}{\rho} e^{-\xi_n z} \right] \cos \frac{n\pi x}{a} + \frac{j}{b\eta_0^2} \sum_{m=1}^M B_m \left[\phi_m \frac{\cosh \phi_m x}{\sinh \phi_m a} + \frac{j m^2 \pi^2 \omega \mu_1 b^2}{\rho c^2 \eta_m} \frac{\cosh \eta_m x}{\sinh \eta_m a} \right] \sin \frac{m\pi z}{c}, \quad \dots (19)$$

and similarly for H_z .

3 Calculation of eddy current distribution

It now remains to state the relevant boundary conditions for the problem. In region 1, Fig. 2, the field stimulus, which does not include the field of the eddy currents, is the normal component of tooth ripple flux density over the stator surface, νw . The boundaries w and ws are assumed to be flux lines. On the first iteration, when the retaining ring is represented as an impermeable surface, the part of the boundary prs is also a flux line. At the rotor surface, up , the scalar magnetic potential is arbitrarily set to zero. The potential function calculated by the finite element method of section 2.2 simultaneously meets these boundary conditions and satisfies the field equation (1).

The tangential field, H_y , at the surface of the retaining ring is calculated from

$$\underline{H} = -\nabla V_m.$$

Thus the constants in the solutions of section 2 can be evaluated.

A correction to the normal component of the field at the surface of the ring is found directly in terms of the parameters derived from the boundary condition, and immediately incorporated into the finite element formulation. In this way interaction between the ring and the airspace can be calculated to any desired accuracy. It will be noted that the 'source' distribution is modified on successive iterations whilst the coefficient matrix for the finite element solution need be assembled only once.

Finally, the eddy current density is obtained from equation (2).

Conclusions

Analytical solutions have been formed in three-dimensional Cartesian coordinates for the diffusion equation applying to a conducting annulus in a rotating harmonic field. Additionally, a numerical solution is presented for Laplace's equation in three-dimensional cylindrical coordinates. These solutions have been applied to the calculation of eddy currents induced in the rotor retaining ring of a turbogenerator by the tooth ripple field. The conducting and non-conducting regions are connected by the continuity of the field between the regions.

An alternative iterative solution could be developed for regions of high permeability where the present method breaks down.

The solutions may be applied to the study of eddy currents induced by rotating harmonic fields over a wide frequency range. At low frequencies, however, the magnetising force at the inner surface of the ring may no longer be negligible. Therefore in calculating the effect of asynchronous operation, for example, it will be necessary to apply the general solutions and include the area occupied by the rotor end windings as an additional connected region.

Acknowledgements

The authors wish to thank C.A. Parsons and Company Limited for permission to publish this paper.

References

- 1 VICKERS, V.J. Recent trends in turbogenerators. Proc. IEE, 1974, 121, (11R), p1273-1306.
- 2 PHEMISTER, T.G. An analytical method of calculating magnetic fields in slotted regions. COMPUMAG, 1976.

APPENDIX

Condition for the convergence of the iterative procedure

It is possible to investigate the convergence of the iterative procedure in a simple model. A two-dimensional field will be considered, with the retaining ring represented by a semi-infinite slab whose boundary with a semi-infinite airspace is at $x = 0$. All fields will be proportional to $e^{j(\omega t - y/b)}$.

If H_0 is the value of H_y on the boundary of the slab, then the solutions of equations (9) to (13) are

$$H_y = H_0 e^{-\phi_0 x},$$

$$H_x = \frac{-j\mu_2 e^{-\phi_0 x}}{\phi_0 b \mu_1},$$

where ϕ_0 is given by equation (15).

Using

$$H_x = \frac{-j\mu_2 H_0}{\phi_0 b \mu_0}$$

as the boundary condition for the solution in air gives

$$H_x = \frac{-jH_0 e^{x/b}}{\phi_0 b} \frac{\mu_2}{\mu_0},$$

$$H_y = \frac{-H_0}{\phi_0 b} \frac{\mu_2 e^{x/b}}{\mu_0}.$$

The iterative procedure will be exponentially convergent if the ratio of the new H_y to the old H_y is less than 1 in absolute value. Thus the iteration will converge if

$$\frac{\mu_0 b |\phi_0|}{\mu_2} > 1.$$

Because the space harmonic number is high and the skin-depth in the retaining ring is small compared with the radius, this criterion for convergence can be applied with little error to the problem of tooth ripple. For the particular generators considered, it guaranteed convergence if $\mu_2 < 10 \mu_0$ for two-pole or $\mu_2 < 14 \mu_0$ for four-pole machines. These conditions are certainly satisfied over the heavily saturated parts of the retaining ring since

$$\mu_2 = \frac{\partial B}{\partial H}.$$

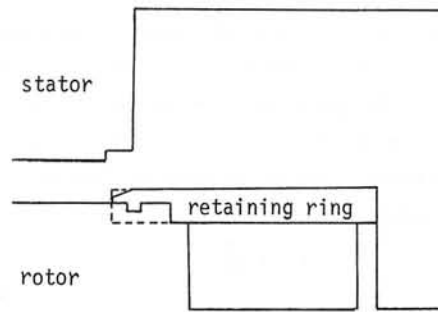


FIG. 1 Representation of rotor retaining ring by tubular region

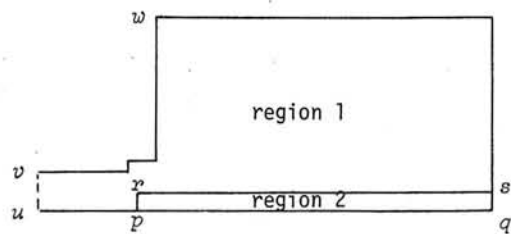


FIG. 2 Model of the field regions

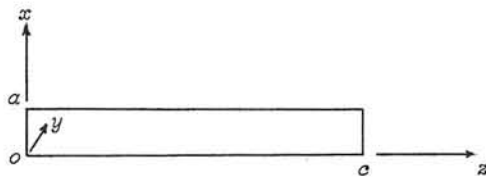


FIG. 3 Model of retaining ring

AN ANALYTICAL APPROACH FOR SOLVING TWO-DIMENSIONAL
SATURABLE EDDY-CURRENT PROBLEMS

by J. Muhlhaus, C.E.R.L. Leatherhead

1. INTRODUCTION

The solution of saturable (i.e. non-linear) eddy-current problems is important in many branches of heavy electrical engineering, in particular, with reference to static and rotating electrical machines. The magnetic characteristic of the iron present is usually represented by an algebraic approximation and for one-dimensional problems, numerical solution of the resulting non-linear differential equations is nearly always necessary. For two- and three-dimensional problems, until now, it has always been necessary. Numerical solutions, of course, imply large computing expenditure and anxiety over convergence. A new analytical method for solution of one- and two-dimensional eddy-current problems is presented here and results checked for a one-dimensional case against existing results obtained by a numerical method.

2. THEORY

The eddy-current problem to be solved is that of a semi-infinite ferromagnetic slab excited on its surface by a travelling magnetic field caused, for example, by a sinusoidal current sheet. In other words, both normal and transverse magnetic fields exist at the surface. The origin of coordinates is taken on the surface, the y-axis along the surface and the x-axis into the material. All currents flow in the z-direction, thus giving a two-dimensional problem with x and y variations only (e.g. the screening of a transformer tank from adjacent heavy current bus bars).

There are many algebraic approximations to the B-H curve, but if these B-H relations are substituted into Maxwell's equations, the eventual non-linear differential equations lend themselves only to solution by numerical methods. If power-series solutions are attempted, fields which are infinite at infinite depth (ascending powers of n) or infinite at the surface (ascending powers of $\frac{1}{x}$) are found. Series solutions in ascending powers of $\exp(-x)$ were found by the author to be invalid for various representations of the magnetisation curve. Power-series solutions are anyway very unmanageable.

For the present problem, however, four simplifications can be made which will eventually lead to an analytical solution.

(1) All time harmonics can be ignored. Although there will be harmonic loss components, they will in general be much smaller than the

loss due to fundamental frequency fields. This means that $\frac{\delta}{\delta t}$ in real time can be replaced by $j\omega$ in the complex domain.

(2) All transverse spatial harmonics can be ignored, that is, the spatial variation in the y-direction parallel to the surface can be considered as $\exp(-jqy)$. Thus if $H_x = h_x(x)\exp(-jqy)$, etc., the equations to be solved are

$$\frac{dh_y}{dx} + jqh_x = J \quad \dots (1)$$

$$J = (\omega\sigma/q)b_x \quad \dots (2)$$

$$\frac{dJ}{dx} = j\omega\sigma b_y \quad \dots (3)$$

$$\frac{db_x}{dx} = jqb_y \quad \dots (4)$$

(The capital letter J is used for current density to avoid confusion with $j = \sqrt{-1}$).

In the one-dimensional problem of a semi-infinite slab excited on the surface by a sinusoidal tangential magnetic field strength, analytical solutions are possible if the relationship between B and H is assumed to be a step-function, or of the step-function type. In this case a "separating surface" is postulated below the top surface of the slab beyond which no fields exist and at which the magnetic field strength is zero. The magnetic flux density is generally finite or indeterminate at the separating surface, which itself may vary in position with time. The permeability, therefore, will be infinite at the separating surface. An idea of Neiman (1949) was to postulate a separating surface of fixed depth β and to let the permeability variation be

$$\mu = \alpha/(\beta - x)^2, \quad 0 \leq x \leq \beta \quad \dots (5)$$

This idea is used in the present two-dimensional problem.

It is a necessary criterion that the pole-pitch should be large. This means that in the slab the flux density is predominately transverse. It is assumed that when the slab is saturated, the transverse magnetic field strength H_y in the slab is much larger than the radial magnetic field strength H_x and that H_x is small; consequently, while the relationship between B_y and H_y is non-linear, that between B_x and H_x is linear.

Combining this statement with the discussion of the previous paragraph, the final two assumptions are therefore

$$(3) \quad B_x = \mu_x H_x \quad \text{where } \mu_x \text{ is a constant, } \mu$$

$$(4) \quad B_y = \mu_y H_y \quad \text{where } \mu_y = \alpha / (\beta - x)^2$$

Appendix 1 gives the analysis of the behaviour of the magnetic field in a slab subject to assumptions (1) to (4) and it is shown that the implied B-H relationship is

$$B = kH^{1-2/n} \quad \dots (6)$$

3. COMPARISON OF THE NEW NON-LINEAR THEORY WITH EXISTING ONE-DIMENSIONAL THEORY

It is useful to consider the new non-linear theory under one-dimensional circumstances (i.e. $q=0$) with existing theories. In effect, the loss is being considered for a semi-infinite slab with tangential sinusoidal magnetic field strength on the surface. Equation (A1.38) is used.

The table shows results for rotor steel of conductivity 5×10^6 mho/m and Ferrosil 253 (a silicon steel) of conductivity 2.5×10^6 mho/m. The best existing non-linear theory is a finite-difference scheme using a Fröhlich approximation to the B-H characteristic, built into a computer program PIFE01 at the C.E.G.B. The values of loss per unit surface area and skin depth at 50 Hz predicted by this program are shown as case nos. 4 and 6 in the table. The other cases are calculations based upon the best-fitted first harmonic curves for rotor steel and Ferrosil 253, the first harmonic curve of the Fröhlich approximation to rotor steel and, for comparison, the actual d.c. curve for rotor steel. The loss per unit area for this last case (case no. 3) gives lower than predicted values at high magnetic field strengths (and thus high saturation) but the other cases agree very well with predictions.

All these results are very encouraging and seem to indicate that the new theory is practical for one-dimensional problems. It is reasonable to expect similarly reliable results for the two-dimensional problem subject to the assumptions of Section 2.

4. CONCLUSION

A new non-linear theory for ferromagnetic material has been developed which agrees closely with existing numerical solutions for one-dimensional eddy-current loss in iron.

5. REFERENCE

Neiman, L.R., 1949, "Surface Effects in Ferromagnetic Bodies". (In Russian), Gosenergoizdat, Moscow-Leningrad.

6. LIST OF SYMBOLS

B	magnetic flux density
H	magnetic field strength
I	current
J	current density
W	total power loss per unit surface area
k, n	constants in the magnetic characteristic $B = kH^{1-2/n}$
m	see equation (A1.10)
q	π /(pole pitch of travelling wave)
α, β	constants in the permeability relation $\mu = \alpha / (\beta - x)^2$
δ	skin depth
μ_x, μ_y	permeability in x and y directions
σ	conductivity
w	angular frequency

APPENDIX I

ANALYSIS OF LOSS IN A NON-LINEAR SLAB

If only fundamental frequency behaviour is required, Maxwell's equations for a non-linear material occupying the half plane $x > 0$ with $\frac{\partial}{\partial z} \equiv 0$ are

$$\frac{\partial H_y}{\partial x} - \frac{\partial H_x}{\partial y} = J_z \quad \dots (A1.1)$$

$$\frac{\partial J_z}{\partial x} = j\omega\sigma B_y \quad \dots (A1.2)$$

$$\frac{\partial J_z}{\partial y} = -j\omega\sigma B_x \quad \dots (A1.3)$$

$$\frac{\partial B_x}{\partial x} + \frac{\partial B_y}{\partial y} = 0 \quad \dots (A1.4)$$

where $B_x = \mu_x H_x$ and $B_y = \mu_y H_y$

If only the fundamental component of transverse spatial variation is required, $H_x = h_x(x) \exp(-jqy)$, $H_y = h_y(x) \exp(-jqy)$, etc. The equation relating h_x and h_y then becomes

$$\frac{d^2 h_y}{dx^2} = (j\omega\mu_x\sigma + q^2) (\mu_y/\mu_x) h_y \quad \dots (A1.5)$$

If the field distribution is linear in the x-direction, such that $\mu_x = \mu$, but non-linear in the y-direction, such that $\mu_y = \alpha/(\beta-x)^2$, then within the region $0 < x < \beta$,

$$\frac{d^2 h_y}{dx^2} = h_y \alpha (j\omega\sigma + q^2/\mu) / (\beta-x)^2 \quad \dots (A1.6)$$

Substituting a solution of the form $h_y = A(\beta-x)^{p_1} + B(\beta-x)^{p_2}$ requires that p_1 and p_2 are the roots of the equation

$$p^2 - p - \alpha(j\omega\sigma + q^2/\mu) = 0 \quad \dots (A1.7)$$

The required root for the present problem is the one whose real part is positive, so that h_y is zero and not infinite at $x = \beta$, and appropriately, either A or B must be zero. The solution can therefore be written as

$$h_y = H_t (1-x/\beta)^{n+jm} \quad \dots (A1.8)$$

where

$$n = \frac{1}{2} \left\{ 1 + \frac{1}{\sqrt{2}} \left[1 + 4\alpha q^2/\mu + \sqrt{(1 + 4\alpha q^2/\mu)^2 + (4\alpha\omega\sigma)^2} \right] \right\}^{\frac{1}{2}} \quad \dots (A1.9)$$

and

$$m = \omega\sigma\alpha/(2n-1) = \sqrt{\{n(n-1) - q^2\alpha/\mu\}} \quad \dots (A1.10)$$

Therefore

$$h_x = (H_t q/\beta) (m-jn) (1-x/\beta)^{n-1+jm} / (q^2 + j\omega\mu\sigma) \quad \dots (A1.11)$$

$$b_x = \mu h_x \quad \dots (A1.12)$$

$$b_y = (\alpha H_t / \beta^2) (1-x/\beta)^{n-2+jm} \quad \dots (A1.13)$$

As $H_Y = h_y \exp(j\omega t - jqy)$ and $B_Y = b_y \exp(j\omega t - qy)$, it is seen that the transverse B-H relation in the slab is given by

$$|B| = k|H|^{1-2/n} \quad \dots (A1.14)$$

where k is a material constant and the modulus of field strength H, of course, removes its oscillatory variation.

From equation (A1.9), the quantity α can be derived:-

$$\alpha = \{-q^2 + \sqrt{q^4 + 4n(n-1)\omega^2\sigma^2\mu^2/(2n-1)^2}\} (2n-1)^2 / (2\omega^2\sigma^2\mu) \quad (A1.15)$$

and from equation (A1.14), the penetration depth β can be deduced:-

$$\beta = H_t^{1/n} \sqrt{(\alpha/k)} \quad \dots (A1.16)$$

After further algebraic rearrangement, the field distribution can be written as

$$H_y = H_t (1-x/\beta)^{n+jm} \exp(-jqy) \quad \dots (A1.17)$$

$$H_x = -\{(H_t/\beta)(\alpha q/\mu)/[m-j(n-1)]\} (1-x/\beta)^{n-1+jm} \exp(-jqy) \quad \dots (A1.18)$$

$$B_y = (\alpha H_t / \beta^2) (1-x/\beta)^{n-2+jm} \exp(-jqy) \quad \dots (A1.19)$$

$$B_x = \mu H_x \quad \dots (A1.20)$$

As $x^{jm} = \exp\{jm \ln(x)\}$ it is seen that the fields decay in an oscillatory fashion as x approaches β . Clearly, given the appropriate values of k and n for the material under consideration, equations (A1.15), (A1.16) and (A1.10) can be used to define the field distribution uniquely in terms of surface tangential magnetic field strength H_t . In particular, the surface normal magnetic flux density is

$$B_n = -(H_t \alpha q/\beta) / [m-j(n-1)] \quad \dots (A1.21)$$

The power loss per unit surface area can be deduced either from the Poynting vector or from the integral of $\frac{1}{2\sigma} J_z J_z^*$ over the region $0 < x < \beta$. The result is

$$W = \frac{1}{2} (\omega\alpha H_t^2 m/\beta) / [m^2 + (n-1)^2] \quad \dots (A1.22)$$

It is useful to examine the skin depth δ . This quantity is different from the depth of penetration β , which marks where the magnetic field strength and current density become zero. It can be calculated only from one-dimensional fields and is defined as that depth within which the actual total current induced would, if uniformly distributed, produce the actual total loss. One-dimensional fields are given when $q = 0$, so the total one-dimensional current is

$$I = \int_0^\beta J_z dx = -\{H_t (2n-1)\sqrt{(n^2-n)}\} / \{[\sqrt{(n^2-n)} - j(n-1)] [n + j(n^2-n)]\} \quad \dots (A1.23)$$

The total loss per unit surface area is $\frac{1}{2} II^*/(\sigma\delta)$, and the one-dimensional

loss from equation (A1.22) is $\frac{1}{2} H_t^2 n / (\sigma\beta)$. Equating the two losses gives

$$\delta = \beta/n \quad \dots (A1.24)$$

To demonstrate that the field distribution reduces to the well-known distribution for the linear case as $n \rightarrow \infty$ and $k = \mu$, it is sufficient to express m and α in terms of n and then proceed to the limit. From equation (A1.16), $\beta \rightarrow \sqrt{(\alpha/k)}$ and from equation (A1.15), $\alpha \rightarrow \infty$. Thus and $\mu_y \rightarrow \alpha/\beta^2 = k = \mu$. By expanding $(n + jm)\ln(1-x/\beta)$ as a series, it is found that

$$\lim_{n \rightarrow \infty} (n+jm)\ln(1-x/\beta) = -x\sqrt{(q^2 + j\omega\mu\sigma)} \quad \dots (A1.25)$$

if the following identity is used:-

$$\sqrt{(q^2 + j\omega\mu\sigma)} = \frac{1}{\sqrt{2}} \{q^2 + \sqrt{(q^4 + \omega^2 \mu^2 \sigma^2)}\}^{\frac{1}{2}} + j \frac{1}{\sqrt{2}} \{-q^2 + \sqrt{(q^4 + \omega^2 \mu^2 \sigma^2)}\}^{\frac{1}{2}} \quad \dots (A1.26)$$

The consequent linear relations are

$$H_y = H_t \exp\{-x\sqrt{(q^2 + j\omega\mu\sigma)}\} \exp(-jqy) \quad \dots (A1.27)$$

$$H_x = -jqH_t \exp\{-x\sqrt{(q^2 + j\omega\mu\sigma)}\} \exp(-jqy) / \sqrt{(q^2 + \omega\mu\sigma)} \dots (A1.28)$$

The power loss reduces to

$$W = \frac{1}{2} (\omega\mu H_t^2 / \sqrt{2}) \left\{ \left[-q^2 + \sqrt{(q^4 + \omega^2 \mu^2 \sigma^2)} \right] / \left[q^4 + \omega^2 \mu^2 \sigma^2 \right] \right\}^{\frac{1}{2}} \quad \dots (A1.29)$$

and the skin depth becomes the well-known relation, $\delta = \sqrt{2} / \sqrt{(\omega\mu\sigma)}$.

When $n = 2$ and $k = B_s$, the B-H characteristic becomes the non-linear limiting curve, i.e., a step-function curve. (In actual practice, n will be very close to 2). Under such circumstances,

$$\alpha = 9 \{-q^2 + \sqrt{(q^4 + 8\omega^2 \sigma^2 \mu^2 / 9)}\} / (2\omega^2 \sigma^2 \mu) \quad \dots (A1.30)$$

$$m = (\omega\sigma\alpha) / 3 \quad \dots (A1.31)$$

$$\beta = H_t^{\frac{1}{2}} \sqrt{(\alpha/B_s)} \quad \dots (A1.32)$$

$$W = \frac{3}{2} \omega^2 \sigma (\alpha^3 H_t^3 B_s^3)^{\frac{1}{2}} / (9 + \omega^2 \sigma^2 \alpha^2) \quad \dots (A1.33)$$

and for a one-dimensional field with sinusoidal tangential excitation, $q = 0$ so that

$$W = \sqrt{(\omega B_s / \sigma)} H_t^{3/2} / \sqrt{(3/2)} \quad \dots (A1.34)$$

For small q and general n , the important parameters are:

$$\alpha = (2n-1)\sqrt{(n^2-n)} / (\omega\sigma) \quad \dots (A1.35)$$

$$m = \sqrt{(n^2-n)} \quad \dots (A1.36)$$

$$\beta = H_t^{1/n} \sqrt{(\alpha/k)} \quad \dots (A1.37)$$

$$W = \frac{1}{2} H_t^{2-1/n} \sqrt{(k\omega/\sigma)} \sqrt{\{n\sqrt{(n^2-n)} / [(n-1)(2n-1)]\}} \quad \dots (A1.38)$$

APPENDIX 2

DERIVATION OF THE BEST-FITTING B-H EQUATION

It is required to derive the best-fitting equation $B = kH^{1-2/n}$, where k and n are constants to be determined, to relate the first harmonic components of magnetic flux density and field strength for a given ferromagnetic material.

For an applied magnetic field strength $H = \hat{H} \cos \omega t$, the d.c. magnetisation curve can be used to obtain the waveform of the flux density B , which can be expanded in harmonics as

$$\Sigma B_r = \Sigma \hat{B}_r \cos r\omega t,$$

that is,

$$B(\omega t) = \hat{B}_1 \cos \omega t + \hat{B}_3 \cos 3\omega t + \hat{B}_5 \cos 5\omega t \dots \quad \dots (A2.1)$$

The amplitude of the first harmonic B_1 in particular is given by,

$$\hat{B}_1 = \frac{1}{\pi} \int_{-\pi}^{\pi} B(\omega t) \cos \omega t d(\omega t) \quad \dots (A2.2)$$

As $B(\omega t)$ is an odd function of H ,

$$\hat{B}_1 = \frac{4}{\pi} \int_0^{\pi/2} B(\omega t) \cos \omega t d(\omega t) \quad \dots (A2.3)$$

When the d.c. magnetisation curve is a step-function, the integral is soluble.

$$\hat{B}_1 = \frac{4B_s}{\pi} \int_0^{\pi/2} \cos \theta d\theta = \frac{4B_s}{\pi} = 1.273B_s \quad \dots (A2.4)$$

Otherwise, the integration must be done numerically, and a first harmonic characteristic can be drawn.

To obtain the best-fitting equation, its form must be redefined as

$$\log B = \log k + (1-2/n)\log H \quad \dots (A2.5)$$

where logarithms to the base 10 are convenient to use. Linear regression is used to derive the slope and intercept of this straight line:-

$$(1-2/n) = \frac{\{N\sum(\log B \log H) - \sum \log H \sum \log B\}}{\{N\sum(\log H)^2 - (\sum \log H)^2\}} \quad \dots (A2.6)$$

$$\log k = \frac{\{\sum \log B \sum (\log H)^2 - \sum \log H (\log B \log H)\}}{\{N\sum(\log H)^2 - (\sum \log H)^2\}} \quad \dots (A2.7)$$

where the summations are over N data points.

ACKNOWLEDGEMENT

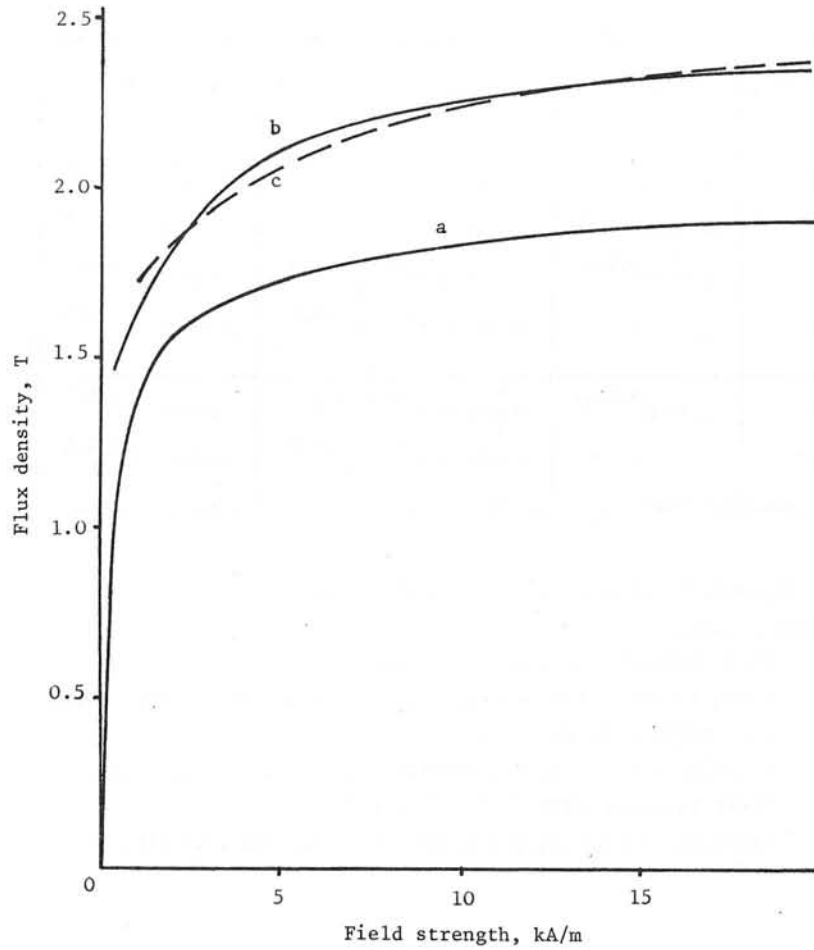
The work was carried out at the Central Electricity Research Laboratories and is published by permission of the Central Electricity Generating Board.

Case	Flux Density (T)	Loss per Unit Area (kW/m ²)	Skin Depth (mm)
1	0.763H ^{0.118}	0.322 x 10 ⁻⁵ H _t ^{1.559}	0.0313 H _t ^{0.441}
2	0.653H ^{0.128}	0.295 x 10 ⁻⁵ H _t ^{1.564}	0.0339 H _t ^{0.436}
3	0.693H ^{0.106}	0.307 x 10 ⁻⁵ H _t ^{1.553}	0.0324 H _t ^{0.447}
4	-	0.18 x 10 ⁻⁵ H _t ^{1.622}	0.0556 H _t ^{0.378}
5	1.18 H ^{0.0661}	0.574 x 10 ⁻⁵ H _t ^{1.533}	0.0348 H _t ^{0.467}
6	-	0.498 x 10 ⁻⁵ H _t ^{1.555}	0.0402 H _t ^{0.445}

N.B. magnetic field strength is in units of A/m

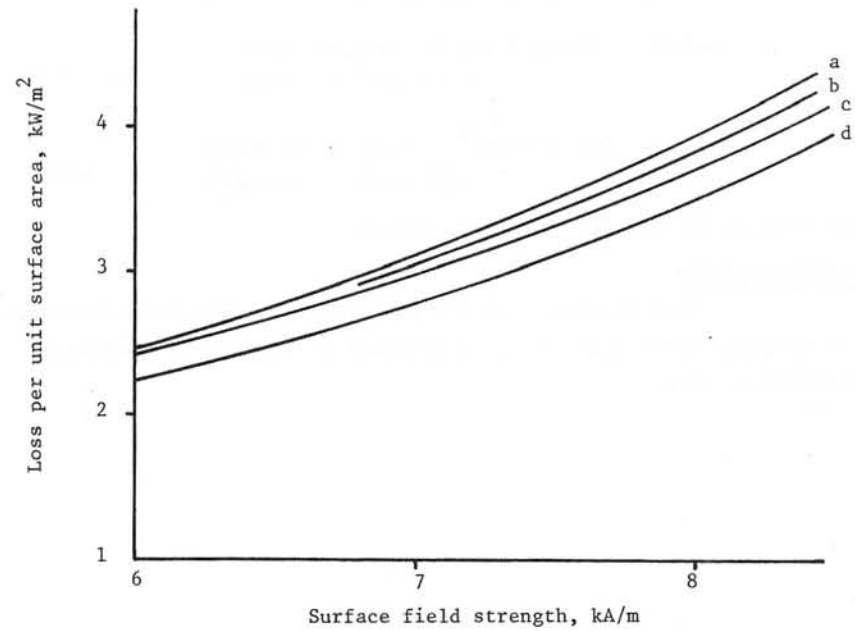
Identity of Cases:

- 1 first harmonic curve of rotor steel
- 2 first harmonic curve of Fröhlich approximation to rotor steel
- 3 d.c. curve of rotor steel
- 4 existing results using a numerical method for rotor steel
- 5 first harmonic curve of Ferrosil 253
- 6 existing results using a numerical method for Ferrosil 253



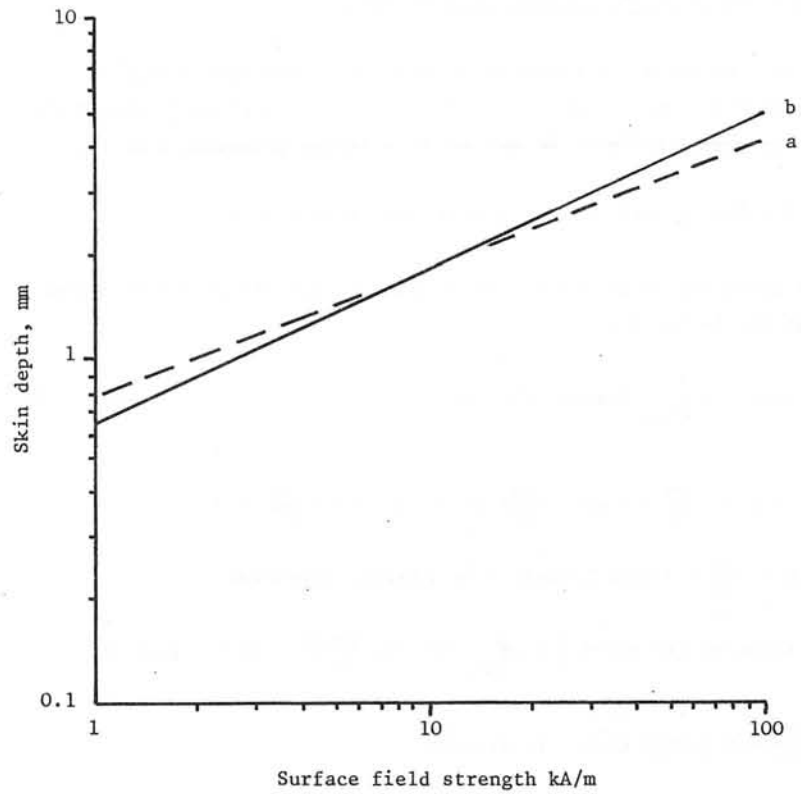
MAGNETIZATION CURVES FOR ROTOR STEEL

- a - d.c. curve
- b - first harmonic curve
- c - best fitted curve of the form $B = kH^\alpha$



LOSS IN ROTOR STEEL CAUSED BY A TANGENTIAL SINUSOIDAL MAGNETIC FIELD

- a - existing results using a numerical method
- b - new theory
- c - new theory using first harmonic curve of Fröhlich approximation
- d - new theory using d.c curve



VARIATION OF SKIN DEPTH IN ROTOR STEEL WITH SURFACE
MAGNETIC FIELD STRENGTH

- a - existing results using a numerical method
- b - new theory

CALCULATION OF EDDY CURRENTS IN A CONDUCTOR AND ITS SHEATH
BY A FINITE ELEMENT METHOD

by J.C. NEDELEC*, J.L. SABRIE** and J.C. VERITE***

INTRODUCTION AND HYPOTHESIS

The purpose of this work is to determine a map of currents everywhere in the set of conductors and sheaths connecting an alternator to its transformer. All these conductors and sheaths are interacting and eddy currents are developed in their volumes. When these currents are known, it will be easy to determine heatings and stresses appearing.

We suppose in this report there is one conductor C and one sheath G. The generalization to the case of several conductors and sheaths does not bring about new theoretical problems.

We consider the following hypothesis :

- The conductor and its sheath are both concentric cylinders in aluminium. They can be curved.

- We only calculate mean values of the currents according to the thickness which is supposed small. So the thickness will be neglected and current densities will be surfacic ones.

- We know the total applied current.

* Ecole Polytechnique - Centre de Mathématiques Appliquées - Palaiseau France.

** Electricité de France - Etudes et Recherches - Service ERMEL - Clamart - France.

*** Electricité de France - Etudes et Recherches - Service IMA - Clamart - France

EQUATIONS VERIFIED BY THE DENSITY OF CURRENT

Let the Maxwell's equations be $\text{curl } H = J$ and $\text{curl } E = -\frac{\partial B}{\partial t}$ where J is the current density, E the electric field, B the magnetic induction and H the magnetic field. We may define a vector potential A by :

$$B = \text{Curl } A \text{ with } \text{div } A = 0 \text{ so we obtain } \Delta A = -\mu J$$

$G(x,y)$ being the Green's function associated with the Dirichlet's problem we obtain for A :

$$A(x) = \mu \int_{G+C} G(x,y) \cdot J(y) \cdot dy \quad (1)$$

and $\text{curl } E = -\frac{\partial B}{\partial t} = -\text{curl} \left(\frac{\partial A}{\partial t} \right)$ gives $\text{curl} \left(E + \frac{\partial A}{\partial t} \right) = 0$

thus, $E + \frac{\partial A}{\partial t} = -\text{grad } V$, where V is a scalar potential.

$$\text{Equation (1) gives } \frac{J}{\sigma} + \mu \int_{G+C} G(x,y) \cdot \frac{\partial J(y)}{\partial t} \cdot dy = -\text{grad } V$$

with $\frac{\partial J(y)}{\partial t} = j\omega J(y)$ when J is harmonic.

Finally, the current density verifies the following equations :

$$\left\{ \begin{array}{l} J(x) + j\omega\sigma\mu \int_{G+C} G(x,y) \cdot J(y) \cdot dy = -\sigma \text{grad } V \end{array} \right. \quad (2)$$

$$\left\{ \begin{array}{l} J \cdot n = 0 \end{array} \right. \quad (3)$$

$$\left\{ \begin{array}{l} \text{div } J = 0 \end{array} \right. \quad (4)$$

Equation (3) expresses that current lines do not leave G or C , equation (4) expresses continuity of electric loads for a stationary mode.

SIMPLIFIED TWO-DIMENSIONAL PROBLEM

These three equations represent the general case of a three-dimen-

sional problem. A preliminary study has been worked out for a two-dimensional problem corresponding to an imaginary configuration of a rectilinear conductor and a sheath by the side of it and parallel to it (see figure 1). The study may then be realized in a plan perpendicular to their axis x, all the quantities being constant according to x.

For a two-dimensional problem $G(x,y) = \frac{1}{2\pi} \text{Log}(x-y)$ and equations (3) and (4) are automatically verified.

We have thus to solve the following equation :

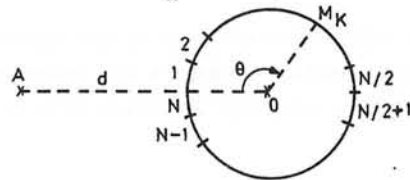
$$J(z) + \frac{j\omega\sigma\mu}{2\pi} \int_{G+C} J(y) \cdot \text{Log}|y-z| \, dS_y = \sigma(\text{grad } V + \lambda)$$

where λ is a constant vector due to the fact that grad V is not completely defined.

The sheath is then discretized in n sectors according to θ (see below), J being constant in each sector, and the equation becomes :

$$J_K = J_0 - \frac{j\omega\sigma\mu}{2\pi} \sum_{k'=1}^n \int_{S_{k'}} J_{k'} \cdot \text{Log}|M_K M_{k'}| \, dS_{k'} - \frac{j\omega\sigma\mu}{2\pi} I_A \text{Log}|AM_K|$$

Letter A refers to the conductor, M_K is a point in the Kth sector.



Thus, we obtain a complex linear system the solution of which gives the current anywhere in the sheath. The constant J_0 is calculated by expressing that the currents in the sheath and in the conductor are equal.

Then the magnetic induction has been calculated near G by the following formulas :

$$B_M = \text{curl } A_M = \begin{cases} \frac{1}{\rho} \frac{\partial A_M}{\partial \varphi} \\ - \frac{\partial A_M}{\partial \rho} \end{cases} \quad \text{with } A_M = \frac{\mu}{2\pi} \int_{G+C} J(M') \cdot \text{Log}|MM'| \, dM'$$

where A_M is the vector potential at point M.

THREE-DIMENSIONAL PROBLEM (see figure 2)

We now have $G(x,y) = \frac{1}{4\pi|x-y|}$

Let $J' \in L^2(R)$ with $\text{div } J' = 0$ in G and C, and let us rewrite equation (2) in a variational form :

$$\int_{G+C} J(x) \cdot J'(x) \cdot dS_x + \frac{j\omega\sigma\mu}{4\pi} \int_{G+C} \int_{G+C} \frac{j(y) \cdot J'(x) \cdot}{|x-y|} \, dS_x \, dS_y = \tag{2'}$$

$$\begin{aligned} \sigma V_{Ce} \int_{\Gamma_{Ce}} J' \cdot n_{Ce} \cdot d\Gamma_{Ce} + \sigma V_{Ge} \int_{\Gamma_{Ge}} J' \cdot n_{Ge} \cdot d\Gamma_{Ge} - \sigma V_{CS} \int_{\Gamma_{CS}} J' \cdot n_{CS} \cdot d\Gamma_{CS} - \\ - \sigma V_{GS} \int_{\Gamma_{GS}} J' \cdot n_{GS} \cdot d\Gamma_{GS} \end{aligned}$$

$\Gamma_{Ce}, \Gamma_{CS}, \Gamma_{Ge}, \Gamma_{GS}$ being respectively the extremities of the conductor and of the sheath.

The problem now is to solve the equations (2'), (3) and (4). We use a finite-element method where $J(x)$ is decomposed in a base of known functions w_i :

$$J(x) = \sum_{i=1}^n a_i \cdot w_i(x)$$

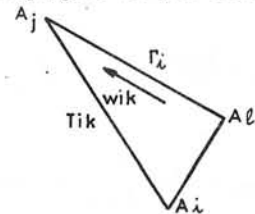
Then the problem is to determine the n unknowns a_i .

DESCRIPTION OF THE FINITE-ELEMENTS AND OF THE BASIC FUNCTIONS

Let T_h be a partition of G and C in triangles the vertices of which, A_i , are on G and C . We then define a set of vectorial functions w_{ik} :

- To one vertex A_i corresponds one function w_i .
 - S_i , support of w_i , is the set of triangles having A_i as vertex.
 - w_i is constant on each triangle and is in the plane of the triangle.
- w_i is then defined in the following manner :

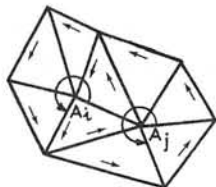
Let Γ_i be the boundary of S_i and n the vector perpendicular to Γ_i in the plane of a triangle T_{ik} of S_i . We take $w_{ik} \cdot n = 0$, w_{ik} being the restriction of w_i on T_{ik} . This condition defines the direction of w_{ik} , parallel to the side of T_{ik} belonging to Γ_i (see below)



The modulus of w_{ik} is defined by the relation :

$$\int_{A_i A_j} |w_{ik}| \cdot n \cdot dS = \pm 1 = - \int_{A_i A_k} |w_{ik}| \cdot n \cdot dS \text{ i.e. } w_{ik} \cdot n \cdot |A_i A_j| = \pm 1$$

We choose +1 or -1 to have the same direction or rotation for all the w_{ik} round the vertices A_i (see below).



w_{ik} are then completely defined.

We have just defined a set of functions but do these functions constitute a base of the functions which are constant on each triangle ?

Let us consider one cylinder C (conductor or sheath). Let N be the number of functions w_i on this cylinder.

It is easy to show that these N functions verify the relation :

$$\sum_{i=1}^N w_i(x) = 0 \quad \forall x \in C$$

Thus these functions don't constitute a base and in particular it can be shown that the circulation of a density of current defined by these functions is zero along any section of the cylinder. If we note that this circulation must be equal to the applied current which is known, the most natural idea is to replace one of the functions w_i by a function the support of which is the whole cylinder, which is constant and equal to the density of the applied current when any electric influence is neglected.

Thus the base of functions for a cylinder is constituted by the $N-1$ former functions w_i and the new special one.

Equations (3) and (4) are automatically verified by these functions. Equation (3) is verified because function w_{ik} is in the plane of triangle T_{ik} and equation (4) because function w_{ik} is constant on T_{ik} , so $\text{div } w_{ik} = 0$ on T_{ik} . We now have to solve only equation (2')

LINEAR SYSTEM OBTAINED

Let us always take the case of one conductor and one sheath. There are two special functions, one for the conductor and one for the sheath. Let w_{N-1} and w_N be these two functions if N is the total number of vertices on $G+C$.

If we replace $J'(x)_N$ in equation (2') successively by the N functions $w_i(x)$ and with $J(x) = \sum_{i=1}^N \alpha_i w_i(x)$ we obtain the following system : for k from 1 to N :

$$\int_{G+C} \left(\sum_i \alpha_i \cdot w_i(x) \right) \cdot w_k(x) \cdot dSx + \frac{j\omega\sigma\mu}{4\pi} \int_{G+C} \int_{G+C} \frac{\left(\sum_i \alpha_i w_i(x) \right) \cdot w_k(y)}{|x-y|} dSy dSx$$

$$= \sigma V_{Ce} \int_{\Gamma_{Ce}} w_k(x) \cdot n_{Ce} \cdot d\Gamma_{Ce} + \sigma V_{Ge} \int_{\Gamma_{Ge}} w_k(x) \cdot n_{Ge} \cdot d\Gamma_{Ge} - \sigma V_{CS} \int_{\Gamma_{CS}} w_k(x) \cdot n_{CS} \cdot d\Gamma_{CS}$$

$$- \sigma V_{GS} \int_{\Gamma_{GS}} w_k(x) \cdot n_{GS} \cdot d\Gamma_{GS}$$

Let us note that by construction, except for the two special functions, the circulation of w_i is equal to zero along the extremities of the cylinders. Thus, we obtain, for k from 1 to N :

$$\sum_{i=1}^N \alpha_i \left[\int_{S_i} w_i(x) \cdot w_k(x) \cdot dSx + \frac{j\omega\sigma\mu}{4\pi} \int_{S_i} \int_{S_k} \frac{w_i(x) \cdot w_k(y)}{|x-y|} dSx \cdot dSy \right]$$

$$= \begin{cases} 0 & \text{for } k < N-1 \\ \sigma V_e \int_{\Gamma_e} w_k(x) \cdot n_e \cdot d\Gamma_e - \sigma V_s \int_{\Gamma_s} w_k(x) \cdot n_s \cdot d\Gamma_s & \text{for } k = N \text{ or } N-1 \end{cases}$$

It is a symmetrical, linear and complex system of N equations with N unknowns α_i .

Let us rewrite it in the following partitionned form where A is an $(N-2) \times (N-2)$ matrix, u_N and u_{N-1} are vectors :

$$\begin{pmatrix} A & u_{N-1} & u_N \\ u_{N-1}^T & w_{N-1} & v_N \\ u_N^T & v_N & w_N \end{pmatrix} \begin{pmatrix} \alpha \\ \alpha_{N-1} \\ \alpha_N \end{pmatrix} = \begin{pmatrix} 0 \\ \beta_{N-1} \\ \beta_N \end{pmatrix}$$

α_{N-1} and α_N can be determined by expressing that the circulation of the current density at an extremity of each cylinder is equal to the applied

current, which is known.

Let I_C and I_G be the applied currents on the conductor and on the sheath and R_C and R_G be the radius.

$$\text{We have } \int_{\Gamma_{Ge}} J(x) \cdot n_{Ge} \cdot d\Gamma_{Ge} = I_G = \alpha_{N-1} \cdot w_{N-1} \cdot 2\pi R_G$$

$$\text{and } \int_{\Gamma_{Ce}} J(x) \cdot n_{Ce} \cdot d\Gamma_{Ce} = I_C = \alpha_N \cdot w_N \cdot 2\pi R_C$$

$$\text{Taking } w_{N-1} = I_G / 2\pi R_G \text{ and } w_N = I_C / 2\pi R_C \text{ we have } \alpha_{N-1} = \alpha_N = 1$$

We can then rub out the last two equations from the system. β_{N-1} and β_N which are the only terms where appear the applied tensions, are eliminated from the system. So we have only to know the applied currents and the system reduces to :

$$A\alpha + u_{N-1} \cdot \alpha_{N-1} + u_N \cdot \alpha_N = 0 \quad \text{i.e. } A\alpha = -u_{N-1} - u_N$$

It is an $(N-2) \times (N-2)$ linear, symmetrical and complex system.

CALCULATION OF THE COEFFICIENTS OF THE SYSTEM

Let a_{ij} be a term of the matrix A .

$$a_{ij} = \int_{S_i} w_i(x) \cdot w_j(x) \cdot dSx + \frac{j\omega\sigma\mu}{4\pi} \int_{S_i} \int_{S_j} \frac{w_i(x) \cdot w_j(y)}{|x-y|} dSx \cdot dSy$$

Thus, it is necessary, in order to determine the terms of A (or u_{N-1} and u_N), to calculate two types of integrals :

$$S_{ik} = \int_{S_i} w_i(x) \cdot w_k(x) \cdot dSx \quad \text{and} \quad D_{ik} = \int_{S_i} \int_{S_k} \frac{w_i(x) \cdot w_k(y)}{|x-y|} dSx \cdot dSy$$

In fact, S_i and S_k are sets of triangle. Thus, we have to calculate integrals over triangles :

$$\int_{T_j} w_{ij}(x) \cdot w_{kl}(x) \cdot dS_k \quad \text{and} \quad \int_{T_j} \int_{T_\ell} \frac{w_{ij}(x) \cdot w_{kl}(y)}{|x-y|} dS_x \cdot dS_y$$

$w_{ij}(x)$ and $w_{kl}(x)$ are constant or equal to zero on each triangle. So we can put the scalar products $w_{ij}(x) \cdot w_{kl}(x)$ and $w_{ij}(x) \cdot w_{kl}(y)$ out the integrals and we have to calculate :

$$\int_{T_j} dS_x \quad \text{and} \quad \int_{T_j} \left[\int_{T_e} \frac{dS_y}{|x-y|} \right] dS_x$$

The first integral is equal to the surface of T_j .

As for the second integral we have to consider several cases, according as the triangles are far from each other, adjacent or identical.

- If they are far from each other, we calculate the product of the surfaces divided by the distance between the centers of gravity.

- if they are adjacent we use twice a Gauss product formula of degree 5 with 7 points.

- if they are identical the inner integral is analytically calculated and the outer one by a 64 points, 15 th degree triangular Gauss product formula.

RESOLUTION OF THE SYSTEM

The resolution of the system has been performed by a classical direct method which is not necessary to describe here.

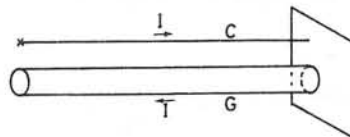


FIGURE 1

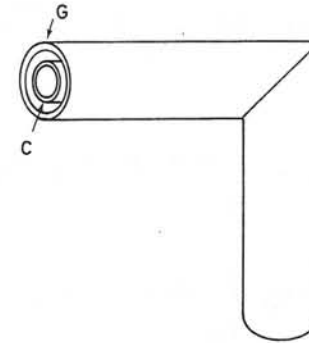


FIGURE 2

BIBLIOGRAPHY

- [1] J.L. SABRIE - Liaison alternateur-transformateur ; Examen des méthodes possibles d'étude des efforts et échauffements. EDF - Rapport interne M16/369 - Novembre 1974
- [2] J.C. VERITE - Influences réciproques d'un conducteur filiforme et d'un conducteur cylindrique parcourus par un courant alternatif. EDF - Rapport interne - HI 1806/02 - Mars 1975
- [3] H.A. STROUD - Approximate calculation of multiple integrals. Prentice-Hall - 1971
- [4] J.L. HESS and A.M.O. SMITH - Calculation of potential flow about arbitrary bodies.
- [5] O.C. ZIENKIEWICZ and Y.K. CHEUNG - The finite element method in structural and continuous mechanics - Mc Graw-Hill - 1967
- [6] R.L. STOLL - The analysis of eddy currents. Clarendon-Press - Oxford - 1974
- [7] J.C. NEDELEC - Curved finite element methods for the solution of singular integral equations on surfaces in R^3 . Rapport - Centre de Mathématiques Appliquées - Ecole Polytechnique - 1976.
- [8] M. DJAOUA - Méthode d'éléments finis pour la résolution d'un problème extérieur dans R^3 . Rapport - Centre de Mathématiques Appliquées - Ecole Polytechnique - 1976.

NUMERICAL RESULTSTwo-dimensional problem

The density of current and the induction near the sheath have been calculated.

Curve 1 shows the tangential induction at 1 mm outside G and curve 2 at 1 mm inside G.

Three-dimensional problem

Numerical results have been obtained with the configuration of the figure 2 for two cases :

- Case 1 : The length of the sheath is supposed infinite but there are finite-elements only on a length D. The sheath is isolated from the conductor.

- Case 2 : The sheath is truncated at the distance D from the knee-pipe. The sheath is still isolated from the conductor.

Many tests have been realized with various numbers of vertices and triangles. We give there the results corresponding to the greatest number of elements, with the following values :

Applied current : 375 A	Length D : 2 m
Ray of the sheath : 10 cm	Ray of the conductor : 5 cm
Thickness of the sheath : 0,9 cm	Thickness of the conductor : 0,5 cm
Number of vertices : 496	Number of triangles : 960

Diagram 3 shows the modulus of the density of current obtained in cases 1 and 2 along the generating lines AA' and BB' of the following figure (for the sheath only) :

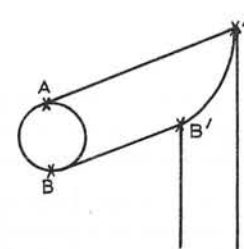


Diagram 4 shows a spreading out in the plane of the diagram of the sheath near the knee-pipe and on both sides of it, in case 1. We can see the finite-elements. Little vectors represent the average density of current on each triangle.

Diagram 5 in the same in case 2.

Conclusion

Obviously, this study has not yet been brought to an end and we have to make several remarks and to underline some difficulties. First of all experimental verifications have to be realized and are worked on at the moment. There are two main difficulties for the numerical results. The first one is that we obtain only average values over triangles and thus it is difficult to well describe the areas where the density of current rapidly change in direction or modulus because the number of triangles is bounded by the power of the computer, all the more so that we shall have to consider the case of three conductors and three sheaths. The second one is that we don't know very well what hypothesis is to be taken at the extremities of G in order to be in the same conditions as in the experimental device. As for the experimental measurements, it is quite difficult to interpretate them.

Nevertheless, because of the heavy difficulties, especially efforts and heatings, appearing in the new power-stations and our high-power laboratory, we go an actively studying both experimental and numerical aspects of the problem.

DIAGRAM 1

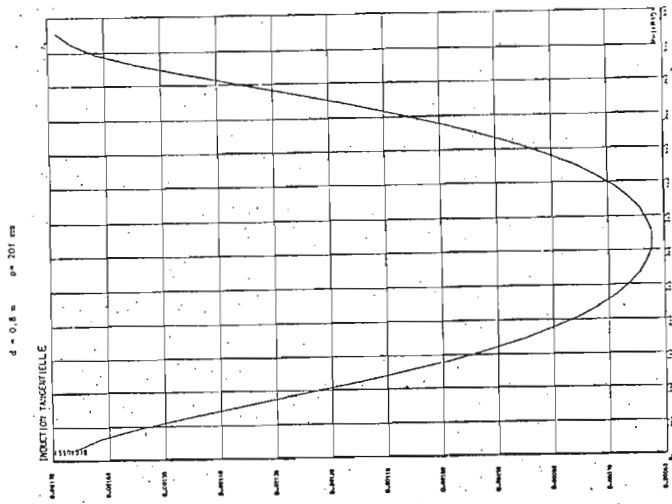
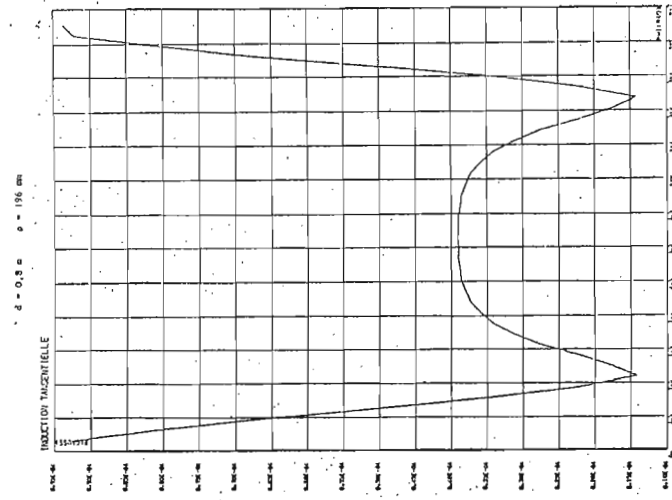


DIAGRAM 2



Curve 1 shows tangential induction outside the sheath.

Curve 2 shows tangential induction inside the sheath.

DIAGRAM 3

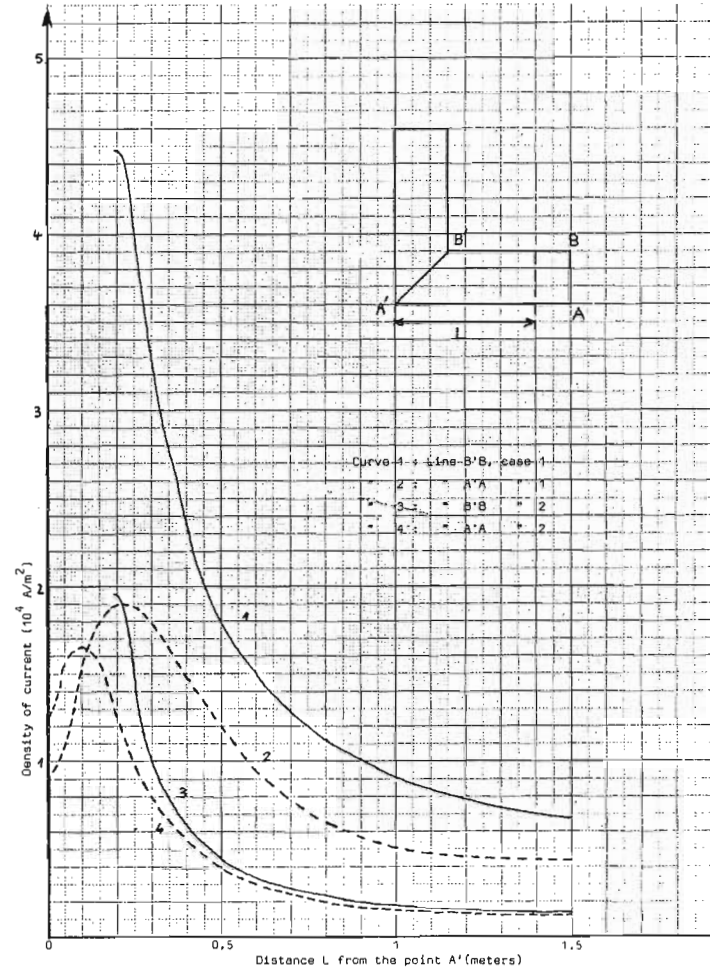


DIAGRAM 5

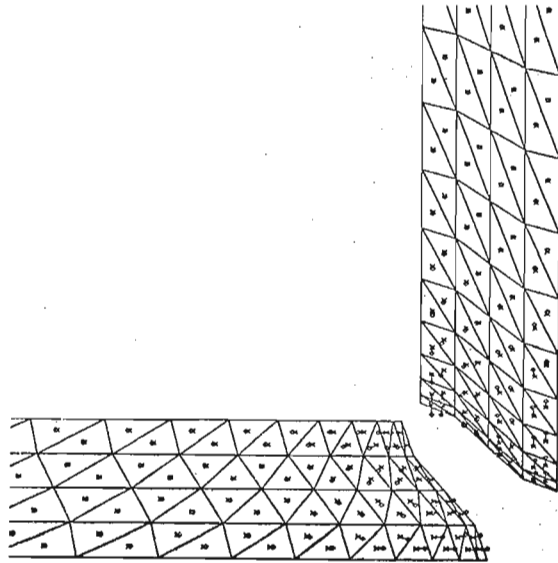
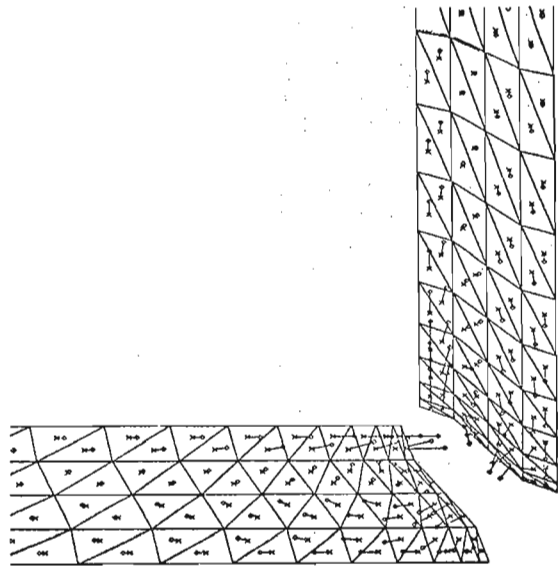


DIAGRAM 4



SIMPLIFIED INTEGRAL EQUATIONS FOR ALTERNATING-CURRENT
DISTRIBUTION IN STRIP-CONDUCTORS AND STRIP-LINE WITH
MINIMIZED PROXIMITY EFFECT

Branko D. Popović, D. Sc.
Department of Electrical Engineering
University of Belgrade, Yugoslavia

1 Introduction

In integral equations for alternating-current distribution in parallel cylindrical conductors enter double integrals which are relatively difficult and time-consuming to integrate when solving these equations numerically. This is true even in the case when the conductors are in the form of thin strips. Only when the strips are flat can the integrals be integrated once explicitly.¹

This paper shows that in the case of thin strip conductors of arbitrary cross-sectional shape the double integrals can be approximated with high accuracy by simple ordinary integrals. Thus the simultaneous integral equations for current distribution in any number of parallel, cylindrical thin strips of arbitrary cross-sectional shape contain only single integrals, and the system can easily be approximately solved using any of the known numerical methods.

If we consider these equations in the case of two identical, symmetrical parallel curved strip conductors, it becomes possible to consider the integral equations not only as equations in current distribution, but also in the shape of the line cross-section. In particular, by shaping the conduc-

tors and their distance appropriately, it is possible to have approximately uniform current distribution in the conductors, i.e. to minimize losses. This appears to be the first attempt to reduce skin and proximity effects by an optimization process.

2 Integral equations for current density in parallel conductors

Consider n very long, parallel nonferromagnetic conductors situated in a vacuum, of constant, but otherwise arbitrary cross-sections. Let the z -axis of a coordinate system be parallel to the conductors, and let the conductors stretch from $z=-b$ to $z=b$, with b much larger than the distance between two most distant points of the cross-sections S_j and S_k of any two conductors of the system. Assume that the currents $i_m(t)$, $m=1,2,\dots,n$, in the conductors are time-harmonic of angular frequency ω , and that, in the complex notation,

$$\sum_{k=1}^n I_k = 0. \quad (1)$$

It can be then shown that complex current densities $J_m(x,y)$, $m=1,2,\dots,n$, in the n conductors satisfy the following set of simultaneous integral equations:

$$J_m(x,y) = \frac{j\omega\mu_0\sigma}{4\pi} \sum_{k=1}^n \int_{S_k} J_k(x',y') \times \\ \times \ln\{(x-x')^2 + (y-y')^2\} dx'dy' + J_{0m}, \\ m = 1,2,\dots,n. \quad (2)$$

The J_{0m} are complex constants to be determined, and current density functions are subject to constraints

$$\int_{S_m} J_m(x,y) dx dy = I_m, \quad m=1,2,\dots,n. \quad (3)$$

Consider now a conductor system consisting of n thin, not necessarily flat strips, of thicknesses d_1, d_2, \dots, d_n (Fig.1). Assume that the strips are such that the middle lines of their cross-sections can be represented by single-valued functions $f_m(x)$, having finite derivatives $f'_m(x)$ at all points of the strips. (By rotating the coordinate system and/or by subdividing the conductors' cross-sections appropriately this condition can be fulfilled in most cases. The other cases, for which $f'_m(x)$ becomes infinite at some points, can be treated by a somewhat more complicated technique, not to be mentioned here.) Let us designate by $g_m(x)$ the functions representing the upper border-lines of the conductors' cross-sections (see Fig.1), i.e.

$$g_m(x) = f_m(x + \Delta x) + \frac{d_m}{2} \sqrt{1 + f'_m(x)^2}, \quad (4)$$

where

$$\Delta x = \frac{d_m}{2} \frac{f'_m(x)}{\sqrt{1 + f'_m(x)^2}}. \quad (5)$$

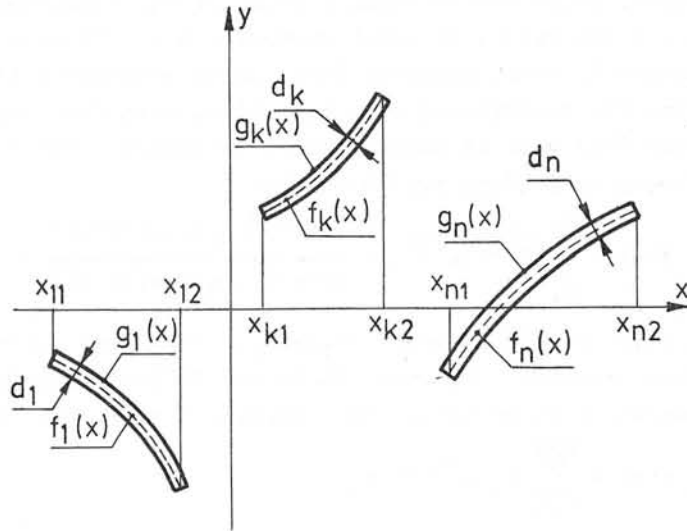


Fig.1. Geometry of cross-section of strip-conductors.

The strips being thin, current density can be assumed constant across the strip thickness, and we can substitute

$$J_k(x', y') dx' dy' \text{ by } J_k(x') d_k \sqrt{1 + f'_k(x')^2} dx'. \quad (6)$$

If $k \neq m$ we can set

$$y - y' = f_m(x) - f_k(x'), \quad m \neq k, \quad (7)$$

but for $m=k$ this would lead to singular integrals. Therefore we put

$$y - y' = g_m(x) - f_k(x'), \quad (m, k=1, 2, \dots, n). \quad (8)$$

Thus from eqn.2 we obtain the following set of approximate integral equations valid for thin strips:

$$J_m(x) = \frac{j\omega\mu_0\sigma}{4\pi} \sum_{k=1}^n d_k \int_{x_{k1}}^{x_{k2}} J_k(x') \sqrt{1 + f'_k(x')^2} \times \ln\{(x-x')^2 + [g_m(x) - f_k(x')]^2\} dx' + J_{0m}, \quad m = 1, 2, \dots, n. \quad (9)$$

Similarly, with approximation in eqn.6, eqn.3 becomes

$$d_k \int_{x_{k1}}^{x_{k2}} J_k(x) \sqrt{1 + f'_k(x)^2} dx = I_k, \quad k=1, 2, \dots, n. \quad (10)$$

To solve approximately the system of integral equations (9), subject to the n constraints (10), different methods can be used. Perhaps the simplest, and from the computing time probably most convenient, is the so-called point-matching method with polynomial approximation of $J_k(x)$ of the form¹

$$J_k(x) = \sum_{i=1}^{n_k+1} C_{ki} x^{i-1}, \quad k=1, 2, \dots, n. \quad (11)$$

Here, C_{ki} are complex current-distribution parameters to be determined, and n_k is the order of the polynomial approximation in strip k . With assumed current distribution (11), eqns.9 and 10 become

$$\sum_{i=1}^{n_m+1} C_{mi} x^{i-1} = \sum_{k=1}^n \sum_{i=1}^{n_k+1} C_{ki} G_{ki}(x) + J_{0m},$$

$$m = 1, 2, \dots, n, \quad (12)$$

$$\sum_{i=1}^{n_k+1} C_{ki} b_{ki} = I_k, \quad k=1, 2, \dots, n, \quad (13)$$

where

$$G_{ki}(x) = \frac{j\omega\mu_0\sigma d_k}{4\pi} \int_{x_{k1}}^{x_{k2}} x'^{(i-1)} \sqrt{1 + f_k'(x')^2} \times$$

$$\times \ln\{(x-x')^2 + [g_m(x) - f_k(x')]^2\} dx',$$

$$k = 1, 2, \dots, n, \quad (14)$$

and

$$b_{ki} = d_k \int_{x_{k1}}^{x_{k2}} x^{i-1} \sqrt{1 + f_k'(x)^2} dx. \quad (15)$$

Alltogether we have $N = \{ \sum_{k=1}^n (n_k+1) + n \}$ unknowns (i.e., all the current-distribution parameters C_{ki} and the n constants J_{0m} , $m=1, 2, \dots, n$). In addition to the n equations (13) we therefore need another $(N-n)$ equations, which we obtain by stipulating that eqns.12 hold for (n_k+1) points of the k -th conductor, $k=1, 2, \dots, n$. The simplest choice for these "matching points" is that they be equispaced along the x -axis, i.e.

$$x_{kj} = x_{k1} + (j-1) \frac{x_{k2} - x_{k1}}{n_k}, \quad k=1, 2, \dots, n,$$

$$j=1, 2, \dots, (n_k+1). \quad (16)$$

Eqns.12 thus become

$$\sum_{i=1}^{n_k+1} C_{mi} x_{mj}^{i-1} = \sum_{k=1}^n \sum_{i=1}^{n_k+1} C_{ki} G_{ki}(x_{mj}) + J_{0m},$$

$$m = 1, 2, \dots, n, \quad j = 1, 2, \dots, (n_m+1). \quad (17)$$

These $(N-n)$ equations, together with the n equations (13), have to be solved for the $(N-n)$ current-distribution parameters C_{ki} and the n constants J_{0m} . Both numerical evaluation of the integrals in eqns.14 and 15 and solution of the N complex linear equations (13) and (17) is today a relatively simple matter, and we shall not discuss these topics here.

3 Synthesis of strip-line with minimized proximity effect

In the case of two strip conductors ($n=2$), symmetrical with respect to the origin and to the x -axis, we have $I_1 = -I_2 = I$, $J_1(x) = -J_2(x) = J(x)$. The equations (9) become two identical equations, of the form

$$J(x) = \frac{j\omega\mu_0\sigma d}{4\pi} \int_{-x_1}^{x_1} J(x') \sqrt{1 + f'(x')^2} \times$$

$$\times \ln \frac{(x-x')^2 + \{g(x) - f(x')\}^2}{(x-x')^2 + \{g(x) + f(x')\}^2} dx' + J_0. \quad (18)$$

By physical reasoning it can be concluded that, in principle, there should exist a shape of the conductors for which $J(x) = \text{constant}$, at least approximately. If this is approximately true, equation (18) can be considered as an equation for determining $f(x)$ for which, with $J(x) = \text{constant}$, equation (18) will be approximately satisfied. Obviously, this leads to finding $f(x)$ such that

$$R(x) = \int_{-x_1}^{x_1} \sqrt{1 + f'(x')^2} \ln \frac{(x-x')^2 + \{g(x) - f(x')\}^2}{(x-x')^2 + \{g(x) + f(x')\}^2} dx' \quad (19)$$

be constant on the segment $-x_1 < x < x_1$. This $f(x)$ cannot be obtained directly. However, it is not difficult to find it approximately by assuming, for example, $f(x)$ in the form

$$f(x) = \sum_{k=1}^{p+1} F_k x^{2(k-1)}, \quad (20)$$

and determining the unknown parameters F_k by an optimization

process so that the expression

$$A = \sum_{i=1}^q \left| \frac{R(x_i) - R(0)}{R(0)} \right|^2, \quad (21)$$

with x_i representing any set of arbitrary number q of points on the segment $[0, x_1]$, be minimal. This optimization process can also be performed relatively easily by means of an electronic digital computer.

4 Numerical results

Using the theory described in Section 2, numerical results were first obtained for several cases of thin strip conductors for which numerical results already existed. For all the cases of flat thin strips considered in References 1-4, practically the same results were obtained by the present theory. This proved the validity of the present theory which, however, is simpler than any of the available methods for determining current distribution in strip conductors known to the author, particularly if the strips are not flat. As a new example, Fig.2 shows current distribution in three-phase balanced line consisting of three flat strips as shown in the insert of Fig.2. Note considerable asymmetry of current distribution in the strips. Current distributions obtained theoretically in the three strips were practically identical and shifted in phase as expected, although the complete system was solved without postulating the symmetry.

As an example of minimization of skin and proximity effects in a symmetrical two-strip line by shaping the conductors, consider a strip-line having minimal distance of 10 cm, maximal width of 20 cm, made of copper strips ($\sigma=5.7 \times 10^7$ S/m) of thickness $d=2$ mm. By the optimization process using the trial function of the conductor's shape of the form

$$f(x) = 0.05 + F_3 x^4 \quad (x \text{ in metres}), \quad (22)$$

it was found that $F_3=836 \text{ m}^{-4}$, i.e.

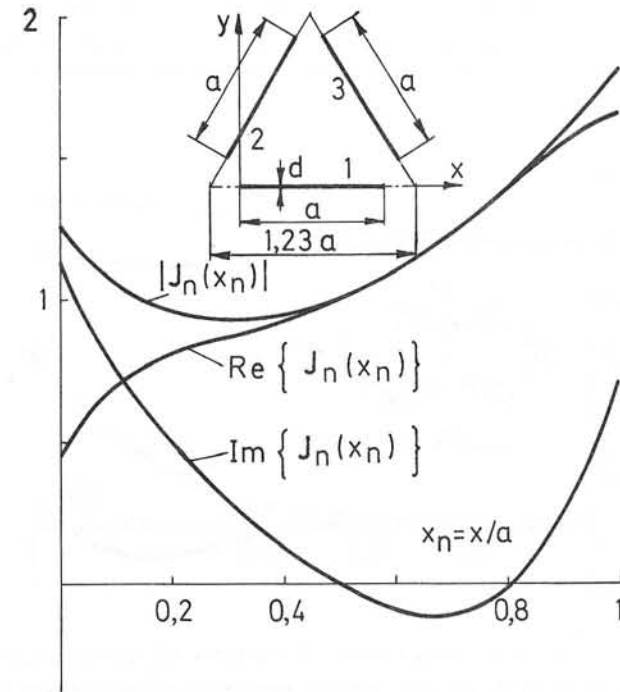


Fig.2. Real part, imaginary part and magnitude of normalized current density $J_n(x_n)=J(x_n)/J(0.5)$ in strip 1 of the symmetrical three-phase strip line shown in the insert. The conductors carry balanced sinusoidal currents, with clockwise phase sequence. $a=20$ cm, $d=0.2$ cm, $\sigma=5.7 \times 10^7$ S/m, $f=50$ Hz, $n=4$.

$$[f(x)]_{\text{optimal}} = 0.05 + 836 x^4 \quad (x \text{ in metres}). \quad (23)$$

For that shape of the conductors current distribution was computed using the present method. The results for real and imaginary parts of current density are shown in Fig.3. For comparison, the results for parallel flat strips of the same width (measured along the x -axis) and the distance equal to

the minimal distance between the curved strips are shown in dashed lines. In spite of relatively crude modelling of the strips (using only one optimization parameter, as in eqn.22), the combined skin and proximity effects are seen to be reduced appreciably.

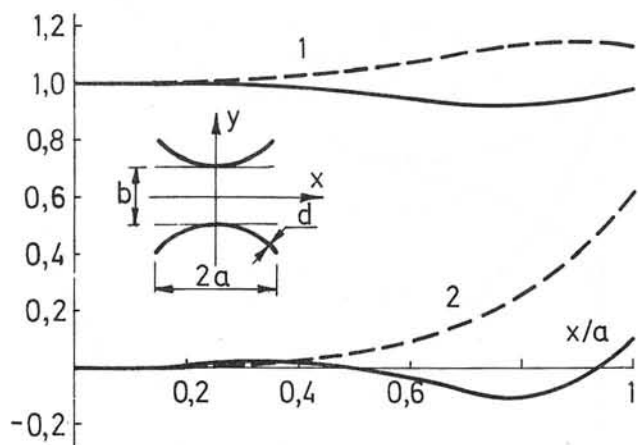


Fig.3. Real (1) and imaginary (2) parts of normalized current density $J(x/a)/J(0)$ in optimized two-strip-conductor line (solid lines) and two parallel flat strips (dashed lines). Cross-sections of the two systems are shown in the insert. $a=10$ cm, $b=10$ cm, $d=0.2$ cm, $\sigma=5.7 \times 10^7$ S/m, $f=50$ Hz, $n=6$.

5 Conclusion

A simple method is presented for determining alternating-current distribution in parallel thin strip-conductors of any cross-sectional shape. It is assumed that the strips are thin enough that current density is practically constant across their thickness.

It is shown in addition that a symmetrical two-strip line can be synthesized with approximately constant current

density at all points of a strip, i.e. with minimized skin and proximity effects. This appears to be the first attempt to minimize the proximity effect by shaping the conductors.

Numerical results obtained by the present method are in excellent agreement with available experimental and theoretical results. However, the present method appears to be the simplest of all the existing methods, particularly if the strips are of a curved cross-section. Numerical results obtained for an optimized two-strip line show pronounced uniformity of current distribution across the optimal line when compared with similar line consisting of two flat strips.

6 Acknowledgement

The author is grateful to Mr. Antonije Djordjević for preparing the computer programs and for obtaining the numerical results presented in the paper.

7 References

- 1 POPOVIĆ, B. D., and FILIPOVIĆ, D. N.: "Theory of power-frequency proximity effect for strip conductors", Proc. IEE, 122, (8), pp.839-842
- 2 HAEFNER, S. J.: "Alternating-current resistance of rectangular conductors", Proc.Inst.Rad.Eng., 1937, 25, pp.434-447
- 3 SILVESTER, P.: "Skin effect in multiple and polyphase conductors", IEEE Trans., PAS-88, (3), pp.231-238
- 4 POPOVIĆ, B. D., and POPOVIĆ, Z. D.: "Method of determining power frequency current distribution in cylindrical conductors", Proc.IEE, 119, (5), pp.569-574

The piece-by-piece solution of eigenvalue problems

by

G. J. Rogers, B.Sc.(Eng.), F.I.M.A.

and

D. S. Benaragama, B.Sc.(Eng.)

Department of Electrical Engineering
The University
Southampton

Summary

A piece-by-piece method is applied to the determination of the eigenvalues and the eigenvectors of the two dimensional scalar Helmholtz Equation. Examples are given for boundary shapes which occur in eddy current problems in electrical machines.

1. Introduction

A piece-by-piece method for the approximate solution of elliptic boundary value problems has been described by Rogers and Cambrell⁽¹⁾. It has been applied to simple electrical machine problems by Hammond and Rogers⁽²⁾. In this paper we extend the technique to the determination of the eigenvalues and the eigenvectors of the scalar Helmholtz equation.

$$\nabla^2 u + \lambda^2 u = 0 \tag{1}$$

with homogeneous boundary conditions.

In machine problems the effect of eddy currents can be represented by equivalent circuits which can be defined in terms of these eigenvalues and eigenvectors⁽³⁾. Here we examine two regions: a basic L-shaped region (Fig. 1) which can represent an induction motor rotor T-bar or the salient pole of a synchronous machine; and the region shown in fig. 2 which represents a cross section through the rotor of a turbo-alternator.

2. The Piece-by-Piece Method

The method is applicable to regions which may be split into sub-regions of such shapes that elementary methods of field solutions may be used in each taken in isolation. At the interface between two sub-regions the field u and its normal derivative $\partial u / \partial n$ must be continuous. We may postulate conceptual sources on the interface to guarantee continuity of

one of these quantities. The other continuity constraint then enables integral equations to be formulated for the distribution of the conceptual sources.

Consider the region (R) shown in fig. 3. Let it be divided into two sub-regions R_a and R_b . Within R the field satisfies the scalar Helmholtz equation

$$\nabla^2 u + \lambda^2 u = 0 \tag{1a}$$

with

$$u = 0 \quad \text{on } S_1 \tag{1b}$$

$$\frac{\partial u}{\partial n} = 0 \quad \text{on } S_2 \tag{1c}$$

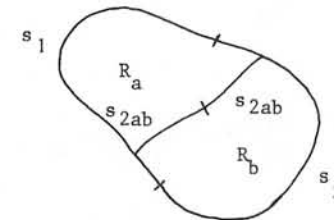


Fig. 3

In each sub-region we may calculate the field u by means of a Green's function, in terms of the field specified on the interface between two regions. On s_{1ab} we assume that u is specified and on s_{2ab} we assume that $\partial u / \partial n$ is specified.

If $G_a(\underline{r}/\underline{r}_o)$ is the Green's function for region R_a , satisfying

$$\nabla^2 G(\underline{r}/\underline{r}_o) + \lambda^2 G(\underline{r}/\underline{r}_o) = -\delta(\underline{r} - \underline{r}_o) \tag{2}$$

$$\text{then } u(\underline{r}) = \int_{s_{2ab}} G_a(\underline{r}/s) \frac{\partial u(s)}{\partial n} ds - \int_{s_{1ab}} \frac{\partial G_a(\underline{r}/s)}{\partial n_o} u(s) ds \tag{3}$$

\underline{r} in R_a

and similarly

$$u(\underline{r}) = - \int_{s_{2ab}} G_b(\underline{r}/s) \frac{\partial u(s)}{\partial n} ds - \int_{s_{1ab}} \frac{\partial G_b(\underline{r}/s)}{\partial n_o} u(s) ds \quad \underline{r} \text{ in } R_b \quad (4)$$

For \underline{r} on s_{2ab} u must be continuous and for \underline{r} on s_{1ab} $\partial u/\partial n$ must be continuous in order to satisfy the remaining continuity constraints.

Thus

$$\int_{s_{2ab}} \{G_a(s_{2ab}/s) + G_b(s_{2ab}/s)\} \frac{\partial u(s)}{\partial n} ds + \int_{s_{1ab}} \left\{ \frac{\partial G_b(s_{2ab}/s)}{\partial n_o} - \frac{\partial G_a(s_{2ab}/s)}{\partial n} \right\} u(s) ds = 0 \quad (5)$$

$$\int_{s_{2ab}} \left\{ \frac{\partial G_a(s_{1ab}/s)}{\partial n} - \frac{\partial G_b(s_{1ab}/s)}{\partial n} \right\} \frac{\partial u(s)}{\partial n} ds - \int_{s_{1ab}} \left\{ \frac{\partial^2 G_a(s_{1ab}/s)}{\partial n \partial n_o} + \frac{\partial^2 G_b(s_{1ab}/s)}{\partial n \partial n_o} \right\} u(s) ds = 0 \quad (6)$$

These coupled integral equations may be solved approximately by Galerkin's method, which leads to a non-linear eigenvalue problem,

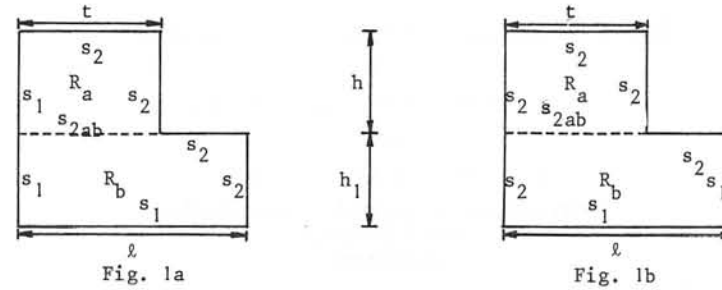
$$[A(\lambda)] [B] = 0 \quad (7)$$

where each root of $\text{Det } [A(\lambda)] = 0$ is an approximate eigenvalue and the corresponding B is related to the eigenvector.

3. Applications

3.1 The L-shaped Region

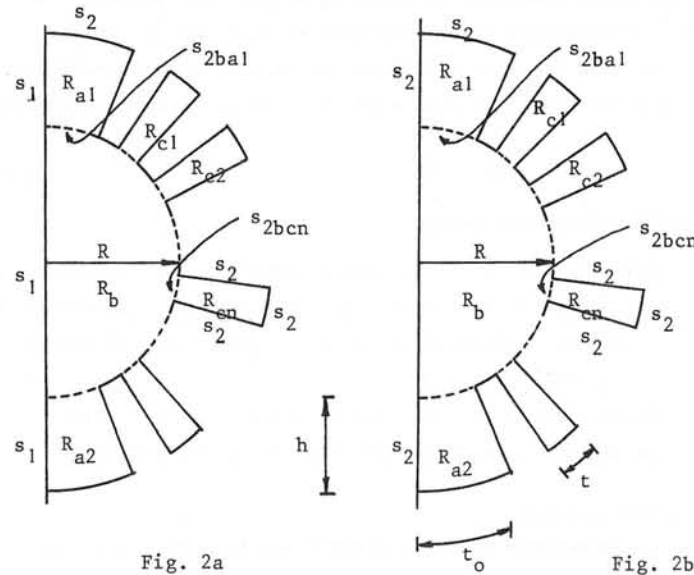
With the boundaries specified as shown, figures 1.a and 1.b illustrate the two-axis representation of one half of a salient pole.



The dominant eigenvalues associated with the direct and quadrature axes for two-pole geometries are given in table 1. Ferriss⁽⁴⁾ has calculated the eigenvalues for the L-shaped region (A) and his values are given in parenthesis.

3.2 Cross-section Through the Rotor of a Turbo-alternator

The specification of the boundaries in figures 2.a and 2.b, once again correspond to the two-axis representation of the rotor.



A list of the dominant eigenvalues associated with the two axes for a typical turbo-alternator rotor is given in table 2.

Table 1

Table 2

(A)		(B)			
$\bar{t}=0.5$	$\bar{h}=0.5$	$\bar{t}=0.53$	$\bar{h}=0.73$	$t_o=0.58$	$\bar{t}=0.0323$
$\bar{h}_1=0.5$		$\bar{h}_1=0.33$			$\bar{h}=0.414$
$\bar{\lambda}^2$	$\bar{\lambda}^2$	$\bar{\lambda}^2$	$\bar{\lambda}^2$	$\bar{\lambda}^2$	$\bar{\lambda}^2$
D-Axis	Q-Axis	D-Axis	Q-Axis	D-Axis	Q-Axis
11.499	3.221	11.207	2.438	2.298	1.599
(11.499)	(3.214)				
17.255	21.808	25.667	20.573	7.821	6.580
(17.218)	(21.792)				
37.698	34.561	35.321	36.610	10.564	10.065
(37.697)	(34.548)				
70.319	46.810	64.505	45.889	11.810	11.580
(70.181)	(46.740)				
79.749	63.501	79.318	54.515	29.397	12.376
(79.745)	(63.404)				
$\bar{t} = t/\ell, \bar{h} = h_1/\ell, \bar{h} = h_1/\ell, \bar{\lambda} = \lambda\ell$				$\bar{t}=t/R, \bar{t}_o=t_o/R, \bar{h}=h/R, \bar{\lambda}=\lambda R$	

References

1. Rogers, G.J. and Cambrell, G.K.: 'The piece-by-piece solution of elliptic boundary value problems', Journal Phys. D, Vol. 8, 1975 pp 1615 - 1623
2. Hammond, P. and Rogers, G.J.: 'Use of equivalent fields in electrical-machine studies', Proc. IEE, Vol. 121, 1974, pp 500 - 507
3. Rogers, G.J. and Smith, J.R.: 'Synchronous-machine model including eddy currents', Proc. IEE, Vol. 120, 1973, pp 461 - 468
4. Ferriss, D.H.: 'Solution of mixed boundary value problems in finite domains by Fourier's method', NPL, NAC 16, 1972

SECTION D TRANSIENT

USE OF THE FAST FOURIER TRANSFORM FOR TRANSIENT MAGNETIC FIELDS

T J E Miller BSc AFIMA Mem IEEE

Professor P J Lawrenson DSc AFIMA FeI IEEE FIEE CEng

1. INTRODUCTION

In many engineering problems it is important to know how transient electromagnetic fields diffuse through conducting or permeable bodies. Such problems include the design of protective shields (for superconductors or instruments), and of many components in machines, transformers and magnets. Of interest usually are the transient distribution of force and heat associated with eddy currents, variations of impedances, and the transient distributions of magnetic flux and current.

Several methods of analysis have been applied to the transient diffusion problem, ranging from 'classical' analysis to purely numerical methods of relatively recent origin. The numerical methods are generally more powerful, but have not been developed to the stage where their use can be regarded as routine or even efficient. This paper develops the solution of transient field problems by Fourier transform techniques, and by means of the digitally calculated fast Fourier transform it enables solutions to be obtained very efficiently and flexibly.

The method has the important advantage of evaluating at an intermediate stage the frequency-response function of the field quantity of interest. This function is itself of considerable value in understanding and estimating the penetration of the diffusing field, and may be obtained by any conventional method: analytical, numerical or experimental. The frequency response function entirely characterises the field quantity of interest in a way which makes the calculation of the time response a routine and efficient matter using the fast Fourier transform. The response to almost any transient excitation function can be computed rapidly and easily.

The paper begins with a review of methods available for solving this class of problem and discusses the relative advantages of the integral

transform method. The analytical methods for obtaining the frequency response function of interest involve the solution of the complex Poisson equation, for which powerful methods are already available and are still developing.

The application of the general method is then explained in relation to the particular problem of screening a superconducting winding from an externally applied, transient magnetic field. The example is taken from the design of a superconducting a.c. generator. It is essential to limit the magnitude and the rate of change of magnetic field in the region of the superconductor, and this is done by interposing a cylindrical screen (or screens) between the superconducting winding (with which it rotates) and the machine's armature (transient currents in which would be responsible for the most troublesome changes in magnetic field). It is necessary to be able to calculate reliably the way in which flux inside the screen changes following a sudden change in armature current. The shielding property of the screen is characterised by the screening ratio frequency response function $S(f)$, which is the complex ratio between the magnetic field at a point at frequency f and at zero frequency. The transient response is then evaluated using the F.F.T. and $S(f)$ for the illustrative case of a step change of armature current. A brief discussion of screening properties is given for single and double screens. It has been found that interactions between concentric screens, and between screens and field winding, can have a degrading influence on the shielding effectiveness, and this is discussed briefly.

2. METHODS AVAILABLE FOR TRANSIENT DIFFUSION

The general linear diffusion process is described by the equation

$$\text{curl curl } H = -\frac{\mu}{\rho} \frac{\partial H}{\partial t} \quad (1)$$

in which H is the magnetic field strength vector. Three main methods for solving this equation are: direct analytical solution; direct numerical solution; and solution by integral transform. The analytical method⁶ is restricted to the simplest geometries with a small number of field components, and produces solutions in the form of an infinite sum of exponential terms e^{-t/τ_n} , which may be slow to converge. The method is best used with step or impulse excitation functions; more general excitation functions require Duhamel's integral, which is cumbersome; the approach is comparatively inflexible, limited and inefficient. Direct

numerical methods (e.g. Crank & Nicolson⁷, Dufort & Frankel⁹, Alternating Direction Implicit method⁸) are much more powerful, in that a larger number of field components can be dealt with, extending the application to more complicated geometries. (They are also the only methods capable at present of dealing with nonlinearities.) However, it is often necessary to solve large numbers of simultaneous equations at every time step, and convergence problems in both space and time domains are possible. The entire solution must be repeated for every new excitation function to which the response is required, and this involves the computation of the field quantities at all points in the problem even when only localised values are needed.

The transform method escapes from most of the limitations of these two methods: by dividing the problem into a 'space-dependent' part and a 'time-dependent' part, which in linear problems can be solved independently, it makes possible a 'once for all' space solution which can subsequently be used in the calculation of the transient response to any excitation function. The space solution is in the form of a frequency response function for each point in the field of interest, and this function is itself often of physical significance and of considerable value in understanding and characterising the diffusion properties of the device in question. The set of frequency response functions for all points in the field are the solution to the complex Poisson equation, for which powerful analytical and numerical methods are available. The frequency response functions can also be obtained experimentally. Because the same functions are used to characterise the spatial variation of the field in the calculation of transient response for all excitation functions, experimental or analytical work is greatly reduced. A further reduction in computational effort is possible when the field is of interest at only a few points, since the transient response at each of these points can be obtained by the transform from the appropriate local frequency response functions independently of all other field points.

Although the integral transform approach is by no means new, its advantages can be realised only if a reliable and efficient method of computing inverse transforms is available. In recent years the fast Fourier transform^{2,3,4} calculated by the method of Cooley and Tukey has

greatly advanced the efficiency of the Fourier transform approach, and whereas this development has been fully exploited in communications and circuit theory there appear to be few applications to electromagnetic field transients.

3. BASIS AND FORMULATION OF THE TRANSFORM METHOD

The Fourier transformation of equation 1 replaces the operator $\partial/\partial t$ by $j\omega$ to produce the complex Poisson equation:

$$\text{curl curl } H(j\omega) = -j\omega \frac{\mu}{\rho} H(j\omega) \quad (2)$$

which is solved for a range of values of ω ($=2\pi f$). If the phasor solution is written

$$H(f) = S(f) H_0 e^{j2\pi ft} \quad (3)$$

where $H_0 e^{j2\pi ft}$ is the excitation function phasor at frequency f , then $S(f)$ is a frequency-response function which characterises the magnetic field at each point. The physical interpretation of $S(f)$ is usually important, and examples of this will be seen below, but its main usefulness here is in the determination of transient response. For any excitation function $H_0(t)$ whose Fourier transform is $H_0(f)$, the transient response of the field is given immediately by

$$H(t) = \mathcal{F}^{-1} \{ S(f) H_0(f) \} \quad (4)$$

The inverse transformation is computed efficiently by means of the F.F.T. algorithm. At this stage the flexibility of the method is clear. The same function $S(f)$ can be used for all excitation functions $H_0(f)$. Of course the transient response of the entire field can only be obtained by repeated application of equation (4) for each field point in turn, but since $S(f)$ is known at all points from the solution of equation (2), this is a straightforward and routine calculation which, because of the F.F.T., is also economical.

The flexibility of the method is further enhanced by the ease with which, if necessary, the excitation transform $H_0(f)$ can be calculated from $H_0(t)$ using the F.F.T. This important advantage extends the method to excitation functions of virtually any waveshape. The essential characteristics of the field are implicit in $S(f)$ and not locked up in a particular transient response to a particular excitation function, as would be the case with an analytical or direct numerical method. At the

same time, the responses to particular excitation functions can be easily and quickly obtained.

There remains the difficulty of solving the complex Poisson equation. Although this is complex, it at least has one independent variable fewer than equation (1). Powerful methods are available for its solution, particularly in problems of only one or two space dimensions, and considerable effort is at present directed towards methods for three-dimensional solutions. Even where direct physical measurement is the only available means of analysis, frequency response functions like $S(f)$ are the most economical and generally useful quantities to measure.

The F.F.T. algorithm calculates the discrete Fourier transform (D.F.T.) and/or its inverse, which are given by

$$g_d(k\Delta t) = \frac{1}{T} \sum_{\ell=0}^{N-1} G_d(\ell\Delta f) e^{j2\pi k\ell/N}, \quad k=0,1,2,\dots,N-1 \quad (5)$$

$$G_d(\ell\Delta f) = \sum_{k=0}^{N-1} g_d(k\Delta t) e^{-j2\pi k\ell/N}, \quad \ell=0,1,2,\dots,N-1$$

This relation may be regarded as the digital equivalent of the continuous Fourier Transform. Several standard papers^{2,3,4} describe the formation of the sampled and truncated functions $g_d(k)$ and $G_d(\ell)$ from the corresponding continuous functions $g(t)$ and $G(f)$, and only the briefest outline is given here. First, the periodic 'aliased' functions

$$g_a(t) = \sum_{m=-\infty}^{\infty} g(t + mT) \quad (6)$$

$$G_a(f) = \sum_{m=-\infty}^{\infty} G(f + mF)$$

are formed by the juxtaposition at intervals of T (or F) of the central or most significant part of $g(t)$ or $G(f)$, as in Fig 1. Then one period of each of the aliased functions is sampled at N equally spaced points:

$$g_d(k) = g_a(k\Delta t), \quad k=0,1,2,\dots,N-1 \quad (7)$$

$$G_d(\ell) = G_a(\ell\Delta f), \quad \ell=0,1,2,\dots,N-1$$

This procedure is illustrated for an example $G(f)$ in Fig 1. F and T are related by $FT = N$, so that $\Delta f = F/N = 1/T$ and $\Delta t = T/N = 1/F$. The inverse D.F.T. of $G_d(\ell)$ is $g_d(k)$ which approximates $g(t)$ for $t < T/2$ just as $G_d(\ell)$ approximates $G(f)$ for $f < F/2$.

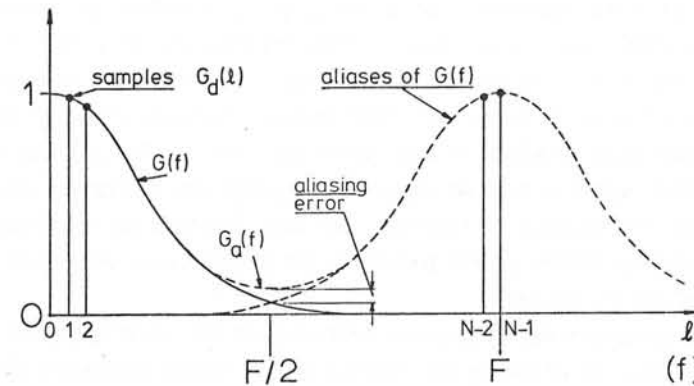


Fig 1 Aliasing and sampling

Two possible sources of error need to be mentioned. First, the 'truncation' of the aliased function, which arises because only a finite number N of samples are taken, is equivalent to multiplying $G(f)$ by a rectangular 'data window' so that the resulting transform $g(t)$ is convolved with a $(\sin t)/t$ function. This appears as a ripple on $g(t)$ around $t = 0$ (Gibbs' phenomenon), and may be avoided by multiplying $G(f)$ by a smoother data window, such as the Hanning or the Dolph-Chebyshev⁴. Secondly, the Nyquist frequency $F/2$ must be chosen to be higher than the highest frequency component present in $G(f)$, so as to avoid aliasing errors.

4. TRANSIENT MAGNETIC FIELDS IN CYLINDRICAL SCREENS

4.1 Application of the Transform Method

The transform method has been applied to the transient screening problem in the superconducting a.c. generator. Fig 2 is a schematic diagram showing the positions of the principal components in a 2-dimensional model of this. A rotating field configuration has been assumed. The superconducting winding, of radius r_f , must be protected from magnetic field transients caused by changes in armature current. For this purpose a cylindrical screen (or a double screen) is fixed to the rotor, and it is here assumed to rotate synchronously with the field winding. It is

necessary to calculate the way in which the magnetic field inside the screen changes following changes in armature current, and to determine the way in which the properties of the screen affect these changes. This study is later extended to include the effect of a short-circuited field winding.

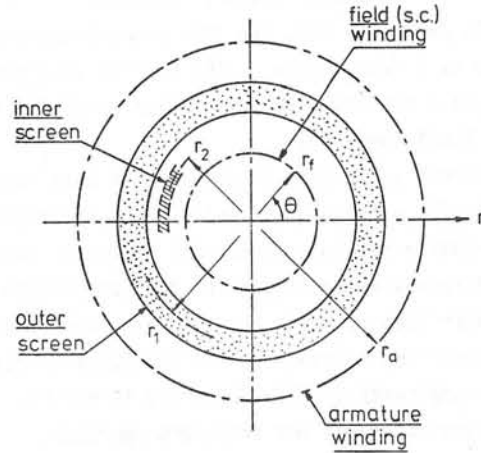


Fig 2 Basic superconducting machine configuration

Frequency response

The first step is to determine the field under harmonic excitation. With only an axial component of current (and thereafter also of vector potential) this can be obtained from the solution of equation (2). Assuming a sinusoidal distribution of armature current, equation (2) reduces to

$$\frac{d^2H}{dr^2} + \frac{1}{r} \frac{dH}{dr} - \left[\frac{p^2}{r^2} + j\omega \frac{\mu}{\rho} \right] H = 0 \tag{8}$$

The solution of this equation is described in detail in Ref 1 and can be written

$$H_{\theta} = \frac{K}{2} \left(\frac{r}{r_a} \right)^{p-1} S(f) e^{j2\pi ft} \sin p\theta \tag{9}$$

for the tangential component inside the screen. $S(f)$, the screening ratio frequency response function, is the ratio between the phasor value of H_{θ} at frequency f and at zero frequency. It is a complex expression

involving Bessel functions (see Ref 1). In simple cases it can be evaluated algebraically, but when the number of concentric components exceeds three the algebra becomes cumbersome and the transfer-matrix method described by Freeman¹⁰ is useful. Where the full three-dimensional variation of the field is necessary numerical methods may be necessary to find $S(f)$.

In the simple case of a single screen with a field winding (which may be short circuited), at low frequencies it is possible to obtain an appropriate expression for $S(f)$ by using asymptotic expressions for the Bessel functions when these have small arguments. This formula is

$$S(f) = 1 / [1 + j2\pi f T_D (1 - \lambda)] \tag{10}$$

where $\lambda = (r_f/r_1)^2$. In this form it applies to the case with the short-circuited field winding, the armature current being symmetrically disposed about the direct axis. When the field winding is open, or when the armature current is symmetrical about the quadrature axis, $\lambda = 0$. The time constant T_D is given approximately by $T_D = \mu_0 r_1 h / 2\rho$. It can be seen that the effect of a short-circuited field winding is to shorten the effective time constant of the screen, which weakens the screening effectiveness; this effect is discussed in Section 4.2.

Transient response

The transient response to any excitation function can now be obtained directly from equation (4). The particular excitation function to be considered here is a step of armature current from 0 to K (see Appendix). This type of change is one of the most severe in the machine and corresponds closely to the effective d.c. transient following a sudden terminal short circuit. The excitation function in terms of H_{θ} is

$$H_{\theta 0} = - \frac{K}{2} \left(\frac{r}{r_a} \right)^{p-1} \sin p\theta u(t) = H_{\theta 0} u(t) \tag{11}$$

where $u(t)$ is the unit step function. The necessary Fourier transform of this can be obtained analytically as

$$H_{\theta 0}(f) = - \frac{K}{2} \left(\frac{r}{r_a} \right)^{p-1} \sin p\theta \left[\pi\delta(f) + \frac{1}{j2\pi f} \right] \tag{12}$$

and equation (4) gives the transient response as

$$H_{\theta}(t) = - \frac{K}{2} \left(\frac{r}{r_a} \right)^{p-1} \sin p\theta \mathcal{F}^{-1} \left\{ \left[\pi\delta(f) + \frac{1}{j2\pi f} \right] S(f) \right\} = h_{\theta}(t) H_{\theta 0} \tag{13}$$

$h_{\theta}(t)$, the normalised transient response, is evaluated by means of the F.F.T. and is used in presenting results. $S(f)$ is first sampled at equally spaced frequencies $\ell\Delta f$, $\ell=0,1,2,\dots,N-1$; then the function $S(\ell\Delta f)/j2\pi\ell\Delta f$ is formed sample by sample, and the step response is given in discrete form by

$$h_{\theta}(k t) = \frac{1}{2}S(0) + \mathcal{F}^{-1} \left\{ \frac{S(\ell\Delta f)}{j2\pi\ell\Delta f} \right\}, \quad k=0,1,2,\dots,N-1 \quad (14)$$

In the Appendix, it is shown that the discrete transform is to be evaluated in the form

$$\mathcal{F}^{-1} \left\{ \frac{S(\ell\Delta f)}{j2\pi\ell\Delta f} \right\} = \frac{4}{T} \left\{ \frac{1}{2}R(0) + \sum_{\ell=1}^{N/2-1} R(\ell) \cos \frac{2\pi k \ell}{N} + \frac{1}{2}R\left(\frac{N}{2}\right) \cos \pi k \right\} + \frac{1}{2} \quad (15)$$

$k=0,1,2,\dots,N-1$

where $R(\ell) = \text{Re}[S(\ell\Delta f)/j2\pi\ell\Delta f]$, $\ell=0,1,2,\dots,N-1$. Δt and Δf are, of course, related by $\Delta t = 1/N\Delta f$. The principle of causality is needed to obtain equation (15) (see Appendix). The real and imaginary parts of $S(f)/j2\pi f$ may not always both have a limit as $f \rightarrow 0$. In screening problems it will usually be possible to formulate $S(f)$ so that as $f \rightarrow 0$, $S(f)/j2\pi f$ tends to a purely real or purely imaginary number; for example, in the formulation used here for the single screen, as $f \rightarrow 0$, $S(f)$ tends to the value given by equation 10, and

$$R(\ell) = \text{Re}[S(\ell\Delta f)/j2\pi\ell\Delta f] \rightarrow -T_D \quad \text{as } \ell \rightarrow 0 \quad (16)$$

In cases more complicated than the one with a single screen, the first sample $R(0)$ was formed by backward extrapolation to $\ell = 0$ ($f = 0$). The imaginary part $\text{Im}[S(\ell\Delta f)/j2\pi\ell\Delta f]$ does not have a limit as $\ell \rightarrow 0$, which is why the cosine transform was used rather than the sine transform.

An alternative way of avoiding the problem of the limit at $f = 0$ in this problem would have been to operate with $1 - S(f)$ and the sine transform, since $\text{Im}[\{1 - S(\ell\Delta f)\}/j2\pi\ell\Delta f]$ has a limit as $\ell \rightarrow 0$. Physically this implies operating purely on the magnetic 'reaction' field of the screen currents, as contrasted with $S(f)$ which implies operating on the total magnetic field (reaction + applied).

The use of the cosine transform halves the computer storage and time requirements as compared with the full exponential transform. This saving is valuable if accurate results are required, particularly when the transient is oscillatory or varies especially rapidly through time. In such cases the errors, and particularly the d.c. error, are reduced by

taking a larger number $N/2$ of samples, so that the fine structure of both the frequency response and the time response can be adequately represented (i.e. $\Delta f, \Delta t$ small). The time taken to compute the time response is proportional to $N \log_2 N$ and is otherwise independent of the complexity of the excitation or frequency response functions. For all the results presented in this paper $N = 512$, and this proved adequate for 1% accuracy without recourse to a data window. The Fortran programme used to compute the transforms was a standard library routine requiring 4 sec execution time (on an ICL 1906A computer).

It is of interest to compare this time with that required to compute $S(f)$. Typically for a 'double screen' problem a Fortran programme based on the transfer-matrix method computed 256 frequency samples of $S(f)$ in 20 sec. In a three-dimensional problem the computation of $S(f)$ would certainly take much longer, while the time required to evaluate the transient response would not increase at all (except as a result of any increase in the complexity of $S(f)$ requiring larger N). This comparison emphasises the flexibility of the transform approach.

4.2 Results

General The results presented below* describe the screening behaviour of cylindrical screening systems in terms of both the screening ratio frequency response function $S(f)$ (Figs 3 and 5) and the transient response to the step of armature current (Figs 4 and 6) computed by F.F.T. In all cases the screening system has the nature of a low-pass filter, as can be seen from the shape of the curves in Figs 3 and 5. Correspondingly the step responses have, broadly, the characteristic 'overdamped' shape of Figs 4 and 6. So far as $S(f)$ is concerned, the frequencies 2 Hz (near the natural oscillation frequency of the rotor), 50 Hz (the system frequency) and 100 Hz (effective negative sequence frequency) are important, whereas the important feature of the transient responses is the maximum rate of change of field. It is difficult to specify precisely what would be acceptable levels for $S(f)$ and dB/dt at the field winding, but values of the order of 0.1 at 2 Hz are 0.001 at 50 Hz for $S(f)$, and a maximum of 1 T/sec for dB/dt , are desirable.

The first pair of graphs (Figs 3 and 4) show the characteristics of a

* All results are for the case $p = 1$ only

single screen with the field winding open-circuited. The second pair (Figs 5 and 6) show, first, the screening characteristics of a double screening system; and secondly, the effect of short-circuiting the field winding.

Single screens (Figs 3 & 4)

The materials, diameters and thicknesses of the screens are typical of those receiving attention. The solid lines denote stainless steel, and the dotted lines aluminium alloy screens, with the screen thickness marked (in mm) on each curve. As would be expected, $S(f)$ decreases with rising frequency. The transient rise of field strength is shown in terms of the normalised circumferential component h_{θ} because when the field winding is short-circuited (see below) this is the only component which exists. The screens with the lower $S(f)$ curves produce the slowest rate of rise in H_{θ} . Screening is improved by increasing both the conductivity and the thickness of the screen. The straight line on Fig 4 shows the constant rate of rise in h_{θ} corresponding to 1 T/sec, and illustrates that in this particular example, aluminium alloy would be preferable from screening considerations alone.

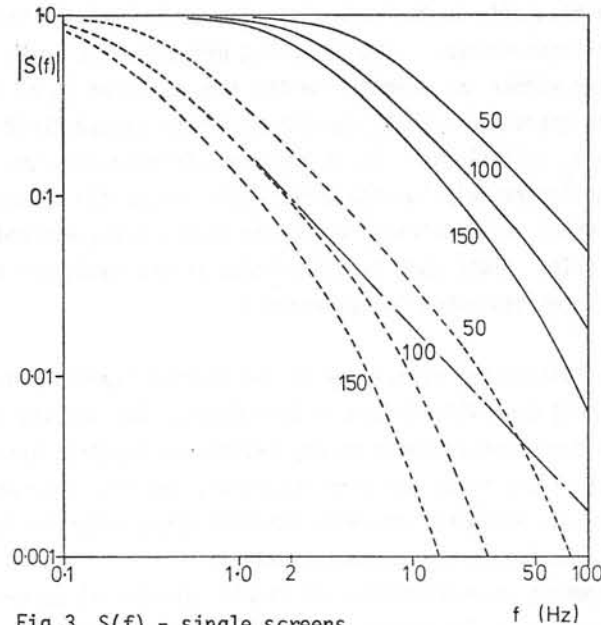


Fig 3 $S(f)$ - single screens

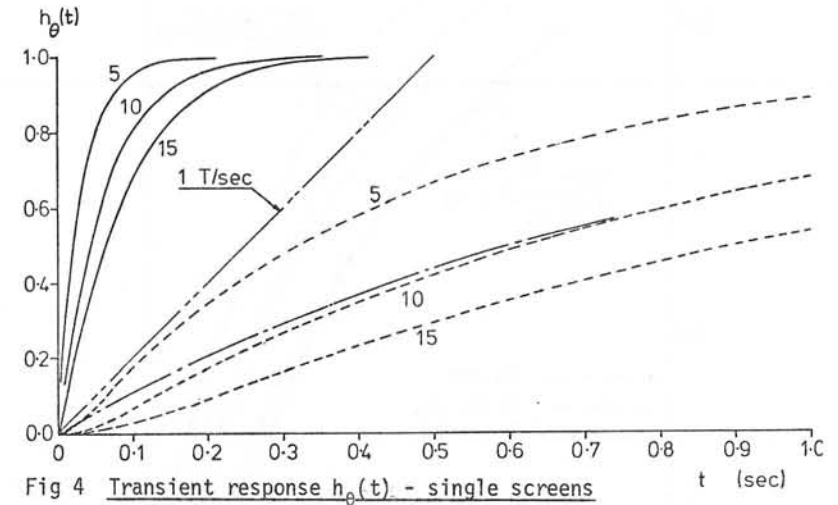


Fig 4 Transient response $h_{\theta}(t)$ - single screens

In the single screen case an approximate formula is possible (equation 16) and results obtained using this and its inverse transform $1 - e^{-t/T_D}$ are also plotted in Figs 3 and 4. In this simple case the agreement in $S(f)$ is good up to about 5Hz, and the transient response is quite adequate, making it possible to characterise the screening conveniently in terms of the parameter $T_D = \mu r_1 h / 2\rho$. The diameter of the screen has little extra effect except through T_D (and $1 - \lambda$, see Section 4.1 and below. $\lambda(r_f/r_1)^2$)

Double screens, with field-winding open-circuited

The double screen arrangement has been proposed for its mechanical and thermodynamic advantages⁵. Figs 5 and 6 show some of the properties of a double screen in which the inner has a long time constant ($T_{D2} = 1$ sec) for good screening, while the outer is designed for maximum mechanical strength and has a shorter time constant $T_{D1} = 0.1$ sec). Figs 5 and 6 are plotted for three separations between the screens, altered by changing the radius of the inner, and it can be seen from the lower $S(f)$ curves in Fig 5 that when the field winding is open circuited, the separation between the screens has little effect. The lower of the two straight lines on Fig 6 corresponds to 1 T/sec when the field winding is open-circuited and shows that this screening system meets the broad

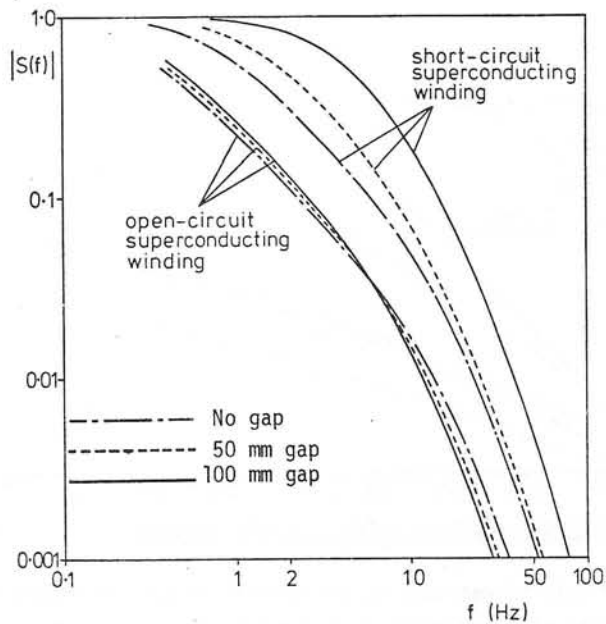


Fig 5 $S(f)$ - double screens

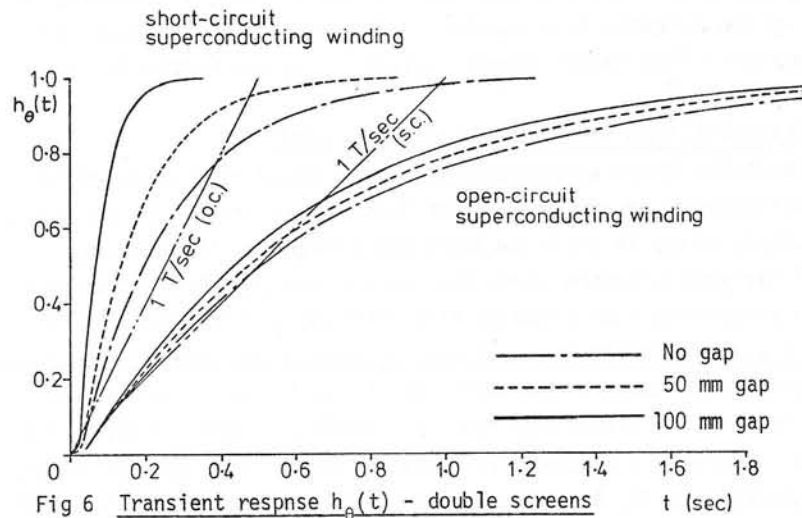


Fig 6 Transient response $h_{\theta}(t)$ - double screens

requirement mentioned earlier in terms of dB/dt .
Double screen with field winding short-circuited

The superconducting winding short circuited at its terminals, or closed through a low* resistance, has a long time constant and behaves effectively in the direct axis as a diamagnetic cylinder of radius r_f . The associated change in the form of the magnetic field inside the screens influences their screening properties, and this can be seen in Figs 5 and 6. Under these conditions the normal field H_r (or B_r) is zero at r_f , while H_{θ} is increased by a maximum factor of 2. Fig 5 shows that the effect of short-circuiting the field winding is to force $S(f)$ to higher values and, correspondingly, to increase the rate of change of field inside the screen. The effectiveness of the screen is diminished by an amount which depends mainly on the separation between the inner screen and the field winding. In Figs 5 and 6 as the gap between screens widens the approach of the inner screen to the field winding worsens the degradation of screening. In the particular example shown here, Fig 6 shows that the degradation of screening by the field winding causes the maximum rate of rise of field to considerably exceed the prescribed 1 T/sec, particularly in the case with minimum gap between the field winding and the inner screen. The screening effectiveness could be recovered by increasing either the diameter or the time constant T_D of the inner screen. In approximate terms the effect of the closed field winding is to increase T_D to $T_D(1-\lambda)$. It is important to note that the degradation of screening occurs only 'on the direct axis' (i.e. for armature current excitation which is symmetrical about the direct axis) and not on the quadrature axis. This fact is significant in the design of the 'heteropervious' screen described in Reference 1.

CONCLUSION

The flexibility and efficiency of the Fourier Transform method using the F.F.T. have been illustrated in this paper. The ability of the method to find the transient response to any excitation function arises from the independence of the space and time solutions, and this also gives rise to the intermediate frequency response function whose value in physical terms is well illustrated in the screening problem.

The screening characteristics of single cylindrical screens have been briefly described. The double screen has been examined and it has been

* i.e. one which makes the field-winding L/R time constant $\gg T_D$

shown that the separation between screens of fixed time constants has little effect on screening when the field winding is open-circuited. When the field winding is closed through a low resistance, it can have a degrading influence on the screening properties. This influence is worse when the screen is close to the field winding.

REFERENCES

1. Miller T J E and Lawrenson P J: 'Penetration of transient magnetic fields through conducting cylindrical structures', Proc IEE to be published (1976)
2. Cooley J W, et al: 'Application of the FFT to computation of Fourier integrals, Fourier series, and convolution integrals', IEEE Trans, vol AU-15, pp 79-84 (1967)
3. Cooley J W, et al: 'The Finite Fourier Transform', IEEE Trans, vol AU-17, pp 77-85 (1969)
4. Bergland G D: 'A guided tour of the FFT', IEEE Spectrum, vol 6, pp 41-52 (1969)
5. Luck D L and Thullen P: 'Double Shielded Superconducting Field Winding', US Patent No 3 764 835 (October 1973)
6. Smythe W S: 'Static and Dynamic Electricity' (McGraw-Hill, New York, 2nd Edn 1950)
7. Crank J and Nicolson P: Proc Cambridge Phil Soc, Vol 43, pp 50-67 (1947)
8. Smith G D: 'Numerical Solution of Partial Differential Equations' (O.U.P., 1974)
9. Lim K K and Hammond P: 'Numerical Method for determining the electro-magnetic field in saturated steel plates', Proc IEE, vol 119, No 11, pp 1667-1674 (1972)
10. Freeman E M: 'Equivalent circuits from electromagnetic theory: low frequency induction devices', Proc IEE, 121 (10), pp 1117-1121 (1974)

APPENDIX

Since h_{θ} is real, from equation (14)

$$h_{\theta}(k\Delta t) = \frac{1}{T} \sum_{\ell=0}^{N-1} \left\{ R(\ell) \cos \frac{2\pi k\ell}{N} - X(\ell) \sin \frac{2\pi k\ell}{N} \right\} + \frac{1}{2}$$

with $R(\ell)$ even and $X(\ell)$ odd in ℓ . Splitting h_{θ} into odd and even parts, $h_{\theta} = h_{O_d} + h_{E_v} + 1/2$, with $h_{O_d} \leftrightarrow X$ and $h_{E_v} \leftrightarrow R$. If the system is causal, i.e., $h_{\theta}(-k) = 0$, then it can be shown that $h_{\theta}(k) = 2h_{E_v}(k) + 1$.

$h_E(k)$ is evaluated by F.F.T. as

$$h_{E_v}(k) = \frac{1}{T} \sum_{\ell=0}^{N-1} R(\ell) \cos \frac{2\pi k\ell}{N} \quad k = 0, 1, 2, \dots, N-1$$

from which equation (15) follows since $R(\ell)$ is even in ℓ .

Evaluation of $H_{\theta 0}$ with $K = 1$ (step change K of armature current)

If the per-unit synchronous reactance x_d is 0.5 pu and the rated flux-density at the armature winding B_{s0} is 1.0 Tesla (these may be regarded as typical values), then 1 per-unit armature current flowing in all three phase windings will produce a flux-density $x_d B_{s0}$ everywhere inside the armature winding; thus $B_{\theta 0} = x_d B_{s0} i_a$ and $H_{\theta 0} = B_{\theta 0} / \mu_0$.

Discussions following paper:

(Trowbridge) Will you please comment on the way you solve for space part of the problem in your program.

(Miller) See comment by Prof Laurenson (co-author)

(Freeman) I should like to congratulate the authors on the elegant technique they describe in their paper. I would like to comment on the calculation of the frequency response using the transfer matrix method. It is now possible to greatly reduce the time required to calculate the elements of the matrices. Principally, Bessel functions can be completely avoided. Finally, could the authors comment on the calculation of the upper end of the frequency spectrum? How high a frequency is required, and is it possible to use an approximation for the screening ratio?

(Miller) The use of the transfer matrix method is only a particular example of a way of calculating the frequency response in a particular illustrative problem. In a more complicated problem, particularly in three dimensions, the transfer matrix method would not be appropriate with or without Bessel functions. There is no particular difficulty calculating the kind of Bessel functions described in the paper (see also Ref 1).

In the case of cylindrical screens it is possible to use an approximation for the screening ratio of the form $1/(1+j\omega T)$, or even one with more than one pole, provided appropriate values of T can be estimated. In complicated or 3-D problems this often is not possible. It is not necessary to have information at the high frequency end of the spectrum because this only affects the early part of the transient. Roughly speaking, a spectrum truncated at 1KHz will give a corrupt transient response for $t < 1$ msec only. The degree of corruption is small in this example because S is very small at 1KHz.

(Lawrenson) The space-variable part of the problem is reduced effectively to the solution of the complex Poisson equations and all the well known and efficient methods can be applied to their solution.

Accordingly the boundary shapes, conditions etc use no more limited than they are in the static (time-transient) case. The FFT then provides an extremely efficient means of converting their space-variable solution over a range of frequencies (frequency response) into whatever time response is required.

(Steel, CERL) Do the authors anticipate any difficulties in using their fourier transform method if they apply it to system studies which include the power system, the turbine and steam generator? The latter two items have significant non-linearities notably those related to the governor system and therefore the fourier transform must be used with great caution.

(Miller) We do not use the FFT itself to solve the 'system equations' of the governed turbine generator, but only to solve transient magnetic field problems. We are also working on the 'system' problem which includes electric circuit equations and non linear differential equations describing the turbine and a.v.r. controls; for this we use a specially formulated method of the 'state space' type which takes into account not only non-linearities but also the frequency dependence of the machine parameters. Incidentally the FFT can be useful here in obtaining frequency-response characteristics from measured time responses on a model machine. Used in this 'identification' problem, the FFT is being used for quite a different application from that described in the paper, namely the computation of transient magnetic fields.

(Umstatter, CERN) You mentioned computing times of 20 sec for evaluating the spectrum and 4 sec for the transform. I confirm this experience that the time for transformation of the spectrum is often negligibly short compared to the time required for obtaining it. Could you comment on the speed referred to other, faster computers? I remember computing times of 30 ms for transformation compared to 1 sec for evaluation of the spectrum on a CDC7600.

(Miller) The time taken for the transformation depends on the speed of the computer and the number of samples in the frequency response (or time response). We used a 256-point transform ($N=512$) on an ICL 1906A

computer, taking 4 sec. I think there are computers capable of doing this much faster but I am not exactly sure what is the fastest possible speed. When the transform takes 4 sec compared with a much longer time for $S(f)$, one is not generally too worried to reduce this time.

(Yeh, Oak Ridge National Lab) How many frequencies are needed to get a good representation for the time-dependent pulse or step function?

(Miller) In the particular examples I have used to illustrate the method, we have smooth frequency response functions and smooth time responses, and reasonable results can be obtained with as few as 64 or even 32 points. In general one trades the number of points against accuracy, even with smooth functions, and I have used 256 points ($N=512$) in all the examples. With a complicated frequency or time functions of course the number of samples must be large enough to reproduce the fine structure.

THE CALCULATION OF MAGNETIC FIELDS IN AIR CORED ELECTRIC MACHINES

Turner D.R., Prior D.L., and Rahim Y.H.A.

Department of Electrical Engineering and Electronics, The University of Liverpool, Liverpool, L69 3BX.

1. Introduction

The work which gave rise to the magnetic field calculations described in this paper, is concerned with the transient terminal performance of air cored alternators, particularly the proposed designs of superconducting a.c. generators. ⁽¹⁾ The prediction of transient performance is obtained by a step by step solution of the electric circuit equations, ⁽²⁾ and thus the role of the field analysis was the determination of inductances, both self and mutual. This meant that the methods used in the field analysis did not have to produce accurate values of flux density at all points in space, rather the requirement was for the integral of the flux over a surface (bounded by winding) to be reasonably accurate. There was also the practical requirement that as part of a larger programme the field analysis had to be economical of time.

These two considerations led to the development of a hybrid analytical numerical technique described in the paper and which has proved very successful for the model tested.

2. Description of the Laboratory Model

Plate 1 shows the laboratory model which has been used in the work. It is seen that it has the salient features of the earlier proposals ⁽¹⁾ for a.c. superconducting generators, an iron-less magnetic circuit and an outer eddy current environmental screen. Because of the linearity of the problem considered low flux densities are acceptable, and hence room temperature windings are used and these are supported by wooden structures. One feature not shown on the plate is the rotor screen, which is required in the full sized machine to protect the superconducting winding from time changing fields experienced during faults etc. This screen is a thin walled aluminium cylinder which is a sliding fit onto the rotor structure. The latter is connected to a shunt D.C. machine and is balanced to allow operation at 3000 r.p.m.

3. Calculation of the magnetic field including the environmental screen.

a) Numerical solution

The field due to the stator (or rotor) saddle type windings in air is calculated using the Biot-Savart equation ⁽³⁾

$$\frac{dB}{4\pi r^2} = \frac{\mu J}{4\pi r^2} \frac{dl \times r}{r^2}$$

where dl is the vector current element and r is a unit vector from the element to the point under consideration. The calculation is organized in such a way that the components of flux density at a point due to the straight portion and the end winding are available separately.

b) Analytical Solution

Because the environment screen, and subsequently the rotor screen, is expected to play a significant role in modifying the field, a solution which includes its effects is necessary. An exact numerical solution would be difficult so a two dimensional analytical solution is obtained and the results modified as explained in subsequent sections.

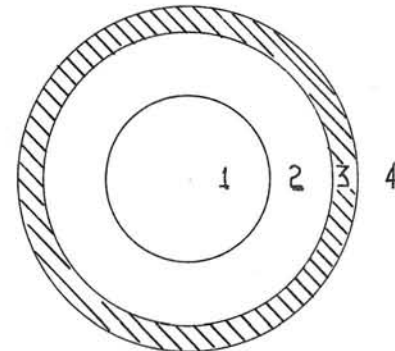


Fig. 1.

Region 1	Winding interior
2	Air
3	Screen
4	Exterior (Air)

Neglecting displacement currents and assuming $\text{div } A = 0$ then Maxwells equations reduce to

$$\frac{\delta^2 A}{\delta r^2} + \frac{1}{r} \frac{\delta A}{\delta r} + \frac{1}{r^2} \frac{\delta^2 A}{\delta \theta^2} = 0 \text{ regions 1 2 and 4}$$

and

$$\frac{\delta^2 A}{\delta r^2} + \frac{1}{r} \frac{\delta A}{\delta r} + \frac{1}{r^2} \frac{\delta^2 A}{\delta \theta^2} = \frac{\mu}{\sigma} \frac{\delta A}{\delta t} \text{ region 3}$$

for the infinitely long system whose cross-section is shown in figure 1. The current in the rotor winding between regions 1 and 2 (considered to be the exciting winding) is represented by a Fourier series

$$k_z = Rc \sum_{n=1}^{\infty} k_{zn} e^{-jn\theta} e^{j\omega t}$$

where k_z is line current density.

Application of the appropriate boundary conditions yields the values of the constants in the solutions of the differential equations and hence the radial and tangential flux densities are found using

$$B_r = \frac{1}{r} \frac{\delta A}{\delta \theta} \text{ and } B_\theta = - \frac{\delta A}{\delta r}$$

c) Modification for finite length

Consider a portion AB of a straight wire. (fig. 2). The flux density at P due to a current in this wire is given by

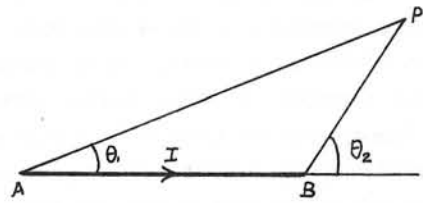


Fig. 2.

$$B_p = B_\infty \frac{\cos \theta_1 - \cos \theta_2}{2}$$

where B_∞ field due to infinitely long straight wire. Now the model used for the analytical solution may be assumed to have an exciting winding consisting of an infinite number of such current elements, each of which is thus modified by a factor $\frac{\cos \alpha' - \cos \beta'}{2}$, which varies around the machine. Hence the modified, finite length, value of flux density is given by

$$B_{ss} = B_\infty \frac{\cos \alpha - \cos \beta}{2}$$

where B_{ss} is the modified flux density (either radial or tangential) due to the straight length of the exciting winding in the presence of the outer screen,

B_∞ is the solution of the analytical method

and $(\cos \alpha - \cos \beta)$ is the average value of the individual element terms $(\cos \alpha' - \cos \beta')$

The evaluation of this average value showed that it could be obtained by a rapidly convergent series. This modification of the analytical solution yields information about the components of flux density due to the straight portion of the exciting winding, but ignores the end windings which in an ironless machine are important.

d) Derivation of the effect of the endwindings in the presence of the environmental screen

Let B_{sa} be the component of flux density (either radial or tangential) due to the straight portion of the exciting winding, with no screen
 B_{ss} as above but with the environmental screen.

B_{ea} the component of flux density due to the end winding, with no screen.

and B_{es} the component of flux density due to the endwinding with screen.

The values of B_{sa} and B_{ea} are derived from the Biot-Savart calculations and B_{ss} by the method described in 3 c). It is assumed that under the steady state operation considered the eddy current screen has a demagnetising effect given by

$$\frac{B_{ss}}{B_{sa}}$$

and hence the value of flux density due to the endwinding with the screen present is given by

$$B_{es} = B_{ea} \frac{B_{ss}}{B_{sa}}$$

and then the total flux density at a point is

$$B_{ss} = B_{ss} + B_{es}$$

This calculation is performed on the spatial components. B_r, B_θ, B_z in turn.

From the solution of the field problem the inductances - stator and rotor self and stator to rotor mutual - are derived by an integration of the radial component of flux density over appropriate surfaces bounded by the windings.

4. Comparison of Predicted and Experimental results

Measurements of flux density at various points in the model were made by search coil techniques under steady state conditions. Some of the results are presented in graphs 1 and 2 which show the measured and predicted flux densities in the axial centre of the machine and at stator and screen radii respectively. In graph 2 the predicted and measured radial flux density were both sensibly zero when the screen was in position.

It is seen that the agreement between predicted and measured values is good, and good correlation of the tangential component at the screen radius (graph 2) is particularly encouraging.

Further evidence of the accuracy of the technique is afforded by a comparison of measured and predicted inductances shown in table 1.

TABLE 1

Parameter	Predicted Value	Measured Value
L _a stator self ind	240 mH	242 mH
L _F field self ind	94 mH	93 mH
M _F field to mutual ind	51 mH	49 mH

The agreement between predicted and measured values of flux density is less accurate near the ends of the screen at radii similar to the screen radius. This is because the technique ignores the circumferential currents in the screen. The effect is however localised and acceptable for the problem considered.

5. Determination of the effect of the rotor screen

Unlike the environmental screen where the steady state performance is the more important, the rotor screen is primarily concerned with transient conditions such as faults. For "thin" screens which could be represented by circuits with constant parameters, it was thought that the steady state parameters would be suitable for the prediction of transient behaviour. Additionally the calculation of the steady state field distribution for the different positions of the screen and exciting winding would be a useful check of the validity of the technique. Some of these field values are given in graph 3, which shows the measured radial flux density at two radii between the rotor and the stator, and the distribution calculated by the analytical/numerical technique. It is seen that the agreement is good.

In the prediction of the transient terminal performance of the machine, the rotor screen is represented by short circuited windings, whose inductance parameters are determined from the field solution.

To evaluate the resistance as a lumped parameter either the technique of Laithwaite⁽⁴⁾ could be used, or the power loss of the screen can be evaluated and then it be assumed that the screen is replaced by a specific winding whose resistance is such as to give the appropriate loss. Using the second technique the power loss in a conducting plate of thickness 2b in a magnetic field is such as to give an effective resistance per unit surface area of

$$R = \frac{1}{2\sigma\delta} \frac{\sinh(2b/\delta) + \sin(2b/\delta)}{\cosh(2b/\delta) - \cos(2b/\delta)}$$

In this instance it was assumed that the winding which replaces the screen is the same as the rotor winding at the screen radius, whence (6)

$$R = \frac{3\rho}{4\delta} \frac{l_t N^2}{\pi r} \frac{\sinh(2b/\delta) + \sin(2b/\delta)}{\cosh(2b/\delta) - \cos(2b/\delta)}$$

where ρ = resistivity
 δ = skin depth
 l_t = length of mean turn
 N = number of turns
 r = mean radius

In addition to calculating the magnetic field by the previously described technique, the idea of the replacement winding was employed. Once the inductance and resistance parameters of the winding have been determined it is a simple matter to determine the current in the screen by circuit analysis (for steady state operation in this instance), and hence the field distribution can be found using the Biot-Savart equation. The results of this are also presented on graph 3 (broken line) and whilst it is seen that the technique is not as accurate as the analytical numerical technique the results are encouraging.

6) Prediction of Transient Performance

Using the step by step technique of Reddy and Jones⁽²⁾ and the values of circuit parameters derived from the field analysis, the short circuit performance of the machine can be predicted. Graph 4 shows the experimental and predicted results for a line-line short circuit on the model machine, the agreement between the measured and the predicted values is seen to be good. The broken peaks on the graph of field current show its value when the rotor screen is removed, illustrating the small but definite screening effect of the thin aluminium cylinder.

References

- (1) Appleton, A.D. and Anderson, A.F. "A Review of the Critical Aspects of Superconducting A.C. Generators". Proc. of the 1972 Applied Superconductivity Conference, IEEE Pub. No. 72 CH0682-5-TABSC, p 136
- (2) Reddy, I.C.T. and Jones C.V. "Line-Line Short Circuit of Synchronous Machines: Illustration of Computer Aided Machine Analysis" Proc. IEE Vol 118, Jan 1971, p 161.
- (3) Lawrenson P.J. "The Magnetic Fields of End-Winding of Turbo-Generators" Proc IEE, Vol 108, March 1961, p 538
- (4) Laithwaite, E.R. "Induction Machines for Special Purposes" Newnes, London 1966.
- (5) Hammond P. "Applied Electromagnetism" Pergamon Press, London 1971
- (6) Rahim Y.H.A. Ph.D Thesis "Predictions of the Transient Parameters of an Air Cored Alternator" Liverpool University (1975)

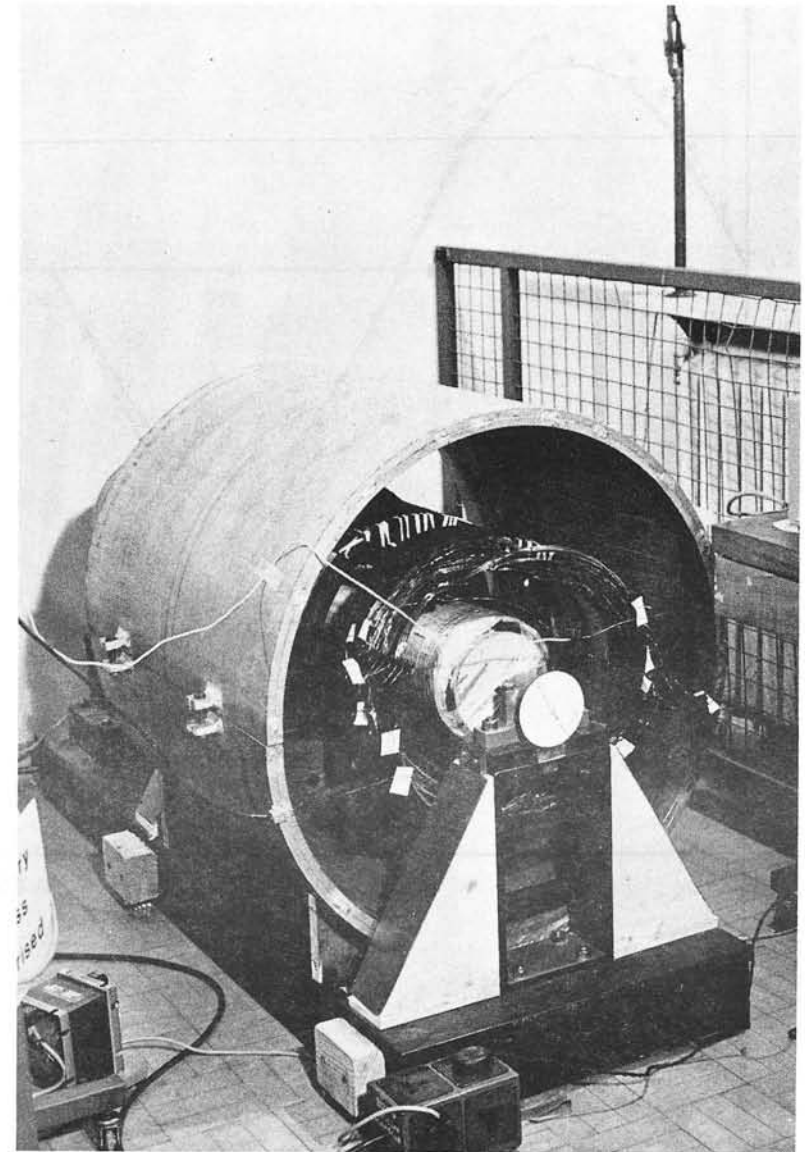
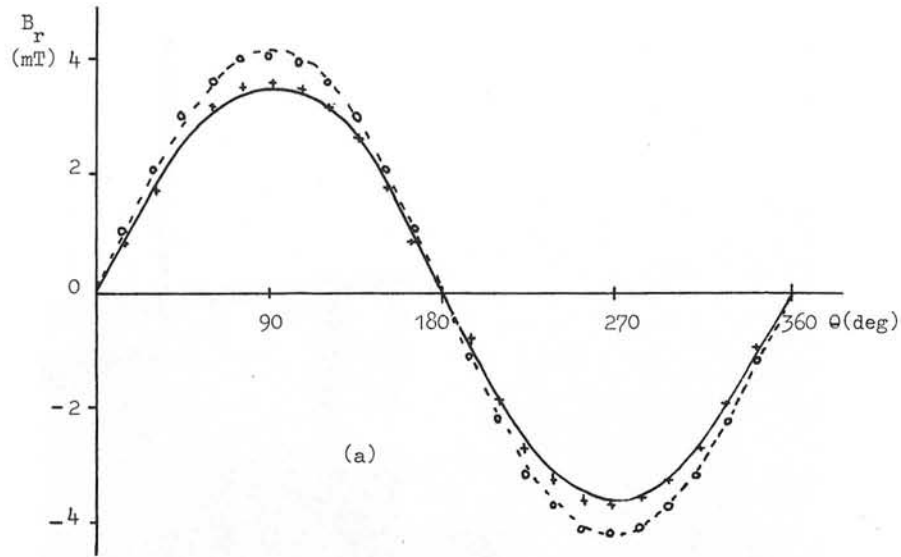
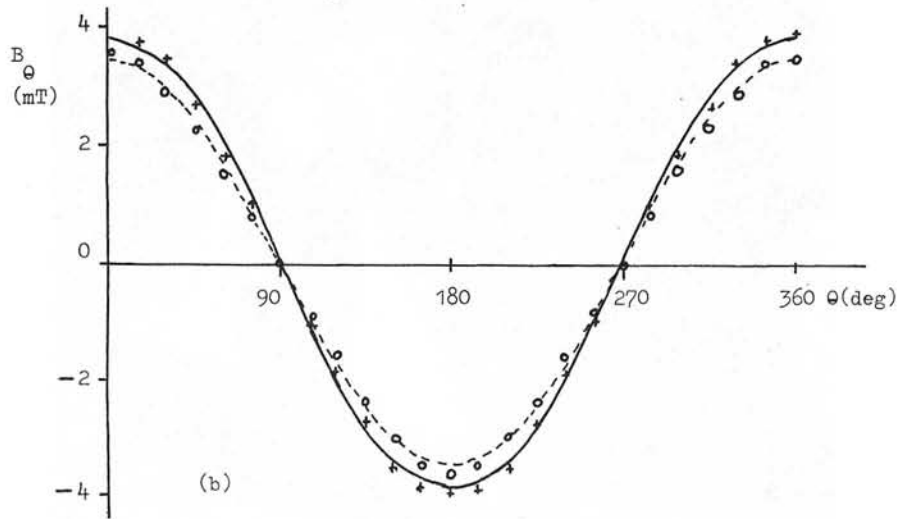


Plate 1 - The laboratory model

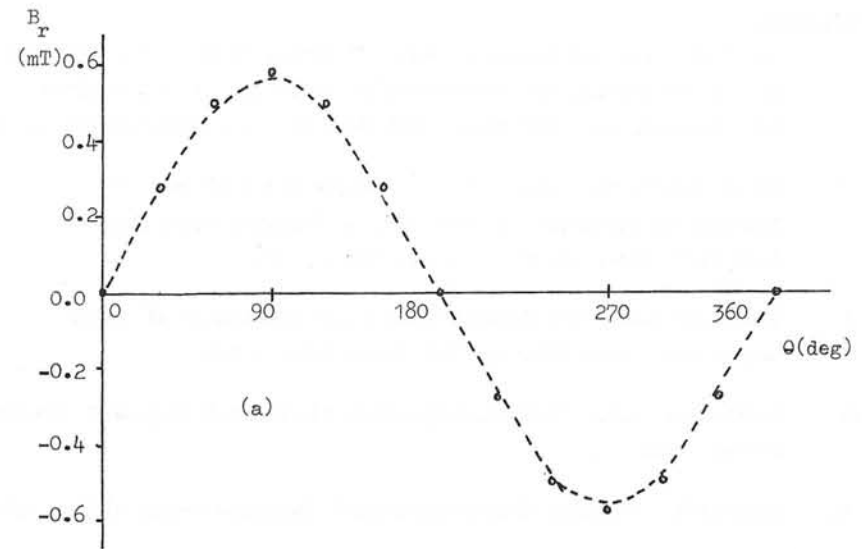


(a)

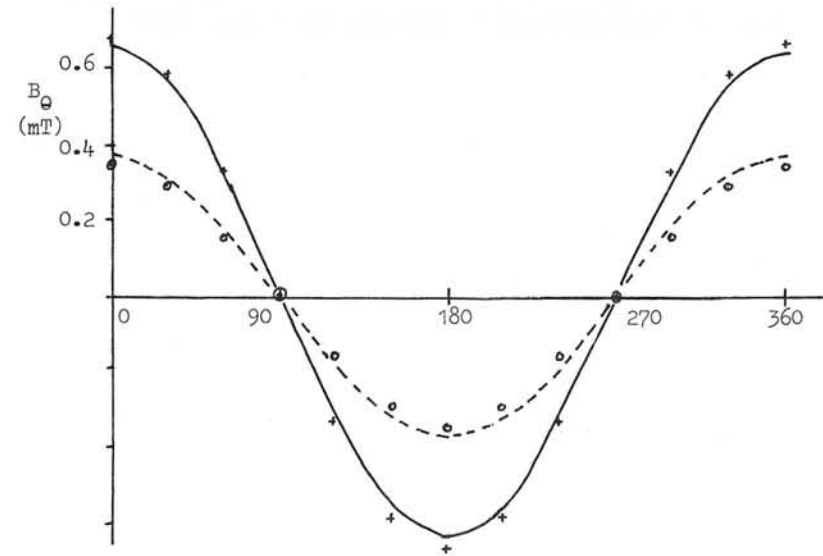


(b)

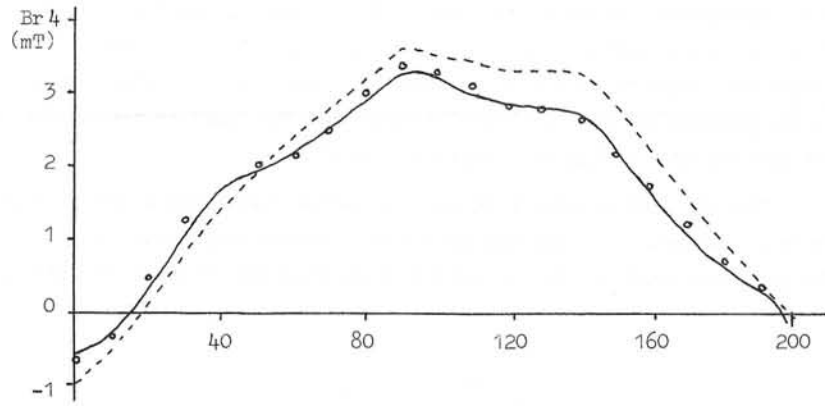
Graph 1 - Flux density at the centre of the stator
 a - radial, b - tangential
 + + + predicted in presence of the screen
 - - - measured " " " " "
 predicted in air
 measured " " "



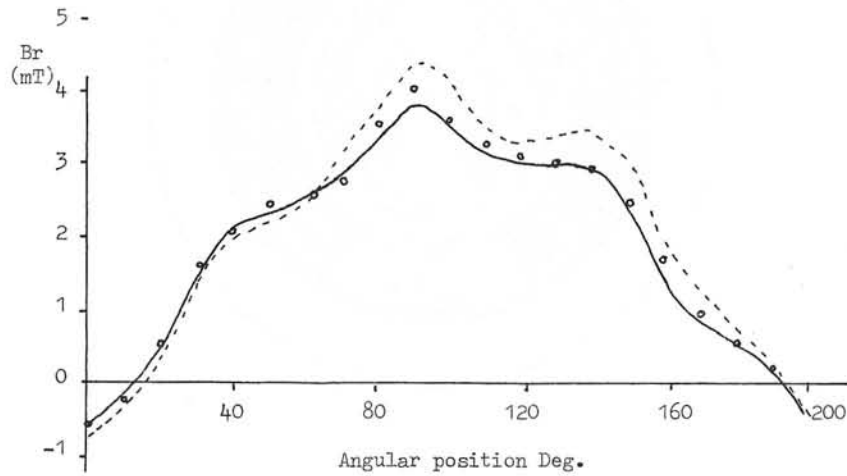
(a)



Graph 2 - Flux density at the centre of the screen,
 a - radial, b - tangential
 - - - predicted in presence of screen,
 predicted in air
 + + + measured in presence of screen,
 measured in air



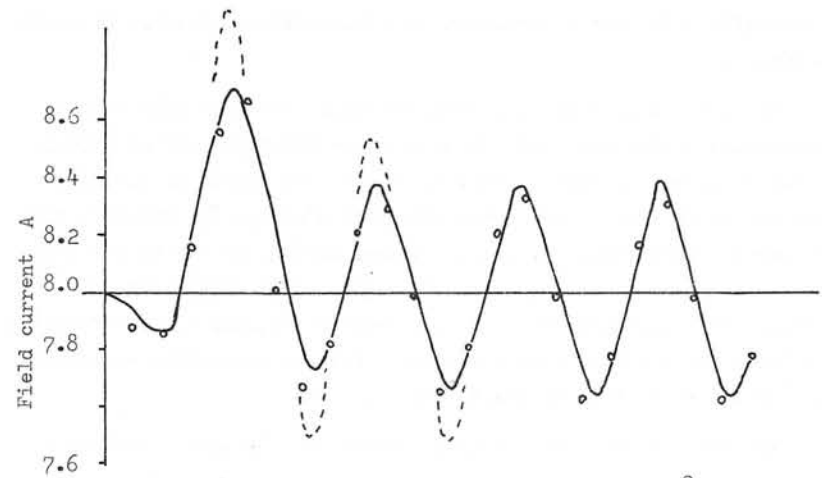
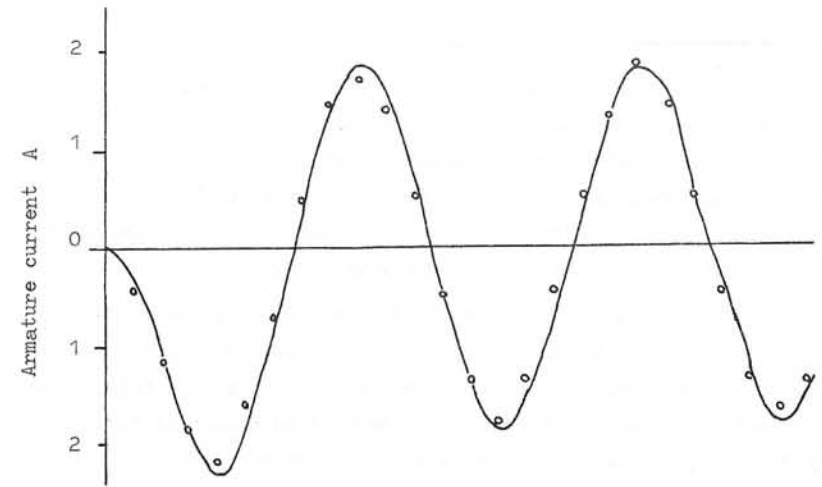
(a)



(b)

Graph 3 - Variation of radial flux density with angular position at $t = 0$, and $a - r = 13.5$ & $b - r = 15$ cm, using the thin screen.

- analytical numerical method
- - - numerical method using winding replacement
- measured



Graph 4 - Line-line short-circuit at $\theta = 90^\circ$
 $V_F = 90$ V $I_F = 8$ A

- predicted
- measured

P. DEL VECCHIO^(°); G. SACERDOTI^(o) and G.M. VECA^(°)

Electromagnetic Behaviour of a Rotating Screen for a Superconducting Inductor of a Synchronous Machine.

1. - INTRODUCTION

The present tendency to increase the specific power of a single unit has led to the study of generators with a power higher than 1000 MVA. For such a power it was thought convenient (1), both economically and technically, to propose the use of units with a superconducting inductor, in spite of the large number of problems involved in their operation at cryogenic temperatures.

In these machines, the magnetic fields in the stator are higher than those of conventional units, with a dissipation in excitation that is practically equal to zero. The power being equal, this allows a reduction in size, weight and cost, as well as potential advantages (4)(6) during operation, thanks to the comparatively low per-unit synchronous reactance, characteristic of these machines.

The morphology (1)(4)(5)(6) of the synchronous cylindrical symmetry machines, presently under study in various countries, is practically only one; a section of an illustrative character is shown in fig. 1.

The s.c. field winding externally shows, integral with it a cylindrical conducting screen to which many functions are entrusted; in the first place, that of magnetic shield for fields at any rate variable in respect of the superconductive winding; secondarily, that of damper of the rotor swing oscillations during the little and great perturbations. Furthermore, with its high thermal diffusivity, it protects the superconductor from the dangers deriving from overheating. The last, but not the least function is that of preventing vibrations and overstresses in a non stationary state (4).

All these numberless functions cannot be effectively performed

(o) of the National Laboratories of CNEN in Frascati.

(°) of the the Electrotechnics Institute of the University of Roma.

by one single conducting cylinder, as proposed in the early works on s.c. generators, as some functions call for characteristics in conflict with one another. It thus became apparent (5) that at least two concentric shields are required: the outer, at room temperature, performing the function of damper, and the inner at the liquid He temperature, acting as a magnetic shield.

For the sake of concreteness, the Authors have considered in this work the screen of a 1300 MVA alternator, with a morphology similar to that indicated in fig. 1, presently in progress of study at ANSALDO

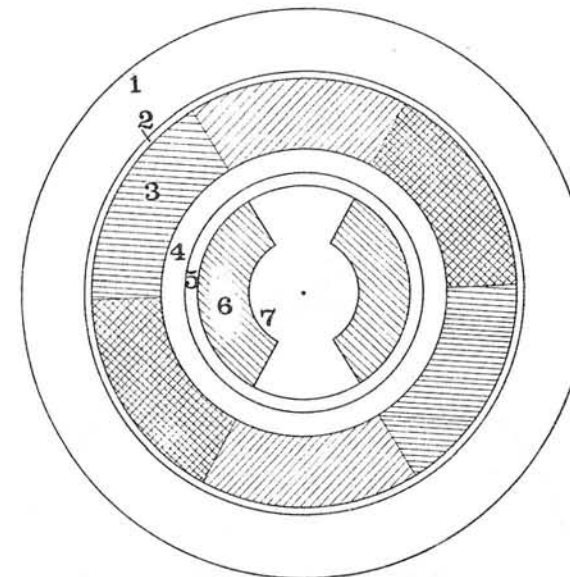


Fig. 1 - Cross sectional view (not in scale) of a synchronous machine with a superconducting inductor. 1) - Iron magnetic screen
2) - Air gap 3) - Stator windings 4) - Air gap and dewar's place
5) - Electromagnetic screen 6) Superconducting winding
7) - Rotor

of Genoa, and have studied, using the potential vectors analytical method (2)(3)(7), its behaviour at the stationary state providing numerical results for a special case.

The method, however, has a more general validity and is used also in non stationary cases, as summarily described hereunder.

2. Method for the Determination of the Current Induced in the Screen, and equivalent alternator circuit.

It was pointed out (2)(3)(7), that inside a machine with a morphology similar to that shown in fig. 1, the principle of the superimposition of the effects is valid with an optimal approximation, even if the presence of iron is found outside the stator, on the condition that its saturation is still distant; with regard to the magnetic field computation within the screen, the additive property was thus applied to the potential vectors determined each time as shown hereunder.

Once a reference system in cylindrical coordinates, fig. 2a) and 2b), is chosen, which is integral with the stator; and if we neglect the edge effect^(°), the Poisson-like equation, developed in Fouruer's series for the partial harmonics due to the J current density distribution, will be, as it is well-known, as follows (2)(3):

$$\nabla^2 A_z = - \sum_n J_n \cos n \theta \quad (1)$$

where

$$J_n = \frac{4}{\pi n} J \sin n \theta_0 \quad (n = 1, 3, 5, \dots)$$

with "n" being the harmonic order, θ_0 the geometric angle with the indicative meaning in fig. 2, and J the current density generating the field, constant along r.

(°) that is, in the assumption of a very long machine in respect of the diameter.

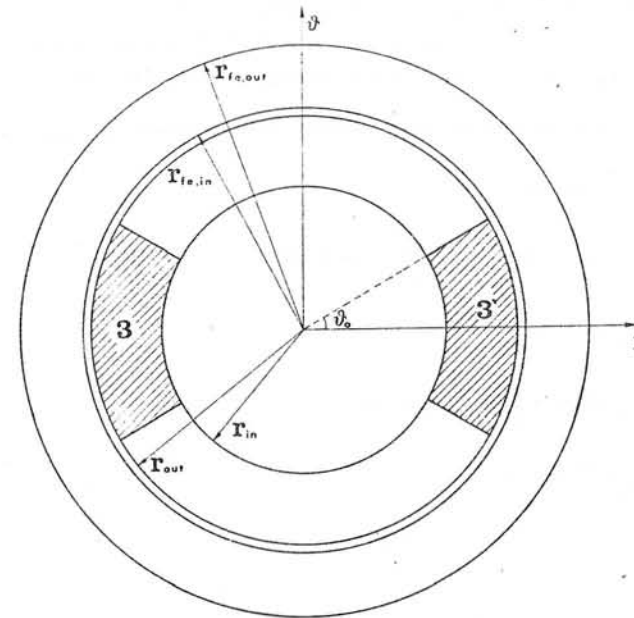


Fig. 2a)
Cross sectional view of stator in which are indicated the geometrical parameters used in the formulas.

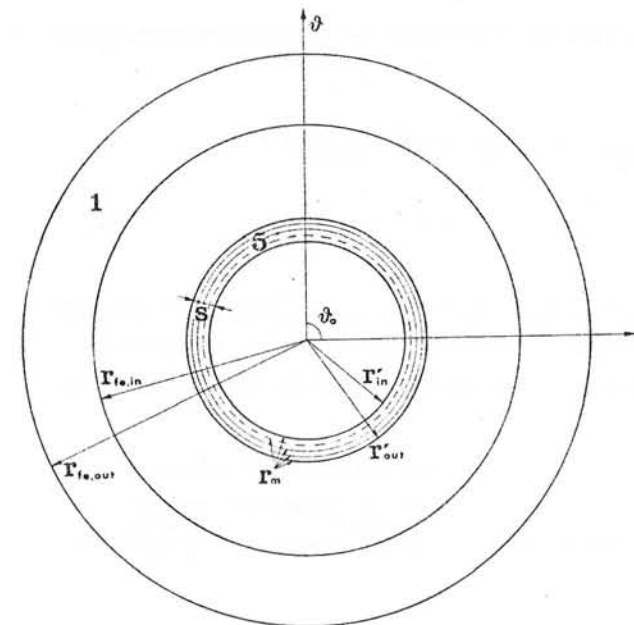


Fig. 2b)
Cross sectional view of electro-magnetic screen in which are indicated the geometrical parameters as well as some shells.

From (1), taking into account the fact that physically the magnetic field has a finite value for $r = 0$ and 0 for r tending to the infinite, the potential vectors relative to the general harmonic "n" in the various regions of the machine are given by the following expressions derived from Coupland⁽²⁾:

$$A_{I,n} = J_n A_{i,n} r^n \cos n\theta$$

$$A_{II,n} = J_n (K r^2 + a_{2,n} r^n + a_{3,n} r^{-n}) \cos n\theta$$

$$A_{III,n} = J_n (a_{4,n} r^n + a_{5,n} r^{-n}) \cos n\theta$$

$$A_{IV,n} = J_n (a_{6,n} r^n + a_{7,n} r^{-n}) \cos n\theta$$

$$A_{V,n} = J_n a_{7,n} r^{-n} \cos n\theta$$

where

$$K = - \frac{\mu_0}{4-n^2}$$

and the indices I, II, III, IV, V indicate the following regions of the machine, respectively:

$$(I): r < r_{in}; (II): r_{out} < r < r_{in}; (III) r_{fe,in} < r < r_{out}$$

$$(IV): r_{fe,out} < r < r_{fe,in}; (V): r > r_{fe,out}$$

where by r_{in} and r_{out} there were indicated, respectively, the internal and external radius of the cylindrical symmetry winding involved by the current generating field, and the other radiuses have the meaning indicated in fig. 2.

The coefficients $a_{1n}, a_{2n}, \dots, a_{8n}$ are derived from relations 2 bearing in mind that in correspondence of the separation surfaces of the various regions, components $B_{rin} = \frac{1}{r} \frac{\partial A_{in}}{\partial \theta}$ and $H_{\theta in} = \frac{1}{\mu} \frac{\partial A_{in}}{\partial r}$, for

$i = I, II, III, IV, V$, are continuous. These coefficients are a function of the geometric parameters alone, and are practically independent from the relative permeability of the iron of stator's outer screen, on condition that $m_{rf} > 20$ (2) (3); they are of the following type:

$$a_{1,n} = -K \frac{n+2}{2n} (r_{out}^{2-n} - r_{in}^{2-n}) + K \frac{n-2}{2n} (r_{out}^{n+2} - r_{in}^{n+2}) \cdot \frac{(r_f^2 - 1) (r_{fe,out}^{2n} - r_{fe,in}^{2n})}{r_{fe,in}^{2n} [(\mu_f + 1)^2 r_{fe,out}^{2n} - (\mu_{rf} - 1)^2 r_{fe,in}^{2n}]}$$

The relations mentioned above and obtained for a case of current density distribution constant over a period of time, can be generalised, for application to the case of rotating machines with a geometry similar to that indicated in fig. 1, taking into account the fact that the J_n density of current will be expressible by means of an analytical law of the following type:

$$J_n(t, \theta) = J_n e^{i(n\theta - \omega_{nt})}$$

characteristic of the rotating magnetic field, consequent to the presence of three windings, of the type shown in fig. 2a), suitably placed in the space, through which there circulate sinusoidal currents dephased in time. In the case in which the three currents form a balanced system, they give birth to a field synchronous with the rotor, without interacting, therefore, with the screen. If we consider instead the presence of the space and time harmonics of an order higher than the first one, and the presence of a dissymmetry in the values of the currents circulating in the three phases owing to a dissymmetrical load, are generated which fields of pulsations $\omega_n = -\frac{n-1}{n} \omega$ not synchronous with the rotor. Therefore, in these assumptions, the magnetic fields that will interact with the screen, will be derived from potential vectors of the type:

$$A_n(t, \theta) = A_n J_n e^{i(n\theta - \omega_{nt})}$$

If the screen is divided into "M" shells, as shown in fig. 2b),

the potential vectors due to the stator, calculated in the mid point of the m-nth shell and having a relative movement in respect to it, are given by:

$$A_{n,m}^0 = a_{1,n} r_m^{*n} J_{0,n} e^{j(n\theta - \omega_n t)} \quad (m = 1, 2 \dots M)$$

where r_m^* is the mean radius of the m-nth shell and 'o' is the index used for denominating the stator.

Since the screen is divided into M shells, of any Δ_m thickness (the smaller Δ_m the better the approximation made by assuming density $J_{m,n}$ as being constant along r), the potential vector of m-nth shell will be given by the sum of the following M+1 terms:

$$\begin{aligned} A_{n,m}^0 &= F_{0,n}(r_m^*) J_{0,n} e^{j(n\theta - \omega_n t)} \\ A_{n,m}^1 &= F_{1,n}(r_m^*) J_{1,n} e^{j(n\theta - \omega_n t + \alpha_{1,n})} \\ A_{n,m}^2 &= F_{2,n}(r_m^*) J_{2,n} e^{j(n\theta - \omega_n t + \alpha_{2,n})} \\ &\dots\dots\dots \\ A_{n,m}^M &= F_{M,n}(r_m^*) J_{M,n} e^{j(n\theta - \omega_n t + \alpha_{M,n})} \end{aligned}$$

where, by $F_{1,n}(r_m^*)$ we intended to indicate the analytical expression of the geometrical parameters relative to the i-nth shell, that contributes in the formation of the field, an expression calculated for $r = r_m^*$, the medium radius of the shell in which the field is considered.

For example, for the first shell

$$\begin{aligned} F_{0,n}(r_1^*) &= a_{1,n} r_1^{*n} \\ F_{1,n}(r_1^*) &= k r_1^2 + a_{2,n} r_1^{*n} + a_{3,n} r_1^{*-n} \\ &\dots\dots\dots \\ F_{M,n}(r_1^*) &= a_{4,n} r_1^{*n} + a_{5,n} r_1^{*-n} \end{aligned}$$

where $a_{1,n}, a_{2,n}, a_{3,n}, a_{4,n}, a_{5,n}$ are calculated as previously indicated.

From the expression $\bar{E} = -\frac{\partial \bar{A}}{\partial t}$, written in cylindrical coordinates, taking into account the situation under examination and recalling that $\bar{E}_n = \rho \bar{J}_n$, we obtain:

$$\rho_m J_{m,n} e^{j(n\theta - \omega_n t + \alpha_{m,n})} = \sum_{i=0}^M -\frac{\partial A_{n,m}^i}{\partial t} \quad (m = 1, 2 \dots M) \quad (3)$$

where by ρ_m we indicated the resistivity of the m-nth shell^(°). If we neglect in (3) the dependence on time and angle, we obtain:

$$(4) \quad \rho_m J_{m,n} e^{j\alpha_{m,n}} = \sum_{i=0}^M -j\omega_n F_{i,n}(r_m^*) J_{i,n} e^{j\alpha_{i,n}} \quad (m=1, 2 \dots M)$$

it being a system of equations in the unknowns $J_{m,n} e^{j\alpha_{m,n}}$ with known terms equal to $j\omega_n F_{0,n}(r_m^*) J_{0,n}$, that admits univocal solutions, and the greater the fractioning of the screen, the more accurate such solutions will be.

Being thus made known for each shell the $J_{m,n} e^{j\alpha_{m,n}}$ distribution of the current density, the determination of the magnetic field within all the points of the machine is immediate, because, the additive property being valid, we will have:

$$(5) \quad \begin{aligned} \bar{B}_{r,n}(r,t,\theta) &= \sum_{i=0}^M B_{r,n}^i = \sum_{i=0}^M \frac{1}{r} \frac{\partial A_n^i(r,t,\theta)}{\partial \theta} \\ \bar{B}_{\theta,n}(r,t,\theta) &= \sum_{i=0}^M B_{\theta,n}^i = \sum_{i=0}^M -\frac{\partial A_n^i(r,t,\theta)}{\partial r} \end{aligned}$$

where the analytical expression of each A_n^i is known, and where all its numeric coefficients are also known.

The effectiveness the screen is thus determined by means of the attenuation coefficient as defined by the following ratio:

(°) This resistivity may change with the index "m" as a result of the disuniform distribution of temperature in the screen, and also and chiefly if we consider a multi-shield configuration of the screen, such shields being made of different materials.

$$G_n = \frac{|\overline{B}_{r,n}(r'_{in}, t, \theta)|}{|\overline{B}_{r,n}(r'_{out}, t, \theta)|}$$

where r'_{in} and r'_{out} are the inner and outer radiuses of the screen, respectively.

It is further possible to determine the Joule power dissipated in the screen as a result of the induced currents, through the following expression:

$$P_n = \sum_{m=1}^M P_m = \frac{1}{2} \sum_{m=1}^M \rho_m |\overline{J}_m|^2 (r_{m,out}^2 - r_{m,in}^2)$$

where $r_{m,out}$ and $r_{m,in}$ are the outer and inner radius of the m -nth shell, respectively.

Again, it is also possible to determine the equivalent impedance of a phase of the stator, when the alternator works in a steady condition.

If we indicate by r_o^* the value of the radius which identifies the mean circumference of the stator, the potential vector $A_{n,o}^*(t)$ calculated in r_o^* is given by the sum of its own field plus the summatory of the fields due to the M shells plus the potential due to the field winding:

$$A_{n,o}^*(t) = A_{n,o}^o(t) + \sum_{i=1}^M A_{n,o}^i(t) + A_{n,o}^{field}$$

Therefore, the electric field in r_o^* will be due to the field of the currents circulating in the stator plus that due to the derivative made in respect of the time of the total potential vector:

$$\overline{E}_n = \rho_{stator} \overline{J}_{o,n} + \frac{\partial A_{n,o}^*}{\partial t} = (\rho_{stator} + \rho') \overline{J}_{o,n} + j\omega_n L' \overline{J}_{o,n}$$

where by ρ' we indicated an equivalent fictitious resistivity to be summed up to that of stator, which does not represent anything but the sum of the all the contributions in phase with $\overline{J}_{o,n}$ of the summatory

$\frac{\partial A_{n,o}^*}{\partial t}$, while L' is the imaginary part.

The equivalent impedance of a stator phase results, therefore, from the following expression:

$$Z_{eq,n} = \frac{(\rho_{stator} + \rho') + j \omega_n L'}{\rho_{stator}} R_o$$

where R_o is the resistance of the winding of a stator phase. As it is obvious, to calculate $Z_{eq,n}$ with a higher degree of approximation, one should not confine oneself to the calculation of the potential vector $A_{n,o}^*(t)$ on the mean radius r_o^* , but it would be necessary to calculate both the potential vector and the electric field, turn by turn, with reference to the actual winding distribution.

Finally, if we want to consider the more general case of currents at any rate variable throughout time and with no relation between the phases and the amplitudes flowing through the three stator windings, for the determination of the field generated by the stator, the three distinct contributions of the single windings will have to be considered in order to determine both the current distribution in the M shells of the screen and the mutual couplings of the three phases. Therefore, the total field in any point of the machine shall be calculated by an expression of the following type:

$$(6) \quad A(t) = A_{s,1}(t) + A_{s,2}(t) + A_{s,3}(t) + A_{s,f}(t) + \sum_{m=1}^M A_m$$

where $A_{s,1}$, $A_{s,2}$ and $A_{s,3}$ are the potential vectors due to the three stator phases, $A_{s,f}$ is the potential due to the field winding, and the summatory indicates the contributions offered by the M shells.

Assuming to be able to express, by first approximation, for each stator winding, the distribution of the turns with the following formulae:

$$N_{s,1} = N_1 \cos \theta + N_2 \cos(2\theta + \beta_2) + N_3 \cos(3\theta + \beta_3) + \dots + N_k \cos(k\theta + \beta_k)$$

$$N_{s,2} = N_1 \cos(\theta + \frac{2}{3}\pi) + \dots$$

$$N_{s,3} = N_1 \cos(\theta + \frac{4}{3}\pi) + \dots$$

where β_k is the angle which takes into account the pitch of the winding, the current density for each phase and for a given harmonic will be given by:

$$J_{n,s,k} = \frac{I_k(t)}{r_0 \Delta r d\theta} N_{sk} \quad (k = 1,2,3)$$

where r_0^* is the value of the radius which identifies the mean circumference of the stator whose thickness is Δr .

On the other hand, the voltage induced, by length unit, on each stator winding will be given by:

$$E_k = - \int_0^{2\pi} \frac{\partial A}{\partial t}(t) N_{sk} d\theta \quad k = 1,2,3$$

where the potential vector $A(t)$ will be expressible with relation (6).

Using the above mentioned expressions it will be thus possible to solve all the problems considered for the case in a steady state and also for the unsteady state, even though in the latter instance computations will be more laborious.

Conclusive considerations

For the sake of brevity, the Authors have shown a diagram giving the Joule power dissipated in the screen in the case of one single shield and considering one single amplitude shell proportional to the penetration depth of the frequency field (fig. 3).

The method may attain an accuracy at any rate high, by reducing the thickness of the shells into which the screen and the stator are divided. This clearly occurs with a marked proliferation of the equations required for the determination of the necessary quantities; the basic value of the method is its intuitiveness and simplicity if a fair compromise is maintained with the desired accuracy. This method also allows to identify a mathematical model, very close to the actual one, that simulates its dynamic behaviour.

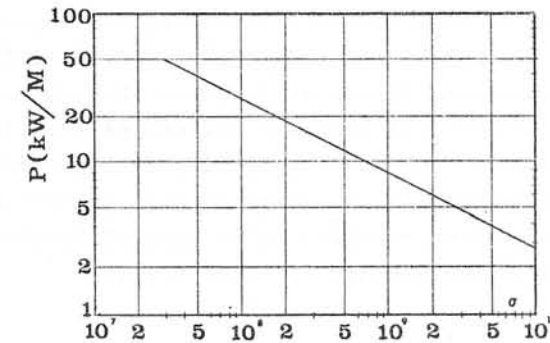


Fig. 3 - Diagram giving the Joule power dissipated in the screen in the case of one single shield and considering one single amplitude shell proportional to the penetration depth of the frequency field. $r_{Fe,out} = 1.550$ M, $r_{Fe,in} = 0.950$ M, $r_{out} = 0.900$ M, $r_{in} = 0.575$ M, $r'_{out} = 0.510$ M, $r'_{in} = 0.500$ M 0.169 A/mm² backward density current due to an unsymmetrical load.

BIBLIOGRAPHY

- (1) - M.J.Jefferies et al., Prospects for superconductive generators in the electric utility industry, IEEE Transactions paper n.T 73.252-4 (1973)
- (2) J.H.Coupland, Equations and formulae for magnets with air cored windings of "saddle coil" type, Rutherford High Energy Laboratory Report RHEL/R 203 (1970)
- (3) G.Veca et al., Determinazione della distribuzione di corrente negli induttori di turboalternatori con avvolgimenti superconduttivi, Atti e Memorie dell'Accademia Patavina di Scienze, Lettere ed Arti, vol.LXXXVI, (1973-1974), Parte II
- (4) T.A.Keim et al., Electromechanically driven and tuned vibrations in superconducting alternators, IEEE PES Winter-Meeting N.Y. January 25-30 1976
- (5) D.Luck et al., Double shielded superconducting field winding, U.S.Patent n°3,764,835, Oct.9, 1973
- (6) T.H.Einstein - System performance characteristics of superconducting alternators for electric utility power generation, IEEE Trans. PAS-94, n°2, March/April 1975
- (7) P.Del Vecchio et al. Comportamento elettromagnetico dello schermo rotorico di un turboalternatore con induttore superconduttore, LNF-75/51(R)

COMPUTER AIDED STEADY-STATE AND TRANSIENT SOLUTIONS OF
QUASI-ONE DIMENSIONAL FIELD PROBLEMS IN INDUCTION DEVICES

by Dr. E.M. Freeman
Department of Electrical Engineering, Imperial College, London.

1.1 Introduction

Many induction devices can be represented, in cross-section, by multi-region models, as depicted in Figs. 1 and 2. The excitation is provided by an infinitesimally thin current sheet, which can be sinusoidally distributed in space. The problem is to solve the field equations for the various field components so that the complex power flow and the forces, if any, can be determined. The object of the paper is to show how, by suitable formulation of the problem, a computer may be used to advantage. Initially, the method of solution was purely algebraic and the coming of computers simply saved calculation time. Over the years, computers have been employed at earlier and earlier stages in the solution. Now the point has been reached where very little preliminary algebra is required before the computer can take over both the steady state and transient solutions of the problem.

This is done using two methods based on transmission line analogues. In the first, the transmission line model is represented by strings of micro-T-circuits, each one of which models a short section of line. Then by using a circuit analysis package, such as ECAP or SPICE, the steady state and transient behaviour may be determined. In the second, a scalar Riccati equation is derived for the wave impedance of the model. This method is suitable for sinusoidal steady state problems only.

To illustrate the historical development, reference will be made to two problems. The first is the planar problem with a travelling wave of excitation, Fig. 1, and the second is that of a rotating magnetic field, as in a rotary induction motor, Fig. 2.

The term "quasi-one dimensional" is used in the title. This is because cisoidal variations of the field in one direction can be included in the analysis. Under certain conditions devices with

cisoidal variation in two directions can be modelled, but great care is required.

1.2 Historical development

Purely algebraic approaches to the planar and cylindrical problems can be found frequently in the literature, e.g. references 1, 2 and 3. Separation of variable theory was used to produce a solution in each region. Enclosed regions required two arbitrary constants and unbounded regions, one constant. Using the appropriate boundary conditions, algebraic expressions were derived and hence, algebraic expressions obtained for the field variables. Lengthy algebra was often required to obtain closed expressions for power and forces. The advent of computers initially made little difference. The computer was used simply to calculate numerical values from the algebraically derived expressions. The number of regions was limited by the vast amount of algebraic manipulation required. As a first step in introducing the computer to the problem, as other than a calculator, some authors solved numerically for the arbitrary constants, e.g. ref. 4. For an N-region problem, there are $(2N - 2)$ arbitrary constants. It was thus necessary to invert a $(2N - 2) \times (2N - 2)$ matrix with complex coefficients. This is time consuming and could require a large computer.

It was possibly Pipes⁵, who first showed, in a machines context, that a transfer matrix could be used to simplify the problem, by linking a pair of unknown quantities on either side of a region. The technique was used later for the travelling and rotating wave problems^{6,7}. The transfer matrix can be derived algebraically, or numerically, with the aid of a computer. The use of a transfer matrix completely removes the limitation on the number of regions.

The transfer matrix form of solution suggests a transmission line. Indeed, a search of the literature showed that Cullen and Barton⁸ had already appreciated this point in a 1958 paper. They took the problem one step further, making use of the concept of "wave impedance" in a machine. This idea was extended in ref. 9 to develop an equivalent circuit, as seen from the terminals, using circuital rather than field quantities. The equivalent T-circuit for a single enclosed region can

be called a macro-T-Circuit. This is to distinguish it from a micro-T-circuit¹⁰, which can represent a very thin or elemental region. The advantages of a macro-T equivalent circuit are obvious, but there are also advantages in sub-dividing conducting regions down into a large number of micro-T-circuits. If this is done, then the device can be represented by a long string of such circuits, in cascade. On most computers some form of circuit analysis package is available. Thus the behaviour of the equivalent circuit can be studied, under both steady state and transient conditions. The transient solution for a multi-region model might otherwise be extremely difficult to obtain¹¹⁻¹³. The use of higher transcendental functions can be avoided completely, for both transient and steady state operation.

An alternative method has also been developed based on the scalar Riccati equation. This is suitable for sinusoidal steady state solutions only. The custom, in the past, has been to obtain values for the field variables in a device. If, instead one thinks in terms of wave impedance, then the Riccati form of equation may be employed. In its generalised form, it links the wave impedance to the rate of change of wave impedance, with respect to the direction of interest. It was found that the Riccati method was much faster, easier to program and easier to understand, than many of the other methods. Higher transcendental functions are completely avoided, one only needs Maxwell's equations and a suitable integration sub-routine.

In the following sections the two new methods are described in detail.

2.1 Theory of the transmission line for the planar model

The excitation is of the form $K_x = \text{Re } K \exp(j(\omega t - ky))$. Hence only E_x , H_y and H_z exist; E_y , E_z and H_x are all zero. Furthermore, there is no variation of the field in the x-direction. It follows that E_x and H_y are linked by the equations⁸:

$$\frac{\partial E_x}{\partial z} = -j\omega\mu H_y \quad \text{and} \quad \frac{\partial H_y}{\partial z} = -E_x(\sigma + k^2/j\omega\mu) \quad (1)$$

where μ is the permeability of the region under consideration
 σ is the conductivity

$$k = 2\pi/\lambda, \quad \lambda = \text{wavelength}$$

The "transmission line" equations are:

$$\frac{\partial V}{\partial z} = -ZI \quad \text{and} \quad \frac{\partial I}{\partial z} = -YV \quad (2)$$

where Z and Y are the impedance and admittance per unit length of line.

Hence, comparing coefficients:

$$Z = j\omega\mu \quad \text{and} \quad Y = \sigma + k^2/j\omega\mu \quad (3)$$

Thus a short section of line, of length g , can be modelled by the circuit shown in Fig. 3.

By joining a number of these micro-T-circuits in cascade, a complete circuit can be assembled, which represents a multi-layer model. The steady state sinusoidal behaviour can then easily be established. The transient behaviour, for any applied E or H waveform, can be found by using a circuit analysis package. At present the author is using ECAP and SPICE. It should not be overlooked that it is unnecessary to feed the details of the circuit into the computer directly. It is usually possible to feed the basic model parameters into the computer, and let the program generate the circuit parameters for the circuit analysis package.

As a check on the method, a simple problem was tried. This was the problem of a conducting semi-infinite half space with a step E or H waveform applied at the surface. This problem is discussed in many text-books, either in the field form, or as an infinite length transmission line.

To model it, as described above, the wavelength is set to zero, and the circuit parameters calculated using equations (3). The transient E and H waveforms were everywhere found to agree very closely with the exact analytical results. Of course, it is necessary to do a certain amount of experimenting in order to find the optimum thickness of a sub-region and the number of such regions. Much depends on the shape of the applied transient and the degree of accuracy required.

2.2 Theory of the transmission line for the cylindrical model

The excitation takes the form $K_z = \text{Re } K \exp(j(\omega t - \alpha\theta))$. Hence, only E_z , H_θ and H_r exist. It follows that E_z and H_θ are linked by the relationships:

$$\frac{\partial E_z}{\partial r} = j(\omega\mu/r)(rH_\theta) \quad \text{and} \quad \frac{\partial(rH_\theta)}{\partial r} = E_z(\sigma r + \alpha^2/jr\omega\mu) \quad (4)$$

$$\text{Hence } Z = j\omega\mu/r \quad \text{and} \quad Y = \sigma r + \alpha^2/jr\omega\mu \quad (5)$$

Thus a short section of line, of length g , can be modelled by the circuit shown in Fig. 4. Note the change of variable from H_θ to rH_θ . Students of Kron's work¹⁴ will appreciate that such transformations are necessary, once one gets away from the cartesian coordinate system.

The range of devices which can be modelled using this technique is wide⁷. It includes not only rotary induction devices, but also the transverse screening problem (where $\alpha = 1$) and the plated conductor problem (where $\alpha = 0$).

The transmission line impedances are a function of radius. The line is thus a non-uniform transmission line¹⁵, closely related to the Heaviside-Bessel line¹⁶.

3.1 The Riccati method

The book by Watson¹⁷ provides a most useful introduction to the Riccati equation. It was named after Count Riccati, who was one of several people interested in a certain form of linear differential equation in the early part of the eighteenth century. In ref. 18 can be found a list of basic references, which the present author has found extremely useful in studying the Riccati equation.

The general form of the scalar Riccati equation¹⁷ is:

$$\frac{dZ}{dr} = P + QZ + RZ^2 \quad (6)$$

where P , Q and R are given functions of r .

In a transmission line context, this equation relates the rate of change of wave impedance (or admittance) to the wave impedance (or

admittance)¹⁸. Normally, the solution to a transmission line problem implies that the voltage and current distributions along the line are to be established. However, very often distributions are of no use at all, one simply requires to know the input impedance to the line. The object is then to derive an equation of the form shown above. Then, instead of seeking an analytical solution, which could involve higher transcendental functions, the equation is solved by numerical integration.

3.2 The planar model Riccati equation

Looking in the positive z direction, the wave impedance is: $Z = E_x/H_y$. Substituting this in equations (1), and solving for Z , results in the following:

$$\frac{dZ}{dz} = -j\omega\mu + Z^2(\sigma - jk^2/\omega\mu) \quad (7)$$

To solve numerically, start at $z \gg z_7$ and with Z set to almost any arbitrary value, integrate towards $z = z_4$. Simply remember to change the material parameters at region boundaries and avoid large changes in Z , if necessary by reducing the step length.

This method was tried successfully against the analytical solution for a wide range of planar models. The exercise can be repeated looking downwards, and hence the input wave impedance can be determined at the current sheet, together with the power and forces. Some experimenting is required to get the optimum integration step length. It is usually fairly safe to start with a step length less than 5% of the skin depth of a region.

The method can be extended to determine the macro-equivalent circuit model. This involves three integrations across each region, two in one direction and one in the other direction.

3.3 The cylindrical model Riccati equation

Repeating the exercise for the cylindrical model, looking outwards, one obtains:

$$\frac{dZ}{dr} = -j\omega\mu + Z^2(\sigma - j\alpha^2/\omega\mu r^2) + Z/r \quad (8)$$

Note the extra term Z/r , but otherwise the equation is of the same basic form.

The advantages of using the Riccati equation are greater here than for the planar model. No Bessel functions are required, and in the case of anisotropic regions, one is spared the problem of dealing with Bessels of non-integer argument¹⁸.

Again the numerical solution was checked against the analytical solution for a wide range of models, very close agreement was obtained.

3.4 General comments

A Riccati type equation can also be obtained for cylindrical induction devices having axially travelling waves¹⁷. The extension to include simple anisotropy is straightforward and is described in ref. 18.

It is worth noting the following fact. The wave impedance at a point, is purely inductive if, up to that point, no conducting material has been encountered in the integration. The wave 'inductance' can thus be obtained, so saving time, if another frequency is to be considered.

4. Conclusions

Two methods for solving field problems in multi-region induction devices have been described. In the first, it was shown that an equivalent circuit, consisting of micro-T-circuits, could be obtained, which could then be analysed using a circuit analysis package. The method is only limited by the number of nodes that can be accommodated by the package. Any E or H waveform can be applied, and one avoids completely the mathematical difficulties inherent in some of the alternative methods.

In the second method, suitable only for the steady state problem, it has been shown that a Riccati type equation could be easily derived, thus avoiding the use of higher transcendental functions.

Both methods require only the basic field equations and some elementary knowledge of field theory. They are also within, or almost within, the capacity of existing programmable calculators. Bearing the

various advantages in mind, it would appear that these techniques could be taught at a much lower level in undergraduate courses than is possible using conventional analytical techniques.

5. References

- 1 LAWRENSON, P.J., REECE, P. and RALPH, M.C.: "Tooth-ripple losses in solid poles", Proc. IEE, 1966, 113, (4), pp.657-662.
- 2 PARTS, I.R.: "Electromagnetic field distribution in liquid metal acyclic converters", Magnitnya Gidrodinamika, 1965, VI, 3, pp.127-138.
- 3 HAGUE, B.: "Electromagnetic problems in electrical engineering", O.U.P., 1929.
- 4 WILSON, J.C., ERDELYI, E.A. and HOPKINS, R.E.: "Aerospace composite-rotor induction motors", IEEE Trans., 1965, AES-3, Suppl., pp.18-23.
- 5 PIPES, L.A.: "Matrix theory of skin effect in laminations", J. Franklin Inst., 1965, 262, pp.127-138.
- 6 GREIG, J. and FREEMAN, E.M.: "Travelling-wave problem in electrical machines", Proc. IEE, 1967, 114, (11), pp.1681-1683.
- 7 FREEMAN, E.M.: "Equivalent circuits from electromagnetic theory: low-frequency induction devices", *ibid*, 1974, 121, (10), pp.1117-1121.
- 8 CULLEN, A.L. and BARTON, T.H.: "A simplified electromagnetic theory of the induction motor, using the concept of wave impedance", *ibid*, 1958, 105C, pp.331-336.
- 9 FREEMAN, E.M.: "Travelling waves in induction machines: input impedance and equivalent circuits", *ibid*, 1968, 115, pp.1772-1776.
- 10 CARPENTER, C.J.: "Three-dimensional numerical solution of eddy currents in thin plates", *ibid*, 122, 1975, (6), pp.681-688.
- 11 SMYTHE, W.R.: "Static and dynamic electricity", McGraw Hill, 1950.
- 12 CARSLAW, H.S. and JAEGGER, J.C.: "Operational methods in applied mathematics", O.U.P., 1948, 2nd ed, Chapters 9 and 10.
- 13 BRATOLJIC, T.: "Electromagnetic transients in superconducting turbogenerators", City University Electrical Machines Conference, 1974.

- 14 KRON, G.: "Equivalent circuit of the field equations of Maxwell - I", Proc. IRE, 1944, pp.289-299.
- 15 KAZANSKY, B.G.: "Outline of a theory of non-uniform transmission lines", Proc. IEE, 1958, 105C, (7), pp.126-138.
- 16 McLACHLAN, N.W.: "Bessel functions for engineers", O.U.P., 1961, Chapter 6.
- 17 WATSON, G.N.: "A treatise on the theory of Bessel functions", C.U.P., 1966.
- 18 FREEMAN, E.M.: "Wave impedance of induction devices using the scalar Riccati equation", Proc. IEE, 1976, 123, (2), pp.145-148.

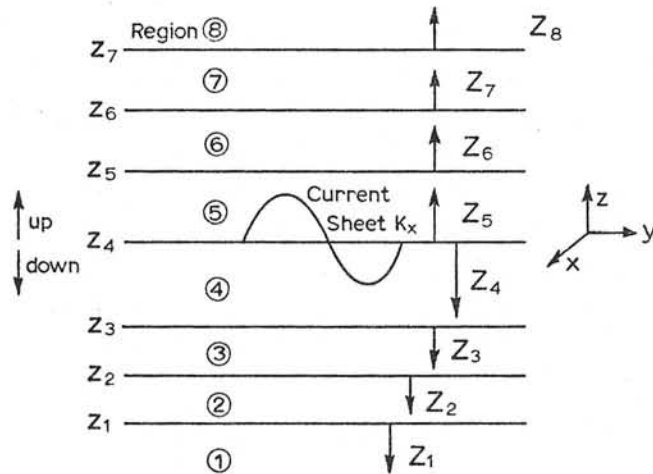


Fig. 1 Multi-region planar model.

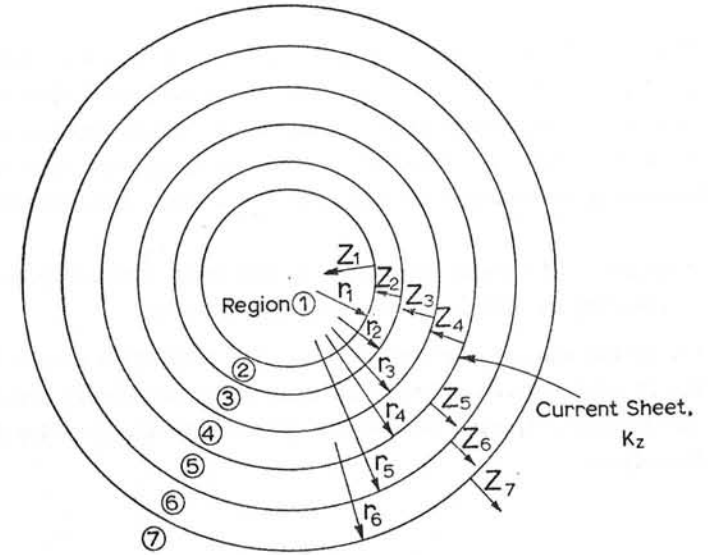


Fig. 2 Multi-region cylindrical model.

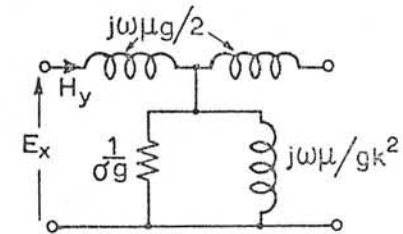


Fig. 3 Planar model micro-T-circuit.

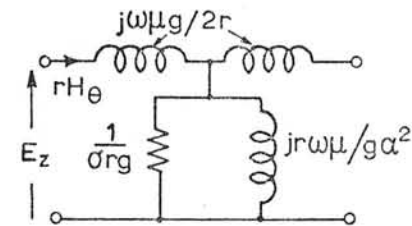


Fig. 4 Cylindrical model micro-T-circuit.

Discussions following paper:

(Miller) I would like to know how the field values at more general field points than at the interfaces can be extracted when using this method. I would also like to know if Dr Freeman can see any way in which the principle of splitting up solid conductors into multiple layers can be extended to deal with fully three dimensional problems?

(Freeman) The field quantities at any point may easily be obtained by introducing an artificial boundary at that point.

The method can only accommodate material variations in one direction. The so called three dimensional multi-layer treatments are really only one-dimensional, with sinusoidal variation of the exciting field in two dimensions.

THE INTEGRAL EQUATION METHOD APPLIED TO EDDY CURRENTS

C S Biddlecombe, C J Collie, J Simkin, C W Trowbridge
 *Rutherford Laboratory, Chilton, Didcot, Oxon. OX11 0QX

ABSTRACT

An algorithm for the numerical solution of eddy current problems is described, based on the direct solution of the integral equation for the potentials. In this method only the conducting and iron regions need to be divided into elements, and there are no boundary conditions.

Results from two computer programs using this method for iron free problems for various two-dimensional geometries are presented and compared with analytic solutions.

1. INTRODUCTION

In this paper the general eddy current problem is formulated as an integral equation for the potentials and an algorithm for its solution is presented. Results from two programs dealing with two-dimensional limits to the iron free problem are described. The method is an extension of the technique used in the GFUN⁽¹⁾ magnetostatics program.

Formulations of the eddy current problems have been classified by Carpenter⁽²⁾, who points out that in the integral formulation the scalar potential ϕ has to be included somehow to ensure that the current cannot flow normal to the surface of the conductor. The formulation in A developed here seems the simplest for the general problem, though a formulation in H is also possible for linear problems. A direct solution in terms of J was also considered but in that case the direct imposition of a boundary condition seemed unavoidable, thus nullifying the main advantage of the integral equation method.

2. FORMULATION FOR IRON FREE REGIONS

2.1 The integral equation for the potentials. The basic field equations for eddy currents are⁽³⁾ in SI units.

$$\nabla \times E = -\partial B/\partial t \quad (2.1.1) \quad \nabla \times H = J \quad (2.1.2)$$

$$\nabla \cdot B = 0 \quad (2.1.3) \quad \nabla \cdot J = 0 \quad (2.1.4)$$

$$J = \sigma E \quad (2.1.5) \quad B = \mu H \quad (2.1.6)$$

that is, displacement currents are neglected, free charges are only present on surfaces, and Ohms Law applies. Also the vector potential A, whose existence follows from (2.1.3), is defined in the Coulomb gauge, so:

$$B = \nabla \times A \quad (2.1.7) \quad \nabla \cdot A = 0 \quad (2.1.8)$$

The integral equation is to be set up for the potentials so first eliminate B between (2.1.1) and (2.1.7):

$$\nabla \times (E + \partial A/\partial t) = 0 \quad (2.1.9)$$

There is therefore a scalar potential ϕ satisfying from (2.1.5) and (2.1.9):

$$J = \sigma E = -\sigma(\partial A/\partial t + \nabla\phi) \quad (2.1.10)$$

For a region of constant conductivity (2.1.4) implies that ϕ is harmonic within the region ($\nabla^2\phi = 0$).

The eddy currents are to be calculated in some (multiply connected) conducting region under the influence of a known driving field. That is:

$$A(\underline{r}) = A_0(\underline{r}) + \frac{\mu_0}{4\pi} \int \frac{J(\underline{r}')}{|\underline{r}-\underline{r}'|} dV \quad (2.1.11)$$

in which $A_0(\underline{r})$ represents the driving field and the 2nd term is the vector potential at \underline{r} due to the eddy currents in terms of the current produced at the source point \underline{r}' . The integration is over the conducting regions of interest. It is only in the Coulomb gauge that (2.1.11) gives the solution of (2.1.2) for the vector potential due to a current. So in the

integral equation formulation nothing is gained by eliminating \emptyset from (2.1.10) by using a different gauge as can be done for differential formulations⁽²⁾, since \emptyset would have to be reintroduced into (2.1.11) to give the equation the right divergence.

Substituting (2.1.10) into (2.1.11) yields the integral equation for $\partial A/\partial t$:

$$A(\underline{r}) = A_0(\underline{r}) - \frac{\mu_0}{4\pi} \int \frac{\sigma(\underline{r}')}{|\underline{r}-\underline{r}'|} \left(\frac{\partial A(\underline{r}')}{\partial t} + \nabla \emptyset(\underline{r}') \right) dV \quad (2.1.12)$$

The equation for \emptyset is obtained by taking the divergence of (2.1.12) and applying (2.1.8) and Gauss's theorem:

$$\begin{aligned} -4\pi\sigma(\underline{r})\emptyset(\underline{r}) &= \int \left\{ \frac{\sigma(\underline{s}')}{|\underline{r}-\underline{s}'|} \frac{\partial A(\underline{s}')}{\partial t} + \sigma(\underline{s}')\emptyset(\underline{s}')\nabla \left(\frac{1}{|\underline{r}-\underline{s}'|} \right) \right\} dS \\ &- \int \left\{ \nabla\sigma(\underline{r}') \cdot \left(\frac{1}{|\underline{r}-\underline{r}'|} \right) \frac{\partial A(\underline{r}')}{\partial t} + \emptyset(\underline{r}')\nabla \left(\frac{1}{|\underline{r}-\underline{r}'|} \right) \right\} dV \end{aligned} \quad (2.1.13)$$

Where \underline{s}' is a point on the surface of the conductor and the 1st integral is over the surface S of the conductor. Physically this expresses the condition that no charge can leave the conductor surface, as can be seen immediately in the constant conductivity, harmonic \emptyset situation by taking Green's theorem⁽⁴⁾ for a harmonic function and inserting the condition $(\partial A/\partial t + \nabla \emptyset) \cdot d\underline{S} = 0$, which by (2.1.10) stipulates that no current leaves the conductor. (2.1.13) shows the condition to be imposed at the internal boundary if the conductor contains more than one material, but most commonly the 2nd term in (2.1.13) is zero, which is assumed in what follows. The treatment of the scalar potential is then similar to the integral boundary method formulation for magnetostatics used in⁽⁵⁾.

2.2 Discretisation. To solve (2.1.12) and (2.1.13) for $\partial A/\partial t$ and \emptyset the conductor is divided into N elementary volumes: L facets of these elements form the surface of the conductor (see Figure 2.2.1). To evaluate the integrals some functional form for the variation of $\partial A/\partial t$ and $\nabla \emptyset$ within each element must be assumed. For the existing programs,

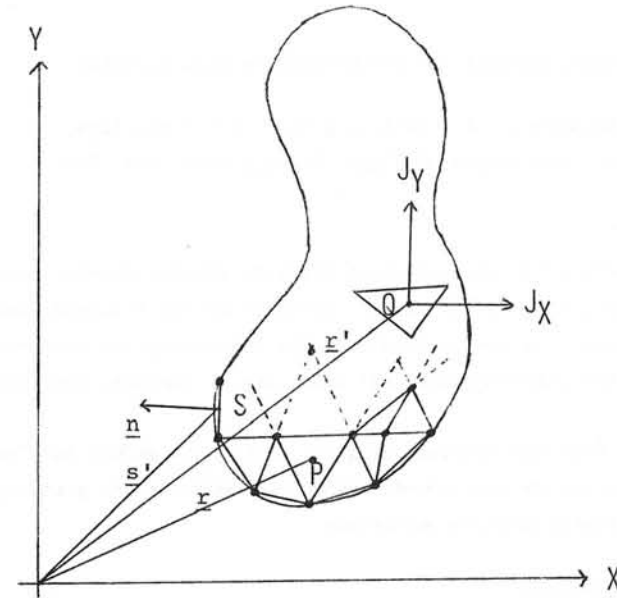


FIGURE 2.2.1 - MESH IMPOSED ON THE CONDUCTING REGION

results from which are described in Section 3, the simplest scheme of constant values for each component of $\partial A/\partial t$ and for \emptyset was adopted. Thus (2.1.12) (2.1.13) are approximated by:

$$A(\underline{r}) = A_0(\underline{r}) + \sum_{N \text{ elements } j} \left\{ R_j \left(\frac{\partial A}{\partial t} \right)_j + R_j (\nabla \emptyset)_j \right\} \quad (2.2.1)$$

$$\emptyset(\underline{r}) = \sum_{L \text{ facets } k} \left\{ T_k (\emptyset)_k + U_k \left(\frac{\partial A}{\partial t} \cdot \underline{n} \right)_k \right\} \quad (2.2.2)$$

$$\nabla \emptyset(\underline{r}) = \sum_{L \text{ facets } k} \left\{ V_k (\emptyset)_k - T_k \left(\frac{\partial A}{\partial t} \cdot \underline{n} \right)_k \right\} \quad (2.2.3)$$

where \underline{n} is the unit vector normal to surface facet k , and (2.2.3) is obtained by differentiating (2.1.13) wrt the coordinates of the field point \underline{r} .

The coupling coefficients (R , T , U , V) are simple integrals over the volume or surface of the elements, for example:

$$R_j = -\frac{\mu_0 \sigma}{4\pi} \int_{\text{elements}_j} \frac{dV}{|\underline{r}-\underline{r}'|}$$

Expressions for these integrals are given in (6).

By setting the field point \underline{r} to the centre of each element in turn a matrix is constructed acting on $3N$ components of $\partial A/\partial t$ and L surface values of \emptyset :

$$\begin{bmatrix} G_A & G_B \\ G_C & G_D \end{bmatrix} \begin{bmatrix} \frac{\partial A}{\partial t} \\ \emptyset \end{bmatrix} = \begin{bmatrix} A - A_0 \\ 0 \end{bmatrix} \quad (2.2.4)$$

Note that the equations for the components of $\partial A/\partial t$ are coupled through the scalar potential \emptyset . This formulation in terms of a constant value for $\partial A/\partial t$ and \emptyset within each element accepts a certain mismatch between the facet centre value in (2.2.3) and the element centre values needed when the coupled equations are formed by substituting the $\nabla\emptyset$ values from (2.2.3) into (2.2.1). This disadvantage would not apply to a higher order variation based on nodal values as the parameters.

Note also that the formulation can be readily adapted to employing a driving electric field \emptyset_0 instead of the magnetic field A_0 .

2.3 Computational procedure. Direct solution of (2.2.4):

$$\begin{bmatrix} \frac{\partial A}{\partial t} \\ \emptyset \end{bmatrix} = G^{-1} \begin{bmatrix} A - A_0 \\ 0 \end{bmatrix} \quad (2.3.7)$$

yields $\partial A/\partial t$ values in terms of the unknown values of A . To complete the solution this set of $3N$ first order differential equations has to be solved in terms of the initial conditions. Less expensively, the steady state solution for sinusoidal drive fields can be solved by replacing $\partial A/\partial t$ in (2.3.1) by $j\omega$ and obtaining the amplitude and phase lag at each element from the real and imaginary parts of the solution. For the general transient case the numerical solution can be obtained with the following procedure:

- Divide the conductor into elements.
- Construct G matrix
- Set the initial conditions, that is $A = A_0$ at $t = 0$.
- Solve for $\partial A/\partial t$ and \emptyset .
- Advance the solution of $3N$ differential equations through some time increment.
- Update $A_0 = A_0(t)$.
- Iterate steps (d) - (f) until the required time interval is covered.

Currents, fields and forces may then be obtained at any space time point by using $J = -\sigma(\partial A/\partial t + \nabla\emptyset)$ and $B = \nabla \times A$, with $\nabla\emptyset$ from (2.2.3) and $\nabla \times A$ obtained analogously to (2.2.3) by differentiating (2.1.12) so that no numerical differentiation is required.

3. RESULTS FROM EXISTING PROGRAMS

3.1 The scope of the programs. Two special cases of the general iron free problem formulated above have been coded in order to assess the practicability of the method. Both are two-dimensional in the sense that no variation in the Z direction is allowed either for field variables or conductor cross-sections and the conductors extend to $\pm \infty$ in the Z direction.

The first program, called EDDY ONE, allows for only one component of A and J , parallel to the Z axis. For this case there is no \emptyset since the electric field is everywhere parallel to the surface. Therefore (2.2.4) reduces to:

$$G_A \begin{bmatrix} \frac{\partial A}{\partial t} \end{bmatrix} = \begin{bmatrix} A_0 - A \end{bmatrix}$$

There is also no mismatch problem (Section 2.2) for this case.

The second program, called EDDY TWO, allows for A_x, A_y, J_x, J_y , but no Z components. For this case the eddy current field is zero outside the conductors. Results from both programs are compared with analytic solutions⁽⁷⁾ calculated by applying the Laplace transform method for simple geometries and a uniform step function driving field of 1 Tesla.

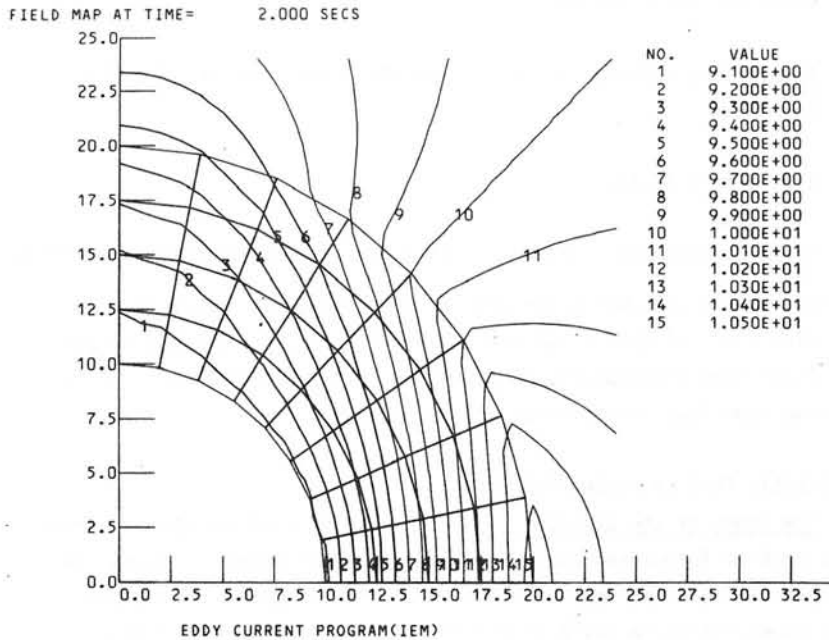


FIGURE 3.2.1 - ELEMENT STRUCTURE AND FIELD LINES IN HOLLOW CYLINDER

3.2 Results from EDDY ONE. Here the analytic comparison is with a hollow cylinder. The cross-section and element structure used by EDDY ONE for one quadrant are shown in Figure 3.2.1, symmetry being exploited to imply the other three quadrants. Figures 3.2.2 to 3.2.4 show the error as a function of time for varying numbers of elements at 3 points: respectively inside the hollow, in the conductor and outside. In all cases the elements were of roughly uniform size including those near the surface so

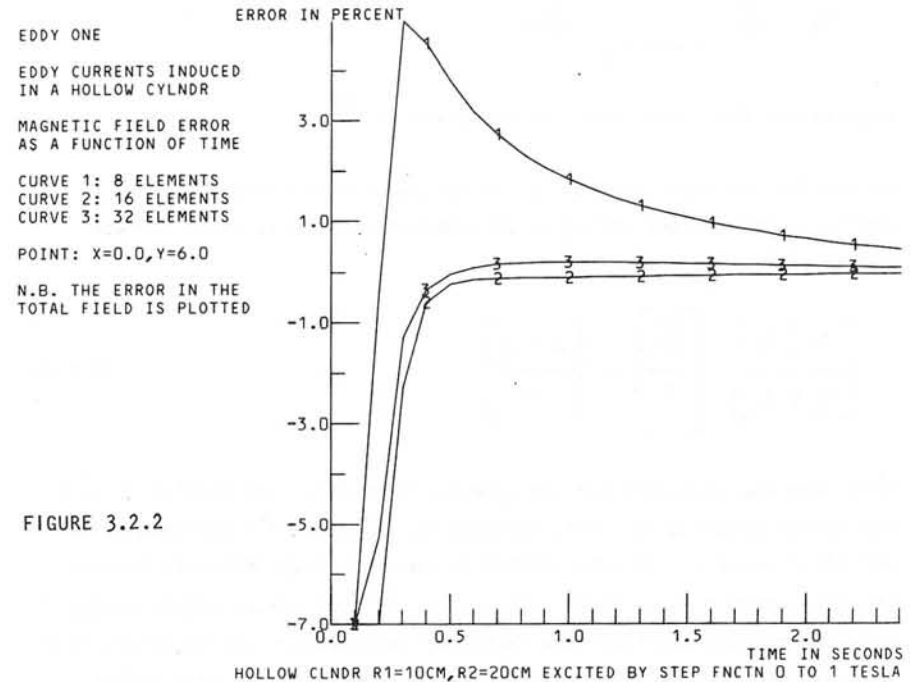


FIGURE 3.2.2

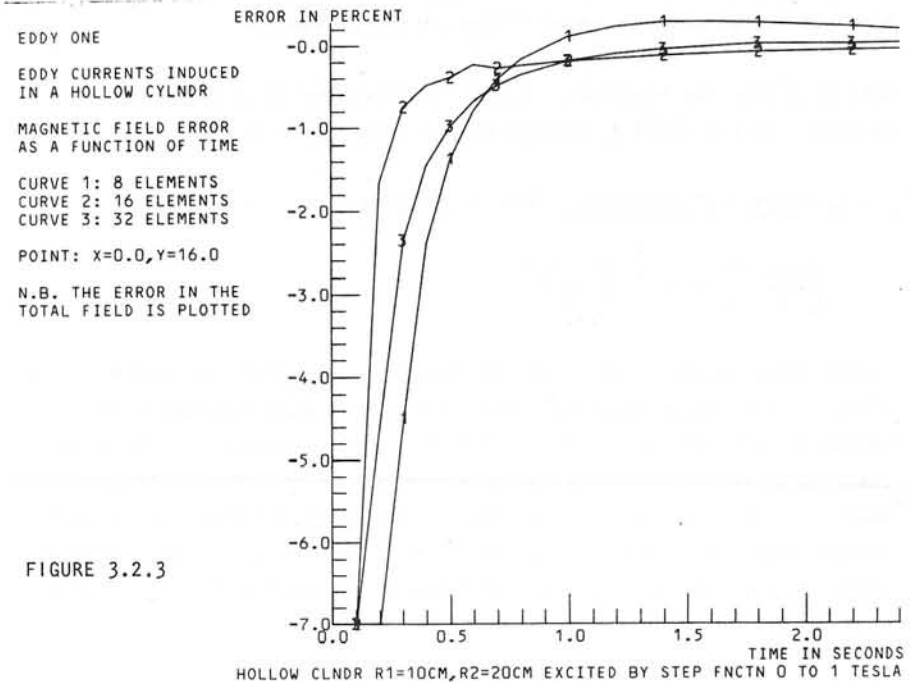
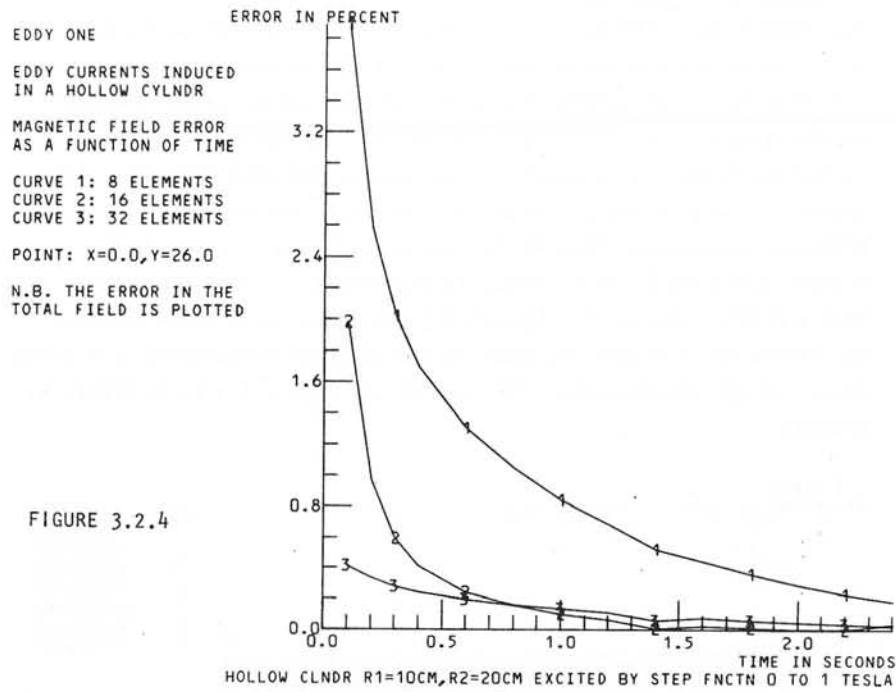


FIGURE 3.2.3



that the element structure is not exploiting knowledge of the skin effect. Convergence for increasing numbers of elements is apparent and the rather greater error for the point within the conductor is to be expected since the further away from the elements the field point is, the less the error introduced by the assumption of constant $\partial A/\partial t$ and ϕ .

Figure 3.2.5 shows another configuration, with the driving field provided by a 50 Hz current (for $t > 0$) in the 4 outer bars and the penetration of flux into the rectangular tube is illustrated at different times in Figures 3.2.5 to 3.2.7, the latter showing the flux of the eddy currents alone as the driving field crosses the zero axis. The transient eddy current response in one element is shown in Figure 3.2.8.

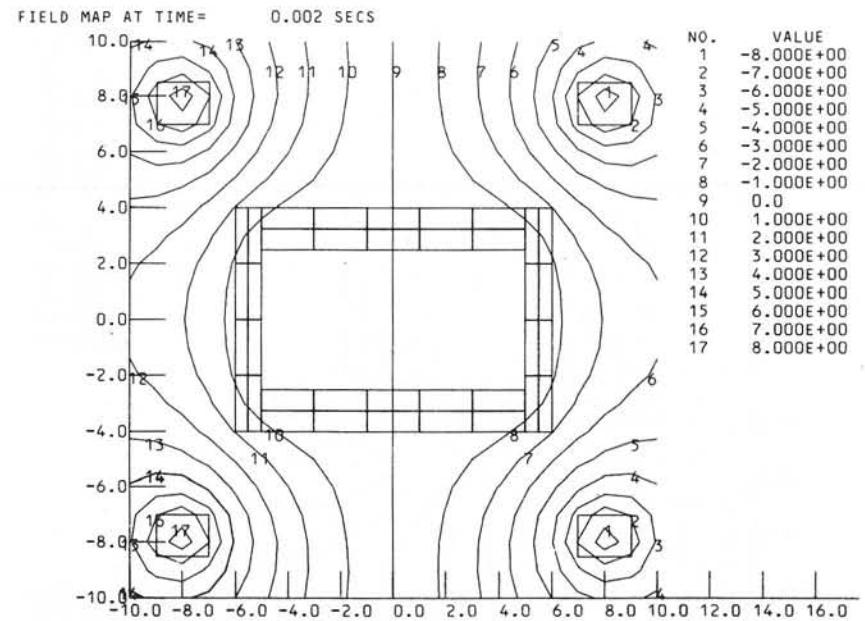


FIGURE 3.2.5 - FLUX PENETRATION INTO RECTANGULAR TUBE, AFTER 0.002 SECS

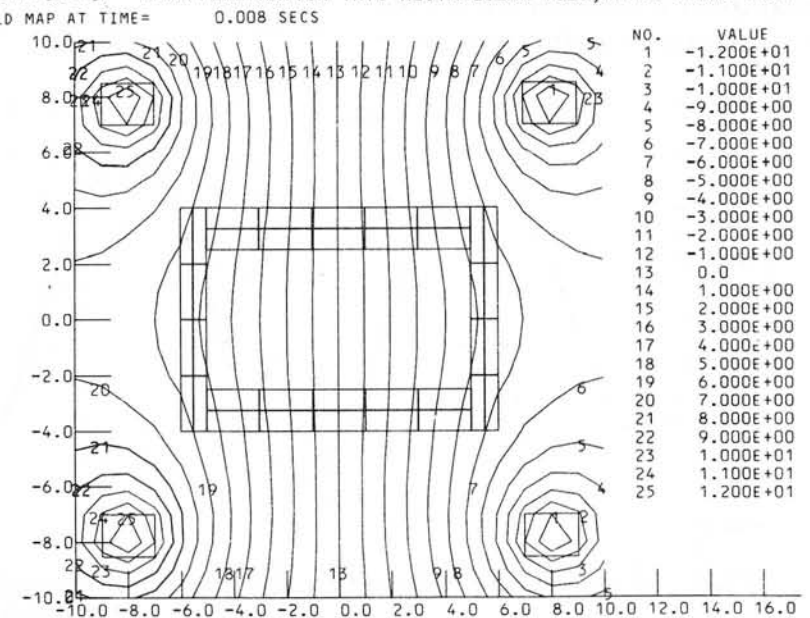


FIGURE 3.2.6 - FLUX PENETRATION INTO RECTANGULAR TUBE, AFTER 0.008 SECS.

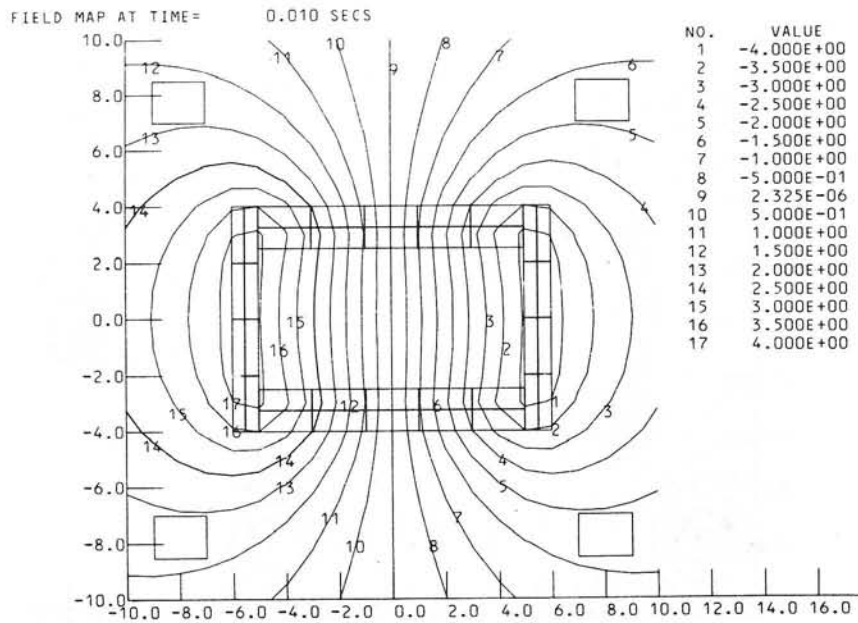


FIGURE 3.2.7 - FLUX MAP AT ZERO OF DRIVING FIELD CURRENT DENSITY AS FUNCTION OF TIME IN ELEMENT 6

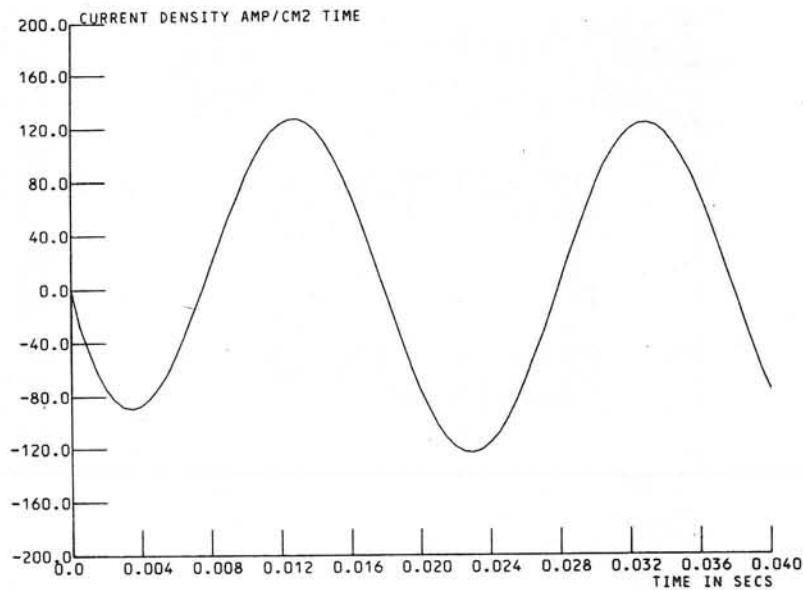


FIGURE 3.2.8 - TRANSIENT EDDY CURRENT RESPONSE TO SINUSOIDAL DRIVE

3.3 Results from EDDY TWO. Here the analytic comparison is with a rectangular bar. The calculated response is illustrated by Figure 3.3.1 the arrows indicating both direction and magnitude of the current. The errors are shown graphically at 3 different points on the diagonal of the rectangle in Figures 3.3.2 to 3.3.4. The convergence with increasing numbers of elements is less happy than with EDDY ONE. The effect of the position of the field relative to the element mesh is probably responsible. Thus at the centre, Figure 3.3.2, in the 96 element model the point is common to 8 elements but to 4 elements in both the other cases. In Figure 3.3.3 the point is in all 8 cases at the centre of an element boundary so the observed convergence to a wrong answer is not unreasonable. The best point, Figure 3.3.4, is within an element.

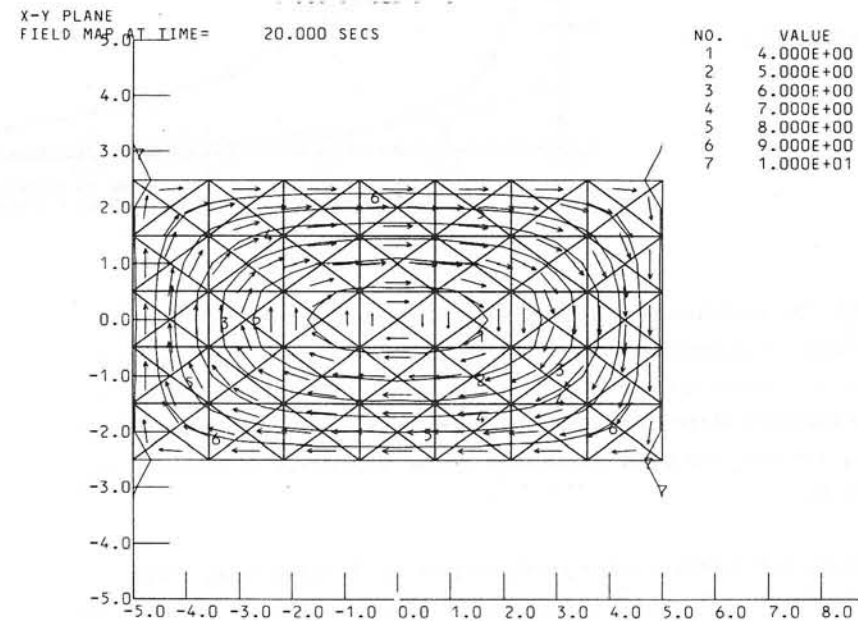
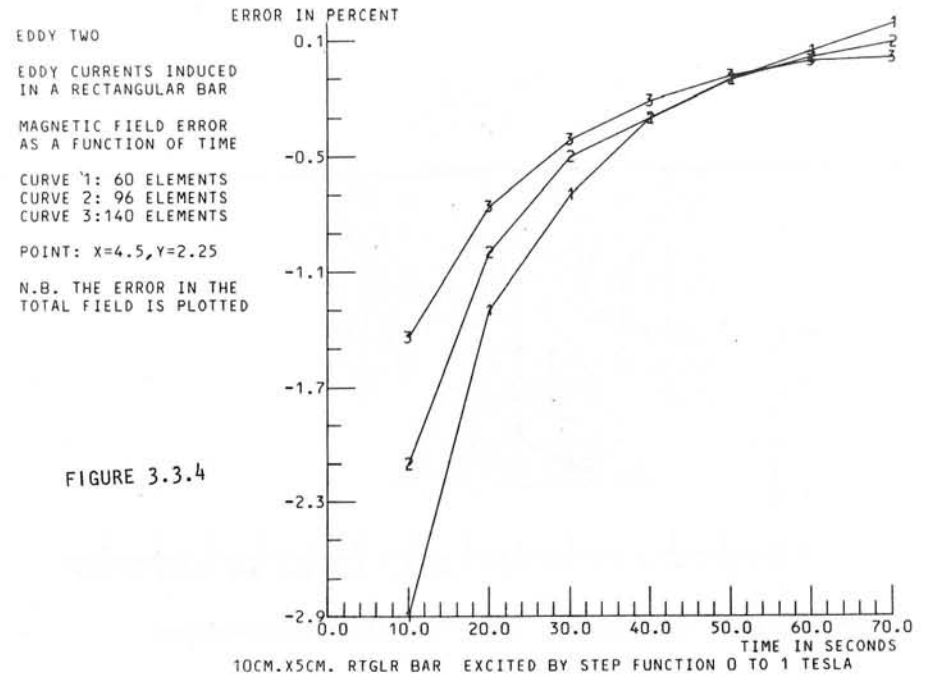
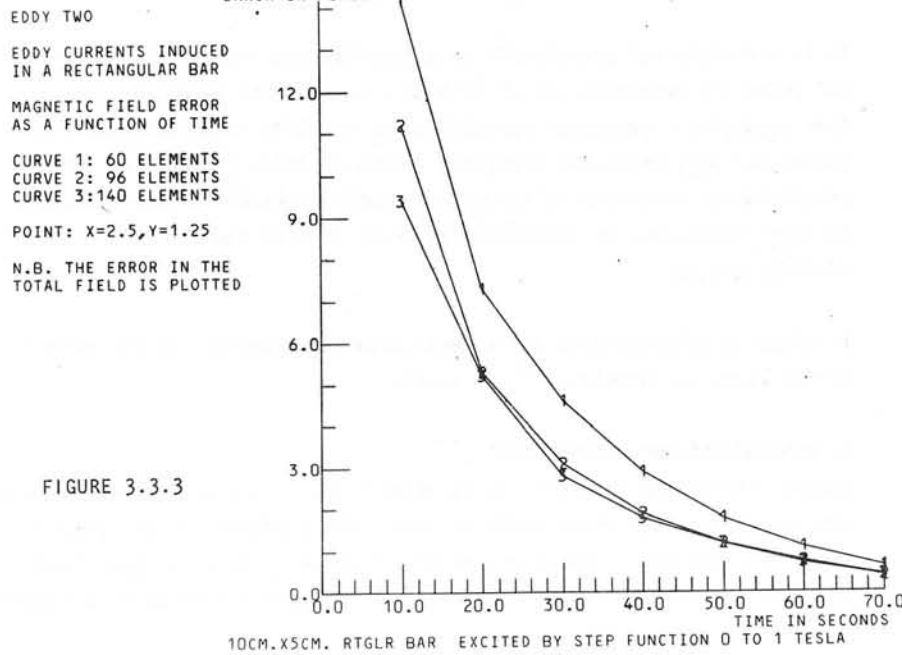
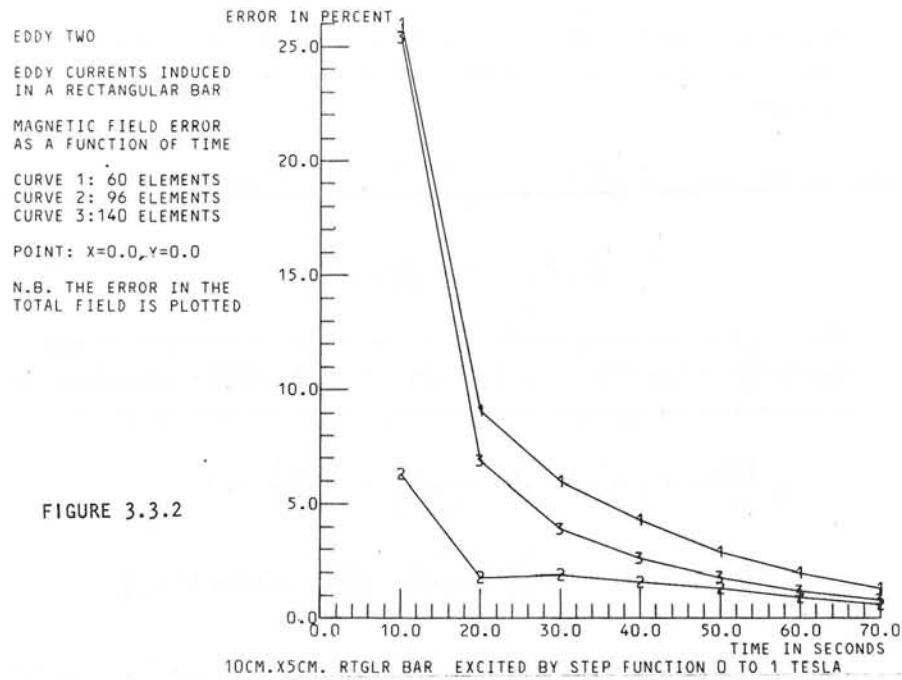


FIGURE 3.3.1 - ELEMENT STRUCTURE, FIELD LINES AND ARROWS REPRESENTING EDDY CURRENTS IN RECTANGULAR BAR



Though the field contours follow the boundary almost perfectly for the case of a rectangle, the final illustration, Figures 3.3.5 and 3.3.6, show the breakdown of this for a more complex shape, and the current direction in the corner is clearly wrong. Hopefully this is due to mismatch error.

4. INCLUSION OF IRON REGIONS

The method could be extended to include regions of magnetically permeable

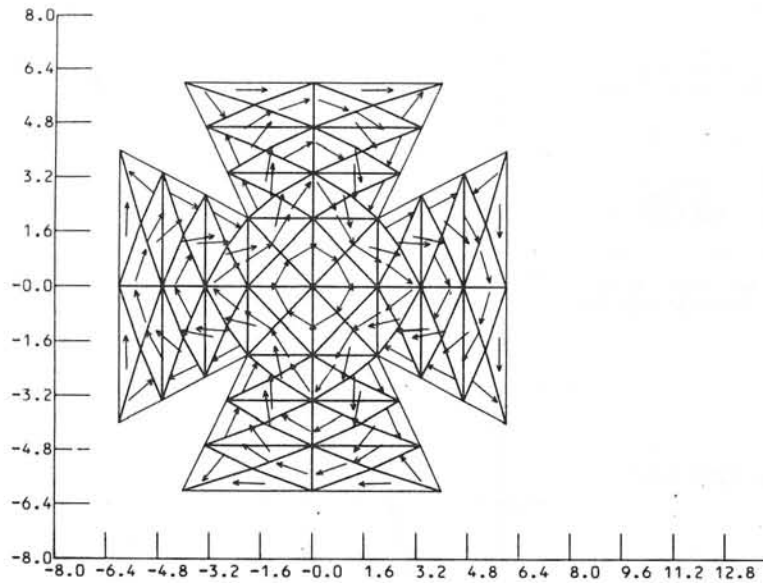


FIGURE 3.3.5 - EDDY CURRENTS IN BAR WITH CROSS SECTION SHOWN

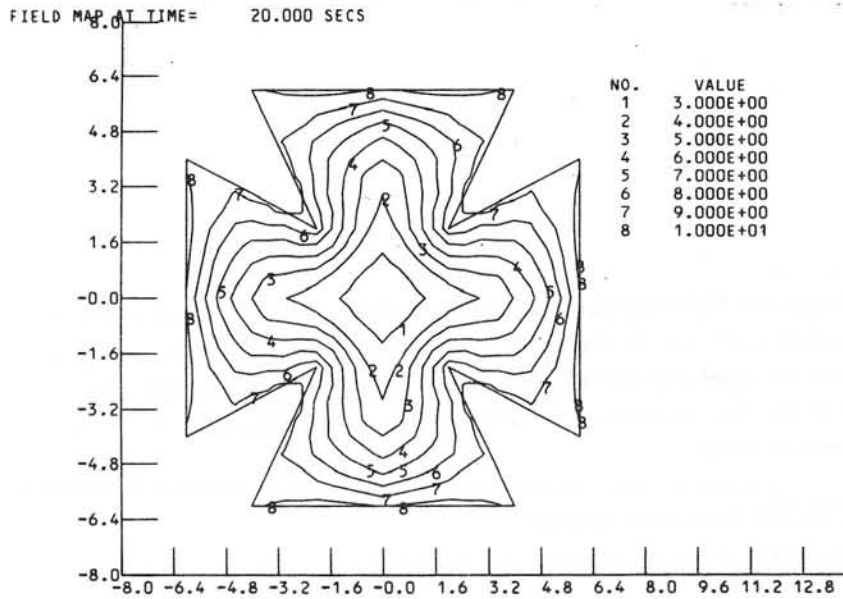


FIGURE 3.3.6 - FIELD LINES IN BAR WITH CROSS SECTION SHOWN

materials by adding a term for the vector potential due to the magnetised region to the integral equation (2.1.12) which becomes (for constant σ):

$$A(\underline{r}) = A_o(\underline{r}) - \frac{\mu_o}{4\pi} \int \frac{\sigma}{|\underline{r}-\underline{r}'|} \left(\frac{\partial A(\underline{r}')}{\partial t} + \nabla\phi(\underline{r}') \right) dV + \frac{\mu_o}{4\pi} \int M(\underline{r}') \times \nabla \left(\frac{1}{|\underline{r}-\underline{r}'|} \right) dV \quad (4.1)$$

where $M(\underline{r})$ is the magnetisation at \underline{r}' and the second integral is over the volume of the iron. The ϕ equation (2.1.13) remains unchanged, and the constitution equation is obtained by taking the curl of (4.1):

$$\mu_o \frac{M(\underline{r})}{\chi} = \nabla \times A_o(\underline{r}) - \frac{\mu_o}{4\pi} \int \left\{ \frac{\sigma}{|\underline{r}'-\underline{r}|} \nabla \times \frac{\partial A(\underline{r}')}{\partial t} \right\} dV + \frac{\mu_o}{4\pi} \int \left\{ \frac{\sigma}{|\underline{r}'-\underline{r}|} \frac{\partial A(\underline{s}')}{\partial t} + \nabla\phi(\underline{s}') \right\} \times \underline{dS} + \frac{\mu_o}{4\pi} \int \{ (M(\underline{r}') \cdot \nabla) \nabla \left(\frac{1}{|\underline{r}-\underline{r}'|} \right) \} dV \quad (4.2)$$

It is certainly not practicable to discretise the iron into M elements and solve the resulting set of $3N + 3M + L$ equations simultaneously. Some predictor - corrector approach seems feasible in which (4.2) is solved for $M(\underline{r})$ using the predicted values of $\partial A/\partial t$ and $\nabla\phi$, the same problem which is solved by the magnetostatic program⁽¹⁾. The solutions for $M(\underline{r})$ could then be substituted in (4.1) to find the corrected values of $\partial A/\partial t$ and $\nabla\phi$.

It might be preferable to use a magnetostatic potential for the effect of the iron, as formulated⁽⁸⁾ by Iselin.

5. CONCLUSIONS AND FUTURE WORK.

Having established that this formulation leads to a useful program there are some extensions which could be made. The exploitation of symmetry would considerably increase the detail in which symmetrical geometries could be mapped. Improved accuracies can be hoped for by using a higher

order basis for the variation within elements, and also by using a more suitably distributed element mesh within the conductors. The coupling coefficients in (2.2.1) to (2.2.3) can be evaluated in a general three-dimensional element⁽⁶⁾. Collectively this should result in a general three-dimensional program for iron free problems.

The major task is to bring the induced current and magnetisation formulations of the Integral Equation Method together and to compare the result with the Finite Element Method, or with a Boundary Integral Method. Any very general program along these lines may be prohibitively expensive and there is clearly a place for steady state versions or, for linear problems, a Fourier transform version.

6. ACKNOWLEDGEMENTS

The authors would like to express their thanks to all the staff of the Rutherford Laboratory who have helped in this work, especially Dr D B Thomas for his encouragement and Mrs E Dawson for her patience with the manuscript.

7. REFERENCES

1. A G A M Armstrong et al. New Developments in the Magnet Design Program GFUN. RL-75-066.
2. C J Carpenter. Computation of Magnetic Fields and Eddy Currents. Proc. 5th Int. Conf. on Magnet Technology, Frascati, 1975.
3. R Stoll. Analysis of Eddy Currents, page 4. Clarendon Press, Oxford, 1974.
4. G T Symm. Potential Problems in Three Dimensions. Numerical Solution of Integral Equations, Ch. 24. Clarendon Press, Oxford, 1974.
5. J Simkin, C W Trowbridge. Magnetostatic Fields using an Integral Equation derived from Green's Theorems. Proc. COMPUMAG Conference on the Computation of Magnetic Fields, Oxford, 1976.

6. C J Collie. Magnetic Fields and Potentials of Linearly Varying Current or Magnetisation in a Plane Bounded Region. Proc. COMPUMAG Conference on the Computation of Magnetic Fields, Oxford, 1976.
7. J C Jaeger. Magnetic Screening by Hollow Circular Cylinders. Phil.Mag. Vol.29, 1940.
8. Ch. Iselin. A Scalar Integral Equation for Magnetostatic Fields. Proc. COMPUMAG Conference on the Computation of Magnetic Fields, Oxford, 1976.

Discussions following paper:

(Becker, University of Texas) 1. Experience with boundary integral equation methods in stress analysis problems has shown that the use of linear (or higher) variation within elements can increase the accuracy per unit of computing cost tremendously. Have you considered the use of higher order elements in GFUN?

2. In our finite element method for transient field problems we have included interfaces between a) different materials.

b) moving and stationary media

Would these present difficulties in the integral formulation?

(Collie) 1. We certainly intend to put in linear variation as soon as possible; the present constant variation technique was adopted simply for speed of implementation, given the existing GFUN coding and is not recommended.

There are problems in introducing higher order variations into the magnetisation routines in GFUN because of singularities on the element corners, these do not occur in the eddy current problem.

2. a) Different materials present no problem, though we should need surface elements over the interfaces between regions.

b) We have not given moving media serious thought. If the media is providing the driving field it should be OK, otherwise we need to do some thinking.

(Yeh) Would you please comment on the amount of computer time needed for solving the transient?

(Collie) Most of the pictures shown took about 1 minute on a 360/195. The present version of EDDY TWO makes no use of symmetry, and when we put this in it should take a few seconds only.

(Newman) To people familiar with finite difference techniques you appear to achieve impressive results with elements whose size is comparable with the dimension of irregularities in the boundary. Is this a feature of the integral equation method?

(Collie) Integration is an intrinsically accurate process numerically, so that for example the constant variation assumption gives a very reasonable average for the effect of 1 element, especially a few element sizes away. However, we pay for our small matrix by having it dense and non-symmetrical.

(Miller) The method appears to solve for four dependent variables, although these are not independent of one another. I would like to know whether there is any special physical significance in the use of the scalar potential ϕ , and whether the problem could in fact be solved solely with the three components of A ?

(Collie) ϕ certainly has a simple physical interpretation: charges build up on the conductor surface until their field, $-\Delta\phi$, forces the currents to flow parallel to the surface. This provides the dependence between ϕ and the vector potential.

Mathematically, the integral equation formulation seems tied to the Coulomb gauge, since only then does

$$A_i = \int \frac{j_i}{r} \text{ hold .}$$

A PERTURBATION EXPANSION WITH SEPARATED TIME DEPENDENCE
FOR EDDY CURRENT CALCULATIONS*

K. H. Carpenter and H. T. Yeh

Oak Ridge National Laboratory
Oak Ridge, Tennessee 37830 USA

Abstract

A particular solution to the eddy current integro-differential equations is found in the form of a perturbation expansion with separated time dependence. No reference to field values outside the conductor is required and a full three-dimensional treatment is maintained. Transient behavior of the eddy currents is obtained by this method through the technique of fitting the time variation of the driving field with a polynomial in time. As an example, the case of a thin plate of constant conductivity is studied. The eddy current distribution is obtained as a function of time for the external magnetic field of a dipole having ramp time dependence, and with the dipole axis perpendicular to the plate. The effects of the boundary charges in modifying the eddy current pattern are illustrated.

Introduction

Design of structures where pulsed magnetic fields of high magnitude are encountered (e.g., in tokamak fusion reactors¹) requires knowledge of the eddy currents the fields will produce. Further, because most such systems are quite complex, it is desirable to adopt an integral formulation for the eddy current problem.² In the integral formulation, the field values need to be determined only for points in the conductor, but the total external field must be known in advance. This is usually the case. (In the tokamak example the fields due to magnets and plasma are known since the charging and discharging of these currents are programmed or controlled. During quench of a superconductor, although the currents are not programmed, they follow approximately the solutions of the lumped circuit equations, provided the coupling between the induced eddy current

and the magnets and plasma is not strong.) Any nearby conductors whose eddies couple strongly to the region of interest need to be treated as a part of the region included in the integral formulation.

Furthermore, in nearly all cases the external vector potential imposed on the conductor can be presented as a finite sum of terms of the form $\underline{a}_0(\underline{r})f(t)$. Thus provided that the conductor is linear (conductivity and permeability independent of field), it is natural to separate out the time dependence from the integral equation by making a perturbation expansion in terms of f and its derivatives.³ This method still allows for arbitrary time dependence in the external field but avoids the need for introducing a time stepping numerical technique with its related stability problems.

In the following we will develop a perturbation expansion that separates the time dependence from the space dependence of an integral formulation of the potential equations for a linear conducting medium. We will then discuss the convergence of the expansion and show how it can be applied to cases where transient behavior is important by making polynomial fits to the time variation of the exciting fields. Several examples will be presented.

Derivation of Expansion

A. Basic Equations

The basic differential equations for the magnetic vector potential \underline{A} and the electrostatic vector potential ψ in Coulomb gauge inside a linear homogeneous and isotropic conducting medium are

$$\nabla^2 \underline{A} = \mu_0 \left(\sigma \frac{\partial \underline{A}}{\partial t} + \sigma \nabla \psi - \nabla \times \underline{M} \right) \quad (1)$$

$$\nabla^2 \psi = - \frac{\rho}{\epsilon} \quad (2)$$

$$\frac{\partial \rho}{\partial t} + \frac{\sigma}{\epsilon} \rho = 0 \quad (3)$$

(All equations are in mks units, and symbols are defined at the end of the paper.) Eq. (3) shows that for typical conductors for which σ/ϵ is large, ρ will be zero except for charges on the conductor surfaces. Surface charges will require ψ to be nonzero if $\nabla \cdot \underline{A} = 0$ is maintained.

*Research sponsored by the U.S. Energy Research and Development Administration under contract with Union Carbide Corporation.

The integral formulation of Eq. (1) is

$$\underline{A}(\underline{r}, t) = \underline{A}_0(\underline{r}, t) - \frac{\mu_0 \sigma}{4\pi} \int \frac{\frac{\partial \underline{A}}{\partial t}(\underline{r}', t) + \nabla' \psi(\underline{r}', t)}{|\underline{r} - \underline{r}'|} d^3 r' + \frac{1}{4\pi} \left(1 - \frac{\mu_0}{\mu}\right) \int \frac{(\nabla' \times \underline{A})(\underline{r}', t) \times (\underline{r} - \underline{r}')}{|\underline{r} - \underline{r}'|^3} d^3 r' \quad (4)$$

where integration is over the region occupied by the conducting medium and \underline{A}_0 is the part of \underline{A} due to all sources external to this region. Since $\frac{\sigma}{\epsilon}$ is large, equations (2) and (3) are replaced by

$$\nabla^2 \psi = 0 \quad (5)$$

$$\frac{\partial \psi}{\partial n} = - \frac{\partial \underline{A}_n}{\partial t} \quad (6)$$

Eq. (6) is the boundary condition forcing the normal component of the current density to be zero at the surface of the conductor.

As mentioned in the introduction, linearity makes it sufficiently general to consider the case where \underline{A}_0 has the form of $\underline{\alpha}_0 f$. In order to obtain a dimensionless form in the expansions to follow we shall normalize the space coordinates of $\underline{\alpha}_0$ by some characteristic length L of the conductor region, and normalize the time argument of f to some characteristic time t_0 . Thus all succeeding equations will be in normalized variables.

$$\underline{x} = \frac{\underline{r}}{L} \text{ and } \tau = \frac{t}{t_0} \quad (7)$$

B. Perturbation Series

One can obtain a particular solution for \underline{A} in terms of the external driving field \underline{A}_0 by expanding \underline{A} and ψ in a perturbation series in terms of the derivative of f , with expansion parameter Γ .

$$\Gamma = \frac{\mu_0 \sigma L^2}{4\pi t_0} \quad (8)$$

The result is

$$\underline{A}(\underline{r}, t) = \sum_{m=0}^{\infty} \underline{a}_m(\underline{x}) (-\Gamma)^m \frac{d^m f}{d\tau^m} \quad (9)$$

$$\psi(\underline{r}, t) = \frac{1}{t_0} \sum_{m=1}^{\infty} \zeta_{m-1}(\underline{x}) (-\Gamma)^{m-1} \frac{d^m f}{d\tau^m} \quad (10)$$

where the \underline{a}_m, ζ_m are recursively related by ($m \geq 0$),

$$\underline{a}_m(\underline{x}) = \underline{\alpha}_m(\underline{x}) + \frac{1}{4\pi} \left(1 - \frac{\mu_0}{\mu}\right) \int \frac{(\nabla_{\underline{x}'} \times \underline{a}_m) \times (\underline{x} - \underline{x}')}{|\underline{x} - \underline{x}'|^3} d^3 x' \quad (11)$$

$$\nabla^2 \zeta_m = 0 \quad \text{with B. C. } \frac{\partial \zeta_m}{\partial \underline{x}_n} = - (\underline{a}_m)_n \quad (12)$$

$$\underline{\alpha}_{m+1}(\underline{x}) = \int \frac{\underline{a}_m(\underline{x}') + \nabla_{\underline{x}'} \zeta_m}{|\underline{x} - \underline{x}'|} d^3 x' \quad (13)$$

For magnetic conductors ($\mu \neq \mu_0$) recursion relation Eq. (11) is itself an integral equation. Solution of Eq. (11) could perhaps be approached in a manner similar to that of Karmacher & Robertson⁴. We shall restrict ourselves here to non-magnetic case ($\mu = \mu_0$) in which Eq. (11) is eliminated and $\underline{\alpha}_m \equiv \underline{a}_m$. Thus, given $\underline{\alpha}_0$ and f , solution for \underline{A} and ψ reduces to a sequence of solvings of the Laplace's equation with Neumann boundary conditions inside the conductor, and integrations over the volume of the conductor.

The eddy current density and the total field may then be obtained as

$$\underline{j}(\underline{r}, t) = - \frac{\sigma}{t_0} \sum_{m=0}^{\infty} (-\Gamma)^m \left[\underline{a}_m(\underline{x}) + \nabla_{\underline{x}'} \zeta_m \right] \frac{d^{(m+1)} f}{d\tau^{m+1}} \quad (14)$$

$$\underline{B}(\underline{r}, t) = \frac{1}{L} \sum_{m=0}^{\infty} (-\Gamma)^m \left\{ \nabla_{\underline{x}'} \times \left[\underline{a}_m(\underline{x}) + \nabla_{\underline{x}'} \zeta_m \right] \right\} \frac{d^m f}{d\tau^m} \quad (15)$$

C. Convergence of Series and Handling of Transients

In general, the convergence of an expansion such as Eq. (4) requires successive terms to be smaller in magnitude. If the normalization conditions L and t_0 are chosen properly this reduces to a requirement $\Gamma < 1$. This condition is similar to that encountered in previous power series solutions of magnetic field problems.⁵ Further, as noted above, the solution for \underline{A} provided by Eq. (9) vanishes when $\underline{\alpha}_0$ vanishes and hence is only the particular solution to the (time-dependent) differential equation and not the complete solution.

Choice of the proper characteristic length L to make $\Gamma < 1$ the convergence criterion depends on both the conductor geometry and the distribution of the source field \underline{A}_0 in the conductor. Note that for conductors which are thin surfaces, the successive integrations of Eq. (13) each introduce a factor of $(\Delta L/L)$ in addition to a factor of L^{-2} times the mean of the area weighted by the integrand. Thus, the choice of L should be $L = (\Delta L \times \text{mean area})^{1/3}$ to cause successive α_m 's to be of the same order of magnitude for thin (non-magnetic) conductive surfaces. Hence, for very thin surfaces L is small and so $\Gamma \ll 1$ - which yields an eddy current \underline{j} that is essentially the first term in Eq. (14).

The solutions to Eq. (4) with $\underline{A}_0 = 0$ will be combinations of exponential decays with time constants proportional to Γt_0 . Thus, for small Γ , transient effects die out quickly and \underline{j} is proportional to $\frac{df}{d\tau}$. However, for the case of $\Gamma \lesssim 1$, transient effects cannot be ignored. One way to include them is to replace any discontinuous time functions $f(\tau)$ with an analytic approximation which is valid over a time interval that extends to several times the longest transient decay time constant prior to the time for which Eq. (9) is to be evaluated. Thus any transient effects that are introduced at the beginning of the time interval become negligible by the time we reach the instant for evaluation. Further, if the analytic function used to approximate $f(\tau)$ is a polynomial in τ the series in Eq. (9) terminates, eliminating, technically at least, the convergence question.

In the following examples we use the technique of approximating f by a finite polynomial in τ , assuming that if the polynomial approximates f closely, the results for \underline{j} are also approximated in the same sense. This indeed seems to be the case when the method is applied to an analogous one-dimensional problem where the problem can also be solved analytically.³

Examples

A. Numerical Method

We shall illustrate the above method with examples of eddy currents induced in a thin plate by an external dipole, which has a ramp time dependence ($f = 0, \tau < 0; f = \tau, \tau > 0$) in the dipole strength. Numerical calculations were carried out using a PDP-10 computer. f was approximated over a specified range of t by an unweighted least squares fit to a

polynomial. (Both α_0 and f could be modified by changing the appropriate numerical subroutines). ζ_m of Eq. (12) was determined to within an unknown constant by a standard numerical program for the Poisson equation.⁶ $\nabla \zeta_m$ was calculated by central differences. The integration in Eq. (13) was carried out by a two-dimensional trapezoidal rule, with special handling of the element containing the singularity of the integrand.

The numerical method settled quickly to a unique solution as the number of mesh point was increased. Checks on a typical case showed results from a 7×7 grid deviated from those of a 21×21 grid by less than 4%.

B. Results when $\Gamma \ll 1$

The first case to consider is for the expansion parameter $\Gamma \ll 1$. For this case, transients will die away almost immediately following the external excitation, hence \underline{j} is given by the first term of Eq. (14) and no approximation for f is needed.

For the example of a linear ramp, $\frac{df}{d\tau} = 1$ and $\frac{d^m f}{d\tau^m} = 0, m \neq 1$. For such a linear ramp there is no time t_0 that can be considered a "natural" normalizing value. Instead t_0 is chosen to set the time scale to show the amount of detail in t desired while the interval used for τ is fixed - say at $-1 < \tau < 1$. Thus t_0 can always be made large, forcing Γ to be small and hence yielding information about only the equilibrium condition. Fig. 1 shows the resulting equilibrium solution for eddy current \underline{j} induced by a dipole of ramp time dependence located half the width of a square plate from the plate with dipole axis perpendicular to the plate and passing through the center of the plate. (If the plate has width 2 m and values of $\sigma = 1.4 \times 10^6 \Omega^{-1} \text{m}^{-1}$, $\mu = 4\pi \times 10^{-7} \text{H/m}$, and $\Delta L = 0.01 \text{ m}$ are chosen, corresponding to a stainless steel at 4 K, the effective value of the expansion parameter is $\Gamma = 6.5 \times 10^{-3}$ for $t_0 = 1 \text{ sec}$ and effective area assumed to be 1 m^2 .)

Fig. 2 compares the current density for points along the line connecting the center of the plate to the midpoint of one side for the case above and for the case where the plate is of infinite area and the case where a lumped circuit approximation is used. j_b corresponds to the square plate case of Fig. 1. j_a corresponds to an infinite plate (no edge charge effect), and j_c corresponds to the lumped circuit approximation of a round plate of radius 1.05 m, divided into eleven concentric circular rings each of width 0.1 m. We see that j_c follows j_b closely, passing

through a peak near 0.7 m away from center, while j_a increases monotonically as we move away from the center.

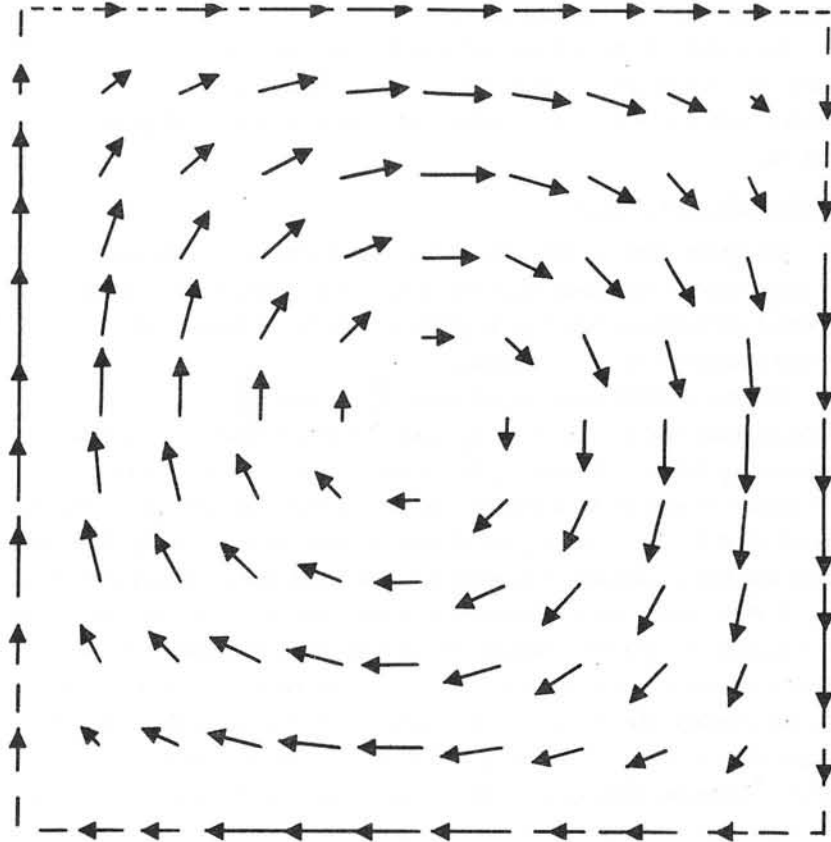


Fig. 1 Eddy current induced in a square plate by a dipole pointing toward the center.

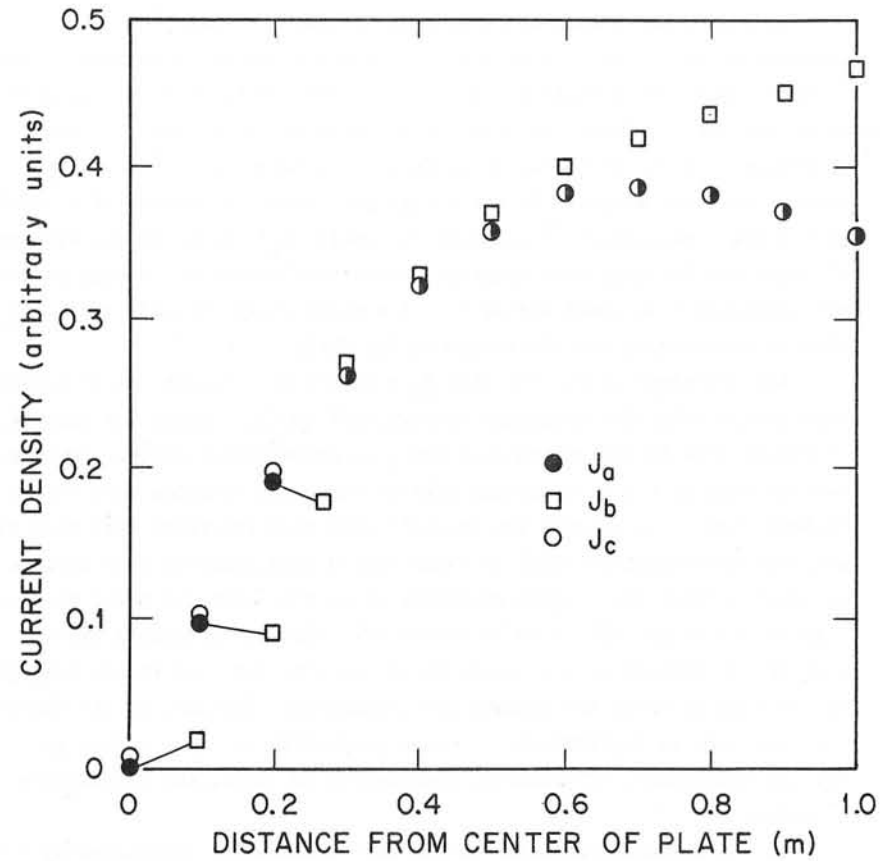


Fig 2 Induced eddy current density along line from center outward of a thin plate for: j_a - infinite plate by perturbation series method; j_b - finite square plate by perturbation series method; j_c - round plate by lumped circuit method.

Another illustration of the edge effect is given in Fig. 3, where the eddy current pattern is shown for the upper right quadrant of the plate in Fig. 1, assuming that the rest of the plate is cut away. We notice that the new boundary significantly modifies the eddy current flow pattern.

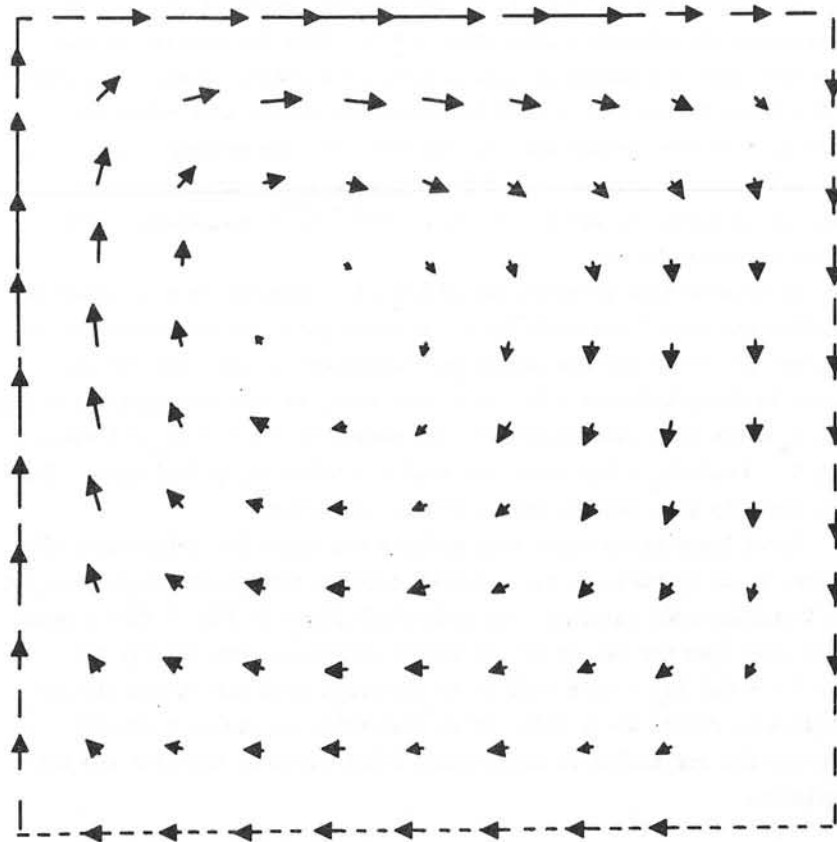


Fig. 3 Eddy current induced in a square plate with dipole pointing at one corner.

C. Transient Effects

We have also evaluated \underline{j} for the case of Fig. 1 by fitting $f(\tau)$ by a 10th order polynomial f_a in the range $-1 < \tau < 1$, and taking $\Gamma = 6.5 \times 10^{-3}$. For those instants for which $\frac{df_a}{d\tau} = 1$, the results agree with the equilibrium solution. This is not surprising, since the sum in Eq. (14) is dominated by its first term for $\Gamma \ll 1$. Hence the accuracy of the method is largely dependent upon the accuracy of the factor $\frac{df_a}{d\tau}$. The more terms used in f_a , the better approximation it gives for $\frac{df_a}{d\tau}$. To reduce the deviation of $\frac{df_a}{d\tau}$ from $\frac{df}{d\tau}$ to less than 10% for most of the range of interest ($0 < \tau < 1$), an eleven term polynomial is satisfactory. The fits of f_a and $\frac{df_a}{d\tau}$ are illustrated in Figs. 4 and 5.

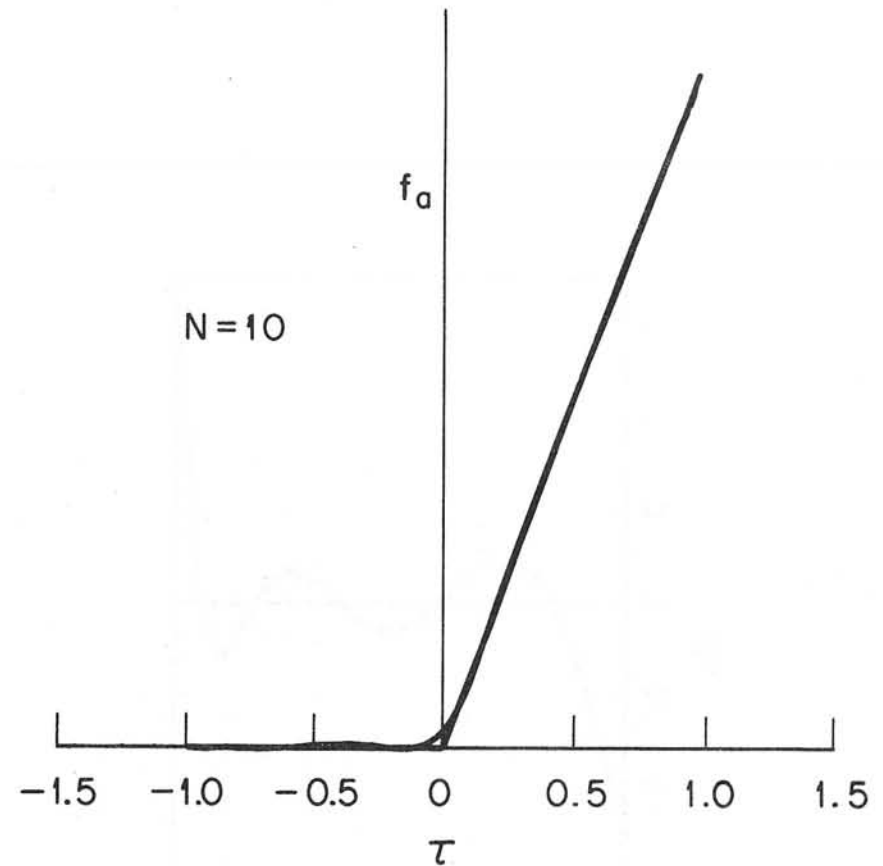


Fig. 4 The fitting of a linear ramp by a 10th order polynomial over the range $-1 < \tau < 1$.

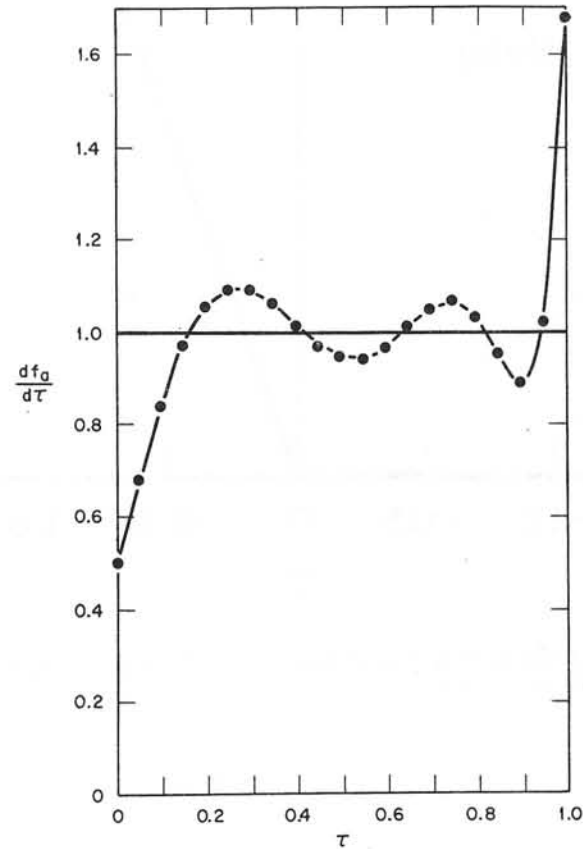


Fig. 5 Comparison of $\frac{df}{d\tau}$ ($=1$) with $\frac{df_a}{d\tau}$ for a 10th order polynomial fit over the range $0 < \tau < 1$.

Having established a limit on the goodness of fit of f_a to f we next investigate the transient case where $\Gamma \lesssim 1$. From the results of Fig. 2, we expect that the lumped circuit solution for points close to the center of the plate should give a good approximation to the true transient behavior. We have solved the problem with the same geometry as Fig. 1, but with larger values of Γ (which correspond to changing the plate material to copper at 150 K - $\sigma = 1.4 \times 10^7 \Omega^{-1} \text{m}^{-1}$) and giving t_0 the values indicated below.

It is necessary to shift the origin of τ relative to t in order to optimize the detail obtained for $t > 0$ while still leaving enough of an interval for $t < 0$ for the transients introduced at the time the fit begins to decay before $t = 0$. As a test case, we have successively fitted f by f_a a ten term polynomial over the ranges $-1 < \tau < 1$ ($t_0 = 1$ sec), $-1.6 < \tau < 0.4$ ($t_0 = 0.5$ sec), and $-1.2 < \tau < 0.8$ ($t_0 = 0.25$ sec). The last two fits give results very close to each other.

For a large plate where edge effects are small for points near the center, it is possible to use a lumped circuit approximating solution for the transient eddy current. The comparison given in Fig. 6 (for a point 0.5 m away from the center of the plate) indicates that the fit for $-1.2 < \tau < 0.8$ ($t_0 = 0.25$ sec) is in agreement with the lumped circuit solution to within about 15%. It is reasonable to assume a similar accuracy for our method in cases where other means of solution are not available.

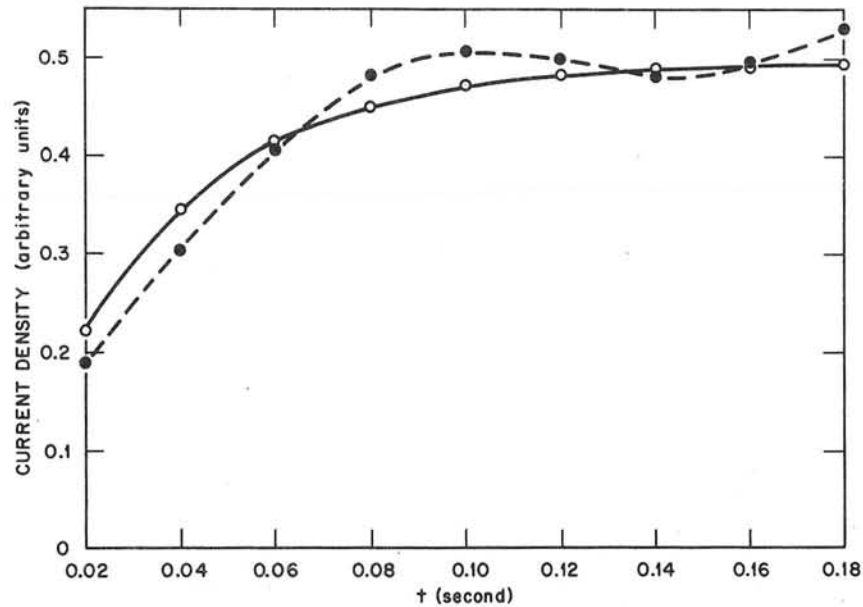


Fig. 6 Comparison of the eddy current transient behavior as calculated by lumped circuit (O) and by the perturbation expansion method (●).

Conclusion

The method of eddy current calculation using the perturbation expansion of the integral equations has been shown to give reasonable results for the equilibrium cases tested. These results agree with lumped circuit approximations and analytic solutions when these are available.

The transient solution for a linear ramp excitation can be obtained by fitting a polynomial to the ramp function over an appropriate interval. In principle, the expansion parameter Γ can always be made small by choosing a very large t_0 . Then one must use enough terms in the polynomial fit to show the desired detail in the transient region.

There appears to be no fundamental difficulty in applying the above method to three-dimensional materials or linear magnetic materials. We intend to extend our work to these cases. We are also investigating alternative schemes for fitting f to f_a (such as fitting $\frac{df}{dt}$ directly)

which should improve the numerical accuracy of \underline{j} for a given order polynomial.

References

1. M. Roberts and E. S. Bettis, "Oak Ridge Tokamak Experimental Power Reactor Study - Reference Design," ORNL-TM-5042, Oak Ridge National Laboratory, Oak Ridge, Tenn. (Nov. 1975).
2. C. J. Carpenter, "Computation of Magnetic Fields and Eddy Currents," Int. Conf. on Magnet Tech., Vol. 5 (1975).
3. The approach of using perturbation expansion with separated time dependence in diffusion equation type problems is derived and verified in: K. H. Carpenter, "Solution of the Diffusion Equation by a Perturbation Approach with Polynomial Approximations to the Driving Term," to be published.
4. H. C. Karmaker, S.D.T. Robertson, "Integral Equation Formulation for the Solution of Magnetic Field Problems, Part II, Magnetization Vector Approach," Trans. IEEE, PAS 92, 815 (1973).
5. R. L. Stoll, J. Muhlhaus, "Power-Series Method of Calculating Eddy Currents in Non-magnetic Conductors," Proc. IEE, 119, 1616 (1972).
6. P. Swartrauber and R. Sweet, "Efficient FORTRAN Subprograms for the Solution of Elliptic Partial Differential Equations," NCAR-TN/1A-109, National Center for Atmospheric Research, Boulder, Colorado (July 1975).

Symbols

$\underline{A}, \underline{A}_0$	Magnetic vector potential
$\underline{\alpha}_0$	Spatial part of the external vector potential
$\underline{\alpha}_m, \underline{\alpha}_m^{\text{th}}$	m^{th} order term of the spatial part of the vector potential
\underline{B}	Magnetic Induction
ϵ	Dielectric constant
f	Time-dependent part of the external vector potential
f_a	Polynomial approximation to f
Γ	Perturbation expansion parameter
\underline{j}	Current density
L	Characteristic length of the conductor
ΔL	Thickness of the conductor
M	Magnetization vector

Symbols (cont.)

μ_0 (μ)	Magnetic permeability in vacuum (conductor)
n	Subscript to indicate normal component
ψ	Electrostatic scalar potential
$\underline{r}, \underline{r}'$	Spatial variables
ρ	Charge density
σ	Conductivity of the conductor
t	Time
t_0	Characteristic time of f
τ	Dimensionless Time (t/t_0)
$\underline{x}, \underline{x}'$	Dimensionless spatial variables ($\underline{r}/L, \underline{r}'/L$)
ζ_m	m^{th} order terms of the spatial part of the scalar potential

The Solution of Transient Fields by the Nodal Method

A.Y. Hannalla & D.C. Macdonald
Ain Shams University Cairo & Imperial College London

Abstract

The transient field in a machine cross-section is obtained numerically in terms of vector potential, full account being taken of saturation and eddy currents in a manner akin to that of the finite element method. Oscillations in the transient solution which are very pronounced in a solid rotor are avoided by making the first time at the start of a transient a special case. Accurate solutions are obtained for simple transients although the computing/real time ratio is approximately 10^4 . As it stands the method is a means to a better understanding and a design tool.

1. Introduction

Magnetic field problems have been studied by finite difference and finite element techniques under steady-state conditions. The ability of the finite element method to accommodate awkward geometries without a very large number of nodes makes it preferable. The nodal method¹ has all the advantages of the first-order finite element method, but gives a more accurate distribution of current to nodes. It also indicates that obtuse-angled triangles give a poor representation. When applied to rectangular elements it has been shown to have the same approximation as that of the finite difference method. In transient conditions the nodal method, being an application of Ampere's law is unquestionably valid. It is therefore an attractive approach, for the derivation through the calculus of variations requires careful justification.

Here the nodal method is used to establish equations for the values of vector potential (A) at nodes in an alternator cross section. In the steady state these are similar to those obtained by the first-order finite element approach. The steady state equations are solved by the Newton-Raphson method for the initial current distribution - here constant field current. The field decrement test is then simulated, the field supply voltage being short-circuited, the stator winding being open. A transient solution of the field is obtained and the field current decrement calculated compares well with measured values when the effect of field winding end-leakage is included.

The transient solution requires a good representation of the conduct-

ing paths in the machine cross-section and this is obtained with a conductivity matrix. The current induced in a multi-turn winding is made dependent on the values of $\frac{\partial A}{\partial t}$ over all of its cross-section. The Newton-Raphson method is used to provide the solution at each time instant for the augmented equations including time effects, reluctance being iterated at the same time.

Solutions have been obtained for field current decrement for a 3kVA micro-alternator and a 325 MVA 4-pole solid rotor machine. The solution for the latter indicates that eddy currents in the solid rotor may have both positive and negative values which may be explicable in terms of higher modes of oscillation.

Equations have also been formulated for a loaded machine, including rotational voltages. This requires representation over a full pole-pitch and very large computing times would be involved in obtaining a solution. With the field decrement calculations over half-a-pole pitch containing 300 nodes, a computed to real time ratio of 10^4 is obtained. For the full pitch analysis 1,000 nodes are required and the ratio might well be 10^5 .

The ultimate aim of the work is to find a model of a solid rotor which will represent it correctly under power system transient conditions. Thus secondary effects, such as tooth ripple, have been neglected and the rotor and stator are considered in a single position with respect to each other.

2. Governing equations

The two-dimensional field is obtained in terms of magnetic vector potential, A , normal to the plane of cross-section. J the current density is also normal to this plane and is distributed in the conducting paths presented by the machine. The field is governed by the equation

$$\nabla_{\wedge} r (\nabla_{\wedge} A) = -J + c' \frac{\partial A}{\partial t} \quad (1)$$

where r is the reluctance of the medium, J represents constant current density, c' is the material conductivity, and the last term represents currents induced by the changing field pattern within the machine. At a point in a closed winding the pattern is more complicated because the resultant current is dependent on the value of $\frac{\partial A}{\partial t}$ throughout the winding. Motion may also produce induced voltage and is omitted in the above.

The boundary conditions in a machine are taken to be those of Dirichlet, Neumann and periodicity. At the inner and outer bore of the

rotor and stator; flux is assumed to be completely contained ($A = \text{constant}$) the leakage flux being negligible. In the field decrement test the field is symmetrical about each pole and only half a pole need be considered. No flux crosses the pole axis ($A = \text{constant}$) and flux crosses the quadrature axis normally ($\frac{\partial A}{\partial n} = 0$). In more general transient problems in the presence of load currents a pole-pitch must be considered and a periodicity condition applied along the radial boundaries.

3. Numerical formulation

The machine cross-section is divided into acute-angled triangles (Plate 1) the sides of which lie along iron and copper boundaries. Within each triangle A varies linearly, giving uniform flux density and reluctance and takes the much used form:

$$A = \frac{1}{2\Delta} (\text{sum of } (a_i + b_i x + c_i y) A_i), \quad i=1,2,3$$

where Δ is the area of the triangle, A_i are values at the vertices, and a_i, b_i and c_i are defined typically as

$$\begin{aligned} a_1 &= x_2 y_3 - x_3 y_2 \\ b_1 &= y_2 - y_3 \\ c_1 &= x_3 - x_2 \end{aligned}$$

the remainder being obtained by cyclic permutation.

Equation 1 is the infinitesimal representation of Ampere's law and here in the nodal method, Ampere's law is used along the orthogonal grid shown in Fig 1 around each internal node and those on the interpolar boundary. This immediately relates the value of current within the contour and associated with the node, with the values of A at the node and at surrounding nodes. The matrix equation obtained is thus

$$S A = c \frac{\partial A}{\partial t} - I \quad (2)$$

where the elements of S on the diagonal are:

$$S_{pp} = \frac{1}{4} (\text{sum of } r_j (b_{1j}^2 + c_{1j}^2) / \Delta_j) \quad j=1, m \quad (3)$$

and on the p th row of the k th column

$$S_{pk} = \frac{r_j}{4\Delta_j} (b_{1j} b_{3j} + c_{1j} c_{3j}) + \frac{r_{j+1}}{4\Delta_{j+1}}$$

$$+ \frac{r_{j+1}}{4\Delta_{j+1}} (b_{1j+1} b_{2j+1} + c_{1j+1} c_{2j+1}) \quad (4)$$

where b_{1j} and c_{1j} are the b_1 and c_1 of the j th triangle, and node k is coupled to node p by the common side of the j and $(j+1)$ th triangles around node p . I represents a vector of constant currents.

S is symmetrical and has n rows ($n = \text{no. of active nodes}$). The inactive nodes on the Dirichlet boundaries are set to zero.

The right-hand side of equation (2) is zero at nodes where there is no conducting path, i.e. in air and laminated material. In the field winding, current may flow and the conductivity matrix has the form

$$c = \begin{bmatrix} 0 & 0 & 0 \\ 0 & c_1 & 0 \\ 0 & 0 & c_2 \end{bmatrix} \quad (5)$$

The sub-matrices c_1 and c_2 represent the damping circuits and the field circuit. In the damping circuits current point is dependent on the value of $\frac{\partial A}{\partial t}$ at each node, and c_1 is a diagonal matrix of elements representing conductivity \times area for each node. c_2 is a full matrix by which the current concentrated at any node is related to the values of $\frac{\partial A}{\partial t}$ at all nodes within the field winding cross-section and the resistance of the field circuit:

$$c_2 = \frac{c' N}{\Delta_s k_s k_i n_f} W W^T \quad (6)$$

where W is the column vector of areas associated with the n_f nodes in the field winding cross-section over half a pole of total area Δ_s . N is the no. of turns/pole, k_s is the field winding space factor and k_i the mean length of turn/2 \times rotor effective length.

The two parts of the conductivity matrix are kept distinct by ensuring that conducting regions are separated by a set of small non-conducting elements.

4. Time approximations

An implicit method is used to obtain $\frac{\partial A}{\partial t}$ at the end of each time step,

$$\text{dt:} \quad \frac{\partial A}{\partial t} \Big|_{t+t} = - \frac{\partial A}{\partial t} \Big|_t + \frac{2}{\text{dt}} (A_{t+\text{dt}} - A_t) \quad (7)$$

The error starts from the third derivative and the time interval is independent of the size of the elements. The initial time step has to be considered separately.

5. Initial values and the first time-step

At nodes in non-conducting regions $\frac{\partial A}{\partial t}$ does not give rise to current and may be allowed to vary freely from zero at the start of the transient.

The solution of equation (2) at the end of the first time step requires a value of $\frac{\partial A}{\partial t} \Big|_{dt}$, or, more exactly, $c \frac{\partial A}{\partial t} \Big|_{dt}$. Equation (7) would appear to give this if $c \frac{\partial A}{\partial t} \Big|_0$ is known. In conductors initially carrying current immediately following the transient, current is maintained by $\frac{\partial A}{\partial t}$, i.e.

$$c \frac{\partial A}{\partial t} = I_0$$

However the use of equation (7) at $t=0$ gives rise to oscillations in the solution (Fig.2 & 3) as was also found by Flatabo² in a thermal diffusion problem.

In conducting paths not initially carrying current, currents rise from zero at $t=0$ and therefore $\frac{\partial A}{\partial t} \Big|_0 = 0$. For a short time after the start of the transient $\frac{\partial A}{\partial t}$ remains constant, changing by dA in successive time steps dt . Using equation (7) at the end of the first time step:

$$\begin{aligned} \frac{\partial A}{\partial t} \Big|_{dt} &= 0 + \frac{2}{dt} (dA) \\ &= 2 \frac{dA}{dt} \end{aligned}$$

which is clearly wrong and at the next instant gives $\frac{\partial A}{\partial t} \Big|_{2dt} = 0$.

A better solution is obtained if in the first time step a first-order approximation is used for $\frac{\partial A}{\partial t}$

$$\frac{\partial A}{\partial t} \Big|_{dt} = \frac{1}{dt} (A_{dt} - A_0),$$

with a very small value for dt .

A further difficulty occurs if nodes are situated on a common boundary between two conducting regions, one of which is initially carrying current (the field winding) and the other is not (the damper winding or solid iron). When driving voltage is suddenly removed (from the field circuit) current

is maintained constant by $\frac{\partial A}{\partial t} \Big|_{t=0}$. However in the conductor that is initially dead $\frac{\partial A}{\partial t} \Big|_{t=0} = 0$ for current rises from zero. If no special provision is made the latter condition is not satisfied and current is calculated in the damping circuits at $t=0$. A full consideration of this situation would have to include the effect of the end leakage of the field winding for it must be the change of flux linkage there which initially contributes to the maintenance of current at the boundary.

However ignoring end effects a solution may be obtained when the field winding consists of many small conductors connected in series. The initial distribution of $\frac{\partial A}{\partial t}$ may then be obtained by assuming uniform rate of change of current density, which gives rise to $\frac{\partial A}{\partial t}$. The total voltage induced is at $t=0$

$$c_2 \frac{\partial A}{\partial t} = I_0$$

$\frac{\partial A}{\partial t} = 0$ is also satisfied at the common boundary. If the field conductors are large a better approximation would probably be to keep the total conductor current constant.

Here these difficulties have been avoided by putting a set of small non-conducting elements between conducting regions and by allowing $\frac{\partial A}{\partial t} \Big|_0$ to have a uniform value over conductors initially carrying current.

6. Choice of Grid

The nodal method allows for triangles or rectangles to be chosen as elements. Rectangles have been used in stator slots (Plate 1) where permeability is constant, and flux distribution is of minor importance in field decrement conditions. Many small elements have been used where gradients of flux density are large, but the overall aim is to use few, large elements, so as to minimise the number of nodes. In transient conditions Carpenter has shown that the surfaces of magnetic material must have at least one layer of elements in the depth of penetration if serious error is to be avoided. Here under transient conditions penetration depth does not have a clear meaning and the grid used has been laid out rather arbitrarily with a coarse grid and with smaller elements towards the air gap surface. As is shown later, higher modes of oscillation appear to be excited by the sudden transient and clearly the representation will limit the modes which can appear in the solution.

The choice of elements in the rotor slots requires to be sufficiently detailed to represent the distribution of $\frac{\partial A}{\partial t}$ over the conductor. Six nodes have been used in each slot and are about the minimum necessary to obtain the distributions shown for $t=0$ and after the first time step in Fig.2.

Nodes are numbered as far as possible so that the s-matrix has a strip of elements about its leading diagonal, i.e. the numbers of adjacent nodes are kept as near together as possible. There are exceptions to this rule in respect of:

inactive boundary nodes
nodes within the field winding cross-section
nodes within the damper winding cross-section, or
in solid iron,

These are numbered in three groups within each of which numbers follow consecutively.

7. The iterative method

The initial values having been obtained by Newton-Raphson successive iteration, time steps are made in the same way with augmented equations. However, the solution to be obtained at the next instant involves $\frac{\partial A}{\partial t}$ and the value given by equation (7) is used save at the first instant. The vector of errors G is given by

$$G = S A + I - c \frac{\partial A}{\partial t}$$

and the solution is obtained for minimal G. The starting values of A at the instant $t+dt$ are those at t, and at the (j+1)th iteration are

$$A_{j+1} = A_j - H_j^{-1} G_j$$

where H_j is the first order derivative of G_j with respect to A. Thus at

$$G_j = S_j A_j + 2 \frac{c}{dt} (A_j - A_t) + I_t$$

and

$$H_j = H_s + \frac{2}{dt} c.$$

H_s is the differential of S as given by Silvester³. At the first time step in a transient the first order approximation gives

$$H_j = H_s + \frac{c}{dt}.$$

Jennings⁴ sparsity techniques are used and very good solutions are normally obtained in under ten iterations. The values of reluctivity are adjusted

at each iteration and the method is unconditionally stable, the size of time step being restricted by the accuracy sought, not by stability.

Applications

The method has been successfully applied to the calculation of simple transients, the field decrement test. The first machine, a 3kVA micro-alternator, has a laminated stator and rotor, damping currents occurring only in the cage damper winding. Fig.3 shows the growth of damper current following the short-circuiting of the field supply voltage. It will be seen that the current density increases fastest at A nearest to the field winding. Current at point B is slightly slower and is followed by the current at the top of the bar (c). Damper current density having reached a maximum uniform value, the damper and field currents decay away together. The fast rise in damper current shown is associated with the initial swift drop in field current.

Fig.3 also shows the oscillation in the solution associated with the use of the second-order approximation throughout.

A typical solution for the solid rotor 4-pole machine are shown in Plate II. The field current decrement is shown in Fig.4. Curves C and D show the oscillations obtained using the second order approximation throughout. E shows the effect of using the first order approximation at $t=0$ and taking full account of the switching operation (current in the discharge resistor was initially in the reverse direction), and F allows for the effect of field leakage reactance at the ends of the machine.

Fig.5 gives the eddy current density at the centre of a tooth at successive instants. A negative current is clearly indicated towards the front of the tooth and in the rotor body. These may be thought of as evidence of excitation of the higher natural modes of oscillation of the rotor, and several other explanations have been considered which would tend to confirm what at first was a surprising result. It would be interesting to confirm these results by measurements.

Conclusions

It has been shown that general transient conditions may be calculated with due regard to eddy currents, varying permeability and awkward geometry. The method is limited at the moment by the poor computing/real time ratio, and this must inhibit its use. If the time of calculation is reduced substantially the method may have a very wide significance. As it

is, it is an interesting tool giving considerable insight and holds promise as a means of devising more approximate machine models.

Acknowledgement

Thanks are due to A.B.J. Reece of GEC Power Engineering Ltd. who supplied the data of the solid rotor machine.

References

1. Hannalla, A.Y and Macdonald, D.C. 'A nodal method for the numerical solution of transient field problems in electrical machines', *IEEE Trans on Magnetics*, September 1975, pp.1544-46.
2. Flatabo, N. 'Transient heat conductance problems in power cables solved by the finite element method', *IEEE Trans. PAS-92* 1973 pp.56-63.
3. Silvester, P., Cabayan, H.S. and Browne, B.T. 'Efficient techniques for finite element analysis of electrical machines', *IEEE Trans. on Power App. & Syst. Vol. PAS-92*, 1973, pp.1274-81.
4. Jennings, A. 'A compact scheme for the solution of symmetric linear simultaneous equations', *Computer Journal* 1966, pp.281-5.

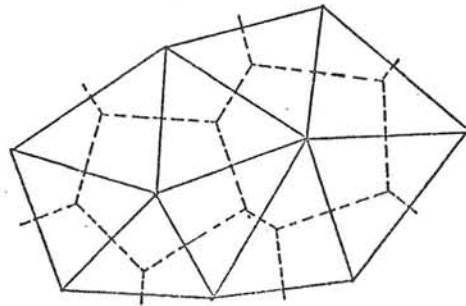


Figure 1 Orthogonal grid

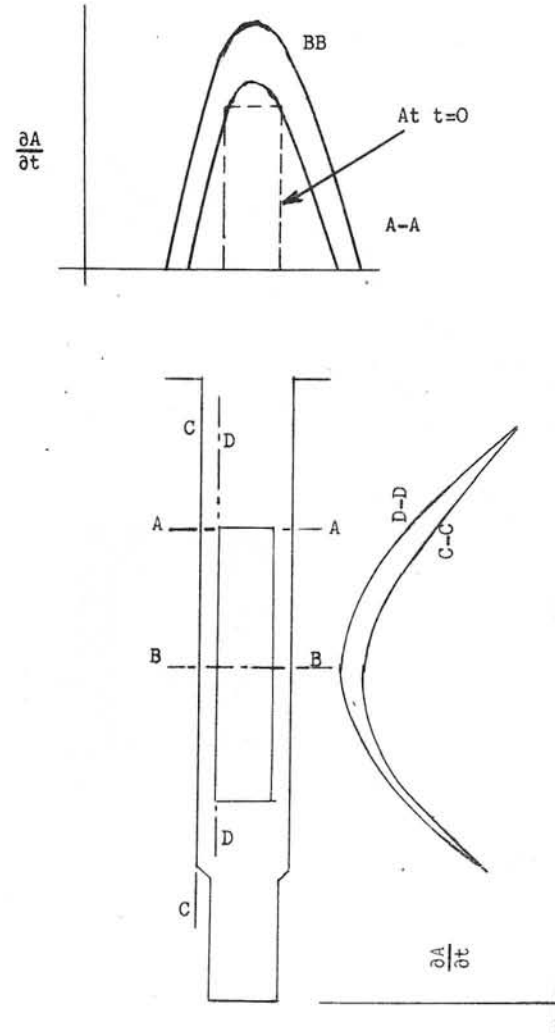


Figure 2 Distribution of $\frac{\partial A}{\partial t}$ in a rotor slot after the first time step

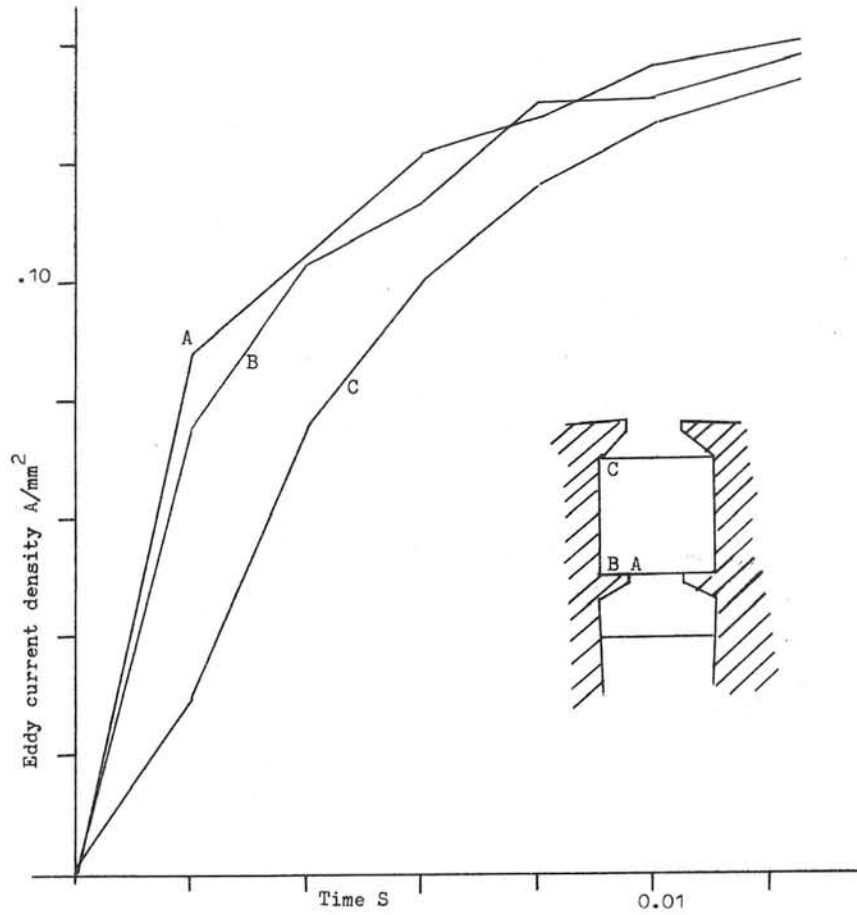


Figure 3 Growth of current in a rotor damper winding

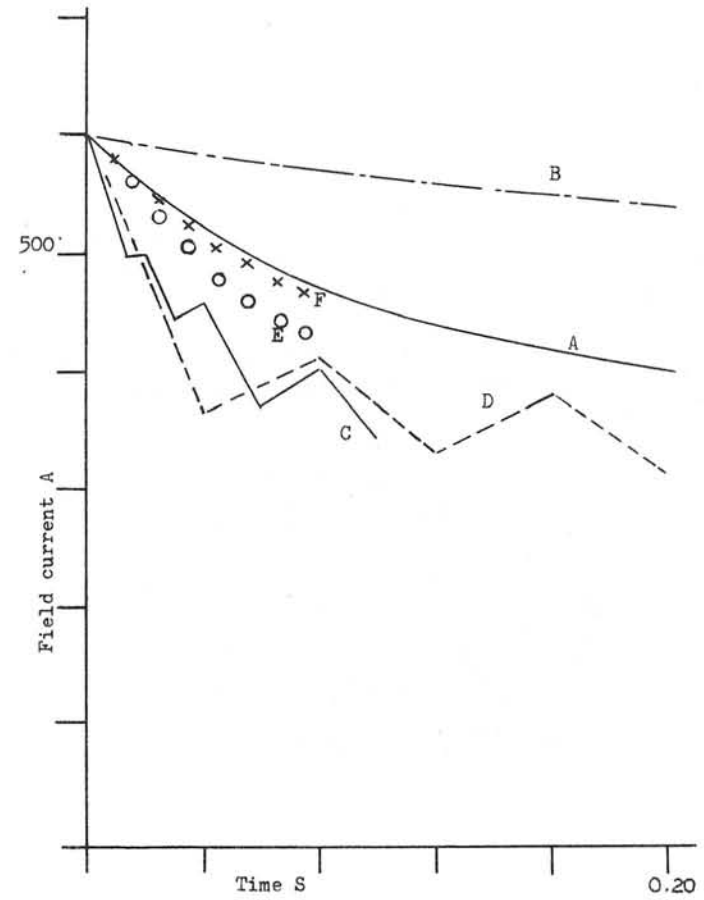


Figure 4 Field current decrement of a solid rotor machine

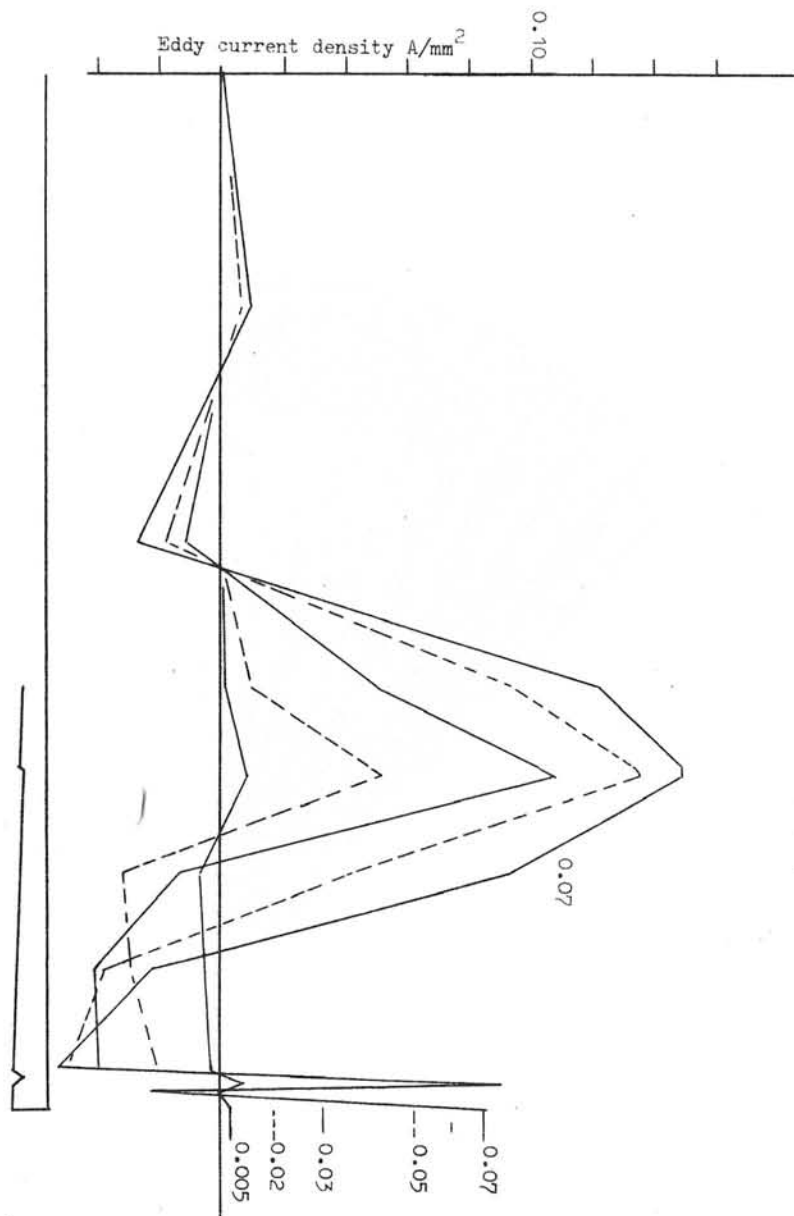


Figure 5 Growth of current along the centre line of a tooth at times from .005 - .075.

Correction Fig.5 shows values of current density scaled from $\frac{\partial A}{\partial t}$ values at nodes directly. These are not correct for in the consideration of the solid pole work current taken to act at a node is also dependent on $\frac{\partial A}{\partial t}$ values at adjacent nodes. When this process is followed only positive values of current density occur.

A.Y.H. and D.C.M.

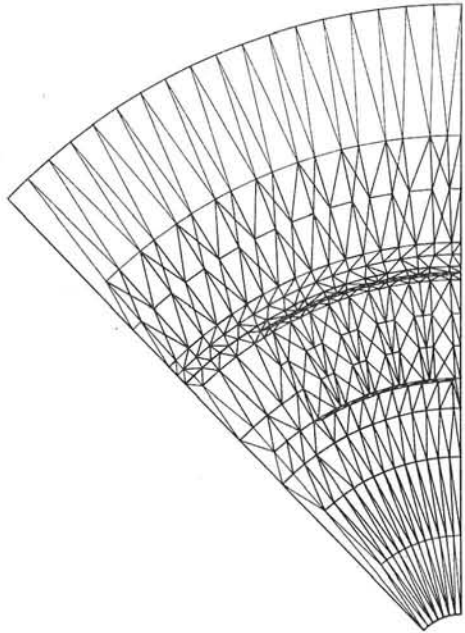


Plate 1 Grid of triangles used over half a pole pitch of a 325 MVA machine.

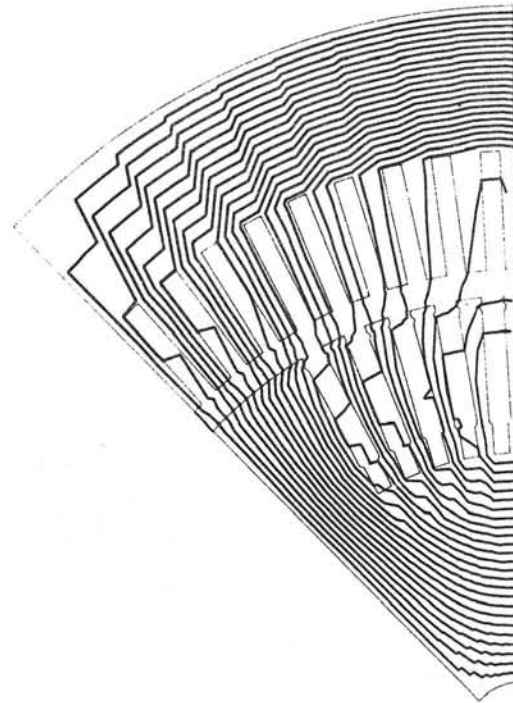


Plate 2 Flux distribution 0.035s after the start of the field decrement test.

CALCULATION OF THE DYNAMIC BEHAVIOUR OF ELECTROMAGNETIC
ACTUATORS*

B. Aldefeld[†]

ABSTRACT

A method for the calculation of the dynamic behaviour of electromagnetic actuators is described which uses finite difference techniques and solves the magnetic field equation for successive time steps. Results of numerical investigations of the convergence of the SLOR method are discussed. As an application the dynamic behavior of a print needle actuator is shown.

INTRODUCTION

Electromagnetic actuators are found in a variety of technical devices e.g. in printers or paper tape and punch card equipment. They are used to provide mechanical energy at a given stroke and in a given time interval. Strokes of the order of 1 mm and times of action in the ms range are typical for many applications. For the excitation usually a voltage pulse of short duration is applied.

In the design and optimization of these devices requirements have to be met as to power consumption, magnetic force, mechanical energy, and speed of action. From the mathematical point of view, the main problem is the solution of Maxwell's field equations for time-varying excitation and moving media taking non-linear magnetization characteristics into account. Because of the dynamic nature of the problem a large number of field distributions for successive time steps have to be calculated, and it is of major importance that efficient methods of solution are used.

*Work supported by the Bundesministerium für Forschung und Technologie of the Federal Republic of Germany.

[†]Philips GmbH Forschungslaboratorium Hamburg, 2 Hamburg 54

The work of which some aspects will be described in this paper is aimed at a complete digital simulation of electromagnetic actuators. As yet, only magnets with rotational symmetry have been taken into consideration and eddy currents have been neglected. However, the eddy current effect is considered to be important, and the methods have been chosen with respect to include this effect at a later time.

METHOD

The dynamic behaviour of an electromagnetic actuator is described by three differential equations, which in common notation read

$$iR = U - \frac{d}{dt} (Li) \quad (1)$$

for the calculation of the current in the coil,

$$m \frac{d^2 z}{dt^2} = \text{magnetic force} + \text{spring force} + \text{frictional force} \quad (2)$$

for the displacement of the armature, assuming that only one mass and one spring are present, and

$$\frac{\partial}{\partial r} \left(\frac{1}{r\mu} \frac{\partial}{\partial r} (rA) \right) + \frac{\partial}{\partial z} \left(\frac{1}{r\mu} \frac{\partial}{\partial z} (rA) \right) = -j \quad (3)$$

for the vector potential, which has only a tangential component in rotationally symmetrical geometries.

The basic principle used in this paper for the solution of these differential equations is shown in the simplified flowchart Fig. 1. The magnetic force and the inductance can be obtained by simple integrations from the magnetic field distribution^{1,2}, and the ordinary differential equations (1) and (2) can be solved by standard methods. The main problem is the solution of the non-linear partial differential equation (3), which will be discussed in more detail in the following.

The finite difference approach is used applying similar techniques as described by Erdélyi³. This method allows for sufficiently accurate discretization for the geometrical con-

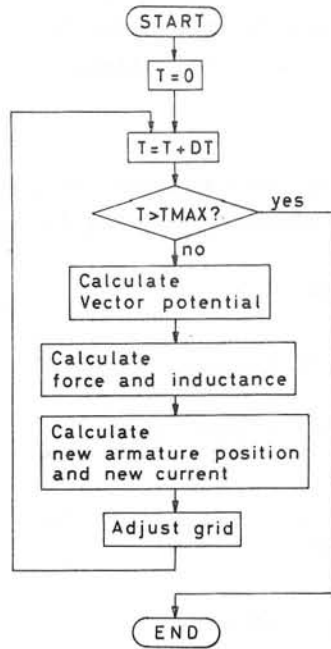


Fig.1 Simplified Flowchart for Calculation of Dynamic Behaviour

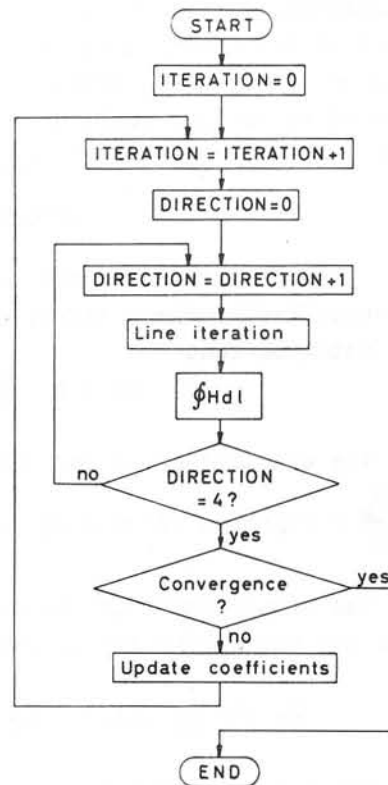


Fig.2 Flowchart of Iteration Method

figurations considered here, and the generation of the grid and its adaption to the time-varying geometry is easy to perform.

The iteration procedure consists of an inner and an outer cycle (Fig. 2). In the inner cycle new vector potentials are calculated by successive line iteration using the Thomas algorithm for the solution of the tridiagonal systems.

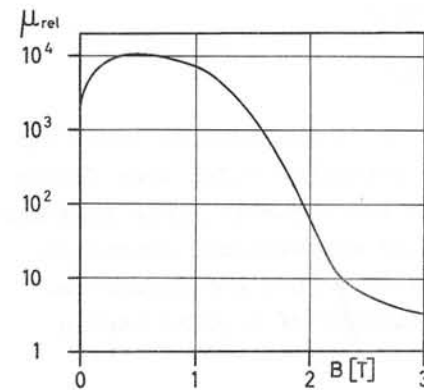


Fig.3 Magnetization Curve

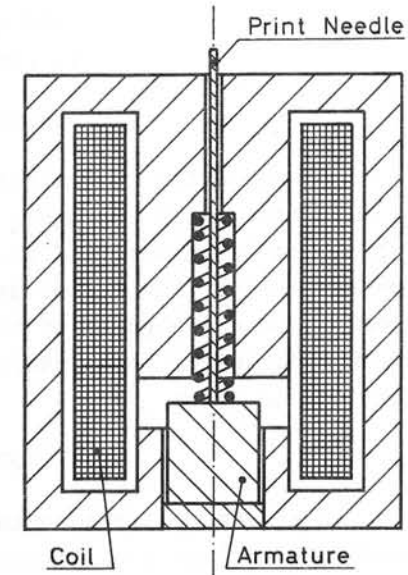


Fig.4 Print Needle Actuator

The vector potentials $A_{J,K}$ are overrelaxed according to

$$A_{J,K}^{(M)*} = A_{J,K}^{(M-1)} + ORF (A_{J,K}^{(M)} - A_{J,K}^{(M-1)}) \quad (4)$$

where J,K refer to the nodes of the grid, M denotes the number of completed iterations of the inner cycle, and ORF is the overrelaxation factor. Additional acceleration of convergence is obtained by the multiplicative method based on Ampere's law, which has been described by Ahamed⁴.

The outer iteration cycle consists of four inner cycles performed in alternating directions followed by updating the coefficients. The reluctivities $v_{J,K}$ are calculated from the flux density and the magnetization curve and underrelaxed according to

$$v_{J,K}^{(I)*} = v_{J,K}^{(I-1)} + URF (v_{J,K}^{(I)} - v_{J,K}^{(I-1)}) \quad (5)$$

where I denotes the number of completed iterations of the outer cycle and URF the underrelaxation factor.

The initial values for the start of the iterative procedure are obtained from the field distribution of the previous time step, except for the first field calculation, which starts from $A_{J,K} = 0$. The convergence of the solution is monitored by three quantities:

- Percentage change in the magnetic force in two successive iterations
- Deviation of $\frac{1}{Ni} \oint Hdl$ from 1
- Euclidean norm of the difference vector divided by the average vector potential.

NUMERICAL INVESTIGATIONS

In several publications the convergence of iterative solutions has already been discussed. However, the results obtained by different authors, e.g. as to optimum relaxation factors, indicate that there is a strong dependence on the special problem and the method used. Additional investigations have therefore been carried out. The convergence of the solution for a number of different electromagnets, including open magnets (without flux return yoke), has been examined for low and high excitation currents and the magnetization curve shown in Fig. 3. Also the influence of the position of the integration path for the evaluation of $\oint Hdl$ has been investigated. The number of cells was chosen between 650 and 1500, which gives sufficient accuracy for the design applications under consideration. The following results have been obtained.

The position of the path of integration is not critical and the convergence is at least five times more rapid than without this acceleration.

On the relaxation factors there is a significant dependence. The underrelaxation factor had to be chosen lower than 0.12 and the overrelaxation factor lower than 1.8 to

avoid instabilities in the solution. Suitable values were found to be 0.1 and 1.7 respectively, for which convergent solutions were obtained for all configurations and currents. Figures 5 and 6 illustrate the typical convergence of magnetic force and $\oint Hdl$ for different overrelaxation factors and an underrelaxation factor of 0.1. The test sample is the magnet shown in Fig. 4 subdivided into 1500 cells.

Fewer iterations are needed at very high excitation when the flux density in large parts of the magnetic circuit exceeds two Tesla. This is obviously due to the facts that at high saturation the differences between the permeabilities in air and iron are reduced and that the slope of the magnetization curve becomes less steep.

The number of iterations required to reach sufficient convergence in each time step is strongly dependent on the rate of change of armature position and current. Typical curves are given in Fig. 7. They apply to the dynamic characteristic shown in Fig. 8a (magnet Fig. 4 subdivided into 650 cells, time increment 0.05 ms). The thresholds for the termination of the iterations were preset to give an accuracy of the numerical solution of about 3 per cent: change in the magnetic force < 0.005 , norm of the difference vector divided by the average vector potential < 0.05 , $|\frac{1}{Ni} \oint Hdl - 1| < 0.005$.

The shape of the curves in Fig. 7 can be characterized, somewhat simplified, as follows:

- Many iterations at the beginning where the iterative process starts from $A_{J,K} = 0$
- Few iterations where the field distribution varies slowly because the armature is not yet moving
- Many iterations where the field distribution varies rapidly because both the position of the armature and the current change.

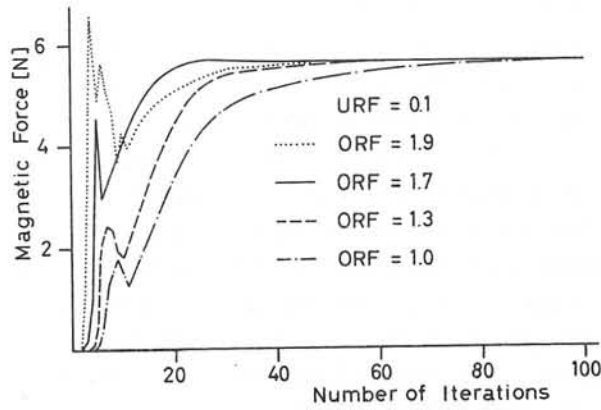


Fig. 5
Convergence of
Magnetic force

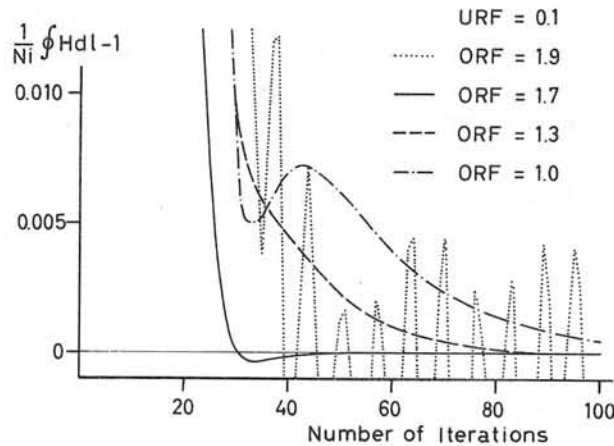


Fig. 6
Convergence of
 $\oint Hd l$

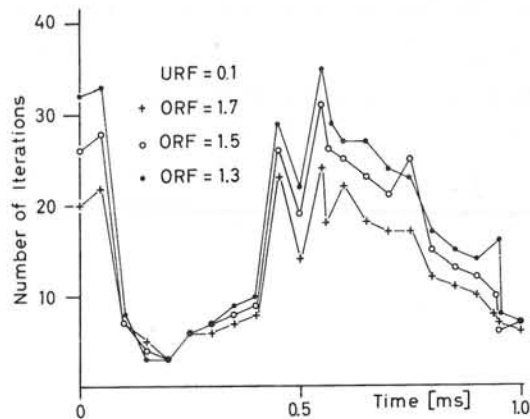


Fig. 7
Number of Itera-
tions as a Func-
tion of Time

For smaller time increments fewer iterations are required per time step because successive field distributions are more similar. For the example in Fig. 7 the average number of iterations per time step decreased from 14 to 10 (for ORF = 1,7) when an increment of 0.025 ms was chosen instead of 0.05 ms. For the determination of a suitable time increment no general rule can be given because there is a strong dependence on the special shape of the curves that describe the dynamic behaviour. On the one hand, the increment should be chosen as great as possible to keep the total number of iterations low, on the other hand, the increment should be chosen small enough to ensure that the magnetic force and the inductance can be interpolated with sufficient accuracy between the points of calculation.

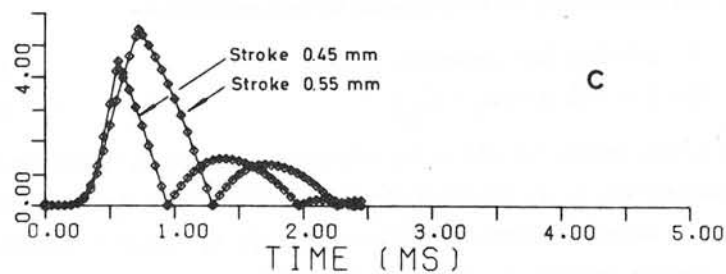
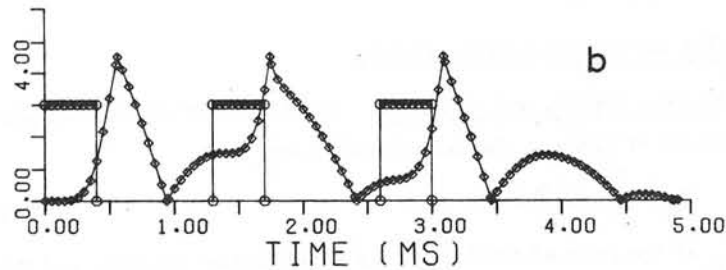
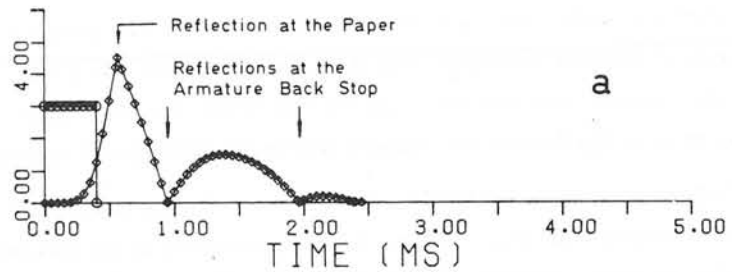
APPLICATION

A computer programme has been developed on the basis of the techniques described and is used currently to assist the design of print needle actuators. The programme produces curves of magnetic force, armature displacement, velocity, mechanical energy, current, and inductance as functions of time and allows for taking 'snapshots' of vector potential, flux density, and flux lines at any time step.

An example is given in Fig. 8 showing the displacement of armature and print needle of the magnet in Fig. 4. Fig. 8a shows the dynamic behaviour under pulse excitation at low repetition rate. Fig. 8b displays the behaviour in the case of three successive pulses at a high repetition rate which causes interference between the pulses. In Fig. 8c the behaviour for different initial positions of the armature is compared.

REFERENCES

1. P. Hammond, Forces in electric and magnetic fields, Bull. Electrical Eng. Educ. 25, pp. 17-23, 1960
2. R.S. Mamak and E.R. Laithwaite, Numerical evaluation of inductance and a.c. resistance, Proc. IEE 108C, pp. 252-258, 1961
3. E.A. Erdélyi and E.F. Fuchs, Nonlinear magnetic field analysis of dc machines, IEEE Trans. Power Apparatus and Systems, Vol. PAS-89, pp. 1546-1583, 1970
4. S.V. Ahamed, Accelerated convergence of numerical solution of linear and non-linear vector field problems, Computer J., Vol. 8, pp. 73-75, 1965



○ Voltage (10A per Division)
 ◇ Displacement (0.1 mm per Division)

Fig.8 Dynamic Behaviour of a Print Needle Actuator

Discussions following paper:

(Chevalley CERN) Have you any comparisons with experimental datas? They would show the influence of neglecting the eddy current effects?

(Alderfeld) Some measurements on a print needle actuator have been performed and compared with the computations. It was found that the computed average force was too large by about 20 per cent for that electromagnet and it is supposed that this is mainly due to the eddy current effects. In order to improve the accuracy it is therefore planned to include the eddy currents in the computations.

A THREE-DIMENSIONAL ANALYTIC MODEL FOR CALCULATING
EDDY-CURRENT EFFECTS APPLIED TO A TOKAMAK BLANKET
AND SHIELD*

L. R. Turner, S. T. Wang, and J. R. Purcell
Argonne National Laboratory
Argonne, Illinois 60439 U. S. A.

SUMMARY

A method has been developed for calculating the induced fields due to eddy currents, in order to determine whether the conducting material is finely enough subdivided that eddy current effects do no harm. In using the method, the conducting material is divided into rectangular bricks. With suitable assumptions about the acting magnetic field, the current densities can be described by third-power equations. Consequently, the induced field from each brick can be written analytically. The method has been applied to flux penetration of the blanket and shield of Argonne National Laboratory's proposed design for a Tokamak Experimental Power Reactor.

1. INTRODUCTION

In a tokamak fusion reactor, as in other kinds of electrical machinery, time-varying magnetic fields can produce undesirable eddy currents. The eddy currents can be reduced by laminating or otherwise subdividing the metal parts; however, to make the pieces smaller than necessary may be expensive, inconvenient, or even inconsistent with their functioning. Thus it seems desirable to develop a general-purpose method of calculating eddy currents and the fields they produce, in order to determine how fine a subdivision is needed.

In a tokamak, the toroidal plasma is surrounded by a toroidal energy-absorbing blanket and radiation shield. In the Argonne design of a Tokamak Experimental Power Reactor (TEPR), these are made of

stainless steel, plus non-conducting material. The blanket and shield experience both the pulsed field from the plasma current and the pulsed vertical field required to hold the plasma in equilibrium.

Eddy currents induced in the blanket and shield will produce magnetic fields which may interfere with the plasma current. In addition, those eddy currents may interact with the field from the toroidal-field coils to create large forces and torques within the blanket and shield.

In Sec. 2, below, we develop the mathematical model used to calculate eddy current effects. Section 3 is a description of the blanket and shield of a tokamak. Section 4 shows the calculation of eddy current effects in the blanket and shield. Finally, Sec. 5 describes possible extensions to the model.

2. THE MATHEMATICAL MODEL

2.1 Blocks, Fields, and Currents. The induced magnetic field due to eddy currents is given by the Biot-Savart Law:

$$B_{in} = \frac{\mu_0}{4\pi} \int \frac{J \times r}{r^3} dV \quad (2.1)$$

where B_{in} is the induced field, J is the eddy current density, and r is the displacement from the source point (x, y, z) to the field point (x_0, y_0, z_0) . The eddy current density is determined by two conditions:

$$J \cdot n = 0 \text{ on the conductor surface} \quad (2.2)$$

$$\nabla \times J = -\sigma \dot{B} = -\sigma (\dot{B}_a + \dot{B}_{in}) \quad (2.3)$$

when n is a unit vector normal to the conductor surface, σ is the electrical conductivity, B_a is the applied field, and the dot designated differentiation with respect to time. Solution of Eq. (2.1) - (2.3) is a difficult problem, and no general algorithm for their solution exists.

Let us make sufficient assumptions that the equations have convenient analytic solutions. Limitations on the applicability of the model due to these assumptions are discussed below in Sec. 2.3.

- (1) The conductivity is sufficiently low that the induced field is small relative to the applied field. Thus $\dot{B}_a + \dot{B}_{in}$ may be

*Work performed under the auspices of the U. S. Energy Research Development Administration.

replaced in Eq. (2.3) by \dot{B}_a .

- (2) All conductors can be represented as rectangular solids aligned parallel to the coordinate axes. Let a conductor be centered at the origin and have length $2a$, $2b$, $2c$ in the x , y , z directions respectively.
- (3) The field B_a is everywhere in the z direction; consequently J is everywhere parallel to the x - y plane.
- (4) The field B_a varies across a rectangular conductor according to

$$B_a = B_o \left(1 - \frac{x^2 + y^2}{a^2 + b^2} \right) \quad (2.4)$$

2.2 Expression for Induced Fields. Under the above assumptions, Eq. (2.2) and (2.3) are satisfied by a current density J with components

$$J_x = \sigma \dot{B}_o y \frac{a^2 - x^2}{a^2 + b^2} \quad (2.5)$$

$$J_y = -\sigma \dot{B}_o x \frac{b^2 - y^2}{a^2 + b^2} \quad (2.6)$$

Eq. (2.1) then has a z component which can then be written:

$$B_{in} = \frac{\sigma \dot{B}_o}{a^2 + b^2} \iiint \left[(y_o - y) y (a^2 - x^2) + (x_o - x) x (b^2 - y^2) \right] / r^3 dy dz \quad (2.7)$$

Substituting:

$$u = x - x_o, \quad v = y - y_o, \quad w = z - z_o,$$

and carrying out the integration, we find the following equation for the z component parallel to B_a :

$$B_{in} = -\frac{\mu_o}{4\pi} \frac{\sigma}{a^2 + b^2} \dot{B}_o \left[\tan^{-1} \frac{uv}{wr} \left\{ \frac{1}{2} w^2 (x_o^2 - a^2 + y_o^2 - b^2) - w^4 / 6 \right\} + \tan^{-1} \frac{uw}{vr} \left\{ v y_o (a^2 - x_o^2) + \frac{1}{2} v^2 (a^2 - x_o^2 + y_o^2 - b^2) + v^3 y_o + \frac{1}{2} v^4 \right\} + \tan^{-1} \frac{vw}{ur} \left\{ u x_o (b^2 - y_o^2) + \frac{1}{2} u^2 (b^2 - y_o^2 + x_o^2 - a^2) + u^3 x_o + \frac{1}{2} u^4 \right\} + \right]$$

$$+ \ln(r + u) \left\{ w v (b^2 - y_o^2 - 2v^2 / 3) - w y_o (a^2 - x_o^2 + 3v^2 / 2) - \frac{1}{2} w^3 y_o \right\} + \\ + \ln(r + v) \left\{ w u (a^2 - x_o^2 - 2u^2 / 3) - w x_o (b^2 - y_o^2 + 3u^2 / 2) - \frac{1}{2} w^3 x_o \right\} + \\ + \ln(r + w) \left\{ u y_o (u^2 + x_o^2 - a^2) + v x_o (v^2 + y_o^2 - b^2) + 2x_o y_o (u^2 + v^2) \right\} + \\ + r \left\{ uvw / 6 + \frac{1}{2} x_o v w + \frac{1}{2} y_o u w + 2x_o y_o w \right\} \quad (2.8)$$

where σ is the electrical conductivity, $r = \sqrt{u^2 + v^2 + w^2}$, and u , v , and w are evaluated at their upper and lower limits $\pm a - x_o$, $\pm b - y_o$, $\pm c - z_o$ respectively.

2.3 Limitations Due to Assumptions. Let us look at the consequences of the four assumptions listed above. For the type of application intended, subdividing the conductor to control the effects of eddy currents, assumption (1) holds definitely, in that the conductor is not adequately subdivided unless the assumption holds. Depending upon the degree of subdivision required, assumption (2) may or may not hold. In some cases, a more detailed treatment may be needed for nearby conductors, and the model used for more distant conductors. There is a class of problems for which assumption (3) is good, but certainly the model would be improved by including all three components of J and B . Assumption (4) is the most questionable; if the field B_a were actually uniform and equal to B_o , then the above expression would probably underestimate B_{in} , but by less than one third. An extension of the model to make the next approximation beyond assumption (4) is discussed in Sec. 5 below.

3. THE BLANKET AND SHIELD AND THE EQUILIBRIUM FIELD

3.1 The TEPR Blanket and Shield. In a tokamak power reactor, most of the energy is carried out of the plasma by 14 MeV neutrons. The blanket surrounding the plasma captures almost all (approximately 99%) of these neutrons and contains a circulating coolant (water or helium) to carry the energy to the generator outside. Surrounding the blanket is

the shield, designed to stop the remaining neutrons. An early design for the Argonne TEPR blanket and shield is shown in Fig. 1. It consists of a torus with alternating layers of stainless steel and boron carbide; the layers are between 5 and 15 cm thick, with a total thickness of 80 cm of stainless steel. The torus was unbroken toroidally or poloidally. After the calculations described below were performed, the design was changed to that shown in Fig. 2, which consists of thirty segments toroidally, each divided into rings of 16 blocks poloidally.

3.2 The Equilibrium Field. A tokamak must have, superimposed upon the other magnetic fields, a vertical magnetic field throughout the plasma region to keep the plasma current in equilibrium. In the Argonne TEPR, the field is 3 kG, it must be established during the one second rise time of the plasma current; and it is produced by coils outside the blanket and shield. It is this equilibrium field which produces eddy currents in the blanket and shield.

4. CALCULATING THE EDDY CURRENTS AND INDUCED FIELD

4.1 A Simpler Model. Because the blanket and shield shown in Fig. 1 consists of thin toroidal rings, it can be approximated by a toroidal shell, with toroidal and poloidal currents, but no radial currents. Furthermore, unless the aspect ratio is too low, the toroidal shell can in turn be replaced by a cylindrical shell, with the toroidal and poloidal currents replaced by axial and azimuthal currents.

If we take the equilibrium field to be vertical and perpendicular to the axis of the cylindrical blanket and shield, then when the equilibrium field changes, there will be, in the low conductivity limit, an axial current

$$J = -\sigma a \sin \theta \dot{B}_0, \tag{4.1}$$

when a is the radius of the cylindrical shell, and θ is the azimuthal angle. This current will produce a field in the plasma

$$B_{in} = -\frac{\mu_0}{2} h a \sigma \dot{B}_0, \tag{4.2}$$

where h is the thickness of the cylindrical shell.

4.2 Calculation of Unbroken Toroidal Shell and Modification of the Model.

For the blanket and shield design shown in Fig. 1 with a rise time of one second, the induced field at the plasma as calculated by Eq. (4.2) is more than three times the applied field. This non-physical result would not actually occur; the induced fields would induce additional currents which in turn would produce fields, limiting the net induced field to a value sufficient to cancel the applied field.

Although we have not correctly calculated the field, we can draw two conclusions about what will happen if the blanket and shield are unbroken.

- (1) The induced field is large (comparable to the applied field).
- (2) Fields induced by the induced field are significant.

Consequently, it appears that we must break up the iron into pieces small enough so that:

- (1) The induced field at the plasma is negligible.
- (2) Fields induced by the induced field are negligible.

If the cylinder is broken into segments of length $2l$ which is small compared with the diameter, the current density has components

$$J_\theta = \sigma y \cos \theta \dot{B}_0 \tag{4.3}$$

$$J_y = -\frac{\sigma}{2a} (l^2 - y^2) \sin \theta \dot{B}_0 \tag{4.4}$$

where y is measured axially from the center of the segment. The field on axis a distance y_0 along the axis is given by

$$B_{in} = \frac{\mu_0 \sigma h a}{8} \dot{B}_0 \left[\frac{y(a^2 + y_0^2 - l^2)}{a^2 \sqrt{a^2 + y^2}} - \ln(\sqrt{a^2 + y^2} + y) \right]_{y=-l-y_0}^{y=l-y_0} \tag{4.5}$$

4.3 Results for a Segmented Shell. For 16 segments and an applied field of 3 kG, the induced field at the plasma is calculated by Eq. (4.5) to be 566 G; for 32 segments, it is reduced to 144 G, or five percent of the applied field. Plasma physics considerations suggest that even this value is uncomfortably large; it seems safest to try to further reduce the eddy currents. To do so requires making the blanket and shield of blocks weighing a few tons each.

4.4 Results with the Brick Model. For calculating the effects of further subdivision, the design in Fig. 1 was divided into thirty segments toroidally; and each of those was divided into sixteen regions poloidally. In addition, the division into from four to six regions radially is maintained. Each segment is represented by 92 rectangular stainless steel bricks. The bricks closest to the plasma are 30 cm thick, the others are 10 cm thick. Widths vary from 112 cm to 153 cm, and lengths from 80 cm to 180 cm to correctly represent the volume of stainless steel.

A FORTRAN program, BRICK, was written to establish the vertices of the bricks in one segment, to translate and rotate the bricks to represent the other segments, and to calculate the induced field at a specified point by Eq. (2.8). The calculation shows that the maximum induced field in the center of the plasma is only 0.86% of the equilibrium field, of which the two nearest segments contribute 0.79%. The effect of repeated subdivision is shown in Table I. The induced field was judged to be sufficiently low with a subdivision of 16 cuts. The actual blanket and shield design suggested as a result of this calculation is shown in Fig. 2.

Table I. Effect of Segmenting and Subdividing the Blanket and Shield

Condition	Peak induced field on plasma axis as percent of applied field.	Calculated by
Unsegmented	325%*	Eq. (4.2)
16 segments	19%	Eq. (4.5)
32 segments	5%	Eq. (4.5)
30 segments, each with 16 cuts	0.9%	Eq. (2.8)

*Assumptions of calculation invalid in this case.

4.5 Forces and Torques. The torque on a horizontal block due to the 40 kG toroidal field can readily be found from Eq. (2.5):

$$N = \iiint J_x y B_T dV \tag{4.6}$$

$$= 16 \dot{B}_O \sigma B_T a^3 b^3 c / 9(a^2 + b^2) \tag{4.7}$$

where N is the torque and B_T the toroidal field. For one of the largest blocks, Eq. (4.7) yields a value of 36000 foot lb.

5. EXTENSIONS OF THE MODEL

5.1 Fifth-Power Equations for J. The model described in Sec. 2 can be extended in several ways. Most important, perhaps, is relaxing the condition that the field must vary across a brick according to Eq. (2.4), which was imposed so that the current density would obey the simple expression Eq. (2.5) and (2.6). If we allow fifth-power terms in the expressions for current, we get

$$J_x = \sigma \dot{B}_O y \left[a^2 - x^2 + \left\{ a^2 b^2 (a^2 - b^2) + (a^4 - a^2 b^2 + b^4) x^2 + 2 a^2 b^2 y^2 - 2 b^2 x^2 y^2 - a^2 x^4 \right\} / \left\{ a^4 + 5 a^2 b^2 + b^4 \right\} \right] / (a^2 + b^2) \tag{5.1}$$

$$J_y = -\sigma \dot{B}_O x \left[b^2 - y^2 + \left\{ a^2 b^2 (b^2 - a^2) + (a^4 - a^2 b^2 + b^4) y^2 + 2 a^2 b^2 x^2 - 2 a^2 x^2 y^2 - b^2 y^4 \right\} / \left\{ a^4 + 5 a^2 b^2 + b^4 \right\} \right] / (a^2 + b^2) \tag{5.2}$$

$$B_a = B_O \left[1 - \frac{a^2 x^4 + 6 x^2 y^2 (a^2 + b^2) + b^2 y^4}{(a^2 + b^2)(a^4 + 5 a^2 b^2 + b^4)} \right] \tag{5.3}$$

Equation (5.1) - (5.3) obey

$$J \cdot n = 0 \text{ on the conductor surface}$$

and $\nabla \times J = -\sigma \dot{B}_a$

Moreover Eq. (5.3) approximates $B_a = B_O$ over much more of the conductor volume than Eq. (2.4) does. When Eq. (5.1) and (5.2) are substituted into Eq. (2.1) and the integration carried out, an analytic expression for B_{in} results, involving the same functions as the simpler expression in Eq. (2.8). When calculations with that expression are compared with those described above, the limitations of assumption (4) can be understood.

5.2 Other Extensions. Three other useful extensions of the model would be:

- (1) Using the J_x , J_y , and B_a which approximate a linear variation of the magnetic field.
- (2) Incorporating all three components of J, B_a , and B_{in} .
- (3) Going beyond the low-conductivity limit by including B_{in} in

B_a , thus producing a set of linear equations to be solved for the eddy currents.

Extensions (1) and (2) in particular would be straightforward because the same kinds of expressions occur there as were determined for the equations of Sec. 2 and 5.1

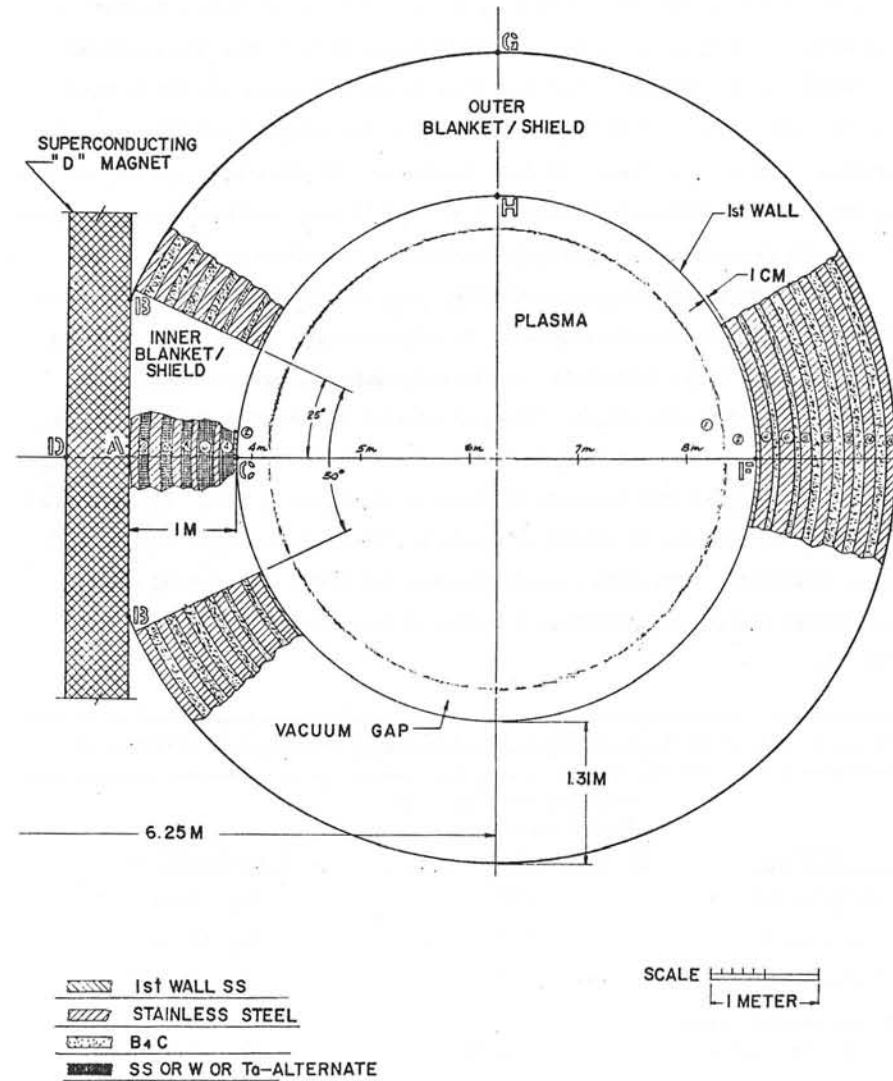


Fig. 1 Unbroken Blanket and Shield Design for the Argonne TEPR

Discussions following paper:

(Yeh) What is the duration for which the perturbing field due to eddy is comparable with VF, since eddy will dive away at flat top of pulses?

(Turner, Argonne) During the first 15 msec or so, while both the applied and induced field are less than 2 gauss.

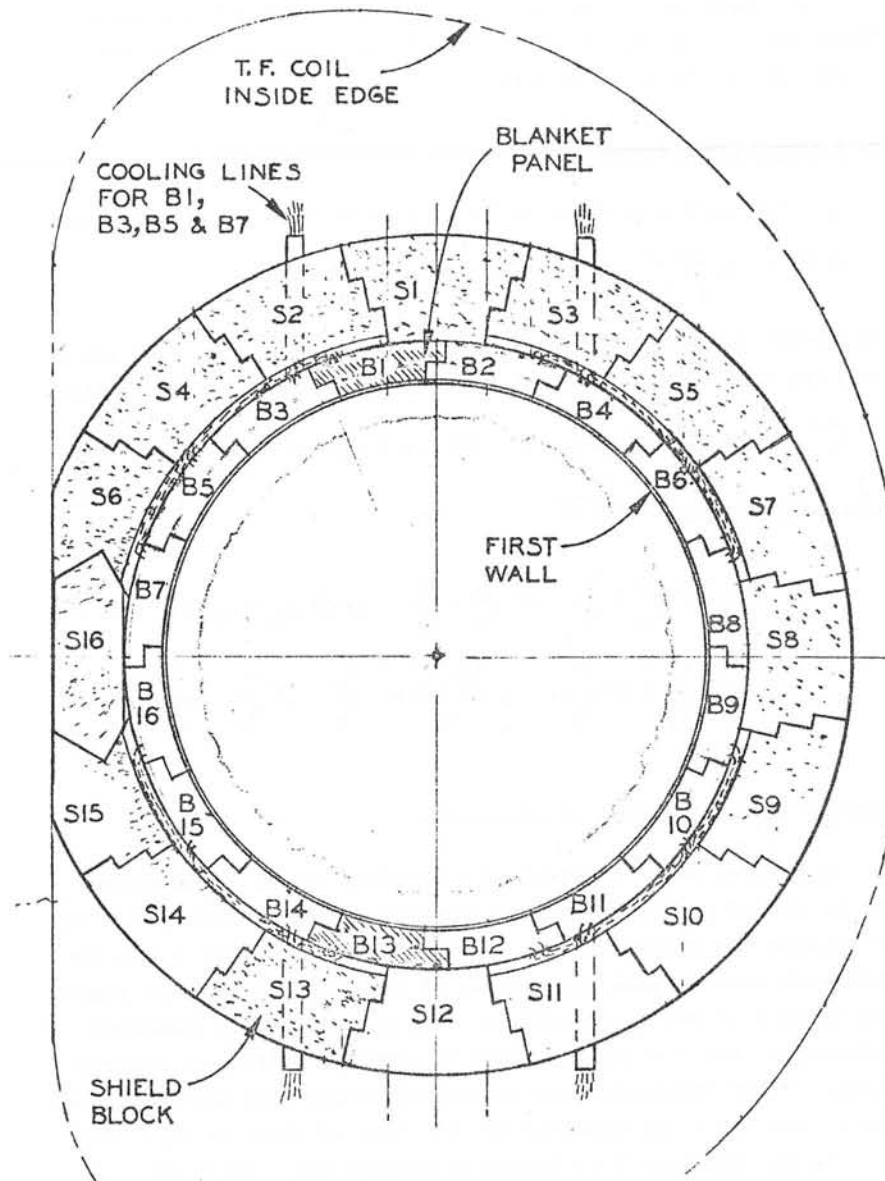


Fig. 2 Blanket and Shield Design for the Argonne TEPR, with 16 Cuts Poloidally to Reduce Eddy-Current Effects

Induction Motor Analysis and Field Calculation
using Anisotropic Layer Theory

S. Williamson

Introduction

'Layer theory' is a technique of analysis that has been developed over a number of years (see introduction and bibliography of ref.1). Its chief use is for the analysis of induction machines. The basic philosophy lies in replacing the regions of a real machine by a series of separate layers. These layers may be arranged concentrically or stacked one on top of the other, depending on the geometry of the machine under analysis. The physical properties of the layers are determined by the physical properties of the regions they represent, composite regions being modelled using an averaging process. The layers are assumed to be magnetically linear, so that the principle of superposition can be evoked to enable a solution to be obtained, harmonic by harmonic. Maxwell's field equations are solved for each layer separately, matching solutions at the boundaries. This is then repeated for all significant harmonics to allow the calculation of an input impedance matrix. The solution is now essentially complete, and the various fields, forces and torques can be readily obtained.

A recent paper¹ has extended layer theory to allow the effects of both electric and magnetic anisotropy to be taken into account. This extension has become necessary with the introduction of the new transverse flux linear induction motors²⁻⁴. In many of these machines the path which the flux takes is governed by the direction in which the back-iron is laminated. In addition, certain flux-paths may be actively discouraged by grouping the laminations into packets, with air-spaces between. Windings have been proposed which are apt for both longitudinal-flux and transverse-flux machines⁴.

The author is with the Department of Engineering, Marischal College, University of Aberdeen, Aberdeen AB9 1AS.

This paper deals with the application of the anisotropic layer-theory to the analysis of one of the new linear machines, with particular respect to the field in the airgap.

Anisotropic Layer Theory

It may readily be shown that if a harmonic solution of the form

$$e_x^{k,l} = \operatorname{Re} \left\{ \bar{E}_x^{k,l}(z) \exp(j(\omega t - ky - lx)) \right\} \quad (1)$$

is assumed for all the field quantities in a region, where the x and y axes lay in the plane of motion, then $\bar{E}_x^{k,l}$ can be expressed in the form

$$\bar{E}_x^{k,l}(z) = D_1 \cosh \epsilon_1 z + D_2 \sinh \epsilon_1 z + D_3 \cosh \epsilon_2 z + D_4 \sinh \epsilon_2 z \quad (2)$$

$$\text{where } \epsilon_1, \epsilon_2 = \alpha \pm \sqrt{\alpha^2 - \beta} \quad (3)$$

$$\alpha = \frac{1}{2} \left\{ \ell^2 \left(\frac{\sigma_x}{\sigma_z} + \frac{\mu_x}{\mu_z} \right) + k^2 \left(\frac{\sigma_y}{\sigma_z} + \frac{\mu_y}{\mu_z} \right) + j\omega(\sigma_y \mu_x + \sigma_x \mu_y) \right\} \quad (4)$$

$$\beta = \left(\ell^2 \frac{\mu_x}{\mu_z} + k^2 \frac{\mu_y}{\mu_z} + j\omega \frac{\sigma_z \mu_x \mu_y}{\mu_z} \right) \left(\ell^2 \frac{\sigma_x}{\sigma_z} + k^2 \frac{\sigma_y}{\sigma_z} + j\omega \frac{\mu_z \sigma_x \sigma_y}{\sigma_z} \right) \quad (5)$$

and $D_1 - D_4$ are constants of integration.

A total of twelve constants of integration result. This number may be reduced to four by applying Maxwell's equations, and then to two by assuming the regions are electrically isolated. Finally a transfer matrix can be calculated, relating field quantities at the upper boundary to those at the lower boundary. This enables surface impedances 'looking up' and 'looking down' from the excitation layer to be determined. If the excitation layer is assumed to have zero thickness, then the winding input impedances may be calculated as shown in ref.1, but if a finite thickness of excitation is incorporated, then thick-excitation formulae should be used⁶. This produces a surface input impedance given by

$$\bar{Z}_{IN}^{k,l} = \frac{-1}{\eta \epsilon^2} \left[\frac{\eta(Z_U + Z_D)(\epsilon S - \tanh \epsilon S) + \tanh \epsilon S(2 \tanh(\frac{\epsilon S}{2}) - \epsilon S \eta^2(Z_U Z_D + 1))}{\eta(Z_U + Z_D) - (\eta^2 Z_U Z_D + 1) \tanh \epsilon S} \right] \quad (6)$$

where $\eta = \frac{jk^2}{\omega \epsilon \mu_z}$ $S =$ thickness of excitation layer
 $\epsilon =$ solution of equation 3
 $Z_U =$ surface impedance looking up from the excitation
 $Z_D =$ surface impedance looking down from the excitation

For a voltage-forced solution the windings are firstly resolved into a complex double Fourier series. If the x-directed conductor distribution of winding 1 is given by

$$n_{x1} = \sum_{l=-\infty}^{+\infty} \sum_{k=-\infty}^{+\infty} N_{x1}^{k,l} e^{-j(ky+l_x)} \quad (7)$$

then the coupling impedance between this winding and a second can be shown to be given by the expression

$$\bar{Z}_{12} = 4\tau_x \tau_y \sum_k \sum_l \frac{1}{k} \frac{1}{l} N_{x2}^{k,l} N_{x1}^{*k,l} \bar{Z}_{IN}^{k,l} + N_{x1}^{k,l} N_{x2}^{*k,l} \bar{Z}_{IN}^{-k,l} \quad (8)$$

Calculation of the coupling impedances enables the winding currents, and hence the excitation layer current density harmonics, to be calculated. This then enables the fields at the excitation layer boundaries to be determined, and these in turn allow the fields in any region to be calculated, via the transfer matrices.

Of particular interest is the field at the surface of the rotor plate, since this can conveniently be measured for verification purposes, and can also be used in conjunction with the Maxwell stress technique to calculate the forces on the rotor assembly. In terms of the field quantities normally calculated using the transfer matrices (i.e. B_z and H_y) the lift, propulsion and transverse forces may be shown to be given respectively by the expressions

$$F_z = \frac{2\tau_x \tau_y}{\mu_0} \operatorname{Re} \left\{ \sum_{l=1}^{+\infty} \sum_{k=-\infty}^{+\infty} \left\{ |H_y^{k,l}|^2 - |B_z^{k,l}|^2 \right\} \right\} N \quad (9)$$

$$F_y = -4\tau_x \tau_y \operatorname{Re} \left\{ \sum_{l=1}^{+\infty} \sum_{k=-\infty}^{+\infty} H_y^{k,l} B_z^{*k,l} \right\} N \quad (10)$$

$$F_x = -8\tau_y \operatorname{Im} \left\{ \sum_k \frac{1}{k} \sum_{l_1}^{+\infty} \sum_{l_2}^{+\infty} H_y^{k,l_1} B_z^{*k,l_2} \left\{ \frac{l_1 l_2}{l_1^2 - l_2^2} \right\} (1 - (-1)^{l_1 + l_2}) \tau_x / \pi \right\} N \quad (11)$$

The 'infinite' summations are, of course, intended to imply that as many terms as necessary should be considered. This is best determined in an empirical basis and is discussed in a later section.

It is interesting to note that the transverse forces arise out of an interaction between odd and even harmonics. This arises because of the nature of the transverse modelling. For a given harmonic pair, B_y and B_z are constrained to vary sinusoidally with x , whilst B_x varies cosinusoidally. The transverse (i.e. x-directed) force is therefore calculated by integrating products of the form $\sin l_1 x \cos l_2 x$ over one transverse pole-pitch. Such integrals are zero unless one of the pole numbers is odd and the other even.

The 'Herringbone' Motor^{4,5} and its Mathematical Model

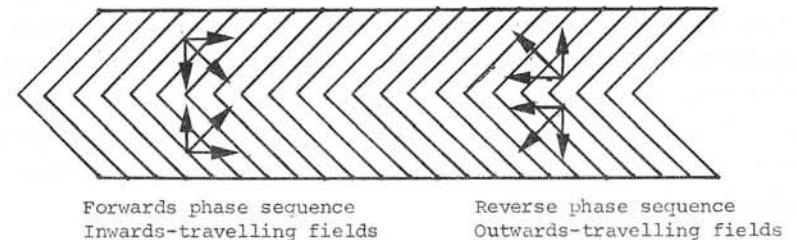


Fig.1 Plan view of Herringbone motor stator, showing doubly-skewed slots and field velocity vectors.

The 'Herringbone' motor was originally designed to enable the self-stabilising properties of doubly-skewed stator slots to be examined. A plan view of the stator is shown in fig.1. When the phase sequence is in the 'forwards' sense the transverse components of the field-velocity vectors produce an 'inwards'-travelling field, as shown. When the phase sequence is reversed an 'outwards'-travelling field is produced. The machine is laminated in the conventional sense, i.e. it is an axial-flux machine. The stator is fitted with a four-pole Gramme-ring winding in sixty slots. The rotor consists of a single sheet of aluminium, backed by a single block of laminated iron. The plane of lamination for the rotor back-iron is the same as that of the stator as indicated in fig.2.

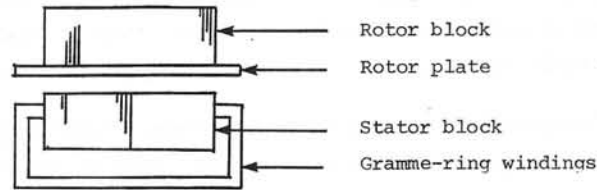


Fig.2 End-view of Herringbone motor

To model the herringbone motor, it was assumed to be one of an infinite two-dimensional array in keeping with the normal layer-theory practice. Longitudinally the machines are arranged in a nose-to-tail fashion at an appropriate separation as shown in fig.3. This allows the windings to be Fourier-analysed in the longitudinal direction, with a period equal to the spacing of the stators. In practice a mark to space ratio of 1:1 was used, since at standstill the flux fringing beyond the stator ends is negligible. In the transverse direction the machines are arranged as shown in fig.4.

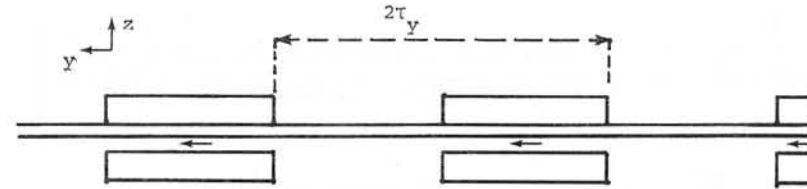


Fig.3 Longitudinal arrangement of stators for Fourier analysis of windings.

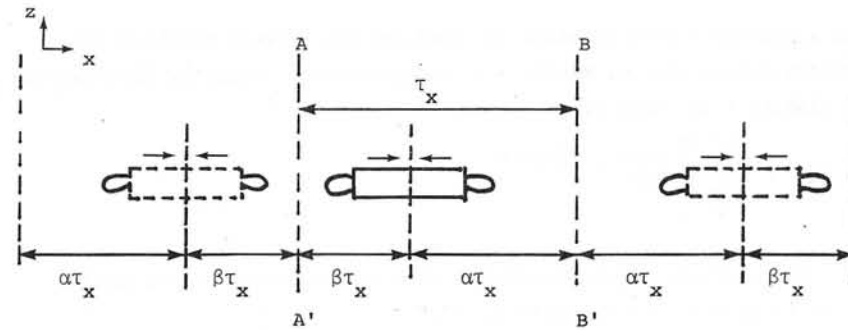


Fig.4 Transverse arrangement of slots for Fourier analysis of windings

Adjacent machines are connected in opposite senses so that the plate current does not cross the lines of symmetry given by AA' and BB' in fig.4. By varying the ratio of $\alpha:\beta$ the effect of off-setting the rotor plate can be simulated. It will, however, be appreciated that this model is only valid when plate widths equivalent to or greater than the stator width are used.

The two-dimensional array is subsequently replaced by a multi-layer model. For the herringbone motor a total of eleven regions was used. These are indicated on fig.5.

Of the eleven regions only two (Nos. 2 and 10) are fully anisotropic. This arises because the stator slot and tooth regions must be assumed non-conducting, and when this is the case $\epsilon_1 = \epsilon_2$ (see equa-

tion 2). The same result is obtained for the (isotropic) air and rotor conductor regions.

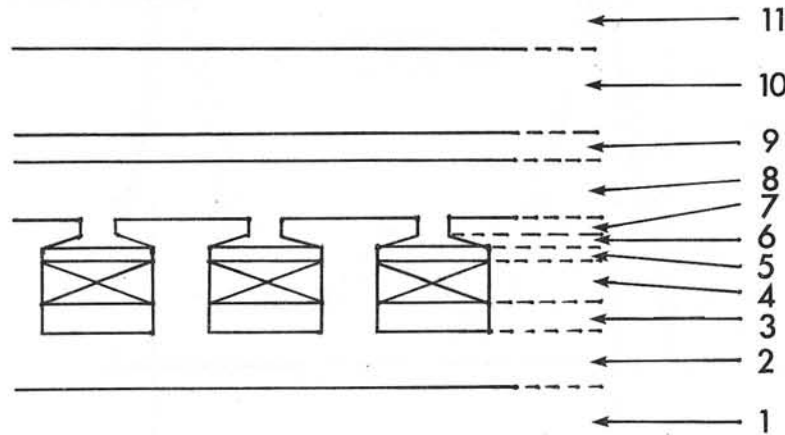


Fig.5 Regional representation of Herringbone motor.

- | | |
|-----------------------------|---------------------|
| 1. Air | 7. Stator tooth tip |
| 2. Stator back-iron | 8. Airgap |
| 3. Stator slot bottom wedge | 9. Rotor plate |
| 4. Stator excitation | 10. Rotor back-iron |
| 5. Stator slot top wedge | 11. Air |
| 6. Stator tooth neck | |

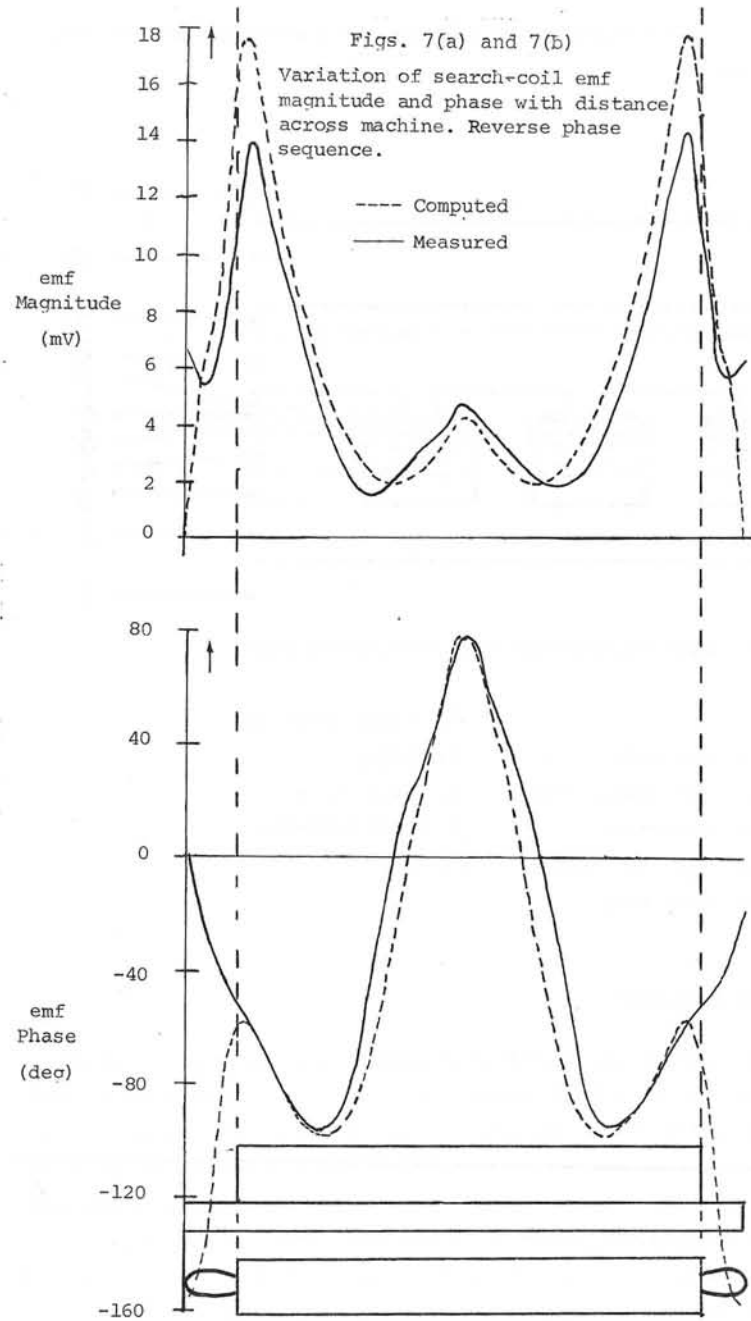
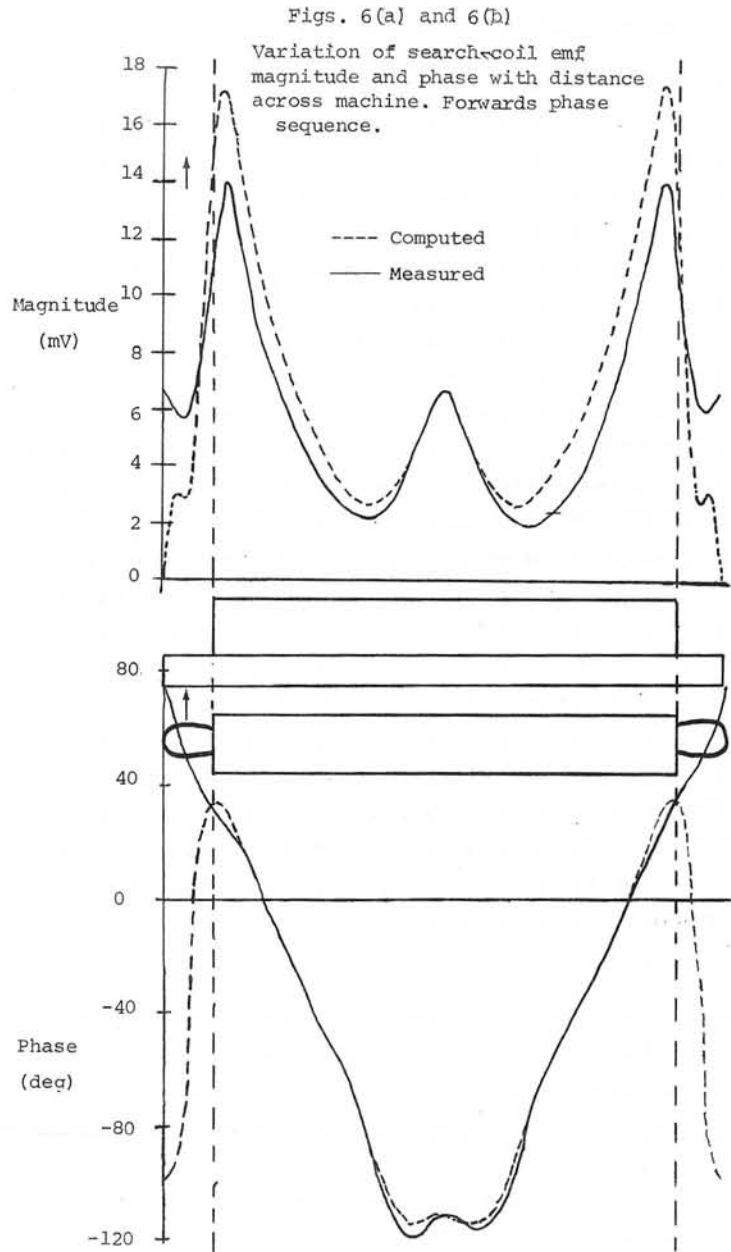
Experimental Procedure

The herringbone was tested at standstill with an aluminium plate rotor 25 cm wide and 3.25 mm thick. This represents an overhang of some 2.4 cm either side of the stator, the plate being in the central position. The clearance airgap was set to 6.15 mm and the machine excited in firstly the forwards and then the reverse sense. For each case a search-coil was used to measure the variation in the flux normal to the rotor plate surface with position across the width of the machine. The rotor surface temperature was held at a steady 60°C ($\pm 4^\circ\text{C}$) throughout both tests.

Comparison of Experimental Results with Theory

As pointed out above the herringbone motor was fitted with Gramme-ring windings. These are excessively leaky and, in fact, the machine impedance is dominated by leakage reactance. This leakage accentuates the unbalance inherent in any normally-wound linear motor, and has to be accurately calculated if a voltage-forced solution is required. In order to overcome this difficulty a current-forced solution was obtained. The unbalanced currents used in the experiments were fed into the program as input data, and as output the program predicted the magnitude and phase of the search-coil voltages. Figure 6(a) and 6(b) show the computed and measured search-coil emf magnitudes and phases for the 'forwards' phase sequence, and figures 7(a) and 7(b) do the same for the 'reverse' phase sequence. It will be seen from these figures that the agreement between theory and practice is reasonable. The greatest discrepancy occurs in the plate overhang regions, where the predicted direction of travel (i.e. the slope of the phase variation) is the opposite to that measured. There are two probable causes of this. Firstly, the layer theory model ignores the lateral discontinuities in the iron blocks. In other words the back-iron is assumed to be as wide as the rotor plate. Secondly, the Gramme-ring windings are modelled as if they are conventional (i.e. drum-type) windings. This means that the winding overhang in the model must carry longitudinal currents, whereas in the real machine the stator currents return at the back of the stator iron. The first of these probable causes is inherent to layer-theory in general. The second is a feature of the test machine only.

This phase discrepancy occurs over a narrow width of the machine. It will be seen that over the majority of the plate surface the agreement is very good. In addition, it will be seen that the direction of field travel across the rotor plate surface is, indeed, determined by the angled field. The results shown required a total of 40 transversely-directed and 60 longitudinally-directed harmonics, and represented a medium-sized job, requiring 2½ mins on the Aberdeen University ICL 4/70 machine.



Conclusion

The anisotropic layer theory has been shown to be capable of predicting the airgap field in the herringbone motor to a reasonable accuracy. Further work must now be done to test its value in predicting the performance of a wide variety of machines, in particular those with unusual geometries.

References

1. WILLIAMSON, S.: 'The Anisotropic Layer Theory of Induction Machines and Induction Devices', J. Inst. Maths. Applics., 1976, 17, (1), pp.69-84.
2. LAITHWAITE, E.R., EASTHAM, J.F., BOLTON, H.R. and FELLOWS, T.G.: 'Linear Motors with Transverse Flux', Proc.IEE, 1971, 118, (12), pp.1761-67.
3. EASTHAM, J.F. and ALWASH, J.H.: 'Transverse Flux Tubular Motors', *ibid.*, 1972, 119, (12), pp.1709-18.
4. EASTHAM, J.F. and LAITHWAITE, E.R.: 'Linear-Motor Topology', *ibid.*, 1973, 120, (3), pp.337-343.
5. EASTHAM, J.F. and WILLIAMSON, S.: 'Experiments on the Lateral Stabilisation and Levitation of Linear Induction Motors', Trans.IEEE, 1974, MAG-10, (3), pp.470-473.
6. BALCHIN, M.J. and EASTHAM, J.F.: 'Performance of Linear Induction Motors with Airgap Windings', Proc.IEE, 1975, 122, (12), pp.1382-1290.

Discussions following paper:

(Wyatt, Imp College) First, I congratulate Dr Williamson on a fine piece of work. In the model used, a series of stators is assumed in the transverse direction and I would ask him what the inter-stator distance corresponding to the results shown is. It seems that the accuracy of the method presented must suffer as the plate width approaches the stator width and I would appreciate Dr Williamson's comments on this point.

(Williamson) I would like to thank Mr Wyatt for his kind remarks. The transverse modelling requires the 'inter-stator' distance to be equal to the width of the rotor plate when the plate is central. This constraint is imposed so that there is no current flow between adjacent machines. When the rotor plate is offset the 'inter-stator' distance is varied as shown in fig 4 of my paper, where T_x is the plate width. I should also point out that the discontinuous stator iron is replaced by a continuous slab in the model, and it is this approximation which I believe, produces the phase error at the plate edges. Regarding Mr Wyatt's last point, I would like to comment that because of the inability to model the transverse discontinuity in the iron, I would expect the accuracy of the model to increase rather than decrease as the plate width approaches the stator width.

(Freeman) My congratulations to Dr Williamson for producing an analysis for an anisotropic model. I should like to ask two questions. Firstly is the material in each region continuous or discontinuous? Second, what is the effect of the transverse flux on the iron losses in the machine?

(Williamson) I should like to thank Dr Freeman for his congratulations. The material in each region is continuous in the plane of motion. The results presented in the paper represent a preliminary investigation, in which only the normal component of airgap flux was both measured and calculated. It is hoped that the anisotropic modelling will be able to predict eddy current loss in the backing-iron with a reasonable accuracy, but hysteresis loss is outside the scope of the analysis. No calculation of eddy-current loss in the laminated iron has yet been made,

but I would like to thank Dr Freeman for pointing out a useful means of comparing isotropic and anisotropic working.

CALCULATION OF TRANSIENT SKIN-EFFECT IN CONDUCTORS EMBEDDED IN SLOTS

S.P. Verma, Member IEEE S.E. Abo-Shady, Student Member IEEE

Power Systems Research Group
 Department of Electrical Engineering
 University of Saskatchewan
 Saskatoon, Canada

ABSTRACT

Skin-effect has a marked influence on the steady-state performance of electrical machines. In order to study the phenomenon of skin-effect during transients, the general partial differential equation of the vector potential is developed on the basis of two-dimensional analysis. Numerical techniques for solving the field equations obtained from two- and single-dimensional analyses are presented. With the consideration of single-dimensional analysis, a transient analytical solution is derived for the case of a sinusoidal total current applied to a rectangular bar embedded in a slot. The two specific cases of a step total current and a sinusoidal total current applied to a rectangular bar are considered for investigating the skin-effect during transients. The excellent agreement between numerical and analytical results verifies the numerical techniques developed in the paper. The results show the importance of the phenomenon of skin-effect and the need for its incorporation in the transient analysis of electrical machines.

INTRODUCTION

It is well known that the phenomenon of skin-effect has a marked influence on the steady-state performance of electrical machines. The investigations related to this phenomenon for the steady-state conditions are well established in the published literature. It is interesting to note that the behaviour of the phenomenon of skin-effect during transients is quite different from that during the steady-state conditions. This is revealed by the studies conducted on an isolated bar by Tuohy et al.¹ and on a bar embedded in a slot by Mocanu² and Probst³.

In several applications of induction, synchronous and induction-synchronous machines, accurate information about their transient performance with special reference to starting, synchronizing, switching-over and load-changes is required. This

necessitates the incorporation of the transient skin-effect in the analysis of the machine under consideration. Important as it is, unfortunately the transient analysis of electrical machines in itself is very complex. In order to study the transient behaviour which takes into account the skin-effect successfully, one requires, firstly, a suitable method of analysis⁴ which simulates the machine in a manner suitable for incorporating the skin-effect during transients and, secondly, an appropriate technique to determine the variation of skin-effect with respect to time. This paper is devoted to the investigations of the transient skin-effect in cage windings.

Eddy currents are produced in conductors carrying alternating currents by the virtue of the changing magnetic field. These currents result in a non-uniform distribution of the current density. In the case of a conductor carrying a steady-state alternating current, as well known, the current tends to flow in the outer layers of the conductor. This causes an increase in the effective resistance of the conductor and a decrease in its effective inductance. In general, at any instant of time the amount of skin-effect due to a time-varying current depends on the rate of change of the current at that instant and on the conditions prior to it. It is, therefore, to be expected that the current distribution in a conductor during transients is quite different from the steady-state distribution.

It is worthwhile to mention that although the approaches based on single-dimensional analyses can be successfully applied to the cases of deep bars, such approaches are not suitable for treating end-ring segments or bars having a small height to width ratio. Further, the representation of bars by series and parallel combinations of resistances and inductances requires the development of a suitable technique to solve such a network which in itself is a problem.

In view of the above, it is the main object of this paper to present the general form of the partial differential equation of the vector potential on the basis of two-dimensional analysis and to develop a numerical technique by formulating the difference equations in a form which is suitable for the computation

of transients in electrical machines. This technique can be applied to bars and end-ring segments provided that the boundary conditions are completely defined. Since in the case of deep bars the use of single-dimensional analysis is quite satisfactory and it requires much less computation time, a numerical technique is also presented for the determination of instantaneous distribution of the magnetic field intensity, the current density and the instantaneous voltage drop of a deep bar embedded in a slot. In order to verify the results delivered by the two-dimensional analysis and to determine the degree of its accuracy, the case of a sinusoidal total current applied to a deep bar embedded in a slot is treated and an analytical transient solution is obtained on the basis of single-dimensional analysis. Expressions for the magnetic field intensity, the current density and the voltage drop are presented.

The numerical techniques are applied to study the transient skin-effect of a deep bar embedded in a slot by considering the following two specific cases:

- (i) a step total current,
- (ii) a sinusoidal total current.

A comparison is then drawn between the numerical results of the two- and single-dimensional analyses. In addition, the analytical results of the single-dimensional analyses are used for further verification.

DEVELOPMENT OF TWO-DIMENSIONAL ANALYSIS

In general, the variation of currents as a function of time in the various bars and end-ring segments of an electrical machine is not known during transients. These currents can, however, be calculated at each instant of time through the numerical solution of the non-linear differential equations of the machine. It is practically impossible to obtain an analytical solution for the purpose of investigating the transient skin-effect in electrical machines. This calls for the development of numerical techniques for studying the skin-effect during transients. The analysis is commenced by formulating the field equations in a manner most suitable for the transient investigations.

General Partial Differential Equation of Vector Potential

Considering two-dimensional variation of the electromagnetic field, the following equations are obtained from the general form of Maxwell's equations:

$$\frac{\partial H_y}{\partial x} - \frac{\partial H_x}{\partial y} = \sigma, \quad (1)$$

$$\frac{\partial \sigma}{\partial y} = -\frac{\mu}{\rho} \cdot \frac{\partial H_x}{\partial t}, \quad (2)$$

$$\text{and} \quad \frac{\partial \sigma}{\partial x} = \frac{\mu}{\rho} \cdot \frac{\partial H_y}{\partial t}. \quad (3)$$

In order to simplify the calculations of the field, one makes use of vector potential A , which is so defined that its line integral around any closed path is equal to the total flux enclosed by the path¹⁶. As the area of a surface bounded by the path approaches zero, the limiting value of the line integral per unit area, (i.e. curl A), is equal to the flux density B . Hence,

$$\text{curl } A = B = \mu H, \quad (4)$$

where the direction of A is in a plane perpendicular to the direction of B .

With the help of equations (1) to (4), the general partial differential equation of the vector potential A is developed as:

$$\frac{\partial^2 A}{\partial x^2} + \frac{\partial^2 A}{\partial y^2} = \frac{\mu}{\rho} \cdot \frac{\partial A}{\partial t} + f(t) = -\mu \sigma, \quad (5)$$

where $f(t)$ is a function dependent on time and independent of the co-ordinates x and y . The physical meaning of this function will be interpreted later.

The vector potential equation for some particular cases which are of considerable importance in practice can be derived from the general form given by equation (5).

Physical Interpretation of $f(t)$

As mentioned earlier, $f(t)$ is dependent on time and independent of the co-ordinates x and y . It is a well-known

fact that at any instant of time the voltage drop between two points located at the two ends of a current-carrying conductor is the same irrespective of the location of these two points. As the voltage drop is the only physical quantity which possesses such a property for any mode of operation (e.g., transient or steady-state), there must be a relationship which correlates $f(t)$ with the voltage drop of the current-carrying conductor. This interpretation is confirmed through the mathematical proof given in the following.

Consider a conductor of an arbitrary cross-section and having a unit length, as shown in Fig. 1, which is located in a magnetic field described by the vector potential A . Such a magnetic field may be produced due to a current in the conductor itself and/or due to currents in other conductors. If the vector potential is defined at a point within the conductor, the flux linking with an infinitesimal filament δS situated at that point will be $(A-A_0)$ due to the magnetic field bounded by a flux line whose vector potential is A_0 . Further, the voltage drop per unit length of this filament caused by its resistance is " $\rho\sigma$ ". Hence, the total drop of the filament under consideration due to the resistance and the magnetic field is given by:

$$v = \rho\sigma + \frac{\partial(A-A_0)}{\partial t}, \quad (6)$$

which is actually the voltage drop across the conductor as a whole.

Since the line $A = A_0$ is a flux line, the value of A_0 is independent of x and y but may be a function of time depending on the mode of operation. Accordingly, equation (5) may be rewritten as:

$$\frac{\partial^2(A-A_0)}{\partial x^2} + \frac{\partial^2(A-A_0)}{\partial y^2} = \frac{\mu}{\rho} \frac{\partial(A-A_0)}{\partial t} + f(t) + \frac{\mu}{\rho} \frac{\partial A_0}{\partial t} = -\mu\sigma. \quad (7)$$

From equations (6) and (7), the following relationship is obtained:

$$[f(t) + \frac{\mu}{\rho} \frac{\partial A_0}{\partial t}] = -\frac{v\mu}{\rho}. \quad (8)$$

The above equation represents the general relationship between $f(t)$ and the voltage drop v . The two terms,

$(f(t))$ and $(\frac{\mu}{\rho} \frac{\partial A_0}{\partial t})$, of equation (8) can be combined to form another function directly proportional to the voltage drop across the conductor under consideration. Further, it is much more convenient, if not the only appropriate way, to deal with the quantity $(A-A_0)$ as a vector potential variable. By doing so, the partial differential equation of the vector potential assumes the following form:

$$\frac{\partial^2 A}{\partial x^2} + \frac{\partial^2 A}{\partial y^2} = \frac{\mu}{\rho} \cdot \frac{\partial A}{\partial t} - \frac{v\mu}{\rho} = -\mu\sigma. \quad (9)$$

Finite Difference Representation

As stated earlier, a numerical technique is required for obtaining the solution of field equations during transients. The finite difference method is adopted for developing the numerical technique.

In order to replace the partial differential equation of the vector potential by a set of finite difference algebraic equations which inter-relate the values of the vector potential at discrete points, any spatial distribution of these points may be chosen. However, it is preferable to make the points lie on the "nodes" of a regular mesh which may consist of squares as is the case presented here. Fig. 2 shows a simple rectangular field region. At a certain time t_n , any node within the boundary is positioned with respect to the neighbouring nodes (including those on the boundary) as shown in Fig. 3 and Fig. 4. As the symmetrical star shown in Fig. 3 is merely a special case of the asymmetrical star, Fig. 4, the difference equation of the latter is presented.

To derive the difference equation of a node (e.g., "i, j, n"), the vector potential function is expanded at the node by using Taylor's series. Expressions for:

$$\left(\frac{\partial^2 A}{\partial x^2}\right)_{i,j,n}, \quad \left(\frac{\partial^2 A}{\partial y^2}\right)_{i,j,n} \quad \text{and} \quad \left(\frac{\partial A}{\partial t}\right)_{i,j,n}$$

are then obtained in terms of the values of the vector potential at this and the neighbouring nodes. The results thus obtained are substituted in equation (9), which gives the following general difference equation:

$$\frac{2(k_1 A_{i-1,j,n} + k_3 A_{i+1,j,n})}{k_1 k_3 (k_1 + k_3)} + \frac{2(k_2 A_{i,j-1,n} + k_4 A_{i,j+1,n})}{k_2 k_4 (k_2 + k_4)} - \left\{ \frac{\lambda \mu}{\rho} + 2 \left(\frac{1}{k_1 k_3} + \frac{1}{k_2 k_4} \right) \right\} A_{i,j,n} + (\Delta x)^2 \left(\frac{\nu \mu}{\rho} \right)_n = - \frac{\lambda \mu}{\rho} A_{i,j,n-1}, \quad (10)$$

where $\lambda = (\Delta x)^2 / \Delta t$

and $(A_{i,j,n-1})$ is the vector potential of the node (i,j,n) at the time interval preceding the one under consideration.

For nodes outside the current-carrying regions, equation (10) becomes:

$$\frac{2(k_1 A_{i-1,j,n} + k_3 A_{i+1,j,n})}{k_1 k_3 (k_1 + k_3)} + \frac{2(k_2 A_{i,j-1,n} + k_4 A_{i,j+1,n})}{k_2 k_4 (k_2 + k_4)} - 2 \left(\frac{1}{k_1 k_3} + \frac{1}{k_2 k_4} \right) A_{i,j,n} = 0. \quad (11)$$

At all boundary points, which may be situated on an iron-air interface or on a magnetic flux line or on an interface between a current-carrying region and a non-current-carrying region, the corresponding difference equation can be suitably developed¹⁶ by modifying equations (10) and (11). Corresponding to the number of nodes "m", a set of m equations similar to equations (10) and (11) can then be formulated. To obtain a complete solution of the vector potential at a given specific instant, one more equation is required for the variable $(\frac{\nu \mu}{\rho})_n$. This particular equation is obtained by equating the line-integral of the magnetic field intensity around a current-carrying conductor to the instantaneous value of the current in the conductor. This integral depends on the vector potential of various nodes. It should be mentioned that in the presence of more than one current-carrying conductor, say v conductors, a corresponding equation has to be obtained for each conductor due to the fact that each conductor has its own value for $(\frac{\nu \mu}{\rho})_n$. The problem is, therefore, converted to a set of simultaneous algebraic equations having the form:

$$[G] [P]_n = [C]_n, \quad (12)$$

where

$[G]$ is a square matrix of order $(m + v)$,
 $[P]_n$ is a column of m vector potentials at the various nodes in addition to v variables of $(\frac{\nu \mu}{\rho})_n$ and
 $[C]_n$ is a column of order $(m + v)$.

It is evident that the matrix $[G]$ is independent of time. As the solution of the algebraic equations during transients is required at each instant of time, from computation time considerations it is not advisable to solve these equations by employing iterative methods. Instead, the inverse of $[G]$ should be determined and stored in the computer. By calling $[G]^{-1}$ from the storage, the vector potential at the various nodes and the variable $(\frac{\nu \mu}{\rho})_n$ can then be evaluated at a specific instant from the following simple algebraic equation:

$$[P]_n = [G]^{-1} [C]_n. \quad (13)$$

Knowing the vector potential at every node of the region under consideration, any other variables (e.g., current density, magnetic field intensity, flux density) can be easily determined at these nodes with the help of simple algebraic equations.

SINGLE-DIMENSIONAL ANALYSIS

In studying the skin-effect of deep bars in electrical machines, the problem can be simplified to a single-dimensional one without committing great errors. This is achieved by assuming the flux lines in the slots to be parallel to the periphery of the rotor. With this assumption, the partial differential equation of the magnetic field intensity in a rectangular bar as shown in Fig. 5 assumes the following form:

$$\frac{\partial^2 H_x}{\partial y^2} = \frac{\mu}{\rho \alpha} \frac{\partial H_x}{\partial t}, \quad (14)$$

where $\alpha = \frac{b}{a}$.

It should be pointed out that the boundary conditions of the magnetic field intensity are much easier to define than those of the current density. It is, therefore, preferable to deal with the magnetic field intensity H_x instead of the current

density σ . Equation (14) is a parabolic differential equation. In order to solve such an equation, both an initial condition and subsequent time-dependent boundary conditions are required. In the case of a rectangular bar, Fig. 5, the boundary conditions are:

$$H_x = 0 \quad \text{at} \quad y = 0 \quad (15)$$

and
$$H_x = \frac{i}{b} \quad \text{at} \quad y = h \quad (16)$$

where i is the total current carried by the bar. Having recognized the initial and the boundary conditions, equation (14) can be solved either numerically or analytically.

Analytical Solution

A transient analytical solution can be obtained for equation (14) only if the total current is defined by an explicit function with respect to time. Although this condition is not satisfied in electrical machines during transients, the analytical solution of the case of a sinusoidal total current applied to a rectangular bar embedded in a slot is derived, firstly, to use the solution for confirming the validity of the numerical techniques presented in this paper and, secondly, because such a solution is not available in the published literature.

Equation (14) can be rewritten as:

$$\frac{\partial^2 H_x}{\partial y^2} = \frac{1}{k^2} \frac{\partial H_x}{\partial t}, \quad (17)$$

where $k^2 = \frac{\alpha \rho}{\mu}$.

Considering the boundary conditions given by equations (15) and (16), the solution for a sinusoidal applied total current is obtained as:

$$H_x(t) = \frac{i}{b} \left[\sum_{\eta=1}^{\infty} \left\{ \frac{2\eta\pi k^2 \omega (-1)^{\eta+1}}{h^2 (\omega^2 + (\eta\pi k/h)^4)} e^{-(\eta\pi k/h)^2 t} \cdot \sin(\eta\pi y/h) \right\} + \sqrt{\frac{(\sinh(y/AA) \cdot \cos(y/AA))^2 + (\cosh(y/AA) \cdot \sin(y/AA))^2}{(\sinh(h/AA) \cdot \cos(h/AA))^2 + (\cosh(h/AA) \cdot \sin(h/AA))^2}} \cdot \sin(\omega t + \alpha_1) \right], \quad (18)$$

where $AA = k \sqrt{2/\omega}$

and
$$\alpha_1 = \tan^{-1}(\cotanh(y/AA) \cdot \tan(y/AA)) - \tan^{-1}(\cotanh(h/AA) \cdot \tan(h/AA)).$$

Differentiating equation (18) partially with respect to y and multiplying the results thus obtained by $(-a)$, the transient distribution of the current density is obtained as:

$$\sigma(t) = \frac{i}{a} \left[\sum_{\eta=1}^{\infty} \left\{ \frac{2\eta^2 \pi^2 k^2 \omega (-1)^{\eta+1}}{h^3 (\omega^2 + (\eta\pi k/h)^4)} e^{-(\eta\pi k/h)^2 t} \cdot \cos(\eta\pi y/h) \right\} + \sqrt{\frac{(\cosh(y/AA) \cdot \cos(y/AA))^2 + (\sinh(y/AA) \cdot \sin(y/AA))^2}{(\sinh(h/AA) \cdot \cos(h/AA))^2 + (\cosh(h/AA) \cdot \sin(h/AA))^2}} \cdot \frac{\sqrt{2}}{AA} \sin(\omega t + \alpha_2) \right], \quad (19)$$

where
$$\alpha_2 = \pi/4 + \tan^{-1}(\tanh(y/AA) \cdot \tan(y/AA)) - \tan^{-1}(\cotanh(h/AA) \cdot \tan(h/AA)).$$

The voltage drop per unit length can be obtained by replacing the variable y by h in equation (19) and multiplying the results thus obtained by ρ .

COMPUTED RESULTS

The various results presented here were calculated for a rectangular bar embedded in a slot by considering the two specific cases of a step applied total current and a sinusoidal applied total current. In the latter case, the frequency is assumed to be 50 Hz.

The dimensions of the bar under consideration are:

$$a = b = 10 \text{ mm}, \quad h = 50 \text{ mm},$$

and the length of the bar is assumed to be unity, i.e. 1 meter.

For the generalization of the results, the different variables are normalized as follows:

$$t_{p.u.} = \frac{t\rho}{\mu h^2}, \quad H_{p.u.} = \frac{Hb}{i},$$

$$\sigma_{p.u.} = \frac{\sigma ah}{i} \quad \text{and} \quad v_{p.u.} = \frac{vah}{\rho i}.$$

A computer programme was developed for the numerical calculation of the instantaneous voltage drop across the bar on the basis of the two-dimensional analysis. Also, a computer programme was developed by considering the single-dimensional analysis for the analytical and numerical determination of the instantaneous voltage drop across the bar and the instantaneous distribution of the magnetic field intensity & the current density along the height of the bar.

Case 1 - Step Applied Total Current

Fig. 6 shows the variation of the instantaneous normalized voltage drop versus the normalized time for a step applied total current. It is interesting to note that the voltage drop reaches a value of more than 15 times the steady-state value. Although the application of a step total current is not actually encountered in electrical machines, nevertheless this important result shows the significance of the transient skin-effect.

Case 2 - Sinusoidal Applied Total Current

The variation of the instantaneous normalized voltage drop versus the normalized time is shown in Fig. 7 for a sinusoidal applied total current. It may be observed that the variation of the voltage drop during the first cycle is quite different from the steady-state variation.

The distribution of the normalized magnetic field intensity along the height of the bar at different values of $t_{p.u.}$ was obtained by using the single dimensional analysis and it is shown in Fig. 8(a) and Fig. 8(b). The results shown are for the first cycle of the applied current. It is observed that initially the magnetic field is concentrated in the upper layers of the bar and as time lapses, the field spreads down to the lower layers.

The variation of the normalized current density along the height of the bar is shown in Fig. 9(a) and Fig. 9(b) at different values of $t_{p.u.}$. As in the case of the magnetic field intensity, initially the current is concentrated in the upper layers of the bars and then it spreads downwards as time increases.

It should be pointed out that the difference between the numerical and analytical results shown in Figs. 6 to 9

is practically negligible, which supports the accuracy of the numerical techniques presented in this paper.

CONCLUSIONS

The general partial differential equation of the vector potential has been developed on the basis of two-dimensional analysis. The corresponding vector potential equations have been derived from the general equation. The numerical solution of such equations has been described in a manner which is suitable for transient conditions.

In the case of deep bars embedded in slots, the phenomenon of skin-effect can be investigated with sufficient accuracy by using the single-dimensional analysis. For this purpose, the procedure for solving the field equations numerically has been presented. In addition, the transient analytical solutions of the magnetic field intensity, the current density and the voltage drop have been derived for the case of a sinusoidal total current applied to a rectangular bar in a slot.

The transient skin-effect in a deep bar embedded in a slot has been investigated by considering the two specific cases of a step and a sinusoidal applied total current. The excellent agreement between the analytical results and the results obtained by using the numerical techniques developed on the basis of two and single dimensional analyses verifies the validity of the numerical techniques.

NOMENCLATURE

A	= Vector potential
B	= Flux density
a	= Width of the bar
b	= Slot opening
H	= Magnetic field intensity
h	= Height of the bar
i	= Instantaneous total current
k_1, k_2, k_3, k_4	= Constants less than or equal to unity
m	= Number of nodes
t	= Time, sec.
x, y	= x and y Cartesian co-ordinates
v	= Instantaneous voltage drop per unit length
ω	= Frequency of the applied current, rad./sec.
σ	= Current density
ρ	= Resistivity
μ	= Permeability

- v = Number of current-carrying conductors
- Δx = Width of a square mesh
- Δt = Time increment

Subscripts:

- i = The variable at the i^{th} x co-ordinate
- j = The variable at the j^{th} y co-ordinate
- n = The variable at the n^{th} interval of time
- p.u. = The normalized value of the variable
- x = The variable component in the x direction
- y = The variable component in the y direction

ACKNOWLEDGEMENT

The authors are thankful to the National Research Council of Canada for the financial support of this project. They also wish to thank the Department of Electrical Engineering, University of Saskatchewan, Saskatoon, for the facilities in connection with this work.

REFERENCES

1. Tuohy, E.J., Lee, T.H. and Fullerton, H.P., "Transient resistance of conductors", IEEE Trans., Vol. PAS-87, No. 2, Feb. 1968, pp. 455-462.
2. Mocanu, C.I., "Transient skin-effect in a rectangular conductor in a slot", Archiv für Elektrotechnik, Bd. 55, 1973, pp. 164-170.
3. Probst, R., "Transient behaviour of asynchronous motors in the case of system switchover, taking into account the skin effect in the rotor bars", ETZ-A, Bd. 94, H.9, 1973, pp. 515-520.
4. Abo-Shady, S.E. and Verma, S.P., "A novel approach for the analysis of rotor cage windings of salient-pole machines", Paper no. C 75 129-2, IEEE PES Meeting, New York, N.Y., January 1975.
5. Štafl, M., "Electrodynamics of Electrical Machines", Iliffe Books Ltd., London, 1967.
6. Dwight, H.B., "Electrical Elements of Power Transmission Lines", The Macmillan Company, New York, 1954.
7. Babb, D.S. and Williams, J.E., "Circuit analysis method for determination of A.C. impedances of machine conductors", AIEE Trans., Vol. 70, Part I, 1951, pp. 661-666.
8. Babb, D.S. and Williams, J.E., "Network analysis of A.C. machine conductors", AIEE Trans., Vol. 70, 1951, pp. 2001-2005.
9. Liwschitz-Garik, M., "Skin-effect bars of squirrel-cage rotors", AIEE Trans., Vol. 73, Part III-A, April 1954, pp. 255-258.
10. Liwschitz-Garik, M., "Computation of skin-effect in bars of squirrel-cage rotors", AIEE Trans., Vol. 74, Part III, August 1955, pp. 768-771.
11. Dwight, H.B., "Effective resistance of isolated nonmagnetic rectangular conductors", AIEE Trans., Vol. 66, 1947, pp. 549-552.
12. Silvester, P., "Modal network theory of skin effect in flat conductors", Proc. of IEEE, Vol. 54, No. 9, Spt. 1966, pp.1147-1151.

13. Silvester, P., "A.C. resistance and reactance of isolated rectangular conductors", IEEE Trans., Vol. PAS-86, No. 6, 1967, pp. 770-774.
14. Silvester, P., "The accurate calculation of skin-effect in conductors of complicated shape", IEEE Trans., Vol. PAS-87, No. 3, March 1968, pp. 735-742.
15. Silvester, P., "Dynamic resistance and inductance of slot-embedded conductors", IEEE Trans., Vol. PAS-87, No. 1, Jan. 1968, pp. 250-256.
16. Binns, K.J. and Lawrenson, P.J., "Analysis and Computation of Electric and Magnetic Field Problems", The Macmillan Company, New York, 1963.
17. Lammeraner, J. and Štafl, M., "Eddy Currents", Iliffe Books Ltd., London, 1966.

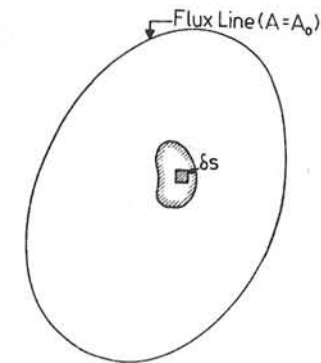


Fig.1. Conductor in a magnetic field

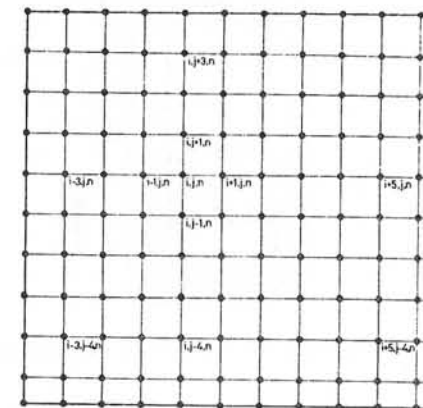


Fig.2. Simple rectangular field region at t_n

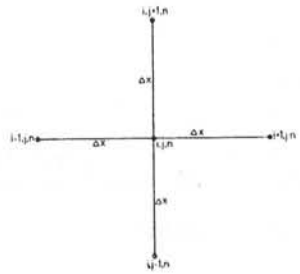


Fig. 3. Symmetrical star

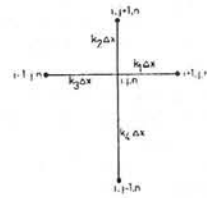


Fig. 4. Asymmetrical star

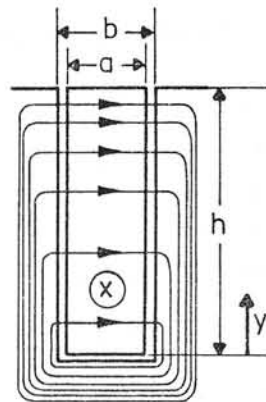


Fig. 5. Flux distribution of a deep bar embedded in a slot

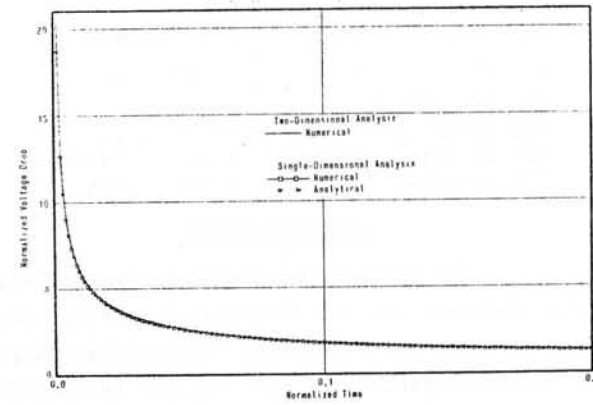


Fig. 6. Instantaneous value of the normalized voltage drop due to a step total current

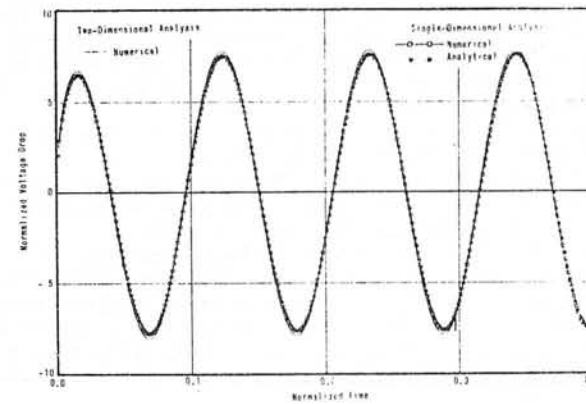
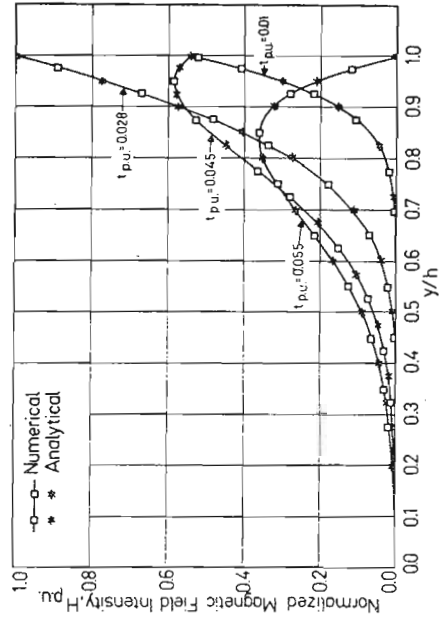
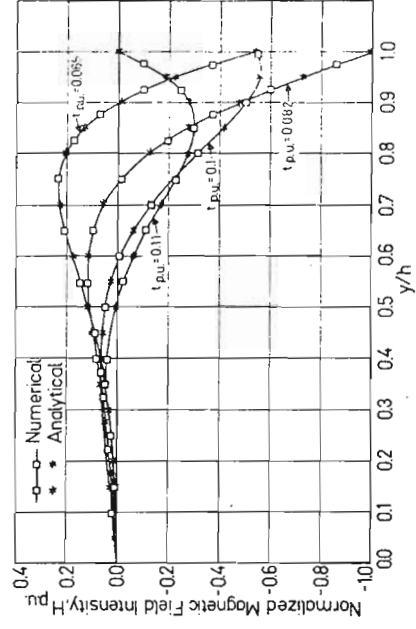


Fig. 7. Instantaneous value of the normalized voltage drop due to a sinusoidal total current of frequency 50 Hz

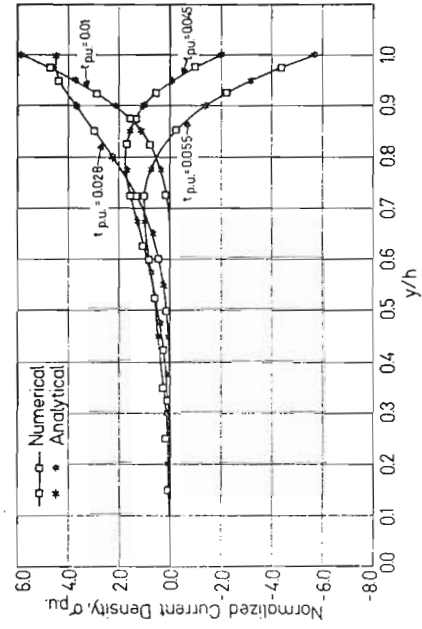


(a)

Fig. 8. Distribution of the magnetic field intensity at different values of time due to a sinusoidal total current of frequency 50 Hz

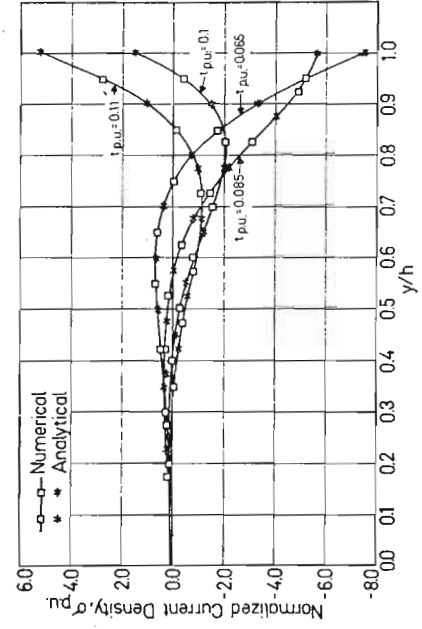


(b)



(a)

Fig. 9. Distribution of the current density at different values of time due to a sinusoidal total current of frequency 50 Hz



(b)

Discussions following paper:

(Reichert) What boundary conditions were assumed in the airgap over the slot? There are two possibilities, either field parallel in the airgap or perpendicular on the iron.

(Verma, Univ of Saskatchewan) In the case of a deep bar embedded in a slot as presented in the paper, the field is considered to be parallel to the periphery of the rotor. The main purpose here was to verify the validity of the numerical techniques developed in the paper.

The method can, however, be applied to the cases where the airgap field is radial on iron by considering the boundary conditions properly.

MAGNETIC FIELD DIFFUSION IN FAST DISCHARGING
HOMOPOLAR MACHINES: A FINITE ELEMENT APPROACH

E. B. Becker, R. D. Pillsbury, M. D. Driga
Energy Storage Group and Texas Institute for
Computational Mechanics
The University of Texas Austin, Texas

The Energy Storage Group at The University of Texas have engaged in the preliminary design of several homopolars for fusion reactor applications, have designed and built two experimental homopolar machines and are currently designing and will build a very fast discharging experimental homopolar machine. This machine, shown in Figure 1, consists of two counter-rotating rotors which turn in a field with a maximum strength of approximately 8 Tesla produced by the circumferential field coil. The 6" diameter rotors, at their initial velocity of 28000 rpm, produce an open circuit voltage of 100 volts. The shaping of the rotors is to reduce the stored energy while maintaining the voltage, thereby reducing, as far as possible, the discharge time. It is expected that the .35 MJ of stored energy will be discharged in approximately 1.25 msec. with a peak current of some 2.8×10^6 amps. The forces and torques produced in the rotors and brushes by the large currents and fields (both applied and induced) are a limiting factor in the mechanical design of the machine; thus the accurate prediction of the force distribution is required. Since the penetration time for a conductor of dimensions comparable to the rotors is roughly the same as the discharge time of 1.25 msec., the determination of the current distribution in the system is truly a transient problem, the driving function of which is the motion of the rotating conductors in the (relatively) steady magnetic field.

Formulation of the Boundary Value Problem

With a few exceptions, notably Silvester (1), computational approaches to field penetration problems have been limited to either the a.c. steady state case, or, as in the work of Miya (2), to situations in which the field is driven

by a current whose spatial as well as temporal distribution is assumed to be known. In these situations the penetration is conveniently expressed in terms of the magnetic field H which satisfies an homogeneous diffusion equation driven by boundary values of H which can be inferred from the assumed conditions.

In the present application, as in many instances involving, say, electrical machines, commutating gear or fusion experiments, there is a conversion of energy that is stored in one form and converted into another, in the process of which the magnetic fields and currents are unknown and cannot reasonably be assumed a priori.

In order to employ the driving function $v \times B$ directly we introduce the electric potential Ψ and the magnetic vector potential A as primary dependent variables. Standard definitions of the potentials (1), Ohm's law for moving media (2), and Maxwell's equations (3) (neglecting displacement current) are the basis of our formulation.

$$\begin{aligned} -\nabla \Psi &= E + \frac{\partial A}{\partial t} \\ B &= \nabla \times A \end{aligned} \quad (1)$$

$$J = \sigma (E + v \times B_0) \quad (2)$$

$$\begin{aligned} \nabla \times H &= J \\ \nabla \cdot B &= 0 \\ \nabla \times E &= -\frac{\partial B}{\partial t} \\ \mu H &= B \end{aligned} \quad (3)$$

To these equations we adjoin the constraints that J and A be divergence free - the first on physical grounds and the second on mathematical ones. Combining these conditions we see that the field equations are equivalent to

$$\sigma \dot{A} + \nabla \times \frac{1}{\mu} \nabla \times A - \sigma (\nabla \times \nabla \times A_0 + \nabla \psi) = 0 \quad (4)$$

$$\nabla \cdot \sigma \nabla \psi - \nabla \cdot \sigma (\nabla \times \nabla \times A_0 - \dot{A}) = 0$$

SUBJECT TO

$$\nabla \cdot A = 0 \quad (5)$$

Because both the rotor motion ∇ and the potential of the applied magnetic field A_0 are axisymmetric and have only Θ components the problem separates into two weakly coupled ones, namely, (6) which governs the distribution of the steady applied field and (7) in which the vector A has only r and z components.

$$\nabla \times \frac{1}{\mu} \nabla \times A_0 = J \quad (6)$$

$$\begin{aligned} \sigma \dot{A} + \nabla \times \frac{1}{\mu} \nabla \times A + \sigma \nabla \psi &= \sigma \nabla \times \nabla \times A_0 \\ \nabla \cdot \sigma \dot{A} + \nabla \cdot \sigma \nabla \psi &= \nabla \cdot \sigma \nabla \times \nabla \times A_0 \\ \nabla \cdot A &= 0 \end{aligned} \quad (7)$$

The finite element solution of (6), although necessary to our problem, is a standard one and need not be discussed further here.

In addition to the equations (7) we have as side conditions the vanishing of the potentials at large distance from the conductors and the usual continuity or jump conditions on current and field. These take the form (8) and (9).

$$A_r = A_z = \psi = 0 \quad \vec{r} \rightarrow \infty \quad (8)$$

$$\begin{aligned} \llbracket \frac{1}{\mu} \nabla \times A \rrbracket &= 0 \\ \llbracket \sigma (\nabla \times \nabla \times A_0 - \nabla \psi - \dot{A}) \rrbracket &= 0 \end{aligned} \quad (9)$$

In (8) the brackets denote the jump in the enclosed quantity across an interface between different materials or between moving and stationary materials. In the finite element model of the region shown in Figure 1, the symmetry about $r = 0$ and

anti-symmetry about $z = 0$ give rise to the following additional boundary conditions

$$\begin{aligned} A_r &= 0 & \text{ON } r &= 0 \\ A_z = \psi &= 0 & \text{ON } z &= 0 \end{aligned} \quad (10)$$

Finite Element Formulation

We seek solutions to (7) and (9) subject to the conditions (8) and (10) in the weak or Galerkin sense. To this end we introduce a Lagrange multiplier λ corresponding to the constraint (7c) and the test functions u, η , and \bar{c} corresponding to A, ψ and λ . The weak statement of the problem is

$$\sum_i \left\{ \iiint_{\Omega_i} [\sigma \dot{A} + \nabla \times \frac{1}{\mu} \nabla \times A + \sigma \nabla \psi - \sigma \nabla \times \nabla \times A_0] \cdot u \, da - \int_{\partial \Omega_i} \llbracket \frac{1}{\mu} \nabla \times A_0 \rrbracket \cdot u \, ds \right\} = 0 \quad \text{FOR ALL } u \quad (11)$$

AND

$$\sum_i \left\{ \iiint_{\Omega_i} [\nabla \cdot \sigma \dot{A} + \nabla \cdot \sigma \nabla \psi - \nabla \cdot \sigma \nabla \times \nabla \times A_0] \eta \, da - \int_{\partial \Omega_i} \llbracket \sigma (\nabla \times \nabla \times A_0 - \nabla \psi - \dot{A}) \rrbracket \cdot m \, \eta \, ds \right\} = 0 \quad (12)$$

FOR ALL η

In (11) and (12) the regions Ω_i are regions within which all fields are continuous i.e. all the jumps are across the boundaries $\partial \Omega_i$ of these regions. Applying the divergence theorem to each region Ω_i and introducing the constraint (7c) with its multiplier and test function leads to the final weak form

$$\sum \left\{ \iiint [\sigma u \dot{A} + \frac{1}{\mu} (\nabla \times A) \cdot (\nabla \times A) + \sigma u \cdot \nabla \psi + \lambda \nabla \cdot u + \bar{c} \nabla \cdot A - \sigma \nabla \times \nabla \times A_0 \cdot u] \, da \right\} = 0$$

$$\sum \{ \int \int \int [-\sigma \nabla \eta \cdot \nabla \psi - \dot{\lambda} \cdot \nabla \eta + \sigma \nabla \times \nabla \times A_c \cdot \nabla \eta] da \} = 0$$

FOR ALL u, η , AND ζ .

(13)

for arbitrary u, η , and ζ vanishing at ∞ .

It is significant that the jump terms have equilibrated the boundary integrals from the integration by parts i.e. the jump conditions are natural conditions that follow as a consequence of (13).

The discrete form of (13) is obtained by introducing the finite element approximation of the fields $A, u, \psi, \eta, \lambda$ and ζ . The elements are quadrilaterals and the shape functions are quadratic for A, u, ψ , and η and linear for λ and ζ . Thus each corner node of the mesh has a total of four unknowns, i.e. A_n, A_z, ψ and λ , while the midside nodes have only A_n, A_z and ψ . If the set of nodal point values is denoted q then the discrete form of (13) can be written as

$$C \dot{q} + K q = f$$
(14)

In (14) C and K are, for an element, 28×28 matrices whose elements are the integrals of products of shape functions. It is apparent from (13) that neither C nor K is symmetric. The forcing function f in (14) contains terms proportional to $\nabla \times \nabla \times A_c$. The motion of the rotor is treated as given in this analysis and the value of the applied field A_c is known from an initial finite element solution for the single component A_c .

Although, in some designs, there is iron shielding around the field coil making the equations for A_c non linear, the

complete compensation of the machine as shown in Figure 1 confines the magnetic field governed by (14) to the region within the return conductor. There is no iron in the machine itself - the rotors being aluminum to reduce the capacitance of the machine - and so (14) is linear.

The initial value problem for q is solved using a combination of algorithms. Using the approximation

$$\dot{q} \approx (q^{n+1} - q^n) / \Delta t$$

leads either to

$$\left(\frac{2}{\Delta t} C + K \right) q^{n+1/2} = \frac{2}{\Delta t} C q^n + f^{n+1/2}$$
(15)

$$\left(\frac{1}{\Delta t} C + K \right) q^{n+1} = \frac{1}{\Delta t} C q^n + f^{n+1}$$
(16)

In (15) $q^{n+1/2} \equiv \frac{1}{2} (q^{n+1} + q^n)$ is taken as the value of at $(n+1/2)\Delta t$. Both (15) and (16) are implicit and clearly each involves the same amount of computation. We find that, once started adequately, longer time steps can be used with (15) but that the use of (15) for the first few time steps leads to unacceptably noisy solutions. Since, with either scheme, a change in time step means reassembly and decomposition, there is no computational penalty paid in changing scheme when the initial small time step is increased.

It is of great significance that, although neither C nor K is symmetric, $(\alpha C + K)$ can be made symmetric simply by dividing the ψ equations thru by α . We have employed both symmetric band solvers and a frontal solver to reduce (15) and (16).

Results

The computational sequence begins with the solution of (6) for the values of the applied field $\vec{B}_0 = \nabla \times \vec{A}_0$. The values of \vec{B}_0 are calculated at the integration points of each element and saved for use in calculating the forcing function in the transient problem. Figure 2 shows a flux plot (contours of constant values of $n\vec{B}_0$) for a current density of 1.18×10^8 amps/m² in the field coil. Incidentally this coil, which is LN₂ cooled copper, is energized by the discharge of a 5 MJ homopolar machine. This pulse is of the order of a second, quite long compared to the transient phenomena under consideration.

The computation proceeds using (15) and/or (16). Figures 3, 4, and 5 show contours of constant values of the magnetic field \vec{B}_0 induced by the current at an early time, $t = 20 \times 10^{-6}$ sec. an intermediate time, $t = 200 \times 10^{-6}$ sec., and a time, $t = 1000 \times 10^{-6}$ sec. The diffusion of the current into the rotor the brushes and the return conductor is apparent. At selected time steps the body force density $\vec{J} \times \vec{B}$ is calculated and used as input to a finite element stress analysis. Both azimuthal and inplane forces give rise to significant stresses. In addition to the stress calculation it is possible to accumulate the time integral of ohmic heating in each element obtaining a detailed map of the resulting temperature distribution.

For reference, Figure 6 shows the long time distribution of \vec{B}_0 together with the finite element mesh used to model the problem. This state is not actually reached in the course of discharging the machine since the rotor speed decreases to zero before the steady state could be reached.

Comments

The formulation described above, in conjunction with finite element techniques, makes possible the solution of quite a general class of problems involving transient magnetic phenomena. Arbitrary geometries, material interfaces etc. can be treated routinely. This formulation has evolved only after a good many false starts. The formulation is cumbersome

and the computations expensive, but can furnish approximate solutions to problems that are otherwise unapproachable.

References

- [1] Silvester, P., "Modal Network Theory of Skin Effect in Flat Conductors," Proceedings of the I.E.E.E., Vol. 54, No. 9, 1960.
- [2] Mita, K., Ando, Y., Ohta, M., and Suzuki, Y., "Application of F.E.M. to Electro-Magneto-Mechanical Dynamics of Superconducting Magnet Coil and Vacuum Vessel," Symposium on Engineering Problems of Fusion Research, San Diego, California.
- [3] Stratton, J. A., Electromagnetic Theory, McGraw-Hill, 1941.
- [4] Rowberg, R. E., Becker, E. B., Rylander, H. G., and Woodson, H. H., "Characteristics of a Homopolar Machine as a Power Supply for Large Pulsed Magnetic Fields for Fusion Experiments," 1973 S.W.I.E.E. Conference Record of Technical Papers, p. 453, April 1973.
- [5] Driga, M. D., Nasar, S. A., Rylander, H. G., Weldon, W. F., and Woodson, H. H., "Fundamental Limitations and Topological Considerations for Fast Discharge Homopolar Machines," I.E.E.E. Trans. on Plasma Science, Vol. PS-3, No. 4, December 1975.

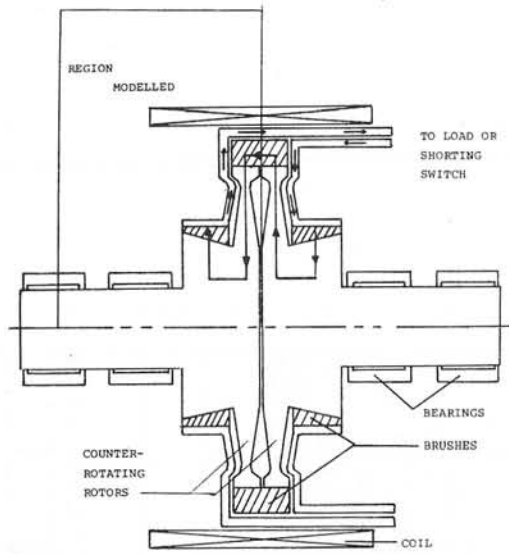


FIGURE 1. MACHINE CONFIGURATION

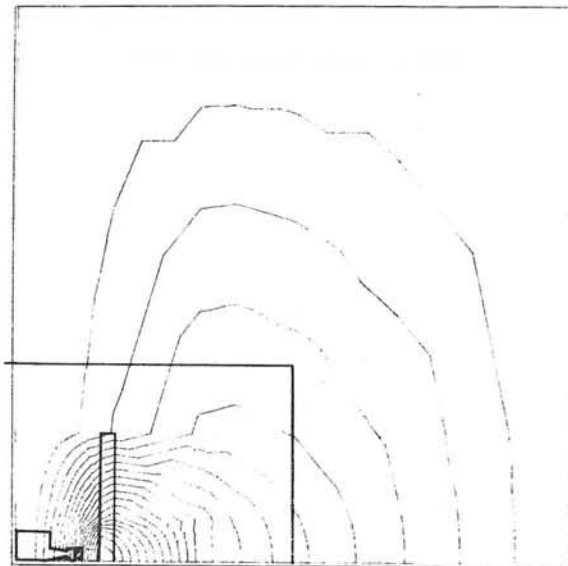


FIGURE 2. APPLIED MAGNETIC POTENTIAL A_0

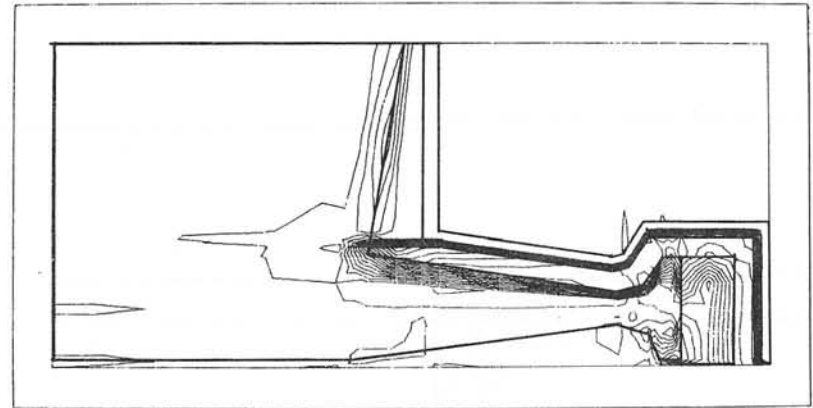


FIGURE 3. INDUCED FIELD B_0 AT $t = 20 \mu\text{sec}$.

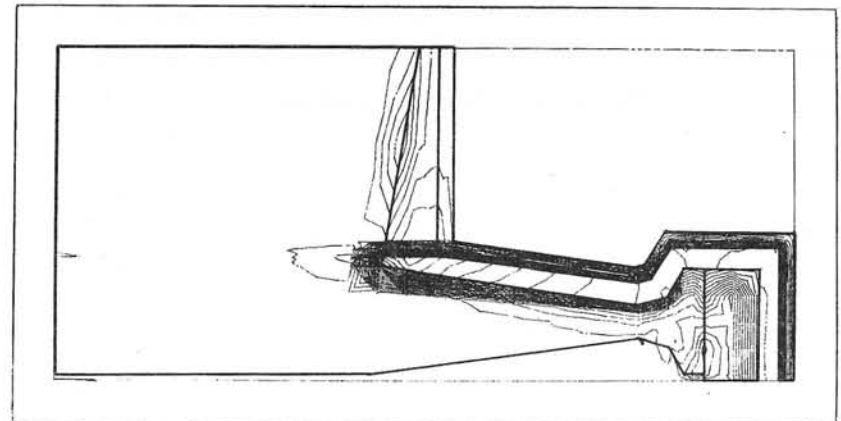


FIGURE 4. INDUCED FIELD B_0 AT $t = 200 \mu\text{sec}$.

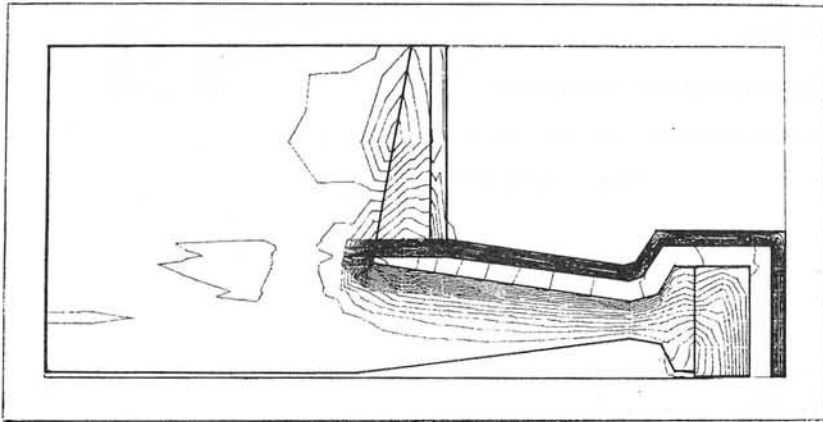


FIGURE 5. INDUCED FIELD B_0 AT $t = 1000 \mu \text{ sec}$.

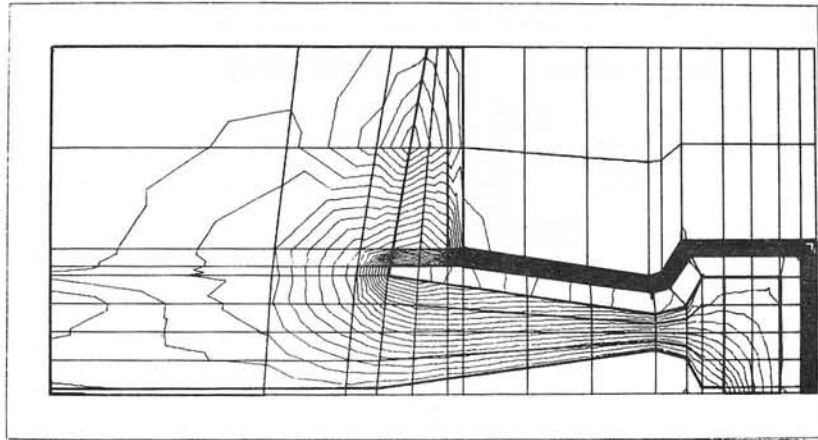


FIGURE 6. INDUCED FIELD B_0 STEADY STATE

FIELD PENETRATION INTO A VARIABLE- μ MATERIAL

I. Gumowski
CERN, Geneva, Switzerland

Abstract

A non-linear partial differential equation is formulated which describes the distribution of H inside a material of non-constant relative permeability μ . The assumption $\mu = \mu(H)$ leads to the existence of solutions differing qualitatively from those obtained with the assumption $\mu = \text{const}$. One of these solutions suggests that remanence is not an independent phenomenon, but merely a consequence of $\mu = \mu(H)$. Conditions are established for the field penetration to be of the usual diffusion type. A recursive method of calculating H is proposed.

1. INTRODUCTION AND STATEMENT OF THE PROBLEM

In field calculations the internal properties of magnetic materials are rarely specified microscopically, in terms of molecular and crystalline structure. The specifications are usually macroscopic ones, in terms of remanence, hysteresis, static-, incremental-, a.c.- and effective-relative permeability. Since an explicit relation between the microscopic and macroscopic descriptions is not yet available, the Ising model notwithstanding, the macroscopic description is obtained phenomenologically, in the form of a set of flux-density versus field curves (B versus $\mu_0 H$, μ_0 = permeability of vacuum, MKSA units used in this paper). The corresponding mathematical problem is extremely complex, because these curves are not single-valued. If it is assumed that the knowledge of the geometric configuration and of the relative permeability μ is sufficient for a complete description of H, then μ is a function of instantaneous as well as past values of H and $\partial H/\partial t$.

The problem of constructing macroscopic models of field penetration of minimal mathematical complexity constitutes in essence a problem of successive approximation, each approximation step describing a physically richer situation. The coarsest possible approximation is based on the assumption $\mu = \mu_e = \text{const}$, describing some "mean" or "effective" static state of the material. The next step, discussed in this paper, is based on the assumption that μ depends also on the instantaneous value of H. The assumption $\mu = \mu(H)$ involves some dynamic effects excluded by the simplification

$\mu = \text{const}$. For example, the diffusion of H changes into a wave propagation with finite velocity (unrelated to displacement currents), and remanence appears as a limiting case.

The paper emphasizes qualitative aspects, i.e. conditions of physically distinct behaviour of H. When the propagation of H corresponds to the usual diffusion process, a computation method based on successive corrections is proposed. In order to reduce the notational bulk and render the procedure physically transparent a very simple geometric configuration is used. The resulting mathematical model is one-dimensional. A generalization to more dimensions is straightforward.

2. FORMULATION OF THE MATHEMATICAL MODEL

Let the magnetic material have the form of a rather thick C in the x-z plane and be quite long along y. The origin of the rectangular coordinates is placed so that the x-axis bisects horizontally the rectangular air gap of the C, $x = 0$ and $x = \bar{x}$ representing the inner and outer edges of the latter. Let $h = \text{const}$ be the height of the air gap and ℓ the length of a flux line inside the magnetic material. If $\mu = \text{const}$ and $\ell = \text{const}$, the time scale can be so chosen that the product $\sigma\mu_0$, σ = electrical conductivity, is absorbed into t , and the field $H(x,t)$ inside the air gap is described by

$$\frac{\partial}{\partial x} \left(k \frac{\partial H}{\partial x} \right) = \frac{\partial H}{\partial t}, \quad t > t_0, \quad 0 < x < \bar{x}, \quad (1)$$

where $k = h/\ell + 1/\mu$ and $t_0 = \text{const}$. A unique solution of eq. (1) is defined, for example, by the boundary conditions

$$H(0,t) = G_1(t), \quad H(x,t_0) = G_2(x), \quad (2)$$

G_1, G_2 being two given (sufficiently smooth) functions.

When $\mu = \mu(H)$ and $\ell = \ell(H)$, the form of eq. (1) changes only slightly (cf. Appendix):

$$\frac{\partial}{\partial x} \left[F(H) \frac{\partial H}{\partial x} \right] = \frac{\partial H}{\partial t}, \quad t > t_0, \quad 0 < x < \bar{x}, \quad (3)$$

$$F(H) = \frac{h}{\ell} + \frac{1}{\mu} + \frac{1}{\ell} H \frac{\partial}{\partial H} \left(\frac{\ell}{\mu} \right). \quad (3a)$$

The specific problem consists at this stage in ascertaining properties of $\mu(H)$, and eventually of $\ell(H)$, which define qualitatively different solutions of eqs. (1), (2) and (3), (2), respectively. From the theory of non-linear parabolic equations it is known that eq. (3) is singular when

$$F(H) = 0 \quad (4)$$

for some real $H = H_c$. Near the critical field H_c there exist no solutions of eq. (3) in the usual sense, i.e. there is no function $H(x,t)$ possessing a continuous second derivative with respect to x and verifying eq. (3) identically. Normal numerical methods are known to yield meaningless results under these circumstances. Physically significant solutions exist in a mathematically generalized sense, subject to the condition that $F(\partial H/\partial x)$ is a continuously differentiable function with respect to x . The function $\partial H/\partial x$ need not be continuous¹⁾. Appropriate numerical methods have already been worked out²⁾. Moreover, some analytical solutions are known when F has a special form. Such solutions are mainly a source of physical insight. Equations of type (3) arise also in other fields, for example, in plasma physics³⁾, heat conduction⁴⁾, and filtration of fluids by porous media^{5,6)}.

The question arises whether eq. (4) is ever satisfied in the case of a magnetic material. As a preliminary step it is necessary to fit $\mu(H)$ and $\ell(H)$ by some analytically simple functions, because otherwise the physical content of eq. (4) is obscured by the mathematical manipulations in eq. (3a). It is obvious that the μ involved in eq. (3a) is intermediate between the conventional a.c.- and static- μ 's. $\mu(H)$ is thus a single-valued function possessing one maximum, say μ_m at H_m , which implies $\partial\mu/\partial H > 0$ for $H < H_m$ and $\partial\mu/\partial H < 0$ for $H > H_m$. Physical concepts, like leakage flux and edge effects near an air gap, suggest that $\partial\ell/\partial H \geq 0$. An elementary analysis of $F(H)$ shows then that $F > 0$ when $\partial\mu/\partial H \leq 0$, and a real H_c can only exist when $\partial\mu/\partial H > 0$. Whether H_c actually exists depends on the specific values of $\max(h/\ell)$, $\min \mu$ and $\partial\mu/\partial H$. A good fit to experimental data is provided by

$$\mu(H) = \mu_i + H^n (\mu_m - \mu_i) / (H_0^n + H^n), \quad 0 \leq H < H_m, \quad (5)$$

where $\mu_i = \mu(0)$, and H_0, n are determined numerically. The parameters H_0 and n characterize the scale of H and the rate of increase of μ , respectively. For a typical silicone steel $\mu_i = 1.2$, $\mu_m = 8.5$, $H_m = 100$, $H_0 = 17$, $n = 3.5$, whereas for a low- μ ferrite (type U60) $\mu_i = 3$, $\mu_m = 33$, $H_m = 1000$, $H_0 = 376$, $n = 2.3$.

Consider first the simplest possible case $\ell = \text{const}$. Combining eqs. (3a) and (5) yields a ratio of two quadratic polynomials in H^n . The vanishing of the numerator being equivalent to eq. (4), the critical field H_c can be expressed explicitly as a function of h/ℓ and the parameters of eq. (5). Two simple roots of eq. (4) exist when $h/\ell \ll 1$, $n > 1$ and μ_i is not too large. In the case of the above examples: $H_{c1} = 9.3$, $H_{c2} = 14$ when $h/\ell = 0.1$; $H_{c1} = 8.2$, $H_{c2} = 20$ when $h/\ell \approx 0$ for silicone steel, and $H_{c1} = 140$, $H_{c2} = 360$, $h/\ell \approx 0$ for the ferrite. The non-existence of real H_c as h/ℓ increases describes simply the diminishing role of the magnetic material compared to that of the air gap. For small n the dynamic effect of $\partial\mu/\partial H$ is weaker than the static effect of the constant part of μ . When $\ell = \text{const}$ is replaced by $\ell = \ell(H)$, eq. (4) becomes too complicated to allow an explicit solution. Numerical tests with particular forms of $\ell(H)$ have shown that flux-line lengthening has a rather weak effect on the roots of eq. (4); they tend, however, to be slightly more separated.

The existence of critical fields H_c permits a rough qualitative assessment of the solutions of eq. (3). Assume, in fact, that the boundary conditions (2) place $H(x,t)$ into the interval $H_{c1} < H < H_{c2}$. In this interval $F(H) < 0$. Replacing t by $-t$ reduces eqs. (3), (2) to a "normal" diffusion problem, with $F(H) > 0$, except that the new time runs backwards. In the original t there exists therefore a process of "inverse" diffusion, with a possible steepening of the spatial profile of H .

3. SOME INVERSE DIFFUSION EFFECTS

Consider eq. (3) in the field range defined by $F(H) \leq 0$. Replace $H - H_{c1}$ by H in order to render H_{c1} a static reference solution, and t by $-t$ in order to make all terms nominally positive. When only the largest term is kept in the transformed F , eq. (3) simplifies into

$$a \frac{\partial}{\partial x} \left(H \frac{\partial H}{\partial x} \right) = \frac{\partial H}{\partial t}, \quad 0 \leq H < H_{c2} - H_{c1}, \quad (6)$$

where $a = F'(H_{c1})$. The usefulness of eq. (6) consists in the fact that some of its solutions can be found in explicit form. These solutions can be verified by direct substitution. For conciseness, the statement " $H(x,t) \equiv 0$ outside the specified range of x " is omitted below. All symbols not mentioned explicitly are positive constants whose values are given by the boundary conditions (2) after insertion of the relevant $H(x,t)$.

In contrast to normal diffusion, eq. (6) admits a non-constant stationary state

$$H(x,t) = H_1 (x_0 - x)^{\frac{1}{2}}, \quad 0 \leq x \leq x_0, \quad (7)$$

where H_1 and x_0 represent the boundary field intensity and the field penetration depth, respectively. From a physical point of view, solutions of type (7) represent a spatially non-uniform remanence. Hence, remanence does not appear to be an independent phenomenon, distinct from the non-linearity introduced by $\mu(H)$.

Various wave-type solutions are also possible. The simplest case is

$$H(x,t) = \frac{c}{a} (ct + x_0 - x), \quad 0 \leq x \leq x_0 + ct, \quad (8)$$

where the propagation velocity c is defined indirectly by the boundary field intensity H_1 . A wave with a steepening profile and a non-propagating front is described by

$$H(x,t) = (x_0 - x)^2 / [6a(c - t)], \quad 0 \leq x \leq x_0. \quad (9)$$

Variable velocity waves are represented by the family of functions

$$H(x,t) = H_1 (c + t)^m f(u), \quad u = \frac{x}{A} \left[a H_1 (c + t)^{m+1} \right]^{-\frac{1}{2}}, \quad 0 \leq u \leq 1, \quad (10)$$

where $f = v(u)$ is a particular solution of the ordinary differential equation

$$v'' + \frac{1}{v^2} + \frac{1}{2} (1 + m) A^2 u v' - mA^2 v = 0. \quad (11)$$

When $(1+m)A^2 = B$, one solution of eq. (11) is

$$v(u) = \frac{w}{B} \sum_{i=0}^{\infty} b_i w^i, \quad B = \sum_{i=0}^{\infty} b_i, \quad (12)$$

where $w = 1 - u$, $b_0 = 1$, $b_1 = 1/4$, $b_2 = -1/24$, ...

Non-constant stationary states, and wave propagation with a finite velocity exist also in two- and three-dimensional inverse diffusion problems. There is no inherent need for symmetry as far as the different spatial

directions are concerned. The resulting macroscopic anisotropy is also a mere consequence of $\mu(H)$.

4. A RECURSIVE SOLUTION METHOD FOR THE NON-SINGULAR CASE

When the field penetration problem is described by eq. (3) and $F(H) > 0$, the analytical fitting (5) is inappropriate. A convenient replacement, emphasizing the range $\partial\mu/\partial H < 0$, is

$$\mu(H) = \mu_1 + mH_0H^n / (H_0^{n+1} + H^{n+1}), \quad H > H_{C2} \quad (H \geq 0 \text{ if } \text{Im } H_C \neq 0), \quad (13)$$

where, as before, the constants are empirically determined. For silicone steel, for example, $\mu_1 = 1.2$, $H_0 = 82$, $m = 13$, $n = 2.8$, and for a low- μ ferrite (type K12, $\mu_m = 34$, $H_m = 2700$), $\mu_1 = 18$, $H_0 = 2090$, $m = 27$, $n = 2.4$. Let ℓ_e, μ_e be the effective values used in the linearization (1), where $k = h/\ell_e + 1/\mu_e$. The difference $g = F(H) - k$ represents therefore the effect of the non-constancy of ℓ and μ . Since the effective values are well chosen by definition, g is a small correction of k . Formally this property is described by

$$F(H) = k + \epsilon g(H), \quad 0 < \epsilon \leq 1, \quad (14)$$

where ϵ is the coefficient of the dominant non-constant term of $F(H)$, or simply an auxiliary ordering parameter (set to unity in the final result). If a solution of eqs. (3), (2) and (14) is written in the form

$$H(x,t) = \sum_{i=0}^{\infty} H_i(x,t) \epsilon^i, \quad H_1(0,t) = H_1(x,t_0) \equiv 0, \quad i > 0, \quad (15)$$

then the non-linear problem reduces to a sequence of linear ones

$$\left. \begin{aligned} k \frac{\partial^2 H_0}{\partial x^2} - \frac{\partial H_0}{\partial t} &= 0 \\ k \frac{\partial^2 H_1}{\partial x^2} - \frac{\partial H_1}{\partial t} &= - \frac{\partial}{\partial x} \left[g(H_0) \frac{\partial H_0}{\partial x} \right] \\ k \frac{\partial^2 H_2}{\partial x^2} - \frac{\partial H_2}{\partial t} &= - \frac{\partial}{\partial x} \left[g(H_0) \frac{\partial H_1}{\partial x} + g'(H_0) H_1 \frac{\partial H_0}{\partial x} \right] \\ &\dots \end{aligned} \right\} \quad (16)$$

the first to be solved with the boundary conditions (2), and the other with homogeneous ones given in eq. (15). The boundary-value problems (16)

can be solved by standard analytical or numerical methods. When k represents a good linearization, the corrections $H_1(x, t)$ diminish rapidly as i increases. It is noteworthy that no direct analytical methods of solving eqs. (3), (2) and (14) are known. Numerical methods require the solving of sets of non-linear algebraic equations, which is a considerable complication compared to the computations involved in solving eq. (16).

CONCLUSION

When the assumption $\mu = \text{const}$ is replaced by $\mu = \mu(H)$ the field penetration into a magnetic material constitutes a non-linear diffusion process. In the range $\partial\mu/\partial H > 0$ an inverse diffusion is possible. Two distinct inverse diffusion effects are illustrated. The full set of such effects, and their stability with respect to small structural perturbation of the differential equation, are still unknown. The most relevant structural perturbation appears to be a dependence of μ on $\partial H/\partial t$, which can be made to simulate the presence of hysteresis.

APPENDIX

Consider the geometric configuration described in Section 2. For conciseness, let $H_z = H$, $\ell = \ell(x, y)$, $\ell(\Delta x) = \ell(x + \Delta x, y)$, and similarly for other variables. Integrate H around two flux lines separated by Δx in the x - z plane of the air gap:

$$\begin{aligned} \oint \vec{H} \cdot d\vec{s} &= \left(h + \frac{\ell}{\mu} \right) H - \left[h + \ell(\Delta x)/\mu(\Delta z) \right] H(\Delta x) \\ &= - \left[H \frac{\partial}{\partial x} \left(\frac{\ell}{\mu} \right) + \left(h + \frac{\ell}{\mu} \right) \frac{\partial H}{\partial x} \right] \Delta x + \dots = J_y \ell \Delta x, \end{aligned}$$

where J is the current density. Neglecting $\partial\ell/\partial y$, $\partial\mu/\partial y$ and keeping only terms of first order in Δx yields

$$-J_y = + \frac{H}{\ell} \frac{\partial}{\partial x} \left(\frac{\ell}{\mu} \right) + \left(\frac{h}{\ell} + \frac{1}{\mu} \right) \frac{\partial H}{\partial x}, \quad J_x = \left(\frac{h}{\ell} + \frac{1}{\mu} \right) \frac{\partial H}{\partial y}, \quad J_z = 0.$$

Inside the air gap $(1/\sigma) \text{curl } \vec{j} = -\mu_0(\partial\vec{H}/\partial t)$, which implies

$$\left(\frac{h}{\ell} + \frac{1}{\mu} \right) \frac{\partial^2 H}{\partial y^2} + \frac{\partial}{\partial x} \left[\left(\frac{h}{\ell} + \frac{1}{\mu} \right) \frac{\partial H}{\partial x} + \frac{H}{\ell} \frac{\partial}{\partial x} \left(\frac{\ell}{\mu} \right) \right] = \sigma \mu_0 \frac{\partial H}{\partial t}.$$

Equation (3) is obtained by neglecting the dependence on y , and replacing $\mu(x, y)$, $\ell(x, y)$ by $\mu(H)$, $\ell(H)$, respectively.

REFERENCES

- 1) O.A. Oleink, A.S. Kalashnikov and Chou-Jui-Lin, *Izv. Akad. Nauk. Ser. Mat.* 22, 667-704 (1958).
- 2) A.A. Samarskii, *Zh. vych. mat.* 3, No. 2, 266-298 (1963).
- 3) N.V. Zmitrenko and S.P. Kurdiumov, *Dokl. Akad. Nauk.* 218, 1306-09 (1974).
- 4) L.K. Martinson and K.B. Pavlov, *Zh. vych. Mat. mat. Fiz.* 12, No. 4, 1048-53 (1972).
- 5) G.I. Barenblatt, *Prikl. mat.* 16, No. 1, 67-78 (1952).
- 6) D.G. Aronson, *SIAM J. Appl. Math.* 17, No. 2, 461-467 (1969).

Use of Bubnow - Galerkin Method for Calculation of Transient Skin Effect in Foil Wound Chokes

P. Rolicz*

Abstract

It is shown that the Bubnow - Galerkin method can be applied for the analysis of non - steady states in conductors. The Joule power dissipated in a foil wound choke with an air gap is calculated in this paper. The particular case, when the excitation current is sinusoidal, is also considered.

1 Introduction

The steady state in foil wound chokes and transformers has been investigated by using numerical⁴ experimental⁶ and analytical^{1,5} methods. The transient skin effect in the winding lying in the window of a foil wound choke with an air gap is examined in this paper by using the Bubnow - Galerkin method.

2 Use of Bubnow - Galerkin method for parabolic equation

The theory of the application of the Bubnow - Galerkin method for the parabolic equation has been considered by Sobolevskii⁷. Let H be a real Hilbert space with a countable base, and C a linear positive and self - adjoint operator in H . The operator equation

$$CE + \frac{\partial E}{\partial t} = 0, \quad 0 \leq t \leq T \quad (1)$$

is given with the initial condition $E = E_0$ at $t = 0$. We chose the sequence $\{\varphi_i\}$, φ_i belongs to the domain of the operator C , complete in the energetic space H_C of the operator C such that the elements $\varphi_1, \varphi_2, \dots, \varphi_n$ are linear independent for arbitrary n . In order to find the approximate solution of equation (1) we take

$$E^{(n)} = \sum_{i=1}^n E_i \varphi_i \quad (2)$$

and we solve this equation with the initial condition $E_0^{(n)} = P_n E_0$ at $t=0$, where P_n denotes the orthogonal projection onto the n - dimensional subspace spanned upon the elements $\varphi_1, \varphi_2, \dots, \varphi_n$. This leads to the following system of equations

$$\sum_{i=1}^n \left[E_i (C \varphi_i | \varphi_m) + \frac{dE_i}{dt} (\varphi_i | \varphi_m) \right] = 0, \quad m=1, 2, \dots, n \quad (3)$$

where $(x|y)$ denotes the scalar product in the space H . The following theorem holds⁷ (Theorem 1 c at $\alpha = 1/2$).

Theorem 1. If E , $E^{(n)}$ denote the exact solution of the equation (1) and the approximate solution of one obtained by the Bubnow - Galerkin method, then

$$\lim_{n \rightarrow \infty} \sup_{0 \leq t \leq T} \sqrt{t} \|E^{(n)} - E\| = 0,$$

where $\|x\|$ denotes the norm of x in the space H_C .

Hence and from positive definition of the operator C results the convergency in the initial space H .

Let L_2 denotes the real Hilbert space of quadratically integrable functions in a closed and bounded set Ω . The scalar product of the elements $f, g \in L_2(\Omega)$ is defined as follows

$$(f | g) = \int_{\Omega} f g \, d\Omega. \quad (4)$$

The operator $-\nabla^2$ is positive definite and self - adjoint³ in $L_2(\Omega)$ for homogeneous boundary problems: Dirichlet, Neumann and mixed.

The Joule power (formula (10)) dissipated in windings lying in the window of a choke is proportional to square of the norm of E in the space $L_2(\Omega)$. Thus, by Theorem 1, the Bubnow - Galerkin method can be used for the calculation of the Joule power.

*The author is with Dept. of Electrical Engineering, Polytechnic of Białystok, Poland

3 Joule power dissipated in winding of choke

3.1 Non - steady state

The choke section is shown in fig.1. We assume that the permeability of ferromagnetic substance is infinitely great, the field in the gap is homogeneous and that foils are such thin that the current density is independent of x in each of them.

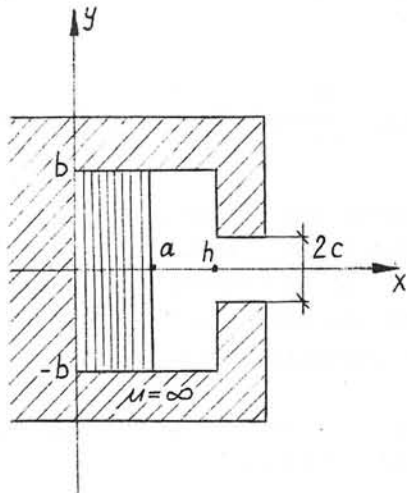


Fig.1 Choke section

The z component E of the electric field fulfils the following equation

$$\nabla^2 E = \begin{cases} \mu_0 \gamma w \frac{\partial E}{\partial t} & \text{for } 0 \leq x \leq a \\ 0 & \text{for } a < x \leq h \end{cases} \quad (5)$$

where μ_0, γ, w denote the permeability, the conductance and the filling factor, respectively. By the received assumptions, the Green's formula and (1) - (5), the Bubnow - Galerkin system of equations has the form

$$\int_0^h \int_{-b}^b \text{grad} \varphi_i \text{grad} E \, dy + \mu_0 \gamma w \frac{d}{dt} \int_0^h \int_{-b}^b \varphi_i E \, dy = \frac{\mu_0}{2c} \frac{dI_x}{dt} \int_{-c}^c \varphi_i \Big|_{x=h} \, dy, \quad (6)$$

where $I_x = n I$, I - a current flowing in a foil, n-number of foils. We assume that I has the form

$$I = I_0 \sin(\omega t + \alpha_0) + \sum_{i=1}^N I_i e^{-\alpha_i t}, \quad I=0 \text{ at } t \leq 0. \quad (7)$$

The Stone-Weierstrass Theorem² can be used for the determination of the sequence $\{\varphi_i\}$. By one, any even (with respect to the y - axis) continuous function on $\Omega = \{(x,y) : 0 \leq x \leq h, |y| \leq b\}$ may be uniformly approximated by linear combinations of functions of the sequence

$$\left\{ \cos h \left(m 0,65 \pi \frac{x}{h} \right) \cdot \cos \left(l \pi \frac{y}{b} \right) \right\} \quad m, l = 0, 1, 2, \dots$$

We admit that E has the following form

$$E = E_1 + E_2 \cos h \left(0,65 \frac{\pi x}{h} \right) \cdot \cos \pi \frac{y}{b}. \quad (8)$$

From (6) - (8) it follows that

$$E_1 = \frac{I_x}{2ab\gamma w} \quad (9a)$$

$$E_2 = n \left\{ \left[\frac{\omega \cos(\omega t + \alpha_0 - \psi) + \delta \sin(\alpha_0 - \psi) e^{-\delta t}}{\sqrt{\delta^2 + \omega^2}} + \sum_{i=1}^N I_i \frac{\delta e^{-\delta t} - \alpha_i e^{-\alpha_i t}}{\delta - \alpha_i} \right] \right\}, \quad (9b)$$

where

$$\delta = 7,8 \mu_0 \gamma \frac{\sin \pi \frac{c}{a}}{\pi \frac{c}{a}}, \quad \delta = \left(25,7 \frac{b}{h} + 80,7 \frac{h}{b} \right) \gamma,$$

$$\rho = \left\{ \mu_0 \gamma w a b \frac{h}{4,08a} \left[\sin h \left(\frac{4,08a}{h} \right) + 1 \right] \right\}^{-1}, \quad \psi = \tan^{-1} \frac{c}{\delta}$$

The Joule power dissipated in the foils lying in the window of the choke is equal to

$$P = w \gamma \int_0^a dx \int_{-b}^b E^2 dy = \frac{I^2}{2abw\gamma} + \frac{1}{2\mu_0\rho} E_2^2 \cdot \left[\frac{W}{m} \right] \quad (10)$$

3.2 Steady state

The steady state in the choke is considered later on. From (9b) it follows that

$$E_2 = n \left\{ I_0 \frac{\omega \cos(\omega t + \alpha_0 - \psi)}{\sqrt{\delta^2 + \omega^2}} \right\} \quad (11)$$

The mean value of P is equal to

$$\hat{P} = \frac{1}{T} \int_0^T P dt = \frac{n^2 I_0^2}{4w\gamma a b} \left[1 + \frac{\xi^2 \omega^2 \gamma w a b}{\mu_0 \rho (\delta^2 + \omega^2)} \right] \cdot \left[\frac{W}{m} \right] \quad (12)$$

The current density J may be written

$$J = \gamma E = \text{Im} \left[\sqrt{2} \underline{J} e^{j(\omega t + \alpha_0)} \right] \quad (13)$$

where Im denotes imaginary part and

$$\underline{J} = J_0 \left[1 + \frac{2j\xi\omega\gamma w a b}{\delta + j\omega} \cos h \left(2,04 \frac{x}{h} \right) \cos \frac{\pi y}{b} \right] = |\underline{J}| e^{j\psi} \quad (14)$$

$$J_0 = \frac{n I_0}{2 \sqrt{2} a b w \gamma}$$

In¹, using the serial reactions of eddy currents method, the following formula has been worked out

$$\underline{J} = \underline{J}_1 \left[1 + j\alpha \sum_{n=1}^{\infty} (\cos n\pi \frac{y}{b} - \cos n\pi) F_n(x) \right], \quad (15)$$

where

$$\underline{J}_1 = J_0 \frac{1 + j\alpha \sum_{n=1}^{\infty} (\cos n\pi \frac{y}{b} - \cos n\pi) F_n(x)}{1 - j\alpha \sum_{n=1}^{\infty} F_n(x) \cos n\pi},$$

$$F_n(x) = \frac{\sin \pi \frac{c}{b}}{n^2 \sin h(n\pi \frac{h}{b})} \cos h \left(n\pi \frac{x}{b} \right),$$

$$\alpha = \frac{2 \omega \mu_0 \gamma w a b^2}{\pi^2 c}$$

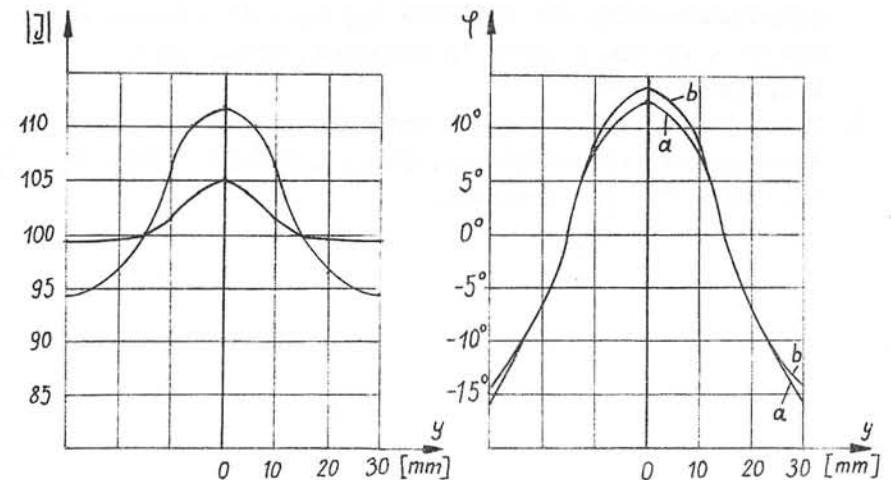


Fig.2 Diagrams of the function |J| and phi for x = 0 a) according to (15), b) according to (14).

In order to compare the results, the calculations were made for $c = 1$ mm, $a = 4c$, $b = 30c$, $h = 20c$, $w = 1$, $J_0 = 100$, $\omega\mu_0\gamma = 12600$ m⁻² - Al at $f = 50$ Hz. On the ground of them fig.2 is made. The differences between $|\underline{J}|$ and φ given by (14) and the exact values of these parameters given by (15) are not greater than 7 %.

References

1. W. Lipiński, "Analysis of Current Density Distribution in Foil Windings of Chokes", *Archiwum Elektrotechniki*, 1974, 23, (3), pp. 667 - 675 (in Polish)
2. K. Maurin, "Methods of Hilbert Spaces" (PWN, 1967)
3. S. G. Mikhlín, "The Problem of the Minimum of a Quadratic Functional" (Holden - Day, 1966)
4. N. Mullineux, J. Reed, I. Whyte, "Current Distribution in Sheet and Foil Wound Transformers", *Proceedings IEE*, 1969, 116, (1), pp. 127 - 130
5. P. Rolicz, "Calculation of Impedance of Conductors by Direct Methods of Functional Analysis", Doctoral Thesis, Polytechnic of Szczecin, 1973 (in Polish)
6. I. Sieradzki, "Stromverteilung im Leiterquerschnitt bei Wechselstromspulen mit Al - Folienwicklung und Optimierungsmassnahmen für Drosseln von Hg - Etlandungslampen mit Al - Folienspulen", *XI Internat. Wiss. Koll. T.H. Ilmenau*, 1966
7. P. E. Sobolevskii, "Bubnow - Galerkin Method for Parabolic Equation in Hilbert Space", *Dokl. A.N.SSSR*, 1968, 178, (3), pp. 548 - 551 (in Russian).

SECTION E COMPUTER AIDED DESIGN

APPLICATION OF INTERACTIVE GRAPHICS TECHNIQUES TO MAGNET DESIGN

M J Newman

Rutherford Laboratory, Chilton, Didcot, Oxon, OX11 0QX

1. INTRODUCTION

The purpose of this paper is to show how the techniques of interactive graphics can be used as an effective tool to enable a designer to make the best use of the power of modern computers. The design process is analysed to see which functions are suitable for computers and which need experienced human intervention.

The capabilities of interactive graphics techniques are reviewed, and areas of the design process where they can be of assistance are identified. Existing programs for magnet design which use these techniques are reviewed, and finally, a general purpose computer-aided design system which is being implemented at the Rutherford Laboratory is described.

2. ANALYSIS OF THE DESIGN PROCESS

The problem of designing a magnet is a particular case of the general problem of minimising a non-linear function of many variables, subject to non-linear constraints. Algorithms for solving such general problems are not known even for local minima, let alone global minima. Unfortunately, the magnet design problem is even more difficult than this. Figure 1 shows a block diagram of a typical optimisation algorithm to find a local minimum with say linear constraints and where first derivations of the function are available.

When we attempt to interpret this diagram in terms of magnet design we see immediately why the problem is difficult. It is usually not too difficult to specify the constraints and the function to be minimised. For example the function might be the inhomogeneity of the field strength over a given volume of space. Typical constraints would be the minimum central field strength, and the minimum aperture needed to gain access to the uniform field region. However, the number and form of the independent variables cannot be specified so easily, and in general may be said to be unlimited. The experience of the designer is immediately invoked to limit the number of variables and impose further constraints

which he hopes will result in a solution not too far from the true minimum. Of course, if he decides not to use iron for concentrating the flux, and if he limits the complexity of the conductor configuration, he will be able to solve the problem automatically on a computer using known algorithms - always providing that he can provide an initial guess that will lead to a sensible local minimum.

However, for most designs the problem will be approximately as shown in Figure 2. Having decided on the constraints and the function he wishes to minimise, the designer makes a guess at a configuration of iron and conductors and at values for their properties (ie. permeability curve and current density) which his experience indicates will meet the constraints and produce a reasonable design. This is the step which we are furthest from being able to do on a computer.

The next step is to set up a discrete model. As is usual with a continuum problem such as this, a model must be constructed which approximates the real problem by a finite number of discrete elements. As the number of elements is increased and their size decreased, the results of the analysis should converge to a true solution of the continuum problem. Figure 5 shows an example of such a mesh. The total number of elements will be limited in practice by the computing power available. It is therefore important to suit the size of elements to the local needs of the geometry. The decision on how to distribute the elements has normally been taken by the designer, although some progress is being made towards allowing the program to optimise this choice.⁽¹⁾

The next step of analysing the model is the only step which can be done without human intervention.

For a given guess at the geometry and current densities, it will be necessary to try several models of increasing refinement to get a reliable measure of the error introduced by the model. The decision as to what criteria to apply to the results of the analysis in deciding whether the model is sufficiently refined is certainly also a long way from being suitable for an automatic algorithm.

Similarly, the designer is almost always involved in deciding whether a particular guess has satisfied his constraints. It is usually much easier for him to make this decision than it is for him to specify his constraints to a computer in a general form. Usually his constraints will not be met until he has refined his guess at the solution several times. Indeed, sometimes this loop is never left because of time limitation, and the resulting design is a compromise. When the constraints are satisfied, he may refine his guess in order to try to reduce the value of the function he is trying to minimise.

It is clear from this description of the design process, that most of the decisions are taken by a human. We hope to show that the techniques of interactive graphics are a valuable tool in making these decision as easy and as fault-free as possible.

3. REVIEW OF INTERACTIVE GRAPHICS TECHNIQUES

An interactive graphics system consists of the hardware and software necessary to allow a fluent dialogue between man and computer with input and output in some graphical form. Systems with a wide range of sophistication and cost are employed in many applications. The usual medium for high speed graphical output is some form of cathode-ray tube (CRT). One convenient way of classifying these is into storage tube devices and refresh devices. Refresh devices can be either raster scan or directed beam. Each type of device has advantages and disadvantages which make them best suited to certain applications.

In a refresh CRT (of which the domestic television set is an example) an image is sustained by repeatedly reproducing the necessary electron beam at a rate which is fast compared with the natural persistence of the phosphor on the screen. A small computer or part of a large computer is devoted to this task of refreshing. With a raster scan device the information is stored in the computer in a line by line digital form. This data is scanned and reproduced on a TV type monitor. With a directed beam device, the electron beam can be directed to any part of the screen. Different parts of the screen can be illuminated in any order.

In a storage tube, each image is produced once and is continuously

refreshed by the hardware of the device. The picture can be added to indefinitely and will remain in view. When a different picture is needed, the whole screen is erased with a bright flash, and a new picture can be stored. Storage devices all use directed beam techniques.

Various hardware options are available to perform graphics functions more quickly than with software. The following list gives an indication of what is available:

1. Character Generation.
2. Vector Generation.
3. Curve Generation.
4. Blinking or Flashing.
5. Dotted or Dashed Vectors.
6. Range of Character Sizes and Fonts.
7. Translation.
8. Scaling.
9. Rotation.
10. 3D Transformations
11. Windowing and Clipping.
12. Multiple Intensity Levels.

The advantages of directed beam refresh devices are that the picture can be partially or completely changed between refresh cycles thus simulating dynamically changing data, and hardware transformations can be implemented comparatively easily. All refresh devices can support a range of intensity levels. The disadvantages are that they are comparatively expensive (£10K - £40K), and the amount of information which can be displayed is limited by the onset of an irritating flicker when the time taken to reconstruct the picture becomes greater than the persistence time of the phosphor. They also require either an extra independent small computer, or some fraction of the store and processing power of a large computer. They are most suitable for applications involving a limited amount of information which is changing rapidly (eg. monitoring air traffic).

The advantages of raster scan refresh devices is that the information content can be much greater, and the monitors can be good quality TV tubes which are comparatively cheap. Several monitors can be attached to

one controller. Domestic colour TV sets can also be adapted. The cost is in the region of £10K. They are most suitable where good quality pictures containing much detail including grey scales are needed and when the data changes rapidly. They become economical when several monitors are required all showing the same picture. The disadvantage is that hardware transformations are more difficult because of the way in which the information is stored.

The advantages of storage tubes are that they are cheap (£2½K - £5½K), that they never flicker, and that an unlimited amount of information may be displayed. The disadvantage is that even if only a small part of a picture is to be changed, the whole screen must be erased (½ sec) and the whole picture redrawn. The time taken to redraw will depend on the amount of information and the line speed. Most cannot support a range of intensity levels. They are most suitable for applications where a large amount of data is to be displayed and erasure is only necessary at comparatively infrequent intervals.

One device is available which attempts to obtain the best of both worlds. This stores the picture on a small storage tube with the facility for selective erasure, and repeatedly scans this tube to reproduce the picture on a TV tube. Selective erasure is obtained by switching the device into erase mode and 'drawing' the vector or character. These devices are not common in the United Kingdom, and no first-hand experience of their use is available.

For graphical input, a range of devices is available:

1. Keyboard.
2. Function switches.
3. Cursor control device.
4. Light Pen.

For some purposes, such as providing numerical values, the keyboard is probably the best device. The function switches are really a special purpose extension of the keyboard. Typically a bank of 16 push buttons is provided with a choice of metallic overlays which identify the meaning allocated to each switch for a particular application program.

However, for many purposes it is more convenient to be able to interact directly with the picture. The most universal way of doing this is to provide a small cross on the screen called a cursor, which can be moved around the screen in a continuous manner by some mechanical device under manual control of the user. Even storage tubes can have a cursor which operates in a dynamic refresh mode. The user will move the cursor until it coincides with the part of the screen he wishes to indicate and then operate some switch which will cause the two co-ordinates of the cursor position to be sent to the program. Many devices are available to control the cursor position. The device which is currently gaining most popularity is called a Mouse. This is a hand-held object which runs on wheels over any horizontal surface. Two orthogonal wheels keep track of the movements. A few finger-operated button switches may be included, thus adding limited function switch capabilities. Other devices are a tablet with stylus, a tracker ball, a joystick, or a pair of orthogonal wheels mounted on the graphics terminal.

The light pen, which is only available on refresh devices, operates by detecting light on the screen when held next to a part of the picture. It can inform a program immediately which picture component is being indicated. Some recent refresh devices allow the light pen to return the co-ordinates of the screen position within a limited accuracy. The light pen can also be used as a cursor control device.

The advantages of cursor techniques are that they can be used on both storage and refresh devices, and that they can indicate positions on the screen which are not illuminated. The disadvantage is that in order to find which part of a picture is being indicated, a software search of the picture co-ordinates must be performed. This may be a slow process for a large amount of data.

The advantages of the light pen are that it can indicate picture parts without a search and that it is a more natural way for a user to operate. The disadvantages are that it cannot be used with storage tubes, and that it cannot indicate positions on the tube which are not illuminated. Some users of light pens find the arm position tiring over a long period and object to the arm obscuring part of the screen.

Connections, between graphics terminals and the computer containing the application program, can range from intercontinental satellite and telephone lines to short fast dedicated lines. If a refresh tube is to be connected over a distance (by telephone line for example) a local small computer will be needed to refresh it. This should be taken into account in cost comparisons.

Computers to which such devices are attached range from a small mini-computer acting as a message switcher in a network, through dedicated medium-sized computers, to large multiprogramming computers.

Since software is becoming an increasingly expensive component of any system, portability between different computers and different graphics devices is becoming of paramount importance. Standardisation amongst graphics packages is a long way from that obtained by Fortran for example. To some extent this represents an inherent difference in capabilities between different types of device.

The choice of a configuration will depend on what equipment is already available, whether the equipment chosen must also suit other applications apart from magnet design, and what the demands on the facilities are likely to be. At the Rutherford Laboratory we have chosen storage tubes with limited cursor control attached to a medium-size real-time computer (GEC 4080) with a fast link to a number crunching host computer. The magnet design application can be programmed in such a way that the disadvantages of a storage tube are not serious compared with the advantage of being able to afford several terminals in simultaneous use to service a large user population. Experiments are also in progress with a refresh device to which hardware for three-dimensional rotation, scaling, and translation, developed at the Laboratory⁽²⁾, has been added. The value of dynamic rotation to portray three-dimensional depth is being estimated.

4. AREAS WHERE THESE TECHNIQUES CAN BE APPLIED

The techniques of interactive graphics have five main uses in the design process.

1. Making subtle errors in the data clearly obvious.

2. Allowing these errors to be corrected immediately.
3. Displaying the mesh model for evaluation.
4. Allowing this model to be edited easily.
5. Displaying the results of the analysis in graph or contour map form for rapid evaluation.

Four areas of application will be examined in detail.

4.1 Data Specification. The main functions of interactive graphics in data preparation are assistance in detection of errors and allowing immediate correction of errors. There are two types of error. The first can be detected by the program because of internal inconsistency. (For example, if two adjacent nodes in a polyhedron are given identical co-ordinates.) The interactive facility allows the user to be informed at the time he inputs the faulty data, and he can correct it immediately while his attention is still focussed on the problem.

The second type of error is more serious because no program can detect it. A typical example is a mis-typed figure which results in data which is completely consistent but totally false. If Figure 3 is compared with Figure 4, the benefits of graphics should be obvious. A good interactive graphics program will display each item of data graphically as it is entered. It will also take every opportunity, subsequently, of displaying all aspects of the data to the user in the hope that subtle errors will be detected as soon as possible. In the batch mode, much computing time and designer time is wasted on such faulty data. Indeed many subtle errors are never detected with disastrous consequences for the accuracy of the results.

Several methods have been used to facilitate the definition of three-dimensional objects. Sutherland's original Sketchpad⁽³⁾ system was extended to three dimensions by Johnson.⁽⁴⁾ This allows the user to define dimensions on the screen with a light pen. Sutherland⁽⁵⁾ has also developed a technique for simultaneously digitising orthogonal views of a three-dimensional object. The accuracy of such methods is generally not sufficient for defining details of the geometry of magnets. Numerical data is best input on a keyboard. Notley⁽⁶⁾ devised a

language for describing the creation of 3D objects. This would need developing to make it competitive with alternatives. Braid⁽⁷⁾ uses a finite set of unit primitives which can be moved, rotated and scaled to synthesise a general solid. His work is aimed at producing tapes for numerically controlled machines. Newman et al^(8,9,10,11) in the original implementation of the GFUN program used a set of shape codes whose dimensions were defined using a parameter format. Newman's MOD3D package (see Section 6) also uses a set of primitives to synthesise a general solid. His POLLY language forms an efficient way of specifying the dimensions in a natural way which is easy to use.

4.2 Generation of the Mesh Model.

4.2.1 Two Dimensions. Much work has been done on algorithms for automatically sub-dividing generally shaped two-dimensional regions into suitably graded finite element meshes. Pathological geometries can usually be found for which any algorithm will either fail, or produce unsuitably distorted meshes. With a range of algorithms available, it is generally possible to select one which will solve the problem. Alternatively details of meshes can be refined by hand using light pen or cursor techniques. Reid's algorithm⁽¹²⁾ for triangulating multiple regions with included voids consists of superimposing a single equilateral triangle over the whole domain, and sub-dividing until local boundary constraints are met. The user can specify local grading of the mesh size. Beretta et al⁽¹³⁾ use a different approach. A general polygon is automatically divided into a combination of triangles or quadrilaterals by joining nodes. Algorithms are available for further sub-division allowing for all the special cases which may arise. Andrews et al⁽¹⁴⁾ use a version of the Winslow⁽¹⁵⁾ technique. They superimpose a regular triangular mesh over a general polygram (optional arcs for sides) and move nodes near the boundary to lie on the boundary. Finally, internal nodes are relaxed to remove local distortions by moving each in turn to the average of its neighbour's co-ordinates. This algorithm at present only handles single regions and cannot grade the mesh size within a region. Newman⁽¹⁶⁾ produced an interactive graphics version of the TRIM⁽¹⁷⁾ mesh generator. This is aimed at producing a mesh over a rectangular domain including all conductors and air spaces for a finite difference program. Mesh size can be graded within the

limitation that the mesh must be topologically uniform. Jones⁽¹⁸⁾, Zienkiewicz et al⁽¹⁹⁾, Gordon et al⁽²⁰⁾, and Newman et al^(8,9,10,11) all use variations of a common algorithm. A general polygonal region is mapped on to a unit regular polygon of the same order by a polynomial mapping. Butlin's method⁽²¹⁾ is similar and has been extensively developed for interactive use. Libraries of meshed sub-structures can be created for subsequent use. These methods are simple and inexpensive to implement and work well provided the polygon is convex and not too far distorted from the regular polygon. Frederick et al⁽²²⁾ have yet another algorithm which synthesises a mesh based on a crude set of nodes digitised by the user. Martin et al⁽²³⁾ use a combination of automatic fitting of a regular mesh to the boundary and use of a light pen to touch up unsuitable areas.

4.2.2 Three Dimensional. No algorithm is known which will automatically generate a suitably graded mesh for a generally shaped three-dimensional domain. If the problem is 2½D (ie. problem of finite length with uniform cross-section) the two-dimensional algorithms can be used for generating a mesh over the cross-section and some simple algorithm used to sub-divide the length.

For truly three-dimensional problems, most success has been obtained by extending the two-dimensional method of polynomial mapping to handle general polyhedra. Newman et al^(8,9,10,11) have used this technique in the GFUN magnet design program. Hexahedra are mapped on to a unit cube, for example. This can be sub-divided by a specified number of planes in each of the three basis directions. Each sub-cuboid can be further sub-divided into a specified number of tetrahedra. Kamel et al⁽²⁴⁾, and Cook⁽²⁵⁾ each adopt a similar approach. Grading of the mesh size is not automatic. The full power of interactive graphics techniques is needed to allow the user to display sub-sections of his mesh so that he can visualise the process, and decide how to distribute his available elements for maximum efficiency and accuracy. The mesh shown in Figure 5 was obtained from the GFUN program using this technique.

4.3 Refining the Mesh Model. If his analysis shows model dependence, the designer will want to examine his mesh and refine it. He will use his

judgement to decide which parts of the model need a finer mesh, and which parts are possibly unnecessarily refined. This process is highly interactive, and clever use of graphics techniques is needed to highlight the problem area amongst a wealth of data.

4.4 Evaluating the Results. Sometimes the efficiency of a design can be computed as a single number, or a small table of numbers. More usually, the designer will require to know the variation of some property (field uniformity for example) over a one, two or three dimensional domain. He will want this information displayed as a graph or contour map. His choice of domain may depend on the results themselves, and so he needs to be able to interact quickly with the results to re-display them in the best way. This is another ideal application of interactive graphics. Figure 6 was created by the GFUN program. It shows the position and value of the peak field experienced by some superconductors.

5. REVIEW OF MAGNET DESIGN PROGRAMS USING INTERACTIVE GRAPHICS

The first reported use of interactive graphics for magnet design was a conversion of the TRIM⁽¹⁷⁾ batch program. This is a two-dimensional program using finite difference methods and including variable permeability iron regions. The regions in real space are mapped on to a regular triangular mesh in logical space by allocating each real node a pair of logical co-ordinates. The numerical process invoked simulates the effect of pinning an infinitely elastic sheet containing the regular mesh to the real boundaries at the specified positions. The resulting shape of the mesh is identical to the minimum energy configuration of the elastic sheet.

Colonias⁽²⁶⁾ has adapted TRIM to use a refresh graphics device with light pen on a CDC 6600 computer. Logical co-ordinates are picked out using the light pen and the corresponding real co-ordinates are input on the keyboard. The resulting mesh is displayed and can be edited with the light pen. Contour maps of flux distributions resulting from the finite difference analysis are also displayed. Newman⁽¹⁶⁾ has also written the MNEMONIC program which is a similar adaptation of TRIM. This is implemented on a Computek 400/15 storage tube attached to an IBM 360/195 computer. No cursor facility is available, so all input is via the

keyboard. Lari⁽²⁷⁾ implemented a system using a Tektronix T4012 Storage Tube with cursor on an IBM computer. The cursor is used to specify the logical co-ordinates and to edit the mesh. The results are displayed as tables, graphs, or contour maps. Lari⁽²⁸⁾ also adapted the MAGNET⁽²⁹⁾ program for the same hardware. This program allows a limited variety of infinitely permeable iron boundaries.

The next major program to be produced was GFUN^(8,9,10,11) which was the first magnet design program written to make use of interactive graphics. The formulation involves an integral equation which has the advantage of needing a mesh only in the non-linear iron regions. It was also easily extended to three dimensions. All input is by keyboard using a convenient parameter format. The hardware is identical to that described for MNEMONIC. The geometry and the mesh are displayed and can be edited. Data defining particular designs can be stored as a named file on a private data-set. Simple problems can be analysed on-line and also some automatic optimisation can be invoked. A harmonic analysis of the resulting field can be displayed. Results can be displayed as tables, graphs, or contour maps. GFUN has been implemented on many systems in many countries. Work is currently in hand (see Section 6) to improve the interactive graphics facilities and to split the tasks between a minicomputer and the main computer.

Martin⁽³⁰⁾ has written the MAGINT program for conductors only, which is aimed at plasma containment problems for fusion research. Data input is by keyboard, and graphics output is on a Cossor CSD 1000 refresh tube. Display of results includes surface plots with removal of hidden lines.

6. RUTHERFORD LABORATORY COMPUTER-AIDED DESIGN SYSTEM

Apart from a few special programs, the operation of the central computer at the Rutherford Laboratory, an IBM 360/195, is aimed at satisfying a large demand for batch processing. The GFUN interactive graphics magnet design program (one of the special programs) occupies 210 Kbytes of memory for several hours each day, but only uses the central processor for a few per cent of that time. We are in the process of transferring the interactive graphics part of the program, which does not need such a powerful computer, into a medium size computer, a GEC 4080. The hardware

and software of this computer is aimed at the interactive environment. When functions are requested which do need the power of the main frame, a batch job will be launched via a high speed link, and the output from this job retrieved along the same route. This method of operation will improve both the batch efficiency in the main frame and the interactive service. Several simultaneous users will be allowed without the schedule being restricted to two hours for a single user as at present. Since it was necessary to redesign the program for a new environment, we are taking the opportunity of splitting the program into several well defined modules. Each of these will take the form of a Fortran package which could be used for many applications apart from magnet design. With a view to such future developments, a data-base has been designed so that a stress analysis program, for example, could use files containing data for a magnet design and calculate the forces in such a structure. Figure 7 shows the structure of the GFUNMINI system. Five main processes are incorporated:

1. GEOM Geometry Definition
2. MATP Material Properties Definition
3. FEMG Finite Element Mesh Generation
4. ANAL Analysis
5. RESU Result Interpretation.

These processes communicate via files on the database. The file management process FILM handles all GFUNMINI files which are accessed through the data-base manager DBM process. The DCOD process does syntax decoding and error diagnostics for messages received from the keyboard. The DOCU process provides the user with instant up-to-date documentation, also from the data-base. The JOBS process handles communication with the main frame.

6.1 Geometry Definition (GEOM). The purpose of this package is to allow the designer to specify the geometry of iron and conductor regions to the computer with the minimum amount of information. The package also provides graphics illustration of the data as it is being specified, so that errors can be detected and corrected immediately. The keyboard is the main input device since specific numerical values for dimensions need to be supplied.

To facilitate data entry, only a limited number of simple shapes can be defined, and complex general shapes must be synthesised from these. Only closed surfaces which are convex and homeomorphic to a sphere (ie. genus zero) may be used. However, surfaces may intersect, and a region may be defined to be a logical combination of the union or intersection of two or more surfaces or their negations. The three-dimensional shapes are based on the following set of two-dimensional shapes:

1. Triangle
2. Quadrilateral
3. Parallelogram
4. Polygram
5. Circle
6. Sector

A polygram is a polygon, each side of which may optionally be an arc of a circle. Three families of three-dimensional shapes are built from these

1. Cone
2. Prism
3. Surface of Revolution

A cone is defined to be the closed surface formed by a line with one end at a fixed point (vertex) and the other tracing out a closed two-dimensional curve (directrix). The directrix may be any of the six two-dimensional shapes.

A prism is defined to be the closed surface formed by joining corresponding nodes of two similar two-dimensional shapes taken from the same set. The end faces are planar. Each other face must be either planar, or part of the surface of a cylinder or cone. For similarity, both end shapes must have the same number of nodes, and corresponding sides must have the same curvature. Each end face of the prism may be optionally inclined to the axis of the prism which itself may be in any direction. The end faces may be defined as congruent.

A surface of revolution consists of the closed surface defined by rotating

one of the two-dimensional shapes about a given axis by a given angle.

The following set of three-dimensional primitives are available at present. The user specifies a four letter name, and the system understands the symmetry inherent in each figure.

FAMILY	2D SHAPE	CONGRUENCE	NAME
CONE	TRIANGLE	-	TETRAhedron
CONE	QUADRILATERAL	-	PYRAmid
CONE	CIRCLE	-	CONE
PRISM	TRIANGLE	YES	TPRISM
PRISM	TRIANGLE	NO	WEDGE
PRISM	QUADRILATERAL	YES	QPRISM
PRISM	QUADRILATERAL	NO	HEXAhedron
PRISM	PARALLELOGRAM	YES	BRICK
PRISM	CIRCLE	YES	CYLinder
PRISM	POLYGRAM	YES	PPRISM
REVOL.	CIRCLE	-	SPHERE
REVOL.	CIRCLE	-	TORUS

These primitives are illustrated in Figure 8. The designer first conceptually divides his general three-dimensional shape into regions which can be formed from these primitives. Each surface is defined using the POLLY language which is decoded by the package and stored as a set of three-dimensional co-ordinates. The co-ordinates of a node can be specified in four ways.

1. Three numeric values separated by one or more spaces.
2. If only one or two of the co-ordinates differ from the last node defined, one or two alphanumeric fields in free format.
3. An incremental version of 2.
4. By the cursor, if it coincides with any previously defined node.

The incremental alphabetic codes are U or D for up or down, L or R for left or right, and O or I for out or in, each with respect to the screen basis. For codes to define absolute co-ordinates as opposed to incremental, T is added to these codes. If the direction of the edge being defined is not along the screen basis directions, several codes can be combined on a single line, and a vector sum will be taken. The numeric value follows immediately after the code letter in free format.

For example, to define an orthogonal block 40 x 20 x 5 units, the commands would be:

```

SHAP = BRIC (defines 3D primitive)

Ø ^ Ø ^ Ø (defines co-ordinates of corner)

R4Ø (defines the first edge)

U5 (defines next edge and complete end face, since
    opposite edges of a brick are parallel)

02Ø (defines third basis vector, and the complete brick)

```

The object is developed on the graphics tube as each item of data is specified. Any error can be immediately erased by typing the privileged code E.

Various display options will be available. The user will be able to scale, move or rotate his objects, and view them with one of the following set of projections:

1. Cabinet projection (default)
2. View from infinity
3. Perspective view
4. Hidden line perspective

5. Stereo wire frame perspective pair.

An example of the hidden line perspective view is shown in Figure 4. If the object has planes of symmetry, these can be specified to reduce the amount of data even further. The data can be edited and stored on the data-base.

6.2 Finite Element Mesh Generation This will be a suite of packages, each of which can take a geometry file and sub-divide it as automatically as possible into small elements (tetrahedra, or triangular or quadrilateral prisms). The first to be implemented uses the same technique as the present GFUN program. A hexahedron, for example, is mapped by a polynomial mapping on to a unit cube. The user may specify a number of planes in each of the basis directions to sub-divide this cube. Each smaller cuboid can be further sub-divided into a specified number of elements in a regular way. The mapping is inverted to find the co-ordinates of the elements in the original hexahedron. (See Figure 5.) This method is cheap to compute and effective, provided the general polyhedron is not too far distorted from the equivalent regular polyhedron. Other algorithms will be added in a modular fashion. Mesh files are also stored on the data-base.

The analysis process (ANAL) will collect data from a specified set of geometry and mesh files and material property files, and submit a batch job to the main frame. When the result file is available on the data-base, the RESU process will be used to display the results in a similar fashion to that employed in the present GFUN program (eg. Figure 6).

Each process is coded in standard ANSI Fortran to ensure a high degree of portability between machines. The data-base manager uses the standard data management software available on all similar computers, the unit of data being a sequential file. The graphics package is GINO-F.⁽³¹⁾ This is also almost all in Fortran and provides a high degree of device independence. It is also available at many centres.

Such a system could form a basis for a network of interactive graphics computing facilities. A small remote station could consist of a cheap storage tube (eg. Tektronix T4010) connected by telephone line to a

remote graphics computer (eg. GEC 4080) containing the CAD system software. Users whose demands were greater could have a local graphics computer serving several terminals.

7. CONCLUSIONS

Magnet design has progressed a long way since 1960 when the beam transport magnets for the Nimrod Accelerator at the Rutherford Laboratory were designed. Computers were much less powerful, and experience in even two-dimensional magnetostatics programs was limited in the United Kingdom. The design process consisted of building small-scale model magnets (6 months from start of paper design to delivery of model) and constructing special apparatus to measure the very accurate fields involved. Refinement of the model in the best case consisted of using non-magnetic jacks to support varying thicknesses of steel shim on the pole-pieces, and experimentally determining the optimum shim size. In the worst case, part or all of the model had to be machined.

Not only can the whole design be done in a fraction of the time now, but the resulting design is often closer to the ideal requirement because experimenting on the computer is a comparatively rapid process. When a large project is to be designed and built, it is important to keep the design time within reasonable limits without launching into production with an inferior design. It is this problem to which the techniques of interactive graphics are so well suited. The designer is able to make full use of the computer while being able to concentrate on the aspects of the design for which he is best suited.

There is still room for refinement of techniques in several areas. General three-dimensional mesh generators with automatic grading of the mesh size will be a major step forward. Several techniques for displaying three-dimensional objects on a two-dimensional screen need to be experimented with. The possibilities of networks need to be exploited.

Magnet design is a large potential growth area for interactive graphics. As hardware costs come down; as machine and device-independent code becomes a reality; and as networking makes powerful facilities available remotely, it will be surprising if such techniques do not become

common-place for magnet design within 5 years.

8. REFERENCES

1. Leyvraz, R. Iterative Generation of Optimal Triangular Grids for the Solution of 2-Dimensional Field Problems. Proc. COMPUMAG Conf. on the Computation of Magnetic Fields, Oxford, April 1976.
2. Holmes, M and Thorne, A R. The Design of a Graphics Processor. RL-75-190, 1975.
3. Sutherland, I E. Sketchpad, a Man-Machine Communication System. Proc. Spring Joint Computer Conf., Michigan, May 1963.
4. Johnson, T E. Sketchpad III; A Computer Program for Drawing in Three Dimensions. Proc. Spring Joint Computer Conf., Michigan 1963.
5. Sutherland, I E. Three-Dimensional Data Input by Tablet. Proc. IEEE 62, No.4, April 1974, p.453.
6. Notley, M G. A Graphical Picture Drawing Language. Comput. Bull. 14, No.3, March 1970, p.68.
7. Braid, I C. The Sythesis of Solids Bounded by Many Faces. Commun. Ass. Comput. Mach. 18, No.4, April 1975.
8. Newman, M J, Trowbridge, C W, and Turner, L R. GFUN: An Interactive Program as an Aid to Magnet Design. Proc. 4th Int. Conf. on Magnet Technology, Brookhaven, 1972.
9. Newman, M J, Simkin, J, Trowbridge, C W and Turner, L R. GFUN User's Guide - A User Guide to an Interactive Graphics Program for the Computer-Aided Design of Magnets. RHEL/R244, 1972.
10. Collie, C J, Diserens, N J, Newman, M J and Trowbridge, C W. Progress in the Development of an Interactive Computer Program for Magnetic Field Design and Analysis in Two and Three Dimensions. RL-73-077. Also in Proc. Conf. on Analysis of Magnetic Fields, Nevada, 1973.
11. Armstrong, A G A M, Collie, C J, Diserens, N J, Newman, M J. Simkin, J, and Trowbridge, C W. New Developments in the Magnet Design Computer Program GFUN. RL-75-066. Also in Proc. 5th Int. Conf. on Magnet Technology, Rome, 1975.
12. Reid, J K. Mesh Generation. Proc. Finite Element Symposium, Atlas Computer Laboratory, Chilton, March 1974.
13. Beretta, L, d'Amico, G and Tiramani, A R. TMG - A Program for the Automatic Discretisation of a Plane Region. G2/28-6, ENEL, Milan. 1974.
14. Andrews, D H and Marshall, J F. GFUN Mesh Generator: Status on 27 June 1975. RL-74-108 (revised) 1975.
15. Winslow, A M. Numerical Solution of the Quasilinear Poisson Equation in a Non-Uniform Triangular Mesh. Jnl. of Computational Phys. 1, No.2, 1966.
16. Newman, M J. MNEMONIC: An Interactive Graphics Program to Generate a Triangular Mesh for TRIM. RL-73-126, RHEL/R238, 1972.
17. Winslow, A M. Numerical Calculation of Static Magnetic Fields in an Irregular Triangle Mesh. UCRL.7784.
18. Jones, R E. A Self Organising Mesh Generation Program. J.Press. Vessel Tech. August 1974.
19. Zienkiewicz, O C and Phillips, D V. An Automatic Mesh Generation Scheme for Plane and Curved Surfaces by 'Isoparametric' Co-ordinates. Int. J. Num. Meth. Eng. 3, No.4, pp.519.
20. Gordon, W J and Hall, C A. Construction of Curvilinear Co-ordinate Systems and Applications to Mesh Generation. Int. J. Num. Meth. Eng. 7, pp. 461, 1973.

21. Butlin, G A. Interactive Graphics for Finite Elements. Proc. Finite Element Symposium, Atlas Computer Laboratory, Chilton, March 1974.
22. Frederick, C O, Wong, Y C and Edge, F W. Two-Dimensional Automatic Mesh Generation for Structural Analysis. Int.J. Num. Meth.Eng. 2, No.1. p. 133, 1970.
23. Martin, T J and Sykes, A. Applications of Interactive Computing in a Scientific Environment. Proc. Int. Conf. on On-line Interactive Computing, Brunel, 1972, Vol.2, p.747.
24. Kamel, H A and Shanta, P J. A Solids Mesh Generator and Result Display Package. J. Press. Vessel Technology, August 1974, p.207.
25. Cook, W A. Body Oriented (Natural) Co-ordinates for Generating Three-Dimensional Meshes. Int. J. Num. Meth. Eng. 8, p.27, 1974.
26. Colonias, J S. Calculation of Two-Dimensional Magnetic Fields by Digital Display Techniques. Proc. 2nd Int. Conf. Magnet Technology, Oxford, 1967.
27. Lari, R J. A Graphic, Time-Sharing Version of the Computer Program TRIM for Magnet Design. ANL/RJL-10, Feb. 1974.
28. Lari, R J. A Graphic, Time-Sharing Version of the Computer Program MAGNET for Magnet Design. RUL-R6209, ANL/RJL-11, Nov. 1974.
29. Lamb, W H. Instructions for using Program MAGNET. ANL/WHL-1, April 1964.
30. Martin, T J. The Interactive Design of Magnetic Fields for Controlled Thermonuclear Research. Proc. COMPUMAG Conf. on Computation of Magnetic Fields, Oxford, April 1976.
31. Gino-F, A Brief Introduction to the Facilities. Computer Aided Design Centre, Cambridge, 1973.

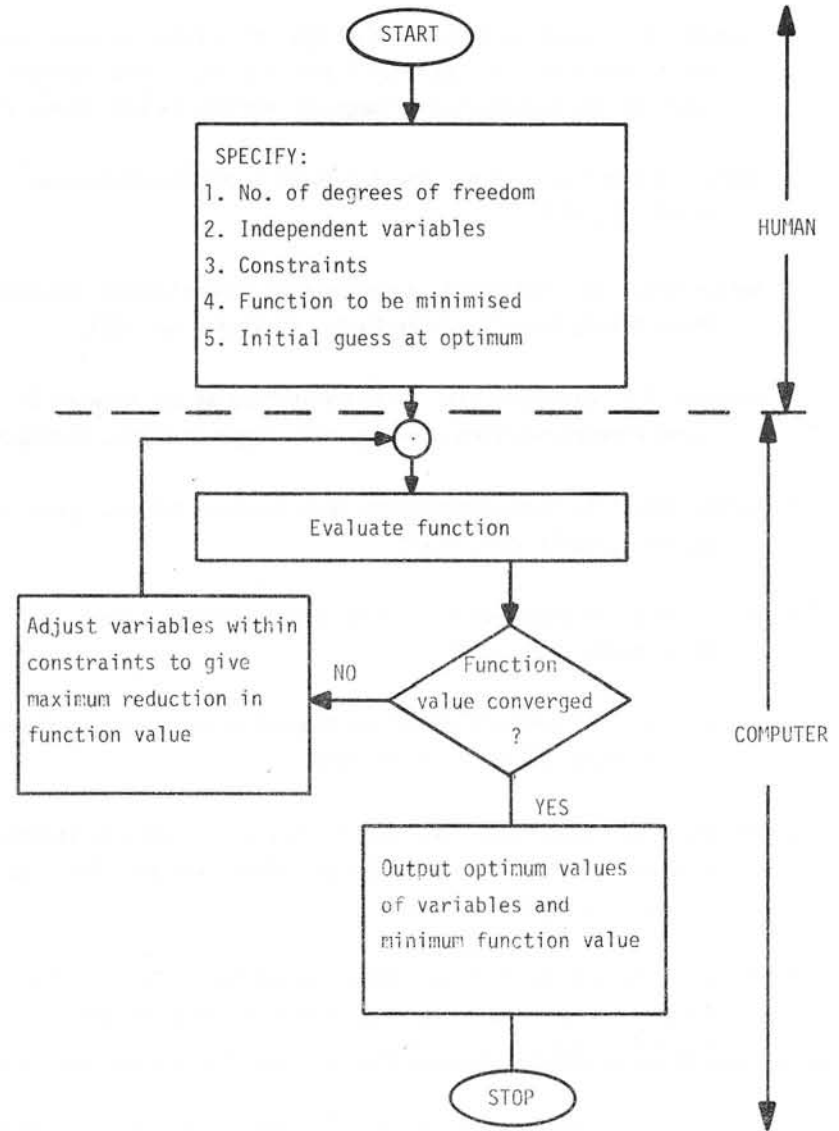


FIGURE 1 - BLOCK DIAGRAM OF OPTIMISATION ALGORITHM

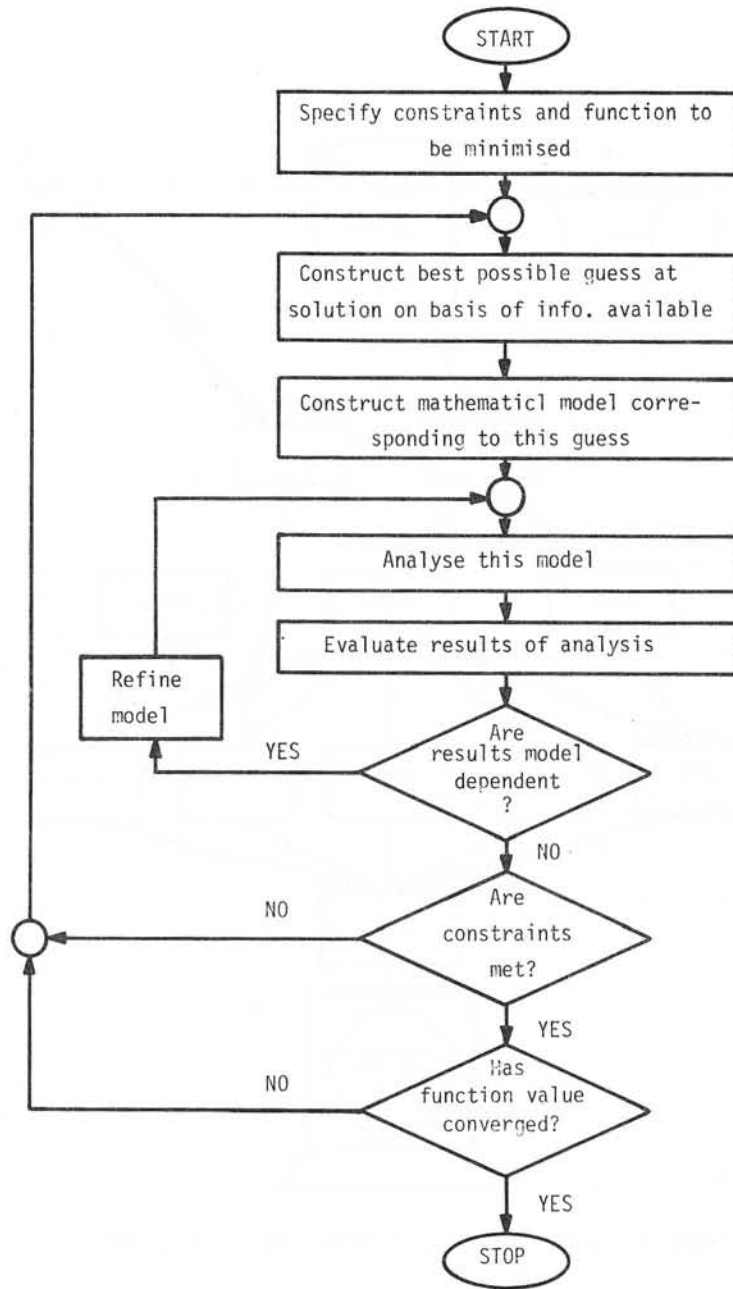


FIGURE 2 - BLOCK DIAGRAM OF DESIGN PROCEDURE

0.0	0.0	0.0	6.83	3.41	0.0	6.83	13.65	0.0
27.3	0.0	0.0	20.48	3.41	0.0	8.19	10.24	0.0
27.3	3.41	0.0	19.11	6.83	0.0	19.11	10.24	0.0
0.0	3.41	0.0	8.19	6.83	0.0	20.48	13.65	0.0
0.0	0.0	27.3	6.83	3.41	27.3	6.83	13.65	27.3
27.3	0.0	27.3	20.48	3.41	27.3	8.19	10.24	27.3
27.3	3.41	27.3	19.11	6.83	27.3	19.11	7.24	27.3
0.0	3.41	27.3	8.19	6.83	27.3	20.48	13.65	27.3
0.0	13.65	0.0	0.0	3.41	0.0	23.89	3.41	0.0
27.3	13.65	0.0	3.41	3.41	0.0	27.3	3.41	0.0
27.3	20.48	0.0	3.41	13.65	0.0	27.3	13.65	0.0
0.0	20.48	0.0	0.0	13.65	0.0	23.89	13.65	0.0
0.0	13.65	27.3	0.0	3.41	27.3	23.89	3.41	27.3
27.3	13.65	27.3	3.41	3.41	27.3	27.3	3.41	27.3
27.3	20.48	27.3	3.41	13.65	27.3	27.3	13.65	27.3
0.0	20.48	27.3	0.0	13.65	27.3	23.89	13.65	27.3

FIGURE 3 - TABLE OF CO-ORDINATES CONTAINING SINGLE DIGIT ERROR

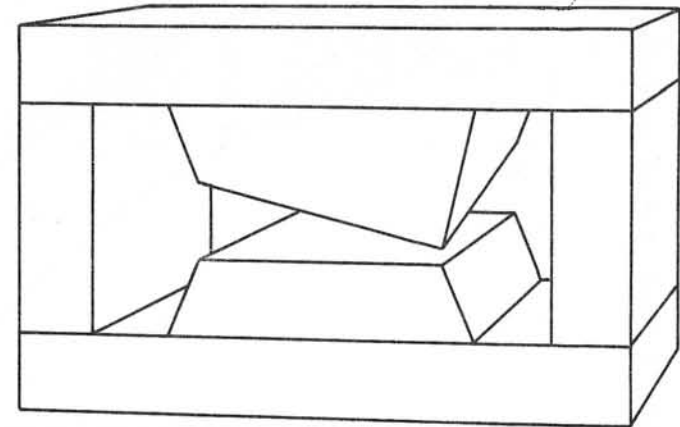


FIGURE 4 - COMPUTER DISPLAY SHOWING ERROR

GFPI92 FRAME 8 DATE 7/ 10/ 75 TIME 11.34.58
 0 CONDUCTOR ELEMENTS 192 IRON ELEMENTS
 Z-X PLANE

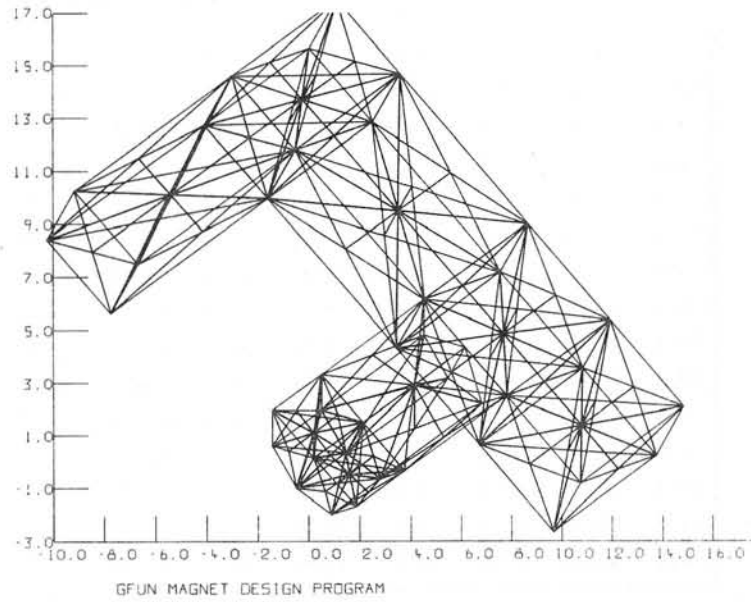


FIGURE 5 - EXAMPLE OF 3D MESH

GFUNWMP, 21 11/ 9/72 AT 12.46. 9 FRAME 14

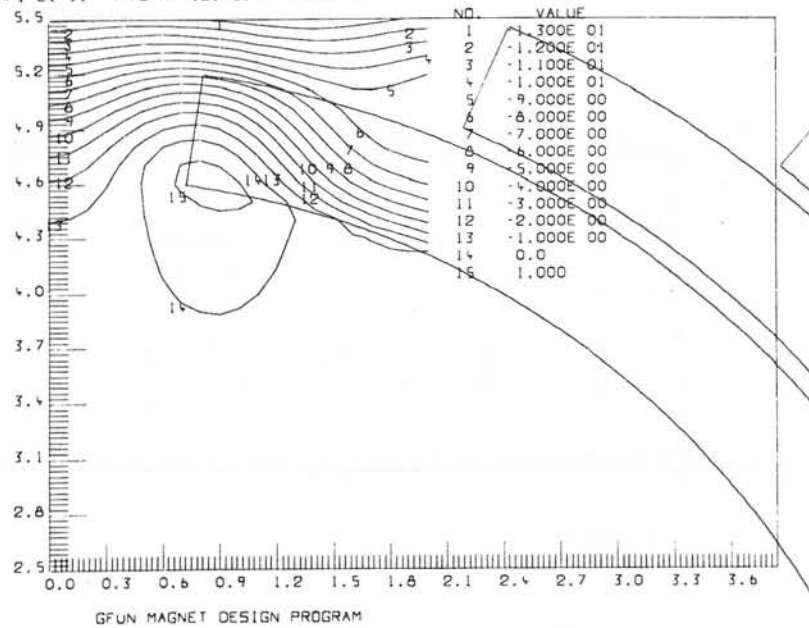


FIGURE 6 - EXAMPLE OF CONTOUR MAP

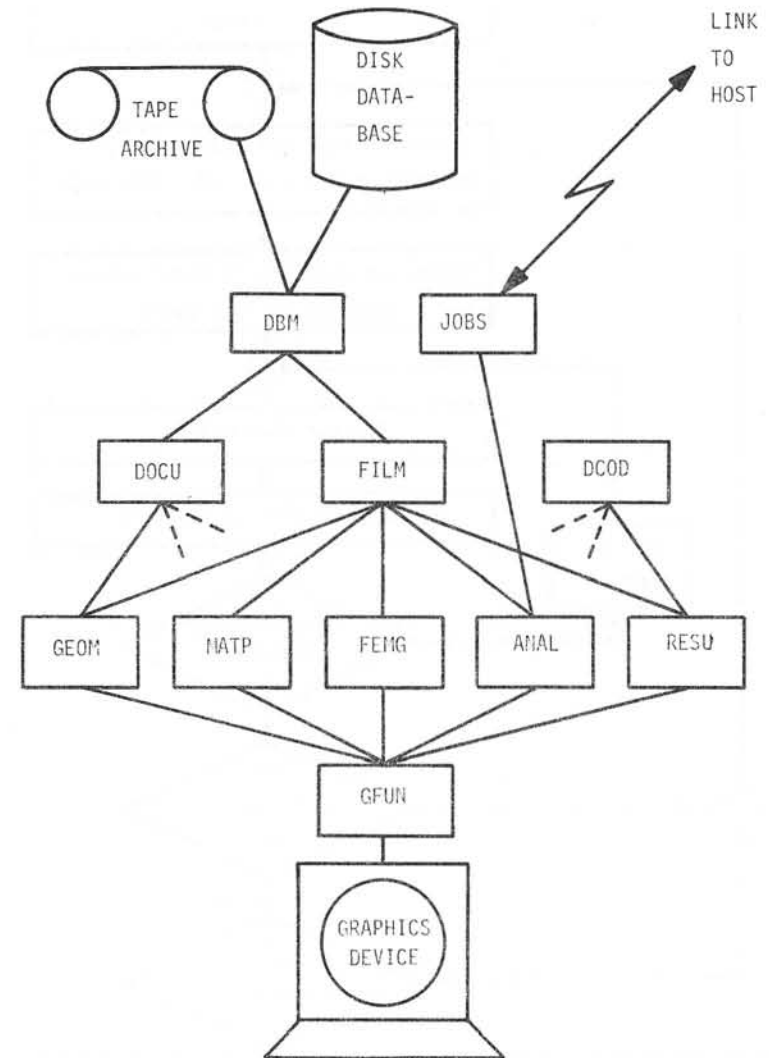


FIGURE 7 - BLOCK DIAGRAM OF GFUNMINI SYSTEM STRUCTURE

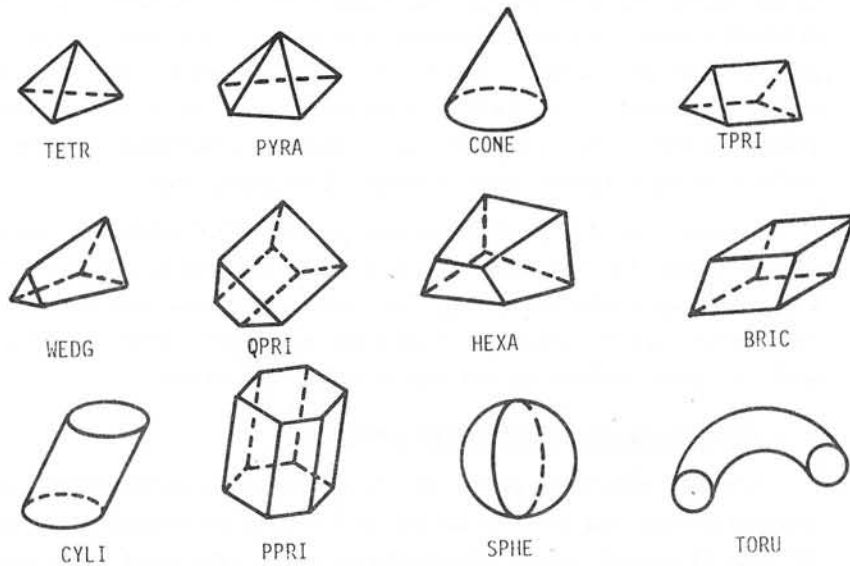


FIGURE 8 - SAMPLE OF 3D PRIMITIVES

Discussion following paper:

(Diserens, Rutherford) What is the future of colour displays in interactive graphics?

(Newman) The development of colour displays is of less immediate importance than monochrome techniques for displaying three dimensional objects. Dynamic rotation and hardware perspective, hidden lines, and intensity variation with depth should be exploited first. If colour can be added independently it would be useful for separating conductors from iron and for distinguishing iron regions of differing permeabilities.

(Jacobs, CERL) You mentioned the development of software to assist users to find mistakes in data input, etc; this must extend to all software development and program usage in the future as software costs increase comparatively fast yet hardware costs will decrease. Could we have your views please?

(Newman) Yes I agree. Fortran, in spite of its lack of flexibility is already accepted as the first language simply because of the guarantee of portability. Standards in graphics packages are already showing some signs of appearing and this again is encouraged by the demand for portable software. There will always be applications for which these standards are in agreement but the vast majority of users will be happy to conform if this saves on software development time. High level interaction packages such as those being developed at the Rutherford Laboratory are a natural extension.

(Luciano, ENEL CRA) I have seen in your review an example of discretization of a plane region ("the front of a church") with holes subdivided into subregions for its discretization. In an improved and more efficient version of that program (paper is available) the mesh may be obtained treating the region with its holes like a whole region, without the need to tear it into subregions.

This means also that data input is much reduced.

THE INTERACTIVE DESIGN OF MAGNETIC FIELDS FOR CONTROLLED
THERMONUCLEAR RESEARCH

T.J. Martin

Culham Laboratory, Abingdon, Oxon, OX14 3DB, UK
(Euratom/UKAEA Fusion Association)

1. INTRODUCTION

The controlled release of energy from nuclear fusion depends on the ability to heat and contain an ionised gas (plasma) of deuterium and tritium for sufficient lengths of time, which may be of the order of seconds. Since the particles are charged, a natural choice for the containment system is one based on magnetic fields. Many such experimental systems have been proposed and built to contribute to the understanding of the problems involved in plasma physics.

In the first instance, the magnetic field topology must satisfy certain constraints and much optimisation must take place before an experiment is eventually built. The cost of these devices demands that extensive calculations and evaluations are made at the design stage thus providing the motivation for the development of the computer program MAGINT described in this paper.

It will be appreciated that many physicists and engineers engaged in the design of magnetic containment systems are not interested in programming for its own sake and are understandably reticent about using computer programs which require complex procedures for setting up data and producing results. A good user image is essential therefore, if manpower (and computing power) is to be utilised in the most efficient and productive manner. To this end, the interactive, magnetic field design program MAGINT offers comprehensive facilities for the optimisation and evaluation of possible conductor configurations, the results where possible being presented in readily assimilated graphical form.

The vacuum magnetic field is regarded as a superposition of one or more elementary, pre-defined analytic fields (e.g. uniform fields) together with any combination of components produced by the following sets of conductor types:

- i. Circular filamentary loops
- ii. Rectangular filamentary loops

- iii. Linear filaments
 - iv. Finite, rectangular cross-section solenoids with constant current density distribution
- and
- v. General curvilinear filaments represented by sets of spatial coordinates joined by straight segments.

A whole range of operations are provided to manipulate and calculate these fields within a versatile and easy-to-use framework.

The program is written almost wholly in standard FORTRAN and runs on the Culham ICL 4-70 computer operating under the MULTJOB regime which provides a fully interactive working environment. Data input to the program is primarily through a conventional teletype and on-line graphical output (generated by the GHOST^[1] package) is directed to a COSSOR CSD1000 refresh display. The total store size required by MAGINT is 120 Kbytes and typical runs consume about a minute of processor time.

Section 2 of this paper introduces the philosophy adopted during the initial design and development stage of the program while section 3 describes the facilities in detail. The numerical methods used for field calculations and for following fieldlines are briefly mentioned and in section 5 some examples in the uses of MAGINT are given.

2. PROGRAM DESIGN AND STRUCTURED DEVELOPMENT

For this program we prefer the interactive mode of operation, rather than batch mode, for not only is the user's train of thought uninterrupted, but he will possess specialised knowledge and/or experience which completes the 'iteration loop' in a manual optimisation^[2]. Additional benefits are that errors in data input and incorrect usage of the program are picked up immediately, resulting in faster turnaround and minimisation of computer time. Disadvantages with the interactive mode are normally restrictions on the size of the program and the complexity of the problem to be analysed, the first being obviated by suitable segmentation of the program. Again by careful programming and selection of optimal numerical methods, it is our experience that useful calculations can be performed on-line for this type of problem. This question is raised again at the end of this section.

During the initial development stage of the program, the following precepts were kept firmly in mind:

- i. The program must be easy to use by both inexperienced and expert computer users.
- ii. The data input should be kept to an absolute minimum.
- iii. The facilities should reflect current requirements and be easily extensible to accommodate growing needs.
- iv. Good protection must be provided against misuse of the program.
- v. Printed output should be minimal unless specifically requested - immediate graphical output being a more efficient vehicle for the transmission of information.

The strategy adopted for data input consistent with the first requirement is that of a command structure. Every program action is invoked by a four-letter mnemonic keyword and an associated parameter. Any additional information required by the program is requested by issuing a prompt at the terminal. After the action has been carried out, the program returns to the command mode in readiness for the next task. As an example, the following command generates sixteen circular loops equispaced around a given torus (hereinafter, all user-typed information will be underlined):-

```
CMND? TOR 16
RMAJ,RMIN,CURRENT?
? 1.0 0.15 1.27E6
16 TYPE 1 TOROIDAL COILS ADDED
CMND?
```

For the user who is familiar with the program, a facility is provided to switch off the prompts so that faster interaction is made possible. At present about sixty commands are available and are described in more detail in section 3. This form of data input has two main advantages; firstly it is easy to learn and use, and secondly it serves to document particular runs of the program.

The minimisation of information typed by the user is achieved in several ways. All program parameters such as contouring matrix size, accuracy criteria etc. are given sensible default values, commands being provided to change them if necessary. In the same vein, to avoid identifying the type of conductor each time some geometric manipulation is performed, the program assumes a "Currently Active Conductor" type with provision for selecting the alternatives. To avoid repeated input of the

same configuration each time the program is executed, sequences are included for storing the geometric details in a magnetic disc file. Finally, specialised commands have been written to take into account any particular configuration symmetry.

The third precept implies a modular program structure so that new facilities can be simply 'plugged in' - an additional advantage being that selected pieces of code may be easily incorporated into other programs.

The final two points are largely self-explanatory; a comprehensive set of diagnostic and error messages being provided to guide the unwary user.

Fig. 1 shows a schematic diagram illustrating the program in its operating environment, the arrows indicating all possible directions of information flow between MAGINT and its hardware peripherals and file storage.

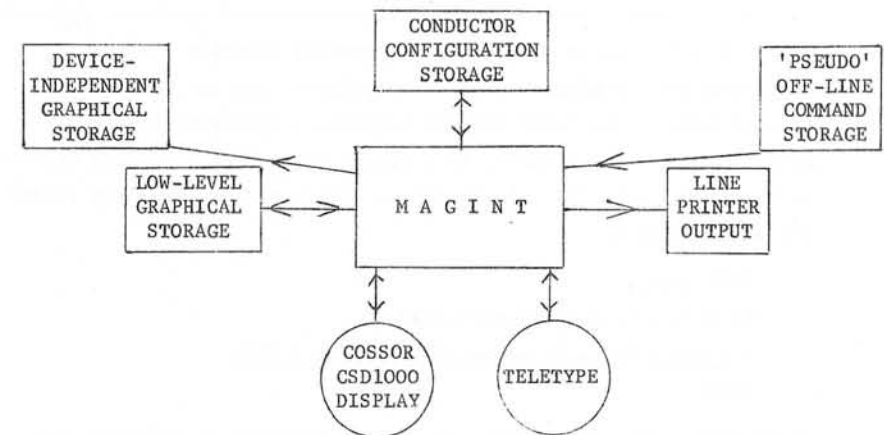


Fig. 1 : Information routes between MAGINT and peripherals

There are of course some aspects of containment system design which require complicated and prolonged calculations such as magnetic surface generation, charged particle and guiding centre trajectory plots. However, MAGINT can be used to set up and verify the configuration before embarking on long (and expensive) batch program runs. A subset of the MAGINT commands that handle conductor manipulation have been incorporated

into a separate input package shared by all the Culham magnetic field programs, thereby creating a completely compatible and uniform user image - a very desirable feature.

3. PROGRAM FACILITIES

All but one of the commands can be classified into five logical subsets, each of which are described in detail below. The exception is the 'USER' command. Provision has been made for executing program actions tailored to suit individual user's requirements. Generally these operations are only of interest to particular people and therefore do not warrant a place in the overall command structure - nevertheless they play an important rôle in ensuring that the designer can perform precisely the operation he has in mind. This facility is introduced by the simple expediency of supplying a FORTRAN subroutine with a pre-defined framework.

3.1 Conductor Manipulation Commands

All of these commands act on the pre-selected conductor type and form a powerful basis with which to speedily assemble the desired configuration. Conductors can be introduced into the system by several means. The 'ADD' command requires a complete geometric specification - for example, if a single solenoid is required centred at the origin with its axis at 45° to the x and y axes, the following would be used:-

```
CMND? ADD 1
XS,YS,ZS,AL,AM,AN,RI,RO,W,CUR?
? 0.0 0.0 0.0 1.0 1.0 0.0 0.5 0.7 0.1 2.75E5
CMND?
```

Right hand screw conventions are used throughout in defining the direction of positive current. Taking symmetries into account, coaxial and toroidal coils can be conveniently distributed by the 'COAX' and 'TOR' commands. For stellarator experiments, 'THLX' is available for generating the toroidal helical windings. It is also possible to interact with the refresh display to draw arbitrarily shaped planar conductors using a tracker cross and ball.

Having established the basic conductor set, commands are provided to perform mirror reflections in any of the three principal planes and to spatially translate and rotate all or specified

conductors together with the option of retaining the originals.

A group of commands to alter specific geometric properties of the conductors is also available, thereby saving a user the task of retyping the complete specification. Centres of coils and their orientation together with currents and individual points on curvilinear conductors may be quickly changed.

Finally, the ability to delete all or selected conductors is introduced through the 'DEL' command, the conductors being uniquely identified by a number assigned at generation time.

The use of these commands is demonstrated in section 5 and it can be seen that a particular construction may be performed in many different ways, the user choosing the one which is most convenient.

3.2 Parameter Setting Commands

On entry to the program, certain common variables used throughout the various sections are given sensibly selected values in order to avoid repeated specification. For example, circular filamentary loops are assumed to be the currently active conductor type, others being invoked by use of the commands 'RECT', 'LINE', 'SLND' or 'CURV'. The user can also set up his own limits for graphs (the default being automatic limits); he can specify the relative accuracy at which the solenoid routines operate or select the type of three-dimensional projection for viewing the conductor configuration. Suppression of data prompts (for experienced users) and altering the matrix size containing the magnetic field components are effected through the 'MSG', 'MU' and 'MV' commands.

Commonly used, predefined analytic magnetic fields are selected by 'ANAL' e.g. an I/R toroidal field being established by the sequence

```
CMND? ANAL 4
TOROIDAL CURRENT?
? 2.96E6
CMND?
```

giving the field

$$B_{\phi} = \frac{2.96 \times 10^6 \mu_0}{2\pi R}$$

3.3 Graphics Commands

Picture information can be handled at two levels; in low-level hardware form using the special instructions related to the COSSOR display or at high, device independent level enabling selected pictures to be processed onto any locally available plotter. 'PSTR' controls whether picture information is retained in a file on disc or only shown once and subsequently lost. In this way picture files can be built up that only contain frames of interest. Commands are available for reshowing, combining and overwriting stored pictures and converting all or selected frames into the device-independent format.

Before any field calculation takes place, it is reassuring for the user to 'VIEW' the conductor configuration in some three-dimensional projection to establish its correctness. (see figs. 2, 3, 4, 5, 6, 7 and 8)

After the magnetic field has been evaluated over some plane, selected quantities can either be contoured (see fig. 10) or three-dimensional, isometric developments of the surfaces can be plotted by the command 'PLTM' (see fig. 11). The matrices of field components are not destroyed, enabling the maximum amount of information to be derived from the relatively costly field evaluations. In addition, the 'BDRN' command plots scaled arrows representing the projected direction and magnitude of the field at each of the matrix gridpoints giving an overall picture of the field without resorting to expensive fieldline calculations.

3.4 Field Evaluation Commands

This important class of commands uses the Culham magnetic field subroutine library to perform the various operations. 'FLDP' and 'FLDL' respectively calculate the cartesian components of the field and its strength at specified points and along an arbitrary line in space, the latter producing a graph of the four quantities together with an optional table printout. 'FLDC' allows the field to be found around a given plotting circle, the results being presented graphically in either a global or natural local coordinate system (see fig. 9). Again, detailed printout may be obtained if required. The user can also specify an arbitrary, rectangular plane over which the field components are evaluated by the 'FLDM' command, graphical

interpretation of the results being performed by 'PLTM' as described in 3.3.

Detailed information about the fieldline structure is obtained from 'FLIN'. The ordinary differential equations of the fieldline

$$\frac{dr}{ds} = \frac{B_z}{|B|}$$

are integrated from a given starting point in both directions until certain stopping criteria operate, the points so obtained being projected onto a given plane and displayed. These pictures can be superimposed on $|B|$ plots to give a comprehensive idea of the field characteristics (see fig. 10).

Fieldlines for the axisymmetric experiments such as the superconducting Levitron are cheaply generated by the 'RAFI' facility where contours of the quantity $R.A\phi$ (where $A\phi$ is the azimuthal component of the vector potential) can be plotted.

3.5 Housekeeping Commands

All or part of the conductor configuration geometry can be directed to the teletype or display by using 'LIST' while the contents of the field component matrices and associated quantities can be sent to an output file which is processed on a line-printer at job termination.

Conductors can be stored and retrieved from a disc file using the 'FILE' and 'READ' options. This facility not only reduces the data input when analysing the same configuration over several runs of the program but also offers additional security against possible system/program failures.

The normal input channel to MAGINT is a teletype, but it is possible, through the 'OBEY' command, to redirect this channel to read commands from a disc file. If any errors are encountered, the program immediately returns to interactive mode for corrective action. In its simplest application, the user might require the same sequence of commands for several different runs of the program.

Finally, provisions are made for adding titles to graphs, obtaining summaries of the assembled configuration and parameter

values and for correctly terminating the program.

4. NUMERICAL METHODS

Closed, algebraic forms derived from the Biot-Savart law for the field due to linear and circular filamentary conductors (the latter involving elliptic integrals of the first and second kind) are well known and are not reproduced here. The rectangular loops and general curvilinear conductors both use the linear segment approximation. Fields due to finite, rectangular cross-section solenoids are calculated from a method by Snow^[3]. Essentially, an infinite series representation of the field is generated for a solid, semi-infinite cylinder, four of which are superimposed to form the solenoid, the current directions being arranged in such a manner as to cancel except in the region of interest.

The method used for integrating the fieldline equations is an eighth order hybrid multistep/Runge-Kutta process described by Butcher^[4]. To advance the integration from one point to the next, derivatives and function values are used from the previous three steps together with intermediate values calculated within the new step. Large steps can be taken with this method whilst maintaining a high degree of accuracy - in fact the step can prove too coarse for some plotting purposes. This is overcome by fitting a seventh order Hermite polynomial to the last four function values and associated derivatives enabling accurate interpolation within the current integration interval.

5. EXAMPLES OF USE

To illustrate the use of MAGINT, we reproduce below the commands which could be used to construct and view the superconducting Levitron configuration shown in fig. 2.

<u>PROGRAM RESPONSES</u>	<u>COMMENTARY</u>
CMND? <u>COAX 3</u>	} Input 3 circular loops coaxial with the z-axis
AXIS 1,2 OR 3?	
? <u>3</u>	
HT, RAD, CUR?	
? <u>0.0 0.3 0.5E5</u>	Superconducting ring
? <u>0.23 0.158 -0.4E5</u>	Inner vertical field coil

PROGRAM RESPONSES
(continued)

COMMENTARY
(continued)

? <u>0.237 0.6 -0.125E5</u>	Outer vertical field coil
3 TYPE 1 COAXIAL COILS ADDED	Confirmatory message
CMND? <u>TRAN -2</u>	} Generates remaining B_v coils in upper plane by the save and translate method
COND NO,DX,DY,DZ?	
? <u>2 0.0 0.0 0.048</u>	Create 2nd inner B_v coil
COND NO,DX,DY,DZ?	
? <u>3 0.0 0.0 -0.044</u>	Create 2nd outer B_v coil
CMND? <u>RFLT 3</u>	} Reflect the four coils in the x-y plane (N.B. Coils in the reflection plane are not duplicated)
4 TYPE 1 CONDUCTORS REFLECTED	
CMND? <u>RECT 1</u>	Select rectangular, filamentary loops
CMND? <u>TOR 12</u>	Generate 12 toroidal B_ϕ coils
RMAJ,A,B,C?	
? <u>0.5325 1.2 0.935 0.83333E5</u>	
12 TYPE 2 TOROIDAL COILS ADDED	Confirmatory message
CMND? <u>PROJ 2</u>	Select conical projection
CMND? <u>VIEW 6</u>	Look at complete configuration (fig.2)
XC,YC,ZC,XE,YE,ZE,RI?	
? <u>0.0 0.0 0.0 90.0 100.0 100.0 1.5</u>	} Specify centre of interest, position of eye and the radius of the sphere of interest
CMND?	

A further example demonstrating the power of MAGINT is in the design of a poloidal field coil assembly for the proposed Joint European Torus experiment (JET). We sought to quantify the magnitude of the perturbations in the field caused by the physical connections to the windings and to find the optimum positions such that the perturbations were minimized. Each connection was represented by a five point general conductor and the final distribution is shown in fig. 8 and the corresponding field perturbations around a plotting circle in fig. 9. This calculation would have been prohibitively tedious to perform without the sophisticated conductor manipulations provided by the program.

6. CONCLUSIONS

The computer program described in this paper was developed in collaboration with those people most closely associated with the design of magnetic containment systems and forms the foundation on which future computational aids will be built.

It was pointed out in the introduction that the program is extensible and new facilities are being added all the time as the need arises. Currently, sections to calculate forces on conductors are being implemented and in the future it is hoped to include the effects of magnetic materials.

7. ACKNOWLEDGEMENTS

The author would like to thank his colleagues at Culham Laboratory, particularly C.M. Wilson and C.J.H. Watson, for their helpful comments and criticisms which have greatly contributed to the shaping of the program as it now exists.

8. REFERENCES

- [1] Prior, W.A.J., "The GHOST graphical output system user manual" Culham Report CLM-PDN 8/71, Issue 2, 1973.
- [2] Martin, T.J. Sykes, A. 'Applications of interactive computing in a scientific environment', ONLINE72, Brunel University, Uxbridge, England, 4 - 7 Sept. 1972.
- [3] Snow, Chester 'Magnetic fields of cylindrical and annular coils', U.S. Dept. of Commerce, N.B.S. App. Maths. Series 38, Dec. 1953.
- [4] Butcher, J.C. 'A multistep generalisation of Runge-Kutta methods with 4 or 5 stages', J.A.C.M. Vol. 14, no. 1, Jan. 1967, pp. 34 - 99.

Discussions following paper:

(Wind, CERN) Does your program take into account the current flowing in the plasma?

(Martin) Not explicitly- however the modular structure of the program makes it very easy to add such a facility. The plasma could of course be modelled by existing filamentary conductors.

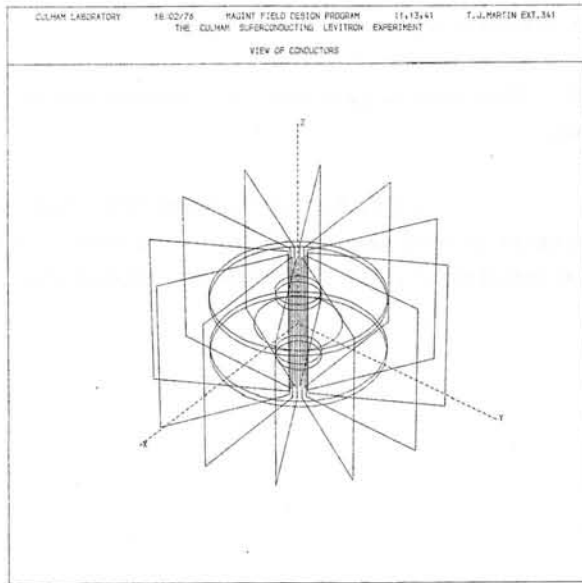


Fig.2 The Culham Superconducting Levitron assembly.

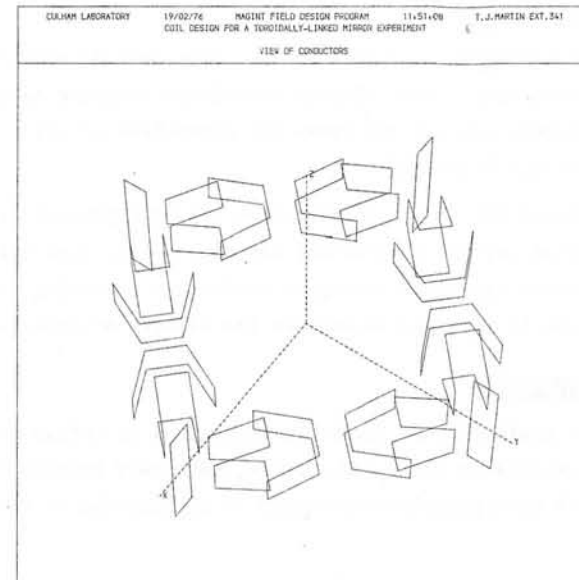


Fig.4 A proposed, toroidally-linked mirror experiment using Yin-Yang coils.

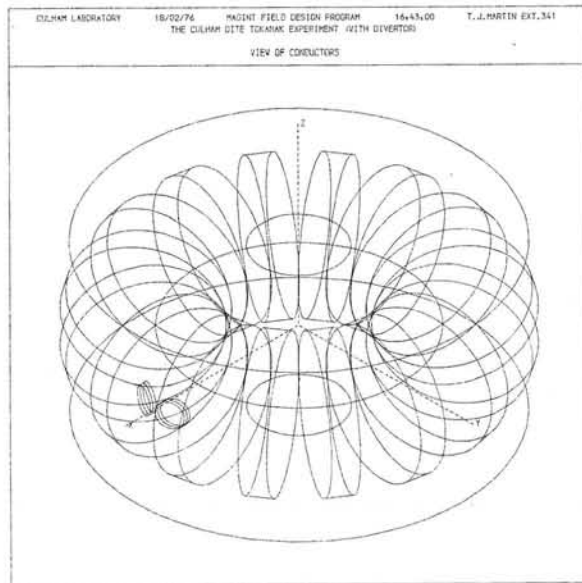


Fig.3 The Culham Dite tokamak experiment with divertor.

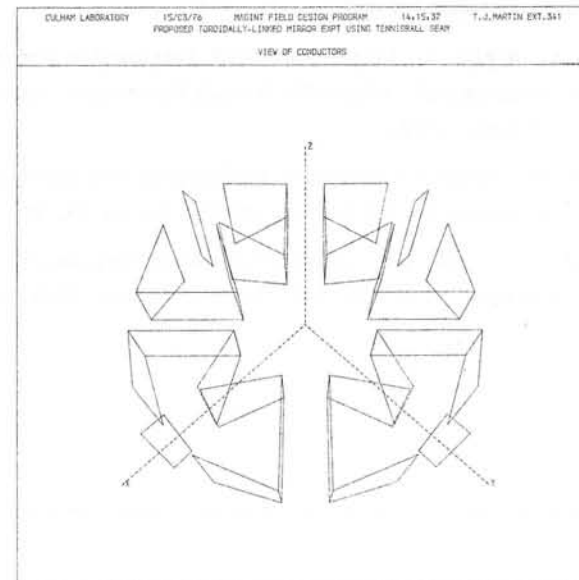


Fig.5 A proposed, toroidally-linked mirror experiment using tennis ball seam conductors.

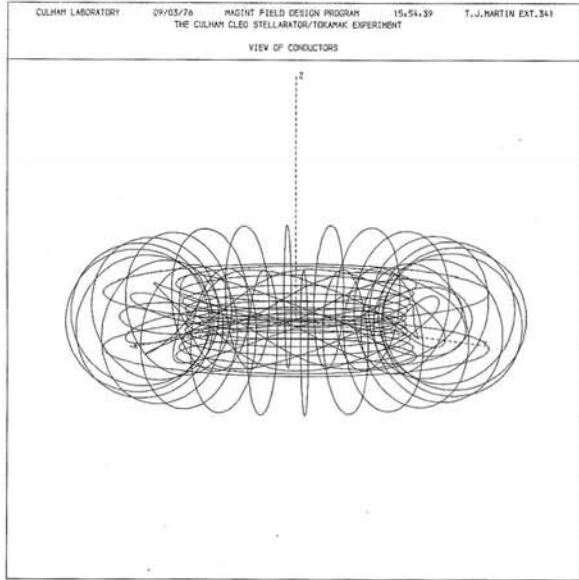


Fig.6 The Culham Cleo Stellarator/Tokamak experiment (general view).

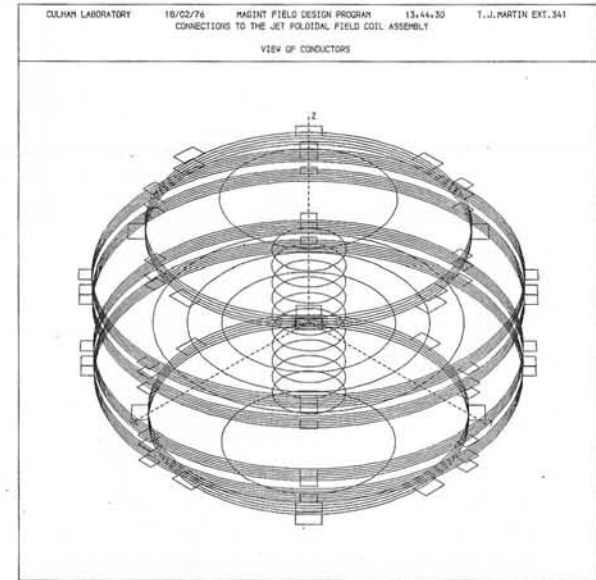


Fig.8 Connections to the poloidal field coils of the proposed JET experiment.

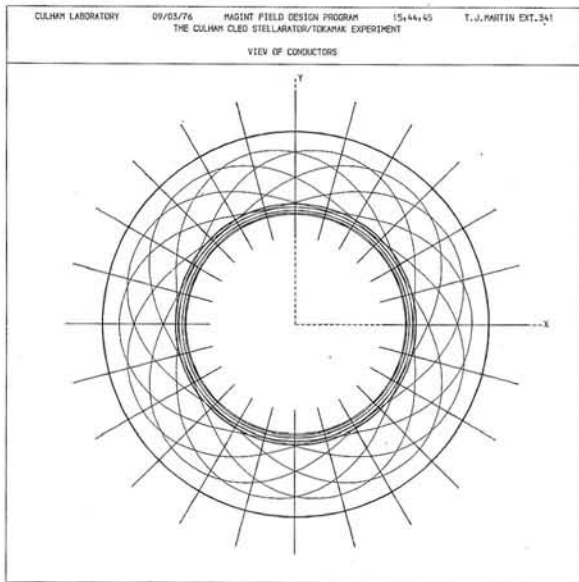


Fig.7 The Culham Cleo Stellarator/Tokamak experiment (plan view).

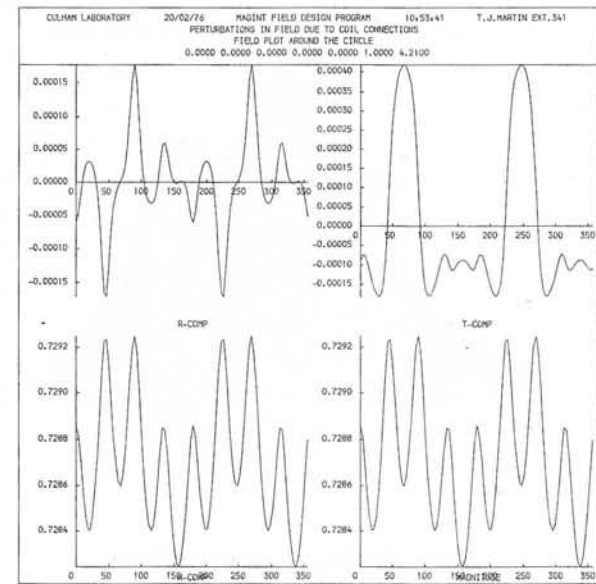


Fig.9 Perturbations in field caused by coil connections (see above).

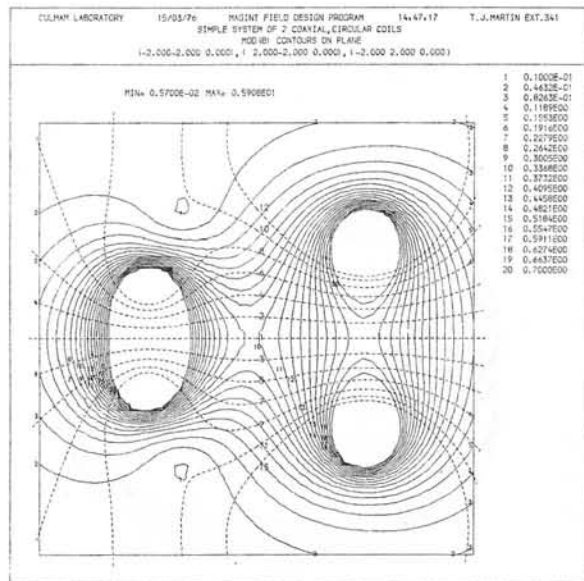


Fig.10 Field lines and $|B|$ contours for a simple 2 coil system.

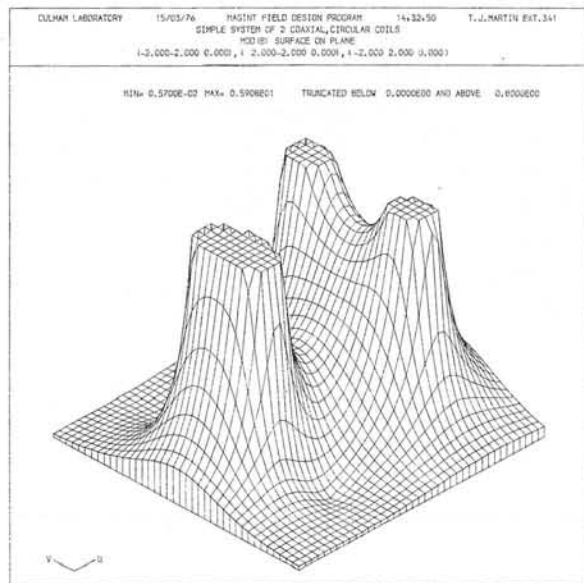


Fig.11 $|B|$ surface for a simple 2 coil system.

DESIGN METHODS FOR TOKAMAK
OHMIC HEATING WINDINGS

A. J. Federowicz, Lois C. Lintner & J. H. McWhirter

Westinghouse Research Laboratories
Pittsburgh, PA 15235
U.S.A.

SUMMARY

The Tokamak Fusion Test Reactor (TFTR) is a device proposed to be completed by 1981 at the Princeton University Plasma Physics Laboratory [1,2]. The device (Figure 1) is planned to achieve a "breakeven" fusion reaction with the assistance of high energy beams of neutral deuterium particles injected into a plasma containing tritium.

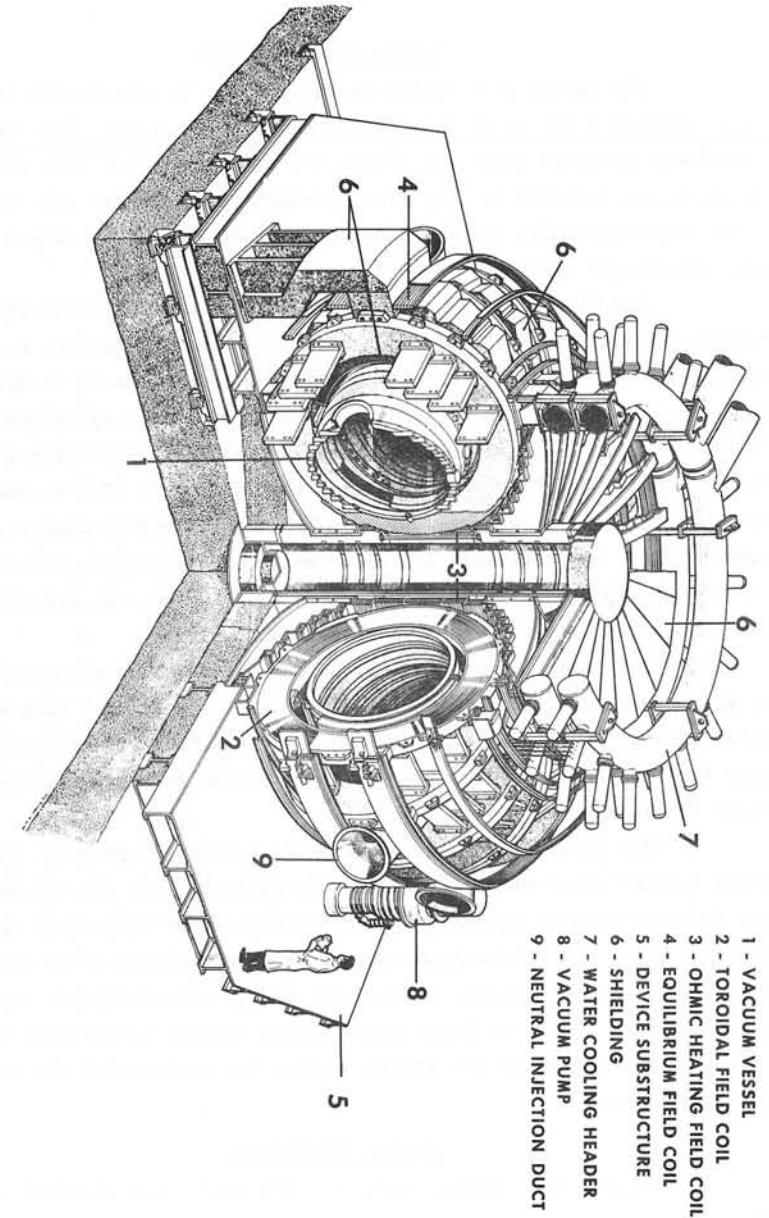
The plasma of a Tokamak device is also heated by an electrical current which is electro-magnetically induced by a changing flux generated by an ohmic heating (OH) winding.

The initiation of the plasma is controlled by a hexapole null. A winding to generate this null could be separate but it has been proposed that both the ohmic heating and the formation of a hexapole null be accomplished by means of the same winding. At this reported stage of development the winding to accomplish the hexapole has been considered as a perturbation on the ohmic heating winding and this perturbation is designed in a separate process. However, it is anticipated that, eventually, both design processes should be combined into one. The techniques which have been used in the conceptual design of the OH winding and the hexapole null are the subject of this paper.

The main intent in this paper is to describe mathematical and computational design processes rather than Tokamak technology or design results. The basis of the design method has been the formulation of the design problem in terms of linear expressions and the optimal solution of the design problem by means of linear programming computer codes.

Other approaches to similar design problems are reported in references 3-5.

Fig. 1 Tokamak Fusion Test Reactor



- 1 - VACUUM VESSEL
- 2 - TOROIDAL FIELD COIL
- 3 - OHMIC HEATING FIELD COIL
- 4 - EQUILIBRIUM FIELD COIL
- 5 - DEVICE SUBSTRUCTURE
- 6 - SHIELDING
- 7 - WATER COOLING HEADER
- 8 - VACUUM PUMP
- 9 - NEUTRAL INJECTION DUCT

DESIGN CONSIDERATIONS

The design description is facilitated by considering the device in a right-hand (R, θ , Z) cylindrical coordinate system. The fields have rotational symmetry about the Z axis and are symmetrical with respect to positive and negative Z. The field parameters which vary only with R and Z are termed poloidal and the winding currents which have only a θ component are called toroidal.

The OH field winding provides a large magnetic flux linking the toroidal plasma current. A rapid change in this flux induces a toroidal current in the plasma. Considering this function alone it is desirable that the flux density in the plasma be very small as compared to other fields. It is also desirable that the mechanical intersection of the OH field with the currents that produce a toroidal field (TF) be small. Although the subject device will have TF coils at higher than room temperatures, later devices are expected to have superconducting TF coils. It will be important to limit the pulsed flux in these superconducting coils in order to preserve their superconductivity.

The initiation of plasma ionization will tend to occur at points of zero magnetic field intensities. A multipole null will have a definite point null (in the R-Z plane) and the field strength will increase rapidly away from this null point. The region of plasma formation is thus accurately controlled.

The OH winding is one of several sources of poloidal fields. Other sources are equilibrium field (EF) coils [2] and the plasma. The OH and EF coils compete with each other and with other functional devices for the same space. A rational resolution of this conflict is an important part of the design problem. Mechanical design considerations favor the use of a fewer number of turns and a higher current (preserving the product). This accentuates the design problem associated with the resolution of integer turns.

LINEAR PROGRAMMING

Linear programming computer codes will solve problems of the type

$$\text{Minimize } \sum_{j=1}^n a_{0j} x_j$$

Subject to constraints

$$x_j \geq 0.0 \text{ and}$$

$$\sum_{j=1}^n a_{ij} x_j \begin{matrix} < \\ > \end{matrix} b_i \quad i = 1, M$$

where the a_{ij} and b_i are known numerical constants, and the x_j are the unknown optimal values of the variables. The symbol $\begin{matrix} < \\ > \end{matrix}$ indicates a choice for each expression i of the relationships \leq , $=$, or \geq .

The codes which solve such problems are mathematically well founded and are essentially guaranteed to produce an optimum solution if a feasible solution exists or to indicate without excessive computation that there is no feasible solution if such is the case.

The output information from a problem solution contains additional numbers which provide insight into the problem economics. For example, there are sensitivity constants which disclose the way in which the minimized function is affected by changes in the constants.

MATHEMATICAL PROGRAMMING - AN ENGINEERING TOOL

Mathematical programming, which to these authors includes geometric programming and linear programming, has been found to be a very powerful design tool. In contrast to other design methods we see the following advantages:

1. The engineering design problem can usually be literally and precisely stated so as to lead to a unique optimum solution.
2. The technique requires the designer to focus on, and think clearly about, the tradeoffs among the cost and various performance characteristics. This also permits a systematic and logical compromise among these considerations.

3. If a solution exists, the code is essentially guaranteed to find it. If several solutions exist the best of these will be found. If no solution is possible the code will determine this without excessive searching. A problem with no feasible solution can be viewed as having a solution of infinite cost.

4. A solution yields by-products in the form of partial derivatives of cost with respect to the many constraint parameters. Through these sensitivity parameters it may be found, for example, that a small change of one unit of performance parameter A is worth the same amount of money as 10 units of performance parameter B. If the present value of parameter B is marginal and the value of A more than is needed, we can trade evenly a large improvement in B for a small worsening in A.

DESIGN RESULTS

The fields resulting from the design processes are shown in the form of lines of flux in Figures 2 and 3. The final design result would be to superimpose the ampere turn distributions of these two windings to produce the design of an OH winding yielding a hexapole null.

ACKNOWLEDGMENTS

The authors wish to acknowledge the contributions to this work of the staff of the Princeton University Plasma Physics Laboratory. This work was performed for the Plasma Physics Laboratory under ERDA Contract E(11-1), subcontract 192.

REFERENCES

1. TFTR Papers, Transactions American Nuclear Society, 1975, Vol. 21.
2. D. K. Davies, A. J. Federowicz, and J. H. McWhirter, Design of Poloidal Field Windings for TFTR, Symposium on Engineering Problems of Fusion Research, San Diego, California, November, 1975.
3. D.I. Brown and U. R. Christensen, The Magnetic Design of the PDX Poloidal Coil System, Ibid.
4. M. Pelovitz, A computer Code for Generating a Magnetic Field Free Region in an Ohmic Heating Coil System, Ibid.

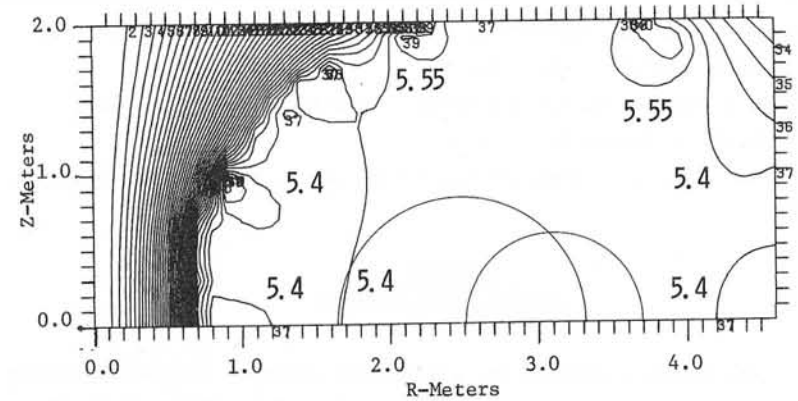


Fig. 2 Lines of Flux From Ohmic Heating Winding

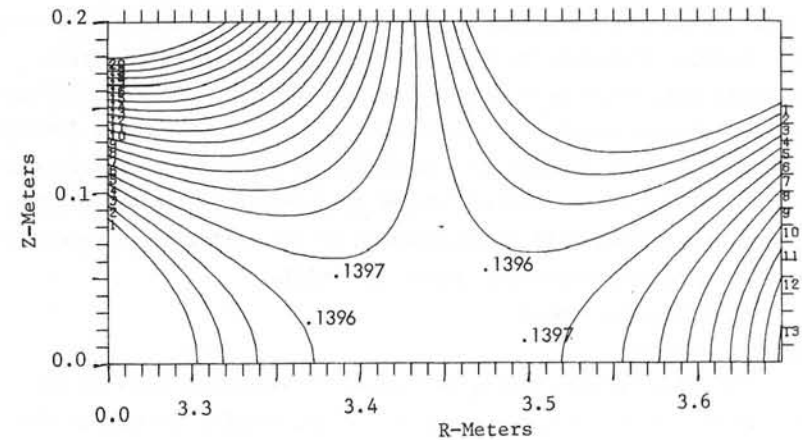


Fig. 3 Lines of Flux From Hexapole Null Winding

5. Y.-K.M. Peng, F. B. Marcus, R. A. Dory, and J. A. Moore, Optimal Poloidal Field Coil Design for Tokamak Experimental Power Reactor (EPR), Ibid.
6. J. H. McWhirter, Optimum Design by Geometric Programming, IEEE Power Engineering Society, July, 1971.
7. William R. Smythe, Static and Dynamic Electricity, pp. 290, 291, Third Edition, McGraw-Hill, 1968.
8. Princeton University Plasma Physics Laboratory, Private Communication, 1974.

APPENDIX A
DESIGN OF OH WINDING

Model

The design variables are filamentary currents of unknown magnitude, $x(j)$. These are assumed at a large number of locations, e.g. 98, in the upper half plane; the linear programming (LP) solution typically contains a smaller set of non-zero values and thus selects these winding locations from the larger set. A symmetrical set of solution values is assumed in the lower half plane. Each turn should carry the same current and thus feasible $x(j)$ must be integral multiples of the same current. This discrete constraint is somewhat difficult to meet without degrading the performance with respect to other constraints. The technique developed for dealing with discrete (integer) variables is described in Appendix B and would be useful here. Because linear programming variables can only take on positive values, $x(j)$ is represented as the difference between its positive and negative components, $x_p(j)$ and $x_m(j)$.

$$x(j) = x_p(j) - x_m(j)$$

Minimization of Cost

The cost of the winding is assumed to be proportional to its volume. If we assume a constant winding current density throughout the winding, the volume is also proportional to ohmic loss. As a consequence of this same assumption, the number of turns at any location is proportional

to the absolute value of $x(j)$ which is given by

$$|x(j)| = x_p(j) + x_m(j)$$

The length of a turn at location j is proportional to the radial position $R(j)$. Therefore the total volume is proportional to

$$\sum_j R(j)(x_p(j) + x_m(j))$$

which is to be minimized.

Magnetic Flux Constraint

The magnetic flux linking the plasma is a linear combination of the $x(j)$ and must be at least equal to a specified value $\bar{\phi}$. That is,

$$\sum_j \phi_{oj} x(j) \geq \bar{\phi}.$$

ϕ_{oj} is the flux linking the plasma due to a unit positive value of $x(j)$ [7] and involves the computation of elliptic integrals [8].

Field Strength Constraints

At points i within the plasma cross-section (or wherever we may wish to place them), we require that the absolute values of both B_Z and B_R be less than a given maximum value. This is imposed by the constraints derived as follows. The Z component of \underline{B} at location i is defined by the equality

$$\sum_j B_{Zij} x(j) - B_{Zi} = 0$$

This is subject to a constraint that

$$-\bar{B} \leq B_{Zi} \leq \bar{B}$$

where B_{Zij} is a constant involving an elliptic integral.

B_{Zi} is a variable, the Z component of \underline{B} at field point i .

\bar{B} is the maximum magnitude of B_{Zi} .

The difficulty with these constraints is that B_{Zi} should be free to take on positive and negative values. We introduce the auxiliary variable

$$B_{Zi}^* = B_{Zi} + \bar{B}$$

and our constraints become

$$\sum_j B_{Zij} x(j) - B_{Zi}^* = -\bar{B} \quad \text{and}$$

$$B_{Zi}^* \leq 2\bar{B} \quad i = 1, NI.$$

In a similar manner we can arrive at the constraints

$$\sum_j B_{Rij} x(j) - B_{Ri}^* = -\bar{B} \quad \text{and}$$

$$B_{Ri}^* \leq 2\bar{B} \quad i = 1, NI.$$

It may be desirable and necessary to constrain components of \underline{B} at points within the toroidal field coils. The constrained components of \underline{B} may be in the direction either perpendicular or parallel to the toroidal field current or both.

At field points k we require that the component of \underline{B} in the direction of a unit vector \underline{V}_k with R and Z components (a_k, b_k) be limited to \bar{B}_V . If the component of \underline{B} in the direction of \underline{V}_k is B_{Vk} , this is defined as

$$a_k \sum_j B_{Rkj} x(j) + b_k \sum_j B_{Zkj} x(j) - B_{Vk} = 0$$

and the constraint is

$$-\bar{B}_V \leq B_{Vk} \leq \bar{B}_V$$

By defining the variable

$$B_{Vk}^* = B_{Vk} + \bar{B}_V$$

we arrive at the constraints

$$\sum (a_k B_{Rkj} + b_k B_{Zkj}) x(j) - B_{Vk}^* = -\bar{B}_V \quad \text{and} \quad B_{Vk}^* \leq 2\bar{B}_V$$

We have a set of constraints specifying that the maximum value $|x(j)|$ may have is $\bar{x}(j)$. That is

$$x(j) = x_p(j) + x_m(j) \leq \bar{x}(j)$$

In working toward an engineering solution we find useful a set of constraints

$$x(j) = x'(j).$$

That is, $x(j)$ must be equal to a given value $x'(j)$.

APPENDIX B
DESIGN OF HEXAPOLE NULL

Model

The model for the hexapole null winding is much the same as that for the OH winding.

The field from the OH winding is known and this known field plus the field from the winding to be designed are to form a hexapole null. In the discussion to follow, the effect of the OH winding is neglected for the sake of simplicity and clarity.

The minimization of cost is identical to that of the OH winding.

Null

The Z component of \underline{B} must be within given tolerances from zero at the null point. The field at the null is defined by

$$\sum_j B_{Zoj} x(j) - B_{Zo} = 0$$

and the constraint is

$$-\bar{B}_{Zo} \leq B_{Zo} \leq \bar{B}_{Zo}.$$

In order to eliminate variables which take on negative values we define

$$B_{Zo}^* = B_{Zo} + \bar{B}_{Zo}$$

and our constraints become

$$\sum_j B_{Zoj} x(j) + B_{Zo}^* = -\bar{B}_{Zo}$$

$$B_{Zo}^* \leq 2\bar{B}_{Zo}$$

Hexapole Lobes

The contours of $|B|$ for an ideal hexapole are circles concentric about the null point. We define the hexapole in terms of a small circle with radius α having the null point as its center and radius vectors i from the null point making an angle θ_i with the R axis. We also consider that $|B|$ will ideally go as the inverse square of the distance from the null point.

The hexapole is to be controlled at values for θ_i , of 0, 30, 60, 90, 120, 150, 180 degrees and on the small circle with radius α ; symmetry about the R axis will take care of the field in the lower half plane. At $\theta_i = 30^\circ$ and 150° , B should ideally be radially outward from the null and at $\theta_i = 90^\circ$, B should be radially inward. At $\theta_i = 0^\circ$ and 120° B should be perpendicular to the radius vectors in a counter-clockwise sense and at $\theta_i = 60^\circ$ and 180° , B should be perpendicular to the radius vectors in a clockwise sense.

The definition of the radial and tangential components of B which are to be constrained are

$$\sum_j (B_{Rij} \cos \theta_i + B_{Zij} \sin \theta_i) x(j) - B_i = 0 \quad i = 2 \text{ and } 6$$

$$\sum_j (B_{Rij} \cos \theta_i + B_{Zij} \sin \theta_i) x(j) + B_i = 0 \quad i = 4$$

$$\sum_j (B_{Rij} \sin \theta_i - B_{Zij} \cos \theta_i) x(j) - B_i = 0 \quad i = 1 \text{ and } 5$$

$$\sum_j (B_{Rij} \sin \theta_i - B_{Zij} \cos \theta_i) x(j) + B_i = 0 \quad i = 3 \text{ and } 7$$

Our requirement is that the B_i should have positive values at least equal to some minimum field strength $\bar{B}\alpha^2$ and less than some value $(1+K)\bar{B}\alpha^2$. This is expressed as

$$\bar{B}\alpha^2 \leq B_i \leq (1+K)\bar{B}\alpha^2.$$

This bounding of a variable is often handled by a specialized feature of a linear programming code. If this is not available it is handled as a double set of ordinary constraints. If K is made zero, the

hexapole will be quite regular. Non-zero values of K permit a distortion of the hexapole.

The hexapole winding should not provide flux linking the plasma. This requires a constraint.

$$\sum_j \phi_{oj} x(j) = 0$$

Integer Turns

The constraint of integer turns is restrictive in the case of a null. Rounding of a non-integer solution is not sufficient. An integer programming code was investigated but appeared to be awkward, costly, and a more powerful tool than was required. The following technique was developed. The candidate current locations were divided into groups k and the following constraints are imposed.

$$\sum_j x_k(j) - S_k = 0$$

$$\bar{S}_{k1} \leq S_k \leq \bar{S}_{k2}$$

The values \bar{S}_{k1} and \bar{S}_{k2} correspond to integer turns. If one of the constraints is active, the sum of the turns is an integer. If the upper and lower bounds are the same, the sum must be an integer. If the bounds correspond to one turn, the sum must be one turn. By successive solutions, each increasing the number of groups, it is possible to reach an integer turn solution with very tight tolerances on the design performance.

If the location of a turn can be judged to lie within bounds in R and Z, the four corners of the bounding square can be proposed as locations. The solution will be fractional turns at two or more of these four locations.

An average of the coordinates of these points weighted with their partial turn solution value provides an estimate of the location of one turn.

Discussions following paper:

(Moses, University of Wisconsin) I would like to comment that a very similar problem was solved for the shield in the FERMLAB pulsed energy storage device. This was published at the Applied Superconductivity Conference, Oakbrook, Illinois (1974) by Moses and Ballou.

(McWhirter, Pittsburgh) I believe that the problem solution which Mr Moses has mentioned is obtained by a method other than linear programming, of course we did not intend to infer that we were the first to solve this type of problem. Our contribution is thought to be the use of linear programming with the advantage mentioned in the paper.

MAGNETIC FIELD COMPUTATION AND STRESS ANALYSIS IN TOROIDAL CIRCULAR AND DEE SHAPED COILS FOR TOKAMAK FUSION EXPERIMENTS

N J Diserens

Rutherford Laboratory, Chilton, Didcot, Oxon, OX11 0QX

ABSTRACT

Data preparation for stress analysis of windings for Tokamak fusion reactors can be a very time-consuming process. A program 'TOK' is described in which simple data input can be used to compute fields and forces in toroidal systems of circular and Dee shaped coils. In addition a complete data deck can be output for use as input to a special version of the 'FINESSE' stress analysis program.

1. INTRODUCTION

The future generation of fusion experiments will require very large TOKAMAK devices. These machines will contain toroidal field windings which will produce a very high magnetic field. In addition there will be poloidal windings which are used to shape and excite the plasma.

Because of the high magnetic fields and high currents involved in the superconducting toroidal windings, the forces on these coils will be very large, and careful design is required to minimise the shear stresses.

A dee shaped toroidal coil will avoid large in-plane shear stresses but it will still be necessary to know what the maximum stresses are likely to be.

Poloidal coil fields will exert a twisting force on the toroidal coils and so the designer must know what stresses are produced by these.

This paper describes a suite of computer programs which have been written at the Rutherford Laboratory to handle this work. Results are given for one possible experiment and details of future developments are also outlined.

2. THE TOK PROGRAM

2.1 General Description. The computer program TOK⁽¹⁾ will accept a simple data input, consisting of a command followed by a string of sub-parameters, similar to that used in the on-line magnetostatic program GFUN.^(2,3) Figure 2.1 shows a sample data deck. Starting with the basic parameters of a toroidal coil system, such as the number of coils, cross section of coils, major radius of torus and outer radius of torus, the command DOPT will produce an optimisation of the shape of the dee to give zero in-plane shear along a specified filament of the coil. This optimisation process has been described by Collie.⁽³⁾

Alternatively, the full geometry of the coil could be read in.

Poloidal coils of rectangular cross section can be described and also the plasma is treated as a coil which has a curvilinear polygon for its cross section and also has varying radial current.

Commands DISP and PRINT produce a graphical display of the coils (Figures 2.2 and 2.3) and also a print out of the coil parameters (Figure 2.4).

Command GETB will enable magnetic fields to be plotted along any given line.

The GETF command will produce a mesh of points at which fields and body forces are computed over the toroidal coil. Failure conditions can be reproduced by 'switching off' any of the desired coils.

The CODA command will enable a complete data deck to be assembled for input to the Swansea University stress analysis program FINESSE.^(4,5) At the same time a cladding of a suitable supporting material can be added to the inside, outside or ends of coils.

2.2 Field Computations. Three types of conductor element are used in the TOK program, these are:

1. Circular coils

```

TITL TBX OPTIMISATION AND FIELDS AND FORCES
GEOM COILS=20, NIT=6, ROPT=0.11, ZOPT=0., J=1340, MARC=7, RADI=157.2, CORE=157.2,
RADB=1008.4, LENG=44, UNITS=MIXED, SHAP=RECT, THICK=66
OPTI
PRINT
GEOM GROU=PLASMA, R1=352.5, R2=410, R3=506, R4=563.5, H1=0, H2=158,
H3=158, H4=0, C1=-0.05, C2=.0167, C3=-.005, J=0, J1=.1392, J2=0, REFL=YES
GEOM GROU=COAX, J=-2000, H1=650, H2=670, R1=657.2, R2=677.2, REFL=YES
GEOM GROU=COAX, J=-2000, R1=1007.2, R2=1027.2, H1=320, H2=340, REFL=YES
GEOM GROU=COAX, J=-2000, R1=150, R2=151.83, H1=0, H2=423, REFL=YES
PRINT
DISP XMAX=1600, XMIN=-1600, YMAX=1600, YMIN=-1600, PLAN=XY, COOR=GLOB, GROU=BOTH
DISP ZMIN=-1600, ZMAX=1600, PLAN=XZ, COOR=GLOB, GROU=BOTH
DISP COOR=BOTH, YMIN=-1600, YMAX=1600
GETP IPRN=0, NR=2, NZ=2, GROU=TORR, C1=1, C2=20, COOR=POLA, OUTP=YES
CODA E1=0.2E+08, C1=0.33, NTMAX=3, NZMAX=9, NZMIN=1, NTHIN=1
END

```

FIGURE 2.1 - SAMPLE INPUT DATA DECK FOR TOK PROGRAM

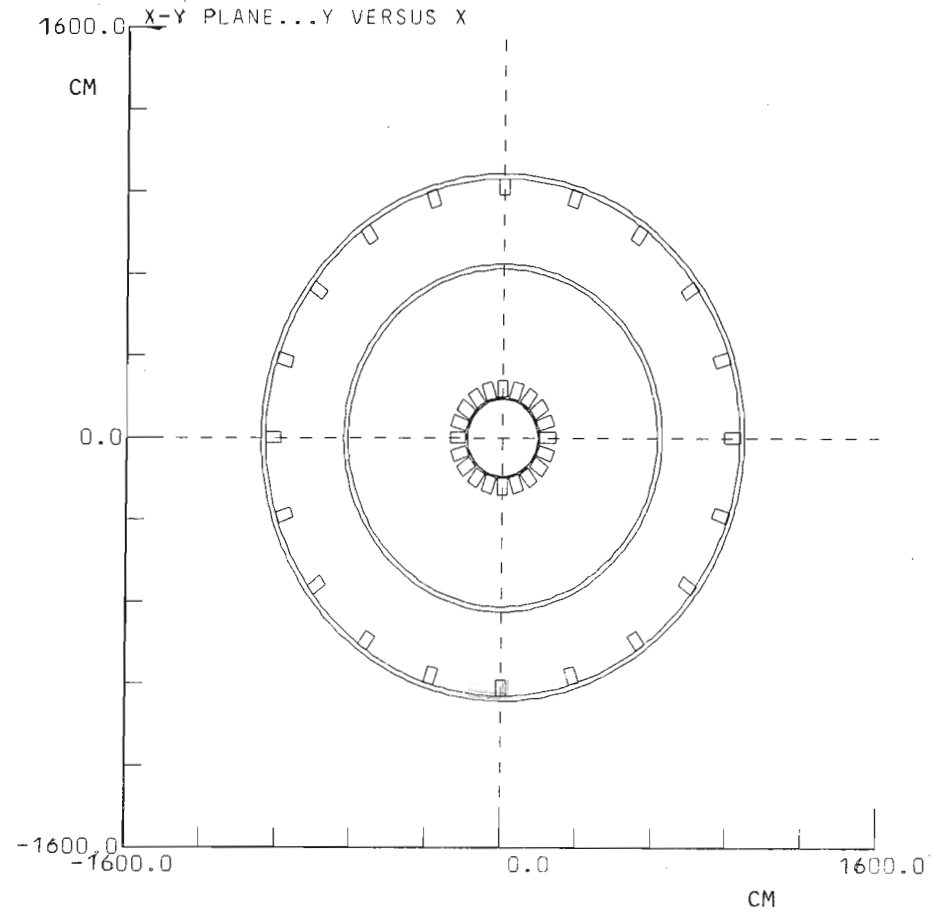


FIGURE 2.2 - SECTION THROUGH Z= 0 PLANE OF TBX TOKAMAK

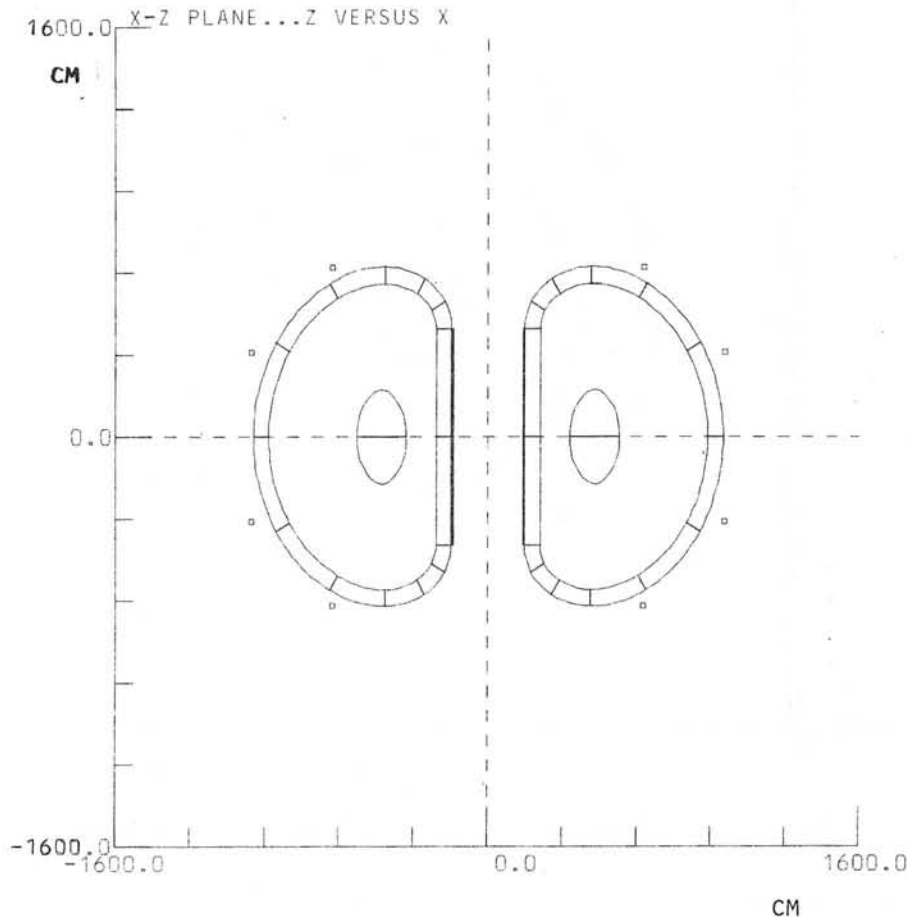


FIGURE 2.3 - SECTION THROUGH $\theta = 0$ PLANE OF TBX TOKAMAK

UNITS
 SPACE DIMENSIONS IN CENTIMETRES
 CURRENTS IN AMPERES
 FIELDS IN KILOGAUSS
 FORCES IN LBS
 STRESSES IN PSI

TORROIDAL SYSTEM OF DEE SHAPED COILS
 CORE RADIUS= 157.200 NUMBER OF COILS= 20
 COIL THICKNESS= 66.000 NUMBER OF ARCS= 7

R OF CUR	ANGLE	XCEN	YCEN
0.0	-90.000	423.069	0.0
205.476	-60.000	423.069	205.476
246.626	-30.000	402.494	241.113
336.052	0.0	325.048	285.826
473.658	30.000	187.442	285.826
628.502	60.000	53.344	208.404
735.189	90.000	0.0	116.010

COIL LENGTH= 44.000 CURRENT DENSITY= 1340.000

COAXIAL SYSTEM OF COILS

IR	OR	H1	H2	C-DEN	REFLECT
657.200	677.200	650.000	670.000	-2000.000	YES
1007.200	1027.200	320.000	340.000	-2000.000	YES
150.000	151.830	0.0	423.000	-2000.000	YES

PLASMA

H	R	C
0.0	352.500	0.005
158.000	410.000	0.017
158.000	506.000	0.005
0.0	563.500	0.0

REFLECT= 1
 CURRENT DENSITY COEFFICIENTS
 0.0 0.1392E+00 0.0

FIGURE 2.4 - PRINT OUT OF COIL PARAMETERS FOR TOK PROGRAM

2. Arc elements of rectangular cross section.
3. Straight elements of rectangular cross section.

Fields due to circular coils are computed by regarding the coil as an array of thin current carrying cylinders, the numerical integration is done radially. This enables coils of varying cross sectional thicknesses to be handled, and with radially varying current density. The method has been previously described.⁽⁶⁾

Arc elements are computed by regarding the element as an array of infinitesimal wedges, the numerical integration being done in the azimuthal direction. It is possible to handle elements with varying thicknesses in the radial direction or in the transverse (Z) direction, and this will be shortly included in the program. This method has been described by Mansfield.⁽⁷⁾

Straight elements are calculated analytically by a subroutine written by Ch. Iselin.⁽⁸⁾ At present the elements must have rectangular cross section but it is intended to include trapezoidal elements shortly.

3. FINESSE

The Swansea Stress Analysis program FINESSE has been modified at the Rutherford Laboratory to handle coil body force data. A special version of the output routines enables the stresses to be output as radial or tangential components. Graphical output is available for the three components of tensile stress and three components of shear stress, plotted along a coil filament.

Anisotropic elastic properties can be input to FINESSE, such that one set of properties hold in a given direction and a second set hold in any plane transverse to this direction. The program is being modified to allow the properties to rotate around with the coil elements so as to maintain their correct orientation. A short treatise by Collie⁽⁹⁾ has shown that two values of elasticity E, two of Poisson's ratio ν and one value of shear modulus G should be adequate to describe the elastic behaviour of a layered superconducting coil.

Before entering the data into FINESSE, after output from the TOK program, it is possible to add additional elements or to change the data as required.

4. RESULTS

Preliminary results⁽¹¹⁾ have been described by the author.

Further work is in progress. A proposal for a European superconducting TOKAMAK known as 'Tritium Burning Experiment' (TBX) is at present being investigated. This has a torus comprising 20 Dee shaped coils, each having an axial length of 0.44 metres and a radial thickness of 0.66 metres.

The shape has been optimised to give pure tension on a filament one third of the radial thickness in distance from the inside of the coil, and on the mid plane. This is the line of mean body force in the coil. Figures 4.1 to 4.3 show the tangential stresses due to the toroidal field, in the mid plane of the TBX Dee coils, for the inner radius, the central filament, and the outer radius, respectively. The stresses are plotted along a filament, in the direction of the current, over 180 degrees of the coil. The coils are assumed to be clamped such that the outer surface of the straight section, facing the centre of the torus, cannot move radially, but can expand along its length. In order to resist the poloidal field forces, it will, of course, be necessary to support the sides of the coil, but these supports are not allowed for at this stage.

Figure 4.4 shows the shear stress in the plane of the coil, along a filament which is radially in the centre of the winding and half way between the mid plane and the end of the coil. It can be seen that the values are quite low, only a few hundreds of pounds per square inch. (Compare this with the typical results for a Dee coil which is not optimised for shape (Figure 4.5) which has a maximum shear stress of about 7000 PSI in the plane of the coil.)

It can be seen from Figure 4.6 that the shear stress in a plane transverse to the direction of current is not insignificant. This is due to the finite axial length of the coil and the field 'leakage' in between the individual windings.

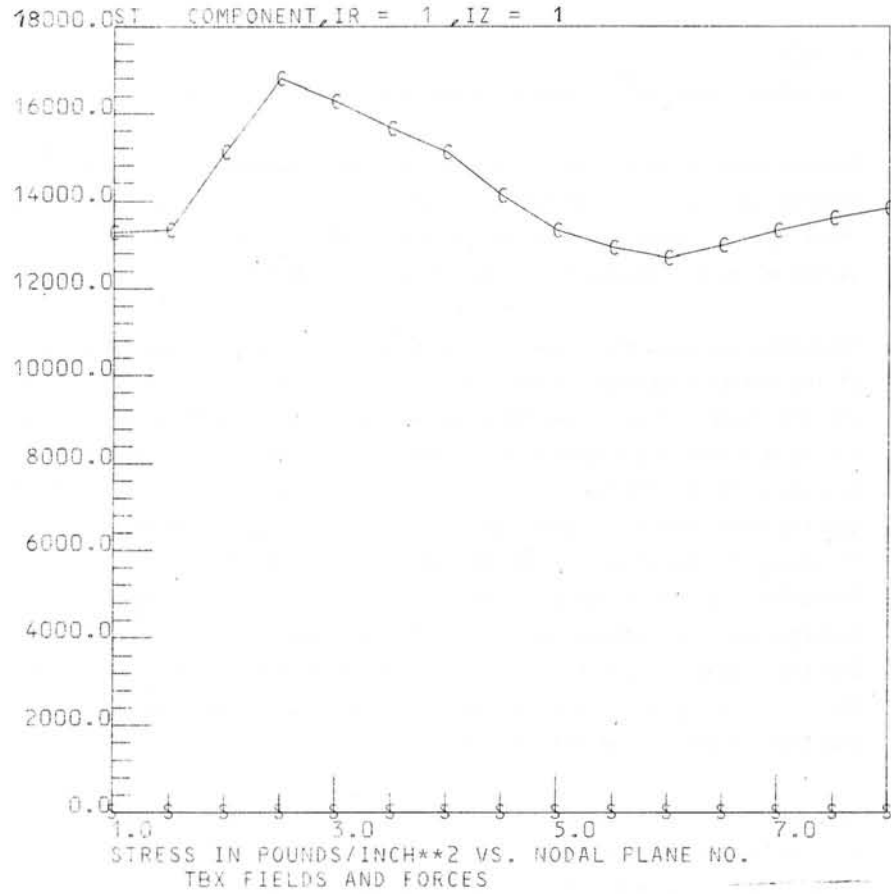


FIGURE 4.1 - HOOP STRESS ALONG INNER SURFACE OF MID PLANE OF TBX TOKAMAK

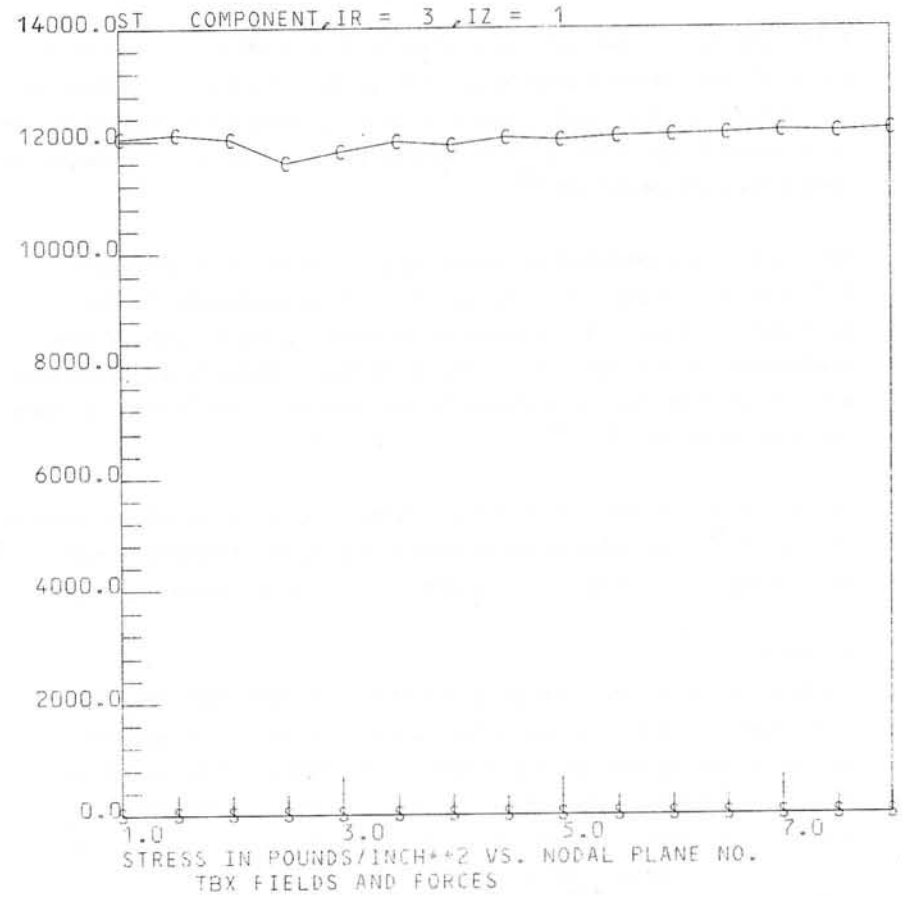


FIGURE 4.2 - HOOP STRESS ALONG CENTRAL FILAMENT OF MID PLANE OF TBX TOKAMAK

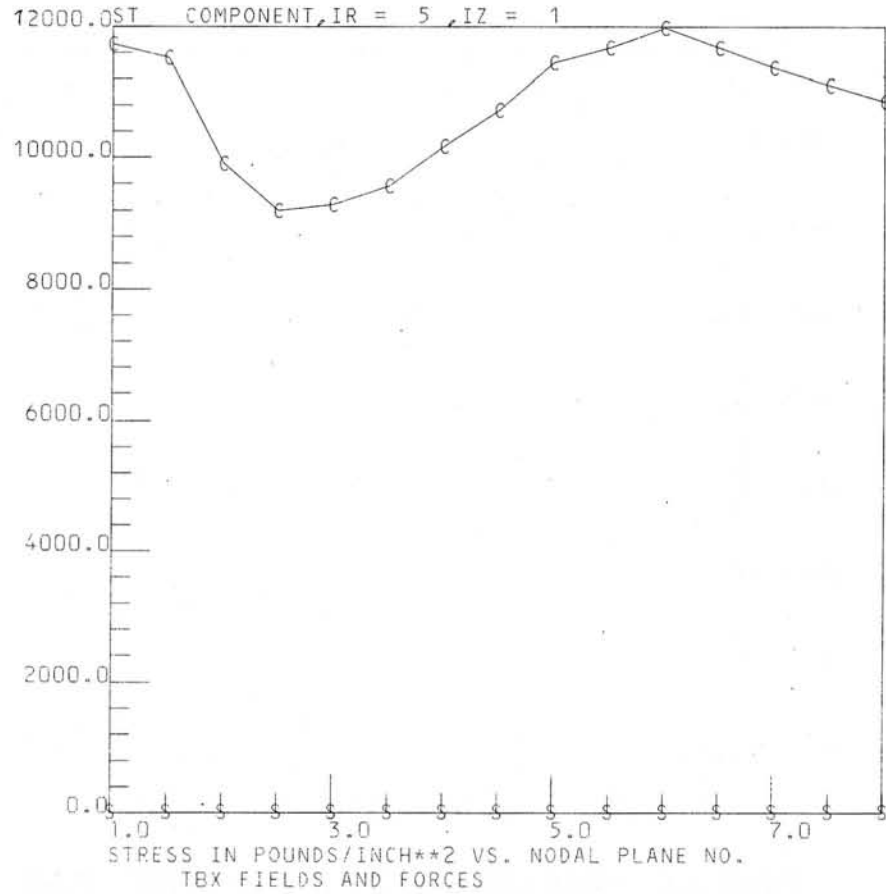


FIGURE 4.3 - HOOP STRESS ALONG OUTER SURFACE OF MID PLANE OF
TBX TOKAMAK

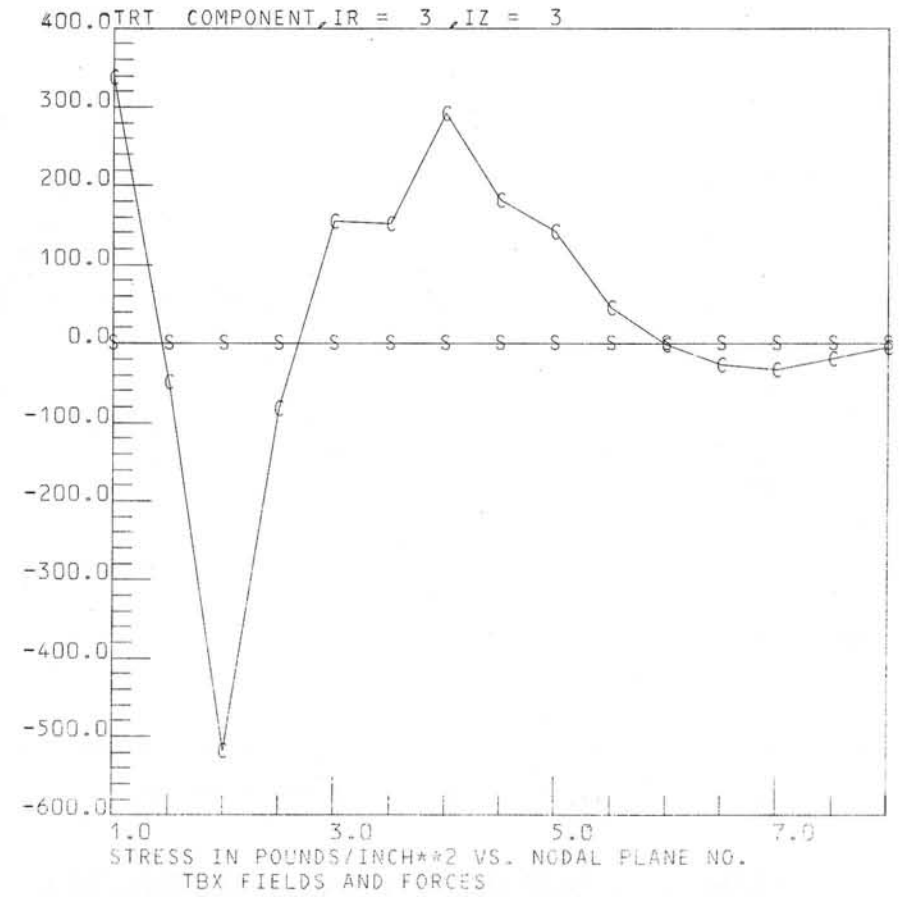


FIGURE 4.4 - SHEAR STRESS IN PLANE OF DEE COIL AT Z = 11.0 CM,
ALONG A CENTRAL FILAMENT

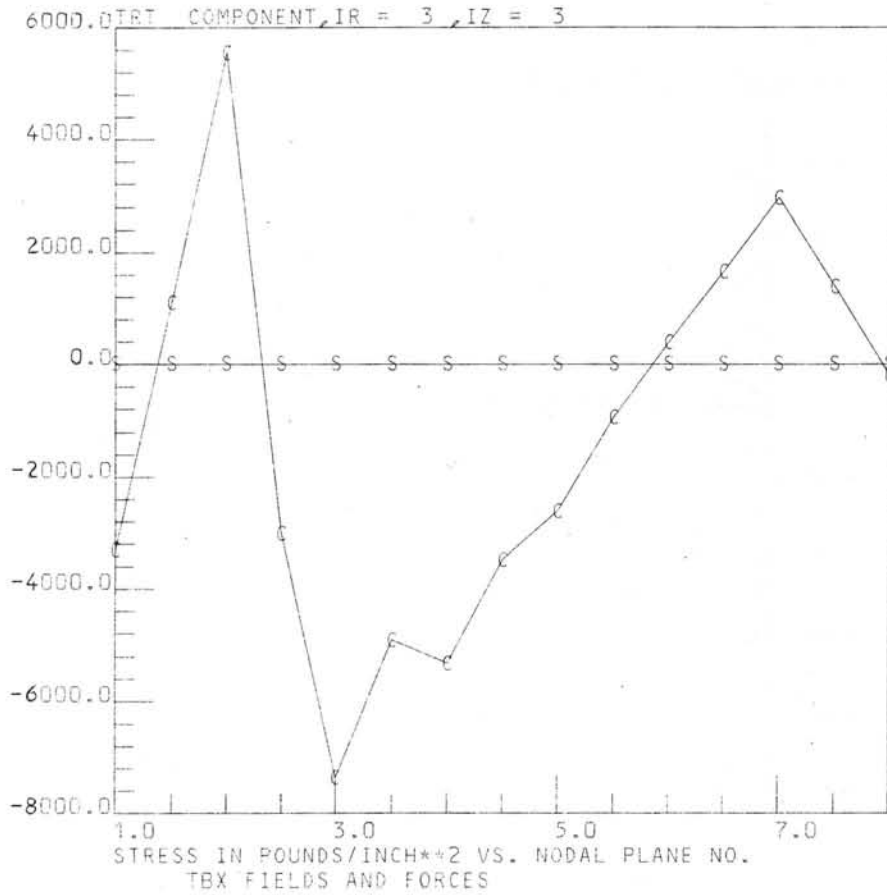


FIGURE 4.5 - SHEAR STRESS IN PLANE OF DEE COIL FOR A
NON-OPTIMISED SHAPE

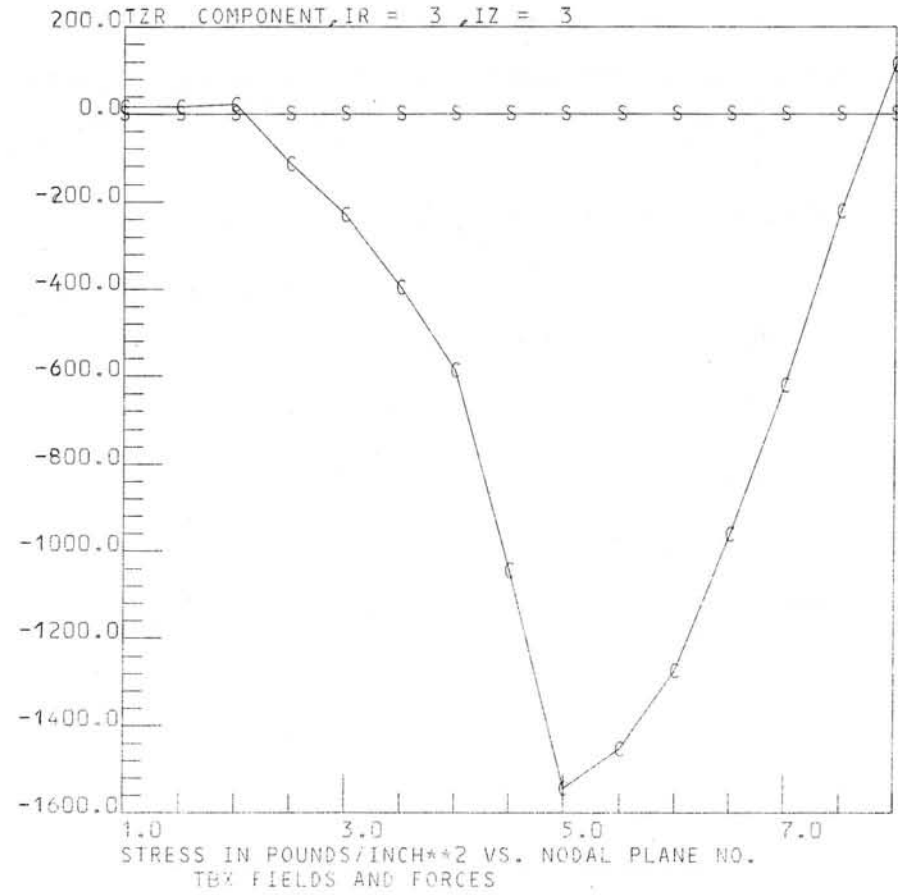


FIGURE 4.6 - SHEAR STRESS AT Z = 11.0 cm IN LOCAL PLANE
DUE TO TOROIDAL FIELD

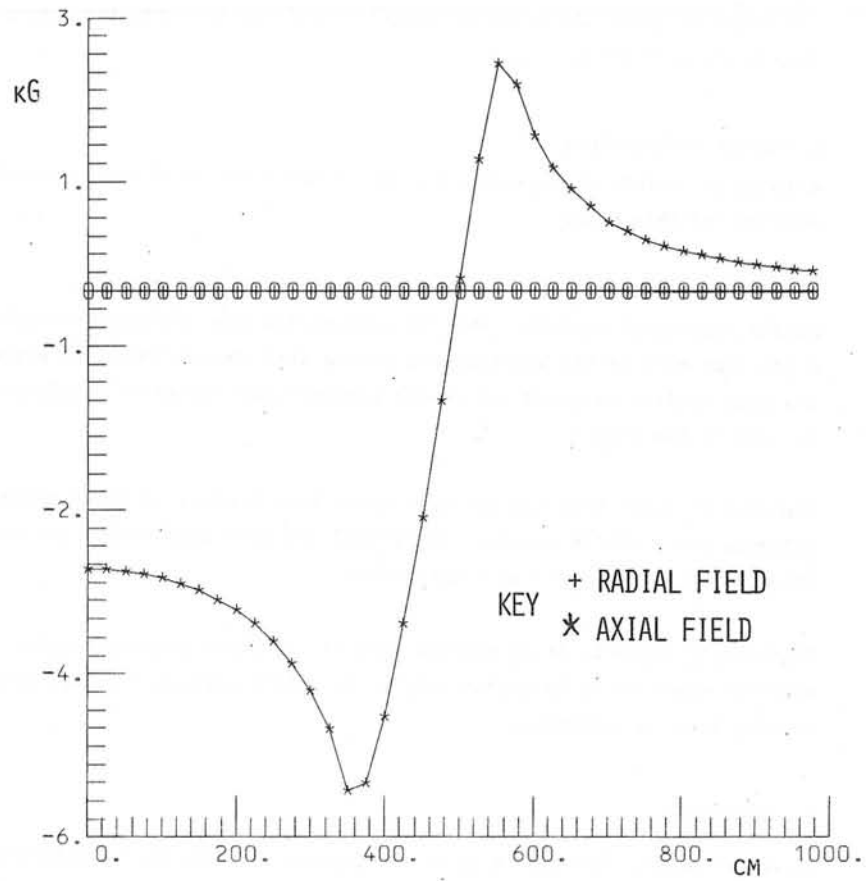


FIGURE 4.7 - MAGNETIC FIELD AT $Z = 0$, DUE TO POLOIDAL COILS AND PLASMA IN TBX TOKAMAK

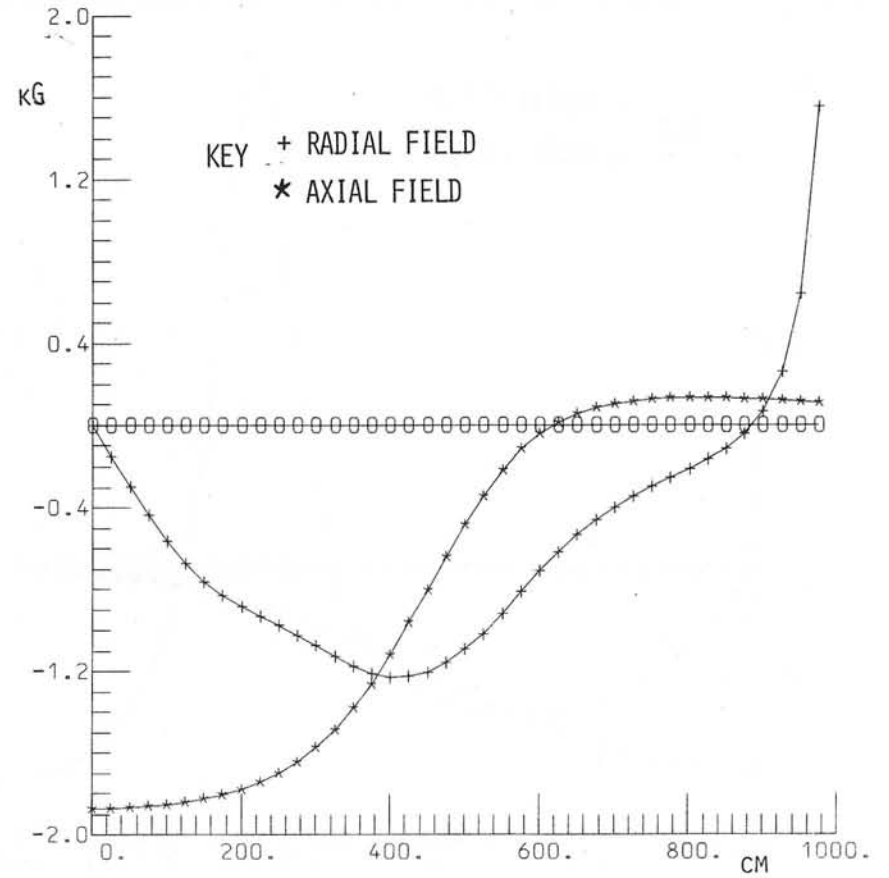


FIGURE 4.8 - MAGNETIC FIELD AT $Z = 3m$, DUE TO POLOIDAL COILS AND PLASMA IN TBX TOKAMAK

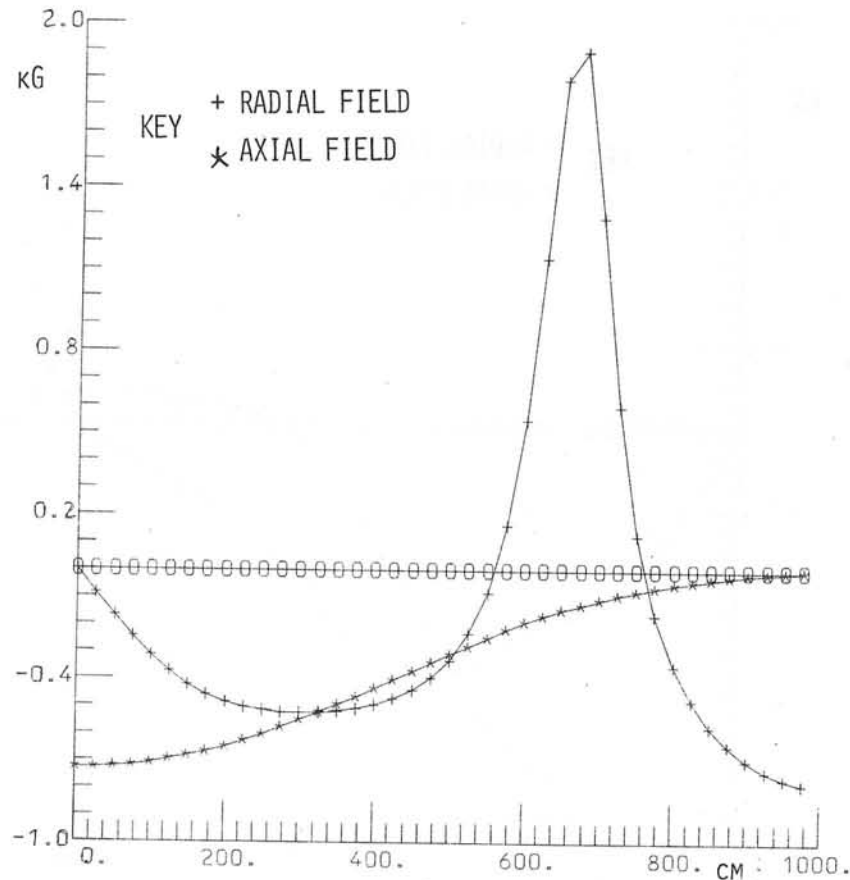


FIGURE 4.9 - MAGNETIC FIELD AT $Z = 6M$, DUE TO POLOIDAL COILS AND PLASMA IN TBK TOKAMAK

Graphical plotting of fields is available. Figures 4.7 to 4.9 show the three components of field due to the poloidal coils in Figure 2.2 along radial lines at $Z = 0$, $Z = 3.0 M$ and $Z = 6.0 M$.

The poloidal coils shown are a typical example rather than the actual design which might be used.

5. FUTURE DEVELOPMENTS

A number of points of development have already been mentioned in previous sections of this paper.

In addition it is intended to develop a version of the program to handle iron cored systems. The TOK program has been designed in such a way that many of the routines are shared with the on-line GFUN program, and thus facilities which are in one program need little or no adaptation for use in the other.

Cooldown stresses have not yet been taken into account in these computations, but a facility exists in FINESSE and will need to be used in a complete evaluation of a working system.

Plotting of magnetic field vectors upon the geometry display diagram is a facility which would be useful and, as it exists already in GFUN, would be very easy to implement.

6. REFERENCES

1. N J Diserens. TOK User's Guide. A Computer Program for Calculating Magnetic Fields and Forces in Toroidal Coil Systems. RL-75-111 (1975).
2. N J Diserens, M J Newman, J Simkin, C W Trowbridge. GFUN User's Guide (2-Dimensional Version). RHEL/R.244 (Release 2) (1975).
3. J Simkin, C W Trowbridge. GFUN3D User's Guide. RL-76-029 (1976)

4. FINESSE Abstract. CNME/AS/18. National Research and Development Corporation.
5. FINESSE - Rutherford Laboratory Version User's Guide. RL-75-144(1975)
6. C J Collie, N J Diserens, M J Newman, C W Trowbridge. Progress in the Development of an Interactive Computer Program for Magnetic Field Design and Analysis in Two and Three Dimensions. RL-73-077 (1973).
7. P Mansfield. Magnetic Fields of Curved Conductors. RL-75-184(1975).
8. Ch Iselin. Private communication.
9. C J Collie. The Optimisation of Dee Shaped Coils. Rutherford Laboratory CAG/75-7 (1975).

Discussions following paper:

(Turner, Argonne Nat. Lab) Jim, you mentioned that when you used the wrong shape for the dee coil, the shear stress changed from a few hundred psi to a few thousand psi. How much did that shape differ from the correct shape?

(Diserens) The coil was quite a long way out of shape. The straight section was lengthened from 4M to 6M which increased the height of the coil by about 30%.

(Leloup, Euratom-CEA) You mentioned that your calculation is not completely general because you can only represent plasma current distributions varying with R. You can make it general provided that you do not need to compute the magnetic field inside the plasma: in such a case, any plasma current distribution can be represented by surface currents determined using the "virtual casing artifice".

R Levyraz

Iterative Generation of Optimal Triangular Grids for the Solution of 2-Dimensional Field Problems
1. Principle and Applications

Engineers who apply the Finite Element Method need computer programs which solve with a minimum of input data problems with very complex and widely different geometries whereby the calculating effort must remain reasonable. A fundamental problem is the subdivision of the region into elements, i.e. the grid generation. The algorithm given here generates 2-dimensional optimal grids for many classes of applications and leads to quantitative information about the discretisation error. The optimisation principle is to minimise the total discretisation error, which means to get best information about the whole considered system. Triangular elements of first order are chosen, because they can easily be treated and allow a good representation of the geometry.

For the construction of such an optimal element subdivision the potential distribution must be known at least approximately, but a potential distribution can only be calculated within a grid. From this it is clear that more than one grid must be used and therefore the grid generation is an iterative process. Since the calculation effort increases with the number of gridpoints, the transient grids should be as coarse as possible. By this consideration the principle of the flow diagram in fig. 1 is obvious.

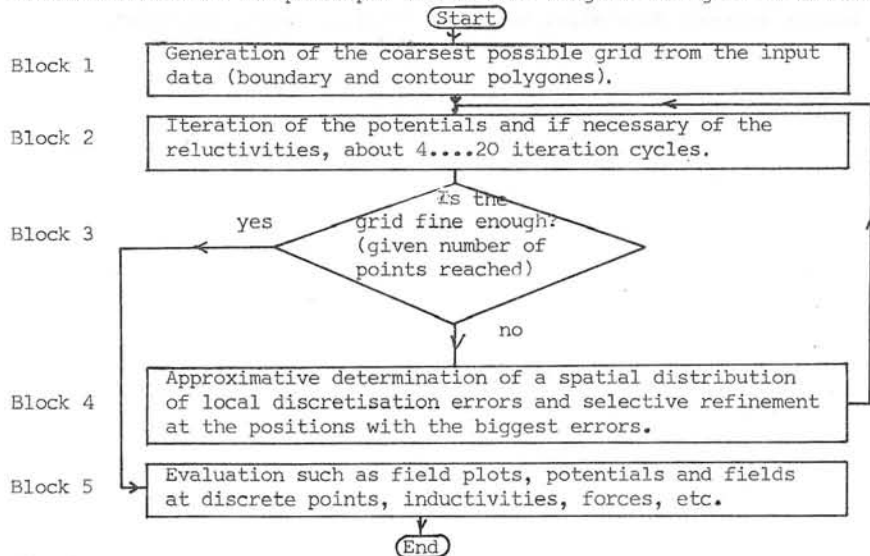


Fig. 1

The above process is very advantageous if few or nothing is known about the potential distribution and the optimal grid and the behaviour of the total system is the principal objective. Nevertheless the algorithm may easily be adapted to other situations, particularly to the following ones:

- The optimal grid density distribution is approximately known: refinement to a given density in block 1.
- There is a special interest in the potential of a partial region: A modified block 1 is used which eliminates from a former grid the elements outside the new boundary and defines the potentials taken from the former calculation as fixed on the new boundary.
- As above, but with a simultaneous change of the geometry: A new grid is built up from the beginning and at block 1 boundary values from the former potential distribution are interpolated.
- A generated grid turns out to be too coarse: Entry at block 4 with the former final grid.
- A present grid is used to calculate a new potential distribution, for instance to determine a nonlinear characteristic: Only blocks 2, 3 and 5 are used.

2. Mathematical Optimisation Objective and General Procedure

The definition of an optimal grid depends first of all on the field equation, but also on material properties, boundary conditions, coordinate system etc.. The selection presented here is given by the practice and the mathematical difficulties. The following field equations are considered:

$$\begin{aligned} \operatorname{div} (\epsilon (-\operatorname{grad} V)) &= Q, & (\text{capacitive electrostatic field}) \\ \operatorname{curl} (\nu \operatorname{curl} \vec{A}) &= \vec{J}_0, & (\text{magnetostatic field}) \\ \operatorname{curl} (\nu \operatorname{curl} \vec{A}) &= j\omega \epsilon \vec{A} + \vec{J}_0, & (\text{harmonic eddy current field}) \end{aligned}$$

where $\vec{A} = (0, 0, A)$, $\vec{J} = (0, 0, J)$

The first equation includes the electrostatic conductance field and the thermostatic field. The problems are treated in 2 dimensions, i.e. cartesian x, y - or axisymmetric r, z-coordinates. The material properties ν, ϵ , etc. are considered as constant over partial regions or scalar functions of the square of the field strength. The first two equations are equivalent to the minimisation of the total energy W in the given region. For the eddy current equation the corresponding principle is not so simple.

In order to get a very general grid optimisation we must choose a discretisation error definition which represents the behavior of the total system and does not degenerate in any case. It is obvious to take the energy difference ΔW_N between the energy W_N calculated within a grid of N points and the real energy W of the system. This value is $\geq 0, \neq \infty$ and approaches 0 if the grid is made infinitely fine under very general conditions. We may therefore declare a grid to be optimal if for a given number N of grid points the energy difference ΔW_N is minimum.

Unfortunately, a direct numerical optimisation with the well-known methods is practically excluded due to the great number ($\approx 2N$) of unknown coordinates and the almost infinite number of possible topologies. On the other side, the primary objective is the potential distribution, and practice has shown that with the successive application of very simple grid changes it is possible to reach ΔW_N by a factor of about 1.2. Furthermore it is not necessary to generate a grid of exactly N points. By these reasons the successive grid refinement given in fig. 1 is justified. The intermediate grids should be optimal as soon as possible in order to reduce the calculation effort.

As elementary grid changes we choose a minimal set of simple operations, because changes in an irregular grid are not easy to program and because the effect of each operation on ΔW_N must be estimated.

The most simple but fully sufficient operation to increase the number of grid points is the segment halving (see fig. 2). Thereby the starting potential of the new point is interpolated according to the potential distribution in the adjacent elements. For the selection of the segments to be halved, there must be a halving index related to each segment which represents the discretisation error in the neighbourhood of a segment and/or the effect of the segment halving on this error. The segments with the greatest indices are halved, which leads as fast as possible to an optimal grid.

As mentioned above it is very important how the grid points are interconnected. The most simple topological change is the diagonal transposition (see fig. 3) which changes two triangles into two different ones. A simple example (fig. 6) shows that after a segment halving all useful transpositions becoming possible by this halving must be executed immediately. This complicates the program but avoids grid degenerations and restricts the possible transpositions to a neighbourhood of the new gridpoint.

To consider the effect of a segment halving it is assumed that in the grid before the execution of the halving the potentials are the exact solution of the corresponding system of equations. The situation after the halving is as follows:

- There is a new equation for the new point which is in general not fulfilled by the starting value of the new potential.
- The equations of the immediately neighbored points P_1, P_2, P_3, P_4 are in general changed and not further fulfilled.
- The sum of the equations of P_1, P_2, P_3, P_4 before the halving is identical with the sum including the new point after the halving if the latter lies inside the calculated region or on a Neumann boundary.
- The total energy remains unchanged.

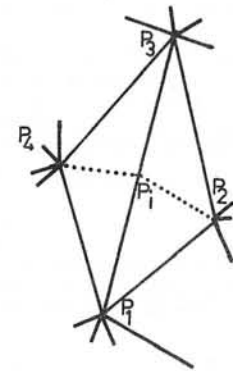
From this it may be concluded that:

- By the halving a part of the discretisation error ΔW is changed to residual error which is eliminated by the following iterations.
- The residues in the new system of equations are bounded to a close neighbourhood of the new point and mostly add to zero.
- If the system is linear, the difference between the new and the old field may be seen as the field produced by the residues. It diminishes with the distance from the new point at least as much as a dipole field.

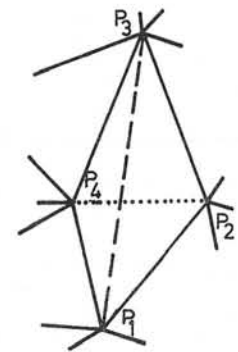
Therefore the total effect of the halving, which practically cannot be calculated exactly, may be approximated as the effect on the immediate neighbourhood of the halved segment. A further reason of the approximation is that the exact determination of all potentials before each refinement would take too much time. The estimation must be chosen such that in doubt halving indices get rather too big. Because of all these approximations it is not necessary to sort halving indices explicitly. A rough logarithmic classification and a scanning is completely sufficient.

To find a diagonal transposition criterion there are similar considerations. As a starting point we choose the energy in the concerned quadrangle to decide if the existing or the other diagonal is better, but also in this case it must be considered that the exact potential distribution is not known. Different from the effect of the halvings, most of the energy gain by the transpositions is realised immediately in the refinement stage.

Experience has shown that after a grid change all new segments should get new halving indices in order to guarantee a principally unlimited refinement. The other possibility, namely to allow only the segments present at the start of the refinement stage to be halved restricts very much the number of new points and therefore needs much more refinement stages.



Segment halving
..... new segment
Fig. 2



Diagonal transposition
--- eliminated segment
Fig. 3

3. Determination of the Halving Indices, Remainder Potential

Since the effect of a segment halving is mainly local it is obvious to try to define the halving index as the energy which can be gained by the change of the potential of the new point with all other potentials fixed. In the following it is shown that this definition may be used with some necessary modifications.

Firstly it is assumed that the potential A is real and the system of equations is linear. The energy gain by the introduction of the new point i then is

$$H_i = k_i / 2 \cdot (\Delta A_i)^2 \tag{3.1}$$

where k_i is the diagonal element of the coefficient matrix and ΔA_i the potential difference between the starting value given by the discrete potential and the value which fulfills equation i . If the system is non-linear, particularly if the relativity is field strength dependent, there must be taken the total differential for k_i which is the 2nd derivative of the energy with respect to A_i . If the potential is complex i.e. for eddy current problems, the problem cannot be taken as a minimisation of an energy, but an interpretation of the factors in (3.1) leads to reasonable grids. It is clear that

$$(\Delta A_i)^2 \rightarrow (\text{Re } \Delta A_i)^2 + (\text{Im } \Delta A_i)^2 \tag{3.2}$$

For k_i there are the following two possibilities:

$$k_i \rightarrow |\text{Re } k_i| + |\text{Im } k_i| \tag{3.3}$$

$$k_i \rightarrow |k_i| \tag{3.4}$$

For grids with a fairly small discretisation error there is anyway

$|\text{Im } k_i| \ll |\text{Re } k_i|$
The maximum difference between (3.3) and (3.4) is a factor of $\sqrt{2}$ which is tolerable with respect to all other simplifications.

Unfortunately there are some types of situations in which (3.1) together with the above definitions fails; these are mainly the following cases:

- The energy gain is mainly or wholly realised only by the diagonal transpositions becoming possible by the halving.

- There is only a considerable energy gain if several neighbored new points are generated (see example fig. 4)

In the first case it would be possible to consider the effect as an additional energy in (3.1) but in the second case the effort would be too big. Since all these problems arise because $(\Delta A_1)^2$ is too small an approximation must be found which represents the behaviour of A in the neighbourhood of the new point and by this the local discretisation error.

The real potential A may be split into the discrete potential A_0 and the remainder potential A':

$$A' = A - A_0, \quad \vec{B}' = \vec{B} - \vec{B}_0 \quad (3.5)$$

For first order elements A_0 is a linear or similar function. To get an approximation for the discretisation error it is in general sufficient to define A' as a quadratic function of the coordinates with the new point i as origin. (3.1) then leads to

$$H_i = k_i / 2 \cdot A'^2(P_i) \quad (3.6)$$

where P_i is one of the end points of the halved segment. The assumption is that the potentials of all points are correct and only the potential between the points is subject to discretisation error. The use of A' mainly eliminates degenerations of the second type.

The remainder potential in its most general form is

$$A' = c_1 x^2 + c_2 xy + c_3 y^2 \quad (3.7)$$

$$\vec{B}' = (c_2 x + 2c_3 y, -2c_1 x - c_2 y) \quad (3.8)$$

Since (3.7) is only valuable in a small neighbourhood of its origin considerations about A' may be performed in cartesian coordinates even if the whole system is defined in cylindrical coordinates.

A' can be transformed to its main axes x', y' :

$$A' = c_1' x'^2 + c_3' y'^2, \quad \vec{B}' = 2(c_3' y'_1, -c_1' x') \quad (3.9)$$

If the signs of c_1' and c_3' are different the equipotentials of A' are hyperbolae with asymptotes of value zero. The fact that in a region with existing discretisation error there may be segments of any length with zero halving indices makes a reasonable grid generation impossible. As an example all boundary segments with fixed constant potential belong to this class which represents the first type of degeneration. A simple modification from A' to A'' eliminates the degeneration but keeps the main information about the local discretisation error:

$$A'' = |c_1'| x'^2 + |c_3'| y'^2, \quad \vec{B}'' = 2(|c_3'| y', -|c_1'| x') \quad (3.10)$$

A'' is positive definite, leads to the same halving indices as A' for segments lying in the directions of the main axes and enlarges halving indices for all other segments if A' is hyperbolic. A'' only vanishes outside the origin if at least one main axis coefficient is zero. It is interesting that

$$B''^2 \equiv B'^2 \quad (3.11)$$

and therefore the fictitious field energy of A' remains unchanged by the modification to A''. It may be said that the modification leaves the same local discretisation error but increases the part which will probably be eliminated. Instead of (3.6), the modified definition

$$H_i = k_i / 2 \cdot A''^2(P_i) \quad (3.12)$$

will be used.

The coefficients c_1, c_2, c_3 are interconnected by the differential equation. As shown in the following the relation

$$c_1' + c_3' = 0 \quad (3.13)$$

is systematically true for certain classes of problems. Then

$$A'' = |c_1'| (x'^2 + y'^2) \quad (3.14)$$

This isotropic A'' leads under fairly general conditions to an isotropic grid, i.e. a grid consisting of approximately equilateral triangles.

In the most general case the equipotentials of A'' are ellipses with the axes in the main axis directions and an axis relation of

$$q_a = \sqrt{|c_3' / c_1'|} \quad (3.15)$$

The relation and the direction of the axes varies over the region; therefore an optimal grid has a location dependent anisotropy which is mainly influenced by the spatial distribution of c_1, c_2, c_3 . The axis relation q_a can systematically get values of 10...30 in practical applications. Hence it is not possible to avoid the local vanishing of c_1' or c_3' by a limitation of q_a .

If the potential is complex it is most natural to modify real and imaginary part separately. By this the equipotentials of $(\text{Re}A''^2 + \text{Im}A''^2)$ are no more ellipses but have in general a slightly different shape. This more general shape can be replaced by an ellipse with good approximation which facilitates the programming of segment halving and transposition.

In the following the relation between c_1, c_2, c_3 is determined starting from

$$\text{curl}(\nu \vec{B}) = J \quad [\text{div}(\epsilon \cdot \vec{E}) = Q] \quad (3.16)$$

When "curl" or a vector product is used as a scalar, the z component of x,y,z or the φ component of r, z, φ is meant.

If ν, ϵ is regionwise constant, with the aid of (3.5) and (3.8) we get

$$\text{curl} \vec{B}' = -2(c_1 + c_3) = R \quad [\text{div} \vec{E}' = 2(c_1 + c_3) = R] \quad (3.17)$$

$$R = -\text{curl} \vec{E}'_0 + J/\nu \quad [R = -\text{div} \vec{E}'_0 + Q/\epsilon] \quad (3.18)$$

Under the further assumptions

$$J = 0 \quad [Q = 0] \quad (3.19)$$

$$\text{and} \quad \text{curl} \vec{E}'_0 = 0 \quad [\text{div} \vec{E}'_0 = 0] \quad (3.20)$$

$$\text{we get} \quad \text{curl} \vec{B}' = 0 \quad [\text{div} \vec{E}' = 0] \quad (3.21)$$

which means that (3.13) is valid and that the optimal grid is isotropic.

The condition (3.19) says that isotropy may only be awaited in current-free (charge-free) regions. Equ. (3.20) is always fulfilled for linear A_0 in cartesian coordinates, but not in cylindrical coordinates:

$$\text{curl} \vec{E}'_0 = A_0 / r^2, \quad [\text{div} \vec{E}'_0 = E_{or} / r] \quad (3.23)$$

which means an unfavorable anisotropy even in current-free regions and in general a significant increase in discretisation error. It can be avoided by using

$$\vec{E}_0 = \vec{e}_1 + \vec{e}_2 r^2 + \vec{e}_3 z, \quad \vec{B}_0 = (\vec{e}_3 / (2\pi r), -\vec{e}_2 / \pi) \quad (3.24)$$

$$[V_0 = V_1 + V_2 \ln r + V_3 z, \quad \vec{E}'_0 = -\text{grad} V_0] \quad (3.25)$$

Besides the much better discretisation error behaviour (3.24) and (3.25) have disadvantages, i.e. there is no continuity of potential on the element boundaries and the discrete field strengths become infinite on the rotation axis. When using the definition (3.7) is slightly different if (3.8) is kept:

$$\vec{e}' = 2\pi r_0 (c_1 x^2 + c_2 xy + c_3 y^2) ; \quad (3.7')$$

for r_0 we can put in most cases the radius of the new point. In case of the eddy current field most quantities are complex and equ (3.18) is replaced by

$$\vec{R} = -\text{curl } \vec{B}_0 + (\gamma \omega \vec{A} + \vec{J})/\nu. \quad (3.18')$$

In case of a field strength dependent material value the relation between c_1, c_2, c_3 is more complicated. The procedure to get it is shown for the example

$$\text{curl}(\nu \vec{B}) = \vec{J}, \quad \nu = \nu(B^2) \quad (3.26)$$

in cartesian coordinates. In the following for each spatial dependent factor the value at the position of the new point is put. Equ. (3.26) can be transformed into

$$\nu \text{curl } \vec{B}' - [\vec{B}', \text{grad } \nu] = \vec{J} \quad (3.27)$$

$$\text{and } \nu \text{curl } \vec{B}' - [\vec{B}_0, \text{grad } \nu] = \vec{J}. \quad (3.28)$$

Replacing grad ν in (3.28) we get

$$\nu \text{curl } \vec{B}' - \partial \nu / \partial B^2 \cdot [\vec{B}_0, \text{grad } B^2] = \vec{J}, \quad (3.30)$$

$$\nu \text{curl } \vec{B}' - 2 \partial \nu / \partial B^2 \cdot [\vec{B}_0, \text{grad } (\vec{B}_0, \vec{B}')] = \vec{J}. \quad (3.31)$$

Putting (3.8) into (3.31) we get

$$\begin{aligned} k_1 c_1 + k_2 c_2 + k_3 c_3 &= J \\ k_1 &= -2\nu - 4B_{0y}^2 \cdot \partial \nu / \partial B^2 \\ k_2 &= 4 \cdot B_{0x} \cdot B_{0y} \cdot \partial \nu / \partial B^2 \\ k_3 &= -2\nu - 4B_{0x}^2 \cdot \partial \nu / \partial B^2 \end{aligned} \quad (3.32)$$

or transformed to main axes

$$\begin{aligned} k_1' c_1' + k_3' c_3' &= J \\ k_1' &= -2\nu - 4B_{0y'}^2 \cdot \partial \nu / \partial B^2 \\ k_3' &= -2\nu - 4B_{0x'}^2 \cdot \partial \nu / \partial B^2. \end{aligned} \quad (3.33)$$

Usually J is zero; then A' is hyperbolic. In general A'' is anisotropic, the main axis relation depends on \vec{B}_0 . The anisotropy is maximum when \vec{B}_0 lies in a main axis direction; then the relation is

$$q_a = \sqrt{(\nu + 2B_{0y}^2 \cdot \partial \nu / \partial B^2) / \nu} \quad (3.34)$$

with the minor axis (shorter segments) in the \vec{B}_0 direction. For common magnetisation curves values of $q_a = 4 \dots 5$ can be reached. If \vec{B}_0 lies in an asymptotic direction of A' there is a local isotropy.

Also for the factor k_1 a modification should be made for the following reasons:

- k_1 depends on the grid topology in the region of the point, but this topology is in general changed after the halving by diagonal transpositions.
- The triangles' shapes approach automatically an optimal shape as the

grid is getting finer.

- If some triangles differ extremely from the optimal shape a determination of H using optimal triangles results in a better estimation of the discretisation error than a calculation with the real triangles as is shown in the example of fig. 4.
- The application of normalised triangle shapes leads to simpler formulae for k_i ; in most cases even to an approximate independency on the segment's angle. The influence of several factors on the mesh size of an optimal grid can better be seen.

In a iteratively generated grid the optimal triangles shape is not necessarily the same as in a static grid. If for instance a segment of a regular triangular grid is halved the grid loses its regularity. A reasonable definition for the dynamically optimal triangles shape is as follows: In a parallelogram composed by two optimal triangles both possible diagonals have the same halving index. From (3.12) it follows that all corners must have the same value of A'' . For a fixed A'' the area of the parallelogram must be maximum.

If A'' is isotropic the optimal triangle is rectangular and equilateral. A rotation of the concerned segment with respect to the new point changes the value of k_i few or not at all if the material value ν etc. is constant.

If A'' is anisotropic the diagonals of the parallelogram are conjugate with respect to A'' . If the segment to be halved lies in a main axis direction the triangles are equilateral but not rectangular. For constant material value the maximum change due to the different positions of the segment to be halved is 5/4 which may be neglected.

The factor k_i for optimal triangles can be partitioned with good approximation:

$$k_i \approx k_m \cdot k_a + k_e, \quad (3.35)$$

where:

k_m = material property factor

m For constant material value $m (= \nu, \epsilon, \lambda, \sigma, \dots)$

$$k_m = 2m \quad (3.36)$$

(if on both sides of the segment different values m_1, m_2 , then $k_m = m_1 + m_2$). For field dependent material property $\nu(B^2)$,

$$k_m = 2(\nu + k_\nu \cdot 2B^2 \cdot \partial \nu / \partial B^2), \quad (3.37)$$

where $0 \leq k_\nu \leq 1$, k_ν is dependent on the main axis relation and the relative directions of \vec{B}_0 and the main axes.

k_r = radius factor.

For cartesian coordinates;

$$k_r = 1. \quad (3.38)$$

For cylindrical coordinates r, z and for scalar potential V or vector potential A :

$$k_r \approx 2\pi r_s, \quad (3.39)$$

for the flux function \vec{a}

$$k_r \approx 1/(2\pi r_s). \quad (3.40)$$

For segments on the rotation axis the mean radius of the adjacent triangle can be put for r_s , in all other cases the radius of the new point.

k_a = anisotropy factor

$$k_a \approx q_a + 1/c_a \quad (3.41)$$

For isotropic A'', $q_a = 1$ and

$$k_a = 2 \quad (3.42)$$

k_e = eddy current factor

For real potential

$$k_e = 0, \quad (3.43)$$

for eddy current problems

$$k_e = \frac{s}{3} \omega (\sigma_1 + \sigma_2), \quad (3.44)$$

where s is the area of the optimal triangle and σ_1, σ_2 the electrical conductivities in the adjacent triangles.

Some general conclusions about optimal grids can be drawn. The assumption is that the halving indices of all segments are equal.

In the most simple case where all k_i in the whole grid are identical all segment end points must have the same A'' value. For an isotropic A'' the length ℓ of a segment is by (3.14)

$$\ell \sim 1/\sqrt{|c_1|} \quad (3.45)$$

where $|c_1|$ may be called "local potential curvature". In the anisotropic case this "curvature" is dependent on the direction.

On the other side it is interesting to consider the influence of other effects on ℓ when the "curvature" is given. Equ. (3.13) leads to

$$\ell \sim k_i^{-1/4} \quad (3.46)$$

The influence is only significant if the coefficients of equ. (3.35) vary very much. The material value can change ℓ by factors 5...10 in the case of ν or the thermal conductivity λ . The direct effect of cylindrical symmetry is only significant near the axis. The anisotropy does not matter very much; with a geometrical relation of 1:32 the segment become shorter by a factor of 2. The eddy current factor is significant only for very coarse grids.

The following example shows a degeneration of the second type and how it is removed by the modification of A' and k_i . It also makes clear that in some cases the halving indices of boundary and contour segments must be adapted.

The grid of fig. 4a in taken as a starting point, where all points have fixed potentials according to the assumptions

$$A' = x^2 - y^2, \quad A'' = x^2 + y^2, \quad \nu = 1; \quad (3.47)$$

which leads to

$$A(P_1, P_2, P_5, P_6) = 1 - \xi^2, \quad A(P_3, P_6) = -1, \quad W_6 \approx 4 \quad (3.48)$$

An additional condition is that the segments P_1P_5 and P_2P_4 cannot be transposed because they are contour segments. Fig. 4b and 4c show optimal grids with one and two additional points.

The use of A'' and of k_i for optimal triangles leads to

$$k_{opt.} = 4, \quad A'' \approx 1, \quad H_7 = H_8 \approx 2 \quad (3.49)$$

which is in the same order of magnitude as

$$W_8 \approx 2, \quad \Delta W_{6-8} \approx 2 \quad (3.50)$$

If the halving indices are determined by an attempted introduction of one of the points we get

$$k_{Real} \approx 1/(2\xi), \quad \Delta A_7 \approx -4\xi, \quad H_7 = H_8 \approx 4\xi, \quad (3.51)$$

$$W_7 \approx 4 - 4\xi, \quad \Delta W_{6-7} \approx 4\xi$$

The halving indices are much too small because the estimation of the final potential of the new points in this way is much worse than by A''. On the other side the use of A'' and k_{Real} leads to

$$H_7 = H_8 \approx 1/\xi \quad (3.52)$$

which is much too big

The arrangement given in fig. 4a shows another difficulty. The segment P_2P_5 gets a slightly higher halving index than P_1P_5 and P_2P_4 , but a halving of P_1P_5 would be very unfavourable because the small distance 2ξ between some points would be reduced to ξ due to the impossibility of transposition of P_1P_5 and P_2P_4 . The difficulty is removed if P_1P_5 or P_2P_4 is halved first and P_2P_5 eliminated by transposition.

The general problem can be described as follows:

A new point besides a boundary (or contour) is generated which has a smaller value of A'' than the end points of a boundary segment with the origin of A'' on the segments center. This degeneration can be eliminated by an eventual enlargement of boundary segment halving indices such that these are greater than the indices of segments which can produce such near-boundary points.

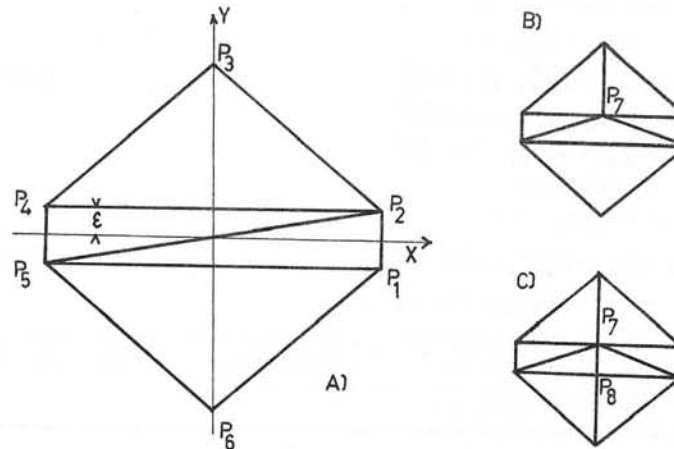


Fig. 4

4. Diagonal Transposition

Transposition Criterion

The transposition has to lead to the segment distribution with the least energy for a given gridpoint distribution. Here too it is not possible to determine the exact effect of a transposition. To get a reasonable approximation only the energy in the concerned quadrangle is considered and the potentials of the corners are taken as fixed.

The analysis is firstly made for an isotropic case, i.e. Laplace's equation in cartesian coordinates with constant reluctivity γ . At the points $P_1 \dots P_4$ of fig. 3 the potential values $A_1 \dots A_4$ are assumed, leading to a field strength \vec{B} in the respective triangles. The potential A can be divided into

$$\begin{aligned} A &= A_e + A_r, \quad \vec{B} = \vec{B}_e + \vec{B}_r \quad \text{with} \\ A_e(P_1, P_2, P_3, P_4) &= A_1, A_2 - k, A_3, A_4 - k, \\ A_r(P_1, P_2, P_3, P_4) &= 0, k, 0, k, \\ k &= A_{D24} - A_{D13} \end{aligned} \quad (4.1)$$

where A_{D24}, A_{D13} are the potential values in the intersection point for the respective diagonal. The quadrangles energy is

$$W_q = \gamma/2 \cdot \int \vec{B}^2 da = \gamma/2 \cdot [\int \vec{B}_e^2 da + 2 \int (\vec{B}_e, \vec{B}_r) da + \int \vec{B}_r^2 da] \quad (4.2)$$

The first integrand is the same for both diagonals; the second integral is zero for each diagonal. In case of nonzero k the evaluation of the third integral leads to the result that the diagonal with greater product of heights on it is better. An identical condition is that this diagonal is better for which the circumscribed circles of the triangles do not include the respective fourth point of the quadrangle. The diagonals are equivalent if all four points lie on a circle.

If k is equal to zero the energy criterion leads to the obviously wrong conclusion that both diagonals are of equal value irrespective of the shape of the quadrangle. The geometrical criteria are better because they do not degenerate in this way and are less subject to rounding errors.

It is remarkable that the above criteria are invariant with respect to rotation, even the energy criterion with the degeneration excluded. This fact further justifies the transition from A' to A''. Indeed a collaboration of an extremely position dependent halving index with a rotation-invariant transposition criterion seems not to be possible.

In an anisotropic optimal grid the above criteria are no more correct. Similar derivations starting with the energy of the quadrangle could be made, but the formulae replacing (4.2) are substantially more complicated and degenerate in more cases than (4.2). It is therefore better to introduce the modified potential A'' which also represents the anisotropy but contains security against degeneration. The geometrical criteria of the isotropic case can be brought into the following formulation which is also applicable to the anisotropic grids:

- The origin of A'' is put such that all corners of one partial triangle get the same values of A''.
- If the fourth point of the quadrangle has a greater/equal/ smaller value of A'', the existing diagonal is better/equal /worse.

For complex potential there are the following two possibilities: If A'' is adapted such that |A''| is quadratic as mentioned in chapter 3, the above criterion may be used with |A''|. If this has not been done, the origins

of real and imaginary part may be determined separately and the comparison is then applied to $(\text{Re } A'')^2 + (\text{Im } A'')^2$.

An important property of the criterion is that in parallelograms the diagonal with the smaller halving index is considered to be better. Since all pairs of optimal triangles form parallelograms the transposition in general reduces the sum of the halving indices significantly.

There are some cases of the linear Poisson equation in cartesian coordinates in which also for an anisotropic A'' the A''-criterion may easily be compared with the energy criterion. The assumption is that the four grid point potentials coincide with A''. If A' is elliptic the energy criterion leads to an identical condition as the A''-criterion for equivalent diagonals, since A_e and B_r are zero. For hyperbolic A' and anisotropic A'' both criteria differ; for instance for a rhombus with diagonals in the main axes of A' the length relation for equivalent diagonals may differ by a factor $\sqrt{3}$ between both criteria.

Sequence of Transpositions and Transposition Tests

As mentioned in chapter 2 the grid is optimized by transpositions immediately after each halving. It is assumed that for given gridpoints there is only one energy minimum and that any sequence of transpositions in which every worse diagonal is transposed reaches that minimum. A simple algorithm which organises this sequence is the following:

- 1) Put all possibly worse diagonals into a queue
- 2) Test the last diagonal in the queue, reduce the number of diagonals by 1.
- 3) If the result of the transposition test is negative, test if the number of diagonals in the queue is 0. If true, the optimal grid is reached. If not, pass to point 2.
- 4) If the result of the transposition test is positive, perform the transposition. Put all segments into the queue which have possibly become worse diagonals by the preceding transposition. Pass to point 2.

Due to the optimality of the grid before the halving the initial content of the queue consists of a very restricted set of segments. These are the radial segments $P_N P_1, P_N P_2, P_N P_3, P_N P_4$ and the peripheral segments $P_1 P_2, P_2 P_3, P_3 P_4, P_4 P_1$ in fig. 5. For all other segments the adjacent triangles are the same as before the halving. A short analysis shows that all radial segments must be optimal; $P_N P_2, P_N P_3, P_N P_4$ for purely geometrical reasons and $P_N P_1$ due to the optimality of the grid before the halving (if $P_2 P_4$ is better than $P_1 P_3$, then it is also better than $P_1 P_2$). Thus the queue contains only the four peripheral segments at the beginning.

If the transposition test on a segment, for instance on $P_2 P_3$ is positive, the effect is:

- $P_2 P_3$ is replaced by $P_N P_5$.
- There is a new radial segment $P_N P_5$.
- A peripheral segment is removed by two different ones.

Principally the radial segments $P_N P_2, P_N P_3$ and the peripheral segments $P_2 P_5, P_5 P_3$ may have become worse diagonals, but for the radial segments it may be shown that this assumption is contradictory to the optimality of the grid before the halving. Thus it may be said that the transposition process after a halving is restricted to the connection of the new point N with additional neighbour points. For n transpositions the algorithm needs $2n + 4$ transposition tests. In a statically optimal infinitely fine grid each point has got 6 neighbours; therefore we could expect a mean

value of 2 transpositions and 8 transposition tests per new point, which is in fairly good agreement with practice. In starting grids there may be much more transpositions per new point as can be seen in the example of fig. 6. For both examples isotropy was assumed.

If A'' is anisotropic a segment arrangement may be shifted out of optimality by iteration and subsequent recalculation of A''. Theoretically in this case there should be an additional transposition run for the whole grid with the new A'' before the first halving of the new refinement stage. In practice this is omitted because during the normal process unfavorable diagonals are transposed or halved.

Since for the optimisation of the starting grid A'' is in general not known, isotropy is assumed. If the grid generation is started at the coarsest possible grid, all N points lie on boundaries or contours. The maximum possible number of transpositions then is about $N^2/4$.

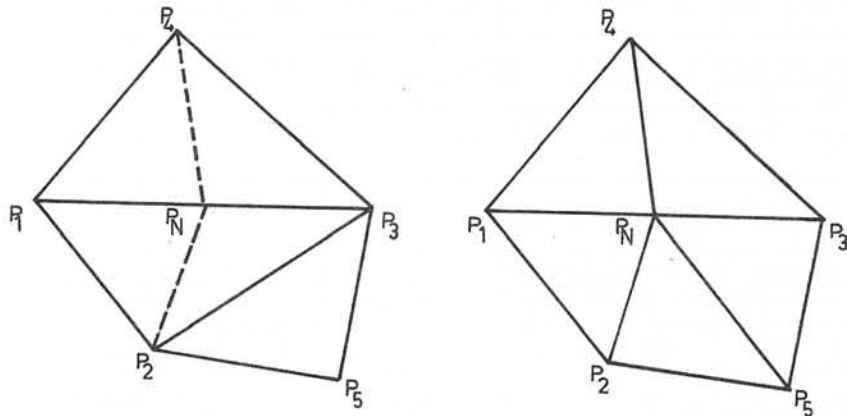


Fig. 5

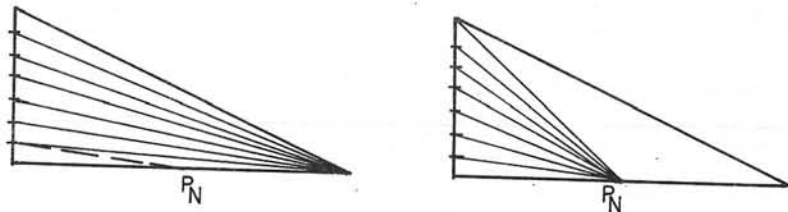


Fig. 6

5. Methods for the Numerical Determination of the Remainder Potential

The calculation must be simple and stable with respect to bad grids and residual errors, but represent significant changes within few elements. In practice the following method has proved to be good:

- The coefficients c_1, c_2, c_3 of the remainder potential are attributed to the triangles, mainly from reasons of programming technique.
- The numerical condition is formulated in terms of \vec{B} . A neighbourhood is selected, which contains the reference triangle and the adjacent triangles with the same material properties (ν, J) as the reference triangle. For each triangle i the discrete field strength \vec{B}_{Di} is determined. The condition is that the energy of the difference field $\vec{B}_0 + \vec{B}' - \vec{B}_{Di}$ within the neighbourhood is minimum. The equation (3.17) or (3.32) is used, such that at least 3 triangles are needed.
- By positioning the origin of \vec{B}' into or nearby the centre of gravity of the neighbourhood the minimisation can be partitioned into two separate calculations of \vec{B}_0 and \vec{B}' . After the calculation of \vec{B}_0 the field dependent quantities in (3.32) or if present in (3.17) can be numerically determined.
- The subsequent calculation of c_1, c_2 leads to two linear equations in case of (3.32); for (3.17) their coefficients matrix is even diagonal. c_3 then is determined by (3.17) or (3.32).

The discretisation to \vec{B}_{Di} and the use of the relation between c_1, c_2, c_3 gives a great numerical stability. The algorithm yields reasonable values even if all grid points lie on boundaries. In some rare cases there can be degenerations, particularly if locally A'' vanishes in a main axis direction. To avoid this it is the best to enlarge the coefficients if necessary such that they reach at least a certain fraction of the coefficients in the adjacent triangles with the same material properties.

6. Effect of the Refinement on the Distribution of Halving Indices, Criterion to Stop the Refinement Step

The effects of the refinement process are best described with the frequency distribution of the halving indices $n(H)$, the related distribution $H \cdot n(H)$ and its integral $\sum H$. In order to get reasonable plots of the distributions the H-axis must have a logarithmic scale.

Fig. 7 shows the selective refinement in a simple arrangement, namely the determination of the carter factor with the analytical value of $W = 2.277437$ in this case. The strong refinement near the singular point is obvious. Fig. 9 gives the distributions $n(H)$ and $H \cdot n(H)$ for the different refinement steps at the beginning of each refinement. In the end phase the distributions approach standard forms with relatively small deviations, whereas at the beginning the deviation is much greater. The selective refinement compresses the distributions from the right to a certain broadness; later they are more or less shifted, which means a uniform refinement.

To halve all segments in a grid multiplies the number of grid points by 4. Under the assumption of an invariant A'' which is fulfilled for fine grids and arrangements with no singularities, we get the following equations:

$$n_{(new)}(H/16) \cdot d(H/16) = 4 \cdot n_{(old)}(H)dH, \tag{6.1}$$

$$\sum H_{(new)} = \frac{1}{4} \sum H_{(old)}. \tag{6.2}$$

This means, that for uniform refinement

$$\Delta W_N \approx \sum H \sim N^{-1}, \tag{6.3}$$

which is a well-known relation for first order elements. The real error for the arrangement of fig. 7, which is shown in fig. 8 is in good agreement for the last refinement steps, if the refinement is done starting from the coarsest possible grid (curve A). The rule (6.3) may be used to estimate the discretisation error of the energy and other results, sometimes even to extrapolate more accurate values. At the beginning the decrease of the total error is much faster because the refinement process is selective. The agreement between ΔW_N and ΣH (curve D) is fairly good in spite of the many simplifications.

The deviation of the distributions in the end phase cannot be avoided since the refinement process is discontinuous. A single halving changes a segment with a halving index H into two segments with indices H/16 each; because of some additional effects the deviation is in general slightly greater, but such a grid is by no means as bad as it seems. Under the very optimistic assumption that we may apply (6.1) in a continuous way to any position of the distribution we get

$$\Delta n(H/\alpha) \cdot d(H/\alpha) = -\sqrt{\alpha} \cdot \Delta n(H) \cdot dH. \quad (6.4)$$

Theoretically, from a grid with the distribution $n(H)$ a grid with uniform indices H_0 could be built up, for which

$$N(H_0) = \sum \sqrt{H} / \sqrt{H_0}. \quad (6.5)$$

If the number of gridpoints is the same as in the original grid, ΣH reduces by a quality factor

$$G = (\sum \sqrt{H})^2 / (N \cdot \Sigma H). \quad (6.6)$$

G is shown in fig. 8 for each grid; the first value is calculated before the iteration and the second after the recalculation of the halving indices. For the last grids values of 0.85 are reached, which means that by an optimal distortion of the grid the error could be reduced by about 15%. But even for the grids with higher number of points there is a considerable change by the iteration in the quality factor due to the singular point which causes a dispersion of the distributions. Fig. 10 shows this dispersion at a coarse and fine grid.

Curve B of fig. 8 shows energy error, quality factor and ΣH for a different way of refinement, namely a uniform refinement at the beginning which is obviously much worse than the selective refinement. By some selective refinement stages this bad quality may be removed if there are not too many points in the uniform grid. The proceeding B sometimes needs less calculation effort than A. The quality factor G for the first grid of B is very small; the least possible error for a grid with the same number of points is in good agreement with the real values of A. Point C also represents a uniform grid and shows that uniform refinement in general is worse than (6.3) if singularities are present.

Knowledge about the distributions may be used to stop the refinement step and to start the iteration. It is clear that the refinement step must be stopped if the halving indices are no more significant. On the other side refinement and iteration steps should not interchange too often because of the effort to determine the halving indices and the equations. In chapter 8 it is shown that the total effort for a grid with N points is about $N/(1-q_p)$, where q_p is the quotient of the point-numbers of two subsequent grids. It may be concluded that an enlargement of q_p beyond $\frac{1}{2}$ is not of great use, which means that a duplication of the point number at each refinement stage should be attempted if the distribution of the indices allows it. From (6.3) there is in this case also a halving of the energy error and of ΣH .

Obviously for very bad grids a duplication of the number of points is far from optimal. On the other side the refinement process in these cases gets very slow if each refinement stage is stopped when ΣH is halved. It is a fairly good compromise to stop the refinement if

$$\frac{N - N_0}{N_0} \cdot \frac{(\Sigma H)_0}{\Sigma H} \geq k, \quad (6.7)$$

where the values at the beginning of the refinement step are signed by indices 0. For uniform refinement, i.e. $(\Sigma H)_0 / \Sigma H = N/N_0$, (6.7) leads to

$$(N - N_0)/N_0 = \frac{1}{2} (\sqrt{1 + 4k} - 1), \quad (6.8)$$

which leads to a duplication of the number of gridpoints if $k = 2$ and to the simple rule

$$\text{eliminated error} \approx \text{remaining error} \quad (6.9)$$

In very bad grids, the number of points may be increased by only 10%, but in this case ΣH diminishes by a factor of 20 according to (6.7). Naturally it is not necessary to check with (6.7) after each halving; it is sufficient to apply the rule after each scanning cycle.

7. Effects of the Grid Refinement on the Iteration

The convergence of a normal iteration process is given in fig. 11, curves A and B. They represent a complete iteration process in the final grid of fig. 7; no overrelaxation was applied. At the beginning the residues have a rather random distribution and in general different signs, which makes the convergence fast. Later there is a transition to a situation with equal signs for all residuals and an error distribution which diminishes uniformly; the convergence is significantly slower.

A grid refinement step changes a part of the discretisation error into residual error, i.e. new residues are introduced. As mentioned in chapter 3 the signs of these new residues are well intermixed. That is why the convergence after a refinement step is in general similar to the starting phase of a normal iteration, as may be seen from the part of curve C which concerns the final grid. For the coarse grids the slower convergence is not reached at all. Curve D shows the total energy error, whereby the generation and elimination of residual error is obvious. A part of the discretisation error is eliminated directly by the diagonal transpositions, particularly in the starting grids. It is interesting that sometimes an iterative grid generation needs not only fewer iterations of single potentials but also fewer iteration cycles to reach the same accuracy as in the present case. The reason is that convergence in coarse grids is in general faster. Experience shows that in few cases of slow convergence even the total effort of refinement and iteration may be smaller than that of a complete iteration in the final grid.

The consideration of the different energy errors allows to establish a reasonable criterion to stop the iteration. In order to ensure a good estimation of the halving indices for the following refinement step the residual error should be an order of magnitude less than the discretisation error. On the other side a very small residual error does not contribute much to the overall accuracy. As a rough approximation it is assumed that the total energy error is proportional to the square of the mean potential error (which is exact if the potential error diminishes uniformly). In order to get a relation of 1:5...10 between the residual and the discretisation error in the potential which allows a reasonable estimation there must be an energy relation of 1:25...100.

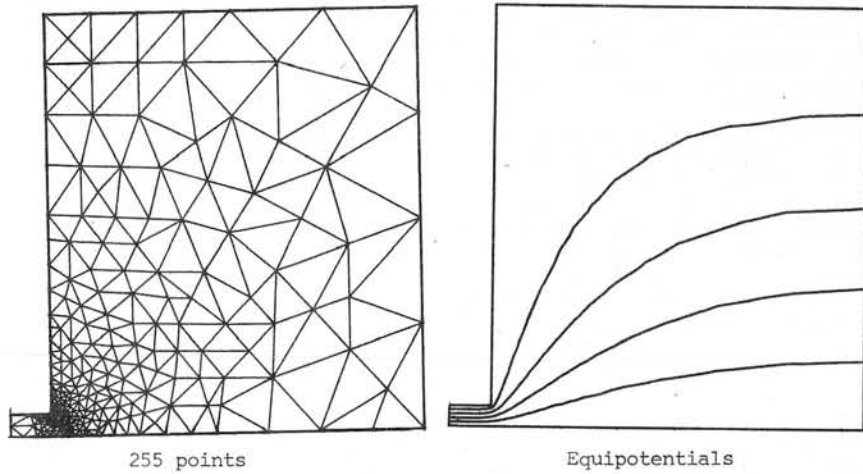
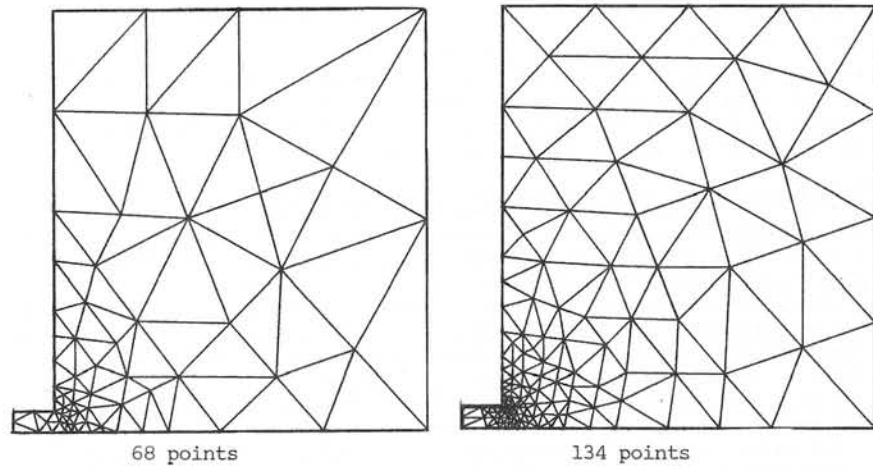
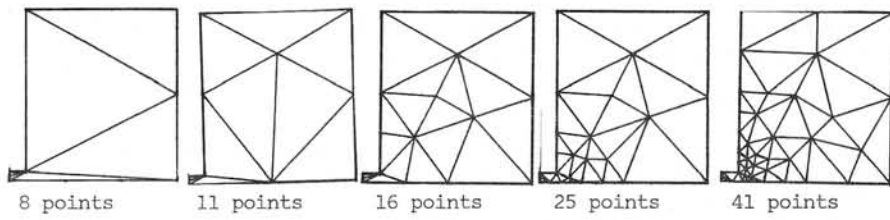
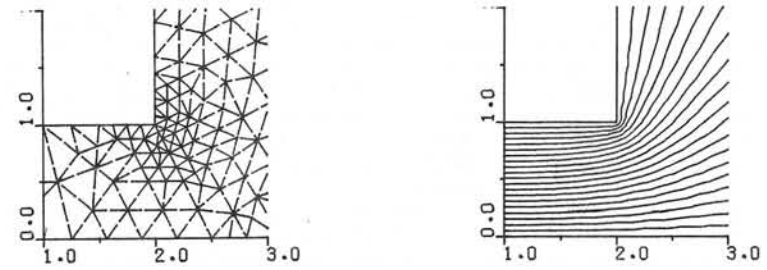


Fig. 7



Detail of Final Grid Fig. 7 (continued)

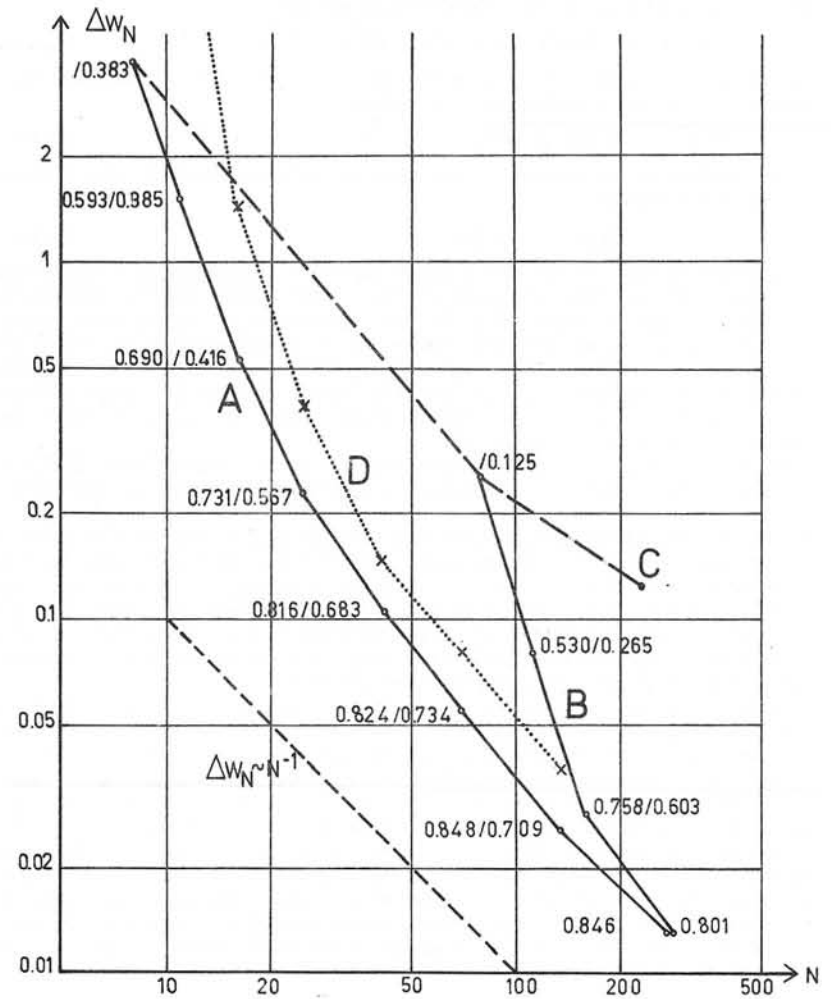


Fig. 8

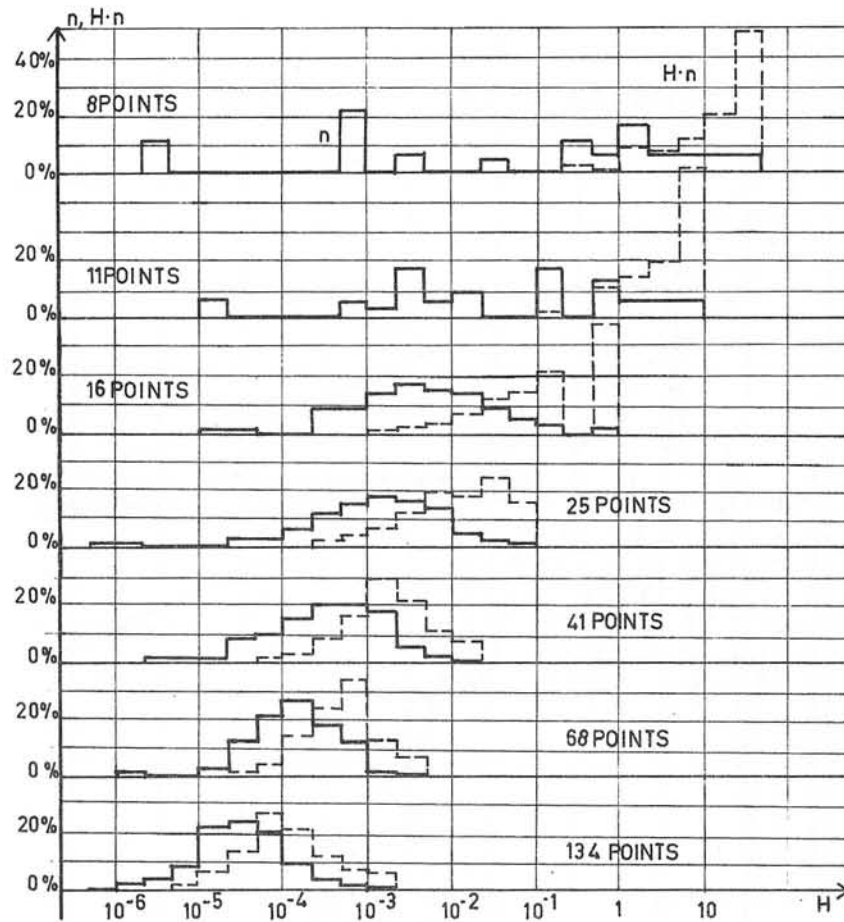


Fig. 9

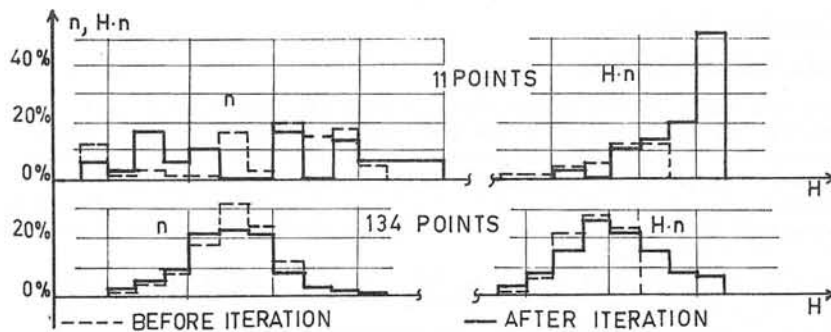


Fig. 10

The discretisation error contained in a grid is determined only at the subsequent refinement step, i.e. too late to be used to stop the iteration. It is much easier to use the relation (6.9) which equals the remaining discretisation error to the eliminated discretisation error. It must be noticed that (6.9) is only valid for uniform refinement, but in case of selective refinement all other estimations of the remaining discretisation error are also quite uncertain. In general a great part of the eliminated discretisation error is changed to residual error and usually the residual error remaining from the former iterations is much smaller. Thus it may be concluded that the iterations can be stopped when the probable remaining residual error is 1/25...1/100 of the eliminated or total residual error.

In the following it is assumed that the convergence speed is uniform, which means that the relation of two subsequent energy reductions is constant:

$$\Delta W_{i+1} / \Delta W_i = \lambda, \tag{7.1}$$

$$S_{NT} = \sum_{i=N+1}^{\infty} \Delta W_i, \tag{7.2}$$

where S_{NT} is the remaining error after N iterations. From (7.1)

$$S_{NT} / S_{OT} = \lambda^N. \tag{7.3}$$

The relation

$$S_{NT} / S_{OT} \approx q_I^2 \tag{7.4}$$

is reached when

$$N \approx 2 \ln q_I / \ln \lambda. \tag{7.5}$$

The following table shows the necessitated number of iterations for the realistic value $\ln q_I = -2$ ($q_I = 0.1353$) and for different convergence speeds:

N	4	6	10	15	20
λ	0,37	0,51	0,67	0,77	0,82

20 iterations correspond to a quite slow convergence, namely a diminution of a potential error of about 10% by each iteration cycle.

There is a certain contradiction between the assumption of a constant convergence speed and the fact that the convergence is getting slower during the iteration, but the variable convergence speed is a quite general problem for the estimation of the remaining residual error. A more accurate estimation for the error relation in case of a variable λ_i consists in

$$S_{NT} \approx \lambda_N \cdot \Delta W_N / (1 - \lambda_N), \quad S_{OT} = \sum_{i=1}^N \Delta W_i + S_{NT}. \tag{7.6}$$

In case of slow convergence ($\lambda > 0,8$) convergence speed should be accelerated. The knowledge about λ can be used to optimize the over-relaxation factor. If this is not sufficient, additive block relaxation can be applied. For automated grid generation the selection of the block boundaries must also be automated because the grids are not known when the input data are prepared. It is a certain advantage of the automated grid generation that it tends to decrease bad convergence outcoming from the grid definition.

(7.4) and (7.5) are based on stable relations between the different energy errors in the whole process. These assumption are sometimes not fulfilled, particularly at the beginning or if only a part of the whole

process is performed. It is obvious that when the refinement passes from selective to uniform the residual errors pass very quickly to the stable relations mentioned above. For the cases in which these relations are not reached one could add special convergence criteria for the final grid.

8. Calculation Effort

In general most effort is used in blocks 2 and 4 of the flow diagram in fig. 1. Experience has shown that the partial efforts for the algorithms performed there are with a good approximation proportional to the number of gridpoints if a fixed number of iteration cycles is assumed. Therefore the effort for a refinement step and the following iterations (a refinement loop) is

$$t_L \approx N \cdot (t_R + t_{It}), \tag{8.1}$$

where N is the number of points in the finer grid and t_R , t_{It} the effort per point for refinement and iterations. For a computer IBM 370/158 the following CPU times have been measured:

$$\begin{aligned} t_R &\approx 0.015 \text{ sec.} \\ t_{It} &\approx 0.010 \dots 0.200 \text{ sec.} \end{aligned} \tag{8.2}$$

While the time needed for refinement is fairly constant, the time for the iteration depends strongly on the type of the equations, the number of iteration cycles and the application of block relaxation.

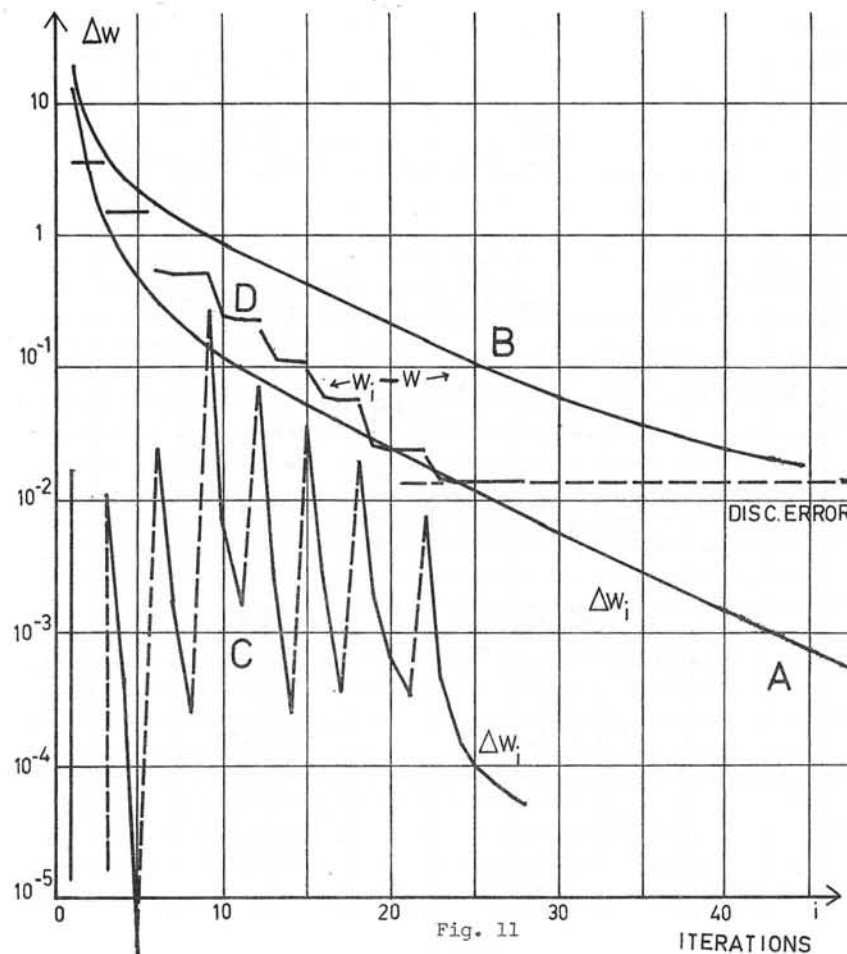
In case of uniform refinement the efforts for the different refinement loops form a geometrical progression. If the ratio q_r between the point number of two successive grids is $\frac{1}{2}$ and the starting grid has a negligible number of points the total time is

$$t_{total} \approx 2 \cdot N_F \cdot (t_R + t_{It}), \tag{8.3}$$

where N_F is the number of points in the final grid. For selective refinement the sum factor is greater than 2. The total effort for reasonable final grids of 300 - 1000 points lies between the extreme values of 15 and 400 sec. For uniform refinement a simple relation between the total effort and the overall accuracy can be established by (6.3) and (8.3):

$$t_{total} \sim \Delta w_N^{-1}. \tag{8.4}$$

A comparison between the efforts of iterative grid generation and the input of the final grid can be done. It shows that for the same calculation time in the final grid 60 - 100 iteration cycles could be performed, where the higher value holds for good convergence. In this case the input of an optimal final grid would need less calculation time, but the absolute values are relatively small. If medium or bad convergence is present, there is in general no advantage to perform all iterations in the final grid. However, if a very good starting potential distribution is known, the use of a given final optimal grid needs less time, which can be used for the determination of nonlinear characteristics.



9. Practical Examples

Static Field of a Magnet

The main parts of the Magnet shown in fig. 12. have a rotational symmetry. For the calculation the yoke has been modified to rotational symmetry with unchanged cross section. The r-axis represents a symmetry plane. The m.m.f. is 32'000 ampere-turns per coil, the magnetic characteristic of the iron is given by the following ν -values in A/m for equidistant B^2 -values with $\Delta B^2 = 0.25$; the first value is at $B^2 = 0$, the last at $B^2 = 4.75 \text{ T}^2$:

150, 150, 150, 155, 170, 205, 285, 440, 750, 1250, 2100, 3300, 4900, 6700, 8800, 11600, 15000, 20900, 35500, 55000.

For $B^2 \geq 4.75$, $\partial H / \partial B = 1/\mu_0$ is assumed.

Fig. 13 contains the final grid with 925 points. There is a considerable grid density at the criterial points on the pole. In general the grid in regions with $\nu = \nu_0$ is much finer than in the iron due to the influence of ν on the discretisation error. In the coil a varying grid anisotropy can be observed which is principally independent on the field strength direction. At some regions in the iron, particularly at the corners where the flux lines are nearly concentric circles there is an anisotropy whose direction is dependent on the direction of \vec{B} . The following table shows the refinement steps and some characteristic results for the different grids. The program takes 200 sec for the whole process. It may be concluded that the energies in the final grid have relative discretisation errors of approximately 0.2%, whereas the accuracy of the force on the coil is about 1% and of the B-values about 2-5%. To know \vec{B} very accurately near the origin a separate refinement of a partial grid in this region is appropriate.

Number of Grid Points N	Field energy $\int dv \int HdB$ [J]	Coil Energy $\int A \cdot Jdv$ [J]	Total Energy [J]	F_z =Force on the coil [kN]	B_z at $z=0, r=0$ [T]	B_z at $z=0, r=0.02m$ [T]
23	371.8	-656.4	-284.6	3.04	0.182	0.181
26	383.5	-667.1	-283.6	3.15	0.342	0.192
36	539.4	-1063.9	-524.5	2.47	1.125	1.048
44	473.9	-1009.0	-535.1	2.05	0.915	0.990
68	496.3	-1062.0	-565.7	2.45	1.187	1.527
124	484.4	-1063.6	-579.2	2.39	1.373	1.526
228	485.8	-1069.1	-583.3	2.40	1.346	1.555
454	482.7	-1068.6	-585.9	2.41	1.376	1.582
925	483.7	-1070.6	-586.9	2.42	1.442	1.577

Eddy Current Losses in a Conductor-Tank-Arrangement

Fig. 14 shows a quarter of the arrangement. On the y-axis the potential is 0 (inverse current signs for $x < 0$), the x-axis is a Neumann boundary (equal current signs for $y < 0$). The tank is made of ferromagnetic steel with an electrical conductivity of $7 \cdot 10^6 \Omega^{-1}m^{-1}$; it is considered as a nonlinear complex boundary condition [5] which takes into account the eddy currents and the field dependent reluctivity. The conductor is of copper with conductivity $5 \cdot 10^7 \Omega^{-1}m^{-1}$, its total current is $\hat{I} = (14.14, 0.)$ kA. Fig. 14 and 15 show the flux lines in the moments of maximum and zero conductor current. The entrance of the flux lines into the tank is far from perpendicular because of the considerable eddy currents. The grid shown in Fig. 16 is concentrated on the conductor where a systematic anisotropy can be seen. The smaller grid density in the conductors centre coincides with the smaller current density. Some results are given in the following table for different grids; the calculation took 60 sec. on an IBM 370/158 computer. The calculation is made for a frequency of 50Hz.

Number of Grid Points N	\hat{u} =conductor voltage [V/m]		Conductor power loss [kW/m]	\hat{I} =current in a quarter of the tank, [kA]		Power loss in a $\frac{1}{4}$ tank [kW/m]
	Real	Imaginary		Real	Imaginary	
18	0.710	1.310	1.205	-7.53	-2.13	4.51
27	0.955	2.120	1.262	-9.18	-2.97	6.11
41	1.029	2.185	1.283	-8.58	-2.63	5.78
63	1.029	2.324	1.195	-8.64	-2.73	5.96
116	1.029	2.391	1.212	-8.71	-2.75	5.95
209	1.013	2.418	1.199	-8.67	-2.76	5.94

10. References

1. G.E. Forsythe, W.R. Wasow: Finite-Difference Methods for partial Differential Equations. J. Wiley and Sons, N.Y., 1965
2. R. Courant, K. Friedrichs und H. Lewy: Ueber die partiellen Differenzengleichungen in der math. Physik. Math. Ann. 100, 1928, 32-74
3. L. Collatz: The Numerical Treatment of Differential Equations. Springer Verlag, Berlin 1960
4. S. Gerschgorin: Fehlerabschätzungen für das Differenzenverfahren zur Lösung partieller Differentialgleichungen. Zeitschr. für angew. Math. und Mech., Band 10, Heft 4 August 1930, S. 373...382.
5. R. Leyvraz: Losses in the internal Parallel Bus-Bars in Transformers and the Adjacent Tank Material. Bulletin Oerlikon, Nr. 389/390, June 1969
6. R. Leyvraz: Field Calculation by an Automatic and Iterative Grid Generation with Minimum Discretisation Error. International High Voltage Symposium 1975, Bulletin of Swiss Electrotechnical Institution.

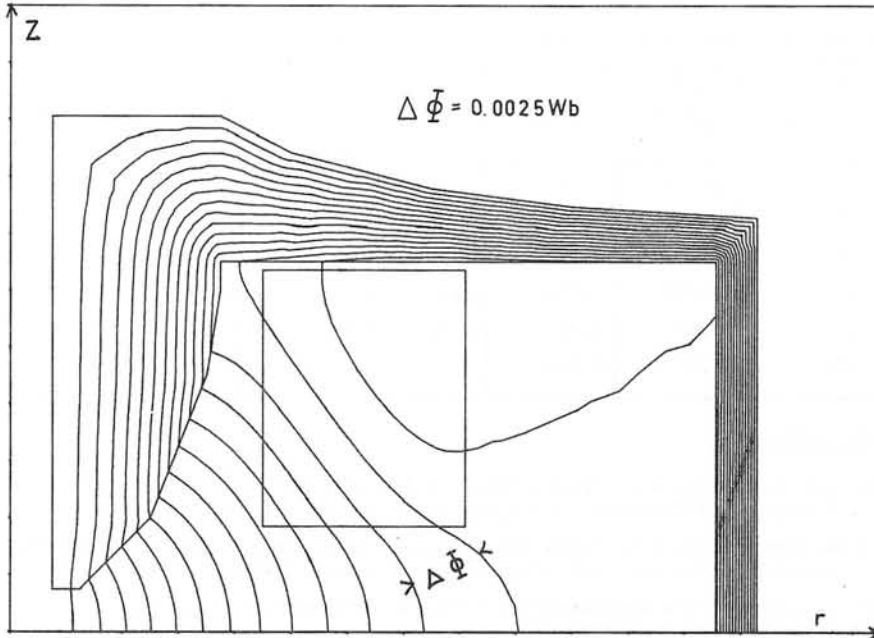


Fig. 12

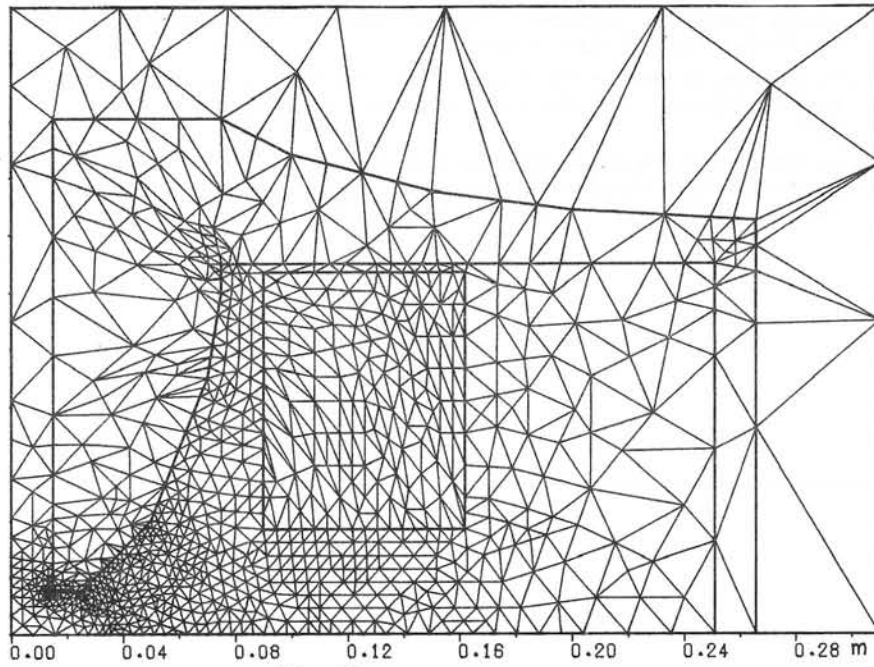


Fig. 13

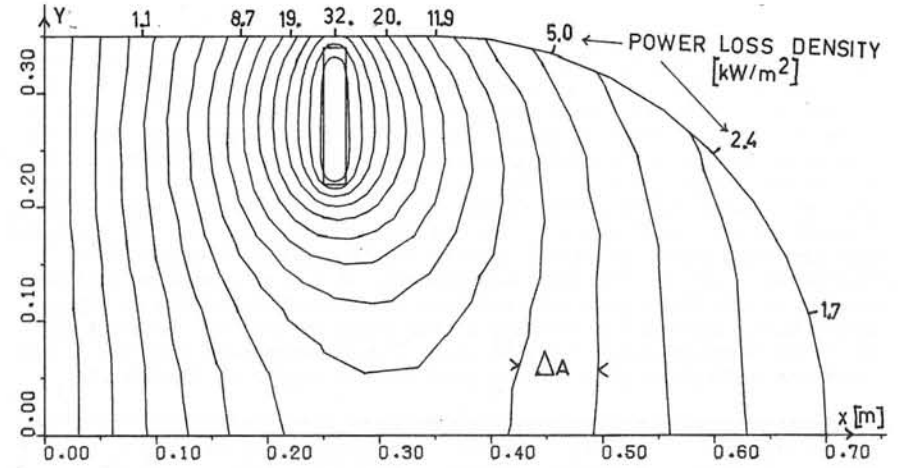


Fig. 14

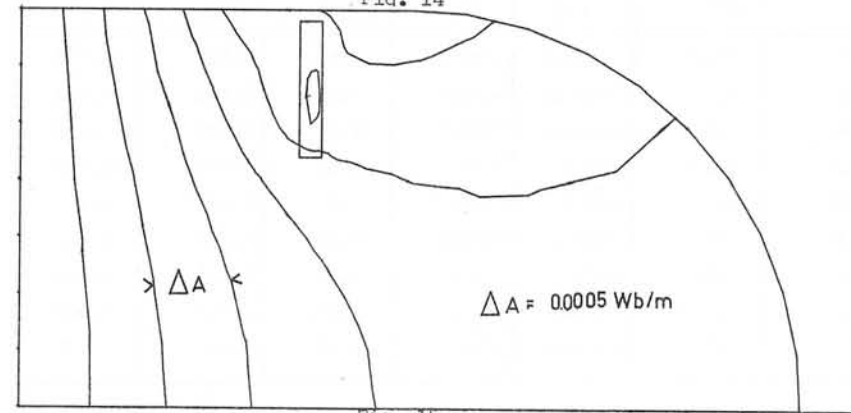


Fig. 15

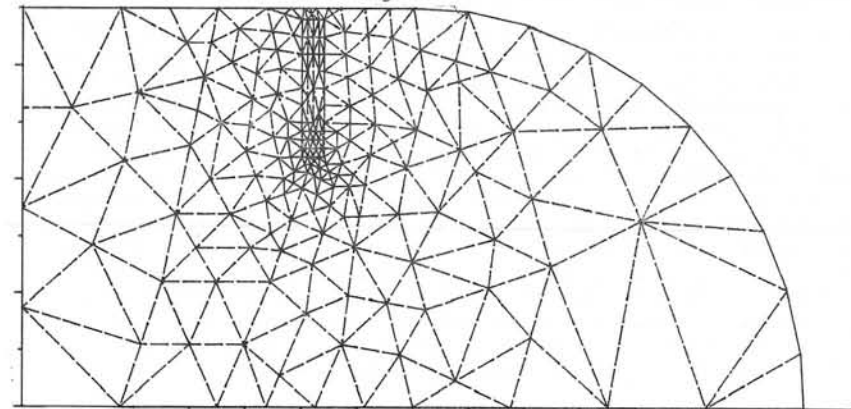


Fig. 16

Discussions following paper:

(Newman) 1) You do not include algorithms to remove mesh points. Did you not find this to be necessary

2) Could you comment on the feasibility of extending this method to three dimensions.

(Leyvraz, Zurich) 1. An algorithm to remove grid points is in general not necessary for the complete generation of a grid from the coarsest possible starting grid. However, it would be very useful in some other situations for instance if an existing grid has to be adapted to a different potential distribution. The grid density change would then be quasi-reversible. Additional rules for the grid change sequence (selection of segments) would be needed, because the frequency distribution of the halving indices is not only compressed from the right, but also from the left.

2. The automated generation of optimal grids in 3 dimensions is even more useful than in 2 dimensions. I can not see any principal obstacles, but there are several detail problems, as the construction of the first grid, selection of elementary operations for topology optimisation, etc. There will be also considerable problems in programming the algorithms.

(McWhirter) You mentioned solving for the eddy currents in the non-linear transformer tank wall. Could you say more about this method. Does it assume that the fields and currents resulting from the iron will not be sinusoidal.

(Leyvraz) The boundary condition used there is described in reference (5) First, the transient eddy current equation is solved in 1 dimension for the given magnetisation curve and a sinusoidal tangential H . Then the harmonics of the total flux Φ , which are fairly small, are neglected. The result can be expressed as a non linear complex boundary condition $\underline{H} = f(|\underline{\Phi}|^2) \cdot \underline{\Phi}$. The assumption is that everywhere in the tank there is a practically fluxless zone outside, where \underline{A} can be normalised to 0 which leads to \underline{A} (inside) = $\underline{\Phi}$ and \underline{H} (tangential, inside) = $f(|\underline{A}|^2) \cdot \underline{A}$ (inside). By this function the equations for the inside boundary nodes can be completed, for instance by choosing the way in which Stokes' theorem

is applied. In some other cases the \underline{A}_0 - value of the fluxless zone is not known, but there is a condition of zero total current in the iron. In this case the function must be taken at $|\underline{A}-\underline{A}_0|^2$ and \underline{A}_0 must be adapted such that $\oint \underline{H} d\mathbf{l} = 0$ over the iron conductor.

The use of a boundary condition is based on the fact that the flux lines inside the solid iron are practically parallel to the boundary.

STRESSES COMPUTATION PRODUCED BY A SUPERCONDUCTING NORMAL SINGLE COIL TRANSITION, IN A TOROIDAL MAGNET FOR FUSION RESEARCH TOKAMAK

by M. Caciotta and G. Sacerdoti

Summary

One discuss a procedure to evaluate the bending moments that might arise for the collapse of a s.c. coil, without the neighborhood transition in the toroidal magnet.

All the computing programs are not reported but are available if request.

1. - INTRODUCTION

As known the large dimension Tokamak, if realized with cheap criteria need to utilize s.c. toroidal magnet.

The magnet is realized with narrow radial coils. In the example the number is of 36. If one of the coils collapse from s.c. to normal state, for some fault, in the neighborhood winding over currents are induced.

The calculation is conceptually easy, if the coils are short-circuited. The magnetic field on the coils is changed with regard to the normal excitation of the magnet. The extra stresses are due both to the change of magnetic field shape and to the overcurrent. The normal excited D-shaped coils should be stressed only by traction. Bending stresses arise with the fault conditions currents distribution. To protect the coils from mechanical overstresses, we might try to discharge the magnetic energy on external loads or, otherwise to locked copper rings all around the coils shape able to "absorb" the overcurrents during the transition time.

Both the systems present some limits and difficulties.

The toroidal magnet energy for Tokamak is between 10^{10} and 10^{11} joule. The magnet protection with fast discharge in external loads needs a high voltage electrical insulation of the windings of the magnet.

If conductors current is 10^4 A, the insulation voltage about $2 \cdot 10^3$ V with N the number of coils, we may get, the magnitude order of discharge time by the formula:

$$N(2 \cdot 10^3) \cdot (10^4) = 6 \cdot 10^{10}$$

with: $6 \cdot 10^{10}$ magnetic energy in joule

$2 \cdot 10^3$ insulating voltage in volt

$1 \cdot 10^4$ current in Ampere

If $N = 36$, we obtain $\tau = 66$ sec. There are researches, in some laboratories, to realize few tens KV electrical insulation. The copper rings protection needs of a mechanical structure able to resist to the bending moments of the magnitude order of that should be requested in the s.c. coils without protection.

The relation between ring thickness s and the time τ in which the rings might to screen the coils, in approximately given by relation

$$s = \left(\frac{\rho \tau}{\mu_0 4\pi} \right)^{\frac{1}{2}}$$

ρ is the electrical resistivity of copper.

The rings presence produces approximately a delay τ in the perturbation passing from one coil to the next. With a N coils magnet, the propagation time of collapse effect shall be:

$$T = \frac{N}{2} = \frac{N s^2 \mu_0 4\pi}{2 \rho}$$

If

$$\rho = \frac{1}{65} \cdot 10^{-6} \Omega \cdot \text{m}; \quad s = 0,20 \text{ m}$$

$$N = 36 ; \quad T = 40 \div 45 \text{ sec}$$

This time should be increased because of the ring self-inductance.

In the present work the stresses evaluation in the worst conditions is done; this is the case in which there are no protection at all and the magnetic flux in each coil will remain constant (naturally excluded the collapsed one).

For more realistic evaluation, we should have done hypotheses on the reasons and on the causes that give arise to the coils collapse and from these to evaluate the phenomenon intrinsic constant time.

We have done some hypotheses that make a more pessimistic evaluation; they are:

- a) the very fast collapse of the coil
- b) the neighbourhoo coils should be enough strong to succeded to support the raised overcurrent, without other transictions;
- c) no external protection limits the currents values.

For a best explanation we apply the proposed procedure to a Tokamak fusion reactor studied at Frascati Laboratories in the 1974 (FINTOR) [1]. The different steps are:

- 1) the mutual inductance measurements between the magnet coils on the little size model
- 2) the coils overcurrents calculation when one of the coils quenches; this calculation is done with the mutual inductances measured values. If the coils are many, the mutual inductances measurements must be very precise to avoid some overcurrents oscillations with the azimuth. So it is necessary to correct some little, the mutual inductances value to get a not oscillating behaviour.
- 3) By the measurement on the model, one obtains the magnetic field component perpendicular to the coil plane value, versus linear development of the coil, in all the azimuthal possible positions. The field has been measured along the four corner-edges of the winding. From the measurements data that are about two thousands and five hundreds relieved by an Hall probe gaussmeter, we carry out a magnetic field analytical expression function of the azimuth and the linear development of the coil.
- 4) By using the just obtained formula and the overcurrents values, one calculate by a computer, the bending moments and the mechanical overstresses in the more excited coil with the following hypothesis:
 - a) the magnet with the coils supported by a central cylinder;
 - b) the magnet coils supported in a point of an ideal central circumference.
- 5) One discuss the possibility to compute both the mutual inductances and the magnetic field instead to measure its.

2. - MUTUAL INDUCTANCES MEASUREMENTS OF TOROIDAL MAGNET COILS

The calculation of the mutual inductance of the D-shaped coils, probably needs the magnetic field computation. Very good programs for the magnetic field calculation in every geometry of windings are available (see bibliography [2] for an example). We for this work have considered easier and quicker to measure on the model the mutual inductances. Its will be:

$$L = 1S \frac{(N_t)^2}{(N_m)^2}$$

where:

L: mutual or self-inductance of the magnet coils of Tokamak

l: mutual or self-inductance measured on the model

S: scale factor

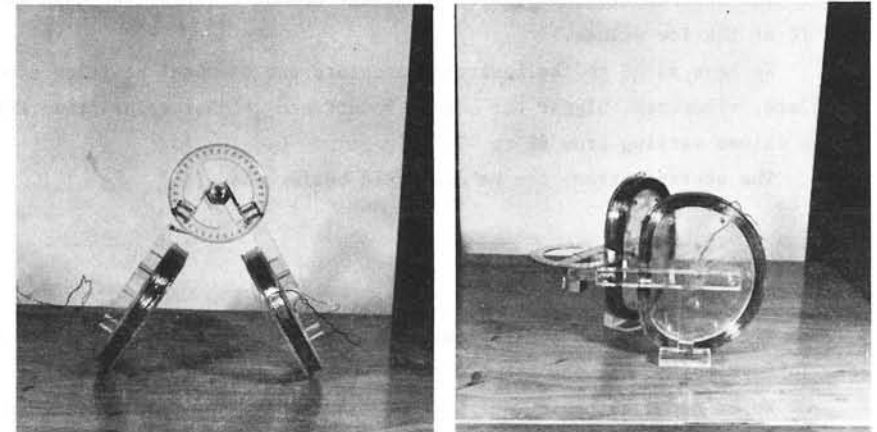
N_t : number of coils of winding

N_m : number of coils of model

We have $N_t = 700$ $N_m = 554$ $s = 50$

The model is realized by two copper wires on plexiglass support fixed on the compass arms.

The machine inner diameter (in scale) is equal to the compass arm length to reproduce easily the all possible reciprocal coils positions. In fig.1 is reproduced the apparatus photos.

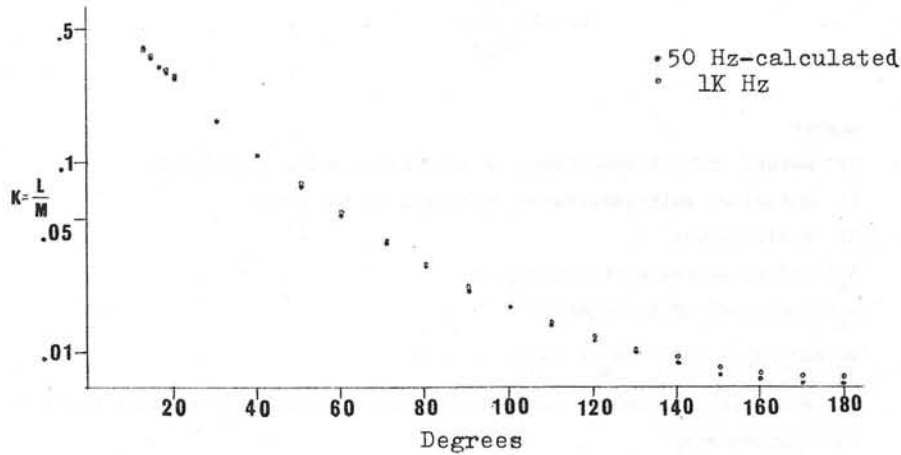


- FIG.1 -

To measure the different angles mutual inductances a volt-ampere-
metric method has been used.

To be sure that the model metallic parts do not have influence we ha
ve accomplished the measurements at 50 Hz and at 1 KMz.

In fig.2 there are reported the experimental relieves and the two dif
ferent frequencies curves are sufficiently overlapped.



- FIG.2 -

The instruments errors are: 2% at the mutual inductances high values
and 7% at the low values.

We have added to the instruments errors the azimuthal position errors
that are, viceversa, bigger for mutual inductance higher values than the
lower values varying from 6% to 1%.

The average errors can be evaluated better than 7%

3. - OVERCURRENTS CALCULATION

With the measured coefficients the overcurrents that are induced in
the Tokamak coils when one or more collapse it is possible to compute.

We do the hypothesis (see introduction) that the magnetic flux in all
the s.c. coils shall remain constant.

So we can get the 35 equations in the 35 unknown currents.

The coefficients matrix is carried out by the mutual inductances measured
values, and it results

$$K_{1,1} = \sum_{j=1}^{36} K_{1,j} \Delta I_j; \quad K_{1,j} = \frac{M_{1,j}}{M_{1,1}}$$

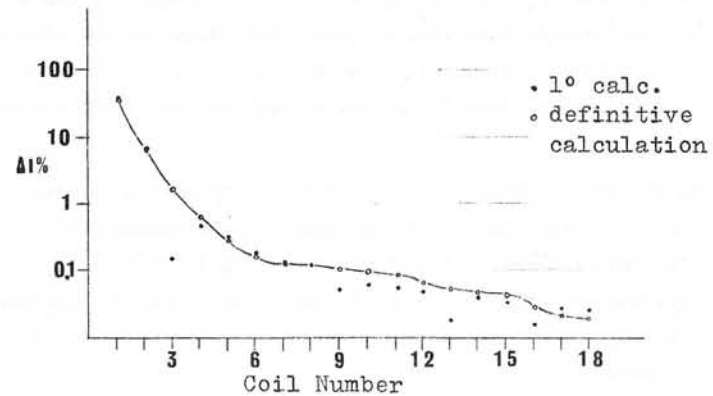
$$M_{1,j} = M(\varphi_{1,j}); \quad \varphi_{1,j} = 10^\circ |1 - j| \quad (3.1)$$

$$j = 1, 2, \dots, 35$$

Similarly when two coils collapse we may write the 34 equations in
the 34 unknown currents

$$K_{1,1} + K_{1,2} = \sum_{j=3}^{36} K_{1,j} \Delta I'_j$$

The over currents obtained resolving the sistem (3.1) are effected
by oscillations (see fig.3) increasing the azimuth that, we believe, are due
to the mutual inductances measurements errors on the model



- FIG.3 -

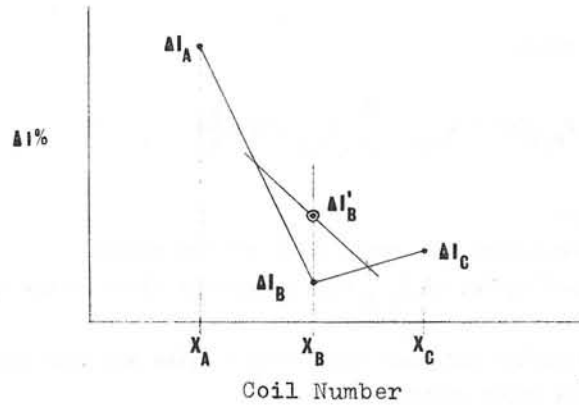
The experimental values have been modified to eliminate oscillations
by the following on the computer procedure.

From the overcurrents versus the azimuth graphic, we connect the mi
nimum with the firsts neighborhood, with two segments then connecting with

a straight-line the average points of the segments. At the minimum ascissa, we evaluate the corrected overcurrent. Easy geometrical considerations allow us to write:

$$\Delta I'_B = \frac{1}{4} (\Delta I_A + 2\Delta I_B + \Delta I_C)$$

By this method (see fig.4) we take off all the minimum points.



- FIG.4 -

We recalculate the mutual inductances new values to get the modified over-current distribution.

We may write

$$K_{1,1} = \sum_{j=2}^{36} K_{1,j} \Delta I_j$$

$$K_{1,1} + \Delta K_{1,1} = \sum_{j=2}^{36} (K_{1,j} + \Delta K_{1,j}) (\Delta I_j + \delta \Delta I_j)$$

$$\Delta K_{1,1} = \sum_{j=2}^{36} K_{1,j} \delta \Delta I_j$$

These relations constitute a system to evaluate the mutual inductances corrections. With the new values set we recalculate the over currents not having oscillations; otherwise we repeat the procedure.

We have controlled that always the mutual inductances values should be in the experimental errors field; otherwise, one reduces all the values by an equal coefficient to arrange the values into the experimental errors range. The coefficients set that eliminates the oscillations in surely precise better than 7%.

The mutual inductances graphic so evaluated is coincident with the fig.2 (50Hz).

Degrees	$K = \frac{L}{M}$		Degrees	$K = \frac{L}{M}$	
	50 Hz	Calculated		50 Hz	Calculated
0	1.00	1.00	100	.018	.019
10	.46	.45	110	.014	.015
20	.28	.24	120	.012	.012
30	.17	.18	130	.010	.010
40	.11	.12	140	.0088	.0090
50	.075	.081	150	.0080	.0081
60	.052	.056	160	.0074	.0074
70	.039	.042	170	.0070	.0071
80	.029	.031	180	.0069	.0069
90	.022	.024			

- TABLE I -

The Table I shows the initial and final mutual inductances. In fig.3 is reported the overcurrents evaluations. |3|

4.1 - MAGNETIC FIELD CALCULATION |4|

On the above described model the azimuthal magnetic field has been relieved. One of the two model coils has been excited by a 1A, D.C. current and the azimuthal magnetic field has been relieved along the four corner-edges of the other coil by an Hall gaussmeter (model Booton ind. 3265).

Because of the magnetic field low value the measurement has been replaced changing the current from 1 A to -1 A to eliminate the earth magnetic field influence.

The bigger errors was principally done in the self-field measurements and in the more far coils the errors were due:

- a) to the strummental causes

- b) to the Hall probe positioning
- c) to the Hall probe physical dimensions

The strummental errors are of the 2% order.

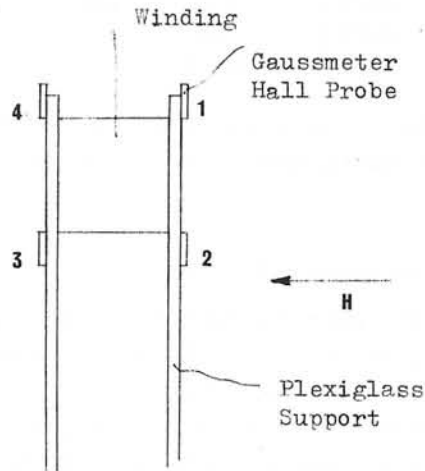
The Hall probe physical dimensions were of about 6 mm x 6 mm.

The field measurements consists in about 2500 relieves (15 for each corner-edge; 4 corner-edges, 18 coils, 2 relieves for the earth magnetic field eliminations).

To utilize the data for the mechanical stresses computation we have to get an analitical magnetic field expression by a best-fit method. We have the aim to get the formula of the botton tipe.

$$B_{r,j} = f_j(s, \vartheta)$$

where j is the coil corner-edge; $B_{r,j}$ is the perpendicular to the coils plane magnetic field component; s is the corner-edge linear development, ϑ is the azimut.



- FIG.5 -

4.2 - THE MAGNETIC FIELD EXPERIMENTAL DATA ELABORATIONS AND THE MAGNETIC INDUCTION ANALYTICAL EXPRESSION

We describe the followed procedure. For simmetry considerations the $B_{r,j}$ for $s = 0$ and $s = s_m$ (the half perimeter of the coil j corner-edge) may have the first derivation equal to zero.

$$\left. \frac{dB_{r,j}}{ds} \right|_{s=0} = \left. \frac{dB_{r,j}}{ds} \right|_{s=s_m} = 0$$

Varying ϑ we can write:

$$B_{r,j}(s) = A_{0,j} + \sum_{i=1}^N A_{i,j} \cos i \frac{\pi s}{s_m}$$

for every ϑ value.

In our computation N is equal 5 for all the angles.

The computed values of $A_{i,j}$ give a magnetic field in the range of experimental errors.

The coefficients get lower when index i arise and your behaviour is strongly sharp for lower angles.

We have represented with an high degree of accuracy the coefficients behaviour versus angles by two functions the first taking the sharp behaviour into account and the second the great angles behaviour.

The functions are reported below:

$$A_{i,j} = \exp(b_0 + b_1 \vartheta^2 + b_2 \vartheta^3 + b_3 \vartheta^4) - 20 \quad \text{for } \vartheta \leq \vartheta_0$$

$$A_{i,j} = \frac{A}{\vartheta} + \frac{B}{\vartheta^2} \quad \text{for } \vartheta > \vartheta_0$$

Where A and B are completely determinated by the junction conditions and where ϑ_0 is the junction angle.

We obtain, for each coil corner-edge, a 6 x 5 matrix, which raws are constituted by the four $A_{i,j}$ coefficients with $\vartheta \leq \vartheta_0$ and the fifth element is the junction angle.

Corner-edge 1(°)					
	b_0	b_1	b_2	b_3	θ_0
A ₀	1.1660	33.747	-72.032	41.631	40
A ₁	2.8599	4.6023	-9.7299	5.5434	40
A ₂	2.9102	1.2804	-2.0755	.91609	50
A ₃	2.8826	.79753	-1.0725	.39813	60
A ₄	2.9843	-1.0357	2.9100	-2.0023	30
A ₅	2.9842	-.42325	.11695	-.77607	30

Corner-edge 2					
	b_0	b_1	b_2	b_3	θ_0
A ₀	4.2507	.0	-64.882	142.21	16
A ₁	3.0370	19.477	-38.811	-20.644	18
A ₂	2.9026	14.781	-60.810	68.545	18
A ₃	2.9162	.97724	-1.5672	.68109	50
A ₄	2.9512	2.1311	-23.651	49.857	18
A ₅	2.9555	-.76093	1.9121	-.70984	20

Corner-edge 3					
	b_0	b_1	b_2	b_3	θ_0
A ₀	4.2514	.0	-126.16	310.47	16
A ₁	3.0497	6.9380	-22.315	15.449	18
A ₂	2.9056	5.9675	-21.255	20.511	20
A ₃	2.9333	.0	8.2799	-20.499	16
A ₄	2.9559	.0	4.8434	-11.271	16
A ₅	2.9596	2.0302	-7.1288	6.7337	20

Corner-edge 4					
	b_0	b_1	b_2	b_3	θ_0
A ₀	1.1613	92.706	-330.74	319.94	20
A ₁	2.8581	1.9272	-3.1459	1.4026	50
A ₂	2.9087	1.0035	-1.6593	.75309	50
A ₃	2.8810	1.1608	-1.9262	.87844	50
A ₄	2.9831	.87159	-3.0789	2.9249	20
A ₅	2.9831	.46941	-1.4200	1.1247	30

(°) See fig. 5

- TABLE II -

The four matrixes are reported in tab.II

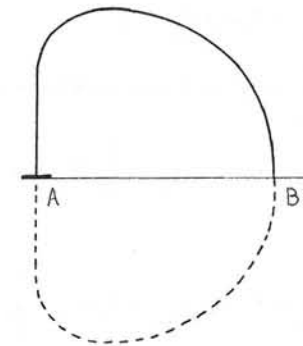
In tab.III is reported the magnetic field versus the linear development of winding both for the normal and collapsed conditions.

Sector Number	Sector Co-ordinates		Linear Development	Normal Field	Collap. Field
	X	Y			
0	6.16	.0	.0	3.96	4.20
1	6.16	1.11	1.11	4.01	4.28
2	6.16	2.22	2.22	4.15	4.42
3	6.21	3.29	3.30	4.13	4.44
4	6.52	4.20	4.27	3.94	4.25
5	7.55	5.42	5.86	3.45	3.77
6	9.05	6.14	7.54	3.04	3.31
7	9.19	6.18	7.69	3.03	3.29
8	10.51	6.26	9.02	2.89	3.15
9	12.73	5.45	11.37	2.81	3.04
10	14.20	4.16	13.36	2.66	2.89
11	15.10	2.73	15.07	2.61	2.84
12	15.63	.92	16.95	2.70	2.95
	Meters	Meters	Meters	Teslas	Teslas

- TABLE III -

5.1 - BENDING MOMENTS CALCULATION WHEN A COIL COLLAPSED [5]

We consider an half coil determined by the single simmetry axis, fig.6.

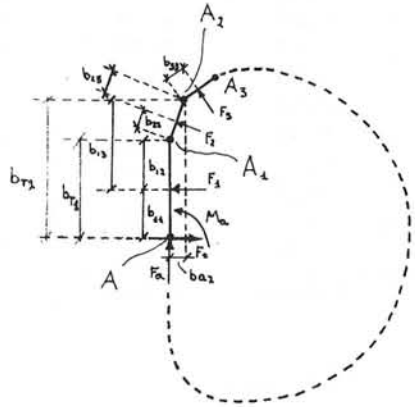


- FIG.6 -

Through the section A a force F_a and a bending moment M_a is transmitted. For symmetry reasons we think the half coil fitted in A and we can say that:

- 1) the section B cannot rotate
- 2) the section B displacement can be only along the symmetry axis.

With the above conditions we can compute F_a and M_a . We divide the half coil in segments fig.7



- FIG.7 -

We can write:

$$\vartheta_j = E_j J_j l_j M_j$$

If E_j and J_j are constant varying j the condition 1) can be written as:

$$\vartheta_{tot} = \sum_j^N l_j M_j = \sum_j^N \vartheta_j = 0 \quad (5.1)$$

where

$$M_j = M_a + F_a b_{a,j} + F_T b_{T,j} + \sum_i^j F_i b_{i,j} \quad (5.2)$$

$b_{i,j}$ is the force F_i -beam referred to the segment center.

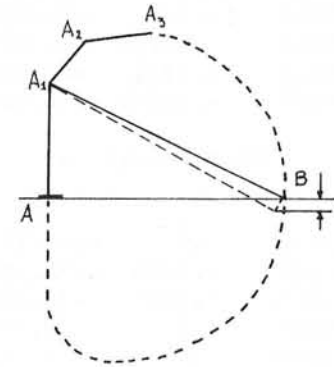
$b_{T,j}$ and $b_{a,j}$ are the F_T and F_a beams referred to the point in which the moment is calculated.

The force F_T in fig.6 is the half-strength reaction that opposes the displacement toward the inside. The F_T is computed adding the components along the symmetry axis of all, the F_i acting on the non constrained part of the half coil.

The (5.1) condition using the (5.2) becomes

$$M_a \sum_j^N l_j + F_a \sum_j^N b_{a,j} l_j + F_T \sum_j^N b_{T,j} l_j + \sum_j^N \sum_i^j F_i b_{i,j} l_j = 0 \quad (5.3)$$

In the fig.8 it is possible to observe that the generical displacement is computed from the segment $(A_j B)$ rotation.



- FIG.8 -

We can write:

$$\sum_j s_j = 0$$

from above we have

$$s_j = \overline{(A_j B)}_x \vartheta_j$$

Where $\overline{(A_j B)}_x$ is the geometrical projection on the symmetry axis of the segment $(A_j B)$ we can so obtain the second equation:

$$M_a \sum_{j=1}^N l_j \overline{(A,B)}_x + F_a \sum_{j=1}^N l_j b_{a,j} \overline{(A,B)}_x + F_T \sum_{j=1}^N l_j b_{Tj} \overline{(A,B)}_x + \sum_{j=1}^N \sum_{i=1}^j F_i b_{i,j} l_j \overline{(A,B)}_x = 0 \tag{5.4}$$

Where $F_i = B_i I_i l_i$, and B_i is the magnetic induction in the segment i ; l_i is the length of segment i ; I_i is the current on the segment i .

A variation to the above calculation to evaluate the bending moments behaviour when the coils have the straightrib supported.

In this case the moments on the supported rib are zero, because the constrain reaction balance the electromagnetic forces.

The support can give only oriented reactions, and we might evaluate as far from A the constrain supports the rib.

For this evaluation we make a constrain displacement along the support surface with F_T equal to the projection on the simmetry axis of electromagnetic forces and from section A to section B.

F_a and M_a can be calculated from(5.3). In the table V are reported the results for thecase with central rib support and in table VI the case with supported rib both in the collapse and in the normal conditions.

Sector Number	Normal Bending Moment	Collapsed Bending Moment
0	-43.7	-59.8
1	-35.6	-48.8
2	-23.8	-32.6
3	-9.3	-12.6
4	3.3	4.7
5	20.2	27.8
6	30.5	41.9
7	31.1	42.6
8	32.2	44.1
9	20.9	28.6
10	4.6	6.3
11	-12.8	-17.4
12	-33.8	-46.1
—	KTons x Meter	KTons x Meter

Note: positive moments are clockwise (fig. 7)

- TABLE V -

Sector Number	Normal Bending Moment	Collapsed Bending Moment
0	.0	.0
1	.0	.0
2	.7	1.0
3	4.5	6.0
4	7.4	9.9
5	10.3	13.7
6	10.7	14.2
7	10.6	14.1
8	8.7	11.5
9	1.6	2.2
10	-4.3	-5.5
11	-8.8	-11.3
12	-12.6	-16.0
—	KTons x Meter	KTons x Meter

Note: positive moments are clockwise (fig. 7)

- TABLE VI -

From table VI the support both in the collapse and in the normal case, is equally far from section A.

If we interpolate the results by the displaced support ones we obtain a difference of about 3 cm.

We foresee a better calculation with a shorter segments structure subdivision.

One can see that the bending moments in the normal conditions are not zero as it should be for a D-shaped coil.

This result is given to the causes below reported:

- 1) the zero bending moment shape is in the continuous toroidal solenoid hypothesis: in the radiate coils realization the bending moment arise;
- 2) the internal-external ratio influences the residual bending moment: in creases with the ratio;
- 3) in our realization the D-shaped is the internal coils perimeter;
- 4) in the calculation we have placed the currents in the windings center, displaced of .5 m from the D-shape;
- 5) our calculation consider the coil divided in linear segments instead of a continuous curve;

6) we consider that magnetic field should be evaluate in the winding center by a linear interpolation of the four corner-edges values.

The bending moment that arise in the normal action one think to be of the acceptable magnitude for the above reasons.

We think correct the problem resolution. In these conditions because of the stresses increase in the case of one coil collapse, is mainly due to the overcurrent than to a change of the magnetic field shape as it should be if the bending moment should be zero in normal excitation.

We intend to develop a computer program to evaluatate the bending moments considering the current distribution in the space.

6. - CONCLUSIONS

To evaluate the bending strains in a s.c. Tokamak with the D-shaped coil we have resolved some problems.

We have evaluate the mutual inductances to compute the overcurrents in the collapse case.

We have preferred a measurements serie on the model because of the complex coils shape, instead of the resolution by a computer calculation.

The computer evaluation needs a program optimization that requires more time than the model realization and the measurements execution.

With the overcurrent we have evaluated the collapsed magnetic field.

Even in this case the experimental relieves have been preferred with a great loss of time.

In the future this procedure is not advisable because of the availability of very good programs for the magnetic field calculation. Our attention have been pointed to the bending moments evaluation.

We have carried out a computer program for the bending moments evaluation in the complex structure proposed.

The program input is the magnetic field and the currents distribution. We have carried out in a reasonable time the unknown moments distribution, but the procedure cannot easily iterate because a new model needs for the mutual inductances evaluation. We are working to replace the measurements on the model with a computer program.

Aknowledgments

We want to thank the candidate for degree Mr.F.Nesci for your accurate measurements and Mr.M.Tidei for your assistance in the drawing up the paper.

BIBLIOGRAPHY

- [1] E.BERTOLINI et al: Design of a minimum size toroidal D. experimental reactor (FINTOR) - International Atomic Energy Agency - Plasma Physics and Controlled Nuclear Fusion Research - Wien 1975
- [2] YANG.: A Magnetic Field Code for Handling General Current Carrying Conductors in Three Dimensions (MAFCO-W) - 4/'75 MT5 pp 203 - 208
- [3] J.FILE: The Princeton Fusion Power Plant s.c. Magnet System and Cost 4/'75 MT5 pp 281 - 289
- [4] BROSER et al: The Toroidal Magnetic Field Coils for the ASDEX Tokamak 4/'75 MT5 pp 332 - 336
- [5] POHLCHEN-HUGUET: Shape Field and Mechanical Analysis of the JET Toroidal Field coils - 4/'75 MT5 pp 325 - 331

MECHANICAL AND THERMAL STRESSES IN

DOUBLER DIPOLE MAGNETS

S.C. Snowdon

October 1975

Summary

An analytical solution for stresses has been found for a structural composite that models the Doubler dipole. Structural cylinders represent the material inside and outside of the excitation current which is represented by two cosine theta sheet current distributions. A pretensioned structural cylinder surrounds the aforementioned materials. Thermal stresses are represented only in so far as a uniform temperature differing from room temperature alters the stress-strain relation. Temperature gradients are not considered. The mechanical energy stored in the elastic field is calculated. Numerical results are given.

Thermo Elasticity

The effect of a temperature change in elasticity is obtained by considering the elastic energy density to have the form:¹

$$W = C_{ij} \epsilon_{ij} + \frac{1}{2} C_{ijkl} \epsilon_{ij} \epsilon_{kl} \quad (1)$$

where the summation convention for repeated indices is used. The stress tensor is related to the strain tensor using

$$\sigma_{ij} = \frac{\partial W}{\partial \epsilon_{ij}} = C_{ij} + C_{ijkl} \epsilon_{kl} \quad (2)$$

For homogeneous isotropic materials

$$C_{ij} = -k(3\lambda + 2\mu) \cdot \delta_{ij} \quad (3)$$

and

$$C_{ijkl} = \lambda \delta_{ij} \delta_{kl} + \mu (\delta_{ik} \delta_{jl} + \delta_{il} \delta_{jk}) \quad (4)$$

where k is the thermal expansion coefficient integrated from 4.2°K to room temperature, λ and μ are the Lamé constants which are related to the more familiar constants Y (Young's modulus) and ν (Poisson's ratio) as follows.

$$\lambda = \frac{\nu}{(1+\nu)(1-2\nu)} Y \quad , \quad \mu = \frac{1}{2(1+\nu)} Y \quad (5)$$

Under these restrictions Hooke's Law becomes

$$\sigma_{ij} = \frac{\nu}{(1+\nu)(1-2\nu)} Y \delta_{ij} \epsilon_{kk} + \frac{1}{1+\nu} Y \epsilon_{ij} - \frac{kY}{1-2\nu} \delta_{ij} \quad (6)$$

The condition of equilibrium is then

$$\frac{\partial \sigma_{ij}}{\partial x_j} + f_j = 0 \quad (7)$$

where f_j is the body force which in our case will be the Lorentz force $\vec{j} \times \vec{B}$. Finally, since some of the boundary conditions relate to the material displacement \vec{u} , one needs the connection between strain and displacement

$$\epsilon_{ij} = \frac{1}{2} \left(\frac{\partial u_i}{\partial x_j} + \frac{\partial u_j}{\partial x_i} \right) \quad (8)$$

For the problem at hand the body force is handled by a surface traction and, therefore, the equilibrium condition Eq. (7) may be satisfied identically through the use of the Airy stress function ϕ :

$$\sigma_{ij} = \delta_{ij} \nabla^2 \phi - \frac{\partial^2 \phi}{\partial x_i \partial x_j} \quad (9)$$

The equation satisfied by the Airy stress function is determined from the equations of compatibility which are imposed on strains since the six strains in Eq. (8) must be interrelated in order to be derivable from three displacements. If Hooke's Law, Eq. (6), is used the equations of compatibility for stresses may be found

$$\nabla^2 \sigma_{ij} + \frac{1}{1+\nu} \frac{\partial^2 \sigma_{kk}}{\partial x_i \partial x_j} = 0 \quad (10)$$

By introducing the approximation known as generalized plane strain² one reduces the problem to manageable proportions. In this approximation one neglects the shear strains connected with the longitudinal or axial direction but permits a free expansion characterized by a uniform strain. For the normal stresses Eq. (4) gives

$$\sigma_{11} = \lambda(\epsilon_{11} + \epsilon_{22} + \epsilon_{33}) + 2\mu\epsilon_{11} - k(3\lambda + 2\mu) \quad (11)$$

$$\sigma_{22} = \lambda(\epsilon_{11} + \epsilon_{22} + \epsilon_{33}) + 2\mu\epsilon_{22} - k(3\lambda + 2\mu) \quad (12)$$

$$\sigma_{33} = \lambda(\epsilon_{11} + \epsilon_{22} + \epsilon_{33}) + 2\mu\epsilon_{33} - k(3\lambda + 2\mu) \quad (13)$$

Suppose that the index 3 represents the longitudinal direction. Then, from Eqs. (5, 11, 12, 13) one has

$$\sigma_{33} = \nu(\sigma_{11} + \sigma_{22}) + Y\epsilon_{33} - kY \quad (14)$$

Since ϵ_{33} is considered constant in this approximation, Eq. (10) becomes

$$\nabla^2 \sigma_{ij} + \frac{\partial^2}{\partial x_i \partial x_j} (\sigma_{11} + \sigma_{22}) = 0 \quad (15)$$

or, using Eq. (9) this becomes

$$\delta_{ij} \nabla^4 \phi - \frac{\partial^2}{\partial x_i \partial x_j} \nabla^2 \phi + \frac{\partial^2}{\partial x_i \partial x_j} (2\nabla^2 \phi - \nabla^2 \phi) = 0 \quad (16)$$

Hence the Airy stress function satisfies the biharmonic equation

$$\nabla^4 \phi = 0 \quad (17)$$

Virial Theorem

One might expect that the boundary conditions which provide for continuity of displacement and discontinuity of normal and shear stresses according to known surface tractions would be sufficient to specify all the unknowns in solving Eq. (17).

However, in this plane strain approximation, information relative to the longitudinal ends is lost and must be supplied by some integral condition. For this problem it is sufficient to invoke the virial theorem which may be found as follows³. Let τ_{ij} be the Maxwell stress tensor for the magnetic field introduced by the current sheet. The body force f_j in Eq. (7) is then given by

$$f_j = \frac{\partial \tau_{ij}}{\partial x_i} \quad (18)$$

To form the virial multiply Eq. (7) by x_j and utilize Eq. (18). Thus, after integrating over a volume

$$\int x_j \frac{\partial}{\partial x_i} (\sigma_{ij} + \tau_{ij}) d^3x = 0 \quad (19)$$

Integrate by parts using

$$\frac{\partial}{\partial x_i} (x_j \beta_{ij}) = \delta_{ij} \beta_{ij} + x_j \frac{\partial \beta_{ij}}{\partial x_i} \quad (20)$$

to give

$$\int_S x_j (\sigma_{ij} + \tau_{ij}) dS_i - \int \delta_{ij} (\sigma_{ij} + \tau_{ij}) d^3x = 0 \quad (21)$$

Notice that the integrand in the volume integral is just the trace of the tensor. But the trace of the Maxwell stress tensor is the

negative of the energy density⁴. Hence

$$\int \delta_{ij} \tau_{ij} d^3x = -W_B, \tag{22}$$

the magnetic energy. Since, in the problem considered σ_{ij} is zero on the boundary but τ_{ij} exists on the iron shield, one has

$$\int \delta_{ij} \sigma_{ij} d^3x = \int_S x_j \tau_{ij} dS_i + W_B. \tag{23}$$

It should be noted that τ_{ij} is taken to be zero on the end walls. Hence one visualizes that the magnet structure has terminating ends. Equation (23) indicates that, since the right hand side is positive, a net tensile structure is required to contain magnetic forces in static equilibrium.

Pretensioned Band

A method of characterizing a pretensioned member may be found by utilizing the concept of rotational dislocation⁵ whereby discontinuity in rotational displacement is permitted. Thus $u_\theta(2\pi) - u_\theta(0)$ is given a preassigned value. This condition will be used in the outer band rather than the customary continuity of displacement.

Magnetic Field

Since a continuously distributed body force as given by the Lorentz force $J \times B$ is more difficult to handle in the equations of elasticity, the region of conduction current in the dipole will be approximated by two current sheets, one at the inner edge of the region and one at the outer edge of the region. Thus the model to be considered consists of two cylindrical current sheets each carrying an axial current density of

$$i = \begin{Bmatrix} i_0 \\ i_1 \end{Bmatrix} \cos\theta \text{ at } \begin{Bmatrix} r=b \\ r=c \end{Bmatrix}. \tag{24}$$

See Fig. 1 for geometrical details. From the current density as given and an iron shield located at $r = r_s$, one finds the following magnetic field components.

$$H_r = -2\pi \begin{Bmatrix} i_0(1+b^2r_s^{-2}) + i_1(1+c^2r_s^{-2}) \\ i_0(b^2r^{-2}+b^2r_s^{-2}) + i_1(1+c^2r_s^{-2}) \\ i_0(b^2r^{-2}+b^2r_s^{-2}) + i_1(c^2r^{-2}+c^2r_s^{-2}) \end{Bmatrix} \sin\theta, \tag{25}$$

$$H_\theta = -2\pi \begin{Bmatrix} i_0(1+b^2r_s^{-2}) + i_1(1+c^2r_s^{-2}) \\ i_0(-b^2r^{-2}+b^2r_s^{-2}) + i_1(1+c^2r_s^{-2}) \\ i_0(-b^2r^{-2}+b^2r_s^{-2}) + i_1(-c^2r^{-2}+c^2r_s^{-2}) \end{Bmatrix} \cos\theta. \tag{26}$$

where the top entry refers to $0 < r < b$, the middle entry to $b < r < c$ and the bottom entry to $c < r < r_s$. In order to calculate the forces one needs the average field at the current sheets.

$$\langle H_r \rangle_{Av} = -2\pi \begin{Bmatrix} i_0(1+b^2r_s^{-2}) + i_1(1+c^2r_s^{-2}) \\ i_0(b^2c^{-2}+b^2r_s^{-2}) + i_1(1+c^2r_s^{-2}) \end{Bmatrix} \sin\theta, \tag{27}$$

$$\langle H_\theta \rangle_{Av} = -2\pi \begin{Bmatrix} i_0b^2r_s^{-2} + i_1(1+c^2r_s^{-2}) \\ i_0(-b^2c^{-2}+b^2r_s^{-2}) + i_1c^2r_s^{-2} \end{Bmatrix} \cos\theta. \tag{28}$$

Lorentz Force on Current Sheets

The force on a current sheet is given by

$$d\vec{F} = ids \hat{k} \times (\vec{i}_r \langle H_r \rangle_{Av} + \vec{i}_\theta \langle H_\theta \rangle_{Av}), \tag{29}$$

where i is given by Eq. (24) and

$$ds = \begin{Bmatrix} b \\ c \end{Bmatrix} d\theta . \tag{30}$$

If \vec{f} denotes the force per unit area on the current sheet, then

$$f_r = \pi \begin{Bmatrix} i_0^2 b^2 r_s^{-2} + i_0 i_1 (1+c^2 r_s^{-2}) \\ i_0 i_1 (-b^2 c^{-2} + b^2 r_s^{-2}) + i_1^2 c^2 r_s^{-2} \end{Bmatrix} (1+\cos 2\theta) , \tag{31}$$

$$f_\theta = -\pi \begin{Bmatrix} i_0^2 (1+b^2 r_s^{-2}) + i_0 i_1 (1+c^2 r_s^{-2}) \\ i_0 i_1 (b^2 c^{-2} + b^2 r_s^{-2}) + i_1^2 (1+c^2 r_s^{-2}) \end{Bmatrix} \sin 2\theta \tag{32}$$

Maxwell Stress Tensor

The Maxwell stress tensor is found by noting that the Lorentz force may be written as the divergence of a tensor. Thus

$$\vec{J} \times \vec{B} = \nabla \cdot \vec{\tau} , \tag{33}$$

where, in cartesian components⁴

$$\vec{\tau} = \frac{1}{4\pi} \begin{pmatrix} B_x^2 - \frac{1}{2}B^2 & B_x B_y & B_x B_z \\ B_x B_y & B_y^2 - \frac{1}{2}B^2 & B_y B_z \\ B_x B_z & B_y B_z & B_z^2 - \frac{1}{2}B^2 \end{pmatrix} . \tag{34}$$

From this it may be seen that the trace of the Maxwell stress tensor is

$$\text{tr } \vec{\tau} = -\frac{1}{8\pi} B^2 , \tag{35}$$

the negative of the energy density.

Application to Doubler Dipole Magnet

Since generalized plane strain is characterized by

$$\epsilon_{rz} = \epsilon_{\theta z} = 0 , \quad \epsilon_{zz} = \text{constant} , \tag{36}$$

the corresponding stress in Eq. (6) becomes

$$\sigma_{rr} = (\lambda+2\mu)\epsilon_{rr} + \lambda\epsilon_{\theta\theta} + \lambda\epsilon_{zz} - k(3\lambda+2\mu) \tag{37}$$

$$\sigma_{\theta\theta} = \lambda\epsilon_{rr} + (\lambda+2\mu)\epsilon_{\theta\theta} + \lambda\epsilon_{zz} - k(3\lambda+2\mu) \tag{38}$$

$$\sigma_{zz} = \lambda\epsilon_{rr} + \lambda\epsilon_{\theta\theta} + (\lambda+2\mu)\epsilon_{zz} - k(3\lambda+2\mu) . \tag{39}$$

$$\sigma_{r\theta} = 2\mu\epsilon_{r\theta} . \tag{40}$$

Inversion gives

$$\epsilon_{rr} = \frac{1}{2\mu(3\lambda+2\mu)} \cdot [2(\lambda+\mu)\sigma_{rr} - \lambda(\sigma_{\theta\theta} + \sigma_{zz})] + k \tag{41}$$

$$\epsilon_{\theta\theta} = \frac{1}{2\mu(3\lambda+2\mu)} \cdot [2(\lambda+\mu)\sigma_{\theta\theta} - \lambda(\sigma_{rr} + \sigma_{zz})] + k \tag{42}$$

$$\epsilon_{zz} = \frac{1}{2\mu(3\lambda+2\mu)} \cdot [2(\lambda+\mu)\sigma_{zz} - \lambda(\sigma_{rr} + \sigma_{\theta\theta})] + k \tag{43}$$

$$\epsilon_{r\theta} = \frac{1}{2\mu}\sigma_{r\theta} . \tag{44}$$

Utilizing Eq. (5) one has

$$\epsilon_{rr} = \frac{1}{Y} [\sigma_{rr} - \nu\sigma_{\theta\theta} - \nu\sigma_{zz}] + k \tag{45}$$

$$\epsilon_{\theta\theta} = \frac{1}{Y} [-\nu\sigma_{rr} + \sigma_{\theta\theta} - \nu\sigma_{zz}] + k \tag{46}$$

$$\epsilon_{zz} = \frac{1}{Y} [-\nu\sigma_{rr} - \nu\sigma_{\theta\theta} + \sigma_{zz}] + k \tag{47}$$

$$\epsilon_{r\theta} = \frac{1+\nu}{Y}\sigma_{r\theta} . \tag{48}$$

Since ϵ_{zz} is taken to be constant in this approximation, Eq. (47) may be used to eliminate σ_{zz} . Thus

$$\epsilon_{rr} = \frac{1+\nu}{Y} \cdot [(1-\nu)\sigma_{rr} - \nu\sigma_{\theta\theta}] - \nu\epsilon_{zz} + (1+\nu)k \tag{49}$$

$$\epsilon_{\theta\theta} = \frac{1+\nu}{Y} [-\nu\sigma_{rr} + (1-\nu)\sigma_{\theta\theta}] - \nu\epsilon_{zz} + (1+\nu)k . \tag{50}$$

The relation between the stresses and the Airy stress function, Eq. (9), becomes in cylindrical coordinates

$$\sigma_{rr} = \frac{1}{r} \frac{\partial \phi}{\partial r} + \frac{1}{r^2} \frac{\partial^2 \phi}{\partial \theta^2} \quad (51)$$

$$\sigma_{\theta\theta} = \frac{\partial^2 \phi}{\partial r^2} \quad (52)$$

$$\sigma_{r\theta} = -\frac{\partial}{\partial r} \left(\frac{1}{r} \frac{\partial \phi}{\partial \theta} \right) \quad (53)$$

For the problem under consideration one may take in each annular region functions of the form

$$\phi = A \ln r + G r^2 \ln r + B r^2 + (C r^2 + D r^4 + E r^{-2} + F) \cos 2\theta \quad (54)$$

The constant G is related to a multivalued azimuthal displacement and is set equal to zero except in the outer band where it is used to characterize pretension.

Stresses, Strains and Displacements

One finds that Eqs. (52-55) gives

$$\sigma_{rr} = \left\{ \begin{array}{l} A_1 r^{-2} + 2B_1 - (2C_1 + 6E_1 r^{-4} + 4F_1 r^{-2}) \cos 2\theta \\ A_2 r^{-2} + 2B_2 - (2C_2 + 6E_2 r^{-4} + 4F_2 r^{-2}) \cos 2\theta \\ A_3 r^{-2} + 2G_3 \ln r + G_3 + 2B_3 - (2C_3 + 6E_3 r^{-4} + 4F_3 r^{-2}) \cos 2\theta \end{array} \right\} \quad (55)$$

$$\sigma_{\theta\theta} = \left\{ \begin{array}{l} -A_1 r^2 + 2B_1 + (2C_1 + 12D_1 r^2 + 6E_1 r^{-4}) \cos 2\theta \\ -A_2 r^2 + 2B_2 + (2C_2 + 12D_2 r^2 + 6E_2 r^{-4}) \cos 2\theta \\ -A_3 r^2 + 2G_3 \ln r + 3G_3 + 2B_3 + (2C_3 + 12D_3 r^2 + 6E_3 r^{-4}) \cos 2\theta \end{array} \right\} \quad (56)$$

$$\sigma_{r\theta} = \left\{ \begin{array}{l} (2C_1 + 6D_1 r^2 - 6E_1 r^{-4} - 2F_1 r^{-2}) \sin 2\theta \\ (2C_2 + 6D_2 r^2 - 6E_2 r^{-4} - 2F_2 r^{-2}) \sin 2\theta \\ (2C_3 + 6D_3 r^2 - 6E_3 r^{-4} - 2F_3 r^{-2}) \sin 2\theta \end{array} \right\}, \quad (57)$$

where the top entry is the bore tube region $a < r < b$; the middle entry is the region of conductors $b < r < c$; and the last entry represents the pretensioned band $c < r < d$.

Substituting Eqs. (55-57) into Eqs. (48-50) gives for the strains

$$\frac{\nu}{1+\nu} [\epsilon_{rr} + \nu \epsilon_{zz} - (1+\nu)k] = \left\{ \begin{array}{l} A_1 r^{-2} + 2(1-2\nu_1)B_1 \\ -[2C_1 + 12\nu_1 D_1 r^2 + 6E_1 r^{-4} + 4(1-\nu_1)F_1 r^{-2}] \cos 2\theta \\ A_2 r^{-2} + 2(1-2\nu_2)B_2 \\ -[2C_2 + 12\nu_2 D_2 r^2 + 6E_2 r^{-4} + 4(1-\nu_2)F_2 r^{-2}] \cos 2\theta \\ A_3 r^{-2} + 2(1-2\nu_3)G_3 \ln r + (1-4\nu_3)G_3 + 2(1-2\nu_3)B_3 \\ -[2C_3 + 12\nu_3 D_3 r^2 + 6E_3 r^{-4} + 4(1-\nu_3)F_3 r^{-2}] \cos 2\theta \end{array} \right\} \quad (58)$$

$$\frac{\nu}{1+\nu} [\epsilon_{\theta\theta} + \nu \epsilon_{zz} - (1+\nu)k] = \left\{ \begin{array}{l} -A_1 r^{-2} + 2(1-2\nu_1)B_1 \\ + [2C_1 + 12(1-\nu_1)D_1 r^2 + 6E_1 r^{-4} + 4\nu_1 F_1 r^{-2}] \cos 2\theta \\ -A_2 r^{-2} + 2(1-2\nu_2)B_2 \\ + [2C_2 + 12(1-\nu_2)D_2 r^2 + 6E_2 r^{-4} + 4\nu_2 F_2 r^{-2}] \cos 2\theta \\ -A_3 r^{-2} + 2(1-2\nu_3)G_3 \ln r + (3-4\nu_3)G_3 + 2(1-2\nu_3)B_3 \\ + [2C_3 + 12(1-\nu_3)D_3 r^2 + 6E_3 r^{-4} + 4\nu_3 F_3 r^{-2}] \cos 2\theta \end{array} \right\} \quad (59)$$

$$\frac{\nu}{1+\nu} \epsilon_{r\theta} = \left\{ \begin{array}{l} (2C_1 + 6D_1 r^2 - 6E_1 r^{-4} - 2F_1 r^{-2}) \sin 2\theta \\ (2C_2 + 6D_2 r^2 - 6E_2 r^{-4} - 2F_2 r^{-2}) \sin 2\theta \\ (2C_3 + 6D_3 r^2 - 6E_3 r^{-4} - 2F_3 r^{-2}) \sin 2\theta \end{array} \right\} \quad (60)$$

The relation between strain and displacement given in Eq. (8) expressed in cylindrical coordinates becomes

$$\epsilon_{rr} = \frac{\partial u_r}{\partial r} \tag{61}$$

$$\epsilon_{\theta\theta} = \frac{u_r}{r} + \frac{1}{r} \frac{\partial u_\theta}{\partial \theta} \tag{62}$$

$$\epsilon_{r\theta} = \frac{1}{2} \left(\frac{\partial u_\theta}{\partial r} - \frac{u_\theta}{r} + \frac{1}{r} \frac{\partial u_r}{\partial \theta} \right) . \tag{63}$$

Utilizing Eqs. (58-60) one finds by partial integration

$$\frac{Y}{1+\nu} [u_r + \nu \epsilon_{zz} r - (1+\nu)kr] = \left\{ \begin{array}{l} -A_1 r^{-1} \qquad \qquad \qquad +2(1-2\nu_1)B_1 r \\ -[2C_1 r + 4\nu_1 D_1 r^3 - 2E_1 r^{-3} - 4(1-\nu_1)F_1 r^{-1}] \cos 2\theta \\ -A_2 r^{-1} \qquad \qquad \qquad +2(1-2\nu_2)B_2 r \\ -[2C_2 r + 4\nu_2 D_2 r^3 - 2E_2 r^{-3} - 4(1-\nu_2)F_2 r^{-1}] \cos 2\theta \\ -A_3 r^{-1} + 2(1-2\nu_3)G_3 r + (1-4\nu_3)G_3 r + 2(1-2\nu_3)B_3 r \\ -[2C_3 r + 4\nu_3 D_3 r^3 - 2E_3 r^{-3} - 4(1-\nu_3)F_3 r^{-1}] \cos 2\theta \end{array} \right\} \tag{64}$$

$$\frac{Y}{1+\nu} \cdot u_\theta = \left\{ \begin{array}{l} 2[C_1 r + (3-2\nu_1)D_1 r^3 + E_1 r^{-3} - (1-2\nu_1)F_1 r^{-1}] \sin 2\theta \\ 2[C_2 r + (3-2\nu_2)D_2 r^3 + E_2 r^{-3} - (1-2\nu_2)F_2 r^{-1}] \sin 2\theta \\ 4(1-\nu_3)G_3 r + 2[C_3 r + (3-2\nu_3)D_3 r^3 + E_3 r^{-3} - (1-2\nu_3)F_3 r^{-1}] \sin 2\theta \end{array} \right\} \tag{65}$$

$$u_z = \epsilon_{zz} z . \tag{66}$$

The unknown functions in the partial integration are set to zero in order not to introduce rigid body rotations.

Boundary Conditions

At $r=a$ no traction is transmitted. Hence

$$\sigma_{rr} = \sigma_{r\theta} = 0 , \tag{67}$$

or

$$A_1 a^{-2} + 2B_1 = 0 \tag{68}$$

$$2C_1 + 6E_1 a^{-4} + 4F_1 a^{-2} = 0 \tag{69}$$

$$2C_1 + 6D_1 a^2 - 6E_1 a^{-4} - 2F_1 a^{-2} = 0 . \tag{70}$$

At $r=b$ the equilibrium condition is

$$\sigma_{rr}^{(+)} - \sigma_{rr}^{(-)} + f_r = 0 , \tag{71}$$

and

$$\sigma_{r\theta}^{(+)} - \sigma_{r\theta}^{(-)} + f_\theta = 0 , \tag{72}$$

where f_r and f_θ are given by Eqs. (31-32). Thus

$$(A_2 - A_1)b^{-2} + 2(B_2 - B_1) = -\pi i_0 [i_0 b^2 r_s^{-2} + i_1 (1+c^2 r_s^{-2})] \tag{73}$$

$$-2(C_2 - C_1) - 6(E_2 - E_1)b^{-4} - 4(F_2 - F_1)b^{-2} = -\pi i_0 [i_0 b^2 r_s^{-2} + i_1 (1+c^2 r_s^{-2})] \tag{74}$$

$$2(C_2 - C_1) + 6(D_2 - D_1)b^2 - 6(E_2 - E_1)b^{-4} - 2(F_2 - F_1)b^{-2} = \pi i_0 [i_0 (1+b^2 r_s^{-2}) + i_1 (1+c^3 r_s^{-2})] \tag{75}$$

Also at $r=b$ the displacements are continuous.

$$u_r^{(+)} - u_r^{(-)} = u_\theta^{(+)} - u_\theta^{(-)} = 0 . \tag{76}$$

From Eqs. (64-65) one obtains

$$\frac{1+\nu_2}{Y_2} [-A_2 b^{-1} + 2(1-2\nu_2)B_2 b] - \frac{1+\nu_1}{Y_1} [-A_1 b^{-1} + 2(1-2\nu_1)B_1 b]$$

$$-(v_2-v_1)\epsilon_{zz}b = -(1+v_2)k_2b+(1+v_1)k_1b \quad (77)$$

$$\frac{1+v_2}{Y_2}[-2C_2b-4v_2D_2b^3+2E_2b^{-3}+4(1-v_2)F_2b^{-1}] - \frac{1+v_1}{Y_1}[-2C_1b-4v_1D_1b^3+2E_1b^{-3}+4(1-v_1)F_1b^{-1}] = 0 \quad (78)$$

$$\frac{1+v_2}{Y_2}[2C_2b+2(3-2v_2)D_2b^3+2E_2b^{-3}-2(1-2v_2)F_2b^{-1}] - \frac{1+v_1}{Y_1}[2C_1b+2(3-2v_1)D_1b^3+2E_1b^{-3}-2(1-2v_1)F_1b^{-1}] = 0 \quad (79)$$

At $r=c$ the equilibrium condition is

$$\sigma_{rr}^{(+)} - \sigma_{rr}^{(-)} + f_r = 0, \quad \sigma_{r\theta}^{(+)} - \sigma_{r\theta}^{(-)} + f_\theta = 0 \quad (80)$$

Hence, using Eqs. (55) and (57)

$$(A_3-A_2)c^{-2} + (2\ell nc+1)G_3+2(B_3-B_2) = -\pi i_1[i_0(-b^2c^{-2}+b^2r_s^{-2})+i_1c^2r_s^{-2}] \quad (81)$$

$$-2(C_3-C_2) - 6(E_3-E_2)c^{-4} - 4(F_3-F_2)c^{-2} = -\pi i_1[i_0(-b^2c^{-2}+b^2r_s^{-2})+i_1c^2r_s^{-2}] \quad (82)$$

$$2(C_3-C_2) + 6(D_3-D_2)c^2 - 6(E_3-E_2)c^{-4} - 2(F_3-F_2)c^{-2} = \pi i_1[i_0(b^2c^{-2}+b^2r_s^{-2})+i_1(1+c^2r_s^{-2})] \quad (83)$$

At $r=c$ u_r is continuous or

$$u_r^{(+)} - u_r^{(-)} = 0 \quad (84)$$

The pretension condition in the band is formulated by utilizing

the notion of rotational dislocation⁵ whereby a small angle α is removed from the band. Subsequently this angle is closed up and held by welding, slippage between the band and region 2 being permitted. Thus, for region 3 and $r=c$

$$u_\theta(2\pi) - u_\theta(0) = c\alpha \quad (85)$$

After removal of the term responsible for pretensioning, subsequent slippage is not allowed and then for $r=c$

$$u_\theta^{(+)} \text{ minus term prop. to } \theta = u_\theta^{(-)} \quad (86)$$

The conditions of Eqs. (84-86) yield

$$\frac{1+v_3}{Y_3}[-A_3c^{-1}+2(1-2v_3)G_3c(\ell nc-1)+(1-4v_3)G_3c+2(1-2v_3)B_3c] - \frac{1+v_2}{Y_2}[-A_2c^{-1}+2(1-2v_2)B_2c] - (v_3-v_2)\epsilon_{zz}c = -(1+v_3)k_3c+(1+v_2)k_2c \quad (87)$$

$$\frac{1+v_3}{Y_3}[-2C_3c-4v_3D_3c^3+2E_3c^{-3}+4(1-v_3)F_3c^{-1}] - \frac{1+v_2}{Y_2}[-2C_2c-4v_2D_2c^3+2E_2c^{-3}+4(1-v_2)F_2c^{-1}] = 0 \quad (88)$$

$$4\frac{(1-v_3^2)}{Y_3}G_3c2\pi = c\alpha \quad (89)$$

$$\frac{1+v_3}{Y_3}[C_3c+(3-2v_3)D_3c^3+E_3c^{-3}-(1-2v_3)F_3c^{-1}] - \frac{1+v_2}{Y_2}[C_2c+(3-2v_2)D_2c^3+E_2c^{-3}-(1-2v_2)F_2c^{-1}] = 0 \quad (90)$$

At $r=d$ no traction is transmitted. Hence

$$\sigma_{rr} = \sigma_{r\theta} = 0 \tag{91}$$

or

$$A_3 d^{-2} + (2\ell nd + 1)G_3 = 0 \tag{92}$$

$$-2C_3 - 6E_3 d^{-4} - 4F_3 d^{-2} = 0 \tag{93}$$

$$2C_3 + 6D_3 d^2 - 6E_3 d^{-4} - 2F_3 d^{-2} = 0 . \tag{94}$$

Note that Eqs. (68-70, 73-75, 77-79, 81-83, 87-90, 92-94) provide 19 conditions among the 20 variables $A_1 B_1 C_1 D_1 E_1 F_1$

$A_2 B_2 C_2 D_2 E_2 F_2 A_3 G_3 B_3 C_3 D_3 E_3 F_3 \epsilon_{zz}$.

Use of Virial Theorem

The virial theorem in Eq. (23) may be expressed as

$$\int_V \text{tr} \vec{\sigma} dV = \int_S \vec{r} \cdot \vec{\tau} \cdot \vec{n} dS + W_B . \tag{95}$$

But the traction on the surface is⁶

$$\vec{\tau} \cdot \vec{n} = \frac{1}{4\pi} [\vec{H}(\vec{H} \cdot \vec{n}) - \frac{1}{2} H^2 \vec{n}] . \tag{96}$$

It is assumed that the magnet is of finite length and that the end surfaces used to specify S are sufficiently far removed so that no fields are present. On the cylindrical iron surface $r=r_s$

$$\vec{r} \cdot \vec{\tau} \cdot \vec{n} = \frac{1}{8\pi} (H_r^2 - H_\theta^2) r_s . \tag{97}$$

Using Eq. (25-26) for the fields

$$\int_S \vec{r} \cdot \vec{\tau} \cdot \vec{n} dS = \frac{2\ell\pi^2}{r_s^2} (i_0 b^2 + i_1 c^2)^2 . \tag{98}$$

The magnetic energy is given by Eqs. (25-26) and (35)

$$W_B = \ell\pi^2 [i_0^2 b^2 + 2i_0 i_1 b^2 + i_1^2 c^2 + (i_0 b^2 + i_1 c^2)^2 r_s^{-2}] , \tag{99}$$

which, together with Eq. (98), gives

$$\int_V \text{tr} \vec{\sigma} dV = \ell\pi^2 [i_0^2 b^2 + 2i_0 i_1 b^2 + i_1^2 c^2 + 3(i_0 b^2 + i_1 c^2)^2 r_s^{-2}] . \tag{100}$$

Then, using Eq. (14) to eliminate σ_{zz} one has after cancelling the effective length ℓ

$$\iint [(1+\nu)(\sigma_{rr} + \sigma_{\theta\theta}) + Y(\epsilon_{zz} - k)] r dr d\theta = \pi^2 [i_0^2 b^2 + 2i_0 i_1 b^2 + i_1^2 c^2 + 3(i_0 b^2 + i_1 c^2)^2 r_s^{-2}] . \tag{101}$$

Using Eqs. (55-56) this gives the condition

$$\begin{aligned} & 4\pi(1+\nu_1)(b^2 - a^2)B_1 + 4\pi(1+\nu_2)(c^2 - b^2)B_2 \\ & + 2\pi(1+\nu_3)[d^2(2\ell nd + 1) + c^2(2\ell nc + 1)]G_3 + 4\pi(1+\nu_3)(d^2 - c^2)B_3 \\ & + \pi[Y_1(b^2 - a^2) + Y_2(c^2 - b^2) + Y_3(d^2 - c^2)]\epsilon_{zz} \\ & = \pi[k_1 Y_1(b^2 - a^2) + k_2 Y_2(c^2 - b^2) + k_3 Y_3(d^2 - c^2)] \\ & + \pi^2 [i_0^2 b^2 + 2i_0 i_1 b^2 + i_1^2 c^2 + 3(i_0 b^2 + i_1 c^2)^2 r_s^{-2}] , \end{aligned} \tag{102}$$

which provides the last condition necessary for determining all of the unknowns. The current densities i_0 and i_1 can be chosen in many ways. The following choice comes from equating respectively the current and radial moment of the current in the two sheet dipoles to the same quantities in the thick cosine theta dipole and expressing the result in terms of the central magnetic field H_0 . Thus Eq. (24) becomes

$$i = \left\{ \begin{matrix} cb^{-1+2} \\ bc^{-1+2} \end{matrix} \right\} \cdot \frac{H_0 \cos\theta}{12\pi [1 + \frac{1}{3}(b^2 + bc + c^2)r_s^{-2}]} . \tag{103}$$

Internal Energy

The expression for the internal energy in Eq. (1) may be obtained using the strains in cylindrical coordinates by partially integrating Eq. (2) using Eqs. (37 - 40). Thus

$$W = \frac{1}{2}(\lambda+2\mu)(\epsilon_{rr}^2 + \epsilon_{\theta\theta}^2 + \epsilon_{zz}^2) + \lambda(\epsilon_{rr}\epsilon_{\theta\theta} + \epsilon_{\theta\theta}\epsilon_{zz} + \epsilon_{zz}\epsilon_{rr}) + \mu\epsilon_{r\theta}^2 - k(3\lambda+2\mu)(\epsilon_{rr} + \epsilon_{\theta\theta} + \epsilon_{zz}) \quad (104)$$

After rearrangement and use of Eqs. (37-40), the strain energy may be written in terms of stresses and strains:

$$W = \frac{1}{2} \left\{ [\sigma_{rr} - k(3\lambda+2\mu)]\epsilon_{rr} + [\sigma_{\theta\theta} - k(3\lambda+2\mu)]\epsilon_{\theta\theta} + [\sigma_{zz} - k(3\lambda+2\mu)]\epsilon_{zz} + \sigma_{r\theta}\epsilon_{r\theta} \right\} \quad (105)$$

Stress Distribution in Iron Shield

In the region of the iron shield between $r=r_s$ and $r=R_s$ the Airy stress function may be taken as

$$\phi = A\ln r + Br^2 + (Cr^2 + Dr^4 + Er^{-2} + F) \cos 2\theta \quad (106)$$

Equations (51-54) then give

$$\sigma_{rr} = Ar^{-2} + 2B - (2C + 6Er^{-4} + 4Fr^{-2}) \cos 2\theta \quad (107)$$

$$\sigma_{\theta\theta} = -Ar^{-2} + 2B + (2C + 12Dr^2 + 6Er^{-4}) \cos 2\theta \quad (108)$$

$$\sigma_{r\theta} = (2C + 6Dr^2 - 6Er^{-4} - 2Fr^{-2}) \sin 2\theta \quad (109)$$

The boundary conditions at $r=r_s$ are $(\sigma_{rr}^{(-)} = \tau_{rr}^{(+)} = 0)$

$$\sigma_{rr}^{(+)} - \tau_{rr}^{(-)} = 0 \quad (110)$$

$$\sigma_{r\theta}^{(+)} = 0 \quad (111)$$

where, from Eqs. (96) and (25)

$$\tau_{rr}^{(-)} = \frac{1}{8\pi} H_r^2 = \pi(i_0 b^2 + i_1 c^2)^2 r_s^{-4} (1 - \cos 2\theta) \quad (112)$$

Hence

$$Ar_s^{-2} + 2B = -\pi(i_0 b^2 + i_1 c^2)^2 r_s^{-4} \quad (113)$$

$$-2C - 6Er_s^{-4} - 4Fr_s^{-2} = \pi(i_0 b^2 + i_1 c^2)^2 r_s^{-4} \quad (114)$$

$$2C + 6Dr_s^2 - 6Er_s^{-4} - 2Fr_s^{-2} = 0 \quad (115)$$

At $r=R_s$ the boundary conditions are

$$\sigma_{rr} = \sigma_{r\theta} = 0 \quad (116)$$

Hence

$$AR_s^{-2} + 2B = 0 \quad (117)$$

$$2C + 6Er_s^{-4} + 4Fr_s^{-2} = 0 \quad (118)$$

$$2C + 6Dr_s^2 - 6Er_s^{-4} - 2Fr_s^{-2} = 0 \quad (119)$$

Note that Eqs. (113-115, 117-119) provide six equations for determining the six unknowns (A-F).

As in the previous problem the generalized plane strain approximation will be used. Since this introduces one more unknown, the longitudinal strain, the virial theorem will be used to provide the last condition. Thus using Eq. (95) and (97) with an inwardly directed normal gives

$$\iint (\sigma_{rr} + \sigma_{\theta\theta} + \sigma_{zz}) r dr d\theta = -2\pi^2 (i_0 b^2 + i_1 c^2)^2 r_s^{-2} \quad (120)$$

Equation (47) may be used to eliminate σ_{zz} . In this case since the iron shield remains at room temperature $k=0$. Thus

$$\iint [(1+\nu)(\sigma_{rr} + \sigma_{\theta\theta}) + Y\epsilon_{zz}] r dr d\theta = - 2\pi^2 (i_0 b^2 + i_1 c^2)^2 r_s^{-2} . \quad (121)$$

Integrating after using Eqs. (107-108) for the stresses gives

$$\pi (R_s^2 - r_s^2) [4(1+\nu)B + Y\epsilon_{zz}] = - 2\pi^2 (i_0 b^2 + i_1 c^2)^2 r_s^{-2} . \quad (122)$$

Thus the longitudinal strain is determined.

Numerical Calculations

The stresses and strains that exist in the three nested hollow cylinders have been calculated as a function of the central magnetic field. Twenty algebraic relations in Eqs. (68, 69, 70, 73, 74, 75, 77, 78, 79, 81, 82, 83, 87, 88, 89, 90, 92, 93, 94, 102) among the nineteen coefficients in the Airy stress functions ($A_1, B_1, C_1, D_1, E_1, F_1, A_2, B_2, C_2, D_2, E_2, F_2, A_3, B_3, C_3, D_3, E_3, F_3$) and the longitudinal strain ϵ_{zz} have been solved. Thus the stress and strain of any point in the dipole model structure may be found. For simplicity in the presentation of numerical results, however, only the values on the median plane are given. It is usually clear whether a quantity is stress or strain. Otherwise, R is radial, T is theta or azimuthal, Z is axial or longitudinal. With regard to position A, B, C, D are the points on the median plane at the cylindrical boundaries between the various media. To indicate the side of the point, P is used for positive and M for negative. Thus, for example, RTBP indicates the (r, θ) component at the positive side of point B.

The boundary between elastic and plastic isotropic media is a function of the invariants of the tensor representing the deviation of stress from the mean stress. A generally accepted simplification

of this condition regards the onset of plastic flow as being determined only by the second invariant of this tensor⁶

$$J_2 = \frac{1}{6} [(\sigma_{rr} - \sigma_{\theta\theta})^2 + (\sigma_{\theta\theta} - \sigma_{zz})^2 + (\sigma_{zz} - \sigma_{rr})^2] + \sigma_{r\theta}^2 . \quad (123)$$

Since the condition may be stated as

$$3J_2 = Y_t^2 , \quad (124)$$

where Y_t is the yield stress in tension, the $\sqrt{3J_2}$ has been tabulated for ready comparison of the state of stress with the yield point. Note that for 45 kG the band stress slightly exceeds the elastic limit.

A comment relative to the appearance of negative elastic energies is in order. Equation (1) is actually an expression for the density of free energy $(u - T\eta)$ where u is the internal energy and η is the entropy density⁷. However, the term in $T\eta$ that depends only on the temperature has been dropped since it does not affect the state of stress. Hence, negative values of the free energy are caused by positive values of the entropy density.

For completeness the effect of the distortions caused by banding, cooldown, and magnetic excitation are indicated by their multipole contribution⁸ to an otherwise pure dipole field. At the reference radius let

$$\Delta B = \Delta B_1 + \Delta B_3 \quad (125)$$

where ΔB_1 is the change in the dipole component and ΔB_3 is the change in the sextupole component of the resulting field. Further,

let

$$\Delta B_1 = \Delta B_{1c} + \Delta B_{1s} \quad \Delta B_3 = \Delta B_{3c} + \Delta B_{3s} , \quad (126)$$

where the subscript c refers to the contribution due to the conductor alone and the subscript s refers to the contribution from the shield. Also let

$$R_1 = \frac{\Delta B_1}{B} \quad R_3 = \frac{\Delta B_3}{B} , \quad (127)$$

where B is the original magnetic field for zero mechanical displacement field. Thus, the output lists ΔB_{1c} , ΔB_{1s} , R_1 and ΔB_{3c} , ΔB_{3s} , R_3 for the displacement field that results from each state of strain.

No calculations have been made for the stresses in the iron since the inner iron surface field is modest.

References

1. R.W. Little, Elasticity, Prentice Hall, Inc., Englewood Cliffs, New Jersey, 1964, p. 78.
2. Chi-Teh Wang, Applied Elasticity, McGraw Hill Book Co., New York, 1953, p. 44. Note that the auxiliary condition does not apply in the presence of body forces.
3. G. Schmidt, Physics of Fluids 3, 481 (1960); see also C.L. Longmire, Elementary Plasma Physics, Interscience Publishers, New York, 1963, p. 68. Note that his sign convention regarding both the Maxwell stress tensor and the mechanical stress tensor is different from that normally used; see also C. Truesdell and R. Toupin, Classical Field Theories, Handb. der Physik III, Springer-Verlag, Berlin, 1960, pp. 586-577, who discuss the history of the virial theorem.
4. J.A. Stratton, Electromagnetic Theory, McGraw Hill Book Co., Inc., New York, 1940, p. 97.
5. R.W. Little, Elasticity, Prentice Hall Inc., New Jersey, 1944, p. 162. See also A.E.H. Love, A Treatise on the Mathematical Theory of Elasticity, Dover Publications Inc., New York, 1944, p. 221.
6. R. Hill, The Mathematical Theory of Plasticity, Clarendon Press, Oxford, p. 20 (1950).
7. B.A. Boley and J.H. Weiner, Theory of Thermal Stress, John Wiley and Sons, Inc., p. 27 and p. 269 (1960); See also, A.M. Freudenthal and H. Geiringer, The Inelastic Continuum, Handb. der Physik 6, p. 263 (1958).
8. S.C. Snowdon, Magnetic Multipoles Induced by Mechanical and Thermal Stresses in Doubler Dipole, TM-621.

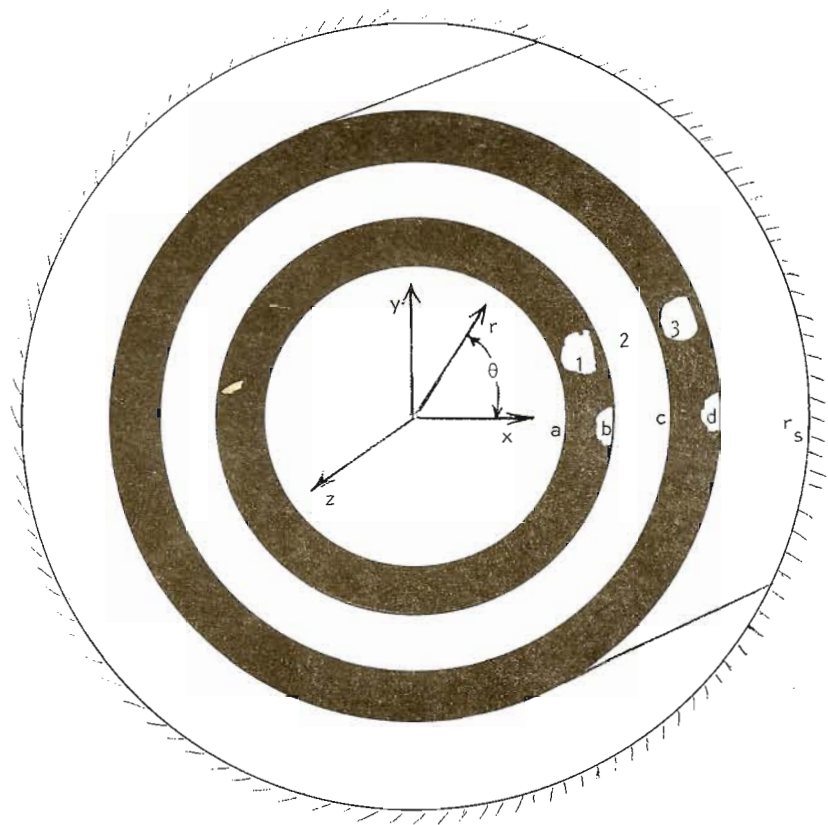
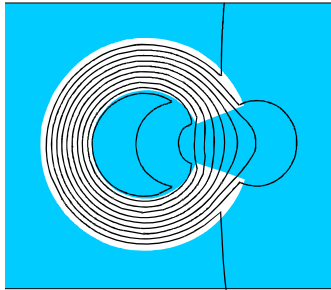


Fig. 1. Geometric Details of Doubler Dipole Model



International Compumag Society

Facsimile of the proceedings of the first Compumag Conference October 23, 2006